

Springer Series in Optical Sciences 219

Eugene Kamenetskii · Almas Sadreev  
Andrey Miroshnichenko *Editors*

# Fano Resonances in Optics and Microwaves

Physics and Applications

 Springer

# Springer Series in Optical Sciences

Volume 219

## **Founded by**

H. K. V. Lotsch

## **Editor-in-chief**

William T. Rhodes, Florida Atlantic University, Boca Raton, FL, USA

## **Series editors**

Ali Adibi, School of Electrical and Computer Engineering, Georgia Institute of Technology, Atlanta, GA, USA

Toshimitsu Asakura, Hokkai-Gakuen University, Sapporo, Hokkaido, Japan

Theodor W. Hänsch, Max-Planck-Institut für Quantenoptik, Garching, Bayern, Germany

Ferenc Krausz, Garching, Bayern, Germany

Barry R. Masters, Cambridge, MA, USA

Katsumi Midorikawa, Laser Technology Laboratory, RIKEN Advanced Science Institute, Saitama, Japan

Bo A. J. Monemar, Department of Physics and Measurement Technology, Linköping University, Linköping, Sweden

Herbert Venghaus, Ostseebad Binz, Germany

Horst Weber, Berlin, Germany

Harald Weinfurter, München, Germany

**Springer Series in Optical Sciences** is led by Editor-in-Chief William T. Rhodes, Georgia Institute of Technology, USA, and provides an expanding selection of research monographs in all major areas of optics:

- lasers and quantum optics
- ultrafast phenomena
- optical spectroscopy techniques
- optoelectronics
- information optics
- applied laser technology
- industrial applications and
- other topics of contemporary interest.

With this broad coverage of topics the series is useful to research scientists and engineers who need up-to-date reference books.

More information about this series at <http://www.springer.com/series/624>

Eugene Kamenetskii · Almas Sadreev  
Andrey Miroshnichenko  
Editors

# Fano Resonances in Optics and Microwaves

Physics and Applications

 Springer

*Editors*

Eugene Kamenetskii  
Department of Electrical and Computer  
Engineering  
Ben-Gurion University of the Negev  
Beersheba, Israel

Andrey Miroshnichenko  
School of Engineering and Information  
Technology  
University of New South Wales  
Canberra, ACT, Australia

Almas Sadreev  
Federal Research Center KSC SB RAS  
Kirensky Institute of Physics  
Krasnoyarsk, Russia

ISSN 0342-4111                      ISSN 1556-1534 (electronic)  
Springer Series in Optical Sciences  
ISBN 978-3-319-99730-8              ISBN 978-3-319-99731-5 (eBook)  
<https://doi.org/10.1007/978-3-319-99731-5>

Library of Congress Control Number: 2018953587

© Springer Nature Switzerland AG 2018

This work is subject to copyright. All rights are reserved by the Publisher, whether the whole or part of the material is concerned, specifically the rights of translation, reprinting, reuse of illustrations, recitation, broadcasting, reproduction on microfilms or in any other physical way, and transmission or information storage and retrieval, electronic adaptation, computer software, or by similar or dissimilar methodology now known or hereafter developed.

The use of general descriptive names, registered names, trademarks, service marks, etc. in this publication does not imply, even in the absence of a specific statement, that such names are exempt from the relevant protective laws and regulations and therefore free for general use.

The publisher, the authors and the editors are safe to assume that the advice and information in this book are believed to be true and accurate at the date of publication. Neither the publisher nor the authors or the editors give a warranty, express or implied, with respect to the material contained herein or for any errors or omissions that may have been made. The publisher remains neutral with regard to jurisdictional claims in published maps and institutional affiliations.

This Springer imprint is published by the registered company Springer Nature Switzerland AG  
The registered company address is: Gewerbestrasse 11, 6330 Cham, Switzerland

# Preface

Scattering of waves involves different phenomena, but the most common one is the interference. It has different manifestations, including constructive interference, corresponding to the field enhancement, and destructive interference, leading to the field suppression. One of the interesting phenomena is resonant scattering when coexistence of resonant transmission and resonant reflection can be reduced to the interference of discrete resonant states with a continuum of nonresonant propagation modes. It results in an asymmetric profile of the resonant lineshapes. These are known as Fano resonances. It turns out to be a common situation in any complex system describing wave propagation regardless of their nature, including classical and quantum mechanical systems. These effects are intimately related to the presence of quasibound states resonantly interacting with a continuum of scattering states. All this makes the Fano resonance a very generic phenomenon. The Fano resonances have been extensively studied in nanoparticles, plasmonic, dielectric, and magnonic structures, and metamaterials as well. With their unique physical properties and unusual combination of classical and quantum effects, Fano resonances have a huge application potential in a wide range of fields, from telecommunication to ultrasensitive biosensing, medical instrumentation, and data storage.

This book enables readers to acquire the multifaceted understanding required for these multidisciplinary challenges. The book has 23 chapters in total covering various aspects of the Fano resonances manifestation. The chapters were written by international experts from 16 countries (Turkey, South Korea, India, Italy, Switzerland, Japan, China, France, Russia, Morocco, USA, Belgium, Brazil, Germany, Australia, and Israel), who have contributed to the advancement of science and engineering of the Fano resonance in optical and microwave systems. The spectrum of the problems presented in this book is very wide. It is shown that Fano resonances manifesting novel phenomena both in linear and nonlinear response of plasmonic nanomaterials can extend the lifetime of plasmonic excitations, enabling the operation of nanolasers. A new pathway toward nonmagnetic excitation of an optical spin angular momentum based on the spin-dependent excitation of Fano resonances is introduced. A new concept based on polarization Mueller matrix analysis for tuning the Fano interference effect and the resulting asymmetric

spectral line shape in anisotropic optical system is discussed. A comprehensive review of recent theoretical and experimental advances in the field of Fano resonances and bound states in the continuum for light transport in evanescently coupled optical structures is provided including arrays of dielectric optical waveguides and coupled resonator optical waveguides. The review of different forms of coupled oscillator models for Fano resonant optical and microwave systems is given. There are studies of tunable metamaterials that realize the storage and retrieval of electromagnetic waves in the same way as the atomic electromagnetically-induced transparency system. The temporal coupled-mode theory formalism to describe the coupling process and the interference effect involved with optical scattering and absorption in nanostructures is shown. To unveil the origin of Fano lineshapes in the scattering efficiency of a spherical nanoparticle, the analysis of the full-wave scattering in terms of a set of eigenmodes independent of its permittivity is derived. Based on symmetry considerations, with the theoretical and experimental evidence, it is shown that electromagnetically induced-transparency and dark mode excitation are not necessarily associated. The feasibility of realizing the light-tunable Fano resonance in the metal-dielectric multilayer structures is demonstrated.

In the book, the reader can find a study of the core-level absorption of an impurity in a one-dimensional semiconductor superlattice with the use of the complex spectral analysis. One can see the results of investigation of the Fano resonances in high-index dielectric nanowires for directional scattering. There are chapters with studies of total wave reflection in band networks due to impurities, disorder, and quasiperiodic potentials; the theory of the multiple resonance interference in metallic nanohole array systems based on spatial and temporal coupled-mode methods; and the theory describing the Fano asymmetry by expanding the transmission amplitude with respect to states with point spectra, including not only bound states, but also resonant states with complex eigenvalues. It is shown that the Fano resonances can be effectively engineered with the use of multilayered hyperbolic metamaterials with either metal-dielectric or graphene-based multilayers. For Fano resonance generation, a new type of structures—3D folding metamaterials—is introduced. It is demonstrated that the concept of Fano resonance can be of significant interest in the context of a new emerging topic of topological photonics. Analytically, it is shown that the Purcell factor related to a dipole emitter oriented orthogonal or tangential to the spherical surface can exhibit the Fano or Lorentzian line shapes in the near-field. It is also discussed that almost any resonant response, either in directional or total scattering light scattering, can be efficiently described in terms of Fano resonances. Tuning of Fano resonance by waveguide rotation is considered in a non-axisymmetric acoustic-wave structure. It is shown that interaction of magnetic-dipolar-mode ferrite particles with a microwave-field continuum is distinguished by broken dual (electric–magnetic) symmetry. A unified vision of strong, weak, and critical coupling is provided based on a simple coupled oscillator model with a nonresonant background usually employed to describe Fano resonances in nanophotonic structures.

We hope that the book will be a valuable aid to understand the current research of the Fano resonance phenomena in optical and microwave structures for scientists, researchers, and graduate students working in the fields of electronic engineering, materials science, and condense matter physics. We are thankful to all authors who accepted our invitation to contribute the respective chapters. We would like to express our gratitude to Dr. Claus Ascheron, Executive Editor, Springer, for his initial support of the book proposal and collaboration with us during preparation of the book. We are thankful to Adelheid Duhm, Jayanthi Krishnamoorthi, and Elke Sauer from the Springer Production Department for their assistance at the book production.

Beersheba, Israel  
Krasnoyarsk, Russia  
Canberra, Australia

Eugene Kamenetskii  
Almas Sadreev  
Andrey Miroshnichenko



# Contents

<b>1</b>	<b>Fano Resonances in the Linear and Nonlinear Plasmonic Response</b> . . . . .	<b>1</b>
	Mehmet Emre Taşgın, Alpan Bek and Selen Postacı	
1.1	Plasmonics . . . . .	1
1.2	Fano Resonances in Linear Response . . . . .	5
1.3	Fano Resonances in Nonlinear Response . . . . .	10
1.3.1	Overlap Integrals and Selection Rules . . . . .	12
1.3.2	Enhancement and Suppression of SHG . . . . .	15
1.3.3	Silent Enhancement of SERS . . . . .	23
1.3.4	Interference of Multiple Conversion Paths and FWM . . . . .	25
1.4	Summary . . . . .	26
	References . . . . .	27
<b>2</b>	<b>Fano-resonant Excitations of Generalized Optical Spin Waves</b> . . . . .	<b>33</b>
	Xianji Piao, Sunkyu Yu and Namkyoo Park	
2.1	Introduction . . . . .	33
2.2	Coupled Mode Theory for Optical Spin Waves . . . . .	34
2.2.1	TCMT Analysis of 2D non-Hermitian Chirality . . . . .	36
2.2.2	TCMT Analysis of 3D Bulk Chirality with Circular Birefringent Mirrors . . . . .	37
2.3	Fano-resonant Excitation of Optical Spin . . . . .	42
2.3.1	Fano Line Shapes Toward Spectral Spin Separation . . . . .	42
2.3.2	Spin-Dependent Antisymmetric Fano Resonances . . . . .	44
2.3.3	Spin Fano Parameters . . . . .	46
2.4	Applications and Metamaterial Realizations . . . . .	47
2.4.1	Fano-resonant Optical Spin Switching . . . . .	47
2.4.2	Fano-resonant ‘Net’ Spin Excitation for Unpolarized Light . . . . .	49

2.4.3	Metamaterial Realizations . . . . .	50
2.5	Conclusions . . . . .	52
	References . . . . .	52
<b>3</b>	<b>Mueller Matrix Approach for Engineering Asymmetric Fano-resonance Line Shape in Anisotropic Optical System . . . . .</b>	<b>57</b>
	A. K. Singh, S. Chandel, S. K. Ray, P. Mitra and N. Ghosh	
3.1	Introduction . . . . .	58
3.2	Basics of Polarization . . . . .	59
3.2.1	Polarization Algebra . . . . .	60
3.2.2	Comprehensive Polarimetric Platform for Plasmonic Study . . . . .	65
3.3	Fano Resonance in Scattering . . . . .	67
3.4	Plasmonic Waveguiding Photonic Crystal . . . . .	69
3.4.1	Resonant Anomaly in Metal Dielectric Grating . . . . .	70
3.4.2	Rayleigh Anomaly in Metal Dielectric Grating . . . . .	72
3.5	Polarization Mediated Tuning of Fano-resonance . . . . .	72
3.5.1	Plasmonic Oligomers . . . . .	73
3.5.2	Polarisation Controlled Tuning of Fano Asymmetry . . . . .	74
3.6	Conclusion and Outlook . . . . .	81
	References . . . . .	82
<b>4</b>	<b>Fano Resonances and Bound States in the Continuum in Evanescently-Coupled Optical Waveguides and Resonators . . . . .</b>	<b>85</b>
	Stefano Longhi	
4.1	Introduction . . . . .	85
4.2	Fano Resonance and Bound States in the Continuum in Optical Waveguide Lattices with Side-Coupled Waveguides . . . . .	86
4.3	Fano Resonance and Particle Statistics . . . . .	93
4.4	Dynamical Control of Fano Resonances . . . . .	99
4.5	Fano Resonances in Non-Hermitian Photonic Structures . . . . .	102
	References . . . . .	106
<b>5</b>	<b>Model of Coupled Oscillators for Fano Resonances . . . . .</b>	<b>109</b>
	Benjamin Gallinet	
5.1	Introduction . . . . .	110
5.2	Oscillator Model . . . . .	110
5.3	Coupled Oscillator Model . . . . .	113
5.4	Resonance Formulas . . . . .	117
5.4.1	Derivation of Resonance Formula Without Intrinsic Damping . . . . .	118
5.4.2	Derivation of Formula Including Intrinsic Damping . . . . .	121

5.5	Electromagnetically Induced Absorption . . . . .	125
5.6	Radiative and Non-radiative Lifetimes in Strongly Coupled Systems . . . . .	127
5.6.1	Extended Coupled Oscillator Model . . . . .	129
5.6.2	Superradiance and Subradiance in Hybridized Modes . . . . .	131
5.7	Summary . . . . .	135
	References . . . . .	136
<b>6</b>	<b>Storage and Retrieval of Electromagnetic Waves in Metamaterials by Dynamical Control of EIT-Like Effect . . . . .</b>	<b>137</b>
	Toshihiro Nakanishi and Masao Kitano	
6.1	Introduction . . . . .	137
6.2	Electromagnetically Induced Transparency in Atomic Systems . . . . .	138
6.3	Metamaterial Analog to Atomic EIT Effect . . . . .	141
6.3.1	Coupled Resonator Model . . . . .	141
6.3.2	Design of EIT-like Metamaterials . . . . .	142
6.4	Storage and Retrieval of Electromagnetic Waves in Metamaterials . . . . .	143
6.4.1	Procedures for Storage and Retrieval of Electromagnetic Waves . . . . .	143
6.4.2	Tunable EIT-Like Metamaterial . . . . .	144
6.4.3	Storage and Retrieval of Electromagnetic Waves . . . . .	147
6.4.4	Frequency Conversion of Electromagnetic Waves . . . . .	149
6.5	Loss Compensation by Parametric Amplification for Extension of Storage Time . . . . .	150
6.5.1	Parametric Amplification of Continuous Waves . . . . .	151
6.5.2	Extension of Storage Time by Loss Compensation . . . . .	152
6.6	Conclusion . . . . .	154
	References . . . . .	154
<b>7</b>	<b>Temporal Coupled-Mode Theory for Light Scattering and Absorption by Nanostructures . . . . .</b>	<b>157</b>
	Yisheng Fang and Zhichao Ruan	
7.1	Introduction . . . . .	157
7.2	Temporal Coupled-Mode Theory for Light Scattering . . . . .	158
7.2.1	General Scattering Theory for Arbitrarily Shaped Scatterers . . . . .	158
7.2.2	Temporal Coupled-Mode Theory with a Single-Resonance . . . . .	161
7.3	General Line Shapes of Scattering and Absorption Cross Sections . . . . .	162

7.4	Temporal Coupled-Mode Theory for Scattering with Two Coupled Resonances . . . . .	166
7.5	Fano Resonance in the Scattering of Nanostructures . . . . .	168
	7.5.1 Fano Resonances in Plasmonic Resonators . . . . .	168
	7.5.2 Fano Resonances in All-Dielectric Resonators . . . . .	172
7.6	All-Optical Analog to Electromagnetically Induced Transparency . . . . .	174
7.7	Design of Super-Scattering Nanoparticles . . . . .	177
7.8	Summary . . . . .	180
	References . . . . .	180
<b>8</b>	<b>A Full-Retarded Spectral Technique for the Analysis of Fano Resonances in a Dielectric Nanosphere . . . . .</b>	<b>185</b>
	Carlo Forestiere, Giovanni Miano, Mariano Pascale and Roberto Tricarico	
8.1	Introduction . . . . .	185
8.2	Material Independent Modes for Electromagnetic Scattering . . . . .	188
	8.2.1 Differences Between Material Independent Modes and Quasi Normal Modes . . . . .	190
8.3	Spectral Theory of Electromagnetic Scattering from a Sphere . . . . .	191
	8.3.1 Coupling with an External Excitation . . . . .	197
	8.3.2 Radiation Pattern and Scattering Efficiency . . . . .	199
8.4	Resonances' Properties of a Homogeneous Sphere . . . . .	201
8.5	Resonances and Interferences in the Scattering by Si and Ag Spheres . . . . .	205
8.6	Backscattering Cancellation . . . . .	210
8.7	Conclusions and Outlook . . . . .	213
	References . . . . .	215
<b>9</b>	<b>Dark-Mode Characteristics of Metasurfaces Engineered by Symmetry Matching of Resonant Elements and Electromagnetic Fields . . . . .</b>	<b>219</b>
	A. Lupu, E. Bochkova, S. N. Burokur and A. de Lustrac	
9.1	Plasmonic EIT Viewed as Bright and Dark Modes Fano Interference . . . . .	219
	9.1.1 Symmetry-Broken Dolmen Metamolecules . . . . .	222
	9.1.2 Symmetry-Broken Ring-Disk Nanocavities . . . . .	223
	9.1.3 Plasmonic Oligomer Clusters . . . . .	223
9.2	Plasmonic EIT Revisited . . . . .	224
9.3	Direct Dark Mode Excitation Mechanism Based on Symmetry Matching . . . . .	226
9.4	Fano Interference is a System with Identical Coupled Resonators . . . . .	232

9.5	Summary and Conclusions . . . . .	236
	References . . . . .	237
<b>10</b>	<b>Light-Tunable Fano Resonance in Metal-Dielectric Multilayer Structures</b> . . . . .	<b>241</b>
	Shinji Hayashi, Dmitry V. Nesterenko and Zouheir Sekkat	
10.1	Introduction . . . . .	241
10.2	How to Realize Fano Resonances in Metal-Dielectric Multilayer Structures . . . . .	243
10.2.1	SPP Mode in MD Structure and PWG Modes in DDD Structure . . . . .	243
10.2.2	Fano Resonance in MDDD Structure . . . . .	246
10.2.3	Experimental Observation of Fano Resonance in MDDD Structure . . . . .	250
10.3	Light-Tunable Fano Resonance . . . . .	252
10.3.1	Experimental Results . . . . .	252
10.3.2	Analysis of Experimental Results and Mechanism of Light Tuning . . . . .	255
10.4	Concluding Remarks . . . . .	258
	References . . . . .	259
<b>11</b>	<b>Study of Fano Resonance in the Core-Level Absorption Spectrum in Terms of Complex Spectral Analysis</b> . . . . .	<b>261</b>
	Satoshi Tanaka, Taku Fukuta and Tomio Petrosky	
11.1	Introduction . . . . .	261
11.2	Absorption Spectrum in the Infinite Chain . . . . .	263
11.2.1	Model and Complex Eigenvalue Problem . . . . .	263
11.2.2	Absorption Spectrum . . . . .	268
11.3	Absorption Spectrum in the Semi-infinite Chain . . . . .	273
11.3.1	Model and Complex Eigenvalue Problem . . . . .	273
11.3.2	Absorption Spectrum . . . . .	275
11.4	Summary . . . . .	280
	References . . . . .	280
<b>12</b>	<b>Fano-resonances in High Index Dielectric Nanowires for Directional Scattering</b> . . . . .	<b>283</b>
	Peter R. Wiecha, Aurélien Cuche, Housseem Kallel, Gérard Colas des Francs, Aurélie Lecestre, Guilhem Larrieu, Vincent Larrey, Frank Fournel, Thierry Baron, Arnaud Arbouet and Vincent Paillard	
12.1	Introduction . . . . .	284
12.1.1	Plasmonics . . . . .	284
12.1.2	High Refractive Index Dielectric Nano-particles . . . . .	285
12.1.3	General Applications of Dielectric Nano-structures . . . . .	286

12.2	Fano Resonances and Kerker's Conditions . . . . .	287
12.2.1	Fano in Nano-optics . . . . .	288
12.2.2	Kerker's Conditions at Optical Frequencies . . . . .	289
12.2.3	Directional Scattering From Nanoparticles . . . . .	290
12.2.4	Applications of Nanoscale Directional Scattering . . . . .	291
12.3	Mie Theory . . . . .	292
12.3.1	Directional Scattering from Spheres and Cylinders . . . . .	293
12.3.2	Nanowires: Resonant Enhancement of the Electric and Magnetic Field . . . . .	295
12.3.3	Nanowires: Multipolar Contributions to Directional Scattering . . . . .	296
12.4	Directional Scattering from Silicon Nanowires . . . . .	297
12.4.1	Cylindrical Nanowires . . . . .	298
12.4.2	Rectangular Nanowires . . . . .	300
12.4.3	Coupled Nanowires . . . . .	303
12.5	Conclusion and Outlook . . . . .	303
	References . . . . .	304
<b>13</b>	<b>Fano Resonances in Flat Band Networks . . . . .</b>	<b>311</b>
	Ajith Ramachandran, Carlo Danieli and Sergej Flach	
13.1	Introduction . . . . .	311
13.1.1	Fano Resonances . . . . .	312
13.1.2	Flat Band Networks . . . . .	314
13.2	Single Local Defects . . . . .	317
13.3	Disorder . . . . .	318
13.4	Nonlinearities . . . . .	322
13.5	Conclusions . . . . .	326
	References . . . . .	327
<b>14</b>	<b>Multiple-Resonance Interference in Metallic Nanohole Arrays . . . . .</b>	<b>331</b>
	Munehiro Nishida and Yutaka Kadoya	
14.1	Introduction . . . . .	331
14.2	Surface Plasmon Polariton in a Metallic Nanohole Array . . . . .	333
14.3	Method . . . . .	334
14.3.1	Spatial Coupled-Mode (SCM) Method . . . . .	334
14.3.2	Temporal Coupled-Mode (TCM) Method . . . . .	337
14.4	Waveguide Modes in a Metallic Nanohole . . . . .	341
14.5	Fano Resonance and Short-Circuit Effect . . . . .	342
14.6	SPP Molecule and Spoof Surface Plasmon . . . . .	343
14.7	Multipole Surface Plasmon Polariton . . . . .	346
14.8	Multiple Fano Resonance Interference . . . . .	348

14.9	EIT-like Phenomena . . . . .	351
14.10	Summary . . . . .	353
	References . . . . .	354
<b>15</b>	<b>Resonant-State Expansion of the Fano Peak in Open Quantum Systems</b> . . . . .	<b>357</b>
	Naomichi Hatano and Gonzalo Ordóñez	
15.1	Introduction: Resonant States . . . . .	357
15.1.1	Landauer Formula and the Transmission Probability . . . . .	357
15.1.2	Siegert Boundary Condition: A Tutorial Example . . . . .	359
15.1.3	Resonant and Anti-resonant States . . . . .	360
15.2	Resonant-State Expansion: Another Tutorial Example . . . . .	363
15.2.1	Transmission Probability and the Green’s Function . . . . .	363
15.2.2	Feshbach Formalism for the Tight-Binding Model . . . . .	364
15.2.3	Green’s Function of the Effective Hamiltonian . . . . .	365
15.2.4	Calculation of the Self-energy . . . . .	366
15.2.5	Quadratic Eigenvalue Problem . . . . .	367
15.2.6	Resonant-State Expansion of the Green’s Function . . . . .	372
15.2.7	New Formula for the Transmission Probability . . . . .	373
15.3	Fano Asymmetry . . . . .	376
15.4	Summary . . . . .	381
	References . . . . .	381
<b>16</b>	<b>Fano Resonances in Slanted Hyperbolic Metamaterial Cavities</b> . . . . .	<b>383</b>
	F. Vaianella and B. Maes	
16.1	Introduction . . . . .	383
16.2	Design . . . . .	384
16.3	Effective Medium Theory . . . . .	385
16.4	Rigorous Calculations and Analysis . . . . .	389
16.5	Graphene Multilayers . . . . .	394
16.6	Loss Effect . . . . .	398
16.7	Conclusion . . . . .	401
	References . . . . .	401
<b>17</b>	<b>Fano Resonance Generation and Applications in 3D Folding Metamaterials</b> . . . . .	<b>403</b>
	Z. Liu, S. Y. Yang, J. J. Li and C. Z. Gu	
17.1	Fano Resonances Excited in Composite Structures . . . . .	404
17.2	Fabrication of 3D Folding Metamaterial . . . . .	405

17.2.1	Combination of Traditional Planar Techniques . . . . .	406
17.2.2	Brand New Techniques . . . . .	407
17.3	Fano Resonances in 3D Folding Metamaterials . . . . .	409
17.3.1	Unusual Fano Resonance in Composite 3D Structures . . . . .	410
17.3.2	Mechanism of Fano Resonance Excitation . . . . .	410
17.3.3	Conductive Coupling and Capacitive Coupling . . . . .	413
17.4	Applications . . . . .	416
17.4.1	Refractive Index Sensing . . . . .	417
17.4.2	SERS Detection . . . . .	418
17.5	Conclusion . . . . .	420
	References . . . . .	420
<b>18</b>	<b>Fano Resonances in Topological Photonic Systems . . . . .</b>	<b>425</b>
	Xiang Ni, Maxim A. Gorlach, Daria A. Smirnova, Dmitry Korobkin and Alexander B. Khanikaev	
18.1	Introduction . . . . .	425
18.2	Theoretical Description of Topological Fano Resonances: Coupled Mode Theory Approach . . . . .	426
18.3	Fitting of Experimental Data with the Analytical Model . . . . .	430
18.4	Constructing the Effective Hamiltonian Using the Plane Wave Expansion Method . . . . .	431
18.5	Perturbative Electromagnetic Theory of Radiative Losses . . . . .	436
18.6	Numerical Calculation of Transmissivity Using Tight-Binding-Based Coupled Mode Theory . . . . .	439
18.7	Conclusion . . . . .	442
	References . . . . .	442
<b>19</b>	<b>Fano Resonances in Plasmonic Core-Shell Particles and the Purcell Effect . . . . .</b>	<b>445</b>
	Tiago José Arruda, Alexandre Souto Martinez, Felipe A. Pinheiro, Romain Bachelard, Sebastian Slama and Philippe Wilhelm Courteille	
19.1	Introduction . . . . .	446
19.2	Light Scattering by Core-Shell Spheres: Conventional and Unconventional Fano Resonances . . . . .	447
19.2.1	The Lorenz-Mie Theory for Single-Layered Spheres . . . . .	448
19.2.2	Fano Resonances in Optical Cross Sections . . . . .	450
19.3	Spontaneous Emission of a Dipole Emitter Near a Plasmonic Nanoshell . . . . .	457
19.3.1	Radiative and Non-radiative Decay Rates of a Dipole Emitter . . . . .	458
19.3.2	Decay Rates and Radiation Efficiency Near a Plasmonic Nanoshell . . . . .	461



19.3.3	The Purcell Effect and Fano Resonances in Plasmonic Nanoshells . . . . .	464
19.4	Conclusion . . . . .	468
	References . . . . .	469
<b>20</b>	<b>Fano Resonances in Light Scattering by Finite Obstacles . . . . .</b>	<b>473</b>
	Andrey Miroshnichenko	
20.1	Introduction . . . . .	473
20.2	Analysis of the Scattered Field . . . . .	474
20.2.1	Scattering Coefficients . . . . .	474
20.2.2	Parity and Mirror Symmetries of the Spherical Harmonics . . . . .	476
20.2.3	Forward and Backward Scattering . . . . .	478
20.3	Light Scattering by a Single Particle . . . . .	479
20.3.1	Directional Fano Resonance . . . . .	479
20.3.2	Vanishing Partial Wave Scattering and <i>Anapole</i> modes . . . . .	481
20.3.3	Fano Profile of the Scattering Coefficients . . . . .	483
20.4	Fano Resonance in <i>Oligomer</i> nanostructures . . . . .	486
20.4.1	Linear Response . . . . .	486
20.4.2	Chiral Structures and Optical Activity . . . . .	489
20.4.3	Harmonic Generation . . . . .	490
20.5	Conclusions . . . . .	491
	References . . . . .	492
<b>21</b>	<b>Tuning of Fano Resonance by Waveguide Rotation . . . . .</b>	<b>497</b>
	Almas Sadreev, Artem S. Pilipchuk and Alina A. Pilipchuk	
21.1	Introduction . . . . .	497
21.2	Acoustic Coupled Mode Theory for Open Cylindrical Resonators . . . . .	499
21.3	Trapping in Non Coaxial Waveguide Under Variation of the Resonator Length $L$ . . . . .	503
21.3.1	$\Delta\phi = 0$ . . . . .	505
21.3.2	$\Delta\phi = \pi/4$ . . . . .	506
21.4	Wave Faucet . . . . .	507
21.5	BSCs in Two Continua Different in Phase . . . . .	512
21.5.1	The Mode with $m = 0$ Crosses the Modes with $\pm M$ . . . . .	513
21.5.2	The Modes $\pm 112$ Cross the Modes $\pm 211$ . . . . .	518
21.6	Conclusions . . . . .	522
	References . . . . .	523

**22 Interaction of MDM Ferrite Particles with a Microwave-Field Continuum** . . . . . 527  
 Eugene Kamenetskii

22.1 Introduction . . . . . 527

22.2 Quasistatic Eigenvalue Problems for Plasmon and Magnon Oscillations in Subwavelength Particles . . . . . 529

22.3 The Spectral Problem for Magnetostatic-Potential Wave Function . . . . . 533

    22.3.1 MDMs in a Ferrite Rod . . . . . 533

    22.3.2 MDMs in a Ferrite-Disk Particle . . . . . 537

22.4 Magnetoelectric Fields and Helical Bound States in a Microwave-Field Continuum . . . . . 539

22.5 *G*- and *L*-Magnetic Dipolar Modes . . . . . 544

22.6 Conclusion . . . . . 547

References . . . . . 548

**23 Weak Coupling, Strong Coupling, Critical Coupling and Fano Resonances: A Unifying Vision** . . . . . 551  
 Simone Zanotto

23.1 Introduction . . . . . 551

23.2 Model System, Parametrization, and Linear Response . . . . . 552

23.3 Lineshape Inheritance to the Strong Coupling Regime . . . . . 555

23.4 Absorption Properties . . . . . 558

    23.4.1 Universal Absorption Lineshapes . . . . . 558

    23.4.2 A Detour on Coherent (Perfect) Absorption . . . . . 560

    23.4.3 Universal Coherent Absorption Lineshapes . . . . . 562

23.5 Weak, Strong, and Critical Coupling . . . . . 564

23.6 Conclusions . . . . . 568

References . . . . . 568

**Index** . . . . . 571

# Contributors

**Arnaud Arbouet** CEMES, Université de Toulouse, CNRS, Toulouse, France

**Tiago José Arruda** Instituto de Física de São Carlos (IFSC), Universidade de São Paulo (USP), São Paulo, São Carlos, Brazil

**Romain Bachelard** Departamento de Física, Universidade Federal de São Carlos (UFSCar), São Paulo, São Carlos, Brazil

**Thierry Baron** LTM, Université Grenoble-Alpes, CNRS, Grenoble, France

**Alpan Bek** Department of Physics, Middle East Technical University, Ankara, Turkey

**E. Bochkova** Centre de Nanosciences et de Nanotechnologies, CNRS, Université Paris-Sud, Université Paris-Saclay, Orsay, France

**S. N. Burokur** LEME, UPL, Université Paris Nanterre, Ville d'Avray, France

**S. Chandel** Indian Institute of Science Education and Research (IISER) Kolkata, Kolkata, India

**Gérard Colas des Francs** ICB, Université Bourgogne-Franche Comté, CNRS, Dijon, France

**Philippe Wilhelm Courteille** Instituto de Física de São Carlos (IFSC), Universidade de São Paulo (USP), São Paulo, São Carlos, Brazil

**Aurélien Cuche** CEMES, Université de Toulouse, CNRS, Toulouse, France

**Carlo Danieli** Center for Theoretical Physics of Complex Systems, Institute for Basic Science, Daejeon, South Korea

**A. de Lustrac** Centre de Nanosciences et de Nanotechnologies, CNRS, Université Paris-Sud, Université Paris-Saclay, Orsay, France; UPL, Université Paris Nanterre, Ville d'Avray, France

**Yisheng Fang** Department of Physics, Zhejiang University, Hangzhou, China

**Sergej Flach** Center for Theoretical Physics of Complex Systems, Institute for Basic Science, Daejeon, South Korea

**Carlo Forestiere** Department of Electrical Engineering and Information Technology, Università degli Studi di Napoli Federico II, Napoli, Italy

**Frank Fournel** CEA-LETI, Université Grenoble-Alpes, Grenoble, France

**Taku Fukuta** Department of Physical Science, Osaka Prefecture University, Sakai, Japan

**Benjamin Gallinet** CSEM SA, Neuchâtel, Switzerland

**N. Ghosh** Indian Institute of Science Education and Research (IISER) Kolkata, Kolkata, India

**Maxim A. Gorlach** ITMO University, Saint Petersburg, Russia

**C. Z. Gu** Beijing National Laboratory for Condensed Matter Physics, Institute of Physics, Chinese Academy of Sciences, Beijing, China; CAS Key Laboratory of Vacuum Physics, School of Physical Sciences, University of Chinese Academy of Sciences, Beijing, China; Collaborative Innovation Center of Quantum Matter, Beijing, China

**Naomichi Hatano** Institute of Industrial Science, The University of Tokyo, Kashiwa, Chiba, Japan

**Shinji Hayashi** Graduate School of Engineering, Kobe University, Kobe, Japan; Optics and Photonics Center, Moroccan Foundation for Science, Innovation and Research (MAScIR), Rabat, Morocco

**Yutaka Kadoya** Graduate School of Advanced Science of Matter, Hiroshima University, Higashi-Hiroshima, Japan

**Houssem Kallel** CEMES, Université de Toulouse, CNRS, Toulouse, France

**Eugene Kamenetskii** Microwave Magnetic Laboratory, Department of Electrical and Computer Engineering, Ben Gurion University of the Negev, Beersheba, Israel

**Alexander B. Khanikaev** The City College of the City University of New York, New York City, NY, USA; ITMO University, Saint Petersburg, Russia

**Masao Kitano** Department of Electronic Science and Engineering, Kyoto University, Kyoto, Japan

**Dmitry Korobkin** The City College of the City University of New York, New York City, NY, USA; ITMO University, Saint Petersburg, Russia

**Vincent Larrey** CEA-LETI, Université Grenoble-Alpes, Grenoble, France

**Guilhem Larriau** LAAS, Université de Toulouse, CNRS, Toulouse, France

**Aurélie Lecestre** LAAS, Université de Toulouse, CNRS, Toulouse, France

**J. J. Li** Beijing National Laboratory for Condensed Matter Physics, Institute of Physics, Chinese Academy of Sciences, Beijing, China; CAS Key Laboratory of Vacuum Physics, School of Physical Sciences, University of Chinese Academy of Sciences, Beijing, China

**Z. Liu** Beijing National Laboratory for Condensed Matter Physics, Institute of Physics, Chinese Academy of Sciences, Beijing, China

**Stefano Longhi** Dipartimento di Fisica e Istituto di Fotonica e Nanotecnologie del Consiglio Nazionale delle Ricerche, Politecnico di Milano, Milan, Italy

**A. Lupu** Centre de Nanosciences et de Nanotechnologies, CNRS, Université Paris-Sud, Université Paris-Saclay, Orsay, France

**B. Maes** Micro- and Nanophotonic Materials Group, Faculty of Science, University of Mons, Mons, Belgium

**Alexandre Souto Martínez** Faculdade de Filosofia, Ciências e Letras de Ribeirão Preto (FFCLRP), Universidade de São Paulo (USP), São Paulo, Ribeirão Preto, Brazil

**Giovanni Miano** Department of Electrical Engineering and Information Technology, Università degli Studi di Napoli Federico II, Napoli, Italy

**Andrey Miroshnichenko** School of Engineering and Information Technology, University of New South Wales, Canberra, ACT, Australia

**P. Mitra** Indian Institute of Science Education and Research (IISER) Kolkata, Kolkata, India

**Toshihiro Nakanishi** Department of Electronic Science and Engineering, Kyoto University, Kyoto, Japan

**Dmitry V. Nesterenko** IPSI RAS - Branch of the FSRC “Crystallography and Photonics” RAS, Samara, Russia; Faculty of Information Technology, Samara National Research University, Samara, Russia

**Xiang Ni** The City College of the City University of New York, New York City, NY, USA

**Munehiro Nishida** Graduate School of Advanced Science of Matter, Hiroshima University, Higashi-Hiroshima, Japan

**Gonzalo Ordóñez** Department of Physics and Astronomy, Butler University, Indianapolis, IN, USA

**Vincent Paillard** CEMES, Université de Toulouse, CNRS, Toulouse, France

**Namkyoo Park** Photonic Systems Laboratory, Department of Electrical and Computer Engineering, Seoul National University, Seoul, Korea, South Korea

**Mariano Pascale** Department of Electrical Engineering and Information Technology, Università degli Studi di Napoli Federico II, Napoli, Italy

**Tomio Petrosky** Center for Complex Quantum System, University of Texas at Austin, Austin, USA; Institute of Industrial Science, The University of Tokyo, Tokyo, Japan

**Xianji Piao** Photonic Systems Laboratory, Department of Electrical and Computer Engineering, Seoul National University, Seoul, Korea, South Korea

**Alina A. Pilipchuk** Federal Research Center KSC SB RAS, Kirensky Institute of Physics, Krasnoyarsk, Russia

**Artem S. Pilipchuk** Federal Research Center KSC SB RAS, Kirensky Institute of Physics, Krasnoyarsk, Russia

**Felipe A. Pinheiro** Instituto de Física, Universidade Federal do Rio de Janeiro (UFRJ), Rio de Janeiro, Brazil

**Selen Postacı** Department of Physics, Middle East Technical University, Ankara, Turkey

**Ajith Ramachandran** Center for Theoretical Physics of Complex Systems, Institute for Basic Science, Daejeon, South Korea

**S. K. Ray** Indian Institute of Science Education and Research (IISER) Kolkata, Kolkata, India

**Zhichao Ruan** State Key Laboratory of Modern Optical Instrumentation, Department of Physics, Zhejiang University, Hangzhou, China

**Almas Sadreev** Federal Research Center KSC SB RAS, Kirensky Institute of Physics, Krasnoyarsk, Russia

**Zouheir Sekkat** Optics and Photonics Center, Moroccan Foundation for Science, Innovation and Research (MAScIR), Rabat, Morocco; Faculty of Sciences, Mohammed V University in Rabat, Rabat, Morocco; Graduate School of Engineering, Osaka University, Suita, Japan

**A. K. Singh** Indian Institute of Science Education and Research (IISER) Kolkata, Kolkata, India

**Sebastian Slama** Physikalisches Institut, Eberhardt-Karls-Universität Tübingen, Tübingen, Germany

**Daria A. Smirnova** The City College of the City University of New York, New York City, NY, USA

**Satoshi Tanaka** Department of Physical Science, Osaka Prefecture University, Sakai, Japan

**Mehmet Emre Taşgın** Institute of Nuclear Science, Hacettepe University, Ankara, Turkey

**Roberto Tricarico** Department of Electrical Engineering and Information Technology, Università degli Studi di Napoli Federico II, Napoli, Italy

**F. Vaianella** Micro- and Nanophotonic Materials Group, Faculty of Science, University of Mons, Mons, Belgium

**Peter R. Wiecha** CEMES, Université de Toulouse, CNRS, Toulouse, France

**S. Y. Yang** Beijing National Laboratory for Condensed Matter Physics, Institute of Physics, Chinese Academy of Sciences, Beijing, China; CAS Key Laboratory of Vacuum Physics, School of Physical Sciences, University of Chinese Academy of Sciences, Beijing, China

**Sunky Yu** Photonic Systems Laboratory, Department of Electrical and Computer Engineering, Seoul National University, Seoul, Korea, South Korea

**Simone Zanotto** NEST, Istituto Nanoscienze - CNR and Scuola Normale Superiore, Pisa, Italy

# Chapter 1

## Fano Resonances in the Linear and Nonlinear Plasmonic Response



Mehmet Emre Taşgın, Alpan Bek and Selen Postacı

**Abstract** Fano resonances manifest novel phenomena both in linear and nonlinear response of plasmonic nanomaterials. They can extend the lifetime of plasmonic excitations, enabling the operation of nanolasers, or they can increase the fluorescence of quantum emitters. They also provide control over nonlinear optical processes such as second harmonic generation and surface enhanced Raman scattering. Fano resonances can both enhance and suppress nonlinear response. Interference of two or more absorption/conversion paths is responsible for the appearance of these effects. In this Chapter, we demonstrate explicitly—on a single equation—how path interference takes part in linear and nonlinear Fano resonances.

### 1.1 Plasmonics

Plasmons are collective oscillations of free electrons in metals and semiconductors. Plasmonic oscillations can be induced in the bulk and surface of the metals [1]. In order for surface plasmons to be excited, conservation of momentum has to be satisfied. When it is desired to excite plasmons on the surface of metal films using light, the match between the momenta of photons and surface plasmons can be satisfied by using a glass prism in Kretschman configuration [2]. In metal nanoparticles (MNPs) such a constraint does not apply since MNPs provide a wide range of reciprocal lattice vectors in Fourier domain due to their small sizes [3]. Interestingly, MNPs can trap light from a spatial range much larger than the wavelength of the incident light [4].

Localized surface plasmon (LSP) modes provide a strong enhancement of the incident field, as large as a factor of  $10^5$ , at the nm-size hot spots [5]. Such a confinement of light can be increased even further using self-repeating cascaded nanostructures

---

M. E. Taşgın (✉)

Institute of Nuclear Science, Hacettepe University, 06532 Ankara, Turkey  
e-mail: metasgin@hacettepe.edu.tr

A. Bek · S. Postacı

Department of Physics, Middle East Technical University,  
06800 Ankara, Turkey

© Springer Nature Switzerland AG 2018

E. Kamenetskii et al. (eds.), *Fano Resonances in Optics and Microwaves*, Springer Series in Optical Sciences 219, [https://doi.org/10.1007/978-3-319-99731-5\\_1](https://doi.org/10.1007/978-3-319-99731-5_1)



[6, 7]. MNPs and semiconductor nanoparticles (NPs) have surface plasmon resonances at optical and infrared regimes, respectively. Such a strong localization of the electromagnetic (EM) field presents numerous advantages both in technological and fundamental physics research [1].

Plasmonics contributed to the technological advance in the past two decades significantly. Some applications have already been used in the industry, while more implementations and new phenomena are studied intensively for industrial interest. As a basic example, the smart drugs used in thermal therapy of cancer [8] rely on localization and heating features of MNPs selectively attached on/in the cancer cells. In the smart glass (window) applications, localized field of MNPs heat vanadium oxide (VO) particles for obtaining VO phase transition at smaller temperatures [9].

Metal nanostructure (MNS)-decorated surfaces of thin film solar cells help the incident sun light to be trapped (scattered) in (into) the active regions [10, 11]. Nanoholes on MNSs demonstrate a phenomenon called extraordinary transmission [12] which can be used in ultra sensitive detectors [13]. Nanoscale detector size also provides ultra fast (e.g. tens of picoseconds) response time which is limited by the transmission of the excited carriers into the intrinsic region of the detector [1]. Such fast detectors are important in observing ultra fast process such as chemical processes in biological activities [14]. Nanohole arrays are also used in imaging devices [15].

The localized EM field can also be used to trap and manipulate the nanosize objects. An interesting example to plasmonic tweezers [16] is the trapping of DNA with the metallic hot spots [17]. Surface plasmon resonance (SPR) is also in use for the detection of the specific types of viruses via change of refractive index. Ligands over a thin metal film attach only to a specific type of analyte (virus). This changes the propagation direction of the light [18]. Field localization near nanomechanical oscillators results an optomechanical (plasmomechanical) system where plasmons couple to the mechanical motion via a strong radiation-pressure-type interaction [19, 20].

As much as plasmonics found applications in biology, biology has found applications in plasmonics. The optical properties of plasmons can be tuned by changing the length of DNA arrays. When the DNA arrays of a certain length is mixed in a solution of MNPs, tetramer, pentamer, hexamer structures of MNPs get self-assembled [21]. The structure is completely determined by the length of the DNA arrays used.

When an AFM tip is covered with nm-thick metal coating (e.g. 5–10 nm), the sharp edge of the AFM tip localizes the field on the sample it scans. Measuring the near field of the sample (apertureless scanning near field optical microscopy: aSNOM) nm-resolution optical imaging becomes possible [22, 23]. It is appealing that a similar dielectric response is observed from metal clusters of different sizes [24–28]. Fortunately, this makes 3D Maxwell simulation of MNPs possible and reliable.

In computers of the present day, data can be processed with a high speed. But capacity of interconnects –responsible for carrying data to other parts of the device– limits the process speed. Plasmons can carry data  $\sim 1000$  times faster as compared to electronic communications [29]. A nanowire (NW) both can conduct electricity and at the same time can route the light in form of surface plasmon polaritons (SPPs)

in nanodimensions. Hence, plasmonics make the current technology scalable into nanodimensions. When the dimensions of a MNS is tuned properly, it can act as a nanoresonator for SPPs [30], similar to an optical cavity. MNSs not only can guide the light, but they can also emit it directionally: nanoantenna working at optical frequencies [31]. When an electronically excited quantum dot is placed at the hot spot of a metal nanoantenna, it transfers its energy to the radiating antenna. Radiation pattern is determined by the plasmon eigenmode of the antenna into which quantum dot transition frequency overlaps.

Nanodimensions of MNSs, as already mentioned, provides fast response time in photo-detector applications. Small decay time of the plasmon excitations can also be adopted for the manufacturing of fast response devices. Spasers (surface plasmon amplification by stimulated emission of radiation [32]) are nanolasers which necessitate a large pump threshold, but much smaller lasing onset times as an advantage [33, 34]. Lasing (spacing) is based on the enhanced stimulated emission of large number of quantum emitters within the presence of more and more plasmons in the medium.

A spaser functions as follows: When quantum emitters (QEs) within a plasmonic medium are illuminated, (i) plasmons on the MNS are excited resonantly by the pump. Pump also (ii) couples to the QEs directly. Coupling of the incident light to the MNS is order of magnitude larger compared to its coupling to the QE. (iii) The strong plasmon field also excites the nearby QEs. (iv) Presence of plasmons also stimulates the decay of QEs into the MNS. (v) Spontaneous emission rate of QEs is also enhanced orders of magnitude [35] due to the increase in the photon density of states (DOS) for plasmon excitations.<sup>1</sup> This enhances the decay and stimulation rates. Lasing onsets more quickly in a spaser, compared to standard lasers. Enhanced decay rate is also related with Fano resonance [36] as discussed in the following section.

A light source, of nanodimensions and with tens of THz onset and reset frequencies, has vital importance in ultra fast processing. To achieve this goal, similar to spasers, MNPs are doped in fibers for fast response (small reset-time) fiber lasers [33, 34].

Field enhancement due to the localization of the light at the hot spots also enhances the nonlinearities. Nonlinear response of frequency converting materials (e.g. molecules) can be enhanced when they are placed near a MNS hot spot [37]. Localization also enhances the nonlinearity of MNSs themselves. Second (third) harmonic generation (SHG, THG) and four-wave mixing (FWM) of plasmonic materials can be enhanced orders of magnitude at the hot spots [38]. One of the most important applications of this nonlinearity enhancement is surface enhanced Raman scattering (SERS) which finds applications over all fields of science [39–45]. The field enhancement near metal surfaces (hot spots) enhances the Raman signal quadratically [46]. SERS can be used to reveal the presence of a molecule and types of chemical bonds

---

<sup>1</sup>One should note that the strong coupling of the incident light to MNSs is also related with the high DOS, that is the Purcell effect.

within. SERS not only gives way to make single-molecule detection possible but it can also image the inner structure of a single molecule with 0.2 nm resolution [40].

In the next sections, we show that all of these nonlinearities can be enhanced 3 orders of magnitude, on top of the localization enhancement. Path interference effects in the nonlinear response, due to Fano resonances, make the extra enhancement possible.

Strong field confinement and presence of nonlinearity are also important for light modulation purposes. In electro-optical (plasmonic) modulators, electrical signal is encoded into the optical signal [1, 47–49]. Small input voltage swings can produce large electric field changes for the encoding, at the region where field localization takes place [1]. All-optical modulation and switching of light is also possible via the nonlinearity induced by the field localization. The presence of one of the pulses can change the refractive index of the medium by inducing Kerr-type nonlinearity. This is due to intensity concentration. The probe (second) pulse can be modified due to the temporal change in the index [50, 51].

Plasmonics also made a great impact on the field of quantum optics, the science of the new age [52–54]. Hot spots provide strong light-matter interaction. QEs placed at these hot spots couple to the polarization field of the plasmon excitation. This is several orders of magnitude larger compared to the coupling of the QE to the incident light. This introduces the new field plasmon quantum optics (or simply quantum plasmonics [55]). For instance, two QEs coupled to the two hot spots of the same plasmon excitation can be strongly entangled [56]. A recent study [57] shows that it is also possible to entangle many QEs: many-particle entanglement [58].

Despite their large damping rate,  $\gamma \sim 10^{13} - 10^{14}$  Hz, plasmons can keep the nonclassical feature (entanglement, single-mode nonclassicality) for much longer times. Experiments [59, 60] show that both quadrature-squeezing and sub-Poissonian statistics (squeezing in the number uncertainty) remain for  $\sim 10^{-11} - 10^{-10}$  s. For this reason, propagating surface plasmon polaritons (SPPs) are studied to carry entanglement between many QEs [61, 62]. The nm dimensions of the nanowires or nanoarays possess the scaling properties for the nanodimensional information processing. Enhancement in the nonlinearity of MNPs, due to localization, enables the production of nonclassical features, such as entanglement and single-mode nonclassicality [63], in the nm dimensions. Many-particle entanglement generated in these systems can increase the signal to noise ratio above the standard quantum level (SQL) [64, 65].

Almost all of the phenomena, mentioned above, rely on the enhancement of the electromagnetic (EM) field via localization into nm dimensions. In the following, we show that coupling of auxiliary particles (e.g. quantum objects or dark plasmon modes) introduces additional absorption or frequency conversion paths, i.e. Fano resonances. Controlling the interference of these paths (e.g. via coupling strength,  $f$ , or auxiliary particle's level spacing,  $\omega_{eg}$ ) one can enhance the localized field even more. In addition, one can both enhance and suppress the nonlinear processes without altering the hot spot fields.

We like to keep things simple. We obtain a single expression by setting up a simple analytical model. We demonstrate why enhancement and suppression emerge

out of this single equation. The understanding, provided by the simplicity, leads us in obtaining better enhancement schemes by introducing more than two interfering paths. We also demonstrate that exact solutions of 3-dimensional Maxwell equations confirm the predictions of our simple analytical results. What is more, we also discuss these schemes on the experiments conducted by our group.

## 1.2 Fano Resonances in Linear Response

Fano resonance is the plasmonic analog of electromagnetically induced transparency (EIT). Path interference effects play the key role in both phenomena: the excited state becomes weakly hybridized into two, see Fig. 1.1. The two hybridized states rely in the broadening of the excited state ( $\gamma_{eg} \sim 10^9$  Hz for QDs and  $\gamma_p \sim 10^{13} - 10^{14}$  Hz for plasmon excitation) and they cannot be resolved [36, 66]. The two paths operate out of phase to each other. One of the paths absorbs the incident radiation while the second one emits the radiation. Hence, a transparency window shows up where absorption vanishes.

The major difference between EIT and Fano resonance is the former (latter) one is an active (passive) medium. In EIT, the weak hybridization of the excited state is induced by the strong microwave pump (driving), which couples the excited state  $|e\rangle$  to an auxiliary state  $|a\rangle$  of the same atom, see Fig. 1.1a. The coupling is over the magnetic field since the  $|e\rangle \rightarrow |a\rangle$  transition is dipole forbidden. Fano resonance does not necessitate a driving field. An auxiliary object with larger lifetime (e.g. a quantum object or a dark plasmon state) is placed at the hot spot of the MNP. Coupling between MNP and the auxiliary particle is induced by the plasmon (polarization) field

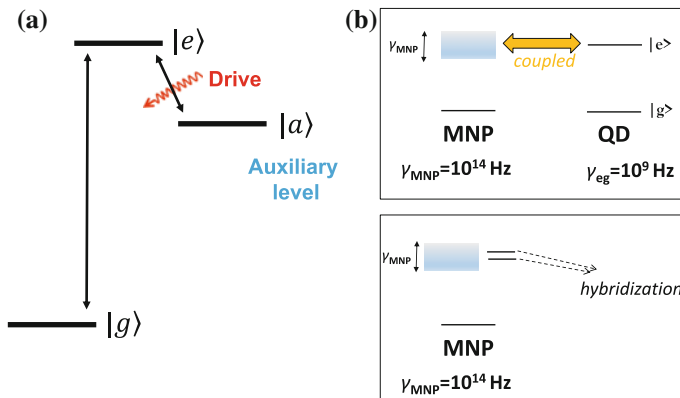


**Fig. 1.1** Analogy between **a** EIT [100] and **b** Fano resonance [36, 66, 67]. In EIT, coupling to an auxiliary level introduces the weak hybridization in  $|e\rangle$ . In a Fano resonance, coupling of the plasmon excitation to an auxiliary object (e.g. QD) introduces the weak hybridization. In both cases, hybridization is weak enough so that hybridized levels cannot be resolved in the excitation band

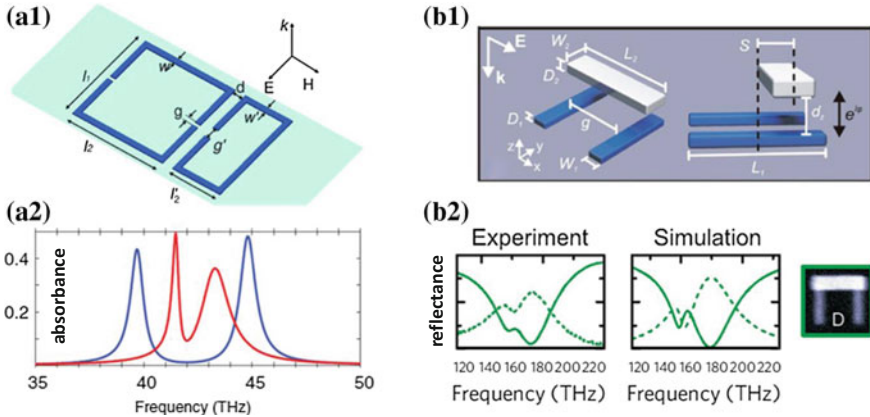


**Fig. 1.2** Experimental demonstration of Fano resonances **a** with split ring resonators in the THz regime [68] and **b** with nanobars in the optical regime [69]. Resonance appears due to the coupling of dipole-like oscillator with a long-live quadrupole-like oscillator in both cases

of the MNP itself. One does not need a driving field. So, Fano resonances can appear in passive media.

Fano resonance is not a pure quantum effect. It also has a classical correspondence which is clearly observed in the experiments. For instance, a plasmon mode of long lifetime (e.g. a quadrupole-like dark mode) can do the job of a quantum object. In Fig. 1.2a1 and a2, two split ring resonators (SRRs) are coupled to each other capacitively [68]. The one on the right hand side is a dipole SRR and couples to the incident radiation of  $\sim$ THz frequency. The one on the left hand side is a quadrupole SRR which does not couple to (cannot be directly excited by) the incident radiation. But it has a 10 times longer lifetime compared to the dipole one. Due to the capacitive coupling between the two, we observe the Fano resonance dip in Fig. 1.2a2. The same effect has also been observed in the optical frequency with a similar set up at Fig. 1.2b1 [69]. Light-color nanobar behaves like a dipole resonator while the two grey bars (below) display a quadrupole-like response. When the light-color nanobar is excited, we observe the absorption dip at the eigen-frequency of the quadrupole grey nanorods. One can also observe the Fano dip when a material of sharp dielectric function is placed at the hot spot of a gold MNP, Fig. 1.3.

One of the major problems in communication with propagating SPPs is that they decay very quickly due to the large damping rates of the metal.<sup>2</sup> The phenomenon of Fano resonance is not only the appearance of a dip in the absorption spectrum. Fano resonances are clearly shown to increase the lifetime of plasmon oscillations [71–73]. Fano resonance may avoid the excitation of the plasmonic oscillations in the steady-state (after long times), but, this is not the case for initial times. Fano-enhanced lifetime of plasmons results in the further accumulation of the field strength at the hot

<sup>2</sup>Decay rate is determined by the dielectric response of the metal at the resonance frequency [70]. It is independent of the MNP shape.

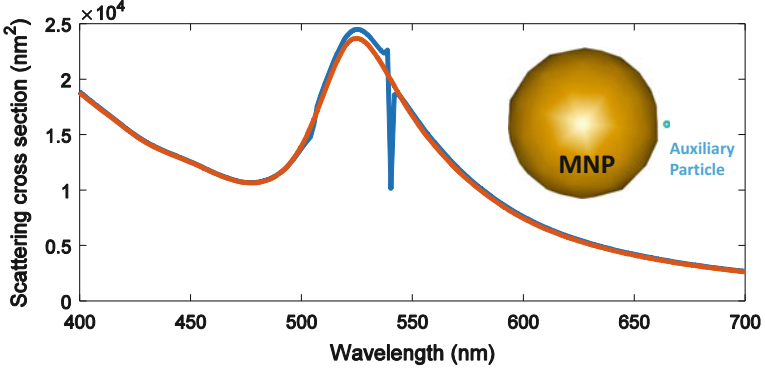


**Fig. 1.3** The Fano dip forms when an auxiliary particle of sharp dielectric function is placed at the hot spot of a gold MNP. The 3D simulation is performed with the MNPBEM toolbox [89, 90] with actual dielectric function for gold

spots. This gives rise to much stronger field enhancements in the hot spots, dark-hot resonances [74], which becomes maximum exactly at the center of the transparency window. This phenomenon is adopted cleverly to further enhance the nonlinear processes. Both hot spots –excited one and the one into which converted frequency emerges– are tuned to coincide with two such dark-hot resonances in four-wave-mixing (FWM) [75] and SERS [7, 76, 77] processes. Nonlinearity enhancement is possible also without altering the field at the hot spots, hot spots (Sect. 1.3.3) via path interference effects in the nonlinear response [78].

In fact, Fano resonances can further enhance the hot spot field not only in the initial times. Below, we show that the hot spot field can also be enhanced in the steady state via path interference effects. We describe the physics of the coupled (MNP-QE) system, derive a Hamiltonian and obtain a single expression, (1.8), for the linear response (plasmon amplitude) of the MNP.

A MNS is illuminated with an EM field of frequency  $\omega$ . The plasmon mode of the MNS, into which  $\omega$  overlaps, is excited strongly. Plasmon resonance of the MNS,  $\Omega$ , need not be tuned with  $\omega$ . A quantum emitter, QE (e.g. a color center in nanosize diamond or a molecule), is placed into the hot spot of the MNS. The near-field of the localized plasmon (polarization) interacts strongly with the dipole moment of the QE. The localized plasmon field is incomparably intense (e.g. five orders of magnitude [79]) compared to the incident one. So, one can neglect the coupling of the QE to the incident light. Therefore, Hamiltonian contains the energy of the plasmon mode, excitation energy of the QE, interaction of the QE with the plasmon mode and the coupling of the  $\omega$  field driving the MNS hot spot

$$\hat{H} = \hbar\Omega\hat{a}^\dagger\hat{a} + \hbar\omega_{eg}|e\rangle\langle e| + \hbar(f|e\rangle\langle g|\hat{a} + H.c.) + \hbar(\hat{a}^\dagger\varepsilon_p e^{-i\omega t} + H.c.), \quad (1.1)$$

where  $\hat{a}^\dagger\hat{a}$  gives the number of excited plasmons and  $|e\rangle$ ,  $|g\rangle$  are the excited, ground states of the QE. We set ground state energy of the QE to zero. In the interaction

term, a plasmon is annihilated and the QE is pumped from ground state to the excited one. Here, we work in terms of quantized field  $\hat{a}$  for plasmon, because it is easier to track and derive the equations of motion (EOM) using, e.g.  $i\hbar\dot{\hat{a}} = [\hat{a}, \hat{H}]$ , and they are ready to be used in quantum optics calculations on non-classical features [35]. If we define  $\hat{\rho}_{i,j} = |i\rangle\langle j|$  for the density matrix operator of the QE,  $i, j = e, g$ , the equation of motion (EOM) can be obtained as

$$\dot{\hat{a}} = (-i\Omega - \gamma)\hat{a} - if^*\hat{\rho}_{ge} + \varepsilon_p e^{-i\omega t}, \quad (1.2)$$

$$\dot{\hat{\rho}}_{ee} = -\gamma_{ee}\hat{\rho}_{ee} - if\hat{a}\hat{\rho}_{ge}^\dagger + if^*\hat{a}^\dagger\hat{\rho}_{ge}, \quad (1.3)$$

$$\dot{\hat{\rho}}_{ge} = (-i\omega_{eg} - \gamma_{eg})\hat{\rho}_{ge} + if^*\hat{a}(\hat{\rho}_{ee} - \hat{\rho}_{gg}), \quad (1.4)$$

where we introduce  $\gamma \sim 10^{13} - 10^{14}$  Hz for plasmon decay rate and  $\gamma_{eg} \sim 10^9$  Hz for quantum dots (QDs), or  $10^{12}$  Hz for molecules. We note that this treatment does not take the Purcell and the retardation effects into account. One can take the Purcell effect into account partially by considering a higher effective decay rate for the QE [35]. The effect of the retardation is rather small due to the nm dimensions of the MNSs. In the nonlinear response, retardation leads to a narrowing in the band where enhancement appears due to the Fano resonances. In the steady-state, both QE and the plasmon mode oscillates with the driving frequency  $\sim e^{-i\omega t}$ ,  $\hat{\alpha} = \tilde{\alpha}e^{-i\omega t}$  and  $\hat{\rho}_{ge} = \tilde{\rho}_{ge}e^{-i\omega t}$ . Equations for the steady-state amplitudes become

$$[i(\Omega - \omega) + \gamma]\tilde{\alpha} = -if^*\tilde{\rho}_{ge} + \varepsilon_p, \quad (1.5)$$

$$[i(\omega_{eg} - \omega) + \gamma_{eg}]\tilde{\rho}_{ge} = if\tilde{\alpha}(\tilde{\rho}_{ee} - \tilde{\rho}_{gg}), \quad (1.6)$$

$$\gamma_{ee}\tilde{\rho}_{ee} = -if\tilde{\alpha}\tilde{\rho}_{ge}^* + if^*\tilde{\alpha}^*\tilde{\rho}_{ge}. \quad (1.7)$$

When one plugs (1.6) in (1.5), the steady-state amplitudes for the plasmon excitation can be obtained as

$$\tilde{\alpha} = \frac{\varepsilon_p}{[i(\Omega - \omega) + \gamma] - \frac{|f|^2 y}{[i(\omega_{eg} - \omega) + \gamma_{eg}]}}. \quad (1.8)$$

Equation (1.8) is easy to interpret in this simple form. First thing to note: if QE-MNS coupling is absent,  $f = 0$ ,  $\tilde{\alpha}$  becomes the response of a field<sup>3</sup> in a damped cavity [20]. When the coupling is significant, the second term in the denominator modifies the nonlinear response. Secondly, transparency for  $\omega = \omega_{eg}$  can be seen explicitly in (1.8). When  $\omega = \omega_{eg}$  and  $f$  is significant, the second term of the denominator becomes  $f^2\Omega y\gamma_{eg}^{-1}$ . When we scale all the frequencies by the optical drive,  $\omega$ ,  $\gamma_{eg}^{-1}$  becomes very large. We note that  $\gamma_{eg}$  is very small compared to  $\omega$ . In this case, the

---

<sup>3</sup>There exists a small difference between the response of a field in the cavity and of a damped harmonic oscillator. In the former, damping  $-\gamma\hat{a}$  is introduced on the field amplitude [34, 35]. In the latter, damping is introduced “only” on the momentum operator  $-\gamma\hat{p}$ . Whereas, in the former  $\gamma$  appears in both  $\hat{x}$  and  $\hat{p}$  operators. One can realize this best in an opto-chemical system [80]. As already used in [34, 35], the former one is more appropriate for the plasmon (field) decay.

second term dominates the denominator and results a very small  $\tilde{\alpha}$  which yields the observed transparency.<sup>4</sup> One can note that transparency always appears at the frequency of the QE's level spacing  $\omega_{eg}$ .

Thirdly, we observe a contrary effect. We can choose  $\omega_{eg}$  such that the real part of the second term of the denominator cancels the real part of the first (nonresonant) term  $[i(\Omega - \omega) + \gamma]$ . Hence, resonant plasmon excitation ( $\omega = \Omega$ ) can be achieved at an off-resonant frequency ( $\omega \neq \Omega$ ), or even at a far-off-resonance frequency, when  $\omega_{eg}$  introduces the correct interference of the paths. One can observe the similar effects by coupling MNS with a non-quantum object, e.g. a quadrupole dark plasmon mode of larger lifetime. Equations are similar to the one we obtain here [73].

One can also obtain information about the time evolution of the coupled system by numerically iterating (1.2)–(1.4) in time with  $\hat{a} \rightarrow \alpha$  and  $\hat{\rho}_{ij} \rightarrow \rho_{ij}$  [35]. We observe that plasmon decay can be slowed down by the long excitation lifetime of the QE [71–73]. Similarly, plasmon lifetime enhancement effect can also be observed in an all-plasmonic (classical) system. In [73], we also present this in 3-dimensions. A gold MNP is coupled to a nanostructure with a longer decay time. When the gold MNP is excited by a Gaussian pulse, solutions of the 3-dimensional Maxwell equations indicate a 5 times slower decay of the plasmons in the MNP.

In [73], we observe something which is much more important than the enhancement in the mean lifetime of plasmons: An ambient field remains in the coupled system even after very long times. We also confirm the presence of the ambient field by fitting two exponentials to the longer-time response of the coupled system. Presence of such an ambient field for long-times can be beneficial for applications such as light harvesting and photovoltaic solar cells.

A reverse (in fact a complementary) effect occurs in the QE's side. When the QE is initially in the excited state  $\rho_{ee}(0) = 1$ , within the absence of plasmonic excitation  $\alpha(0) = 0$ , it decays  $\sim 10$  times faster in the coupled system [36], see Fig. 1.4a. Such an effect has been observed also in experiments [82], Fig. 1.4b. Fluorescence rate of a QE increases for closer spacing to a MNS, till quenching appears due to very strong coupling, Fig. 1.4b [83]. In some experiments thousands of times enhancement is observed in the fluorescence rate [84]. In the calculation of the enhanced decay rate for a QE, one needs to consider the combination (multiplication) of the following two factors: First factor is the enhanced damping of the QE in the coupled system, that is (1.2)–(1.4). The second factor is the change of density of states into which the QE can spontaneously decay, in the presence of the nearby MNS, that is the Purcell effect. One may also desire to compare the results of the simple model, (1.2)–(1.4), with the 3-dimensional simulations. In this case, one also needs to take care of the change in the modes trapped between the two particles.

Engineering the lifetime of plasmons and quantum emitters are important in technological applications. Controlling (turning on/off) the coupling between a QE and a MNS, one can read, write and store a quantum bit with desired speeds and time.

---

<sup>4</sup>The most famous phenomenon with the EIT is the slow-light propagation. A similar phenomenon also appears with Fano resonances [81].



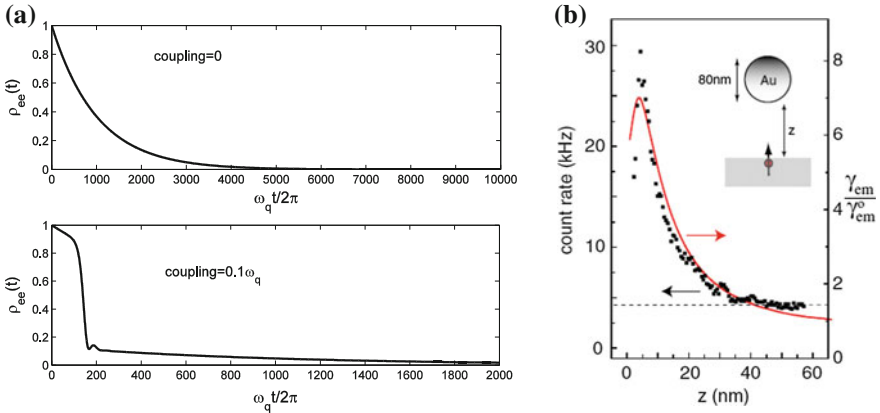


**Fig. 1.4** **a** Comparison of the durations for the excited quantum emitter to decay into the ground state [36]. **b** Fluorescence rate as a function of particle-surface distance for a vertically oriented molecule [83]

In quantum optics, this is studied in single-photon sub/superradiant systems [85]. In such systems, however, preservation of coherence is a big challenge.

### 1.3 Fano Resonances in Nonlinear Response

There are three factors, multiplying each other, plasmonics can provide for the enhancement of nonlinear processes. (i) Localization of the incident radiation into hot spots can increase the local intensity 5 orders of magnitude. The enhanced intensity also enhances the nonlinear processes which are proportional to the higher powers of the local electric field [38]. This is the major contribution to the nonlinear enhancement, e.g., enabling surface enhanced Raman scattering (SERS). This enhancement factor can be  $10^5$  in SHG [86],  $10^6$  in FWM [87] and  $10^{10}$  in SERS [88]. (ii) Fano resonances in the linear response can enhance the localized field furthermore [74]. This further enhancement in the hot spot field enhances the nonlinear process more. (iii) Finally, another factor, multiplying (i) and (ii), originates from the path interference effect in the nonlinear response. Nonlinear processes can be enhanced and suppressed by constructive and destructive interferences of the frequency conversion paths. This enhancement is called “silent”, since the enhancement takes place with unmodified hot spot intensity [78].

Path interference effects in the nonlinear response appear both for coupling to a classical and a quantum auxiliary object. Similar to the Fano resonances in the linear response, coupling of the frequency converter with an auxiliary dark (long-live) plasmon mode can enhance and suppress the nonlinear processes.

In this section, we examine the enhancement and suppression phenomena due to path interference in the nonlinear response, for SHG, FWM and SERS. We obtain the plasmon amplitudes of the generated (converted) frequencies in the steady-state. The form of the nonlinear amplitudes, see (1.23), (1.28), (1.29) and (1.30), is common to all processes. Furthermore, it is also common to the linear response demonstrating path interferences, see (1.8). That is, the reason for the enhancement and suppression to appear is common to linear and nonlinear responses. They can be explicitly demonstrated via cancellations in the denominator of a simple equation.

We calculate amplitudes for the plasmons oscillating at the converted frequency, i.e.  $2\omega$ , in SHG. Frequency-converted plasmons can radiate to the far-field (observed) directly by radiation reaction or via a fluorescent molecule resonant to the generated frequency. The intensity, observed in the experiments, is proportional to the number of plasmons oscillating at the nonlinear frequency. Hence, by comparing the number of plasmons one can also compare the far-field intensities.

In the following, we first study the SH response of a MNS coupled to a QE, in Sects. 1.3.2.1 and 1.3.2.2. We desire to control the SH response of the MNS via the presence of a QE. We use a basic model and obtain the steady-state amplitude for the generated SH plasmons. We examine the denominator of this amplitude, (1.23), and demonstrate why enhancement and suppression take place. Then, in Sect. 1.3.2.3, we compare the predictions of our model with the exact solutions of the 3-dimensional Maxwell equations. We confirm that enhancement of the SHG process is observed in the predicted spectral position even when the retardation effects are taken into account. Enhancement appears in a narrower spectrum due to the retardation effect. In Sect. 1.3.2.4, we show that SHG enhancement emerges also when a dark plasmon mode (of long lifetime) is coupled to the SHG converter in place of the QE. We present our experiment on SHG with coupled metal nanowire (MNW)-metal bipyramid system. We explore that, in the experiment, such a Fano enhancement enables the observation of the SH signal with a continuous wave (CW) laser source. Path interference is introduced by coupling of the MNW to the long-live dark plasmon mode bipyramid supports. In Sect. 1.3.2.5, we discuss another experiment of our group where we demonstrate the background-free excitation of molecules via SHG. Molecules are placed in the vicinity of a plasmonic SH converter. The molecules, of resonance close to the SH frequency, can both enhance the SHG and report the quadrupolar SH plasmon oscillations to the far-field. In Sect. 1.3.3, using the exact 3-dimensional solutions of the Maxwell equations, we demonstrate that SERS can be enhanced *silently* via path interference in the nonlinear response. This is the enhancement factor (iii). In Sect. 1.3.4, on FWM process, we discuss utilizations of path interference effects. When multiple plasmonic conversion paths interfere, nonlinearity can be enhanced 15 times more compared to interference of two paths. That is, the enhancement factor (iii) can further be multiplied by 15. One could also define the enhancement due to multiple interferences as a (iv)th factor.

Before all of this, in Sect. 1.3.1, we introduce the overlap integrals since they play a key role in determining the strengths of the linear and nonlinear processes. They yield the selection rules. We also study the physics of excitation and frequency conversion processes via these overlap integrals.

### 1.3.1 Overlap Integrals and Selection Rules

#### 1.3.1.1 Excitation of a Plasmon Mode

In typical experiments and solar cell applications, source behaves like a plane wave (PW) at the MNSs. PW excitation drives the localized surface plasmon (LSP) mode into which its frequency matches. Interaction of the PW source with the polarization field of the plasmon can be written as

$$H_{\text{drive}} = \int d^3\mathbf{r} \epsilon(\mathbf{r}) \mathbf{E}_1(\mathbf{r}) \mathbf{E}_0 e^{ikz} e^{-i\omega t} + H.c. \quad (1.9)$$

where  $\mathbf{E}_1(\mathbf{r})$  is the spatial profile of the excited plasmon mode. For brevity, we consider a single plasmon mode, but it is straight forward to generalize to a multi-mode system. The profile  $\mathbf{E}_1(\mathbf{r})$  can be calculated using softwares for plasmonic calculations, e.g. using the *eigenstat* command in the freeware toolbox MNPBEM [89, 90].  $\epsilon(\mathbf{r})$  is the dielectric function of the MNS, which can be described with a 3D step-function. It is constant in the MNS and zero elsewhere. We can move to second-quantized scheme by  $\mathbf{E}_1(\mathbf{r}) \rightarrow \mathbf{E}_1(\mathbf{r}) \hat{a}_1$  where  $\hat{a}_1^\dagger$  creates a plasmon in the  $E_1$ -mode [91]. Then, (1.9) becomes,

$$H_{\text{drive}} = \left( E_0 \int d^3(\mathbf{r}) \epsilon(\mathbf{r}) \mathbf{E}_1(\mathbf{r}) \cdot \hat{\mathbf{x}} e^{ikz} \right) \hat{a}_1 e^{-i\omega t} + H.c. \quad (1.10)$$

The integral in the parenthesis, in dimensions of energy, can also be written as  $H_{\text{drive}} = \hbar \left( \hat{a}_1^\dagger \varepsilon_p e^{-i\omega t} + H.c. \right)$ , where  $\varepsilon_p$  is proportional to the amplitude of the driving field  $E_0$  and determined by the integral in the parenthesis. Equation (1.10) shows that PW source cannot excite a quadrupole plasmon mode for a symmetric MNS. Because, overlap integral  $\varepsilon_p$  vanishes for an odd integrand function. This is the reason quadrupole modes are dark-plasmon modes. A quadrupole plasmon mode can be excited via a near-field interaction, e.g. interaction with an excited dipole-like plasmon mode. A quadrupole mode also has a longer lifetime since its radiation (coupling) to the far-field (PW-modes) vanishes. This is again due to the vanishing overlap integral with the vacuum modes. We observe this phenomenon in our experiment [92] and use molecules to report quadrupole plasmon excitation to the far-field. On the other hand, PW can excite a dipole-like plasmon mode. Because, the integrand in (1.10) becomes even and integration does not vanish. Due to similar considerations, dipole plasmon modes can radiate to far-field.

#### 1.3.1.2 Second Harmonic Generation

It is experimentally demonstrated that localized plasmon modes are responsible for the SHG process in MNSs [86, 93]. That is, two plasmons in  $\hat{a}_1$ -mode, oscillating

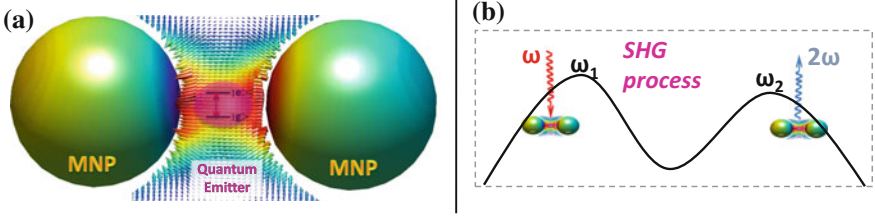


**Fig. 1.5** **a** Coupling of MNS with a quantum emitter (QE) whose decay rate is small. QE is placed at the hot spot of the MNP dimer. **b** Schematic representation of the SHG process [99]

with  $\omega$ , combine to yield a single plasmon in  $\hat{a}_2$ -mode oscillating with  $2\omega$  (we depict this in Fig. 1.5). Actually, involvement of plasmons are apparent considering the following observation. Both the excited ( $\omega$ ) and the converted ( $2\omega$ ) field intensities are enhanced at two (input and output) hot spots. This yields a quadratic enhancement of nonlinear processes [46]. The Hamiltonian for such a process can be written as

$$H_{\text{SH}} = \int d^3\mathbf{r} \hat{\mathbf{E}} \cdot \hat{\mathbf{P}} = \int d^3\mathbf{r} \mathbf{E}_2^{(-)}(\mathbf{r}) \chi_2(\mathbf{r}) \mathbf{E}_1^{(+)}(\mathbf{r}) \mathbf{E}_1^{(+)}(\mathbf{r}) + H.c. \quad (1.11)$$

where  $\chi_2(\mathbf{r})$  is the second order polarization in dimensions of  $[\epsilon_0]/[\text{E-field}]$ . One can also consider  $\chi_2(\mathbf{r})$  as a 3D step function.

The process in (1.11) is: annihilate two  $\omega$  plasmons in the  $\hat{a}_1$ -mode and create a  $2\omega$  plasmon in the  $\hat{a}_2$ -mode [91]. Using  $\mathbf{E}_i^{(+)}(\mathbf{r}) = E_i(\mathbf{r})\hat{a}_i$  and  $\mathbf{E}_i^{(-)}(\mathbf{r}) = E_i^*(\mathbf{r})\hat{a}_i^\dagger$ , one obtains

$$\hat{H}_{\text{SH}} = \left( \int d^3\mathbf{r} E_2^*(\mathbf{r}) E_1^2(\mathbf{r}) \chi_2(\mathbf{r}) \right) \hat{a}_2^\dagger \hat{a}_1 \hat{a}_1 + H.c., \quad (1.12)$$

where the overlap integral  $\hbar\chi^{(2)} = \int d^3(\mathbf{r}) E_2^*(\mathbf{r}) E_1^2(\mathbf{r}) \chi_2(\mathbf{r})$  determines the strength of the SHG process.  $\chi_2(\mathbf{r})$  is constant over the MNS and zero outside.

$\chi^{(2)}$  integral demonstrates us a well-known selection rule for the SHG process; SHG is not observed in the far-field for a centro-symmetric MNS. The reason for this observation is as follows. Since we externally drive the  $\hat{a}_1$ -mode,  $E_1(\mathbf{r})$  is dipole-like. So,  $E_1^2(\mathbf{r})$  is an even function. If  $E_2(\mathbf{r})$  is an odd function, integration in (1.12) vanishes since  $\chi_2(\mathbf{r})$  is even for a centro-symmetric MNS. Therefore, SHG ( $2\omega$  oscillations) takes place into an even  $\hat{a}_2$ -mode only. However, an even plasmon mode does not couple to the far-field as discussed in (1.10). Its coupling with the vacuum modes vanishes. Consequently, in a centro-symmetric MNS, one cannot observe the SH generated plasmons in the far-field. This is why, in the experiment [92] we place molecules in the vicinity of MNSs. They report the  $2\omega$  plasmons to the far-field. On the other hand, when  $\chi_2(\mathbf{r})$  is not centro-symmetric,  $\chi^{(2)}$  integral does not vanish completely.

In third harmonic generation (THG) process, overlap integral is  $\chi^{(3)} \sim \int d^3(\mathbf{r}) \chi_3(\mathbf{r}) E_2^*(\mathbf{r}) E_1^3(\mathbf{r})$ .  $E_2(\mathbf{r})$ -mode supports the  $3\omega$  oscillations. When the  $E_2(\mathbf{r})$  is

dipole-like,  $\chi^{(3)}$  does not vanish even the MNS is centro-symmetric. THG can be observed since  $E_2(\mathbf{r})$  can couple to the far-field.

Integral in (1.12) also explains why plasmons are involved in the SHG process [93]. Lets suppose that  $2\omega$  oscillations did not emerge into the  $\hat{a}_2$ -mode, but directly coupled into the free space. In this case,  $E_2(\mathbf{r})$  would be a PW, or another unlocalized wave. This would yield a much smaller  $\chi^{(2)}$  integral. Thus, SHG with two localized modes dominates over the one where frequency converted directly to the free-space, as unlocalized photons.

### 1.3.1.3 Four Wave Mixing

Four wave mixing (FWM) is governed by the third order susceptibility,  $\chi_3$ . Two plasmon modes are pumped with  $\omega_1$  and  $\omega_2$  frequencies and a different frequency, e.g.  $\omega_3 = 2\omega_1 - \omega_2$ , emerges in another mode, see Fig. 1.13. Two  $\omega_1$  plasmons in  $\hat{a}_1$ -mode is annihilated and two plasmons of different frequencies  $\omega_2$  and  $\omega_3$  are created in  $\hat{a}_2$  and  $\hat{a}_3$ -modes. Creation of  $\hat{a}_2$ -mode plasmons are stimulated by the pump laser. Similar to SHG, Hamiltonian can be written as

$$\hat{H}_{\text{FWM}} = \left( \int d^3(\mathbf{r}) E_3^*(\mathbf{r}) \chi_3(\mathbf{r}) E_2^*(\mathbf{r}) E_1^2(\mathbf{r}) \right) \hat{a}_3^\dagger \hat{a}_2^\dagger \hat{a}_1^2 + H.c., \quad (1.13)$$

where the integration in parenthesis can be defined as  $\hbar\chi_{\text{FWM}}$ . We note that  $\chi_{\text{FWM}}$  does not vanish even if all 3 plasmon modes have dipole symmetry. Better overlap of the profiles of the three plasmon modes implies a strong FWM process.

### 1.3.1.4 Surface Enhanced Raman Scattering

Field localized at the hot spots also enhance the Raman process. Localized plasmon polarization interacts with the vibrational modes of a molecule. In the Stokes shift, a plasmon ( $\omega$ ) is absorbed by the molecule, on return exciting a vibrational mode ( $\nu$ ) and another plasmon of lower energy ( $\omega_R$ ). It is experimentally demonstrated [94] that emergence of the generated frequency into a second plasmon mode yields a much larger Raman intensity. One can write the Hamiltonian for the process similarly as

$$\hat{H}_R = \left( \int d^3(\mathbf{r}) \rho(\mathbf{r}) E_1^*(\mathbf{r}) E_2(\mathbf{r}) \right) \hat{b}^\dagger \hat{a}_1^\dagger \hat{a}_2 + H.c., \quad (1.14)$$

where  $\hat{b}^\dagger$  creates a phonon in the vibrational mode of the molecule. Molecule density  $\rho(\mathbf{r})$  can be considered as a 3D step function. The overlap integral in (1.14) defines the selection rules for Raman process [95]. The same form of the Hamiltonian can be derived from an opto-mechanical type coupling between the oscilla-

tions of the molecule and the plasmon field [19, 20]. One merely need to consider  $\hat{E}(\mathbf{r}) = \hat{E}_1(\mathbf{r})\hat{a}_1 + \hat{E}_2(\mathbf{r})\hat{a}_2$  in  $\hat{H} = \hbar g(\hat{b}^\dagger + \hat{b})\hat{E}^\dagger(\mathbf{r})\hat{E}(\mathbf{r})$  [78].

A control and knowledge on the overlap integrals has crucial importance in technical applications. A better overlap between  $\hat{E}_1(\mathbf{r})$  and  $\hat{E}_2(\mathbf{r})$  may result a stronger Raman intensity. Equation (1.14), however, tells us that; if the two plasmon modes are engineered to overlap at small (sharp) spatial regions, a better spatial resolution in Raman imaging can be achieved [40, 78].

### 1.3.2 Enhancement and Suppression of SHG

In this part, (a) we present a basic model for the SHG in a MNS. We examine the effect of the presence of a QE, at the hot spot, on the SHG process. We obtain a steady-state amplitude, (1.23), which demonstrates us why enhancement and suppression is observed in the experiments [82]. This is simply due to the interplay of the two terms in the denominator. (b) We perform exact solutions of the 3D Maxwell equations and confirm the predictions of the simple model in the presence of retardation effects. (c) We present our experiment [96], and an accompanying theoretical model, demonstrating that SHG enhancement takes place also in an all-plasmonic system. (d) A second experiment [92] of our group shows that molecules can be used both for the SHG enhancement as well as for reporting the SH signal to the far-field.

#### 1.3.2.1 Basic Model

The physics of a MNS, performing SHG process, can be described as follows. A strong incident laser field of frequency  $\omega$  strongly couples to the first (low-energy) plasmon mode ( $\hat{a}_1$ ) and excites plasmon oscillations  $\sim e^{-i\omega t}$ , see Fig. 1.5. The two of the plasmons in the  $\hat{a}_1$ -mode combine, due to the strong overlap integral, (1.12), and creates a single  $2\omega$  plasmon in the  $\hat{a}_2$ -mode, oscillating as  $e^{-i2\omega t}$ . The resonances of the modes,  $\omega_1$  and  $\omega_2$  respectively, need not be resonant to  $\omega$  and  $2\omega$ . If a QE is present at the hot spot (of the  $\hat{a}_2$ -mode), the generated  $2\omega$  plasmon strongly couple to that QE. We observe that presence of the QE can modify the SH process dramatically, depending on its level spacing,  $\omega_{eg}$ .

Hamiltonian of the system can be written as the sum of the terms  $\hat{H}_p = i\hbar(\hat{a}_1^\dagger \varepsilon_p e^{-i\omega t} - \hat{a}_1 \varepsilon_p^* e^{i\omega t})$ ,  $\hat{H}_{\text{MNS}} = \hbar\omega_1 \hat{a}_1^\dagger \hat{a}_1 + \hbar\omega_2 \hat{a}_2^\dagger \hat{a}_2$ ,  $\hat{H}_{\text{QE}} = \hbar\omega_{eg} |e\rangle\langle e|$ ,  $\hat{H}_{\text{SH}} = \hbar\chi^{(2)}(\hat{a}_2^\dagger \hat{a}_1 \hat{a}_1 + \hat{a}_1^\dagger \hat{a}_1^\dagger \hat{a}_2)$ ,  $\hat{H}_{\text{int}} = \hbar(f_1 \hat{a}_1^\dagger |g\rangle\langle e| + f_1^* |e\rangle\langle g| \hat{a}_1 + f_2 \hat{a}_2^\dagger |g\rangle\langle e| + f_2^* |e\rangle\langle g| \hat{a}_2)$ , where  $\hat{H}_p$  is the interaction of the pump laser with the  $\hat{a}_1$ -mode,  $\hat{H}_{\text{MNS}}$  and  $\hat{H}_{\text{QE}}$  are the energies of the two plasmon modes and the QE,  $\hat{H}_{\text{SH}}$  is the SHG process of origin described in (1.12),  $\hat{H}_{\text{int}}$  is the interaction of the SH generated plasmons in the  $\hat{a}_2$ -mode, with the QE placed at the hot spot. We choose  $\omega_{eg}$  around  $2\omega$ , far off-resonant to the  $\hat{a}_1$ -mode. So, we neglect  $f_1$  interaction.

In this work, we are not interested in the quantum optical features of the modes. We replace the  $\hat{a}_i$  operators by complex amplitudes  $\alpha_i$  [35]. Before doing that, however, we use the advantage of Heisenberg equation,<sup>5</sup> e.g.  $i\hbar\hat{a}_i = [\hat{a}_i, \hat{H}]$ , to determine the equations of motion (EOM) for  $\hat{a}_i$ . Then, we perform the replacement  $\hat{a}_i \rightarrow \alpha_i$  and obtain [99]

$$\dot{\alpha}_1 = (-i\omega_1 - \gamma_1)\alpha_1 - i2\chi^{(2)}\alpha_1^*\alpha_2 - if_1\rho_{ge} + \varepsilon_p e^{-i\omega t} \quad (1.15)$$

$$\dot{\alpha}_2 = (-i\omega_2 - \gamma_2)\alpha_2 - i\chi^{(2)}\alpha_1^2 - if_2\rho_{ge} \quad (1.16)$$

$$\dot{\rho}_{ge} = (-i\omega_{eg} - \gamma_{eg})\rho_{ge} + i(f_1\alpha_1 + f_2\alpha_2)(\rho_{ee} - \rho_{gg}) \quad (1.17)$$

$$\dot{\rho}_{ee} = -\gamma_{ee}\rho_{ee} + i[(f_1\alpha_1^* + f_2\alpha_2^*)\rho_{ge} - (\alpha_1 + \alpha_2)\rho_{ge}^*] \quad (1.18)$$

for the plasmon amplitudes  $\alpha_{1,2}$  and the density matrix of the QE [100]. We introduce the decay rates  $\gamma_{1,2} \sim 10^{14}$  Hz and  $\gamma_e \sim 10^9$  Hz for the MNP and the QE respectively, with  $\gamma_{eg} = \gamma_e/2$ . The typical decay rates for molecules are  $\gamma_{ee} \sim 10^{12}$  Hz [83] and  $\gamma_{ee} \sim 10^9$  Hz for quantum dots [31]. We also have  $\rho_{ee} + \rho_{gg} = 1$ .

We seek for the steady-state solutions where  $\alpha_1$  and  $\alpha_2$  oscillate as  $e^{-i\omega t}$  and  $e^{-i2\omega t}$ . When we use  $\alpha_1(t) = \tilde{\alpha}_1 e^{-i\omega t}$ ,  $\alpha_2(t) = \tilde{\alpha}_2 e^{-i2\omega t}$ ,  $\rho_{ge}(t) = \tilde{\rho}_{ge} e^{-i2\omega t}$ ,  $\rho_{ee}(t) = \tilde{\rho}_{ee}$ , we obtain the equations for amplitudes [99]

$$[i(\omega_1 - \omega) + \gamma_1]\alpha_1 + i2\chi^{(2)}\alpha_1^*\alpha_2 = \varepsilon_p, \quad (1.19)$$

$$[i(\omega_2 - 2\omega) + \gamma_2]\alpha_2 + i\chi^{(2)}\alpha_1^2 = -if_2\rho_{ge}, \quad (1.20)$$

$$[i(\omega_{eg} - 2\omega) + \gamma_{eg}]\rho_{ge} = if_2\alpha_2(\rho_{ee} - \rho_{gg}), \quad (1.21)$$

$$\gamma_{ee}\rho_{ee} = if_2(\alpha_2^*\rho_{ge} - \alpha_2\rho_{ge}^*). \quad (1.22)$$

One does not need to solve (1.19)–(1.22) in order to gain understanding on the path interference effect. Eliminating  $\tilde{\rho}_{eg}$  in (1.20) and (1.21), we obtain

$$\tilde{\alpha}_2 = \frac{i\chi^{(2)}}{\frac{|f_2|^2 y}{i(\omega_{eg} - 2\omega) + \gamma_{eg}} - [i(\omega_2 - 2\omega) + \gamma_2]} \tilde{\alpha}_1^2. \quad (1.23)$$

Once noting that the number of SH generated plasmons are exceedingly small, one can realize that  $\tilde{\alpha}_1$  is not altered much by the strength of the SHG process. So, (i)  $\tilde{\alpha}_1$  can be considered as almost fixed throughout the SHG process. (ii) QE interacts with the plasmons in the  $\hat{a}_2$ -mode. Thus, the population inversion  $y = \rho_{ee} - \rho_{gg}$  is very close to  $y \simeq -1$ .

---

<sup>5</sup>Use of Heisenberg EOM possesses some serious advantages especially in performing separation of variables in nonlinear differential equations [97, 98].

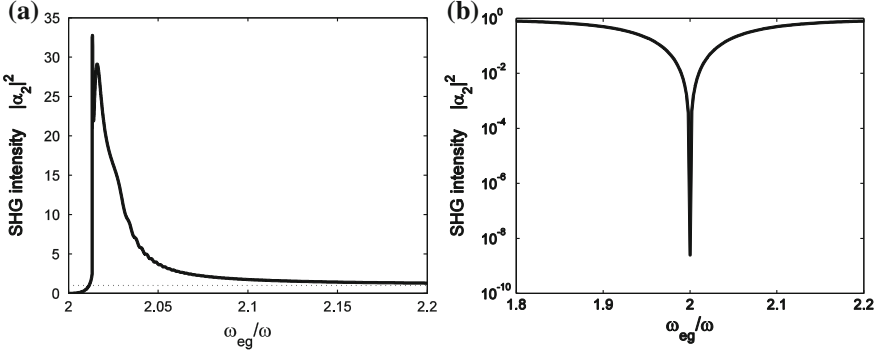


**Fig. 1.6** **a** Enhancement and **b** suppression of SHG in a MNS [99].  $\omega_{eg}$  is the level-spacing of the quantum emitter (QE) attached to the MNS

### 1.3.2.2 Enhancement and Suppression

Equation (1.23) tells us the whole story on the origin of the enhancement and suppression phenomena for the SHG process. (1) In the denominator of (1.23), imaginary part of the first term,  $|f|^2 y / [i(\omega_{eg} - 2\omega) + \gamma_{eg}]$ , can be tuned to cancel the imaginary part of the second, the nonresonant  $[i(\omega_2 - 2\omega) + \gamma_2]$  term. That is, for the choice of the level spacing

$$\omega_{eg} = 2\omega + \frac{|f|^2 y}{\omega_2 - 2\omega} + \sqrt{\frac{|f_2|^4 |y|^2}{(\omega_2 - 2\omega)^2} - 4\gamma_{eg}^2}, \quad (1.24)$$

SHG can be *enhanced* about 30 times, see Fig. 1.6a. This enhancement factor (EF) is for the choice  $\gamma_2/\omega \sim 0.1$ . EF can be as large as 4 orders of magnitude when a high quality MNS, e.g.  $\gamma_2/\omega \sim 10^{-3}$  in [101] is considered. In (1.23), one can also observe that EFs like  $\sim 5$  does not necessitate a small  $\gamma_{eg}$ .

(2) *Suppression* of the SHG process can be read also from the denominator of (1.23) as follows. When the QE level spacing is chosen close to the SH frequency  $\omega_{eg} \approx 2\omega$ , the first term becomes  $|f_2|^2 y / \gamma_{eg}^2$ . Since  $\gamma_{eg} \sim 10^{-6}\omega$  for a QD and  $\gamma_{eg} \sim 10^{-3}\omega$  for a molecule, with  $f_2 \approx 0.1\omega$  and  $y \approx -1$ ,  $|f_2|^2 y / \gamma_{eg}^2$  term becomes very large. Then SHG is suppressed 2–7 orders of magnitude, Fig. 1.6b. Suppression phenomenon is also observed experimentally [82].

It is worth noting that results in Fig. 1.6 are obtained by the time evolution of (1.15)–(1.18), rather than using (1.23).



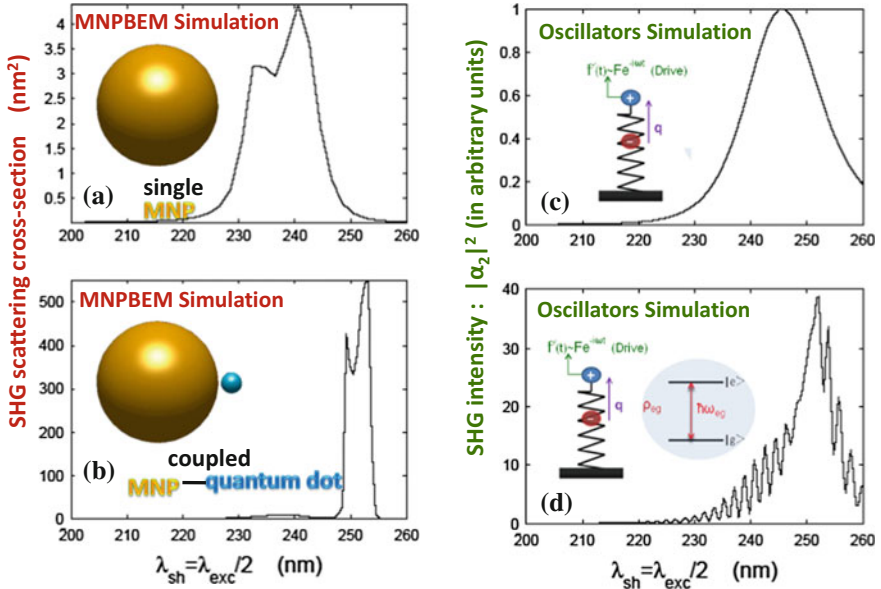


**Fig. 1.7** Comparison of the **a, b** exact solutions of the Maxwell equation with the **c, d** results of our analytical model, (1.15)–(1.18). We compare the SH response [99]. The simple model predicts both the presence of Fano enhancement and the spectral position of the Fano resonance correctly. MNPBEM [89, 90] is used in the simulations

### 1.3.2.3 Comparison with 3D Solutions

The simple model we study treats the system as if interaction and frequency conversion take place at a single point (position). It does not account the finite time for the oscillations of the plasmon field over the MNS. So, we test if the predicted enhancement effect would indeed appear, by performing 3-dimensional exact solutions of the Maxwell equations. We simulate SHG signal from a gold NP of 70 nm diameter in the (i) absence and (ii) presence of a 12 nm auxiliary object with a sharp spectral width. In the Maxwell simulations, for the  $\epsilon(\omega)$  of the gold NP, we use the Drude model with experimental parameters in MNPBEM [89, 90]. We model the auxiliary object by a Lorentzian,  $\epsilon(\omega) = 1 + \omega_p^2 / (\omega_{eg}^2 - \omega^2 - i\gamma_{eg}\omega)$ , where  $\omega_p$  determines the strength of the polarization. 12 nm is the typical dimensions of a quantum dot (QD). Although the damping rate of a QD can be as low as  $10^9$  Hz, we consider a moderate rate at  $10^{11}$  Hz in the Lorentzian.

Figure 1.7a, b demonstrate the SHG response of the gold NP with and without the presence of the auxiliary particle. We plot the spectrum of the generated SH field. We choose the polarization of the incident field along the x-direction, along the axis connecting the two particles, in order to obtain a hot spot of the gold NP near the auxiliary particle. In Fig. 1.7, we make a comparison with our simple analytical model using similar parameters with the 3D simulations. Comparing Fig. 1.7a, c, we observe a similar spectral width for the produced SH field. When an auxiliary object

(e.g. a QD) is present, in Fig. 1.7b, d, we observe the enhanced SH response (about 100 times) in a spectral region around  $\lambda_{\text{sh}} = 253$  nm in both 3D and analytical simulations. Spectral width for the Fano enhancement, however, is narrower in the 3D simulations. This is due to the presence of retardation effects in the interaction between the two particles. Analytical model treats the interaction as if it happens at a single point. A similar phenomenon is observed also in the SERS process, in a more apparent way, since the auxiliary particle is not close to the molecule producing the Raman process, see Fig. 1 in [78].

As a conclusion, one can appreciate that the analytical model is very successful in predicting the spectral position, here  $\lambda_{\text{sh}} = 253$  nm, where maximum SHG enhancement takes place.

### 1.3.2.4 Experiment 1: All-Plasmonic Fano Resonance

As already mentioned, Fano resonances in the linear response show up also in an all-plasmonic system. When the lifetime of a plasmonic mode (either belonging to the same MNP or to an auxiliary MNP) is larger than the excited plasmon mode, Fano resonances appear. This is due to the near-field coupling between the two modes, i.e. via  $f \sim \int d^3\mathbf{r} E_b^*(\mathbf{r}) E_2(\mathbf{r})$  overlap integral, with  $E_{2,b}(\mathbf{r})$  are the mode profiles for the short/long lifetime LSP modes, respectively. We show that, a similar phenomenon appears also in the nonlinear response due to the path interferences in the all-plasmonic system [96].

In our experiment [96], we measure the SH signal from (i) a silver nanowire (AgNW), (ii) silver bipyramid (AgBP), and (iii) a coupled AgNW-AgBP structure. While SH signal from a (i) AgNW is 1 (unity) and (ii) a AgBP is only 1/6, the coupled system (iii) produces a SH signal of 30 units. A bipyramid structure may not be a good SH converter, but it can support many long-live dark modes due to its size and symmetry. We measure the plasmon spectrum of the AuNW, see Fig. 1.8a. We depict the linear response of the AgNW and show the two plasmon modes, which the CW pump excites and the one into which SH oscillations emerge. We calculate the SH response of AgNW in the presence of coupling to AgBP. We show that a  $\sim 30$  times enhancement can take place due to the path interference, if the bipyramid supports a dark mode of lifetime only 10 times larger than that of AgNW, see Fig. 1.9b. We discuss that such a Fano enhancement makes the observation of SH signal possible with a CW light source in the experiment.

A simple analytical model can be derived also for the path interferences in an all-plasmonic system. In the Hamiltonian, given in Sect. 1.3.2.1, one need to perform the replacements  $\hat{H}_{\text{QE}} = \hbar(\omega_e|e\rangle\langle e| + \omega_g|g\rangle\langle g|) \rightarrow \hat{H}_b = \hbar\omega_b\hat{b}^\dagger\hat{b}$  and  $\hat{H}_{\text{int}} = \hbar(f_2|e\rangle\langle g|\hat{a}_2 + f_2^*\hat{a}_2^\dagger|g\rangle\langle e|) \rightarrow \hat{H}_{\text{int}} = \hbar(f_2\hat{b}^\dagger\hat{a}_2 + f_2^*\hat{a}_2^\dagger\hat{b}) + \hbar(f_1\hat{b}^\dagger\hat{a}_1 + f_1^*\hat{a}_1^\dagger\hat{b})$ . Here, second LSP mode of the converter MNP,  $\hat{a}_2$ , into which SH oscillations emerge, couples with a dark plasmon mode  $\hat{b}$ , e.g. a quadrupolar plasmon mode.  $\hat{b}$ -mode may belong to the SH converter MNP or, as well, it may belong to an auxiliary MNP placed near to the SH converter MNP.

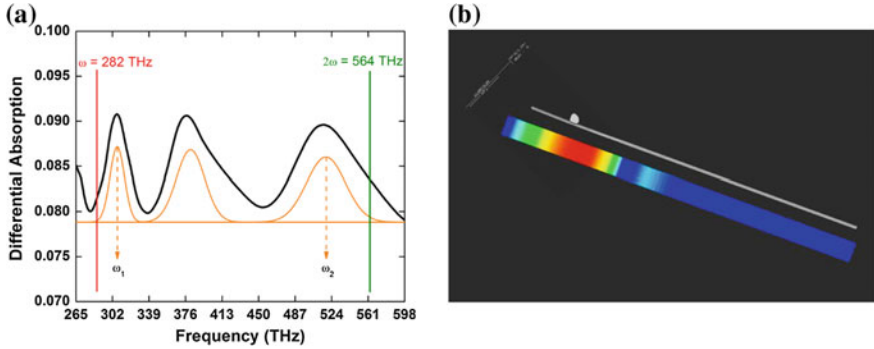


**Fig. 1.8** **a** Linear response of silver nanowire. The excited plasmon mode (282 THz) and the one into which SH signal (564 THz) emerges, are depicted [96]. **b** The SHG integral signal intensity as a colour bar. The enhancement originates from coupling of the AgNW with the silver bipyramid

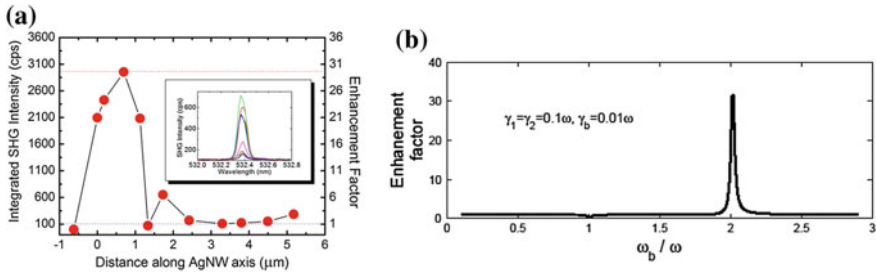


**Fig. 1.9** **a** SHG intensity and the enhancement factor (EF) obtained at different positions along the body of the AgNW, see Fig. 1.8b. **b** EF from the analytical model for different choices of the resonance ( $\omega_b$ ) of the auxiliary mode [96]. Enhancement appears due to Fano resonance

In difference to path interference via a QE, in Sect. 1.3.2.1, here we also consider the interaction of the quadrupolar (long-live) mode with the low energy plasmon mode ( $\hat{a}_1$ ) of the SH converter MNP, see Fig. 1.5. This is because, spectral width of the auxiliary plasmon mode is not as sharp as linear response of a QE. Its spectrum can overlap with the one of  $\hat{a}_1$ -mode.

Similar to Sect. 1.3.2.1, one can obtain [96]

$$\dot{\alpha}_1 = (-i\omega_1 - \gamma_1)\alpha_1 - f_1\alpha_b + \varepsilon_p e^{-i\omega t} - 2i\chi^{(2)}\alpha_1^*\alpha_2, \quad (1.25)$$

$$\dot{\alpha}_2 = (-i\omega_2 - \gamma_2)\alpha_2 - f_2\alpha_b - i\chi^{(2)}\alpha_1^2, \quad (1.26)$$

$$\dot{\alpha}_b = (-i\omega_b - \gamma_b)\alpha_b - f_1\alpha_1 - if_2\alpha_2, \quad (1.27)$$

using the Heisenberg EOM and making the replacement  $\hat{a}_i \rightarrow \alpha_i$  [35]. Once again, nonclassical features of the states are out of interest.

In this case, coupling of the auxiliary mode  $\hat{b}$  to the  $\hat{a}_1$ -mode allows the transfer of  $2\omega$  oscillations into the  $\hat{a}_1$ -mode, and,  $\omega$  oscillations into the  $\hat{b}$ -mode and into the  $\hat{a}_2$ -

mode indirectly. So, we need to consider  $\alpha_i(t) = \tilde{\alpha}_i^{(1)} e^{-i\omega t} + \tilde{\alpha}_i^{(2)} e^{-i2\omega t}$  for all  $i = 1, 2$ , b modes. Thus, we time evolve (1.25)–(1.27) and obtain the SH components  $\tilde{\alpha}_i^{(2)}$  from the Fourier transform of  $\alpha_i(t)$ . We consider the long time behaviour. The total number of  $2\omega$  plasmons is  $N = |\tilde{\alpha}_1^{(2)}|^2 + |\tilde{\alpha}_2^{(2)}|^2 + |\tilde{\alpha}_b^{(2)}|^2$ , is depicted in Fig. 1.9b.

We can also obtain an analytical form for the SH plasmon amplitude

$$\tilde{\alpha}_2 = \frac{i\chi^{(2)}}{\frac{|f|^2}{i(\omega_b - 2\omega) + \gamma_b} - i(\omega_2 - 2\omega) + \gamma_2} \tilde{\alpha}_1^2, \quad (1.28)$$

when the coupling of  $\hat{b}$  and  $\hat{a}_1$  mode is neglected. This is similar to the QE case, (1.23).

In Fig. 1.8a we depict the measured cross section (linear response) of the AgNW. The  $\omega = 282$  THz and  $2\omega = 564$  THz lines show the  $\lambda = 1064$  nm pump and the  $\lambda_{\text{sh}} = 532$  nm SH generated fields. The plasmon modes, these lines overlap,  $\omega_1$  and  $\omega_2$ , are the excited (driven) plasmon mode and the one into which  $2\omega$  oscillations emerge. When we use parameters similar with the experiment, we can obtain a  $\sim 30$  times enhancement in the SH field compared with the AgNW alone. In the analytical model we assign only a 10 times higher lifetime to the dark mode supported by the Ag bipyramid. We note that, in Fig. 1.9b the spectral width of the enhancement is wider compared to the one with a QE. Larger spectral width of a dark plasmon state makes Fano resonance appear in a wider band. So, they are easier to observe in experiments.

One may raise the following question. Could the enhancement in the SH signal be due to the formation of a hot spot region between the AgNW and AgBP? In our SHG simulation with the 3-dimensional Maxwell equations, we observe that SHG signal starts to decrease if the auxiliary particle is placed closer to the converter MNP, see Fig. 6 in [99]. We observe the similar behaviour in our simulations with 3D Maxwell equations for the SERS enhancement [78]. This is because, Fano resonance appears for weak hybridization between the two particles. When the interaction is very large, that is two MNPs are very close to each other, our simple analytical treatment fails. Because, one cannot treat the plasmon mode and the mode of the auxiliary particle as two different modes. It is noteworthy that the experiment (even though it is just a single data point between 1 and 2  $\mu\text{m}$ ) displays a behaviour in line with this discussion.

### 1.3.2.5 Experiment 2: Molecule(s) Enhancement and Reporter Agents

Activation of a single molecule (or a group of molecules) is important for switching and data storage applications. One can activate the molecules plasmonically when they are placed at the hot spots of the MNS. Such a method is not quite controllable, since the background field can also excite molecules undesirably. One can circumvent this difficulty as follows. We excite the MNS with a CW source of frequency  $\omega$ , but choose the energy level spacing of the molecule about  $\omega_{eg} \sim 2\omega$ . SH response of the

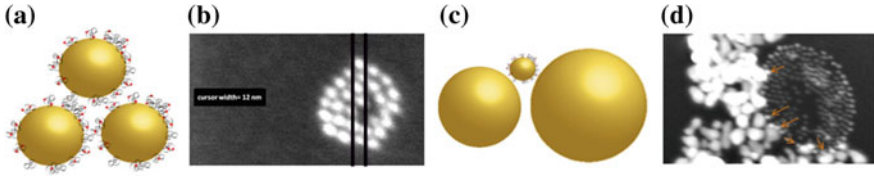


**Fig. 1.10** **a, b** 12 nm size gold NPs decorated with EYFP molecules. No SH signal is observed. We do not observe SHG also from the cluster of AuNPs of dispersed sizes 70–120 nm. **c, d** When the two clusters brought together, we observe SH signal at the interface [92]

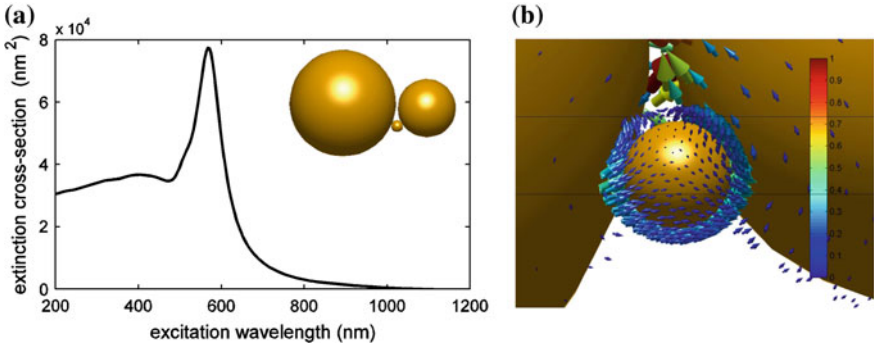


**Fig. 1.11** **a** The extinction cross-section of three hybridized AuNPs. Even though, SHG at  $\lambda/2 = 532$  nm is off-resonant with the second plasmon mode, insertion of a molecule with an absorption peak at  $\lambda_{eg} = 514$  nm enhances the SHG substantially. **b** Distribution of the electric field. An EYFP molecule attached to the 12 nm AuNP interacts with the 532 nm oscillations created in the quadrupole mode. This interaction leads to the Fano resonance and results in the 2–3 orders of magnitude enhancement of the SH conversion process [92]

MNS generates plasmons of  $2\omega$  frequency whose near-field excites the  $\omega_{eg} \sim 2\omega$  molecule. This way, only the peak of the activation pulse ( $\omega$ ) achieves to activate the molecule(s). However, SH response of MNSs is small even after accounting the effect of the localized field.

In our experiment [92], molecules both (i) Fano-enhance the SH signal about 3 orders of magnitude and (ii) report the excited  $2\omega$  quadrupolar plasmons to the far-field.

(a) We decorate 12 nm gold NPs (AuNPs) with enhanced yellow fluorescent (EYFP) molecules. When we illuminate the cluster of these NPs, see Fig. 1.10a, b, we can observe no SH signal. (b) We prepare a cluster of AuNPs of sizes dispersed between 70 and 120 nm. This is to break up the centro-symmetry and to obtain a better excitation for  $\lambda = 1064$  nm, see the tail in Fig. 1.11a. When we illuminate the cluster, we still do not observe SH signal. That is, a non-vanishing (but probably small)  $\chi^{(2)}$  overlap integral, (1.11), is not enough for an observable SHG. We remind that for the direct observation of SH generated plasmons,  $E_2(\mathbf{r})$ -mode needs to be a dipole-like one. Driven mode  $E_1(\mathbf{r})$  is also dipole-like. This yields a small  $\chi^{(2)}$  in

(1.11) even for a broken centro-symmetry. (c) However, when the two clusters are brought together, see Fig. 1.10c and d, we observe SH signal at the interface of the two clusters.

In Fig. 1.11a, we plot the plasmonic excitation spectrum (linear response) of three AuNPs of 110, 60 and 12 nm in sizes. The tail extends to longer wavelengths due to the hybridization compared to a 12 nm AuNP alone. When we calculate the eigen plasmon modes of the 3 coupled AuNPs, using *eigenstat* in MNPBEM [89, 90], we observe the following. The plasmon eigenmode at  $\lambda_2 \sim 400$  nm, into which  $2\omega$  (532 nm) signal emerges, display a quadrupole nature on the 12 nm MNP, see Fig. 1.11b. We also check the nature of the 1064 nm excitation. We observe that it has a dipole shape on the 12 nm AuNP. That is, (i) the overlap integral  $\chi^{(2)}$ , (1.11), attains a larger value on the 12 nm AuNP since  $E_1(\mathbf{r})$  is dipole and  $E_2(\mathbf{r})$  is quadrupole. A  $\chi^{(2)}$  due to centro-symmetry breaking, when both  $E_{1,2}(\mathbf{r})$  have dipole characteristic, has contributions only from small regions. However, overlap integral on 12 nm AuNP non-vanishes over all of the particle. The non centro-symmetric larger size AuNPs work as bedding for the SHG of 12 nm AuNP.

(ii) Localization of the E-field on the 12 nm AuNP, Fig. 1.11b, results a strong interaction between the  $\hat{a}_2$ -mode ( $E_2(\mathbf{r})$ ) and the EYFP molecules. This creates the path interference and enhances the SHG. Using the parameters in Fig. 1.11a, our analytical model predicts a SHG enhancement in the order of  $\sim 1000$ . (iii) Quadrupole  $\hat{a}_2$  plasmon mode cannot radiate far-field due to the vanishing coupling of quadrupole mode to vacuum modes, see Sect. 3.1.1. However, the SH signal created in the plasmons of the  $\hat{a}_2$ -mode [93] transfers also to other EYFP molecules on the 12 nm AuNP. This (these) molecule(s) radiate to far-field enabling the observation of SH signal in our experiment. That is, EYFP molecules can both enhance the SHG and behave as far-field reporters.<sup>6</sup>

Finally we note that, the nonlinearity enhancement achievable by facilitating a quantum emitter is one order larger compared to Fano resonances with long-live dark plasmon modes.

### 1.3.3 Silent Enhancement of SERS

Similar to other nonlinearities, Raman signal can also be enhanced by field localization, when Raman-active molecule is placed into the hot spots. This is called surface enhanced Raman scattering (SERS). For instance, 6–8 orders of magnitude enhanced Raman signal can be retrieved from a molecule when it is placed into the nm-size gap between a gold surface and a gold AFM tip, see Fig. 1.12. The hot spot field can be enhanced using a double resonant scheme where excitation ( $\omega$ ) and generated from ( $\omega_R$ ) frequencies overlap two plasmon modes [94]. This way, the fields at both input and output hot spots are enhanced. Input and output hot spots can be further

---

<sup>6</sup>EYFP molecules do not have a two photon absorption response at 1064 nm.

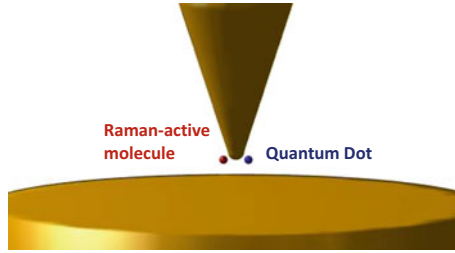


**Fig. 1.12** A Raman-active molecule is placed inside the hot spot gap which appears between a gold coated AFM tip and a gold surface. Molecule is placed slightly to the left of that particle. The Raman signal can be enhanced due to localization. On top of this, SERS can be enhanced 3-orders or more when a QD is present, e.g. on the right of the tip [78]. The second enhancement is *silent*. It does not change the hot spot field

enhanced by increasing the hot spot fields by linear Fano resonances [7, 76], dark-hot resonances [74].

These enhancement schemes are useful up to a hot spot intensity above which the molecule is damaged or the vibrational modes get modified. In this situation, path interference in the nonlinear response (Raman signal) helps us. Similar to other plasmonic non-linearities, we can obtain [78]

$$\tilde{\alpha}_R = \frac{-i\chi\varepsilon_{\text{ph}}^*}{\beta_{\text{ph}} \left( [i(\Omega_R - \omega_R) + \gamma_R] - \frac{|f|^2 y}{[i(\omega_{\text{eg}} - \omega_R) + \gamma_{\text{eg}}]} \right) - |\chi|^2 |\tilde{\alpha}|^2} \tilde{\alpha} \quad (1.29)$$

for the steady-state Raman amplitude with  $\beta_{\text{ph}} = [-i(\Omega_{\text{ph}} - \omega_{\text{ph}}) + \gamma_{\text{ph}}]$ . Here  $y = \rho_{ee} - \rho_{gg}$  is the population inversion and  $f$  denotes the interaction between the MNS and the QE.  $\Omega_R$  is the second plasmon mode of the MNP converter, while  $\gamma_R$  and  $\gamma_{\text{eg}}$  are the damping rates of the  $\Omega_R$ -mode and the QE, respectively.<sup>7</sup> Again similar to other non-linearities, the denominator of (1.29) can be reduced by cancellations. We note that the cancellation only increases the value of  $\tilde{\alpha}_R$ . The driven plasmon mode ( $\tilde{\alpha}$ ) need not be modified. That is, one can increase the Raman signal *silently*, without increasing the hot spot field.

One more time, we test our analytical model with the exact solutions of 3-dimensional Maxwell equations. We again use the freeware program MNPBEM [89, 90]. We clearly observe that Raman signal is enhanced 3 orders of magnitude when an auxiliary particle is placed at the other side of the hot spot, see Fig. 1, 2 in [78]. That is, the Raman-active molecule and the auxiliary particle do not interact. We also confirm that the field on the Raman-active molecule does not increase in the presence of the auxiliary particle, compared to the absence of the auxiliary particle.

Imaging of the vibrational modes reveals the band types in unknown molecules and nanostructures like carbon nanotubes. It is invaluable in determining the finger prints of molecules for detection purposes. This makes SERS an important tool for

<sup>7</sup>Detailed description of the process can be found in [78].

all the fields of science. Under these considerations, one can appreciate the impact of 3 orders of magnitude enhancement without modulating the modes of the sample.

### 1.3.4 Interference of Multiple Conversion Paths and FWM

Four wave mixing (FWM) process in plasmonic structures can also be enhanced and suppressed similar to SHG, THG and SERS processes. One can obtain the plasmon amplitude for the converted  $\omega_3 = 2\omega_1 - \omega_2$  frequency [102] as

$$\tilde{\alpha}_3 = \frac{i\chi_{FWM}}{\frac{|f_2|^2 y}{i(\omega_{eg} + \omega_2 - 2\omega_1) + \gamma_{eg}}} - [i(\Omega_3 + \omega_2 - 2\omega_1) + \gamma_3]} \tilde{\alpha}_2^* \tilde{\alpha}_1^2, \quad (1.30)$$

which is in the common form with other processes. Here,  $\alpha_{1,2}$  are the plasmon amplitudes of the pumped  $\hat{a}_{1,2}$  plasmon modes.  $\alpha_3$  is the plasmon mode into which generated frequency  $\omega_3$  emerges, see Fig. 1.13.  $\alpha_3$  is coupled to a QE. Using the  $\omega_{eg}$  of the QE, one can obtain 80 times enhancement in the FWM signal, see Fig. 1.14a. We note that  $\alpha_{1,2}$  in (1.30) are plasmon amplitudes which are not affected by the interference in the denominator. Hence, the hot spots are not modified in this enhancement process, too.

The basic understanding, provided through out this chapter, now drives us to raise the following question. Can we perform better cancellations in the denominator of  $\tilde{\alpha}_3$  by introducing the interference of more than two conversion paths? We find that using 2 QEs, instead of a single QE, one can obtain  $\sim 1200$  times enhancement in the FWM signal, see Fig. 1.14b. For the 2 QEs case we need to add two new terms. When one considers the interaction of the second QE with the  $\hat{a}_3$ -mode,

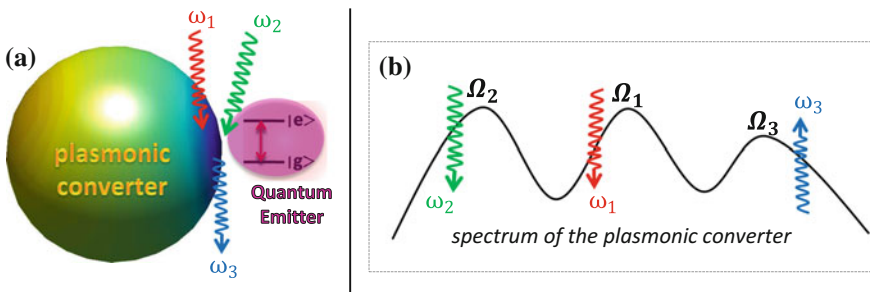


**Fig. 1.13** Fano-enhancement of a plasmonic FWM process. QE is coupled to the  $\Omega_3$ -mode into which converted frequency  $\omega_3 = 2\omega_1 - \omega_2$  emerges. **a** A quantum emitter (QE) is placed on the hot spot of a plasmonic converter. Field localization provides a strong plasmon-QE interaction. **b** Two lasers of frequencies  $\omega_1$  and  $\omega_2$  drive the plasmon modes of resonances  $\Omega_1$  and  $\Omega_2$ . Two plasmons oscillating with  $\omega_1$ , combine and decay into two plasmons with different frequencies,  $\omega_2$  and  $\omega_3$  [102]



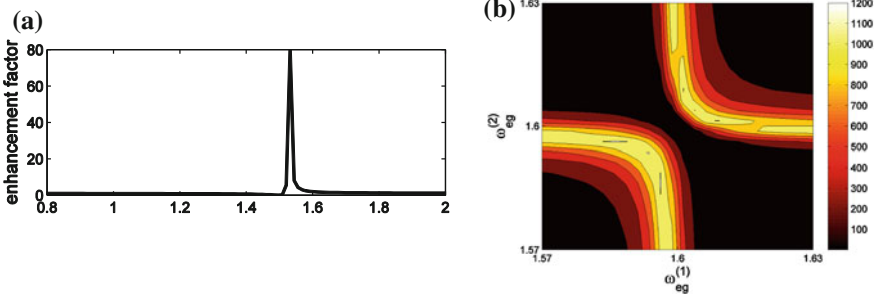


**Fig. 1.14** **a** Relative enhancement of the FWM process in the presence of coupling to the QE, compared to a bare plasmonic converter. **b** When the plasmonic converter is coupled to two QEs, additional terms are introduced. A 1200 times larger enhancement can be achieved on top of the localization enhancement [102]

$\hat{H}_{\text{int}} = \hbar(g|e_2\rangle\langle g_2| \times |g_1\rangle\langle e_1| + H.c.)$ , and the interaction between the two QEs,  $\hat{H}_{\text{QE-QE}} = \hbar(f_1\hat{a}_3^\dagger|g_1\rangle\langle e_1| + f_2\hat{a}_3^\dagger|g_2\rangle\langle e_2| + H.c.)$ , steady-state FWM amplitude becomes

$$\tilde{\alpha}_3 = \frac{i\chi_{FWM}(\beta_1\beta_2 + y_1y_2|g|^2)}{(y_1|f_1|^2\beta_2 + y_2|f_2|^2\beta_1) + iy_1y_2(f_1f_2^*g^* + f_1^*f_2g) - \xi_3(\beta_1\beta_2 + y_1y_2|g|^2)} \tilde{\alpha}_2^* \tilde{\alpha}_1^2 \quad (1.31)$$

where  $\xi_3 = i(\Omega_3 + \omega_2 - 2\omega_1) + \gamma_3$  and  $\beta_j = i(\omega_{eg}^{(j)} + \omega_2 - 2\omega_1) + \gamma_{eg}^{(j)}$ . Here, (1.31) has more terms in the denominator and hence has more parameters for the cancellations. Better cancellations yield a  $\sim 1200$  times FWM enhancement, in Fig. 1.14b. Once again, this enhancement is *silent*.

## 1.4 Summary

We demonstrate that enhancement and suppression both in the linear and nonlinear responses have the same origin. Amplitude of the excited plasmon in the linear response and the amplitude of the frequency converted plasmons in the nonlinear response have a common structure, see (1.8), (1.23), (1.28), (1.29) and (1.30). Coupling to an auxiliary object (a QE or a dark plasmon mode) introduces an extra term in the denominator. (i) When  $\omega_{eg}$  of the auxiliary particle is tuned properly, the new term can cancel the non-resonant term in the conversion. This creates the enhancement. (ii) When the denominator is enriched with coupling to more than one auxiliary particle, the cancellation can be made better. This yields even a better enhancement in the nonlinear signal. (iii) When the auxiliary particle has a longer lifetime (i.e.  $> 100$  times) and one chooses  $\omega_{eg} = \omega_{\text{converted}}$ , the extra term grows dramatically. This results the suppression. (iv) In the nonlinear processes, the auxiliary particle must be coupled to the plasmon mode into which converted frequency emerges. (v) All of the nonlinearity enhancement obtained in this way are *silent* in

the sense that hot spot fields are not enhanced. (vi) The enhancement does not always increase with a stronger interaction between the frequency converted plasmon mode and the auxiliary particle. For stronger hybridization, one cannot talk about two different modes and the simple model fails. (vii) For the suppression phenomenon to appear, coupling to a long-live auxiliary particle is necessary. On the other hand, enhancement, cancellation in the denominator, can take place also for coupling to an auxiliary particle with an ordinary lifetime. However, enhancement is larger with a long lifetime auxiliary object. (viii) Retardation effects cause the enhancement to appear in a narrower  $\omega_{eg}$  band.

## References

1. J.A. Schuller, E.S. Barnard, W. Cai, Y.C. Jun, J.S. White, M.L. Brongersma, Plasmonics for extreme light concentration and manipulation. *Nat. Mater.* **9**, 193–204 (2010)
2. E. Kretschmann, H. Raether, Radiative decay of non radiative surface plasmons excited by light. *Zeitschrift für Naturforschung A* **23**, 2135–2136 (1968)
3. M. Moskovits, The case for plasmon-derived hot carrier devices. *Nat. Nanotechnol.* **10**, 6–8 (2015)
4. F.C. Bohren, How can a particle absorb more than the light incident on it? *Am. J. Phys.* **51**, 323–327 (1983)
5. X. Wu, S.K. Gray, M. Pelton, Quantum-dot-induced transparency in a nanoscale plasmonic resonator. *Opt. Express* **18**, 23633–23645 (2010)
6. C. Höppener, Z.J. Lapin, P. Bharadwaj, L. Novotny, Self-similar gold-nanoparticle antennas for a cascaded enhancement of the optical field. *Phys. Rev. Lett.* **109**, 017402 (2012)
7. J. He, C. Fan, P. Ding, S. Zhu, E. Liang, Near-field engineering of Fano resonances in a plasmonic assembly for maximizing CARS enhancements. *Sci. Rep.* **6**, 20777 (2016)
8. C.S.S.R. Kumar, F. Mohammad, Magnetic nanomaterials for hyperthermia-based therapy and controlled drug delivery. *Adv. Drug Deliv. Rev.* **63**, 789–808 (2011)
9. J. Zhou, Y. Gao, Z. Zhang, H. Luo, C. Cao, Z. Chen, L. Dai, X. Liu, VO2 thermochromic smart window for energy savings and generation. *Sci. Rep.* **3** (2013)
10. M.L. Brongersma, N.J. Halas, P. Nordlander, Plasmon-induced hot carrier science and technology. *Nat. Nanotechnol.* **10**, 25–34 (2015)
11. H.A. Atwater, A. Polman, Plasmonics for improved photovoltaic devices. *Nat. Mater.* **9**, 205–213 (2010)
12. J.S. White, G. Veronis, Z. Yu, E.S. Barnard, A. Chandran, S. Fan, M.L. Brongersma, Extraordinary optical absorption through subwavelength slits. *Opt. Lett.* **34**, 686–688 (2009)
13. E. Laux, C. Genet, T. Skauli, T.W. Ebbesen, Plasmonic photon sorters for spectral and polarimetric imaging. *Nat. Photonics* **2**, 161–164 (2008)
14. W. Wang, K. Foley, X. Shan, S. Wang, S. Eaton, V.J. Nagaraj, P. Wiktor, U. Patel, N. Tao, Single cells and intracellular processes studied by a plasmonic-based electrochemical impedance microscopy. *Nat. Chem.* **3**, 249–255 (2011)
15. M. Najiminaini, F. Vasefi, B. Kaminska, J.J.L. Carson, Nanohole-array-based device for 2D snapshot multispectral imaging. *Sci. Rep.* **3** (2013)
16. C. Min, Z. Shen, J. Shen, Y. Zhang, H. Fang, G. Yuan, L. Du, S. Zhu, T. Lei, X. Yuan, Focused plasmonic trapping of metallic particles. *Nat. Commun.* **4** (2013)
17. M. Belkin, S.H. Chao, M.P. Jonsson, C. Dekker, A. Aksimentiev, Plasmonic nanopores for trapping, controlling displacement, and sequencing of DNA. *ACS Nano* **9**, 10598–10611 (2015)
18. J. Homola, Surface plasmon resonance sensors for detection of chemical and biological species. *Chem. Rev.* **108**, 462–493 (2008)

19. M.K. Schmidt, R. Esteban, A. González-Tudela, G. Giedke, J. Aizpurua, Quantum mechanical description of raman scattering from molecules in plasmonic cavities. *ACS Nano* **10**, 6291–6298 (2016)
20. P. Roelli, C. Galland, N. Piro, T.J. Kippenberg, Molecular cavity optomechanics as a theory of plasmon-enhanced Raman scattering. *Nat. Nanotechnol.* **11**, 164–169 (2016)
21. S.J. Barrow, X. Wei, J.S. Baldauf, A.M. Funston, P. Mulvaney, The surface plasmon modes of self-assembled gold nanocrystals. *Nat. Commun.* **3**, 1275 (2012)
22. A. Bek, R. Vogelgesang, K. Kern, Apertureless scanning near field optical microscope with sub-10 nm resolution. *Rev. Sci. Instrum.* **77**, 043703 (2006)
23. N. Rotenberg, L. Kuipers, Mapping nanoscale light fields. *Nat. Photonics* **8**, 919–926 (2014)
24. W. Harbich, S. Fedrigo, J. Buttet, The optical absorption spectra of small silver clusters ( $n=5-11$ ) embedded in argon matrices. *Chem. Phys. Lett.* **195**, 613–617 (1992)
25. J. Tiggesbäumker, L. Köller, K.H. Meiwes-Broer, A. Liebsch, Blue shift of the Mie plasma frequency in Ag clusters and particles. *Phys. Rev. A* **48**, R1749 (1993)
26. V. Bonačić-Koutecky, V. Veyret, R. Mitrić, Ab initio study of the absorption spectra of Ag  $n$  ( $n=5-8$ ) clusters. *J. Chem. Phys.* **115**, 10450–10460 (2001)
27. S.M. Morton, D.W. Silverstein, L. Jensen, Theoretical studies of plasmonics using electronic structure methods. *Chem. Rev.* **111**, 3962–3994 (2011)
28. L. Jensen, C.M. Aikens, G.C. Schatz, Electronic structure methods for studying surface-enhanced Raman scattering. *Chem. Soc. Rev.* **37**, 1061–1073 (2008)
29. E. Ozbay, Plasmonics: merging photonics and electronics at nanoscale dimensions. *Science* **311**, 189–193 (2006)
30. E.S. Barnard, J.S. White, A. Chandran, M.L. Brongersma, Spectral properties of plasmonic resonator antennas. *Opt. Express* **16**, 16529–16537 (2008)
31. A.G. Curto, G. Volpe, T.H. Taminiau, M.P. Kreuzer, R. Quidant, N. van Hulst, Unidirectional emission of a quantum dot coupled to a nanoantenna. *Science* **329**, 930–933 (2010)
32. M.A. Noginov, G. Zhu, A.M. Belgrave, R. Bakker, V.M. Shalae, E.E. Narimanov, S. Stout, E. Herz, T. Suteewong, U. Wiesner, Demonstration of a spaser-based nanolaser. *Nature* **460**, 1110 (2009)
33. S. Derom, A. Berthelot, A. Pillonnet, O. Benamara, A.M. Jurdyc, C. Girard, G.C. des Francs, Metal enhanced fluorescence in rare earth doped plasmonic core-shell nanoparticles. *Nanotechnology* **24**, 495704 (2013)
34. M.I. Stockman, The spaser as a nanoscale quantum generator and ultrafast amplifier. *J. Opt.* **12**, 024004 (2010)
35. M. Premaratne, M.I. Stockman, Theory and technology of SPASERs. *Adv. Opt. Photon.* **9**, 79–128 (2017)
36. M.E. Taşgın, Metal nanoparticle plasmons operating within a quantum lifetime. *Nanoscale* **5**, 8616–8624 (2013)
37. Y. Pu, R. Grange, C.L. Hsieh, D. Psaltis, Nonlinear optical properties of core-shell nanocavities for enhanced second-harmonic generation. *Phys. Rev. Lett.* **104**, 207402 (2010)
38. M. Kauranen, A.V. Zayats, Nonlinear plasmonics. *Nat. Photonics* **6**, 737–748 (2012)
39. S. Schlücker, Surface-Enhanced raman spectroscopy: concepts and chemical applications. *Angew. Chem. Int. Edition* **53**, 4756–4795 (2014)
40. R. Zhang, Y. Zhang, Z.C. Dong, S. Jiang, C. Zhang, L.G. Chen, L. Zhang, Y. Liao, J. Aizpurua, Y. Luo, Chemical mapping of a single molecule by plasmon-enhanced Raman scattering. *Nature* **498**, 82 (2013)
41. J. Kneipp, H. Kneipp, K. Kneipp, SERS-A single-molecule and nanoscale tool for bioanalytics. *Chem. Soc. Rev.* **37**, 1052–1060 (2008)
42. K. Kneipp, H. Kneipp, I. Itzkan, R.R. Dasari, M.S. Feld, Surface-enhanced Raman scattering and biophysics. *J. Phys. Condens. Matter* **14**, R597 (2002)
43. B. Fazio, C. D’Andrea, A. Foti, E. Messina, A. Irrera, M.G. Donato, V. Villari, N. Micali, O.M. Maragò, P.G. Gucciardi, SERS detection of Biomolecules at Physiological pH via aggregation of Gold Nanorods mediated by Optical Forces and Plasmonic Heating. *Sci. Rep.* **6**, 26952 (2016)

44. X. Qian, X.H. Peng, D.O. Ansari, Q. Yin-Goen, G.Z. Chen, D.M. Shin, L. Yang, A.N. Young, M.D. Wang, S. Nie, In vivo tumor targeting and spectroscopic detection with surface-enhanced Raman nanoparticle tags. *Nat. Biotechnol.* **26**, 83–90 (2008)
45. N. Yi, C. Zhang, Q. Song, S. Xiao, A hybrid system with highly enhanced graphene SERS for rapid and tag-free tumor cells detection. *Sci. Rep.* **6**, 25134 (2016)
46. S.Y. Ding, J. Yi, J.F. Li, B. Ren, D.Y. Wu, R. Panneerselvam, Z.Q. Tian, Nanostructure-based plasmon-enhanced Raman spectroscopy for surface analysis of materials. *Nat. Rev. Mater.* **1**, 16021 (2016)
47. T. Nikolajsen, K. Leosson, S.I. Bozhevolnyi, Surface plasmon polariton based modulators and switches operating at telecom wavelengths. *Appl. Phys. Lett.* **85**, 5833–5835 (2004)
48. M.J. Dicken, L.A. Sweatlock, D. Pacifici, H.J. Lezec, K. Bhattacharya, H.A. Atwater, Electrooptic modulation in thin film barium titanate plasmonic interferometers. *Nano Lett.* **8**, 4048–4052 (2008)
49. K.F. MacDonald, Z.L. Sámsón, M.I. Stockman, N.I. Zheludev, Ultrafast active plasmonics. *Nat. Photonics* **3**, 55–58 (2009)
50. A.V. Krasavin, N.I. Zheludev, Active plasmonics: controlling signals in Au/Ga waveguide using nanoscale structural transformations. *Appl. Phys. Lett.* **84**, 1416–1418 (2004)
51. R.A. Pala, K.T. Shimizu, N.A. Melosh, M.L. Brongersma, A nonvolatile plasmonic switch employing photochromic molecules. *Nano Lett.* **8**, 1506–1510 (2008)
52. J.I. Cirac, H.J. Kimble, Quantum optics, what next? *Nat. Photonics* **11**, 18–20 (2017)
53. I.A. Walmsley, Quantum optics: science and technology in a new light. *Science* **348**, 525–530 (2015)
54. Horizon 2020 EU-funds Quantum Technology Projects
55. M.S. Tame, K.R. McEnery, Ş.K. Özdemir, J. Lee, S.A. Maier, M.S. Kim, Quantum plasmonics. *Nat. Phys.* **9**, 329–340 (2013)
56. J. Hakami, M.S. Zubairy, Nanoshell-mediated robust entanglement between coupled quantum dots. *Phys. Rev. A* **93**, 022320 (2016)
57. A. Castellini, H.R. Jauslin, A. Messina, S. Guérin, Quantum plasmonics with multi-emitters: application to adiabatic control (2007). [arXiv:1710.11530](https://arxiv.org/abs/1710.11530)
58. M.E. Taşgın, Many-particle entanglement criterion for superradiantlike states. *Phys. Rev. Lett.* **119**, 033601 (2017)
59. A. Huck, S. Smolka, P. Lodahl, A.S. Sørensen, A. Boltasseva, J. Janousek, U.L. Andersen, Demonstration of quadrature-squeezed surface plasmons in a gold waveguide. *Phys. Rev. Lett.* **102**, 246802 (2009)
60. G. Di Martino, Y. Sonnefraud, S. Kéna-Cohen, M. Tame, Ş.K. Özdemir, M.S. Kim, S.A. Maier, Quantum statistics of surface plasmon polaritons in metallic stripe waveguides. *Nano Lett.* **12**, 2504–2508 (2012)
61. M.C. Dheur, E. Devaux, T.W. Ebbesen, A. Baron, J.C. Rodier, J.P. Hugonin, P. Lalanne, J.J. Greffet, G. Messin, F. Marquier, Single-plasmon interferences. *Sci. Adv.* **2**, e1501574 (2016)
62. A.V. Akimov, A. Mukherjee, C.L. Yu, D.E. Chang, A.S. Zibrov, P.R. Hemmer, H. Park, M.D. Lukin, Generation of single optical plasmons in metallic nanowires coupled to quantum dots. *Nature* **450**, 402–406 (2007)
63. S.L. Braunstein, P. Van Loock, Quantum information with continuous variables. *Rev. Mod. Phys.* **77**, 513 (2005)
64. K. Wodkiewicz, P.L. Knight, S.J. Buckle, S.M. Barnett, Squeezing and superposition states. *Phys. Rev. A* **35**, 2567 (1987)
65. M. Kitagawa, M. Ueda, Squeezed spin states. *Phys. Rev. A* **47**, 5138 (1993)
66. C.L. Garrido Alzar, M.A.G. Martínez, P. Nussenzveig, Classical analog of electromagnetically induced transparency. *Am. J. Phys.* **70**, 37–41 (2002)
67. B. Luk'yanchuk, N.I. Zheludev, S.A. Maier, N.J. Halas, P. Nordlander, H. Giessen, C.T. Chong, The Fano resonance in plasmonic nanostructures and metamaterials. *Nat. Mater.* **9**, 707–715 (2010)
68. P. Tassin, L. Zhang, T.H. Koschny, E.N. Economou, C.M. Soukoulis, Low-loss metamaterials based on classical electromagnetically induced transparency. *Phys. Rev. Lett.* **102**, 053901 (2009)

69. N. Liu, L. Langguth, T. Weiss, J. Kästel, M. Fleischhauer, T. Pfau, H. Giessen, Plasmonic analogue of electromagnetically induced transparency at the Drude damping limit. *Nat. Mater.* **8**, 758–762 (2009)
70. F. Wang, Y.R. Shen, General properties of local plasmons in metal nanostructures. *Phys. Rev. Lett.* **97**, 206806 (2006)
71. S.M. Sadeghi, W.J. Wing, R.R. Gutha, Undamped ultrafast pulsation of plasmonic fields via coherent exciton-plasmon coupling. *Nanotechnology* **26**, 085202 (2015)
72. M. ElKabbash, A.R. Rashed, B. Kucukoz, Q. Nguyen, A. Karatay, G. Yaglioglu, E. Ozbay, H. Caglayan, G. Strangi, Ultrafast transient optical loss dynamics in exciton? plasmon nano-assemblies. *Nanoscale* **9**, 6558–6566 (2017)
73. B.C. Yıldız Karakul, Enhancement of plasmonic nonlinear conversion and polarization lifetime via fano resonances, Middle East Technical University (2017)
74. M.I. Stockman, Nanoscience: Dark-hot resonances. *Nature* **467**, 541–542 (2010)
75. Y. Zhang, F. Wen, Y.R. Zhen, P. Nordlander, N.J. Halas, Coherent Fano resonances in a plasmonic nanocluster enhance optical four-wave mixing. *Proc. Natl. Acad. Sci.* **110**, 9215–9219 (2013)
76. J. Ye, F. Wen, H. Sobhani, J.B. Lassiter, P. Van Dorpe, P. Nordlander, N.J. Halas, Plasmonic nanoclusters: near field properties of the Fano resonance interrogated with SERS. *Nano Lett.* **12**, 1660–1667 (2012)
77. Y. Zhang, Y.R. Zhen, O. Neumann, J.K. Day, P. Nordlander, N.J. Halas, Coherent anti-Stokes Raman scattering with single-molecule sensitivity using a plasmonic Fano resonance. *Nat. Commun.* **5**, 4424 (2014)
78. S. Postacı, B.C. Yıldız, A. Bek, M.E. Taşgın, Silent enhancement of SERS with unmodified hot spots (2017). [arXiv:1709.09230](https://arxiv.org/abs/1709.09230)
79. M.I. Stockman, Nanoplasmonics: past, present, and glimpse into future. *Opt. Express* **19**, 22029–22106 (2011)
80. C. Genes, A. Mari, P. Tombesi, D. Vitali, Robust entanglement of a micromechanical resonator with output optical fields. *Phys. Rev. A* **78**, 032316 (2008)
81. N. Papasimakis, N.I. Zheludev, Metamaterial-induced transparency: sharp Fano resonances and slow light. *Opt. Photonics News* **20**, 22–27 (2009)
82. J. Berthelot, G. Bachelier, M. Song, P. Rai, G.C. Des Francs, A. Dereux, A. Bouhelier, Silencing and enhancement of second-harmonic generation in optical gap antennas. *Opt. Express* **20**, 10498–10508 (2012)
83. P. Anger, P. Bharadwaj, L. Novotny, Enhancement and quenching of single-molecule fluorescence. *Phys. Rev. Lett.* **96**, 113002 (2006)
84. H. Yuan, S. Khatua, P. Zijlstra, M. Yorulmaz, M. Orrit, Thousand-fold enhancement of single-molecule fluorescence near a single gold nanorod. *Angew. Chem. Int. Edition* **52**, 1217–1221 (2013)
85. M.O. Scully, Single photon subradiance: quantum control of spontaneous emission and ultrafast readout. *Phys. Rev. Lett.* **115**, 243602 (2015)
86. M.L. Ren, S.Y. Liu, B.L. Wang, B.Q. Chen, J. Li, Z.Y. Li, Giant enhancement of second harmonic generation by engineering double plasmonic resonances at nanoscale. *Opt. Express* **22**, 28653–28661 (2014)
87. E. Poutrina, C. Ciraci, D.J. Gauthier, D.R. Smith, Enhancing four-wave-mixing processes by nanowire arrays coupled to a gold film. *Opt. Express* **20**, 11005–11013 (2012)
88. E.C. Le Ru, E. Blackie, M. Meyer, P.G. Etchegoin, Surface enhanced Raman scattering enhancement factors: a comprehensive study. *J. Phys. Chem. C* **111**, 13794–13803 (2007)
89. U. Hohenester, A. Trügler, MNPBEM-A Matlab toolbox for the simulation of plasmonic nanoparticles. *Comput. Phys. Commun.* **183**, 370–381 (2012)
90. F.J.G. De Abajo, A. Howie, Retarded field calculation of electron energy loss in inhomogeneous dielectrics. *Phys. Rev. B* **65**, 115418 (2002)
91. M. Finazzi, F. Ciccacci, Plasmon-photon interaction in metal nanoparticles: second-quantization perturbative approach. *Phys. Rev. B* **86**, 035428 (2012)

92. M.E. Taşgın, I. Salakhutdinov, D. Kendziora, M.K. Abak, D. Turkpence, L. Piantanida, L. Fruk, M. Lazzarino, A. Bek, Fluorescence excitation by enhanced plasmon upconversion under continuous wave illumination, *Photonics Nanostructures Fundam. Appl.* **21**, 32–43 (2016)
93. N.B. Grosse, J. Heckmann, U. Woggon, Nonlinear plasmon-photon interaction resolved by k-space spectroscopy. *Phys. Rev. Lett.* **108**, 136802 (2012)
94. Y. Chu, M.G. Banaee, K.B. Crozier, Double-resonance plasmon substrates for surface-enhanced Raman scattering with enhancement at excitation and stokes frequencies. *ACS Nano* **4**, 2804–2810 (2010)
95. A. Jorio, N.S. Mueller, S. Reich, Symmetry-derived selection rules for plasmon-enhanced Raman scattering. *Phys. Rev. B* **95**, 1–10 (2017)
96. B.C. Yıldız, M.E. Taşgın, M.K. Abak, S. Coskun, H.E. Unalan, A. Bek, Enhanced second harmonic generation from coupled asymmetric plasmonic metal nanostructures. *J. Opt.* **17**, 125005 (2015)
97. M.E. Taşgın, Ö.E. Müstecaplıoğlu, L. You, Creation of a vortex in a Bose-Einstein condensate by superradiant scattering. *Phys. Rev. A* **84**, 063628 (2011)
98. P. Das, M.E. Taşgın, Ö.E. Müstecaplıoğlu, Collectively induced many-vortices topology via rotatory Dicke quantum phase transition. *New J. Phys.* **18**, 093022 (2016)
99. D. Turkpence, G.B. Akguc, A. Bek, M.E. Taşgın, Engineering nonlinear response of nano-materials using Fano resonances. *J. Opt.* **16**, 105009 (2014)
100. M.O. Scully, M.S. Zubairy, *Quantum Optics* (Cambridge University Press, New York, 1997)
101. B. Min, E. Ostby, V. Sorger, E. Ulin-Avila, L. Yang, X. Zhang, K. Vahala, High-Q surface-plasmon-polariton whispering-gallery microcavity, *Nature* **457** (2009)
102. S.K. Singh, M.K. Abak, M.E. Taşgın, Enhancement of four-wave mixing via interference of multiple plasmonic conversion paths. *Phys. Rev. B* **93**, 035410 (2016)

# Chapter 2

## Fano-resonant Excitations of Generalized Optical Spin Waves



Xianji Piao, Sunkyu Yu and Namkyoo Park

**Abstract** While chiral materials possess spin-form wave functions as their eigenmodes, optical spin excitations cannot be obtained solely in chiral materials due to a lack of spin impedances. To date, spin excitation has generally been induced through non-conservative methods, such as circular dichroism or magneto-optical effects. In this chapter, we describe a conservative approach to optical spin excitation and control based on the spin-dependent appearance of Fano resonance. Starting from the development of the spin-form temporal coupled mode theory for 2D and 3D chiral resonances, the origin of the spin-Fano interactions is demonstrated in terms of the link between the spin eigenmodes in the polarization domain and anti-symmetric Fano resonances in the spectral domain. By comparing this spin-dependent Fano-resonant system with other optical spin materials, such as chiral, circular dichroic, and birefringent media, we discuss the impact of our results toward the realization of optical spintronics, such as applications of highly selective spin switching and unpolarized spinning operations.

### 2.1 Introduction

Due to the ultrafast and low-loss nature of light, photonics has provided revolutionary contributions to communication, information, and energy technologies. To continue this photonic revolution, serious efforts have been devoted to the fields of nanophotonics [1], plasmonics [2], and metamaterials [3] during the last decade. In these fields, optical phenomena in the subwavelength regime and their applications allow for the realization of “spatially” integrated optical devices that can overcome the conventional diffraction limit. Although this approach provides a useful tool for the design of future photonic devices, it is still difficult to overcome the fundamental limiting length scale of photons [4–6], even with state-of-the-art photonics.

---

X. Piao (✉) · S. Yu · N. Park  
Photonic Systems Laboratory, Department of Electrical and Computer Engineering,  
Seoul National University, Seoul, Korea 08826, South Korea  
e-mail: xjpiao227@gmail.com

© Springer Nature Switzerland AG 2018  
E. Kamenetskii et al. (eds.), *Fano Resonances in Optics and Microwaves*, Springer  
Series in Optical Sciences 219, [https://doi.org/10.1007/978-3-319-99731-5\\_2](https://doi.org/10.1007/978-3-319-99731-5_2)

Next-generation photonics requires an alternative to the “sub-wavelength” approach that has become widespread over the last decade.

As a logical starting point, it is necessary to revisit the physical quantities of photons and their interactions. While previous approaches toward the integration of optical information have focused on “spatial integration”, recent works have paid more attention to *other physical axes*: spin [7–13] and orbital [14, 15] angular momenta of light and their interactions toward topological photonics [16–19], temporal evolution of light-matter interactions [20–22], and disordered formation of materials for controlling light spreading [23–27]. By utilizing these uncultivated degrees of freedom, light information can now be better stacked inside the same spatial footprint, maximizing the capability of photons as information carriers.

Among the various physical parameters utilized for optical information integration, in this chapter, we focus on the *spinning* of light, which is one of the fundamental motions in physics. Spin angular momentum (SAM) of light, which corresponds to the handedness of photons [28], is an active research field that studies circular polarizations in classical optics [29], an optical analogy of quantum phenomena [9, 28], and the application of molecular sensing [30]. In general, to access the SAM “eigenmode” in optics, coupling between electric and magnetic fields is necessary, which can be achieved in 3D chiral structures [31–36] or gyrotropic media [37–39]. As another route, 2D chiral structures [40–42], including parity-time symmetric systems [12, 43, 44], also allow the realization of SAM eigenmodes. Although the effects of these SAM platforms on properties such as spectral quality and field enhancement can be significantly enhanced by utilizing optical resonance structures, an intuitive analytical method for SAM resonances is still missing.

For the realization of spin-controlled photonic processing, we focus on “selective” manipulation of optical spin, especially in the spectral domain. For this goal, in this chapter, we will review our studies on the link between Fano resonance and polarization space and show an intriguing phenomenon: optical spin-dependent Fano resonances. We will show that the realization of spin-dependent Fano resonances allows highly sensitive control of the optical spin state for the building block of optical spin switching. Due to the steep response in the spectral domain, Fano resonance will provide a new perspective on various spin-based applications, including sensors, modulators, switches, and lasers, in the context of optical spintronics [45].

In Sect. 2.2, we introduce a theoretical model for the generalized spin wave excitations in 2D and 3D optical chirality, using a temporal coupled mode theory. Using the developed temporal coupled mode theory, the origin of spin-dependent Fano resonance and its control are discussed in Sect. 2.3. Metamaterial-based applications of spin-dependent Fano resonances are discussed in Sect. 2.4.

## 2.2 Coupled Mode Theory for Optical Spin Waves

Coupled mode theory (CMT) provides platform-transparent analysis of universal coupled oscillatory systems, including guided optical systems [46], transmission lines [47], electronic circuits [48], and acoustic systems [49]. From its intuitive



and generalized representation, CMT allows for a phenomenological understanding of various wave phenomena, such as directional coupling [46], Fano resonances [50–52], isospectral energy spectra [53, 54], disordered optics [27, 55], slow light [56], optical switching [57, 58], and wireless power transfer [59]. In spite of its simple form, CMT also leads to quantitatively acceptable results within the weakly coupled regime compared with those from full wave analysis.

By assigning the coupling-induced perturbation to a simplified model, the basic form of the coupled mode equation includes (i) the on-site energy that defines the self-oscillation of each element and (ii) interaction energy that represents the magnitude of the perturbation driven by the coupling. The equation for a general  $N$ -oscillator system is

$$\frac{d}{d\xi} a_j = i\rho_j a_j + i \sum_{k=1}^N \delta_{jk} a_k + \gamma_j S_j, \quad (2.1)$$

where  $a_j$  and  $\rho_j$  represent the field amplitude and self-oscillation terms of the  $j$ -th element, respectively;  $\gamma_j$  and  $S_j$  represent the excitation coefficient and external source of the  $j$ -th element, respectively;  $\delta_{jk}$  is the coupling coefficient between the  $j$ -th and  $k$ -th elements; and  $\xi$  is the physical axis for the self-oscillation, which can be a spatial or temporal axis. In harmonic systems ( $\partial\xi \rightarrow i\rho$ ), (2.1) becomes the matrix equation  $i \cdot [\rho \cdot \mathbf{I} - \text{diag}(\boldsymbol{\rho}) - \mathbf{K}] \mathbf{a} = \mathbf{S}$ , where  $\mathbf{I}$  is the identity matrix,  $[\boldsymbol{\rho}]_j = \rho_j$ ,  $[\mathbf{K}]_{jk} = \delta_{jk}$ , and  $[\mathbf{S}]_j = \gamma_j S_j$ . Using this simple matrix equation, eigenmode problems (no excitation with  $\mathbf{S} = \mathbf{O}$ ) or excitation behaviours from external sources ( $\mathbf{S} \neq \mathbf{O}$ ) can be analysed. The Hermiticity of the matrix determines whether the coupled system is conservative.

While spatial CMT (the wave vector  $\rho$  and  $\xi = z$ ) historically provides a comprehensible description of the directional coupling in guided optics [46], temporal coupled mode theory (TCMT, the resonant frequency  $\rho$  and  $\xi = t$ ) [60] has attracted particular attention in the field of nanophotonics for the interpretation of coupled resonant structures. Because the results from the TCMT provide a reasonable fit in the weakly coupled regime with a quality ( $Q$ -) factor of over  $\sim 10$ , various optical resonant systems, including dielectric [52, 58, 61] or metallic resonators [50, 51, 62, 63], meet the requirement of TCMT. By obtaining the quantified parameters of coupling coefficients, resonance frequencies, and resonator  $Q$ -factors, the temporally varying flows of light, such as the field excitation and storage of resonators as well as scattering to external waveguides, are successfully predicted in general platforms, e.g., guided optics [60], photonic crystals [52, 56, 58, 61], and plasmonic structures [50, 51, 62, 63].

It should be noted that most previous studies have not fully exploited the generality of TCMT and solely focused on the “spatial” optical mode with a specific polarization (TE or TM), rather than a “polarization” mode with an optical spin. Considering spin-related localized resonances in nanophotonics, which can be obtained in chiral nanostructures [33], metamaterial films [40–42], and parity-time (PT) symmetric

resonances [12, 44], the development of TCMT for spin resonant systems is strongly required.

In this section, as a tool for the later discussion of Fano-resonant spin waves (Sects. 2.3 and 2.4), we introduce TCMT analysis for different types of optical spin waves: (i) from 2D non-Hermitian structures and (ii) 3D chiral structures. In both works, we consider the polarization space of the planewave propagation, constructing two-coupled-oscillator TCMT models.

### 2.2.1 TCMT Analysis of 2D non-Hermitian Chirality

A representative optical spin phenomenon in 2D structures is circular dichroism [40–42], which exhibits different dissipation for each spin wave. Considering that any 2D structure can be expressed as a two-level non-Hermitian system with gain or loss, we extend the physics of circular dichroism by exploring the condition of spin-form eigenmodes in a universal two-level non-Hermitian system, which allows 2D non-Hermitian chirality.

First, consider a nonmagnetic two-level resonant system in polarization space. When each resonant mode has a linear polarization orthogonal to each other ( $h$ : horizontal,  $v$ : vertical) and coupling from the perturbation is assumed, the “non-Hermitian” TCMT equation becomes

$$\frac{d}{dt} \begin{bmatrix} a_h \\ a_v \end{bmatrix} = i \begin{bmatrix} \omega_h + i\lambda_h & \kappa \\ \kappa & \omega_v + i\lambda_v \end{bmatrix} \begin{bmatrix} a_h \\ a_v \end{bmatrix}, \quad (2.2)$$

where  $\omega_{h,v}$  and  $\lambda_{h,v}$  are the resonant frequency and non-Hermitian component of each polarization mode ( $\lambda_{h,v} < 0$  for amplification and  $\lambda_{h,v} > 0$  for dissipation),  $\kappa$  is the coupling coefficient, and all of the parameters are real-valued. The corresponding eigenfrequency and eigenmode are

$$\omega_{\text{eig}1,2} = \frac{\omega_h + \omega_v + i(\lambda_h + \lambda_v)}{2} \pm \frac{\sqrt{(\omega_h - \omega_v)^2 + 4\kappa^2 - (\lambda_h - \lambda_v)^2 + 2i(\omega_h - \omega_v)(\lambda_h - \lambda_v)}}{2}, \quad (2.3)$$

$$\mathbf{v}_{\text{eig}1,2} = \begin{bmatrix} \frac{\omega_h - \omega_v + i(\lambda_h - \lambda_v)}{2} \pm \frac{\sqrt{(\omega_h - \omega_v)^2 + 4\kappa^2 - (\lambda_h - \lambda_v)^2 + 2i(\omega_h - \omega_v)(\lambda_h - \lambda_v)}}{2} \\ \kappa \end{bmatrix}. \quad (2.4)$$

When considering the form of the spin states  $[1, \pm i]^T$ , it is observed that the emergence of the spin-form eigenmode originates from different non-Hermitian components  $\lambda_h \neq \lambda_v$ . If  $\lambda_h = \lambda_v = \lambda_o$ , the eigenfrequency and eigenmode become

$$\omega_{\text{eig}1,2} = \frac{\omega_h + \omega_v}{2} + i\lambda_o \pm \frac{\sqrt{(\omega_h - \omega_v)^2 + 4\kappa^2}}{2}, \quad (2.5)$$

$$\mathbf{v}_{\text{eig}1,2} = \left[ \begin{array}{c} \frac{\omega_h - \omega_v}{2} \pm \frac{\sqrt{(\omega_h - \omega_v)^2 + 4\kappa^2}}{2} \\ \kappa \end{array} \right], \quad (2.6)$$

which leads to the “phase-matched” resonance between horizontal and vertical linear polarizations in  $\mathbf{v}_{\text{eig}1,2}$ , constructing the oblique linearly polarized resonance. In addition, each eigenmode supports a different resonant frequency. However, if  $\omega_h = \omega_v = \omega_o$  the eigenfrequency and eigenmode become

$$\omega_{\text{eig}1,2} = \omega_o + \frac{i(\lambda_h + \lambda_v)}{2} \pm \frac{\sqrt{4\kappa^2 - (\lambda_h - \lambda_v)^2}}{2}, \quad (2.7)$$

$$\mathbf{v}_{\text{eig}1,2} = \left[ \begin{array}{c} \frac{i(\lambda_h - \lambda_v)}{2} \pm \frac{\sqrt{4\kappa^2 - (\lambda_h - \lambda_v)^2}}{2} \\ \kappa \end{array} \right], \quad (2.8)$$

which derives a uniquely existing spin eigenmode,  $\mathbf{v}_{\text{eig}1,2} = [1, i]^T$  and  $\omega_{\text{eig}} = \omega_o + i(\lambda_v - \kappa)$  with the condition of  $\lambda_h - \lambda_v = -2\kappa$ . Therefore, the non-Hermitian resonant system realizes chirality from the unique existence of a pure spin eigenmode at a certain condition, which corresponds to the exceptional point in polarization space [12, 43, 44]. The cases of  $\omega_h \neq \omega_v$  or  $\lambda_h - \lambda_v \neq -2\kappa$  result in elliptic eigenmodes with different amplifications and dissipations, encompassing the systems with circular dichroism.

Figure 2.1 represents TCMT eigenmode analysis of 2D non-hermitian chirality: the evolutions of the spin densities of the eigenmodes (Fig. 2.1a, b), as well as their eigenfrequencies (Fig. 2.1c, d) and amplification or dissipation (Fig. 2.1e, f), for eigenmodes 1 (Fig. 2.1a, c, e) and 2 (Fig. 2.1b, d, f). On the parameter space of  $\omega_\Delta = (\omega_h - \omega_v)/2$  and  $\lambda_\Delta = (\lambda_h - \lambda_v)/2$ , we calculate the spin density for each eigenmode  $C_{1,2} = (|a_+|^2 - |a_-|^2)/(|a_+|^2 + |a_-|^2)$  from the spin amplitudes of  $a_+ = (a_h - ia_v)/2^{1/2}$  and  $a_- = (a_h + ia_v)/2^{1/2}$ . The approach to the pure spin state is apparent in the  $\text{EP}^+$  ( $\lambda_\Delta = -\kappa$ ) and  $\text{EP}^-$  ( $\lambda_\Delta = \kappa$ ) points, while other regimes allow for elliptic eigenmodes with level splitting (Fig. 2.1c, d) and different non-conservative evolutions of gain or loss features (Fig. 2.1e, f), covering the case of circular dichroism [40–42].

## 2.2.2 TCMT Analysis of 3D Bulk Chirality with Circular Birefringent Mirrors

We now investigate the application of TCMT for 3D chiral resonant structures [11] maintaining the “Hermitian” condition (or energy conservation). A chiral structure [31–36], distinguishable from its mirror image, has attracted much attention in optics

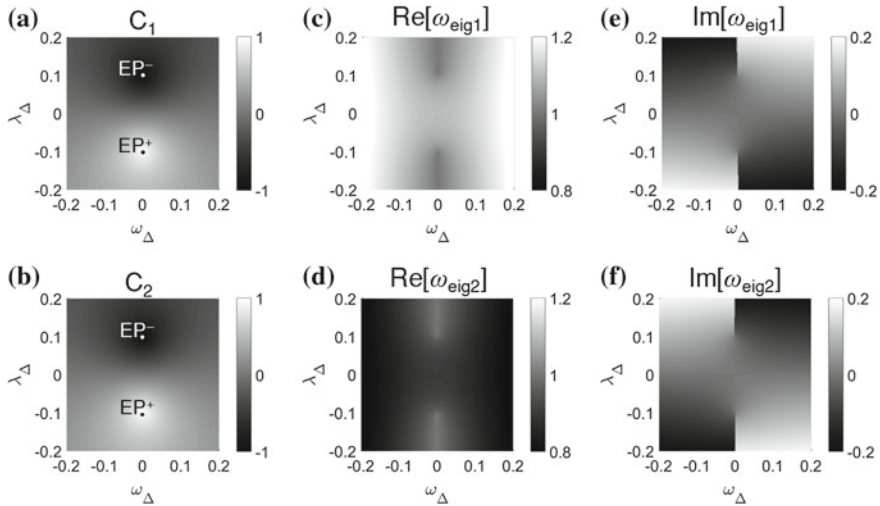


**Fig. 2.1** TCMT analysis of 2D non-hermitian chirality: **a, b** spin density of eigenmodes, **c, d** eigenfrequencies, and **e, f** amplification or dissipation coefficients for eigenmodes 1 **a, c, e** and 2 **b, d, f**.  $\omega_o = 1$ ,  $\lambda_o = 0$ , and  $K = 0.1$ .  $EP^+$  (or  $EP^-$ ) presents the exceptional point with the + (or -) spin eigenmode

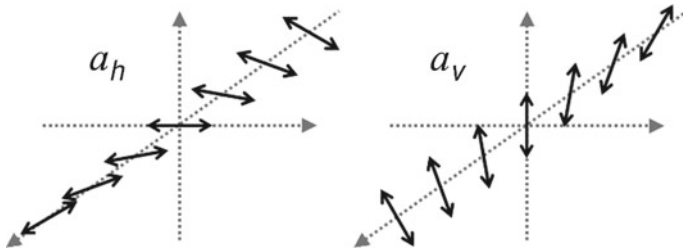


**Fig. 2.2** Natural optical rotation in the resonant linear polarization basis

for the sensing of natural chirality in chemical and biological molecules [30, 64, 65] and for novel phenomena in artificial chiral materials, such as negative refraction [34, 35]. The representative feature of 3D chiral structures is the chiral “velocity” of light [66], i.e., different phase velocities of each circular polarization. The spatio-temporally varying interference between right and left circular polarizations from their different velocities generates the “natural optical rotation” of linear polarizations [66] (Fig. 2.2).

To model 3D chiral phenomena with the TCMT, the resonance mode in the 3D chiral structure has to be defined on the spatially “rotated” coordinates ( $h$ - and  $v$ -axes in Fig. 2.2) for a chiral medium. For planewave propagation, because two polarization axes are considered, the TCMT resonance mode can have two degrees of freedom from the linear combination of the resonator field amplitudes  $a_h$  (horizontal linear

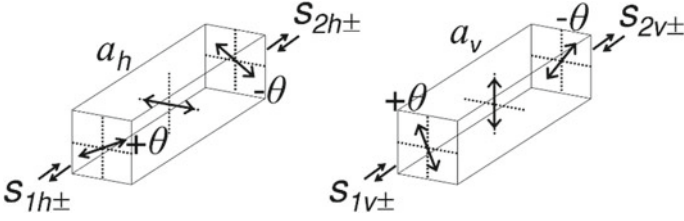


**Fig. 2.3** Two-port scattering of 3D chiral resonance. Each incoming and outgoing wave has its polarization aligned to the horizontal and vertical resonant mode with the spatially rotated polarization axis

polarization at the resonator centre) and  $a_v$  (vertical linear polarization at the resonator centre) of the resonance modes, with the same directional rotation (Fig. 2.2).

The TCMT equation for Hermitian  $h$ - and  $v$ -resonances then becomes

$$\frac{d}{dt} \begin{bmatrix} a_h \\ a_v \end{bmatrix} = \begin{bmatrix} i\omega_{h0} & 0 \\ 0 & i\omega_{v0} \end{bmatrix} \cdot \begin{bmatrix} a_h \\ a_v \end{bmatrix}, \quad (2.9)$$

where  $\omega_{h0}$  and  $\omega_{v0}$  are the resonant frequencies of the  $a_h$  and  $a_v$  modes, respectively, and then, the rotational modes of  $a_h$  and  $a_v$  become the eigenmodes of the system. It is worth mentioning that the resonant frequencies  $\omega_{h0}$  and  $\omega_{v0}$  have the same value when the permittivity of the chiral material is isotropic.

While the 3D chiral structure has simple linearly polarized eigenmodes, the scattering from external light sources requires special consideration. Consider the two-port system for the planewave, as shown in Fig. 2.3. For the case of the incoming ( $S_{1,2h+}$ ,  $S_{1,2v+}$ ) and outgoing ( $S_{1,2h-}$ ,  $S_{1,2v-}$ ) waves through ports 1 and 2, which each have an “aligned” polarization to the horizontal and vertical resonant mode with the spatially rotated polarization axis, the scattering TCMT has the following form:

$$\begin{aligned} \frac{d}{dt} \begin{bmatrix} a_h \\ a_v \end{bmatrix} &= \begin{bmatrix} i\omega_h - \frac{1}{\tau_{1h}} - \frac{1}{\tau_{2h}} & 0 \\ 0 & i\omega_v - \frac{1}{\tau_{1v}} - \frac{1}{\tau_{2v}} \end{bmatrix} \cdot \begin{bmatrix} a_h \\ a_v \end{bmatrix} \\ &+ \begin{bmatrix} \sqrt{\frac{2}{\tau_{1h}}} & 0 \\ 0 & \sqrt{\frac{2}{\tau_{1v}}} \end{bmatrix} \cdot \begin{bmatrix} S_{1h+} \\ S_{1v+} \end{bmatrix} + \begin{bmatrix} \sqrt{\frac{2}{\tau_{2h}}} & 0 \\ 0 & \sqrt{\frac{2}{\tau_{2v}}} \end{bmatrix} \cdot \begin{bmatrix} S_{2h+} \\ S_{2v+} \end{bmatrix} \end{aligned} \quad (2.10)$$

$$\begin{aligned}
\begin{bmatrix} S_{1h-} \\ S_{1v-} \end{bmatrix} &= -I \cdot \begin{bmatrix} S_{1h+} \\ S_{1v+} \end{bmatrix} + \begin{bmatrix} \sqrt{\frac{2}{\tau_{1h}}} & 0 \\ 0 & \sqrt{\frac{2}{\tau_{1v}}} \end{bmatrix} \cdot \begin{bmatrix} a_h \\ a_v \end{bmatrix} \\
\begin{bmatrix} S_{2h-} \\ S_{2v-} \end{bmatrix} &= -I \cdot \begin{bmatrix} S_{2h+} \\ S_{2v+} \end{bmatrix} + \begin{bmatrix} \sqrt{\frac{2}{\tau_{2h}}} & 0 \\ 0 & \sqrt{\frac{2}{\tau_{2v}}} \end{bmatrix} \cdot \begin{bmatrix} a_h \\ a_v \end{bmatrix}
\end{aligned} \tag{2.11}$$

where  $\tau_{1,2h}$  and  $\tau_{1,2v}$  are the resonant-modal decay times determined by the radiation  $Q$ -factor for ports 1 and 2.

We now reformulate (2.10) and (2.11) using the spinor representation, with the resonator structural parameters defined on the universal axes  $x$  and  $y$ . First, if we consider the natural optical rotation of  $2\theta$  inside the resonator ( $\theta = \omega\chi L_{\text{eff}}/2c$ , where  $\chi$  is normalized chirality,  $L_{\text{eff}}$  is the effective path of the resonator, and  $c$  is the speed of light) [67, 68], we can rewrite the scattering fields from the representations on the rotated axes  $h$  and  $v$  to those of the universal axes  $x$  and  $y$ , as

$$\begin{bmatrix} S_{1h\pm} \\ S_{1v\pm} \end{bmatrix} = U \cdot \begin{bmatrix} S_{1x\pm} \\ S_{1y\pm} \end{bmatrix}, \quad \begin{bmatrix} S_{2h\pm} \\ S_{2v\pm} \end{bmatrix} = U^{-1} \cdot \begin{bmatrix} S_{2x\pm} \\ S_{2y\pm} \end{bmatrix}, \quad \text{where } U = \begin{bmatrix} \cos \theta & \sin \theta \\ -\sin \theta & \cos \theta \end{bmatrix}, \tag{2.12}$$

if the rotated axis  $h$  (or  $v$ ) is parallel to the  $x$  (or  $y$ ) axis at the resonator centre. On this coordinate representation, by considering the evanescent power flow to the resonator, we can obtain the decay times along the rotated axes from those along the universal axes, as  $1/\tau_{1,2h} = \cos^2 \theta/\tau_x + \sin^2 \theta/\tau_y$  and  $1/\tau_{1,2v} = \sin^2 \theta/\tau_x + \cos^2 \theta/\tau_y$ , where  $\tau_x$  and  $\tau_y$  are the decay times along the  $x$ - and  $y$ -axis. This representation allows consideration of the chiral resonator ‘‘boundary’’, which usually possesses the birefringence effect ( $\varepsilon_x \neq \varepsilon_y$ ).

Second, we transform the resonator and scattering fields from the linear polarization to the spinor representation

$$\begin{aligned}
\begin{bmatrix} a_+ \\ a_- \end{bmatrix} &= \frac{1}{\sqrt{2}} \begin{bmatrix} 1 & i \\ 1 & -i \end{bmatrix} \cdot \begin{bmatrix} a_h \\ a_v \end{bmatrix} = C_{\text{SL}} \cdot \begin{bmatrix} a_h \\ a_v \end{bmatrix} = C_{\text{LS}}^{-1} \cdot \begin{bmatrix} a_h \\ a_v \end{bmatrix} \\
\begin{bmatrix} S_{1x+} \\ S_{1y+} \end{bmatrix} &= C_{\text{LS}} \cdot \begin{bmatrix} S_{1L+} \\ S_{1R+} \end{bmatrix}, \quad \begin{bmatrix} S_{2x+} \\ S_{2y+} \end{bmatrix} = C_{\text{LS}}^* \cdot \begin{bmatrix} S_{2L+} \\ S_{2R+} \end{bmatrix} \\
\begin{bmatrix} S_{1x-} \\ S_{1y-} \end{bmatrix} &= C_{\text{LS}}^* \cdot \begin{bmatrix} S_{1L-} \\ S_{1R-} \end{bmatrix}, \quad \begin{bmatrix} S_{2x-} \\ S_{2y-} \end{bmatrix} = C_{\text{LS}} \cdot \begin{bmatrix} S_{2L-} \\ S_{2R-} \end{bmatrix}
\end{aligned} \tag{2.13}$$

where  $C_{\text{SL}}$  (or  $C_{\text{LS}}$ ) is the linear-to-spin (or spin-to-linear) transformation matrix and the  $*$  sign denotes the complex conjugate. By applying (2.12) and (2.13) to (2.11), we now derive the TCMT equation for the scattering as

$$\begin{aligned}
\frac{d}{dt} \begin{bmatrix} a_+ \\ a_- \end{bmatrix} &= C_{\text{SL}} \cdot \begin{bmatrix} i\omega_h - \frac{1}{\tau_{1h}} - \frac{1}{\tau_{2h}} & 0 \\ 0 & i\omega_v - \frac{1}{\tau_{1v}} - \frac{1}{\tau_{2v}} \end{bmatrix} \cdot C_{\text{LS}} \cdot \begin{bmatrix} a_+ \\ a_- \end{bmatrix} \\
&+ C_{\text{SL}} \cdot \begin{bmatrix} \sqrt{\frac{2}{\tau_{1h}}} & 0 \\ 0 & \sqrt{\frac{2}{\tau_{1v}}} \end{bmatrix} \cdot U_1 \cdot C_{\text{LS}} \cdot \begin{bmatrix} S_{1L+} \\ S_{1R+} \end{bmatrix} + C_{\text{SL}} \cdot \begin{bmatrix} \sqrt{\frac{2}{\tau_{2h}}} & 0 \\ 0 & \sqrt{\frac{2}{\tau_{2v}}} \end{bmatrix} \cdot U_2 \cdot C_{\text{LS}}^* \cdot \begin{bmatrix} S_{2L+} \\ S_{2R+} \end{bmatrix},
\end{aligned} \tag{2.14}$$

which can handle the resonance mode on a chiral medium between birefringent mirrors.

For further insight, we introduce reasonable assumptions for simplicity: (1) spatial symmetry between ports 1 and 2 ( $\tau_{1h} = \tau_{2h} = \tau_h$  and  $\tau_{1v} = \tau_{2v} = \tau_v$ ), (2) single port excitation ( $S_{2L+} = S_{2R+} = 0$ ), and (3) an isotropic chiral material ( $\omega_{h0} = \omega_{v0} = \omega_0$ ). Equation (2.14) then becomes

$$\begin{aligned}
\frac{d}{dt} \begin{bmatrix} a_+ \\ a_- \end{bmatrix} &= \begin{bmatrix} i\omega_0 - (\frac{1}{\tau_h} + \frac{1}{\tau_v}) & -(\frac{1}{\tau_h} - \frac{1}{\tau_v}) \\ -(\frac{1}{\tau_h} - \frac{1}{\tau_v}) & i\omega_0 - (\frac{1}{\tau_h} + \frac{1}{\tau_v}) \end{bmatrix} \cdot \begin{bmatrix} a_+ \\ a_- \end{bmatrix} \\
&+ \frac{1}{2} \begin{bmatrix} (\sqrt{\frac{2}{\tau_h}} + \sqrt{\frac{2}{\tau_v}})e^{-i\theta} & (\sqrt{\frac{2}{\tau_h}} - \sqrt{\frac{2}{\tau_v}})e^{i\theta} \\ (\sqrt{\frac{2}{\tau_h}} - \sqrt{\frac{2}{\tau_v}})e^{-i\theta} & (\sqrt{\frac{2}{\tau_h}} + \sqrt{\frac{2}{\tau_v}})e^{i\theta} \end{bmatrix} \cdot \begin{bmatrix} S_{1L+} \\ S_{1R+} \end{bmatrix}.
\end{aligned} \tag{2.15}$$

For a more clear representation, we introduce the coupling coefficient  $\kappa_{h,v} = (2/\tau_{h,v})^{1/2}$ , where  $\kappa_0 = (\kappa_h + \kappa_v)/2$  and  $\Delta\kappa = (\kappa_h - \kappa_v)/2$ , and then, (2.16) is simplified as

$$\begin{aligned}
\frac{d}{dt} \begin{bmatrix} a_+ \\ a_- \end{bmatrix} &= \begin{bmatrix} i\omega_0 - (\frac{1}{\tau_h} + \frac{1}{\tau_v}) & -(\frac{1}{\tau_h} - \frac{1}{\tau_v}) \\ -(\frac{1}{\tau_h} - \frac{1}{\tau_v}) & i\omega_0 - (\frac{1}{\tau_h} + \frac{1}{\tau_v}) \end{bmatrix} \cdot \begin{bmatrix} a_+ \\ a_- \end{bmatrix} \\
&+ \begin{bmatrix} \kappa_0 e^{-i\theta} & \Delta\kappa e^{i\theta} \\ \Delta\kappa e^{-i\theta} & \kappa_0 e^{i\theta} \end{bmatrix} \cdot \begin{bmatrix} S_{1L+} \\ S_{1R+} \end{bmatrix}.
\end{aligned} \tag{2.16}$$

Equation (2.16) represents the ‘‘birefringent’’ boundary effect, which is the origin of the interfered mixing between spin modes. If there is no birefringence boundary ( $\tau_h = \tau_v$ ) for chiral resonances, every off-diagonal term in (2.16) vanishes, and thus, each spin mode is independently excited, leading to the simple Lorentzian resonant response. However, when the birefringent boundary effect occurs ( $\tau_h \neq \tau_v$ , or  $\tau_x \neq \tau_y$  from  $1/\tau_h = \cos^2\theta/\tau_x + \sin^2\theta/\tau_y$  and  $1/\tau_v = \sin^2\theta/\tau_x + \cos^2\theta/\tau_y$ ), the mixing between the (+) and (−) spin modes is obtained in both (1) the resonance mode from  $-(1/\tau_h - 1/\tau_v)$  and (2) the scattering from  $\Delta\kappa \cdot \exp(\pm i\theta) = [(2/\tau_h)^{1/2} - (2/\tau_v)^{1/2}] \cdot \exp(\pm i\theta)/2$ . We also note that this spin mixing effect accompanies the frequency-dependent interference from the value of the natural optical rotation  $\theta = \omega\chi L_{\text{eff}}/2c$ ,

leading to the possibility of spectral interference phenomena, such as Fano resonances [51] and electromagnetically induced transparency [50].

Based on this phase-dependent mixing of spin modes, in Sect. 2.3, we explore the emergence of spin-dependent Fano resonances in 3D chiral resonators with birefringent mirrors.

## 2.3 Fano-resonant Excitation of Optical Spin

A Fano resonance [69] is a universal phenomenon that occurs in coupling between resonances of different bandwidths. From the different phase evolutions of each resonance on the spectral axis, the coupling between these resonances results in spectral “interference”, which transforms the traditional Lorentzian resonance with a symmetric line shape to an “asymmetric” line shape. In addition to the classical emergence of Fano resonances for inelastic electron scattering [69], the universality of Fano-resonant phenomena has been observed in various fields, including condensed matter physics, microwave engineering, and optics.

Due to its spectral response and universal nature, Fano resonance provides a valuable tool for achieving superior spectral sensitivity in general wave devices. In optics, to achieve more sensitive spectral dispersion within the inherent  $Q$ -factor, which is usually limited by the utilized optical materials, the design of Fano resonance systems has been broadly studied for several applications, such as selective sensors [51, 70, 71], power-efficient modulators [11, 50, 72, 73], narrowband absorbers [52], controlled lasing [74], and wave transport in disordered systems [75].

In this section, we utilize Fano resonances to achieve spin separation in the spectral domain by focusing on the Fano resonance in polarization space. In Sect. 2.3.1, we show that by realizing an antisymmetric Fano resonance upon each spin component, i.e., spin-dependent Fano spectral asymmetry, the spectral separation of optical spin can be achieved as a route toward spin manipulation. In Sect. 2.3.2, the basic mechanism and origin of this phenomenon will be discussed based on the TCMT model of Sect. 2.2.2. For quantitative analysis, the definition and application of a spin-density Fano parameter are introduced in Sect. 2.3.3.

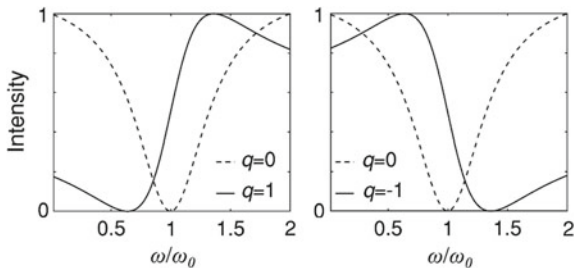
### 2.3.1 Fano Line Shapes Toward Spectral Spin Separation

The distinctive feature of Fano resonances is the spectral asymmetry in its line shape, usually described by the following formula [45, 74, 76, 77],

$$I(\omega) \propto \frac{(q\gamma + \omega - \omega_0)^2}{(\omega - \omega_0)^2 + \gamma^2}, \quad (2.17)$$



**Fig. 2.4** Normalized scattering cross section defined by the Fano formula (2.17) for opposite signs of Fano parameters: (left)  $q = 1$ , (right)  $q = -1$



where  $q$  is the famous Fano parameter representing the strength of the Fano spectral asymmetry;  $\omega_0$  and  $\gamma$  denote the resonance frequency and bandwidth of the system, respectively; and  $I$  is the scattering cross section. Along with its spectral asymmetry, Fano resonances also lead to the spectral shift governed by the Fano parameter  $q$  as

$$\omega_{\min} = \omega_0 - q\gamma, \quad (2.18)$$

where  $I(\omega_{\min}) = 0$ . Because the magnitude and sign of the Fano parameter  $q$  determine the strength and direction of both spectral asymmetry and the minimum scattering frequency  $\omega_{\min}$  (Fig. 2.4), the introduction of “spin dependence” on the Fano parameter allows spectral separation of each spin mode, e.g., the high frequency scattering of the positive spin and low frequency scattering of the negative spin.

The comparison of Fano-resonant spin separation with conventional spin materials in optics demonstrates the novelty of the proposed Fano system (Fig. 2.5). First, optical chiral materials (Fig. 2.5a, b) allow circular birefringence for light from the spin-form eigenmodes with different phase velocities. Although the circular birefringence derives the natural optical rotation for linear polarizations, it does not provide mixing of optical spins during scattering due to the lack of a spin-dependent impedance. Therefore, the chiral material cannot derive the “net” achievement of optical spins by itself (Fig. 2.5a, b).

A conventional method for the excitation of optical spin is circular dichroism, by imposing different absorptions on each optical spin mode (Fig. 2.5c, d). Although the use of circular dichroic materials, or more broadly non-Hermitian materials (Sect. 2.2.1), enables a scattering difference between each spin mode, the inherent dissipation from circular dichroism not only degrades the intrinsic  $Q$ -factor of the system but also decreases the signal strength of the target spin mode (Fig. 2.5c, d).

By contrast, because Fano-resonant spin separation (Fig. 2.5e, f) is achieved in a conservative manner, the original intrinsic  $Q$ -factor and signal strength of the optical spin mode can be maintained. Moreover, the Fano-induced spectral asymmetry provides additional spectral sensitivity (Fig. 2.5e, f). Therefore, spin-dependent Fano-resonance provides the optimum platform for achieving conservative and precise control of optical spin.

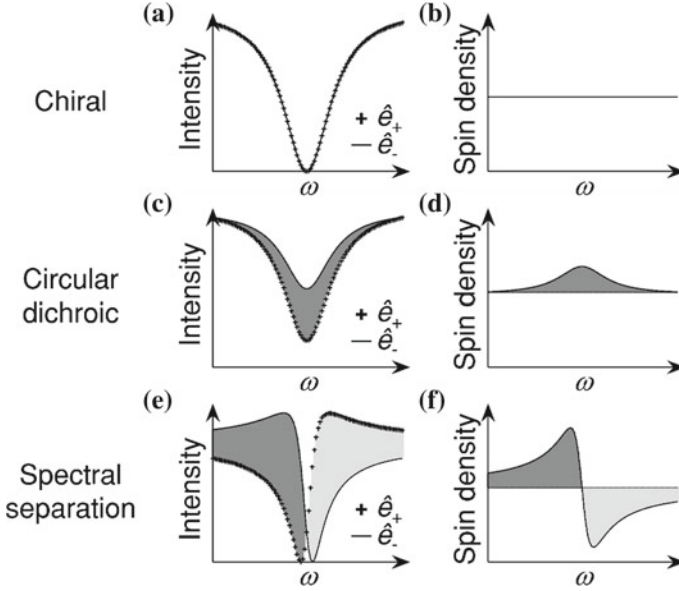


**Fig. 2.5** Schematics of the spectra for the **a, c, e** scatterings and **b, d, f** optical spin densities induced by **a, b** a chiral material, **c, d** circular dichroic material, and **e, f** Fano-induced spin separation structure [11]

### 2.3.2 Spin-Dependent Antisymmetric Fano Resonances

In this section, we develop the proposed Fano-resonant system for spin separation by utilizing the theoretical analysis from Sect. 2.2.2. For spin-dependent Fano resonance, each spin mode  $\hat{e}_{\pm} = (x \pm iy)/2^{1/2}$  has to experience Fano interference with the opposite direction of spectral asymmetry and resonance shift. If we rewrite (2.16) for each spin as

$$\begin{aligned} \frac{da_+}{dt} &= \left[ i\omega_0 - \left( \frac{1}{\tau_h} + \frac{1}{\tau_v} \right) \right] a_+ - \left( \frac{1}{\tau_h} - \frac{1}{\tau_v} \right) a_- + (\kappa_0 e^{-i\theta} S_{1L+} + \Delta\kappa e^{+i\theta} S_{1R+}) \\ \frac{da_-}{dt} &= \left[ i\omega_0 - \left( \frac{1}{\tau_h} + \frac{1}{\tau_v} \right) \right] a_- - \left( \frac{1}{\tau_h} - \frac{1}{\tau_v} \right) a_+ + (\kappa_0 e^{+i\theta} S_{1R+} + \Delta\kappa e^{-i\theta} S_{1L+}) \end{aligned} \quad (2.19)$$

the frequency-dependent “phase interference” inside the external source [the third terms of the right side in (2.19)] is obtained from the natural optical rotation  $\theta = \omega\chi L_{\text{eff}}/2c$ , and from its spin-dependent phase information, we can expect the opposite phase interference for each spin resonance mode  $a_{\pm}$ .

To demonstrate this antisymmetric mixing between (+) and (−) spin modes, which occurs in the chiral resonator with birefringent boundaries (Sect. 2.2.2), we construct a Fabry–Pérot resonator composed of a chiral medium between a pair of birefringent

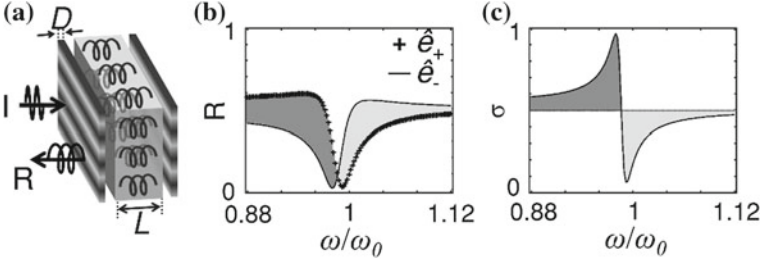


**Fig. 2.6** Demonstration of the spin-dependent Fano resonance [11]. **a** A schematic of a Fabry–Pérot chiral resonator with indefinite mirrors. **b** The corresponding reflectance spectra  $R_{\hat{e}_{\pm}}$  and **c** spin density  $\sigma$ . The chirality and permittivity of the chiral material is  $\chi=0.05$  and  $\varepsilon_{\text{chiral}}=9$ , respectively. The resonator structure parameters are  $L=0.29\lambda_0$  and  $D=\lambda_0/60$ , where  $\lambda_0=2\pi c/\omega_0$  and  $\omega_0$  is the normalization frequency

mirrors. Because the relative magnitude of the mixing  $\Delta\kappa=[(2/\tau_h)^{1/2}-(2/\tau_v)^{1/2}]$  increases with the strength of the birefringence, we utilize an “indefinite” material [78] mirror, which has a metallic permittivity value in one axis ( $\varepsilon_x=\varepsilon_{\text{metal}}<0$ ) and a dielectric permittivity value in the other axis ( $\varepsilon_y=\varepsilon_{\text{dielec}}>0$ ) (Fig. 2.6a). Thus, this FP resonator provides two different resonances, a narrow- (or broad-) band resonance of  $x$ - (or  $y$ -) polarized light from the highly reflected metallic (or from highly transparent dielectric) mirror. These two resonances of different bandwidths lead to Fano interference. Based on the derived TCMT model in (2.16), the spectral response of the scattering spin density  $\sigma(\omega)=(R_{\hat{e}_-}-R_{\hat{e}_+})/(R_{\hat{e}_-}+R_{\hat{e}_+})$  is obtained as

$$\sigma = \frac{\sin(2\theta)[\kappa_h^2/(\omega-\omega_h)-\kappa_v^2/(\omega-\omega_v)]}{1+\kappa_h^4[\cos\theta/(\omega-\omega_h)]^2+\kappa_v^4[\cos\theta/(\omega-\omega_v)]^2}. \quad (2.20)$$

where  $R_{\hat{e}_{\pm}}$  is the reflectance of each spin from the system.

Figure 2.6b and c show the reflectance spectra and scattering spin density for  $\varepsilon_x=-80$  and  $\varepsilon_y=2.25$ , where  $\sigma=\pm 1$  denotes the pure spin state. For a clear comparison with circular dichroism, we assume real values for the material parameters (see Sect. 2.4.1 for the influence of material loss). As expected from (2.19), introduction of an indefinite mirror for the birefringent boundary condition of a chiral resonator leads to the emergence of spin-dependent “antisymmetric” Fano resonance, satisfying the condition for spectral separation and net achievement of optical spin (Fig. 2.6c vs. Fig. 2.5f). From the sharp and antisymmetric Fano reflectance spectra  $R_{\hat{e}_{\pm}}$ , the state of the spin changes very rapidly between pure spin states close to  $\sigma=0.998$ .

The temporal interpretation of the Fano dynamics [74] also provides a comprehensible understanding of its spectral nature. Figure 2.7 shows the temporal analysis of the spin-dependent Fano resonance based on the TCMT model in (2.16) with impulse excitation  $S_{1,x}^{\text{in}}=\delta(t)$ . While no temporal shift is observed with isotropic mirror realization (Fig. 2.7a), the indefinite mirror for the spin-dependent Fano resonance stimulates the time leading and lagging phenomena for each spin state. These

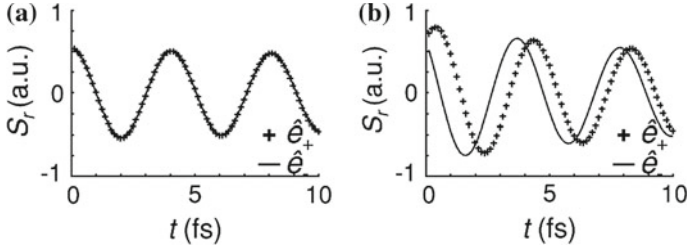


**Fig. 2.7** Impulse responses of chiral resonators sandwiched between a pair of **a** isotropic mirrors and **b** birefringent indefinite mirrors [11]

opposite temporal shifts correspond to spectral shifts toward the opposite direction, resulting in antisymmetric Fano resonance line shapes.

### 2.3.3 Spin Fano Parameters

The proper definition of a Fano parameter [69] provides excellent quantification of Fano resonances in terms of the degree of spectral asymmetry and resonance shift. Following the definition of the Fano parameter in [69], we define the “spin” Fano parameter  $q_s$  as the ratio of indirect to direct excitation of the chiral resonator. From the external source term in (2.19), because the coefficient of the indirect coupling is  $\kappa_d e^{i\theta}$  while the direct one is  $\kappa_s e^{-i\theta}$ , the spin Fano parameter becomes

$$q_s = \frac{\kappa_d}{\kappa_s} e^{i2\theta}. \quad (2.21)$$

As shown in (2.21), this complex Fano parameter has two degrees of freedom: the argument  $\arg(q_s) = 2\theta$  from the strength of natural optical rotation (or optical chirality) and modulus  $|q_s| = \kappa_d/\kappa_s$  from the strength of the birefringence. We examine the dependence of the spin density spectra on  $q_s$  (Fig. 2.8). Figure 2.8a, b show spin density spectra for different values of  $\arg(q_s)$  and  $|q_s|$ , respectively. First, smaller values of the material chirality (Fig. 2.8a) lead to a narrower bandwidth of the spin density spectra, directly associated with smaller spectral separation between optical spins (see Sect. 2.4.1 for its application to a spin switching device). Figure 2.8b also shows that larger values of  $|q_s|$  lead to a narrower bandwidth of the spin density spectrum. From this quantitative analysis, the tuning approach toward spin switching can be achieved, as demonstrated in the next section.

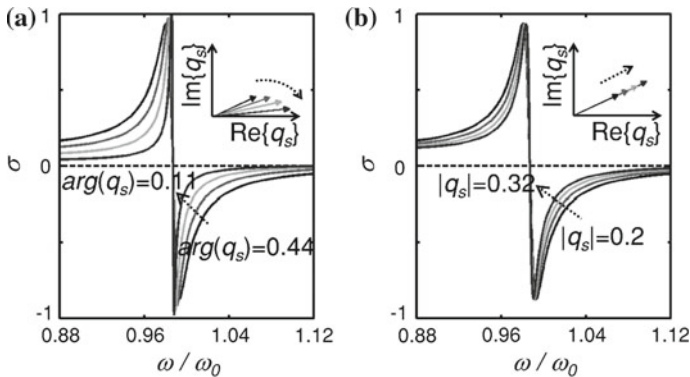


**Fig. 2.8** Control of the optical spin density spectra ( $\sigma$ ) in terms of the spin Fano parameter  $q_s$  [11]. The control parameters are **a** chirality for  $\arg(q_s)=0.44-0.11$  and **b** birefringence for  $|q_s|=0.2-0.32$

## 2.4 Applications and Metamaterial Realizations

In this section, we show the applications of the spin-dependent Fano resonance for Sect. 2.3, focusing on (i) its spectral sensitivity toward a spin switching implementation (Sect. 2.4.1) and (ii) its robust spinning nature to unpolarized light, in contrast to a conventional birefringent material (Sect. 2.4.2). We also provide the detailed design criteria for the birefringent metamaterial mirror of the chiral resonator (Sect. 2.4.3), the core control part of the spin-dependent Fano resonance.

### 2.4.1 Fano-resonant Optical Spin Switching

On the road to optical spintronics, achieving precise control of the optical spin states is essential. The flow and magnitude of each spin state needs to be freely manipulated using devices such as spin filters, splitters, absorbers, and amplifiers. Among these devices, realization of highly efficient spin switching [79–81] between the (+) and (−) states will be the fundamental building block for light-based spintronics circuits and applications of circular polarized light. The spectral sensitivity of antisymmetric Fano resonances for optical spin modes (Figs. 2.6 and 2.8 in Sect. 2.3) provides the optimum platform for the implementation of spin switching.

Figure 2.9 shows the Fano-resonant optical spin switching operation, derived by the refractive index change of the chiral material (Fig. 2.9a). As shown in Fig. 2.9b, the sharp transition of the spin density  $\sigma$  from +1 to −1 occurs within the spectral difference  $\Delta\omega \sim 0.004 \omega_c$ . Because the  $\sigma$  spectrum is strongly dependent on the phase of the Fano parameter  $\arg(q_s) = 2\theta = \omega\chi L_{\text{eff}}/c$  (Fig. 2.8 in Sect. 2.3.3), i.e., natural optical rotation, we change the amount of natural optical rotation by

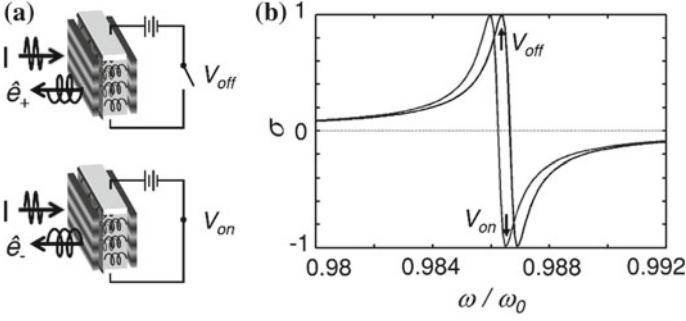


**Fig. 2.9** Fano-resonant optical spin switching [11]. **a** A schematic of switching with on/off states, as determined by refractive index modulation. **b** Spin reversal from the positive ( $\sigma = +0.998$ ) to negative ( $\sigma = -0.993$ ) spin state, derived by refractive index modulation with the assumed electrical bias ( $V_{on}$  for  $\Delta n = 10^{-3}$ )

applying a refractive index change of the chiral material, which can be obtained through electrical or optical modulation of the material carrier density or optical nonlinearity, such as the optical Kerr effect. For the small refractive index change of  $\Delta n = 10^{-3}$ , which is an acceptable value guaranteed from previous literature (e.g.,  $\Delta n \sim 8 \times 10^{-3}$  can be achieved with the bias voltage of  $\sim 1$  V [82–84]), the obtained shift of the spin density spectra leads to a sharp transition of  $\sigma$  (Fig. 2.9b): from  $\sigma = +0.998$  (bias off) to  $\sigma = -0.993$  (bias on) at the working frequency  $\omega = 0.987 \omega_c$  and chirality value  $\chi = 5 \times 10^{-3}$ .

Figure 2.10 shows the detailed performance analysis of Fano-resonant spin switching, demonstrating its superior features in terms of spin purity and operating power. Interestingly, much smaller values of the material chirality  $\chi$  ( $= 10^{-1}$  to  $10^{-4}$ ) allow for significantly decreased index modulation  $\Delta n$  ( $10^{-2}$  to  $10^{-5}$ , Fig. 2.10a) for high purity spin switching, with the sacrifice of signal strength ( $0.4$  to  $10^{-4}$ , Fig. 2.10b). Such a counterintuitive feature (small chirality for efficient spin switching) greatly increases the design degrees of freedom for optical spin switching devices when considering the material chirality values in nature [66, 68] as well as the required electric or optical bias. We also note that chiral metamaterials of larger  $\chi$  ( $\chi \sim 1$ ) [32, 33, 36, 85] enable larger signal strengths with the index tuning of  $\Delta n > 10^{-3}$ , which can be achieved in liquid crystals.

For practical implementation, we also analyse the influence of material loss (Fig. 2.10c, d), which degrades the intrinsic  $Q$ -factor of the system. The intrinsic  $Q$ -factor of each mode ( $Q_{int} = Re[\omega_{h,v0}] / (2 \cdot Im[\omega_{h,v0}])$ ) is included as the complex values of  $\omega_{h0}$  and  $\omega_{v0}$  in the TCMT model (Sect. 2.2.2). Owing to the broadening in the signal spectrum and deviation from the critical coupling condition by material loss, the purity in the spin switching operation is degraded (Fig. 2.10c). However, the broadened spectrum provides enhancement of the signal strength for switching states (Fig. 2.10d).

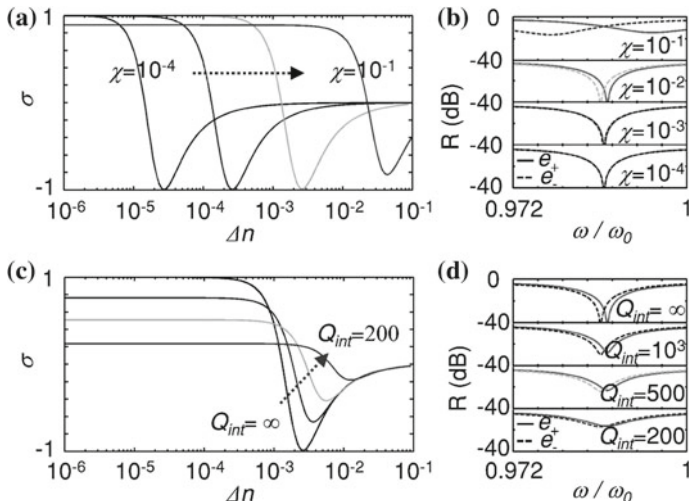


**Fig. 2.10** Performance analysis of Fano-resonant optical spin switching [11]. **a, c** The spin density  $\sigma$  as a function of the refractive index modulation  $\Delta n$  and **b, d** reflectance spectra for different **a, b** material chirality values  $\chi$  and **c, d** intrinsic quality factors  $Q_{\text{int}}$

### 2.4.2 Fano-resonant ‘Net’ Spin Excitation for Unpolarized Light

While birefringent media conventionally enable the excitation of optical spin (or circular polarization), the spin-dependent Fano-resonant system provides unique features compared with the conventional one in the context of spin switching (Sect. 2.4.1): exhibiting a “robust spinning nature” to unpolarized light. Figure 2.11a, b shows the polarization-angle-dependency of the optical spin excitation in the platforms using the birefringent medium (Fig. 2.11a) and Fano-resonant system (Fig. 2.11b). The Fano-resonant chiral system realizes an asymmetric line shape for any polarization angle (Fig. 2.11b vs. 2.11a). Most interestingly, in the Fano-resonant system, there exists the “net” excitation of optical spin for the incidence of unpolarized light (Fig. 2.11d vs. Fig. 2.11c). Such a robust spinning nature originates from the participation of the natural optical rotation from a chiral material, leading to Fano-interfered mixing of the narrowband ( $x$ -axis) and broadband ( $y$ -axis) birefringent scattering paths. This result enables “universal” operation of circular polarizers, which can be applied to chiral filters, lasers, and absorbers.

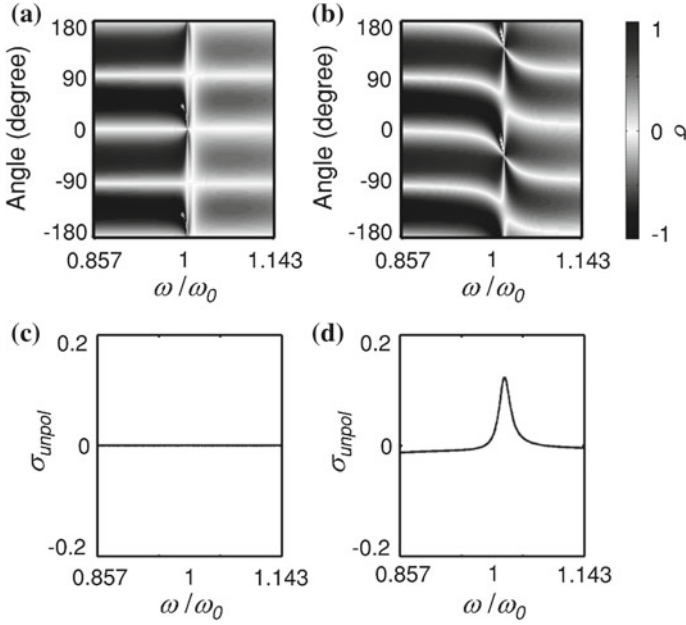


**Fig. 2.11** The ‘net’ excitation of the optical spin through spin-dependent Fano-resonance. **a, b** Angular dependence of the spin density spectra, and **c, d** excitation of optical spin from unpolarized light excitation for **a, c** a birefringent medium and **b, d** the spin-dependent Fano-resonant system (supplementary information in [11])

### 2.4.3 Metamaterial Realizations

As demonstrated in the TCMT analysis (Sect. 2.2.2), the physical origin of the spin mixing in spin-dependent Fano-resonance is the birefringent boundaries of the chiral resonator. Therefore, significant and tunable birefringence over the natural material response is the core design parameter for the applications in optical spintronics.

Specifically, birefringent mirrors should satisfy the following criteria; (1) a ‘flat’-type mirror for the serial deposition of a core and claddings; (2) an indefinite ( $\epsilon_x < 0$  and  $\epsilon_y > 0$ ) non-resonant mirror for significant spin mixing; and (3) precise control of effective material parameters for controlling Fano interferences. These criteria can be satisfied by using metamaterials. Figure 2.12 shows an implementation example of metamaterial mirrors. While a natural chiral medium is enough for the core medium of the resonator, due to the chirality-sensitive operation of the spin-dependent Fano resonance (Sect. 2.4.1), we utilize an indefinite ( $\epsilon_x < 0$  and  $\epsilon_y > 0$ ) birefringent mirror for significant spin mixing, which is composed of a gold (Au) grating embedded in a polyimide film (Fig. 2.12a). Figure 2.12b shows the effective material parameters of this artificial film operating in the infrared regime ( $h_{poly} = 100$  nm,  $h_{Au} = 40$  nm,  $w = 40$  nm, and  $P = 400$  nm). We note that the change of the structural parameters (filling ratio of metal  $w/P$ , metal width  $w$ , material thicknesses  $h_{poly}$  or  $h_{Au}$ ) allows for



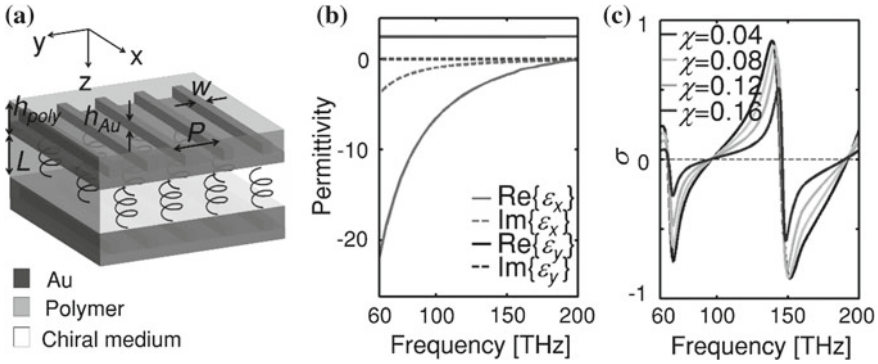


**Fig. 2.12** Realization of metamaterial mirrors for Fano-resonant spin excitation. **a** A schematic for the chiral resonator, embedded between indefinite metamaterial mirrors. **b** Anisotropic effective permittivity of the metamaterial mirror, calculated from the 3D finite element method. **c** Spin density spectra for different  $\chi$ , with practical material values in the infrared regime (supplementary information in [11])

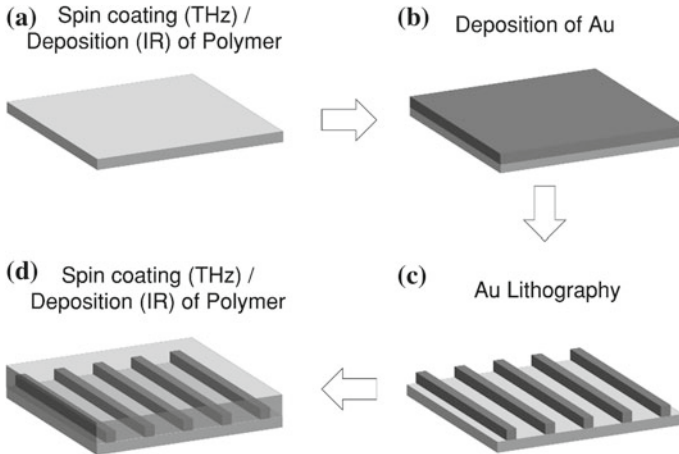


**Fig. 2.13** A schematic for the fabrication process of an indefinite birefringent mirror (supplementary information in [11])

precise control of the effective material parameters. The desired “sharp” transition between the positive and negative spins is successfully achieved even if the practical degradation factors, such as material loss and spectral dispersion, are involved (Fig. 2.12c). The spectral broadening can also be manipulated by changing the value of chirality.

Figure 2.13 shows the detailed fabrication process of the indefinite mirror. Conventional fabrication technologies, such as spin coating, chemical vapour deposition (CVD), electron-beam or thermal evaporation, lithography or imprinting, chemical-mechanical polishing (CMP), allow tunable realization of the indefinite mirror.

## 2.5 Conclusions

In this chapter, we introduced a new pathway toward nonmagnetic excitation of optical SAM based on the spin-dependent excitation of Fano resonances. We first developed the analytical method of spin-form TCMT for 2D and 3D chiral resonances to achieve a comprehensible understanding of the optical spin eigenmodes and their scattering with external light sources. This theoretical approach reveals the origin of the “anti”-symmetric line shapes of the spin-dependent Fano resonance to be the opposite temporal phase shift of each spin, in perfect agreement with the full-wave scattering matrix calculations. We also showed that a spin-density Fano parameter derived by the TCMT plays a critical role in identifying the quantitative control of the spin excitation. This result enables energy-conservative separation of optical spins without any need for magneto-optical or circular dichroic materials, allowing pure spin density superior to conventional approaches. Along to the access to 3D optical spin components [13], spin-dependent Fano resonances for confined light will be an avenue for the spectral manipulation of 3D spin components.

**Acknowledgements** We acknowledge financial support from the National Research Foundation of Korea (NRF) through the Korea Research Fellowship Program (2016H1D3A1938069), the Basic Science Research Program (2016R1A6A3A04009723), and the Global Frontier Program (2014M3A6B3063708), all funded by the Korean government.

## References

1. R. Kirchain, L. Kimerling, A roadmap for nanophotonics. *Nat. Photon.* **1**, 303–305 (2007)
2. S.A. Maier, *Plasmonics: Fundamentals and Application* (Springer Science & Business Media, 2007)
3. N. Engheta, R.W. Ziolkowski, *Metamaterials: Physics and Engineering Explorations* (John Wiley & Sons, 2006)
4. D.A. Miller, Are optical transistors the logical next step? *Nat. Photon.* **4**, 3–5 (2010)
5. T. Baehr-Jones, T. Pinguet, P.L. Guo-Qiang, S. Danziger, D. Prather, M. Hochberg, Myths and rumours of silicon photonics. *Nat. Photon.* **6**, 206–208 (2012)
6. D. Sanvitto, S. Kéna-Cohen, The road towards polaritonic devices. *Nat. Mater.* **15**, 1061–1073 (2016)
7. A.Y. Bekshaev, K.Y. Bliokh, F. Nori, Transverse spin and momentum in two-wave interference. *Phys. Rev. X* **5**, 011039 (2015)
8. K.Y. Bliokh, F. Nori, Transverse and longitudinal angular momenta of light. *Phys. Rep.* **592**, 1–38 (2015)
9. K.Y. Bliokh, F. Rodríguez-Fortuño, F. Nori, A.V. Zayats, Spin-orbit interactions of light. *Nat. Photon.* **9**, 796–808 (2015)
10. K.Y. Bliokh, D. Smirnova, F. Nori, Quantum spin hall effect of light. *Science* **348**, 1448–1451 (2015)
11. X. Piao, S. Yu, J. Hong, N. Park, Spectral separation of optical spin based on antisymmetric Fano resonances. *Sci. Rep.* **5**, 16585 (2015)
12. S. Yu, H.S. Park, X. Piao, B. Min, N. Park, Low-dimensional optical chirality in complex potentials. *Optica* **3**, 1025–1032 (2016)
13. X. Piao, S. Yu, N. Park, Design of transverse spinning of light with globally unique handedness. *Phys. Rev. Lett.* **120**, 203901 (2018)

14. N. Bozinovic, Y. Yue, Y. Ren, M. Tur, P. Kristensen, H. Huang, A.E. Willner, S. Ramachandran, Terabit-scale orbital angular momentum mode division multiplexing in fibers. *Science* **340**, 1545–1548 (2013)
15. E. Karimi, S.A. Schulz, I. De Leon, H. Qassim, J. Upham, R.W. Boyd, Generating optical orbital angular momentum at visible wavelengths using a plasmonic metasurface. *Light Sci. Appl.* **3**, e167 (2014)
16. D.L. Vitullo, C.C. Leary, P. Gregg, R.A. Smith, D.V. Reddy, S. Ramachandran, M.G. Raymer, Observation of interaction of spin and intrinsic orbital angular momentum of light. *Phys. Rev. Lett.* **118**, 083601 (2017)
17. A.B. Khanikaev, S.H. Mousavi, W.K. Tse, M. Kargarian, A.H. MacDonald, G. Shvets, Photonic topological insulators. *Nat. Mater.* **12**, 233–239 (2013)
18. M.C. Rechtsman, J.M. Zeuner, Y. Plotnik, Y. Lumer, D. Podolsky, F. Dreisow, S. Nolte, M. Segev, A. Szameit, Photonic floquet topological insulators. *Nature* **496**, 196–200 (2013)
19. L. Lu, J.D. Joannopoulos, M. Soljačić, Topological photonics. *Nat. Photon.* (2014)
20. B. Plansinis, W. Donaldson, G. Agrawal, What is the temporal analog of reflection and refraction of optical beams? *Phys. Rev. Lett.* **115**, 183901 (2015)
21. Y. Xiao, D.N. Maywar, G.P. Agrawal, Reflection and transmission of electromagnetic waves at a temporal boundary. *Opt. Lett.* **39**, 574–577 (2014)
22. Z. Yu, S. Fan, Complete optical isolation created by indirect interband photonic transitions. *Nat. Photon.* **3**, 91–94 (2009)
23. M. Florescu, S. Torquato, P.J. Steinhardt, Designer disordered materials with large, complete photonic band gaps. *Proc. Natl. Acad. Sci.* **106**, 20658 (2009)
24. W. Man, M. Florescu, K. Matsuyama, P. Yadak, G. Nahal, S. Hashemizad, E. Williamson, P. Steinhardt, S. Torquato, P. Chaikin, Photonic band gap in isotropic hyperuniform disordered solids with low dielectric contrast. *Opt. Express* **21**, 19972–19981 (2013)
25. S. Torquato, Hyperuniformity and its generalizations. *Phys. Rev. E* **94**, 022122 (2016)
26. S. Yu, X. Piao, J. Hong, N. Park, Bloch-like waves in random-walk potentials based on super-symmetry. *Nat. Commun.* **6**, 8269 (2015)
27. S. Yu, X. Piao, J. Hong, N. Park, Metadisorder for designer light in random systems. *Sci. Adv.* **2**, e1501851 (2016)
28. S. Van Enk, G. Nienhuis, Spin and orbital angular momentum of photons. *Europhys. Lett.* **25**, 497 (1994)
29. E. Collett, Polarized light. Fundamentals and applications, in *Optical Engineering* (Dekker, New York, 1992)
30. Y. Tang, A.E. Cohen, Optical chirality and its interaction with matter. *Phys. Rev. Lett.* **104** (2010)
31. Y. Cui, L. Kang, S. Lan, S. Rodrigues, W. Cai, Giant chiral optical response from a twisted-arc metamaterial. *Nano Lett.* **14**, 1021–1025 (2014)
32. M. Thiel, M.S. Rill, G. von Freymann, M. Wegener, Three-dimensional bi-chiral photonic crystals. *Adv. Mater.* **21**, 4680–4682 (2009)
33. J.K. Gansel, M. Thiel, M.S. Rill, M. Decker, K. Bade, V. Saile, G. von Freymann, S. Linden, M. Wegener, Gold helix photonic metamaterial as broadband circular polarizer. *Science* **325**, 1513–1515 (2009)
34. S. Zhang, Y.-S. Park, J. Li, X. Lu, W. Zhang, X. Zhang, Negative refractive index in chiral metamaterials. *Phys. Rev. Lett.* **102** (2009)
35. J.B. Pendry, A chiral route to negative refraction. *Science* **306**, 1353–1355 (2004)
36. Y. Zhao, M. Belkin, A. Alù, Twisted optical metamaterials for planarized ultrathin broadband circular polarizers. *Nat. Commun.* **3**, 870 (2012)
37. S.H. Mousavi, A.B. Khanikaev, J. Allen, M. Allen, G. Shvets, Gyromagnetically induced transparency of metasurfaces. *Phys. Rev. Lett.* **112**, 117402 (2014)
38. V. Agranovich, Y.N. Gartstein, A. Zakhidov, Negative refraction in gyrotropic media. *Phys. Rev. B* **73**, 045114 (2006)
39. L. Lu, L. Fu, J.D. Joannopoulos, M. Soljačić, Weyl points and line nodes in gyroid photonic crystals. *Nat. Photon.* **7**, 294–299 (2013)

40. A. Papakostas, A. Potts, D.M. Bagnall, S.L. Prosvirnin, H.J. Coles, N.I. Zheludev, Optical manifestations of planar chirality. *Phys. Rev. Lett.* **90** (2003)
41. E. Plum, X.-X. Liu, V. Fedotov, Y. Chen, D. Tsai, N. Zheludev, Metamaterials: optical activity without chirality. *Phys. Rev. Lett.* **102**, 113902 (2009)
42. E. Plum, J. Zhou, J. Dong, V. Fedotov, T. Koschny, C. Soukoulis, N. Zheludev, Metamaterial with negative index due to chirality. *Phys. Rev. B* **79**, 035407 (2009)
43. S. Yu, X. Piao, N. Park, Acceleration toward polarization singularity inspired by relativistic  $E \times B$  drift. *Sci. Rep.* **6**, 37754 (2016)
44. M. Lawrence, N. Xu, X. Zhang, L. Cong, J. Han, W. Zhang, S. Zhang, Manifestation of PT symmetry breaking in polarization space with terahertz metasurfaces. *Phys. Rev. Lett.* **113**, 093901 (2014)
45. M.F. Limonov, M.V. Rybin, A.N. Poddubny, Y.S. Kivshar, Fano resonances in photonics. *Nat. Photon.* **11**, 543–554 (2017)
46. A. Yariv, Coupled-mode theory for guided-wave optics. *IEEE J. Quantum Electron.* **9**, 919–933 (1973)
47. S. Miller, Coupled wave theory and waveguide applications. *Bell Labs Tech. J.* **33**, 661–719 (1954)
48. N. Yin, G. Xu, Q. Yang, J. Zhao, X. Yang, J. Jin, W. Fu, M. Sun, Analysis of wireless energy transmission for implantable device based on coupled magnetic resonance. *IEEE Trans. Magn.* **48**, 723–726 (2012)
49. D.N. Maksimov, A.F. Sadreev, A.A. Lyapina, A.S. Pilipchuk, Coupled mode theory for acoustic resonators. *Wave Motion* **56**, 52–66 (2015)
50. X. Piao, S. Yu, N. Park, Control of Fano asymmetry in plasmon induced transparency and its application to plasmonic waveguide modulator. *Opt. Express* **20**, 18994–18999 (2012)
51. X. Piao, S. Yu, S. Koo, K. Lee, N. Park, Fano-type spectral asymmetry and its control for plasmonic metal-insulator-metal stub structures. *Opt. Express* **19**, 10907–10912 (2011)
52. S. Yu, X. Piao, J. Hong, N. Park, Progress toward high- $Q$  perfect absorption: a Fano antilaser. *Phys. Rev. A* **92**, 011802 (2015)
53. M.-A. Miri, M. Heinrich, R. El-Ganainy, D.N. Christodoulides, Supersymmetric optical structures. *Phys. Rev. Lett.* **110**, 233902 (2013)
54. S. Yu, X. Piao, J. Hong, N. Park, Interdimensional optical isospectrality inspired by graph networks. *Optica* **3**, 836–839 (2016)
55. S. Yu, X. Piao, N. Park, Target decoupling in coupled systems resistant to random perturbation. *Sci. Rep.* **7** (2017)
56. S. Yu, X. Piao, N. Park, Slow-light dispersion properties of multiatomic multiband coupled-resonator optical waveguides. *Phys. Rev. A* **85**, 023823 (2012)
57. S. Yu, X. Piao, S. Koo, J.H. Shin, S.H. Lee, B. Min, N. Park, Mode junction photonics with a symmetry-breaking arrangement of mode-orthogonal heterostructures. *Opt. Express* **19**, 25500–25511 (2011)
58. M.F. Yanik, S. Fan, M. Soljačić, J.D. Joannopoulos, All-optical transistor action with bistable switching in a photonic crystal cross-waveguide geometry. *Opt. Lett.* **28**, 2506–2508 (2003)
59. A. Karalis, J.D. Joannopoulos, M. Soljačić, Efficient wireless non-radiative mid-range energy transfer. *Ann. Phys.* **323**, 34–48 (2008)
60. C. Manolatu, M. Khan, S. Fan, P.R. Villeneuve, H. Haus, J. Joannopoulos, Coupling of modes analysis of resonant channel add-drop filters. *IEEE J. Quantum Electron.* **35**, 1322–1331 (1999)
61. Y. Tanaka, J. Upham, T. Nagashima, T. Sugiyu, T. Asano, S. Noda, Dynamic control of the  $Q$  factor in a photonic crystal nanocavity. *Nat. Mater.* **6**, 862–865 (2007)
62. H. Lu, X. Liu, D. Mao, Plasmonic analog of electromagnetically induced transparency in multi-nanoresonator-coupled waveguide systems. *Phys. Rev. A* **85**, 053803 (2012)
63. R.D. Kekatpure, E.S. Barnard, W. Cai, M.L. Brongersma, Phase-coupled plasmon-induced transparency. *Phys. Rev. Lett.* **104**, 243902 (2010)
64. Y. Tang, A.E. Cohen, Enhanced enantioselectivity in excitation of chiral molecules by superchiral light. *Science* **332**, 333–336 (2011)

65. E. Hendry, T. Carpy, J. Johnston, M. Popland, R.V. Mikhaylovskiy, A.J. Laphorn, S.M. Kelly, L.D. Barron, N. Gadegaard, M. Kadodwala, Ultrasensitive detection and characterization of biomolecules using superchiral fields. *Nat. Nanotechnol.* **5**, 783–787 (2010)
66. I.V. Lindell, A. Sihvola, S. Tretyakov, A. Viitanen, *Electromagnetic Waves in Chiral and Bi-Isotropic Media* (Artech House Antenna Library, 1994)
67. S.J. Orfanidis, *Electromagnetic Waves and Antennas* (Rutgers University New Brunswick, NJ, 2002)
68. A. Serdyukov, I. Semchenko, S. Tretyakov, A. Sihvola, *Electromagnetics of Bi-Anisotropic Materials: Theory and Applications* (Gordon and Breach Science, 2001)
69. U. Fano, Effects of configuration interaction on intensities and phase shifts. *Phys. Rev.* **124**, 1866 (1961)
70. F. Shafiei, F. Monticone, K.Q. Le, X.-X. Liu, T. Hartsfield, A. Alù, X. Li, A subwavelength plasmonic metamolecule exhibiting magnetic-based optical Fano resonance. *Nat. Nanotech.* **8**, 95–99 (2013)
71. P. Fan, Z. Yu, S. Fan, M.L. Brongersma, Optical Fano resonance of an individual semiconductor nanostructure. *Nat. Mater.* (2014)
72. K. Nozaki, A. Shinya, S. Matsuo, T. Sato, E. Kuramochi, M. Notomi, Ultralow-energy and high-contrast all-optical switch involving Fano resonance based on coupled photonic crystal nanocavities. *Opt. Express* **21**, 11877–11888 (2013)
73. X. Yang, C. Husko, C.W. Wong, M. Yu, D.-L. Kwong, Observation of femtojoule optical bistability involving Fano resonances in high-Q/V m silicon photonic crystal nanocavities. *Appl. Phys. Lett.* **91**, 051113-051113-051113 (2007)
74. C. Ott, A. Kaldun, P. Raith, K. Meyer, M. Laux, J. Evers, C.H. Keitel, C.H. Greene, T. Pfeifer, Lorentz meets Fano in spectral line shapes: a universal phase and its laser control. *Science* **340**, 716–720 (2013)
75. A.N. Poddubny, M.V. Rybin, M.F. Limonov, Y.S. Kivshar, Fano interference governs wave transport in disordered systems. *Nat. Commun.* **3**, 914 (2012)
76. A.E. Miroschnichenko, S. Flach, Y.S. Kivshar, Fano resonances in nanoscale structures. *Rev. Mod. Phys.* **82**, 2257–2298 (2010)
77. B. Luk'yanchuk, N.I. Zheludev, S.A. Maier, N.J. Halas, P. Nordlander, H. Giessen, C.T. Chong, The Fano resonance in plasmonic nanostructures and metamaterials. *Nat. Mater.* **9**, 707–715 (2010)
78. D.R. Smith, D. Schurig, Electromagnetic wave propagation in media with indefinite permittivity and permeability tensors. *Phys. Rev. Lett.* **90** (2003)
79. M. Johnson, Bipolar spin switch. *Science* **260**, 320–323 (1993)
80. D. Frustaglia, M. Hentschel, K. Richter, Quantum transport in nonuniform magnetic fields: Aharonov-Bohm ring as a spin switch. *Phys. Rev. Lett.* **87**, 256602 (2001)
81. A. Tartakovskii, T. Wright, A. Russell, V. Fal'ko, A. Van'kov, J. Skiba-Szymanska, I. Drouzas, R. Kolodka, M. Skolnick, P. Fry, Nuclear spin switch in semiconductor quantum dots. *Phys. Rev. Lett.* **98**, 026806 (2007)
82. J.A. Dionne, K. Diest, L.A. Sweatlock, H.A. Atwater, PlasMOSstor: a metal-oxide-Si field effect plasmonic modulator. *Nano Lett.* **9**, 897–902 (2009)
83. H.W. Lee, G. Papadakis, S.P. Burgos, K. Chander, A. Kriesch, R. Pala, U. Peschel, H.A. Atwater, Nanoscale conducting oxide PlasMOSstor. *Nano Lett.* **14**, 6463–6468 (2014)
84. J. Aitchison, D. Hutchings, J. Kang, G. Stegeman, A. Villeneuve, The nonlinear optical properties of AlGaAs at the half band gap. *IEEE J. Quantum Electron.* **33**, 341–348 (1997)
85. S. Droulias, V. Yannopoulos, Broad-band giant circular dichroism in metamaterials of twisted chains of metallic nanoparticles. *J. Phys. Chem. C* **117**, 1130–1135 (2013)

# Chapter 3

## Mueller Matrix Approach for Engineering Asymmetric Fano-resonance Line Shape in Anisotropic Optical System



A. K. Singh, S. Chandel, S. K. Ray, P. Mitra and N. Ghosh

**Abstract** The Fano resonances observed in diverse micro and nano optical systems have received particular attention due to their numerous potential applications like sensing, switching, lasing, filters and robust color display, nonlinear and slow-light devices, invisibility cloaking, and so forth. For most of these applications, it is highly desirable that the asymmetric spectral line shape of Fano resonance can be controlled or modulated by some experimentally accessible parameters. In this chapter, we discuss a new concept based on polarization Mueller matrix analysis for tuning the Fano interference effect and the resulting asymmetric spectral line shape in anisotropic optical system. The approach is founded on a generalized model of anisotropic Fano resonance and exploits the differential polarization response (anisotropy) of the two interfering modes to achieve unprecedented control over Fano resonance. Illustrative results on the use of the model for tuning Fano resonance in coupled plasmonic systems are presented. In this context, the fundamentals of polarized light, the mathematical framework of Stokes-Mueller formalism and the basic polarimetry parameters encoded in Mueller matrix are discussed. The specifics of a novel dark field Mueller matrix spectroscopy system and its use for studying the polarization response of Fano resonance in plasmonic systems is illustrated with selected examples. The chapter concludes with an outlook on the prospects of the

---

A. K. Singh · S. Chandel · S. K. Ray · P. Mitra · N. Ghosh (✉)  
Indian Institute of Science Education and Research (IISER) Kolkata, Kolkata 741246, India  
e-mail: nghosh@iiserkol.ac.in

A. K. Singh  
e-mail: aks13ip027@iiserkol.ac.in

S. Chandel  
e-mail: sc14rs013@iiserkol.ac.in

S. K. Ray  
e-mail: skr13rs007@iiserkol.ac.in

P. Mitra  
e-mail: pmitra@iiserkol.ac.in

polarization-optimized anisotropic Fano resonant systems for applications involving control and manipulation of electromagnetic waves at the nano scale.

### 3.1 Introduction

Resonance phenomenon has been known to mankind for very long as it is present widely in all sort of vibrations or waves e.g. Electromagnetic resonance, Acoustic resonance, Mechanical resonance, resonance of quantum wave function and many more. When a system stores and transfers energy easily between two or more different modes, resonance is obtained. All these resonant system resonates or oscillates at some natural frequency, and in the presence of losses or damping it follows a Lorentzian profile. For a long time, the Lorentzian profile was considered to be the fundamental line shape for a resonance. U. Fano discovered a new type of resonance (line shape) in the atomic auto-ionization of Helium [1], which now bears his name, Fano resonance. In resonances other than Fano resonance the spectral line shape is the sum of intensity of individual resonances, it also implies that the resonance spectral line shape lacks the interference of individual resonances, whereas Fano resonance is result of an interference effect. Fano resonances differ from other resonances in two major distinct ways, (a) Interference induced resonance, (b) Asymmetric Spectral line shape. The asymmetric profile of the Fano resonance is achieved due to the constructive and destructive interference of broad mode or continuum with a discrete mode. The inherent nature of interference has made Fano resonance being observed in both quantum and classical domain [1–9]. Plasmonics is one among the major contributors in the area of Fano resonance and here in this chapter we will focus on the aspects of Fano resonance in Plasmonics [6, 10]. Fano resonance in plasmonics has attained a lot of attraction due to the real life potential applications [11–21]. Various plasmonic structures have been fabricated to show the Fano resonance in different wavelength domain and varying asymmetry [6]. In the realm of Fano resonance, tuning has been of great importance and researchers have tried various ways to attain tunability due to its potential advantages. Tuning of Fano resonance can be achieved in various ways like varying the shape, size, orientation, arrangement, polarization etc [9, 22–27]. Most of the above mentioned ways except polarization require the fabrication of different samples with variation in any of the parameter to attain the prescribed tunability. On the other hand, polarization can be used as an effective tool to tune the asymmetry of the spectral line shape as well as the resonance peak/dip positions from an external input without modifying the structure [22, 25, 27].

Interaction of Polarized light with plasmonic system has not been explored extensively, partly due to weak scattering from the system in comparison with background, intermixed polarization effects, focusing affecting polarization etc. This has an adverse effect on plasmonic studies because polarization offers interesting control on excitation-emission in the field of plasmonics, and a wealth of information of potential interest and relevance to plasmonic sensing and characterization [28–35]. Such negligence is gradually being readdressed, as novel experimental techniques

for polarization studies, enhanced models for understanding the interactions, and sophisticated interpretation, are coming up [27, 35–41]. In this chapter we will be providing the fundamentals and mathematical formulations of polarized light interacting with plasmonic systems, details of polarimetric systems, discussion about the various aspects of polarization mediated tuning of Fano resonance and its possible potential applications.

The chapter is organized as follows. In Sect. 3.2 the basics of polarization have been provided that will help the readers to connect and understand the connection between the polarization and Fano resonance, which effectively is being used as a mechanism for tuning the asymmetric Fano resonance profile. The forthcoming subsections cover the polarization algebra, describing the two major polarization formalisms. This is followed by the short description of the comprehensive plasmon polarimetry platform which enabled the recording of scattering polarization signals from the plasmonic system. Section 3.3 contains a short description of Fano resonance followed by special emphasis on Fano resonance in scattering regime. In Sect. 3.4 we discuss about scattering from plasmonic waveguiding photonic crystal, and origin of resonant and Rayleigh anomalies in metal dielectric grating. Further in Sect. 3.5 we discuss the results of polarization controlled tuning of Fano resonance from the coupled plasmonic system of Oligomers and plasmonic waveguided system. The chapter concludes with a discussion of the immense potential and various possible applications of polarization mediated tuning of Fano resonance.

## 3.2 Basics of Polarization

Polarization is one of the distinct inherent properties of light and is known to mankind from centuries. Light matter interaction from polarization perspective has been explored and has proved to be extremely useful. A lot has been studied and still much more has to be studied in the context of interaction of polarized light with matter. Definitions and properties of polarization have been discussed extensively in literature [42–44]. Here we will provide some basics, a brief overview and important connections in order to understand the role of polarization in the context of Fano resonance.

Polarization of light can be understood as the direction specific to the oscillation of the transverse electromagnetic wave. Conventionally the oscillations of the electric field or the direction of the electric field is referred as the plane of polarization. From polarization point of view, Light can be divided into two main sections: Unpolarized and Polarized. In unpolarized light, the electric field randomly oscillates in all planes containing direction of propagation whereas for polarized light it oscillates in a correlated manner. Polarized light can further be classified as Linear, Circular and elliptical polarizations. A linear polarized light has the electric field component of electromagnetic wave confined in a plane containing the line of propagation, for circular polarization the temporal evolution of electric field vector traces a circle normal to the direction of propagation, whereas for elliptical polarization the electric



field follows an ellipse as the wave propagates. These two (linear and circular) polarization states can be considered as the two particular cases of elliptical polarization. However, there exist a mixed state where light is not completely polarized in such case the extent of polarization is quantified using a parameter known as degree of polarization, where completely polarized light will have degree of polarization 1, that of unpolarized light 0 and partially polarized light having magnitude in between 0 and 1. We now extend the discussion to polarization algebra that contains the two major formalisms.

### 3.2.1 Polarization Algebra

There are two formalisms that deal with the polarization property of light, Jones formalism and Stokes-Mueller formalism. These two formalisms are quite useful, important and different from each other. On one hand Jones formalism is field based, on the other Stokes-Mueller formalism is intensity based representation. Jones formalism works for fully polarized light, whereas Stokes-Mueller formalism deals with partially polarized light too. Both these formalisms will be useful for studying interaction of polarized light with plasmonic system generating Fano resonance.

#### 3.2.1.1 Jones Formalism

This formalism was proposed by R. C. Jones in 1942 to define the polarization properties of light, and light matter interaction. He proposed a two-dimensional matrix algebra for expressing the polarization of light and the properties of different optical components for the completely polarized interactions. As mentioned earlier this approach is field based and electromagnetic wave can be represented by a  $2 \times 1$  Jones vector obtained using the electric field of the wave. The Jones vector of an electromagnetic wave propagating in  $z$  direction having frequency  $\omega$  can be written as

$$\mathbf{E}(z, t) = \begin{bmatrix} E_x \\ E_y \end{bmatrix} = \begin{bmatrix} E_{0x} e^{i(kz - \omega t + \phi_x)} \\ E_{0y} e^{i(kz - \omega t + \phi_y)} \end{bmatrix} \quad (3.1)$$

Here  $E_{0x}$  and  $E_{0y}$  are the amplitudes,  $\phi_x$  and  $\phi_y$  are the phases of electromagnetic wave for  $x$  and  $y$  polarized components respectively and  $k$  is the wave vector associated with the wave, the phase factor  $e^{i(kz - \omega t)}$  is common/redundant and can be dropped. Thus, the polarization of wave can be expressed only using the amplitude and phase derived parameters  $\alpha$  and  $\phi$  given as,

$$\tan \alpha = \frac{E_{0x}}{E_{0y}}, \quad \phi = \phi_x - \phi_y \quad (3.2)$$

The intensity of electromagnetic field in terms of Jones vector can be written as

$$I = |E_x|^2 + |E_y|^2 = \mathbf{E} \cdot \mathbf{E}^\dagger \tag{3.3}$$

Here,  $\mathbf{E}^\dagger$  represents the conjugate transpose of  $\mathbf{E}$ . Some of the fully polarized states represented in the form of Jones vector look like as given in the table below.

Polarization state	$H(0^\circ)$	$+45^\circ$	$V(90^\circ)$	$135^\circ/-45^\circ$	Right circular polarized (RCP)	Left circular polarized (LCP)
Jones vector	$\begin{bmatrix} 1 \\ 0 \end{bmatrix}$	$\begin{bmatrix} 1 \\ 1 \end{bmatrix}$	$\begin{bmatrix} 0 \\ 1 \end{bmatrix}$	$\begin{bmatrix} 1 \\ -1 \end{bmatrix}$	$\begin{bmatrix} 1 \\ i \end{bmatrix}$	$\begin{bmatrix} 1 \\ -i \end{bmatrix}$

The Jones vector depicts polarization property of electromagnetic wave. Similarly there is Jones matrix ( $J$ ) which describes the polarization properties of the optical components like polarizer, retarder, mirrors etc. Mathematically, Jones matrix ( $J$ ) is a  $2 \times 2$  transformation matrix encoding the polarization response of sample for the Jones vector of light incident on the sample. It describes how the polarization property of incident light (Jones vector) is altered/modulated when it passes through these components (Jones matrices). The Jones matrix for some of the optical components are given below.

Polarization component	Linear polarizer (Horizontal axis)	Linear polarizer (Vertical axis)	Quarter wave plate (Horizontal axis)	Half wave plate (Horizontal axis)
Jones matrix ( $J$ )	$\begin{bmatrix} 1 & 0 \\ 0 & 0 \end{bmatrix}$	$\begin{bmatrix} 0 & 0 \\ 0 & 1 \end{bmatrix}$	$e^{i\pi/4} \begin{bmatrix} 1 & 0 \\ 0 & i \end{bmatrix}$	$e^{i\pi/2} \begin{bmatrix} \cos 2\theta & \sin 2\theta \\ \sin 2\theta & -\cos 2\theta \end{bmatrix}$

As mentioned above the Jones calculus only covers pure polarization components and is a field based technique. However, the formalism is of not much practical use as in most cases we observe the time average intensity instead of the field amplitude, also most of the optical scattering phenomena implicitly involves depolarization phenomenon. To overcome these challenges Stokes-Mueller formalism is extensively used for practical purposes.

### 3.2.1.2 Stokes-Mueller Formalism

G. G. Stokes in 1852 proposed that the polarization of light can be expressed in terms of experimentally observable quantities and gave a  $4 \times 1$  vector now known after him as Stokes vector ( $\mathbf{S}$ ). The Stokes vector elements (or Stokes parameter) termed as I, Q, U and V can be formed by recording six different (prescribed) intensities. The Stokes vector can be written as

$$\mathbf{S} = \begin{bmatrix} I \\ Q \\ U \\ V \end{bmatrix} = \begin{bmatrix} I_H + I_V \\ I_H - I_V \\ I_P - I_M \\ I_{RCP} - I_{LCP} \end{bmatrix} \quad (3.4)$$

Here, these six intensity measurements correspond to intensity of various polarization states as:  $I_H$  as Horizontal polarization,  $I_V$  as Vertical polarization,  $I_P$  as  $45^\circ$  polarization,  $I_M$  as  $135^\circ$  (or  $-45^\circ$ ) polarization,  $I_{RCP}$  as Right Circular Polarization, and  $I_{LCP}$  as Left Circular Polarization respectively.  $I$  characterizes the total intensity,  $Q$  and  $U$  tell about the orientation and degree of linear polarization ( $H/V$  and  $+45^\circ/-45^\circ$  polarization state respectively) and  $V$  contains information of degree and orientation of circular polarization. The Stokes parameters are related to each other by the relation given as

$$I^2 \geq Q^2 + U^2 + V^2 \quad (3.5)$$

Here the equality sign is valid in the case of pure polarization states and inequality for the rest of the partial polarization states. The parameter Degree of polarization (DOP) can be extracted from Stokes vector as

$$\text{DOP} = \frac{\sqrt{Q^2 + U^2 + V^2}}{I} \quad (3.6)$$

It can be seen from the above given equation that the degree of polarization for a completely polarized light will be 1 (as  $Q^2 + U^2 + V^2 = I^2$ ) and for unpolarized light 0 (as  $Q, U, V = 0$ ). It is to be noted that for a polarized light the Stokes vector can be written in terms of the Jones vector as,

$$S = A(\mathbf{E} \otimes \mathbf{E}^\dagger) \quad \text{where,} \quad A = \begin{bmatrix} 1 & 0 & 0 & 1 \\ 1 & 0 & 0 & -1 \\ 0 & 1 & 1 & 0 \\ 0 & i & -i & 0 \end{bmatrix} \quad (3.7)$$

Here,  $\otimes$  represents the tensor product.

Now as we see the polarization property of light can be described using Stokes vector, we will move focus to the polarization properties of interacting medium. As discussed before, the interaction of polarized light with any medium usually alters the polarization of output light. If we write two Stokes vectors, one before interaction and one after interaction, we will come up with a linear equation like

$$\mathbf{S}_o = M\mathbf{S}_i \quad (3.8)$$

Here,  $\mathbf{S}_o$  and  $\mathbf{S}_i$  are the output and input Stokes vector, whereas the Mueller matrix " $M$ " is the transfer function that encodes the polarization properties of the interacting medium. This transfer function  $M$  is a  $4 \times 4$  matrix which gives a mathematical description of the change of polarization after the interaction of polarized light

with any arbitrary medium, incorporates the complete polarization properties of the medium. Mueller matrix can also be thought of as the polarization fingerprint of the medium, for completely polarized/coherent interaction the Mueller matrix can be written in terms of Jones matrix as

$$M = A(J \otimes J^\dagger)A^{-1} \quad (3.9)$$

Every Jones matrix has a corresponding Mueller matrix however the inverse is not true, because of the incoherent interactions/depolarization. The necessary and sufficient condition for a  $4 \times 4$  matrix to be a physically realisable Mueller matrix is that the matrix map to a physical output Stokes vector (satisfying the relation  $I^2 \geq Q^2 + U^2 + V^2$ ) for all the possible incident polarized states. The different elements of the Mueller matrix “ $M$ ” encode the three basic polarization properties diattenuation, retardance and depolarization, which are explained below.

**Diattenuation:** Diattenuation ( $d$ ) stands for the differential attenuation between orthogonal polarizations for both circular and linear components of polarization. Linear diattenuation is thus the difference in amplitude for the two orthogonal linear polarizations (Horizontal/Vertical,  $+45^\circ/-45^\circ$  polarization state) and circular diattenuation is defined as differential attenuation of Right and Left circularly polarized state. Diattenuation parameter is akin to dichroism but much more generalized as it can result due to various effects like reflection, absorption, scattering etc. Mathematically the Mueller matrix of a linear diattenuator with diattenuation  $d$  oriented at an angle of  $\theta$  can be written as

$$M_D = \begin{bmatrix} 1 & d \cos 2\theta & d \sin 2\theta & 0 \\ d \cos 2\theta & \cos^2 2\theta + \sqrt{1-d^2} \sin^2 2\theta & (1 - \sqrt{1-d^2}) \sin 2\theta \cos 2\theta & 0 \\ d \sin 2\theta & (1 - \sqrt{1-d^2}) \sin 2\theta \cos 2\theta & \sin^2 2\theta + \sqrt{1-d^2} \cos^2 2\theta & 0 \\ 0 & 0 & 0 & \sqrt{1-d^2} \end{bmatrix} \quad (3.10)$$

The ideal example of a linear diattenuator can be a linear polarizer which let pass one polarization and blocks the corresponding orthogonal component having the diattenuation value  $d = 1$ . The diattenuation of an arbitrary system in terms of a diagonal Jones matrix can be given as,

$$d = \frac{|J_{11}|^2 - |J_{22}|^2}{|J_{11}|^2 + |J_{22}|^2} \quad (3.11)$$

In terms of Mueller matrix element the diattenuation can be given as,

$$d = \frac{\sqrt{M_{12}^2 + M_{13}^2 + M_{14}^2}}{M_{11}} \quad (3.12)$$

It is to be noted that the diattenuation parameter  $d$  is a dimensionless quantity and ranges from 0 – 1.

**Retardance:** Retardance parameter is defined as the difference in phase for two orthogonal polarizations (both linear and circular). In other words it is the difference in the phase velocity of the two orthogonal linear (Horizontal/Vertical,  $+45^\circ/-45^\circ$ ) and circular (*RCP/LCP*) polarizations, the difference for linear polarizations provide linear retardance and for circular polarizations it yields circular retardance or optical rotation. It originates from the anisotropy in the refractive indices of the system, it has proven itself to be an excellent parameter to probe such phase anisotropies, like in the cases of tissues, proteins, lipids, glucose, plasmonics and many more [45, 46]. The general form of the Mueller matrices of linear retarder can be written as,

$$M_R = \begin{bmatrix} 1 & 0 & 0 & 0 \\ 0 & \cos^2 2\theta + \sin^2 2\theta \cos \delta & \sin 2\theta \cos 2\theta (1 - \cos \delta) & -\sin 2\theta \sin \delta \\ 0 & \sin 2\theta \cos 2\theta (1 - \cos \delta) & \sin^2 2\theta + \cos^2 2\theta \cos \delta & \cos 2\theta \sin \delta \\ 0 & \sin 2\theta \sin \delta & -\cos 2\theta \sin \delta & \cos \delta \end{bmatrix} \quad (3.13)$$

and the Mueller matrices of circular retarder can be written as,

$$M_R = \begin{bmatrix} 1 & 0 & 0 & 0 \\ 0 & \cos 2\psi & -\sin 2\psi & 0 \\ 0 & \sin 2\psi & \cos 2\psi & 0 \\ 0 & 0 & 0 & 1 \end{bmatrix} \quad (3.14)$$

Here  $\theta$  is the orientation angle of the fast axis and,  $\delta$  and  $\psi$  are the linear and circular retardance respectively. The retardance of an arbitrary system in terms of a diagonal Jones matrix can be given as,

$$\delta = \arg(J_{11}) - \arg(J_{22}) \quad (3.15)$$

In terms of Mueller matrix element the retardance can be given as,

$$\delta, \psi = \cos^{-1} \left( \frac{\text{Tr}(M_R)}{2} - 1 \right) \quad (3.16)$$

**Depolarization:** It is defined as the loss in degree of polarization and is generated in most of the cases due to the multiple scattering of photons (a/o particle behavior) or the randomly oriented birefringent domains, the incoherent addition of amplitude and phase of the scattered field which give rise to the scrambled output polarization state. The general form of a depolarizer matrix can be written as

$$M_\Delta = \begin{bmatrix} 1 & 0 & 0 & 0 \\ 0 & a & 0 & 0 \\ 0 & 0 & b & 0 \\ 0 & 0 & 0 & c \end{bmatrix} \quad (3.17)$$

Here,  $|a|$ ,  $|b|$ ,  $|c| \leq 1$ . The depolarization parameter for a linear polarization is  $1 - |a|$ , and  $1 - |b|$ , whereas for the circular polarization it is  $1 - |c|$ . Please note that the depolarization factor presented here is different from the one presented for the Stokes vector. Here it represents the loss of polarization due to the interaction from the material (depolarization transfer function of medium) whereas the degree of polarization for Stokes vector is a measure of polarized component of the light beam, for example a material having higher magnitude of  $\Delta$  is considerably depolarizing in nature, therefore a polarized light beam after interacting with this material will have lower degree of polarization.

These three parameters enable one to precisely probe the individual polarization effects and the corresponding physics related to the same, resulting in better understanding as well as it works as a pointer/parameter for quantification of such effects. In many cases these individual polarization effects occur simultaneously causing these lumped effects hindering the extraction and unique interpretation. In last few decades few robust decomposition technique like polar and log decomposition [47–50], and various accurate inverse techniques have been developed and made available to overcome such challenges.

We now provide a short description of the experimental polarimetric system (comprehensive polarimetric platform) used for studying the polarization properties from the plasmonic structures.

### 3.2.2 *Comprehensive Polarimetric Platform for Plasmonic Study*

Recording of complete polarization information via Mueller matrix from plasmonic system is a tough task due to the major challenges like, weak scattering signal incorporated with large background, simultaneous occurrence and intermixing of individual polarization effects, requirement of high NA microscopic geometry (which itself alters the polarization) for recording of Mueller matrices over broad wavelength range and corresponding spatial maps, analysis, quantification, understanding and interpretation of plasmon polarimetry results from the recorded polarization signal [37]. These outstanding challenges were addressed by integrating a dark field microscope (removes background signal by recording pure scattering signal from sample) with Mueller matrix measurement scheme (records spectral Mueller matrix for broad wavelength range) and a robust Eigen Value calibration technique (corrects for all sort of polarization alteration/transformation due to high NA focusing or non-ideal behaviour of polarization optics or misalignments) [51, 52].

Mueller matrix measurement scheme shown in Fig. 3.1 consist of a set of fixed linear polarizers aligned orthogonal to each other, one after the light source (P1) and other before detector (P2). Two motorized, rotating quarter wave plates (QWP1 and QWP2) are used in combination with these polarizers (QWP1 kept after P1 and QWP2 before P2) to generate and analyse the polarization states respectively.

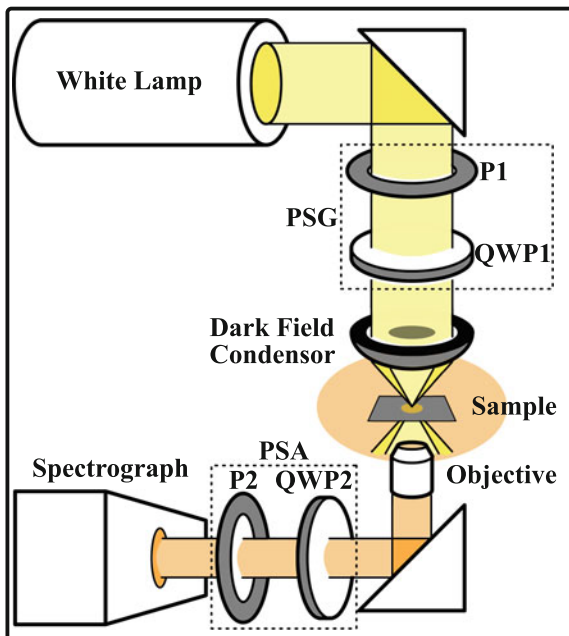


**Fig. 3.1** Schematic of Polarimetric Platform for Plasmonic study, built using an inverted dark-field microscope. The white light emitted from Mercury lamp is passed through the Polarization state generator (PSG) unit, then focused on the sample site through an annular condenser. The scattered light is collected with an objective below the sample, and passes it through the Polarization state analyzer (PSA) unit. The resultant spectral intensity signal is recorded through a spectrograph. P1, P2: fixed linear polarizers and QWP1, QWP2: achromatic quarter waveplates. Taken from Chandel et al. [53]

The set of P1 and QWP1 makes Polarization State Generator (PSG) unit which can generate any polarization state by rotating the quarter wave plate and the linear polarizer, whereas QWP2 and P2 forms Polarization State Analyser (PSA) unit which is used in similar fashion to analyse the polarization states. Four optimized elliptical polarization states are generated using PSG unit (with fixed axis of P1 and changing fast axis of QWP1 to the optimized angles  $\theta = 35^\circ, 70^\circ, 105^\circ$  and  $140^\circ$ ) and the scattered polarized state is analyzed using similar four optimized polarized state of PSA unit, (rotating fast axis of QWP2 to the optimized angles  $\theta_o = 35^\circ, 70^\circ, 105^\circ$  and  $140^\circ$ ). Four optimized elliptical polarizations basis states for PSG and PSA in combination are utilized to generate and record 16 sequential wavelength resolved intensities. These spectrally resolved intensities are grouped in a  $4 \times 4$  matrix  $M_i$  which can be used to obtain the scattering Mueller matrix (M) from the scattering sample with the help of known PSG and PSA matrices (obtained using the Stokes vectors corresponding to the four states at the optimized angles, denoted by  $W$  and  $A$  respectively) as,

$$M_i = AMW; M = A^{-1}M_iW^{-1} \quad (3.18)$$

Once the scattering spectral Mueller matrix is recorded the individual polarization properties were extracted and quantified using robust Polar decomposition or differential decomposition technique. In polar decomposition technique the Mueller matrix is decomposed into a sequence of three basis matrices, a diattenuator matrix, a retarder matrix and a depolarization matrix as

$$M \Leftarrow M_{\Delta} \cdot M_R \cdot M_D = M_{\Delta} \cdot M_{\text{Pol}} \quad (3.19)$$

These basis matrices incorporate the individual polarization properties and are used to extract and quantify these polarization properties in terms of polarization parameters named as diattenuation, retardance and depolarization. The  $M_{\text{Pol}} (= M_R \cdot M_D)$  matrix contains the information about completely polarized part of interaction. On the other hand, in differential decomposition technique a differential matrix  $m$  is related to the Mueller matrix and decomposed as a combination of an anti-symmetric and symmetric matrix. The individual components of these two matrices integrate the elementary polarization properties and the corresponding deviations. The polarization parameters are thus extracted from the Mueller matrix and utilized. The details of this Comprehensive Polarimetry Platform can be found elsewhere [37, 54].

As we have covered the basics of polarization algebra and the system for recording polarization signal from plasmonic system in scattering geometry. We now move forward towards the short description of Fano resonance. As the book is dedicated to Fano resonance and a lot is already conveyed, therefore we will restrain ourselves from a detailed description of Fano resonance, however a short description will be provided along with the model of Fano resonance in scattering domain.

### 3.3 Fano Resonance in Scattering

Fano resonance was first introduced in the study of auto ionizing states of atoms by U. Fano (hence the name) in 1961, the resonance is characterized by a typical asymmetric spectral line shape in contrast to the general Lorentzian resonances [1]. Its a universal resonance phenomenon which originates due to the interference of a discrete narrow mode with a broad spectral line shape or continuum mode giving a characteristic asymmetric line shape ( $\sigma$ ) with constructive/destructive interference on one side of the narrow resonance while destructive/constructive on the other side of it. The spectral response of a Fano resonant system is given as

$$\sigma = \frac{(\epsilon + q)^2}{1 + \epsilon^2} \quad (3.20)$$

Here,  $q$  decides the asymmetry in line shape and  $\epsilon = (\omega - \omega_o)/(\gamma/2)$  is the reduced energy scale. Where,  $\omega_o$  and  $\gamma$  are the resonance frequency and width of the discrete mode, respectively.



Although the Fano resonance is a feature specific to quantum systems but it is observed in various classical optical systems because of the ubiquitous nature of interference phenomenon. In fact first experimental observation of the Fano type line shape could be traced back to the observation of Woods anomaly in metallic grating in 1902 [55], however the origin of the anomaly was recently explained in term of the interference of incoming waves with the leaky waves of the metallic grating [56–59], since then Fano resonant line shape have been observed in various classical optical systems for example metamaterials, various plasmonic and photonic systems, simple Mie scatterer and many other scattering systems [6–9, 23, 24, 60, 61]. There has been an intensive study of the resonance in various optical systems because of its potential application in various micro/nano optical devices such as sensors, switches, slow light devices, filters and many others, for which the ability to control the line shape using various physically accessible parameters is crucial.

In general optical system (3.20) is not strictly valid, and for lossy mediums (for details see [62, 63]) a Lorentzian background in addition to the Fano line shape is obtained. It has been shown using a phenomenological model that the scattered field of a Fano resonant scatterer could be given as [27]

$$E_s(\omega) \approx \frac{q-i}{\epsilon+i} + B(\omega) = \frac{\sqrt{(q^2+1)}}{(\epsilon+i)} e^{i\varphi_F} + B(\omega) \quad (3.21)$$

where,  $B$  is the relative amplitude of the continuum mode and the first term correspond to the discrete Lorentzian mode of amplitude  $\sqrt{q^2+1}$ , and the Fano phase shift “ $\varphi_F$ ” is the additional phase shift of the Lorentzian mode which is directly related to the asymmetry parameter “ $q$ ” as

$$\varphi_F = -\tan^{-1}\left(\frac{1}{q}\right) \quad (3.22)$$

Assuming relative amplitude of the continuum mode to be frequency independent (ideal continuum), the scattered intensity can be given as,

$$I_s(\omega) = |E_s(\omega)|^2 = B^2 \frac{(q^{\text{eff}} + \epsilon)^2}{\epsilon^2 + 1} + \frac{(B-1)^2}{\epsilon^2 + 1} \quad (3.23)$$

The first term yields the asymmetric spectral line shape with an effective asymmetry parameter  $q^{\text{eff}} (= q/B)$  while the second term corresponds to the non-interfering Lorentzian background. In case  $B = 1$ , the scattered intensity reduces to an ideal Fano profile as in (3.20), leading to perfect destructive ( $I_s(\omega) = 0$ ) interference at Fano frequency ( $\omega_F = \omega_o - q\gamma/2$ ). The relative amplitude parameter “ $B$ ” thus controls the contrast of interference between the continuum and discrete mode.

In the forthcoming section, a short description of the theory of plasmonic grating waveguides will be presented and the origin of different waveguiding anomalies and their effects in scattered spectral response from waveguiding systems will be discussed.

### 3.4 Plasmonic Waveguiding Photonic Crystal

The potential applications of Fano resonance in optical domain has led to a quest of a suitable optical system/structure with highly dispersive and tunable Fano profile which could help designing more sensitive optical devices, several plasmonic structures like oligomers, dolmen, ring-disk cavity, waveguiding plasmonic crystals (WPC) and many others have shown Fano resonances in optical domain [6–9, 23, 24, 60, 61]. In most of the above structures except WPC, Fano resonance occurs because of interference between super-radiant (bright) mode and sub-radiant (dark) mode, where both the modes originate because of the collective oscillation of conduction band electrons (plasmonic resonances) i.e. electronic in nature, while in case of WPC Fano resonance originates due to interference between the sharp waveguide resonance (excited by the grating Bragg resonances) and a broad electronic resonance (originates from the plasmonic grating) forming waveguide-plasmon polariton [6, 9, 22, 23]. WPCs offers a huge tunability of the Fano spectral response just like other plasmonic structures by varying structure parameters as well as angle of incidence but it differs with them in its origin, i.e. interaction/interference of plasmonic and photonic mode. WPC enables a very strong coupling between the contributing photonic and plasmonic mode which leads to an anti-crossing behavior in the spectral response of the system [9, 22]. Indeed, the properties could offer huge technical applications in optical domain. Here, we will discuss about one dimensional WPC only, however the observations are quite general and could be seen for higher dimensions too.

One dimensional WPC consist of plasmonic nanowire grating, deposited on the top of a thin waveguiding layer (refractive index,  $n_{wg}$ ) over a dielectric substrate (refractive index,  $n_{sub} < n_{wg}$ ) with a period  $d_x$  as shown in Fig. 3.2a, the schematics of WPC taken into consideration are shown in the figure. The wavevector ( $\mathbf{k}$ ) corresponding to a plane wave of frequency  $\omega_o$  incident on the system with an angle  $\theta$

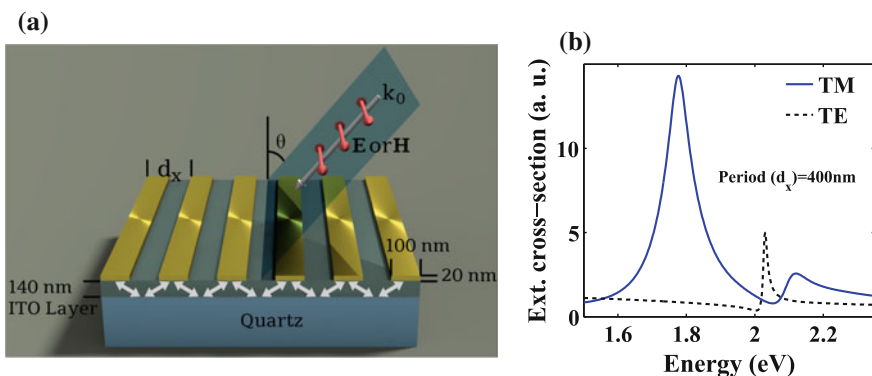


**Fig. 3.2** **a** Schematic view of one dimensional waveguiding plasmonic crystal on quartz substrate; **b** the FEM simulated extinction spectra with 140 nm thick ITO layer for TE and TM polarization states at normal incidence with grating period  $d_x = 400$  nm. Taken from Chandel et al. [53]

from the normal to grating plane (z-axis) and  $\phi$  with the direction of periodicity of grating (x-axis) can be written as

$$\mathbf{k} = (k_x, k_y, k_z) = k_o(\sin \theta \cos \phi, \sin \theta \sin \phi, \cos \theta) \quad (3.24)$$

where,  $k_o = \frac{\omega_o}{c}$  where c is the speed of light in vacuum, and the wavevector ( $\mathbf{k}_{\text{sca}}^{\text{vac/sub}}$ ) corresponding to light diffracted from grating into vacuum (air)/substrate can be written as

$$\mathbf{k}_{\text{sca}}^{\text{vac/sub}} = \left( k_x + \frac{2\pi n}{d_x}, k_y, -/+ \sqrt{\epsilon_{\text{vac/sub}} k_o^2 - \left( k_x + \frac{2\pi n}{d_x} \right)^2 - k_y^2} \right) \quad (3.25)$$

Here,  $n = 0, \pm 1, \pm 2, \pm 3, \dots$  represent different orders of Braggs resonance of the grating, which could add/reduce momentum along x-axis into the diffracted light. The “-/+” sign in z component corresponds to the light reflected/transmitted into vacuum/substrate with permittivity  $\epsilon_{\text{vac/sub}}$ .

The spectral response of the light transmitted from the system can show a huge deviation from the response of the individual nanowires as shown in Fig. 3.2b (Simulated using FEM), the deviation in spectral response of the grating system arises because of: (a) coupling between the individual nanowires depending on their periodicity and dimensions, (b) waves propagating along the periodic structure because of collective response of nanowire array which could be related to the diffraction phenomenon called Woods anomaly. The anomaly could be classified into two categories: (a) resonant or waveguiding anomaly because additional resonances in the waveguiding layer below grating, (b) diffractive or Rayleigh anomaly, associated with opening of new diffraction channel into the substrate or air. The two anomalies are briefly discussed in the following sections.

### 3.4.1 Resonant Anomaly in Metal Dielectric Grating

These are the anomalies observed in the transmission spectra producing a characteristic asymmetric line shape and are responsible for the Fano resonance in the WPC. The grating structure of the crystal excites the momentum matched bound waveguide modes of the waveguiding layer through the Bragg resonances, the bound guided modes couple with the metallic grating and start radiating or become leaky forming a quasi-guided/polaritonic modes [9, 22]. It is to be noted that there exist lower limit on frequency of the guided mode that could exist in a given waveguiding layer called the cut off frequency of the waveguide, given as

$$\omega_{\text{cut}} = \frac{c \tan^{-1} \left( \frac{\epsilon_{\text{sub}} - \epsilon_{\text{vac}}}{\epsilon_{\text{ITO}} - \epsilon_{\text{vac}}} \right)}{d \sqrt{\epsilon_{\text{ITO}} - \epsilon_{\text{sub}}}} \quad (3.26)$$

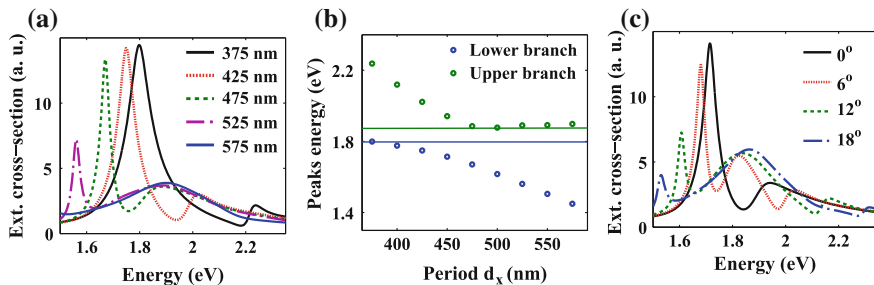


**Fig. 3.3** The FEM simulated, **a** extinction spectra for normally incident TM polarization states with varying grating period, **b** dispersion curve of TM waveguide modes showing upper and lower branch of waveguided polaritons with varying grating period. **c** Extinction spectra for incident TM polarization states with varying angle of incidence, at grating period  $d_x = 450$  nm. Adopted from [22]

As shown in Fig. 3.2b, the transmission of incident transverse electric (TE) and transverse magnetic (TM) polarizations at normal incidence ( $\theta = 0^\circ$ ) shows a clear Fano-type asymmetric line shape for a WPC consisting of gold nanowire grating (periodic arrangement of infinite nanowires of width 100 nm and height 20 nm) deposited on 140 nm thick waveguiding layer of Indium Tin Oxide (ITO) coated on quartz substrate. The incident polarization dependence of the transmission spectra originates because of the anisotropy of the plasmon resonance of the metallic nanowire which are excited only for TM polarization, the polarization dependence of the plasmonic resonance also leads to different origin of the asymmetric Fano resonances, (a) for TM polarization the excited discrete waveguided modes interfere with the broad plasmonic mode to give the asymmetric Fano line shape, the excited plasmon mode also ensures at least two peaks in the transmission spectra, (b) for TE polarization the broad plasmonic mode is absent, however the excited waveguided modes interfere with the incident photon continuum to give the characteristic Fano line shape.

In Fig. 3.3 the transmission spectra for incident TM polarization is shown with varying periodicity of the grating structure and angle of incidence of light. It can be observed from the Fig. 3.3a that at normal incidence ( $\theta = 0^\circ$ ) with varying periodicity (a) the position of discrete mode shifts, which is a direct signature of the shifting of the Bragg resonances ( $2\pi n/d$ , here  $n = 1$ ) of the grating (b) the two peaks corresponding to the upper and lower branch of the polaritonic system show an anti-crossing behavior (the two peaks cannot be observed at same frequency), which signifies the strong coupling between plasmon and waveguided modes forming leading to an energy gap between higher and lower energy resonant modes (peaks) as shown by their dispersion in Fig. 3.3b (c) due to the mirror symmetry of the system at  $\theta = 0^\circ$ , instead of three only two peaks are observed in the transmission spectra. However, at  $\theta \neq 0^\circ$  the mirror symmetry of the system is broken leading to three peaks in the transmission spectra, one corresponding to the plasmon resonance and the other two asymmetric resonances corresponding to the waveguide modes of the

two Bragg resonances ( $\pm 2\pi/d$ ) for  $n = 1$ , as shown in Fig. 3.3c. The momentum of the waveguided mode shifts as  $k_x \pm 2\pi/d$  leading to a symmetrical shift in the resonance position of the waveguided modes with increasing  $\theta$ . A pretty similar and analogous behavior in the transmission spectra is found even for the incident TE polarization, however here the plasmon modes is absent.

### 3.4.2 Rayleigh Anomaly in Metal Dielectric Grating

This anomaly can be observed in the transmission from grating producing a characteristic cusp in the spectra. It has been observed that with varying periodicity of the grating, the spectral behavior show that (a) a cusp appears in the spectra at different frequencies with varying periodicity, (b) effect of the anomaly on the spectral response is dominant only near plasmonic resonances and (c) the position of anomalies are independent of the polarization of incident light and the cusp are observed at same frequencies for both TE and TM polarization [9, 22]. The anomaly/cusp-like structure in transmission spectra can be associated with opening of new diffraction channel in substrate or vacuum, or the field corresponding to a Bragg resonance becomes radiative abandoning its evanescent nature. The condition for Rayleigh anomaly is

$$k_o = \frac{\omega_o}{c} = \frac{1}{\sqrt{\epsilon_{\text{vac/sub}}}} \sqrt{\left(k_x + \frac{2\pi n}{d}\right)^2 + k_y^2} \quad (3.27)$$

It is clear from the above equation that the transmission spectra should show a grating period and incident angle dependence of cusp-like structure similar to the resonant anomalies.

In the next section, we will demonstrate the polarization controlled tuning of the spectral response of plasmonic Oligomers and two dimensional plasmonic grating. A self consistent theoretical model is introduced to demonstrate the polarization control from the anisotropic Fano resonant systems.

### 3.5 Polarization Mediated Tuning of Fano-resonance

As shown in the previous section, WPC shows polarization dependence of the transmission spectra from the system. However, the polarization dependence of the Fano resonant asymmetric line shape in transmission spectra is not limited to the WPC only, it can be demonstrated in various system like oligomers, dolmen and many other. The presence of polarization dependent scattering/transmission spectra provides the ideal tool to modulate, control and tune the spectral response and resonances like Fano resonance. The origin of such polarization dependence lies in the anisotropic polarization response of the structure/system. Indeed, full polarization information

about the system could be very useful to controllably tune the light scattered from the system, and as mentioned above the complete polarization information of any system could be easily obtained from its Mueller matrix [27]. The polarization mediated tuning of Fano resonance in plasmonic systems is demonstrated on plasmonic oligomers, and Mueller matrix approach is used to demonstrate the spectral tuning of WPC. Next, we will be exploring the origin and polarization controlled tuning of Fano resonance in these systems.

### 3.5.1 Plasmonic Oligomers

Plasmonic oligomer is a coupled system, which consists of a ring of metallic nanodisks and a disk at the centre [6, 24, 25, 60]. Oligomers have been reported to have sharp asymmetric Fano spectral profile. As discussed above, the origin of Fano resonance in oligomers is different from waveguiding photonic crystal in terms of the interfering modes. Here the collective oscillations or the collective dipole moment of ring particles interferes with the dipole moment of centre particle. They form the broad super-radiant and discrete subradiant mode for constructive and destructive interference of the collective ring particles with center particle respectively [6, 24, 25, 60]. The interference of these two (super-radiant and sub-radiant) modes gives rise to the asymmetric line profile of Fano resonance. The broad nature of superradiant mode is due to the dipolar nature of resonance whereas for subradiant mode it is the presence of higher order (quadrupolar) mode at the central particle. In the plasmonic oligomer systems the spectral profile, dip/peak are directly dependent on the participating disk size, inter particle separation, material etc. Keeping this in mind, the tuning of Fano resonance in oligomers has been achieved by varying the particle size, inter-particle separation, displacement of particles etc. But such tuning resulted when oligomer structure had been re-fabricated, which itself is a cumbersome task. Polarization based tuning is kind of the perfect solution of the problem posed here. The participating modes are mainly modulated using the polarization which effectively alters the interference of the two participating modes, as a result the Fano profile or the dip is changed. The fabricated oligomer had the central disk diameter larger than ring particles so that there is effective cancellation of dipole moment of the ring and disk particles. In an ideal case, the subradiant mode has zero dipole moment, does not couple to light easily and is non-radiative in nature. But in the sub-wavelength domain or near field limit, the plasmonic resonance mediates a weak interaction resulting in a frail coupling between this superradiant and subradiant mode. This weak coupling commences an asymmetric Fano dip in the broad dipolar resonance at the wavelength/energy of subradiant mode. In cases where the subradiant mode radiates faintly the linewidth is slightly broadened in comparison to the ideal sharp asymmetric Fano profile.

The Fano dip is thus quite useful as it contains crucial information like the strength of cancellation (destructive interference), wavelength of discrete resonance and coupling of the two participating modes. These properties of Fano dip provides us with the perfect handle to probe and control the Fano resonance. The polarization depen-

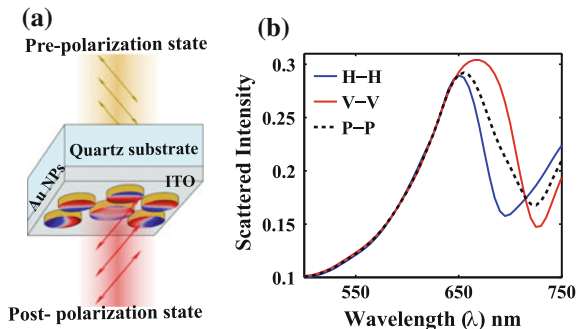


**Fig. 3.4** **a** A schematic showing the geometry of symmetry broken oligomer deposited on quartz substrate, with pre and post selection of polarization state excited and collected from the system, respectively. **b** Polarization controlled tuning of Fano spectral asymmetry in a symmetry broken plasmonic oligomer sample

dence of discrete mode makes it very crucial in this regard and can be exploited for various applications.

Figure 3.4 represents the results of polarization based tuning. Here the pre and post selection of polarization (excitation and detection) was taken to be same. The position of the dip can be seen to be shifted from 685 to 735 nm for the different pre-post polarization states. The shifting of the Fano dip is caused due to the polarization dependent modulation of dipole moments (of nano disks) and the higher order modes (mainly quadrupolar mode). The polarized excitation and detection affects the quadrupolar arrangement (strength and position) in between the participating disks and central disk according to the orientation of polarization state. As a result altering the subradiant mode energy and strength is seen as a shifted Fano dip and altered asymmetric spectral profile.

We further extend this application to an anisotropic Fano resonant system, study and model the polarization mediated tuning of Fano asymmetry.

### 3.5.2 Polarisation Controlled Tuning of Fano Asymmetry

The polarization response of an anisotropic Fano resonant system can be modelled using Jones-Mueller formalism, and such a model can be used to predict the spectral response of the system for various polarizations. The Jones Matrix ( $J(\omega)$ ) of a Fano resonant system can be written as [27]

$$J(\omega) = \begin{bmatrix} j_x^R + B_x & 0 \\ 0 & j_y^R + B_y \end{bmatrix}; \quad \text{where,} \quad j_{x/y}^R = \frac{q_{x/y} - i}{\epsilon_{x/y} + i} \quad (3.28)$$

The observed field scattered ( $E_s(\omega)$ ) from such system for an incident pre ( $E_\alpha$ ) and subsequent post ( $E_\beta$ ) selection of polarization state after the scattering can be given

as

$$E_s(\omega) = \mathbf{E}_\beta^\dagger \mathbf{J}(\omega) \mathbf{E}_\alpha \quad (3.29)$$

And corresponding intensity is given as

$$I_s(\omega) = |\mathbf{E}_\beta^\dagger \mathbf{J}(\omega) \mathbf{E}_\alpha|^2 = \frac{1}{2} \mathbf{S}_\beta^\dagger \mathbf{M}(\omega) \mathbf{S}_\alpha \quad (3.30)$$

Here, pre and post states are chosen to be a general elliptical polarization state given as  $\mathbf{E}_\alpha = [\cos \alpha \quad \sin \alpha e^{i\phi_\alpha}]^T$  and  $\mathbf{E}_\beta = [\cos \beta \quad \sin \beta e^{i\phi_\beta}]^T$ ;  $\mathbf{S}_\alpha$  and  $\mathbf{S}_\beta$  are the corresponding Stokes vectors (see (3.7)).  $\mathbf{M}(\omega)$  denotes the Mueller matrix corresponding to the Jones matrix ( $\mathbf{J}(\omega)$ , see (3.9)). Assuming  $\epsilon_x = \epsilon_y = \epsilon$ , the scattered field for pre and post selected linear ( $\phi_\alpha = \phi_\beta = 0$ ) state can be given as

$$E_s(\omega) = \frac{q_x \cos \alpha \cos \beta + q_y \sin \alpha \sin \beta - i \cos(\alpha - \beta)}{\epsilon + i} + B_x \cos \alpha \cos \beta + B_y \sin \alpha \sin \beta \quad (3.31)$$

And for  $\cos(\alpha - \beta) \neq 0$  the corresponding scattered intensity is given as

$$I_s(\omega) = |E_s(\omega)|^2 = \cos^2(\alpha - \beta) \left( B^2 \frac{(q^{\text{eff}} + \epsilon)^2}{\epsilon^2 + 1} + \frac{(B - 1)^2}{\epsilon^2 + 1} \right) \quad (3.32)$$

where,

$$q^{\text{eff}} = \frac{q}{B}; \quad q = \frac{q_x \cos \alpha \cos \beta + q_y \sin \alpha \sin \beta}{\cos(\alpha - \beta)}; \quad (3.33)$$

$$B = \frac{B_x \cos \alpha \cos \beta + B_y \sin \alpha \sin \beta}{\cos(\alpha - \beta)}$$

When  $\cos(\alpha - \beta) = 0$  the scattered intensity can be easily evaluated. However it can be seen from above equations that the polarization can be used as tool to tune/manipulate the Fano line shape either by tuning the asymmetry parameter “q” or relative amplitude of the continuum “B” in an anisotropic medium. It is to be noted that  $J_{11} \neq J_{22}$  in (3.28) represents an anisotropic Fano resonant case showing a differential polarization response from the system, the anisotropy could be basically classified as either amplitude ( $|J_{11}| \neq |J_{22}|$ , associated with diattenuation) or phase ( $\arg(J_{11}) \neq \arg(J_{22})$ , associated with retardation). However, on the basis of origin of anisotropy two cases are of particular interest, case 1-amplitude and phase anisotropic discrete mode ( $q_x \neq q_y$ ) and case 2-a perfectly diattenuating discrete mode ( $j_x^R \neq 0$  and  $j_y^R = 0$ ).

### Case 1—Amplitude and phase anisotropic discrete mode ( $q_x \neq q_y$ )

In this type of system anisotropy arises because of the contributions from discrete modes only, which have a difference in the Fano phase “ $\varphi_F$ ” associated with them.



Here the Fano line shape can be tailored by tuning “ $\varphi_F$ ” with the linear polarization states. Assuming that the resonant frequency of the two discrete modes ( $\omega_{ox}$  and  $\omega_{oy}$  for x and y polarizations respectively) such that ( $\omega_{ox} - \omega_{oy} \ll \gamma$ ) where  $\gamma$  is the mean of the width of the two discrete modes; the parameters of the line shape could be reduced to

$$q^{\text{eff}} = \frac{q}{B}; q = \frac{q_x \cos \alpha \cos \beta + q_y \sin \alpha \sin \beta}{\cos(\alpha - \beta)}; B = B_x = B_y \quad (3.34)$$

Figure 3.5a demonstrates the tuning of Fano-type spectral line shape for pre selection of  $\mathbf{E}_\alpha = [1 \ 1]^T$  and subsequent post selection of  $\mathbf{E}_\beta = [\cos \beta - \sin \beta]^T$  with isotropic continuum  $B_x = B_y = 0.5$ ; and strongly anisotropic discrete mode  $q_x = 1.5, q_y = 0.5$  with resonance frequency  $\omega_o = 1.78$  eV and line width  $\gamma = 0.107$  eV. As observed, considerably wider and different interesting regimes of the asymmetry parameter ( $q^{\text{eff}}$ ) can be tuned by directly modifying the Fano phase factor ( $\varphi_F$ ) by polarization state control.

With varying polarization the Fano phase  $\varphi_F$  can be gradually tailored, from  $\varphi_F = -33.7^\circ$  to  $-63.44^\circ$  (corresponding to  $q^{\text{eff}} = +3 \rightarrow +1$ ), from  $\varphi_F = -63.4^\circ \rightarrow +49.1^\circ$  corresponding to a Fano phase reversal (negative  $q$ -parameter regime leading to the reversal of spectral asymmetry), to a symmetric Lorentzian line shape canceling the Fano phase ( $q^{\text{eff}} \rightarrow \infty, \varphi_F \rightarrow 0^\circ$ ).

### Case 2—A perfectly diattenuating discrete mode ( $j_x^R \neq 0$ and $j_y^R = 0$ )

These kind of systems will have a discrete mode only in one of the eigenstate of the system. In contrast to case 1, here the anisotropy arises due to the change in the relative amplitude of continuum with the pre and post selection of polarization state. The parameters of the line shape of the scattered intensity could be reduced to

$$I_s(\omega) = |E_s(\omega)|^2 = \cos^2 \alpha \cos^2 \beta \left( B^2 \frac{(q^{\text{eff}} + \epsilon)^2}{\epsilon^2 + 1} + \frac{(B - 1)^2}{\epsilon^2 + 1} \right); \quad (3.35)$$

$$q^{\text{eff}} = \frac{q}{B}; q = q_x; B = \frac{B_x \cos \alpha \cos \beta + B_y \sin \alpha \sin \beta}{\cos \alpha \cos \beta}.$$

In Fig. 3.5b, we have demonstrated the tuning of Fano-type spectral line shape for pre selection of  $\mathbf{E}_\alpha = [1 \ 1]^T$  and subsequent post selection of  $\mathbf{E}_\beta = [\cos \beta - \sin \beta]^T$  with  $B_x = B_y = 0.5$  and  $q_x = 1.5$  with resonance frequency  $\omega_o = 1.78$  eV and line width  $\gamma = 0.107$  eV. Different interesting regimes can be achieved - starting from a modest asymmetry ( $q^{\text{eff}} \sim +3$ ), high degree of asymmetry can be obtained ( $q^{\text{eff}} \sim +1.5$ ), the negative  $q$ -parameter regime can be tailored ( $q^{\text{eff}} \sim -2.1$ ), and finally symmetric Lorentzian line shape ( $q^{\text{eff}} \rightarrow \infty$ ) can be produced. These are illustrative examples, and many other interesting possibilities emerge on appropriately designed anisotropic Fano resonant systems.

The above analysis is strictly valid for non-depolarizing systems, which is not in general the case in experimental scenarios. However, the study can be implemented in such scenarios once we can filter out the depolarizing component ( $M_\Delta$ )

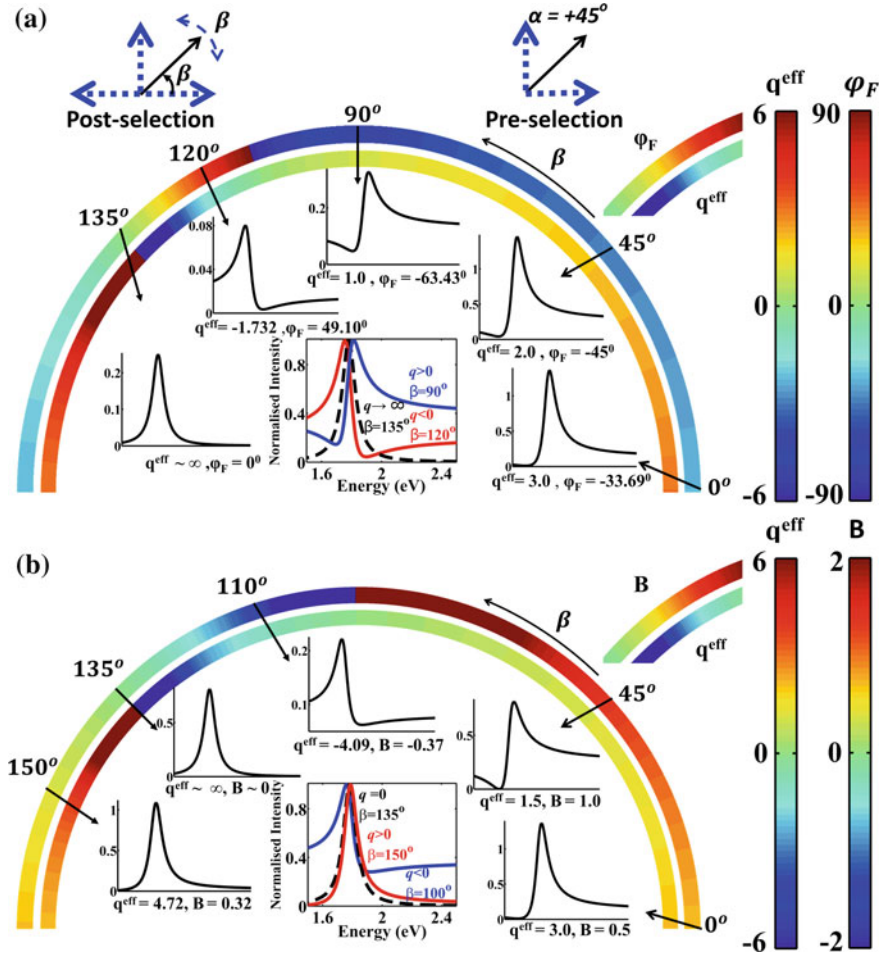


**Fig. 3.5** Demonstration of Polarization controlled tuning of Fano spectral asymmetry in **a** Amplitude and phase anisotropic discrete mode (case-1), and **b** a perfectly diattenuating discrete mode (case-2) with parameters mentioned in the text. The pre-selected state is linear ( $\alpha = 45^\circ, \phi_\alpha, S_\alpha = [1 \ 0 \ 1 \ 0]^T$ ) in both the cases and the post-selections are at different linear polarization angles  $\beta$  ( $S_\beta = [1 \ \cos 2\beta \ \sin 2\beta \ 0]^T$ ) (marked by arrows). The frequency dependence of the scattered intensities for different  $\beta$  (obtained using respective  $S_\alpha$  and  $S_\beta$  in (3.30)) were fitted to (3.23), and the resulting parameters ( $B, q^{\text{eff}}$ , Fano phase  $\phi_F$  or  $q$ ) are noted. The insets highlight the change in the spectral line shapes with varying post-selection (including the reversal of spectral asymmetry for negative  $q$ ). While, in (a)  $q^{\text{eff}}$  is tuned by directly modifying the Fano phase  $\phi_F$  (or  $q$ ), in (b) regulated control is achieved by controlling  $B$  alone. The magnitudes of the continuously tuned Fano phase  $\phi_F$  and  $q^{\text{eff}}$  in case 1, and  $B$  and  $q^{\text{eff}}$  in case 2, parameters are represented by color code and the corresponding color bar is displayed. Adopted from Chandel et al. [53] and Ray et al. [27]

from the recorded Mueller matrix using matrix decomposition methods discussed in Sect. 3.2.2 and use the remaining non-depolarizing part ( $M_{\text{pol}}$ ) of Mueller matrix

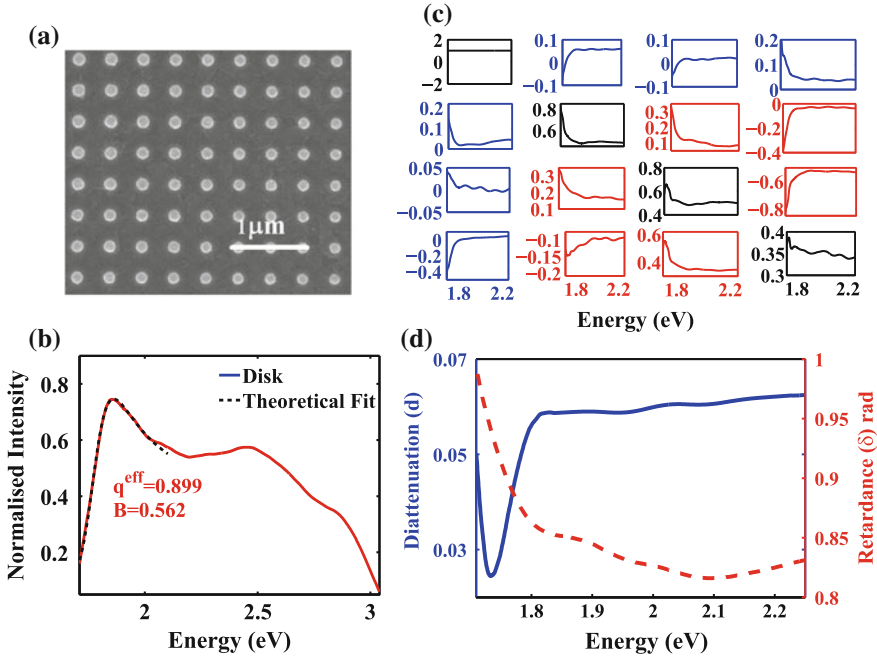


**Fig. 3.6** **a** SEM image of an array of gold nanodisks; **b** the scattering spectra from the gold nanodisk array showing asymmetry at the farther end ( $\approx 690$  nm) with theoretical fitting using (3.23), the fitted  $q$  and  $B$  parameters are specified. **c** The recorded Mueller matrix from the disk array obtained using Dark field set up. The parameter of the system are as follows: the Au circular disk array were of diameter  $D = 160$  nm, height  $h = 30$  nm, center to center distance  $L = 480$  nm; and the thickness of ITO was 190 nm, **d**) Spectral variation of the Mueller matrix-derived linear retardance  $\delta$  (red dashed line, right axis) and linear diattenuation  $d$  (blue solid line, left axis). A characteristic signature of anisotropic Fano resonance is observed in the rapid variation of  $d$  and  $\delta$  parameters across the narrow resonance peak of the quasiguided mode ( $E \approx 1.8$  eV or  $\lambda \approx 690$  nm). Adopted from Ray et al. [27]

(see (3.19)) for the analysis. The experimental validation of above analysis is shown using a WPC.

Figure 3.6a shows a two dimensional WPC with a plasmonic nano-disk (diameter  $D = 160$  nm and height  $h = 30$  nm) made of gold deposited on top of 190 nm thick ITO coated quartz substrate with a period of 480 nm in both x and y direction (as shown in SEM image) with an electron beam lithography technique. As discussed previously such structure gives a Fano resonant scattering spectra (peak at  $E_m \sim 1.896$  eV,  $\lambda_m \sim 654$  nm) due to interference of the broad isotropic plasmon mode of the gold nano-disk with the discrete waveguided mode (peak at  $E_o = \hbar\omega_o \sim 1.777$  eV,  $\lambda_o \sim 698$  nm) of thin ITO layer, which can be observed in the polarization blind scattering spectra of the sample shown in Fig. 3.6b, obtained using a dark field microscope. The scattered profile were fitted using (3.23) and the effective asymmetry parameter “ $q^{\text{eff}}$ ” was found to be  $\sim +0.90$  and corresponding Fano phase “ $\varphi_F$ ” to be  $\sim 63.2^\circ$ . The polarizing part of the Mueller matrix of sample and the polariza-

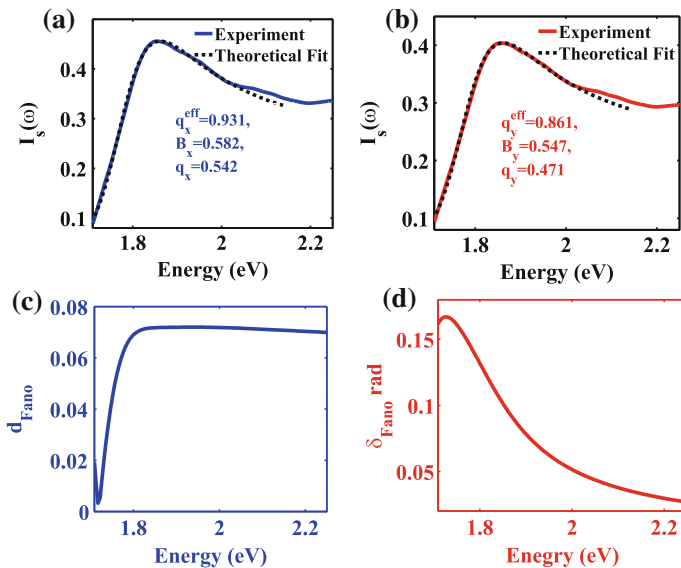


**Fig. 3.7** The spectral variation of scattered intensities for **a** TM (x polarization) and **b** TE (y polarization). The resonance parameters were obtained using theoretical fit with (3.23), the parameters are noted in the figure. The spectral variation of **c** linear diattenuation ( $d_{\text{Fano}}$ ) and **d** linear retardance ( $\delta_{\text{Fano}}$ ) using the theoretically predicted parameters ( $q_x/q_y$ ,  $B_x/B_y$ ). Taken from Ray et al. [27]

tion parameters are shown in Fig. 3.6c and Fig. 3.6d respectively. The off-diagonal element of the matrix represents the anisotropic polarization response of the system, which can be subsequently quantified by the polarization parameters of the system namely retardance ( $\delta$ ) and diattenuation ( $d$ ) corresponding to phase and amplitude anisotropy respectively. It is to be noted that the origin of such anisotropy is the differential response of TE and TM narrow waveguided modes, as the circular nanodisk provides an isotropic and broad continuum. The sharp variation of polarization parameters across the waveguided mode/Fano resonance peak ascertain the origin of anisotropy due to the waveguided modes, and (3.11), (3.15) along with (3.28) imply its relation with the Fano asymmetry.

In order to establish the fact, the parameters for orthogonal x and y polarizations were obtained using projection on approximately block diagonal  $M_{\text{Pol}}$  matrix which gives an appropriate estimate of the corresponding parameters of its Jones matrix. The parameters showed a small phase as well as amplitude anisotropy as shown in Fig. 3.7a, b. These parameters were obtained by pre- and postselection of corresponding polarization states (Stokes vector:  $[1 \ 1 \ 0 \ 0]^T$  for x and  $[1 \ 1 \ 0 \ 0]^T$  for y) on the  $M_{\text{Pol}}$  matrix. In order to quantify and estimate the anisotropy, the parameters were used to obtain the retardance and diattenuation polarization parameters which showed a good match with the experimental behaviour as shown in Fig. 3.7c, d, establishing the connection between the asymmetry parameters  $q_x$ ,  $q_y$  and the anisotropy of the Fano resonance. The method shows the self-consistency as well as provides a check

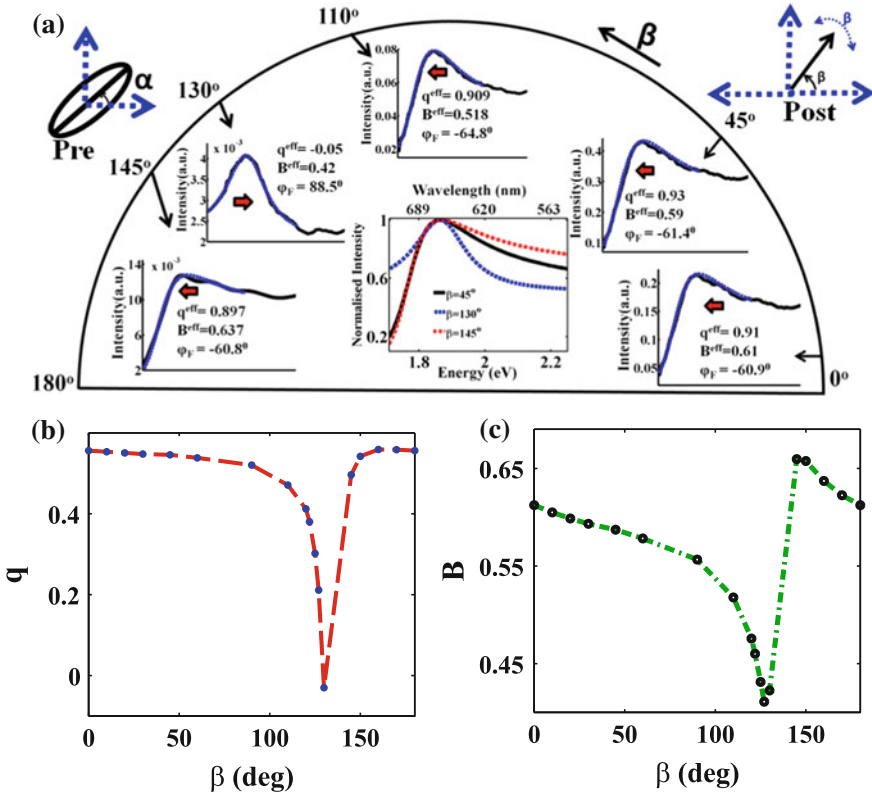


**Fig. 3.8** a Polarization controlled tuning of Fano spectral asymmetry in a moderately anisotropic experimental waveguided plasmonic crystal sample. The pre-selected state is chosen to be elliptical ( $\Phi_\alpha - \Phi_\beta = 0.8$  to compensate the background retardance) and post-selections at different linear polarization angles  $\beta$  (value marked by arrows). The spectral variations of the scattered intensities for different post selection angles ( $\beta$ , obtained using 3.30) were fitted to (3.23), and the resulting parameters ( $q_{\text{eff}}$ , Fano phase  $\varphi_F$ , or  $q$ ) are noted. The dependence of the derived effective Fano asymmetry parameter **b**  $q$ -parameter and **c** the relative amplitude factor  $B$ , on the post selection of linear polarization angle  $\beta$ , for the case 1 anisotropic experimental waveguided plasmonic crystal sample. Taken from Ray et al. [27]

on the accuracy of parameters obtained through fitting. The results demonstrate that the physical parameters such as Fano phase  $\varphi_F$  and the relative amplitude parameter ( $B$ ) can be mapped to spectral asymmetry of the resonance. The difference in these parameters leads to Fano resonance anisotropy, and indeed causes a peculiar rapidly varying spectral retardance and diattenuation effects in the Mueller matrix. Thus, the  $\delta$  and  $d$  parameters could provide novel experimental tool to probe and analyze anisotropic Fano resonances.

The tuning of Fano spectral line shape with pre and post selection of polarization state for the WPC is demonstrated in Fig. 3.8. The pre-selected state was optimized

to an elliptical polarized state to compensate the background retardance observed ( $\alpha = 45^\circ$ ,  $\phi_x - \phi_y \sim 0.8$ , see Fig. 3.6) with varying linearly polarized post selected state. The system is equivalent to the case 1 discussed above with linear pre and post selected polarization state. Its to be noted that here an effective tuning of relative amplitude of the continuum is observed due to  $B_x \neq B_y$ . Although chosen system is weakly anisotropic ( $q_x - q_y \sim 0.1$ ), it shows a considerable amount of tuning of effective asymmetry by modulating the Fano phase. Figure 3.8b, c shows a range of asymmetry parameter “q” and relative amplitude “B” obtained through polarization tuning respectively, negative  $q$  parameter region was obtained at  $\beta = 130^\circ$  implying the reversal of asymmetry of spectra (i.e.  $\omega_F > \omega_o$  to  $\omega_F < \omega_o$ ). However the variation of the parameters with post selection angle  $\beta$  is slightly deviated from the behavior predicted by (3.33), the possible reason for such deviation could be remnant contribution of the background retardance due to complexity involved in the focused geometry or smaller magnitude of the detected intensities (within the noise level of the experimental measurement system).

### 3.6 Conclusion and Outlook

In conclusion, this chapter presents and explores the studies of asymmetric Fano resonance from the aspect of polarization, which has immense potential for both fundamental understanding and numerous applications but has not been investigated in details. Basics of polarization along with Fano resonance has been provided for better understanding of connections and implementations for the polarization based modulation of Fano resonance. A brief description of the Plasmonic polarimetry platform is also provided, which was used to record the complete polarization response in the form of spectral scattering Mueller matrix from plasmonic nanostructures along with the accurate extraction and quantification of individual polarization properties. Experimental results of polarization based tuning of Fano resonance, from the coupled plasmonic system like Plasmonic Oligomers as well as from waveguided photonic crystals has been presented backed by theoretical ones. We have also presented a new model of anisotropic Fano resonance in the scattering of electromagnetic waves. The model enables interpretation of the Fano spectral asymmetry via a set of physically meaningful parameters, namely, the Fano phase shift and the relative amplitudes of the interfering modes. Experimental control on these parameters and engineering of the resulting spectral line shape is achieved in anisotropic Fano resonant system by Mueller matrix-based polarization analysis. It is further shown that the Mueller matrix-derived retardance and diattenuation parameters capture exclusive information on the anisotropy of Fano phase shift and relative amplitude factors (respectively), and that these can be utilized for optimal pre and post selection of the polarization states for desirably tuning the spectral line shape. The principle is demonstrated on waveguided plasmonic crystals exhibiting moderate level of anisotropy, and a much more dramatic control is envisaged in strongly anisotropic systems. The ability to probe, manipulate and desirably tune the interference effect

enables remarkable control on the spectral line shape, leading to realization of several exotic regimes of Fano resonance from the same system. This promising approach should therefore stimulate further studies enabling new applications of polarization-optimized anisotropic Fano resonant systems, which may potentially lead towards development of novel polarization controlled optical meta-devices. In general, this approach may open a new avenue in analyzing/interpreting and controlling Fano resonance in diverse systems.

## References

1. U. Fano, Phys. Rev. **124**(6), 1866 (1961)
2. A.C. Johnson et al., Phys. Rev. Lett. **93**(10), 106803 (2004)
3. I. Mazumdar, A.R.P. Rau, V.S. Bhasin, Phys. Rev. Lett. **97**(6), 062503 (2006)
4. A.R. Schmidt et al., Nature **465**(7298), 570 (2010)
5. P. Fan et al., Nat. Mater. **13**(5), 471 (2014)
6. B. Luk'yanchuk et al., Nat. Mater. **9**(9), 707 (2010)
7. C. Ott et al., Science **340**(6133), 716 (2013)
8. Y. Sonnefraud, ACS Nano **4**(3), 1664 (2010)
9. A. Christ et al., Phys. Rev. Lett. **91**(18), 183901 (2003)
10. S.A. Maier, *Plasmonics: Fundamentals and Applications* (Springer Science & Business Media, 2007)
11. J.N. Anker et al., Nat. Mater. **7**(6), 442 (2008)
12. W.-S. Chang et al., Nano Lett. **12**(9), 4977 (2012)
13. A. Bärnthaler et al., Phys. Rev. Lett. **105**(5), 056801 (2010)
14. C. Wu et al., Nat. Mater. **11**(1), 69 (2012)
15. K. Nozaki et al., Opt. Express **21**(10), 11877 (2013)
16. A. Kaldun et al., Phys. Rev. Lett. **112**(10), 103001 (2014)
17. M.R. Shcherbakov et al., Phys. Rev. Lett. **108**(25), 253903 (2012)
18. C. Wu, A.B. Khanikaev, G. Shvets, Phys. Rev. Lett. **106**(10), 107403 (2011)
19. B. Zhang, Light Sci. Appl. **1**(10), e32 (2012)
20. N.I. Zheludev et al., Nat. Photonics **2**(6), 351 (2008)
21. Y. Zhu et al., Adv. Opt. Mater. **1**(1), 61 (2013)
22. A. Christ, Phys. Rev. B **70**(12), 125113 (2004)
23. G. Gantzounis, N. Stefanou, N. Papanikolaou, Phys. Rev. B **77**(3), 035101 (2008)
24. M. Hentschel, ACS Nano **5**(3), 2042 (2011)
25. J.B. Lassiter et al., Nano Lett. **10**(8), 3184 (2010)
26. M. Lisunova et al., J. Phys. D: Appl. Phys. **46**(48), 485103 (2013)
27. S.K. Ray, ACS Nano **11**(2), 1641 (2017)
28. C.-L. Du et al., Plasmonics **4**(3), 217 (2009)
29. T.K. Sau et al., Adv. Mater. **22**(16), 1805 (2010)
30. C. Sönnichsen et al., Phys. Rev. Lett. **88**(7), 077402 (2002)
31. J. Müller et al., Appl. Phys. Lett. **81**(1), 171 (2002)
32. K. Drozdowicz-Tomsia et al., Chem. Phys. Lett. **468**(1), 69 (2009)
33. Z. Gryczynski et al., Chem. Phys. Lett. **421**(1), 189 (2006)
34. O. Schubert et al., Nano Lett. **8**(8), 2345 (2008)
35. N. Lippok et al., Nat. Photonics **11**(9), 2017 (2017)
36. J. Soni, H. Purwar, N. Ghosh, Opt. Commun. **285**(6), 1599 (2012)
37. S. Chandel et al., Sci. Rep. **6**, 26466 (2016)
38. Y. Huang, D.-H. Kim, Nanoscale **3**(8), 3228 (2011)
39. L. Li et al., Light Sci. Appl. **4**(9), e330 (2015)

40. D. Li, Nat. Photonics **11**(6), 336 (2017)
41. T. Shegai et al., Proc. Natl. Acad. Sci. **105**(43), 16448 (2008)
42. D.H. Goldstein, *Polarized Light* (CRC Press, 2016)
43. S.D. Gupta, N. Ghosh, A. Banerjee *Wave Optics: Basic Concepts and Contemporary Trends*, (CRC Press, 2015)
44. C. Brosseau, *Fundamentals of Polarized Light: A Statistical Optics Approach* (Wiley-Interscience, 1998)
45. N. Ghosh, M.F.G. Wood, I.A. Vitkin, J. Biomed. Opt. **13**(4), 044036 (2008)
46. N. Ghosh, I.A. Vitkin, J. Biomed. Opt. **16**(11), 110801 (2011)
47. S.-Y. Lu, R.A. Chipman, JOSA A **13**(5), 1106 (1996)
48. N. Ortega-Quijano, J.L. Arce-Diego, Opt. Lett. **36**(10), 1942 (2011)
49. R. Ossikovski, Opt. Lett. **36**(12), 2330 (2011)
50. S. Kumar et al., J. Biomed. Opt. **17**(10), 105006 (2012)
51. F. Stabo-Eeg, Dissertation, Norges teknisk-naturvitenskapelige universitet, Fakultet for naturvitenskap og teknologi, Institutt for fysikk (2009)
52. A.D. Martino et al., Thin Solid Films **455**, 112 (2004)
53. S. Chandel, Curr. Nanomater. **2**(1), 60 (2017)
54. J. Soni et al., Opt. Express **21**(13), 15475 (2013)
55. R.W. Wood, Proc. Phys. Soc. Lond. **18**(1), 269 (1902)
56. F.J.G. De Abajo, Rev. Mod. Phys. **79**(4), 1267 (2007)
57. A. Hessel, A.A. Oliner, Appl. Opt. **4**(10), 1275 (1965)
58. C. Billaudeau et al., Opt. Express **17**(5), 3490 (2009)
59. M. Sarrazin, J.-P. Vigneron, J.-M. Vigoureux, Phys. Rev. B **67**(8), 085415 (2003)
60. N.A. Mirin, K. Bao, P. Nordlander, J. Phys. Chem. A **113**(16), 4028 (2009)
61. A.E. Miroshnichenko, S. Flach, Y.S. Kivshar, Rev. Mod. Phys. **82**(3), 2257 (2010)
62. B. Gallinet, O.J.F. Martin, ACS Nano **5**(11), 8999 (2011)
63. B. Gallinet, O.J.F. Martin, Phys. Rev. B **83**(23), 235427 (2011)



# Chapter 4

## Fano Resonances and Bound States in the Continuum in Evanescently-Coupled Optical Waveguides and Resonators



Stefano Longhi

**Abstract** This chapter provides a comprehensive review of some recent theoretical and experimental advances in the field of Fano resonances and bound states in the continuum for light transport in evanescently-coupled optical structures, including arrays of dielectric optical waveguides and coupled resonator optical waveguides. The review will be focused on the occurrence of Fano resonances and bound states in static photonic structures, the role of particle (photon) statistics, dynamical control of Fano resonances, and Fano resonances in non-Hermitian optical structures.

### 4.1 Introduction

Fano resonances were introduced in a pioneering work by Ugo Fano in 1935 [1] and formalized in 1961 [2] to explain certain asymmetric profiles of spectral absorption lines in atoms [3]. The theoretical description of these resonances was developed independently by Feshbach [4] in nuclear physics. In contrast to a more conventional symmetric-shaped Lorentzian (Breit-Wigner) resonance, a Fano resonance is generally associated to an asymmetric line shape which arises from the constructive and destructive interference of discrete resonance states by broadband continuum states. Nowadays, Fano resonances are ubiquitous in several areas of physics. A recent comprehensive review can be found, for instance, in [5]. Among the different physical fields where Fano resonances are found, light transport in photonic structures has provided since more two decades a feasible laboratory tool to observe the rich physics embodied in Fano resonances, with important applications to optical switching and optical sensing. Photonic systems where Fano resonance can occur can be roughly

---

S. Longhi (✉)

Dipartimento di Fisica e Istituto di Fotonica e Nanotecnologie del Consiglio Nazionale delle Ricerche, Politecnico di Milano, Piazza L. da Vinci 32, 20133 Milan, Italy  
e-mail: longhi@fisi.polimi.it; stefano.longhi@polimi.it

speaking classified into four classes: photonic crystal structures, arrays of coupled optical waveguide and resonators, plasmonic nano structures, and metamaterials. Recent progress on Fano resonances in photonic crystal, plasmonic and metamaterial structures is reviewed in [6–8]. In this chapter we provide an overview of Fano resonance and related physical aspects, such as the existence of bound states in the continuum, for light transport in waveguide lattices with side-coupled waveguides or coupled resonator optical waveguides (CROW) structures, which has attracted great and increasing interest in the past decade [9–31]. In particular, we focus on the occurrence of static Fano resonances and related bound states in the continuum (BIC) in waveguide lattices with side-coupled waveguides, the role of particle (photon) statistics on Fano resonances, dynamical control of Fano resonances in CROW structures, and Fano resonances in non-Hermitian coupled waveguide systems.

## 4.2 Fano Resonance and Bound States in the Continuum in Optical Waveguide Lattices with Side-Coupled Waveguides

Light transport in an array of evanescently-coupled optical waveguides with side-coupled waveguides provides the simplest optical structure where the physics of Fano resonance and related phenomena come into play [15, 16, 21, 23, 27]. Light propagation in a chain of optical waveguides is described, within a tight-binding approximation, by coupled mode equations [32–34] which provide an optical analogue to single-particle quantum transport in quantum wires and quantum waveguides, where Fano resonance phenomena are commonplace [35–43]. A rather general waveguide lattice, that shows Fano-like resonance profiles and bound states in the continuum (BIC) [44–49], is shown in Fig. 4.1a. It comprises a set of  $N$  optical waveguides  $|1\rangle, |2\rangle, \dots, |\alpha\rangle, \dots, |N\rangle$  which are side-coupled to a linear array of evanescently-coupled optical waveguides. The side-coupled waveguides play the role of discrete states which decay into the common continuum of states provided by the tight-binding array (the optical analogue of a quantum wire); see Fig. 4.1b. The side waveguide  $|\alpha\rangle$  is assumed to be weakly coupled, with a coupling rate  $\kappa_\alpha$ , to the waveguide of index  $n_\alpha$  in the array ( $\alpha = 1, 2, \dots, N$ ), whereas the coupling rate between adjacent waveguides in the linear array is  $\kappa$ . Indicating by  $b_n(z)$  the field amplitude of light waves trapped in the waveguide  $n$  of the linear array, and by  $c_\alpha(z)$  the field amplitude of light waves trapped in the side waveguide  $|\alpha\rangle$ , in the nearest-neighbor tight-binding approximation the evolution of modal amplitudes along the spatial propagation distance  $z$  is governed by the following set of coupled-mode equations [21]

$$i \frac{db_n}{dz} = -\kappa(b_{n+1} + b_{n-1}) - \sum_{\alpha=1}^N \kappa_\alpha c_\alpha \delta_{n,n_\alpha} \quad (n = 0, \pm 1, \pm 2, \dots) \quad (4.1)$$

$$i \frac{dc_\alpha}{dz} = -\kappa_\alpha b_{n_\alpha} + \omega_\alpha c_\alpha \quad (\alpha = 1, 2, \dots, N) \quad (4.2)$$

where  $\omega_\alpha$  is the propagation constant mismatch of the side waveguide  $|\alpha\rangle$  as compared to the propagation constant of waveguides in the linear array. Light transport in the waveguide array set-up of Fig. 4.1a provides a photonic simulator of the  $N$ -level Fano-Anderson model, which describes rather generally the decay of  $N$  discrete states into a common continuum [50–53]. Fano resonances and bound states in the continuum arise from interference of the various decay channels. To highlight the optical-quantum analogy, it is worth rewriting (4.1) and (4.2) using a Bloch basis  $|k\rangle$  rather than a Wannier basis for the linear array (see, for instance, [16, 21, 53, 54]). To this aim, let us introduce the amplitude  $c(k, z)$ , which is a function of the Bloch wave number  $k$  defined inside the first Brillouin zone  $-\pi \leq k < \pi$ , according to

$$c(k, z) = -\frac{1}{\sqrt{2\pi}} \sum_{n=-\infty}^{\infty} b_n(z) \exp(ikn), \quad (4.3)$$

so that the inversion relation

$$b_n(z) = -\frac{1}{\sqrt{2\pi}} \int_{-\pi}^{\pi} dk c(k, z) \exp(-ikn) \quad (4.4)$$

holds. Using (4.3) and (4.4), from (4.1) and (4.2) the following coupled-mode equations are obtained for the amplitudes  $c_\alpha(z)$  and  $c(k, z)$

$$i \frac{dc}{dz} = \omega(k)c(k, z) + \sum_{\alpha=1}^N g_\alpha(k)c_\alpha(z) \quad (4.5)$$

$$i \frac{dc_\alpha}{dz} = \omega_\alpha c_\alpha(z) + \int_{-\pi}^{\pi} dk g_\alpha^*(k)c(k, z) \quad (\alpha = 1, 2, \dots, N) \quad (4.6)$$

where we have set

$$\omega(k) = -2\kappa \cos k, \quad g_\alpha(k) = \frac{\kappa_\alpha}{\sqrt{2\pi}} \exp(ikn_\alpha). \quad (4.7)$$

In their present form, (4.5) and (4.6) describe the decay of  $N$  discrete states  $|1\rangle, |2\rangle, \dots, |N\rangle$  of energies  $\hbar\omega_1, \hbar\omega_2, \dots, \hbar\omega_N$  coupled to a common tight-binding continuum (a band) of states  $|k\rangle$  with energy  $\hbar\omega(k)$  as derived by the Schrödinger equation with the Hamiltonian (see Fig. 4.1b)

$$H = \hbar \sum_{\alpha=1}^N \omega_\alpha |\alpha\rangle \langle \alpha| + \hbar \int dk \omega(k) |k\rangle \langle k| + \hbar \sum_{\alpha=1}^N \int dk [g_\alpha(k) |\alpha\rangle \langle k| + g_\alpha^*(k) |k\rangle \langle \alpha|] \quad (4.8)$$

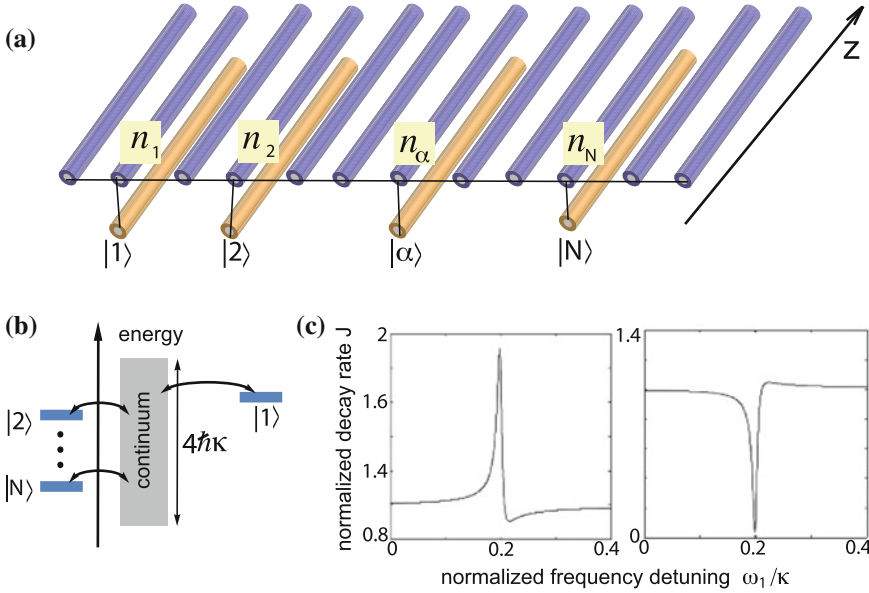


**Fig. 4.1** **a** Schematic of a linear array of straight evanescently-coupled optical waveguides with  $N$  side-coupled waveguides  $|1\rangle, |2\rangle, \dots, |N\rangle$ . Light propagates along the paraxial  $z$  direction. **b** The quantum analogue of the optical waveguide system describing the coupling of  $N$  discrete states with a common continuum. **c** Fano resonance for  $N = 2$  side waveguides. The panels show the behavior of the decay rate  $J$  of light from the waveguide  $|1\rangle$ , weakly coupled to the array, in the presence of the strongly-coupled second waveguide  $|2\rangle$ , versus the normalized detuning parameter  $\omega_1/\kappa$ . The decay rate  $J$  is normalized to the one observed in the absence of the second waveguide. Parameter values are  $\kappa_1/\kappa = 0.04$ ,  $\kappa_2/\kappa = 0.1$ ,  $\omega_2/\kappa = 0.2$  and  $n_0 = 3$  in the left panel,  $n_0 = 4$  in the right panel. Note the asymmetric line shape of  $J$  at around  $\omega_1 = \omega_2$ , which is a typical signature of a Fano resonance

where  $g_\alpha(k)$  is the coupling amplitude between states  $|\alpha\rangle$  and  $|k\rangle$ . Note that in the optical analogue of the quantum mechanical decay problem the temporal evolution of the quantum state is replaced by the spatial propagation dynamics along the waveguide axis  $z$ , and the fractional light power  $|c_\alpha(z)|^2$  trapped in waveguide  $|\alpha\rangle$  plays the role of the population for level  $|\alpha\rangle$  in the scheme of Fig. 4.1b.

The multi-level Fano-Anderson model is known to provide a fertile system to study Fano resonance and the appearance of BIC states via destructive interference of decay channels into the common continuum (an effect also known as population trapping in atomic physics). The simplest case, which is amenable to an analytical treatment and capable of providing the main physical insights into Fano resonance and BIC, is when the discrete states are weakly coupled with the continuum [21], i.e.  $\kappa_\alpha \ll \kappa$ . Following a standard procedure (see, for instance, [55]), the amplitudes  $c(k, z)$  of the continuous states can be eliminated from (4.5) and (4.6), yielding a set of integro-differential equations for the field amplitudes  $c_\alpha(z)$  in the side waveguides

$$\frac{dc_\alpha}{dz} = -i\omega_\alpha c_\alpha(z) - \sum_{\beta=1}^N \int_0^z d\xi \Phi_{\alpha,\beta}(z-\xi) c_\beta(\xi) \quad (4.9)$$

where

$$\Phi_{\alpha,\beta}(\tau) \equiv \int_{-\pi}^{\pi} dk g_\alpha^*(k) g_\beta(k) \exp[-i\omega(k)\tau] \quad (4.10)$$

are the ‘memory functions’. For our specific model (4.7), the form of  $\Phi_{\alpha,\beta}$  reads explicitly

$$\Phi_{\alpha,\beta}(\tau) = i^{n_\alpha - n_\beta} \kappa_\alpha \kappa_\beta J_{n_\alpha - n_\beta}(2\kappa\tau) \quad (4.11)$$

where  $J_n$  is the Bessel function of order  $n$ . Under the assumption  $\kappa_\alpha \ll \kappa$  and after setting  $c_\alpha(z) = q_\alpha(z) \exp(-i\omega_\alpha z)$ , for ‘frequencies’  $\omega_\alpha$  sufficiently far from the band edges  $\pm 2\kappa$  the amplitudes  $q_\alpha$  vary slowly with  $z$  over the characteristic spatial period  $\sim 1/\kappa$  of the memory function as estimated from (4.11). By invoking the markovian approximation, (4.9) then simplify into the coupled differential equations

$$\frac{dc_\alpha}{dz} \simeq -i\omega_\alpha c_\alpha - \sum_{\beta=1}^N \Delta_{\alpha,\beta} c_\beta \quad (4.12)$$

where we have set

$$\begin{aligned} \Delta_{\alpha,\beta} &= \int_0^\infty d\tau \Phi_{\alpha,\beta}(\tau) \exp(i\omega_\beta \tau) = \kappa_\alpha \kappa_\beta i^{|n_\alpha - n_\beta|} \times \\ &\times \frac{\left(\sqrt{4\kappa^2 - \omega_\beta^2} + i\omega_\beta\right)^{|n_\alpha - n_\beta|}}{(2\kappa)^{|n_\alpha - n_\beta|} \sqrt{4\kappa^2 - \omega_\beta^2}} \end{aligned} \quad (4.13)$$

To observe a Fano resonance and BIC, a minimum of two side waveguides is required, and therefore we will focus our study to the simplest case of  $N = 2$  side waveguides. After setting  $n_1 = 0$  and  $n_2 = n_0 > 0$ , in the markovian approximation the amplitudes of light waves in the two side waveguides  $|1\rangle$  and  $|2\rangle$  evolve according to the coupled equations

$$\frac{dc_1}{dz} = -(\Delta_{11} + i\omega_1)c_1 - \Delta_{12}c_2 \quad (4.14)$$

$$\frac{dc_2}{dz} = -\Delta_{21}c_1 - (\Delta_{22} + i\omega_2)c_2 \quad (4.15)$$

where the  $2 \times 2$  matrix  $\{\Delta_{n,m}\}$  is determined by (4.13).

Let us first consider the limiting case where the coupling  $\kappa_1$  of waveguide |1) with the linear array (continuum) is much weaker than the coupling  $\kappa_2$  of the other side waveguide |2) with the continuum. In this case, we can view the decay of light in waveguide |1) as a result of its evanescent coupling with a ‘structured’ continuum obtained by the strong coupling of the linear array with the side waveguide |2). The features of the structured continuum appear at frequencies close to  $\omega_2$ , and therefore according to Fano theory [2, 55] the decay of state |1) into the structured continuum is expected to be strongly modified for  $\omega_1 \simeq \omega_2$ , with a characteristic asymmetric profile of the decay rate versus  $\omega_1$  at around  $\omega_1 = \omega_2$ . The profile of the decay rate versus  $\omega_1$  can be analytically calculated by elimination of  $c_2(t)$  from (4.14) and (4.15) taking the limit  $\kappa_1 \ll \kappa_2$ . This yields the following equation for the decay of amplitude  $c_1(z)$

$$\frac{dc_1}{dz} \simeq \left[ -(\Delta_{11} + i\omega_1) + \frac{\Delta_{12}\Delta_{21}}{\Delta_{22} + i(\omega_2 - \omega_1)} \right] c_1. \quad (4.16)$$

Note that the decay law that one would observe in the absence of the second waveguide |2) which structures the continuum, i.e. in a featureless continuum, is simply obtained from (4.16) by taking  $\kappa_2 = 0$ , i.e.  $\Delta_{12} = \Delta_{21} = \Delta_{22} = 0$ . The behavior of the decay rate  $R$  versus  $\omega_1$ , normalized to its value  $\Delta_{11}$  in absence of the second side waveguide, is then given by

$$J \equiv \frac{R}{\Delta_{11}} = 1 - \text{Re} \left\{ \frac{\Delta_{12}\Delta_{21}}{\Delta_{11}[\Delta_{22} + i(\omega_2 - \omega_1)]} \right\} \quad (4.17)$$

The curve  $J(\omega_1)$  shows an asymmetric shape around  $\omega_1 = \omega_2$  which strongly depends on  $n_0$  being an even or an odd number. Typical behaviors of  $J$  for an odd and for an even value of  $n_0$  are shown in Fig. 4.1c. Note that, for  $\omega_1$  near  $\omega_2$ , a strong peak is observed when  $n_0$  is odd, corresponding to an increase of the decay rate, whereas a strong deep in the behavior of  $J$  is observed when  $n_0$  is even, corresponding to a deceleration of the decay. In particular, the minimum of the normalized decay rate  $J$  is found to vanish at  $\omega_1 = \omega_2$  when  $\omega_2 = 0$ , leading to a complete suppression of the decay (population trapping). Such a suppression of the decay is related to the existence of a BIC when  $\omega_1 = \omega_2 = 0$  and for an even value of  $n_0$ . In the markovian limit, population trapping and the appearance of a BIC state are associated to the vanishing of the real part of one of the two eigenvalues of the  $2 \times 2$  matrix  $\{\Delta_{n,m}\}$  which governs the decay dynamics of the two states |1) and |2) according to (4.14) and (4.15). In the optical waveguide system of Fig. 4.1a, the trapping mechanism and the existence of a BIC can be physically explained in a simple way as a destructive interference effect among different tunneling paths into the common continuum. From such a perspective, the trapping mechanism is thus analogous to the one found in chains of tunneling-coupled quantum dots [39, 40, 42]. In fact, if we consider two side waveguides |1) and |2) connected to the linear array at sites  $n_1 = 0$  and  $n_2 = n_0 > 0$ , for  $\omega_1 = \omega_2 = 0$  and for an even value of  $n_0$  the coupled mode equations (4.1) and (4.2) admit of the trapped state

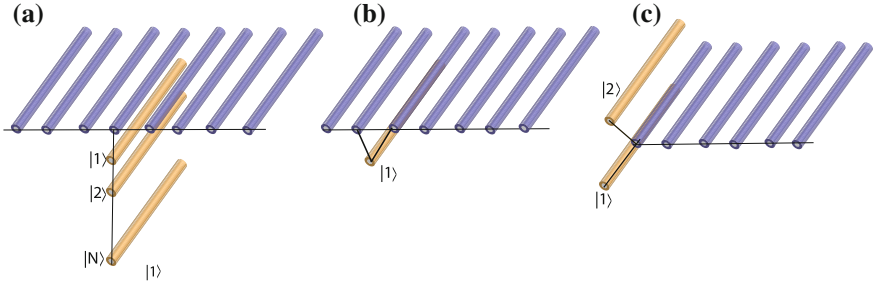


**Fig. 4.2** Other configurations of side-coupled waveguides to either **a** an infinite linear waveguide array, and **b, c** a semi-infinite linear waveguide array where Fano resonances and BIC can be observed

$$b_n = 0 \text{ for } n < 0, \quad n > n_0, \quad n = 0, 2, 4, \dots, n_0 \quad (4.18)$$

$$b_1 = -\frac{\kappa_1}{\kappa}, \quad b_3 = \frac{\kappa_1}{\kappa}, \quad b_5 = -\frac{\kappa_1}{\kappa}, \quad \dots, \quad b_{n_0-1} = (-1)^{n_0/2} \frac{\kappa_1}{\kappa} \quad (4.19)$$

$$c_1 = 1, \quad c_2 = -(-1)^{n_0/2} \frac{\kappa_1}{\kappa_2}. \quad (4.20)$$

such that the waveguides in the linear array at sites  $n \leq 0$  and  $n \geq n_0$  decouple from the other waveguides of the structure. Decoupling is made possible owing to the vanishing of the tunneling rates  $-\kappa b_1 - \kappa_1 c_1$  and  $-\kappa b_{n_0-1} - \kappa_2 c_2$  for the two waveguides in the array at sites  $n = 0$  and  $n = n_0$ , respectively. BIC arising from such a decoupling mechanism (also called a dark state) has been experimentally observed in [56, 57]. Interestingly, by adiabatically varying the ratio  $\kappa_1/\kappa_2$ , according to (4.20) one can transfer excitation between the two side waveguides  $|1\rangle$  and  $|2\rangle$  using the waveguide lattice as a virtual bus. Such an interesting possibility provides the photonic analogue of adiabatic population transfer via a continuum and has been experimentally demonstrated using femtosecond laser written waveguide arrays in [56].

It should be noted that, as the previous analysis has been focused to the case of two side waveguides, trapping effects may occur for more than two side-coupled waveguides. Assuming, for the sake of definiteness,  $n_N > n_{N-1} > \dots > n_1$ , a trapping state is found provided that a non-decaying solution to (4.1) and (4.2) does exist with  $b_n = 0$  for  $n \leq n_1$  and  $n \geq n_N$ . In the markovian approximation, where the continuum degrees of freedom are eliminated, the trapping state corresponds to an eigenmode of (4.12) with a vanishing decay rate. As an example, in case of  $N = 3$  side waveguides with  $n_1 = 0$ ,  $n_2 = 1$  and  $n_3 = 2$ , a trapping state with  $b_n = \delta_{n,1} \exp(-i\omega_1 z)$ ,  $c_1 = -(\kappa/\kappa_1) \exp(-i\omega_1 z)$ ,  $c_2 = -(\omega_1/\kappa_2) \exp(-i\omega_1 z)$ ,  $c_3 = -(\kappa/\kappa_3) \exp(-i\omega_1 z)$  does exist provided that  $\omega_3 = \omega_1$  and  $\omega_2 = \omega_1 - \kappa_2^2/\omega_1$ .

We briefly mention that different side-coupling configurations can be used to observe Fano resonances and BIC using waveguide lattices. Some of other possible configurations are shown in Fig. 4.2 and discussed in [14, 16, 23, 27]. In the configuration of Fig. 4.2a, an infinitely-extended linear waveguide array is coupled to a

system of  $N$  side defect states. In this simple system transmission and reflection of propagating waves can be tailored through engineering Fano resonances. In particular, perfect reflections and transmissions can be observed due to either destructive or constructive interferences [14]. In the configurations of Fig. 4.2b, c, one or two waveguides are side-coupled to a semi-infinite waveguide lattice [23, 27]. In this case a BIC can be regarded as a surface state localized at the edge of the semi infinite waveguide array, and can coexist with other more conventional bound states outside the continuum with exponential localization. In particular, in the setting of Fig. 4.2b, experimentally realized in [23], simultaneous Fano and Fabry-Perot resonances are found. The surface mode, related to the BIC, is a compact state with all energy concentrated in a few waveguides at the edge and no field penetration beyond the side-coupled waveguide position. Similar behavior is found for BIC in the configuration of Fig. 4.2c, which was realized in the experiment of [27]. It should be noted that BIC in waveguide lattices are not necessarily related to Fano interference, and can be observed without any side-coupled waveguides in specially-engineered lattices with non-uniform coupling constants. For example, in [58] a BIC with non-compact support and algebraic localization has been experimentally observed in a semi infinite waveguide array with inhomogeneous hopping rates. Finally, we mention that the Fano-Anderson model (4.1, 4.2) has been recently extended assuming imaginary (non-Hermitian) couplings  $\kappa_\alpha$  [59], which makes the dynamics non-unitary. Remarkably, by flipping the coupling from Hermitian ( $\kappa_\alpha$  real) to non-Hermitian ( $\kappa_\alpha$  imaginary) time reversal of the subsystem of discrete states can be achieved, while the continuum of states is not reversed. Exact time reversal requires frequency degeneracy of the discrete states, or large frequency mismatch among the discrete states as compared to the strength of indirect coupling mediated by the continuum. Interestingly, periodic and frequent switch of the discrete-continuum coupling results in a frozen dynamics of the subsystem of discrete states.

Finally, we mention that several results and physical phenomena previously discussed in waveguide lattices can be found in other optical structures, notably in photonic crystal waveguides (see, for instance, [49, 60–62] and references therein). A photonic crystal waveguide is realized by a defect line which forms directed continuum for propagative guided electromagnetic waves. Defect rods in the vicinity of the defect line interact with the continuum and give rise to scattering of ingoing waves in a similar fashion as discussed above. A quantum-mechanical analog of the non-Hermitian Hamiltonian of the open system with complex eigenvalues can be derived for this system [60], which describes a scattering of electromagnetic waves by the defect rods. In this formalism a BIC is found by tailoring the dielectric constant of the defect rods so that one of the complex eigenvalues becomes real. Interestingly, two o-channel nonlinear defects coupled to the photonic waveguide serve as self-adjusted Fano mirrors and can self-induce a BIC [61, 62].



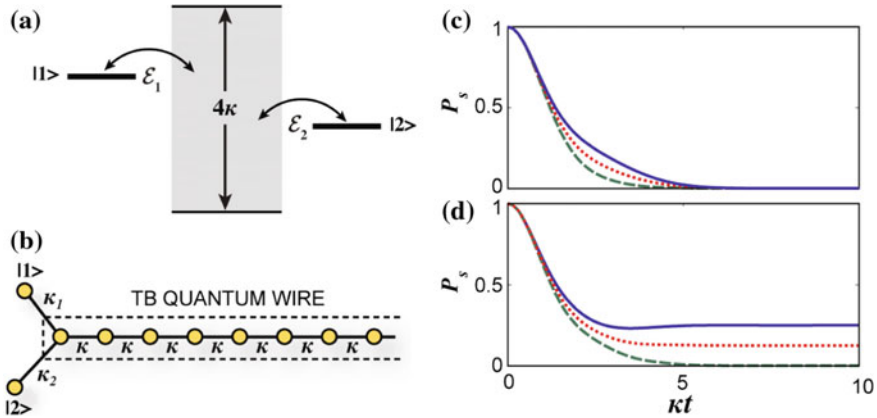


**Fig. 4.3** **a** Schematic of two discrete levels coupled to a common tight-binding (TB) continuum, and **b** physical realization based on two quantum wells side-coupled to a tight binding quantum wire. In the photonic simulation of the two-level Fano-Anderson Hamiltonian with two indistinguishable particles, the quantum wells and the quantum wire are replaced by evanescently-coupled optical waveguides in the geometrical setting schematically shown in Fig. 4.2c. Excitation of the side waveguides  $|1\rangle$  and  $|2\rangle$  with two polarization-entangled photons with a phase offset  $\varphi$  enables to effectively simulate the evolution of two non-interacting bosonic (for  $\varphi = 0$ ) and fermionic (for  $\varphi = \pi$ ) particles. **c, d** Evolution of the survival probability  $P_s(t)$  for bosons (solid curves), fermions (dashed curves) and for two distinguishable particles (dotted curves) for  $\kappa_1/\kappa = \kappa_2/\kappa = 0.5$  and for  $\epsilon_1/\kappa = 0, \epsilon_2/\kappa = 0.8$  in (c) and  $\epsilon_1/\kappa = \epsilon_2/\kappa = 0.8$  in (d)

### 4.3 Fano Resonance and Particle Statistics

Quantum decay processes, Fano resonances and BIC are generally regarded as single-particle effects and have been observed in different systems using particles with either bosonic (e.g. neutral atoms, photons) or fermionic (e.g. electrons) nature. However, recent works [27, 53, 60–65] showed that particle statistics and contact interactions can deeply modify the decay dynamics as well as the appearance of Fano resonance and BIC in a many-body system. Even in the absence of particle interaction, fermions and bosons may show very different decay behavior, in particular in many cases fermions tend to decay faster. Interestingly, under certain circumstances Fano resonance and BIC can disappear when particle statistics is switched from bosonic to fermionic. The latter phenomenon has been theoretically predicted in [53] and experimentally observed in [27] in a waveguide photonic lattice probed by non-classical states of light.

The simplest model to investigate the role of particle statistics on quantum decay, BIC and Fano resonance is the two-level Fano-Anderson model, which is schematically shown in Fig. 4.3a. The model describes rather generally the decay of two discrete states  $|1\rangle$  and  $|2\rangle$ , such as two quantum wells, into a common tight-binding continuum represented, for example, by a semi-infinite linear quantum wire (Fig. 4.3b). The tight-binding lattice band spans the energy interval  $-2\kappa < E < 2\kappa$ ,

where  $\kappa$  is the hopping rate between two adjacent wells in the wire, whereas the energy offsets  $\epsilon_1$  and  $\epsilon_2$  of the discrete states  $|1\rangle$  and  $|2\rangle$  from the center of the tight-binding lattice band is generally (but not necessarily) assumed to be embedded into the continuum, i.e.  $|\epsilon_{1,2}| < 2\kappa$ . If the couplings  $\kappa_1$  and  $\kappa_2$  of the discrete states  $|1\rangle$  and  $|2\rangle$  with the quantum wire is weak, i.e. provided that  $\kappa_{1,2} \ll \kappa$ , for the single particle case quantum decay, Fano resonance and the appearance of BIC can be described within the markovian approximation following a similar analysis to the one developed in the previous section. An interesting property of the system shown in Fig. 4.3b is the existence of one BIC when  $\epsilon_1 = \epsilon_2$ , even beyond the markovian limit. As discussed in the previous section, the BIC arises because of a destructive Fano interference between different decay channels, which leads to fractional decay when a single particle is initially placed in either one of the two wells  $|1\rangle$  or  $|2\rangle$ .

For the two-particle case, the system is assumed to be prepared, at time  $t = 0$ , with one particle occupying the well  $|1\rangle$  and the other one the well  $|2\rangle$ . Quantum decay is described by the survival probability  $P_s(t) = |\langle \psi(0) | \psi(t) \rangle|^2$ , which is the probability that at time  $t$  none of the two particles has decayed into the continuum (the wire). For non-interacting particles, the expression of  $P_s(t)$  can be derived in terms of the single-particle scattering matrix  $\mathcal{S}(t) = S_{n,m}(t)$  ( $n, m = 1, 2$ ), where  $S_{n,m}(t)$  is the amplitude probability that a particle, occupying at  $t = 0$  the well  $|m\rangle$ , is found at time  $t$  in the well  $|n\rangle$ . The expression for  $P_s(t)$  depends on the statistics of the two particles and reads explicitly [53]

$$P_s^{(\text{bos})}(t) = |S_{1,1}S_{2,2} + S_{1,2}S_{2,1}|^2 = |\text{perm } \mathcal{S}(t)|^2 \quad (4.21)$$

for bosonic particles, and

$$P_s^{(\text{ferm})}(t) = |S_{1,1}S_{2,2} - S_{1,2}S_{2,1}|^2 = |\det \mathcal{S}(t)|^2 \quad (4.22)$$

In a photonic simulation of the the decay dynamics of the two indistinguishable particles, the temporal evolution of the two-level Fano-Anderson Hamiltonian is mapped into the spatial propagation of two polarization-entangled photons in an array of evanescently-coupled optical waveguides in the geometrically setting shown in Fig. 4.2c. Let us indicate by  $\hat{a}_{n,T}^\dagger$  the creation operator of photons in the fundamental mode of waveguide  $|n\rangle$  with polarization states  $T = H$  (horizontal) or  $T = V$  (vertical), respectively. The optical structure is excited at the input  $t = 0$  plane by two photons in a polarization entangled state, injected into waveguides  $|1\rangle$  and  $|2\rangle$ , namely

$$|\psi(t=0)\rangle = \frac{1}{\sqrt{2}} \left( a_{1,H}^\dagger a_{2,V}^\dagger + \exp(i\varphi) a_{1,V}^\dagger a_{2,H}^\dagger \right) |0\rangle \quad (4.23)$$

where  $\varphi$  is a controllable phase. As shown in [66], by switching the phase  $\varphi$  from  $\varphi = 0$  to  $\varphi = \pi$ , one can effectively simulate the evolution of two non-interacting bosonic and fermionic particles, respectively. In a linear optical network, the photon state  $|\psi(t)\rangle$  at a propagation distance  $t$  is obtained from (4.23) by the formal replacement [66, 67]

$$\hat{a}_{n,T}^\dagger \rightarrow \sum_{j=1}^{\infty} S_{j,n}^{(T)}(t) \hat{a}_{j,T}^\dagger, \quad (4.24)$$

where  $S_{j,n}^{(T)}(t)$  is the amplitude probability that one photon with polarization state  $T$ , injected at  $t = 0$  in waveguide  $|n\rangle$ , is found in the waveguide  $|j\rangle$  after a propagation length  $t$ . The amplitudes  $S_{j,n}^{(T)}(t)$  for the waveguide structure can be readily calculated from coupled-mode theory that describes propagation of classical light waves in the optical network. Substitution of (4.24) into (4.23) yields

$$\begin{aligned} |\psi(t)\rangle = & \frac{1}{\sqrt{2}} \left[ \left( S_{1,1}^{(H)} S_{1,2}^{(V)} + \exp(i\varphi) S_{1,1}^{(V)} S_{1,2}^{(H)} \right) \hat{a}_{1,H}^\dagger \hat{a}_{1,V}^\dagger \right. \\ & + \left( S_{1,1}^{(H)} S_{2,2}^{(V)} + \exp(i\varphi) S_{2,1}^{(V)} S_{1,2}^{(H)} \right) \hat{a}_{1,H}^\dagger \hat{a}_{2,V}^\dagger \\ & + \left( S_{2,1}^{(H)} S_{1,2}^{(V)} + \exp(i\varphi) S_{1,1}^{(V)} S_{2,2}^{(H)} \right) \hat{a}_{2,H}^\dagger \hat{a}_{1,V}^\dagger \\ & + \left( S_{2,1}^{(H)} S_{2,2}^{(V)} + \exp(i\varphi) S_{2,1}^{(V)} S_{2,2}^{(H)} \right) \hat{a}_{2,H}^\dagger \hat{a}_{2,V}^\dagger \\ & \left. + \dots \right] |0\rangle \end{aligned} \quad (4.25)$$

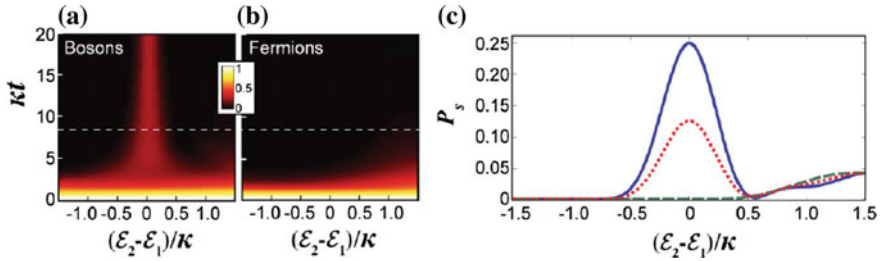
where  $\dots$  is a sum of operator products  $\hat{a}_{j,H}^\dagger \hat{a}_{n,V}^\dagger$  with either  $n$  or  $j$  greater than 2. From (4.25) one can readily calculate the *coincidence probability*  $P^{(1,1)}(t)$  to find, at propagation distance  $t$ , one photon (with either polarization H or V) in waveguide  $|1\rangle$  and the other photon (with polarization V or H) in waveguide  $|2\rangle$ . Assuming that the amplitude probabilities  $S_{n,j}$  (for  $n, j = 1, 2$ ) do not depend on the polarization state, i.e.  $S_{n,j}^H = S_{n,j}^V \equiv S_{n,j}$ , one obtains

$$\begin{aligned} P^{(1,1)}(t) = & \frac{1}{2} |S_{1,1}(z) S_{2,2}(z) + \exp(i\varphi) S_{1,2}(z) S_{2,1}(z)|^2 \\ & + \frac{1}{2} |S_{1,1}(z) S_{2,2}(z) + \exp(-i\varphi) S_{1,2}(z) S_{2,1}(z)|^2 \end{aligned} \quad (4.26)$$

Note that, for bosonic particles ( $\varphi = 0$ ), one has  $P^{(1,1)}(t) \equiv P^{(\text{bos})}(t) = |\text{perm } \mathcal{S}(t)|^2$ , whereas for fermions ( $\varphi = \pi$ ) one has  $P^{(1,1)}(t) \equiv P^{(\text{ferm})}(t) = |\det \mathcal{S}(t)|^2$ , which provide the survival probabilities for bosonic and fermionic particles in the two-level Fano-Anderson model according to (4.21) and (4.22). The coincidence probabilities  $P^{(\text{bos})}(t)$  and  $P^{(\text{ferm})}(t)$  for indistinguishable photons with  $\varphi = 0, \pi$  should be compared with the coincidence probability for distinguishable photons, which is simply obtained by neglecting quantum interference and reads

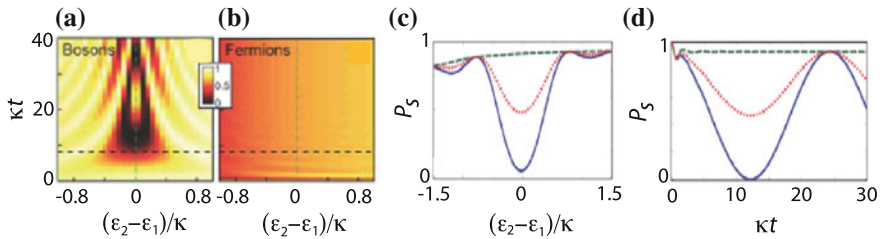
$$P^{(\text{dis})}(t) = |S_{1,1}(t) S_{2,2}(t)|^2 + |S_{1,2}(t) S_{2,1}(t)|^2. \quad (4.27)$$

Figure 4.3c shows, as an example, the behavior of  $P^{(\text{bos})}(t)$ ,  $P^{(\text{ferm})}(t)$  and  $P^{(\text{dis})}(t)$ , defined by (4.21), (4.22) and (4.27), predicted by coupled-mode equation analysis for parameter values  $\kappa_1/\kappa = \kappa_2/\kappa = 0.5$ ,  $\epsilon_1/\kappa = 0$  and  $\epsilon_2/\kappa = 0.8$ . For



**Fig. 4.4** Map of the survival probability  $P_s$  as a function of  $t$  and  $(\epsilon_2 - \epsilon_1)/\kappa$  for **a** bosons, and **b** fermions. Parameter values are:  $\kappa_1/\kappa = \kappa_2/\kappa = 0.5$  and  $\epsilon_1/\kappa = 0.8$  (Fan interference regime). In **c** the behavior of  $P_s$  versus  $(\epsilon_2 - \epsilon_1)/\kappa$  is shown at the normalized time  $t = 8/\kappa$  for bosons (solid curve), fermions (dashed curve) and for distinguishable particles (dotted curve)

such parameter values, the Fano-Anderson Hamiltonian does not sustain a BIC, and a single particle, initially placed at either wells  $|1\rangle$  or  $|2\rangle$ , decays toward zero (complete decay). As shown in Fig. 4.3c, the same behavior occurs for bosonic and fermionic particles, the decay being faster for fermions than for bosons. More interesting is the case  $\epsilon_1 = \epsilon_2$ , where a BIC with energy  $\epsilon = \epsilon_1 = \epsilon_2$  arises as a result of destructive Fano interference of decay channels. Figure 4.3d shows, as an example, the behavior of  $P^{(\text{bos})}(t)$ ,  $P^{(\text{ferm})}(t)$  and  $P^{(\text{dis})}(t)$  for parameter values  $\kappa_1/\kappa = \kappa_2/\kappa = 0.5$ , and  $\epsilon_1/\kappa = \epsilon_2/\kappa = 0.8$ . Remarkably, as  $P^{(\text{bos})}(t)$  shows a fractional (limited) decay owing to the existence of a BIC,  $P^{(\text{ferm})}(t)$  shows a complete decay. Such a result is basically a signature of the Pauli exclusion principle and can be explained observing that no more than one fermion can be accommodated into the dressed bound state, the remaining one decaying into the continuous (scattering) states. This means that for two fermions Fano interference, responsible for the existence of a BIC and fractional decay, is suppressed. To better highlight the suppression of Fano interference in the quantum decay of two fermionic particles, in Fig. 4.4 we plot the behavior of the probabilities  $P^{(\text{bos})}(t)$  and  $P^{(\text{ferm})}(t)$  versus  $t$  as a function of the normalized energy detuning  $(\epsilon_2 - \epsilon_1)/\kappa$  for  $\kappa_1/\kappa = \kappa_2/\kappa = 0.5$  and  $\epsilon_1/\kappa = 0.8$ . Note that, for two bosonic particles, at a given time  $t = t_0$   $P^{(\text{bos})}(t_0)$  shows a Fano resonance at  $\epsilon_2 = \epsilon_1$ , which is the signature of destructive quantum interference of decay channels and fractional decay. On the other hand, the Fano resonance is completely suppressed for two fermionic particles. This is clearly shown by plotting the behavior of at a given propagation distance, e.g.  $t = t_0 = 8/\kappa$ , as shown Fig. 4.4c. Disappearance of the Fano resonance for fermionic particles has been demonstrated in a recent experiment [27]. In the experiment, to determine the survival probability for indistinguishable particles, two photons at 810 nm wavelength, generated by a spontaneous parametric down-conversion source, were coupled to single-mode optical fibres and injected simultaneously in waveguides  $|1\rangle$  and  $|2\rangle$ . Output light from the same waveguides was collected by an objective, coupled to multimode fibres and detected by single-photon avalanche photodiodes. Coincidence-detection counts, in equal temporal gates, were performed for different input states: indistinguishable vertically polarized photons, polarization-entangled photons in antisymmetric state



**Fig. 4.5** Map of the survival probability  $P_s$  as a function of  $t$  and  $(\epsilon_2 - \epsilon_1)/\kappa$  for (a) bosons, and (b) fermions. Parameter values are:  $\kappa_1/\kappa = \kappa_2/\kappa = 0.5$  and  $\epsilon_1/\kappa = 4$  (Rabi oscillations regime). In (c) the behavior of  $P_s$  versus  $(\epsilon_2 - \epsilon_1)/\kappa$  at the time  $t = 8/\kappa$  is shown, whereas (d) depicts the behavior of  $P_s$  versus  $t$  for  $\epsilon_2 = \epsilon_1$ . Solid curve: bosons; dashed curves: fermions; dotted curves: distinguishable particles

and distinguishable photons. The latter were generated by introducing, for each of the previous states, a temporal delay for one of the photons. These conditions correspond to identical bosons, identical fermions and distinguishable particles. From coincidence counts and by varying the offset  $\epsilon_2 - \epsilon_1$  in different manufactured waveguide array samples, the survival probabilities for effective fermionic and bosonic particles were retrieved, clearly showing the disappearance of the Fano resonance according to the theoretical prediction (Fig. 4.4c).

So far we have considered the case where the energies  $\epsilon_{1,2}$  of the discrete states  $|1\rangle$ ,  $|2\rangle$  are embedded in the continuum of scattered states. A different scenario is found when  $\epsilon_1$  and  $\epsilon_2$  fall outside the continuous band of the lattice. In this case, the Fano-Anderson Hamiltonian sustains *two* bound states *outside* the continuum, and the survival probability for a single particle, initially placed in either one of the sites  $|1\rangle$  or  $|2\rangle$ , shows fractional decay and Rabi-like oscillations for  $\epsilon_2$  close to  $\epsilon_1$ . In this case the two fermions can be now accommodated in the two bound dressed states, and thus fractional decay is observed for fermions as well. However, while for bosons the survival probability shows Rabi-like oscillations with time when  $\epsilon_2$  is close to  $\epsilon_1$  (like for the single-particle problem), Rabi oscillations are suppressed for fermionic particles. This is shown in Fig. 4.5, which depicts the behavior of  $P^{(\text{bos})}(t)$  and  $P^{(\text{ferm})}(t)$  for the same parameter values as in Fig. 4.4, except for  $\epsilon_1 = 4\kappa$ . Note that, as expected, the survival probability for fermions now shows a fractional (i.e. not complete) decay owing to the existence of *two* bound dressed states. However, as compared to bosons, for fermions Rabi oscillations in the survival probability at  $\epsilon_2 \simeq \epsilon_1$  are suppressed. The theoretical analysis of Rabi oscillations for the two-particle state can be given in a rather simple form when the energies  $\epsilon_1$  and  $\epsilon_2$  of the discrete states  $|1\rangle$  and  $|2\rangle$  are far outside the continuous band of scattered states, and the couplings  $\kappa_1$  and  $\kappa_2$  are of the same order of magnitude. In this case, the amplitude occupation probabilities of continuous states are weak and can be eliminated from the dynamics, leading to an effective (second-order) coupling of states  $|1\rangle$  and  $|2\rangle$  mediated by the scattered states (see, for instance, [68, 69]). Assuming  $|\epsilon_{1,2}| \gg \kappa_{1,2}, \kappa$  and a small detuning  $|\epsilon_2 - \epsilon_1|$  (of the same order of magnitude or smaller than

$\sim \kappa_1^2/\epsilon_1$ ), for the single-particle problem the following effective coupled equations for the occupation amplitudes  $c_1(t)$  and  $c_2(t)$  of sites  $|1\rangle$  and  $|2\rangle$  can be obtained

$$i \frac{dc_1}{dt} = \kappa_e c_2 - \Delta c_1, \quad i \frac{dc_2}{dt} = \kappa_e c_1 + \Delta c_2 \quad (4.28)$$

where we have set

$$\kappa_e = \frac{\kappa_1 \kappa_2}{\epsilon_1}, \quad 2\Delta = \epsilon_2 - \epsilon_1 + \frac{\kappa_2^2 - \kappa_1^2}{\epsilon_1}. \quad (4.29)$$

Note that (4.28) describe detuned Rabi oscillations of a two-level system. The single-particle scattering matrix  $\mathcal{S}(t) = \{S_{n,m}(t)\}$  ( $n, m = 1, 2$ ) can be readily calculated from (4.28) and reads

$$\begin{aligned} S_{1,1}(t) &= \cos(\Omega t) + i \frac{\Delta}{\Omega} \sin(\Omega t) \\ S_{1,2}(t) &= S_{2,1}(t) = -i \frac{\kappa_e}{\Omega} \sin(\Omega t) \\ S_{2,2}(t) &= \cos(\Omega t) - i \frac{\Delta}{\Omega} \sin(\Omega t) \end{aligned} \quad (4.30)$$

where  $\Omega = \sqrt{\kappa_e^2 + \Delta^2}$ . For a single particle, initially placed at either sites  $|1\rangle$  or  $|2\rangle$ , the survival (revival) probability is given by

$$P_s(t) = |S_{1,1}(t)|^2 = |S_{2,2}(t)|^2 = \cos^2 \Omega t + \frac{\Delta^2}{\Omega^2} \sin^2 \Omega t \quad (4.31)$$

and shows detuned Rabi oscillations. For two indistinguishable particles, the revival probabilities are given by the modulus square of the permanent and determinant of  $\mathcal{S}(t)$  for bosons and fermions, respectively, i.e.

$$P_s^{(\text{ferm})} = |\det \mathcal{S}(t)|^2 = 1 \quad (4.32)$$

and

$$P_s^{(\text{bos})} = |\text{perm } \mathcal{S}(t)|^2 = \left( \cos^2 \Omega t + \frac{\Delta^2 - \kappa_e^2}{\Delta^2 + \kappa_e^2} \sin^2 \Omega t \right)^2 \quad (4.33)$$

Note that for fermions the survival probability is frozen, corresponding to the two fermions occupying the two bound dressed states with no evolution. Conversely, for bosons the survival probability shows Rabi-like oscillations owing to the possibility for the bosons to occupy either one or both the bound dressed states. Note also that, at  $\Delta = 0$  the Rabi oscillations of the two bosons occurs at a frequency twice the single-particle Rabi oscillations.

## 4.4 Dynamical Control of Fano Resonances

In photonics, Fano resonances find interesting applications in the design of optical filters, switches, modulators and sensors, especially at the micro- and nano-scale. For such applications, lineshape engineering, i.e. the possibility to control and tune frequency, shape and width of the Fano resonance, is of major importance. Usually, the Fano lineshape can be tuned over wide spectral ranges by carefully altering the geometry of a nanostructure [70–72]. However, dynamical and fine control of Fano resonances is a highly desirable functionality, which can not be accomplished by material or geometric engineering. Several methods have been suggested for dynamical lineshape engineering, based on two-beam interference [72], phase engineering of the excitation beam [73], the use of hybrid gratings [74], the application of mechanical stress [75], and dynamic modulation of the refractive index in micro cavities [28]. The latter method is based on dynamic modulation of the resonance frequency of a microcavity in a linear CROW structure and provides an example of Fano resonance in time-periodic systems, where the resonance arises from interference of different Floquet channels [76–78]. A CROW consists of a homogeneous chain of resonators in which light propagates by virtue of the evanescent coupling between adjacent cavities [79–81]. CROWs have been explored in a variety of material platforms and resonator types, including photonic-crystal defect cavities, microspheres, microdisks, and microring resonators. While in static CROW structures Fano resonances are usually realized by side-coupled microcavities in the geometrical settings similar to the ones shown in Figs. 4.1a and 4.2 for optical waveguide arrays, a Fano resonance can be dynamically created and tuned by periodic modulation of the resonance frequency of one resonator in a linear chain, without the need to resort to side cavities [28]. Figure 4.6a shows a schematic of the CROW structure that realizes a dynamic and controllable Fano resonance. It consists of a chain of coupled micro/nano resonators with the same resonance frequency  $\omega_0$  and coupling constant  $\kappa$ . The resonance frequency of the resonator at site  $n = 0$  is assumed to be biased and periodically modulated in time. This can be accomplished by modulation of the microcavity refractive index using various physical mechanisms such as free-carrier-plasma dispersion and electro-optic effects [82–85]. Coupled mode equations that describe light hopping in the coupled microrings/resonators read

$$i \frac{da_n}{dt} = \omega_0 a_n + \kappa(a_{n+1} + a_{n-1}) + \delta_{n,0} \Delta\omega_0(t) a_n \quad (4.34)$$

where  $a_n(t)$  is the mode amplitude of the field in the  $n$ -th microring/resonator,  $\Delta\omega_0(t) = \sigma + \Gamma \cos(\omega t)$  is the resonance shift of the resonator at site  $n = 0$ , which comprises a bias (static) term  $\sigma$  and a sinusoidal term of amplitude  $\Gamma$  and frequency  $\omega$ . For  $\Delta\omega_0 \neq 0$ , the resonator at site  $n = 0$  acts as a scattering centre, enabling to reflect light waves propagating along the CROW at some spectral frequencies inside the CROW transmission band ( $\omega_0 - 2\kappa, \omega_0 + 2\kappa$ ). Note that, since the Hamiltonian is time-periodic, scattering is inelastic, i.e. it does not conserve the energy, which can be exchanged with quanta of the driving field. If  $\omega$  and  $\Gamma$  are of the same

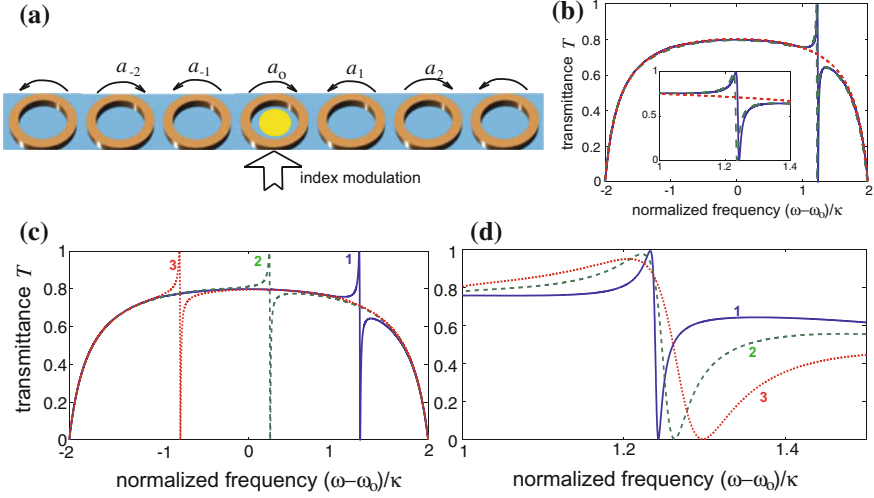


**Fig. 4.6** **a** Schematic of a CROW with dynamic modulation. **b** Transmittance versus normalized frequency  $(\omega(q) - \omega_0)/\kappa$  for  $\sigma/\kappa = 1$ ,  $\omega/\kappa = 1$  and  $\Gamma/\kappa = 0.3$  (solid curve). The dotted curve is the transmittance of the static CROW ( $\Gamma = 0$ ), whereas the dashed curve is the transmittance as predicted by the approximate analytical relation (4.39). Inset: enlargement of the Fano resonance near  $\omega = \omega_0$ . **c**, **d** Fano lineshape engineering: **(c)** Transmittance for  $\sigma/\kappa = 1$ ,  $\Gamma/\kappa = 0.3$  and for  $\omega/\kappa = 1$  (curve 1),  $\omega/\kappa = 2$  (curve 2), and  $\omega/\kappa = 3$  (curve 3); **(d)** Transmittance for  $\omega/\kappa = 1$ ,  $\sigma/\kappa = 1$  and for  $\Gamma/\kappa = 0.3$  (curve 1),  $\Gamma/\kappa = 0.6$  (curve 2), and  $\Gamma/\kappa = 0.9$  (curve 3)

order of magnitude than the coupling constant  $\kappa$ , dynamic Fano resonances can arise because light can hop across the modulated resonator following different Floquet paths [76]. Assuming that a light wave with Bloch number  $q$  ( $0 < q < \pi$ ) and frequency  $\omega(q) = \omega_0 + 2\kappa \cos q$  is incident onto the modulated resonator from the left to the right side of the chain, according to Floquet theory [76] the exact scattered solution to (4.34) has the form

$$a_n(t) = \begin{cases} \sum_{\alpha=-\infty}^{\infty} \{ \delta_{\alpha,0} \exp[-iq_\alpha(n+1)] + r_\alpha(q) \exp[iq_\alpha(n+1)] \} \\ \quad \times \exp(-i\Omega_\alpha t) & n \leq -1 \\ \sum_{\alpha=-\infty}^{\infty} B_\alpha \exp(-i\Omega_\alpha t) & n = 0 \\ \sum_{\alpha=-\infty}^{\infty} t_\alpha(q) \exp[-iq_\alpha(n-1)] \times \exp(-i\Omega_\alpha t) & n \geq 1 \end{cases} \quad (4.35)$$

where  $\Omega_\alpha = \omega(q) + \alpha\omega$ ,  $r_\alpha(q)$  and  $t_\alpha(q)$  are the reflection and transmission amplitudes of the various Floquet (scattered) orders  $\alpha = 0, \pm 1, \pm 2, \pm 3, \dots$ ,  $B_\alpha(t)$  are the harmonic amplitudes of the field in the modulated resonator at  $n = 0$ , and  $q_\alpha$  are defined from the relation

$$\cos q_\alpha = \cos q + \alpha(\omega/2\kappa), \quad (4.36)$$

with  $0 \leq q_\alpha \leq \pi$  if  $q_\alpha$  is real (propagative modes) and  $\text{Im}(q_\alpha) < 0$  if  $q_\alpha$  is complex (evanescent modes). The power transmittance  $T(q)$  and reflectance  $R(q)$  of the modulated resonator can be then calculated as



$$T(q) = \sum_{\langle \alpha \rangle} \frac{v_{g\alpha}}{v_{g0}} |t_\alpha|^2, \quad R(q) = \sum_{\langle \alpha \rangle} \frac{v_{g\alpha}}{v_{g0}} |r_\alpha|^2 \quad (4.37)$$

where  $v_{g\alpha} = 2\kappa \sin q_\alpha$  is the group velocity at the Bloch wave number  $q_\alpha$  and the symbol  $\langle \dots \rangle$  means that the sum is extended over the indices  $\alpha$  corresponding to propagative modes (i.e.  $q_\alpha$  real). For a lossless system one has  $R + T = 1$  and the system is reciprocal, i.e. transmittance is independent of the incidence side. Substitution of the Ansatz (4.35) into (4.34) and eliminating  $r_\alpha$  and  $B_\alpha$  yields the following difference equation for the transmission amplitudes  $t_\alpha$  of various Floquet orders

$$\begin{aligned} & t_\alpha \left( 1 - \exp(2iq_\alpha) + \frac{\sigma}{\kappa} \exp(iq_\alpha) \right) \\ & + \frac{\Gamma}{2\kappa} (t_{\alpha+1} \exp(iq_{\alpha+1}) + t_{\alpha-1} \exp(iq_{\alpha-1})) \\ & = \delta_{\alpha,0} (\exp(-2iq_\alpha) - 1). \end{aligned} \quad (4.38)$$

Let us first notice that, in the absence of the ac modulation, i.e. for  $\Gamma = 0$ , the solution to (4.38) is given by  $t_\alpha(q) = \delta_{\alpha,0} t_{st}(q)$ , where  $t_{st}(q)$  is the transmission amplitude of the static CROW, given by

$$t_{st}(q) = \frac{\exp(-2iq) - 1}{1 - \exp(2iq) + (\sigma/\kappa) \exp(iq)}. \quad (4.39)$$

The transmittance  $T_{st}(q)$  of the static CROW is simply given by  $T_{st}(q) = |t_{st}(q)|^2$ . A typical behavior of  $T_{st}$  versus the normalized frequency  $(\omega(q) - \omega_0)/\kappa$  is shown in Fig. 4.6b, dotted curve. Dynamic Fano resonances can be created by switching on the ac modulation term. Let us first consider the biased case ( $\sigma \neq 0$ ) and let us assume, for the sake of definiteness,  $\sigma > 0$ . In this case the static CROW structure sustains a localized (bound) mode oscillating at the frequency  $\omega_{loc} = \omega_0 + (4\kappa^2 + \sigma^2)^{1/2}$  outside the transmission CROW band. To create a Fano resonance at the frequency  $\omega_F$  inside the CROW transmission band, let us modulate the microcavity refractive index at the frequency  $\omega$  satisfying the condition  $\omega = \omega_{loc} - \omega_F$ . In this case, a light photon at the frequency  $\omega(q)$  close to  $\omega_F$  incident onto the modulated microresonator (incident Floquet channel) can gain one energy quantum  $\hbar\omega$  and drop into the ‘bound’ state. Similarly, photons in the ‘bound’ state can loss one energy quantum  $\hbar\omega$  and jump to the incident channel. Interference between direct and indirect (bound-state mediated) photon crossing creates a Fano-like resonance, as shown in Fig. 4.6b, solid curve. Formally, the onset of the Fano resonance can be explained by considering the small-modulation limit  $\Gamma/\kappa \rightarrow 0$  and looking for a solution to (4.38) as a power series  $t_\alpha = t_\alpha^{(0)} + t_\alpha^{(1)} + t_\alpha^{(2)} \dots$ , where the term  $t_\alpha^{(k)}$  is of the order  $\sim (\Gamma/\kappa)^k$ . At leading order ( $k = 0$ ) one recovers the static case, namely  $t_\alpha^{(0)}(q) = \delta_{\alpha,0} t_{st}(q)$ , whereas at first order one obtains

$$t_\alpha^{(1)}(q) = \begin{cases} 0 & \alpha \neq \pm 1 \\ -\frac{\Gamma}{2\kappa} \frac{t_{st}(q) \exp(iq)}{1 - \exp(2iq_\alpha) + (\sigma/\kappa) \exp(iq_\alpha)} & \alpha = \pm 1 \end{cases} \quad (4.40)$$

While  $t_{-1}^{(1)}(q)$  is a bounded function of  $q$  and of order  $\sim \Gamma/\kappa$ ,  $t_1^{(1)}(q)$  shows a singularity at  $q = q_F = \arccos[(\omega_{loc} - \omega - \omega_0)/2\kappa]$ , which breaks the perturbative analysis. The singularity can be avoided by considering both  $t_0$  and  $t_1$  of the same order  $\sim 1$ . In the two-channel approximation, one obtains at leading order

$$t_0^{(0)}(q) \simeq \frac{\exp(-2iq) - 1}{1 - \exp(2iq) + (\sigma/\kappa) \exp(iq) - \Sigma(q)} \quad (4.41)$$

where we have set  $\Sigma(q) = (\Gamma/2\kappa)^2 \exp[i(q + q_1)]/[1 - \exp(2iq_1) + (\sigma/\kappa) \exp(iq_1)]$ . Note that  $t_0^{(0)}(q)$  differs from the static value  $t_{st}(q)$  because of the complex term  $\Sigma(q)$  in the denominator of (4.41). Since the Floquet channel  $\alpha = 1$  corresponds to an evanescent mode, at leading order the transmittance can be thus calculated as  $T(q) \simeq |t_0^{(0)}|^2$ , which well reproduces the exact shape obtained by exact numerical analysis of (4.37) (see the dashed curve in Fig. 4.6b). Note that, around the frequency  $\omega = \omega_F$ , the transmittance shows a characteristic sharp and asymmetric profile, rapidly varying from zero to (almost) one. The frequency  $\omega_F$  around which the Fano resonance appears can be tuned by changing the modulation frequency  $\omega$  according to the relation  $\omega_F = \omega_{loc} - \omega$ , whereas the resonance width is controlled by the modulation amplitude  $\Gamma$ . This is shown in Fig. 4.6c, d.

The case of unbiased microresonator ( $\sigma = 0$ ) shows a different behavior. Here the static transmittance is unity ((4.39) with  $\sigma = 0$ ), and the structure does not sustain any localized mode. When the modulation is switched on, for  $\omega < 2\kappa$  quite remarkably *two* resonances (rather than one) at the frequencies  $\omega_0 + 2\kappa - \omega$  and  $\omega_0 - 2\kappa + \omega$  are created, symmetrically placed with respect to  $\omega_0$ . The two resonances appear as asymmetric dips in the transmission spectrum. As  $\omega \rightarrow 2\kappa^-$ , the two resonances interference and overlap at  $\omega = \omega_0$ , yielding a more complex resonance pattern comprising a narrow transmission dip with embedded an ultra-narrow resonance peak with unity transmittance at frequency  $\omega = \omega_0$  [28]. The ultra-narrow transmission peak created inside the dark dip and arising from resonance overlapping can be regarded as a kind of electromagnetically-induced transparency (EIT) effect. The entire dynamical process, i.e. creation and overlapping of resonances, can be well described within a five-channel model by considering the amplitudes  $t_\alpha$ ,  $\alpha = 0, \pm 1, \pm 2$  in (4.38), and could be exploited to realize ultra narrow resonances for sensing applications. For such narrow resonances, however, the impact of resonator losses should be included [28] and may be loss compensation is required to reach ultra narrow resonances.

## 4.5 Fano Resonances in Non-Hermitian Photonic Structures

In photonic structures, light transport can be ingeniously tailored by a judicious combination of optical gain and loss which, rather than merely provide amplification or

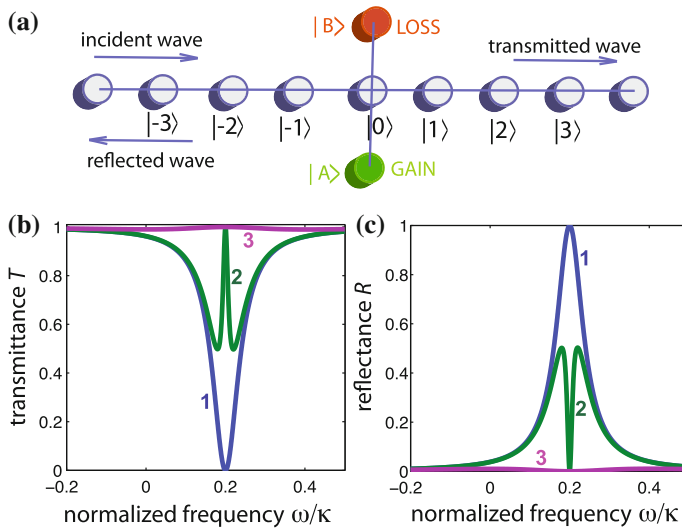


**Fig. 4.7** Fano resonance in a  $\mathcal{PT}$ -symmetric Fano-Anderson model. **a** Schematic of a linear array of optical cavities/resonators with two side-coupled resonators with optical gain and loss. **b** Spectral transmittance  $T$  and **c** reflectance  $R$  versus frequency  $\omega$  of the incident wave for parameter values  $V/\kappa = 0.2$ ,  $\omega_0/\kappa = 0.2$ , and for  $\gamma_0/\kappa = 0$  (curve 1),  $\gamma_0/\kappa = 0.02$  (curve 2) and  $\gamma_0/\kappa = 0.2$  (curve 3)

attenuation of photons, can deeply modify localization and propagation of light in ways impossible to realize with passive structures. One of the most interesting configuration of gain and loss in an optical structure is a balanced distribution that respects the so-called parity-time ( $\mathcal{PT}$ ) symmetry.  $\mathcal{PT}$  photonics is a rapidly emerging area of research, which was initiated about tens years ago in a series of pioneering works [86–91], inspired by the concept of parity-time symmetry in non-Hermitian extensions of quantum mechanics [92, 93], and subsequently demonstrated in a series of seminal experiments [94–97]. The literature on non-Hermitian photonics is extremely broad, and some special issues and review papers are just appearing [98–101]. In this section we are not aimed at discussing all facets of  $\mathcal{PT}$  symmetry in photonics, rather we just provide some insights into Fano resonances in non-Hermitian photonic structures. We also mention that Fano resonance in non-Hermitian transport are found in other physical fields, such as in coherent transport of electrons in mesoscopic solid-state systems [102] and in acoustic systems [103]. The interplay between Fano resonances and exceptional points in non-Hermitian models have been investigated as well [104–106].

The simplest system to theoretically investigate the impact of gain and loss on Fano resonances in photonic structures is to consider a non-Hermitian extension of the Fano-Anderson model [25, 26, 29, 107–109] in a geometrical settings similar to those shown in Figs. 4.1a and 4.2, in which optical gain and loss are introduced in the side coupled waveguides/resonators. When nonlinearity is included in the Fano-

Anderson model, non-reciprocal transmission can be observed [26, 110, 111]. As a first example, let us consider the  $\mathcal{PT}$ -symmetric Fano-Anderson model of Fig. 4.7a, which is studied in [108]. It consists of a linear array of coupled resonators with two side cavities A and B, one with optical gain  $\gamma_0$  and the other with optical loss  $-\gamma_0$ , attached at the site  $n = 0$  of the array. Indicating by  $\kappa$  the coupling constants between adjacent resonators in the linear array and by  $V$  the coupling constants of the two side coupled cavities with the  $n = 0$  resonator in the array, in the linear propagation regime coupled-mode equations for the modal amplitudes  $c_n$ ,  $c_A$  and  $c_B$  in the array and in the two side cavities read

$$\begin{aligned} i \frac{dc_n}{dt} &= -\kappa(c_{n+1} + c_{n-1}) - V\delta_{n,0}(c_A + c_B) \\ i \frac{dc_A}{dt} &= -Vc_0 + (\omega_0 + i\gamma_0)c_A \\ i \frac{dc_B}{dt} &= -Vc_0 + (\omega_0 - i\gamma_0)c_B \end{aligned} \quad (4.42)$$

where  $\omega_0$  is the resonance frequency offset of the side cavities from the ones of the linear array. Let us consider a propagative wave at frequency  $\omega = -2\kappa \cos q$  and Bloch wave number  $q > 0$  incident from the left side. Since scattering is elastic, a solution to (4.42) can be searched in the form

$$\begin{aligned} c_n &= \exp(iqn - i\omega t) + r(\omega) \exp(-iqn - i\omega t) \quad n \leq 0 \\ c_n &= t(\omega) \exp(iqn - i\omega t) \quad n \geq 0 \\ c_A &= A \exp(-i\omega t), \quad c_B = B \exp(-i\omega t) \end{aligned} \quad (4.43)$$

where  $t(\omega)$  and  $r(\omega)$  are the spectral transmission and reflection amplitudes (for left incidence side), respectively. They are readily found after substitution of the Ansatz (4.43) into (4.42) and read

$$t(\omega) = \frac{\sqrt{1 - (\omega/2\kappa)^2}}{\sqrt{1 - (\omega/2\kappa)^2} + i \frac{V^2}{\kappa} \frac{\omega_0 - \omega}{(\omega_0 - \omega)^2 + \gamma_0^2}}, \quad r(\omega) = t(\omega) - 1. \quad (4.44)$$

with  $-2\kappa < \omega < 2\kappa$ . Figure 4.7 shows typical examples of spectrum transmittance  $T(\omega) = |t(\omega)|^2$  and reflectance  $R(\omega) = |r(\omega)|^2$  for increasing values of the normalized gain-loss parameter  $\gamma_0/\kappa$ . The figure demonstrates two noteworthy effects [108]. The first one is the suppression of the transmission by the degenerate side-coupled resonators without the gain and loss, i.e. when  $\gamma_0 = 0$ . In this case excitation of the two side-coupled elements results in the resonant reflection at  $\omega = \omega_0$ , which can be explained in terms of the Fano resonance [5]. A weak balanced gain and loss at the side-coupled cavities, i.e. for  $\gamma_0 \ll \kappa$ , lifts the degeneracy between the attached sites, leading to a transmission profile resembling the EIT effect (curve 2 in Fig. 4.7b, c): a narrow transmission peak, with transmissivity ( $T = 1$  at  $\omega = \omega_0$ ), arises inside the transmission dip. However, for strong balanced gain and loss the

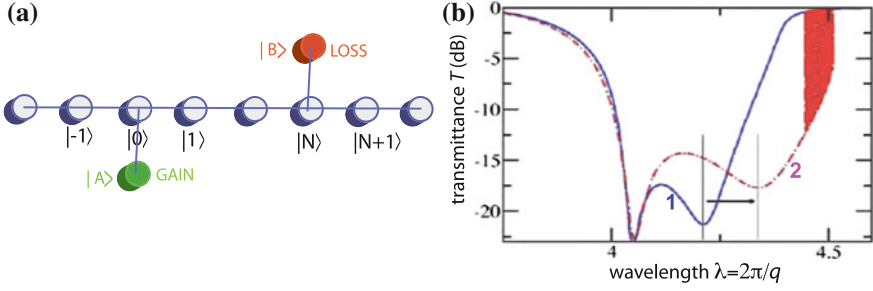


**Fig. 4.8** Nonreciprocal optical transmission based on nonlinear Fano resonance. **a** Schematic of the CROW structure with two side-coupled nonlinear optical resonator with gain (A) and loss (B). **b** Numerically-computed spectral transmittance  $T$  for left (curve 1) and right (curve 2) incidence sides on a log scale. The amplitude of incident wave, for either left and right incidence sides, is set equal to one. Parameter values are:  $\kappa = 1$ ,  $\gamma_0 = 0.02$ ,  $\omega_0 = 0$ ,  $V_A = V_B = 0.5$ ,  $N = 1$ , and  $\chi = 0.0125$ . The wavelength is defined by  $\lambda = 2\pi/q$ , where  $q$  is the Bloch wave number.  $\omega(q) = -2\kappa \cos q$  is the dispersion curve of the tight-binding lattice band. The red-shadowed area on the right of the graph, around  $\lambda = 4.5$ , corresponds to a bistable behavior. The horizontal arrow shows the shift of the Fano resonances due to the Kerr nonlinearity in resonators A and B. Figure (b) is adapted from [26]

side-coupled resonators are out of resonance and any spectral features around  $\omega = \omega_0$  is washed out (curve 3 in Fig. 4.7b, c).

In a linear system, the transmittance is the same for left and right incidence sides. However, when a nonlinearity (usually a Kerr-type nonlinearity) is added to the side-coupled resonators, asymmetric transmission is found, which can be exploited to realize an optical isolator. Experimental observations of optical non-reciprocity involving nonlinear  $\mathcal{PT}$ -symmetric microrings have been recently reported in [110, 111]. Nazari et al. [26] suggested that the observed non-reciprocity may reside in nonlinear Fano resonances, which can be captured by the simple  $\mathcal{PT}$ -symmetric nonlinear Fano-Anderson model shown in Fig. 4.8a. The optical structure is similar to the one previously considered in Fig. 4.7a, apart from that the two side-coupled resonators are attached to different sites of the linear array, the gain resonator at site  $n = 0$  and the loss resonator at site  $n = N$ . Also, different coupling constants  $V_A$  and  $V_B$  of the side resonators A and B with the array are assumed. Coupled mode equations for the modal amplitudes  $c_n$ ,  $c_A$  and  $c_B$  in the array and in the two side cavities read

$$\begin{aligned}
 i \frac{dc_n}{dt} &= -\kappa(c_{n+1} + c_{n-1}) - V_A \delta_{n,0} c_A - V_B \delta_{n,N} c_B \\
 i \frac{dc_A}{dt} &= -V_A c_0 + (\omega_0 + i\gamma_0) c_A - \chi |c_A|^2 c_A \\
 i \frac{dc_B}{dt} &= -V_B c_N + (\omega_0 - i\gamma_0) c_B - \chi |c_B|^2 c_B
 \end{aligned} \tag{4.45}$$

where  $\omega_0$  is the resonance frequency offset of the side cavities from the ones of the linear array,  $\gamma_0$  is the gain/loss parameter, and  $\chi$  measures the strength of the Kerr nonlinearity in resonators A and B. For this model, spectral transmittance and reflectance for left and right incidence sides can be computed numerically, following the procedure detailed in [26]. Owing to nonlinearity, multiple (bistable) states can be found, as discussed in [108]. Figure 4.8b shows a typical example of transmittance curves for a left/right incident wave for the model of (4.45). Note that both the shape and the position of the Fano resonances depend on the direction of the incident wave, and that for a left (gain-side) incoming wave a red-shift in the transmittance resonances is found. Such a shift of the Fano resonances induced by nonlinearity can be exploited to realize non-reciprocal optical transmission and thus an optical isolator. However, it should be mentioned that the use of nonlinear optical effects to achieve effective optical is generally limited by the appearance of so-called dynamical reciprocity [112], although this is not always the case [113].

## References

1. U. Fano, *Nuovo Cimento* **12**, 154 (1935)
2. U. Fano, *Phys. Rev.* **124**, 1866 (1961)
3. H. Beutler, *Eur. Phys. J. A* **93**, 177 (1935)
4. H. Feshbach, *Ann. Phys. (N.Y.)* **5**, 357 (1958)
5. A.E. Miroshnichenko, S. Flach, Y.S. Kivshar, *Rev. Mod. Phys.* **82**, 2257 (2010)
6. B. Lukyanchuk, N.I. Zheludev, S.A. Maier, N.J. Halas, P. Nordlander, H. Giessen, C.T. Chong, *Nat. Mater.* **9**, 707 (2010)
7. W. Zhou, D. Zhao, Y.-C. Shuai, H. Yang, S. Chuwongin, A. Chadha, J.-H. Seo, K.X. Wang, V. Liu, Z. Ma, S. Fan, *Prog. Quantum Electron.* **38**, 1 (2014)
8. M. Rahmani, B. Lukyanchuk, M. Hong, *Laser Photonics Rev.* **7**, 329 (2013)
9. S. Fan, P.R. Villeneuve, J.D. Joannopoulos, H.A. Haus, *Phys. Rev. Lett.* **80**, 960 (1998)
10. Y. Xu, Y. Li, R.K. Lee, A. Yariv, *Phys. Rev. E* **62**, 7389 (2000)
11. S. Fan, J.D. Joannopoulos, *Phys. Rev. B* **65**, 235112 (2002)
12. S. Fan, W. Suh, J.D. Joannopoulos, *J. Opt. Soc. Am. B* **20**, 569 (2003)
13. A.E. Miroshnichenko, S.F. Mingaleev, S. Flach, Y.S. Kivshar, *Phys. Rev. E* **71**, 036626 (2005)
14. A.E. Miroshnichenko, Y.S. Kivshar, *Phys. Rev. E* **72**, 056611 (2005)
15. R.A. Vicencio, A.V. Gorbach, S. Flach, *Phys. Lett. A* **354**, 210 (2006)
16. S. Longhi, *Eur. Phys. J. B* **57**, 45 (2007)
17. S. Longhi, *Phys. Rev. B* **75**, 184306 (2007)
18. M.I. Tribelsky, S. Flach, A.E. Miroshnichenko, A.V. Gorbach, Y.S. Kivshar, *Phys. Rev. Lett.* **100**, 043903 (2008)
19. E.N. Bulgakov, A.F. Sadreev, *Phys. Rev. B* **78**, 075105 (2008)
20. U. Naether, D.E. Rivas, M.A. Larenas, M.I. Molina, R.A. Vicencio, *Opt. Lett.* **34**, 2721 (2009)
21. S. Longhi, *J. Mod. Opt.* **56**, 729 (2009)
22. X. Tu, L.Y. Mario, T. Mei, *Opt. Express* **18**, 18820 (2010)
23. S. Weimann, Y. Xu, R. Keil, A.E. Miroshnichenko, A. Tunnermann, S. Nolte, A.A. Sukhorukov, A. Szameit, Y.S. Kivshar, *Phys. Rev. Lett.* **111**, 240403 (2013)
24. E.N. Bulgakov, A.F. Sadreev, *Phys. Rev. A* **90**, 053801 (2014)
25. H. Ramezani, H.-K. Li, Y. Wang, X. Zhang, *Phys. Rev. Lett.* **113**, 263905 (2014)
26. F. Nazari, N. Bender, H. Ramezani, M.K. Moravvej-Farshi, D.N. Christodoulides, T. Kottos, *Opt. Express* **22**, 9574 (2014)

27. A. Crespi, L. Sansoni, G. Della Valle, A. Ciamei, R. Ramponi, F. Sciarrino, P. Mataloni, S. Longhi, R. Osellame, *Phys. Rev. Lett.* **114**, 090201 (2015)
28. S. Longhi, *Phys. Rev. A* **91**, 063809 (2015)
29. B. Zhu, R. Lü, S. Chen, *Phys. Rev. A* **91**, 042131 (2015)
30. E.N. Bulgakov, K.N. Pichugin, A.F. Sadreev, *Opt. Express* **23**, 22520 (2015)
31. A.F. Sadreev, A.S. Pilipchuk, A.A. Lyapina, *EPL* **117**, 50011 (2017)
32. D.N. Christodoulides, F. Lederer, Y. Silberberg, *Nature* **424**, 817 (2003)
33. S. Longhi, *Laser Photonics Rev.* **3**, 243 (2009)
34. I.L. Garanovich, S. Longhi, A.A. Sukhorukov, Y.S. Kivshar, *Phys. Rep.* **518**, 1 (2012)
35. R.L. Schult, H.W. Wyld, D.G. Ravenhall, *Phys. Rev. B* **41**, 12760 (1990)
36. E.N. Bulgakov, P. Exner, K.N. Pichugin, A.F. Sadreev, *Phys. Rev. B* **66**, 155109 (2002)
37. M.L. Ladrón de Guevara, F. Claro, P.A. Orellana, *Phys. Rev. B* **67**, 195335 (2003)
38. K. Kobayashi, H. Aikawa, A. Sano, S. Katsumoto, Y. Iye, *Phys. Rev. B* **70**, 035319 (2004)
39. I. Rotter, A.F. Sadreev, *Phys. Rev. E* **71**, 046204 (2005)
40. M.L. Ladrón de Guevara, P.A. Orellana, *Phys. Rev. B* **73**, 205303 (2006)
41. E.N. Bulgakov, K.N. Pichugin, A.F. Sadreev, I. Rotter, *JETP Lett.* **84**, 430 (2006)
42. G. Ordóñez, K. Na, S. Kim, *Phys. Rev. A* **73**, 022113 (2006)
43. K.-K. Voo, C.S. Chu, *Phys. Rev. B* **74**, 155306 (2006)
44. J. von Neumann, E. Wigner, *Phys. Z.* **30**, 465 (1929)
45. F.H. Stillinger, D.R. Heerick, *Phys. Rev. A* **11**, 446 (1975)
46. F.H. Stillinger, *Phys. B* **85**, 270 (1977)
47. H. Friedrich, D. Wintgen, *Phys. Rev. A* **31**, 3964 (1985)
48. F. Capasso, C. Sirtori, J. Faist, D.L. Sivco, S.-N.G. Chu, A.Y. Cho, *Nature* **358**, 565 (1992)
49. C.W. Hsu, B. Zhen, A.D. Stone, J.D. Joannopoulos, M. Soljacic, *Nat. Rev. Mater.* **1**, 16048 (2016)
50. G.D. Mahan, *Many-Particle Physics* (Plenum Press, New York, 1990), pp. 272–285
51. G. Sudarshan, in *Field Theory, Quantization and Statistical Physics*, ed. by E. Tirapegui (Reidel, Dordrecht, 1988), pp. 237–245
52. M. Miyamoto, *Phys. Rev. A* **72**, 063405 (2005)
53. S. Longhi, G. Della Valle, *Phys. Rev. A* **86**, 012112 (2012)
54. P. Biagioni, G. Della Valle, M. Ornigotti, M. Finazzi, L. Duó, P. Laporta, S. Longhi, *Opt. Express* **16**, 3762 (2008)
55. P.L. Knight, M.A. Lander, B.J. Dalton, *Phys. Rep.* **190**, 1 (1990)
56. F. Dreisow, A. Szameit, M. Heinrich, R. Keil, S. Nolte, A. Tünnermann, S. Longhi, *Opt. Lett.* **34**, 2405 (2009)
57. Y. Plotnik, O. Peleg, F. Dreisow, M. Heinrich, S. Nolte, A. Szameit, M. Segev, *Phys. Rev. Lett.* **107**, 183901 (2011)
58. G. Corrielli, G. Della Valle, A. Crespi, R. Osellame, S. Longhi, *Phys. Rev. Lett.* **111**, 220403 (2013)
59. S. Longhi, *Sci. Bull.* **62**, 869 (2017)
60. T. Taniguchi, S.I. Sawada, *Phys. Rev. E* **83**, 026208 (2011)
61. A. del Campo, *Phys. Rev. A* **84**, 012113 (2011)
62. G. Garcia-Calderon, L.G. Mendoza-Luna, *Phys. Rev. A* **84**, 032106 (2011)
63. M. Rontani, *Phys. Rev. Lett.* **108**, 115302 (2012)
64. M. Pons, D. Sokolovski, A. del Campo, *Phys. Rev. A* **85**, 022107 (2012)
65. G. Zürn, A.N. Wenz, S. Murmann, A. Bergschneider, T. Lompe, S. Jochim, *Phys. Rev. Lett.* **111**, 175302 (2013)
66. L. Sansoni, F. Sciarrino, G. Vallone, P. Mataloni, A. Crespi, R. Ramoni, R. Osellame, *Phys. Rev. Lett.* **108**, 010502 (2012)
67. J. Skaar, J.C. García Escartín, H. Landro, *Am. J. Phys.* **72**, 1385 (2004)
68. S. Longhi, *Phys. Rev. A* **78**, 013815 (2008)
69. S. Longhi, *Phys. Rev. A* **79**, 023811 (2009)
70. A. Lovera, B. Gallinet, P. Nordlander, O.J. Martin, *ACS Nano* **7**, 4527 (2013)
71. B. Sun, L. Zhao, C. Wang, X. Yi, Z. Liu, G. Wang, J. Li, *J. Phys. Chem. C* **118**, 25124 (2014)

72. T. Hu, P. Yu, C. Qiu, H. Qiu, F. Wang, M. Yang, X. Jiang, H. Yu, J. Yang, *Appl. Phys. Lett.* **102**, 011112 (2013)
73. F. Xiao, W. Zhu, M. Premaratne, J. Zhao, *Opt. Express* **22**, 2132 (2013)
74. Z.-X. Chen, J.-H. Chen, Z.-J. Wu, W. Hu, X.-J. Zhang, Y.-Q. Lu, *Appl. Phys. Lett.* **104**, 161114 (2014)
75. Y. Cui, J. Zhou, V.A. Tamma, W. Park, *ACS Nano* **6**, 2385 (2012)
76. W. Li, L.E. Reichl, *Phys. Rev. B* **60**, 15732 (1999)
77. W. Li, L.E. Reichl, *Phys. Rev. B* **62**, 8269 (2000)
78. K.-H. Ahn, H.C. Park, B. Wu, *Phys. E* **34**, 468 (2006)
79. B.E. Little, S.T. Chu, J. Haus, H.A. Foresi, J.-P. Laine, *J. Lightwave Technol.* **15**, 998 (1997)
80. N. Stefanou, A. Modinos, *Phys. Rev. B* **57**, 12127 (1998)
81. A. Yariv, Y. Xu, R.K. Lee, A. Scherer, *Opt. Lett.* **24**, 711 (1999)
82. M. Först, J. Niehusmann, T. Plötzing, J. Bolten, T. Wahlbrink, C. Moormann, H. Kurz, *Opt. Lett.* **32**, 2046 (2007)
83. Y.S. Lee, G.-D. Kim, W.-J. Kim, S.-S. Lee, W.-G. Lee, W.H. Steier, *Opt. Lett.* **36**, 1119 (2011)
84. S. Manipatruni, L. Chen, M. Lipson, *Opt. Express* **18**, 16858 (2010)
85. H. Lira, Z. Yu, S. Fan, M. Lipson, *Phys. Rev. Lett.* **109**, 033901 (2012)
86. A. Ruschhaupt, F. Delgado, J.G. Muga, *J. Phys. A* **38**, L171 (2005)
87. R. El-Ganainy, K.G. Makris, D.N. Christodoulides, Z.H. Musslimani, *Opt. Lett.* **32**, 2632 (2007)
88. K.G. Makris, R. El-Ganainy, D.N. Christodoulides, Z.H. Musslimani, *Phys. Rev. Lett.* **100**, 103904 (2008)
89. S. Klaiman, U. Günther, N. Moiseyev, *Phys. Rev. Lett.* **101**, 080402 (2008)
90. S. Longhi, *Phys. Rev. Lett.* **103**, 123601 (2009)
91. S. Longhi, *Phys. Rev. A* **82**, 031801(R) (2010)
92. C.M. Bender, S. Boettcher, *Phys. Rev. Lett.* **80**, 5243 (1998)
93. C.M. Bender, *Rep. Prog. Phys.* **70**, 947 (2007)
94. A. Guo, G.J. Salamo, D. Duchesne, R. Morandotti, M. Volatier-Ravat, V. Aimez, G.A. Siviloglou, D.N. Christodoulides, *Phys. Rev. Lett.* **103**, 093902 (2009)
95. C.E. Rüter, K.G. Makris, R. El-Ganainy, D.N. Christodoulides, M. Segev, D. Kip, *Nat. Phys.* **6**, 192 (2010)
96. A. Regensburger, C. Bersch, M.-A. Miri, G. Onishchukov, D.N. Christodoulides, U. Peschel, *Nature* **488**, 167 (2012)
97. L. Feng, Y.-L. Xu, W.S. Fegadolli, M.-H. Lu, J.B.E. Oliveira, V.R. Almeida, Y.-F. Chen, A. Scherer, *Nat. Mater.* **12**, 108 (2013)
98. *Focus on Parity Time Symmetry in Photonics*, *New. J. Phys.* (2015)
99. S.V. Suchkov, A.A. Sukhorukov, J. Huang, S.V. Dmitriev, C. Lee, Y.S. Kivshar, *Laser Photonics Rev.* **10**, 177 (2016)
100. V.V. Konotop, J. Yang, D.A. Zezyulin, *Rev. Mod. Phys.* **88**, 035002 (2016)
101. S. Longhi, *EPL* **122**, 14004 (2018)
102. L. Huang, Y.-C. Lai, H.-G. Luo, C. Grebogi, *AIP Adv.* **5**, 017137 (2015)
103. L. Xiong, W. Bi, Y. Aurégan, *J. Acoust. Soc. Am.* **139**, 764 (2016)
104. W.D. Heiss, G. Wunner, *Eur. Phys. J. D* **68**, 284 (2014)
105. Q. Liu, B. Wang, S. Ke, H. Long, K. Wang, P. Lu, *Opt. Express* **25**, 7203 (2017)
106. L. Schwarz, H. Cartarius, G. Wunner, W.D. Heiss, J. Main, *Eur. Phys. J. D* **69**, 196 (2015)
107. S. Longhi, *Phys. Rev. B* **80**, 165125 (2009)
108. A.E. Miroshnichenko, B.A. Malomed, Y.S. Kivshar, *Phys. Rev. A* **84**, 012123 (2011)
109. N.X.A. Rivolta, B. Maes, *Phys. Rev. A* **94**, 053854 (2016)
110. B. Peng, S.K. Özdemir, F. Lei, F. Monifi, M. Gianfreda, G.L. Long, S. Fan, F. Nori, C.M. Bender, L. Yang, *Nat. Photonics* **10**, 394 (2014)
111. L. Chang, X. Jiang, S. Hua, C. Yang, J. Wen, L. Jiang, G. Li, G. Wang, M. Xiao, *Nat. Photonics* **8**, 524 (2014)
112. Y. Shi, Y. Zongfu, S. Fan, *Nat. Photonics* **9**, 388 (2015)
113. A. Rangelov, S. Longhi, *Appl. Opt.* **56**, 2991 (2017)



# Chapter 5

## Model of Coupled Oscillators for Fano Resonances



Benjamin Gallinet

**Abstract** The use of analogies in numerical simulations and experiments can be a powerful tool to extract useful information, understand and design optical and electromagnetic systems based on the Fano effect. The model of coupled oscillators has been used over decades to interpret the Fano interference effect in a variety of optical, plasmonic and microwave systems. Fano resonances can be modeled with systems of weakly or strongly coupled mechanical oscillators, providing insight into the dynamics of the radiative continuum and the localized resonance. The coupled oscillator model has been revisited and used extensively in optical and electromagnetic analogs of Fano resonances in the recent years, and has also been the subject of further elaborations bringing it quite far from its standard form: this includes an explicit distinction between non-radiative and radiative losses, the relationship between the driving force and the radiative damping of the bright oscillator, its extension to non-linear effects (such as second or third harmonic generation), and the inclusion of a phase in the coupling term. Further work which has been conducted to understand the interplay between the bright mode and the dark mode in Fano-resonant systems is discussed, in particular the effect of modes coupling and non-radiative losses on its spectral lineshape. For this purpose, the Fano formula and its generalization to lossy systems have been derived in the coupled oscillator system. Finally, an extended coupled oscillator model including radiative losses as a result of Abraham-Lorentz force on accelerated charges is discussed. It allows a model of hybridization taking into account radiative losses and radiative coupling. Both phenomena of superradiance and subradiance, as well as the interaction between hybridized modes can be predicted. The purpose of this Chapter is to review these different forms of coupled oscillator models for Fano-resonant optical and microwave systems, and provide theoretical and experimental examples of applications.

---

B. Gallinet (✉)  
CSEM SA, Neuchâtel, Switzerland  
e-mail: benjamin.gallinet@csem.ch

## 5.1 Introduction

In optical and electromagnetic systems, Fano resonances involve the interference between a radiative continuum and a localized resonance [1–3]. They carry a specific spectral signature with an asymmetric lineshape, with an asymmetry depending on the relative phase between the continuum and the localized resonance [4]. In this framework, the classical analog of electromagnetically induced transparency (EIT) effect can be seen as a specific case of a Fano interference, when the role of the continuum is played by a broadband resonance with large radiative losses and the two resonances are almost tuned [5, 6]. The coupling between the continuum and the localized resonance strongly determines the response of the system and can lead to very different types of responses, which do not necessarily qualify as a Fano resonance [3, 7]. The different loss channels of the resonances, radiative or non-radiative, also influence in a complex way the Fano resonance [8]. Modeling these complex resonance and interference effects can be a challenge, and the use of analogies can be a powerful tool to extract useful information, understand and design optical and electromagnetic systems based on the Fano effect.

One of the most widespread modeling tool in physics is obviously the classical oscillator. In particular, the coupled oscillator model has been used extensively in optical and electromagnetic analogs of Fano resonances in the recent years, and has also even been sometimes the subject of further elaborations bringing it quite far from its standard form. The purpose of this Chapter is to review different forms of coupled oscillator models for Fano-resonant optical and microwave systems, and provide theoretical and experimental examples of applications. First, the classical oscillator will be first reviewed and its interpretation to the case of an electromagnetic resonance will be discussed (Sect. 5.2). The role of non-radiative and radiative losses through the Abraham-Lorentz force will be discussed. Then the coupled oscillator model will be introduced and illustrated through examples of applications in plasmonics (Sect. 5.3). This model will be used in Sect. 5.4 to derive the Fano resonance formula and its generalization to lossy localized resonances. Its extension to the electromagnetically induced absorption will be shown. Finally, the generalized coupled oscillator model, introducing radiative coupling between resonators, allows for modeling the interaction of subradiance and superradiance of hybridized photonic modes (Sect. 5.6).

## 5.2 Oscillator Model

This section aims at reviewing the oscillator model applied and interpreted in the context of a structure interacting with electromagnetic radiation. The electrons in the structure oscillate under the excitation of a harmonic electric field generated by an electromagnetic wave. This interaction can enter a resonant state under certain conditions. A collection of modes is available in the structure, each with a given

resonance frequency and damping rate. In general, the full dynamics of the system, including the resonance frequencies and damping rate of the modes, can be calculated using e.g. full-field electromagnetic simulation methods or measured experimentally using far-field or near-field spectroscopy. Around the resonance of a mode at frequency  $\omega_0$ , the bound charges, the polarization density and the electric field show a dispersion which can be modeled with an harmonic oscillator. A model of harmonic oscillator taking into account the radiative and non-radiative damping of a collection of charges in a structure is described in this section. The non-radiative damping originates from collision events with the cores or other electrons, while the radiative damping originates from the emission by electrons of radiation when accelerated.

First, consider a single charge  $q$  with mass  $m$  such as an electron bound to an atom, so that it is subject to a restoring force from the core. The oscillator is characterized by its resonance frequency  $\omega_0$  and damping  $\gamma_i$  (Fig. 5.1a). The resonance frequency depends on the dimensions of the structures and on the material properties, such as the refractive index or the plasma frequency for metals [9]. The damping force accounts for the various collision events with the cores or other electrons. Following Kats et al. [10], in addition to the internal damping force  $m\gamma_i\dot{\mathbf{x}}$ , the charge is experiencing an additional force  $m\gamma_r\ddot{\mathbf{x}}$  due to radiation reaction, where  $\gamma_r = q^2/(6\pi m\epsilon_0 c^3)$  [11]. This term describes the recoil that the charge feels when it emits radiation, and is referred to as the Abraham-Lorentz force or the radiation reaction force. The equation of motion of this charge can be written as:

$$\ddot{\mathbf{x}} + \gamma_i\dot{\mathbf{x}} + \omega_0^2\mathbf{x} = (q/m)\mathbf{E}_0e^{i\omega t} + \gamma_r\ddot{\mathbf{x}}. \quad (5.1)$$

By assuming a harmonic motion ( $\mathbf{x} = c \exp(i\omega t)\mathbf{E}_0/|\mathbf{E}_0|$ ), the steady-state solution of (5.1) can be written down as:

$$c = \frac{(q|\mathbf{E}_0|/m)}{(\omega_0^2 - \omega^2) + i\omega(\gamma_i + \omega^2\gamma_r)}. \quad (5.2)$$

The damping rate of the resonance is therefore the some of the contributions from non-radiative and radiative damping, respectively  $\gamma_i$  and  $\gamma_r$ . For a collection of charges participating to the oscillation in a structure of volume  $V$ , each electron is subject to the same restoring and damping force from the cores. If the structure is small compared the wavelength, all charges oscillate in phase, with a relative position  $\mathbf{x}'$  from the core. The local polarization field is related to the oscillator amplitude by  $\mathbf{P}_{\text{loc}} = nq\mathbf{x}$  where  $n$  is the charge density. Due to the influence of other charges (screening effect) or the geometry of the structure, only a subset  $N$  of the bound charges oscillate, possibly under different directions. Defining the average polarization vector  $\mathbf{P}$  by:

$$\mathbf{P} = q \frac{\int_V n(\mathbf{r})\mathbf{x}'(\mathbf{r})d\mathbf{r}}{\int_V d\mathbf{r}} \simeq \frac{qN\mathbf{x}}{V}. \quad (5.3)$$

where  $\mathbf{x}$  is an average amplitude. The total radiation reaction force is proportional to  $N^2$  and assumed to be equally distributed between the charges, which implies that the radiation reaction force on a single oscillator is proportional to  $N$ . This leads to the following equation for the average polarization vector for the structure:

$$\ddot{\mathbf{P}} + \gamma_i \dot{\mathbf{P}} + \omega_0^2 \mathbf{P} = \alpha \omega_0^2 \mathbf{E}_0 e^{i\omega t} + \frac{V\omega_0^2}{6\pi\epsilon_0 c^3} \alpha \ddot{\mathbf{P}}. \quad (5.4)$$

where  $\alpha = \frac{Nq^2}{Vm\omega_0^3}$  is the polarizability, defined as the system response for a DC electric field (i.e.  $\ddot{\mathbf{P}} = \dot{\mathbf{P}} = \mathbf{P} = 0$ ). The oscillator model can be equivalently used from a description in terms of amplitude of charge displacement or polarization field. Another interpretation uses an effective susceptibility to describe analytically the system, provided that the resonating structure is much smaller than the wavelength:

$$\mathbf{P} = \chi \epsilon_0 \mathbf{E}_0, \quad (5.5)$$

where the susceptibility:

$$\chi = \frac{Nq^2/(Vm\epsilon_0)}{\omega_0^2 - \omega^2 + i\omega(\gamma_i + N\omega^2\gamma_r)}. \quad (5.6)$$

The power loss channels from internal friction and from radiation can be distinguished using this model. For a single charge, the absorbed power  $P_{\text{abs}}(t)$  is given by:

$$P_{\text{abs}}(t) = \text{Re}[-m\gamma_i \dot{x}(t)] \text{Re}[\dot{x}(t)] = -m\gamma_i \omega^2 |c|^2 \sin^2(\omega t + \phi). \quad (5.7)$$

The average power over one period of oscillation  $T = 2\pi/\omega$  is:

$$\langle P_{\text{abs}} \rangle = -\frac{m\gamma_i \omega^2}{2} |c|^2. \quad (5.8)$$

Similarly, the power lost by radiation  $P_{\text{rad}}(t)$  is given by:

$$P_{\text{rad}}(t) = \text{Re}[-m\gamma_r \ddot{x}(t)] \text{Re}[\dot{x}(t)] = -m\gamma_r \omega^4 |c|^2 \sin^2(\omega t + \phi), \quad (5.9)$$

and the average power over one period of oscillation by:

$$\langle P_{\text{rad}} \rangle = -\frac{m\gamma_r \omega^4}{2} |c|^2. \quad (5.10)$$

Comparing (5.8) and (5.10), the frequency dependence of the power is different, which results in a shift of the peak of absorption or scattering cross sections with respect to the near-field amplitude [10]. Furthermore, both far-field cross sections are

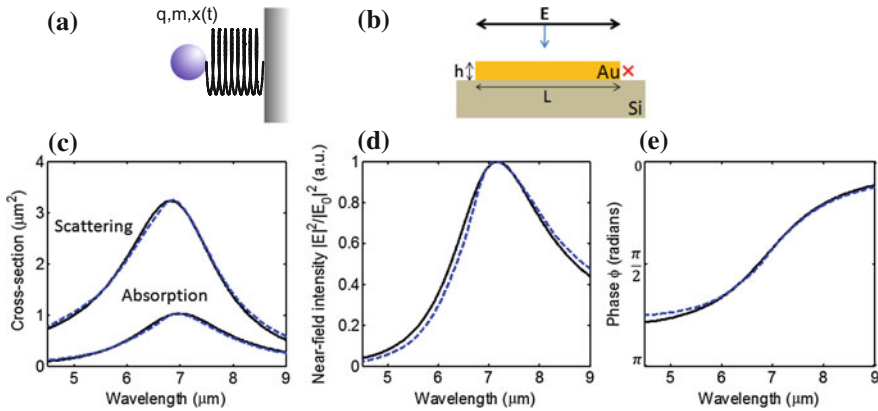


**Fig. 5.1** **a** Oscillator model of a moving charge in an electric field, where  $q$  is the charge,  $m$  is the inertial mass, and  $x(t)$  is the displacement from the equilibrium position. **b** Schematic of a gold optical antenna (length  $L = 1 \mu\text{m}$ , height  $h = 50 \text{ nm}$ , width  $w = 130 \text{ nm}$ ) on a silicon substrate, illuminated by a normally incident plane wave polarized along the antenna axis. The cross represents the point 4 nm away from the antenna edge where the near-field is calculated. **c** Scattering and absorption cross-sections numerically calculated (dashed lines) and the model (solid lines). **d** Near-field intensity enhancement calculated by the model (solid line) and numerically (dashed line) at the location identified by the cross, with the incident field subtracted off. **e** Oscillator phase (which also represents the phase of the near-field). Adapted with permission from [10]. Copyright Optical Society of America

red-shifted from the near-field amplitude which can be modeled with the oscillator amplitude  $|c|^2$  [10, 12]. As an example, a gold linear plasmonic antenna on a silicon substrate is considered (Fig. 5.1b) [10]. In Fig. 5.1c–e are shown the scattering and absorption cross-sections, the near-field intensity at the edge, and the near-field phase, respectively, for the antenna as calculated numerically (dashed lines). The simulation results presented in Fig. 5.1c with (5.8) and (5.10) are fitted to obtain the parameters  $q$ ,  $m$ ,  $\omega_0$  and  $\gamma_i$ . These parameters are used to reconstruct the spectral position and lineshape of the near-field intensity (Fig. 5.1d), as well as the phase response of the antenna (Fig. 5.1e).

### 5.3 Coupled Oscillator Model

This section aims at introducing the model of coupled oscillators for Fano resonances [2, 6, 13–19]. In this model, an oscillator A with a large damping rate is subject to an external driving force. This oscillator is the equivalent of the radiative continuum and is referred sometimes to the bright oscillator. Another oscillator with a low damping rate, not driven, is the equivalent of the discrete state. After the derivation of the main equations, their application to plasmonic and microwave systems is discussed as an example.

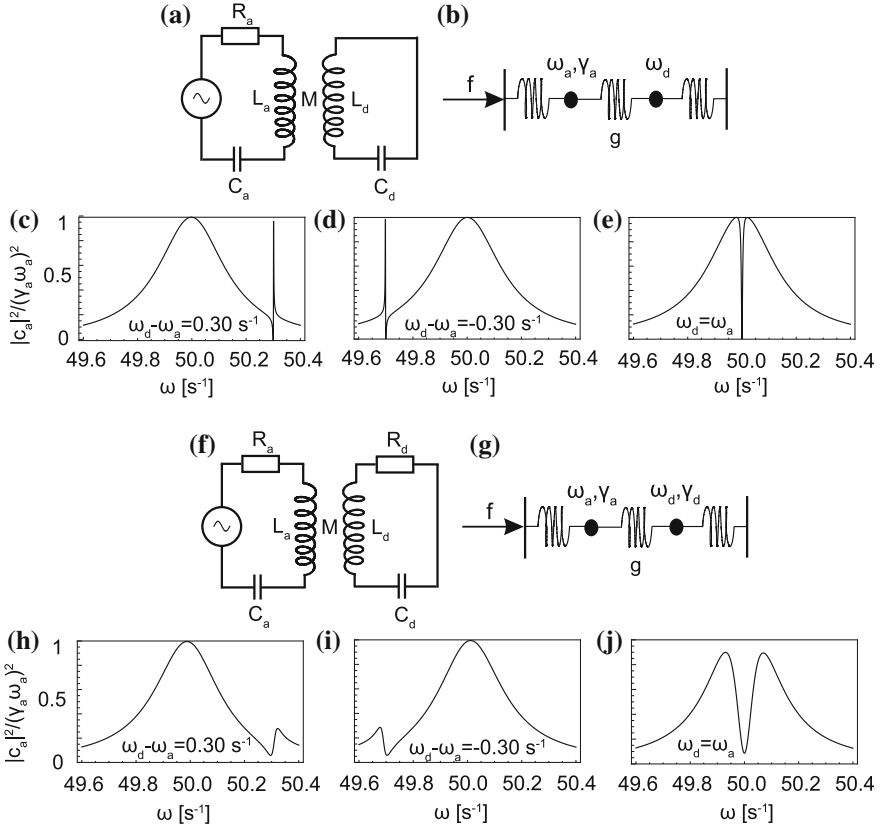


**Fig. 5.2** a–e Fano resonance in a conservative system. (a) Electrical circuit analog of Fano resonances: the LC circuit is excited only through its inductive coupling to an RLC circuit. (b) Mechanical model of Fano resonances: two coupled oscillators A and D with resonance frequencies  $\omega_a$  and  $\omega_d$  respectively. The oscillator A has a damping  $\gamma_a$  and is forced by an external excitation with amplitude  $f$ . Their coupling constant is  $g$ . (c–e) Amplitude of the forced oscillator as a function of the excitation frequency for different values of detuning  $\omega_d - \omega_a$  (with  $\omega_a = 50.00 \text{ s}^{-1}$ ,  $g = 6.00 \text{ s}^{-2}$  and  $\gamma_a = 0.30 \text{ s}^{-1}$ ). f–j Fano resonance in nonconservative systems. (f) A resistance  $R_d$  is added to the LC circuit. (g) A damping constant  $\gamma_d$  is added to the oscillator D. (h–j) Amplitude of the forced oscillator as a function of the excitation frequency for different values of detuning  $\omega_d - \omega_a$  (with  $\omega_a = 50.00 \text{ s}^{-1}$ ,  $g = 6.00 \text{ s}^{-2}$ ,  $\gamma_a = 0.30 \text{ s}^{-1}$  and  $\gamma_d = 0.02 \text{ s}^{-1}$ )

Consider two oscillating charges A and D coupled by a spring of constant  $g$  (Fig. 5.2). Their resonance frequency are  $\omega_a$  and  $\omega_d$ , respectively, and their damping are  $\gamma_a$  and  $\gamma_d$ . A time-harmonic force is applied to oscillator A. The equations of motion for this system can be written as:

$$\ddot{\mathbf{x}}_a + \gamma_a \dot{\mathbf{x}}_a + \omega_a^2 \mathbf{x}_a + g \mathbf{x}_d = (q \mathbf{E}_0 / m) e^{i\omega t} \quad (5.11)$$

$$\ddot{\mathbf{x}}_d + \gamma_d \dot{\mathbf{x}}_d + \omega_d^2 \mathbf{x}_d + g \mathbf{x}_a = 0. \quad (5.12)$$

In the following, the force amplitude  $q|\mathbf{E}_0|$  defined in the context of an oscillating charge will be referred sometimes as  $f$  for generality. Assuming a time-harmonic behavior for the response of the oscillators ( $\mathbf{x}_d = c_d \exp(i\omega t)\mathbf{E}_0/|\mathbf{E}_0|$  and  $\mathbf{x}_a = c_a \exp(i\omega t)\mathbf{E}_0/|\mathbf{E}_0|$ ), the amplitude of the response of the oscillator A is given by:

$$c_a = \frac{\omega_d^2 + i\gamma_d\omega - \omega^2}{(\omega_a^2 + i\gamma_a\omega - \omega^2)(\omega_d^2 + i\gamma_d\omega - \omega^2) - g^2} (q|\mathbf{E}_0|/m). \quad (5.13)$$

The amplitude of oscillator A is shown for different parameters in Fig. 5.2. Several observations can be made from (5.13) and Fig. 5.2:

1. The amplitude of oscillator A undergo a local minimum around the resonance frequency of oscillator D.
2. When the frequency of oscillators A and D are equal, a symmetric dip is observed. When they are detuned from each other, an asymmetric lineshape is observed, composed of a local minimum and local maximum. Its symmetry switches together with the detuning. This is a signature of a Fano-like interference.
3. When a damping is added to the oscillator D, the amplitude of constructive and destructive interferences is damped.
4. When the oscillator is damped, the width of the Fano resonance increases with the coupling between the oscillators and the intrinsic damping of the oscillator D.
5. The modulation depth of the Fano resonance increases with the oscillators coupling.

From (5.12), the amplitude of oscillator D is:

$$c_d = -\frac{g}{(\omega_a^2 + i\gamma_a\omega - \omega^2)(\omega_d^2 + i\gamma_d\omega - \omega^2) - g^2} (qE_0/m). \quad (5.14)$$

Considering a large damping and a response of the bright oscillator slowly varying compared to the response of the dark oscillator, the lineshape of (5.14) is a lorentzian-like lineshape around the resonance frequency of the dark oscillator, with amplitude proportional to the coupling  $g$ .

The mechanical power  $P_a(t)$  transferred from the electric field to oscillator A is:

$$P_{\text{tot}}(t) = \text{Re}[F(t)]\text{Re}[\dot{x}(t)] = (qE_0) \cos(\omega t)\omega|c_a| \sin(\omega t + \phi_a) \quad (5.15)$$

where  $\tan(\phi_a) = \text{Im}(\phi_a)/\text{Re}(\phi_a)$ . The average power over one period of oscillation  $T = 2\pi/\omega$  is:

$$\langle P_{\text{tot}}(t) \rangle = \frac{1}{T} \int_0^T P(t) dt = \frac{qE_0\omega}{2} \text{Im}(c_a). \quad (5.16)$$

Replacing  $c_a$  by its expression in (5.13) yields:

$$\langle P_{\text{tot}}(t) \rangle = \frac{(qE_0)^2 \omega}{2m} \text{Im} \left( \frac{\omega_d^2 + i\gamma_d \omega - \omega^2}{(\omega_a^2 + i\gamma_a \omega - \omega^2)(\omega_d^2 + i\gamma_d \omega - \omega^2) - g^2} \right) \quad (5.17)$$

The coupled oscillator model has been refined in [20] to include the coupling of the radiative resonator to the electromagnetic fields. A radiation damping term is introduced in the bright oscillator as well as in the external driving force. The model is able to link surface conductivity to scattering, group delay and absorbance in a meta-material surface. It has been applied experimentally in microwaves metamaterials supporting EIT or electromagnetically induced absorption (EIA).

The coupled oscillator model has been used for example in [21] to quantitatively analyze a Fano-resonant system, more precisely a plasmonic analog of EIT (Fig. 5.3). In this system, a single gold nanorod supporting a dipolar plasmonic mode is placed on top of two parallel nanorods supporting a quadrupolar mode. The dipolar mode interacts strongly with the radiation continuum and has a large bandwidth. On the other hand, the quadrupolar mode has comparatively very small radiative losses. When the single top nanorod is centered with respect to the bottom nanorods, the quadrupolar mode is not excited for symmetry reasons. As the top nanorod is offset  $s$  from the center, a coupling between the dipolar and quadrupolar mode is generated. A dip in the transmittance appears, which is the signature of a Fano-like interference. The width of transmittance dip increases as  $s$  is increased, independently from the resonance frequency or damping of the modes, which makes it an interesting parameter to study. The absorbance spectra are fitted with (5.17) and the values of the fitting parameters reported in Fig. 5.3c. It can be observed that the only parameter which varies as the offset  $s$  is increased is the oscillator coupling. The damping parameter of the quadrupolar mode is comparable to the value of the Drude damping of gold at this frequency range. The low radiative losses can be understood from the cancellation of the dipolar moment. On the other hand, the damping parameter of the dipolar mode is significantly larger due to its high radiative losses. This example has shown how quantitative information on the properties of the resonators can be extracted from a fit with the coupled oscillator model. In another more recent example [22], the line-shape of the transmitted power of a THz split ring resonator array has been fitted with the coupled oscillator model in order to retrieve the coupling and damping coefficients of the modes.

The coupled oscillator model can also be used to understand the Fano resonance in non-linear systems. In [16], the coupled oscillator model is extended to the non-linear regime and applied to the case of metallic photonic crystal slabs. In the anharmonic coupled oscillator model the bright and the dark modes can be treated as classical harmonic oscillators with a third order perturbation term [16]. In [23] a fitting of the measured linear extinction spectra in a dolmen-like structure with the expression for the linear extinction yields the linear optical properties of the coupled oscillator system. Subsequently, the solution in first order perturbation describing the third harmonic (TH) response can be calculated as the third power of the time-dependent



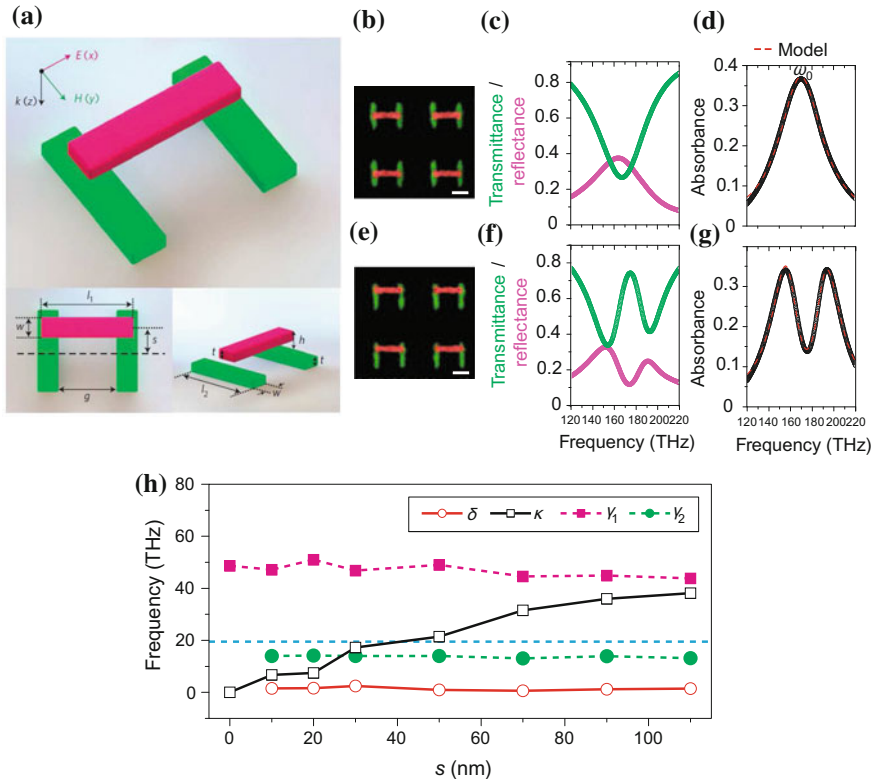


**Fig. 5.3** **a** Scanning electron micrographs of the fabricated structures. **b** Experimental absorbance as a function of frequency for different rod position detuning  $s$ . **c** Result of fitting the absorbance spectra with (5.17). Adapted from [21]

linear response. The transfer of TH energy between both modes, as well as the linear response function at the TH frequency have been neglected since they are small and spectrally flat, respectively. Hence, in the oscillator model the sources of the nonlinearity are the displacements of the unperturbed solution. Applied to a dolmen-like plasmonic structure, this oscillator model successfully predicts the TH spectrum in comparison to the measured and computed spectra with finite elements.

## 5.4 Resonance Formulas

This section aims at deriving the equivalent of the Fano formula from an oscillator model, and its generalization to a lossy system. Such derivations have been reported in [8, 24, 25]. An oscillator is coupled to a continuum which dynamics are determined by a general operator. First, the case of a non-lossy oscillator is considered, from

which the equivalent of the Fano formula is derived. With a lossy oscillator, the Fano interference is damped and its modulation depth depends on the coupling between the oscillator and the continuum. An expression for the different resonance parameters is derived, and applied to the case where the continuum is a highly damped oscillator. The regimes of low, critical and strong coupling are discussed and illustrated with examples.

### 5.4.1 Derivation of Resonance Formula Without Intrinsic Damping

In this model, an oscillator D with displacement  $x_d$  is coupled with coupling constant  $g$  to a continuum with displacement  $x_a$ . For generality, it is assumed that the dynamics of the continuum is determined by the linear time-differential operator  $\mathcal{L}$ . The oscillator D is for the moment not subject to a damping force. An external force  $f(t)$  is applied to the continuum. The equations of motion of this general system are:

$$\mathcal{L}x_a + gx_d = f \quad (5.18)$$

$$\ddot{x}_d + \omega_d^2 x_d + gx_a = 0. \quad (5.19)$$

Taking the Fourier transform of (5.18) and (5.19) yields:

$$\mathcal{L}_\omega c_a + gc_d = \hat{f} \quad (5.20)$$

$$(\omega_d^2 - \omega^2)c_d + gc_a = 0, \quad (5.21)$$

where  $c_a(\omega)$ ,  $c_d(\omega)$ ,  $\mathcal{L}_\omega$  and  $\hat{f}(\omega)$  are the Fourier components of the displacement  $x_a(t)$ ,  $x_d(t)$ , the operator  $\mathcal{L}$  and the force  $f(t)$ , respectively. For simplicity, the dependencies in  $\omega$  are kept implicit, except for the operator  $\mathcal{L}_\omega$ . It is assumed that the continuum slowly varies as a function of  $\omega$  and that around the resonance can be evaluated as  $\mathcal{L}_{\omega_d} = \mathcal{L}_d$ . The amplitude of the response of the continuum is written as:

$$c_a = \frac{\omega_d^2 - \omega^2}{\mathcal{L}_d(\omega_d^2 - \omega^2) - g^2} \hat{f}. \quad (5.22)$$

Around the frequency resonance  $\omega_d$  of the oscillator D, energy is resonantly transferred between the two systems. This transfer occurs at a frequency that is shifted from  $\omega_d$  by:

$$\Delta = -\frac{g^2}{|\mathcal{L}_d|^2} \frac{\text{Re}(\mathcal{L}_d)}{\omega_d}, \quad (5.23)$$

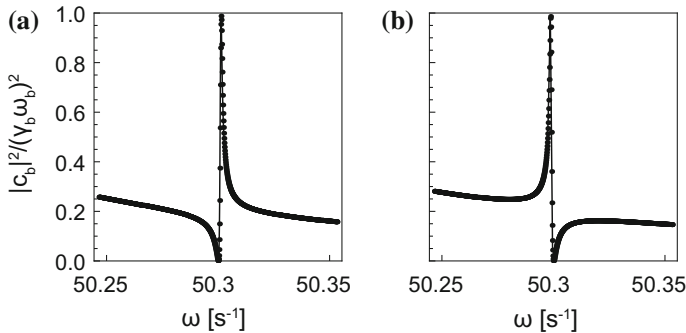


**Fig. 5.4** Amplitude of the forced oscillator as a function of the excitation frequency for **a** a real coupling constant  $g = 2.00 \text{ s}^{-2}$  and **b** an imaginary coupling constant  $g = 2.00i \text{ s}^{-2}$  (with  $\omega_a = 50.00 \text{ s}^{-1}$ ,  $\omega_d = 50.30 \text{ s}^{-1}$  and  $\gamma_b = 0.30 \text{ s}^{-1}$ ). Dots: calculated directly from (5.22); solid line: calculated from (5.25)

The resonance width  $\Gamma$  is solely determined from the coupling between the oscillator and the continuum:

$$\Gamma = g^2 \text{Im}(\mathcal{L}_d) / |\mathcal{L}_d|^2 \quad (5.24)$$

We defined the reduced frequency  $\kappa = (\omega^2 - \omega_d^2 - \omega_d \Delta) / \Gamma$ . From (5.22), we derive the response of the continuum as a function of the reduced frequency:

$$|c_a|^2 = \frac{|\hat{f}|^2 (\kappa + q)^2}{|\mathcal{L}_d|^2 (\kappa^2 + 1)}, \quad (5.25)$$

where the asymmetry parameter  $q$  is given by:

$$q = -\frac{\text{Re}(\mathcal{L}_d)}{\text{Im}(\mathcal{L}_d)}, \quad (5.26)$$

Equation (5.25) is equivalent of the Fano formula such as formulated in [4] applied to a mechanical oscillator. It is valid if the complex amplitude of the continuum does not strongly vary within the Fano resonance frequency interval. In such conditions, the agreement between (5.25) and (5.22) is perfect, as shown in Fig. 5.4a. In the case of a purely imaginary coupling constant  $g = ig'$ , (5.22) becomes:

$$c_a = \frac{\omega_d^2 - \omega^2}{\mathcal{L}_d(\omega_d^2 - \omega^2) + g'^2} \hat{f}. \quad (5.27)$$

A physically meaningful response of the system requires that the resonance has a positive width. As a result, the resonance frequency shift and asymmetry parameter reverse their sign for a purely imaginary coupling:

$$q = \frac{\text{Re}(\mathcal{L}_d)}{\text{Im}(\mathcal{L}_d)}, \quad (5.28)$$

and

$$\Delta = \frac{g^2}{|\mathcal{L}_d|^2} \frac{\text{Re}(\mathcal{L}_d)}{\omega_d}. \quad (5.29)$$

These results imply in particular that if a  $\pi/2$  phase retardation is introduced in the oscillators coupling, the conditions of destructive and constructive interference are reversed (Fig. 5.4b).

The response of the oscillator D around its resonance frequency is derived from (5.21) and normalized to the response of the uncoupled system A:

$$|c_d|^2 \frac{|\mathcal{L}_d|^2}{|\hat{f}|^2} = \frac{|\mathcal{L}_d|^2}{\text{Im}(\mathcal{L}_d)^2 \Gamma_c} \frac{1}{\kappa^2 + 1}. \quad (5.30)$$

Its line shape is a symmetric lorentzian whose amplitude and width are controlled by the coupling between the two systems. As the coupling decreases, the energy transferred from the continuum to the oscillator is stored longer and its amplitude increases.

The role of the radiative continuum can be played by a highly damped oscillator, for example in plasmonic systems. For the case of two coupled oscillators,  $\mathcal{L}_\omega = \omega_a^2 - \omega^2$  and  $\mathcal{L}_d = \omega_d^2 - \omega^2$ . The resonance parameters then become:

$$\Gamma = \frac{2g^2 \gamma_a \omega_d}{|\mathcal{L}_d|^2}, \quad q = \frac{\omega_d^2 - \omega_a^2}{2\omega_d \gamma_a}, \quad \Delta = \frac{g^2}{|\mathcal{L}_d|^2} \frac{\omega_d^2 - \omega_a^2}{\omega_d}. \quad (5.31)$$

For high frequencies (i.e.  $\omega_a, \omega_d \gg \gamma_a$ ), (5.25) can be approximated as a function of single powers of the frequency:

$$\frac{(2\omega_a)^2}{|\hat{f}|^2} |c_a|^2 = \frac{1}{(\omega - \omega_a)^2 + \gamma_a^2} \frac{(\omega - \omega_0 + q\gamma)^2}{(\omega - \omega_0)^2 + \gamma^2}, \quad (5.32)$$

where the spectral width in frequency units is given by:

$$\gamma = \frac{\Gamma}{2\omega_d}, \quad (5.33)$$

the resonance frequency by:

$$\omega_0 = \omega_d + \frac{\Delta}{2}, \quad (5.34)$$

and the asymmetry parameter by:

$$q = \frac{\omega_d - \omega_a}{\gamma_a}. \quad (5.35)$$

### 5.4.2 Derivation of Formula Including Intrinsic Damping

We now introduce a damping force to the oscillator D, from which the impact of intrinsic losses on the resonance properties and lineshape will be assessed. From (5.18) and (5.19), the equations of motion become in this case:

$$\mathcal{L}x_a + gx_d = f \quad (5.36)$$

$$\ddot{x}_d + 2i\gamma_d\dot{x}_d + \omega_d^2x_d + gx_a = 0. \quad (5.37)$$

Taking the Fourier transform of (5.36) and (5.37) yields:

$$\mathcal{L}_\omega c_a + gc_d = \hat{f} \quad (5.38)$$

$$(\omega_d^2 + 2i\gamma_d\omega - \omega^2)c_d + gc_a = 0, \quad (5.39)$$

where  $c_a(\omega)$ ,  $c_d(\omega)$ ,  $\mathcal{L}_\omega$  and  $\hat{f}(\omega)$  are the Fourier components of the displacement  $x_a(t)$ ,  $x_d(t)$ , the operator  $\mathcal{L}$  and the force  $f(t)$ , respectively. For simplicity, the dependencies in  $\omega$  are kept implicit, except for the operator  $\mathcal{L}_\omega$ . It is assumed that the continuum weakly varies as a function of  $\omega$  and that around the resonance can be evaluated as  $\mathcal{L}_{\omega_d} = \mathcal{L}_d$ . The amplitude of the response of the continuum is written as:

$$c_a \simeq \frac{\omega_d^2 + 2i\gamma_d\omega - \omega^2}{\mathcal{L}_d(\omega_d^2 + 2i\gamma_d\omega - \omega^2) - g^2} \hat{f}. \quad (5.40)$$

Around the frequency resonance  $\omega_d$  of the oscillator D, energy is resonantly transferred between the two systems. This transfer occurs at a frequency that is shifted from  $\omega_d$  by:

$$\Delta = -\frac{g^2}{|\mathcal{L}_d|^2} \frac{\text{Re}(\mathcal{L}_d)}{\omega_d}, \quad (5.41)$$

The resonance width is the sum of two contributions  $\Gamma_i = 2\gamma_d\omega_d$  from intrinsic losses and  $\Gamma_c = g^2\text{Im}(\mathcal{L}_d)/|\mathcal{L}_d|^2$  from the coupling between the oscillator D and the system A:

$$\Gamma = \Gamma_i + \Gamma_c. \quad (5.42)$$

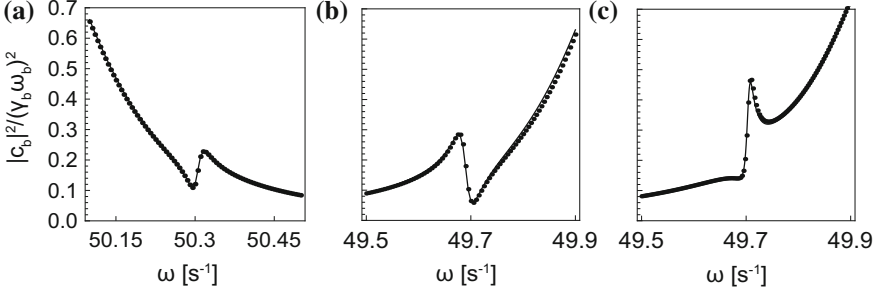


**Fig. 5.5** Amplitude of the forced oscillator as a function of the excitation frequency for **a** a real coupling constant  $g = 4.00 \text{ s}^{-2}$ ,  $\omega_d = 50.30 \text{ s}^{-1}$ , **b**  $g = 6.00 \text{ s}^{-2}$ ,  $\omega_d = 49.70 \text{ s}^{-1}$ , **c**  $g = 4.00i \text{ s}^{-2}$ ,  $\omega_d = 49.70 \text{ s}^{-1}$  (with  $\omega_a = 50.00 \text{ s}^{-1}$ ,  $\gamma_a = 0.3 \text{ s}^{-1}$  and  $\gamma_d = 0.02 \text{ s}^{-1}$ . Dots: calculated directly from (5.40); solid line: calculated from (5.43)

The reduced frequency  $\kappa$  is defined by  $\kappa = (\omega^2 - \omega_d^2 - \omega_d \Delta) / \Gamma$ . From (5.40), we derive the response of the oscillator A as a function of the frequency:

$$|c_a|^2 = \frac{|f|^2}{|\mathcal{L}_\omega|^2} \frac{(\kappa + q)^2 + b}{\kappa^2 + 1}, \quad (5.43)$$

where the asymmetry parameter  $q$  is given by:

$$q = -\frac{\text{Re}(\mathcal{L}_d)}{\text{Im}(\mathcal{L}_d)(1 + \Gamma_i / \Gamma_c)}, \quad (5.44)$$

and the modulation damping parameter  $b$  by:

$$b = \frac{\Gamma_i^2}{(\Gamma_c + \Gamma_i)^2}. \quad (5.45)$$

Equation (5.43) is a generalization of the Fano formula such as formulated in [4] to the case of a resonator with intrinsic losses. It is valid if the complex amplitude of the continuum does not strongly vary within the resonance frequency interval. In such conditions, the agreement between (5.43) and (5.40) is perfect, as shown in Fig. 5.5. A derivation of this formula from Maxwell's equations and the Feschbach formalism [26, 27] has been reported in [8, 24, 25]. The resonance parameters are expressed in terms of the electromagnetic field distributions of the radiative continuum and the localized resonant mode.

The response of the oscillator D around its resonance frequency is derived from (5.39) and normalized to the response of the uncoupled system A:

$$|c_d|^2 \frac{|\mathcal{L}_d|^2}{|\hat{f}|^2} = \frac{|\mathcal{L}_d|^2 \Gamma_c}{\text{Im}(\mathcal{L}_d)^2 (\Gamma_c + \Gamma_i)^2} \frac{1}{\kappa^2 + 1}. \quad (5.46)$$

As the coupling decreases, the intensity  $|c_d|^2$  reaches a maximum value for  $\Gamma_c = \Gamma_i$ . This is the so-called critical coupling condition. As the coupling decreases, the energy is stored longer in the oscillator D but is subject to stronger damping, so that its intensity vanishes.

For the case of two coupled oscillators A and D with respective resonance frequencies  $\omega_a$  and  $\omega_d$  and damping  $\gamma_a$  and  $\gamma_d$ ,  $\mathcal{L}_\omega = \omega_a^2 - \omega^2 + 2i\gamma_a\omega$  and  $\mathcal{L}_d = \omega_d^2 - \omega^2 + 2i\gamma_d\omega$ . The resonance parameters then become:

$$\Gamma_c = \frac{2g^2\gamma_a\omega_d}{|\mathcal{L}_d|^2}, \quad q = \frac{\omega_d^2 - \omega_a^2}{2\omega_d\gamma_a(1 + \Gamma_i/\Gamma_c)}, \quad \Delta = \frac{g^2}{|\mathcal{L}_d|^2} \frac{\omega_d^2 - \omega_a^2}{\omega_d}. \quad (5.47)$$

Equation (5.43) is valid if the complex amplitude of the oscillator A does not strongly vary within the Fano resonance frequency interval.

For high frequencies (i.e.  $\omega_a, \omega_d \gg \gamma_a$ ), (5.43) can be approximated as a function of single powers of the frequency:

$$\frac{(2\omega_a)^2}{|\hat{f}|^2} |c_a|^2 = \frac{1}{(\omega - \omega_a)^2 + \gamma_a^2} \frac{(\omega - \omega_0 + q\gamma)^2 + b\gamma^2}{(\omega - \omega_0)^2 + \gamma^2}, \quad (5.48)$$

where the spectral width in frequency units is given by:

$$\gamma = \frac{\Gamma}{2\omega_d} = \frac{\Gamma_i}{2\omega_d} + \frac{\Gamma_c}{2\omega_d} := \gamma_i + \gamma_c, \quad (5.49)$$

the resonance frequency by:

$$\omega_0 = \omega_d + \frac{\Delta}{2}, \quad (5.50)$$

and the shape parameters by:

$$q = \frac{\omega_d - \omega_a}{\gamma_a(1 + \gamma_i/\gamma_c)}, \quad b = \frac{\gamma_i^2}{(\gamma_c + \gamma_i)^2}. \quad (5.51)$$

The oscillator amplitude in oscillator D becomes from (5.46):

$$|c_d|^2 \propto \frac{\gamma_c}{(\gamma_c + \gamma_i)^2} \quad (5.52)$$

Figure 5.6 shows an example of the critical coupling condition applied to coupled oscillators. The two oscillators have different resonance frequencies, and the Fano modulation is asymmetric. The modulation strength increases monotonously with the coupling. The amplitude of the oscillator D increases as a function of the oscillator coupling and reaches a maximum when the coupling  $\gamma_c$  balances intrinsic losses  $\gamma_i$ . As the coupling increases, the width  $\gamma$  of the modulation becomes comparable to

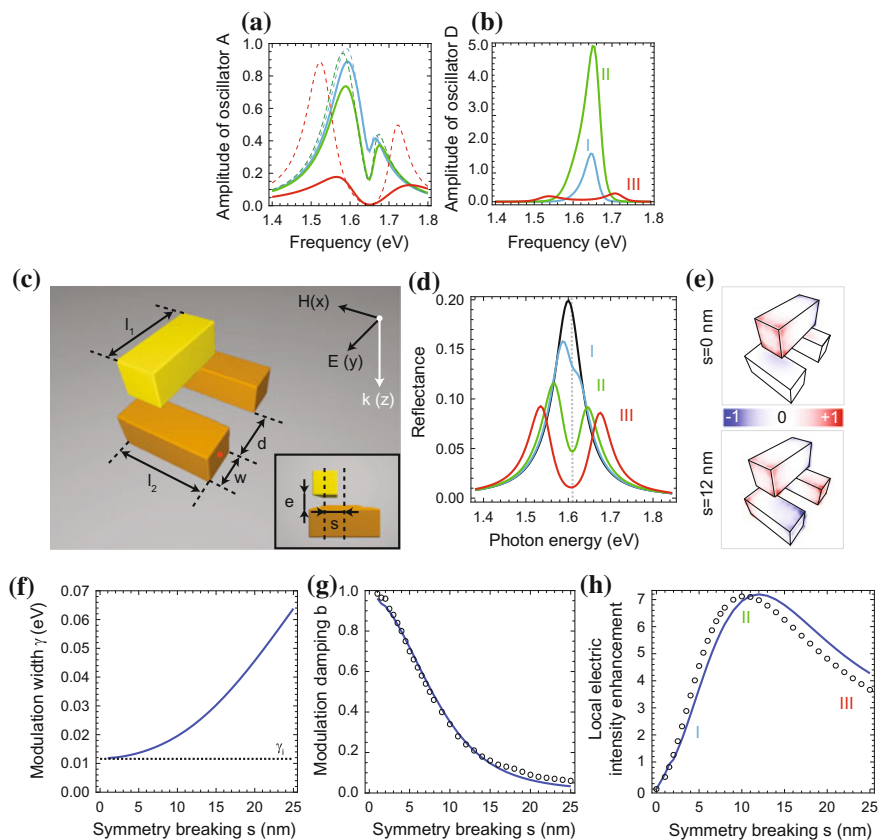


**Fig. 5.6** Amplitude of the oscillators **a** A and **b** D as a function of the frequency, with  $\omega_a = 1.599$  eV,  $\gamma_a = 0.060$  eV,  $\omega_0 = 1.650$  eV, and  $\gamma_i = 0.012$  eV. The blue, green, and red curves correspond to  $\gamma_c = 0.003$  eV,  $\gamma_c = 0.009$  eV, and  $\gamma_c = 0.082$  eV, respectively. The solid and dashed line correspond to the direct evaluation from (5.13) and to the evaluation with (5.48), respectively. **c** Symmetry breaking in a plasmonic nanostructure. **d** Reflectance of a two-dimensional array of such structures. The black, blue, red, and green curves correspond increasing symmetry breaking  $s$ . The symbols I, II, and III represent the three different coupling regimes. **e** Surface charge distribution at a resonant energy 1.61 eV for symmetric and non-symmetric cases, respectively. **f** Spectral width of the reflection dip as a function of the symmetry breaking. The solid blue and the dashed black lines represent the total and the intrinsic width, respectively. **g** Modulation damping  $b$  as a function of the symmetry breaking. The solid blue line corresponds to the ratio of the reflectance at a photon energy of 1.61 eV in the symmetry broken system ( $s \neq 0$ ) to the reflectance in the symmetric system ( $s = 0$ ) at the same energy. The black circles correspond to calculations using panel (f) and the expression of the modulation damping  $b$  in (5.51). **h** Electric field intensity enhancement related to the quadrupolar mode at 1.61 eV as a function of the symmetry breaking (location: red point in panel (c)). The black circles correspond to calculations using panel (f) and (5.52). Adapted from [25] with permission. Copyright American Chemical Society



the width  $\gamma_a$  of the oscillator A. For strong coupling, a splitting in the response of the oscillator D is observed, each individual resonance being a normal mode of the composite system, and the dip in the spectral response of oscillator A of the system is not Fano interference but the sum of two Lorentzians centered on each hybridized mode frequency [25, 28, 29]. This limiting case is the classical analogue of Autler-Townes splitting (ATS) [7, 15, 30–32]. In [32], analytical profiles of EIT and ATS derived from a coupled resonator model are used to fit transmission spectra of coupled whispering gallery modes. A quantitative criterion to discriminate between EIT and ATS is presented. When the coupling strength of the resonators is low and the decay rate  $\gamma_d$  of the dark resonator is much lower than the decay rate of the bright resonator  $\gamma_a$ , the EIT model is favored. If the decay rates of the resonators are comparable and the coupling is strong, the ATS model is favored. Finally, if the decay rates of the resonators are comparable and the coupling is low, the EIT model is favored. A transition regime can occur when the difference in decay rates is comparable to the critical coupling strength. This procedure has also been applied experimentally to a system of coupled mechanical oscillators [19].

Figure 5.6c–h shows an example in a plasmonic system similar to Fig. 5.3, for near-field and far-field properties have been numerically calculated. The offset from the symmetric position allows to directly tune the coupling between the dipolar and quadrupolar modes. As the mode coupling is increased, the modulation becomes more pronounced: the modulation damping ranges from 1 in the weak coupling regime ( $\gamma_c \ll \gamma_i$ ) and decreases monotonically to 0 in the strong coupling regime ( $\gamma_c \gg \gamma_i$ ). For weak coupling, the modulation amplitude is extremely sensitive to the symmetry breaking. In Fig. 5.6h, the electric field intensity enhancement associated with the quadrupolar mode initially increases along with the modes coupling but reaches a maximum for a specific value of the mode coupling and then decreases. The local near-field intensity enhancement depends on the total energy stored by the mode and the modal field distribution (5.52). The values of damping  $\gamma_c$  and  $\gamma_i$  extracted from Fig. 5.6f enables to predict the behavior of the modulation damping (Fig. 5.6g) and the near-field enhancement from the quadrupole (Fig. 5.6h) using (5.51) and (5.52), respectively.

## 5.5 Electromagnetically Induced Absorption

Electromagnetically induced absorption (EIA) differs from EIT in the sense that the destructive interference generating a window of transparency is changed into a constructive interference. In an optical system retardation is present and can be harnessed for phase tuning by increasing the relative distance between resonators. Consider the two oscillators A and D of the standard coupled oscillator mode coupled by a complex spring of constant  $g = |g|e^{i\phi}$  where  $\phi$  is the phase delay in the coupling. This models the classical equivalent of electromagnetically induced absorption [33, 34]. The equation of motion becomes:

$$\ddot{x}_a + \gamma_a \dot{x}_a + \omega_a^2 x_a + |g|e^{i\phi} x_d = (qE_0/m)e^{i\omega t} \quad (5.53)$$

$$\ddot{x}_d + \gamma_d \dot{x}_d + \omega_d^2 x_d + |g|e^{i\phi} x_a = 0. \quad (5.54)$$

This equation can be written under matrix form:

$$\begin{pmatrix} \omega_a^2 - \omega^2 - i\gamma_a \omega_a & |g|e^{i\phi} \\ |g|e^{i\phi} & \omega_d^2 - \omega^2 - i\gamma_d \omega_d \end{pmatrix} \begin{pmatrix} c_a \\ c_d \end{pmatrix} = \begin{pmatrix} f \\ 0 \end{pmatrix}, \quad (5.55)$$

from which the oscillators amplitude can be found by matrix inversion:

$$\begin{pmatrix} c_a \\ c_d \end{pmatrix} = \frac{f}{(\omega_a^2 + i\gamma_a \omega - \omega^2)(\omega_d^2 + i\gamma_d \omega - \omega^2) - |g|^2 e^{2i\phi}} \begin{pmatrix} \omega_d^2 + i\gamma_d \omega - \omega^2 \\ |g|e^{i\phi} \end{pmatrix}. \quad (5.56)$$

The energy absorbed by the system is equal to the energy transferred by the driving force to oscillator A. Following the procedure for the derivation of (5.17) yields the total power transferred to the system:

$$\langle P_{\text{tot}}(t) \rangle = \frac{(qE_0)^2 \omega}{2m} \text{Im} \left( \frac{\omega_d^2 + i\gamma_d \omega - \omega^2}{(\omega_a^2 + i\gamma_a \omega - \omega^2)(\omega_d^2 + i\gamma_d \omega - \omega^2) - |g|^2 e^{2i\phi}} \right). \quad (5.57)$$

Assuming  $\omega_d \simeq \omega_a$  in an EIT-like system, the absorption at  $\omega = \omega_d = \omega_a$  satisfies:

$$\langle P_{\text{tot}}(t) \rangle \propto \left( \frac{\gamma_d \omega_d}{\gamma_a \gamma_d \omega_d^2 + |g|^2 \cos(2\phi)} \right). \quad (5.58)$$

The amplitude of absorption can be therefore be tuned using the phase of the coupling coefficient, resulting to a constructive or destructive interference. However, the phase and amplitude of the coupling coefficient are linked in a realistic system. Those constraints render the optimal condition of absorption enhancement difficult to achieve.

As an example of EIA effect, Figure 5.7 shows the transmittance, reflectance and absorbance calculated numerically in a system similar to the one of Figure 5.3 supporting a plasmonic EIT. Here, the distance  $d_z$  from the top nanorod supporting a dipolar mode to the bottom nanorods support a quadrupolar mode is tuned, which has the effect to change the phase delay in the coupling between the dipolar and the quadrupolar modes. This is equivalent to changing the phase  $\phi$  in (5.53). When the vertical spacing is increased, the near-field coupling between the dipolar and quadrupolar modes is decreased as expected. However, the modulation of the dip in reflectance becomes much stronger than that of the peak in transmittance, indicating a change in absorbance. At the quadrupole resonance position, a very strong absorbance peak is observed for a vertical spacing of approximately  $d_z = 260$  nm

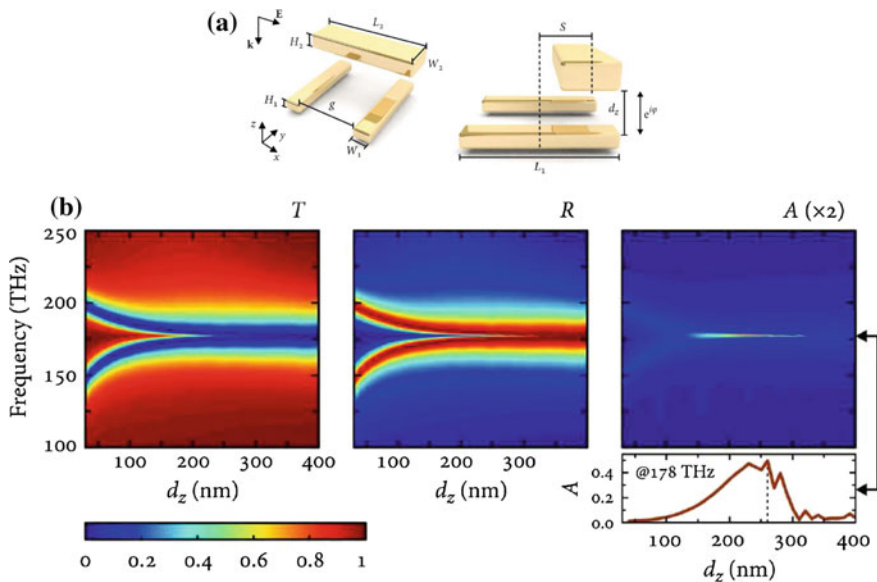


**Fig. 5.7** **a** Parameters of the system supporting the classical equivalent of EIA. The phase difference between the dipolar and the quadrupolar modes can be tuned by changing the vertical spacing  $d_z$ . **b** Resulting calculated transmittance, reflectance, and absorbance spectra as a function of the vertical spacing  $d_z$ . Adapted from [34] with permission. Copyright Optical Society of America

(Fig. 5.7b). In this condition, the retardation phase is matched to obtain constructive interference.

Figure 5.8 shows experimental and numerical spectra corresponding to the structure of Fig. 5.7 fitted to the harmonic oscillator model (5.57). The fitting parameters are plotted and their trend can be visualized. As expected, increasing the offset  $S$  yields an increase in the coupling parameter  $|g|$ . The coupling phase parameter can be extracted from the fit, and shows a dependence in the coupling strength. Finally, the fitting parameters show that the quadrupolar mode damping rate is in fact smaller than the dipolar damping rate, as expected. However, interestingly the dipolar damping rate decreases consistently with increasing coupling strength while the quadrupolar damping rate increases.

## 5.6 Radiative and Non-radiative Lifetimes in Strongly Coupled Systems

In some Fano-resonant systems such as oligomers [35–37] or concentric ring resonators [38, 39], the continuum and the discrete state are supported by the same set of nanostructures. In such systems, hybridization of modes occur to form bonding

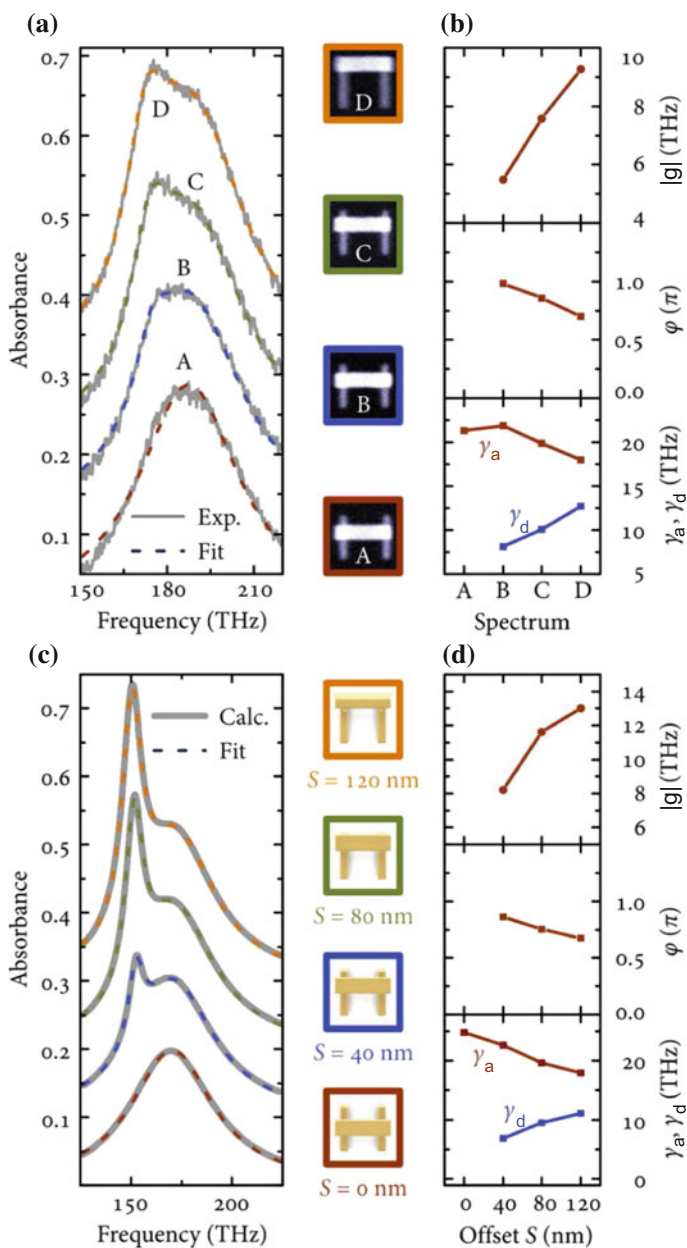


**Fig. 5.8** **a, b** Fit curves (dashed) of the coupled oscillator model with a complex coupling coefficient, (5.57), to the **(a)** experimental and **(b)** calculated absorbance spectra (solid gray curves). **c, d** Retrieved fit parameters  $|g|$ ,  $\phi$ ,  $\gamma_d$ , and  $\gamma_a$ . Adapted from [33] with permission. Copyright American Chemical Society

and anti-bonding modes. One of the resulting modes has a very high dipole moment and radiation loss, is referred as the superradiant mode and plays the role of the continuum. The other mode resulting from the hybridization has a very low dipole moment, almost vanishing, is referred as the subradiant mode and plays the role of the discrete state. Both superradiant and subradiant modes are supported by the same nanostructures. In the standard oscillator model (5.11) the oscillators do not directly have a correspondence with the structure, which makes an interpretation difficult. The Fano interference results in the scattering spectrum by driving only the superradiant mode with an external field and the damping of the two oscillators is prescribed a priori. In this Section, an oscillator model of hybridization taking into account radiative losses and radiative coupling is presented. Both phenomena of superradiance and subradiance, as well as the interaction between hybridized modes are modeled.

### 5.6.1 Extended Coupled Oscillator Model

In Sect. 5.2, an oscillator model taking into the radiation reaction force, proportional to the third derivative of the dipole amplitude, has been described. In this section, the model is extended to a system of two coupled oscillators and is referred as the extended coupled oscillator (ECO) model in the following. In contrast to the standard coupled oscillator model, the oscillators represent the original diabatic modes of the system and are characterized by resonant frequencies  $\omega_1$ ,  $\omega_2$  and damping  $\gamma_1$ ,  $\gamma_2$  accounting for nonradiative losses. Nonradiative damping in a nanoparticle is a local quantity that only depends on the local plasmon oscillation and is independent of any dissipation in nearby systems. In contrast, radiative damping is a collective effect exhibiting interference, i.e., sub- or superradiance. The radiative damping of two dipolar oscillators is proportional to the total dynamical dipole moment of the system, influenced by the individual polarizabilities of the oscillators (5.4). The external excitation is represented by forces applied on both oscillators and is here for simplicity assumed to be in phase, which can be justified when the spatial extension of the system is smaller than a quarter wavelength of the incident light. The net force on each oscillator is proportional to their polarizabilities (5.4). The equations of motion can then be written in terms of polarization of the oscillators [40]:

$$\ddot{\mathbf{P}}_1 + \gamma_{i1}\dot{\mathbf{P}}_1 + \omega_1^2\mathbf{P}_1 + g\mathbf{P}_2 = \alpha_1\omega_1^2\mathbf{E}_0e^{i\omega t} + \frac{1}{6\pi\epsilon_0c^3}[\alpha_1V_1\omega_1^2\ddot{\mathbf{P}}_1 + \alpha_2V_2\omega_2^2\ddot{\mathbf{P}}_2] \quad (5.59)$$

$$\ddot{\mathbf{P}}_2 + \gamma_{i2}\dot{\mathbf{P}}_2 + \omega_2^2\mathbf{P}_2 + g\mathbf{P}_1 = \alpha_2\omega_2^2\mathbf{E}_0e^{i\omega t} + \frac{1}{6\pi\epsilon_0c^3}[\alpha_1V_1\omega_1^2\ddot{\mathbf{P}}_1 + \alpha_2V_2\omega_2^2\ddot{\mathbf{P}}_2]. \quad (5.60)$$

where  $\alpha_1 = (N_1 q)^2 / (V_1 m \omega_1^2)$  and  $\alpha_2 = (N_2 q)^2 / (V_2 m \omega_2^2)$  are the respective polarizability of the oscillators and  $V_1$  and  $V_2$  their respective volume. Assuming an harmonic time-dependence of the polarization, (5.59) and (5.60) can be written in a matrix form:

$$\begin{pmatrix} \omega_1^2 - \omega^2 + i\omega\gamma_{i1} + i\omega^3\gamma_{r1} & g + i\omega^3\gamma_{r2} \\ g + i\omega^3\gamma_{r1} & \omega_2^2 - \omega^2 + i\omega\gamma_{i2} + i\omega^3\gamma_{r2} \end{pmatrix} \begin{pmatrix} \mathbf{P}_1 \\ \mathbf{P}_2 \end{pmatrix} = \begin{pmatrix} \gamma_{r1} \\ \gamma_{r2} \end{pmatrix} \mathbf{E}'_0, \quad (5.61)$$

where the radiative damping coefficient is given by:

$$\gamma_{rn} = (6\pi c^3 \epsilon_0) \alpha_n \omega_n^2, \quad (5.62)$$

and  $\mathbf{E}'_0 = 6\pi c^3 \epsilon_0 \mathbf{E}_0$ . The radiative damping term appears both in the diagonal and coupling elements of the equation of motion matrix in (5.61). Equation (5.61) can be written as:

$$\begin{pmatrix} \Omega_1 & \Gamma_2 \\ \Gamma_1 & \Omega_2 \end{pmatrix} \begin{pmatrix} \mathbf{P}_1 \\ \mathbf{P}_2 \end{pmatrix} = \begin{pmatrix} \gamma_{r1} \\ \gamma_{r2} \end{pmatrix} \mathbf{E}'_0. \quad (5.63)$$

where

$$\Omega_n = \omega_n^2 - \omega^2 + i\omega\gamma_{in} + i\omega^3\gamma_{rn}, \quad (5.64)$$

and

$$\Gamma_n = g + i\omega^3\gamma_{rn}. \quad (5.65)$$

Inverting the matrix in (5.61) leads to

$$\begin{pmatrix} \mathbf{P}_1 \\ \mathbf{P}_2 \end{pmatrix} = \frac{1}{\Omega_1\Omega_2 - \Gamma_1\Gamma_2} \begin{pmatrix} \Omega_2 & -\Gamma_1 \\ -\Gamma_2 & \Omega_1 \end{pmatrix} \begin{pmatrix} \gamma_{r1} \\ \gamma_{r2} \end{pmatrix} \mathbf{E}'_0. \quad (5.66)$$

Such a model can be applied to a system of coupled antennas, as shown in Fig. 5.9. The central antenna is modeled by a diabatic oscillator, while the outer nanorods by the other diabatic oscillator. They are respectively named DN and DA in the following. A fit of the model with measured and simulated scattering spectra shows a good agreement. The squared modulus of the sum of the polarization amplitudes,  $|\mathbf{P}_1 + \mathbf{P}_2|^2$ , represents light scattering efficiency of the system and is used to model the scattering spectrum. A first inspection of the scattering spectrum shows a Fano-type resonance, which takes its origin from the coupling between the hybridized superradiant and subradiant modes (referred as AB and AD, respectively), as will be discussed in the following. The superradiant and subradiant modes can be also individually driven using in-phase or out-of-phase excitation of the individual diabatic oscillators [41].

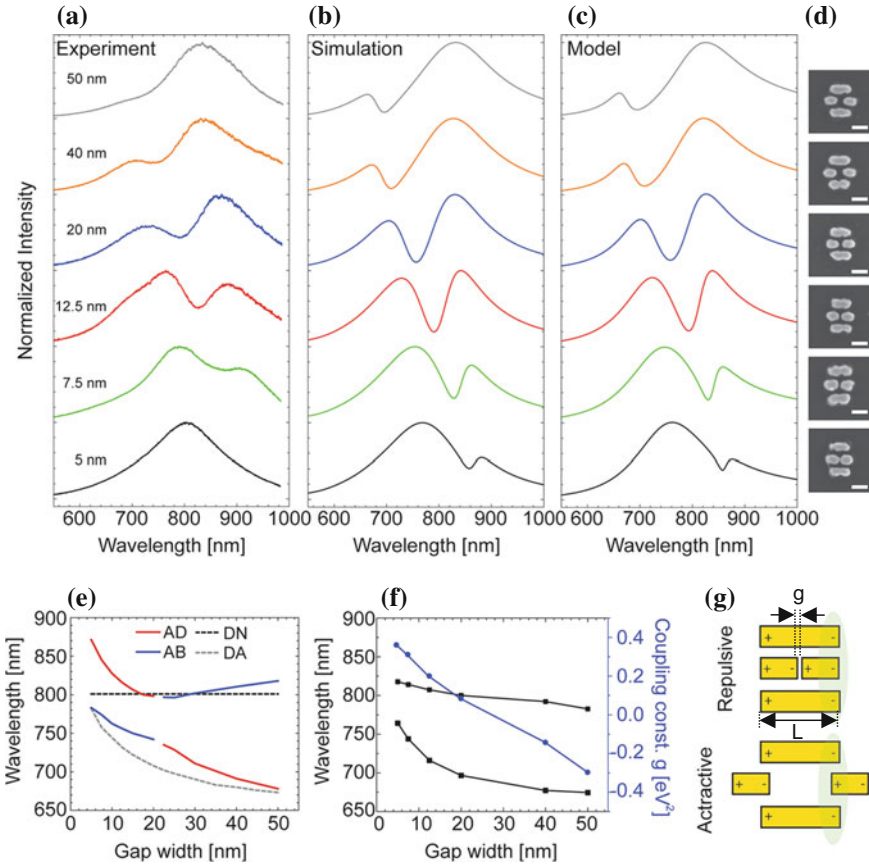


**Fig. 5.9** **a** Dark-field measurements, **b** simulations of scattering cross section, **c** fit with the ECO model, and **d** SEM pictures (scale bar 100 nm) of structures with constant nanorods length  $L = 120$  nm and increasing antenna gap size from 5 to 50 nm. **e** Plasmon hybridization diagram with the spectral position of the diabatic (dashed lines) and adiabatic modes (solid red and blue lines) versus the gap width. **f** Resonance wavelengths of the diabatic modes extracted from the fitting with the ECO model (black) and coupling constant  $g$  (blue). **g** Schematics of Coulomb interaction for different gap widths. For small gaps, the AB mode is at higher energy than AD because of repulsive forces between antenna and nanorods, while for large gaps, forces are attractive and the effect is opposite. Adapted with permission from [40]. Copyright American Chemical Society

### 5.6.2 Superradiance and Subradiance in Hybridized Modes

We now wish to express this equation in terms of hybridized mode, when one is superradiant and the other subradiant. We perform a change of basis expressed from the individual dipoles  $\mathbf{P}_1$  and  $\mathbf{P}_2$  into a basis of dipoles oscillating in phase  $\mathbf{P}_b = 1/\sqrt{2}(\mathbf{P}_1 + \mathbf{P}_2)$  or out of phase  $\mathbf{P}_d = 1/\sqrt{2}(\mathbf{P}_1 - \mathbf{P}_2)$ . The system of (5.63) becomes

$$\begin{pmatrix} \frac{\Omega_1 + \Omega_2 + \Gamma_1 + \Gamma_2}{2} & \frac{\Omega_1 - \Omega_2 - \Gamma_1 + \Gamma_2}{2} \\ \frac{\Omega_1 - \Omega_2 + \Gamma_1 - \Gamma_2}{2} & \frac{\Omega_1 + \Omega_2 - \Gamma_1 - \Gamma_2}{2} \end{pmatrix} \begin{pmatrix} \mathbf{P}_1 + \mathbf{P}_2 \\ \frac{\sqrt{2}}{\sqrt{2}} \\ \mathbf{P}_1 - \mathbf{P}_2 \\ \frac{\sqrt{2}}{\sqrt{2}} \end{pmatrix} = \begin{pmatrix} \frac{(\gamma_{r1} + \gamma_{r2})}{\sqrt{2}} \\ \sqrt{2} \\ \frac{(\gamma_{r1} - \gamma_{r2})}{\sqrt{2}} \\ \sqrt{2} \end{pmatrix} \mathbf{E}'_0. \quad (5.67)$$

Let us define the resonance frequency of the subradiant mode by:

$$\omega_d = \sqrt{\frac{\omega_1^2 + \omega_2^2}{2} - g}, \quad (5.68)$$

and the resonance frequency of the superradiant mode by:

$$\omega_b = \sqrt{\frac{\omega_1^2 + \omega_2^2}{2} + g}. \quad (5.69)$$

Their respective damping coefficient is given by:

$$\gamma_d = \frac{\gamma_{i1} + \gamma_{i2}}{2}, \quad (5.70)$$

and

$$\gamma_b = \frac{\gamma_{i1} + \gamma_{i2}}{2} + \omega^2(\gamma_{r1} + \gamma_{r2}). \quad (5.71)$$

Equation (5.67) then becomes:

$$\begin{pmatrix} \omega_b^2 - \omega^2 + i\omega\gamma_b & \Gamma_{bd} \\ \Gamma_{db} & \omega_d^2 - \omega^2 + i\omega\gamma_d \end{pmatrix} \begin{pmatrix} \mathbf{P}_1 + \mathbf{P}_2 \\ \frac{\sqrt{2}}{\sqrt{2}} \\ \mathbf{P}_1 - \mathbf{P}_2 \\ \frac{\sqrt{2}}{\sqrt{2}} \end{pmatrix} = \begin{pmatrix} \frac{(\gamma_{r1} + \gamma_{r2})}{\sqrt{2}} \\ \sqrt{2} \\ \frac{(\gamma_{r1} - \gamma_{r2})}{\sqrt{2}} \\ \sqrt{2} \end{pmatrix} \mathbf{E}'_0. \quad (5.72)$$

The resonance frequency of the hybridized modes, subradiant and superradiant, corresponds to the well known model of strongly coupled oscillator model, including Rabi splitting and the avoided crossing [42], but also provides an expression for their radiative and non-radiative lifetimes.

An example in a plasmonic structure is shown in Fig. 5.9. The geometry of the plasmonic structure plays a major role in determining the energies of the diabatic and adiabatic modes. Fig. 5.9f shows a dependence on the coupling coefficient  $g$  from the gap width. The coupling between the diabatic oscillators  $g$  is tuned by the gap distance in the central antenna: a fit with the ECO models reveals that it undergoes a change of sign which can be explained from electrostatic arguments (Fig. 5.9g). The sign of the detuning between the superradiant and subradiant modes can be changed. For zero coupling, the adiabatic modes are not defined and there is a discontinuous jump in Fig. 5.9e. This is a fundamentally different behavior from standard avoided crossings, where the interaction remains finite and the two adiabatic states repel each other. The unusual phenomenon of a sign change in the coupling between the antenna



and nanorod modes can be understood from the schematic in Fig. 5.9g: as the antenna gap increases, the Coulomb interaction changes sign from repulsive to attractive.

The coupling coefficients between the superradiant and subradiant modes are:

$$\Gamma_{bd} = \frac{\omega_1^2 - \omega_2^2}{2} + \frac{i\omega(\gamma_{i1} - \gamma_{i2})}{2}, \quad (5.73)$$

and

$$\Gamma_{db} = \frac{\omega_1^2 - \omega_2^2}{2} + \frac{i\omega(\gamma_{i1} - \gamma_{i2})}{2} + i\omega^3(\gamma_{r1} - \gamma_{r2}). \quad (5.74)$$

When the polarizability and intrinsic damping of the oscillators is nearly equal, i.e. the nanoparticles are nearly equal in terms of geometry and amount of carriers, one can approximate  $\gamma_{i1} \simeq \gamma_{i2}$  and  $\gamma_{r1} \simeq \gamma_{r2}$ , yielding:

$$\begin{pmatrix} \omega_b^2 - \omega^2 + i\omega\gamma_b & \frac{\omega_1^2 - \omega_2^2}{2} \\ \frac{\omega_1^2 - \omega_2^2}{2} & \omega_d^2 - \omega^2 + i\omega\gamma_d \end{pmatrix} \begin{pmatrix} \frac{\mathbf{P}_1 + \mathbf{P}_2}{\sqrt{2}} \\ \frac{\mathbf{P}_1 - \mathbf{P}_2}{\sqrt{2}} \end{pmatrix} = \begin{pmatrix} \frac{(\gamma_{r1} + \gamma_{r2})}{\sqrt{2}} \mathbf{E}'_0 \\ 0 \end{pmatrix}. \quad (5.75)$$

This system of equation is equivalent describes a highly damped radiative resonator coupled to a non-radiative resonator. This makes it equivalent to the standard model of coupled oscillators (5.11) and the absorbed power can be calculated equivalently. However, the radiative and non-radiative characters result from hybridization of two radiative resonators. As an illustration, we consider the influence of the nanorods length on the response of the system. Normalized experimental scattering spectra as well as simulations with corresponding oscillator model fitting and SEM pictures for four different nanorods lengths are presented in Fig. 5.10. The calculated spectra agree very well with the measured spectra as well as with the ECO model. Several effects caused by the tuning can be immediately observed: a clear red shift of the superradiant peak, a width tuning of the Fano resonance and the disappearance of the Fano resonance for a specific nanorods length. The first effect is simply due to the fact that increasing the nanorods length causes a red shift of the nanorods mode and a resulting red shift of the hybridized modes. It can be seen from (5.75) that the coupling between the hybridized modes depends on the energy difference between the two diabatic modes. Therefore, from the knowledge on the influence of modes coupling on the Fano resonance (Sects. 5.3 and 5.4), the modulation depth of the Fano resonance can be controlled.

In Fig. 5.10e, a plasmon hybridization diagram illustrates the effects of tuning the energy of nanorods mode. As the uncoupled nanorod resonance (DN, black dashed line) wavelength approaches that of the uncoupled antenna (DA, gray dashed line), the hybridized modes exhibit an avoided crossing behavior. The positions of AB and AD are extracted from the absorption peaks using (5.43). The anticrossing behavior implies that the magnitude and sign of the coupling remains unchanged. When the diabatic modes cross, which occurs for  $L = 87.5$  nm, the width of the Fano resonance goes to a minimum and the Fano line shape is completely damped, leading

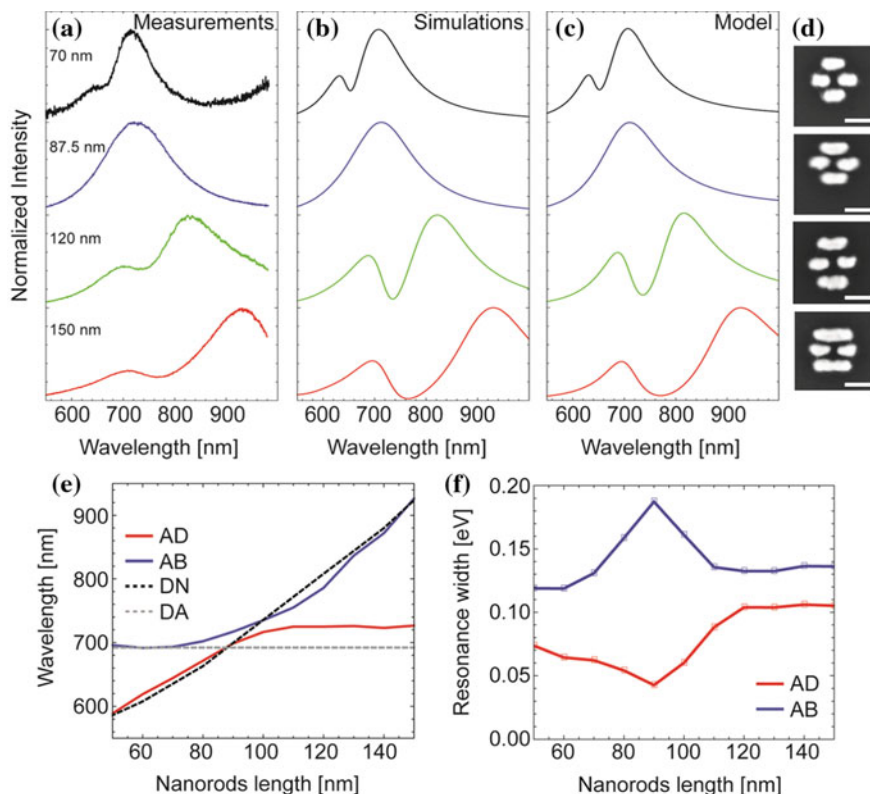


**Fig. 5.10** **a** Dark-field measurements, **b** simulations of scattering cross section, **c** fit with ECO model, and **d** SEM pictures (scale bar 100 nm) of systems with different nanorods lengths ranging from 70 to 150 nm and antenna gap fixed at 25 nm. **e** Plasmon hybridization diagram with the spectral position of diabatic and adiabatic modes versus nanorods length. **f** AB and AD mode resonance widths versus nanorods length extracted with a fitting using (5.43). Adapted from [40] with permission. Copyright American Chemical Society

to a single Lorentzian peak for the scattering cross section that corresponds then to a pure bright mode. In Fig. 5.10f, the width associated with the AD mode goes toward the minimum for nanorod lengths approaching 87.5 nm while the width of the AB mode reaches a maximum. Because of the overlap of the absorption peaks around the anticrossing point, the modal widths cannot be extracted from the absorption spectra but are instead determined using (5.43) that provide position and mode width of the hybridized modes by fitting the scattering cross section.

The ECO model has also been used to predict some effects in the second harmonic generation (SHG) from plasmonics structures [43]. The oscillation amplitudes of the diabatic oscillators have been extracted with the ECO model. The convolution of their

respective SHG emission pattern with the linear oscillator amplitude from the ECO model corresponds very well to the emission pattern of the numerically computed SHG from the system.

## 5.7 Summary

The model of coupled oscillators has been used over decades to interpret the Fano interference effect in a variety of optical, plasmonic and microwave systems. In this model, one resonator with a large damping rate is subject to an external driving force. This so-called bright oscillator is the equivalent of the radiative continuum. Another so-called dark oscillator with a low damping rate, not driven, is the equivalent of the discrete state. The high interest for this model has triggered further research to extend its description to further effects or to more rigorously and accurately model the Fano interference, electromagnetically induced transparency (EIT) and electromagnetically induced absorption (EIA) effects: this includes an explicit distinction between non-radiative and radiative losses, the relationship between the driving force and the radiative damping of the bright oscillator, its extension to non-linear effects (such as second or third harmonic generation), and the inclusion of a phase in the coupling term.

Further work has been conducted to understand the interplay between the bright mode and the dark mode in Fano-resonant system, in particular the effect of modes coupling and non-radiative losses on its spectral lineshape. For this purpose, the Fano formula and its generalization to lossy systems have been derived in the coupled oscillator system. The different resonance parameters are expressed in terms of the oscillator parameters and their coupling. In Fano-resonant systems such as oligomers the continuum and the discrete state are supported by the same set of structures. An extended coupled oscillator model including radiative losses as a result of Abraham-Lorentz force on accelerated charges has been discussed. It allows a model of hybridization taking into account radiative losses and radiative coupling. Both phenomena of superradiance and subradiance, as well as the interaction between hybridized modes can be predicted.

Oscillator models are a simple yet powerful tool to interpret theoretical, numerical or experimental work when it is used for example for fitting, extracted physical parameters and predict effects. Thanks to their universal and versatile character, they will continue to be applied to a variety of optical and microwave systems and even in other fields of research.

## References

1. B. Luk'yanchuk, N.I. Zheludev, S.A. Maier, N.J. Halas, P. Nordlander, H. Giessen, C.T. Chong, *Nat. Mater.* **9**, 707 (2010)
2. A.E. Miroshnichenko, S. Flach, Y.S. Kivshar, *Rev. Mod. Phys.* **82**, 2257 (2010)
3. M.F. Limonov, M.V. Rybin, A.N. Poddubny, Y. Kivshar, *Nat. Photonics* **11**, 543 (2017)
4. U. Fano, *Phys. Rev.* **124**, 1866 (1961)
5. K.J. Boller, A. Imamoglu, S.E. Harris, *Phys. Rev. Lett.* **66**, 2593 (1991)
6. S. Zhang, D.A. Genov, Y. Wang, M. Liu, X. Zhang, *Phys. Rev. Lett.* **101**, 047401 (2008)
7. P.M. Anisimov, J.P. Dowling, B.C. Sanders, *Phys. Rev. Lett.* **107**, 163604 (2011)
8. B. Gallinet, O.J.F. Martin, *Phys. Rev. B* **83**, 235427 (2011)
9. S.A. Maier, *Plasmonics: Fundamentals and Applications* (Springer Science, 2007)
10. M.A. Kats, N. Yu, P. Genevet, Z. Gaburro, F. Capasso, *Opt. Express* **19**, 21748 (2011)
11. J.D. Jackson, *Classical Electromagnetism*, 3rd edn. (Wiley, 1999)
12. J. Zuolaga, P. Nordlander, *Nano Lett.* **11**, 1280 (2011)
13. W.E. Lamb, R.C. Retherford, *Phys. Rev.* **81**, 222 (1951)
14. A.G. Litvak, M.D. Tokman, *Phys. Rev. Lett.* **88**, 095003 (2002)
15. C.L.G. Alzar, M.A.G. Martinez, P. Nussenzveig, *Am. J. Phys.* **70**, 37 (2002)
16. M.W. Klein, T. Tritschler, M. Wegener, S. Linden, *Phys. Rev. B* **72**, 115113 (2005)
17. Y.S. Joe, A.M. Satanin, C.S. Kim, *Phys. Scr.* **74**, 259 (2006)
18. P. Tassin, L. Zhang, T. Koschny, E.N. Economou, C.M. Soukoulis, *Phys. Rev. Lett.* **102**, 053901 (2009)
19. J. Liu, H. Yang, C. Wang, K. Xu, J. Xiao, *Sci. Rep.* **6**, 19040 (2016)
20. P. Tassin, L. Zhang, R. Zhao, A. Jain, T. Koschny, C.M. Soukoulis, *Phys. Rev. Lett.* **109**, 187401 (2012)
21. N. Liu, L. Langguth, T. Weiss, J. Kaestel, M. Fleischhauer, T. Pfau, H. Giessen, *Nat. Mater.* **8**, 758 (2009)
22. L. Cong, M. Manjappa, N. Xu, I. Al-Naib, W. Zhang, R. Singh, *Adv. Opt. Mat.* **3**, 1537 (2015)
23. B. Metzger, T. Schumacher, M. Hentschel, M. Lippitz, H. Giessen, *ACS Photonics* **1**, 471 (2014)
24. B. Gallinet, *Fano Resonances in Plasmonic Nanostructures: Fundamentals, Numerical Modeling and Applications* (Ecole Polytechnique Federale De Lausanne, These 5299, 2012)
25. B. Gallinet, T. Siegfried, H. Sigg, P. Nordlander, O.J.F. Martin, *Nano Lett.* **13**, 497 (2013)
26. H. Feshbach, *Ann. Phys.* **19**, 287 (1962)
27. A.K. Bhatia, A. Temkin, *Phys. Rev. A* **29**, 1895 (1984)
28. E. Prodan, C. Radloff, N. Halas, P. Nordlander, *Science* **302**, 419 (2003)
29. R. Adato, A. Artar, S. Erramill, H. Altug, *Nano Lett.* **13**, 2584 (2013)
30. S.H. Autler, C.H. Townes, *Phys. Rev.* **100**, 703 (1955)
31. N. Liu, S. Kaiser, H. Giessen, *Adv. Mater.* **20**, 4521 (2008)
32. B. Peng, S.K. Oznedir, W. Chen, F. Nori, L. Yang, *Nat. Commun.* **5**, 5082 (2014)
33. R. Taubert, M. Hentschel, J. Kstel, H. Giessen, *Nano Lett.* **12**, 1367 (2012)
34. R. Taubert, M. Hentschel, H. Giessen, *J. Opt. Soc. Am. B* **30**, 3123 (2013)
35. J.A. Fan, C. Wu, K. Bao, J. Bao, R. Bardhan, N.J. Halas, V.N. Manoharan, P. Nordlander, G. Shvets, F. Capasso, *Science* **328**, 1135 (2010)
36. M. Hentschel, M. Saliba, R. Vogelgesang, H. Giessen, A.P. Alivisatos, N. Liu, *Nano Lett.* **10**, 2721 (2010)
37. B. Hopkins, D.S. Filonov, S.B. Glybovski, A.E. Miroshnichenko, *Phys. Rev. B* **92**, 045433 (2015)
38. F. Hao, P. Nordlander, Y. Sonnefraud, P. Van Dorpe, S.A. Maier, *ACS Nano* **3**, 643 (2009)
39. N. Verellen, Y. Sonnefraud, H. Sobhani, F. Hao, V.V. Moshchalkov, P. Van Dorpe, P. Nordlander, S.A. Maier, *Nano Lett.* **9**, 1663 (2009)
40. A. Lovera, B. Gallinet, P. Nordlander, O.J.F. Martin, *ACS Nano* **7**, 4527 (2013)
41. J.B. Lassiter, H. Sobhani, M.W. Knight, W.S. Mielczarek, P. Nordlander, N.J. Halas, *Nano Lett.* **12**, 1058 (2011)
42. L. Novotny, B. Hecht, *Principles of Nano-Optics* (Cambridge University Press, 2006)
43. J. Butet, O.J.F. Martin, *Opt. Express* **22**, 29693 (2014)

# Chapter 6

## Storage and Retrieval of Electromagnetic Waves in Metamaterials by Dynamical Control of EIT-Like Effect



Toshihiro Nakanishi and Masao Kitano

**Abstract** The storage of light is one of the most significant applications of electromagnetically induced transparency (EIT) effects in atomic systems. It is also possible to mimic the EIT effect using artificial media, or metamaterials, which are based on coupled resonators. This chapter focuses on metamaterials that realize the storage and retrieval of electromagnetic waves in the same way as the atomic EIT system. We introduce tunable metamaterials that are loaded with variable capacitors, which realize dynamical modulation of the EIT-like effects and the control of asymmetric spectra unique to the Fano resonance. Experiments are performed to show that electromagnetic waves are stored and released coherently in a multi-layered metamaterial designed for the operation in the microwave region. In addition, we show the frequency conversion of the stored waves and the extension of the storage time using parametric amplification.

### 6.1 Introduction

Electromagnetically induced transparency (EIT) is a nonlinear optical effect that makes an opaque medium become transparent using an incident auxiliary light called a control light [1, 2]. Destructive interference between two excitation pathways causes the EIT effect in a three-level system. The transparency is induced in an extremely narrow spectral region. This indicates that the refractive index, which is related to the absorption through the Kramers-Kronig relation, is also modified in the transparent region. As a result, the group velocity of the light is significantly reduced owing to the highly dispersive characteristics of the medium. This slow-light effect has been applied to the storage of light, or “optical memory,” which is realized by the dynamical modulation of the group velocity [3–6].

It is also possible to mimic EIT effects such as the suppression of absorption and slow propagation by using classical systems, because the phenomenon of interference is universal among waves or oscillations. In fact, similarities to the EIT effect have

---

T. Nakanishi (✉) · M. Kitano

Department of Electronic Science and Engineering, Kyoto University, Kyoto, Japan  
e-mail: t-naka@kuee.kyoto-u.ac.jp

© Springer Nature Switzerland AG 2018

E. Kamenetskii et al. (eds.), *Fano Resonances in Optics and Microwaves*, Springer Series in Optical Sciences 219, [https://doi.org/10.1007/978-3-319-99731-5\\_6](https://doi.org/10.1007/978-3-319-99731-5_6)

137

been found in various classical systems, such as optical waveguides equipped with cavities [7–10], optomechanical systems [11–13], acoustic systems [14], and electric circuits [15]. Recently, the implementation of the EIT effects using metamaterials, or EIT-like metamaterials, has attracted considerable attention. EIT-like metamaterials respond to electromagnetic waves in the same way as atomic EIT media, and this is because the effective medium parameters of EIT-like metamaterials are expressed in the same form as those of the atomic EIT medium. Unlike atomic media, EIT-like metamaterials can be realized in various frequency regions by designing the structure, dimensions, and materials of the metamaterial constituents, or meta-atoms. In fact, since the experimental demonstrations of the EIT-like effect in metamaterials were first reported in the microwave frequency region [16, 17], the investigation of EIT-like metamaterial has been extended to higher frequencies, including terahertz [18–20] and optical regimes [21–25]. Owing to the sharp spectral response and field enhancement of highly localized modes, EIT-like metamaterials are suited to various applications, including high-accuracy sensing [26–29], the manipulation of near fields [30], surface plasmon control [31], nonreciprocal transmission [32–34], lasing spacers [35], the enhancement of nonlinearity [36], and absorption enhancement [37, 38].

For practical applications, active control of the metamaterials is important [39]. In particular, the control of conductivity in metamaterial constituents is often utilized to modulate the function of EIT-like metamaterials. In microwave regions, tunable EIT-like metamaterials have been demonstrated in various ways using nonlinear diodes [40], superconductors [41, 42], and air-discharge plasma [43]. For higher frequencies, conductivity modulation by photocarrier excitation in semiconductors has been widely investigated [44–46] owing to the fast modulation response. In addition, microelectromechanical system (MEMS) technologies enable the tuning of the EIT-like effect by the reconfiguration of metamaterial structures [47].

The above methods have achieved the control of the EIT-related phenomena concerned with the sharp transparency or slow group velocity, but they do not address the storage of electromagnetic waves, which is realized by the dynamical control of the EIT-like effect. In this chapter, we introduce a tunable EIT-like metamaterial loaded with variable capacitors, and we demonstrate the storage and retrieval of electromagnetic waves in the metamaterial. In addition, we demonstrate the frequency conversion during the storage process, and show a way of extending the storage time by parametric amplification using a double EIT-like metamaterial that exhibits two EIT-like properties for fundamental waves and second harmonic waves.

## 6.2 Electromagnetically Induced Transparency in Atomic Systems

The EIT effect can be found in a three-level system interacting with two external fields, as shown in Fig. 6.1. Assume that a probe light with an oscillating electric

**Fig. 6.1** Three-level system interacting with probe and control light

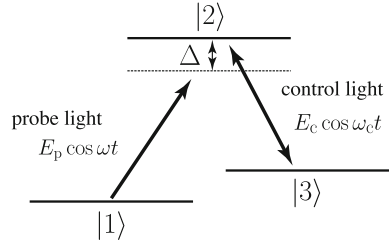
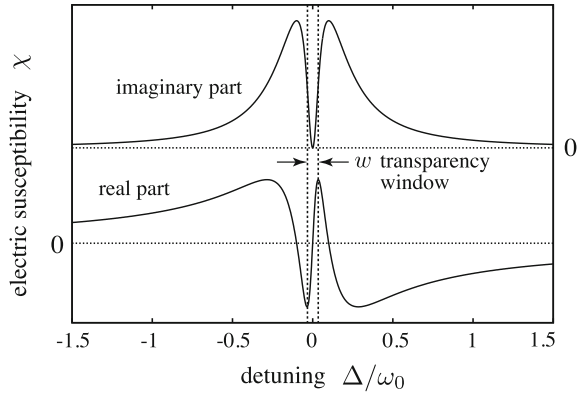


**Fig. 6.2** Electric susceptibility of atomic EIT medium for  $\gamma_2 = 0.5\omega_0$ ,  $\gamma_3 = 0$ ,  $\Omega_c = 0.2\omega_0$ . Imaginary part (top) and real part (bottom). The detuning  $\Delta$  is normalized by the frequency of the  $|1\rangle$ - $|2\rangle$  transition,  $\omega_0$



field  $E_p \cos \omega t$  induces the transition from  $|1\rangle$  to  $|2\rangle$  with a detuning  $\Delta$ , and the other field  $E_c \cos \omega_c t$ , called the control light, connects the transition between  $|3\rangle$  and  $|2\rangle$  with no detuning. We obtain an electric susceptibility for the probe light using the electric dipole moment for the probe-light transition  $p_p$  and the atomic density  $N$  as follows [48]:

$$\chi = \frac{i|p_p|^2 N}{2\epsilon_0 \hbar} \frac{i\Delta + \frac{\gamma_3}{2}}{\left(i\Delta + \frac{\gamma_2}{2}\right)\left(i\Delta + \frac{\gamma_3}{2}\right) + \left|\frac{\Omega_c}{2}\right|^2}. \tag{6.1}$$

The relaxation rate of the coherence between  $|1\rangle$  and  $|2\rangle$  ( $|1\rangle$  and  $|3\rangle$ ) is represented by  $\gamma_2$  ( $\gamma_3$ ), and the frequency of the Rabi oscillation induced by the control light is given by  $\Omega_c$ , which is proportional to the electric field of the control light.

The spectral shape of the susceptibility for the ideal case  $\gamma_3 = 0$  is illustrated in Fig. 6.2. The absorption spectrum given by the imaginary part of the susceptibility exhibits sharp transparency in a broad absorption line, which is a typical characteristic of the EIT effect. The width of the transparency window,  $w$ , is proportional to  $|\Omega_c|^2$ , or the intensity of the control light. In addition to the absorption profile, the refractive index, which is given by the square root of the real part of the susceptibility, is

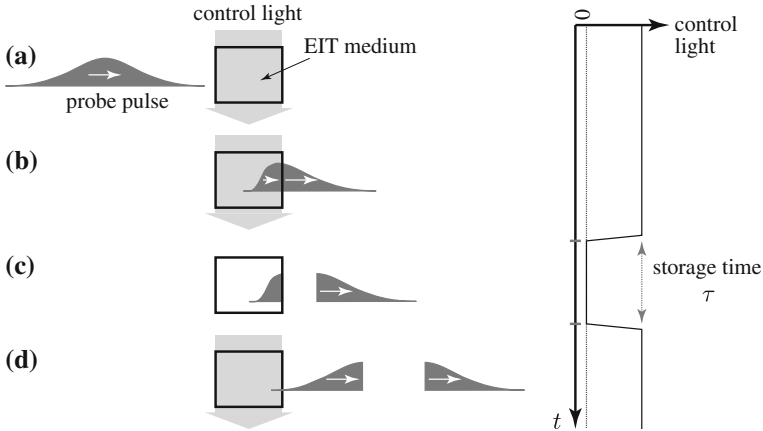


**Fig. 6.3** a Schematic diagram of light storage using EIT effect in an atomic medium. Light-storage procedures are divided into three phases: **b** slow-propagation phase; **c** storage phase; and **d** retrieval phase. The intensity of the control light, which varies as a function of time,  $t$ , is also shown on the right-hand side of the diagram

significantly modified in the transparency window. Consequently, the group velocity of the probe light is dramatically reduced. Hau et al. successfully reduced the group velocity to 17 m/s in a laser-cooled atomic gas [49]. They prepared a single-shot pulse with a duration of  $2.5 \mu\text{s}$  and a pulse length of 750 m in a vacuum, and fed it into the EIT medium. Because of the slow propagation in the medium, the pulse length was compressed into  $43 \mu\text{m}$  in the medium.

It is possible to realize the storage of light in the medium by dynamically controlling the states of the EIT effect. Suppose that a probe pulse interacts with a medium composed of three-level atoms, as shown in Fig. 6.3a. In the first phase, the intensity of the control light is kept constant and the probe pulse slowly travels in the medium, as shown in Fig. 6.3b. Then, the control light is gradually reduced, and the probe pulse is further slowed down. The pulse is stored in the medium when the control light is eventually turned off, as shown in Fig. 6.3c. Then, the stored pulse can be restarted by restoring the control light, as shown in Fig. 6.3d. The duration without the control light,  $\tau$ , determines the storage time. If the medium stores a fraction of the probe pulse, as shown in Fig. 6.3c, the resultant signal is split into two parts with a separation of time  $\tau$ , as shown in Fig. 6.3d. If the medium is sufficiently thick, the whole pulse can be stored in the medium. In that case, the released pulse is identical to the original one because the freezing and releasing processes are carried out coherently.



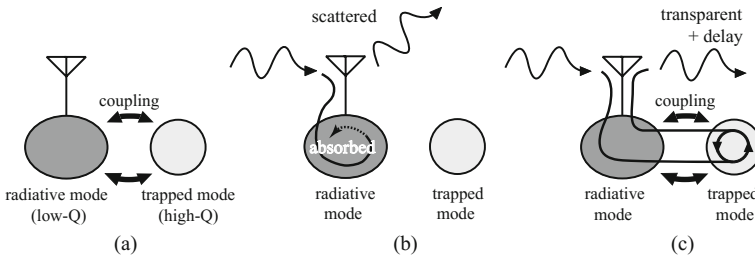


**Fig. 6.4** **a** Coupled resonator model of the EIT-like metamaterial. **b** Interaction with external waves without resonator coupling. **c** Interaction with external waves with resonator coupling

### 6.3 Metamaterial Analog to Atomic EIT Effect

#### 6.3.1 Coupled Resonator Model

The quantum effect based on the wave nature can be partially or perfectly realized even in classical systems, such as coupled oscillators [50, 51]. The EIT effect is also mimicked by the coupled oscillator composed of two resonators with different quality factors [15]. Based on the classical analogy, various types of metamaterials that mimic the EIT effect, or EIT-like metamaterials, have been proposed for various frequency ranges, ranging from microwave to optical regions.

Before showing actual structures of EIT-like metamaterials, we outline the EIT-like effect in metamaterials using the concept model shown in Fig. 6.4a. The circles represent two resonant modes, which are called the “radiative mode” and “trapped mode.” The antenna attached to the radiative mode symbolically shows the function that interacts with propagating electromagnetic waves. In other words, the radiative mode can be directly excited by the incidence of the external waves. However, the trapped mode is uncoupled with the external waves.

In the absence of the coupling between the radiative mode and the trapped mode, as shown in 6.4b, the energy excited by propagating waves in the radiative mode is scattered into free space or absorbed in the radiative mode, and the transmission drops at the resonant frequency. The quality factor of the radiative mode is low owing to the scattering dissipation, called the radiation loss, even in the ideal case where intrinsic losses such as Ohmic or dielectric losses are negligible.

If the radiative mode and the trapped mode are coupled with each other, as shown in 6.4c, the electromagnetic response of the metamaterial is significantly modified. Assuming that the resonant frequencies of these two modes are the same and the dissipation of the trapped mode is negligible, the energy received through the radiative mode is effectively transferred into the trapped mode for the incidence of the propagating waves at the resonant frequency. The energy temporarily stored in the trapped mode is then retransferred into free space through the radiative mode. In the steady state, two excitation pathways of the radiative mode from the incident waves

and from the oscillation in the trapped mode are balanced so that no oscillations are excited in the radiative mode. As a result, the absorption or scattering loss is significantly suppressed owing to the small dissipation of the trapped mode. In the transmission spectrum, the width of the transparency window is proportional to the coupling strength. In addition to the transparency, the temporal storage in the trapped mode causes some delay, and the group velocity of the metamaterial for the input waves is significantly reduced. It is known that the smaller the coupling, the slower the group velocity. This is because the smaller coupling results in longer storage in the trapped mode. The above properties, such as sharp transparency and slow propagation for small coupling, can be regarded as classical counterparts to the atomic EIT effect. In fact, the electric susceptibility of the metamaterial, which determines the electric response of propagating waves, can be expressed in the same form as that of the atomic EIT system given by (6.1) [52].

It should be noted that the EIT-like effect is closely related to the Fano resonance, which is characterized by an asymmetric spectral line shape [53, 54], and various metamaterials with Fano resonances based on coupled resonators have been proposed [55]. The EIT effect can be regarded as a special case of the Fano resonance, where the resonant frequencies of the radiative mode and the trapped mode coincide with each other [56].

### 6.3.2 Design of EIT-like Metamaterials

A straightforward way to implement a metamaterial based on the coupled resonator model described in the previous section is to combine two resonant structures, one of which effectively interacts with external waves, and the other has a low-loss resonant mode. As a typical example, an EIT-like metamaterial is shown in Fig. 6.5a. The unit structure of the metamaterial is decomposed into two structures, as shown in Figs. 6.5b and c, with the charge distributions of the resonant modes. The electric-dipole oscillation in Fig. 6.5b is used as the radiative mode, and the electric quadrupole oscillation in Fig. 6.5c is used as the trapped mode. From the normal incidence of electromagnetic waves with the polarization shown in Fig. 6.5a, only the radiative mode is directly excited. If the separation  $d$  is close enough to induce the coupling

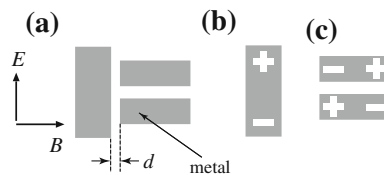
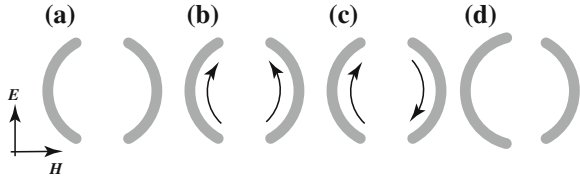


**Fig. 6.5** **a** EIT-like metamaterial proposed by Zhang et al. [52]. **b** Dipole antenna. **c** Pair of metallic stripes. The symbols “+” and “-” represent the charge distributions of each resonant mode

**Fig. 6.6** EIT-like metamaterial proposed in [16]. **a** Symmetric split ring. **b** Radiative mode. **c** Trapped mode. **d** Asymmetric split ring



between these two structures, the EIT-like effects, i.e., sharp transparency and slow propagation, can be observed. A smaller  $d$  results in a wider transparency window.

The sharp transparency in metamaterials was first demonstrated in the microwave band [16]. The design is different from the EIT-like metamaterials composed of two separate resonators, as in the previous example shown in Fig. 6.5a; however, the operation of the metamaterial can also be explained by the coupled resonator model. First, we consider the symmetric split ring resonator composed of two identical metallic arcs, as shown in Fig. 6.6a. The structure has two resonant modes, one of which is formed by symmetric currents in two arcs, as shown in Fig. 6.6b, and the other is formed by anti-symmetric currents, as shown in Fig. 6.6c. The former mode induces an electric dipole moment, which is easily excited by the normally incident plane waves, with the polarization defined as in Fig. 6.6a, and it works as a radiative mode. However, the latter mode induces a magnetic moment, which is uncoupled with the external waves and works as a trapped mode with high quality factor. For the symmetric split ring resonator, because these two modes are eigenmodes, or uncoupled with each other, only the radiative mode is excited by the external waves.

Next, we consider that some asymmetry is introduced in the structure, as shown in Fig. 6.6d. In this configuration, the radiative mode, as shown in Fig. 6.6b, and the trapped mode, as shown in Fig. 6.6c, are no longer eigenmodes, and they are coupled. Consequently, EIT-like effects are induced.

## 6.4 Storage and Retrieval of Electromagnetic Waves in Metamaterials

### 6.4.1 Procedures for Storage and Retrieval of Electromagnetic Waves

In Sect. 6.2, we introduced the procedures for achieving light storage in atomic EIT media, and we explained that dynamical control of the EIT effect is required by modulating the control light. Even in EIT-like metamaterials, dynamical switching between EIT on and EIT off states enables the storage of electromagnetic waves. In this section, we present the procedures for electromagnetic-wave storage in EIT-like metamaterials using the concept model, as illustrated in Fig. 6.7. First, the metamaterial is prepared in an EIT on state, where the radiative and trapped modes are

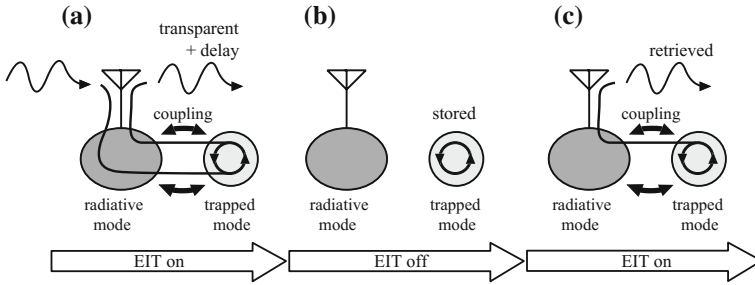


**Fig. 6.7** Procedures for the storage and retrieval of electromagnetic waves. **a** Slow-propagation phase. **b** Storage phase. **c** Retrieval phase

coupled. If the spectrum of the incident pulse is in the transparency window, the pulse is transmitted through the metamaterial with a transit time or group delay, which corresponds to the time taken for the electromagnetic energy received in the radiative mode to be transferred to the trapped mode and to return to the radiative mode through coupling. During the propagation, if the metamaterial is changed into an EIT off state, where the two resonant modes are decoupled, the energy is captured in the trapped mode. Then, this energy is released by returning the metamaterial to the EIT on state to reintroduce the coupling.

### 6.4.2 Tunable EIT-Like Metamaterial

Figure 6.8a illustrates the unit cell of a tunable EIT-like metamaterial for the storage of electromagnetic waves [57]. The design of the EIT-like metamaterial is based on EIT-like metamaterials with broken structural symmetry [16, 20, 58]. It is assumed that one or both of the capacitances of two capacitors, which are denoted by  $C_1$  and  $C_2$ , can be controlled, and that external fields have the polarization as denoted

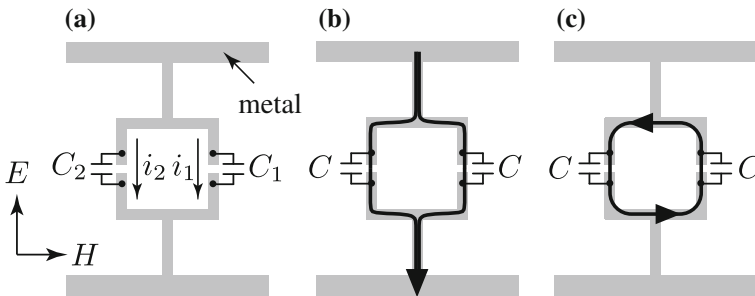


**Fig. 6.8** **a** Unit cell of tunable EIT-like metamaterial. **b** Radiative mode. **c** Trapped mode

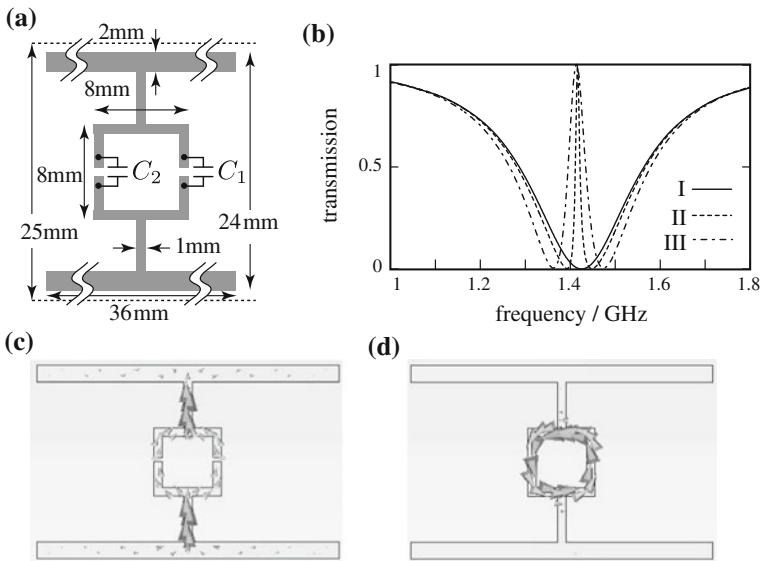


**Fig. 6.9** **a** Unit structure and its dimensions. The thickness and permittivity of the substrate are 0.8 mm and 3.3, respectively. **b** Transmission spectra obtained by electromagnetic simulation for three cases: (I)  $C_1 = C_2 = 2.1$  pF; (II)  $C_1 = 1.91$  pF,  $C_2 = 2.33$  pF; (III)  $C_1 = 1.75$  pF,  $C_2 = 2.63$  pF. **c** Current distribution at the resonance for case (I). **d** Current distribution at the center of transparency for case (II). Periodic boundary conditions are imposed for the unit cell with a size of 120 mm  $\times$  25 mm. The incident waves are vertically polarized. Adapted with permission from [57]. Copyrighted by the American Physical Society

on the left-hand side of the diagram. For the case of  $C_1 = C_2$ , the currents in the structure form two eigenmodes, as shown in Fig. 6.8b, c, which are characterized by the relative phases of the currents flowing in the two capacitors, as expressed by  $i_1$  and  $i_2$ . The symmetric current, which is shown in Fig. 6.8b, forms an electric dipole oscillation, which is excited by external fields and is highly radiative. On the other hand, the anti-symmetric current, as shown in Fig. 6.8c, forms a loop current, or magnetic dipole oscillation, which is less radiative and is uncoupled to the external fields. The former mode could be a radiative mode and the latter mode could be a trapped mode. The resonant frequencies for these two modes should be closely located. In the case of  $C_1 = C_2$ , there is no EIT effect because the two modes are eigenmodes and are decoupled. By breaking the symmetry, i.e.,  $C_1 \neq C_2$ , these two modes are coupled and EIT-like effects can be expected. The degree of the asymmetry determines the coupling strength and the width of the transparency window. The dynamical control of the structural symmetry with variable capacitors contributes to the dynamical modulation of the EIT-like effects, which is required for the storage of electromagnetic waves.

Figure 6.9a shows a unit cell of the metamaterial with its dimensions. The transmission spectra calculated by electromagnetic simulations are shown in Fig. 6.9b

for three cases: (I)  $C_1 = C_2 = 2.1$  pF; (II)  $C_1 = 1.91$  pF,  $C_2 = 2.33$  pF; (III)  $C_1 = 1.75$  pF,  $C_2 = 2.63$  pF. For the symmetric case,  $C_1 = C_2$ , the transmission is depressed over a broad spectrum. At the center of the transmission depression, a resonant current is induced on the metal, as shown in Fig. 6.9c, which corresponds to the radiative mode. On the other hand, for the other cases,  $C_1 \neq C_2$ , sharp transparent regions appear in the broad resonant lines. At the transmission peak, a resonant loop current is induced, as shown in Fig. 6.9d, and this can be regarded as the trapped mode. We confirmed that the increase in the degree of asymmetry leads to the broadening of the transparency window. As shown in this study, it is possible to control the width of the transparency window without changing the center of the window. This is done by keeping the composite capacitance in the loop,  $C_L = C_1 C_2 / (C_1 + C_2)$ , constant. In general cases where  $C_1$  and  $C_2$  are controlled independently, the mismatch of the resonant frequencies between the radiative mode and the trapped mode results in asymmetric transmission spectra that are unique to Fano resonance, and this is demonstrated in Sect. 6.4.4. The tunability of the Fano resonance is one of the significant functionalities of the metamaterials.

The minimum width of the transparency window is limited by the linewidth of an isolated trapped mode, which is determined by the radiation loss of the loop current and the Ohmic loss in the capacitors and metal. The transparency peak is deteriorated by the loss in the trapped mode.

For an experimental demonstration of the tunable EIT-like effect in the microwave band, the unit structures were fabricated using a copper film on a dielectric substrate with dimensions  $(W \times H \times D) = (120 \text{ mm} \times 25 \text{ mm} \times 0.8 \text{ mm})$  and a permittivity of 3.3. For the capacitance  $C_1$ , we used a varactor diode. The capacitance  $C_1$  is a function of the applied bias voltage  $V$ , which is fed through a bias circuit. A 1.2 pF normal capacitor with low Ohmic loss was introduced for the other capacitance  $C_2$ . In this case, unlike the simulation in which  $C_L$  is kept constant, the center and width of the transparent window are expected to change with  $C_1(V)$ .

The results of transmission measurements for a single-layered metamaterial placed in an open-type waveguide are shown in Fig. 6.10a. For  $V = -3.6$  V, we observe a broad depression in the transmission spectrum, which indicates that the unit cell of the metamaterial is symmetric, including the capacitances, i.e.,  $C_1(V) \simeq C_2 = 1.2$  pF. By breaking the symmetry, we can observe transparency windows. When increasing  $C_1(V)$  by reducing  $|V|$ , the asymmetry of the structure is enhanced and the transparency window becomes wider. The transmission peaks shift to lower frequencies because they correspond to the resonant frequencies of the trapped modes, which are determined by the loop capacitance  $C_L$ . This is the reason for the difference with the simulation results, where both capacitances are changed while  $C_L$  is kept constant.

The group delay of the three-layered metamaterial can be estimated by measuring the transit time of pulses. The carrier frequency of the pulse was tuned to a transparent peak for each bias voltage. Figure 6.10b shows observed signal intensity that is transmitted through the three-layered metamaterial with bias voltages of  $V = 0, -0.4$  V, and  $-0.8$  V. For comparison, the output signal in the absence of the metamaterial is also displayed. Each signal passing through the metamaterial is

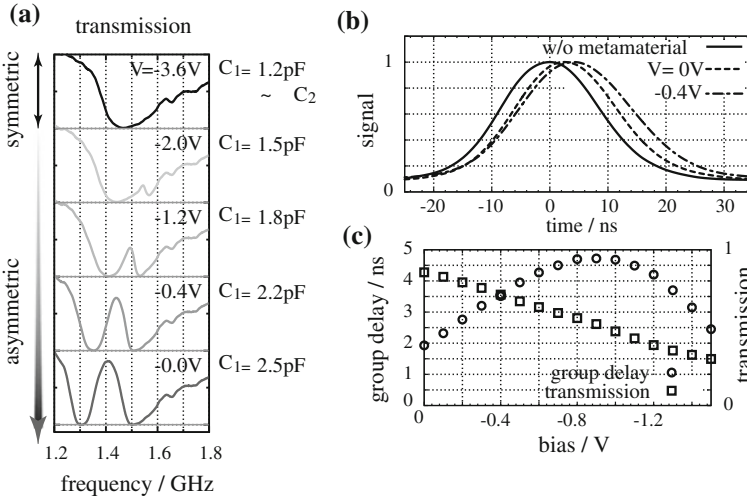


**Fig. 6.10** Experimental results. **a** Transmission spectra of EIT-like metamaterial for  $V = 0, -0.4, -1.2, -2.0, -3.6$  V. **b** Output intensity for pulses propagating through the metamaterial with  $V = 0, -0.4$  V, and for the case without the metamaterial. **c** Group delays and transmission peaks for various  $V$ . Adapted with permission from [57]. Copyrighted by the American Physical Society

delayed, depending on the bias voltage, while the shape of the pulse is maintained. The graph in Fig. 6.10c represents the group delays and transmissions at the center of transparency windows. From  $V = 0$  to  $V = -0.9$  V, the group delay increases with  $|V|$ . This is because the transparency window becomes sharper for larger  $|V|$  and the group velocity in the metamaterial becomes slower. For  $V < -0.9$  V, the transparency windows are corrupted and the group delay is decreased.

### 6.4.3 Storage and Retrieval of Electromagnetic Waves

Dynamical control of the EIT-like effect in metamaterials enables us to realize the storage and retrieval of electromagnetic waves, as discussed in Sect. 6.4.1. For our experimental demonstration, we used two bias voltages:  $V = -0.4$  V for the “EIT on” state and  $V = -3.6$  V for the “EIT off” state. A 35 ns pulse with a carrier frequency of 1.440 GHz, which is located at the center of the transparency window for  $V = -0.4$  V, is fed into the waveguide with the three-layered metamaterial. The initial state of the metamaterial is set to the “EIT on” state with the bias voltage  $V = -0.4$  V. When the rear part of the pulse enters the metamaterial, the state is changed to the “EIT off” state by changing the bias voltage to  $V = -3.6$  V. During this period, the energy of the electromagnetic wave in the metamaterial is captured in the trapped modes. After some time period  $\tau$ , which corresponds to the storage

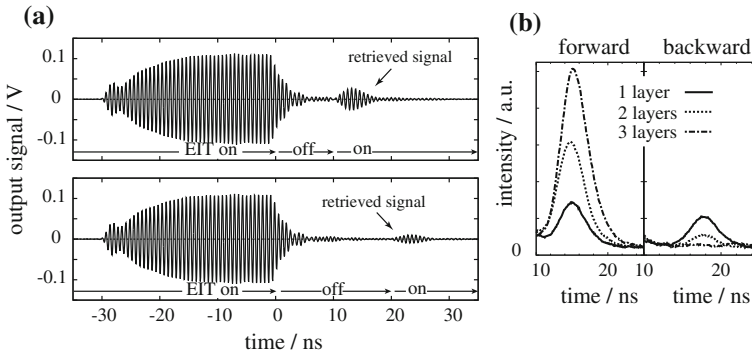


**Fig. 6.11** **a** Demonstration of storage and retrieval of electromagnetic waves for storage times of  $\tau = 10$  ns (top) and  $\tau = 20$  ns (bottom). **b** Intensity of the retrieved signals propagating in forward and backward directions. Adapted with permission from [57]. Copyrighted by the American Physical Society

time, the state is returned to the “EIT on” state to release the stored energy into the waveguide.

Figure 6.11a shows the output signal transmitted through the metamaterial under the modulation of the bias voltage for storage times of  $\tau = 10$  ns and  $\tau = 20$  ns. The states of the metamaterial are superimposed at the bottom of each graph. It is confirmed that the signals are dropped during the “EIT off” state owing to the storage of the electromagnetic waves, and the retrieved signals can be observed after the reintroduction of the EIT effect. This is clear evidence that the tunable EIT-like metamaterial can store and release the electromagnetic waves in the same way as atomic EIT media. From results obtained for various values of  $\tau$ , the height of the retrieved pulses decays exponentially with a time constant of 6.3 ns, which corresponds to the lifetime of the trapped mode.

If the metamaterial “remembers” the phase distribution of the input pulse correctly, the retrieved signal should be released in the forward direction. Figure 6.11b shows the intensity of the retrieved signals released in the forward (backward) direction on the left (right) side for  $n$ -layered metamaterials ( $n = 1, 2, 3$ ). For a single-layered metamaterial,  $n = 1$ , retrieved signals with almost the same amplitudes are released in opposite directions because the energy is radiated from a single meta-atom. As  $n$  increases, the retrieved signals are enhanced in the forward direction and are suppressed in the backward direction. This indicates that the oscillation in each trapped mode during the storage process “inherits” the relative phase of the oscillating electric field of the incident waves at each location, and the retrieved pulse reproduces the phase distributions of the incident waves. These results suggest that by increasing the number of layers, the metamaterial could potentially store the whole of an input pulse that has an arbitrary temporal shape. It is also possible to store waves with arbitrary transverse modes and any polarizations by appropriately distributing the meta-atoms.



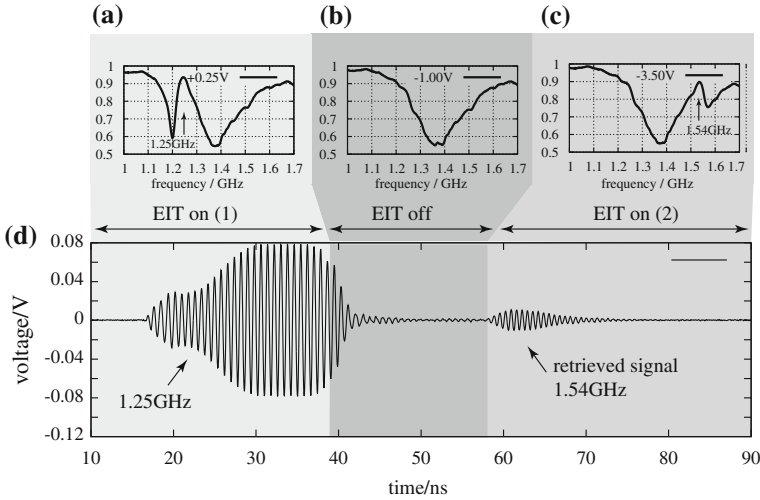


**Fig. 6.12** Transmission spectra for **a**  $V = 0.25$  V, **b**  $V = -1.00$  V, and **c**  $V = -3.50$  V. **d** Demonstration of frequency conversion using the storage and retrieval processes

### 6.4.4 Frequency Conversion of Electromagnetic Waves

Because the stored energy is released from the trapped mode, the frequency of the retrieved signal can be modified by changing the resonant frequency of the trapped mode. For an experimental demonstration of the frequency conversion, only the capacitance  $C_2$  is changed to 1.8 pF. The transmission spectra of the metamaterial for various bias voltages,  $V = 0.25$  V,  $-1.00$  V, and  $-3.50$  V, are shown in Fig. 6.12a–c. The EIT-like effect can be observed for  $V = 0.25$  V and  $V = -3.50$  V. The transparency windows are located at different frequencies, i.e., 1.25 GHz for  $V = 0.25$  V and 1.54 GHz for  $V = -3.50$  V, which correspond to the resonant frequencies of the trapped modes. Both of these cases show asymmetric transmission spectra that are peculiar to the Fano resonance, which results from the resonant-frequency mismatch between the radiative mode and the trapped mode. However, the spectrum for  $V = -1.00$  V shows a single resonant dip without the EIT-like effect.

For the frequency conversion, the varactor diode of the metamaterial is initially biased at 0.25 V, and a pulse at 1.25 GHz is sent to the metamaterial. When the rear part of the pulse enters the metamaterial, the bias voltage is changed to  $V = -1.00$  V in order to deactivate the EIT-like effect for the storage of the pulse. After some time interval  $\tau$ , the bias voltage is changed to  $V = -3.50$  V to release the stored energy. Figure 6.12d shows the output signal transmitted through the metamaterial for the storage time  $\tau = 20$  ns. As expected, the output signal is dropped during the “EIT-off” period ( $V = -1.00$  V) because the energy is captured in the trapped mode. The stored energy is released by activating the EIT-like effect with the bias voltage  $V = -3.50$  V. It should be noted that the retrieved signal is composed of a different

frequency around 1.54 GHz, which corresponds to the center of the transparency window for the final state  $V = -3.50$  V, as shown in Fig. 6.12c. This indicates that the retrieved signal is emitted from the trapped mode, whose resonant frequency is shifted from 1.25 to 1.54 GHz during the storage and retrieval processes. Unlike conventional frequency conversion using frequency mixing, the conversion frequency can be tuned within the linewidth of the radiative mode by changing the capacitance  $C_1$ . In addition, the efficiency of the frequency conversion is independent of the input signal, and even small signals can be converted.

## 6.5 Loss Compensation by Parametric Amplification for Extension of Storage Time

During the process of the electromagnetic-wave storage in the metamaterial, the storage time is limited by the lifetime of the trapped mode. In the ideal case, the storage time is determined by the radiation loss of the trapped mode. For the metamaterial introduced in the previous section, the Ohmic loss in the varactor diode is dominant, and it seriously degrades the function of the electromagnetic-wave storage. It is possible to extend the maximum storage time by introducing some gain in the trapped mode. In this section, we introduce loss compensation to realize an extension of the storage time by parametric amplification.

Parametric amplification is a nonlinear process, where a fundamental mode oscillating at  $\omega$  is amplified by performing parameter modulation at  $2\omega$ . Here, we consider a double EIT-like metamaterial that has EIT-like properties for both the fundamental waves and second harmonic waves. The unit cell of the metamaterial is represented in Fig. 6.13a, which is a composite structure composed of a primary structure, as shown in Fig. 6.13b, and a secondary structure, as shown in Fig. 6.13c. These two structures are printed on each side of a substrate with a lateral shift of  $d$ . Three capacitors,  $C_1$ ,  $C_2$ , and  $C_3$ , are introduced in the primary structure, and only  $C_1$  is a nonlinear element, whose capacitance is a function of the applied voltage,  $C_1(V)$ . The primary structure has three resonant modes and the secondary structure has an electric-dipole resonant mode. All of the resonant modes are summarized in Fig. 6.13d, which are labeled by R1, T1, T2, and R2, respectively. Two of the resonant modes in the primary structure, R1 and T1, are the same as those of the tunable EIT-like metamaterial discussed in the previous section, and they are responsible for the EIT-like effect for fundamental waves. The other resonant mode, T2, which is derived from the additional structure including  $C_3$ , works as a trapped mode for second harmonic waves owing to the low radiation loss. The resonance R2 in the secondary structure works as a radiation mode for the second harmonic waves. The resonant modes T2 and R2 are coupled with each other through the magnetic coupling, which depends on the separation  $d$ .

In the presence of the second harmonic waves, the trapped mode T2 is excited owing to the EIT-like effect induced by the magnetic coupling of the R2 and T2

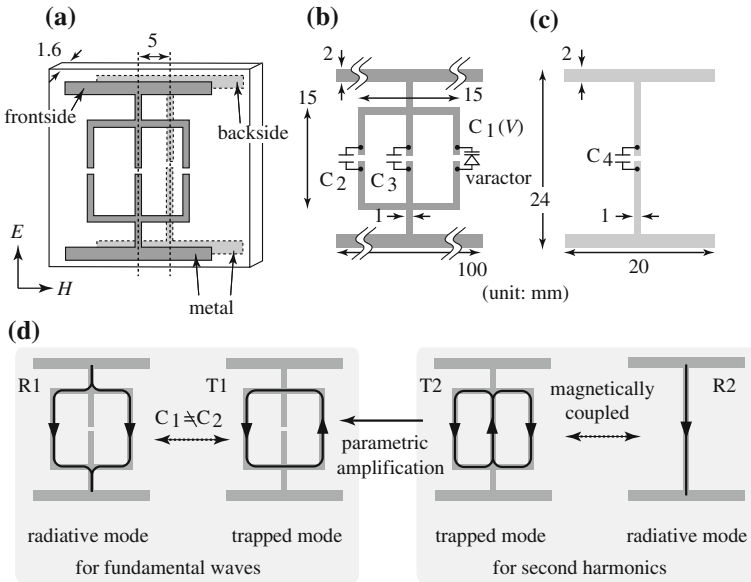


**Fig. 6.13** **a** Unit structure of double EIT-like metamaterial (Capacitances are omitted.). **b** Primary structure. **c** Secondary structure. **d** Resonant modes and their functions

modes, and this effectively modulates the capacitance  $C_1(V)$ . The modulation of the capacitance contributes to the parametric amplification (or attenuation) of the fundamental waves in the trapped mode. In other words, two trapped modes, T1 and T2, are coupled through the parametric process in the nonlinear element, or the varactor diode. The parametric gain depends on the relative phase of the fundamental waves and the second harmonic waves.

### 6.5.1 Parametric Amplification of Continuous Waves

This section deals with the parametric amplification of continuous waves in the double EIT-like metamaterial. The structures are printed on a dielectric substrate with a permittivity of 3.3 and thickness of 1.6 mm. A varactor diode is introduced as  $C_1$ , which varies with the applied voltage. The capacitances are  $C_2 = 1.5$  pF,  $C_3 = 0.7$  pF, and  $C_4 = 2.0$  pF. The shift  $d$  is set to 5 mm. The transmission spectrum for the single-unit structure placed in an open-type waveguide with  $V = 0$  is shown in Fig. 6.14a for small signals. As expected, two EIT spectra are observed around 0.82 and 1.64 GHz. For parametric amplification, the mixed waves of a weak probe signal at  $f_1 = 0.82$  GHz with  $-6.9$  dBm and a strong pump at  $f_2 = 1.64$  GHz with 17 dBm were sent to the waveguide. As discussed, the modulation of  $C_1(V)$  at  $f_2 = 2f_1$  induces some parametric gain (or loss) in the T1 mode oscillating at

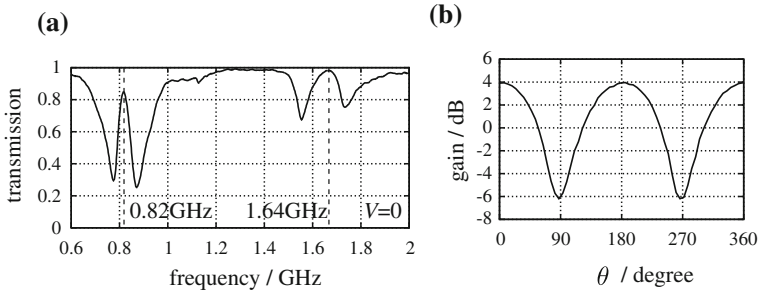


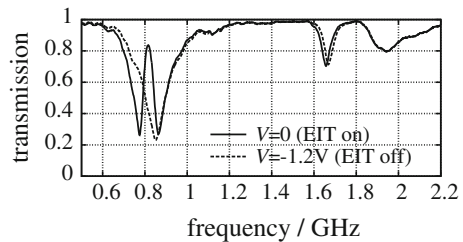
**Fig. 6.14** **a** Transmission spectrum for  $C_2 = 1.5$  pF,  $C_3 = 0.7$  pF, and  $C_4 = 2.0$  pF. **b** Parametric gain as a function of the phase of fundamental waves

the frequency of  $f_1$ . The metamaterial re-radiates the fundamental waves from the trapped mode T1 through the radiative mode R1, and the incident waves are amplified or attenuated, depending on the relative phase  $\theta$  between the fundamental waves and second harmonic waves. Figure 6.14b shows the parametric gain, which is given by the transmission power divided by the input power of the probe waves (The origin of  $\theta$  is chosen at the location to maximize the gain.). The parametric gain varies with a period of  $\pi$ , which is a typical characteristic of the parametric process [59]. The maximum gain is 4 dB. In the case of unity gain (0 dB), the dissipation in the radiation mode and the trapped mode is balanced by the parametric gain, and an ideal EIT-like effect is realized by the loss compensation.

### 6.5.2 Extension of Storage Time by Loss Compensation

In this section, we discuss the extension of the storage time by loss compensation through parametric amplification. The capacitances are  $C_2 = 1.5$  pF,  $C_3 = 0.6$  pF, and  $C_4 = 0.9$  pF. We adopted two states for the storage of electromagnetic waves: the EIT on state with  $V = 0$  and the EIT off state with  $V = -1.2$  V. The transmission spectra for these states are shown in Fig. 6.15. For the EIT on state, two EIT-like spectra are observed around  $f_1 = 0.82$  GHz and  $f'_2 = 1.80$  GHz. For the EIT off

**Fig. 6.15** Transmission spectra for  $C_2 = 1.5$  pF,  $C_3 = 0.6$  pF, and  $C_4 = 0.9$  pF in two cases:  $V = 0$  (solid line) and  $V = -1.2$  V (dotted line)



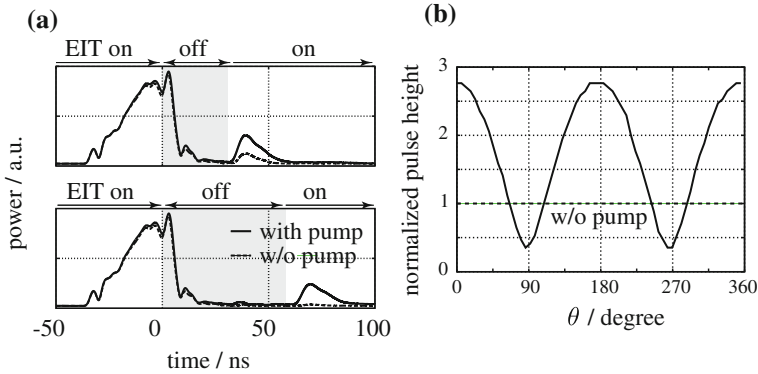


**Fig. 6.16** **a** Demonstration of electromagnetic-wave storage with double EIT-like metamaterial. **b** The height of retrieved signals as a function of the phase of the fundamental waves

state, the transparency window around  $f_1$  disappears. This is because the coupling between the R1 and T1 modes is turned off by satisfying  $C_1(V) \sim C_2$ .

The storage of electromagnetic waves oscillating around  $f_1$  can be demonstrated using the same procedure, as discussed in the previous section. The dotted lines in Fig. 6.16a show the intensity of the output signals from the waveguide with the three-layered metamaterial for the storage time  $\tau = 30$  ns (top) and  $\tau = 60$  ns (bottom). The states of the metamaterial are superimposed at the top of each graph. The retrieved pulse for  $\tau = 60$  ns is weaker than that for  $\tau = 30$  ns. The degradation of the retrieval is attributed to the damping in the T1 mode during the EIT off state.

The storage time can be extended by loss compensation, which is realized by illuminating pump waves to induce the parametric gain in the T1 mode. Note that the resonant frequency of the T1 mode in the EIT off state is around 0.90 GHz, which is slightly shifted from that in the EIT on state. The parametric amplification in the T1 mode can be realized by the incidence of strong pump waves at 1.80 GHz, which coincides with the location of the transparency window  $f'_2$  at a higher frequency. The solid lines in Fig. 6.16a represent the output signals for the probe pulse in the presence of the pump waves with the power of 17 dBm. The phase  $\theta$  of the fundamental wave is adjusted to maximize the retrieval efficiency. It is clear that the retrieved pulses are reinforced owing to the parametric amplification in the T1 mode. Figure 6.16b shows the height of the retrieved signals for various values  $\theta$ . The height is normalized by that in the case without the pump waves, and it is found that the parametric gain can be controlled by  $\theta$ .

In the experiment, the lifetime of the storage signal with the pump waves with 17 dBm is estimated to be about 380 ns, which is much longer than the lifetime 16 ns without parametric amplification. It is also possible to further increase the parametric amplification by increasing the pump power or by decreasing  $d$ , which results in a narrower transparency window at  $f'_2$ . In principle, the storage time could be extended as long as necessary using stable pump waves that are strong enough to offset the

loss by parametric amplification. In addition, we confirmed that the amplification becomes negligible by removing the second structure (Result is not shown here.). This is proof that the double EIT configuration contributes to the enhancement of the pump efficiency. The metamaterial can be considered as a doubly resonant metamaterial [60–62] that effectively enhances nonlinear interactions between the fundamental and second harmonic waves.

## 6.6 Conclusion

In this chapter, we presented dynamically tunable metamaterials that realize the storage and retrieval of electromagnetic waves in the same way as the atomic EIT medium. We demonstrated the “coherent” storage of electromagnetic waves in an EIT-like metamaterial that is designed for operation in the microwave frequency band. In addition, we showed the frequency conversion using the storage process and the extension of the storage time by parametric amplification in the double EIT metamaterial, which effectively enhances the nonlinear interaction between the fundamental and second harmonic waves. The experiments demonstrated the partial storage of an electromagnetic pulse propagating in the waveguide. However, in principle, metamaterials could store the whole pulse with any temporal or spatial modes by distributing the structures in three dimensions.

The EIT-like effect of the metamaterials presented in this chapter is different from the EIT effect in the strict sense, where the auxiliary light, called the control light, induces transparency. A recent study has shown a way to implement the true EIT effect [63], which has the potential to store electromagnetic waves in the exact same way as the atomic EIT system by the modulation of control waves [64].

The storage of electromagnetic waves and frequency conversion always require temporal modulation of the metamaterials. The use of “time-varying” metamaterials may open new avenues as “spatial-varying” metamaterials have led to the rapid development of transformation optics, including invisible cloaks [65, 66].

**Acknowledgements** This research was financially supported by JSPS KAKENHI Grants No. 22560041, No. 22109004, No. 25790065, No. 25287101, and No. 17K05075.

## References

1. S. Harris, *Phys. Today* **50**, 36 (1997)
2. M. Fleischhauer, A. Imamoglu, J.P. Marangos, *Rev. Mod. Phys.* **77**, 633 (2005)
3. M. Fleischhauer, M. Lukin, *Phys. Rev. Lett.* **84**, 5094 (2000)
4. D. Phillips, A. Fleischhauer, A. Mair, R. Walsworth, M. Lukin, *Phys. Rev. Lett.* **86**, 783 (2001)
5. C. Liu, Z. Dutton, C.H. Behroozi, L.V. Hau, *Nature* **409**, 490 (2001)
6. A. Turukhin, V. Sudarshanam, M. Shahriar, J. Musser, B. Ham, P. Hemmer, *Phys. Rev. Lett.* **88**, 023602 (2002)

7. S. Chu, B. Little, W. Pan, T. Kaneko, Y. Kokubun, I.E.E.E. Photon, Technol. Lett. **11**, 1426 (1999)
8. Q. Xu, S. Sandhu, M. Povinelli, J. Shakya, S. Fan, M. Lipson, Phys. Rev. Lett. **96**, 123901 (2006)
9. K. Totsuka, N. Kobayashi, M. Tomita, Phys. Rev. B **98**, 213904 (2007)
10. R.D. Kekatpure, E.S. Barnard, W. Cai, M.L. Brongersma, Phys. Rev. Lett. **104**, 243902 (2010)
11. Q. Lin, J. Rosenberg, D. Chang, R. Camacho, M. Eichenfield, K.J. Vahala, O. Painter, Nat. Photonics **4**, 236 (2010)
12. S. Weis, R. Rivière, S. Deléglise, E. Gavartin, O. Arcizet, A. Schliesser, T.J. Kippenberg, Science **330**, 1520 (2010)
13. A.H. Safavi-Naeini, T.P.M. Alegre, J. Chan, M. Eichenfield, M. Winger, Q. Lin, J.T. Hill, D.E. Chang, O. Painter, Nature **472**, 69 (2011)
14. I. Yoo, C.K. Han, D.S. Shin, K.J.B. Lee, J.W. Wu, H.S. Moon, O.B. Wright, S.H. Lee, Sci. Rep. **4**, 4634 (2014)
15. C.L. Garrido Alzar, M.A.G. Martinez, P. Nussenzveig, Am. J. Phys. **70**, 37 (2002)
16. V.A. Fedotov, M. Rose, S.L. Prosvirnin, N. Papasimakis, N.I. Zheludev, Phys. Rev. Lett. **99**, 147401 (2007)
17. N. Papasimakis, V.A. Fedotov, N.I. Zheludev, S.L. Prosvirnin, Phys. Rev. Lett. **101**, 253903 (2008)
18. S.Y. Chiam, R. Singh, C. Rockstuhl, F. Lederer, W. Zhang, A. Bettiol, Phys. Rev. B **80**, 153103 (2009)
19. Z. Li, Y. Ma, R. Huang, R. Singh, J. Gu, Z. Tian, J. Han, W. Zhang, Opt. Express **19**, 8912 (2011)
20. R. Singh, I.A.I. Al-Naib, Y. Yang, D. Roy Chowdhury, W. Cao, C. Rockstuhl, T. Ozaki, R. Morandotti, W. Zhang, Appl. Phys. Lett. **99**, 201107 (2011)
21. N. Liu, L. Langguth, T. Weiss, J. Kästel, M. Fleischhauer, T. Pfau, H. Giessen, Nat. Mater. **8**, 758 (2009)
22. J. Zhang, S. Xiao, C. Jeppesen, A. Kristensen, N.A. Mortensen, Opt. Express **18**, 17187 (2010)
23. W. Huang, Q. Wang, X. Yin, C. Huang, H. Huang, Y. Wang, and Y. Zhu, J. Appl. Phys. **109**, 114310 (2011)
24. R. Hokari, Y. Kanamori, K. Hane, J. Opt. Soc. Am. B **31**, 1000 (2014)
25. Y. Yang, I.I. Kravchenko, D.P. Briggs, J. Valentine, Nat. Commun. **5**, 5753 (2014)
26. B. Lahiri, A.Z. Khokhar, R.M. De La Rue, S.G. McMeekin, N.P. Johnson, Opt. Express **17**, 1107 (2009)
27. Z.G. Dong, H. Liu, J.X. Cao, T. Li, S.M. Wang, S.N. Zhu, X. Zhang, Appl. Phys. Lett. **97**, 114101 (2010)
28. N. Liu, T. Weiss, M. Mesch, L. Langguth, U. Eigenthaler, M. Hirscher, C. Sönnichsen, H. Giessen, Nano Lett. **10**, 1103 (2010)
29. F. Cheng, X. Yang, J. Gao, Sci. Rep. **5**, 14327 (2015)
30. S. Zhang, Z. Ye, Y. Wang, Y. Park, G. Bartal, M. Mrejen, X. Yin, X. Zhang, Phys. Rev. Lett. **109**, 193902 (2012)
31. X. Zhang, Q. Xu, Q. Li, Y. Xu, J. Gu, Z. Tian, C. Ouyang, Y. Liu, S. Zhang, X. Zhang, J. Han, W. Zhang, Sci. Adv. **2**, e1501142 (2016)
32. Y. Sun, Y. Tong, C. Xue, Y. Ding, Y. Li, H. Jiang, H. Chen, Appl. Phys. Lett. **103**, 091904 (2013)
33. S.H. Mousavi, A.B. Khanikaev, J. Allen, M. Allen, G. Shvets, Phys. Rev. Lett. **112**, 117402 (2014)
34. D. Floess, M. Hentschel, T. Weiss, H.U. Habermeier, J. Jiao, S.G. Tikhodeev, H. Giessen, Phys. Rev. X **7**, 021048 (2017)
35. N. Zheludev, S. Prosvirnin, N. Papasimakis, V. Fedotov, Nat. Photonics **2**, 351 (2008)
36. Y. Yang, W. Wang, A. Boulesbaa, I.I. Kravchenko, D.P. Briggs, A. Poretzky, D. Geohagan, J. Valentine, Nano Lett. **15**, 7388 (2015)
37. R. Taubert, M. Hentschel, J. Kästel, H. Giessen, Nano Lett. **12**, 1367 (2012)
38. L. Verslegers, Z. Yu, Z. Ruan, P.B. Catrysse, S. Fan, Phys. Rev. Lett. **108**, 083902 (2012)

39. I.V. Shadrivov, M. Lapine, Y.S. Kivshar, *Nonlinear, Tunable and Active Metamaterials* (Springer, Switzerland, 2015)
40. D. Meng, S. Wang, X. Sun, R. Gong, C. Chen, Appl. Phys. Lett. **104**, 261902 (2014)
41. C. Kurter, P. Tassin, L. Zhang, T. Koschny, A. Zhuravel, A. Ustinov, S. Anlage, C. Soukoulis, Phys. Rev. Lett. **107**, 043901 (2011)
42. O. Limaj, F. Giorgianni, A. Di Gaspare, V. Giliberti, G. de Marzi, P. Roy, M. Ortolani, X. Xi, D. Cunnane, S. Lupi, ACS Photonics **1**, 570 (2014)
43. Y. Tamayama, K. Hamada, K. Yasui, Phys. Rev. B **92**, 125124 (2015)
44. J. Gu, R. Singh, X. Liu, X. Zhang, Y. Ma, S. Zhang, S.A. Maier, Z. Tian, A.K. Azad, H.T. Chen, A.J. Taylor, J. Han, W. Zhang, Nat. Commun. **3**, 1151 (2012)
45. F. Miyamaru, H. Morita, Y. Nishiyama, T. Nishida, T. Nakanishi, M. Kitano, M.W. Takeda, Sci. Rep. **4**, 4346 (2014)
46. R. Yahiaoui, M. Manjappa, Y.K. Srivastava, R. Singh, Appl. Phys. Lett. **111**, 021101 (2017)
47. P. Pitchappa, M. Manjappa, C.P. Ho, R. Singh, N. Singh, C. Lee, Adv. Opt. Mater. **4**, 541 (2016)
48. M. Scully, M. Zubairy, *Quantum Optics* (Cambridge University Press, Cambridge, 1997)
49. L.V. Hau, S.E. Harris, Z. Dutton, C.H. Behroozi, Nature **397**, 594 (1999)
50. W. Frank, P. Brentano, Am. J. Phys. **62**, 706 (1994)
51. J.L. Rosner, Am. J. Phys. **64**, 982 (1996)
52. S. Zhang, D.A. Genov, Y. Wang, M. Liu, X. Zhang, Phys. Rev. Lett. **101**, 047401 (2008)
53. U. Fano, **124**, 1866 (1961)
54. A. Miroshnichenko, S. Flach, Y. Kivshar, Rev. Mod. Phys. **82**, 2257 (2010)
55. B. Luk'yanchuk, N.I. Zheludev, S.A. Maier, N.J. Halas, P. Nordlander, H. Giessen, C.T. Chong, Nat. Mater. **9**, 707 (2010)
56. M.F. Limonov, M.V. Rybin, A.N. Poddubny, Y. Kivshar, Nat. Photon. **11**, 543 (2017)
57. T. Nakanishi, T. Otani, Y. Tamayama, M. Kitano, Phys. Rev. B **87**, 161110 (2013)
58. M. Kang, H.X. Cui, Y. Li, B. Gu, J. Chen, H.T. Wang, J. Appl. Phys. **109**, 014901 (2011)
59. A. Yariv, *Optical Electronics in Modern Communications* (Oxford University Press, New York, 1997)
60. M.V. Gorkunov, I.V. Shadrivov, Y.S. Kivshar, Appl. Phys. Lett. **88**, 071912 (2006)
61. T. Kanazawa, Y. Tamayama, T. Nakanishi, M. Kitano, Appl. Phys. Lett. **99**, 024101 (2011)
62. T. Nakanishi, Y. Tamayama, M. Kitano, Appl. Phys. Lett. **100**, 044103 (2012)
63. T. Nakanishi, M. Kitano, Phys. Rev. Appl. **4**, 024013 (2015)
64. T. Nakanishi, M. Kitano, Appl. Phys. Lett. **112**, 201905 (2018)
65. D. Schurig, J.J. Mock, B.J. Justice, S.A. Cummer, J.B. Pendry, A.F. Starr, D.R. Smith, Science **314**, 977 (2006)
66. U. Leonhardt, Science **312**, 1777 (2006)



# Chapter 7

## Temporal Coupled-Mode Theory for Light Scattering and Absorption by Nanostructures



Yisheng Fang and Zhichao Ruan

**Abstract** Nanostructures enrich optical resonances in wavelength and even sub-wavelength region and consequently influence scattering and absorption properties profoundly. Temporal coupled-mode theory was initially developed and applied to analyzing waveguide-resonator interactions in integrated optics. In this chapter, we develop the temporal coupled-mode theory formalism to describe the coupling process and the interference effect involved with optical scattering and absorption in nanostructures. We first discuss the temporal coupled-mode theory based on the consideration of energy conservation and time-reversal symmetry and validate the theory with numerical simulations. Based on the theory, we then elucidate that both the Fano interference and electromagnetic induced transparency (EIT)-like effect can be unified in a temporal coupled-mode equation, but with different background phase shifts. Such a model provides a general line shape formula of scattering and absorption cross sections for both cases. At last we discuss the super-scattering effect of a single subwavelength particle, where an arbitrarily large total scattering cross section can be achieved provided that one maximizes the contributions from a sufficiently large number of resonances.

### 7.1 Introduction

The study of light scattering and absorption by nanostructures is of great importance in nanophotonics and electromagnetics. The presence of resonances profoundly influences the scattering and absorption properties of nanostructures, resulting in the enhancement of electromagnetic cross sections far exceeding their geometric cross sections [1], as well as complex resonance-based interference phenomena including

---

Y. Fang

Department of Physics, Zhejiang University, Hangzhou 310027, China  
e-mail: ysfang@zju.edu.cn

Z. Ruan (✉)

Department of Physics, Zhejiang University, and State Key Laboratory  
of Modern Optical Instrumentation, Hangzhou 310027, China  
e-mail: zhichao@zju.edu.cn

© Springer Nature Switzerland AG 2018

E. Kamenetskii et al. (eds.), *Fano Resonances in Optics and Microwaves*, Springer  
Series in Optical Sciences 219, [https://doi.org/10.1007/978-3-319-99731-5\\_7](https://doi.org/10.1007/978-3-319-99731-5_7)

157

Fano interference [2–9], all-optical analogue to electromagnetically induced transparency (EIT) [10–15], super-scattering [16, 17], and the anomalous absorption and scattering [18, 19]. Therefore it is important to develop a theoretical framework that elucidates the role of resonances in these nanostructures.

The temporal coupled-mode theory formalism provides a very useful general framework to study the scattering behavior of obstacles supporting resonances. The scattering process is well modeled as the interference and coupling between the external field and the resonance-assisted leaky radiation field. The temporal coupled-mode theory was initially developed and applied to study the interaction of resonances with external waves in waveguide-resonator coupled systems [20–22], and has also been used to study the interaction of plane waves with grating structures [23–25].

In this Chapter, we introduce the temporal coupled-mode theory formalism, which has been used to study the scattering properties of two- and three-dimensional nanoparticles [2, 16, 17, 26] and planar nanostructures [27, 28]. The Fano resonances [4, 5, 29–31] and optical analog of electromagnetic induced transparency (EIT) [32, 33] are essentially scattering phenomena. In the coupled-mode theory [2, 28, 33], they arise from the interference of two light scattering pathways: the direct pathway of the background scattering, and the indirect pathway of the resonance-assisted scattering. We show that both the Fano interference and EIT-like effects can be unified in the same temporal coupled-mode equation, but with different background phase shifts.

One intriguing topic in nanophotonics is enhancing the scattering cross sections of subwavelength nanoparticles to be much larger than their geometric cross sections. The scattering can be significantly enhanced with the excitation of resonances and can further go beyond the single channel limit by implementing the superscattering formalism [16, 17, 28]. Also, in this chapter, the coupled-mode theory is developed to model the superscattering behavior. With the coupled-mode theory, an arbitrarily large total scattering cross section is predicted by spectrally aligning a sufficiently large number of orthogonal resonances.

## 7.2 Temporal Coupled-Mode Theory for Light Scattering

### 7.2.1 *General Scattering Theory for Arbitrarily Shaped Scatterers*

For the study of individual isolated objects, external waves are naturally expanded in the cylindrical wave basis in two dimensions, or the spherical wave basis in three dimensions. Temporal coupled-mode theory with wave expansion in either the cylindrical or spherical basis has been developed [2, 34]. Considering the great importance of a large number of antennas and nanoparticle structures that do not have a symmetric shape, we first generalize the temporal coupled-mode theory on a cylindrical or spherical wave basis to structures without rotational symmetry.

We start from the general scattering theory in the two-dimensional (2D) case where a scatterer is invariant along the  $z$  direction. Consider the scatterer located at the origin of the coordinate, surrounded by air. When a TM wave (with its magnetic field  $H$  polarized along the  $z$ -direction) impinges on the scatterer, the total field in the air region outside the scatterer can be written as:

$$H_{\text{total}} = \sum_{m=-\infty}^{\infty} A_0 \left( a_m^+ H_{|m|}^{(2)}(k\rho) \exp(im\theta) + a_m^- H_{|m|}^{(1)}(k\rho) \exp(im\theta) \right), \quad (7.1)$$

where  $(\rho, \theta)$  is the polar coordinates oriented at the origin,  $k$  is the wave number in air, and  $H_m^{(1)}$  ( $H_m^{(2)}$ ) is the  $m$ -th order Hankel function of the first (second) kind. Here we take the convention that the field varies in time as  $\exp(-i\omega t)$ . So  $a_m^+$  and  $a_m^-$  can be identified as the incoming and outgoing wave amplitudes, respectively. With the choice of  $A_0 = \sqrt{\frac{\omega\epsilon_0}{2}}$ ,  $|a_m^+|^2$  and  $|a_m^-|^2$  represent the power of the incoming and outgoing cylindrical waves in the  $m$ -th channel. Following [2, 26], we define a “reflection” matrix  $\mathbf{R}$  that connects the incoming coefficients  $\mathbf{a}^-$  with the outgoing coefficients  $\mathbf{a}^+$  as

$$\mathbf{a}^- = \mathbf{R}\mathbf{a}^+. \quad (7.2)$$

where  $\mathbf{a}^\pm$  is a column vector composed by  $a_m^\pm$  as

$$\mathbf{a}^\pm = \begin{bmatrix} \vdots \\ a_{-1}^\pm \\ a_0^\pm \\ a_1^\pm \\ \vdots \end{bmatrix} \quad (7.3)$$

When the scatterer is lossless, by energy conservation,  $\mathbf{R}$  is unitary, i.e.

$$\mathbf{R}^\dagger \mathbf{R} = \mathbf{I}. \quad (7.4)$$

Generally, for a scatterer without rotation symmetry the scattering and absorption cross sections are functions of incident angle. We consider a plane wave with  $H_{\text{inc}} = H_0 \exp(i\mathbf{k} \cdot \mathbf{r})$  incident upon the scatterer with an incident angle of  $\phi$  schematically shown in Fig. 7.1. Here  $\mathbf{k}$  is the wave vector of the incident plane wave. The total field in the air region outside the scatterer is then written as

$$H_{\text{total}} = H_0 \exp(i\mathbf{k} \cdot \mathbf{r}) + \sum_{m=-\infty}^{\infty} A_0 s_m H_{|m|}^{(1)}(k\rho) \exp(im\theta), \quad (7.5)$$

where  $s_m$  is the amplitude of the scattered field in the  $m$ -th channel. To connect (7.5) with (7.1), we expand the plane wave into cylindrical waves as

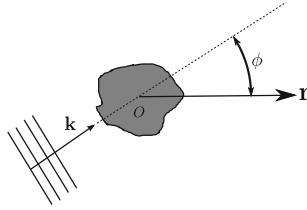


**Fig. 7.1** A plane wave impinges upon a scatterer with an incident angle of  $\phi$ . The scatterer does not have rotational symmetry. Reprinted with permission from [26]. Copyright 2012 by the American Physical Society

$$\exp(i\mathbf{k} \cdot \mathbf{r}) = \sum_{m=-\infty}^{\infty} i^{|m|} \exp(-i\phi m) \left( \frac{H_{|m|}^{(2)}(k\rho) + H_{|m|}^{(1)}(k\rho)}{2} \right) \exp(im\theta).$$

In comparison with (7.1), we then have

$$a_m^+ = \frac{1}{2} f_m \quad (7.6)$$

$$a_m^- = a_m^+ + s_m, \quad (7.7)$$

where

$$f_m = \sqrt{\frac{2}{\omega\epsilon_0}} H_0 i^{|m|} \exp(-i\phi m). \quad (7.8)$$

Below, we will use the symbols  $\mathbf{f}$ ,  $\mathbf{a}^+$ ,  $\mathbf{a}^-$ , and  $\mathbf{s}$  to denote the column vectors with components  $f_m$ ,  $a_m^+$ ,  $a_m^-$ , and  $s_m$  defined above, respectively.

We define a matrix  $\mathbf{S}$  that connects  $\mathbf{s}$  and  $\mathbf{f}$  as  $\mathbf{s} = \mathbf{S}\mathbf{f}$ , and by applying (7.7) we have

$$\mathbf{S} = \frac{1}{2}(\mathbf{R} - \mathbf{I}). \quad (7.9)$$

As a result, the total scattered and absorbed powers are

$$P_{\text{sct}} = \mathbf{s}^\dagger \mathbf{s} = 4(\mathbf{a}^+)^\dagger \mathbf{S}^\dagger \mathbf{S} \mathbf{a}^+ \quad (7.10a)$$

$$P_{\text{abs}} = (\mathbf{a}^+)^\dagger \mathbf{a}^+ - (\mathbf{a}^-)^\dagger \mathbf{a}^- = (\mathbf{a}^+)^\dagger (\mathbf{I} - \mathbf{R}^\dagger \mathbf{R}) \mathbf{a}^+ \quad (7.10b)$$

Following the definition, the scattering and absorption cross sections are evaluated as  $C_{\text{sct}} \equiv P_{\text{sct}}/I_0$  and  $C_{\text{abs}} \equiv P_{\text{abs}}/I_0$ , where  $I_0 = \frac{1}{2} \sqrt{\frac{\mu_0}{\epsilon_0}} |H_0|^2$  is the intensity of the incident plane wave.

### 7.2.2 Temporal Coupled-Mode Theory with a Single-Resonance

We now apply the temporal coupled-mode theory to calculate  $\mathbf{R}$  and then  $\mathbf{S}$  for the case when the scatterer supports a single resonant mode. The amplitude of the resonance  $c$  is normalized such that  $|c|^2$  corresponds to the energy inside the resonator [20]. Using the temporal coupled-mode theory formalism [20, 24], the dynamic equations for the amplitude  $c$  are

$$\frac{dc}{dt} = (-i\omega_0 - \gamma_0 - \gamma) c + \boldsymbol{\kappa}^T \mathbf{a}^+ \quad (7.11a)$$

$$\mathbf{a}^- = \mathbf{B}\mathbf{a}^+ + c\mathbf{d} \quad (7.11b)$$

where  $\omega_0$  is the resonant angular frequency,  $\gamma_0$  is the intrinsic loss rate due to, for example, material absorption,  $\gamma$  is the external leakage rate due to the coupling of the resonance to the outgoing wave, and  $\boldsymbol{\kappa}$  corresponds to the coupling coefficients between the resonance and the incoming wave. Note that such coupled-mode formalism is, strictly speaking, valid only when  $\gamma_0 + \gamma \ll \omega_0$  [20].

As shown in (7.11b) the outgoing waves have contributions from two pathways. The direct pathway, as described by the term  $\mathbf{B}\mathbf{a}^+$ , forms the background in the response spectrum.  $\mathbf{B}$  is the background reflection matrix. In this pathway, scattering occurs without exciting the resonance. The indirect, or the resonant, pathway is described by the term  $c\mathbf{d}$ . The vector  $\mathbf{d}$  can be determined by considering the scenario, where the resonance has amplitude  $c$ , and there is no incoming wave, i.e.  $\mathbf{a}^+ = \mathbf{0}$ . For this scenario, the radiation field outside the scatterer can be written as

$$H_{\text{eigen}} = c \sum_{m=-\infty}^{\infty} A_0 d_m H_{|m|}^{(1)}(k\rho) \exp(im\theta). \quad (7.12)$$

Here the coefficients  $d_m$ , which are components of the column vector  $\mathbf{d}$ , correspond to the radiation coefficients of the resonance.

The coupling coefficients  $\mathbf{B}$ ,  $\mathbf{d}$  and  $\boldsymbol{\kappa}$  in (7.11) are not independent of each other. They are constrained by the energy conservation and time-reversal symmetry [24] as

$$\mathbf{d}^\dagger \mathbf{d} = 2\gamma. \quad (7.13)$$

$$\boldsymbol{\kappa} = \hat{O}\mathbf{d} \quad (7.14)$$

$$\mathbf{B}\hat{O}\mathbf{d}^* + \mathbf{d} = 0 \quad (7.15)$$

Here  $\hat{O}$  has a matrix form of  $\hat{O}_{mn} = \delta_{m,-n}$

$$\hat{O} = \begin{bmatrix} 0 & & & \ddots \\ & & 1 & \\ & & & 1 \\ & & & & \ddots \\ \ddots & & 1 & & & 0 \end{bmatrix}. \quad (7.16)$$

From (7.14), we have a general form of the reflection matrix

$$\mathbf{R} = \mathbf{B} + \frac{\mathbf{d}\mathbf{d}^T \hat{O}}{i\omega_0 - i\omega + \gamma + \gamma_0}. \quad (7.17)$$

Below, we will apply (7.17) to calculate the scattering matrix  $\mathbf{S}$ .

### 7.3 General Line Shapes of Scattering and Absorption Cross Sections

Based on the general temporal coupled-mode formalism developed in the above section, we present a theory for the Fano interference in light scattering by an individual obstacle. We take an infinite long cylindrical scatterer for example. We show that for each angular momentum channel, the Fano interference effect can be modeled by a simple temporal coupled-mode equation, which provides a line shape formula for scattering and absorption cross sections. Though the following analysis is developed in the particular case of a cylindrical scatterer, the presented theory and conclusions can be applied to general scattering processes for scatterers with a single resonance.

In the case where the scatterer has cylindrical symmetry, the resonances in different  $l$ -th orders are orthogonal to each other. Thus the  $l$ -th order incoming wave only excites the same order resonance and outgoing wave. So the coupling coefficients are decoupled and the reflection matrix  $\mathbf{R}$  in the previous section reduces to the diagonal matrix. We define  $R_l$  as

$$R_l \equiv \frac{a_l^-}{a_l^+}, \quad (7.18)$$

which is the reflection coefficient since it relates the outgoing wave to the incoming wave in each channel. If the system is lossless, the background reflection coefficient is  $B = e^{i\phi_l}$ , where  $\phi_l$  is a real phase factor. Thus in this Section, we consider only the  $l$ -th channel, and for notation simplicity we suppress the subscript  $l$  in all variables.

Following the same procedure developed in the previous section, we have

$$R = \frac{i(\omega_0 - \omega) + \gamma_0 - \gamma}{i(\omega_0 - \omega) + \gamma_0 + \gamma} e^{i\phi} \quad (7.19)$$

The scattering coefficient  $S = \frac{R-1}{2}$  can be obtained as

$$S = S_b \left[ -i \frac{\omega - \omega_0 - \gamma_0 + q\gamma}{i(\omega_0 - \omega) + \gamma_0 + \gamma} \right] \quad (7.20)$$

Here  $S_b$  provides the background and determines the Fano asymmetric parameter  $q$ :

$$S_b = \frac{e^{i\phi} - 1}{2} \quad (7.21)$$

and

$$q = -i \left( 1 + \frac{1}{S_b} \right) = -\cot \frac{\phi}{2} \quad (7.22)$$

Substituting (7.20) into (7.10), we then have the scattering and the absorption cross sections as

$$C_{\text{sct}} = \frac{2\lambda}{\pi} \left| \frac{1}{2} \frac{(i(\omega_0 - \omega) + \gamma_0)(e^{i\phi} - 1) - \gamma(1 + e^{i\phi})}{i(\omega_0 - \omega) + \gamma_0 + \gamma} \right|^2 \quad (7.23a)$$

$$C_{\text{abs}} = \frac{2\lambda}{\pi} \frac{\gamma_0\gamma}{(\omega - \omega_0)^2 + (\gamma_0 + \gamma)^2} \quad (7.23b)$$

From (7.23) one can easily prove that the maximum scattering and absorption cross sections in a single channel cannot exceed  $2\lambda/\pi$  and  $\lambda/2\pi$  respectively. In the lossless case where  $\gamma_0 = 0$ ,

$$S = S_b \left[ -i \frac{\omega - \omega_0 + q\gamma}{i(\omega_0 - \omega) + \gamma} \right]. \quad (7.24)$$

Thus the scattering cross section

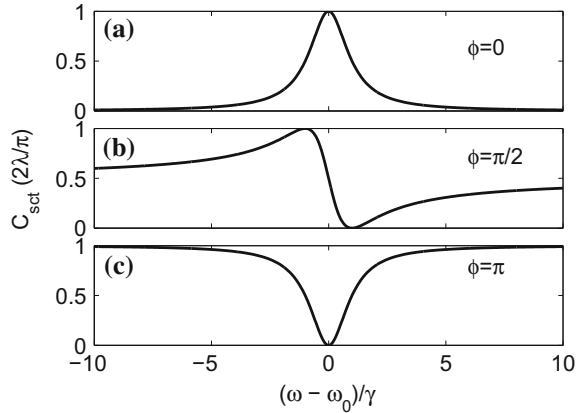
$$C_{\text{sct}} = \frac{2\lambda}{\pi} |S_b|^2 \frac{[(\omega - \omega_0) + q\gamma]^2}{(\omega - \omega_0)^2 + \gamma^2} \quad (7.25)$$

This is obviously the form of the Fano lineshape. From (7.25) we can see that the Fano lineshape of the scattering cross section is determined by the phase of the background scattering through the Fano asymmetry parameter  $q$  [see (7.22)].

To further interpret the physical meaning of the  $q$  parameter more explicitly, we find out the relative amplitude and phase differences between the scattered fields from the direct background scattering pathway and the indirect resonance-assisted scattering pathway at the resonant frequency  $\omega_0$  as

$$\frac{c \cdot d}{(B - 1) \cdot a^+} = -iq - 1 \quad (7.26)$$

**Fig. 7.2** Scattering cross section spectra as given by (7.23) for the lossless case ( $\gamma_0 = 0$ ). **a–c** correspond to  $\phi = 0, \pi/2, \pi$ , respectively. Reprinted with permission from [2]. Copyright 2010 ACS



The Fano asymmetric parameter  $q$  describes the amplitude and phase differences between the fields in the direct and indirect pathways at the resonant frequency, thus describes how these two portions of scattered field interfere and give out different styles of Fano lineshape.

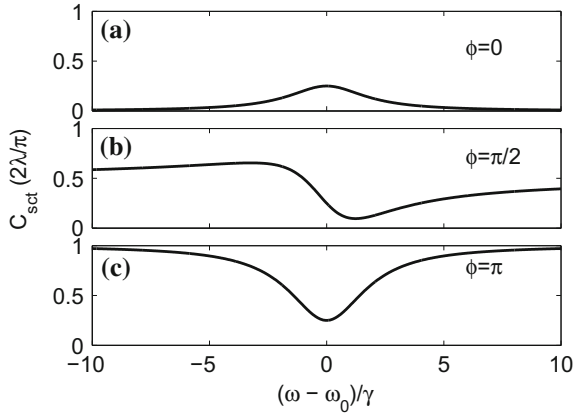
We now use (7.25) to illustrate general line shapes of scattering cross section spectrum in a single channel. Figure 7.2 plots the scattering cross section spectra with different phase factors  $\phi$  as arose from the background reflection. For the phase factor  $\phi = 0$ , the cross section spectrum always has a Lorentzian line shape (Fig. 7.2a). Since  $\phi = 0$  corresponds to a very weak background scattering [ $q = \infty$  in (7.26)], in this case the only contribution to the scattering process is from the resonance-assisted pathway and there is no scattering contribution from the direct pathway. The resonance creates maximal scattering at the resonant frequency  $\omega_0$ , and the resonance line width is determined by the leakage rate  $\gamma$  and the intrinsic loss rate  $\gamma_0$ .

When  $\phi = \pi$ , the cross section spectrum has an anti-Lorentzian line shape (Fig. 7.2c). In this case,  $q = 0$  and the background scattering reaches the maximum. The scattering contributions from the background and resonance interfere destructively at the resonance frequency  $\omega_0$ , according to (7.26). Thus the presence of the resonance creates a dip at  $\omega_0$ —no scattering occurs at the resonance frequency. This effect is closely related to the all-optical analog of EIT.

For all other cases where  $\phi$  is neither equal to 0 nor  $\pi$ , the spectrum is not a Lorentzian, but rather exhibits a Fano asymmetric line shape, which exhibits both enhancement and suppression of scattering in the vicinity of the resonance. For example, Fig. 7.2b shows the scattering cross section spectrum for  $\phi = \pi/2$ . We note that in the Fano line shape, neither the minimum nor the maximum in scattering cross section occurs at the resonant frequency  $\omega_0$ . Through (7.25), we can determine that the resonance peak and dip occur at the frequency  $\omega_{\max} = \omega_0 - \gamma \tan \frac{\phi}{2}$  and  $\omega_{\min} = \omega_0 + \gamma \cot \frac{\phi}{2}$  respectively. Therefore, in order to switch the scattering cross



**Fig. 7.3** Scattering cross section spectra as given by (7.23) for the lossy case with  $\gamma_0 = \gamma$ . Reprinted with permission from [2]. Copyright 2010 ACS



section from the minimum to the maximum, the smallest frequency variation required is  $2\gamma$  in the case of  $\phi = \pm\pi/2$ . In particular, at the resonance dip, we can find out that the fraction in (7.26) equals to  $-1$ , thus interprets the presence of the scattering dip as a result of the destructive interference between the resonance and background.

To show the effect of the intrinsic loss, Fig. 7.3 shows the scattering cross section spectra when  $\gamma_0 = \gamma$  in (7.23a). Compare it with Fig. 7.2, one can see that the line shapes are similar to the corresponding lossless cases, but the presence of the loss reduces the cross section variation as a function of frequency. In particular, the scattering cross sections can no longer reach  $2\lambda/\pi$ , which is the upper limit for a single channel. Neither can the minimum of the scattering cross sections reach zero. In other word, in the presence of loss it is no longer possible to completely eliminate scattering field at a single frequency through Fano interference effect with the presence of a single resonance.

We then consider the absorption cross section spectrum described by (7.23b). In contrast to the scattering cross section spectrum, which varies with the background phase factor, the absorption cross section is independent of the phase factor. Instead, it always has a symmetric Lorentzian line shape with its maximum at the resonant frequency. Thus, Fano interference effect does not affect the absorption properties of the obstacle.

For cylinders and spheres with rotation symmetry, resonances in different channels are orthogonal to each other. When we take multiple channels into consideration and in the situation that there is only one resonance in each channel, the scattering and absorption cross section spectra show the Fano and Lorentzian line shapes respectively in each channel, and the total cross section is simply the sum of the contributions from all channels.

## 7.4 Temporal Coupled-Mode Theory for Scattering with Two Coupled Resonances

In this Section, we consider the coupled-resonator systems where two resonances are supported in a single channel. In other words, the two coupled resonances  $c_1$  and  $c_2$  are of the same  $l$ -th channel. Thus in this Section, we consider only the  $l$ -th channel, and for notation simplicity we suppress the subscript  $l$  in all variables. In such a system, the coupling and interference process for light scattering can be described by the following coupled-mode equations,

$$\frac{d}{dt} \begin{bmatrix} c_1 \\ c_2 \end{bmatrix} = (-i\Omega_0 - \Gamma - \Gamma_0) \begin{bmatrix} c_1 \\ c_2 \end{bmatrix} + \begin{bmatrix} d_1 \\ d_2 \end{bmatrix} a^+ \quad (7.27a)$$

$$a^- = a^+ + [d_1 \ d_2] \begin{bmatrix} c_1 \\ c_2 \end{bmatrix} \quad (7.27b)$$

where  $\Omega_0 = \begin{bmatrix} \omega_1 & 0 \\ 0 & \omega_2 \end{bmatrix}$ ,  $\Gamma_0 = \begin{bmatrix} \gamma_{01} & 0 \\ 0 & \gamma_{02} \end{bmatrix}$ , and  $\Gamma = \begin{bmatrix} \gamma_1 & \gamma_3 \\ \gamma_3^* & \gamma_2 \end{bmatrix}$ . Here  $\omega_i$  and  $\gamma_i$  are the resonant frequencies and leakage rates of each single resonance  $c_i$  ( $i = 1, 2$ ) respectively.  $\gamma_3$  denotes the cross coupling of two resonances,  $\gamma_{0i}$  is the intrinsic loss rate due to material absorption, and  $d_1, d_2$  correspond to the coupling coefficients of two resonances to the incoming wave. To simplify the derivation, in the following discussions, we consider the lossless case, i.e.  $\gamma_{0i} = 0$ .

First of all, we analyze the eigenmodes by solving the eigen-problem equation

$$\det [i(\Omega - \Omega_0) - \Gamma] = 0 \quad (7.28)$$

We assume that  $c_a$  and  $c_b$  are sub-radiant and super-radiant modes with the eigenvalue  $-i\omega_a - \gamma_a$  and  $-i\omega_b - \gamma_b$ , respectively, where  $\gamma_a < \gamma_b$ . These hybridized sub-radiant and super-radiant modes overlap in the spectrum, and their interference leads to the Fano resonance. The coupled-mode equations (7.27) can be further written as

$$\frac{d}{dt} \begin{bmatrix} c_a \\ c_b \end{bmatrix} = \left( -i \begin{bmatrix} \omega_a & 0 \\ 0 & \omega_b \end{bmatrix} - \begin{bmatrix} \gamma_a & 0 \\ 0 & \gamma_b \end{bmatrix} \right) \begin{bmatrix} c_a \\ c_b \end{bmatrix} + \begin{bmatrix} d_a \\ d_b \end{bmatrix} a^+ \quad (7.29a)$$

$$a^- = a^+ + [d_a \ d_b] \begin{bmatrix} c_a \\ c_b \end{bmatrix} \quad (7.29b)$$

Consequently, the scattering coefficient is obtained as

$$S = \frac{\gamma_a}{i(\omega_a - \omega) + \gamma_a} \frac{-i(\omega_a - \omega_b) + i(\gamma_a + \gamma_b)}{(\omega_a - \omega_b) - i(\gamma_a - \gamma_b)} - \frac{\gamma_b}{i(\omega_b - \omega) + \gamma_b} \frac{(\omega_a - \omega_b) + i(\gamma_a + \gamma_b)}{(\omega_a - \omega_b) - i(\gamma_a - \gamma_b)} \quad (7.30)$$

To compare with the single resonance case, (7.30) can be rewritten as

$$S = S_b \left[ -i \frac{\omega - \omega_a + q\gamma_a}{i(\omega_a - \omega) + \gamma_a} \right] \quad (7.31)$$

where

$$S_b = \frac{-\gamma_b}{i(\omega_b - \omega) + \gamma_b} \frac{(\omega_a - \omega_b) + i(\gamma_a + \gamma_b)}{(\omega_a - \omega_b) - i(\gamma_a - \gamma_b)} \quad (7.32)$$

provides the background with a slowly varying Lorentzian line shape and  $q$  is the Fano asymmetry parameter.

We take the approximation that the bandwidth of the super-radiant mode is much larger than the sub-radiant one ( $\gamma_b \gg \gamma_a$ ) and consider a limited spectrum range in the vicinity of the anti-bonding resonance ( $\omega \approx \omega_a$ ). The background scattering coefficient in (7.31) is approximated as

$$S_b = \frac{-\gamma_b}{i(\omega_b - \omega) + \gamma_b}, \quad (7.33)$$

and the Fano asymmetry parameter

$$q \approx -i \left( 1 + \frac{1}{S_b} \right) \quad (7.34)$$

is determined by the background scattering, which coincides with (7.22) in Sect. 7.3. Therefore, we come to the characteristic Fano formula of the scattering cross section for the two-resonance case, which is similar to the single-resonance case of (7.25):

$$C_{\text{sct}} = \frac{2\lambda}{\pi} |S_b|^2 \frac{|\omega - \omega_a + q\gamma_a|^2}{(\omega_a - \omega)^2 + \gamma_a^2}. \quad (7.35)$$

The optical analog of EIT occurs in the particular case of  $q = 0$ . Such condition is realized when resonant frequencies of the two coupling modes nearly match with each other, that is,  $\omega_1 = \omega_2$ .

We can view such a two-resonance interference effect as a two-step process. Firstly the scattering process of the super-radiant mode can be described by the coupled-mode equations for a single resonance as

$$\frac{dc_b}{dt} = (-i\omega_b - \gamma_b)c + d_b a'^+ \quad (7.36a)$$

$$a'^- = a'^+ + c_b d_b \quad (7.36b)$$

Such a super-radiant mode coupling process creates the background scattering  $S_b$  for the sub-radiant mode, which coincides with (7.33). Secondly, under this background path, the coupled-mode equation for the sub-radiant mode is

$$\frac{dc_a}{dt} = (-i\omega_a - \gamma_a)c + d_a a^+ \quad (7.37a)$$

$$a^- = B a^+ + c_a d_a \quad (7.37b)$$

where the background coefficient  $B = 2S_b + 1$ . As results, the Fano resonance corresponds to the case that the radiation path of the sub-radiant mode is out of phase from the background path of the super-radiant mode, while the EIT corresponds to the off-phase case that  $B = -1$  with  $S_b = -1$  and  $q = 0$ . Therefore, in principle, we can unify the pictures of any multiple resonances with the single resonance one in this way.

## 7.5 Fano Resonance in the Scattering of Nanostructures

The Fano resonance was first observed in the autoionizing states of atoms [35]. In contrast to the symmetric Lorentzian line shape for individual resonance, the Fano resonance is featured of its asymmetric line shape which exhibits a successive resonant peak and dip in the spectra. This phenomenon originates from the coupling and interference of a narrowband discrete resonance with a broadband continuum. In the past years, the Fano interference effects in light scattering in classical optical systems have attracted significant attentions [30, 31]. As discussed in the previous sections, in the temporal coupled-mode formalism [2, 26], the Fano resonance for both the single and multiple modes can be unified in the view of the interference between two light scattering pathways: the direct pathway of the background scattering and the indirect pathway of the resonance-assisted scattering. The direct scattering pathway provides a slowly-varying background phase while the scattered light in the resonant pathway has a rapid  $\pi$  phase change near the resonant frequency. Such phase difference results in a steep transition from constructive interference to destructive interference between these two pathways in the vicinity of the resonant frequency, thus gives rise to the scattering peak and dip respectively. The Fano resonances in the scattering and extinction cross section spectra were observed in a variety of optical systems, ranging from plasmonic resonators, all-dielectric resonators to photonic crystals and optomechanical cavities. Below we review these Fano resonance cases and classify them according to the background scattering, whether it arises from the individual scattering or from the super-radiant mode in the multiple-resonance cases.

### 7.5.1 Fano Resonances in Plasmonic Resonators

Metallic nanostructures are able to confine and manipulate light in subwavelength scale and realize subwavelength resonances with strong field enhancement [36–39]. The Fano resonance has been realized in a broad range of nanoscale plasmonic

systems, ranging from individual plasmonic nanoparticles to coupled plasmonic nanostructures.

For individual plasmonic nanoparticles, the Fano resonances in the scattering cross section have been discussed, for both nanocylinders (two-dimensional scattering) and nanospheres (three-dimensional scattering) [2, 7, 13, 40–42]. In these cases, the background scattering field is provided by the direct reflection when the external light illuminates on the particle surface. The out-of-phase interference, between the background scattering and the re-emission of the localized resonances, gives rise to asymmetric Fano line shape in the scattering cross section spectra. The occurrence of such Fano resonances is absent from the Rayleigh scattering diagram, when the wavelength is much larger than the particle size. Thus the plasmonic Fano resonance is named as “anomalous scattering” in previous studies, and can be fully interpreted by applying the Mie scattering theory in the vicinity of the plasmon resonance [18, 40, 41, 43]. For the scattering of a single sphere, the Fano line shapes in the differential scattering cross section spectra, for example, the forward scattering or backward scattering, have been studied [4, 41]. In these cases, the Fano resonances result from the interference between scattering fields in different  $l$ -th orders, thus the Fano resonances occur in differential scattering cross sections rather than total scattering cross sections, because the radiation patterns of resonances with different  $l$ -th orders have different angular distributions. In other studies, the Fano line shape in the total scattering cross section spectra have been realized when two interfered scattering fields are of the same  $l$ -th order, by introducing core-shell coated structures [2, 44, 45].

Apart from individual nanoparticles, Fano resonances were also realized in coupled plasmonic nanostructures. These coupled plasmonic nanostructures are often composed of two or more slightly separated resonators and they each supports a resonance. These metallic nanostructures have characteristic sizes of subwavelength scale and are in the quasi-static regime, thus the most common supported modes are plasmonic dipolar modes. In the coupled plasmonic systems, Fano resonances arise from the interference between the super-radiant and the sub-radiant modes. Here the super-radiant mode provides the broadband background while the sub-radiant mode acts as the narrowband resonance. These sub-radiant narrowband resonances in coupled plasmonic nanostructures can be introduced in two approaches, the hybridization approach [46, 47] and the symmetry-breaking approach [48–52].

The hybridization approach is usually implemented in spatially symmetric plasmonic nanocluster systems, where several individual metallic nanoparticles are placed in proximity in a symmetric configuration with subwavelength separations between each other. In such systems, the two resonances  $c_1$  and  $c_2$  supported by two coupled resonators feature the same  $l$ -th order, typically the dipolar plasmon modes. Interactions of the dipolar modes of these individual nanoparticles form different collective oscillation modes, according to (7.28) in Sect. 7.4. For example, in the ring-disk cluster configuration [46], the central disk and the surrounding ring each supports a dipolar mode respectively (Fig. 7.4a), corresponding to  $c_1$  and  $c_2$  in (7.27). When the two resonators are placed in proximity and their eigenmodes overlap in the spectrum, they hybridize to form two new modes, a lower-energy

bonding mode  $c_b$  and a higher-energy anti-bonding mode  $c_a$ . In the bonding mode  $c_b$ , the dipolar plasmons in the central and the surrounding disks oscillate in phase, resulting in the strong radiative feature of this mode, thus it is referred to as the super-radiant mode. In the anti-bonding mode  $c_a$ , however, dipolar plasmons in the central and the surrounding disks oscillate out of phase, cancelling out the total dipole moments, thus this mode hardly couples to the external field and is referred to as the sub-radiant mode. The coupling and interference process for light scattering in the above-mentioned systems can be generally described by the coupled-mode equations for hybridized modes (7.27). These hybridized sub-radiant and super-radiant modes overlap in the spectrum, and their interference lead to the Fano resonance. Similarly, symmetric four-nanorod configuration was studied, where a gold dipole nanoantenna is placed between two gold nanorods [47]. The hybridization originates from the dipolar modes supported by the central nanoantenna and the nanorod pair (Fig. 7.4b).

As for the symmetry-breaking approach, higher-order multipolar modes are involved by introducing spatial symmetry-breaking into coupled plasmonic nanostructures. In the symmetric structure, the odd-symmetric modes cannot be excited by the incident plane wave and only the even-symmetric modes are accessible from the far field due to the consistence of symmetry. Thus such symmetric nanostructures support only dipolar modes while quadrapolar and higher-order multipolar mode remain dark. When symmetry-breaking is introduced, the higher-order multipolar modes are no longer dark, particularly the quadrupolar mode can be excited. In such a system, the dipolar mode acts as the super-radiant mode and provides the broadband background, while the quadrupolar mode is sub-radiant and acts as the narrowband resonance. By appropriately choosing the geometric parameters of the nanostructure, the sub-radiant quadrupolar mode spatially and spectrally overlaps with the super-radiant dipolar mode, thus their coupling and interference give rise to the Fano resonance as (7.31). What is most interesting in the symmetry-broken coupled plasmonic systems is that the spectral profile of the Fano resonance can be dynamically tuned. By tuning the geometric sizes of and spacing between individual elements in the nanostructure [49–52] (Fig. 7.4c, d), as well as the incident angle and polarization [48, 50, 52] of the incident plane wave, one can dynamically vary the extent of the spatial mode overlapping between the super-radiant and sub-radiant modes, thus the coupling strength between them, which leads to the tunability of the Fano spectral profile.

The most commonly studied coupled plasmonic systems implementing symmetry-breaking are the nonconcentric core-shell structures [48–50] (Fig. 7.4c) and the three-bar configurations [51] (Fig. 7.4d). In the nonconcentric core-shell metallic nanostructure with the diameter of several hundreds nanometers [48], the dipolar modes in the ring and the disk form hybridized dipolar modes. The anti-bonding dipolar mode provides the super-radiant mode. The super-radiant dipolar mode can be directly excited by the incident field, providing a broad background. When the concentric structure evolves into a nonconcentric one, the geometric symmetry is broken and higher-order plasmon modes arise. The sub-radiant quadrupolar mode can be excited indirectly through near-field coupling with the dipolar mode, thus

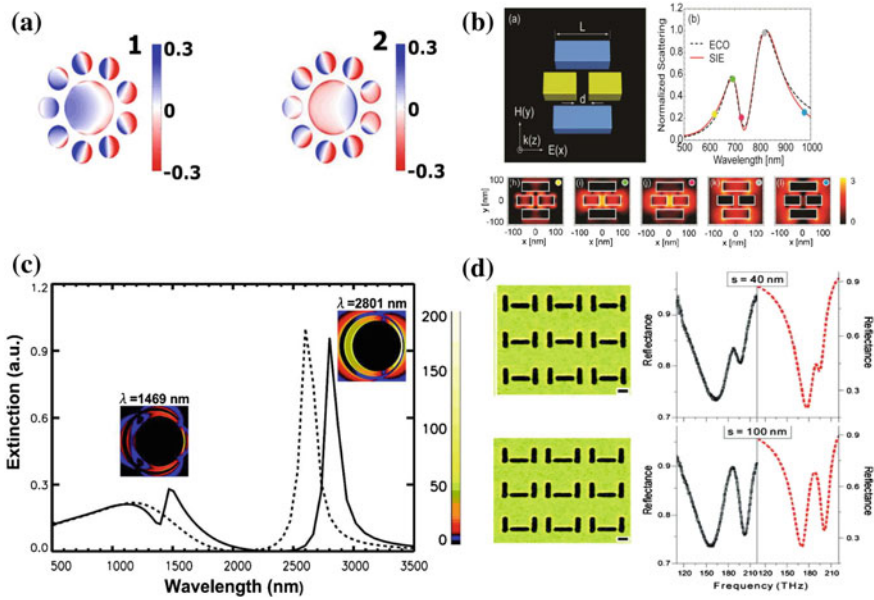


**Fig. 7.4** **a** The calculated charge distributions at the Fano peak and Fano dip, where in the former case the dipolar plasmons in the central and the surrounding disks oscillate in phase, while in the latter case they oscillate out of phase. Reprinted with permission from [46]. Copyright 2016 ACS. **b** Symmetric four-nanorod configuration structure made of gold. The scattering cross sections simulated (red solid line) and fitted by model (black dashed line) are plotted. The bottom panels show the near-field intensity corresponding to the Fano dip and peak positions in the cross section. The right panel shows the electric field distributions at the wavelength of 580 nm. Reprinted with permission from [47]. Copyright 2013 ACS. **c** Extinction spectra for nonconcentric Ag ring/disk cavity (solid line) and the concentric one (dashed line). Insets show the electric field distribution at the resonance. Reprinted with permission from [48]. Copyright 2008 ACS. **d** Experimental (black) and calculated (red) reflectance spectra of the planar three-bar configuration metamaterial. The left column shows the scanning electron microscopy images of the structures.  $s$  denotes the lateral displacement of the central antenna to the symmetric position. Reprinted with permission from [51]. Copyright 2010 ACS

the interference between the narrowband sub-radiant and broadband super-radiant modes leads to the Fano resonance in the infrared region, observed as an asymmetric line shape in the extinction cross section spectrum (Fig. 7.4c). The Fano resonance can be tuned from the visible to the mid-infrared spectrum by changing the geometry parameters [49]. The asymmetric Fano resonances were also observed in the three-bar configurations in near-infrared extinction or reflection spectrum [50–52]. Here a pair of side nanobars act as the quadrupole antenna and support the sub-radiant quadrupolar mode, while the middle nanobar acts as the dipole antenna and supports the super-radiant dipolar mode. With the spatial symmetry breaking, the sub-radiant quadrupolar mode can be excited indirectly through near-field coupling with the dipolar mode. The sub-radiant quadrupolar plasmon mode interferes with

the super-radiant hybridized dipolar mode, leading to the Fano resonance (Fig. 7.4d). Furthermore, experimentally measured and numerically calculated near-field distributions reveal the interactions between the super-radiant and sub-radiant modes and therefore the nature of the Fano resonance [50, 52]. At the Fano resonance dip, the electromagnetic field mainly localizes in the sub-radiative antenna while the super-radiative antenna is absent of field, demonstrating the destructive interference of two excitation pathways.

The Fano resonance possesses narrow spectral linewidth and the resonance frequency displays high sensitivity to the variations of geometry or environment refractive-index. These features altogether promise the Fano resonances as platforms for nanoscale optical sensing. Efficient sensors in the near-infrared region were proposed based on the Fano resonances in metallic nanostructures [48–50, 52].

### 7.5.2 *Fano Resonances in All-Dielectric Resonators*

Fano resonances are also plentiful in dielectric nanoscale resonators. Using the high refractive index dielectric material overcomes the high dissipative losses of the plasmonic systems counterparts, thus gives rise to higher Q-factors of the Fano resonances, and promises applications for sensors [53]. Due to its asymmetric and highly dispersive line shape feature, as well as the steep transition from resonant peak to dip, the Fano resonance can also be implemented to realize optical switches or slow-light devices. One main difference is that while in plasmonic resonators the most common resonances are the dipolar surface plasmon modes, the resonances supported in the dielectric nanostructures are volume cavity modes, which have the field concentrated inside the dielectric resonators. In analogy with the plasmonic systems, Fano resonances in dielectric resonators are also tunable.

In individual dielectric obstacles, Fano resonances in the scattering spectra have been studied. It was revealed that the Mie scattering by individual high-refractive-index dielectric two-dimensional cylindrical nanorods [54, 58] or three-dimensional nanospheres [59, 60] can be represented as a cascade of Fano resonances. The Fano resonances arise from the interference between the direct scattering pathway, which is the slowly varying background provided by non-resonant scattering of the incident wave, and the resonant-assisted indirect scattering pathway, which is the leakage radiation from the excited eigenmode of the cylinder. For homogeneous cylinder with high refractive index, the Fano formula in the scattering cross section can be analytically derived from the Mie theory. By fitting the calculated Mie scattering spectra with the Fano formula, Fano asymmetry parameters for different eigenmodes of the nanorod are extracted (Fig. 7.5a). When individual cylinders are further lined in a periodic linear chain, interference gives rise to even narrower Fano resonances [61]. When the cylinder rows are placed in succession and develop into a two-dimensional cylinder array, the former Fano resonances further develop into narrow Fano bands. Apart from cylindrical and spherical nanoparticles, Fano resonances are also observed in individual planar slab structures. In 2014, Fan et al. studied the



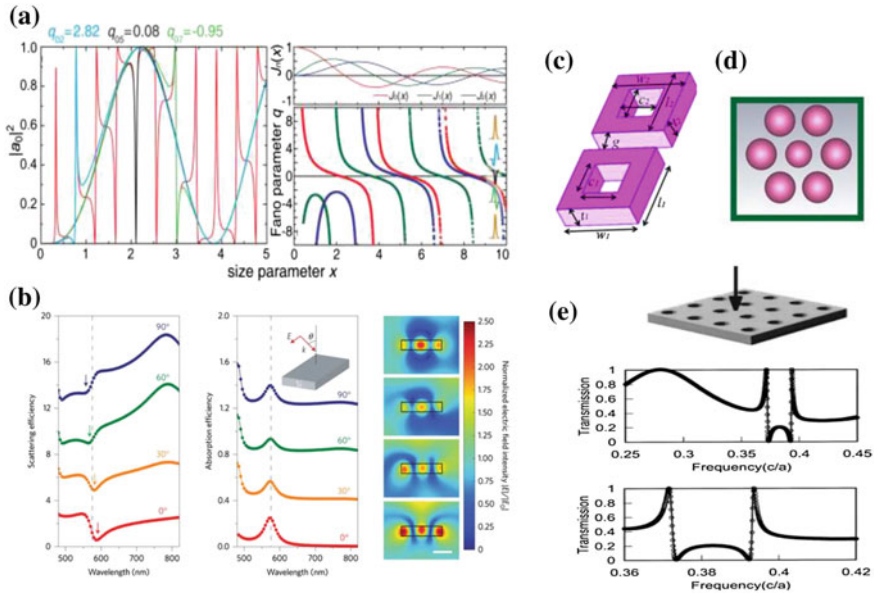


**Fig. 7.5** **a** Red curve presents the normalized amplitude of the scattered light (squared Lorentz-Mie coefficient) for a cylindrical nanorod. Blue, green and black curves present the Fano fitting of TE<sub>02</sub>, TE<sub>05</sub> and TE<sub>07</sub> modes. Reprinted with permission from [54]. Copyright 2013 OSA. **b** Simulated total scattering efficiency spectra and absorption efficiency spectra of a Si slab at different incident angles. The Fano resonances are observed in the scattering spectra. Reprinted by permission from Macmillan Publishers Ltd: [Nature Materials] [55], copyright 2014. **c** Planar nanodimers consisted of two adjacent subwavelength silicon nanoblocks [56]. With permission of Springer. **d** Dielectric symmetric ring-disk clusters made of silicon nanospheres. Reprinted with permission from [57]. Copyright 2012 ACS. **e** Transmission spectrum through a photonic crystal structure under normal incidence. Reprinted with permission from [24]. Copyright 2003 OSA

scattering spectra of the subwavelength semiconductor slab [55]. The Fano resonance was obtained in the visible region at the excitation of the waveguide mode in the slab (Fig. 7.5b). As an advantage of the semiconductor-based nanostructure, the scattering and absorption spectra can be simultaneously analyzed.

Fano resonances in coupled dielectric nanostructures have been widely studied. In asymmetric dielectric metamaterials, Fano resonance arises from the interference between the super-radiant dipolar mode and the sub-radiant quadrupolar mode. One example is the planar nanodimers consisting two adjacent subwavelength silicon nanoblocks [56] (Fig. 7.5c). Dielectric symmetric ring-disk clusters made of silicon nanodisks [62] or nanospheres [57] are also able to achieve Fano resonance (Fig. 7.5d), resulting from the interference between the magnetic dipole mode of the central particle and the collective mode in the surrounding particles. In periodic sphere arrays, the interference between the sub-radiant mode of discrete Bragg band and the super-radiant Mie scattering gives rise to the Fano resonance [63]. Fano resonance also appears in the reflection spectra of the multilayer Bragg gratings [64],

where the excited Bloch surface wave provides the discrete narrow resonance. Interference of two reflection pathways, the direct reflection from the surface and the remission through exciting the surface waves, leads to the Fano resonance.

In two-dimensional (2D) photonic crystal slab (PCS) systems, Fano resonances arise from the coupling of the discrete guided resonance with the background of free space radiation modes. The guided resonances have their field strongly confined within the slab and are leaky modes that can couple to external fields [23]. The Fano resonances can be attributed to the interference of a direct pathway of background reflection/transmission and an indirect resonance-assisted pathway that light couples into guided resonances and then radiates out to the free space. The physical process is described and the asymmetric lineshape is well fitted by the analytical model of temporal coupled-mode theory [24] (Fig. 7.5e).

## 7.6 All-Optical Analog to Electromagnetically Induced Transparency

Electromagnetic induced transparency (EIT) is a coherent quantum interference effect originally observed in three-level atomic gas systems, resulting from the destructive quantum interference of different pathways for excitation of the state [11, 12]. However, the occurrence of EIT-like effects is not necessarily limited to quantum systems. It has been observed in a variety of classical systems, ranging from mechanical systems and electrical circuits to coupled plasmonic and dielectric optical resonators and optomechanical systems, all with the similar mechanism of coupling between two frequency-degenerate modes with remarkable different Q-factors [33]. These EIT-like effects were generally described by several physical diagrams such as the mechanical coupled two-oscillator model [12, 15, 65] and the coupled electrical circuits model [66, 67].

The optical analog of EIT is featured by a narrowband transparency window in the electromagnetic response of a system. The characteristic line shape shows that a narrow transmission window superimposes on the center of a broad scattering background. In optical resonator systems, the EIT-like effect results from the classical destructive interference of different scattering pathways of the electromagnetic waves (Fig. 7.6a). Here the presence of a sub-radiant mode resembles the metastable level in the atomic systems, which is necessary for realizing EIT, and the weak coupling is enabled by spatial overlapping of the modes rather than a pump beam [11, 12].

Following the theory we developed in Sects. 7.3 and 7.4, the optical analog of EIT occurs in the case that resonant frequencies of two coupling modes nearly match with each other, that is,  $\omega_1 \approx \omega_2$ . In this condition, it is easily deduced from (7.31) that  $q \approx 0$  in the vicinity of the resonant frequency, thus the scattering spectrum lineshape exhibits a narrowband anti-Lorentzian dip in the vicinity of the resonant frequency superimposed on the broadband Lorentzian background. Particularly, it can be further derived out that at the resonance, the super-radiant mode and the sub-radiant

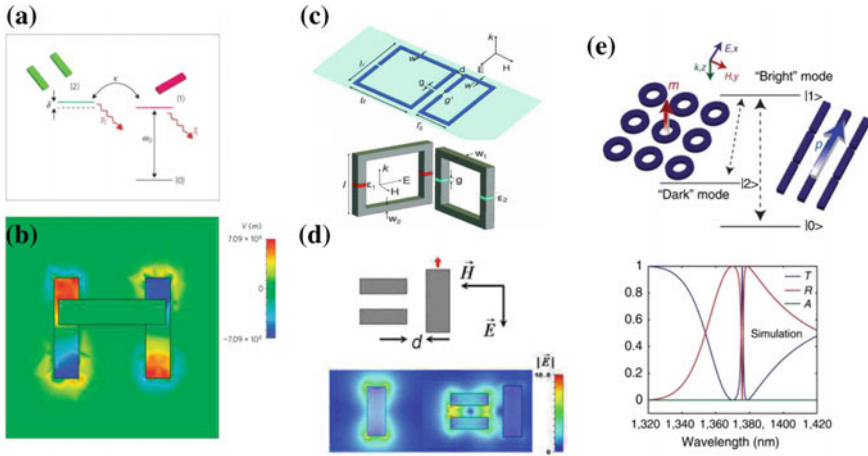


**Fig. 7.6** Plasmonic and dielectric nanostructures supporting EIT. **a** A three-level prototype of the plasmonic EIT nanostructure. The bottom nanobar pair supports the super-radiant mode ( $|1\rangle$ ) and the top bar supports the sub-radiant mode ( $|2\rangle$ ).  $\delta$  denotes the detuning of resonances  $|1\rangle$  and  $|2\rangle$ .  $\kappa$  denotes the coupling strength between resonances  $|1\rangle$  and  $|2\rangle$ .  $\gamma_1$  and  $\gamma_2$  denote the damping rates of resonances  $|1\rangle$  and  $|2\rangle$ . The EIT-like phenomenon arises from the destructive interference between two pathways, the direct pathway  $|0\rangle - |1\rangle$  and the indirect pathway  $|0\rangle - |1\rangle - |2\rangle - |1\rangle$ . **b** Simulated electric field distribution at the resonance. There is nearly no field in the top bar. Reprinted with permission from Macmillan Publishers Ltd: [Nature Materials] [15], copyright 2009. **c** Planar metamaterial composed of two coupled SRRs. Reprinted with permission from [12]. Copyright 2009 by the American Physical Society. **d** Plasmonic three-bar planar metamaterial and the electric field distribution at resonance. Reprinted with permission from [11]. Copyright 2008 by the American Physical Society. **e** All-dielectric metasurface composed of rectangular bars and ring resonators. Reprinted with permission from Macmillan Publishers Ltd: [Nature Communications] [65], copyright 2014

mode have equal amplitudes but with a phase difference of  $\pi$ . Thus the destructive interference of these two modes at the resonance cancels out the total scattering field and results in a narrow transparency window. This is the essential physical mechanism of the optical analog of EIT. In addition, in other studies, temporal coupled-mode theory of two resonances was also developed to describe these coupling processes [33, 68, 69], involving a set of two differential equations describing the dynamics of the super-radiant and sub-radiant modes respectively.

In analogy with the Fano resonances discussed above, EIT can be realized in subwavelength coupled plasmonic systems. The transparency is induced as a result of the interference between the super-radiant and sub-radiant modes. Introducing the spatial symmetry breaking allows the excitation of a sub-radiant higher-order mode. In the scattering process, two pathways contribute to the excitation of the broad plasmon mode, the direct excitation by the external field and the indirect resonant-assisted pathways through the backward coupling of the sub-radiant mode (Fig. 7.6a). At the resonant frequency, two optical pathways destructively interfere, thus result in suppression of the total scattering field (Fig. 7.6b). Coupling strength between the

two modes can be dynamically controlled by changing the geometric size of and the spatial separation between the coupled resonators.

Optical analogs of EIT were experimentally studied in plasmonic three-bar planar [11] (Fig. 7.6c) and stacked [15, 70] metamaterials. By introducing symmetry-broken spatial shift, the sub-radiant quadrupole mode in the pairing bars can be excited through plasmonic coupling with the super-radiant dipolar mode in the perpendicular single bar. At the resonant transparency, simulated near-field distributions show that the electromagnetic field in the radiative dipole antenna is indeed suppressed, while the field mainly localizes in the sub-radiant resonator. EIT effects were also studied in coupled split ring resonators (SRR) systems, composed of two SRRs [12, 71] (Fig. 7.6d), a cut-wire with a double-split SRR [67], an SRR pair separated by a cut-wire [72], or even three-dimensional SRRs [73]. Here one of the SRR or a cut-wire is directly excited by the incident wave and functions as a super-radiant resonator, while another SRR does not couple directly to the external field and functions as a sub-radiant resonator. The EIT-like spectrum results from the interference between the super-radiant resonance and the LC resonance in the sub-radiant SRR. EIT in other planar metamaterial has been studied, for example, bilayer fishlike-pattern metallic strips [10]. In the induced-transparency region, modes in the two layers are excited with a phase shift of  $\pi$  and their far field emissions interfere destructively, thus the reflection is reduced while the transmission is enhanced at the same time.

Optical analogs of EIT were also studied in a wide range of dielectric resonators. For a metasurface with its periodic lattice composed of a rectangular bar and a ring resonator, the EIT effect arises from the interference between the super-radiant electric dipole mode supported by the rectangular bars and the sub-radiant magnetic dipole mode supported by the ring resonator [65] (Fig. 7.6e). EIT in other dielectric systems were also demonstrated, for example, in waveguide-cavity systems [74–78], coupled whispering-gallery-mode microcavities [33, 79–83], and optomechanical cavity systems [84–88].

The distinct features of the EIT line shape give rise to a variety of applications. The induced transparency peak has a narrow spectral width and its resonant frequency is sensitive to changes of the environment refractive index [65, 70] or the structure geometric parameters [89], thus promises high-performance sensors for refractive index or structure displacement. Based on the steep transition from zero to complete transmission, EIT allows dynamical switching on and off of optical processes [90], useful for wave modulations [91] and unidirectional transmissive electromagnetic diode [92]. Steep dispersion of the transparency peak indicates the reduction of group velocity, which can be utilized for slowing of light pulses [32]. Slowing of light pulses have been demonstrated in many dielectric [75, 77, 78, 80] and plasmonic [10–12] nanoresonator systems. Furthermore, EIT effects can be implemented for enhancing nonlinear processes [32], and useful for quantum memory applications [87].

## 7.7 Design of Super-Scattering Nanoparticles

Enhancing the scattering of subwavelength objects is important in nano-optics, and has practical significance for applications such as imaging, biomedicine, optical antenna, and photovoltaics [18, 48, 93–102]. When the subwavelength object is a single atom in three-dimensional (3D) vacuum, one can rigorously prove that in the absence of dephasing, the scattering cross-section due to spontaneous emission of the atom reaches a maximum value of  $(2l + 1)\lambda^2/2\pi$  at the atomic resonant frequency, where  $l$  is the total angular momentum of the atomic transition. Most subwavelength nanoparticles have a scattering cross section less than  $3\lambda^2/2\pi$  since the underlying resonance has a total angular momentum  $l = 1$  [93, 94, 97]. Theoretically, in two-dimension, one can similarly prove that the maximum cross section of an atom cannot exceed  $2\lambda/\pi$  (7.23). Thus for subwavelength rotational symmetry nanostructures, a common observation has been that the scattering cross section is typically less than the single-channel limit, that is,  $2\lambda/\pi$  in two dimensions (such as nanowires) or  $(2l + 1)\lambda^2/2\pi$  in three dimensions (such as nanospheres) [18, 93–97]. Here we refer to a subwavelength particle having a total scattering cross section exceeding  $2\lambda/\pi$  in two dimensions and  $(2l_{\max} + 1)\lambda^2/2\pi$  in three dimensions as a superscatterer, where  $l_{\max}$  is the maximal total angular momentum involved.

In this Section, we answer a fundamental question that how large a scattering cross section can be achieved by an individual subwavelength particle. Following the theoretical suggestion of [16], we show that even though there is a rigorous upper limit of cross sections related with each individual scattering channel, there is no general theoretical constraint on the total cross section for an object with a given geometric dimension. Rather, in principle, arbitrarily large total cross-sections can be reached, provided that one maximizes the contribution from sufficiently large number of channels and creates an accidental degeneracy of resonant modes with different total angular momenta. We numerically demonstrate subwavelength spherical particles with a scattering cross section beyond the single channel limit ( $2\lambda/\pi$  in two dimensions and  $(2l + 1)\lambda^2/2\pi$  in three dimensions), by employing multiple resonances with different total angular momenta, and by ensuring that all these resonances have almost the same frequency and operate in the over-coupling region [16].

We want to mention that although the superscattering and the EIT effect both stem from the superposition of two degenerate resonances, a broad super-radiant one and a narrow sub-radiant one, these two phenomena arise in different conditions. According to the coupled-mode theory [28], the specific conditions for realizing EIT and superscattering are theoretically determined by the degree of orthogonality between the radiation patterns of these two involved eigenmodes. EIT requires destructive interference between these two resonances. The perfect EIT occurs in the extreme case that the radiation patterns of super-radiant and sub-radiant modes are identically aligned. On the contrary, the superscattering is achieved in another extreme case that two modes are exactly orthogonal.

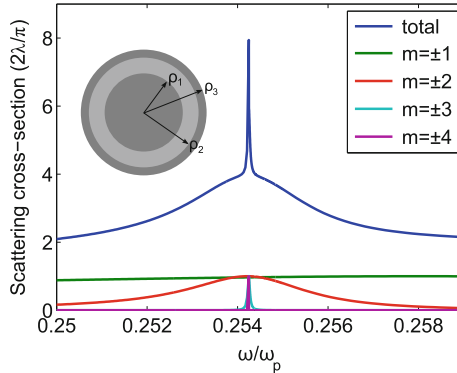


**Fig. 7.7** Total scattering cross section of a nanorod in the lossless case, and the contributions from individual channels. The  $m = \pm 1$  channel is near-resonant in the plotted frequency range. Its resonant line shape is not apparent since its resonant linewidth is much larger than the frequency range plotted here. (Inset) Schematic of the nanorod. The dark and gray areas correspond to a plasmonic material and a dielectric, respectively. The geometry parameters are  $\rho_1 = 0.3485\lambda_p$ ,  $\rho_2 = 0.5623\lambda_p$ , and  $\rho_3 = 0.6370\lambda_p$ , where  $\lambda_p = 2\pi c/\omega_p$ , with  $c$  being the speed of light in vacuum. Reprinted with permission from [16]. Copyright 2010 by the American Physical Society

As a numerical demonstration, we present subwavelength nanorod and nanosphere with a plasmonic-dielectric-plasmonic layer structure, where the scattering cross-section far exceeds the single-channel limit, even in the presence of loss. For the two-dimensional super-scatterer, we consider the nanorod schematically shown in the inset of Fig. 7.7, which consists of multiple concentric layers of dielectric and plasmonic materials. The plasmonic material is described by the Drude model. We consider a lossless structure first. The rod layers' thicknesses are designed to realize near-degeneracy of nanorod resonances at different angular momentum channels and the over-coupling condition. The contribution from each channel between  $m = \pm 1$  and  $m = \pm 4$  has a Lorentzian line shape that peaks with a value of  $2\lambda/\pi$ , at a frequency around  $0.2542\omega_p$  (Fig. 7.7). The leakage rates of these resonances decrease as one increases the angular momentum. The scattering cross section spectra are shown in Fig. 7.7. The total scattering cross-section reaches a peak value of  $7.94(2\lambda/\pi)$ , which is far beyond the single-channel limit, even though the scatterer just has a subwavelength diameter of  $0.32\lambda$ . Such a large total scattering cross-section is a result of near-degeneracy of resonances in multiple channels.

Figure 7.8a plots the real part of the total magnetic field distribution and the pointing vector lines at the frequency of  $0.2542\omega_p$ , when a plane wave, with unity amplitude, illuminates the nanorod. The nanorod leaves a large “shadow” behind it. The size of the shadow is much larger than the diameter of the rod. The presence of the rod also leads to significant redistribution of the power flow around the rod (Fig. 7.8a). We emphasize that the super-scattering effect is not an automatic outcome with the use of plasmonic material. A uniform plasmonic cylinder of the same size has a much smaller scattering cross section (Fig. 7.8b).

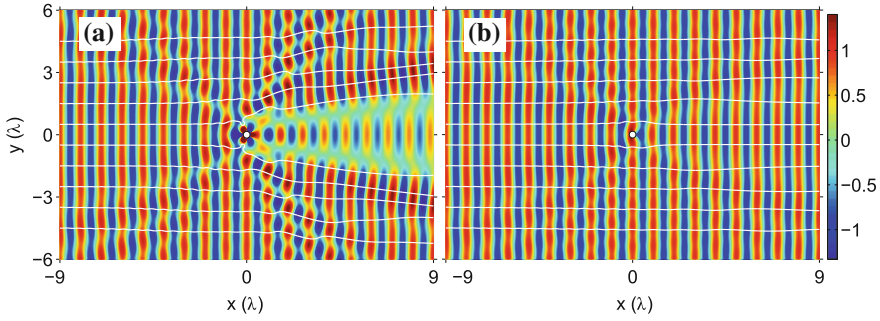


**Fig. 7.8** Real part of the total field distribution and the pointing vector lines at the frequency of  $0.2542\omega_p$  **a** for the nanorod shown in Fig. 7.7, **b** when the rod is replaced by a same-size uniform plasmonic cylinder. Here the amplitude of an incident plane wave is unity. The white circle at the center indicates the size of the rod. Reprinted with permission from [16]. Copyright 2010 by the American Physical Society

Consider the lossy case, the total scattering cross section reaches a maximum value of  $1.92(2\lambda/\pi)$ , which is still about two times the single-channel limit. The contributions to scattering is mostly from the  $m = \pm 1, \pm 2$  channels. In the higher angular momentum channels, the loss rate dominates over the radiation leakage rate. These resonances are therefore no longer in the over-coupled limit and do not contribute significantly to the scattering. Since the radiation leakage rate is generally smaller for higher angular momentum channel [18, 103, 104], the presence of loss has a more significant effect in higher angular momentum channels in general.

For the three-dimensional super-scatterer, similarly, we consider a nanosphere which consists of concentric metal-dielectric-metal layer. We start with lossless case first. With a proper choice of the dielectric layer thickness, we can realize near-degeneracy in the nanosphere between TM modes (with the magnetic field parallel with the interface) with different total angular momenta. The total scattering cross section reaches a peak value of  $15.2(\lambda^2/2\pi)$  or  $2.42\lambda^2$ , in comparison to the geometric cross section of the particle of  $0.18\lambda^2$ , for such a subwavelength particle with a diameter of  $0.485\lambda$ . In consistency with (7.23a), the contribution from different total angular momentum  $l$  each has a Lorentzian lineshape that peaks with a value of  $(2l + 1)\lambda^2/2\pi$ . The total cross section also exceeds  $7\lambda^2/2\pi$  where  $l_{\max} = 3$ . We have thus indeed designed a superscattering nanosphere.

We now consider the lossy case. The total scattering cross section maximum is reduced to  $6.1\lambda^2/2\pi$ , which nevertheless still exceeds  $(2l_{\max} + 1)\lambda^2/2\pi$ , since the contributions to scattering are mostly from the  $l = 1, 2$  channels. The resonances with  $l = 3$  do not contribute, since they are no longer in the over-coupling regime due to the material loss. To summarize, our results show that a superscattering nanosphere can be designed even in the presence of realistic loss.

In the above-mentioned examples, homogeneous core-shell cylindrical and spherical nanoparticles are considered, where the electric modes with different angular momenta are made spectrally aligned. These configurations were extended further

by taking the dispersion of realistic material into consideration [105]. The designing of the multi-layer cylindrical superscatterer at any desired wavelength was also achieved [106]. Furthermore, superscatterers based on the co-existence of electric and magnetic resonances were proposed. For example, the electric dipole and magnetic dipole resonances can be made degenerate in metal-dielectric core-shell nanowires [107], in spherical particles with radial anisotropy [108]. Even further, overlapping of electric quadrupole and magnetic quadrupole resonances was also demonstrated in core-shell nanosphere with nonlocality taken into consideration [109]. Finally, in analogy to the superscattering, one can seek to enhance the absorption cross section to go beyond the single channel limit as well, named as super-absorption. This has been realized in multilayer nanowires [110] and nanoparticles [111].

## 7.8 Summary

In this Chapter, the temporal coupled-mode theory is developed to provide a general description of the scattering behavior for subwavelength obstacles supporting resonances. The scattering process is well modeled as the interference and coupling between the external field and the resonance-assisted leaky radiation. In Sect. 7.2, we first discuss the temporal coupled-mode theory based on the consideration of energy conservation and time-reversal symmetry, and provide the general form of the scattering matrix and the scattering cross section. In Sects. 7.3 and 7.4, we then show that the Fano interference effect and EIT can be modeled by a simple temporal coupled-mode equation, which provides line shape formulas for scattering and absorption cross sections [2]. In Sects. 7.5 and 7.6, a brief review of the optical analog of Fano resonances and EIT in nanostructures is presented, and the temporal coupled-mode theory with the presence of two resonances is developed to provide a general modelling of the Fano and EIT lineshapes in these nanostructures. Finally, in Sect. 7.7, we discuss the super-scattering effect of a single subwavelength particle, where an arbitrarily large total scattering cross section can be achieved provided that one maximizes contributions from a sufficiently large number of resonances. In conclusion, we develop a theoretical framework that elucidates the influence of the resonance in subwavelength obstacles on the scattering properties, including Fano interference, all-optical analog to EIT, and super-scattering.

## References

1. M. Husnik, M.W. Klein, N. Feth, M. König, J. Niegemann, K. Busch, S. Linden, M. Wegener, *Nat. Photonics* **2**(10), 614 (2008)
2. Z. Ruan, S. Fan, *J. Phys. Chem. C* **114**, 7324 (2009)
3. N.J. Halas, S. Lal, W.S. Chang, S. Link, P. Nordlander, *Chem. Rev.* **111**, 3913 (2011)
4. B. Luk'yanchuk, N.I. Zheludev, S.A. Maier, N.J. Halas, P. Nordlander, H. Giessen, C.T. Chong, *Nat. Mater.* **9**(9), 707 (2010)



5. A.E. Miroshnichenko, S. Flach, Y.S. Kivshar, *Rev. Mod. Phys.* **82**(3), 2257 (2010)
6. R.D. Artuso, G.W. Bryant, *Nano Lett.* **8**(7), 2106 (2008)
7. A. Christ, O.J.F. Martin, Y. Ekinci, N.A. Gippius, S.G. Tikhodeev, *Nano Lett.* **8**(8), 2171 (2008)
8. F. Hao, P. Nordlander, Y. Sonnefraud, P.V. Dorpe, S.A. Maier, *ACS Nano* **3**(3), 643 (2009)
9. B. Gallinet, O.J.F. Martin, *Phys. Rev. B* **83**(23), 235427 (2011)
10. N. Papisimakis, V.A. Fedotov, N.I. Zheludev, S.L. Prosvirnin, *Phys. Rev. Lett.* **101**(25), 253903 (2008)
11. S. Zhang, D.A. Genov, Y. Wang, M. Liu, X. Zhang, *Phys. Rev. Lett.* **101**(4), 047401 (2008)
12. P. Tassin, L. Zhang, T. Koschny, E.N. Economou, C.M. Soukoulis, *Phys. Rev. Lett.* **102**(5), 053901 (2009)
13. V.A. Fedotov, M. Rose, S.L. Prosvirnin, N. Papisimakis, N.I. Zheludev, *Phys. Rev. Lett.* **99**(14), 147401 (2007)
14. S.Y. Chiam, R. Singh, C. Rockstuhl, F. Lederer, W. Zhang, A.A. Bettiol, *Phys. Rev. B* **80**(15), 153103 (2009)
15. N. Liu, L. Langguth, T. Weiss, J. Kastel, M. Fleischhauer, T. Pfau, H. Giessen, *Nat. Mater.* **8**(9), 758 (2009)
16. Z. Ruan, S. Fan, *Phys. Rev. Lett.* **105**, 013901 (2010)
17. Z. Ruan, S. Fan, *Appl. Phys. Lett.* **98**, 043101 (2011)
18. M.I. Tribelsky, B.S. Lykyanchuk, *Phys. Rev. Lett.* **97**(26), 263902 (2006)
19. M. Tribelsky, *EPL (Europhys. Lett.)* **94**, 14004 (2011)
20. H. Haus, *Waves and Fields in Optoelectronics* (Prentice-Hall, 1984)
21. C. Manolatu, M.J. Khan, S. Fan, P.R. Villeneuve, H.A. Haus, J.D. Joannopoulos, *IEEE J. Quantum Electron.* **35**(9), 1322 (1999)
22. A. Chutinan, M. Mochizuki, M. Imada, S. Noda, *Appl. Phys. Lett.* **79**, 2690 (2001)
23. S. Fan, J.D. Joannopoulos, *Phys. Rev. B* **65**(23), 235112 (2002)
24. S. Fan, W. Suh, J.D. Joannopoulos, *J. Opt. Soc. Am. A* **20**(3), 569 (2003)
25. Z. Yu, A. Raman, S. Fan, *Proc. Natl. Acad. Sci.* **107**(41), 17491 (2010)
26. Z. Ruan, S. Fan, *Phys. Rev. A* **85**(4), 043828 (2012)
27. L. Verslegers, Z. Yu, P.B. Catrysse, S. Fan, *J. Opt. Soc. Am. B* **27**(10), 1947 (2010)
28. L. Verslegers, Z. Yu, Z. Ruan, P.B. Catrysse, S. Fan, *Phys. Rev. Lett.* (in press) (2012)
29. A.B. Khanikaev, C.H. Wu, G. Shvets, *Nanophotonics* **2**(4), 247 (2013)
30. W.D. Zhou, D.Y. Zhao, Y.C. Shuai, H.J. Yang, S. Chuwongin, A. Chadha, J.H. Seo, K.X. Wang, V. Liu, Z.Q. Ma, *Progress in Quantum Electronics* **38**(1), 1 (2014)
31. M.F. Limonov, M.V. Rybin, A.N. Poddubny, Y.S. Kivshar, *Nature Photonics* **11**(9), 543 (2017)
32. M.D. Lukin, A. Imamoglu, *Nature* **413**(6853), 273 (2001)
33. B. Peng, S.K. Ozdemir, W.J. Chen, F. Nori, L. Yang, *Nat. Commun.* **5**, 5082 (2014)
34. R.E. Hamam, A. Karalis, J.D. Joannopoulos, M. Soljačić, *Phys. Rev. A* **75**(5), 053801 (2007)
35. U. Fano, *Phys. Rev.* **124**(6), 1866 (1961)
36. J.A. Schuller, E.S. Barnard, W.S. Cai, Y.C. Jun, J.S. White, M.L. Brongersma, *Nat. Mater.* **9**(3), 193 (2010)
37. M.L. Brongersma, V.M. Shalae, *Science* **328**(5977), 440 (2010)
38. V. Giannini, A.I. Fernandez-Dominguez, S.C. Heck, S.A. Maier, *Chem. Rev.* **111**(6), 3888 (2011)
39. J.M. Pitarke, V.M. Silkin, E.V. Chulkov, P.M. Echenique, *Rep. Prog. Phys.* **70**(1), 1 (2007)
40. B.S. Luk'yanchuk, M.I. Tribelsky, V. Ternovsky, Z.B. Wang, M.H. Hong, L.P. Shi, T.C. Chong, *J. Opt. A* **9**(9), S294 (2007)
41. M.I. Tribelsky, S. Flach, A.E. Miroshnichenko, A.V. Gorbach, Y.S. Kivshar, *Phys. Rev. Lett.* **100**(4), 043903 (2008)
42. N. Liu, S. Kaiser, H. Giessen, *Adv. Mater.* **20**(23), 4521 (2008)
43. B.S. Luk'yanchuk, M.I. Tribelsky, Z.B. Wang, Y. Zhou, M.H. Hong, L.P. Shi, T.C. Chong, *Appl. Phys. A* **89**(2), 259 (2007)
44. T.J. Arruda, A.S. Martinez, F.A. Pinheiro, *Phys. Rev. A* **87**(4), 043841 (2013)
45. H.L. Chen, L. Gao, *Opt. Express* **21**(20), 23619 (2013)

46. M. Yorulmaz, A. Hoggard, H.Q. Zhao, F.F. Wen, W.S. Chang, N.J. Halas, P. Nordlander, S. Link, *Nano Lett.* **16**(10), 6497 (2016)
47. A. Lovera, B. Gallinet, P. Nordlander, O.J.F. Martin, *ACS Nano* **7**(5), 4527 (2013)
48. F. Hao, Y. Sonnefraud, P. Van Dorpe, S.A. Maier, N.J. Halas, P. Nordlander, *Nano Lett.* **8**(11), 3983 (2008)
49. F. Hao, P. Nordlander, Y. Sonnefraud, P. Van Dorpe, S.A. Maier, *ACS Nano* **3**(3), 643 (2009)
50. N. Verellen, Y. Sonnefraud, H. Sobhani, F. Hao, V.V. Moshchalkov, P. Van Dorpe, P. Nordlander, S.A. Maier, *Nano Lett.* **9**(4), 1663 (2009)
51. N. Liu, T. Weiss, M. Mesch, L. Langguth, U. Eigenthaler, M. Hirscher, C. Sonichsen, H. Giessen, *Nano Lett.* **10**(4), 1103 (2009)
52. W. Khunsin, J. Dorfmueller, M. Esslinger, R. Vogelgesang, C. Rockstuhl, C. Etrich, K. Kern, *ACS Nano* **10**(2), 2214 (2016)
53. J.F. Zhang, W. Liu, Z.H. Zhu, X.D. Yuan, S.Q. Qin, *Opt. Express* **22**(25), 30889 (2014)
54. M.V. Rybin, K.B. Samusev, I.S. Sinev, G. Semouchkin, E. Semouchkina, Y.S. Kivshar, M.F. Limonov, *Opt. Express* **21**(24), 30107 (2013)
55. P.Y. Fan, Z.F. Yu, S.H. Fan, M.L. Brongersma, *Nat. Mater.* **13**(5), 471 (2014)
56. N. Muhammad, A.D. Khan, *Plasmonics* **12**(5), 1399 (2017)
57. A.E. Miroshnichenko, Y.S. Kivshar, *Nano Lett.* **12**(12), 6459 (2012)
58. M.I. Tribelsky, A.E. Miroshnichenko, Y.S. Kivshar, *EPL* **97**(4), 44005 (2012)
59. X.H. Kong, G.B. Xiao, *J. Opt. Soc. Am. A* **33**(4), 707 (2016)
60. M.I. Tribelsky, A.E. Miroshnichenko, *Phys. Rev. A* **93**(5), 053837 (2016)
61. P. Markos, *Phys. Rev. A* **92**(4), 043814 (2015)
62. K.E. Chong, B. Hopkins, I. Staude, A.E. Miroshnichenko, J. Dominguez, M. Decker, D.N. Neshev, I. Brener, Y.S. Kivshar, *Small* **10**(10), 1985 (2014)
63. M.V. Rybin, A.B. Khanikaev, M. Inoue, K.B. Samusev, M.J. Steel, G. Yushin, M.F. Limonov, *Phys. Rev. Lett.* **103**(2), 023901 (2009)
64. I.V. Soboleva, V.V. Moskalenko, A.A. Fedyanin, *Phys. Rev. Lett.* **108**(12), 123901 (2012)
65. Y.M. Yang, I.I. Kravchenko, D.P. Briggs, J. Valentine, *Nat. Commun.* **5**, 5753 (2014)
66. C.L.G. Alzar, M.A.G. Martinez, P. Nussenzevig, *Am. J. Phys.* **70**(1), 37 (2002)
67. P. Tassin, L. Zhang, T. Koschny, E.N. Economou, C.M. Soukoulis, *Opt. Express* **17**(7), 5595 (2009)
68. W. Suh, Z. Wang, S. Fan, *IEEE J. Quantum Electron.* **40**(10), 1511 (2004)
69. R. Adato, A. Artar, S. Erramilli, H. Altug, *Nano Lett.* **13**(6), 2584 (2013)
70. Z.G. Dong, H. Liu, J.X. Cao, T. Li, S.M. Wang, S.N. Zhu, X. Zhang, *Appl. Phys. Lett.* **97**(11), 114101 (2010)
71. R. Singh, C. Rockstuhl, F. Lederer, W.L. Zhang, *Phys. Rev. B* **79**(8), 085111 (2009)
72. X.J. Liu, J.Q. Gu, R. Singh, Y.F. Ma, J. Zhu, Z. Tian, M.X. He, J.G. Han, W.L. Zhang, *Appl. Phys. Lett.* **100**(13), 131101 (2012)
73. S. Han, L.Q. Cong, H. Lin, B.X. Xiao, H.L. Yang, R. Singh, *Sci. Rep.* **6**, 20801 (2016)
74. S.H. Fan, *Appl. Phys. Lett.* **80**(6), 908 (2002)
75. M.F. Yanik, W. Suh, Z. Wang, S.H. Fan, *Phys. Rev. Lett.* **93**(23), 233903 (2004)
76. D.D. Smith, H. Chang, K.A. Fuller, A.T. Rosenberger, R.W. Boyd, *Phys. Rev. A* **69**(6), 063804 (2004)
77. Q.F. Xu, S. Sandhu, M.L. Povinelli, J. Shakya, S.H. Fan, M. Lipson, *Phys. Rev. Lett.* **96**(12), 123901 (2006)
78. X.D. Yang, M.B. Yu, D.L. Kwong, C.W. Wong, *Phys. Rev. Lett.* **102**(17), 173902 (2009)
79. A. Naweed, G. Farca, S.I. Shopova, A.T. Rosenberger, *Phys. Rev. A* **71**(4), 043804 (2005)
80. K. Totsuka, N. Kobayashi, M. Tomita, *Phys. Rev. Lett.* **98**(21), 213904 (2007)
81. M. Tomita, K. Totsuka, R. Hanamura, T. Matsumoto, *J. Opt. Soc. Am. B* **26**(4), 813 (2009)
82. C.H. Dong, C.L. Zou, Y.F. Xiao, J.M. Cui, Z.F. Han, G.C. Guo, *J. Phys. B* **42**(21), 215401 (2009)
83. B.B. Li, Y.F. Xiao, C.L. Zou, X.F. Jiang, Y.C. Liu, F.W. Sun, Y. Li, Q.H. Gong, *Appl. Phys. Lett.* **100**(2), 021108 (2012)

84. S. Weis, R. Riviere, S. Deleglise, E. Gavartin, O. Arcizet, A. Schliesser, T.J. Kippenberg, *Science* **330**(6010), 1520 (2010)
85. C.H. Dong, V. Fiore, M.C. Kuzyk, H.L. Wang, *Science* **338**(6114), 1609 (2012)
86. K.N. Qu, G.S. Agarwal, *Phys. Rev. A* **87**(6), 063813 (2013)
87. A.H. Safavi-Naeini, T.P.M. Alegre, J. Chan, M. Eichenfield, M. Winger, Q. Lin, J.T. Hill, D.E. Chang, O. Painter, *Nature* **472**(7341), 69 (2011)
88. K.Y. Fong, L.R. Fan, L. Jiang, X. Han, H.X. Tang, *Phys. Rev. A* **90**(5), 051801 (2014)
89. N. Liu, M. Hentschel, T. Weiss, A.P. Alivisatos, H. Giessen, *Science* **332**(6036), 1407 (2011)
90. B.D. Clader, S.M. Hendrickson, R.M. Camacho, B.C. Jacobs, *Opt. Express* **21**(5), 6169 (2013)
91. N. Dabidian, I. Kholmanov, A.B. Khanikaev, K. Tatar, S. Trendafilov, S.H. Mousavi, C. Magnuson, R.S. Ruoff, G. Shvets, *ACS Photonics* **2**(2), 216 (2015)
92. Y. Sun, Y.W. Tong, C.H. Xue, Y.Q. Ding, Y.H. Li, H.T. Jiang, H. Chen, *Appl. Phys. Lett.* **103**(9), 091904 (2013)
93. J.B. Jackson, N.J. Halas, *Proc. Natl. Acad. Sci.* **101**(52), 17930 (2004)
94. J. Aizpurua, P. Hanarp, D.S. Sutherland, M. Käll, G.W. Bryant, F.J. Garcia de Abajo, *Phys. Rev. Lett.* **90**(5), 057401 (2003)
95. J.A. Schuller, T. Taubner, M.L. Brongersma, *Nat. Photonics* **3**, 658 (2009)
96. A.E. Miroshnichenko, *Phys. Rev. A* **80**(1), 013808 (2009)
97. R. Bardhan, S. Mukherjee, N.A. Mirin, S.D. Levit, P. Nordlander, N.J. Halas, *J. Phys. Chem. C* **114**, 7378 (2009)
98. H.R. Stuart, D.G. Hall, *Appl. Phys. Lett.* **73**, 3815 (1998)
99. S. Nie, S.R. Emory, *Science* **275**(5303), 1102 (1997)
100. L.R. Hirsch, R.J. Stafford, J.A. Bankson, S.R. Sershen, B. Rivera, R.E. Price, J.D. Hazle, N.J. Halas, J.L. West, *Proc. Natl. Acad. Sci.* **100**(23), 13549 (2003)
101. S. Pillai, K.R. Catchpole, T. Trupke, M.A. Green, *J. Appl. Phys.* **101**, 093105 (2007)
102. H.A. Atwater, A. Polman, *Nat. Mater.* **9**(3), 205 (2010)
103. H.C. van de Hulst, *Light Scattering by Small Particles* (Dover, New York, 1981)
104. Z. Jacob, L.V. Alekseyev, E. Narimanov, *Opt. Express* **14**(18), 8247 (2006)
105. A. Mirzaei, I.V. Shadrivov, A.E. Miroshnichenko, Y.S. Kivshar, *Opt. Express* **21**(9), 10454 (2013)
106. A. Mirzaei, A.E. Miroshnichenko, I.V. Shadrivov, Y.S. Kivshar, *Appl. Phys. Lett.* **105**(21), 011109 (2014)
107. W. Liu, A.E. Miroshnichenko, R.F. Oulton, D.N. Neshev, O. Hess, Y.S. Kivshar, *Opt. Lett.* **38**(14), 2621 (2013)
108. W. Liu, *Opt. Express* **23**(11), 14734 (2015)
109. Y. Huang, L. Gao, *J. Phys. Chem. C* **118**(51), 30170 (2014)
110. A. Mirzaei, I.V. Shadrivov, A.E. Miroshnichenko, Y.S. Kivshar, *Nanoscale* **7**(42), 17658 (2015)
111. K. Ladutenko, P. Belov, O. Pena-Rodriguez, A. Mirzaei, A.E. Miroshnichenko, I.V. Shadrivov, *Nanoscale* **7**(45), 18897 (2015)

# Chapter 8

## A Full-Retarded Spectral Technique for the Analysis of Fano Resonances in a Dielectric Nanosphere



Carlo Forestiere, Giovanni Miano, Mariano Pascale and Roberto Tricarico

**Abstract** We introduce a representation of the electromagnetic field scattered by a homogeneous sphere in terms of a set of full-retarded modes independent of its permittivity. Within this framework, we introduce the orthogonality properties of the modes, their resonance conditions, and their classification into narrow and broad modes. We also discuss the role played by the material properties in determining the resonant width of a given mode and in enabling or preventing the multimode interference. We use this theory to unveil the origin of Fano lineshapes in the scattering efficiency of a spherical nanoparticle, by identifying the interfering modes responsible for peaks and dips. Eventually, by using the introduced theoretical approach, we design the permittivity of a homogeneous sphere of size comparable to the incident wavelength to cancel its backscattering through directional multimode interference.

### 8.1 Introduction

The electromagnetic resonant properties of metal and dielectric nanoparticles (NPs) have attracted the interest of many scientist and engineers. The free electron plasma of metal NPs may display coherent oscillations, named localized surface plasmons [1]. This phenomenon can be exploited to engineer the electromagnetic fields at the nanoscale and to enhance linear and nonlinear optical response of nanomaterials [2], triggering many potential applications, including biosensors of improved sensitivity [3], nonlinear optics [4], and solar energy harvesting [5].

Unfortunately metals are plagued by high losses in the visible and mid-IR part of the spectrum, and this fact is currently inhibiting the development of commercial devices [6]. Therefore, the replacement of metals with high index dielectrics may be beneficial for many applications as pointed out in [7–11], especially to manipulate light and enhance light-matter interactions at the nanoscale. This interest was stimulated by the evidence that the enhancement of electric and magnetic fields in

---

C. Forestiere (✉) · G. Miano · M. Pascale · R. Tricarico  
Department of Electrical Engineering and Information Technology,  
Università degli Studi di Napoli Federico II, via Claudio 21, 80125 Napoli, Italy  
e-mail: carlo.forestiere@unina.it

high-index structures is of the same order of magnitude of the one achievable in plasmonics. However, we should bear in mind that both the electric and magnetic hotspots are found within the dielectric particle, while in plasmonic NPs the hotspot is more easily accessible, being always located outside the metal region. Nevertheless, by using dimers of dielectric particles coupled in the near field zone high values of enhancement of electric and magnetic fields have been demonstrated [12–20].

The strong electromagnetic response of high index NPs suggested an increasing number of applications, including the enhancement of non linear effects [21], Raman scattering [22, 23], enhanced emission from quantum dots [24], and biosensing [25].

The physics governing the scattering from high index dielectric NPs is far richer than the physics behind metal NPs scattering, due to the possibility of exciting magnetic modes, and due to presence of multimode interference, which may lead to the formation of Fano resonances [26]. Magnetic (TE) scattering has been experimentally measured from an isolated nanosphere [27] and nanodisk [28], and high magnetic field enhancement has been also achieved in different geometries [20, 29]. This strong magnetic response has also suggested novel strategies to enhance the weak magnetic transitions of molecules [30–34]. Contrarily to high index nanosphere, the magnetic modes (TE) in isolated metal nanospheres at optical frequencies have never been observed. In this chapter, we also justify this fundamental difference based on the properties of a suitable set of modes that do not depend on the permittivity of the nanosphere.

Fano resonances, which are associated with an asymmetric scattering profile, originate from the interference of broad and narrow modes. They may manifest

- in the spectrum of the total scattered power,
- in the spectrum of the power scattered in a given angular direction (directional Fano resonances).

Fano resonances have been observed in the total scattering spectrum of a Si nanosphere, see Fig. 1a of [28], of isolated disks [35], of oligomers [36–39], and of silicon dolmen structures [40]. Fano resonances are particularly interesting for practical applications, including, for instance, lasing and switching schemes, and for optical sensors which, taking advantage of their sharp resonant lineshape, could potentially offer a significant improvement in sensitivity [26]. It is worth to note that Fano lineshapes in the total scattering spectrum have never been observed in isolated plasmonic spheres. We theoretically justify also this difference in this chapter.

Directional Fano Resonances [26], are often associated with cancellation of the backscattering [41–50], where the scattering is suppressed in one direction, due to destructive multipole interference and enhanced in the opposite direction. Enhancing the directionality of nano-scatterers may have a great impact in optical wireless nano-antenna links.

The correct description of Fano lineshapes, where interference phenomena play a key role, requires not only the identification of the resonant modes but also a rigorous decomposition of the total scattered field in terms of these modes. Only in this way the interfering modes can be unambiguously identified, contrarily to qualitative approaches which are often prone to ambiguities and errors.

In order to accomplish this task we need a full electrodynamic spectral theory. It is worth to point out that the Mie theory cannot be considered a spectral theory. In addition, quasi normal modes (QNM) cannot address these problems, because they diverge at infinity [51], thus the representation of the field scattered in the far zone in terms of QNM is not practical.

However, in the quasi-electrostatic regime, spectral theories enabling the identification of plasmon resonances have been previously proposed. As an example, for a sphere of radius much smaller than the wavelength of the incident field and permittivity  $\varepsilon_r$ , the Fröhlich condition [1], i.e.:

$$|\varepsilon_r(\omega) + 2| = \text{Minimum}_{\omega}, \quad (8.1)$$

enables the calculation of the resonant value of the permittivity. Moreover, many authors introduced quasi-electrostatic techniques allowing the calculation of resonances of arbitrarily shaped particles [52–56]. In the framework of electrostatic approaches, the Fano resonances in complex plasmonic nanostructures have been theoretically modelled in [57]. However, although the applicability domain of these approaches can be reasonably extended using perturbation techniques [55, 56, 58], they break down when the particle size is of the order of the incident wavelength.

In this chapter, we derive a full-retarded spectral theory for the description of the electromagnetic scattering from a sphere. This theory enables the identification of the resonances and interference effects in the electromagnetic scattering from an isolated spherical particle. It is based on a series expansion of the scattered electric field in terms of addends of the form  $(\gamma_h - \varepsilon_r)^{-1} \mathbf{C}_h(\mathbf{r})$ , where  $\gamma_h$  and  $\mathbf{C}_h$  are respectively the  $h$ -th eigenvalue and eigenfunction of the auxiliary eigenvalue problem introduced in [59], which do not depend on the permittivity  $\varepsilon_r$ . For this reason we denote these eigenfunctions as material-independent modes. The investigation of the properties of these eigenvalues and eigenfunctions enables the derivation of the general properties of the electromagnetic scattering from a sphere. Specifically, we explain the differences between the spectrum of the total scattered power of dielectric and metal NPs, which stem from the disjoint subset of narrow modes excited in these two cases [60]. Similar methods have been formulated in previous works [61, 62] and applied to either the quasi-static or long wavelength limit [54–56, 61–64], to the retarded single dipole approximation [65], to the scalar Mie scattering [66], and to the full-wave electromagnetic scattering from a slab [67]. In [59] we presented the spectral theory of electromagnetic scattering from a homogeneous sphere. Subsequently, we extended this approach to a coated sphere [68], and to an arbitrarily shaped homogeneous object exploiting a volume integral formulation of the Maxwell's equations [69].

In particular, in Sect. 8.2, we introduce the material independent modes for the general case of an arbitrarily shaped object, pointing out in 8.2.1 the main differences between the material independent modes and the quasi normal modes. In Sect. 8.3, we particularize the results of Sect. 8.2 to the case of a sphere, deriving the characteristic power series, the expression of the modes, the orthogonality con-

ditions, the expansions of the scattered field. In this framework, we also provide the analytic form of the expansion coefficients of the scattered field, together with the expression of the radiation pattern and of the scattering efficiency, when the incident field is a plane wave. Next, in Sect. 8.4, we investigate the spectral properties of the electromagnetic scattering from a homogeneous sphere, showing the universal loci described by the eigenvalues as a function of the sphere's size parameter, systematizing within this framework the properties of plasmonic and photonic modes. We also classify the modes in terms of their width, separating them into narrow and broad modes, regardless of the excitation conditions. Then, in Sect. 8.5, we apply the introduced theoretical framework to the study of the resonances and interference effects in Silver and Silicon NPs. Eventually, in Sect. 8.6, we demonstrate that the design of the permittivity of a sphere to cancel its backscattering can be greatly simplified by expressing the scattered electromagnetic field in terms of material-independent eigenmodes, exploiting the fact that the expansion coefficients are rational functions of the permittivity.

## 8.2 Material Independent Modes for Electromagnetic Scattering

Let us consider the electromagnetic scattering by an object occupying a regular region  $\Omega$  with boundary  $\partial\Omega$ , sketched in Fig. 8.1. The object is excited by a time harmonic electromagnetic field incoming from infinity  $\text{Re}\{\mathbf{E}_i(\mathbf{r})e^{-i\omega t}\}$ . The medium is a non-magnetic isotropic homogeneous dielectric with relative permittivity  $\varepsilon_r(\omega)$ , surrounded by vacuum. Let  $\mathbf{E}_S^+$  and  $\mathbf{E}_S^-$  be the scattered electric fields in  $\Omega$  and  $\mathbb{R}^3 \setminus \bar{\Omega}$ , respectively. The Maxwell's equations lead to

$$\nabla^2 \mathbf{E}_S^+ + k_0^2 \varepsilon_r(\omega) \mathbf{E}_S^+ = k_0^2 [1 - \varepsilon_r(\omega)] \mathbf{E}_i \text{ in } \Omega, \quad (8.2)$$

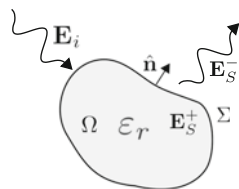
$$\nabla^2 \mathbf{E}_S^- + k_0^2 \mathbf{E}_S^- = \mathbf{0} \quad \text{in } \mathbb{R}^3 \setminus \bar{\Omega}, \quad (8.3)$$

$$\hat{\mathbf{n}} \times (\mathbf{E}_S^- - \mathbf{E}_S^+) = \mathbf{0} \quad \text{on } \partial\Omega, \quad (8.4)$$

$$\hat{\mathbf{n}} \times (\nabla \times \mathbf{E}_S^- - \nabla \times \mathbf{E}_S^+) = \mathbf{0} \quad \text{on } \partial\Omega, \quad (8.5)$$

where  $k_0 = \omega/c_0$ ,  $c_0$  is the light velocity in vacuum and  $\hat{\mathbf{n}}$  is the outgoing normal to  $\partial\Omega$ . Equations (8.2)–(8.5) have to be solved with the radiation conditions for the

**Fig. 8.1** Sketch of the homogeneous scatterer



scattered field, namely the regularity and Silver-Müller conditions at infinity. This problem has a unique solution if  $\text{Im} \{\varepsilon_r\} \geq 0$  [70].

Aiming at the reduction of the scattering problem to an algebraic form, we introduce the following auxiliary eigenvalue problem

$$-k_0^{-2} \nabla^2 \mathbf{C} = \gamma \mathbf{C} \quad \text{in } \Omega, \quad (8.6)$$

$$\hat{\mathbf{n}} \times \nabla \times \mathbf{C} = \mathcal{C}^e \{ \hat{\mathbf{n}} \times \mathbf{C} \} \quad \text{in } \partial\Omega, \quad (8.7)$$

where  $\gamma$  is the eigenvalue. We introduced the exterior outgoing Calderón operator  $\mathcal{C}^e$  [70] that takes the tangential component of the scattered electric field on  $\partial\Omega$ , i.e.  $\hat{\mathbf{n}} \times \mathbf{E}_S^-|_{\partial\Omega}$ , where  $\mathbf{E}_S^-$  is solution of the scattering problem, and returns the tangential component of its curl  $\hat{\mathbf{n}} \times \nabla \times \mathbf{E}_S^-|_{\partial\Omega}$ :

$$\mathcal{C}^e \{ \hat{\mathbf{n}} \times \mathbf{E}_S^-|_{\partial\Omega} \} = \hat{\mathbf{n}} \times \nabla \times \mathbf{E}_S^-|_{\partial\Omega}. \quad (8.8)$$

The Calderón operator only depends on the geometry of  $\partial\Omega$ . The spectrum of the operator  $-\nabla^2$  in  $\Omega$  with the boundary condition (8.7) is countably infinite. This fact is a consequence of the radiation conditions at infinity, which are implicitly accounted for by the exterior Calderón operator. We denote the aforementioned spectrum as  $\{\gamma_r\}_{r \in \mathbb{N}}$ , made of complex eigenvalues with  $\text{Im} \{\gamma_r\} < 0$ .

In this case, the operator  $-\nabla^2$  is symmetric, and the eigenmodes  $\mathbf{C}_r$  and  $\mathbf{C}_s$  corresponding to different eigenvalues  $\gamma_r$  and  $\gamma_s$  are not orthogonal in the usual sense, i.e.  $\langle \mathbf{C}_r^*, \mathbf{C}_s \rangle_\Omega \neq 0$ , where

$$\langle \mathbf{A}, \mathbf{B} \rangle_V = \iiint_V \mathbf{A} \cdot \mathbf{B} \, dV. \quad (8.9)$$

Nevertheless, it can be proved that [59]:

$$\langle \mathbf{C}_r, \mathbf{C}_s \rangle_\Omega = 0 \quad \gamma_r \neq \gamma_s, \quad (8.10)$$

and

$$\gamma_r = \frac{1}{\|\mathbf{C}_r\|_\Omega^2} \left[ \frac{\|\nabla \times \mathbf{C}_r\|_{\mathbb{R}^3}^2}{k_0^2} - \|\mathbf{C}_r\|_{\mathbb{R}^3 \setminus \bar{\Omega}}^2 - i \iint_{S_\infty} \frac{|\mathbf{C}_r|^2}{k_0} \, dS \right] \quad (8.11)$$

where  $\|\mathbf{A}\|_V^2 = \langle \mathbf{A}^*, \mathbf{A} \rangle_V$ . The eigenmodes  $\mathbf{C}_r$  are extended in  $\mathbb{R}^3$  by requiring that they satisfy (8.3), the boundary conditions (8.4)–(8.5) and the radiation conditions at infinity. Equation (8.11) suggests that  $\text{Re} \{\gamma_r\}$  does not have a definite sign, while  $\text{Im} \{\gamma_r\}$  is strictly negative. In particular,  $\text{Im} \{\gamma_r\}$  is proportional to the contribution of the corresponding mode to the power radiated to infinity, accounting for its radiative losses.

In the presence of an arbitrary external excitation  $\mathbf{E}_i$ , the solution of the scattering problem is:



$$\mathbf{E}_S^+ = (1 - \varepsilon_r) \sum_{r=1}^{\infty} \frac{1}{\varepsilon_r - \gamma_r} \frac{\langle \mathbf{C}_r, \mathbf{E}_i \rangle_{\Omega}}{\langle \mathbf{C}_r, \mathbf{C}_r \rangle_{\Omega}} \mathbf{C}_r. \quad (8.12)$$

The eigenvalues  $\gamma_r$  and the eigenfunctions  $\mathbf{C}_r$  are permittivity independent, they only depend on the geometry of the dielectric object. The permittivity appears in the multiplicative factors only as  $1/(\varepsilon_r - \gamma_r)$ .

### 8.2.1 Differences Between Material Independent Modes and Quasi Normal Modes

Open systems are often investigated by using quasi normal modes (QNM) [71]. When applied to a dielectric sphere they are also known as morphology-dependent resonances (MDR's) or whispering gallery modes [72, 73]. Therefore, we feel compelled to highlight the major differences between QNMs and material independent modes.

The QNMs are solution of the following eigenvalue problem:

$$-\nabla^2 \mathbf{F}^+ = \frac{\xi^2}{c^2} \varepsilon_r \mathbf{F}^+ \quad \text{in } \Omega, \quad (8.13)$$

$$-\nabla^2 \mathbf{F}^- = \frac{\xi^2}{c^2} \mathbf{F}^- \quad \text{in } \mathbb{R}^3 \setminus \bar{\Omega}, \quad (8.14)$$

$$\hat{\mathbf{n}} \times (\mathbf{F}^- - \mathbf{F}^+) = \mathbf{0} \quad \text{on } \partial\Omega, \quad (8.15)$$

$$\hat{\mathbf{n}} \times (\nabla \times \mathbf{F}^- - \nabla \times \mathbf{F}^+) = \mathbf{0} \quad \text{on } \partial\Omega, \quad (8.16)$$

with the Silver-Müller conditions at infinity, namely

$$\mathbf{F}^- + \frac{c}{i\xi} \hat{\mathbf{r}} \times \nabla \times \mathbf{F}^- = o\left(\frac{1}{r}\right), \quad (8.17)$$

where  $\xi$  is the eigenvalue.

It is worth noting that in this case the spectral parameter  $\xi$  also appears in the Silver-Müller conditions at infinity. This fact makes the spectral problem (8.13)–(8.17) fundamentally different from the problem of (8.6)–(8.7), where the radiation conditions at infinity are independent of the spectral parameter instead.

The problem (8.13)–(8.17) exhibits a countably infinite spectrum  $\{\xi_r\}_{r \in \mathbb{N}}$  with the property  $\text{Im}\{\xi_r\} < 0$ . This property, together with the radiation condition at infinity, (8.17) has the consequence that QNMs diverge exponentially at large distances [74]. Therefore, to be used in any practical application, they need to be normalized [75]. On the contrary, the material-independent modes approach zero at infinity and no normalization is needed.

Furthermore, an additional major difference is that the eigenvalues  $\{\xi_r\}_{r \in \mathbb{N}}$  and the corresponding QNMs  $\{\mathbf{F}\}_{r \in \mathbb{N}}$  are dependent on the permittivity of the material  $\varepsilon_r$ . This fact makes the QNMs unattractive for the design of the permittivity of an object to achieve a prescribed tailoring of the scattered field, because the expansion in terms of QNMs of the electric field, that solves the inhomogeneous scattering problem, is a very complicated function of the permittivity.

### 8.3 Spectral Theory of Electromagnetic Scattering from a Sphere

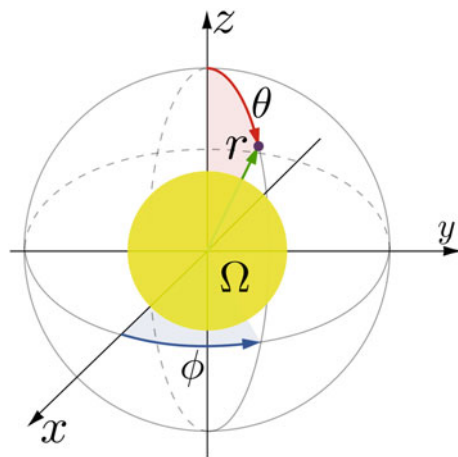
From now on, we assume that the region  $\Omega$  is a sphere of radius  $R$ , sketched in Fig. 8.2, with size parameter  $x = 2\pi R/\lambda$ , where  $\lambda$  is the wavelength. The vector field  $\mathbf{C}$ , solution of the problem (8.6)–(8.7), can be described in  $\Omega$  in terms of the Vector Spherical Wave Functions [76] (VSWFs) expansion:

$$\mathbf{C}(\mathbf{r}) = \sum_{n=1}^{\infty} \sum_{m=0}^n \{ C_{emn} \mathbf{M}_{emn}^{(1)}(\sqrt{\gamma} k_0 \mathbf{r}) + C_{omn} \mathbf{M}_{omn}^{(1)}(\sqrt{\gamma} k_0 \mathbf{r}) + D_{emn} \mathbf{N}_{emn}^{(1)}(\sqrt{\gamma} k_0 \mathbf{r}) + D_{omn} \mathbf{N}_{omn}^{(1)}(\sqrt{\gamma} k_0 \mathbf{r}) \}, \quad (8.18)$$

where the subscripts  $e$  and  $o$  denote even and odd, and the superscript (1), appended to the VSWFs, denotes that the radial dependence is given by the Bessel function  $j_n^{(1)}(\cdot)$ , which are regular at the origin. The explicit expressions of the VSWFs are reported in the Appendix of the present document.

The extension of  $\mathbf{C}$  in the external region  $\mathbb{R}^3 \setminus \Omega$  can be written as:

**Fig. 8.2** Spherical coordinate system centred on the sphere of size parameter  $x$  occupying the region  $\Omega$ . We denote with  $r$  the radial distance, and with  $\theta$  and  $\phi$  the polar and azimuthal angles, respectively (Adapted from [59]. Copyright (2016) by the American Physical Society)



$$\mathbf{C}(\mathbf{r}) = \sum_{n=1}^{\infty} \sum_{m=0}^n \left\{ B_{\text{em}n} \mathbf{M}_{\text{em}n}^{(3)}(k_0 \mathbf{r}) + B_{\text{om}n} \mathbf{M}_{\text{om}n}^{(3)}(k_0 \mathbf{r}) + A_{\text{em}n} \mathbf{N}_{\text{em}n}^{(3)}(k_0 \mathbf{r}) + A_{\text{om}n} \mathbf{N}_{\text{om}n}^{(3)}(k_0 \mathbf{r}) \right\}, \quad (8.19)$$

where the superscript (3), appended to the VSWFs, denotes that the radial dependence is given by the Hankel function  $h_n^{(1)}(\cdot)$ , which satisfies the Silver-Müller condition at infinity.

By enforcing the continuity of the tangential components of  $\mathbf{C}$  and  $\nabla \times \mathbf{C}$  on the surface of the sphere and exploiting the orthogonality of the VSWFs, we obtain, for a given indices pair  $m, n$ , the equations:

$$\begin{pmatrix} h_n^{(1)}(x) & -\sqrt{\gamma} j_n(\sqrt{\gamma}x) \\ \sqrt{\gamma} [x h_n^{(1)}(x)]' - [\sqrt{\gamma}x j_n(\sqrt{\gamma}x)]' \end{pmatrix} \begin{pmatrix} A_{\sigma^{mn}} \\ D_{\sigma^{mn}} \end{pmatrix} = \mathbf{0}, \quad (8.20)$$

$$\begin{pmatrix} h_n^{(1)}(x) & -j_n(\sqrt{\gamma}x) \\ [x h_n^{(1)}(x)]' - [\sqrt{\gamma}x j_n(\sqrt{\gamma}x)]' \end{pmatrix} \begin{pmatrix} B_{\sigma^{mn}} \\ C_{\sigma^{mn}} \end{pmatrix} = \mathbf{0}, \quad (8.21)$$

where the prime denotes differentiation with respect to the argument in parentheses. Non trivial solutions of the linear problems described by (8.20) and (8.21) are obtained by zeroing the determinant of the corresponding matrices, i.e.

$$\begin{aligned} h_n^{(1)}(x) [\sqrt{\gamma}x j_n(\sqrt{\gamma}x)]' - \gamma j_n(\sqrt{\gamma}x) [x h_n^{(1)}(x)]' &= 0, \\ h_n^{(1)}(x) [\sqrt{\gamma}x j_n(\sqrt{\gamma}x)]' - j_n(\sqrt{\gamma}x) [x h_n^{(1)}(x)]' &= 0. \end{aligned} \quad (8.22)$$

We now use the properties of the derivatives of the Bessel and Hankel functions shown below:

$$\begin{aligned} [z h_n^{(1)}(z)]' &= (n+1) h_n^{(1)}(z) - z h_{n+1}^{(1)}(z), \\ [z j_n(z)]' &= (n+1) j_n(z) - z j_{n+1}(z), \end{aligned} \quad (8.23)$$

and we obtain, after some algebraical manipulations:

$$\begin{aligned} \left[ -(n+1) \frac{(\gamma-1)}{x} h_n^{(1)}(x) + \gamma h_{n+1}^{(1)}(x) \right] j_n(\sqrt{\gamma}x) - \sqrt{\gamma} h_n^{(1)}(x) j_{n+1}(\sqrt{\gamma}x) &= 0, \\ h_{n+1}^{(1)}(x) j_n(\sqrt{\gamma}x) - \sqrt{\gamma} h_n^{(1)}(x) j_{n+1}(\sqrt{\gamma}x) &= 0. \end{aligned} \quad (8.24)$$

Thus, we apply the multiplication theorem for the Bessel functions, namely:

$$j_n(\sqrt{\gamma}x) = (\sqrt{\gamma})^n \sum_{h=0}^{\infty} \frac{(-1)^h}{h!} (\gamma-1)^h \left(\frac{x}{2}\right)^h j_{n+h}(x), \quad (8.25)$$

and (8.24) become respectively:

$$\sum_{h=0}^{\infty} \frac{(-1)^h}{h!} \left(\frac{x}{2}\right)^h (\gamma - 1)^h \left\{ -\frac{(\gamma - 1)}{x} (n + 1) h_n^{(1)}(x) j_{n+h}(x) + \gamma \left[ h_{n+1}^{(1)}(x) j_{n+h}(x) - h_n^{(1)}(x) j_{n+h+1}(x) \right] \right\} = 0,$$

$$\sum_{h=0}^{\infty} \frac{(-1)^h}{h!} \left(\frac{x}{2}\right)^h (\gamma - 1)^h \left[ h_{n+1}^{(1)}(x) j_{n+h}(x) - \gamma h_n^{(1)}(x) j_{n+h+1}(x) \right] = 0. \quad (8.26)$$

We recast the equations above in the following power series expansions:

$$\mathcal{P}_n(\gamma) = \sum_{h=0}^{\infty} p_{nh} (\gamma - 1)^h = 0, \quad \mathcal{Q}_n(\gamma) = \sum_{h=0}^{\infty} q_{nh} (\gamma - 1)^h = 0, \quad (8.27)$$

where the coefficients  $p_{nh} = p_{nh}(x)$  and  $q_{nh} = q_{nh}(x)$  are defined for any given  $n$ ,  $x$ , and  $h \geq 1$  as follows:

$$p_{n0} = q_{n0} = h_{n+1}^{(1)}(x) j_n(x) - h_n^{(1)}(x) j_{n+1}(x),$$

$$q_{nh} = -\frac{(-1)^{h-1}}{(h-1)!} \left(\frac{x}{2}\right)^{h-1} \left[ h_n^{(1)}(x) j_{n+h}(x) + \frac{(-1)^h}{h!} \left(\frac{x}{2}\right)^h \left[ h_{n+1}^{(1)}(x) j_{n+h}(x) - h_n^{(1)}(x) j_{n+h+1}(x) \right] \right],$$

$$p_{nh} = q_{nh} - \frac{(-1)^{h-1}}{(h-1)!} \left(\frac{x}{2}\right)^{h-1} \frac{[x h_n^{(1)}(x)]'}{x} j_{n+h-1}(x),$$

$j_n$  are the spherical Bessel functions of the first kind,  $h_n^{(1)}$  are the Hankel functions of the first kind. The infinite countable set of eigenvalues is the union of two sets  $\{\alpha_{nl}\}_{(n,l) \in \mathbb{N}^2}$  and  $\{\beta_{nl}\}_{(n,l) \in \mathbb{N}^2}$ , being  $\alpha_{nl}$  (resp.  $\beta_{nl}$ ) the  $l$ -th root of the power series  $\mathcal{P}_n$  (resp.  $\mathcal{Q}_n$ ). The eigenspaces corresponding to the eigenvalues  $\alpha_{nl}$  and  $\beta_{nl}$  are spanned by the eigenfunctions:

$$\mathbf{C}_{pmnl}^{(\alpha)} = \begin{cases} \mathbf{N}_{pmn}^{(1)}(\sqrt{\alpha_{nl}} k_0 \mathbf{r}) & \mathbf{r} \in \Omega \\ \frac{\sqrt{\alpha_{nl}} j_n(\sqrt{\alpha_{nl}} x)}{h_n^{(1)}(x)} \mathbf{N}_{pmn}^{(3)}(k_0 \mathbf{r}) & \mathbf{r} \in \mathbb{R}^3 \setminus \bar{\Omega} \end{cases}, \quad (8.28)$$

$$\mathbf{C}_{pmnl}^{(\beta)} = \begin{cases} \mathbf{M}_{pmn}^{(1)}(\sqrt{\beta_{nl}} k_0 \mathbf{r}) & \mathbf{r} \in \Omega \\ \frac{j_n(\sqrt{\beta_{nl}} x)}{h_n^{(1)}(x)} \mathbf{M}_{pmn}^{(3)}(k_0 \mathbf{r}) & \mathbf{r} \in \mathbb{R}^3 \setminus \bar{\Omega} \end{cases}. \quad (8.29)$$

The modes  $\mathbf{C}_{pmnl}^{(\alpha)}$  have no radial magnetic field component and are therefore called *electric type* or TM modes. Vice versa the modes  $\mathbf{C}_{pmnl}^{(\beta)}$  have no radial electric field component and are denoted as *magnetic type* or TE modes. The modal indices  $p, m, n, l$  have the following meaning. The subscript  $p \in \{e, o\}$  distinguishes

between even and odd modes with respect to the azimuthal dependence. The numbers  $n \in \mathbb{N}$  and  $0 \leq m \leq n$  define the angular dependence of the mode:  $m$  defines the number of oscillations along the azimuth,  $n$  is associated with the number of lobes of the mode amplitude at any given radial distance. In particular, the modes with  $n = 1$  are the dipolar modes, those with  $n = 2$  are the quadrupolar modes, and so on. The mode number  $l \in \mathbb{N}$  gives the number of maxima of the mode amplitude along the radial direction inside the sphere. We denote the electric and the magnetic modes as *fundamental* when  $l = 1$ , and as *higher order* modes when  $l \geq 2$ . It is worth noting that higher order electric modes and magnetic modes are not contemplated by the electrostatic resonance theory [56], and it is not possible to include them within the electrostatic framework by using perturbation techniques.

In general, due to the bi-orthogonality property of (8.10), we have

$$\langle \mathbf{C}_{pmnl}^{(\delta)}, \mathbf{C}_{p'm'n'l'}^{(\delta')} \rangle_{\Omega} = 0 \quad \forall (\delta, p, m, n, l) \neq (\delta', p', m', n', l') \quad (8.30)$$

where  $\delta, \delta' \in \{\alpha, \beta\}$ . Furthermore, due to the spherical symmetry, we also have that a subset of the modes is orthogonal on every spherical surface

$$\int_0^{2\pi} \int_0^{\pi} \left( \mathbf{C}_{pmnl}^{(\delta)} \right)^* \cdot \mathbf{C}_{p'm'n'l'}^{(\delta')} \sin(\theta) d\theta d\phi = 0 \quad \forall (\delta, p, m, n) \neq (\delta', p', m', n'). \quad (8.31)$$

For instance, two modes sharing the values of all the indices  $\delta, p, m, n$  are not orthogonal, even if they have different values of  $l$ . On the contrary, two modes differing in at least one of the indices  $\delta, p, m, n$  are orthogonal according to the definition (8.31).

As an example, we now show the eigenmodes of a sphere of size parameter  $x = 2\pi$  for  $m = 1$ , associated with the eigenvalues given in Tables 8.1 and 8.2.

Specifically, in Fig. 8.3 we plot the eigenmodes of the electric type  $\mathbf{C}_{e1nl}^{(\alpha)}$  for  $n = 1, 2, 3$  and  $l = 1, 2, 3$ . The eigenmode obtained for  $n = 1$  and  $l = 1$  shows a dipolar character; increasing the index  $l$ , while keeping fixed the order  $n$  to 1, we observe for  $l = 2$  and  $l = 3$  two and three oscillation of the eigenmode as we move away from the center of the sphere. For  $n = 2$  and  $l = 1$  the eigenmode shows a quadrupolar

**Table 8.1** Eigenvalues  $\alpha_{nl}$  of a sphere of size parameter  $x = 2\pi$  for  $n = 1, 2, 3$  and  $l = 1, 2, 3$

$\alpha_{nl}$	$l = 1$	$l = 2$	$l = 3$
$n = 1$	$0.1670 - 0.0812i$	$0.7485 - 0.3238i$	$1.5809 - 0.4144i$
$n = 2$	$0.3147 - 0.2035i$	$1.0223 - 0.4323i$	$2.1294 - 0.4210i$
$n = 3$	$0.4955 - 0.3990i$	$1.3503 - 0.5145i$	$2.7598 - 0.4524i$

**Table 8.2** Eigenvalues  $\beta_{nl}$  of a sphere of size parameter  $x = 2\pi$  for  $n = 1, 2, 3$  and  $l = 1, 2, 3$

$\beta_{nl}$	$l = 1$	$l = 2$	$l = 3$
$n = 1$	$0.4442 - 0.1722i$	$1.1043 - 0.3993i$	$2.2314 - 0.3737i$
$n = 2$	$0.6786 - 0.2832i$	$1.4928 - 0.4007i$	$2.9304 - 0.3464i$
$n = 3$	$0.9159 - 0.3709i$	$1.9836 - 0.3638i$	$3.7095 - 0.3142i$

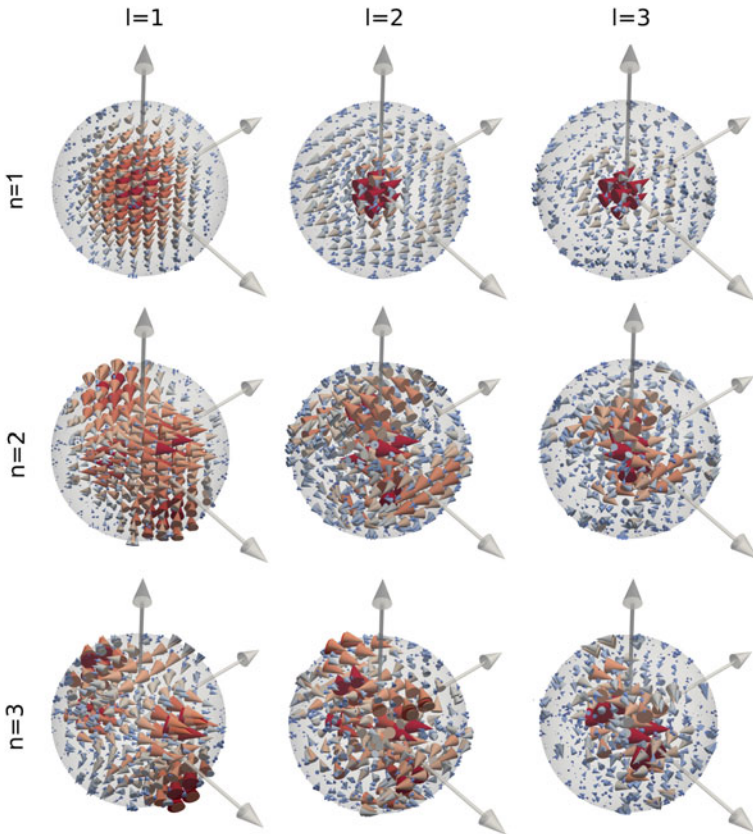


**Fig. 8.3** Cone plots of the real part of the electric type eigenmodes  $C_{elnl}^{(a)}$  for  $n = 1, 2, 3$  and  $l = 1, 2, 3$ . The eigenmodes are calculated for a sphere of size parameter  $x = 2\pi$ . The direction of each cone represents the direction of the eigenmode in the corresponding point of the space, while the length of the cone is proportional to its amplitude (Adapted from [59]. Copyright (2016) by the American Physical Society)

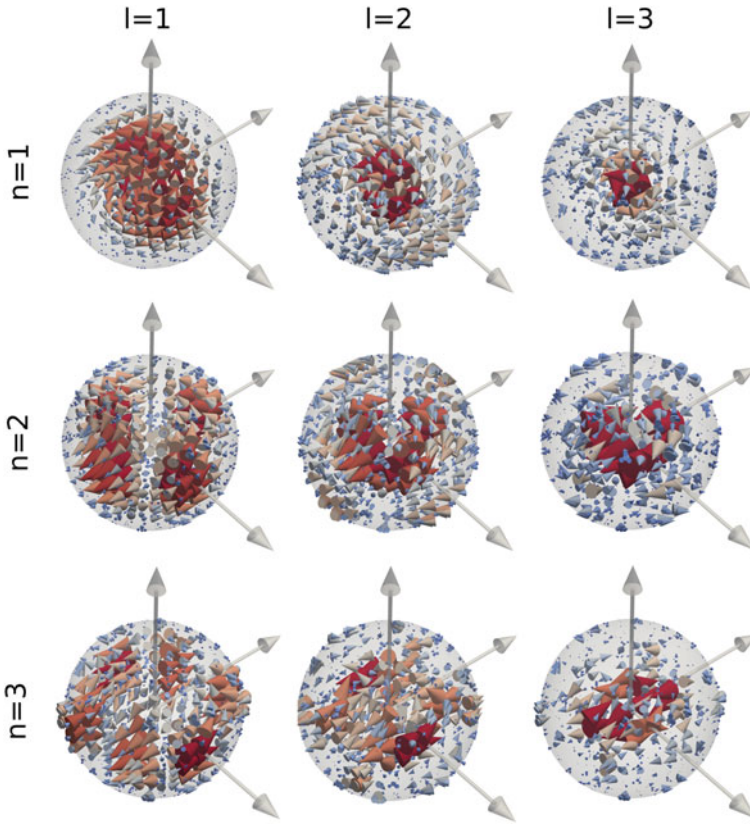


**Fig. 8.4** Cone plots of the real part of the magnetic-type eigenmodes  $\mathbf{C}_{e1nl}^{(\beta)}$  for  $n = 1, 2, 3$  and  $l = 1, 2, 3$ . The eigenmodes are calculated for a sphere of size parameter  $x = 2\pi$ . The direction of each cone represents the direction of the eigenmode in the corresponding point of the space, while the length of the cone is proportional to its amplitude (Adapted from [59]. Copyright (2016) by the American Physical Society)

character, while for  $n = 3$  and  $l = 1$  the eigenmode is of octupolar type. In both cases, by increasing  $l$ , the number of oscillation along the radius increases. In Fig. 8.4 we plot the eigenmodes of the magnetic type  $\mathbf{C}_{e1nl}^{(\beta)}$  for  $n = 1, 2, 3$  and  $l = 1, 2, 3$ . In particular, we show the fundamental magnetic dipole ( $n = 1, l = 1$ ), quadrupole ( $n = 2, l = 1$ ), and octupole ( $n = 3, l = 1$ ). Also in this case, by increasing  $l$ , we notice an increasing number of oscillation along the radial direction.

### 8.3.1 Coupling with an External Excitation

Let us consider an external excitation  $\mathbf{E}_i$ , assumed to be solenoidal and solution of the Maxwell's equations in vacuum. Thus, it can be represented within the spherical region  $\Omega$  in terms of the eigenmodes  $\mathbf{C}_{pmnl}^{(\alpha)}(\mathbf{r})$  and  $\mathbf{C}_{pmnl}^{(\beta)}(\mathbf{r})$ :

$$\mathbf{E}_i(\mathbf{r}) = \sum_{pmnl} \left( A_{pmnl} \mathbf{C}_{pmnl}^{(\alpha)}(\mathbf{r}) + B_{pmnl} \mathbf{C}_{pmnl}^{(\beta)}(\mathbf{r}) \right) \quad \forall \mathbf{r} \in \Omega, f \quad (8.32)$$

where  $\sum_{pmnl} = \sum_{p \in \{e,o\}} \sum_{n=1}^{\infty} \sum_{m=0}^n \sum_{l=1}^{\infty}$ , and

$$A_{pmnl} = \frac{\langle \mathbf{C}_{pmnl}^{(\alpha)}, \mathbf{E}_i \rangle_{\Omega}}{\langle \mathbf{C}_{pmnl}^{(\alpha)}, \mathbf{C}_{pmnl}^{(\alpha)} \rangle_{\Omega}}, \quad B_{pmnl} = \frac{\langle \mathbf{C}_{pmnl}^{(\beta)}, \mathbf{E}_i \rangle_{\Omega}}{\langle \mathbf{C}_{pmnl}^{(\beta)}, \mathbf{C}_{pmnl}^{(\beta)} \rangle_{\Omega}}. \quad (8.33)$$

Therefore, it is straightforward to obtain the scattered field inside the sphere by using (8.12):

$$\mathbf{E}_S^+(\mathbf{r}) = (\varepsilon_r - 1) \sum_{pmnl} \left( \frac{A_{pmnl}}{\alpha_{nl} - \varepsilon_r} \mathbf{C}_{pmnl}^{(\alpha)}(\mathbf{r}) + \frac{B_{pmnl}}{\beta_{nl} - \varepsilon_r} \mathbf{C}_{pmnl}^{(\beta)}(\mathbf{r}) \right), \quad (8.34)$$

where  $\alpha_{nl}, \beta_{nl}$  are the roots of series  $\mathcal{P}_n$  and  $\mathcal{Q}_n$  give in (8.27), while the corresponding eigenfunctions  $\mathbf{C}_{pmnl}^{(\alpha)}, \mathbf{C}_{pmnl}^{(\beta)}$  are provided in (8.28) and (8.29).

#### 8.3.1.1 Coupling with a Plane Wave

We now present the expansion of a plane wave in terms of eigenmodes  $\mathbf{C}_{pmnl}^{(\alpha)}$  and  $\mathbf{C}_{pmnl}^{(\beta)}$ . An  $x$ -polarized plane wave propagating along  $z$  has the following expression:

$$\mathbf{E}_i(\mathbf{r}) = \mathbf{E}_0 e^{ikz} \hat{\mathbf{e}}_x, \quad (8.35)$$

which, expressed in terms of VSWFs, has the form [76]:

$$\mathbf{E}_i(\mathbf{r}) = \sum_{n=1}^{\infty} E_n \left( \mathbf{M}_{o1n}^{(1)}(k_0 \mathbf{r}) - i \mathbf{N}_{e1n}^{(1)}(k_0 \mathbf{r}) \right), \quad (8.36)$$

where:

$$E_n = E_0 i^n \frac{2n+1}{n(n+1)}. \quad (8.37)$$



Starting from the expression (8.36), it is easy to obtain the expansion of  $\mathbf{E}_i$  in the volume  $\Omega$  in terms of the material independent eigenmodes:

$$\mathbf{E}_i(\mathbf{r}) = \sum_{n=1}^{\infty} E_n \sum_{l=1}^{\infty} \left( B_{nl} \mathbf{C}_{o1nl}^{(\beta)} - i A_{nl} \mathbf{C}_{e1nl}^{(\alpha)} \right), \quad (8.38)$$

through the projections:

$$\begin{aligned} A_{nl} &= \frac{\langle \mathbf{N}_{e1n}^{(1)}(\sqrt{\alpha_{nl}} k_0 \mathbf{r}), \mathbf{N}_{e1n}^{(1)}(k_0 \mathbf{r}) \rangle_{\Omega}}{\langle \mathbf{N}_{e1n}^{(1)}(\sqrt{\alpha_{nl}} k_0 \mathbf{r}), \mathbf{N}_{e1n}^{(1)}(\sqrt{\alpha_{nl}} k_0 \mathbf{r}) \rangle_{\Omega}}, \\ B_{nl} &= \frac{\langle \mathbf{M}_{o1n}^{(1)}(\sqrt{\beta_{nl}} k_0 \mathbf{r}), \mathbf{M}_{o1n}^{(1)}(k_0 \mathbf{r}) \rangle_{\Omega}}{\langle \mathbf{M}_{o1n}^{(1)}(\sqrt{\beta_{nl}} k_0 \mathbf{r}), \mathbf{M}_{o1n}^{(1)}(\sqrt{\beta_{nl}} k_0 \mathbf{r}) \rangle_{\Omega}}. \end{aligned} \quad (8.39)$$

In this case, both  $A_{nl}$  and  $B_{nl}$  have an analytical closed-form expression:

$$\begin{aligned} A_{nl} &= \frac{2}{x(\alpha_{nl} - 1)} \frac{\text{num}\{A_{nl}\}}{\text{den}\{A_{nl}\}}, \\ B_{nl} &= \frac{2}{x(\beta_{nl} - 1)} \frac{j_{n-1}(x) j_n(\sqrt{\beta_{nl}} x) - \sqrt{\beta_{nl}} j_{n-1}(\sqrt{\beta_{nl}} x) j_n(x)}{j_n^2(\sqrt{\beta_{nl}} x) - j_{n+1}(\sqrt{\beta_{nl}} x) j_{n-1}(\sqrt{\beta_{nl}} x)}, \end{aligned} \quad (8.40)$$

where:

$$\begin{aligned} \text{num}\{A_{nl}\} &= (n+1) [j_{n-2}(x) j_{n-1}(\sqrt{\alpha_{nl}} x) - \sqrt{\alpha_{nl}} j_{n-2}(\sqrt{\alpha_{nl}} x) j_{n-1}(x)] \\ &\quad + n [j_n(x) j_{n+1}(\sqrt{\alpha_{nl}} x) - \sqrt{\alpha_{nl}} j_{n+1}(x) j_n(\sqrt{\alpha_{nl}} x)], \\ \text{den}\{A_{nl}\} &= (n+1) [j_{n-1}^2(\sqrt{\alpha_{nl}} x) - j_{n-2}(\sqrt{\alpha_{nl}} x) j_n(\sqrt{\alpha_{nl}} x)] \\ &\quad + n [j_{n+1}^2(\sqrt{\alpha_{nl}} x) - j_n(\sqrt{\alpha_{nl}} x) j_{n+2}(\sqrt{\alpha_{nl}} x)]. \end{aligned}$$

Once the coefficients  $A_{nl}$  and  $B_{nl}$  are known, we can write the expression of the internal scattered field:

$$\begin{aligned} \mathbf{E}_S^+(\mathbf{r}) &= (\varepsilon_r - 1) \sum_{n=1}^{\infty} E_n \sum_{l=1}^{\infty} \left[ \frac{B_{nl}}{\beta_{nl} - \varepsilon_r} \mathbf{M}_{o1n}^{(1)}(\sqrt{\beta_{nl}} k_0 \mathbf{r}) \right. \\ &\quad \left. - i \frac{A_{nl}}{\alpha_{nl} - \varepsilon_r} \mathbf{N}_{e1n}^{(1)}(\sqrt{\alpha_{nl}} k_0 \mathbf{r}) \right], \end{aligned} \quad (8.41)$$

while the field outside the sphere is readily obtained using the boundary conditions (8.20)–(8.21):

$$\mathbf{E}_S^-(\mathbf{r}) = (\varepsilon_r - 1) \sum_{n=1}^{\infty} \frac{E_n}{h_n^{(1)}(x)} \sum_{l=1}^{\infty} \left[ \frac{B_{nl} j_n(\sqrt{\beta_{nl}} x)}{\beta_{nl} - \varepsilon_r} \mathbf{M}_{o1n}^{(3)}(k_0 \mathbf{r}) - i \frac{A_{nl} \sqrt{\alpha_{nl}} j_n(\sqrt{\alpha_{nl}} x)}{\alpha_{nl} - \varepsilon_r} \mathbf{N}_{e1n}^{(3)}(k_0 \mathbf{r}) \right]. \quad (8.42)$$

### 8.3.2 Radiation Pattern and Scattering Efficiency

The radiation pattern is defined by [77]

$$\mathbf{E}_S^\infty(\theta, \phi) = \lim_{r \rightarrow \infty} \left[ r e^{-ik_0 r} \mathbf{E}_S^-(r, \theta, \phi) \right]. \quad (8.43)$$

Thus, substituting (8.42) into (8.43), we obtain its explicit form for the problem at hand:

$$\mathbf{E}_S^\infty(\theta, \phi) = \frac{(\varepsilon_r - 1)}{k_0} \times \sum_{n=1}^{\infty} \frac{E_n}{h_n^{(1)}(x)} \sum_{l=1}^{\infty} \left[ \frac{B_{nl} j_n(\sqrt{\beta_{nl}} x)}{\beta_{nl} - \varepsilon_r} \mathbf{M}_{o1n}^{(\infty)}(\theta, \phi) - i \frac{A_{nl} \sqrt{\alpha_{nl}} j_n(\sqrt{\alpha_{nl}} x)}{\alpha_{nl} - \varepsilon_r} \mathbf{N}_{e1n}^{(\infty)}(\theta, \phi) \right], \quad (8.44)$$

where:

$$\begin{aligned} \mathbf{M}_{o1n}^{(\infty)}(\theta, \phi) &= \lim_{r \rightarrow \infty} \left[ k_0 r e^{-ik_0 r} \mathbf{M}_{o1n}^{(3)}(\theta, \phi) \right], \\ \mathbf{N}_{e1n}^{(\infty)}(\theta, \phi) &= \lim_{r \rightarrow \infty} \left[ k_0 r e^{-ik_0 r} \mathbf{N}_{e1n}^{(3)}(\theta, \phi) \right]. \end{aligned} \quad (8.45)$$

The explicit expressions of  $\mathbf{M}_{o1n}^{(\infty)}(\theta, \phi)$  and  $\mathbf{N}_{e1n}^{(\infty)}(\theta, \phi)$  are reported in the Appendix.

The scattering cross section can be defined as [76, 77]:

$$C_{sca} = \frac{1}{\|\mathbf{E}_0\|^2} \frac{c_0}{\omega} \iint_{S_c} \hat{\mathbf{e}}_r \cdot \text{Im} \{ (\nabla \times \mathbf{E}_S^-)^* \times \mathbf{E}_S^- \} dS, \quad (8.46)$$

where  $S_c$  is an auxiliary surface enclosing  $\Omega$ . We also define the scattering efficiency  $\sigma_{sca}$  as [76, 77]:

$$\sigma_{sca} = \frac{C_{sca}}{G}, \quad (8.47)$$

where  $G$  is the particle cross-sectional area projected onto a plane perpendicular to the incident beam (e.g.,  $G = \pi R^2$  for a sphere of radius  $R$ ). By combining (8.42), (8.46), (8.47), assuming the auxiliary surface  $S_c$  to be a spherical surface concentric with  $\Omega$ , and exploiting the orthogonality of the VSWFs, we finally get:

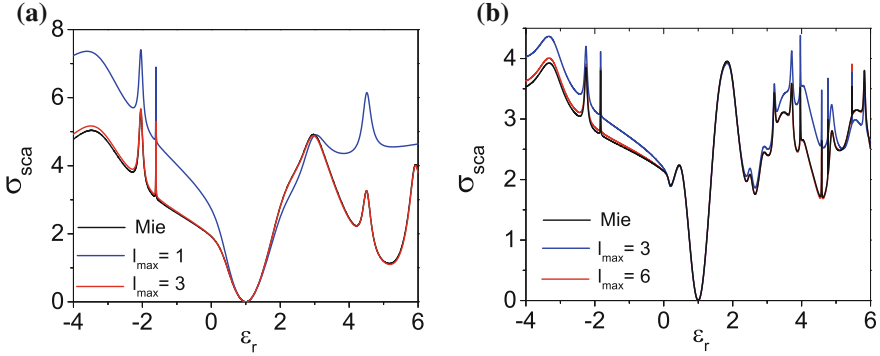


**Fig. 8.5** Scattering efficiency  $\sigma_{sca}$  of a dielectric sphere with size parameter  $x = \pi$  (a) and  $x = 2\pi$  (b) excited by a linearly polarized plane wave, as a function of  $\varepsilon_r \in [-4, 6]$  calculated using (8.48) and with the standard Mie theory. In all the calculations we have assumed  $n_{\max} = 10$  (Panel b was adapted from [59]. Copyright (2016) by the American Physical Society)

$$\sigma_{sca} = x^{-2} \sum_n (|\sum_l u_{nl}|^2 + |\sum_l v_{nl}|^2), \quad (8.48)$$

where:

$$\begin{aligned} u_{nl} &= (\varepsilon_r - 1) \frac{\sqrt{2(2n+1)}}{h_n^{(1)}(x)} \frac{\sqrt{\alpha_{nl}} j_n(\sqrt{\alpha_{nl}} x) A_{nl}}{\alpha_{nl} - \varepsilon_r}, \\ v_{nl} &= (\varepsilon_r - 1) \frac{\sqrt{2(2n+1)}}{h_n^{(1)}(x)} \frac{\sqrt{\beta_{nl}} j_n(\sqrt{\beta_{nl}} x) B_{nl}}{\beta_{nl} - \varepsilon_r}. \end{aligned} \quad (8.49)$$

Equation (8.48) shows that two electric (magnetic) modes sharing the value of the index  $n$ , but having different values of  $l$ , may interfere in the scattering efficiency. On the contrary, two modes differing in  $n$  cannot interfere. Also electric and magnetic modes cannot interference between them. These are all consequences of the orthogonality condition of (8.31).

In order to validate the proposed modal expansion, we now calculate the scattering efficiency  $\sigma_{sca}$  of a sphere, when it is excited by a linearly polarized plane wave of unit intensity. Specifically, in Fig. 8.5 we plot  $\sigma_{sca}$  for  $x = \pi$  (a) and  $x = 2\pi$  (b) as a function of  $\varepsilon_r$ . As a reference solution we use the standard Mie Theory [58], where the scattered electric field has been expanded in terms of VSWFs:

$$\mathbf{E}_S^- = \sum_{n=1}^{n_{\max}} E_n \left( i a_n \mathbf{N}_{e1n}^{(3)}(k_0 \mathbf{r}) - b_n \mathbf{M}_{o1n}^{(3)}(k_0 \mathbf{r}) \right), \quad (8.50)$$

where  $a_n$  and  $b_n$  are the Mie scattering coefficients, which can be found in [58] and  $E_n = i^n (2n+1) / [n(n+1)]$ . The cross section is:

$$\sigma_{sca} = \frac{2}{x^2} \sum_{n=1}^{n_{\max}} (2n+1) (|a_n|^2 + |b_n|^2) \quad (8.51)$$

where we assumed  $n_{\max} = 10$ .

In Fig. 8.5a we plot the scattering efficiency of the sphere with  $x = \pi$ , truncating the inner sum of (8.48) to  $l_{\max} = 1$  (blue line) and to  $l_{\max} = 3$  (red line). When only the fundamental modes ( $l_{\max} = 1$ ) are considered, we have agreement with the standard Mie theory only for small values of  $\varepsilon_r$ , while increasing  $l_{\max}$  to 3 the results of the two approaches closely agree.

The scattering efficiency of the sphere with size parameter  $x = 2\pi$  is shown in Fig. 8.5b. Here, we truncated the inner sum to  $l_{\max} = 3$  (blue line) and to  $l_{\max} = 6$  (red line). Although for  $l_{\max} = 3$  it is apparent a moderate disagreement with the Mie theory, for  $l_{\max} = 6$  the outcomes of the two approaches become almost indistinguishable.

## 8.4 Resonances' Properties of a Homogeneous Sphere

From the expansion (8.34) it is possible to deduce the general properties of the scattering resonances of a sphere. For passive materials ( $\text{Im}\{\varepsilon_r\} \geq 0$ ), the quantities  $|\alpha_{nl} - \varepsilon_r|$  and  $|\beta_{nl} - \varepsilon_r|$  do not vanish as  $\omega$  varies for a given  $R$ , because  $\text{Im}\{\alpha_{nl}\} < 0$  and  $\text{Im}\{\beta_{nl}\} < 0$ . Nevertheless, the mode amplitudes  $A_{pmnl}/(\alpha_{nl} - \varepsilon_r)$  and  $B_{pmnl}/(\beta_{nl} - \varepsilon_r)$  reach their maximum when, for a given  $R$  and  $\varepsilon_r(x)$ , the residua  $r_{nl}^{(\alpha)}$  and  $r_{nl}^{(\beta)}$  are minimum as a  $x$  varies, namely:

$$\begin{aligned} r_{nl}^{(\alpha)} &= |\varepsilon_r(x) - \alpha_{nl}(x)| = \underset{x}{\text{Minimum}}, \\ r_{nl}^{(\beta)} &= |\varepsilon_r(x) - \beta_{nl}(x)| = \underset{x}{\text{Minimum}}, \end{aligned} \quad (8.52)$$

respectively. These are the conditions that maximize the contribution of the modes  $\mathbf{C}_{pmnl}^{(\alpha)}$  and  $\mathbf{C}_{pmnl}^{(\beta)}$  as  $x$  varies and define their resonance frequencies. In other words, (8.34) exemplifies that, for a fixed frequency, when the scatterer's material closely approaches an eigenvalue, the corresponding mode undergoes a boost, namely a *resonance in a material picture*. This picture is dual with respect to the usual *frequency picture*, where the material is instead fixed and the frequency plays the role of the spectral parameter. The *material picture* is particularly relevant in light of the latest advances in the design of Metamaterials and fabrication techniques, which are enabling the effective values of permittivity and permeability of the material to be engineered with increasing precision.

We denote the specific values of  $x$  that minimize the residua introduced in (8.52) as  $x_{nl}^{(\alpha)}$  and  $x_{nl}^{(\beta)}$ , the corresponding values of the poles as  $\hat{\alpha}_{nl}$  and  $\hat{\beta}_{nl}$ , and the minimum

residua as  $\hat{r}_{nl}^{(\alpha)}$  and  $\hat{r}_{nl}^{(\beta)}$ . We also point out that the resonant frequencies can be determined from the values of  $x_{nl}^{(\alpha)}$  and  $x_{nl}^{(\beta)}$  by using the relation  $\omega = c/Rx$ .

The width of a mode is related to the minimum value of the residuum. Specifically, a larger residuum is associated with a *wider* resonance. We denote a given mode as *narrow* if its minimum residuum is less than a given threshold  $\rho$ ,

$$\hat{r}_{nl}^{(\delta)} < \rho, \quad (8.53)$$

as *broad* otherwise. In the following, we assume  $\rho = 5$ . It is worth to note that the resonant conditions (8.52) and the definition (8.53) do not depend on the excitation.

We recall that both  $\alpha_{nl}$  and  $\beta_{nl}$  are independent of the permittivity of the sphere, but they only depend on the size parameter  $x$ . Therefore, they can be exhaustively described by the loci they span in the complex plane as a function of  $x$ . The resulting diagrams are universal, because they apply to any homogeneous sphere, and represent an invaluable tool to investigate NPs resonances.

The real part of  $\alpha_{nl}$  and  $\beta_{nl}$  can be either positive or negative. If negative, the condition (8.52) can be satisfied by metals in the visible spectral range ( $\text{Re}\{\varepsilon_r\} < 0$ ), causing a *plasmon resonances*. If positive, the condition (8.52) is verified by dielectrics ( $\text{Re}\{\varepsilon_r\} \geq 0$ ), causing a *photonic resonances*.

In Fig. 8.6a we plot the locus spanned by the eigenvalue  $\alpha_{11}$ , which is associated with the fundamental electric dipole  $\mathbf{C}_{pm11}^{(\alpha)}$ . For  $x \ll 1$ ,  $\alpha_{11}$  approaches the value  $-2$ , in agreement with the Fröhlich condition [1]. This is consistent with (8.11) that shows that  $\text{Re}\{\gamma_n\} < 0$  in the quasi-electrostatic limit where  $\nabla \times \mathbf{C}_n \approx \mathbf{0}$ . Therefore, for finite values of  $x$ , the condition (8.52) applied to the fundamental dipole represents the natural extension of the Fröhlich condition to the full retarded case. By increasing  $x$ , both the real and the imaginary part of  $\alpha_{11}$  move toward more negative values. The decrease of the real part implies, for low losses Drude metals, a red shift of the corresponding resonant frequency [78]. When  $x \approx 0.72$ , the quantity  $\text{Re}\{\alpha_{11}\}$  reaches a minimum and then starts increasing. For larger  $x$ ,  $\alpha_{11}$  lies in fourth quadrant of the complex plane. Then,  $\text{Re}\{\alpha_{11}\}$  increases until  $x \approx 2$  where it reaches the maximum value of 0.48, and eventually  $\alpha_{11}$  asymptotically approaches the origin of the complex plane.

The loci spanned by higher order electric dipole modes  $\alpha_{1l}$  with  $l = 2, 3, 4, 5$ , shown in Fig. 8.6b, manifest a very different nature. In fact,  $\alpha_{1l}$  always lies in the fourth quadrant of the complex plane irrespectively of the mode order  $l \geq 2$ . Moreover, for  $x \rightarrow 0$ , the real part of  $\alpha_{1l} \rightarrow \infty$ , while  $\text{Im}\{\alpha_{1l}\}$  approaches zero. This fact means that, for  $x \ll 1$ , these modes cannot be practically excited. By increasing  $x$ ,  $\text{Re}\{\alpha_{1l}\}$  moves toward smaller values, while the imaginary part decreases and reaches a minimum. Eventually,  $\alpha_{1l}$  approaches the origin of the complex plane for very high values of  $x$ .

In Fig. 8.6c, e we plot the loci spanned by  $\alpha_{21}$  and  $\alpha_{31}$  of the fundamental ( $l = 1$ ) electric quadrupole and octupole eigenmodes. In this case, for  $x \rightarrow 0$ , the eigenvalues  $\alpha_{21}$  and  $\alpha_{31}$  approach respectively the values  $-1.5$  and  $-1.33$ , which agree with the

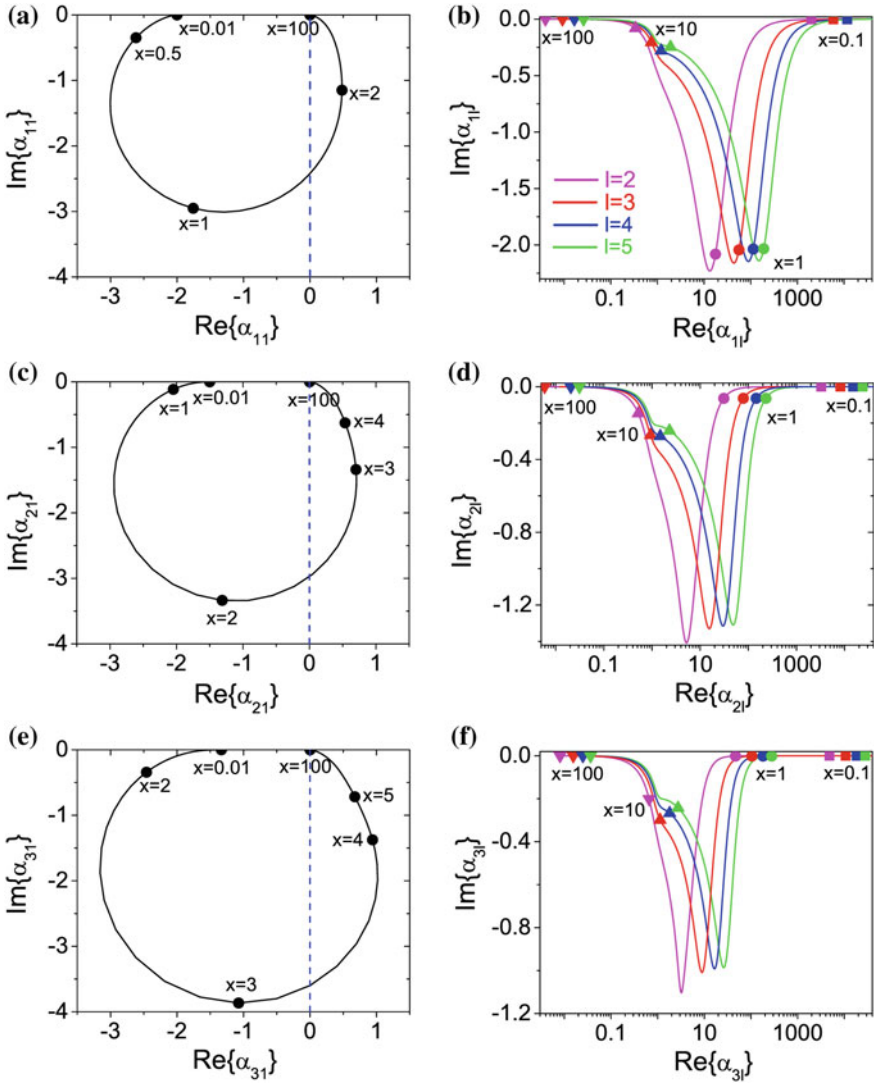


**Fig. 8.6** Universal loci spanned in the complex plane by the eigenvalues  $\alpha_{nl}$  of the electric type eigenmodes of a dielectric sphere by varying its size parameter  $x \in [0.01, 100]$ . We show the eigenvalues of the fundamental (a) and higher order dipole modes (b), fundamental (c) and higher order (d) quadrupole modes, fundamental (e) and higher order (f) octupole modes. The panels a, c, e are in linear scale. The panels (b, d, f) are in semilog scale (Adapted from [59]. Copyright (2016) by the American Physical Society)

quasi-static approximation [55, 56]. In Fig. 8.6d, f we show the loci of higher order electric quadrupole and octupole modes, which display a behavior similar to higher order electric dipole modes.

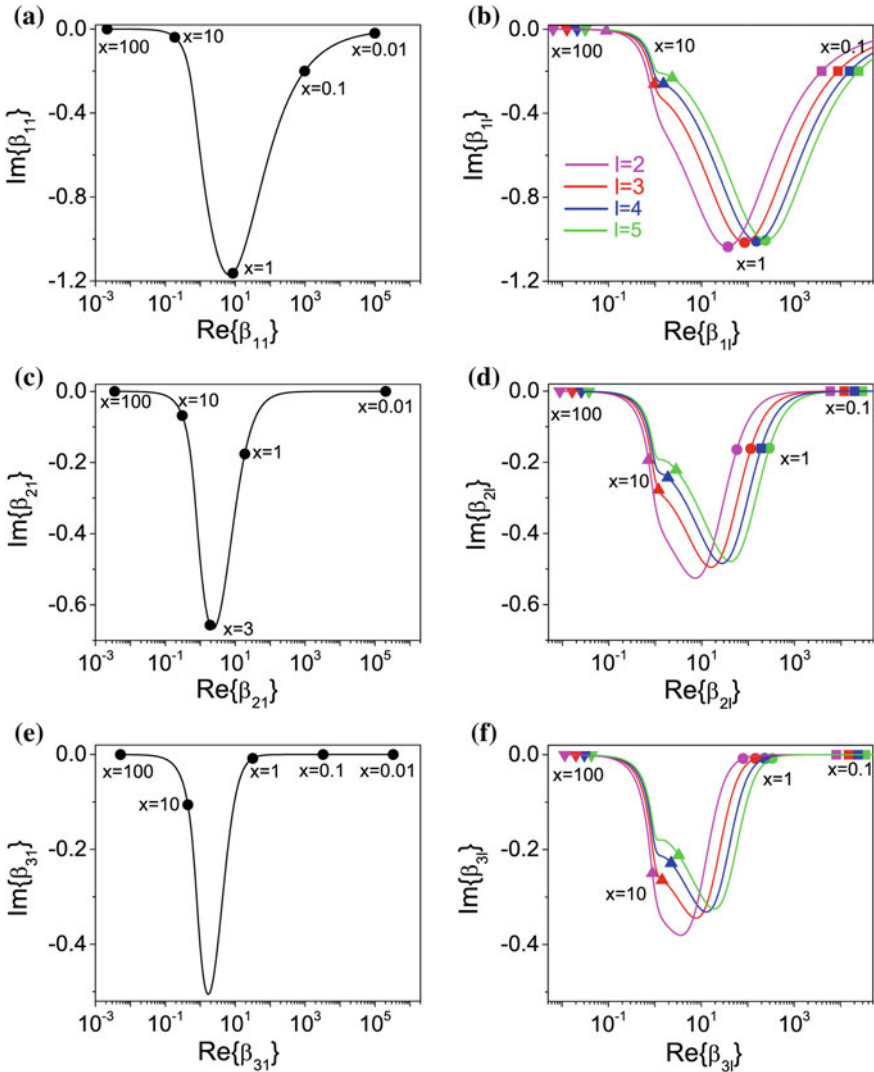


**Fig. 8.7** Universal loci spanned in the complex plane by the eigenvalues  $\beta_{nl}$  of the magnetic-type eigenmodes of a dielectric sphere by varying its size parameter  $x \in [0.01, 100]$ . We show the eigenvalues of the fundamental (a) and higher order (b) dipole modes, fundamental (c) and higher order (d) quadrupole modes, fundamental (e) and higher order (f) octupole modes. The panels a, c, e are in linear scale. The panels b, d, f are in semilog scale (Adapted from [59]. Copyright (2016) by the American Physical Society)

Let us now consider the eigenvalues  $\beta_{nl}$  of the magnetic type eigenmodes. The eigenvalues of both the fundamental magnetic eigenmodes, i.e.  $\beta_{n1}$  shown in Fig. 8.7a, c, e for  $n = 1, 2, 3$ , and higher order magnetic eigenmodes, i.e.  $\beta_{nl}$  shown in

Fig. 8.7b, d, f for  $l = 2, 3, 4, 5$ , exhibit the same behavior of the eigenvalue of higher order electric modes. In particular, in the limit for  $x \rightarrow 0$ , the quantity  $\text{Re} \{\beta_{n1}\}$  diverges. Therefore, the fundamental magnetic eigenmodes cannot be practically excited in the electrostatic limit, consistently with [55, 56].

In conclusion, the loci spanned by the eigenvalues associated with the fundamental electric dipole  $\mathbf{C}_{pm11}^{(\alpha)}$ , quadrupole  $\mathbf{C}_{pm21}^{(\alpha)}$ , and octupole  $\mathbf{C}_{pm31}^{(\alpha)}$  are confined in a limited region of the complex plane, because  $-3 \leq \text{Re} \{\alpha_{11}\} \leq 0.48$ ,  $-2.94 \leq \text{Re} \{\alpha_{21}\} \leq 0.71$ , and  $-3.1578 \leq \text{Re} \{\alpha_{31}\} \leq 1.0176$ , respectively. Therefore, according to the definition of (8.52) and (8.53), these modes are *broad* for spheres with moderately positive permittivity, e.g. Si ( $\epsilon_r \approx 16$ ). Instead, they may be *narrow* for metal spheres in the visible spectral range, whose permittivity belongs to the second quadrant of the complex plane.

The loci spanned by higher order electric modes and by all the magnetic modes have very different properties. These modes always belong to the fourth quadrant of the complex plane, for any value of  $x$ . Thus, they are *broad* in metal sphere and may be *narrow* in particles with moderately positive permittivity. Moreover, they asymptotically approach the positive real axis for  $x \rightarrow 0$ , playing no role in the scattering of any particle much smaller than the incident wavelength.

In conclusion, the only narrow modes in a metal sphere are the fundamental electric ones. These modes form an orthogonal set, according to (8.31). This fact forbids interference among them in the total scattered power. In principle, the interference between a narrow and a broad mode is possible, e.g. between the fundamental and the higher order electric dipoles, but it requires a careful tailoring of the excitation, since broad higher order electric modes poorly couple with a plane wave excitation.

Vice versa, the narrow modes in a dielectric sphere with positive permittivity are the magnetic modes and the higher order electric modes ( $l \geq 2$ ). Some of these modes are non-orthogonal. This fact allows interference phenomena among narrow modes. Moreover, the narrow higher order electric dipole modes are not orthogonal also with the broad fundamental dipole mode, and their interference may give rise to Fano lineshapes in the scattering power spectrum. This interference is easy to observe, because the broad fundamental electric dipole mode efficiently couples with a plane wave, as we will see in Sect. 8.5.

## 8.5 Resonances and Interferences in the Scattering by Si and Ag Spheres

In this section, we analyse the effects of resonances and interferences found in the spectrum of scattered power from silicon (Si) and silver (Ag) spheres with  $R = 100$  nm and 60 nm, respectively. We describe the Ag permittivity  $\epsilon_{r,Ag}$  by using experimental data [79], while for Si we employ a constant permittivity, i.e.  $\epsilon_{r,Si} = 16$ . In Tables 8.3 and 8.4 we list, for some representative modes of the investigated Si and Ag sphere, the quantities  $x_{nl}^{(\alpha)}$  and  $x_{nl}^{(\beta)}$ , which are the values of  $x$  minimizing



**Table 8.3** Values of  $x$  minimizing the residua, corresponding poles and residua for a 100 nm Si sphere

$n$	$l$	$x_{nl}^{(\alpha)}$	$\hat{\alpha}_{nl}$	$\hat{r}_{nl}^{(\alpha)}$	$x_{nl}^{(\beta)}$	$\hat{\beta}_{nl}$	$\hat{r}_{nl}^{(\beta)}$
1	1	2.20	0.48 – 0.96i	15.6	<b>0.75</b>	<b>16.2 –</b> <b>1.07i</b>	<b>1.08</b>
1	2	<b>1.06</b>	<b>16.3 –</b> <b>2.15i</b>	<b>2.17</b>	<b>1.55</b>	<b>15.9 –</b> <b>0.96i</b>	<b>0.97</b>
2	1	2.99	0.70 – 1.33i	15.3	<b>1.09</b>	<b>16.2 –</b> <b>0.21i</b>	<b>0.27</b>
2	2	<b>1.38</b>	<b>16.0 –</b> <b>0.31i</b>	<b>0.31</b>	<b>1.89</b>	<b>16.0 –</b> <b>0.45i</b>	<b>0.45</b>
3	1	3.86	1.00 – 1.67i	15.1	<b>1.42</b>	<b>15.9 –</b> <b>0.04i</b>	<b>0.07</b>

**Table 8.4** Values of  $x$  minimizing the residua, corresponding poles and residua for a 60 nm Ag sphere

$n$	$l$	$x_{nl}^{(\alpha)}$	$\hat{\alpha}_{nl}$	$\hat{r}_{nl}^{(\alpha)}$	$x_{nl}^{(\beta)}$	$\hat{\beta}_{nl}$	$\hat{r}_{nl}^{(\beta)}$
1	1	<b>0.92</b>	<b>–2.42 –</b> <b>2.61 i</b>	<b>3.0</b>	1.08	7.6 – 1.17 i	8.55
1	2	1.25	11.8 – 2.2 i	10.3	1.08	33.0 – 1.04 i	33.9
2	1	<b>1.0</b>	<b>–2.03 –</b> <b>0.11 i</b>	<b>0.35</b>	1.08	16.5 – 0.20 i	17.4
2	2	1.25	19.8 – 0.19 i	17.6	1.08	50.5 – 0.19 i	51.3

the residua introduced in (8.52). We also show the corresponding values of the poles  $\hat{\alpha}_{nl}$  and  $\hat{\beta}_{nl}$ , and the minimum residua  $\hat{r}_{nl}^{(\alpha)}$  and  $\hat{r}_{nl}^{(\beta)}$ . The resonant frequencies can be immediately obtained from  $x_{nl}^{(\alpha)}$  and  $x_{nl}^{(\beta)}$  by using the relation  $\omega = c/Rx$ . We highlight in bold the narrow modes, according to the definition (8.53) with  $\rho = 5$ . We searched for the minima in the range  $x \in [0.01, 100]$  and  $x \in [0.19, 1.08]$  for Si and Ag, respectively.

For the Si sphere, Table 8.3 shows that the minimum residua associated with the fundamental electric modes (dipole, quadrupole, and octupole) are roughly one order of magnitude larger than the ones associated with higher order electric modes and the magnetic modes. For this reason, the fundamental electric modes are *broad*, while the higher order electric modes and to magnetic modes are *narrow*, according to the definition (8.53). This fact is consistent with the conclusions of Sect. 8.4. Furthermore, Table 8.3 shows that the real parts of the poles associated with the higher order electric modes and to the magnetic modes all approach the value of  $\varepsilon_{r,Si} = 16$ .

For Ag particles exactly the opposite happens. Table 8.4 shows that the residua exhibited by all the magnetic modes and by higher order electric modes are much

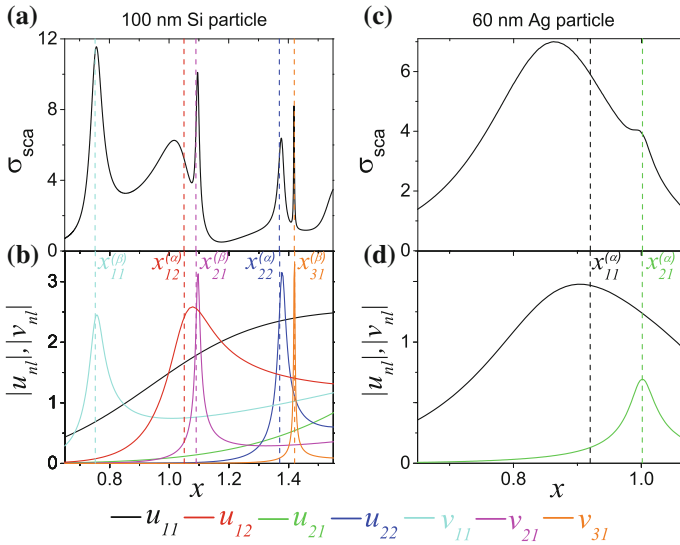


**Fig. 8.8** Scattering efficiency  $\sigma_{sca}$  of the investigated Si (a) and Ag (c) spheres as function of  $x$ . Absolute value of the coefficients  $u_{nl}$  and  $v_{nl}$  as a function of  $x$  for Si (b) and Ag (d) spheres. The vertical dashed lines represent the resonance positions  $x_{nl}^{(\alpha)}$  and  $x_{nl}^{(\beta)}$ , as listed in the third and sixth columns of Tables 8.3 and 8.4 (Adapted from [60]. Copyright (2017) by IOP Publishing)

larger than the ones of the fundamental electric modes. In particular, the former modes are *broad*, while the latter are *narrow*, according to the condition (8.53), consistently with the results of the previous section.

In conclusion, the narrow modes in metal and silicon spheres constitute two disjoint sets. This fact explains why silicon and metal nano-sphere of comparable size exhibit remarkably different resonant behaviour. In particular, magnetic-type modes are always broad in metal spheres, regardless of  $x$ .

We now investigate the scattering efficiency  $\sigma_{sca}$  of Si and Ag spheres as a function of the size parameter  $x$ , when they are excited by a linearly polarized plane wave. Due to the symmetry of  $\mathbf{E}_i$ , only even electric modes and odd magnetic modes with  $m = 1$  are excited. The scattering efficiency  $\sigma_{sca}$  of a sphere excited by a plane wave is provided in (8.48). It is worth noting that the coefficient  $u_{nl}$  and  $v_{nl}$  introduced in (8.49) are associated with the action of the mode  $\mathbf{C}_{e1nl}^{(\alpha)}$  and  $\mathbf{C}_{o1nl}^{(\beta)}$ , respectively. In Fig. 8.8 we plot  $\sigma_{sca}$  of the 100 nm Si (a) and 60 nm Ag (c) sphere as a function of  $x$ . In Fig. 8.8b, d we show the absolute value of the coefficients  $u_{nl}$  and  $v_{nl}$  for the Si and Ag spheres, respectively, as a function of the electric size  $x$ . We also show with vertical dashed lines the resonant values of  $x$ , namely  $x_{nl}^{(\alpha)}$  and  $x_{nl}^{(\beta)}$ , as listed in the third and sixth columns of Tables 8.3 and 8.4. We recall that  $x_{nl}^{(\alpha)}$  and  $x_{nl}^{(\beta)}$  are the values of  $x$  in correspondence of which the amplitudes of  $\mathbf{C}_{e1nl}^{(\alpha)}$  and  $\mathbf{C}_{o1nl}^{(\beta)}$ , respectively, are maximized.

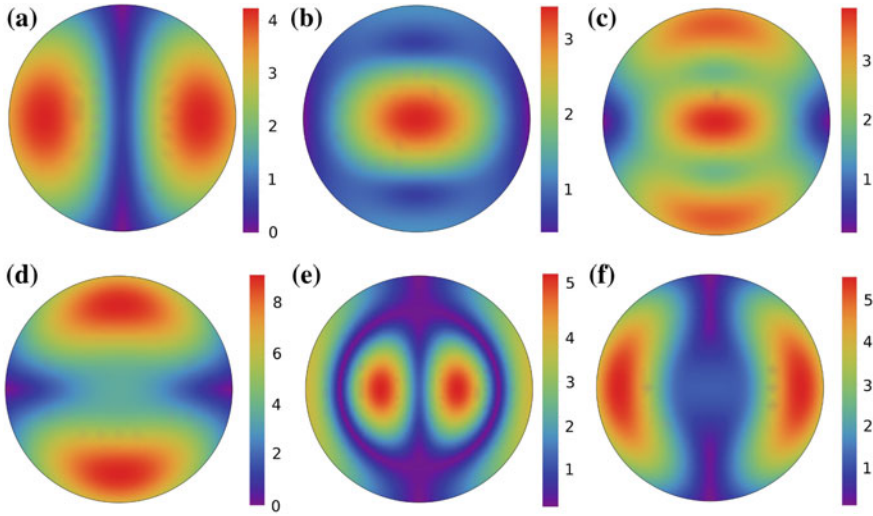


**Fig. 8.9** Near field pattern of the magnitude of the total electric field in the equatorial plane of the Si sphere orthogonal to the propagation direction of the incident field in correspondence of the first peak of  $\sigma_{sca}$  at  $x = 0.91$  (a), second peak at  $x = 1.01$  (b), scattering dip at  $x = 1.076$  (c), third peak at  $x = 1.096$  (d), fourth peak at  $x = 1.376$  (e), fifth peak at  $x = 1.419$  (f)

Now, we describe  $\sigma_{sca}$  of the Si nanosphere, shown in Fig. 8.8a. All  $\sigma_{sca}$  peaks but one can be attributed to the dominant contribution of a single resonant mode. In particular, the first peak from the left occurs exactly at  $x_{11}^{(\beta)}$ , where the contribution of the fundamental magnetic dipole  $\mathbf{C}_{o111}^{(\beta)}$  is maximum. This fact is also demonstrated by Fig. 8.8b, where  $v_{11}$  is also peaked in correspondence of  $x_{11}^{(\beta)}$  and it is dominant compared to the remaining coefficients. In correspondence of this peak, we show in Figs. 8.9a and 8.10a the magnitude of the total electric and magnetic fields in the equatorial plane of the sphere orthogonal to the propagation direction of the incident field. We note that the magnetic field magnitude is enhanced 25 times.

Instead, no mode resonates in correspondence of the second peak. This peak is localized at  $x = 1.02$  and originates from the positive interplay between two off-resonance modes, namely the fundamental electric dipole  $\mathbf{C}_{e111}^{(\alpha)}$  and the second order electric dipole  $\mathbf{C}_{e112}^{(\alpha)}$ , as demonstrated by Fig. 8.8b, where  $u_{11}$  and  $u_{12}$  have comparable magnitude. The near field distributions of the electric and magnetic fields are shown in Figs. 8.9b and 8.10b.

The third  $\sigma_{sca}$  peak is caused by the fundamental magnetic quadrupole  $\mathbf{C}_{o121}^{(\beta)}$ . In correspondence of this peak we have an enhancement of both the electric and magnetic field, as apparent from Figs. 8.9d and 8.10d.

The fourth peak is due to second order electric dipole  $\mathbf{C}_{e122}^{(\alpha)}$ , and the fifth one to the fundamental magnetic octupole  $\mathbf{C}_{o131}^{(\beta)}$ . The corresponding near field plots are shown in Figs. 8.9e, 8.10e and 8.9f, 8.10f, respectively.

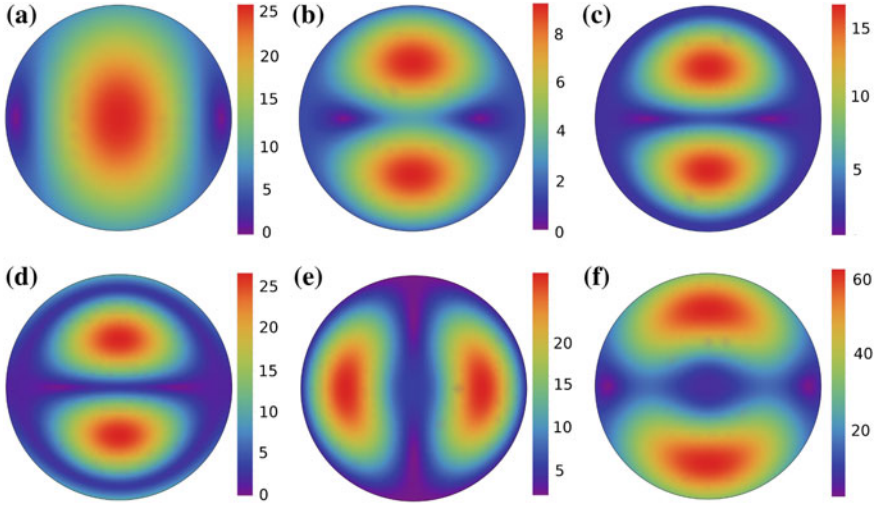


**Fig. 8.10** Near field pattern of the magnitude of the total magnetic field in the equatorial plane of the Si sphere orthogonal to the propagation direction of the incident field in correspondence of the first peak of  $\sigma_{sca}$  at  $x = 0.91$  (a), second peak at  $x = 1.01$  (b), scattering dip at  $x = 1.076$  (c), third peak at  $x = 1.096$  (d), fourth peak at  $x = 1.376$  (e), fifth peak at  $x = 1.419$  (f)

The scattering dip enclosed by peaks 2 and 3 at  $x = 1.076$ , and the corresponding Fano lineshape of  $\sigma_{sca}$  originates from the destructive interference between the *broad* fundamental electric dipole  $\mathbf{C}_{e111}^{(\alpha)}$  and the *narrow* second order electric dipole  $\mathbf{C}_{e112}^{(\alpha)}$ , which are not orthogonal according to the definition (8.31). In correspondence of this dip the values of the coefficients are  $u_{11} = 0.78 - 0.95i$  and  $u_{12} = 0.063 + 1.83i$ . We point out that, although the scattering dip is in the close proximity of the third peak, the magnetic quadrupole  $\mathbf{C}_{o121}^{(\beta)}$  is not responsible for it, because it is orthogonal to both  $\mathbf{C}_{e111}^{(\alpha)}$  and  $\mathbf{C}_{e112}^{(\alpha)}$  due to (8.31), and interference cannot take place.

In conclusion, the scattering efficiency of a Si sphere features a Fano lineshape, where the dip is due to the interference between the fundamental and the higher order electric dipoles, while the peak is due to the fundamental magnetic quadrupole mode. In correspondence of the scattering dip, we plot the near field distribution of the electric and magnetic field in Figs. 8.9c and 8.10c, respectively. Furthermore, the Fano-dip corresponds to a weakly radiative state that features a magnetic near field distribution resembling the one of the magnetic quadrupole, and only slightly smaller values of magnetic field enhancement.

We now investigate the role played by the fundamental electric dipole in the scattering from a Si sphere. The definition (8.53) implies that  $\mathbf{C}_{e111}^{(\alpha)}$  is broad for a Si sphere. Nevertheless, this mode significantly contributes to the scattering efficiency, because the coefficient  $A_{11}$  is very large compared to  $A_{nl}$  and  $B_{nl}$  of the remaining modes. This is due to the fact that the fundamental dipole  $\mathbf{C}_{e111}^{(\alpha)}$  more easily couples with the exciting plane wave and more strongly radiates into the far field.

It is possible to qualitatively compare the  $\sigma_{sca}$  spectrum shown in Fig. 8.8a for a  $R = 100$  nm Si sphere with the dark-field scattering spectrum measured by Kuznetsov et al. [28] for a  $R = 91$  nm Si NP laying on a Si substrate. The experimental and theoretical peaks are found into one to one correspondence.

Next, we investigate the  $\sigma_{sca}$  spectrum of the Ag nanosphere. It can be completely described by considering only the fundamental electric dipole and quadrupole modes, namely  $\mathbf{C}_{e111}^{(\alpha)}$  and  $\mathbf{C}_{e121}^{(\alpha)}$ . These modes are narrow according to (8.53). The peak associated with the mode  $\mathbf{C}_{e111}^{(\alpha)}$  is *wider* compared to  $\mathbf{C}_{e121}^{(\alpha)}$ , due to large imaginary part of the pole  $\hat{\alpha}_{nl}$ , as shown in Table 8.4. Moreover, we found no Fano lineshapes in the spectrum, due to the orthogonality of the fundamental electric modes according to (8.31).

## 8.6 Backscattering Cancellation

More than three decades ago Kerker et al. first demonstrated the suppression of the back-scattering in magneto-dielectric spheres of arbitrary size with  $\varepsilon = \mu$  [80]. In that case, cancellation of the backward scattering results from the destructive interference between magnetic and electric multipoles of corresponding order.

More recently, Nieto et al. [41] predicted that, when the scattering response of a *small* non-magnetic sphere is dominated by the multipolar orders associated with magnetic and electric dipoles, vanishing backscattering can result from their destructive interference. This scenario, that generalizes the Kerker's condition, has been experimentally observed both in the microwaves [42] and in the visible spectral range [43, 44]. An additional extension of the Kerker's conditions, that describes the suppression of the backscattering from a sphere when excited by a local dipole source, has also been introduced in [45]. Furthermore, the generalized Kerker conditions have been also verified in subwavelength metal-dielectric core-shell particles [46], core shell nanowires [47], silicon nanodisks [81], and to particles with cylindrical symmetry [48]. The cancellation of the backscattering have been also achieved in a nanoring antenna by balancing the electric dipole and quadrupole [49], and in a core-shell particle by balancing multipoles of different orders [50].

It is also worth to point out that the backscattering cancellation from a dielectric sphere is also possible even when the size of the particle is comparable with the incident wavelength and many scattering orders are involved, as shown in [59]. The cancellation of the backscattering is often associated with an enhanced directionality of the scattering, which may have a great impact in optical wireless nano-antenna links.

In this section we describe the procedure, introduced in [59], to cancel the backscattering of a homogeneous sphere by designing its permittivity. We assume that the sphere has radius  $R$ , corresponding size parameter  $x = 2\pi R/\lambda$ , and is excited by a  $x$ -polarized plane wave of unit intensity, propagating along the  $z$ -axis. Within the framework of spectral theory introduced in the previous sections, the determina-

tion of the permittivities of the sphere that cancel the backscattering only requires one to find the roots of a polynomial equation.

The radiation pattern is defined in (8.43). Due to symmetry consideration, the only non-vanishing component of the radiation pattern in the backscattering direction ( $\theta = \pi$ ) is  $\mathbf{E}_S^\infty \cdot \mathbf{i}_\theta$ . Our task is to find the zeros of  $\mathbf{E}_S^\infty \cdot \mathbf{i}_\theta$  as a function of  $\varepsilon_r$ , where  $\mathbf{E}_S^\infty \cdot \mathbf{i}_\theta$  can be obtained from (8.44):

$$\mathbf{E}_S^\infty \cdot \mathbf{i}_\theta(\varepsilon_r) = \frac{\varepsilon_r - 1}{k_0} \sum_{n=1}^{\infty} \sum_{l=1}^{\infty} \left\{ \frac{\delta_{nl}(x, \theta, \phi)}{\beta_{nl}(x) - \varepsilon_r} + \frac{\gamma_{nl}(x, \theta, \phi)}{\alpha_{nl}(x) - \varepsilon_r} \right\}, \quad (8.54)$$

where:

$$\begin{aligned} \gamma_{nl}(x, \theta, \phi) &= -i E_n \frac{\sqrt{\alpha_{nl}} j_n(\sqrt{\alpha_{nl}} x)}{h_n^{(1)}(x)} A_{nl} \mathbf{N}_{e1n}^{(\infty)}(\theta, \phi) \cdot \mathbf{i}_\theta, \\ \delta_{nl}(x, \theta, \phi) &= E_n \frac{j_n(\sqrt{\beta_{nl}} x)}{h_n^{(1)}(x)} B_{nl} \mathbf{M}_{o1n}^{(\infty)}(\theta, \phi) \cdot \mathbf{i}_\theta, \end{aligned}$$

$E_n = i^n (2n + 1) / [n(n + 1)]$ ,  $A_{nl}$  and  $B_{nl}$  are defined in (8.39), (8.40)  $\mathbf{M}_{o1n}^{(\infty)} = \lim_{r \rightarrow \infty} [k_0 r e^{-ik_0 r} \mathbf{M}_{o1n}^{(3)}]$ ,  $\mathbf{N}_{e1n}^{(\infty)} = \lim_{r \rightarrow \infty} [k_0 r e^{-ik_0 r} \mathbf{N}_{e1n}^{(3)}]$ , and the functions  $\mathbf{N}_{e1n}^{(3)}$  and  $\mathbf{M}_{o1n}^{(3)}$  are the radiative VSWFs.

Therefore, we put all the terms in the sum of (8.54) over a common denominator, obtaining a rational function of  $\varepsilon_r$  and we zero the resulting numerator, which is a polynomial in  $\varepsilon_r$ .

We apply this procedure to find the permittivity of a homogeneous sphere of radius  $R = \lambda/4$  that cancels the backscattering. We set  $x = \pi/2$ ,  $\theta = \pi$  and  $\phi = 0$  in the expression (8.54) truncated with  $n_{\max} = 10$  and  $l_{\max} = 8$ . Among the different solutions, we choose  $\varepsilon_r = -1.475 + 5.937 \cdot 10^{-3}i$ . To validate this result, we plot in Fig. 8.11a the squared magnitude of the radiation pattern of the sphere with the designed permittivity as a function of the angle  $\theta$  for  $\phi = 0$ , computed by using the standard Mie theory with  $n_{\max} = 10$ . We achieved a ratio between the back- and the forward- scattered power of  $-53$  dB. It is worth noting that the achieved backscattering suppression originates from a complex interplay between the electric dipole, electric quadrupole and magnetic dipole multipolar scattering orders. This fact is demonstrated with the help of Fig. 8.11c, d where we show the magnitude of the Mie coefficients as defined in (8.50). In Fig. 8.11b we show in a semi-logarithmic scale the ratio between the backscattering and the forward scattering as a function of the size parameter  $x$  for the sphere with the designed value of permittivity. As expected, in correspondence of the  $x = \pi/2$  this ratio has a dip.

Now, following the same algorithm, we find the permittivity of a homogeneous sphere of radius  $R = \lambda$  that cancels the backscattering. Among the different solutions, we choose the only one that is physically realizable by a passive material, i.e.  $\varepsilon_r = -2.2747 + 8.188 \cdot 10^{-2}i$ . Then, we plot in Fig. 8.12a the squared magnitude of the radiation pattern of the sphere with  $x = 2\pi$  with the designed permittivity

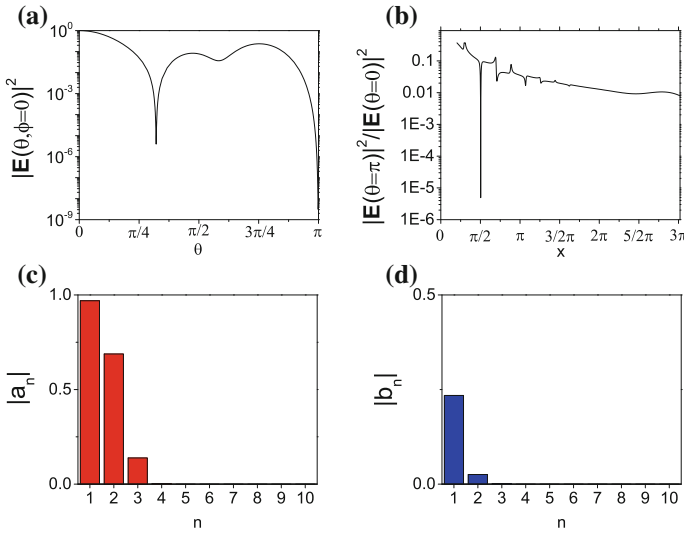


**Fig. 8.11** **a** Squared magnitude of the radiation pattern for  $\phi = 0$  as a function of the angle  $\theta$  for the sphere of size parameter  $x = \pi/2$ . **b** Ratio between the squared magnitudes of the electric field in the back- and forward- scattering direction as a function of the size parameter  $x$ . **c-d** Magnitude of Mie coefficients (as defined by (8.50)) for the sphere of size parameter  $x = \pi/2$ . All the calculations have been performed with the standard Mie theory assuming  $n_{\max} = 10$ . The permittivity of the sphere is the designed value  $\epsilon_r = -1.475 + 5.937 \cdot 10^{-3}i$

as a function of the angle  $\theta$  for  $\phi = 0$  computed by using the standard Mie theory with  $n_{\max} = 10$ . We achieved a ratio between the back- and the forward-scattered power of  $-54$  dB. In this case, since the size of the sphere is equal to the incident wavelength, many electric and magnetic modes take part in the interference. This fact is demonstrated by Fig. 8.12c, d where we show that the magnitude of the Mie coefficients, as defined by (8.50), is significant up to the multipoles of order 9. In Fig. 8.12b we show, in a semi-logarithmic scale, the ratio between the backscattering and the forward scattering as a function of the size parameter  $x$  for the sphere of the designed value of permittivity. As expected, we note that in correspondence of the  $x = 2\pi$  this curve has a dip.

This method can be also used to design the permittivity of the sphere to pursue many different goals, including zeroing or focusing a given field component in an arbitrary point of space, in the near or in the far zone. These objectives can be all easily achieved by zeroing a polynomial. Finally, we note that the proposed method leads to high computational burden when  $x \gg 1$  because many modes have to be considered to accurately describe the field.

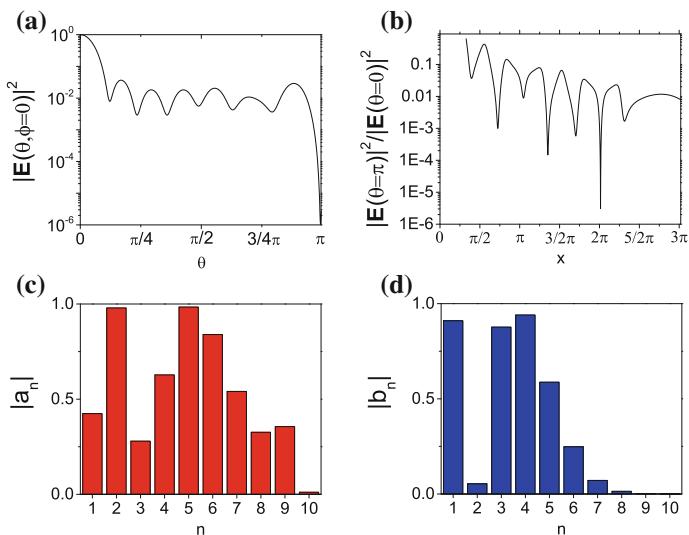


**Fig. 8.12** **a** Squared magnitude of the radiation pattern for  $\phi = 0$  as a function of the angle  $\theta$  for the sphere of size parameter  $x = 2\pi$ . **b** Ratio between the squared magnitudes of the electric field in the back- and forward-scattering direction as a function of the size parameter  $x$ . **c–d** Magnitude of Mie coefficients (as defined by (8.50)) for the sphere of size parameter  $x = 2\pi$ . All the calculations have been performed with the standard Mie theory assuming  $n_{\max} = 10$ . The permittivity of the sphere is the designed value  $\epsilon_r = -2.2747 + 8.188 \cdot 10^{-2}i$

## 8.7 Conclusions and Outlook

We derived a representation of the electromagnetic field for the analysis of the full-wave scattering by a homogeneous sphere in terms of a set of eigenmodes independent of its permittivity. The expansion coefficients are rational functions of the permittivity. Within this framework, we introduced rigorous conditions that define the resonances and the corresponding widths of a nanosphere in the full retarded regime. Moreover, we classified the modes according to their width into narrow and broad modes, independently of the excitation conditions. Then, we showed that the fundamental electric modes are the only narrow modes of a metal sphere with negative permittivity. Vice versa, the magnetic modes and the higher order electric modes are the only narrow modes of a dielectric sphere with moderately positive permittivity. Therefore, since the narrow modes of metal and dielectric spheres constitute two disjoint sets, dielectric and metal nanospheres of comparable size exhibit deeply different resonant behaviours. In particular, magnetic modes are narrow only for a dielectric sphere, but not for a metal one.

Moreover, the narrow modes of a metal sphere constitute an orthogonal set: this fact prevents interference among them in the total scattered power. In a metal sphere, interference among the broad higher order electric modes and the corresponding narrow fundamental electric mode is also difficult to achieve, because broad higher



order electric modes poorly couple with a plane wave excitation, unless a proper tailoring of the excitation is considered.

On the contrary, the narrow modes of a dielectric sphere may be non-orthogonal. This fact enables interference phenomena among them. Moreover, the narrow higher order electric dipole modes are not orthogonal with the broad fundamental electric dipole mode, which efficiently couples with a plane wave excitation, enabling the formation of Fano lineshapes in the scattered power spectrum.

As an example, we investigated the scattered power properties of Ag and Si isolated spheres. In particular, we found that the scattering efficiency of a Si sphere features a Fano lineshape, where the dip is due to the interference between the fundamental and the higher order electric dipole modes, while the peak is due to the fundamental magnetic quadrupole mode. At the position of the scattering dip, we found a great enhancement of electric and magnetic fields.

Eventually, we used the introduced theoretical framework to design the permittivity of a homogeneous sphere of size comparable to the incident wavelength to cancel its backscattering through directional multimode interference. In the investigated examples, where many electric and magnetic multipoles take part in the destructive interference, the scattering in the forward direction exceeded the backscattering more than 50 dB.

This approach can be also extended to interacting spheres by integrating the presented theory with the translation addition theorem for vector spherical wave function. This fact will enable to describe resonances and interferences of more complex dielectric systems, such as dielectric oligomers.

## Appendix: Vector Spherical Wave Functions

The explicit expressions of the vector spherical wave functions (VSWF) are [76]:

$$\begin{aligned}
 \mathbf{N}_{o\,mn}^e(k\mathbf{r}) &= n(n+1) \begin{pmatrix} \cos m\phi \\ \sin m\phi \end{pmatrix} P_n^m(\cos\theta) \frac{z_n(kr)}{kr} \hat{\mathbf{e}}_r \\
 &+ \begin{pmatrix} \cos m\phi \\ \sin m\phi \end{pmatrix} \frac{dP_n^m(\cos\theta)}{d\theta} \frac{1}{kr} \frac{d}{dr} [rz_n(kr)] \hat{\mathbf{e}}_\theta \\
 &+ m \begin{pmatrix} -\sin m\phi \\ \cos m\phi \end{pmatrix} \frac{P_n^m(\cos\theta)}{\sin\theta} \frac{1}{kr} \frac{d}{dr} [rz_n(kr)] \hat{\mathbf{e}}_\phi, \\
 \mathbf{M}_{o\,mn}^e(k\mathbf{r}) &= m \begin{pmatrix} -\sin m\phi \\ \cos m\phi \end{pmatrix} \frac{P_n^m(\cos\theta)}{\sin\theta} z_n(kr) \hat{\mathbf{e}}_\theta - \begin{pmatrix} \cos m\phi \\ \sin m\phi \end{pmatrix} \frac{dP_n^m(\cos\theta)}{d\theta} z_n(kr) \hat{\mathbf{e}}_\phi.
 \end{aligned} \tag{8.55}$$

where the subscripts  $e$  and  $o$  denote even and odd, and  $P_n^m(\cdot)$  are the associated Legendre function of the first kind of degree  $n$  and order  $m$ . Moreover, the superscripts <sup>(1)</sup> and <sup>(3)</sup> are appended to the functions  $\mathbf{M}_{e\,mn}^o$  and  $\mathbf{N}_{e\,mn}^o$  to denote the function  $z_n$ , namely Bessel functions of the first kind  $J_n$  and Hankel functions of the first kind  $h_n$ , respectively.

Starting from (8.55) it is possible to derive the expression of (8.45):

$$\begin{aligned}
\mathbf{N}_{e_{mn}}^{(\infty)}(\theta, \phi) &= (-i)^n \begin{pmatrix} \cos m\phi \\ \sin m\phi \end{pmatrix} \frac{dP_n^m(\cos\theta)}{d\theta} \hat{\mathbf{e}}_\theta + (-i)^n m \begin{pmatrix} -\sin m\phi \\ \cos m\phi \end{pmatrix} \frac{P_n^m(\cos\theta)}{\sin\theta} \hat{\mathbf{e}}_\phi, \\
\mathbf{M}_{e_{mn}}^{(\infty)}(\theta, \phi) &= (-i)^{n+1} m \begin{pmatrix} -\sin m\phi \\ \cos m\phi \end{pmatrix} \frac{P_n^m(\cos\theta)}{\sin\theta} \hat{\mathbf{e}}_\theta - (-i)^{n+1} \begin{pmatrix} \cos m\phi \\ \sin m\phi \end{pmatrix} \frac{dP_n^m(\cos\theta)}{d\theta} \hat{\mathbf{e}}_\phi.
\end{aligned}
\tag{A2}$$

## References

1. U. Kreibig, M. Vollmer, *Optical Properties of Metal Clusters*, vol. 25 (Springer Science & Business Media, 2013)
2. J.A. Schuller, E.S. Barnard, W. Cai, Y.C. Jun, J.S. White, M.L. Brongersma, Plasmonics for extreme light concentration and manipulation. *Nat. Mater.* **9**, 193–204 (2010)
3. J.N. Anker, W.P. Hall, O. Lyandres, N.C. Shah, J. Zhao, R.P. Van Duyne, Biosensing with plasmonic nanosensors. *Nat. Mater.* **7**(6), 442–453 (2008)
4. M. Kauranen, A.V. Zayats, Nonlinear plasmonics. *Nat. Photonics* **6**(11), 737–748 (2012)
5. H.A. Atwater, A. Polman, Plasmonics for improved photovoltaic devices. *Nat. Mater.* **9**(3), 205–213 (2010)
6. J.B. Khurgin, How to deal with the loss in plasmonics and metamaterials. *Nat. Nanotechnol.* **10**(1), 2–6 (2015)
7. A.B. Evlyukhin, C. Reinhardt, A. Seidel, B.S. Luk'yanchuk, B.N. Chichkov, Optical response features of si-nanoparticle arrays. *Phys. Rev. B* **82**, 045404 (2010)
8. A.B. Evlyukhin, C. Reinhardt, B.N. Chichkov, Multipole light scattering by nonspherical nanoparticles in the discrete dipole approximation. *Phys. Rev. B* **84**, 235429 (2011). Dec
9. A. García-Etxarri, R. Gómez-Medina, L.S. Froufe-Pérez, C. López, L. Chantada, F. Scheffold, J. Aizpurua, M. Nieto-Vesperinas, J.J. Sáenz, Strong magnetic response of submicron silicon particles in the infrared. *Opt. Express* **19**(6), 4815–4826 (2011)
10. A.I. Kuznetsov, A.E. Miroshnichenko, M.L. Brongersma, Y.S. Kivshar, B. Luk'yanchuk, Optically resonant dielectric nanostructures. *Science*, **354**(6314) (2016)
11. S. Kruk, Y. Kivshar, Functional meta-optics and nanophotonics govern by mie resonances. *ACS Photonics* **4**(11), 2638–2649 (2017)
12. M.M. Sigalas, D.A. Fattal, R.S. Williams, S. Wang, R.G. Beausoleil, Electric field enhancement between two si microdisks. *Opt. Express* **15**, 14711–14716 (2007)
13. P. Albella, M.A. Poyli, M.K. Schmidt, S.A. Maier, F. Moreno, J.J. Sáenz, J. Aizpurua, Low-loss electric and magnetic field-enhanced spectroscopy with subwavelength silicon dimers. *J. Phys. Chem. C* **117**(26), 13573–13584 (2013)
14. P. Albella, R. Alcaraz de la Osa, F. Moreno, S.A. Maier, Electric and magnetic field enhancement with ultralow heat radiation dielectric nanoantennas: considerations for surface-enhanced spectroscopies. *ACS Photonics* **1**(6), 524–529 (2014)
15. J. Yan, P. Liu, Z. Lin, H. Wang, H. Chen, C. Wang, G. Yang, Directional fano resonance in a silicon nanosphere dimer. *ACS Nano* **9**(3), 2968–2980 (2015)
16. R.M. Bakker, D. Permyakov, Y.F. Yu, D. Markovich, R. Paniagua-Domínguez, L. Gonzaga, A. Samusev, Y. Kivshar, B. Luk'yanchuk, A.I. Kuznetsov, Magnetic and electric hotspots with silicon nanodimers. *Nano Lett.* **15**(3), 2137–2142 (2015)
17. U. Zywiets, M.K. Schmidt, A.B. Evlyukhin, C. Reinhardt, J. Aizpurua, B.N. Chichkov, Electromagnetic resonances of silicon nanoparticle dimers in the visible. *ACS Photonics* **2**(7), 913–920 (2015)
18. G. Boudarham, R. Abdeddaim, N. Bonod, Enhancing the magnetic field intensity with a dielectric gap antenna. *Appl. Phys. Lett.* **104**(2), 021117 (2014)
19. A. Mirzaei, A.E. Miroshnichenko, Electric and magnetic hotspots in dielectric nanowire dimers. *Nanoscale* **7**(14), 5963–5968 (2015)

20. J. van de Groep, T. Coenen, S.A. Mann, A. Polman, Direct imaging of hybridized eigenmodes in coupled silicon nanoparticles. *Optica* **3**, 93–99 (2016). Jan
21. D. Smirnova, Y.S. Kivshar, Multipolar nonlinear nanophotonics. *Optica* **3**, 1241–1255 (2016)
22. M. Caldarola, P. Albella, E. Cortés, M. Rahmani, T. Roschuk, G. Grinblat, R.F. Oulton, A.V. Bragas, S.A. Maier, Non-plasmonic nanoantennas for surface enhanced spectroscopies with ultra-low heat conversion. *Nat. Commun.* **6** (2015)
23. P.A. Dmitriev, D.G. Baranov, V.A. Milichko, S.V. Makarov, I.S. Mukhin, A.K. Samusev, A.E. Krasnok, P.A. Belov, Y.S. Kivshar, Resonant raman scattering from silicon nanoparticles enhanced by magnetic response. *Nanoscale* **8**, 9721–9726 (2016)
24. V. Rutckaia, F. Heyroth, A. Novikov, M. Shaleev, M. Petrov, J. Schilling, Quantum dot emission driven by mie resonances in silicon nanostructures. *Nano Lett.* **17**(11), 6886–6892 (2017). PMID: 28968505
25. A. Krasnok, M. Caldarola, N. Bonod, A. Alú, Spectroscopy and biosensing with optically resonant dielectric nanostructures. [arXiv:1710.10233](https://arxiv.org/abs/1710.10233) (2017)
26. B. Luk'yanchuk, N.I. Zheludev, S.A. Maier, N.J. Halas, P. Nordlander, H. Giessen, C.T. Chong, The fano resonance in plasmonic nanostructures and metamaterials. *Nat. Mater.* **9**(9), 707–715 (2010)
27. A.B. Evlyukhin, S.M. Novikov, U. Zywietz, R.L. Eriksen, C. Reinhardt, S.I. Bozhevolnyi, B.N. Chichkov, Demonstration of magnetic dipole resonances of dielectric nanospheres in the visible region. *Nano Lett.* **12**(7), 3749–3755 (2012)
28. A.I. Kuznetsov, A.E. Miroshnichenko, Y.H. Fu, J. Zhang, B. Luk'yanchuk, Magnetic light. *Sci. Rep.* **2**, 492 (2012)
29. P. Kapitanova, V. Ternovski, A. Miroshnichenko, N. Pavlov, P. Belov, Y. Kivshar, M. Tribelsky, Giant field enhancement in high-index dielectric subwavelength particles. *Sci. Rep.* **7**(1), 731 (2017)
30. M.K. Schmidt, R. Esteban, J.J. Sáenz, I. Suárez-Lacalle, S. Mackowski, J. Aizpurua, Dielectric antennas—a suitable platform for controlling magnetic dipolar emission. *Opt. Express* **20**, 13636–13650 (2012). Jun
31. B. Rolly, B. Bebey, S. Bidault, B. Stout, N. Bonod, Promoting magnetic dipolar transition in trivalent lanthanide ions with lossless mie resonances. *Phys. Rev. B* **85**, 245432 (2012)
32. T. Feng, Y. Xu, Z. Liang, W. Zhang, All-dielectric hollow nanodisk for tailoring magnetic dipole emission. *Opt. Lett.* **41**, 5011–5014 (2016). Nov
33. J. Li, N. Verellen, P. Van Dorpe, Enhancing magnetic dipole emission by a nano-doughnut-shaped silicon disk. *ACS Photonics* **4**(8), 1893–1898 (2017)
34. D.G. Baranov, R.S. Savelev, S.V. Li, A.E. Krasnok, A. Alú, Modifying magnetic dipole spontaneous emission with nanophotonic structures. *Laser Photonics Rev.* (2017)
35. D.-J. Cai, Y.-H. Huang, W.-J. Wang, W.-B. Ji, J.-D. Chen, Z.-H. Chen, S.-D. Liu, Fano resonances generated in a single dielectric homogeneous nanoparticle with high structural symmetry. *J. Phys. Chem. C* **119**(8), 4252–4260 (2015)
36. A.E. Miroshnichenko, Y.S. Kivshar, Fano resonances in all-dielectric oligomers. *Nano Lett.* **12**(12), 6459–6463 (2012)
37. B. Hopkins, A.N. Poddubny, A.E. Miroshnichenko, Y.S. Kivshar, Revisiting the physics of Fano resonances for nanoparticle oligomers. *Phys. Rev. A* **88**(5), 053819 (2013)
38. K.E. Chong, B. Hopkins, I. Staude, A.E. Miroshnichenko, J. Dominguez, M. Decker, D.N. Neshev, I. Brener, Y.S. Kivshar, Observation of fano resonances in all-dielectric nanoparticle oligomers. *Small* **10**(10), 1985–1990 (2014)
39. D.S. Filonov, A.P. Slobozhanyuk, A.E. Krasnok, P.A. Belov, E.A. Nenasheva, B. Hopkins, A.E. Miroshnichenko, Y.S. Kivshar, Near-field mapping of fano resonances in all-dielectric oligomers. *Appl. Phys. Lett.* **104**(2), 021104 (2014)
40. P. Fan, Z. Yu, S. Fan, M.L. Brongersma, Optical Fano resonance of an individual semiconductor nanostructure. *Nat. Mater.* **13**(5), 471–475 (2014)
41. M. Nieto-Vesperinas, R. Gomez-Medina, J. Saenz, Angle-suppressed scattering and optical forces on submicrometer dielectric particles. *JOSA A* **28**(1), 54–60 (2011)

42. J.-M. Geffrin, B. García-Cámara, R. Gómez-Medina, P. Albella, L. Froufe-Pérez, C. Eyraud, A. Litman, R. Vaillon, F. González, M. Nieto-Vesperinas et al., Magnetic and electric coherence in forward-and back-scattered electromagnetic waves by a single dielectric subwavelength sphere. *Nat. Commun.* **3**, 1171 (2012)
43. Y.H. Fu, A.I. Kuznetsov, A.E. Miroshnichenko, Y.F. Yu, B. Luk'yanchuk, Directional visible light scattering by silicon nanoparticles. *Nat. Commun.* **4**, 1527 (2013)
44. S. Person, M. Jain, Z. Lapin, J.J. Saenz, G. Wicks, L. Novotny, Demonstration of zero optical backscattering from single nanoparticles. *Nano Lett.* **13**(4), 1806–1809 (2013)
45. B. Rolly, B. Stout, N. Bonod, Boosting the directivity of optical antennas with magnetic and electric dipolar resonant particles. *Opt. Express* **20**, 20376–20386 (2012)
46. W. Liu, A.E. Miroshnichenko, D.N. Neshev, Y.S. Kivshar, Broadband unidirectional scattering by magneto-electric core-shell nanoparticles. *ACS Nano* **6**(6), 5489–5497 (2012)
47. W. Liu, A.E. Miroshnichenko, R.F. Oulton, D.N. Neshev, O. Hess, Y.S. Kivshar, Scattering of core-shell nanowires with the interference of electric and magnetic resonances. *Opt. Lett.* **38**(14), 2621–2624 (2013)
48. X. Zambrana-Puyalto, I. Fernandez-Corbaton, M.L. Juan, X. Vidal, G. Molina-Terriza, Duality symmetry and kerker conditions. *Opt. Lett.* **38**, 1857–1859 (2013)
49. R. Alae, R. Filter, D. Lehr, F. Lederer, C. Rockstuhl, A generalized kerker condition for highly directive nanoantennas. *Opt. Lett.* **40**, 2645–2648 (2015)
50. W. Liu, J. Zhang, B. Lei, H. Ma, W. Xie, H. Hu, Ultra-directional forward scattering by individual core-shell nanoparticles. *Opt. Express* **22**, 16178–16187 (2014)
51. C. Sauvan, J.-P. Hugonin, I. Maksymov, P. Lalanne, Theory of the spontaneous optical emission of nanosize photonic and plasmon resonators. *Phys. Rev. Lett.* **110**(23), 237401 (2013)
52. F. Ouyang, M. Isaacson, Accurate modeling of particle-substrate coupling of surface plasmon excitation in EELS. *Ultramicroscopy* **31**(4), 345–349 (1989)
53. F. Ouyang, M. Isaacson, Surface plasmon excitation of objects with arbitrary shape and dielectric constant. *Philos. Mag. Part B* **60**(4), 481–492 (1989)
54. F.J. Garcia de Abajo, A. Howie, Relativistic electron energy loss and electron-induced photon emission in inhomogeneous dielectrics. *Phys. Rev. Lett.* **80**, 5180–5183 (1998)
55. D.R. Fredkin, I.D. Mayergoyz, Resonant behavior of dielectric objects (electrostatic resonances). *Phys. Rev. Lett.* **91** (2003)
56. I. Mayergoyz, D. Fredkin, Z. Zhang, Electrostatic (plasmon) resonances in nanoparticles. *Phys. Rev. B* **72**, 155412 (2005)
57. C. Forestiere, L. Dal Negro, G. Miano, Theory of coupled plasmon modes and fano-like resonances in subwavelength metal structures. *Phys. Rev. B* **88**(15), 155411 (2013)
58. C.F. Bohren, D.R. Huffman, *Absorption and Scattering of Light by Small Particles* (Wiley, 1998)
59. C. Forestiere, G. Miano, Material-independent modes for electromagnetic scattering. *Phys. Rev. B* **94**, 201406 (2016)
60. C. Forestiere, G. Miano, On the nanoparticle resonances in the full-retarded regime. *J. Opt.* **19**(075601), 075601 (2017)
61. R. Fuchs, Theory of the optical properties of ionic crystal cubes. *Phys. Rev. B* **11**, 1732–1740 (1975)
62. D.J. Bergman, D. Stroud, Theory of resonances in the electromagnetic scattering by macroscopic bodies. *Phys. Rev. B* **22**(8), 3527 (1980)
63. D.J. Bergman, The dielectric constant of a composite material—a problem in classical physics. *Phys. Rep.* **43**(9), 377–407 (1978)
64. R. Rojas, F. Claro, Electromagnetic response of an array of particles: Normal-mode theory. *Phys. Rev. B* **34**, 3730–3736 (1986)
65. V.A. Markel, Antisymmetrical optical states. *J. Opt. Soc. Am. B* **12**, 1783–1791 (1995)
66. V.A. Markel, Pole expansion of the lorenz-mie coefficients. *J. Nanophotonics* **4**(1), 041555–041555 (2010)
67. A. Farhi, D.J. Bergman, Electromagnetic eigenstates and the field of an oscillating point electric dipole in a flat-slab composite structure. *Phys. Rev. A* **93**(6), 063844 (2016)

68. M. Pascale, G. Miano, C. Forestiere, Spectral theory of electromagnetic scattering by a coated sphere. *JOSA B* **34**(7), 1524–1535 (2017)
69. C. Forestiere, G. Miano, G. Rubinacci, A. Tamburrino, R. Tricarico, S. Ventre, “Volume integral formulation for the calculation of material independent modes of dielectric scatterers”. *IEEE Tran. Antennas and Propag.* **66**(5), 2505–2514 (2018)
70. M. Cessenat, Mathematical methods in electromagnetism, in *Linear Theory and Applications. Series on Advances in Mathematics for Applied Sciences*, vol. 41 (1996)
71. E. Ching, P. Leung, A.M. van den Brink, W. Suen, S. Tong, K. Young, Quasinormal-mode expansion for waves in open systems. *Rev. Mod. Phys.* **70**(4), 1545 (1998)
72. E.J. Davis, G. Schweiger, *The Airborne Microparticle* (Springer, 2002)
73. H.S. C, B.R. E, Morphology-dependent resonances, in *Optical Effects Associated with Small Particles* ed. by P.W. Barber, R.K. Change, chap. 1 (World Scientific, Singapore, 1988)
74. P.T. Kristensen, S. Hughes, Modes and mode volumes of leaky optical cavities and plasmonic nanoresonators. *ACS Photonics* **1**(1), 2–10 (2013)
75. P.T. Kristensen, R.-C. Ge, S. Hughes, Normalization of quasinormal modes in leaky optical cavities and plasmonic resonators. *Phys. Rev. A* **92**(5), 053810 (2015)
76. C.F. Bohren, D.R. Huffman, *Absorption and scattering of light by small particles* (Wiley, 2008)
77. A. Doicu, T. Wriedt, Y. Eremin, *Light Scattering by Systems of Particles* (Springer, 2006)
78. S.A. Maier, *Plasmonics: Fundamentals and Applications* (Springer Science & Business Media, 2007)
79. Y. Jiang, S. Pillai, M.A. Green, Realistic silver optical constants for plasmonics. *Sci. Rep.* **6** (2016)
80. M. Kerker, D.-S. Wang, C. Giles, Electromagnetic scattering by magnetic spheres. *JOSA* **73**(6), 765–767 (1983)
81. I. Staude, A.E. Miroshnichenko, M. Decker, N.T. Fofang, S. Liu, E. Gonzales, J. Dominguez, T.S. Luk, D.N. Neshev, I. Brener, Y. Kivshar, Tailoring directional scattering through magnetic and electric resonances in subwavelength silicon nanodisks. *ACS Nano* **7**(9), 7824–7832 (2013)

# Chapter 9

## Dark-Mode Characteristics of Metasurfaces Engineered by Symmetry Matching of Resonant Elements and Electromagnetic Fields



A. Lupu, E. Bochkova, S. N. Burokur and A. de Lustrac

**Abstract** We revisit the engineering of metasurfaces displaying sharp spectral features and conventionally relying on electromagnetically induced transparency resulting from Fano-type interference between dark and bright resonant elements. The aim of the developed approach based on symmetry considerations is to show that electromagnetically induced transparency and dark mode excitation are not necessarily associated. We bring theoretical and experimental evidence in the microwave domain that electromagnetically induced transparency and dark mode excitation can be achieved in an independent manner by using distinctly different mechanisms. The use of these distinctly different mechanisms provides higher flexibility for metasurfaces engineering and results in a great improvement of their spectral performances.

### 9.1 Plasmonic EIT Viewed as Bright and Dark Modes Fano Interference

The phenomenon of electromagnetically induced transparency (EIT), initially introduced in atomic physics, results from quantum destructive interference of two resonant pathways in atomic three-level system [1]. During the last decade, the classical analogs of this concept widely pervaded the fields of photonics [2, 3], plasmonics [4] and metamaterials [5]. The interest in EIT-like resonances is driven by their ability to demonstrate much narrower linewidths than those of individual resonators.

---

A. Lupu (✉) · E. Bochkova · A. de Lustrac  
Centre de Nanosciences et de Nanotechnologies, CNRS, Université Paris-Sud, Université Paris-Saclay, C2N – Orsay, 91405 Orsay Cedex, France  
e-mail: anatole.lupu@c2n.upsaclay.fr

S. N. Burokur  
LEME, UPL, Université Paris Nanterre, 92410 Ville d'Avray, France

A. de Lustrac  
UPL, Université Paris Nanterre, 92410 Ville d'Avray, France

Applied to plasmonic metasurfaces (MSs), such sharp spectral features with steep intensity variation are highly desirable for sensing applications [6–8]. The sensing principle exploits the high sensitivity of the localized surface plasmons to the change of their immediate dielectric environment. The adsorption of the analyte species on the surface of metamaterial elements results in a shift of the resonance spectral position. The sensing detection limit and accuracy are greatly increased by using narrow width spectral features associated with EIT.

Despite the seemingly great variety of studied designs, most of them actually share the same principle. The interaction of plasmonic resonant elements with the external electromagnetic field causes collective oscillations of conductivity electrons. In the quasi-electrostatic approximation such systems may be described in terms of the plasmonic eigenmodes interacting with the external field. The Fano resonance and its associated EIT effect occur due to the interference between plasmonic eigenmodes. The eigenmodes with strong dipolar momentum correspond to in-phase oscillation of coupled resonators and are called bright or radiative modes. In contrast, the eigenmodes with low dipolar momentum correspond to opposite-phase oscillation of coupled resonators and are called dark modes. Such modes weakly couple with external field because of practically zero net dipolar momentum and therefore demonstrate higher quality factor.

One of the widely used methods for dark modes excitation consists in breaking the symmetry in a system of coupled resonators. Such breaking enables excitation of antisymmetric currents in the near vicinity of the resonance frequency. The radiation emitted by oppositely directed electric dipoles is strongly suppressed, leading thus to the appearance of a transparency window in a narrow frequency range. Strong impetus to this approach was brought by the Fedotov's et al. seminal paper [9] reporting the experimental demonstration of dark mode excitation in the microwave domain. The demonstration was performed by using an array of paired metallic arcs of slightly different length. The narrow maximum observed in the transmission spectrum was associated with antiphase current oscillations in the arcs that induce a dipolar magnetic momentum.

Later a theoretical model introducing a general description of an EIT like plasmonic “molecule” was proposed in [10]. The authors have considered an artificial plasmonic molecule consisting of two “atoms”. The bright resonant element corresponding to the superradiant plasmonic mode  $|a\rangle = \tilde{a}(\omega) \exp(i\omega t)$  strongly couples with the incident field and has a broad resonance linewidth. The dark atom that corresponds to a subradiant plasmonic mode  $|b\rangle = \tilde{b}(\omega) \exp(i\omega t)$  is weakly coupled to the incident light and has a narrow resonance linewidth. The field amplitude of both elements is described by a system of linearly coupled Lorentzian oscillators:

$$\begin{pmatrix} \tilde{a} \\ \tilde{b} \end{pmatrix} = - \begin{pmatrix} \Delta\omega + i\gamma_a & \kappa \\ \kappa & \Delta\omega + i\gamma_b \end{pmatrix}^{-1} \begin{pmatrix} g\tilde{E}_0 \\ 0 \end{pmatrix} \quad (1)$$

where the detuning from resonance  $\Delta\omega = \omega - \omega_0 \ll \omega_0$ , the damping factors of the two resonators satisfy  $\gamma_b \ll \gamma_a \ll \omega_0$ ,  $\kappa$  is the coupling between two atoms

and  $g$  is the factor indicating the coupling of superradiant element with the incident electromagnetic field.

It is assumed that there is no direct coupling between the dark element and the incident field and the polarizability of the plasmonic molecule is proportional to the amplitude of the dipole response of the bright element:

$$\tilde{a} = \frac{-\kappa E_0(\Delta\omega + i\gamma_b)}{(\Delta\omega + i\gamma_a)(\Delta\omega + i\gamma_b) - \kappa^2} \quad (2)$$

It should be noted that such a resonant behavior is typical for many systems, which can be described by a model of coupled oscillators: RLC contour, mechanical systems with masses and springs or nano-particles coupled through the near field. For instance it describes the dynamic of two coupled oscillators with resonant frequencies  $\omega_1$  and  $\omega_2$ , damping factors  $\gamma_1$  and  $\gamma_2$ , and driven by external harmonic forces  $f_1$  and  $f_2$  is described by a system of motion equations:

$$\begin{aligned} \ddot{x}_1 + \gamma_1 \dot{x}_1 + \omega_1^2 x_1 &= \kappa x_2 + f_1 e^{i\omega t} \\ \ddot{x}_2 + \gamma_2 \dot{x}_2 + \omega_2^2 x_2 &= \kappa x_1 + f_2 e^{i\omega t} \end{aligned} \quad (3)$$

where  $\kappa$  is a coupling between two oscillators. The complex steady-state solutions for the displacement of oscillators are periodic and can be written as  $x_1 = c_1 e^{i\omega t}$  and  $x_2 = c_2 e^{i\omega t}$ , where  $c_1$  and  $c_2$  are the complex amplitudes:

$$\begin{aligned} c_1 &= \frac{\kappa f_2 + f_1(\omega_2^2 - \omega^2 + i\gamma_2\omega)}{(\omega_1^2 - \omega^2 + i\gamma_1\omega)(\omega_2^2 - \omega^2 + i\gamma_2\omega) - \kappa^2} \\ c_2 &= \frac{\kappa f_1 + f_2(\omega_1^2 - \omega^2 + i\gamma_1\omega)}{(\omega_1^2 - \omega^2 + i\gamma_1\omega)(\omega_2^2 - \omega^2 + i\gamma_2\omega) - \kappa^2} \end{aligned} \quad (4)$$

In classical analog of Fano resonance, the external force  $f_1$  excites only the heavier damped mode, e.g.  $x_1$ , while the narrow resonance mode  $x_2$  (dark mode) is excited only through the coupling interaction ( $f_2 = 0$ ). The variation of spectral response of the driven oscillator normalized amplitude  $|c_1|$  with resonance frequency detuning  $\delta = \omega_1 - \omega$  is shown in Fig. 9.1a. A characteristic asymmetric Fano type line-shape due to the constructive/destructive interference is observed when the resonance frequencies of the two oscillators are different. In contrast, a marked dip of resonance amplitude corresponding to EIT effect due to destructive type interference is observed in the when the resonance frequencies of both oscillators coincide. It is important to note that efficiency of constructive-destructive interference characteristic for a Fano resonance strongly depends on losses. The impact of the damping strength variation of second oscillator  $\gamma_2$  is depicted in Fig. 9.1b. With the increase of the damping strength  $\gamma_2$  the transmission dip almost completely disappears though  $\gamma_2$  is still much lower than  $\gamma_1$ .

Since the works published in [9, 10] a plethora of EIT effect demonstrations exploiting the concept of interacting bright and dark modes have been reported.



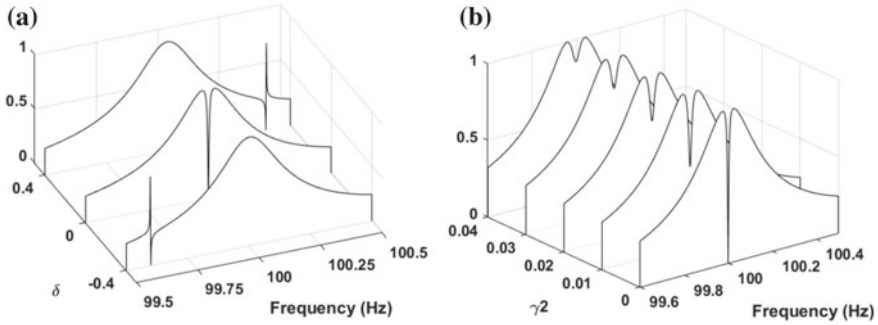


**Fig. 9.1** Normalized amplitude  $|c_1|$  of the driven oscillator in the classical coupled oscillators system. **a** Variation of the resonance frequency detuning  $\delta = \omega_1 - \omega_2$  at  $\omega_1 = 100$  Hz,  $\gamma_1 = 0.25$  Hz,  $\gamma_2 = 0$ ,  $\kappa = 5$  Hz<sup>2</sup>; **b** influence of the damping strength variation  $\gamma_2$  of the second oscillator at  $\delta = 0$

Several designs based on dolmen type geometry [8, 11, 12] plasmonic oligomers [13–16], ring-disk nanocavities [17, 18] nanoshells [19, 20], asymmetric coupled split-ring resonators [9, 21–24] and cut wires plasmonic lattices [25–27] have been proposed and investigated for EIT characteristics.

Selected examples of plasmonic nanostructures reporting the demonstration of EIT effect in the NIR domain are detailed below.

### 9.1.1 Symmetry-Broken Dolmen Metamolecules

Following the conceptual precepts elaborated in [10], the experimental demonstration of EIT-like effects in dolmen type structure was performed later in [10]. The dolmen structure unit cell consists a gold bar stacked above two symmetric gold wires. The top gold bar acting as radiative dipole antenna plays the role of the bright mode strongly coupled to the incident light. The bottom gold wire pair acts as a non-radiative quadrupole antenna and represents the dark mode, which excitation is forbidden for normally incident light. The symmetry breaking renders this normally dark mode active and excitable.

The EIT appears as the consequence of interaction between the narrow dark and broad bright modes. For instance, it was found that in agreement with the general physical considerations, the damping strength of both bright and dark mode are practically constant and do not depend of the asymmetry parameter. In contrast, the coupling strength displays an approximately linear dependence of the lateral displacement.

### 9.1.2 *Symmetry-Broken Ring-Disk Nanocavities*

Similar behavior was also reported for system composed of ring-disk nanocavities [17]. The superradiant antibonding dipolar mode acts as the bright resonant element. The rings' quadrupolar electric mode acts as the dark resonant element. Its excitation is forbidden for normally incident light in concentric ring-disk nanocavities, but becomes allowed when the symmetry of the system is broken.

### 9.1.3 *Plasmonic Oligomer Clusters*

Another family of nanostructures used for the investigation of Fano resonances and EIT concerns plasmonic oligomers [15, 19, 28, 29]. In such structure, the bright dipolar mode is produced by the collective in-phase oscillation of electrons both of the central and of the outer ring nanoparticles. The dark mode is produced by the anti-phase oscillation of collective charges in the outer ring with respect to the central oligomer nanoparticle. One important difference with respect to the previous examples of dolmen and coupled disk-ring nanostructures, is that in the case of oligomer clusters the dark mode cannot be assigned to a separate cluster element. It appears instead as the result of near field interaction between plasmonic nanoparticles, a phenomenon known also as hybridization mechanism [13, 14, 16, 19, 25, 28, 30]. The plasmon hybridization approach is based on a quasi-electrostatic approximation. The dressed eigenmodes of a system of interacting nanoparticles are considered as a hybridized linear combination of the "primitive" or "diabatic" plasmon modes of the individual particles [13, 20]. In the quantum mechanical description, the hybridization process represents the first order approximation in the perturbation theory approach. As known, in the approximation of weak perturbation the solutions of the perturbed Hamiltonian are found as power series of terms using solutions of unperturbed Hamiltonian.

Another notable difference is that Fano interference between the bright and dark modes does not rely on symmetry breaking scheme of the oligomer arrangement. However, as reported in [13], the variation of the geometrical dimensions of the inner oligomer particle can significantly modify the efficiency of Fano interference mechanism. The generation of a marked Fano resonance in the extinction spectrum was argued by matching the dipole moments of the outer ring and the center particle. In a similar manner as for dolmen or ring-disk coupled structures, the EIT effect is by far more pronounced when the bright dressed mode is highly super-radiant and the dark dressed mode is very sub-radiant.

The provided examples show that the simple model of coupled mechanical oscillators captures the essential features of Fano interference occurring in plasmonic systems. However, as it was pointed in several works [31–33] it suffers from a number of deficiencies detailed below. Furthermore, the parameters entering the coupled mode equation are obtained through a fitting procedure from modeling or experi-

mental scattering spectra instead of being calculated directly from the radiative characteristics of the individual unhybridized modes. This issue motivated scientists to develop novel approaches oriented to achieve the predictive power when considering an *ab initio* design.

## 9.2 Plasmonic EIT Revisited

The initial interpretation given to the phenomenon of Fano resonance and EIT in plasmonic systems was based on the concept of interference between a bright mode and a dark mode. The assumption made when using the model of coupled mechanical oscillators is that the incident light is for essential scattered by the bright mode. To verify the validity of this conjecture based on the quasi-electrostatic approach [32] considered the scattering in a plasmonic system with two or more bright modes. The performed analysis showed that the coupling between at least two bright modes gives rise to Fano-like resonances in the scattering spectrum. The authors have determined in a very clear way the contribution of each plasmon mode to the scattering and absorption processes. The obtained results highlighted the fact that the Fano-type interference and its associated plasmonic equivalent of EIT are by far more pronounced as the radiative strengths of both plasmonic modes are similar. In contrast, the interference of two modes with very dissimilar radiative strengths increases the asymmetry of the scattering response but the amplitude of EIT is greatly reduced.

The apparent contradiction with the previous model of bright-dark mode interaction stems from the fact that in [32] Forestiere et al. considered the interaction of dressed and not diabatic eigenmodes of the plasmonic system. The considered approach is fully consistent with the experimental results reported for oligomers clusters, namely what concerns the influence of the size of the central nanoparticle. As reported in [15], Fano interference is by far more pronounced when the size and related with it dipolar moment of the central nanoparticle is matched with that of the outer ring.

Yet one important moment, while not explicitly expressed but *de facto* taken into account in [32] analysis is related to the condition of the orthogonality of the eigenmodes. As known, no interference effect should exist in the case of an orthogonal basis of eigenmodes. By consequence it is not clear why Fano interference is observed, especially when dealing with an oligomer assembly having a high degree of symmetry. The initial explanation of this result was based on the non-Hermitian nature of considered system due to metal related losses. However later results have shown the possibility for occurrence of a Fano resonance in all-dielectric symmetric oligomers [34].

The relevant explanation of this discrepancy was done in [35]. As it was pointed by the authors of this publication “The key is that the symmetry approach produces orthogonal modes by definition, whereas the interaction matrix, which describes the coupling between the dipole moments of each particle, is non-Hermitian.” The non-Hermitian character of interaction matrix is due to the presence of both electric and

magnetic polarizabilities in the system of interacting particles [36]. The resulting eigenvectors form a complete set, but are not orthogonal. The fact that the eigenvectors are not orthogonal means that even though the eigenmodes are themselves decoupled; their excitations are coupled. On this basis it was shown in [35] that the true modes of the oligomer assembly are bright instead of dark and then concluded that “the Fano resonance in this system is explicitly due to the interference between bright modes only, and it does not involve any dark mode.”

It appears thus that the non-Hermiticity of interaction matrix is the key feature to observe Fano-type interference of eigenmodes. This non-Hermiticity can be also viewed as the consequence of the open character of the system where the scattered wave corresponds to resonance-continuum coupling [37, 38].

One elegant way to take into account the open character of the system was proposed in [33]. The authors of this publication proposed an extended coupled oscillator (ECO) model, which consists in introducing in the system of coupled (3) an additional term accounting for the radiative dumping:

$$\begin{aligned}\ddot{x}_1 + \gamma_1 \dot{x}_1 + \omega_1^2 x_1 + \kappa x_2 &= 0.5 \ddot{P}_{tot} + f_1 e^{i\omega t} \\ \ddot{x}_2 + \gamma_2 \dot{x}_2 + \omega_2^2 x_2 + \kappa x_1 &= 0.5 \ddot{P}_{tot} + f_2 e^{i\omega t}\end{aligned}\quad (5)$$

where the total dipole moment of the system  $P_{tot} = P_1 + P_2 = \alpha_1 x_1 + \alpha_2 x_2$  is the sum of the dipole momentum of oscillators 1 and 2,  $\alpha_j = f_j/E_{ext}$  are the polarizabilities related to the diabatic plasmon modes.

On the example of plasmonic assembly made of a gold dipole nanoantenna surrounded by two gold nanorods it was demonstrated that ECO model results are in a very good agreement with numerical modeling simulations obtained by using Surface Integral Equation (SIE) method as well as with experimental measurements [33].

Another highly efficient analytical approach that takes into account the open character of the system of interacting plasmonic resonators is the use of the formalism of the scattering matrix based on temporal coupled mode theory (TCMT), which was originally proposed by H. Haus for a system of coupled optical resonators in [39] and later considerably developed by Fan et al. [40–42]. Following this approach, a resonator system considered to be open can freely couple to free space through radiation. Propagation of electromagnetic waves through such system occurs via two channels that incorporate direct non-resonance pathway and resonance-assisted pathway. In this formalism and by using same notations as in [43], the scattering matrix for the system of coupled resonators can be expressed as:

$$S = C + iV[wI - H_{eff}]^{-1}V^\dagger \quad (6)$$

where  $C$  is the background scattering which does not interact with resonator and accounts also for the higher order resonances far away from considered frequency range,  $V$  is the coupling between radiation and resonator,  $H_{eff}$  is the effective Hamiltonian that can be described as:

$$H_{eff} = H_0 + i \frac{1}{2} V V^\dagger + i \Lambda_L \quad (7)$$

Eigenvalues of unperturbed Hermitian Hamiltonian  $H_0$  represents the discrete resonator states. The second term is the coupling between radiation and discrete states and the third term involves extraneous losses. Owing to the presence of latter terms the effective Hamiltonian become non-Hermitian and possesses non-orthogonal basis of eigenmodes.

It follows thus from all the above that even though we consider open systems with initially bright and dark diabatic modes, the Fano type interference resulting from their non-Hermiticity turns out to occur between bright adiabatic modes. Furthermore, the efficiency of Fano interference and its associated EIT effect is optimal when both interacting modes are having similar strength. An obvious question arising in this context and that we address by the following is whether it is possible to achieve Fano interference in a more efficient manner, by considering from the beginning system with equal strength, i.e. identical resonant elements? Another question associated with the previous one is what in this case the meaning of the dark mode and whether can it be excited without losing the “dark” properties? Based on the symmetry considerations these questions are addressed in the next sections.

### 9.3 Direct Dark Mode Excitation Mechanism Based on Symmetry Matching

The fact that dark mode is forbidden means that it cannot be excited due to zero net electric dipolar momentum. To illustrate the concept of such a mode we consider the archetypical example of cut-wires (CWs) metasurface shown in the inset of Fig. 9.2a. Details on the CWs structure used for this study can be found in [44]. The transmission and reflectance spectral responses of the CWs metasurface calculated using ANSYS HFSS modeling software [45] are displayed in Fig. 9.2a. The transmission dip at  $f_0 = 8.3$  GHz is related to the  $m_0$  fundamental CWs mode excitation that corresponds to that of an electric dipole. The excitation by a plane wave of the first higher mode  $m_1$  sketched in Fig. 9.2b is forbidden by symmetry and consequently this mode remains dark.

Nevertheless the excitation by a plane wave of the first higher mode is possible when considering resonant elements with inversion symmetry geometry. One of the simplest inversion symmetry structures is the example of two connected anti-symmetric V-antennas (AVA), shown as inset in Fig. 9.3a. Under normal incidence, the structure exhibits only fundamental electric dipole excitation at 8.1 GHz corresponding to the dip in transmission spectrum shown in Fig. 9.3a. The excitation of the first higher order mode is forbidden since electric field cannot interact with this antisymmetric dark mode due to zero net dipole moment.

The situation becomes however drastically different for oblique incidence configuration sketched in Fig. 9.3b when the magnetic component of the incident field is

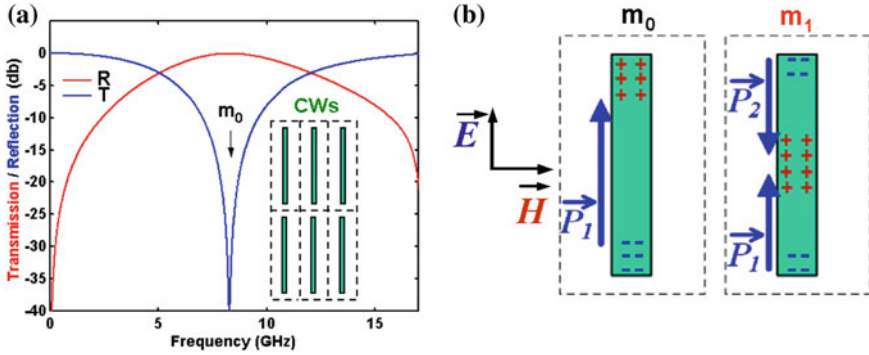


**Fig. 9.2** **a** Normal incidence reflection and transmission spectra of a CWs metasurface shown in inset; **b** Sketch of the charges distribution for the fundamental- $m_0$  and first higher order mode- $m_1$

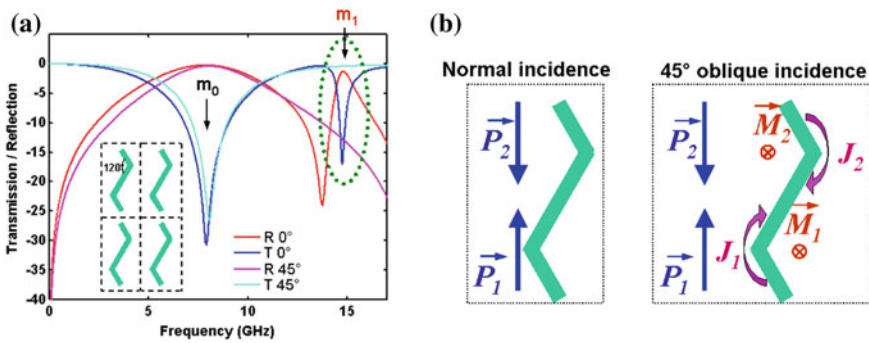


**Fig. 9.3** **a** Normal and  $45^\circ$  oblique incidence reflection and transmission spectra of a AVA metasurface shown in inset; **b** Sketch of the antisymmetric mode electric and magnetic dipole moments induced by normally and obliquely incident field

crossing the metasurface. As it can be seen from Fig. 9.3a, under oblique incidence the transmission and reflection spectra exhibit not only the fundamental dipolar mode at 8.1 GHz but also an additional resonance at 14.8 GHz related to the magnetic dipole excitation. The magnetic momenta induced by opposite currents in the top and bottom V-antennas are oriented in the same direction resulting in a net non-zero magnetic dipolar momentum. Thus, as illustrated in Fig. 9.3b, under oblique incidence the magnetic component of the incident field can produce a direct excitation of the antisymmetric dark mode. Note that the quality factor of the dark mode ( $Q = 9.5$ ) is almost an order of magnitude higher as compared to that of fundamental resonance ( $Q = 1.1$ ).

The provided above results show that even with a raw design that was not subjected to any optimization the excitation at 14.8 GHz of the magnetic dipole instead of electric one indeed provides a significant improvement of the spectral response

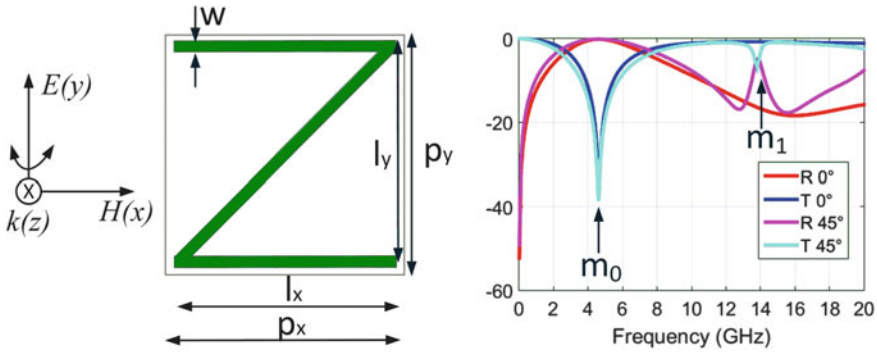


**Fig. 9.4** Dark mode excitation in Z-shaped resonator. Simulated transmission and reflection spectra under normal and oblique incidence

selectivity. By consequence it seems possible to have a room for further performance enhancement.

To this end for a fixed resonator length we consider a unit cell design. where two V-antennas are transformed to the Z-shaped resonator with two legs perpendicular to the E-field as displayed in Fig. 9.4. The dimensions of the unit cell is  $p_x = p_y = 6$  mm. The length of the Z-element along  $x$ - and  $y$ -directions is, respectively,  $l_x = 5.8$  mm and  $l_y = 5.7$  mm, and the width is 0.3 mm.

Similarly to two asymmetric V-antennas design, under normal incidence the Z-shaped resonator displays only one resonance at 4.5 GHz corresponding to the fundamental mode excitation. This is confirmed by instantaneous charges distribution shown in Fig. 9.5a. Under oblique incidence transmission and reflection spectra exhibit an additional resonance feature at 13.7 GHz related to the dark mode excitation. As it can be seen from Fig. 9.5b, at this resonance two opposite currents are excited leading to non-zero magnetic moment. While having a behavior similar to that of two connected V-antennas, Z-shaped design brings a notable improvement of the dark mode resonance quality factor.

As it can be observed from Figs. 9.3 and 9.4, for an identical resonator length, passing from two V-antennas to Z-shaped design reduces the induced electric dipole projection on the direction of external electric field. The narrowing of the fundamental mode frequency bandwidth proves this. The bandwidth narrowing of the antisymmetric dark mode for Z-shaped resonator turns out to be much more significant. In summary for Z-shaped design, the quality factor of fundamental and dark mode resonances is  $Q_{\text{fund}} = 0.9$  and  $Q_{\text{dark}} = 23$ , respectively.

It should be emphasized, that dark mode resonance in the Z-shaped design does not rely on coupling between adjacent resonators but is related only to excitation in individual elements. This is evidenced by spectral characteristics for increased dimensions of unit cell in Fig. 9.6. As it can be seen, both the dark mode and fundamental mode are present when the period of unit cell becomes equal to  $p_x = p_y = 9$  mm. The influence of resonators coupling manifests as frequency shift of resonance

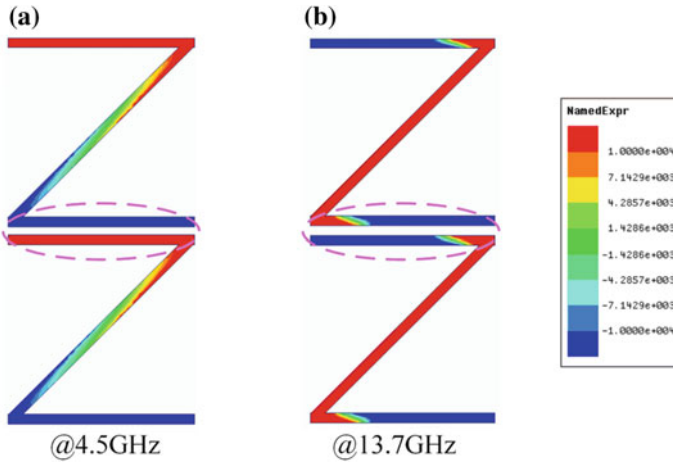


**Fig. 9.5** Instantaneous current distributions: **a** fundamental resonance at 4.5 GHz; **b** magnetic dipole excitation at 13.7 GHz

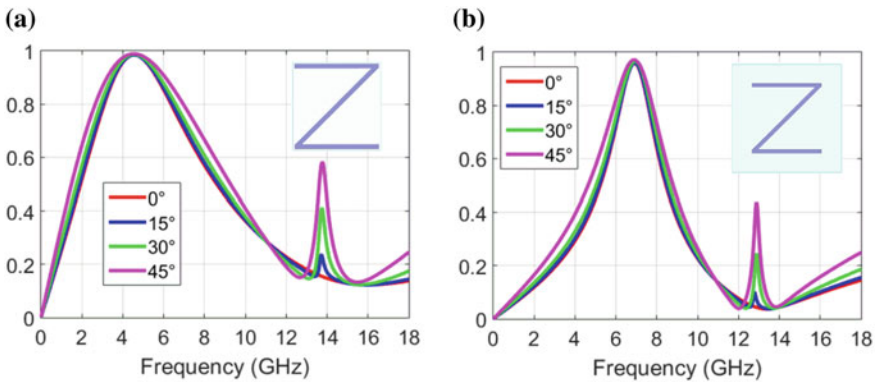


**Fig. 9.6** Reflection under normal and oblique incidence for Z-elements with identical geometry but different size unit cell **a**  $p_x = p_y = 6$  mm; **b**  $p_x = p_y = 9$  mm

positions from 4.5 GHz to 6.9 GHz and from 13.7 GHz to 12.8 GHz for fundamental and dark mode, respectively. In terms of LC-contour, the frequency shift can be explained as the variation of capacitance formed by the top and bottom legs of two adjacent Z (Fig. 9.5). The fundamental resonance moves to higher frequency since the capacitance is decreased when the separation distance between legs is increased. In contrast the frequency of dark mode moves to lower frequency because of same sign charges accumulation on the legs of Z.

It is worthy to mention that the fundamental resonance is little sensitive to the variation of incidence angle while the amplitude of dark mode excitation noticeably increases with the incidence angle, as it can be seen in Fig. 9.6. It is because the



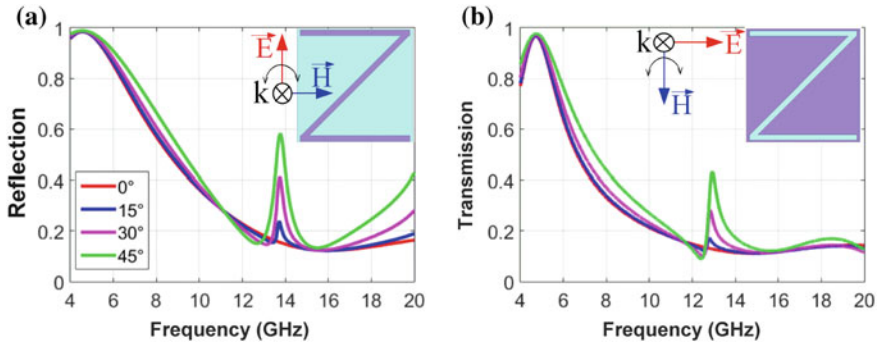


**Fig. 9.7** Dual behavior for Z-shaped resonator: **a** reflection for the original Z; **b** transmission for the complementary Z

resonance amplitude augments for higher projection of the magnetic component of the incident field penetrating the structure. This feature represents an additional evidence of magnetic nature of the dark mode resonance.

Note also that in contrast to the usual case where dark mode excitation is associated with maximum in transmission due to the EIT effect, in the present configuration dark mode manifests as a peak in reflection and minimum in transmission. Considering complementary metasurface design relying on Babinet's principle allows to easily inverse situation and achieve dual to original design electromagnetic behavior [46–50].

To this end, we consider complementary Z-shaped metasurface displayed as inset in Fig. 9.7b. According to Babinet's principle, polarization of complementary incident field is such that its electric component is horizontally orientated while the magnetic field vertically. As it can be observed in Fig. 9.7, the peak in reflection is replaced now by a maximum in transmission for the complementary Z-structure. As it can be seen from Fig. 9.7b, under oblique incidence when electric field component is crossing the metasurface, dark mode resonance is excited at 12.9 GHz.

In order to validate experimentally the modeling results, prototypes of Z-shaped and complementary Z metasurface were fabricated by using classical printed circuit board technology (Fig. 9.8). The total sample size is  $35 \times 35$  cells on a  $210 \text{ mm} \times 210 \text{ mm}$  dielectric substrate. The material parameters of the substrate and the geometrical dimensions used for the experimental validation are the same as in numerical simulations.

The microwave transmission measurements were conducted in an anechoic chamber using an Agilent 8722ES network analyzer and two wide band horn antennas. Oblique incidence measurements were performed by using a goniometric setup schematically shown in Fig. 9.9b. Phase referencing and normalization have been performed in transmission by removing the sample from the signal path, and in reflection, by replacing the sample with a copper plate. Measured reflection and transmission

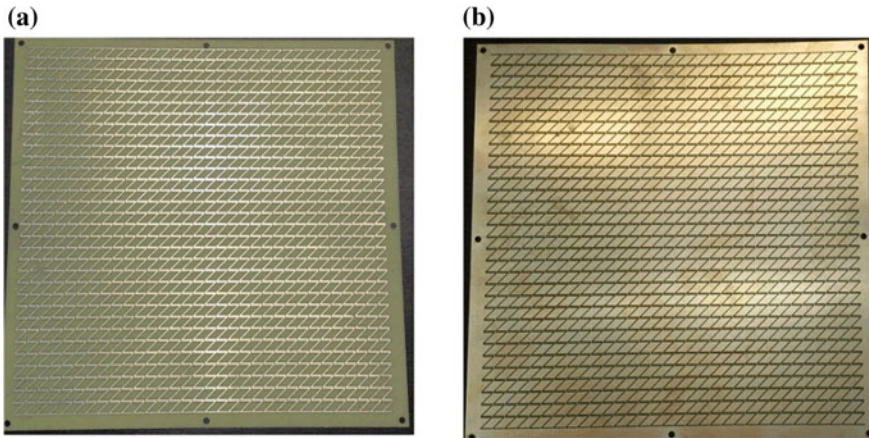


**Fig. 9.8** Prototypes used in microwave experiments. **a** Z-MS; **b** complementary Z-MSs

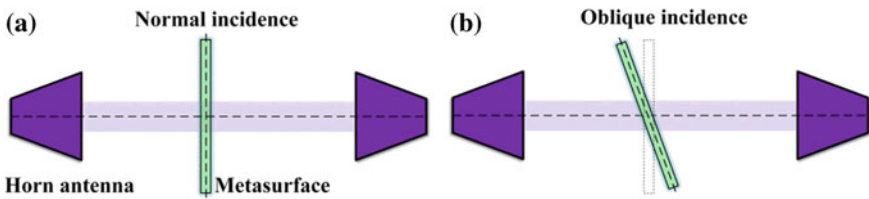


**Fig. 9.9** Microwave measurements experimental setup. **a** Normal; **b** oblique incidence

coefficients are compared to the simulated ones, as represented in Fig. 9.10. A good qualitative agreement between simulations and measurements is found.

It should be noticed that complementary structure also exhibits a significantly higher quality factor for dark mode resonance  $Q_{\text{dark}} = 39$  as compared to fundamental resonance  $Q_{\text{fund}} = 1.8$ . The difference with respect to the original Z-MS, where  $Q_{\text{fund}} = 0.85$  and  $Q_{\text{dark}} = 29$ , results from smaller absorption in dielectric substrate due to less uncovered dielectric surface.

The considered examples show that antisymmetric dark mode indeed provides lower radiative losses. The excitation does not rely on coupling between elements, i.e. mode hybridization, and is related to direct interaction with incident field. The conditions required for antisymmetric dark mode excitation are based only on symmetry matching considerations. Consequently, such a design not relying on hybridization mechanism through near field interaction is expected to be more robust with respect to technological imperfections, especially when considering fabrication of structures intended for operation in the optical domain.

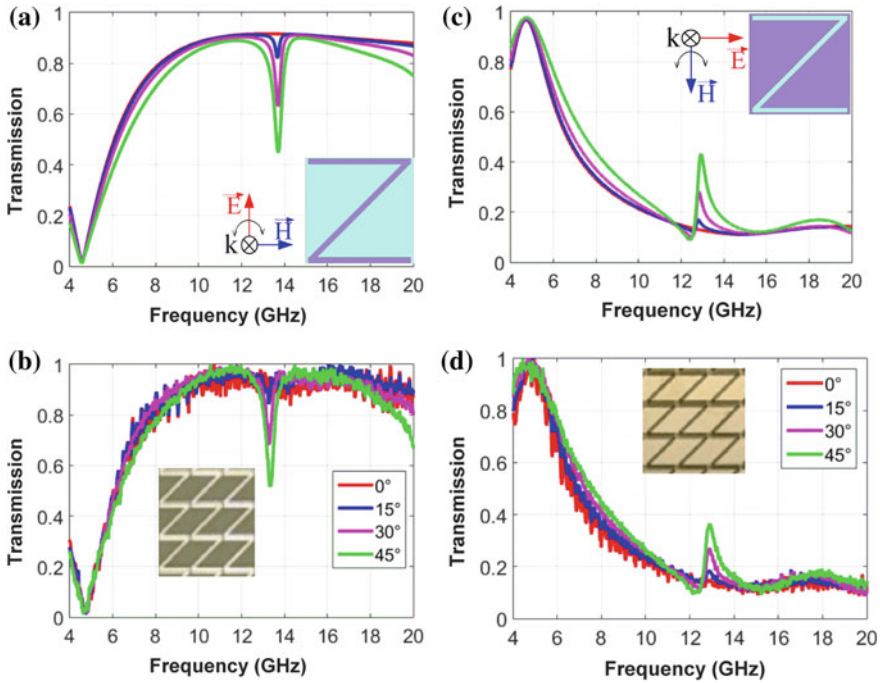


**Fig. 9.10** Normal and oblique incidence transmission spectra for Z-MSs (left column) and complementary Z-MSs (right column): **a, c** HFSS modeling results; **b, d** experimental data

## 9.4 Fano Interference is a System with Identical Coupled Resonators

Our next goal is to provide evidence that Fano type interference can be achieved in a system with two identical coupled resonators. Paradoxically, an example of such a system with identical resonant elements displaying Fano interference was provided in the same seminal paper by Fedotov et al. [9]. The schematic of the investigated structure is displayed in Fig. 9.11a. The metasurface unit cell is composed of an enantiomeric arrangement of circle arcs having a different angular split of  $10^\circ$  and  $30^\circ$  on the left and right side, respectively. The observation that can be done now one decade later is that the design with identical resonant elements has attracted much less attention as compared to its simultaneously proposed asymmetric counterpart. The lack of interest to the considered solution is probably due to the fact that the displayed performances in terms of Fano resonance contrast was substantially lower than that obtained by using asymmetric type design. However no detailed investigations aiming to enhance the performances and assess the potential of this approach were performed so far. To contribute filling this gap, we consider a unit cell design with obliquely oriented cut wires (CWs) sketched in Fig. 9.11b. Basically it repre-

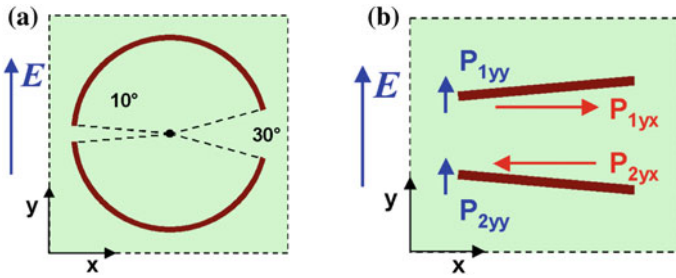


**Fig. 9.11** Enantiomeric arrangement of coupled resonators. **a** Pair of circle arcs with different angular split [9]; **b** Pair of obliquely oriented CWs

sents a simplified version of design shown in Fig. 9.11a. The interest of this simplified version is to facilitate the understanding of Fano interference mechanism occurring in a system with two interacting identical resonant elements.

For practical implementation and HFSS modeling, we consider a rectangular unit cell design with dimensions along  $x$ - and  $y$ -axis  $p_x = 9$  mm and  $p_y = 6$  mm, respectively. The angle  $\theta$  formed by obliquely oriented CWs is  $10^\circ$ . The CWs of length  $l = 5.8$  mm and width  $w = 0.3$  mm used for HFSS simulations are assumed to behave like an ideal metal (perfect conductor). They are printed on a dielectric substrate with  $\epsilon_r = 2.2$ , tangential losses  $\tan(\delta) = 0.0009$  and thickness  $d = 0.5$  mm.

Simulation results for the transmitted and reflected intensity calculated for  $x$ - and  $y$ -polarized normally incident electromagnetic (EM) wave are shown in Fig. 9.12a and 9.12c, respectively. As it can be seen, in contrast to the conventional Lorentzian type resonant behavior observed for  $x$ -polarization, a marked Fano resonance effect occurring at 18.8 GHz is observed for  $y$ -polarized EM wave. As it can be seen in the inset of Fig. 9.12c, the very narrow drop in transmission ( $|S_{12}|^2$ ) is reaching 98%. The resonance quality factor for  $y$ -polarization  $Q_y = 209$  obtained from the absorption line bandwidth is almost two orders of magnitude higher as compared to the  $Q_x = 3.5$  for  $x$ -polarization. Furthermore, a marked difference in the resonance behavior is observed when comparing the phase spectral response of  $x$ - and  $y$ -polarized EM wave shown in Fig. 9.12b and 9.12d, respectively. As it can be seen in the inset of Fig. 9.12d, a characteristic forth and back jump phase of reflected wave is observed in the vicinity of Fano resonance frequency.

To explain the origin of Fano resonance, it is meaningful to examine the instantaneous currents and charges distribution shown in Fig. 9.13 for  $y$ -polarized wave. As it can be seen at all frequencies, the current flow along the  $x$ -axis in the upper and lower CWs are circulating in opposite directions. The dipolar momentums  $P_{1yx}$  and  $P_{2yx}$  shown in Fig. 9.11b corresponding to such charges distribution can be associated to the excitation of antisymmetric dark mode. At the same time the motion of charges along the  $y$ -axis and its associated dipolar momentums  $P_{1yy}$  and  $P_{2yy}$  that are oriented in the same direction corresponds to the excitation of bright mode, for which resonance occurs at much higher frequencies. As discussed above, the non-orthogonality of the eigenmodes leads to the Fano type constructive/destructive interference in the

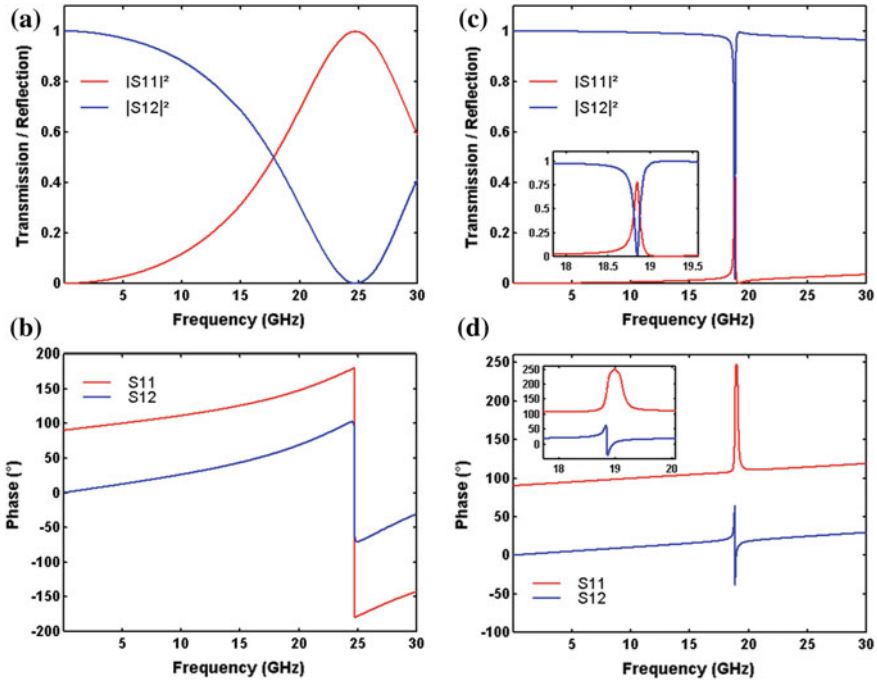


**Fig. 9.12** HFSS numerical modeling results for obliquely oriented CWs. Left column  $x$ -, right column  $y$ -polarized normally incident EM wave; **a, c** Transmitted and reflected intensity; **b, d** Phase of transmitted and reflected wave

vicinity of dark mode resonance frequency, which roughly corresponds to that of  $x$ -polarization CWs redshifted due to the coupling [33].

The main difference with respect to the most of the previous studies is that in the present case the resonance frequencies of the bright and dark mode are not close but rather far apart. The very low slope of reflection and transmission outside the Fano resonance region for  $y$ -polarized EM wave attests the fact that the resonance of the bright mode should occur well beyond the considered frequency range. This feature ensures a high non-resonant transmission and low reflection. As it will be shown below, a very high contrast Fano type interference can be achieved in this case. The considered situation is distinctly different from that when the resonance frequencies of bright and dark mode are close resulting in EIT effect. As detailed above EIT manifests as a narrow maximum occurring in the middle of attenuated transmission band. Here the situation is exactly opposite.

It may seem that the obtained results are in contradiction with previous studies [32] stating that efficient Fano interference is observed when the radiative strengths of both modes are similar. To show that there is no any contradiction we consider the simple model of coupled oscillators described by the (3), which solutions are given

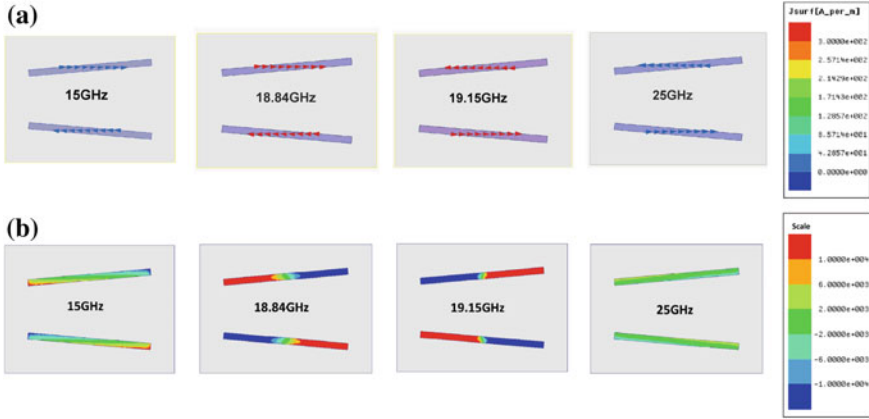


**Fig. 9.13** HFSS numerical modeling results for a pair obliquely oriented CWS: **a** Instantaneous currents flow; **b** Instantaneous charges distribution

by the (4). To this end we examine the solution for the amplitude of bright mode, which is convenient to express as:

$$c_b = \frac{f_b}{(\omega_b^2 - \omega^2 + i\gamma_b\omega) - \frac{\kappa^2}{(\omega_d^2 - \omega^2 + i\gamma_d\omega)}} \quad (8)$$

Since  $\omega_b \gg \omega_d$  the following approximation holds in  $\Delta\omega$  vicinity of dark mode resonance:

$$c_b = \frac{f_b}{(\omega_b^2 + i\gamma_b(\omega_d + \Delta\omega)) - \frac{\kappa^2}{(-2\omega_d\Delta\omega + i\gamma_d(\omega_d + \Delta\omega))}} \quad (9)$$

As evident  $c_b$  may attain very high values when the denominator of (9) approaches zero. This happens when the following condition for the real part of denominator is met:

$$\Delta\omega \approx \frac{\kappa^2}{2\omega_d\omega_b^2} \quad (10)$$

It means that when increasing the bright mode frequency  $\omega_b$ , the coupling coefficient  $\kappa$  should be roughly increased in a similar proportion. The amplitude of bright mode is then determined by the residual imaginary part of the denominator that is inversely to  $\Delta\omega$ . In contrast to the conventional dolmen type [8, 11, 12], plasmonic oligomers [13–16], ring-disk nanocavities [17, 18] arrangements, the present system is operating in the regime of strong coupling. Such a strong coupling cannot be ensured through the tunneling type near field interaction but can be instead

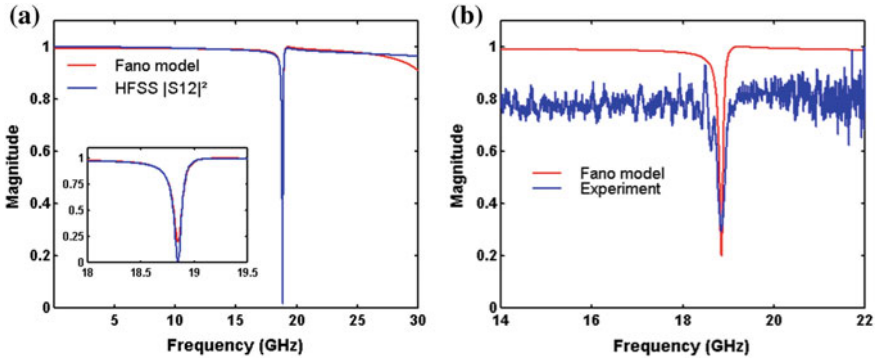


**Fig. 9.14** **a** HFSS  $|S_{11}|^2$  transmission spectrum and Fano model fitted results; **b** Experimentally measured transmission spectrum and Fano model fitted results

achieved through direct electrons driving by the external electric field projection on the obliquely oriented CWs.

The validity of the considered approach was verified by comparing numerical simulations and experimental results for transmission spectrum with those obtained by using the model of bright and dark coupled oscillators. As it can be observed from results shown in Fig. 9.14a there is a good overall agreement between the fit obtained with the Fano model and HFSS numerical simulations. Similar good agreement, except for the absolute value of transmission level, is also observed when comparing experimental data and Fano model results shown in Fig. 9.14b. The parameters of the model of coupled oscillators used for the fitting procedure are:  $\omega_d = 19.25$  GHz,  $\omega_b = 34$  GHz,  $\gamma_d = 0.05$  GHz,  $\gamma_b = 2.5$  GHz,  $\kappa = 120$  GHz<sup>2</sup>.

The considered design based on a pair of obliquely oriented CWs brings a great flexibility for the control of the parameters of the system. Thus the dark mode frequency can be tuned by changing the length of CWs, the dark mode damping factor  $\gamma_d$  can be also tuned on the angles between CWs. For instance a further increase of Fano resonance quality factor can be achieved by using a smaller angle between CWs, the ultimate quality factor being limited essentially by the radiative losses. The considered approach can be easily generalized to other kind of geometries based on an enantiomeric arrangement of identical resonant elements.

## 9.5 Summary and Conclusions

We revisit the engineering of metasurfaces displaying sharp spectral features and conventionally relying on electromagnetically induced transparency resulting from Fano-type interference between dark and bright resonant elements. On the basis of recent theoretical advances we highlight the fact that Fano resonance in such systems is due to the interference between bright modes only. In contrast, Fano interference

between two modes with substantially different radiative strength results in a very weak EIT effect. The origin of this discrepancy is related to the non-orthogonality of eigenmodes base due to non-Hermiticity of interaction matrix as the consequence of the open character of the system.

In this context one of the purposes of our study is to bring evidence of direct dark mode excitation mechanism that does not depend on near-field coupling between resonant elements. On the basis of symmetry matching considerations we show that direct excitation mechanism is possible for an anti-symmetric type higher order mode having a zero net electric dipolar momentum but different from zero magnetic one. The excitation of magnetic dipolar momentum can be achieved under field oblique incidence on metasurface having anti-symmetric unit cell geometry. In our examples we consider single-element-based metasurface composed of two V antennas connected in an anti-symmetric arrangement or more simply Z-shaped meta-atoms. Both experimental and modeling results show an efficient excitation of magnetic dipolar mode in such structures.

The great advantage of the considered approach is that dark mode excitation is entirely determined by structures' geometry symmetry and does not depend on coupling between elements. The considered approach opens promising perspectives for new type of nanostructure designs and greatly relaxes technological constraints for the optical domain.

Another goal of our study is to show that efficient high contrast Fano resonance effect can be achieved by considering a system with identical resonant elements from the beginning. To this end we consider examples of such systems and discuss the condition necessary to achieve sharp Fano resonance features. We provide modeling and experimental demonstration in the microwave domain of such metasurface displaying a high contrast ratio (~98%) and high quality factor (~209) Fano resonance.

## References

1. S.E. Harris, Electromagnetically induced transparency. *Phys. Today* **50**, 36–42 (1997)
2. M.F. Yanik, W. Suh, Z. Wang, S. Fan, Stopping light in a waveguide with an all-optical analog of electromagnetically induced transparency. *Phys. Rev. Lett.* **93**, 233903 (2004)
3. Q. Xu, S. Sandhu, M.L. Povinelli, J. Shakya, S. Fan, M. Lipson, Experimental realization of an on-chip all-optical analogue to electromagnetically induced transparency. *Phys. Rev. Lett.* **96**, 123901 (2006)
4. R.W. Boyd, D.J. Gauthier, Photonics: transparency on an optical chip. *Nature* **441**, 701 (2006)
5. S. Zhang, D.A. Genov, Y. Wang, M. Liu, X. Zhang, Plasmon-induced transparency in metamaterials. *Phys. Rev. Lett.* **101**, 047401 (2008)
6. B. Luk'yanchuk, N.I. Zheludev, S.A. Maier, N.J. Halas, P. Nordlander, H. Giessen, T.C. Chong, The Fano resonance in plasmonic nanostructures and metamaterials. *Nat. Mater.* **9**, 707 (2010)
7. B. Gallinet, O.J.F. Martin, Refractive index sensing with subradiant modes: a framework to reduce losses in plasmonic nanostructures. *ACS Nano* **7**, 6978 (2013)
8. B. Gallinet, O.J.F. Martin, Ab initio theory of Fano resonances in plasmonic nanostructures and metamaterials. *Phys. Rev. B* **83**, 235427 (2011)



9. V.A. Fedotov, M. Rose, S.L. Prosvirnin, N. Papasimakis, N.I. Zheludev, Sharp trapped-mode resonances in planar metamaterials with a broken structural symmetry. *Phys. Rev. Lett.* **99**, 147401 (2007)
10. S. Zhang, D.A. Genov, Y. Wang, M. Liu, X. Zhang, Plasmon-induced transparency in metamaterials. *Phys. Rev. Lett.* **101**, 047401 (2008)
11. N. Liu, L. Langguth, T. Weiss, J.Kästel, M. Fleischhauer, T. Pfau, H. Giessen, Plasmonic analogue of electromagnetically induced transparency at the Drude damping limit. *Nat. Mater.* **8**, 758 (2009)
12. B. Gallinet, O.J.F. Martin, Refractive index sensing with subradiant modes: a framework to reduce losses in plasmonic nanostructures. *ACS Nano* **7**, 6978 (2013)
13. K. Bao, N. Mirin, P. Nordlander, Fano resonances in planar silver nanosphere clusters. *Appl. Phys. A* **100**, 333 (2010)
14. N.A. Mirin, K. Bao, P. Nordlander, Fano resonances in plasmonic nanoparticle aggregates. *J. Phys. Chem. A* **113**, 4028 (2009)
15. J.A. Fan, C. Wu, K. Bao, J. Bao, R. Bardhan, N.J. Halas, V.N. Manoharan, P. Nordlander, G. Shvets, F. Capasso, Self-assembled plasmonic nanoparticle clusters. *Science* **328**, 1135 (2010)
16. P. Nordlander, C. Oubre, E. Prodan, K. Li, M.I. Stockman, Plasmon hybridization in nanoparticle dimers. *Nano Lett.* **4**, 899–903 (2004)
17. F. Hao, Y. Sonnefraud, P.V. Dorpe, S.A. Maier, N.J. Halas, P. Nordlander, Symmetry breaking in plasmonic nanocavities: subradiant LSPR sensing and a tunable Fano resonance. *Nano Lett.* **8**, 3983 (2008)
18. N. Verellen, Y. Sonnefraud, H. Sobhani, F. Hao, V.V. Moshchalkov, P. Van Dorpe, P. Nordlander, S.A. Maier, Fano resonances in individual coherent plasmonic nanocavities. *Nano Lett.* **9**, 1663 (2009)
19. E. Prodan, C. Radloff, N.J. Halas, P. Nordlander, A hybridization model for the plasmon response of complex nanostructures. *Science* **302**, 419 (2003)
20. H. Wang, Y.P. Wu, B. Lassiter, C.L. Nehl, J.H. Hafner, P. Nordlander, N.J. Halas, Symmetry breaking in individual plasmonic nanoparticles. *Proc. Natl. Acad. Sci. U.S.A.* **103**, 10856 (2006)
21. P. Tassin, L. Zhang, T. Koschny, E.N. Economou, C.M. Soukoulis, Low-loss metamaterials based on classical electromagnetically induced transparency. *Phys. Rev. Lett.* **102**, 053901 (2009)
22. R. Singh, C. Rockstuhl, F. Lederer, W. Zhang, Coupling between a dark and a bright eigenmode in a terahertz metamaterial. *Phys. Rev. B* **79**, 085111 (2009)
23. K. Aydin, I.M. Pryce, H.A. Atwater, Symmetry breaking and strong coupling in planar optical metamaterials. *Opt. Express* **18**, 13407 (2010)
24. R. Singh, I.A.I. Al-Naib, Y. Yang, D.R. Chowdhury, W. Cao, C. Rockstuhl, T. Ozaki, R. Morandotti, W. Zhang, Observing metamaterial induced transparency in individual Fano resonators with broken symmetry. *Appl. Phys. Lett.* **99**, 201107 (2011)
25. A. Christ, Y. Ekinci, H.H. Solak, N.A. Gippius, S.G. Tikhodeev, O.J.F. Martin, Controlling the Fano interference in a plasmonic lattice. *Phys. Rev. B* **76**, 201405(R) (2007)
26. Christ, O.J.F. Martin, Y. Ekinci, N.A. Gippius, S.G. Tikhodeev, Symmetry breaking in a plasmonic metamaterial at optical wavelength. *Nano Lett.* **8**, 2171 (2008)
27. X. Duan, S. Chen, H. Yang, H. Cheng, J. Li, W. Liu, C. Gu, J. Tian, Polarization-insensitive and wide-angle plasmonically induced transparency by planar metamaterials. *Appl. Phys. Lett.* **101**, 143105 (2012)
28. L. Chuntonov, G. Haran, Trimeric plasmonic molecules: the role of symmetry. *Nano Lett.* **11**, 2440–2445 (2011)
29. A.E. Miroshnichenko, S. Flach, Y.S. Kivshar, Fano resonances in nanoscale structures. *Rev. Mod. Phys.* **82**, 2257–2298 (2010)
30. M. Hentschel, D. Dregely, R. Vogelgesang, H. Giessen, N. Liu, Plasmonic oligomers: the role of individual particles in collective behavior. *ACS Nano* **5**, 2042 (2011)
31. M. Frimmer, T. Coenen, A.F. Koenderink, Signature of a Fano resonance in a plasmonic metamolecules local density of optical states. *Phys. Rev. Lett.* **108**, 077404 (2012)

32. C. Forestiere, L. Dal Negro, G. Miano, Theory of coupled plasmon modes and Fano-like resonances in subwavelength metal structures. *Phys. Rev. B* **88**, 155411 (2013)
33. A. Lovera, B. Gallinet, P. Nordlander, O.J.F. Martin, Mechanisms of Fano resonances in coupled plasmonic systems. *ACS Nano* **7**, 4527 (2013)
34. A.E. Miroshnichenko, Y.S. Kivshar, Fano resonances in all-dielectric oligomers. *Nano Lett.* **12**, 6459–6463 (2012)
35. B. Hopkins, A.N. Poddubny, A.E. Miroshnichenko, Y.S. Kivshar, Revisiting the physics of Fano resonances for nanoparticle oligomers. *Phys. Rev. A* **88**, 053819 (2013)
36. O. Merchiers, F. Moreno, F. Gonzalez, J.M. Saiz, Light scattering by an ensemble of interacting dipolar particles with both electric and magnetic polarizabilities. *Phys. Rev. A* **76**, 043834 (2007)
37. J. Wiersig, Formation of long-lived, scarlike modes near avoided resonance crossings in optical microcavities. *Phys. Rev. Lett.* **97**, 253901 (2006)
38. T. Lepetit, E. Akmansoy, J.-P. Ganne, J.-M. Lourtioz, Resonance continuum coupling in high-permittivity dielectric metamaterials. *Phys. Rev. B* **82**, 195307 (2010)
39. H.A. Haus, Waves and fields in optoelectronics, in *Solid State Physical Electronics* (Prentice-Hall series, 1984)
40. S. Fan, W. Suh, J.D. Joannopoulos, Temporal coupled-mode theory for the Fano resonance in optical resonators. *J. Opt. Soc. Am. A* **20**, 569 (2003)
41. W. Suh, Z. Wang, S. Fan, Temporal coupled-mode theory and the presence of non-orthogonal modes in lossless multimode cavities. *IEEE J. Quant. Electron.* **40**, 1511 (2004)
42. Z. Ruan, S. Fan, Temporal coupled-mode theory for Fano resonance in light scattering by a single obstacle. *J. Phys. Chem. C* **114**, 7324–7329 (2009)
43. A. Kodigala, T. Lepetit, B. Kante, Engineering resonance dynamics of plasmon hybridized systems. *J. Appl. Phys.* **117**, 023110 (2015)
44. S.N. Burokur, A. Lupu, A. de Lustrac, Direct dark mode excitation by symmetry matching of a single-particle-based metasurface. *Phys. Rev. B* **91**, 035104 (2015)
45. High Frequency Structure Simulator, vol. 15, Ansys Ltd.
46. Y. Guo, L. Yan, W. Pan, B. Luo, K. Wen, Z. Guo, X. Luo, Electromagnetically induced transparency (EIT)-like transmission in side-coupled complementary split-ring resonators. *Opt. Express* **20**, 24348–24355 (2012)
47. Y. Nakata, Y. Urade, T. Nakanishi, M. Kitano, Plane-wave scattering by self-complementary metasurfaces in terms of electromagnetic duality and Babinet's principle. *Phys. Rev. B* **88**, 205138 (2013)
48. M. Navarro-Cía, M. Aznabet, M. Beruete, F. Falcone, O. El Mrabet, M. Sorolla, M. Essaaidi, Stacked complementary metasurfaces for ultraslow microwave metamaterials. *Appl. Phys. Lett.* **96**, 164103 (2010)
49. Y.P. Jia, Y.L. Zhang, X.Z. Dong, M.L. Zheng, J. Li, J. Liu, X.M. Duan, Complementary chiral metasurface with strong broadband optical activity and enhanced transmission. *Appl. Phys. Lett.* **104**, 011108 (2014)
50. N. Liu, S. Kaiser, H. Giessen, Magnetoinductive and electroinductive coupling in plasmonic metamaterial molecules. *Adv. Mater.* **20**, 4521–4525 (2008)

# Chapter 10

## Light-Tunable Fano Resonance in Metal-Dielectric Multilayer Structures



Shinji Hayashi, Dmitry V. Nesterenko and Zouheir Sekkat

**Abstract** Recent progress on Fano resonances exhibited by metal-dielectric multilayer structures is reviewed. The Fano resonance in the multilayer structures is caused by coupling between a surface plasmon polariton mode supported by a metal-dielectric interface and a waveguide mode supported by a system of three dielectric layers. Electromagnetic calculations of attenuated total reflection spectra demonstrate the feasibility of realizing the Fano resonance, and the predicted Fano resonance was indeed observed experimentally. Since the structure is simple, it is easy to add the photofunctionality to the structure. Incorporation of photofunctional dye molecules into the waveguide layer made it possible to tune the Fano resonance by light irradiation.

### 10.1 Introduction

Over the past decade, asymmetric line shapes appearing in optical responses of plasmonic nanostructures and metamaterials attracted much attention and have been analyzed in terms of Fano resonances [1–6]. A variety of nanostructures such as

---

S. Hayashi (✉)

Graduate School of Engineering, Kobe University, Kobe 657-8501, Japan  
e-mail: s.hayashi@dragon.kobe-u.ac.jp

S. Hayashi · Z. Sekkat

Optics and Photonics Center, Moroccan Foundation for Science,  
Innovation and Research (MAScIR), 10100 Rabat, Morocco

D. V. Nesterenko

IPSI RAS - Branch of the FSRC “Crystallography and Photonics” RAS,  
Samara 443001, Russia

D. V. Nesterenko

Faculty of Information Technology, Samara National Research University,  
Samara 443086, Russia

Z. Sekkat

Faculty of Sciences, Mohammed V University in Rabat, 10010 Rabat, Morocco

Z. Sekkat

Graduate School of Engineering, Osaka University, Suita 585-0871, Japan

© Springer Nature Switzerland AG 2018

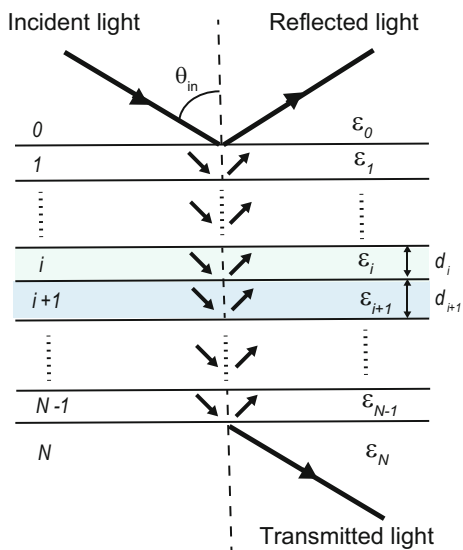
E. Kamenetskii et al. (eds.), *Fano Resonances in Optics and Microwaves*, Springer  
Series in Optical Sciences 219, [https://doi.org/10.1007/978-3-319-99731-5\\_10](https://doi.org/10.1007/978-3-319-99731-5_10)

metallic nanowire arrays [7], clusters of nanoparticles [8–12], disk/ring nanocavities [13–15] and metal-insulator-metal waveguides coupled to resonators [16], are known to exhibit Fano line shapes in their optical spectra. The Fano-resonant nanostructures offer the opportunities for achieving high-Q resonances that induce highly enhanced electromagnetic fields in the vicinities of the nanostructures. Therefore, they have potentials for achieving high performances in photonic devices, such as optical sensors, switches and platforms for surface-enhanced spectroscopies [2, 3, 5]. One of the key issues in developing such devices is the realization of dynamic tuning of the Fano resonance [5]. Cui et al. [17] demonstrated mechanical tuning of Fano resonances supported by a gold heptamer structure embedded in a flexible membrane. Integrating single-layer graphene with plasmonic Fano-resonant metasurfaces, Shvets et al. [18, 19] succeeded in modulating mid-IR Fano resonances using electrostatic gating. Electric-field modulation of the Fano resonance was also demonstrated for gold nanowire gratings [20] and silicon nanohole arrays [21] integrated with liquid crystals. In spite of great efforts made so far, the fabrication of the nanostructures is not always easy and time consuming, preventing their real applications. Therefore, it is highly demanded to exploit structures exhibiting the Fano line shapes that can be fabricated by a low-cost, fast and easy method. The quest for simpler structures that do not require the use of nanofabrication techniques and exhibit high Q Fano resonances still remains a challenge. Realization of the dynamic tuning in such structures is highly demanded.

Very recently, we demonstrated both theoretically and experimentally the feasibility of realizing sharp Fano line shapes in attenuated total reflection (ATR) spectra of planar multilayer structures consisting of a metallic layer and dielectric layers [22–29]. The structures studied do not require the use of nanofabrication techniques and consequently, they are very much suited for realistic applications. The purpose of this Chapter is to discuss the fundamental aspects of the Fano resonances in such simple metal-dielectric multilayer structures. It is common to explain the Fano resonances in nanostructures as due to the interference of a bright mode with a broad resonance and a dark mode with a narrow resonance. The physical origin of the Fano line shape in our multilayer structures has clearly been identified as the coupling between a surface plasmon polariton (SPP) mode localized at a metal-dielectric interface and a planar waveguide (PWG) mode supported by a stack of dielectric layers. The SPP mode can be regarded as a bright mode and the PWG mode as a dark mode. The simplicity in the structure and mechanism of the Fano resonance allows us to develop a novel method for tuning the Fano resonance by light irradiation. In this Chapter, we review recent progress in theoretical and experimental studies on the Fano resonance and its light tuning realized in the metal-dielectric multilayer structures.

The multilayer structure discussed in this Chapter is schematically shown in Fig. 10.1. Each layer can be a metal (M) or a dielectric (D). The dielectric constant and the thickness of the  $i$ -th layer is written as  $\epsilon_i$  and  $d_i$ , respectively. When light is incident from the layer 0, a part is reflected back at the 0–1 interface and the rest is transmitted into the multilayer system. At each interface, the light wave is reflected and transmitted, generating backward and forward waves inside each layer. After multiple reflection and transmission processes of the light waves in the

**Fig. 10.1** Multilayer structure considered



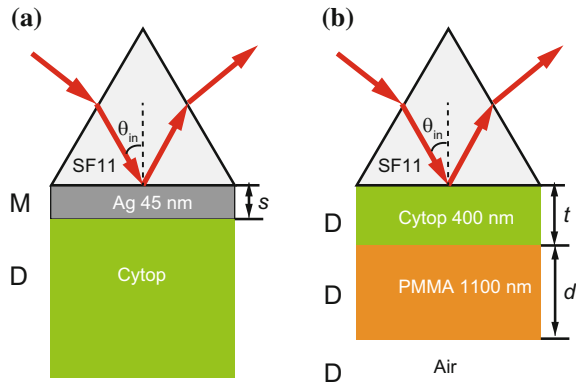
system, reflected light finally exits from the layer 0 and transmitted light exits from the medium  $N$ . When the values of  $\epsilon_i$  and  $d_i$  are known, electromagnetic (EM) theories allow us to calculate the intensities of the reflected and transmitted light as well as the distributions of the electromagnetic fields inside the layers. Methods for the EM calculations are well established [30]; in this Chapter, we present results of EM calculations obtained by a  $2 \times 2$  transfer matrix method [31, 32]. To perform the EM calculations, a light wave (a plane wave) is assumed to be incident on the 0–1 interface at an angle of  $\theta_{in}$ . Throughout this Chapter, the layer 0 is assumed to be a glass prism to discuss the ATR spectra in the Kretschmann configuration [33]. In the following sections, we consider various combinations of a metal and dielectric layers and demonstrate the feasibility of realizing the Fano resonances in the metal-dielectric multilayer structures.

## 10.2 How to Realize Fano Resonances in Metal-Dielectric Multilayer Structures

### 10.2.1 SPP Mode in MD Structure and PWG Modes in DDD Structure

Let us consider the optical responses of simple multilayer systems schematically shown in Fig. 10.2a, b. We consider here two different structures. One consists of a metal layer and a dielectric layer (MD structure) attached to a prism (Fig. 10.2a). This

**Fig. 10.2** MD (a) and DDD (b) structures attached to a glass prism (Kretschmann configuration of ATR spectroscopy)



is a Kretschmann configuration in the ATR spectroscopy [33]. The other is a stack of three dielectric layers (DDD structure) (Fig. 10.2b). It is well known that a MD interface can support a SPP mode, which is a coupled mode of a collective oscillation of free electrons in the metal and an electromagnetic wave that propagates along the interface and decays exponentially away from the interface. The SPP mode can be excited by light incident through the prism. In the angle-scan ATR spectroscopy, a laser beam with a fixed wavelength is used as the incident light and the intensity of reflected light exiting from the prism is measured as a function of the angle of incidence under the total reflection condition. The curve A in Fig. 10.3 shows an ATR spectrum calculated for a MD structure consisting of a 45 nm-thick Ag layer and a fluoropolymer Cytop layer attached to a SF11 glass prism. To obtain the spectrum a freely available Winspall software package was used together with values of the dielectric constants reported in our previous paper [24]. *p*-polarized incident light with a wavelength of  $\lambda = 632.8$  nm (He-Ne laser) was assumed. As can be seen in the figure, the excitation of the SPP mode at the MD interface is manifested by a relatively broad dip in the ATR spectrum. Figure 10.4a shows an electric field distribution generated in the MD structure under the SPP excitation at  $\theta_{in} = 53.865^\circ$ . In this figure, the square of the electric field amplitude normalized to that of the incident light (field enhancement factor) is plotted as a function of the position  $z$  in the structure; the  $z$  axis is normal to the interfaces and the prism/Ag interface is located at  $z = 0$ . We see that a strong electric field is generated at the MD interface and the field decays exponentially away from the interface inside the Cytop layer. The electric field distribution seen in Fig. 10.4a is typical of SPP excitation.

In Fig. 10.3, an ATR spectrum calculated for a DDD structure shown in Fig. 10.2b is also presented as curve B. To obtain the spectrum, a stack of a Cytop layer (400 nm thick) and a poly(methyl methacrylate) (PMMA) layer (1100 nm thick) surrounded by air was assumed. In this DDD structure, the real part of the dielectric constant (refractive index) of the PMMA layer is larger than those of Cytop layer and air. It is well known that this kind of DDD structure can support PWG modes that propagate in the middle dielectric layer (waveguide layer) accompanied by evanescent fields

**Fig. 10.3** ATR spectra of the MD structure (curve A) and the DDD structure (curve B)

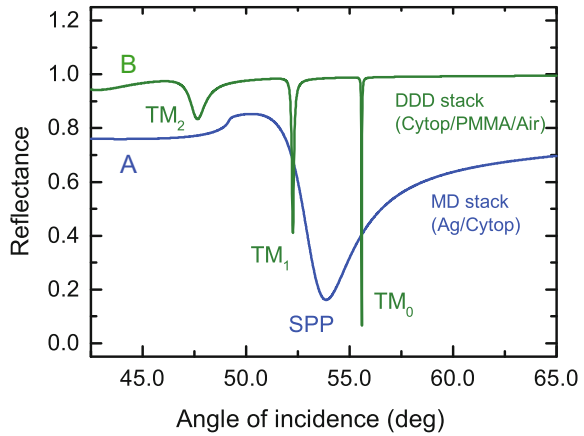
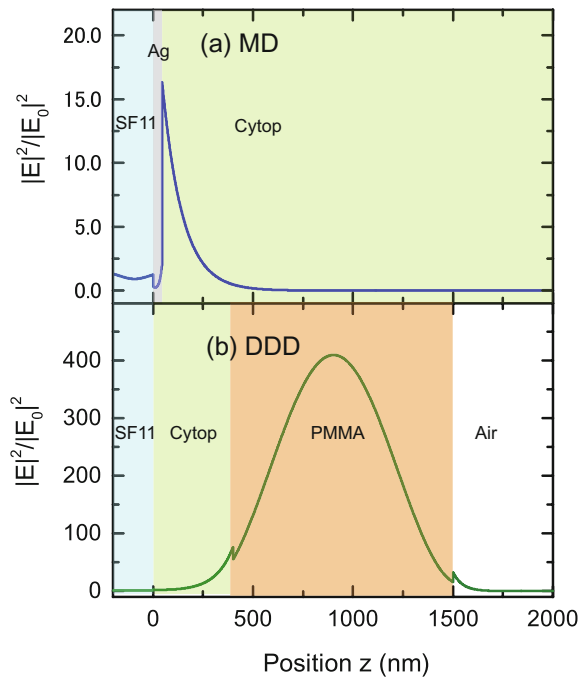


**Fig. 10.4** Electric field distributions corresponding to excitations of the SPP mode in the MD structure (a) and the TM<sub>0</sub> PWG mode in the DDD structure (b)



outside the waveguide layer. The excitation of the PWG modes results in sharp reflection dips in the ATR spectrum. The sharp reflection dips denoted as  $TM_0$ ,  $TM_1$  and  $TM_2$  in Fig. 10.3 correspond to the excitation of 0th-, 1st- and 2nd-order transverse magnetic (TM) PWG modes, respectively. The electric field distribution associated with the excitation of the  $TM_0$  PWG mode at  $\theta_{in} = 55.584^\circ$  is presented in Fig. 10.4b. We see a distribution with highly enhanced electric fields localized in the PMMA waveguide layer, which is typical of PWG mode excitation.

### 10.2.2 Fano Resonance in MDDD Structure

Now we turn to the discussion of a MDDD structure schematically shown in Fig. 10.5a. As can be understood from Fig. 10.5b, this structure can be regarded as a combination of the MD and DDD structures described above. The MD structure can support the SPP mode and the DDD structure can support the PWG modes, and in the MDDD structure, they can interact each other through the overlap of their evanescent electromagnetic fields in the spacer D layer, i.e., the D layer between the metal layer and the waveguide layer. Therefore, it may be possible to generate the Fano resonance based on the interference between a broad SPP resonance and a sharp PWG resonance, provided that the structural parameters of the MDDD structure are appropriately chosen. Indeed, the Fano line shape can be generated as demonstrated by a calculated spectrum shown in Fig. 10.6. To obtain this spectrum the thicknesses of the Cytop spacer layer and the PMMA waveguide layer were set at  $t = 400$  nm and  $d = 1100$  nm, respectively. We see clearly an asymmetric line shape around  $\theta_{in} = 55.5^\circ$ ; the inset shows the line shape in an expanded scale. A comparison between this spectrum and those shown in Fig. 10.3 reveals that the Fano line shape is a

**Fig. 10.5** MDDD hybrid structure that generates a Fano resonance (a), and MD and DDD units before hybridization (b). From [24]

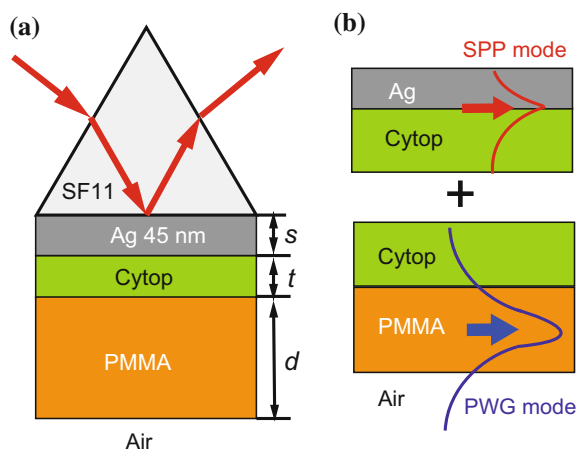
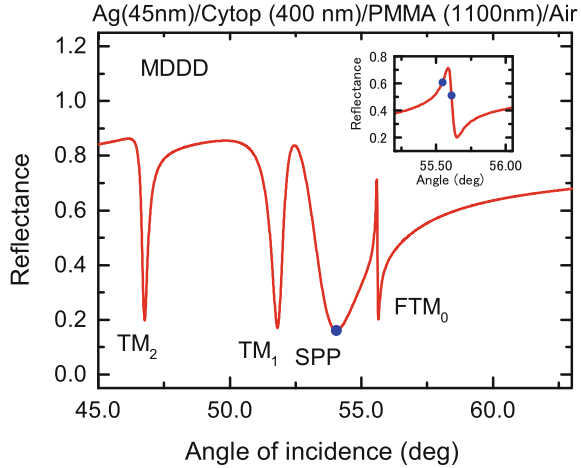




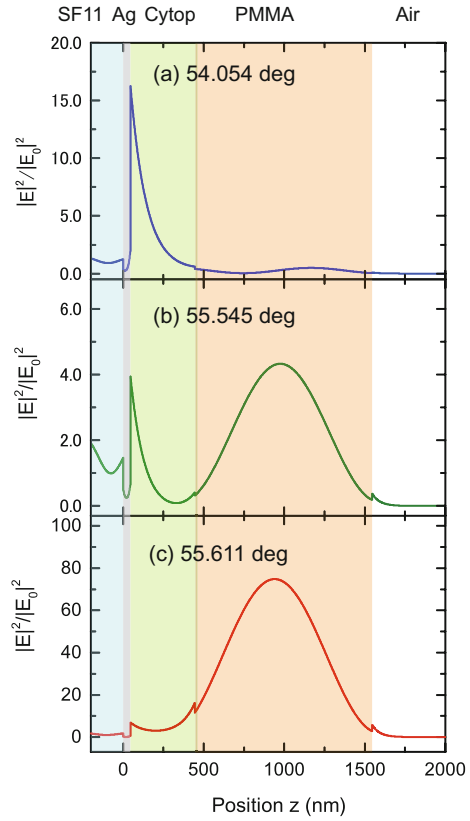
**Fig. 10.6** ATR spectrum of the MDDD structure exhibiting the Fano resonance



consequence of interaction between the broad SPP mode and the sharp  $TM_0$  PWG mode.

To confirm the mechanism of Fano line shape generation, electric field distributions induced in the MDDD structure for three different angles of incidence are presented in Fig. 10.7a–c. The filled circles shown in Fig. 10.6 indicate the angles chosen for the calculations; they correspond to the SPP excitation angle ( $54.054^\circ$ ), the Fano resonance angle ( $55.611^\circ$ ) and an angle ( $55.545^\circ$ ) slightly lower than the Fano resonance angle, respectively. In Fig. 10.7a–c, we see the hybridization of the SPP and PWG modes; their relative contributions vary depending on the angle of incidence. In fact, in Fig. 10.7a corresponding to the SPP resonance angle, we see a strong contribution of the SPP excitation at the Ag/Cytop interface, which is manifested by a strong electric field amplitude at the interface accompanied by an evanescent tail in the Cytop spacer layer. At this angle, the excitation of the PWG mode is weak and gives only a small bump in the PMMA waveguide. Figure 10.7b corresponding to the intermediate angle of  $55.545^\circ$  shows that both the SPP and PWG mode excitations contribute almost equally to the distribution; the field enhancement factor at this angle is very small, because the angle is far from the SPP and PWG mode resonances. In Fig. 10.7c corresponding to the Fano resonance angle, we see that the field distribution is dominated by the PWG mode excitation that induces highly enhanced electric fields around the center of the waveguide. From the behaviors seen in Fig. 10.7a–c, it is clear that the sharp Fano resonance is caused by the excitation of the PWG mode that interacts with the SPP mode. As has been shown in our theoretical paper [23], when the angle of incidence is scanned around the resonance angle of the sharp PWG mode, the phase of the electromagnetic field associated with the PWG mode changes by a factor of  $\pi$  and its sign is reversed (See Fig. 5a in [23]), while that of the SPP mode does not change appreciably, because the angle is located in the tail region of the broad SPP resonance. The constructive and destructive interferences of the two

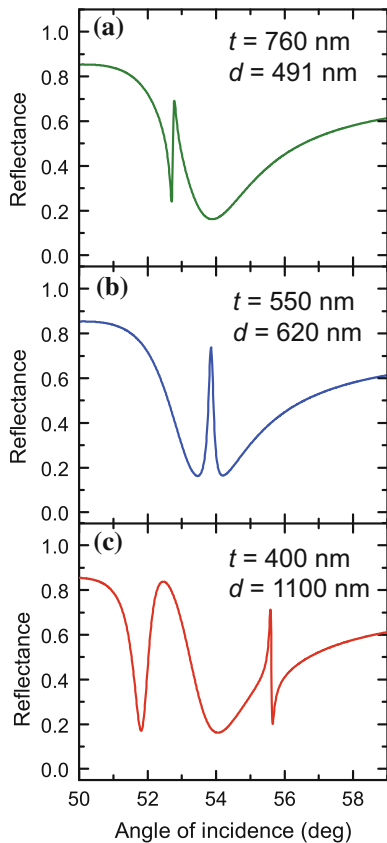
**Fig. 10.7** Field distributions for the MDDD structure calculated at three different angles of incidence, 54.054° (SPP resonance) (a), 55.545° (far from resonances) (b) and 55.611° (Fano resonance) (c), respectively



modes around the PWG mode resonance thus results in the sharp asymmetric Fano line shape.

The simplicity of the present MDDD structure allows us to easily control the Fano line shape by varying the structural parameters, in particular the thicknesses of the Cytop spacer layer  $t$  and the PMMA waveguide layer  $d$ . In Fig. 10.8a–c, we show three different line shapes generated by three different sets of the thicknesses indicated in the figures. The spectrum shown in Fig. 10.8c is the same as that shown in Fig. 10.6. Note that the position of the resonance can be controlled by  $d$ , which determines the resonance position of the PWG mode; as  $d$  increases, the resonance angle of PWG mode increases. The strength of the coupling between the SPP mode and the PWG mode is governed by  $t$ ;  $t$  has to be appropriately chosen to obtain a well shaped resonance. For  $d = 491$  nm, as seen in Fig. 10.8a, the PWG mode resonance is located at the angle lower than that of the SPP resonance and consequently, the Fano line shape is realized at the low-angle side of the broad SPP resonance. For  $d = 1100$  nm, Fig. 10.8c demonstrates that the PWG mode resonance is shifted to the

**Fig. 10.8** Dependence of Fano line shape on the thicknesses of Cytop spacer layer  $t$  and PMMA waveguide layer  $d$ . **a**, **b** and **c** were obtained by assuming values of  $t$  and  $d$  indicated in the figures



angle higher than that of the SPP resonance, resulting in the Fano resonance at the high-angle side of the SPP resonance. For  $d = 620$  nm, Fig. 10.8b shows the line shape quite different from others. In this case, the PWG mode resonance is located at almost the same position as the SPP mode resonance, and the line shape seen is typical of so called electromagnetically induced transparency (EIT). Normally, the line shape of EIT is characterized by a sharp transmission dip appearing inside a broad absorption band. In the present ATR spectra, the decrease in the reflectivity  $R$  is caused by the absorption of light  $A$  in the sample, because the angle of incidence is in the region of the total reflection, and there is no light transmitted from the sample. Therefore, using a relation  $A = 1 - R$ , we can convert the spectrum shown in Fig. 10.8b into that of absorption exhibiting a sharp dip (transparency) in the absorption band.

### 10.2.3 Experimental Observation of Fano Resonance in MDDD Structure

The results of simulations presented in Sects. 10.2.1 and 10.2.2 suggest the possibility of realizing the Fano resonance in simple metal-dielectric multilayer structures. The structures suggested are so simple that they can be prepared without nanofabrication techniques. We have indeed succeeded in observing the Fano resonance in the MDDD structure shown in Fig. 10.5 [24]. To prepare the structure, first the Ag layer was deposited on a SF10 glass substrate by vacuum evaporation, and then the Cytop and PMMA layers were successively deposited by spin coating on top of the Ag layer. The multilayer sample was pasted onto the bottom surface of a 60°-prism made of SF11 glass with the aid of index matching oil. The prism with the sample was mounted on a computer-controlled rotating stage. For the measurements of  $\theta$ -scan ATR spectra,  $p$ -polarized light from a He-Ne laser with a wavelength of 632.8 nm was incident on the prism through a chopper. The intensity of the reflected light was measured as a function of the angle of incidence,  $\theta_{in}$ , using a Si photo-diode connected to a lock-in-amplifier. The reflectance spectra were obtained by normalizing the intensity data recorded with the sample to that recorded for a bare part of the prism.

Typical experimental  $\theta$ -scan ATR spectrum is presented in Fig. 10.9a. The experimental spectrum is quite similar to the theoretical spectrum shown in Fig. 10.6 and exhibit clearly the Fano resonance around 55.25°. In Fig. 10.9b, the experimental Fano line shape (dots) is shown in an expanded scale together with a result of fitting to the Fano line shape function [2, 24]. We see that the observed line shape can be very well reproduced by the Fano function. We also attempted to reproduce the observed spectrum by the EM calculation. The solid line in Fig. 10.9a is the result of EM calculation obtained by a set of parameters:  $s = 45$  nm and  $\epsilon_{Ag} = -15.5075 + i3.1010$  for the Ag layer,  $t = 400$  nm and  $\epsilon_{Cytop} = 1.8117 + i2.6900 \times 10^{-3}$  for the Cytop layer, and  $d = 920$  nm and  $\epsilon_{PMMA} = 2.2141 + i2.9760 \times 10^{-4}$  for the PMMA layer. The overall fit of the calculated spectrum to the experimental points is very good. In our paper [24], we have also reported the dependence of the ATR spectrum on the thicknesses of the spacer Cytop layer and the PMMA waveguide layer and demonstrated the feasibility of controlling the Fano line shape by varying the thicknesses.

Another example of experimental observation of the Fano resonance [29] is given in Fig. 10.10. The ATR spectrum presented in this figure was obtained for a MDDD structure consisting of layers of inorganic materials, namely an Al layer, a SiO<sub>2</sub> layer, an Al<sub>2</sub>O<sub>3</sub> layer and air. The Al layer was prepared by vacuum deposition, and the SiO<sub>2</sub> and Al<sub>2</sub>O<sub>3</sub> layers were prepared by a rf sputtering method. The experimental spectrum (dots) can be well reproduced by the theoretical spectrum (solid curve) obtained by a set of parameters:  $s = 20.95$  nm and  $\epsilon_{Al} = -37.28 + i16.33$  for the Al layer,  $t = 363$  nm and  $\epsilon_{SiO_2} = 2.124 + i2.915 \times 10^{-4}$  for the SiO<sub>2</sub> layer, and  $d = 563$  nm and  $\epsilon_{Al_2O_3} = 2.788 + i3.673 \times 10^{-4}$  for the Al<sub>2</sub>O<sub>3</sub> layer. The figure demonstrates that the observation of the Fano resonance is successful not only for the organic dielectric layers mentioned above, but also for inorganic dielectric layers.

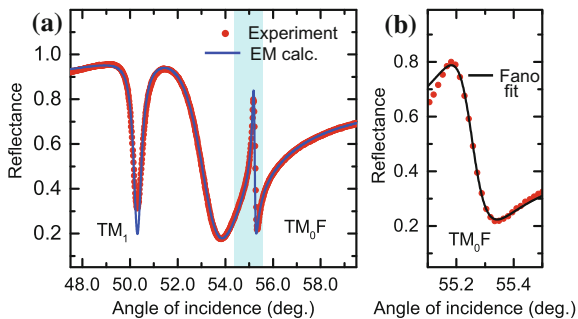
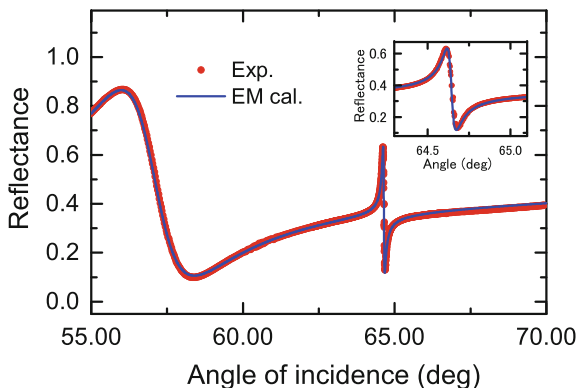


**Fig. 10.9** **a** Experimental  $\theta$ -scan ATR spectrum (dots) obtained for an Ag/Cytop/PMMA/Air (MDDD) system and theoretical fit curve obtained by EM calculation. **b** Experimental spectrum (dots) and result of fitting to Fano function (solid curve) in the vicinity of the resonance. Adapted from [24]

**Fig. 10.10** Experimental  $\theta$ -scan ATR spectrum obtained for an Al/SiO<sub>2</sub>/Al<sub>2</sub>O<sub>3</sub>/Air (MDDD) system and theoretical fit curve obtained by EM calculation. Adapted from [29]



An advantage of using the Al layer is its broadness of the SPP resonance; when the SPP resonance is broad, it is not necessary to control precisely the thickness of the waveguide to tune the PWG mode resonance into the SPP resonance to assure their overlap and interaction. Another advantage of the Al layer is its applicability to the UV plasmonics. The Al layer is known to have low losses in the UV region and consequently, keeps good plasmonic properties, which is not the case for Ag and Au layers. Results of systematic experiments on Fano line shape engineering are reported in our paper [29], where a  $Q$  factor as high as  $\sim 1,500$  is demonstrated.

In Fig. 10.10, we see that the ATR dip corresponding to the SPP excitation at the Al/SiO<sub>2</sub> interface is highly asymmetric exhibiting a long tail extending to large angles. The sharp Fano resonance is superposed on this long tail. According to our analyses presented in [29], the asymmetric SPP dip can be well reproduced by a generalized Fano function derived by Gallinet and Martin [34, 35]. This implies that the SPP resonance can be regarded as the Fano resonance. Furthermore, the sharp Fano resonance superposed on the asymmetric SPP dip was found to be well reproduced by a product of two generalized Fano functions. Therefore, it is appropriate to iden-

tify the resonance presented in Fig. 10.10 as the double Fano resonance. Although the asymmetric line shapes of the SPP dips have long been known, it was common to analyze them using Lorentzian line shapes [33]. Very recently, we have analyzed in detail the Fresnel reflection coefficient at a metal-dielectric interface and that for the 3-layer ATR geometry [36]. We demonstrated that the coefficients contain a nonresonant continuum and a SPP-resonant response that lead to the Fano resonance, when they interfere. The asymmetric SPP resonances can thus be reinterpreted as the Fano resonances.

## 10.3 Light-Tunable Fano Resonance

### 10.3.1 Experimental Results

In Sects. 10.2.2 and 10.2.3, we demonstrated that the Fano resonance can be realized easily in the MDDD structures. Since the structures are simple, it is also easy to add functionalities to the structures for developing various novel optical devices. Normally, once the structural parameters of nanostructures are fixed, the characteristics of the Fano line shape such as the position, width and height are fixed. However, recent studies in nanostructures demonstrated the modification of the Fano line shape caused by external perturbations to the structures, such as mechanical forces [17] and the electric fields [18, 19, 21]. In this section, we introduce a novel method for tuning the Fano resonance by light irradiation. Our strategy for realizing the light-tunable Fano resonance is as follows. Since the Fano resonance in our multilayer structures arises from the coupling between the SPP and PWG modes, a change in the propagation constant of the PWG mode is thought to directly induce a shift of the Fano resonance. When a photosensitive material is used as the waveguide layer and its refractive index could be changed by light irradiation, the change in the refractive index in the waveguide may change the propagation constant of the PWG mode, thus generating a photosensitive shift of the Fano resonance. To make the waveguide layer photosensitive, we prepared PMMA layers doped with disperse red 1 (DR1) molecules.

The DR1 molecule is one of the azobenzene derivatives exhibiting *trans-cis* photoisomerization (see Fig. 10.11a), and its *trans* form is known to be stable [26, 37–41]. Both *trans*- and *cis*-DR1 molecules have absorption bands in the blue region of the spectrum, and they transform into each other by reversible photoisomerization as schematically shown in Fig. 10.11a. *Cis*-DR1 molecules revert to *trans*-DR1 molecules by thermal relaxation as well. Linear and nonlinear optical properties of the DR1-doped PMMA films are governed by the orientation of the *trans* molecules, because they have large transition dipole moments along the long molecular axis. When the photoisomerization of DR1 molecules takes place under the pump irradiation, we can expect to have changes in the refractive index of the DR1-doped PMMA waveguide layer, resulting in the modulation of the Fano resonance.

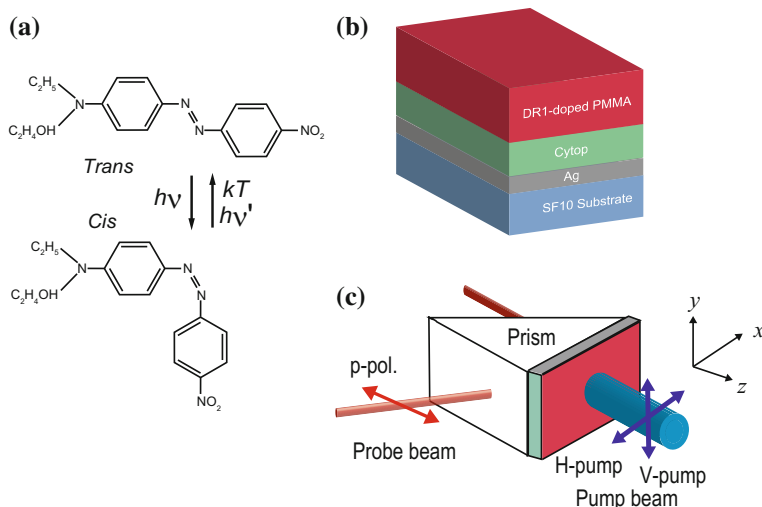


**Fig. 10.11** **a** *Trans*- and *cis*-forms of DR 1 molecule and their mutual transformations. **b** Multilayer stack of Ag/Cytop/DR1-doped PMMA/Air (MDDD) prepared on SF10 substrate. **c** Kretschmann configuration and polarizations of the probe and pump light. From [27]

The multilayer sample used in our studies is schematically shown in Fig. 10.11b. Instead of using the pure PMMA waveguide layer as in our previous work [24], we use the PMMA waveguide layer doped with photofunctional DR1 molecules. The sample consists of a SF10 glass substrate, a Ag layer, a fluoropolymer Cytop layer and a DR1-doped PMMA layer. The estimated thicknesses of the Ag, Cytop and DR1-doped PMMA layers are 45.5, 524 and 720 nm, respectively. To measure the angle-scan ATR spectra in a Kretschmann configuration, the multilayer sample was pasted onto the bottom surface of a 60°-prism made of SF11 glass (Fig. 10.11c).

The optical setup used to measure the ATR spectra under pump light irradiation (pump-probe ATR experiments) is schematically shown in Fig. 10.12. The prism with the sample was mounted on a computer-controlled rotating stage. *p*-polarized light beam from a He-Ne laser with a wavelength of 632.8 nm was used as the probe beam. The diameter of the probe beam is  $\sim 2$  mm. The ATR spectra were measured as a function of the angle of incidence. A pump beam with a wavelength of 488.0 nm from a semiconductor diode laser was directed onto the sample surface. To assure the overlap between the pump beam and the probe beam, the pump beam as large as  $\sim 7$  mm in diameter was used. The pump beam was incident normal to the surface of the DR1-doped PMMA layer (normal pumping) or with an angle of 60° (oblique pumping). The polarization of the pump beam was set to either the vertical or horizontal direction (V-pump or H-pump). Hereafter, we call the normal V-pump, normal H-pump, oblique V-pump and oblique H-pump conditions as NV-, NH-, OV- and OH-pump conditions, respectively.

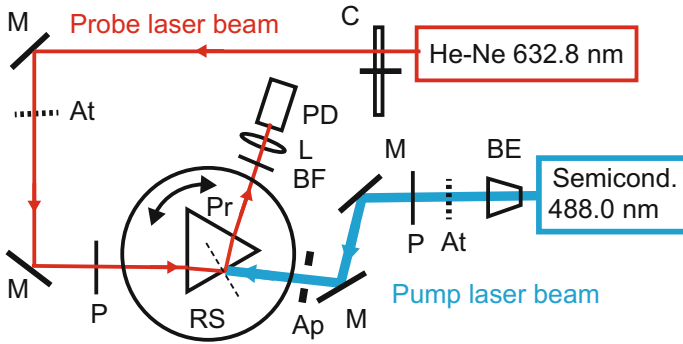


**Fig. 10.12** Optical set up used for pump-probe ATR measurements. Optical elements used are: chopper (C), mirror (M), attenuator (At), polarizer (P), rotation stage (RS), prism (Pr), band-pass filter (BF), lens (L), photodiode (PD), aperture (Ap), and beam expander (BE). Adapted from [28]

**Fig. 10.13** Shift of Fano resonance induced by pump light irradiation. The inset shows a spectrum measured without pump irradiation. From [28]

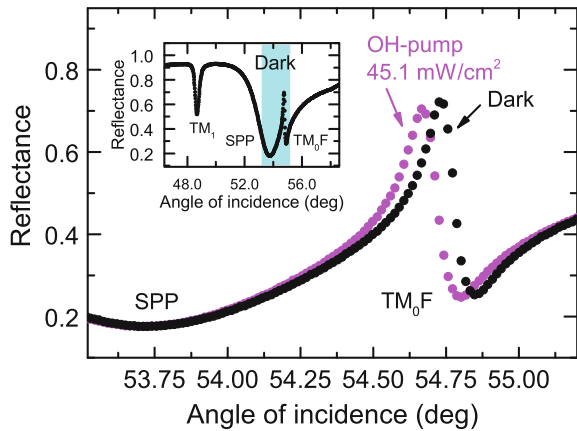
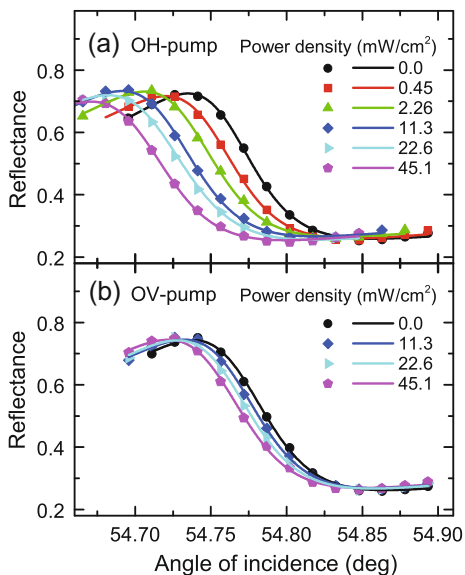


Figure 10.13 compares an ATR spectrum around the Fano resonance obtained under the OH-pump condition with a power density of  $45.1 \text{ mW/cm}^2$  with a spectrum obtained without pump irradiation (dark spectrum). The inset of the figure shows the dark spectrum in a wide angle range. The thicknesses and the dielectric constants of the layers of the present sample determined from a theoretical fit of the dark spectrum are  $s = 45.5 \text{ nm}$  and  $\epsilon_{\text{Ag}} = -16.5837 + i2.3417$  for the Ag layer,  $t = 524 \text{ nm}$  and  $\epsilon_{\text{Cyttop}} = 1.8252 + i8.1100 \times 10^{-3}$  for the Cyttop layer, and  $d = 720 \text{ nm}$  and  $\epsilon_{\text{PMMA}} = 2.2320 + i2.9880 \times 10^{-4}$  for the PMMA layer, respectively [27]. The dark spectrum shown in the inset is very similar to that presented in Fig. 10.9, which was obtained with a pure PMMA waveguide layer. A remarkable feature seen in Fig. 10.13 is the shift of the Fano resonance to a lower angle under pump irradiation; the SPP dip stays at the same angle under pump irradiation. This figure clearly demonstrates that light tuning of the Fano resonance is successful.



**Fig. 10.14** Results of systematic measurements of the Fano resonance performed by varying the pump beam intensity under OH-pump condition (a) and under OV-pump condition. From [28]

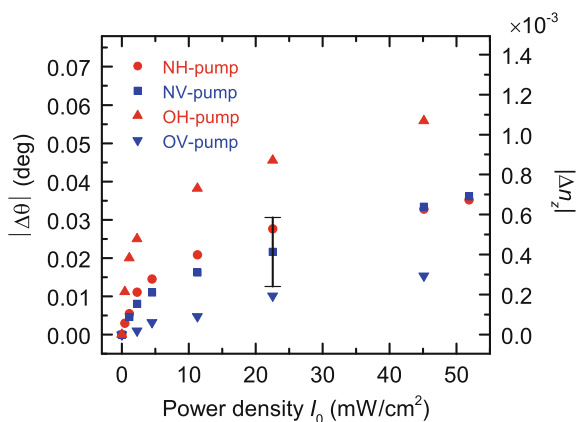


Results of systematic measurements performed by varying the intensity of the pump beam are presented in Fig. 10.14a, b for OH- and OV-pump conditions, respectively. In these figures, we see that the amount of the shift of the Fano resonance increases as the pump power density increases; the shift is larger for the OH-pump than for the OV-pump. The solid curves shown in Fig. 10.14a, b are results of fitting to the Fano function. In Fig. 10.15, the resonance angles obtained from the Fano fit are plotted as functions of the pump power density for the OH- and OV-pump conditions as well as for the NV- and NH-pump conditions. We see that under the normal pumping, the observed shifts are almost the same for V- and H-polarizations, while under the oblique pumping, the observed shifts for the H-polarization are much larger than those observed for the V-polarization. These results imply that the observed light-tuning effect is polarization sensitive presumably due to the polarization sensitive nature of the DR1 molecules embedded in the PMMA matrix.

### 10.3.2 Analysis of Experimental Results and Mechanism of Light Tuning

The shifts of the Fano resonance under the pump light irradiation demonstrated in the above are thought to arise from the changes in the refractive index of the DR1-doped PMMA waveguide layer. Here, we estimate the amount of changes in the refractive index from a comparison between the observed ATR spectra and those calculated by the EM theory. For detailed discussions, we introduce a Cartesian coordinate

**Fig. 10.15** Shifts of Fano resonance angle as functions of the pump power density obtained under NH-, NV-, OH- and OV-pump conditions. From [28]



attached to the sample-prism system as shown in Fig. 10.11c. In this coordinate system, the plane of incidence for the pump and prob beams lies in the  $x - z$  plane. The polarization of the probe beam was set to the  $p$ -polarization; corresponding electric fields have thus  $x$  and  $z$  components,  $E_x$  and  $E_z$ , respectively. Under the normal pump condition, when the probe beam scans the narrow region of the Fano resonance, the pump beam is almost normal to the sample surface. Therefore, the electric field of the pump light can be assumed to have only the  $y$  component ( $E_y$ ) for V-pump, and only the  $x$  component ( $E_x$ ) for H-pump. In case of the oblique pumping, the pump beam is incident obliquely to the sample surface and the electric field of the pump light has  $E_y$  for V-pump and both the  $E_x$  and  $E_z$  components for H-pump. Since the changes in the refractive index are thought to be anisotropic, we introduce anisotropic refractive indices of the layer  $n_x$ ,  $n_y$  and  $n_z$  for the DR1-doped PMMA layer. Note that the present ATR spectra are determined only by  $n_x$  and  $n_z$ , because the probe light is  $p$ -polarized.

Optical phenomena related with the *trans-cis* photoisomerization of DR1 molecules embedded in PMMA matrices have been investigated extensively over two decades [38–45]. It was demonstrated that photoinduced changes in the refractive index of the DR1-doped PMMA film can be well described by a simple model of angular hole burning (AHB) [38, 41, 42], which predicts the depletion of the *trans* molecules in the direction of the polarization of pump light. According to the AHB model, the photoisomerization induces anisotropic changes in the refractive indices described by  $\Delta n_{\parallel}$  and  $\Delta n_{\perp}$ , where  $\Delta n_{\parallel}$  and  $\Delta n_{\perp}$  represent the changes in the directions parallel and perpendicular to the polarization of the pump light, respectively. The AHB model predicts that low irradiation intensities produce a change of refractive index  $\Delta n_{\parallel} = 3\Delta n_{\perp}$ , while for high irradiation intensities, saturation prevails and the ratio  $\Delta n_{\parallel}/\Delta n_{\perp}$  tends towards 1.

We performed EM calculations to examine the influence of the change in the refractive index of the DR1-doped PMMA waveguide on the ATR Fano line shape. The fitting parameters for the dark spectrum were used as initial parameters. In

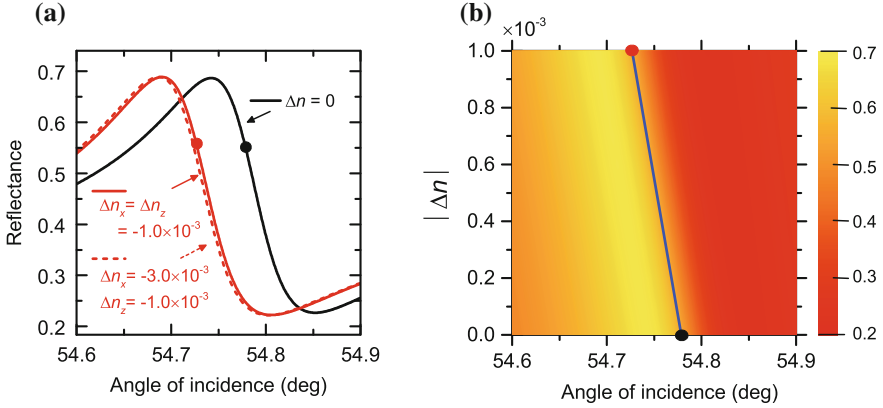


**Fig. 10.16** **a** Fano line shapes theoretically obtained to reproduce the experimental shift. Filled circles represent the resonance angles determined from the Fano fits. **b** Contour plot of the Fano line shape obtained by varying continuously the refractive index of the DR1-doped PMMA layer. The solid line gives the dependence of the resonance angle on the change in the refractive index. The result presented by the solid line allows us to convert the observed shift of the resonance angle into the change in the refractive index. From [27]

case of NV-pump, the pump  $E_y$  fields may induce the changes in  $n_x$  and  $n_z$  given by  $\Delta n_x = \Delta n_z = \Delta n_{\perp}$ . We simply write as  $\Delta n = \Delta n_x = \Delta n_z = \Delta n_{\perp}$ . ATR spectra in the region of the Fano resonance obtained for  $\Delta n = 0$  and  $-1.0 \times 10^{-3}$  are presented in Fig. 10.16a as solid lines. We see that the spectrum calculated with  $\Delta n = -1.0 \times 10^{-3}$  exhibits a low-angle shift similar to that observed experimentally. For NH-pump, the pump  $E_x$  fields may induce the changes given by  $\Delta n_x = \Delta n_{\parallel}$  and  $\Delta n_z = \Delta n_{\perp}$ , respectively. In the limit of high pump intensity, we recover the NV-pump case, since  $\Delta n_{\parallel} = \Delta n_{\perp}$  holds as mentioned above. In the limit of low pump intensity, since  $\Delta n_{\parallel} = 3\Delta n_{\perp}$  holds, we have  $\Delta n_x = \Delta n_{\parallel} = 3\Delta n_{\perp} = 3\Delta n$  and  $\Delta n_z = \Delta n_{\perp} = \Delta n$ . The broken curve in Fig. 10.16a is the Fano line shape obtained with this assumption for  $\Delta n = -1.0 \times 10^{-3}$ . We see that the shift of the Fano line shape relative to that of the high pump intensity limit or NV-pump case is very small and well below the angular precision of the present measurements. This is in good agreement with the experimental results presented in Fig. 10.15, where no appreciable difference between the NV-pump and NH-pump results exceeding the present angular precision is observed. These facts allow us to simplify our theoretical analysis; in what follows, we present calculated results only for the case of  $\Delta n_x = \Delta n_z = \Delta n$ .

Figure 10.16b shows a contour plot of the Fano line shape obtained by continuously varying  $\Delta n$  from 0 to  $-1.0 \times 10^{-3}$ . The calculated Fano line shapes were fitted to the Fano formula to determine the Fano resonance angles. The solid line in Fig. 10.16b represents the shift of the Fano resonance angle as a function of  $|\Delta n|$ . We can define an angular sensitivity of the Fano line shape to the variation of the refractive index as  $S_{\theta} = \lim_{\Delta n \rightarrow 0} (\frac{\Delta \theta}{\Delta n})$ , where  $\Delta \theta$  is the shift of the resonance angle caused by the refractive index change  $\Delta n$ . From the slope of the solid line in Fig. 10.16b

we obtain a value  $S_\theta = -52.27^\circ \text{RIU}^{-1}$ . Since the above arguments are valid also for the OV- and OH-pump, we can use the value of  $S_\theta$  to convert the observed shift  $|\Delta\theta|$  plotted in Fig. 10.15 to the change in the refractive index  $|\Delta n|$ . The right vertical axis of Fig. 10.15 was scaled with  $|\Delta n|$  converted from  $|\Delta\theta|$ . The figure demonstrates that the optical pumping of the present sample with a pump power density of up to  $\sim 50 \text{ mW/cm}^2$  induces the change in the refractive index of up to  $\sim 0.7 \times 10^{-3}$ . The amount of change in the refractive index is in good agreement with experimental results reported so far for similar DR1-doped PMMA films [38, 40–42]. The good agreement further confirms that the present shift is caused by the photoisomerization of DR1 molecules.

Figure 10.15 demonstrates that the shift of the Fano resonance strongly depends on the pumping angle and polarization (polarization sensitive), and the dependence of the shift on the pumping power density is nonlinear. To further analyze these behaviors we have to take into account the changes in the refractive index of the DR1-doped PMMA waveguide layer at the pump wavelength (488.0 nm). In previous experimental studies [37, 41, 42], the decrease in the absorbance of DR1-doped PMMA films at the pump wavelength under pump irradiation has been demonstrated. The decrease in the absorbance implies the decrease in the imaginary part of the refractive index. When the imaginary part changes under pump irradiation, the distribution of the pump light intensity inside the waveguide layer also changes. The EM calculation of the light intensity inside the waveguide layer thus becomes very much complex. Since rigorous EM calculations at the pump wavelength are highly involved and not tractable, we introduced a simple phenomenological treatment described in detail in our recent paper [28]. Our phenomenological treatment is very much successful to reproduce the observed shifts of the Fano resonance under various pumping conditions presented in Fig. 10.15 (see Fig. 5 in [28]). According to our analyses, the large shifts observed under the OH-pump condition can be attributed to the large overlap of the pump and probe electric fields ( $E_z$  component for both).

## 10.4 Concluding Remarks

In this Chapter, starting from the simulation results and proceeding to the experimental results, we demonstrated the feasibility of realizing the Fano resonance in the metal-dielectric multilayer structures. Furthermore, we presented the successful observation of light tuning of the Fano resonance and gave the physical interpretation of the observed shift of the resonance. The multilayer structures are easy to prepare and very much suited for realistic applications to photonic devices such as optical sensors, switches and platforms for enhancing Raman, fluorescence and nonlinear signals. In biosensing, for instance, surface plasmon resonance (SPR) sensors have been widely used [46]. It is common to functionalize metallic surfaces to capture desired biomolecules and monitor changes in the SPP ATR dips caused by the capture of the biomolecules. Our metal-dielectric multilayer structures can be used in

exactly the same manner as the SPR sensors, when the outer surface of the waveguide layer is functionalized.

According to our previous numerical analyses [22, 23, 25], when the change in intensity of the reflected light is monitored, we can expect to have a large figure of merit (FOM) of sensitivity by intensity for a sharp Fano resonance; sharper the resonance, larger the FOM. Although the ultimate enhancement in the sensitivity is determined by the material parameters, in particular the imaginary part of dielectric constant of the waveguide [29], the FOM of sensitivity for an optimized structure is predicted to be enhanced by several orders of magnitude compared to that of the conventional SPR sensor. Numerical results reported in [23, 25] also suggest giant enhancements of electric fields at the waveguide surface under the Fano resonance condition. The enhanced electric fields can be used to enhance Raman and fluorescence signals from molecules adsorbed on the surface. In the metal-enhanced fluorescence spectroscopy, the fluorescence of molecules located very close the metal surface (within  $\sim 10$  nm) is quenched due to the energy transfer from the molecules to the metal and a spacer layer is indispensable to place target molecules away from the metal surface. In contrast, using the multilayer Fano structures, we can avoid the fluorescence quenching, because the molecules placed on the waveguide surface are far from the metal surface. Experimental evidences for the high FOM of sensor sensitivity and the high enhancement of optical signals have not yet been reported. Further extensive experimental and theoretical studies on the metal-dielectric Fano structures toward their real applications are highly required.

**Acknowledgements** This work was supported in part by JSPS KAKENHI Grant Number 16K04979.

## References

1. A.E. Miroshnichenko, S. Flach, Y.S. Kivshar, *Rev. Mod. Phys.* **82**, 2257 (2010)
2. B. Luk'yanchuk, N.I. Zheludev, S.A. Maier, N.J. Halas, P. Nordlander, H. Giessen, C.T. Chong, *Nat. Mater.* **9**, 707 (2010)
3. N.J. Halas, S. Lal, W.S. Chang, S. Link, P. Nordlander, *Chem. Rev.* **111**, 3913 (2011)
4. A.B. Khanikaev, C. Wu, G. Shvets, *Nanophotonics* **2**, 247 (2013)
5. M. Rahmani, B. Luk'yanchuk, M. Hong, *Laser Photonics Rev.* **7**, 329 (2013)
6. M.F. Limonov, M.V. Rybin, A.N. Poddubny, Y.S. Kivshar, *Nat. Photonics* **11**, 543 (2017)
7. A. Christ, Y. Ekinci, H.H. Solak, N.A. Gippius, S.G. Tikhodeev, O.J.F. Martin, *Phys. Rev. B* **76**, 201405(R) (2007)
8. J.B. Lassister, H. Sobhani, J.A. Fan, J. Kundu, F. Capasso, P. Nordlander, N.J. Halas, *Nano Lett.* **10**, 3184 (2010)
9. J.B. Lassister, H. Sobhani, M.W.M.W.S. Knight, P. Nordlander, N.J. Halas. *Nano Lett.* **12**, 1058 (2011)
10. S.N. Sheikholeslami, A. Garcia-Extarri, J.A. Dionne, *Nano Lett.* **11**, 3927 (2011)
11. W.S. Chang, J.B. Lassister, P. Swanglap, H. Sobhani, S. Khatua, P. Nordlander, N.J. Halas, S. Link, *Nano Lett.* **12**, 4977 (2012)
12. Z.J. Yang, Q.Q. Wang, H.Q. Lin, *Appl. Phys. Lett.* **103**, 111115 (2013)
13. Y. Sonnerfraud, N. Verellen, H. Sobhani, G.A.E. Vandenbosch, V.V. Moshchalkov, P.V. Dorpe, P. Nordlander, S.A. Maier, *ACS Nano* **4**, 1664 (2010)

14. Y.H. Fu, J.B. Zhang, Y.F. Yu, B. Luk'yanchuk, *ACS Nano* **6**, 5130 (2012)
15. J. Li, T. Liu, H. Zheng, J. Dong, E. He, W. Gao, Q. Han, C. Wang, Y. Wu, *Plasmonics* **9**, 1439 (2014)
16. J. Qi, C. Z., J. Chen, Y. Li, W. Qiang, J. Xu, Q. Sun. *Opt. Express* **22**, 14688 (2014)
17. Y. Cui, J. Zhou, V.A. Tamma, W. Park, *ACS Nano* **6**, 2385 (2012)
18. S.H. Mousavi, I. Kholmanov, K. Alici, D. Purtseladze, N. Arju, K. Tatar, D.Y. Fozdar, J.W. Suk, Y. Hao, A.B. Khanikaev, R. Ruoff, G. Shvets, *Nano Lett.* **13**, 1111 (2013)
19. N. Dabidian, I. Kholmanov, A. Khanikaev, K. Tatar, S. Trendafilov, S.H. Mousavi, C. Magnusson, R.S. Ruoff, G. Shvets, *ACS Photonics* **2**, 216 (2015)
20. F. Zhang, X. Hu, C. Wu, H. Yang, Q. Gong, *Appl. Phys. Lett.* **105**, 181114 (2014)
21. W. Zhao, H. Jiang, B. Liu, Y. Jiang, C. Tang, J. Li, *Appl. Phys. Lett.* **107**, 171109 (2015)
22. S. Hayashi, D.V. Nesterenko, Z. Sekkat, *Appl. Phys. Express* **8**, 022201 (2015)
23. S. Hayashi, D.V. Nesterenko, Z. Sekkat, *J. Phys. D Appl. Phys.* **48**, 325303 (2015)
24. S. Hayashi, D.V. Nesterenko, A. Rahmouni, Z. Sekkat, *Appl. Phys. Lett.* **108**, 051101 (2016)
25. D.V. Nesterenko, S. Hayashi, Z. Sekkat, *J. Opt.* **18**, 065004 (2016)
26. Z. Sekkat, S. Hayashi, D.V. Nesterenko, A. Rahmouni, S. Refki, H. Ishitobi, Y. Inouye, S. Kawata, *Opt. Express* **24**, 20080 (2016)
27. S. Hayashi, D.V. Nesterenko, A. Rahmouni, H. Ishitobi, Y. Inouye, S. Kawata, *Sci. Rep.* **6**, 33144 (2016)
28. S. Hayashi, D.V. Nesterenko, A. Rahmouni, Z. Sekkat, *Phys. Rev. B* **95**, 165402 (2017)
29. S. Hayashi, U. Fujiwara, B. Kang, M. Fujii, D.V. Nesterenko, Z. Sekkat, *J. Appl. Phys.* **122**, 163103 (2017)
30. M. Born, E. Wolf, *Principles of Optics*, 7th edn. (Cambridge University Press, 1999)
31. C.E. Reed, J. Giergiel, J.C. Hemminger, S. Ushioda, *Phys. Rev. B* **36**, 4990 (1987)
32. C.C. Katsidis, D.I. Siapkas, *Appl. Opt.* **41**, 3978 (2002)
33. H. Raether, *Surface Plasmons on Smooth and Rough Surfaces and on Gratings*, *Springer Tracts in Modern Physics*, vol. 111 (Springer, 1988)
34. B. Gallinet, O.J.F. Martin, *Phys. Rev. B* **83**, 235427 (2011)
35. B. Gallinet, O.J.F. Martin, *ACS Nano* **5**, 8999 (2011)
36. D.V. Nesterenko, S. Hayashi, Z. Sekkat, *Phys. Rev. B* **97**, 235437 (2018)
37. Z. Sekkat, W. Knoll, *Photoreactive Organic Thin Films* (Academic, New York, 2002)
38. Z. Sekkat, M. Dumont, *Appl. Phys. B* **53**, 121 (1991)
39. M. Dumont, D. Morichère, Z. Sekkat, Y. Levy, in *SPIE Vol. 1559 Photopolymer Device Physics, Chemistry, and Applications II* (SPIE-The International Society for Optical Engineering, 1991), p. 127
40. Z. Sekkat, D. Morichère, M. Dumont, R. Loucif-Saïbi, J.A. Delaire, *J. Appl. Phys.* **71**, 1543 (1992)
41. Z. Sekkat, M. Dumont, *Synth. Metals* **54**, 373 (1993)
42. Z. Sekkat, M. Dumont, *Appl. Phys. B* **54**, 486 (1992)
43. R. Loucif-Saïbi, K. Nakatani, J.A. Delaire, M. Dumont, Z. Sekkat, *Chem. Mater.* **5**, 229 (1993)
44. G. Kleideiter, Z. Sekkat, M. Kreiter, M. Dieter Lechner, W. Knoll. *J. Mol. Struct.* **521**, 167 (2000)
45. M. Maeda, H. Ishitobi, Z. Sekkat, S. Kawata, *Appl. Phys. Lett.* **85**, 351 (2004)
46. J. Homola, *Chem. Rev.* **108**, 462 (2008)

# Chapter 11

## Study of Fano Resonance in the Core-Level Absorption Spectrum in Terms of Complex Spectral Analysis



Satoshi Tanaka, Taku Fukuta and Tomio Petrosky

**Abstract** We study theoretically the core absorption spectrum of an impurity embedded in a tight-binding chain in terms of complex spectral analysis. The absorption spectral profile associated with the resonance states in principle exhibits an asymmetric Fano-type structure, even without apparent multiple interference transition paths. The asymmetric Fano absorption profile is attributed to the complex-valued oscillator strength of the transition to the resonance state belonging to the extended Hilbert space. The boundary condition on the continuum causes a large energy dependence of the self-energy, so that it enhances the nonlinearity of the eigenvalue problem of the effective Hamiltonian, yielding several non-analytic resonance states. The optical transitions to these resonance states constitute the overall absorption spectrum structure.

### 11.1 Introduction

Optical absorption spectroscopy is a fundamental tool to experimentally observe an elementary excitation of a material, where the absorption peak energy and spectral width, respectively, correspond to the excitation energy and the damping constant. Lorentz oscillator model has been well known as a classical model to interpret the absorption spectrum as a sum of induced independent oscillators with real-valued oscillator strengths for the excitations [1]. When a discrete excited state is energetically isolated from the others, the absorption peak corresponding to the excitation

---

S. Tanaka (✉) · T. Fukuta  
Department of Physical Science, Osaka Prefecture University,  
Gakuen-cho 1-1, Sakai 599-8531, Japan  
e-mail: stanaka@p.s.osakafu-u.ac.jp

T. Petrosky  
Center for Complex Quantum System, University of Texas at Austin, Austin, USA  
e-mail: petrosky@physics.utexas.edu

T. Petrosky  
Institute of Industrial Science, The University of Tokyo, Tokyo, Japan

shows a distinct Lorentzian peak, but when several excited states are interacting with each other, it sometimes becomes difficult to interpret the spectrum with the simple Lorentz oscillator model.

A typical example of a deviation from the Lorentz oscillator model is the Fano effect, where the absorption spectrum shows a characteristic asymmetric spectral profile first observed in the photoionization of a Helium atom [2–4]. Fano gave an interpretation to the absorption spectrum in terms of the quantum interference between the transition paths of the direct photoionization and the ionization via a resonance state [3, 4] and derived a general formula, known as Fano-profile for the absorption spectrum. Since then, the effect has been paid much attention as a manifestation of the quantum interference and has been found in various systems, such as in atomic physics, nuclear physics, condensed matter physics, circuits, and mesoscopic systems, and so on [5–8].

As the degrees of freedom of a matter increases, it becomes difficult to reveal the elementary excitations inherent to the matter from the analysis of the absorption spectrum. Especially, when discrete states are resonant with a continuum, causing the decaying process that is a prerequisite for the Fano effect, we cannot find an eigenmode corresponding to the decaying state within the ordinary quantum mechanics formulated in the Hilbert space. Therefore, there seems no way to make a direct correspondence of the spectral structure to the intrinsic elementary excitation of the system.

Meanwhile, a new field of the quantum mechanics is arising to expand the realm of the quantum mechanics to interpret an irreversible decay process based on the quantum theory. Such extensions of quantum mechanics have used a phenomenological non-Hermitian effective Hamiltonian, revealing that if we weaken the standard requirement of Hermiticity, the effective Hamiltonian may take the complex eigenvalues [9–15].

Instead of phenomenological methods, a non-Hermitian effective Hamiltonian has been derived from the microscopic total (Hermitian) Hamiltonian with use of the Brillouin-Wigner-Feshbach projection operator method (BWF method) [14–19], where the detailed information about the microscopic interaction with the environment is renormalized into the self-energy. Prigogine and one of the authors (T. P.) et al. have clarified that the eigenvalues of the effective Hamiltonian coincide with those of the total Hamiltonian when we correctly take into account the energy dependence of the self-energy in the effective Hamiltonian. Then the total Hermitian Hamiltonian can have complex eigenvalues for the resonance states in the *extended Hilbert space*, where the Hilbert norm of the eigenvector vanishes [20–28]. It is important to note that the complex eigenvalue problem of the effective Hamiltonian is nonlinear in the sense that the effective Hamiltonian depends on its eigenvalue.

In this chapter, we present an interpretation of the optical absorption spectrum in terms of the complex spectral analysis. We study the core-level absorption of an impurity in a one-dimensional semiconductor superlattice. We show that we make a correspondence of the absorption spectrum structures to the transitions to the discrete resonance states with the complex eigenvalues. We reveal that the absorption spectral structure due to the resonance state takes in principle an asymmetric Fano profile,



reflecting the complex oscillator strength of the transition to the resonance state belonging to the extended Hilbert space. Since this is the eigenstate representation of the Hamiltonian, there is no ambiguity in the interpretation of the absorption spectrum, avoiding the arbitrary interpretation of the quantum interference in terms of a Hilbert space basis.

Also, we found out that introducing an infinite potential barrier at the end of the chain causes a strong energy dependence of the self-energy, which strengthens the nonlinearity of the complex eigenvalue problem of the effective Hamiltonian. As a result, non-analytic resonance states appear in addition to a perturbative analytic resonance state. We found that the transition to the non-analytic resonance state exhibits a strong asymmetric Fano-type absorption structure.

The structure of this chapter is as follows. In Sect. 11.2, we study the core-level absorption spectrum of an impurity atom in the infinite one-dimensional semiconductor with a single intra-atomic transition taken into account. The model and the complex spectral representation method are presented in Sect. 11.2.1. We analyze the absorption spectrum in Sect. 11.2.2 with some calculated results. We study in Sect. 11.3 the core-level optical absorption spectrum of an impurity in a semi-infinite one-dimensional semiconductor. In Sect. 11.3.1 the model and the complex spectral analysis are presented. In Sect. 11.3.2 the absorption spectrum is studied, where the nonlinearity of the complex eigenvalue problem of the effective Hamiltonian plays an important role in the absorption spectrum. We summarize in Sect. 11.4.

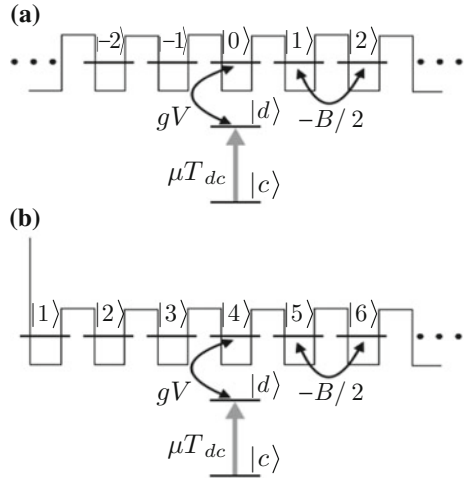
## 11.2 Absorption Spectrum in the Infinite Chain

In this section, we illustrate in terms of a simple physical system that the spectral profile of the absorption transition to a resonance state shows a Fano-type asymmetric profile representing the characteristics of the wavefunction belonging to the extended Hilbert space. We shall show that even with only a single absorption transition path without any interference we can obtain a Fano-type asymmetric profile.

### 11.2.1 Model and Complex Eigenvalue Problem

We consider the intra-atomic absorption transition in a two-level atom that is locally coupled with a one-dimensional semiconductor superlattice by a tunneling interaction as shown in Fig. 11.1a [24]. We describe the system by a one-dimensional single impurity Fano-Anderson model with chain length  $Na$ , where  $a$  is a lattice constant taken as the unit of length in this paper, and with the nearest neighbor transfer integral of  $-B/2$ , and  $N$  is the total number of sites in the chain. The energies of the ground state  $|c\rangle$  and the excited state  $|d\rangle$  of the impurity, coupled to the central site  $n = 0$ , are denoted by  $E_c$  and  $E_d$ , respectively. Then the Hamiltonian of the electronic system reads

**Fig. 11.1** The model of a two level-impurity atom embedded in one-dimensional semiconductor superlattice: The impurity is located at the central site of an infinite chain (a), and it is located at the  $n_0$ -th site of a semi-infinite chain (b)



$$\hat{H} = E_c|c\rangle\langle c| + E_d|d\rangle\langle d| - \frac{B}{2} \sum_{n=-N/2}^{N/2-1} (|n+1\rangle\langle n| + \text{H.c.}) + gV(|0\rangle\langle d| + \text{H.c.})$$

$$= E_c|c\rangle\langle c| + \hat{H}_e, \tag{11.1}$$

where  $V$  is the tunneling interaction between the excited state of the impurity  $|d\rangle$  and the  $|0\rangle$ th site state of the chain with the dimensionless coupling constant  $g$ .

By using the wave number representation of

$$|k\rangle \equiv \frac{1}{\sqrt{N}} \sum_{n=-N/2}^{N/2-1} \exp[ikn]|n\rangle, \tag{11.2}$$

$\hat{H}_e$  in (11.1) reduces to

$$\hat{H}_e = E_d|d\rangle\langle d| + \sum_k E_k|k\rangle\langle k| + \frac{gV}{\sqrt{N}} \sum_k (|k\rangle\langle d| + \text{H.c.}), \tag{11.3}$$

where the energy dispersion of the continuum is given by

$$E_k = -B \cos k. \tag{11.4}$$

In the limit  $N \rightarrow \infty$ ,  $k$  becomes a continuous variable for  $-\pi \leq k \leq \pi$ . Hereafter, we take the half bandwidth as an energy unit, i.e.  $B = 1$ . The density of states of the continuum is given by

$$\rho(E) = \frac{1}{\pi} \frac{1}{\sqrt{1-E^2}}, \quad (11.5)$$

with a divergent *Van Hove singularity* at the band edges  $E = \pm 1$  [26]. As will be shown later, this singularity influences the absorption profile.

We consider the complex eigenvalue problem of  $\hat{H}_e$  in the extended Hilbert space by using the BWF method [16]. The right- and left-eigenvalue problems read

$$\hat{H}_e |\phi_\xi\rangle = z_\xi |\phi_\xi\rangle, \quad \langle \tilde{\phi}_\xi | \hat{H}_e = z_\xi \langle \tilde{\phi}_\xi |, \quad (11.6)$$

where the subscripts  $\xi$  denote the eigenstates of the bound states, the discrete resonance states, or the continuous state.

The projection operator  $\hat{P}$  onto the excited state  $|d\rangle$  of the impurity and its complement  $\hat{Q}$  are defined by

$$\hat{P}^{(d)} \equiv |d\rangle\langle d|, \quad \hat{Q}^{(d)} \equiv 1 - \hat{P}^{(d)} = \sum_k |k\rangle\langle k|. \quad (11.7)$$

By acting with  $\hat{P}^{(d)}$  and  $\hat{Q}^{(d)}$  onto the right-eigenvalue problem, we have

$$E_d \langle d | \phi_\xi \rangle + \frac{gV}{\sqrt{N}} \sum_k \langle k | \phi_\xi \rangle = z_\xi \langle d | \phi_\xi \rangle, \quad (11.8a)$$

$$\frac{gV}{\sqrt{N}} \langle d | \phi_\xi \rangle + E_k \langle k | \phi_\xi \rangle = z_\xi \langle k | \phi_\xi \rangle. \quad (11.8b)$$

Substituting (11.8b) into (11.8a) yields the complex eigenvalue problem of the effective Hamiltonian  $\hat{H}_{\text{eff}}(z)$  as

$$\hat{H}_{\text{eff}}(z_\xi) \langle d | \phi_\xi \rangle = z_\xi \langle d | \phi_\xi \rangle, \quad (11.9)$$

where the scalar effective Hamiltonian is defined by

$$\hat{H}_{\text{eff}}(z) = E_d + \frac{g^2 V^2}{N} \sum_k \frac{1}{z - E_k}. \quad (11.10)$$

It should be noted that the effective Hamiltonian itself depends on the eigenvalue. In this sense, the eigenvalue problem becomes nonlinear [20, 28].

The eigenvalues are obtained by non-perturbatively solving the dispersion equation  $z = \hat{H}_{\text{eff}}(z)$  in the limit  $N \rightarrow \infty$ :

$$z_\xi = E_d + g^2 \Sigma^+(z_\xi), \quad (11.11)$$

where the self-energy  $\Sigma^+(z)$  is explicitly represented by [24, 26]

$$\Sigma^+(z) = \int_{-\pi}^{\pi} dk \frac{V^2}{(z - E_k)^+} = \frac{V^2}{\sqrt{z^2 - 1}}. \tag{11.12}$$

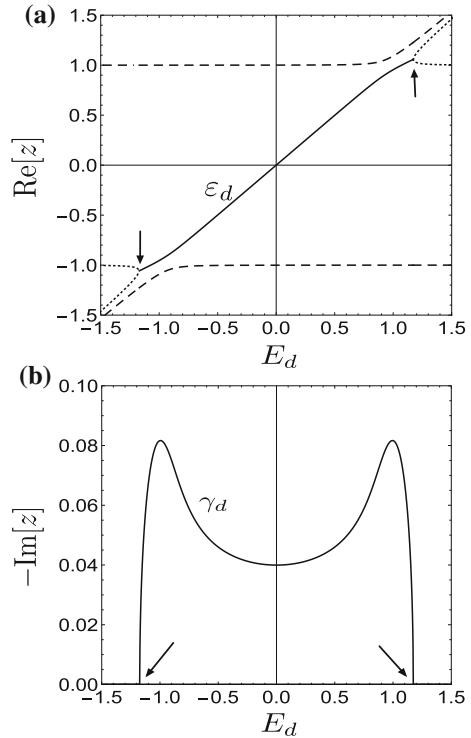
The + symbol in the integrand denotes the analytic continuation from the upper half plane through the branch cut. Substituting (11.12) into (11.11), the dispersion equation reduces to a fourth-order polynomial equation for  $z_\xi$  as

$$(z_\xi - E_d)^2(z_\xi^2 - 1) = g^4 V^4. \tag{11.13}$$

In Fig. 11.2a, b, respectively, we show the real and imaginary values of the four solutions as a function of  $E_d$ , the two of which are localized bound states with real eigenvalues appearing above and below the continuum and the other two are the resonance and anti-resonance states with complex conjugate eigenvalues. For later use, we denote the eigenvalue of the resonance state as

$$z_d(E_d) = \varepsilon_d(E_d) - i\gamma_d(E_d). \tag{11.14}$$

**Fig. 11.2** The real (a) and the imaginary parts (b) of the solutions of the dispersion equation of (11.13) as a function of  $E_d$  for  $g = 0.2$ . The complex eigenvalue of the resonance state is drawn by the solid line, while the two bound states in the first Riemann sheet are denoted by the dashed lines. The arrows indicate the exceptional points where the resonance and anti resonance state pairs are coalesced to be the so-called *virtual bound states* in the second Riemann sheet drawn by the dotted lines [32]



The arrows in the figures indicate the exceptional points at  $|E_d| = E_\gamma$  where the resonance and antiresonance states coalesce together, which is known as an exceptional point [13, 14, 29, 30]. The exceptional point  $E_\gamma$  is given by the non-analytic expansion in terms of  $g$  [24, 29]:

$$E_\gamma = 1 + \frac{3g^{4/3}}{2} - \frac{g^{8/3}}{8} + O(g^{12/3}). \quad (11.15)$$

For  $|E_d| > E_\gamma$ , the resonance and anti-resonance states become the so-called *virtual bound states* (or anti-bound) on the real axis in the second Riemann sheet drawn by the dotted lines in Fig. 11.2a [31, 32].

The right-resonance state is obtained as [20]

$$|\phi_d\rangle = \langle d|\phi_d\rangle \left( |d\rangle + \frac{gV}{\sqrt{N}} \sum_k \frac{1}{(z - E_k)_{z=z_d}^+} |k\rangle \right), \quad (11.16)$$

where the + sign in the denominator in the second term represents the analytic continuation of  $z \rightarrow z_d$  from the upper half plane in the limit  $N \rightarrow \infty$ . The left-resonance state is similarly obtained as

$$\langle \tilde{\phi}_d| = \langle \tilde{\phi}_d|d\rangle \left( \langle d| + \frac{gV}{\sqrt{N}} \sum_k \frac{1}{(z - E_k)_{z=z_d}^+} \langle k| \right). \quad (11.17)$$

It should be emphasized that since the analytic continuations are taken to the same direction in  $|\phi_d\rangle$  and  $\langle \tilde{\phi}_d|$  the Hermite conjugate of  $|\phi_d\rangle$  does not coincide with the left-resonance state  $\langle \tilde{\phi}_d|$ :

$$\langle \tilde{\phi}_d| \neq \langle \phi_d|. \quad (11.18)$$

The normalization constant  $\mathcal{N}_d \equiv \langle d|\phi_d\rangle\langle \tilde{\phi}_d|d\rangle$  is determined from the condition  $\langle \tilde{\phi}_d|\phi_d\rangle = 1$  to give

$$\mathcal{N}_d = \langle d|\phi_d\rangle\langle \tilde{\phi}_d|d\rangle = \left( 1 - g^2 \frac{d}{dz} \Sigma^+(z) \Big|_{z=z_d} \right)^{-1}. \quad (11.19)$$

We differentiate (11.11) with respect to  $E_d$  to find

$$\left( 1 - g^2 \frac{d}{dz_d} \Sigma^+(z_d) \right) \frac{d}{dE_d} z_d(E_d) = 1, \quad (11.20)$$

where  $z_d(E_d)$  is a solution of (11.11) for the resonance state [27]. With use of (11.19) and (11.20), we find the relation of

$$\frac{d}{dE_d} z_d(E_d) = \mathcal{N}_d. \quad (11.21)$$

Note that the normalization constant  $\mathcal{N}_d$  is in general a complex number, contrary to the ordinary case in which  $\langle d|\psi\rangle\langle\psi|d\rangle = |\langle d|\psi\rangle|^2$  is necessarily real and positive for a Hilbert space vector  $|\psi\rangle$ .

The continuous right-eigenstate  $|\phi_k\rangle$  and left-eigenstate  $\langle\tilde{\phi}_k|$  are similarly obtained [20]. Using the contour deformation method [20, 33], the bi-completeness relation can be proved as

$$\sum_{i=1}^2 |\phi_i\rangle\langle\phi_i| + |\phi_d\rangle\langle\tilde{\phi}_d| + \sum_k |\phi_k\rangle\langle\tilde{\phi}_k| = 1, \quad (11.22)$$

where  $|\phi_i\rangle$  ( $i = 1, 2$ ) indicate the two bound states belonging to the Hilbert space,  $|\phi_d\rangle$  ( $\langle\tilde{\phi}_d|$ ) is the resonance state belonging to the extended Hilbert space, and  $|\phi_k\rangle$  ( $\langle\tilde{\phi}_k|$ ) are the continuous states.

### 11.2.2 Absorption Spectrum

Now we consider the absorption spectrum of the intra-atomic transition of the impurity atom. Using the dipole transition approximation under the rotating wave approximation, the photon-atom interaction is given by

$$\hat{T} \equiv \mu(T_{dc}|d\rangle\langle c| + \text{H.c.}), \quad (11.23)$$

where  $\mu T_{dc}$  is coupling strength and  $\mu$  is a dimensionless coupling constant.

For  $\mu \ll 1$ , the absorption spectrum is given by [5, 24]

$$F(\omega) \equiv -\frac{1}{\pi} \lim_{\varepsilon \rightarrow +0} \text{Im} \langle c|\hat{T} \frac{1}{\Omega + E_c - \hat{H} + i\varepsilon} \hat{T}|c\rangle + O(\mu^4), \quad (11.24)$$

where  $\Omega$  is the incident photon frequency. Hereafter, we consider the spectrum up to  $O(\mu^2)$  and define a shifted photon frequency as  $\omega \equiv \Omega + E_c$ .

Substituting (11.23) in (11.24), we have

$$F(\omega) = -\frac{\mu^2 |T_{dc}|^2}{\pi} \lim_{\varepsilon \rightarrow +0} \text{Im} G_{dd}(\omega + i\varepsilon), \quad (11.25)$$

where the Green's function is defined by

$$G_{dd}(z) \equiv \langle d|\frac{1}{z - \hat{H}_e}|d\rangle. \quad (11.26)$$

Using the bi-completeness (11.22), the Green's function (11.26) is decomposed to the discrete state component and the continuum component, which gives the absorption spectrum (11.25) as

$$F(\omega) = -\frac{\mu^2 |T_{dc}|^2}{\pi} \lim_{\varepsilon \rightarrow +0} \text{Im} \left\{ \sum_{i=1}^2 \frac{|d|\phi_i\rangle|^2}{\omega - E_i + i\varepsilon} + \frac{\langle d|\phi_d\rangle\langle\tilde{\phi}_d|d\rangle}{\omega - z_d + i\varepsilon} + \sum_k \frac{\langle d|\phi_k\rangle\langle\tilde{\phi}_k|d\rangle}{\omega - E_k + i\varepsilon} \right\}, \quad (11.27)$$

where the integrated intensity is normalized as

$$\frac{1}{\mu^2 |T_{dc}|^2} \int_{-\infty}^{\infty} d\omega F(\omega) = 1. \quad (11.28)$$

The first term of (11.27) is attributed to the two bound states which gives a delta-function peak with the intensities of  $|d|\phi_i\rangle|^2$  at  $\omega = E_i$  ( $i = 1, 2$ ). In this paper we are concerned with the absorption spectrum for the resonance states and the continuum represented by the second line of (11.27):

$$f(\omega) \equiv -\frac{1}{\pi} \lim_{\varepsilon \rightarrow +0} \text{Im} \left\{ \frac{\langle d|\phi_d\rangle\langle\tilde{\phi}_d|d\rangle}{\omega - z_d + i\varepsilon} + \sum_k \frac{\langle d|\phi_k\rangle\langle\tilde{\phi}_k|d\rangle}{\omega - E_k + i\varepsilon} \right\} \quad (11.29a)$$

$$\equiv f_r(\omega) + f_c(\omega), \quad (11.29b)$$

where  $f_r(\omega)$  and  $f_c(\omega)$  are the resonance state contribution and the continuous state contribution, respectively. We can regard the numerators in (11.29a) as the complex-valued oscillator strengths to the resonance state and the continuous state. Note that the complex-valued oscillator strength  $\langle d|\phi_d\rangle\langle\tilde{\phi}_d|d\rangle$  has given in (11.19) as the normalization constant.

The integrated intensity of  $f(\omega)$  is given by

$$I_f \equiv \int_{-\infty}^{\infty} d\omega f(\omega) = 1 - \sum_{i=1}^2 |d|\phi_i\rangle|^2. \quad (11.30)$$

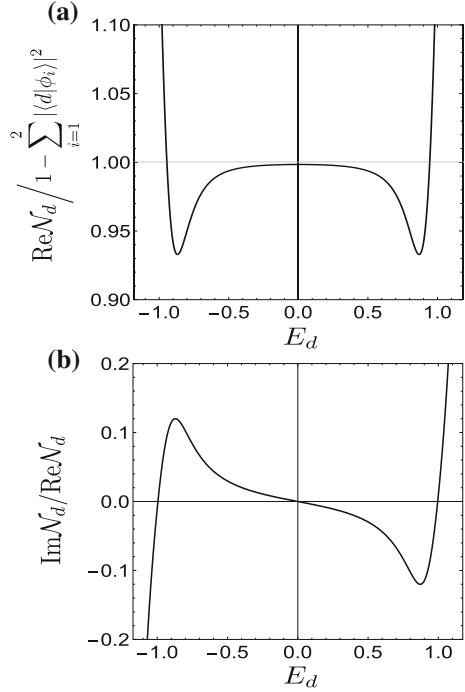
and the integrated area of  $f_r(\omega)$  is given by

$$\int_{-\infty}^{\infty} d\omega f_r(\omega) = \text{Re} \langle d|\phi_d\rangle\langle\tilde{\phi}_d|d\rangle = \text{Re} \mathcal{N}_d, \quad (11.31)$$

where we have used (11.19).

We show in Fig. 11.3a the ratio of the resonance state contribution to the integrated area,  $\text{Re} \mathcal{N}_d / I_f$ , as a function of  $E_d$  for  $g = 0.2$ . It is found that the resonance state contribution is dominant for the region except for the continuum threshold.

**Fig. 11.3** The ratio of the resonance state contribution to the integrated area,  $\text{Re}\mathcal{N}_d/I_f$  (a) and the asymmetry of the absorption profile  $a(E_d, g)$  (b) as a function of  $E_d$  for  $g = 0.2$



As mentioned in (11.21), since the normalization constant  $\mathcal{N}_d$  is a complex number, we decompose  $f_r(\omega)$  as

$$f_r(\omega) = -\frac{1}{\pi} \left\{ \frac{\gamma_d \text{Re}\mathcal{N}_d}{(\omega - \varepsilon_d)^2 + \gamma_d^2} + \frac{(\omega - \varepsilon_d) \text{Im}\mathcal{N}_d}{(\omega - \varepsilon_d)^2 + \gamma_d^2} \right\} \tag{11.32a}$$

$$\equiv f_r^S(\omega) + f_r^A(\omega) , \tag{11.32b}$$

where  $\text{Re}\mathcal{N}_d$  causes a symmetric Lorentzian profile, while  $\text{Im}\mathcal{N}_d$  causes the Fano-type asymmetric spectral profile. The asymmetry is evaluated by the ratio of

$$a(E_d, g) \equiv \frac{\text{Im}\mathcal{N}_d}{\text{Re}\mathcal{N}_d} = \frac{\frac{d}{dE_d} \text{Im}z_d(E_d)}{\frac{d}{dE_d} \text{Re}z_d(E_d)} = \frac{-\frac{d}{dE_d} \gamma_d(E_d)}{\frac{d}{dE_d} \varepsilon_d(E_d)} . \tag{11.33}$$

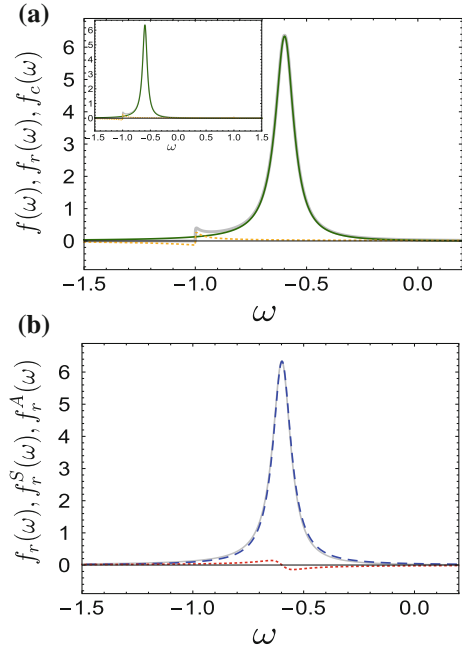
where we have used (11.14) and (11.21).

The behavior of  $a(E_d, g)$  as a function of  $E_d$  for  $g = 0.2$  is shown in Fig. 11.3b. Since  $\gamma_d(E_d)$  takes extremal at  $E_d = 0$  and  $E_d \simeq \pm 1$  as seen in Fig. 11.2b,  $a(E_d, g)$  vanishes at these points. The  $a(E_d, g)$  takes extremal at  $|E_d| \simeq 0.89$  and diverges at the exceptional point,  $E_d = E_\gamma$  given in (11.15).

This characteristic feature of the wavefunction of the resonance state is well reflected in the absorption spectrum. We show in Fig. 11.4 the absorption spectrum



**Fig. 11.4** The absorption spectrum  $f(\omega)$  for  $E_d = -0.6$  and  $g = 0.2$ . **a** The total spectrum  $f(\omega)$ , the resonance state contribution  $f_r(\omega)$ , and the continuous state contribution  $f_c(\omega)$  are drawn by the thick solid, the thin solid, and the dashed lines, respectively. **b** The decomposition of  $f_r(\omega)$  (thin solid line) to  $f_r^S(\omega)$  (dashed line) and  $f_r^A(\omega)$  (dotted line)



$f(\omega)$  when the impurity state energy  $E_d$  is well into the continuum for  $E_d = -0.6$  and  $g = 0.2$ . In Fig. 11.4a, we have shown the resonance state contribution  $f_r(\omega)$ , the continuous state contribution  $f_c(\omega)$  by the thin solid and the dashed lines, respectively, in addition to the total spectrum  $f(\omega)$  by the thick solid line. It is found that the total spectrum  $f(\omega)$  is mostly determined by  $f_r(\omega)$ . In Fig. 11.4b, we further decompose  $f_r(\omega)$  (thin solid line) into  $f_r^S(\omega)$  (dashed line) and  $f_r^A(\omega)$  (dotted line). The resonance state contribution  $f_r(\omega)$  is composed of  $f_r^S(\omega)$ , and the contribution of  $f_r^A(\omega)$  is very small. Therefore the absorption spectral profile is almost symmetric Lorentzian with its peak and the width representing the energy and the damping of the resonance state, respectively.

As  $E_d$  comes close to the band edge,  $f_r^A(\omega)$  becomes prominent. In Fig. 11.5, we show the absorption spectrum for  $E_d = -0.89$  where  $a(E_d, g)$  takes the maximal value. As seen in Fig. 11.5b,  $f_r^A(\omega)$  becomes significant which deviates the resonance state contribution from a symmetric Lorentzian. Even so, the continuous state contribution  $f_c(\omega)$  significantly contributes to the total absorption spectrum  $f(\omega)$  on its lower energy side, which obscures the effect of the asymmetry, as shown in Fig. 11.5a.

We also show in Fig. 11.6 the absorption spectrum for  $E_d = -1.10$ , where the resonance state is the non-analytic solution of the dispersion equation. In this case, since  $a(E_d; g)$  takes a large negative value, the resonance contribution largely distorts the absorption spectrum from Lorentzian as shown in Fig. 11.6b. However, the continuous state contribution becomes large at the same time, so that the resonance state contribution is not dominant contribution to the spectrum, as seen in Fig. 11.6a.

**Fig. 11.5** The absorption spectrum  $f(\omega)$  for  $E_d = -0.89$  and  $g = 0.2$ . **a** The total spectrum  $f(\omega)$ , the resonance state contribution  $f_r(\omega)$ , and the continuous state contribution  $f_c(\omega)$  are drawn by the thick solid, the thin solid, and the dashed lines, respectively. **b** The decomposition of  $f_r(\omega)$  (thin solid line) to  $f_r^S(\omega)$  (dashed line) and  $f_r^A(\omega)$  (dotted line)

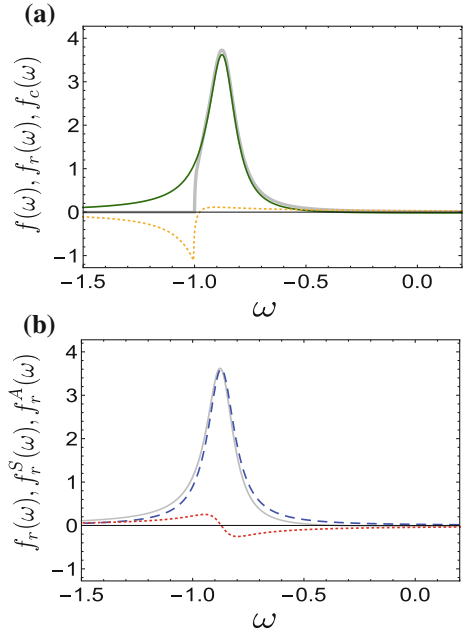
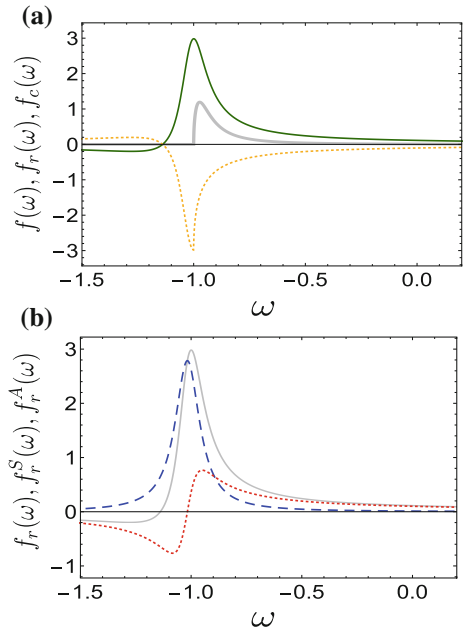


**Fig. 11.6** The absorption spectrum  $f(\omega)$  for  $E_d = -1.10$  and  $g = 0.2$ . **a** The total spectrum  $f(\omega)$ , the resonance state contribution  $f_r(\omega)$ , and the continuous state contribution  $f_c(\omega)$  are drawn by the thick solid, the thin solid, and the dashed lines, respectively. **b** The decomposition of  $f_r(\omega)$  (thin solid line) to  $f_r^S(\omega)$  (dashed line) and  $f_r^A(\omega)$  (dotted line)



### 11.3 Absorption Spectrum in the Semi-infinite Chain

In the previous section, we have shown that a Fano-type asymmetry in the absorption spectrum represents a characteristic feature of the resonance state belonging to the extended Hilbert space. Even though this asymmetry is enhanced when the bare impurity state energy is close to the band threshold, this effect is overwhelmed by the continuous state contributions.

In this section, we show that a boundary condition on the chain leads to a large energy dependence of the self-energy within the continuum. Therefore the complex eigenvalue problem of the effective Hamiltonian becomes highly nonlinear so that more non-analytic resonance states appear as the distance between the impurity and the potential wall increases. As a result, the absorption spectrum of the transitions to the resonance state, especially to the non-analytic resonance states, show a large Fano-type asymmetry even in the case where the bare impurity state energy is well inside the continuum. We shall show in this section that the transitions to these discrete resonance states determine the overall spectral feature.

#### 11.3.1 Model and Complex Eigenvalue Problem

We consider a semi-infinite one-dimensional semiconductor superlattice described by a tight-binding model with an infinite potential wall at the end of the chain, as shown in Fig. 11.1b. We place the same two-level impurity atom as considered in the previous section located at the  $n_0$ th site distance from the boundary. The Hamiltonian reads

$$\begin{aligned}\hat{H} &= E_c|c\rangle\langle c| + E_d|d\rangle\langle d| - \frac{B}{2} \sum_{n=1}^N (|n+1\rangle\langle n| + \text{H.c.}) + g(V|n_0\rangle\langle d| + \text{H.c.}), \\ &= E_c|c\rangle\langle c| + \hat{H}_e,\end{aligned}\quad (11.34)$$

where  $\hat{H}_e$  represents the Hamiltonian for the high energy states consisting of  $|d\rangle$  and the continuum, as in (11.1). The eigenmodes of the continuous state in terms of the wavenumber representation is given by

$$|k\rangle \equiv \sqrt{\frac{2}{N}} \sum_{n=-1}^N \sin(kn)|n\rangle, \quad (11.35)$$

which leads the Hamiltonian  $\hat{H}_e$  to

$$\hat{H}_e = E_d|d\rangle\langle d| + \sum_k E_k|k\rangle\langle k| + g \frac{2}{\sqrt{N}} \sum_k (V_k|k\rangle\langle d| + \text{H.c.}), \quad (11.36)$$

with the same energy dispersion as (11.4). An important difference from the infinite chain system of (11.3) is that the interaction potential depends on the wavenumber as

$$V_k = V \sin(n_0 k) . \quad (11.37)$$

Then the self-energy is given by

$$\Sigma^+(z) = \int_{-\pi}^{\pi} dk \frac{V^2 \sin^2(n_0 k)}{z - E_k} \quad (11.38a)$$

$$= \frac{V^2}{\sqrt{z^2 - 1}} \left\{ 1 - \left( -z + \sqrt{z^2 - 1} \right)^{2n_0} \right\} . \quad (11.38b)$$

Because of the energy dependence, the complex eigenvalue problem of the effective Hamiltonian (11.9) becomes highly nonlinear.

The dispersion equation for the complex eigenvalue problem of the effective Hamiltonian (11.9) reads

$$z = E_d + g^2 \frac{V^2}{\sqrt{z^2 - 1}} \left\{ 1 - \left( -z + \sqrt{z^2 - 1} \right)^{2n_0} \right\} . \quad (11.39)$$

This dispersion equation turns out to be the  $2n_0$ th order polynomial equation with the solutions of the  $(n_0 - 1)$  resonance-and-anti-resonance-states pairs and the two bound states. It should be noted that imposing the boundary on the chain gives rise to the several discrete resonance (antiresonance) states even with the single impurity state placed in the chain. The numbers of the resonance (antiresonance) states increases as  $n_0$  increases.

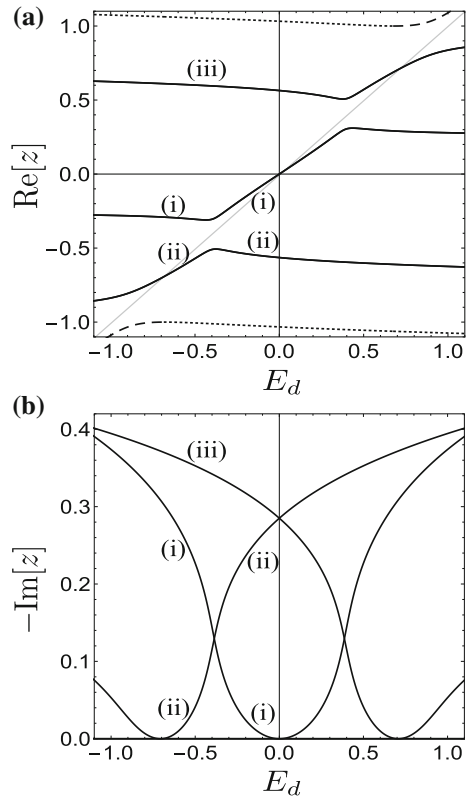
In terms of these discrete eigenstates in addition to the continuous eigenstates of  $\hat{H}_e$ , the bi-completeness is given by

$$\sum_{i \in \mathbb{R}^1} |\phi_i\rangle \langle \phi_i| + \sum_{\alpha=1}^{n_0-1} |\phi_\alpha\rangle \langle \tilde{\phi}_\alpha| + \sum_k |\phi_k\rangle \langle \tilde{\phi}_k| = 1 , \quad (11.40)$$

where the first, the second, and the third terms represent the bound states with the real energies in the first Riemann sheet, the resonance states with the complex energies in the second Riemann sheet, and the continuous states with the real energies on the real axis, respectively. The difference from (11.22) is in the second term, where the summation for the  $(n_0 - 1)$  resonance states are taken.

We show the real and the imaginary parts of the eigenvalues as a function of  $E_d$  for  $g = 0.2$  and  $n_0 = 4$  in Fig. 11.7a, b, respectively, where the thin line also shows the unperturbed impurity energy  $\text{Re}z = E_d$ . There are three resonance states numbered by (i) to (iii) in Fig. 11.7, where we see the real parts of the resonance states repelling each other, while the imaginary parts are crossing each other as  $E_d$  changes.

**Fig. 11.7** The eigenvalues as a function of  $E_d$  for  $g = 0.2$  and  $n_0 = 4$  as a function of  $E_d$ : The real part (a) and the imaginary part (b). The solid curves represent the resonance and anti-resonance state pairs: the three pair of the states are denoted by (i), (ii), and (iii). The dashed curves represent the bound state in the first Riemann sheet, while the dotted curves the bound state in the second Riemann sheet known as the virtual bound state. The thin line represent the bare impurity state energy  $E_d$



At  $E_d = \pm 2/3, 0$ , the imaginary part of one of these resonance states vanishes to be a bound state with no decay. This is known as the bound state in continuum (BIC) [34].

Note that there exist the two resonance states with the large decay rates  $-\text{Im}z \gg g^2$  in addition to the ordinary resonance states, as a result of the nonlinearity of the eigenvalue problem of the effective Hamiltonian. They are numbered by (i) and (iii) for  $E_d < -2/3$  and (ii) and (iii) for  $-2/3 \leq E_d < 0$ , as shown in Fig. 11.7. Those resonance states cannot be obtained by the perturbation method so that they are non-analytic for  $g$ .

### 11.3.2 Absorption Spectrum

With use of the bi-completeness of (11.40), the absorption spectrum is given by

$$f(\omega) = \frac{F(\omega)}{\mu^2 |T_{dc}|^2} = -\frac{1}{\pi} \lim_{\varepsilon \rightarrow +0} \text{Im} \left\{ \sum_{i \in \mathbb{R}^I} \frac{|\langle d|\phi_i\rangle|^2}{\omega - E_i + i\varepsilon} + \sum_{\alpha=1}^{n_0-1} \frac{\langle d|\phi_\alpha\rangle\langle\tilde{\phi}_\alpha|d\rangle}{\omega - z_\alpha + i\varepsilon} + \sum_k \frac{\langle d|\phi_k\rangle\langle\tilde{\phi}_k|d\rangle}{\omega - E_k + i\varepsilon} \right\}. \quad (11.41)$$

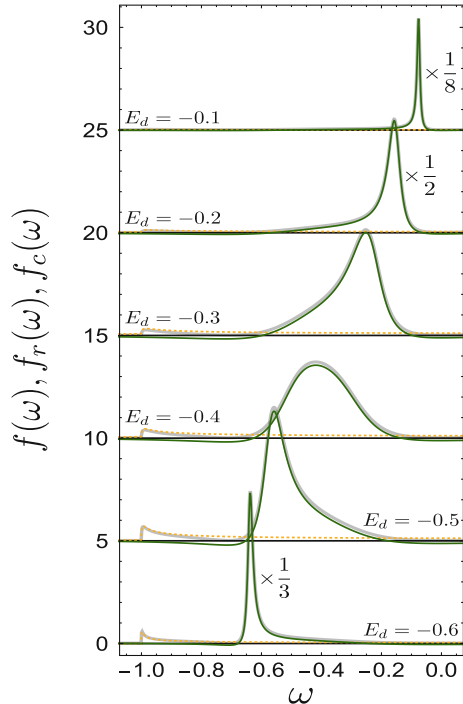
It will be shown that the absorption spectrum in the range of the continuum,  $f(\omega \mid -1 < \omega < 1)$ , is mainly determined by the resonance state contribution

$$f_r(\omega) \equiv -\frac{1}{\pi} \lim_{\varepsilon \rightarrow +0} \text{Im} \sum_{\alpha=1}^{n_0-1} \frac{\langle d|\phi_\alpha\rangle\langle\tilde{\phi}_\alpha|d\rangle}{\omega - z_\alpha + i\varepsilon} \equiv \sum_{\alpha=1}^{n_0-1} f_{r,\alpha}(\omega). \quad (11.42)$$

Each term of  $f_{r,\alpha}(\omega)$  is further decomposed to the symmetric part  $f_{r,\alpha}^S(\omega)$  and asymmetric part  $f_{r,\alpha}^A(\omega)$ :

$$f_{r,\alpha}(\omega) = -\frac{1}{\pi} \left\{ \frac{\gamma_\alpha \text{Re} \mathcal{N}_\alpha}{(\omega - \varepsilon_\alpha)^2 + \gamma_\alpha^2} + \frac{(\omega - \varepsilon_\alpha) \text{Im} \mathcal{N}_\alpha}{(\omega - \varepsilon_\alpha)^2 + \gamma_\alpha^2} \right\} \equiv f_{r,\alpha}^S(\omega) + f_{r,\alpha}^A(\omega). \quad (11.43)$$

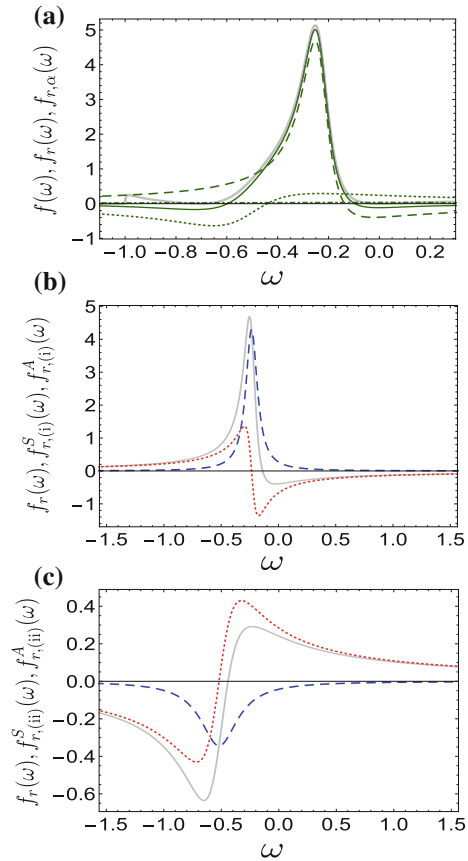
**Fig. 11.8** Absorption spectrum  $f(\omega)$  for various values of  $E_d$  ( $= -0.6 \sim -0.1$ ) for  $g = 0.2, V = 1.0$  and  $T_{dc} = 1.0$ . The calculated  $f(\omega)$  for each  $E_d$  are thick lines, the contribution of the resonance states  $f_r(\omega)$  are continuous lines and the background integral  $f_c(\omega)$  are dotted lines



We show in Fig. 11.8 the absorption spectra  $f(\omega)$  for various values of  $E_d$  ( $-0.6 < E_d < 0$ ), where the spectral contributions of  $f_r(\omega)$  and  $f_c(\omega)$  are also shown. The absorption profile is changed with  $E_d$ , reflecting the exchange of the characters of the resonance states (i) and (ii) in Fig. 11.7. Note that the spectrum is primarily determined by the resonance contribution  $f_r(\omega)$  as mentioned above.

In Fig. 11.9a, we show the three resonance state components of  $f_{r,\alpha}(\omega)$  ( $\alpha =$  (i), (ii), (iii)) at  $E_d = -0.3$ . We see that the sum of  $f_{r,(i)}$  and  $f_{r,(ii)}$  (thin solid line) almost determines the total spectrum  $f(\omega)$  (thick solid line), where the main contribution is due to  $f_{r,(i)}$  (dashed line). On the other hand,  $f_{r,(ii)}$  (dotted line) gives a minor contribution and  $f_{r,(iii)}$  (chain line) is negligibly small. In Fig. 11.9b, we have decomposed the resonance state component of  $f_{r,(i)}$  to the symmetric part  $f_{r,(i)}^S$  and the antisymmetric part  $f_{r,(i)}^A$  shown with the dashed and dotted lines in the figures, respectively. Compared to the infinite chain, the antisymmetric part prominently causes the Fano-type absorption profile even when  $E_d$  is well inside the continuum. As shown in Fig. 11.9c, this antisymmetric part for the resonance state component of

**Fig. 11.9** The decomposition of the absorption spectrum for  $E_d = -0.3$ . **a** Total spectrum is thick line and the resonance contribution  $f_r(\omega)$  is continuous line. The dashed line is a usual resonance state component  $f_{r,(i)}$  and The dotted and dot-dashed line are non-perturbative resonance components  $f_{r,(ii)}$  and  $f_{r,(iii)}$ . **b, c** The panels of (i) and (ii) show the symmetric and antisymmetric components for the resonance state (i) and (ii) in Fig. 11.7. The contribution of the resonance states  $f_r(\omega)$  is a thin solid line and a dashed line and a dotted line are the symmetry term  $f_r^S(\omega)$  and antisymmetry term  $f_r^A(\omega)$ , respectively

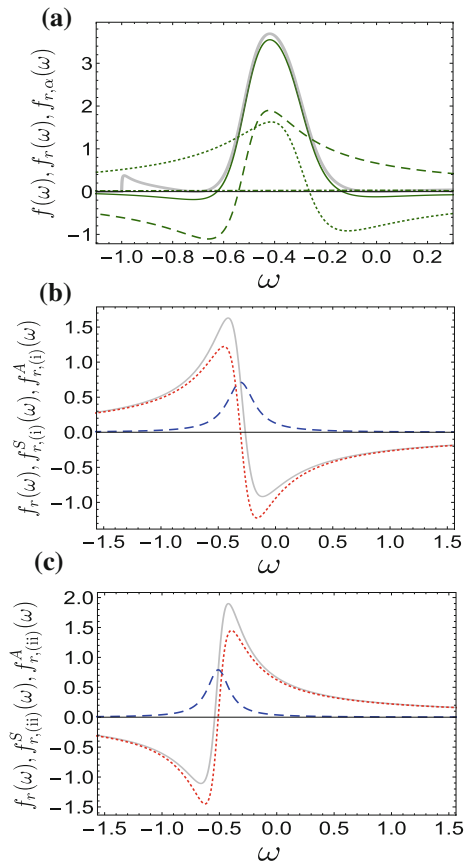


$f_{r,(ii)}$  is more exaggerated, because the resonance state (ii) is the non-analytic state obtained by the non-perturbative method.

Furthermore, the asymmetric part  $f_{r,(ii)}^A$  takes the opposite sign to  $f_{r,(i)}^A$ . This reflects the different signs of the derivatives of imaginary part of the eigenvalues of (i) and (ii) at  $E_d$ :  $\partial_E \text{Im}z_\alpha(E)|_{E=E_d}$ . Note that the symmetric part of  $f_{r,(ii)}^S$  is also opposite to  $f_{r,(i)}^S$ . This reflects the different sign of the derivative of imaginary part of the eigenvalues of (i) and (ii) at  $E_d$ :  $\partial_E \text{Re}z_\alpha(E)|_{E=E_d}$ . Thus, the absorption profile reflects the feature of the resonance states not only for the ordinary ones but also the non-analytic states.

These asymmetric components become much more pronounced for the crossing region of the resonance states of (i) and (ii) near  $E_d \simeq -0.4$  as shown in Fig. 11.7. We have shown in Fig. 11.10a the three resonance state components of  $f_{r,\alpha}(\omega)$  ( $\alpha = (i), (ii), (iii)$ ) at  $E_d = -0.4$ . The decomposition to the symmetric part  $f_{r,(i,ii)}^S$  and the antisymmetric part  $f_{r,(i,ii)}^A$  of the resonance state component of  $f_{r,(i)}$  and  $f_{r,(ii)}$  are shown in Fig. 11.10b, c, respectively. As seen from Fig. 11.7b,  $\partial_E \text{Im}z_\alpha(E)|_{E=E_d}$

**Fig. 11.10** The decomposition of the absorption spectrum for  $E_d = -0.4$ . **a** Total spectrum is thick line and the resonance contribution  $f_r(\omega)$  is continuous line. The dashed line is an usual resonance state component  $f_{r,(i)}$  and The dotted and dot-dashed line are non-perturbative resonance components  $f_{r,(i)}$  and  $f_{r,(ii)}$ . **b, c** The panels of (i) and (ii) show the symmetric and antisymmetric components for the resonance state (i) and (ii) in Fig. 11.7. The contribution of the resonance states  $f_r(\omega)$  is a thin solid line and a dashed line and a dotted line are the symmetry term  $f_r^S(\omega)$  and antisymmetry term  $f_r^A(\omega)$ , respectively

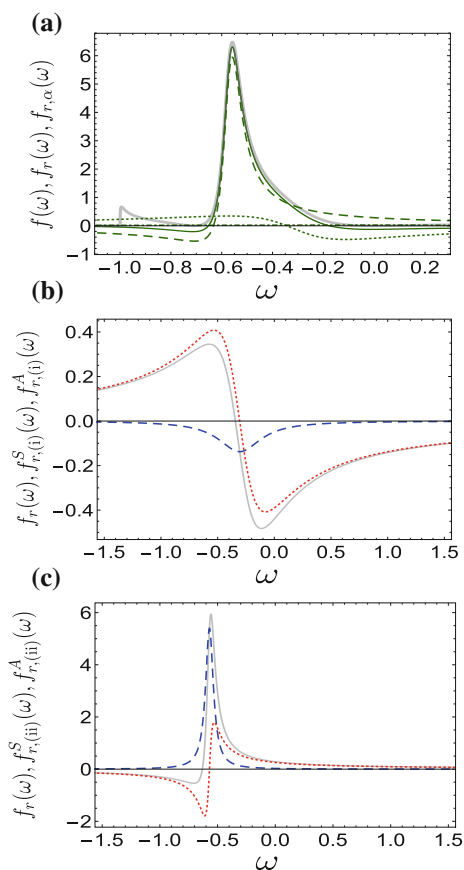




becomes large with opposite signs for both the resonance states of (i) and (ii) at  $E_d = -0.4$ . Therefore, the two resonance state components almost equally contribute to the absorption spectrum, and the antisymmetric part overwhelms the symmetric part for both resonance states. As a sum of these spectral components, the total absorption profile becomes broadened and largely deviates from a simple Lorentzian profile. From this absorption profile, we can see that the resonance states are no more ordinary perturbative resonance states but the non-analytic resonance states.

As  $E_d$  further decreases, the characteristics of the resonance states of (i) and (ii) is exchanged as shown in Fig. 11.7. We show in Fig. 11.11 the absorption spectrum at  $E_d = -0.5$ . The contributions of the resonance states of (i) and (ii) to the absorption spectrum is exchanged and the asymmetry of the absorption spectrum is about opposite to those in Fig. 11.9 with respect to  $\omega = -0.4$ .

**Fig. 11.11** The decomposition of the absorption spectrum for  $E_d = -0.5$ . **a** Total spectrum is thick line and the resonance contribution  $f_r(\omega)$  is continuous line. The dashed line is an usual resonance state component  $f_{r,(ii)}$  and The dotted and dot-dashed line are non-perturbative resonance components  $f_{r,(i)}$  and  $f_{r,(iii)}$ . **b, c** The panels of (i) and (ii) show the symmetric and antisymmetric components for the resonance state (i) and (ii) in Fig. 11.7. The contribution of the resonance states  $f_r(\omega)$  is a thin solid line and a dashed line and a dotted line are the symmetry term  $f_r^S(\omega)$  and antisymmetry term  $f_r^A(\omega)$ , respectively



## 11.4 Summary

We have studied the core-level absorption of an impurity in a one-dimensional semiconductor superlattice with the use of the complex spectral analysis. We have revealed that the absorption spectral structure due to the resonance state takes in principle an asymmetric Fano profile. This reflects the fact that the complex-valued oscillator strength of the transition to the resonance state belonging to the extended Hilbert space is a complex number. Since this is the eigenstate representation of the Hamiltonian, there is no ambiguity in the interpretation of the absorption spectrum, avoiding the arbitrary interpretation of the quantum interference in terms of a Hilbert space basis.

The introduction of an infinite potential barrier at the end of the chain causes a strong energy dependence of the self-energy. This strengthens the nonlinearity of the complex eigenvalue problem of the effective Hamiltonian. As a result, in addition to a perturbative analytic resonance state, there appear non-analytic resonance states. The transition to the non-analytic resonance state exhibits a strong asymmetric Fano-type absorption structure.

We would like to emphasize that the individual transitions have interpreted the absorption spectrum to the discrete resonance states which are the intrinsic eigenstate of the system. The idea is similar to the Bohr's model of the quantum jump between the discrete states of the matter for the photon emission. Our interpretation is the extension of the quantum jump between the resonance states, where the interaction with the decay processes is renormalized into the resonance states not only the complex eigenvalues but also the wave function of the extended Hilbert space. It is interesting to apply our method to interpret other optical spectroscopies, such as resonance fluorescence, four-wave mixing, and so on.

**Acknowledgements** We are very grateful Drs. S. Garmon, K. Noba, and K. Kanki for many valuable discussions. We also thank K. Mizoguchi and Y. Kayanuma for fruitful comments. This work was partially supported by JSPS Grant-in-Aid for Scientific Research No.16H04003, 16K05481, and 17K05585.

## References

1. R. Loudon, *The Quantum Theory of Light* (OUP Oxford, Oxford, 2000)
2. H. Beutler, *Z. Physik A* **93**, 177 (1935)
3. U. Fano, *Nuovo Cimento* **12**, 154 (1935)
4. U. Fano, *Phys. Rev.* **124**, 1866 (1961)
5. C. Cohen-Tannoudji, J. Dupont-Roc, G. Grynberg, *Atom-Photon Interactions: Basic Processes and Applications*. A Wiley-Interscience Publication (Wiley, 1998)
6. A.E. Miroshnichenko, S. Flach, Y.S. Kivshar, *Rev. Mod. Phys.* **82**, 2257 (2010)
7. P. Fan, Z. Yu, S. Fan, M.L. Brongersma, *Nat. Mater.* **13**, 471 EP (2014)
8. S. Yoshino, G. Oohata, K. Mizoguchi, *Phys. Rev. Lett.* **15**, 157402 (2015)
9. N. Hatano, D.R. Nelson, *Phys. Rev. Lett.* **77**, 570 (1996)
10. N. Hatano, D.R. Nelson, *Phys. Rev. B* **56**, 8651 (1997)

11. C. Bender, S. Boettcher, Phys. Rev. Lett. **80**, 5243 (1998)
12. C.M. Bender, D.C. Brody, H.F. Jones, Am. J. Phys. **71**, 1095 (2003)
13. W.D. Heiss, J. Phys. A: Math. Gen. **37**, 2455 (2004)
14. I. Rotter, J. Phys. A: Math. Theor. **42**, 153001 (2009)
15. I. Rotter, J.P. Bird, Rep. Prog. Phys. **78**, 114001 (2015)
16. H. Feshbach, Ann. Phys. **19**, 287 (1962)
17. C. Jung, M. Müller, I. Rotter, Phys. Rev. E **60**, 114 (1999)
18. C. Jung, M. Müller, I. Rotter, J. Mod. Phys. **1**, 303 (2010)
19. H. Eleuch, I. Rotter, Eur. Phys. J. D **69**, 229 (2015)
20. T. Petrosky, I. Prigogine, S. Tasaki, Phys. A: Stat. Mech. Appl. **173**, 175 (1991)
21. T. Petrosky, I. Prigogine, Adv. Chem. Phys. **99**, 1 (1997)
22. T. Petrosky, G. Ordonez, I. Prigogine, Phys. Rev. A. At. Mol. Opt. Phys. **64**, 062101/1 (2001)
23. G. Ordonez, T. Petrosky, I. Prigogine, Phys. Rev. A. At. Mol. Opt. Phys. **63**, 521061 (2001)
24. S. Tanaka, S. Garmon, T. Petrosky, Phys. Rev. B **73**, 115340 (2006)
25. S. Tanaka, S. Garmon, G. Ordonez, T. Petrosky, Phys. Rev. B **76**, 153308 (2007)
26. S. Garmon, H. Nakamura, N. Hatano, T. Petrosky, Phys. Rev. B **80**, 115318 (2009)
27. S. Garmon, I. Rotter, N. Hatano, D. Segal, Int. J. Theor. Phys. **51**, 3536 (2012)
28. S. Tanaka, S. Garmon, K. Kanki, T. Petrosky, Phys. Rev. A **94**, 022105 (2016)
29. T. Kato, *Perturbation Theory for Linear Operators*, 2nd edn. (Springer, Berlin, Heidelberg, 1995)
30. K. Kanki, K. Hashimoto, T. Petrosky, S. Tanaka, *Spontaneous Breakdown of a PT-Symmetry in the Liouvillean Dynamics at a Non-Hermitian Degeneracy Point* (Springer International Publishing, Cham, 2016), pp. 289–304
31. N. Hatano, G. Ordonez, J. Math. Phys. **55**, 122106 (2014)
32. S. Garmon, M. Gianfreda, N. Hatano, Phys. Rev. A **92**, 022125 (2015)
33. S.C.G. Sudarshan, C.B. Chiu, V. Gorini, Phys. Rev. D **18**, 2914 (1978)
34. J. von Neumann, E. Wigner, Phys. Z. **30**, 465 (1929)

# Chapter 12

## Fano-resonances in High Index Dielectric Nanowires for Directional Scattering



Peter R. Wiecha, Aurélien Cuche, Housseem Kallel, Gérard Colas des Francs, Aurélie Lecestre, Guilhem Larrieu, Vincent Larrey, Frank Fournel, Thierry Baron, Arnaud Arbouet and Vincent Paillard

**Abstract** High refractive index dielectric nanostructures provide original optical properties thanks to the occurrence of size- and shape-dependent optical resonance modes. These modes commonly present a spectral overlap of broad, low-order modes (e.g. dipolar modes) and much narrower, higher-order modes. The latter are usually characterized by a rapidly varying frequency-dependent phase, which—in superposition with the lower order mode of approximately constant phase—leads to typical spectral features known as Fano resonances. Interestingly, such Fano resonances occur in dielectric nanostructures of the simplest shapes. In spheroidal nanoparticles, interference between broad magnetic dipole and narrower electric dipole modes can be observed. In high aspect-ratio structures like nanowires, either the electric or the magnetic dipolar mode (depending on the illumination conditions) interferes with higher order multipole contributions of the same nature (electric or magnetic). Using the analytical Mie theory, we analyze the occurrence of Fano resonances in high-index dielectric nanowires and discuss their consequences like unidirectional scattering. By means of numerical simulations, we furthermore study the impact on those Fano resonances of the shape of the nanowire cross-sections as well as the coupling of two

---

P. R. Wiecha · A. Cuche · H. Kallel · A. Arbouet · V. Paillard (✉)  
CEMES, Université de Toulouse, CNRS, Toulouse, France  
e-mail: vincent.paillard@cemes.fr

P. R. Wiecha  
e-mail: peter.wiecha@cemes.fr

G. Colas des Francs  
ICB, Université Bourgogne-Franche Comté, CNRS, Dijon, France

A. Lecestre · G. Larrieu  
LAAS, Université de Toulouse, CNRS, Toulouse, France

V. Larrey · F. Fournel  
CEA-LETI, Université Grenoble-Alpes, MINATEC Campus, Grenoble, France

T. Baron  
LTM, Université Grenoble-Alpes, CNRS, Grenoble, France

parallel nanowires. The presented results show that all-dielectric nanostructures, even of simple shapes, provide a reliable low-loss alternative to plasmonic nanoantennas.

## 12.1 Introduction

Research on effects of light-matter interaction occurring at subwavelength dimensions has been drawing increasing attention during the last three decades. When we talk about subwavelength dimensions, at visible and near-infrared frequencies, we find ourselves at the nanometer scale, a length-scale particularly interesting with regards to applications in information processing and optical computing, single molecule sensing or biomedicine, amongst many other domains. Most applications rely on the possibility to strongly confine far-field radiation to deeply subwavelength small volumes at resonant modes of specifically designed nanoparticles. Resonances are either due to surface plasmons in the case of metals (field of plasmonics) or to constructive optical interference in the case of dielectrics. Usually, all phenomena can be described by classical electrodynamics, i.e. by the set of Maxwell's equations [68].

In the following, we will briefly describe the fields of plasmonic and high index dielectric nanostructures, with a particular attention on their specificity and main differences.

Then, in the other sections of this chapter, we will give an overview on Fano Resonances in dielectric nanostructures, with an emphasis on directional scattering as a result of Fano-like interference phenomena. In particular, we will present the so-called *Kerker's conditions* under which unidirectional scattering occurs in dielectric spherical particles and extend the idea to cylinders. To substantiate the findings on dielectric nanowires, we will compare experimental results to Mie theory and numerical simulations.

Finally, we analyze the directional scattering behavior of nanowires with non-symmetric cross-sections, as well as the case of a system of two coupled nanowires.

### 12.1.1 Plasmonics

One of the main driving forces in nano-optics is the field of *plasmonics* [65, 74]. Electromagnetic waves impinging on metals launch collective oscillations of the free electrons in the conduction band of the metal. The dielectric constant of metals is negative, leading to an imaginary wave vector. Fields are therefore evanescent and confined within a small region at the surface, called the *skin-depth*. In consequence, the collective oscillations of the electrons propagate along the surface and are therefore called *surface plasmon polaritons* (SPP). In small metallic particles, the propagation of SPPs is hindered due to the spatial confinement and localized modes appear, so-called *localized surface plasmon resonances* (LSP).

These confined plasmon oscillations allow to squeeze light into tiny volumes of subwavelength size, far below the diffraction limit and yield extremely high local field enhancements [94]. In the visible spectral range, this results in sizes of several tenths to a few hundreds of nanometers for resonant metallic nanostructures. Such plasmonic particles are often referred to as *optical (nano-)antennas* [74].

In the context on this chapter, we would like to mention a few selected examples for applications of plasmonic nanostructures. Beyond the possibility to obtain strong localized field intensities, plasmonic nanoantennas can be designed to provide directional scattering. This can be achieved for instance by tailoring plasmonic geometries which provide a simultaneous electric and magnetic response [116]. With complex structures like bimetallic antennas, wavelength selective directional color routing can be obtained from individual nanoantennas [98]. Also the directional emission of quantum emitters can be controlled using plasmonic antennas [12, 26, 46]. For an extensive introduction on plasmonics, see e.g. [65].

### 12.1.2 High Refractive Index Dielectric Nano-particles

The focus of this chapter lies on a different kind of nano-antennas than the plasmonic ones. Recently, *dielectric* nanostructures of high refractive index started drawing a lot of attention as promising alternatives to metallic particles, since they offer in a similar way tailorable optical resonances [53].

Even in very simple systems such as nanospheres [54], or cylindrical [20, 49] or rectangular nanowires (NWs) [31], optical resonance modes can be tuned over (and beyond) the whole visible spectral range. Flexible tailoring of the resonant behavior can be achieved using dielectric nanostructures of more complex shapes [108].

A particular advantage of dielectric particles over metallic ones are their very low losses [4, 17, 27]. This property is directly related to the generally low imaginary part of the dielectric function for wavelengths above the direct bandgap. It is demonstrated in the upper spectra of Fig. 12.1a, b, where a gold and a silicon dimer are compared in terms of scattering efficiency and dissipation. Although the electric field-enhancement (as well as the confinement) is usually at least an order of magnitude lower than for plasmonic antennas (see also Fig. 12.1a, b, lower spectra), the reduced dissipative losses are a tremendous advantage and can be a decisive factor in applications such as field enhanced spectroscopy [86, 106].

Another unique feature of dielectric nanoparticles is the possibility to obtain strong magnetic resonances from geometries as simple as a sphere [32, 39, 40, 104]. In contrast, plasmonics require complex geometries to obtain important magnetic resonances [54] (see Fig. 12.1c, d). These magnetic-type resonances allow also to obtain a strong enhancement of the magnetic near-field, which is usually significantly more intense than the magnetic field intensity obtainable using metal nanostructures [4, 9, 70] (see Fig. 12.1a, b, bottom spectra). The magnetic resonances of dielectric nanostructures can be exploited to enhance the decay rate of magnetic dipole transitions [10, 88, 93, 111]. While the optical magnetic near-field and the magnetic

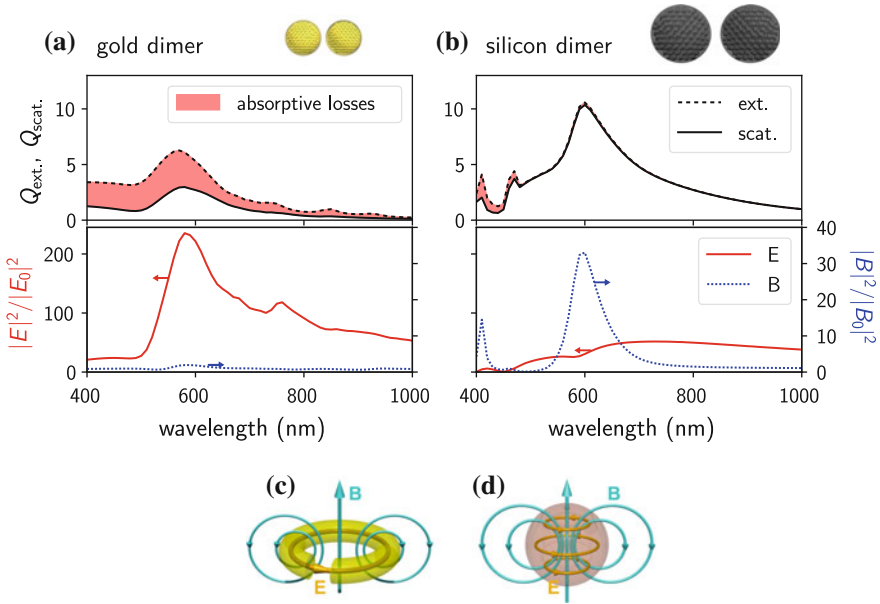


**Fig. 12.1** Extinction and scattering efficiency spectra (top) as well as nearfield enhancement (bottom:  $\mathbf{E}$ -field: red,  $\mathbf{B}$ -field: blue) in the gap of **a** a dimer of two silicon spheres with radius  $R = 80\text{ nm}$  and **b** a gold dimer of nano-spheres with  $R = 40\text{ nm}$ . Gap is  $R/4$  in both cases. Sizes were chosen to obtain resonances around  $\lambda = 600\text{ nm}$ . Incident plane wave polarized along dimer axis. Dimers are placed in vacuum. A sketch of the model and numerical mesh used in the simulations for the gold and silicon dimers is shown above the plots. **c, d** illustration of the mechanism for obtaining strong magnetic fields in (c) plasmonics using a circular current density in a metal nano-ring and (d) in dielectrics, occurring naturally via the curl of the electric displacement current in geometries as simple as spheres (**c, d** reprinted by permission from Macmillan Publishers Ltd from [54], copyright 2012)

contribution to the local density of photonic states (LDOS) in the vicinity of nanostructures can be probed using appropriate SNOM tips (gold-ring coated tips for sensing the  $\mathbf{B}$ -field [16, 28]; tips prepared with rare-earth-ion doped nano-crystals, e.g. using  $\text{Eu}^{3+}$ , for the magnetic LDOS [2, 23]), it is experimentally far more demanding to access the intrinsic field enhancement. While no measurement was reported in the visible regime, strong magnetic field enhancement in dielectric cylinders has recently been experimentally demonstrated at THz frequencies [51].

### 12.1.3 General Applications of Dielectric Nano-structures

High-index dielectric nanostructures are increasingly used in many nano-optical applications, often—but not exclusively—as alternatives to their lossy plasmonic equivalent.

In perfect analogy to plasmonics, it is possible to design color filters [112] and (color) holograms [58, 118] or to use dielectric nano-structures for “color-printing” at the diffraction limit [37, 83].

Field-enhanced spectroscopy can even more benefit by replacing plasmonic-based substrates with dielectric nanoantenna-based substrates for two main reasons. The first reason is the prevention of the reabsorption of the generated fluorescence or Raman signal that occurs in the metal nanostructures [17, 18, 43, 86, 106]. The second reason is that heat generation can be almost completely suppressed using dielectric nanoantennas, while plasmonic structures suffer from strong local heating [4, 5]. This point is important to realize very sensitive biosensors [13], as a slight increase of temperature can be fatal for fragile biomolecules or simply decrease the luminescence intensity.

Further applications of photonic nano-particles based on dielectric materials can be found in photovoltaics: The geometrical structure of the photovoltaic junction can be shaped such that its absorption covers optimally the solar spectrum. It has been shown that already simple geometries like nano-blocks or nanowires can significantly improve the absorptive coverage of the solar spectrum, compared to two-dimensional layers used in commercial photovoltaic cells [21, 50]. A different approach is to design dielectric (low-loss) nano-antennas able to trap and redirect the incoming solar light towards the classical (planar) photovoltaic junction [15, 82].

Finally, the strong field enhancements occurring at the resonant modes of dielectric nanostructures can be used to promote nonlinear optical effects. For instance, it has been shown that surface second harmonic generation (SHG) can be strongly enhanced in dielectric nanoparticles [18, 60, 107, 109]. Also the third harmonic generation (THG) can be significantly enhanced [69, 95] and its emission can be tailored [96, 105] in silicon nano-particles, by making use of their magnetic resonances. Even ultrafast all-optical switching of the optical transmission has been demonstrated using silicon nano-discs [97].

## 12.2 Fano Resonances and Kerker’s Conditions

Fano resonances occur due to the interference between two scattering amplitudes, when a resonant state energetically lies in a background of continuous states. If the scattering amplitudes of the resonance and the background are of comparable magnitude, the cross section of the Fano resonance follows a very characteristic, asymmetric lineshape. Although Ugo Fano originally considered the interference between a single state with a continuum [36], very similar resonance profiles occur if a narrow resonant state interferes with a significantly broader state. Such interference between two resonant states of similar amplitude but different linewidths are nowadays often colloquially called *Fano resonances*. The Fano lineshape can be written as



$$\sigma(E_r) \propto 1 + \frac{q^2 + 2qE_r - 1}{1 + E_r^2} \quad (12.1)$$

with the reduced energy

$$E_r = \frac{E - E_0}{\Gamma/2}, \quad (12.2)$$

where  $E_0$  is the position of the resonance and  $\Gamma$  its spectral width. The amplitude of the background state(s) is considered constant over the spectral range of the Fano profile.  $q$  is called the *Fano parameter*, which corresponds to the ratio between the resonance amplitude and the non-resonant background. Note that in the limit of a very strong resonance on a weak background, (12.1) converges towards a Lorentzian. On the other hand, for  $q \approx 1$  a strong interference between the resonance and the background exists, which results in the typical line shapes. The cases  $q = 0.5$ ,  $q = 1$ , and  $q = 2$  are shown in Fig. 12.2a.

For a detailed coupled mode theory of Fano resonances in optical resonators, see also [35].

### 12.2.1 Fano in Nano-optics

Optical Fano resonances in photonic nanostructures allow to obtain anomalous, usually very sharp mode signatures in the scattering or extinction spectra. The most prominent structure geometry which pronounces Fano-like mode profiles is the class of oligomers: Ordered arrangements of several nano-particles. Tailorable Fano resonances have been observed for example in dielectric oligomers. The resonances occur as a result of an interference between the magnetic resonance of each individual constituent and a collective magnetic response of the entire system and can be tailored by the size and distance between the individual particles [47]. Also in plasmonic oligomers Fano resonances occur, for instance due to interference between electric and magnetic modes [8]. Using an asymmetric arrangement of plasmonic particles, it is even possible to create an optical “Fano-switch” [24]: Via the polarization of the incident light, the Fano resonance can be toggled on and off, as shown in Fig. 12.2b.

But Fano-like scattering profiles are not limited to complex geometrical arrangements like the above mentioned oligomers. In fact, Fano resonances occur in very simple systems such as individual, dielectric nanowires of rectangular cross-section with relatively high aspect-ratio. Narrow Fano lineshapes appear in the scattering spectra of such nanowires, at which the scattering rapidly drops, while absorption strongly rises. This can be explained by a spectrally sharp guided mode along the NW width, which interferes with a spectrally broad leaky mode resonance [34]. A similar kind of Fano resonance due to the interference between guided modes (along the NW axis) and Mie resonances has recently been described in short dielectric nanowires [1]. For a detailed review on Fano resonances in photonics, we would like to point to [59].

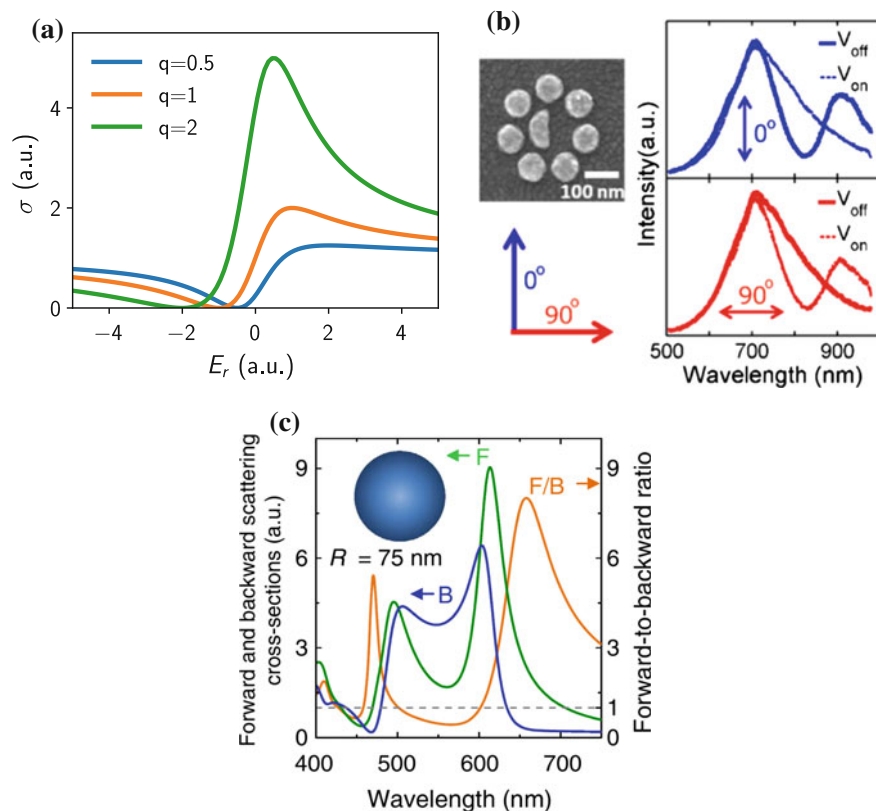


**Fig. 12.2** **a** Fano profiles for Fano parameters  $q = 0.5$ ,  $q = 1$  and  $q = 2$ . **b** Plasmonic “Fano switch”, which allows to toggle the polarization dependent transmittance of a metallic structure embedded in a liquid crystal via a switchable Fano resonance, reprinted with permission from [24]. Copyright 2012 American Chemical Society. **c** Directional resolved scattering spectra from a silicon nano-sphere of radius  $R = 75$  nm, reprinted by permission from Macmillan Publishers Ltd from [38], copyright 2013

### 12.2.2 Kerker’s Conditions at Optical Frequencies

A special type of Fano resonance was studied by Kerker et al. in hypothetical magneto-dielectric nanospheres, for which they found conditions at which exclusive forward (FW) or backward (BW) scattering occurs [52]. Kerker et al. described two possible configurations, called the *Kerker’s conditions*. The first Kerker’s condition requires equal electric permittivity and magnetic permeability ( $\epsilon_r = \mu_r$ ), at which zero-backward scattering occurs. The second Kerker’s condition predicts zero-forward scattering if the first order magnetic Mie coefficient and first order electric Mie coefficient are of equal value but of opposite sign ( $a_1 = -b_1$ ).

In contrast to particularly designed metamaterials [79], no known material in nature has a direct response to rapidly oscillating magnetic fields. Hence,  $\mu_r$  is unitary in dielectric nano-particles. However, equally strong electric and magnetic resonances can *de-facto* fulfill the first Kerker's condition, if they overlap energetically [44, 75]. The second condition on the other hand contradicts the optical theorem and is therefore unphysical. Nevertheless, *almost* zero-forward scattering can still be achieved, however scattering efficiencies are in that case usually considerably lower compared to the first Kerker's condition (zero-backward scattering) [7, 75, 110].

Note that, although the Kerker's conditions were originally derived for spherical particles, it has been shown later that they have their origin in a cylindrical symmetry and can hence be generalized to particles of cylindrical symmetry, excited along their long axis [117].

### 12.2.3 Directional Scattering From Nanoparticles

#### Directional Scattering from Nanospheres and Small Particles

The possibility to *de facto* fulfill the Kerker's conditions at visible wavelengths for unidirectional forward and backward scattering has been first discussed around 2010 for spherical high refractive index dielectric nanoparticles (silicon or germanium) [39, 44, 75]. For instance, spectra showing the directional scattering of light from an individual silicon nanosphere are presented in Fig. 12.2c. It turned out that the directionality of light scattering occurs in many kinds of dielectric nanoparticles, like individual nanocubes or nanocube dimers [19]. It has been shown as well, that the luminescence of emitting dipoles placed near the surface of spherical dielectric nanoparticles can be focused in a preferred direction via simultaneous excitation of electric and magnetic modes in the spheres [91]. The same effect has been predicted for quantum emitters embedded inside dielectric nanodiscs [87].

The experimental demonstration of Kerker-type scattering in the visible range was achieved about two years after the theoretical prediction. In early 2013, two research groups around Novotny and Luk'yanchuk published almost at the same time their results on exclusive forward or backward scattering from dielectric nanoparticles [38, 80]. Since then, similar results have been achieved for different geometries of dielectric nanoparticles, like nanodiscs [102], nanospheroids [64] or nanosphere dimers for switchable directional scattering [6, 100, 114].

The main insight of all these works is that dielectric spheres permit a spectral overlap of electric and magnetic dipolar resonances, thus allowing to effectively satisfy Kerker's conditions and obtain a distinct directional scattering.

#### Directional Scattering from Nanowires

In a nanosphere excited with a linearly polarized plane wave, transverse electric (TE) and transverse magnetic (TM) polarizations are not separable, hence the according modes are always simultaneously excited. In the case of normally illuminated nanowires by the plane wave on the other hand, it is possible to excite either TE or

TM modes by choosing an illumination with a polarization either perpendicular, or parallel, to the NW axis. In that case, it becomes impossible to obtain spectrally overlapping electric and magnetic resonances, so that Kerker's conditions (for instance  $a_1 = -b_1$ ) cannot be satisfied.

Several propositions have been made to overcome this limitation and generate Kerker-type directional scattering from nanowires (NWs) as well. For instance, by using hybrid plasmonic/dielectric materials in core-shell NWs, an electric/magnetic response can be tailored, leading to directional scattering [62] (a concept which, by the way, has been successfully applied also to “non-wire” nano-particles [42]). In this context it has been demonstrated that properly designed plasmonic/dielectric core-shell NWs can be even rendered invisible thanks to destructive interference between electric and magnetic modes [63]. However, the implementation of plasmonic components would increase losses due to absorption in the metal, as well as the complexity of the object fabrication. In that regard, all-dielectric solutions seem advantageous. In analogy to metal/dielectric hybrid NWs, Kerker-type directional scattering can occur in NWs with a radially anisotropic refractive index [61]. Likewise, the invisibility effect can be achieved in multilayer all-dielectric NWs [71].

### **Directional Scattering from Complex Dielectric Nanostructures**

Obviously, complex geometries can be used to tailor the spectral positions of electric and magnetic resonances. Without going in much detail, Let us refer to two examples as illustration.

First, it has been shown that V-shaped dielectric resonators can be designed for bidirectional color routing (in perpendicular directions with respect to the incidence). This directionality has been found to be a result of interference between electric dipolar, magnetic dipolar as well as an electric quadrupolar mode. Furthermore, the left/right color routing effect is observed in addition to the occurrence of an unidirectional forward/backward scattering [56].

As a second example for tailored scattering behavior, we would like to mention a study on semi-hollow nano-discs, i.e. nanorings in which the central hole goes not through the entire height. Such geometry allows to create a bianisotropic directional scattering, which is dependent on the illumination direction. In other words, light is scattered purely in forward direction, or not—depending on its incidence direction. These nanostructures could be used to design reflective metasurfaces, which is only possible thanks to the anisotropy of the individual metasurface unit-cells, inducing a  $2\pi$  phase shift in the reflected amplitude. Off resonance, the dielectric metasurface is transparent, which would be impossible using metallic mirrors, due to their high ohmic losses [3].

### **12.2.4 Applications of Nanoscale Directional Scattering**

The last part of this section is dedicated to an overview on some useful applications of directional scattering by nanoscale particles.

We previously discussed the example of a dielectric metasurface as a lossless mirror, which can be also designed to offer an incidence-dependent reflectivity [3]. Other all-dielectric metasurfaces have been proposed, offering a generalized Brewster effect for arbitrary angles and wavelengths [77]. Such metasurfaces are particularly promising for applications in photovoltaics: Light-trapping could significantly reduce reflective losses and increase the efficiency of state-of-the-art solar cells [57, 66, 73, 82, 101].

The possibility to render a nanowire completely invisible [63, 71] has been proposed as a tool to design invisible electric circuits [33].

Directional scattering of the radiation from quantum emitters by dielectric nanoparticles has been theoretically predicted [89, 91, 115] and recently also experimentally demonstrated [25, 81]. Together with the Purcell effect—the decay rate enhancement for emitters in the proximity of nano-structures [84]—the directionality in the emission renders dielectric particles and nanowires very promising for many applications in field enhanced spectroscopy. However, the position of the emitter with respect to the particle is crucial for the scattering directionality. This sensitivity to the emitter location holds generally, for quantum emitters outside [90] as well as for such embedded inside dielectric nano-particles [87]. On the other hand, this supposed drawback can be actually an advantage and might be used in far-field measurements to gain information about the emitter location on a subwavelength scale. Using Kerker-type scattering effects, the emission from a nanostructure itself, such as photoluminescence [14, 76, 85] or nonlinear effects like second harmonic generation [22, 113], can be focused into a preferred direction, which is useful in the detection of weak signals from individual nanostructures.

## 12.3 Mie Theory

In this section, we will explain Kerker-type directional scattering in the context of Mie theory for nanospheres and adapt the same idea in a slightly modified form to infinitely long cylinders (i.e. nanowires). The results are mainly excerpted from an earlier publication. Therefore, for more details see also [110].

Mie theory provides an analytical description of the response of spherical or cylindrical particles (with an infinitely long axis in the latter case) to an incident optical field. The far-field response to an external illumination is written as a multipole series whose coefficients—the “Mie scattering coefficients”  $a_i$  and  $b_i$ —can be regarded as weights for corresponding electric ( $a_i$ ) and magnetic ( $b_i$ ) multipole moments. The expressions “electric” and “magnetic” also refer to the fact that the magnetic, respectively electric field components, are zero in the scattering plane.

As a short remark we would like to mention that it has been demonstrated, that the Mie coefficients for a cylinder can be written equivalently as a series of Fano profiles, which is explained by the interference between the continuum of modes represented by the incident field and a (sharper) resonant mode (a Mie resonance of the cylinder) [92]. Even though this is not directly linked to the demonstration below,

it is an interesting interpretation of Mie resonances, adding a different viewpoint on them in general.

### 12.3.1 Directional Scattering from Spheres and Cylinders

#### Nanospheres

In the description of the light scattering in spherical particles (which is the “classical” Mie theory), all fields are expanded in vector spherical harmonics, leading to a kind of multipole development. Scattering to the far-field can be written using the scattering amplitude matrix (S-matrix), which connects the incident field  $\mathbf{E}_i$  with the scattered field  $\mathbf{E}_s$  [11]

$$\begin{bmatrix} E_{s,\parallel} \\ E_{s,\perp} \end{bmatrix} = \frac{e^{-ik(R-z)}}{ikR} \begin{bmatrix} S_2 & 0 \\ 0 & S_1 \end{bmatrix} \begin{bmatrix} E_{i,\parallel} \\ E_{i,\perp} \end{bmatrix}. \quad (12.3)$$

$k = 2\pi/\lambda$  is the wavenumber,  $e^{-ikR}/(ikR)$  the scattered (outgoing) wave with  $R$  the distance to the sphere center and  $e^{ikz}$  is the incident plane wave. For simplicity, we will now assume that the sphere is sufficiently small, such that only the first order of the development has a significant magnitude. In this case the two nonzero S-matrix elements write [11, 48]

$$\begin{aligned} S_1 &= \frac{3}{2} (a_1 + b_1 \cos(\varphi)), \\ S_2 &= \frac{3}{2} (a_1 \cos(\varphi) + b_1). \end{aligned} \quad (12.4)$$

In (12.4),  $\varphi$  is the scattering angle with respect to the incident wave vector, and  $\varphi = 0$  corresponds to the forward direction. This directly leads to the well-known conditions for exclusive BW or FW scattering:

$$\begin{aligned} S_i \Big|_{\varphi=0} &\propto (a_1 + b_1) = 0 \quad \text{for pure BW scattering (2. Kerker),} \\ S_i \Big|_{\varphi=\pi} &\propto \pm(a_1 - b_1) = 0 \quad \text{for pure FW scattering (1. Kerker).} \end{aligned} \quad (12.5)$$

#### Nanowires

Infinitely long cylinders can also be treated using Mie theory by developing the fields in vector *cylindrical* harmonics. Under normal incidence, the Mie S-matrix writes in this case [11]

$$\begin{bmatrix} E_{s,\text{TM}} \\ E_{s,\text{TE}} \end{bmatrix} = e^{i3\pi/4} \sqrt{\frac{2}{\pi k R}} e^{ikR} \begin{bmatrix} T_1 & 0 \\ 0 & T_2 \end{bmatrix} \begin{bmatrix} E_{i,\text{TM}} \\ E_{i,\text{TE}} \end{bmatrix}. \quad (12.6)$$

$k = 2\pi/\lambda$  is the wavenumber and  $R$  the distance to the cylinder axis. As for nanospheres, we assume nanowires of sufficiently small diameter, such that only the lowest two orders significantly contribute to scattering, leading to

$$\begin{aligned} T_1 &= b_1 + 2b_2 \cos(\varphi) \\ T_2 &= a_1 + 2a_2 \cos(\varphi). \end{aligned} \quad (12.7)$$

Again,  $\varphi$  is the scattering angle with respect to the incident wave vector with  $\varphi = 0$  the forward direction.

Under normal incidence, the transverse magnetic (TM) polarized components of the scattered field are proportional to the S-matrix component  $T_1$  (respectively, the transverse electric (TE) components are proportional to  $T_2$ ). According to (12.7), scattering from a TE polarized normally incident plane wave ( $\mathbf{E} \perp$  NW axis) is only due to the “electric” multipole contributions  $a_i$ . On the other hand, a TM polarized illumination ( $\mathbf{E} \parallel$  NW axis) induces scattering exclusively via the “magnetic” Mie terms  $b_i$ .

In perfect analogy to (12.5) we find

$$\begin{aligned} T_1 \Big|_{\varphi=0} &= b_1 + 2b_2 = 0 && \text{for pure BW scattering, and} \\ T_1 \Big|_{\varphi=\pi} &= b_1 - 2b_2 = 0 && \text{for pure FW scattering.} \end{aligned} \quad (12.8)$$

The same conditions hold for TE polarization with  $T_2$  and the “electric” coefficients  $a_i$ . The main difference to the case of a sphere is that we do not have an interference of dipolar electric and dipolar magnetic modes anymore, but an interference between dipolar and quadrupolar modes of the same, “electric” or “magnetic”, character, depending on the incident polarization. In the upper panels of Fig. 12.3, the Mie coefficients  $a_1$  and  $b_1$  for a silicon sphere (Fig. 12.3a) are compared to the coefficients  $a_1$  and  $a_2$  of a silicon nanowire as function of the wavelength. Indeed, the coefficients show very similar spectral dependencies, which holds equally for their amplitude and phase. Comparing the FW/BW scattering spectra of both geometries (bottom plots in Fig. 12.3), the similarity in Mie coefficients is reproduced. Please note also the Fano-like profiles in the scattering resonances, shown in Fig. 12.3: The interference of a spectrally narrow mode (electric mode for the sphere, “ $a_2$ ”-mode in the case of the nanowire) with a spectrally large “background-mode” (sphere: magnetic mode, nanowire: “ $a_1$ ”-mode) leads to the directional response and a Fano-like line shape.

We conclude that interference of multiple spectrally overlapping orders of either electric or magnetic modes in dielectric nanowires can lead to similar FW/BW scattering phenomena as interfering electric and magnetic dipole resonances in dielectric nano-spheres. Different behaviors, hence different directions of light scattering, could be addressed by incident light polarization.

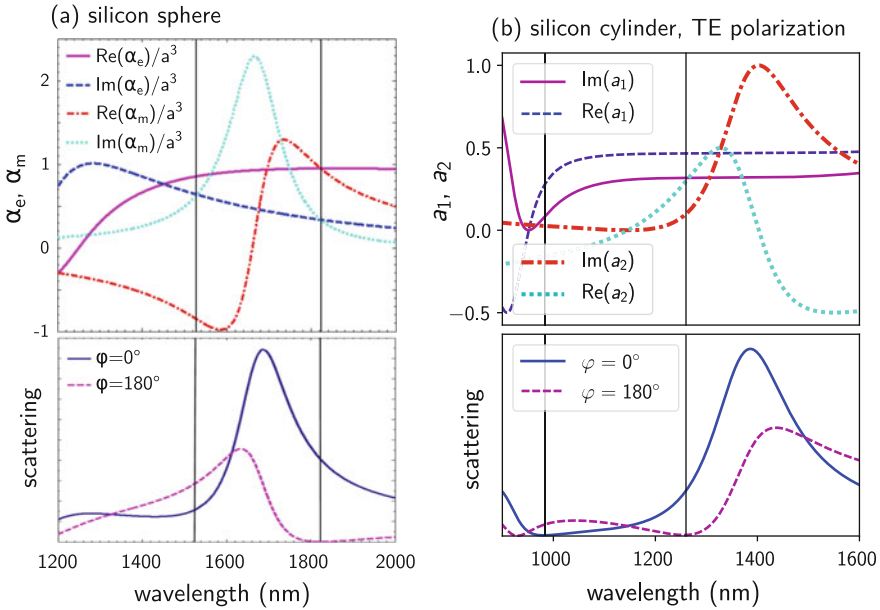


**Fig. 12.3** **a** Electric and magnetic polarizability for a silicon sphere ( $\epsilon = 12$ ) of radius  $R = 230$  nm (top) and directional scattering intensity ( $\varphi = 0^\circ, 180^\circ$  correspond to FW, BW direction). Adapted with permission from [75]. Copyright OSA, 2011. Note that the quantities in the top plot of **(a)** are proportional to the first order (spherical) Mie coefficients:  $\alpha_e \propto ia_1$  and  $\alpha_m \propto ib_1$  [39]. **b** First and second order electric (TE) Mie coefficients  $a_1$  and  $a_2$  for a silicon nanowire with  $R = 230$  nm. Bottom: Scattered intensity in FW ( $\varphi = 0^\circ$ ) and BW ( $\varphi = 180^\circ$ ) direction. Colors are chosen for direct comparison with **(a)**. The vertical black lines indicate a maximum in BW/FW (left line) and FW/BW (right line) scattering ratio, hence positions where the second, respectively first Kerker’s condition are (approximately) satisfied

### 12.3.2 Nanowires: Resonant Enhancement of the Electric and Magnetic Field

It is possible to expand the electromagnetic fields inside the cylinder in the same way as the scattered near- or far-field. For details, please refer to the textbook of Bohren and Huffman [11]. In Fig. 12.4 we show the average field intensity enhancement inside a silicon NW (SiNW) of radius  $R = 50$  nm for illumination with (a) TE and (b) TM polarized plane waves, respectively. The silicon dispersion is taken from the book of Palik [30]. At resonance, we observe for both the TE and for TM cases not only high electric field intensities (blue lines), but also a strong enhancement of the magnetic field (orange lines). The magnetic field increases even far stronger compared to the electric field intensity, an observation which is in agreement with recent experimental results from dielectric cylinders in the GHz regime [51]. We conclude that a simultaneous excitation of strong electric and magnetic fields occurs in dielectric, non-magnetic (i.e.  $\mu_r = 1$ ) NWs, even under pure TE or TM polarized



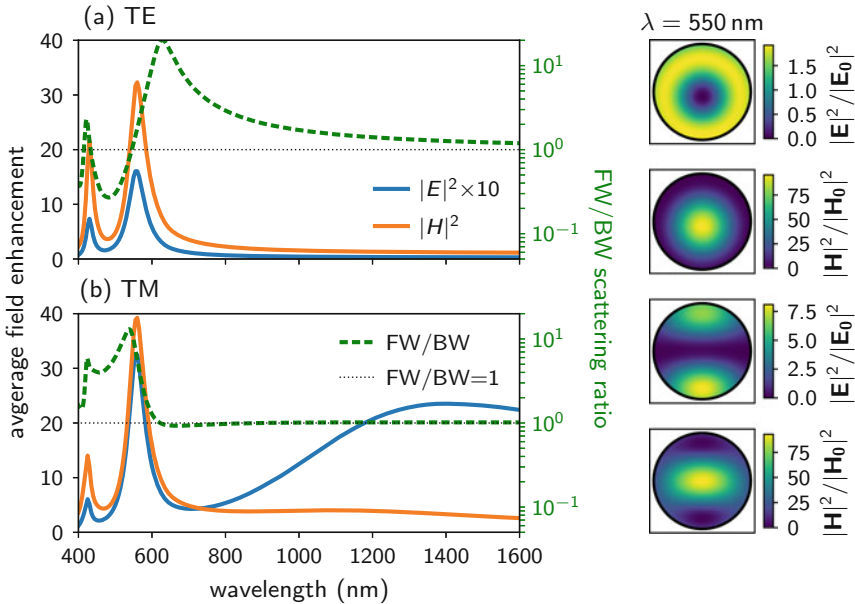


**Fig. 12.4** Spectra of the average electric (blue lines) and magnetic (orange lines) field intensity enhancement inside a silicon nanowire of radius  $R = 50$  nm. Incident plane wave polarized **a** TE and **b** TM. For comparison, the FW/BW ratio of far-field scattering is also shown (dashed green lines, logscale). Right: internal field intensity distributions at  $\lambda = 550$  nm (around the TE<sub>01</sub>/TM<sub>11</sub> mode). Top: electric, bottom: magnetic field enhancement. Incidence from the top. The fields are calculated using Mie theory and normalized to the illumination field intensity

illumination and normal incidence. Hence, in analogy to the findings of Kerker et al., the observed directionality (dashed green lines in Fig. 12.4) can be interpreted as a result of the interference between “effective” electric and magnetic modes. In particular, at the non-degenerate, fundamental TM<sub>01</sub> mode ( $\lambda \approx 1400$  nm), where only the internal electric field shows a resonant enhancement while the magnetic field intensity follows a flat line beyond  $\lambda \gtrsim 700$  nm (see Fig. 12.4b), no directional scattering is obtained. This is also the case for any small diameter nanowire supporting the fundamental resonant mode only. For illustration the electric and magnetic field intensity patterns inside the NW are shown on the right of Fig. 12.4 at  $\lambda = 550$  nm.

### 12.3.3 Nanowires: Multipolar Contributions to Directional Scattering

Previously, we used only the two first coefficients of the field expansion. We want to assess if this approximation remains valid for larger NWs, and how many orders of multipole contributions are necessary to describe with a sufficient agreement the directional scattering phenomena. Let us illustrate this empirically by taking a SiNW

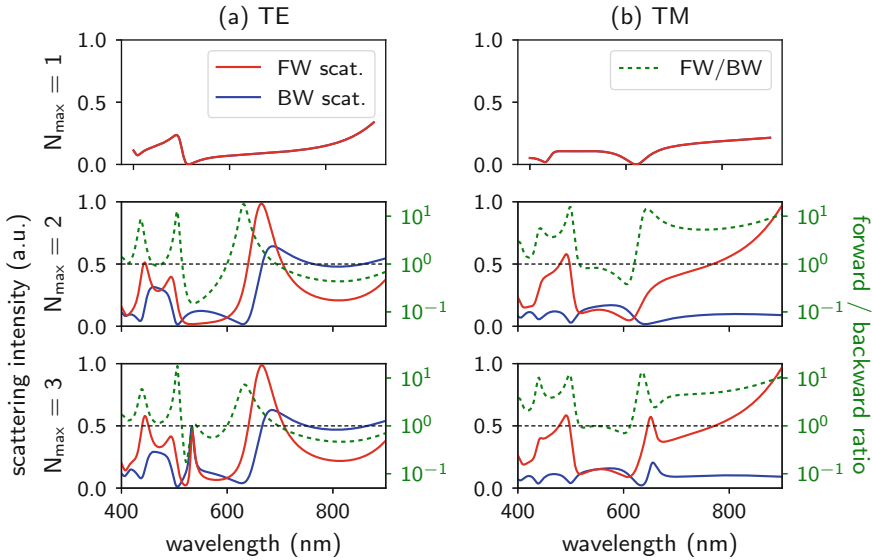


**Fig. 12.5** Mie development of the FW/BW scattering from a SiNW with radius  $R = 100$  nm for the first 3 Mie coefficients (TE:  $a_n$ , TM:  $b_n$ ). **a** TE, **b** TM polarized incident plane wave.  $N_{\max}$  corresponds to the number of Mie terms:  $n = 0$ ,  $n \in \{0, 1\}$ ,  $n \in \{0, 1, 2\}$  (from top to bottom). TE/TM data is normalized separately. FW/BW ratios (green dashed lines) are plotted on a logscale

of radius  $R = 100$  nm for example. Since directional scattering is a result of the interference between multiple simultaneously excited modes, the FW/BW resolved scattered intensity cannot be plotted individually for the different contributing scattering coefficients  $a_n$  and  $b_n$  (for TE and TM polarized, normal incidence, respectively). In Fig. 12.5, the FW and BW scattered intensity from a normally illuminated SiNW ( $R = 100$  nm) is calculated successively for an increasing number of contributing terms. Figure 12.5a shows the scattering under TE polarized illumination, Fig. 12.5b the TM case. We have shown elsewhere [110] that for a NW of  $R = 50$  nm radius, terms higher than the first two orders are negligible. Yet, even for a larger NW as shown in Fig. 12.5, the response is mostly determined by the first two orders of the Mie series, while only few additional features arise if third order modes are considered as well. In conclusion, despite some missing spectral features, using only the first two Mie orders gives already a very good approximation even in the case of large dielectric NWs.

## 12.4 Directional Scattering from Silicon Nanowires

In this section, we present experiments performed on silicon nanowires showing the directional scattering phenomenon as function of size and shape. We compare the experimental data to Mie theory and numerical simulations, confirming the accuracy

of the predictions. Having confirmed the validity of our approach, we analyze theoretically a more sophisticated system of two normally illuminated parallel nanowires, lying on a plane. We find that such a system can be used to switch the scattering direction between forward and backward, simply by changing the distance between the two wires.

### 12.4.1 Cylindrical Nanowires

We start with the simplest possible geometry: A cylindrical SiNW in vacuum. The SiNWs are VLS grown [29] and dispersed on a transparent silica substrate with lithographic markers, so the exactly same NW can be examined on different experimental setups. We perform standard dark field microscopy either in reflection (BW scattering) or in transmission geometry (FW scattering). The measurement setup is schematically shown in Fig. 12.6a, b for FW and BW scattering, respectively. Details on the technique are described elsewhere [110]. The incident light is polarized either perpendicular (TE) or along the NW axis (TM), as illustrated in Fig. 12.6c. We use the scattering from small cylindrical nanowires ( $R \approx 25$  nm) for normalization of the FW and BW spectra: In sufficiently small NWs only the fundamental dipolar  $TM_{01}$  mode is excited, which results in an omni-directional scattering (corresponding to a dipolar source along the NW axis, as explained in the previous section). We hence assume that the FW and BW scattered intensities are of equal strength and normalize all spectra using this reference. We compare our experimental results to Mie theory and 2D simulations by the Green dyadic method (“GDM”, assuming structures of infinite length along  $Y$  [67, 78]). The GDM simulations reproduce Mie with almost perfect agreement (see also [110]).

Results of the scattering experiments on a SiNW of radius  $R \approx 50$  nm are shown in Fig. 12.6d for TE (top) and TM (bottom) illumination. In the case of TE polarized illumination FW scattering occurs for large wavelengths ( $\lambda \gtrsim 550$  nm), while BW scattering takes over at shorter wavelengths ( $\lambda \lesssim 550$  nm). In the TM case on the other hand, FW scattering dominates over the whole accessible spectral range, however with a pronounced peak around 550 nm, where a maximum of scattered FW intensity coincides with a minimum in BW scattering. Near-field plots and corresponding far-field scattering patterns are shown in Fig. 12.6e (top and bottom, respectively) for selected wavelengths, indicated by dashed black lines in Fig. 12.6d. Note that around 480 nm, we obtain the possibility to invert the main scattering direction by simply flipping the polarization from TM to TE (see also Fig. 12.6e, bottom left). Via the NW diameter, this spectral zone can be tuned to other frequencies. At longer wavelengths ( $\lambda \gtrsim 700$  nm), only the nondegenerate  $TM_{01}$  mode exists, leading to very weak overall scattering under TE incidence and to the aforementioned, omni-directional radiation pattern in the TM geometry. Interestingly, while it is possible to induce directional BW scattering in the TE configuration, under TM illumination BW scattering is generally very weak and mainly FW scattering occurs—with the exception of a uniform scattering when only the  $TM_{01}$  mode is excited.

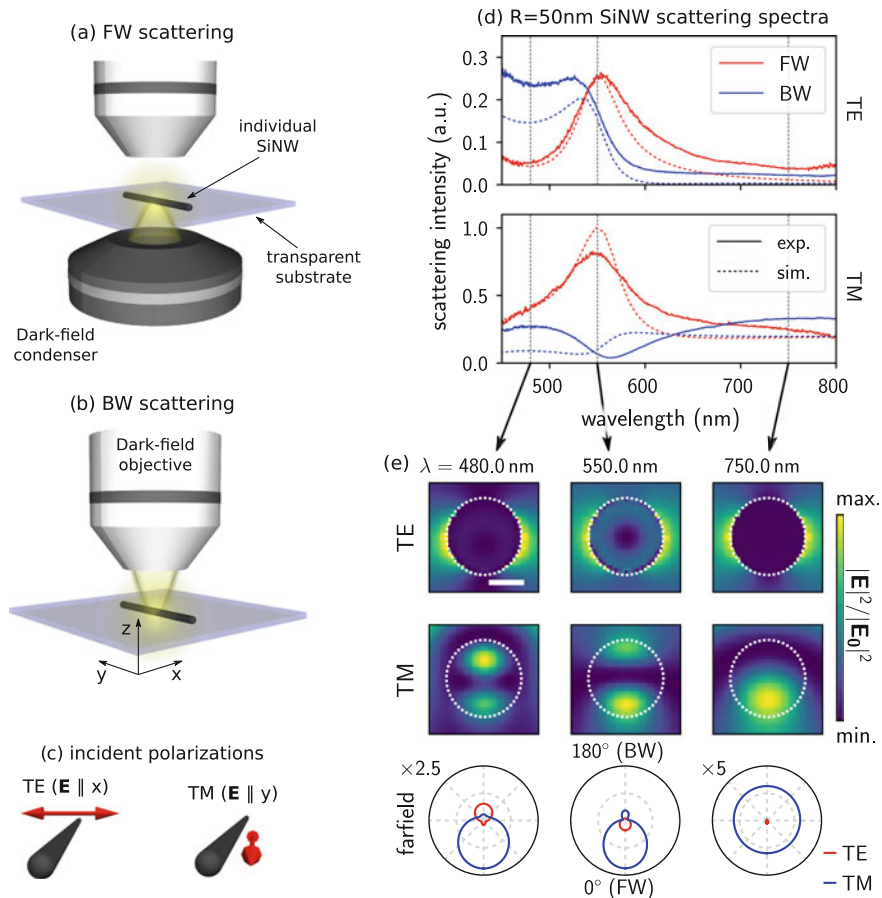


**Fig. 12.6** Sketch of the experimental setup for **a** forward scattering and **b** backward scattering measurements. **c** Incident polarization configurations. The electric field is orientated either perpendicular (TE) or parallel (TM) to the NW axis. **d** Experimental (solid lines) and simulated (dashed lines) FW/BW scattering spectra (red/blue) for a cylindrical silicon NW of diameter  $R \approx 50$  nm. Top and bottom plot show the case of TE and TM polarized incident plane waves, respectively. **e** Mie-calculated nearfield (top row: TE, center row: TM incidence) and farfield patterns (bottom row; TE/TM: red/blue) for a  $R = 50$  nm SiNW diameter at selected wavelengths, indicated by dashed vertical lines and arrows in **(d)**. Plane wave incident from the top. Scale bar is 50 nm

In summary, we note that although we do observe BW scattering (mainly under TE polarization) it mostly remains weak compared to the FW scattered light. In the case of TM polarized illumination, the FW/BW scattering ratio is even almost exclusively  $\gtrsim 1$ .

### 12.4.2 Rectangular Nanowires

In a second step we analyze what happens if the cylindrical symmetry of the nanowire cross section is broken. We therefore fabricate SiNWs of rectangular section by electron beam lithography (EBL) and subsequent dry-etching [41, 45] on a silicon-on-quartz (SOQ) substrate [72]. A great advantage of our top-down approach on SOQ is the possibility to create silicon nanostructures of arbitrary shape by EBL on a transparent substrate from single crystalline silicon. Using this material rather than deposited polycrystalline or amorphous silicon guarantees that the best optical properties of single crystal silicon are kept. Defined by the thickness of the silicon layer on the SOQ substrate ( $H = 90$  nm), the height of the rectangular nanowires is constant. The rectangular section is varied by changing the SiNWs width. The length  $L = 7$   $\mu\text{m}$  is chosen large compared to the focal spot of the illuminating optics in order to obtain a purely Mie-like response [103]. All NWs have excellent surface properties, low roughness and steep flanks, verified by scanning electron microscopy.

The results of our systematic FW/BW scattering measurements are shown in Fig. 12.7c (for TM polarization). Selected spectra for SiNWs of width  $W = 120$  nm and  $W = 180$  nm are shown in Fig. 12.7a, b, respectively, where TE polarized illumination is shown in the top, the TM case in the bottom plot. The comparison of experiments with GDM simulations shows a very good agreement. Having a look at the FW/BW ratios (Fig. 12.7c, TM polarization) we observe that mostly forward scattering occurs. This is similar to our observations on cylindrical SiNWs. Figure 12.7d, e finally show selected simulated near-field plots and far-field scattering patterns for TM polarized illumination. In particular, the first two panels in Fig. 12.7d, e show, for a NW of nearly symmetric section, the excitation of the first strongly directional mode (corresponding to  $\text{TE}_{01}/\text{TM}_{11}$ ) and the region of omnidirectional scattering in the red spectrum (corresponding to  $\text{TE}_{01}/\text{TM}_{11}$ ), which are almost identically found as in cylindrical NWs.

Under TM excitation, we observe branches of a kind of Fano resonance, which do not occur in cylindrical NWs: In narrow spectral zones, the FW/BW ratio is almost unity (see Fig. 12.7b around  $\lambda = 580$  nm and Fig. 12.7c, white diagonal branches). In a confined spectral window the otherwise strong forward scattering is suddenly suppressed, while BW scattering increases. Resonances with such field profiles are observed neither under TE polarization, nor in symmetric SiNWs (see also [110]). These sharp features are a result of horizontal guided modes along the SiNW width ( $X$ -direction, in the NW cross-sectional plane) and their interference with the leaky “background” mode of, in comparison, large spectral width. The wire side facets act as the Fabry-Perot cavity mirrors and the nanowire slab has an effective index of  $n_{\text{eff}} = 3.45$  ( $n_{\text{Si}} \approx 4.0$ ) for the supported guided mode in the case of TM polarized illumination at  $\lambda = 580$  nm. With this effective index, a standing wave pattern with three lobes matches perfectly a nanowire width of 180 nm, in nice agreement to the wavelength and width at which the resonance occurs. The calculated near-field pattern (very right panel of Fig. 12.7d) finally confirms the presence of a guided mode. We verified the guided mode assumption also for the other branches in Fig. 12.7c,

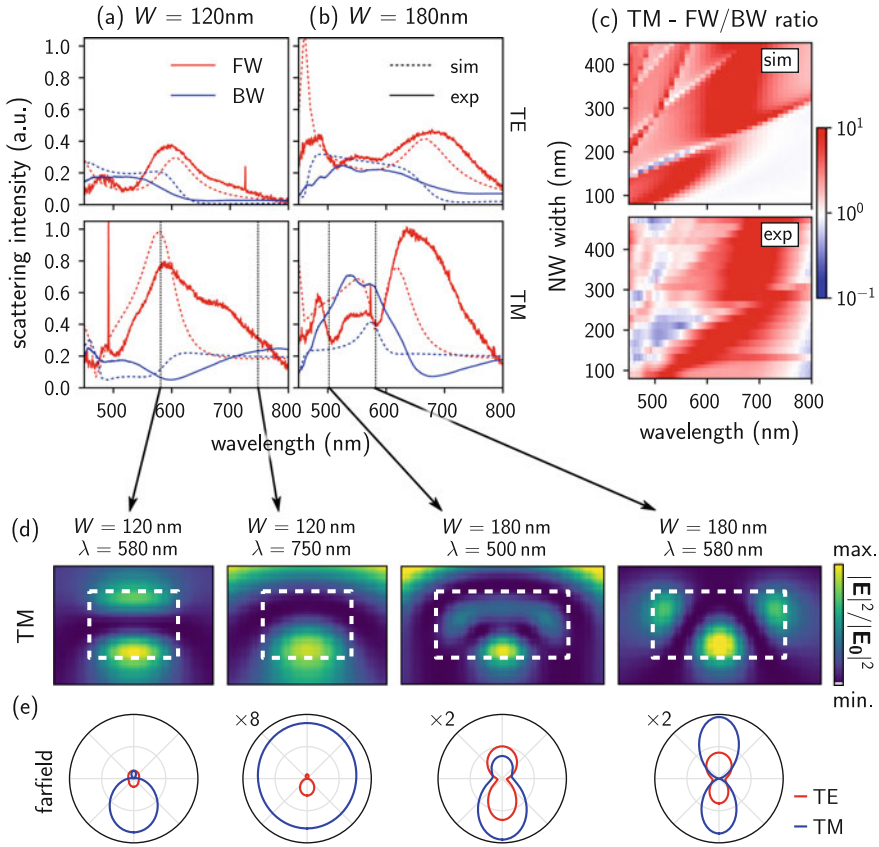


**Fig. 12.7** **a, b** Scattering spectra of rectangular shaped SiNWs of a fixed length and height  $L = 7\ \mu\text{m}$  and  $H = 90\ \text{nm}$ , with widths of **(a)**  $W = 120\ \text{nm}$  and **(b)**  $W = 180\ \text{nm}$ . Plane wave illumination, polarized perpendicular (TE, top) or along the NW axis (TM, bottom). Red lines indicate forward, blue lines backward scattering. Dashed and solid lines represent simulated and experimental data, respectively. **c** Simulated (top) and measured (bottom) FW/BW scattering ratio for TM polarization using a logarithmic color scale. **d** Nearfield intensity distribution in and around the SiNWs at selected wavelengths (indicated by vertical lines in **(a, b)** and by arrows under TM polarized illumination (incident from the top). Dashed white lines illustrate the NW shape. **e** Farfield scattering pattern for the corresponding cases shown in **(d)**. TM: blue, TE: red lines

at each of which the NW width corresponds to an odd integer multiple of half the wavelength divided by the effective index. A standing-wave pattern of increased order can be found at these positions in the near-field plots. We note that former studies on scattering from rectangular dielectric NWs used Fabry-Perot modes, reflected between the side-walls of the wire, for the analytical description of the scattering [34, 55].

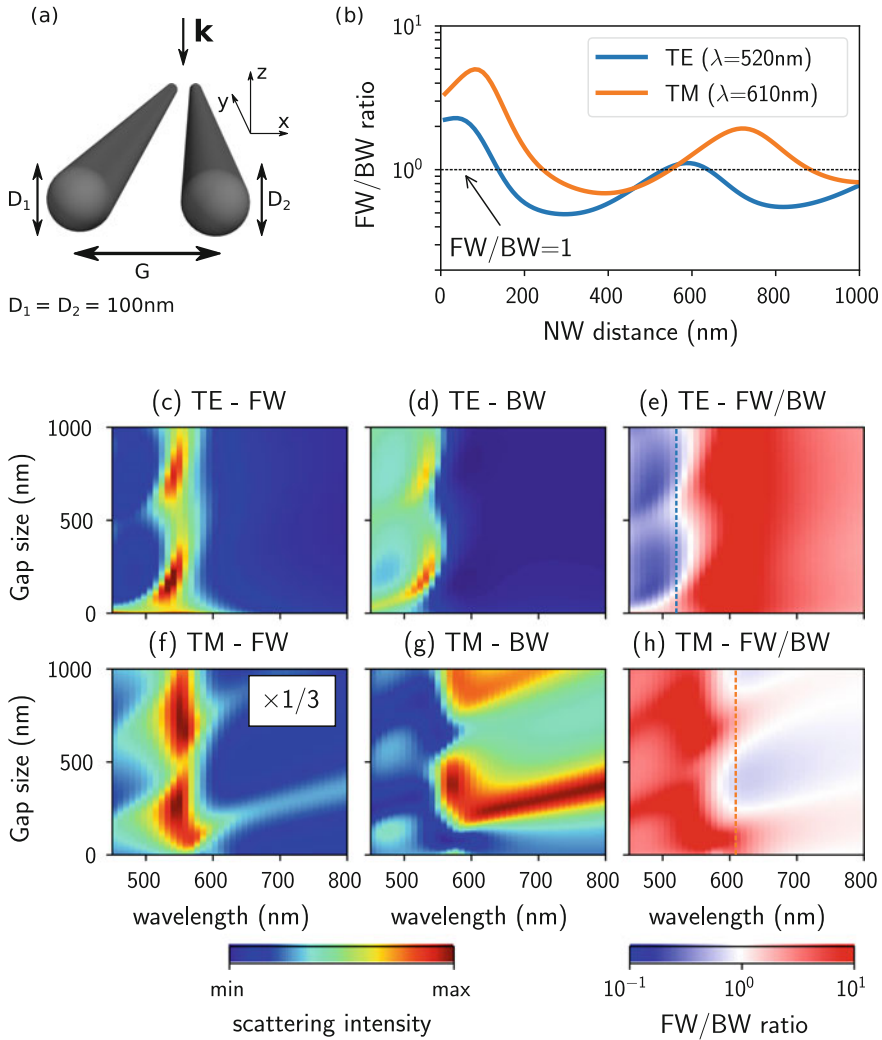


**Fig. 12.8** **a** Sketch of the geometry: Two parallel silicon NWs in the  $XY$ , of equal diameter  $D_1 = D_2 = 100\text{ nm}$  ( $\rightarrow R = 50\text{ nm}$ ) and separated by a “gap”  $G$ , are normally illuminated (along  $\hat{e}_z$ ) by a plane wave, polarized either along the mutual long axis direction (“TM”) or perpendicular to it (“TE”). **b** Simulated forward to backward scattering ratio as function of the distance  $G$  between the two NWs for two TE and TM at fixed wavelengths:  $\lambda_{\text{TE}} = 520\text{ nm}$  and  $\lambda_{\text{TM}} = 610\text{ nm}$ . **c–h** show the simulated FW/BW resolved scattering spectra of the coupled NWs as function of the gap  $G$ . **c–e** show forward scattering, backward scattering and their ratio for TE polarization, (**f–h**) similar but for TM polarization. Vertical dashed lines in (**e**) and (**h**) indicate the spectral positions of the profiles shown in (**b**). The FW/BW ratios in (**b**), (**e**) and (**h**) are shown on a logarithmic scale

### 12.4.3 Coupled Nanowires

Finally we analyze a system composed of two identical, parallel silicon nanowires illuminated normally with respect to the plane defined by their axes, as schematically shown in Fig. 12.8a. The radius of the wires is  $R = 50$  nm, (c.f. also Fig. 12.6), the incident plane wave is polarized either perpendicular (TE) or parallel to the wire axis (TM). Using the GDM, the scattered intensity is calculated in forward and backward direction. The results are shown in Fig. 12.8 as function of the incident wavelength and polarization as well as the distance between the NWs, also labeled “gap”  $G$ .

Figure 12.8c–e show (c) forward, (d) backward scattering and (e) the FW/BW ratio in the case of TE polarization. Figure 12.8f–h show the same for the TM case. We find a strong modulation of the scattering, which is in agreement with former observations in the total scattering signal [70]. Interestingly, not only the scattering intensity itself shows a modulation of high contrast; likewise, the FW/BW ratio shows a significant dependence on the distance between the two SiNWs. Figure 12.8b shows the FW/BW scattering ratio for TE (blue dashed line) and TM polarization (orange dashed line) at two fixed wavelengths of particularly strong contrast in the scattering signal. Obviously, at selected wavelengths, it is possible to toggle between mainly forward, isotropic, and mainly backward scattering simply by varying the gap size between the two nanowires. Furthermore, an interesting feature of coupled nanowires is to increase the scattering efficiency either in forward or backward direction, compared to the case of a single nanowire where it is rather low at Kerker’s conditions [99]. This is due to the fact that Kerker’s conditions are usually fulfilled out of a resonance. This observation opens perspectives for several applications in sensing or field-enhanced spectroscopy by realizing more efficient directional dielectric nanoantennas. We could for instance imagine two parallel dielectric nanowires embedded in a flexible transparent matrix for sub-wavelength optical distance measurements at visible frequencies.

## 12.5 Conclusion and Outlook

We compared plasmonics with the emerging field of high-index dielectric nanostructures and gave an overview about the recent research in nano-optics on directional scattering at the single particle level. We introduced the Kerker’s conditions, their representation for nonmagnetic materials at visible frequencies, and put them in the context of Fano resonances in general. Furthermore, we compared the conditions for unidirectional scattering in Mie theory for spherical particles and cylindrical nanowires. We experimentally demonstrated directional scattering first in the “Mie case” of cylindrical silicon nanowires, where we found the possibility to switch between forward and backward scattering by a simple rotation of the incident polarization. Subsequently, we studied the effects of an asymmetric nanowire shape. For rectangular NWs of increasing height/width aspect-ratio, we observed the apparition



of Fano-like modes due to the occurrence of spectrally sharp guided modes along the NW width. Finally, we theoretically studied a system of two coupled SiNWs and found that such an arrangement allows to toggle between FW and BW scattering, simply by adjusting the distance between the coupled wires. Optical Fano resonances in nanostructures open perspectives for light management and guiding at the nanometer scale, for sub diffraction-limited optical sensing or for applications in field-enhanced spectroscopies.

## References

1. D.R. Abujetas, M.A.G. Mandujano, E.R. Méndez, J.A. Sánchez-Gil, High-contrast fano resonances in single semiconductor nanorods. *ACS Photonics* **4**(7), 1814–1821 (2017)
2. L. Aigouy, A. Cazé, P. Gredin, M. Mortier, R. Carminati, Mapping and quantifying electric and magnetic dipole luminescence at the nanoscale. *Phys. Rev. Lett.* **113**(7), 076101 (2014). 00035
3. R. Alaei, M. Albooyeh, A. Rahimzadegan, M.S. Mirmoosa, Y.S. Kivshar, C. Rockstuhl, All-dielectric reciprocal bianisotropic nanoparticles. *Phys. Rev. B*, **92**(24):245130 (2015). 00010
4. P. Albella, R. Alcaraz de la Osa, F. Moreno, S.A. Maier, Electric and magnetic field enhancement with ultralow heat radiation dielectric nanoantennas: considerations for surface-enhanced spectroscopies. *ACS Photonics* **1**(6), 524–529 (2014)
5. P. Albella, M. Ameen Poyli, M.K. Schmidt, S.A. Maier, J.J. Sáenz, J. Aizpurua, Low-loss electric and magnetic field-enhanced spectroscopy with subwavelength silicon dimers. *J. Phys. Chem. C* **117**(26), 13573–13584 (2013)
6. P. Albella, T. Shibanuma, S.A. Maier, Switchable directional scattering of electromagnetic radiation with subwavelength asymmetric silicon dimers. *Sci. Rep.* **5**, 18322 (2015)
7. A. Alu, N. Engheta, How does zero forward-scattering in magnetodielectric nanoparticles comply with the optical theorem? *J. Nanophotonics* **4**(1), 041590–041590–17 (2010). 00055
8. S. Bakhti, A.V. Tishchenko, X. Zambrana-Puyalto, N. Bonod, S.D. Dhuey, P. James Schuck, S. Cabrini, S. Alayoglu, N. Destouches, Fano-like resonance emerging from magnetic and electric plasmon mode coupling in small arrays of gold particles. *Sci. Rep.* **6**, 32061 (2016)
9. R.M. Bakker, D. Permyakov, Y.F. Yu, D. Markovich, R. Paniagua-Domínguez, L. Gonzaga, A. Samusev, Y. Kivshar, B. Luk'yanchuk, A.I. Kuznetsov, Magnetic and electric hotspots with silicon nanodimers. *Nano Lett.* **15**(3), 2137–2142 (2015)
10. D.G. Baranov, R.S. Savelev, S.V. Li, A.E. Krasnok, A. Alù, Modifying magnetic dipole spontaneous emission with nanophotonic structures. *Laser Photonics Rev.* **11**(3), 1600268–n/a (2017)
11. C.F. Bohren, D.R. Huffman, *Absorption and Scattering of Light by Small Particles* (Wiley, 1998)
12. N. Bonod, A. Devilez, B. Rolly, S. Bidault, B. Stout, Ultracompact and unidirectional metallic antennas. *Phys. Rev. B* **82**(11), 115429 (2010)
13. N. Bontempi, K.E. Chong, H.W. Orton, I. Staude, D.-Y. Choi, I. Alessandri, Y.S. Kivshar, D.N. Neshev, Highly sensitive biosensors based on all-dielectric nanoresonators. *Nanoscale* **9**(15), 4972–4980 (2017). 00000
14. B.J.M. Brenny, D.R. Abujetas, D. van Dam, J.A. Sánchez-Gil, J.G. Rivas, A. Polman, Directional emission from leaky and guided modes in GaAs nanowires measured by cathodoluminescence. *ACS Photonics* **3**(4), 677–684 (2016)
15. M.L. Brongersma, Y. Cui, S. Fan, Light management for photovoltaics using high-index nanostructures. *Nat. Mater.* **13**(5), 451–460 (2014). 00279
16. M. Buresi, D. van Oosten, T. Kampfrath, H. Schoenmaker, R. Heideman, A. Leinse, L. Kuipers, Probing the magnetic field of light at optical frequencies. *Science* **326**(5952), 550–553 (2009)

17. M. Caldarola, P. Albella, E. Cortés, M. Rahmani, T. Roschuk, G. Grinblat, R.F. Oulton, A.V. Bragas, S.A. Maier, Non-plasmonic nanoantennas for surface enhanced spectroscopies with ultra-low heat conversion. *Nat. Commun.* **6**, 7915 (2015)
18. J. Cambiasso, G. Grinblat, Y. Li, A. Rakovich, E. Cortés, S.A. Maier, Bridging the gap between dielectric nanophotonics and the visible regime with effectively lossless gallium phosphide antennas. *Nano Lett.* **17**(2), 1219–1225 (2017). 00004
19. S. Campione, L.I. Basilio, L.K. Warne, M.B. Sinclair, Tailoring dielectric resonator geometries for directional scattering and Huygens' metasurfaces. *Opt. Express* **23**(3), 2293 (2015)
20. L. Cao, P. Fan, E.S. Barnard, A.M. Brown, M.L. Brongersma, Tuning the color of silicon nanostructures. *Nano Lett.* **10**(7), 2649–2654 (2010)
21. L. Cao, P. Fan, A.P. Vasudev, J.S. White, Y. Zongfu, W. Cai, J.A. Schuller, S. Fan, M.L. Brongersma, Semiconductor nanowire optical antenna solar absorbers. *Nano Lett.* **10**(2), 439–445 (2010)
22. L. Carletti, A. Locatelli, D. Neshev, C. De Angelis, Shaping the radiation pattern of second-harmonic generation from AlGaAs dielectric nanoantennas. *ACS Photonics* **3**(8), 1500–1507 (2016). 00015
23. R. Carminati, A. Cazé, D. Cao, F. Peragut, V. Krachmalnicoff, R. Pierrat, Y. De Wilde, Electromagnetic density of states in complex plasmonic systems. *Surf. Sci. Rep.* **70**(1), 1–41 (2015). 00040
24. W.-S. Chang, J. Britt Lassiter, P. Swanglap, H. Sobhani, S. Khatua, P. Nordlander, N.J. Halas, S. Link, A plasmonic Fano switch. *Nano Lett.* **12**(9), 4977–4982 (2012)
25. A.F. Cihan, A.G. Curto, S. Raza, P.G. Kik, M.L. Brongersma, Silicon Mie Resonators for Highly Directional Light Emission from Monolayer MoS<sub>2</sub>. *Nat. Photonics* **12**, 284–290 (2018)
26. A.G. Curto, G. Volpe, T.H. Taminiau, M.P. Kreuzer, R. Quidant, N.F. van Hulst, Unidirectional emission of a quantum dot coupled to a nanoantenna. *Science* **329**(5994), 930–933 (2010). 00954
27. M. Decker, I. Staude, Resonant dielectric nanostructures: a low-loss platform for functional nanophotonics. *J. Opt.* **18**(10), 103001 (2016)
28. E. Devaux, A. Dereux, E. Bourillot, J.-C. Weeber, Y. Lacroute, J.-P. Goudonnet, C. Girard, Local detection of the optical magnetic field in the near zone of dielectric samples. *Phys. Rev. B* **62**(15), 10504–10514 (2000)
29. F. Dhalluin, T. Baron, P. Ferret, B. Salem, P. Gentile, J.-C. Harmand, Silicon nanowires: diameter dependence of growth rate and delay in growth. *Appl. Phys. Lett.* **96**(13), 133109 (2010). 00043
30. D.F. Edwards, Silicon (Si)\*, in *Handbook of Optical Constants of Solids*, ed. by E.D. Palik (Academic Press, Burlington, 1997), pp. 547–569
31. H.-S. Ee, J.-H. Kang, M.L. Brongersma, M.-K. Seo, Shape-dependent light scattering properties of subwavelength silicon nanoblocks. *Nano Lett.* **15**(3), 1759–1765 (2015)
32. A.B. Evlyukhin, S.M. Novikov, U. Zywietz, R.L. Eriksen, C. Reinhardt, S.I. Bozhevolnyi, B.N. Chichkov, Demonstration of magnetic dipole resonances of dielectric nanospheres in the visible region. *Nano Lett.* **12**(7), 3749–3755 (2012)
33. P. Fan, U.K. Chettiar, L. Cao, F. Afshinmanesh, N. Engheta, M.L. Brongersma, An invisible metal-semiconductor photodetector. *Nat. Photonics* **6**(6), 380–385 (2012)
34. P. Fan, Z. Yu, S. Fan, M.L. Brongersma, Optical Fano resonance of an individual semiconductor nanostructure. *Nat. Mater.* **13**(5), 471–475 (2014). 00072
35. S. Fan, W. Suh, J.D. Joannopoulos, Temporal coupled-mode theory for the Fano resonance in optical resonators. *JOSA A* **20**(3), 569–572 (2003)
36. U. Fano, Effects of configuration interaction on intensities and phase shifts. *Phys. Rev.* **124**(6), 1866–1878 (1961)
37. V. Flauraud, M. Reyes, R. Paniagua-Domínguez, A.I. Kuznetsov, J. Brugger, Silicon nanostructures for bright field full color prints. *ACS Photonics* (2017)
38. Y.H. Fu, A.I. Kuznetsov, A.E. Miroshnichenko, Y.F. Yu, B. Luk'yanchuk, Directional visible light scattering by silicon nanoparticles. *Nat. Commun.* **4**, 1527 (2013)

39. A. García-Etxarri, R. Gómez-Medina, L.S. Froufe-Pérez, C. López, L. Chantada, F. Scheffold, J. Aizpurua, M. Nieto-Vesperinas, J.J. Sáenz, Strong magnetic response of submicron Silicon particles in the infrared. *Opt. Express* **19**(6), 4815 (2011)
40. J.C. Ginn, I. Brener, D.W. Peters, J.R. Wendt, J.O. Stevens, P.F. Hines, L.I. Basilio, L.K. Warne, J.F. Ihlefeld, P.G. Clem, M.B. Sinclair, Realizing optical magnetism from dielectric metamaterials. *Phys. Rev. Lett.* **108**(9), 097402 (2012)
41. Y. Guerfi, F. Carcenac, G. Larrieu, High resolution HSQ nanopillar arrays with low energy electron beam lithography. *Microelectron. Eng.* **110**, 173–176 (2013)
42. R. Guo, E. Rusak, I. Staude, J. Dominguez, M. Decker, C. Rockstuhl, I. Brener, D.N. Neshev, Y.S. Kivshar, Multipolar coupling in hybrid metal-dielectric metasurfaces. *ACS Photonics* **3**(3), 349–353 (2016)
43. D. Gérard, J. Wenger, A. Devilez, D. Gachet, B. Stout, N. Bonod, E. Popov, H. Rigneault, Strong electromagnetic confinement near dielectric microspheres to enhance single-molecule fluorescence. *Opt. Express* **16**(19), 15297 (2008)
44. R. Gómez-Medina, B. García-Cámara, I. Suárez-Lacalle, F. González, F. Moreno, M. Nieto-Vesperinas, J.J. Sáenz, Electric and magnetic dipolar response of germanium nanospheres: interference effects, scattering anisotropy, and optical forces. *J. Nanophotonics* **5**(1), 053512–053512–9 (2011). 00000
45. X.-L. Han, G. Larrieu, P.-F. Fazzini, E. Dubois, Realization of ultra dense arrays of vertical silicon nanowires with defect free surface and perfect anisotropy using a top-down approach. *Microelectron. Eng.* **88**(8), 2622–2624 (2011)
46. I.M. Hancu, A.G. Curto, M. Castro-López, M. Kuttge, N.F. van Hulst, Multipolar interference for directed light emission. *Nano Lett.* **14**(1), 166–171 (2014)
47. B. Hopkins, D.S. Filonov, A.E. Miroshnichenko, F. Monticone, A. Alú, Y.S. Kivshar, Interplay of magnetic responses in all-dielectric oligomers to realize magnetic fano resonances. *ACS Photonics* **2**(6), 724–729 (2015)
48. J.P. Hosemann, Computation of angular functions  $n$  and  $n$  occurring in the Mie theory. *Appl. Opt.* **10**(6), 1452–1453 (1971)
49. H. Kallel, A. Arbouet, G. BenAssayag, A. Chehaidar, A. Potié, B. Salem, T. Baron, V. Paillard, Tunable enhancement of light absorption and scattering in  $\text{Si}(1-x)\text{Ge}(x)$  nanowires. *Phys. Rev. B* **86**(8), 085318 (2012)
50. H. Kallel, A. Chehaidar, A. Arbouet, V. Paillard, Enhanced absorption of solar light in Ge/Si core-sheath nanowires compared to Si/Ge core-sheath and  $\text{Si}(1-x)\text{Ge}(x)$  nanowires: a theoretical study. *J. Appl. Phys.* **114**(22), 224312 (2013)
51. P. Kapitanova, V. Ternovski, A. Miroshnichenko, N. Pavlov, P. Belov, Y. Kivshar, M. Tribelsky, Giant field enhancement in high-index dielectric subwavelength particles. *Sci. Rep.* **7**(1), 731 (2017). 00001
52. M. Kerker, D.-S. Wang, C.L. Giles, Electromagnetic scattering by magnetic spheres. *J. Opt. Soc. Am.* **73**(6), 765 (1983)
53. A.I. Kuznetsov, A.E. Miroshnichenko, M.L. Brongersma, Y.S. Kivshar, B. Luk'yanchuk, Optically resonant dielectric nanostructures. *Science* **354**(6314) (2016)
54. A.I. Kuznetsov, A.E. Miroshnichenko, Y.H. Fu, J.B. Zhang, B. Luk'yanchuk, Magnetic light. *Sci. Rep.* **2**, 492 (2012)
55. P.E. Landreman, H. Chalabi, J. Park, M.L. Brongersma, Fabry-Perot description for Mie resonances of rectangular dielectric nanowire optical resonators. *Opt. Express* **24**(26), 29760–29772 (2016). 00000
56. J. Li, N. Verellen, D. Vercruyssen, T. Bearda, L. Lagae, P. Van Dorpe, All-dielectric antenna wavelength router with bidirectional scattering of visible light. *Nano Lett.* **16**(7), 4396–4403 (2016). 00010
57. Y. Li, M. Li, R. Li, F. Pengfei, L. Chu, D. Song, Method to determine the optimal silicon nanowire length for photovoltaic devices. *Appl. Phys. Lett.* **106**(9), 091908 (2015)
58. Z. Li, I. Kim, L. Zhang, M.Q. Mehmood, M.S. Anwar, M. Saleem, D. Lee, K.T. Nam, S. Zhang, B. Luk'yanchuk, Y. Wang, G. Zheng, J. Rho, C.-W. Qiu, Dielectric meta-holograms enabled with dual magnetic resonances in visible light. *ACS Nano* (2017)

59. M.F. Limonov, M.V. Rybin, A.N. Poddubny, Y.S. Kivshar, Fano resonances in photonics. *Nat. Photonics* **11**(9), 543–554 (2017)
60. S. Liu, M.B. Sinclair, S. Saravi, G.A. Keeler, Y. Yang, J. Reno, G.M. Peake, F. Setzpfandt, I. Staude, T. Pertsch, I. Brener, Resonantly enhanced second-harmonic generation Using III-V semiconductor all-dielectric metasurfaces. *Nano Lett.* **16**(9), 5426–5432 (2016)
61. W. Liu, Superscattering shaping for radially anisotropic nanowires through multipolar interferences. [arXiv: 1704.07994](https://arxiv.org/abs/1704.07994) [physics], Apr 2017. 00001
62. W. Liu, A.E. Miroshnichenko, R.F. Oulton, D.N. Neshev, O. Hess, Y.S. Kivshar, Scattering of core-shell nanowires with the interference of electric and magnetic resonances. *Opt. Lett.* **38**(14), 2621–2624 (2013). 00037
63. W. Liu, J. Zhang, B. Lei, H. Haojun, A.E. Miroshnichenko, Invisible nanowires with interfering electric and toroidal dipoles. *Opt. Lett.* **40**(10), 2293 (2015)
64. B.S. Luk'yanchuk, N.V. Voshchinnikov, R. Paniagua-Domínguez, A.I. Kuznetsov, Optimum forward light scattering by spherical and spheroidal dielectric nanoparticles with high refractive index. *ACS Photonics* **2**(7), 993–999 (2015)
65. S.A. Maier, *Plasmonics: Fundamentals and Applications* (Springer US, 2010)
66. S.A. Mann, R.R. Grote, R.M. Osgood, A. Alú, E.C. Garnett, Opportunities and limitations for nanophotonic structures to exceed the Shockley–Queisser limit. *ACS Nano* (2016)
67. O.J.F. Martin, C. Girard, A. Dereux, Generalized field propagator for electromagnetic scattering and light confinement. *Phys. Rev. Lett.* **74**(4), 526–529 (1995)
68. J.C. Maxwell, A dynamical theory of the electromagnetic field. *Philos. Trans. R. Soc. Lond.* **155**, 459–512 (1865)
69. E.V. Melik-Gaykazyan, M.R. Shcherbakov, A.S. Shorokhov, I. Staude, I. Brener, D.N. Neshev, Y.S. Kivshar, A.A. Fedyanin, Third-harmonic generation from Mie-type resonances of isolated all-dielectric nanoparticles. *Philos. Trans. R. Soc. A* **375**(2090), 20160281 (2017). 00000
70. A. Mirzaei, A.E. Miroshnichenko, Electric and magnetic hotspots in dielectric nanowire dimers. *Nanoscale* **7**(14), 5963–5968 (2015)
71. A. Mirzaei, A.E. Miroshnichenko, I.V. Shadrivov, Y.S. Kivshar, All-dielectric multilayer cylindrical structures for invisibility cloaking. *Sci. Rep.* **5**(9574), 00014 (2015)
72. H. Moriceau, F. Fournel, F. Rieutord. Materials and manufacturing techniques for SOI wafer technology, in *Silicon-on-Insulator (SOI) Technology*, ed. by O. Kononchuk, B.-Y. Nguyen (Woodhead Publishing, 2014), pp. 38–46. 00000
73. O.L. Muskens, J.G. Rivas, R.E. Algra, E.P.A.M. Bakkers, A. Lagendijk, Design of light scattering in nanowire materials for photovoltaic applications. *Nano Lett.* **8**(9), 2638–2642 (2008). 00405
74. P. Mühlischlegel, H.-J. Eisler, O.J.F. Martin, B. Hecht, D.W. Pohl, Resonant optical antennas. *Science* **308**(5728), 1607–1609 (2005)
75. M. Nieto-Vesperinas, R. Gomez-Medina, J.J. Saenz, Angle-suppressed scattering and optical forces on submicrometer dielectric particles. *JOSA A* **28**(1), 54–60 (2011). 00107
76. R. Paniagua-Domínguez, G. Grzela, J. Gómez Rivas, J.A. Sánchez-Gil, Enhanced and directional emission of semiconductor nanowires tailored through leaky/guided modes. *Nanoscale* **5**(21), 10582–10590 (2013). 00000
77. R. Paniagua-Domínguez, Y.F. Yu, A.E. Miroshnichenko, L.A. Krivitsky, Y.H. Fu, V. Valuckas, L. Gonzaga, Y.T. Toh, A.Y.S. Kay, B. Luk'yanchuk, A.I. Kuznetsov, Generalized Brewster effect in dielectric metasurfaces. *Nat. Commun.* **7**, 10362 (2016)
78. M. Paulus, O.J.F. Martin, Green's tensor technique for scattering in two-dimensional stratified media. *Phys. Rev. E* **63**(6), 066615 (2001). 00072
79. J.B. Pendry, D. Schurig, D.R. Smith, Controlling electromagnetic fields. *Science* **312**(5781), 1780–1782 (2006)
80. S. Person, M. Jain, Z. Lapin, J.J. Sáenz, G. Wicks, L. Novotny, Demonstration of zero optical backscattering from single nanoparticles. *Nano Lett.* **13**(4), 1806–1809 (2013)
81. M. Peter, A. Hildebrandt, C. Schlickriede, K. Gharib, T. Zentgraf, J. Förstner, S. Linden, Directional emission from dielectric leaky-wave nanoantennas. *Nano Lett.* **17**(7), 4178–4183 (2017)

82. F. Priolo, T. Gregorkiewicz, M. Galli, T.F. Krauss, Silicon nanostructures for photonics and photovoltaics. *Nat. Nanotechnol.* **9**(1), 19–32 (2014)
83. J. Proust, F. Bedu, B. Gallas, I. Ozerov, N. Bonod, All-dielectric colored metasurfaces with silicon Mie resonators. *ACS Nano* (2016)
84. E.M. Purcell, Spontaneous emission probabilities at radio frequencies. *Phys. Rev.* **69**, 681 (1946)
85. M. Ramezani, A. Casadei, G. Grzela, F. Matteini, G. Tütüncüoğlu, D. Ruffer, Fontcuberta i Morral A, Rivas, J.G.: Hybrid semiconductor nanowire-metallic Yagi-Uda antennas. *Nano Lett.* **15**(8), 4889–4895 (2015)
86. R. Regmi, J. Berthelot, P.M. Winkler, M. Mivelle, J. Proust, F. Bedu, I. Ozerov, T. Begou, J. Lumeau, H. Rigneault, M.F. García-Parajó, S. Bidault, J. Wenger, N. Bonod, All-dielectric silicon nanogap antennas to enhance the fluorescence of single molecules. *Nano Lett.* **16**(8), 5143–5151 (2016)
87. D. Rocco, L. Carletti, A. Locatelli, C. De Angelis, Controlling the directivity of all-dielectric nanoantennas excited by integrated quantum emitters. *JOSA B* **34**(9), 1918–1922 (2017)
88. B. Rolly, B. Bebey, S. Bidault, B. Stout, N. Bonod, Promoting magnetic dipolar transition in trivalent lanthanide ions with lossless Mie resonances. *Phys. Rev. B* **85**(24), 245432 (2012)
89. B. Rolly, J.-M. Geffrin, R. Abdeddaim, B. Stout, N. Bonod, Controllable emission of a dipolar source coupled with a magneto-dielectric resonant subwavelength scatterer. *Sci. Rep.* **3** (2013)
90. B. Rolly, B. Stout, S. Bidault, N. Bonod, Crucial role of the emitter-particle distance on the directivity of optical antennas. *Opt. Lett.* **36**(17), 3368 (2011)
91. B. Rolly, B. Stout, N. Bonod, Boosting the directivity of optical antennas with magnetic and electric dipolar resonant particles. *Opt. Express* **20**(18), 20376 (2012)
92. M.V. Rybin, K.B. Samusev, I.S. Sinev, G. Semouchkin, E. Semouchkina, Y.S. Kivshar, M.F. Limonov, Mie scattering as a cascade of Fano resonances. *Opt. Express* **21**(24), 30107–30113 (2013)
93. M.K. Schmidt, R. Esteban, J.J. Sáenz, I. Suárez-Lacalle, S. Mackowski, J. Aizpurua, Dielectric antennas—a suitable platform for controlling magnetic dipolar emission. *Opt. Express* **20**(13), 13636 (2012)
94. P.J. Schuck, D.P. Fromm, A. Sundaramurthy, G.S. Kino, W.E. Moerner, Improving the Mismatch between light and nanoscale objects with gold bowtie nanoantennas. *Phys. Rev. Lett.* **94**(1), 017402 (2005)
95. M.R. Shcherbakov, D.N. Neshev, B. Hopkins, A.S. Shorokhov, I. Staude, E.V. Melik-Gaykazyan, M. Decker, A.A. Ezhov, A.E. Miroshnichenko, I. Brener, A.A. Fedyanin, Y.S. Kivshar, Enhanced third-harmonic generation in silicon nanoparticles driven by magnetic response. *Nano Lett.* **14**(11), 6488–6492 (2014)
96. M.R. Shcherbakov, A.S. Shorokhov, D.N. Neshev, B. Hopkins, I. Staude, E.V. Melik-Gaykazyan, A.A. Ezhov, A.E. Miroshnichenko, I. Brener, A.A. Fedyanin, Y.S. Kivshar, Non-linear interference and tailorable third-harmonic generation from dielectric oligomers. *ACS Photonics* **2**(5), 578–582 (2015)
97. M.R. Shcherbakov, P.P. Vabishchevich, A.S. Shorokhov, K.E. Chong, D.-Y. Choi, I. Staude, A.E. Miroshnichenko, D.N. Neshev, A.A. Fedyanin, Y.S. Kivshar, Ultrafast all-optical switching with magnetic resonances in nonlinear dielectric nanostructures. *Nano Lett.* **15**(10), 6985–6990 (2015)
98. T. Shegai, S. Chen, V.D. Miljković, G. Zengin, P. Johansson, M. Käll, A bimetallic nanoantenna for directional colour routing. *Nat. Commun.* **2**, ncomms1490 (2011)
99. T. Shibanuma, P. Albella, S. Maier, Unidirectional light scattering with high efficiency at optical frequencies based on low-loss dielectric nanoantennas. *Nanoscale* **8**, 14184–14192 (2016)
100. T. Shibanuma, T. Matsui, T. Roschuk, J. Wojcik, P. Mascher, P. Albella, S.A. Maier, Experimental demonstration of tunable directional scattering of visible light from all-dielectric asymmetric dimers. *ACS Photonics* **4**(3), 489–494 (2017)
101. P. Spinelli, A. Polman, Light trapping in thin crystalline Si solar cells using surface Mie scatterers. *IEEE J. Photovolt.* **4**(2), 554–559 (2014)

102. I. Staude, A.E. Miroshnichenko, M. Decker, N.T. Fofang, S. Liu, E. Gonzales, J. Dominguez, T.S. Luk, D.N. Neshev, I. Brener, Y. Kivshar, Tailoring directional scattering through magnetic and electric resonances in subwavelength silicon nanodisks. *ACS Nano* **7**(9), 7824–7832 (2013). 00295
103. D.J. Traviss, M.K. Schmidt, J. Aizpurua, O.L. Muskens, Antenna resonances in low aspect ratio semiconductor nanowires. *Opt. Express* **23**(17), 22771 (2015)
104. V. Valuckas, R. Paniagua-Domínguez, Y.H. Fu, B. Luk'yanchuk, A.I. Kuznetsov, Direct observation of resonance scattering patterns in single silicon nanoparticles. *Appl. Phys. Lett.* **110**(9), 091108 (2017). 00000
105. L. Wang, S. Kruk, L. Xu, M. Rahmani, D. Smirnova, A. Solntsev, I. Kravchenko, D. Neshev, Y. Kivshar, Shaping the third-harmonic radiation from silicon nanodimers. *Nanoscale* **9**(6), 2201–2206 (2017). 00000
106. S.M. Wells, I.A. Merkulov, I.I. Kravchenko, N.V. Lavrik, M.J. Sepaniak, Silicon nanopillars for field-enhanced surface spectroscopy. *ACS Nano* **6**(4), 2948–2959 (2012). 00052
107. P.R. Wiecha, A. Arbouet, C. Girard, T. Baron, V. Paillard, Origin of second-harmonic generation from individual silicon nanowires. *Phys. Rev. B* **93**(12), 125421 (2016). 00000
108. P.R. Wiecha, A. Arbouet, C. Girard, A. Lecestre, G. Larrieu, V. Paillard, Evolutionary multi-objective optimization of colour pixels based on dielectric nanoantennas. *Nat. Nanotechnol.* **12**(2), 163–169 (2017). 00002
109. P.R. Wiecha, A. Arbouet, H. Kallel, P. Periwal, T. Baron, V. Paillard, Enhanced nonlinear optical response from individual silicon nanowires. *Phys. Rev. B* **91**(12), 121416 (2015). 00000
110. P.R. Wiecha, A. Cuche, A. Arbouet, C. Girard, G. Colas des Francs, A. Lecestre, G. Larrieu, F. Fournel, V. Larrey, T. Baron, V. Paillard, Strongly directional scattering from dielectric nanowires. *ACS Photonics* **4**(8), 2036–2046 (2017)
111. P.R. Wiecha, C. Girard, A. Cuche, V. Paillard, A. Arbouet, Decay Rate of Magnetic Dipoles near Non-magnetic Nanostructures. [arXiv:1707.07006](https://arxiv.org/abs/1707.07006) [cond-mat, physics:physics], July 2017
112. T. Wood, M. Naffouti, J. Berthelot, T. David, J.-B. Claude, L. Métayer, A. Delobbe, L. Favre, A. Ronda, I. Berbezier, N. Bonod, M. Abbarchi, All-dielectric color filters using SiGe-based Mie resonator arrays. *ACS Photonics* **4**(4), 873–883 (2017)
113. X.Y.Z. Xiong, L.J. Jiang, W.E.I. Sha, Y.H. Lo, W.C. Chew, Compact nonlinear Yagi-Uda nanoantennas. *Sci. Rep.* **6**, 18872 (2016)
114. J. Yan, P. Liu, Z. Lin, H. Wang, H. Chen, C. Wang, G. Yang, Directional Fano resonance in a silicon nanosphere dimer. *ACS Nano* **9**(3), 2968–2980 (2015). 00049
115. Y. Yang, Q. Li, M. Qiu, Controlling the angular radiation of single emitters using dielectric patch nanoantennas. *Appl. Phys. Lett.* **107**(3), 031109 (2015)
116. K. Yao, Y. Liu, Controlling electric and magnetic resonances for ultracompact nanoantennas with tunable directionality. *ACS Photonics* (2016)
117. X. Zambrana-Puyalto, I. Fernandez-Corbaton, M.L. Juan, X. Vidal, G. Molina-Terriza, Duality symmetry and Kerker conditions. *Opt. Lett.* **38**(11), 1857 (2013)
118. W. Zhao, B. Liu, H. Jiang, J. Song, Y. Pei, Y. Jiang, Full-color hologram using spatial multiplexing of dielectric metasurface. *Opt. Lett.* **41**(1), 147 (2016)

# Chapter 13

## Fano Resonances in Flat Band Networks



Ajith Ramachandran, Carlo Danieli and Sergej Flach

**Abstract** Linear wave equations on Hamiltonian lattices with translational invariance are characterized by an eigenvalue band structure in reciprocal space. Flat band lattices have at least one of the bands completely dispersionless. Such bands are coined flat bands. Flat bands occur in fine-tuned networks, and can be protected by (e.g. chiral) symmetries. Recently a number of such systems were realized in structured optical systems, exciton-polariton condensates, and ultracold atomic gases. Flat band networks support compact localized modes. Local defects couple these compact modes to dispersive states and generate Fano resonances in the wave propagation. Disorder (i.e. a finite density of defects) leads to a dense set of Fano defects, and to novel scaling laws in the localization length of disordered dispersive states. Nonlinearities can preserve the compactness of flat band modes, along with renormalizing (tuning) their frequencies. These strictly compact nonlinear excitations induce tunable Fano resonances in the wave propagation of a nonlinear flat band lattice.

### 13.1 Introduction

In this chapter we will discuss Fano resonances induced by defects, disorder and nonlinearities in flat band networks. More specifically, we will present phenomena of resonant scattering occurring in lattices that, in the crystalline case, exhibit the existence of one (or more) *dispersionless* (or *flat*) band.

One of the main reasons to study the class of flat band networks is the existence of compact localized states (CLS), flatband eigenstates of the system which extend over a strictly finite number of lattice sites. Differently from Anderson localization, where localized states may exist due to uncorrelated disorder, CLS appear in ordered systems, and their existence is protected by local symmetries which induce destructive interference in the lattice that suppress the propagation out of the compact domain of their nonzero amplitudes.

---

A. Ramachandran (✉) · C. Danieli · S. Flach  
Center for Theoretical Physics of Complex Systems,  
Institute for Basic Science, Daejeon, South Korea  
e-mail: ajithstcp@pcs.ibs.re.kr

Introduced around the late 1980s, this class of models recently shifted into the focus of interest of a broad community due to mathematical advancements as well as experimental realizations. Indeed, compact localized states are optimal candidates for transmission in networks of photonic waveguides that minimize the diffraction due to the destructive interference. Furthermore, flat band networks and the observation of compact localized states have been experimentally realized with exciton-polariton and Bose-Einstein condensate.

In several cases, the complete set of compact localized states can be fully detangled from the dispersive bands through suitable unitary transformations. This mathematical procedure allowed to extensively study several physical effects. In the following chapter, we will discuss Fano resonances induced by impurities, onsite perturbations and nonlinear terms in flat band networks. We will discuss our findings using one of the simplest and most re-known flat band networks—the *cross-stitch* lattice—as a test bed to present our results.

This chapter is structured in the following way. In the introduction we will review basic concepts of Fano resonances and of flat-band lattices. We will then discuss how single impurities can induce Fano resonance in the system. This is further discussed in the following section, where we discuss absence of transport in the flat band lattice due to the presence of uncorrelated disorder and quasiperiodic potentials. At last, we present Fano resonances induced in a perfectly periodic flat band structure in the presence of additional nonlinear terms.

### 13.1.1 Fano Resonances

In the quantum mechanical study of auto-ionising atoms, Ugo Fano introduced a new type of resonance mechanism to explain the asymmetric profile of spectral lines [1, 2]. The microscopic origin of the asymmetric line profile is due to constructive and destructive interference of the light continuum of states with a localized state hosted by the atom, giving rise to additional paths for an incoming wave to scatter [3]. The resulting constructive or destructive interference gives rise to either perfect transmission or complete reflection. Fano derived this line shape as [2]

$$T(s) = \frac{(s + q)^2}{s^2 + 1}, \quad (13.1)$$

where  $s = (E - E_R)/(\Gamma/2)$  and  $E_R$  is the resonance energy,  $\Gamma$  the line width and  $q$  the asymmetry parameter. Recently, Fano resonances were observed in a variety of cases such as electronic transport in quantum dots [4–7], wires and tunnel junctions [8], Mie and Bragg scattering in photonic crystals [9, 10], and bilayer graphene nano-structures [11].

The Fano-Anderson model is one of the simplest models that describes the physics and main features of Fano resonances [3]. This model consists of a tight-binding



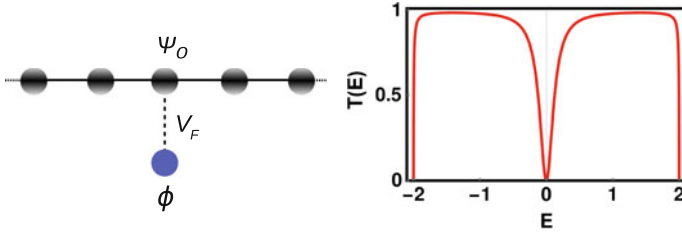


**Fig. 13.1** Schematic view of the Fano-Anderson model (left). Transmission coefficient for the Fano-Anderson model (right). Here:  $C = 1$ ,  $V_F = 0.5$  and  $E_F = 0$

chain with nearest-neighbor hopping, and a side-coupled discrete defect state. The Fano-Anderson Hamiltonian is given by

$$H = C \sum_n (\psi_n \psi_{n-1}^* + c \cdot c) + E_F |\phi|^2 + V_F (\phi^* \psi_0 + c \cdot c). \quad (13.2)$$

In the absence of the coupling  $V_F = 0$  it supports propagation of plane waves with dispersion relation  $\omega_k = 2C \cos k$ , while the isolated defect state has energy  $E_F$ . For nonzero coupling  $V_F \neq 0$  equations of motion read (Fig. 13.1)

$$\begin{aligned} i\dot{\psi}_n &= C(\psi_{n+1} + \psi_{n-1}) + \delta_{n,0} V_F \phi, \\ i\dot{\phi} &= E_F \phi + V_F \psi_0. \end{aligned} \quad (13.3)$$

A traveling wave has now the choice of two scattering channels: it can either bypass the defect state, or populate the state and return back to the chain. The existence of these two paths gives rise to destructive interference, and a Fano resonance. To the left and right of the defect, we write the propagating modes in the usual scattering formulation

$$\psi_n = \begin{cases} \tau e^{kn} + \sigma e^{-ikn}, & n < 0 \\ \rho e^{ikn}, & n \geq 0 \end{cases}; \quad (13.4)$$

where  $\tau$ ,  $\sigma$  and  $\rho$  are the incoming, reflected, and transmitted amplitudes respectively. The transmission coefficient  $T(\omega) = |\rho/\tau|^2$  can be obtained using the transfer matrix method [12]:

$$T(\omega_k) = \frac{\alpha_k^2}{1 + \alpha_k^2}, \quad (13.5)$$

where

$$\alpha_k = c_k \frac{E_F - \omega_k}{V_F^2}, \quad c_k = 2C \sin k. \quad (13.6)$$

For the resonant frequency  $\omega_k = E_F$ , the scattering along the two channels generates destructive interference leading to a complete suppression of the wave transmission.

The resonance width is proportional to the squared coupling strength  $V_F^2$ . The asymmetry parameter of the Fano resonance for the Fano-Anderson model vanishes  $q = 0$  [3], thus the transmission profile is symmetric.

### 13.1.2 Flat Band Networks

Flat band networks are translationally invariant tight binding lattices (also coined continuous time quantum walks) of various dimension and hopping range which support at least one dispersion-less band in the energy spectrum [13]. In this chapter, we will focus on the case of a one-dimensional lattice modeled with nearest-neighbor hopping between unit cells:

$$i\dot{\psi}_n = \epsilon_n \psi_n + H_0 \psi_n + H_1 \psi_{n+1} + H_1^\dagger \psi_{n-1}. \quad (13.7)$$

Here  $\psi_n = (\psi_n^1, \dots, \psi_n^\nu)^T \in \mathbb{C}^\nu$  is a wave function vector with  $\nu$  complex scalar components residing in the  $n$ th unit cell, and  $H_0, H_1 \in M_\nu(\mathbb{R})$  are  $\nu \times \nu$  square matrices representing intra-cell and nearest neighbor inter-cell hoppings, respectively. The optional onsite perturbation  $\epsilon_n$  of (13.7) is given by a diagonal square matrix  $\epsilon_n = \text{diag}(\epsilon_n^a, \epsilon_n^b, \dots, \epsilon_n^\nu)$ , where  $\epsilon_n^i$  are so-called on-site energies originating from some external potential (field). Using the ansatz  $\psi_n = A_n e^{-iEt}$ , the eigenvalue problem reduces to

$$EA_n = \epsilon_n A_n + H_0 A_n + H_1 A_{n+1} + H_1^\dagger A_{n-1}. \quad (13.8)$$

For vanishing onsite energies  $\epsilon_n = 0$  the equations are invariant under discrete lattice translations, and the Bloch theorem leads to the ansatz  $A_n = e^{ikn} \varphi_{\mathbf{k}}$  and a Bloch Hamiltonian  $H(\mathbf{k})$ :

$$E\varphi_{\mathbf{k}} = H(\mathbf{k})\varphi_{\mathbf{k}} \equiv (H_0 + e^{i\mathbf{k}} H_1 + e^{-i\mathbf{k}} H_1^\dagger)\varphi_{\mathbf{k}}. \quad (13.9)$$

Solving the eigenvalue problem for  $H(\mathbf{k})$  we arrive at the band structure with  $\nu$   $\mathbf{k}$ -periodic bands  $E_{1,2,\dots,\nu}(\mathbf{k})$  and the corresponding set of polarization eigenvectors.

For flat band lattices at least one of the energies  $E_m(\mathbf{k}) = \text{const}$  resulting in macroscopic degeneracy. Relevant perturbations can lift the degeneracy and qualitatively change the nature of the eigenstates [14–20]. Due to the degeneracy, Bloch states of the flat band can be superimposed still yielding a valid eigenstate. It turns out, that in many cases superpositions exist which yield not only localized, but even compact localized states (CLS). The origin of these compact localized states is destructive interference that prevents diffraction and effectively decouples them from rest of the lattice. The set of CLS can be orthogonal and linearly independent, and nonorthogonal but still linearly independent. In those cases the CLS set spans the entire Hilbert subspace of the flat band, and there exists some unitary transformation which connects the CLS set with the corresponding Bloch eigenstate set. In dimension  $d \geq 2$ ,

and in the presence of band touchings of the flat band and a dispersive band, it is also possible that the CLS set is linearly dependent and incomplete. However, gapping the flat band away from the dispersive spectrum, or in general in one dimension, linear dependence can be avoided. In one dimension, the CLS can be expressed in the following form:

$$\psi_{n_0}(t) = \left\{ \sum_{l=0}^{U-1} \left[ \sum_{j=1}^{\nu} a_{l,j} A_{l,j} \mathbf{e}_j \right] \delta_{n,n_0+l} \right\} e^{-i\Omega t}. \quad (13.10)$$

where  $\Omega = E_{FB}$ . Here  $\mathbf{e}_j$  are the basis vectors in  $\mathbb{R}^{\nu}$ , and the integers  $a_{i,j} \in \{0, \pm 1\}$  pin down the locations of the nonzero CLS amplitudes  $A_{i,j}$ . The integer number  $U$  counts the number of unit cells occupied by one CLS [13]. This number is also called the *class* of the CLS. If the class  $U$  flat band network is smoothly modified such that the CLS turn linearly dependent, the consequence is that the class  $U$  is reduced. The class  $U = 1$  always possesses an orthogonal and linearly independent CLS set. In Fig. 13.2 we show some examples of flat band networks.

Flat band networks are discrete geometrical structures that find applications in distortion free image transmission through photonic lattices [21, 22], artificial quantum dot arrays [23], ultracold atoms [24], microwaves in dielectric resonator networks [25, 26], light-matter exciton-polariton condensates [27], among others. Furthermore, compact localized states were experimentally observed in photonic lattices [21], structured microcavities for exciton-polariton condensates [27], and electronic circuits [28].

Attempts to construct flat band generators were based on graph theory [29], local cell construction [30], Origami rules in decorated lattices [31], and repetitions of mini arrays [32]. All these generators are focussing on subclasses of flat band networks with some additional symmetry or property. The classification via CLS properties including the class  $U$  is in principle complete [13]. The most general flat band generator for  $U = 1$  was obtained in [13]. The extension to  $U = 2$  proved already to be more involved, but was completed by Walaiymu et al. [33] for one-dimensional networks with two bands (one dispersive, one flat) and nearest neighbour hoppings. A chiral flat band network generator for bipartite networks with majority sub-lattices was obtained in [34], which yields chiral symmetry protected flat bands in any space dimension, and no further restrictions—even the loss of translational invariance is not destroying the macroscopic degeneracy in the energy spectrum and the correspondent CLS. Properly tuned magnetic fields can yield all bands flat [35]. Further results concern non-Hermitian flat band networks [36], Bloch oscillations [37], topological flat Wannier-Stark bands [38], and the existence of nontrivial superfluid weights [39], among others.

Let us consider the most simple and generic flat band case of  $U = 1$ , and of one dispersive and one flat band. This cross-stitch lattice has two spectral bands and is obtained with the following matrices in (13.7) (see Fig. 13.2a):

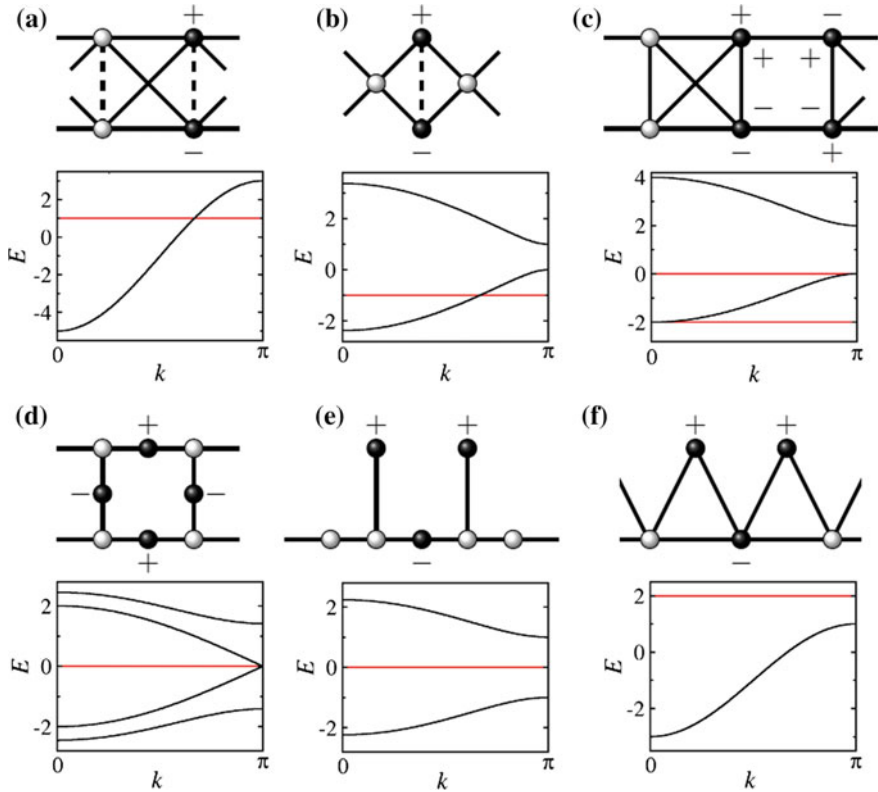


**Fig. 13.2** One-dimensional flat band topologies. **a** cross-stitch,  $\kappa = 1$ ,  $U = 1$ ; **b** diamond,  $\kappa = 1$ ,  $U = 1$ ; **c** one-dimensional pyrochlore,  $U = 1$ ; **d** one-dimensional Lieb  $U = 2$ ; **e** stub,  $U = 2$ ; **f** saw-tooth,  $U = 2$ . Figure taken from [13]

$$H_0 = \begin{pmatrix} 0 & \kappa \\ \kappa & 0 \end{pmatrix}, \quad H_1 = \begin{pmatrix} 1 & 1 \\ 1 & 1 \end{pmatrix}. \quad (13.11)$$

The wave equations read

$$\begin{aligned} i\dot{\psi}_n^1 &= \epsilon_n^a \psi_n^1 - \psi_{n-1}^1 - \psi_{n+1}^1 - \psi_{n-1}^2 - \psi_{n+1}^2 - \kappa \psi_n^2, \\ i\dot{\psi}_n^2 &= \epsilon_n^b \psi_n^2 - \psi_{n-1}^2 - \psi_{n+1}^2 - \psi_{n-1}^1 - \psi_{n+1}^1 - \kappa \psi_n^1. \end{aligned} \quad (13.12)$$

For the dispersive band  $E_{DB}(k) = -\kappa - 4 \cos(k)$ , and for the flat band  $E_{FB} = \kappa$ . The hopping strength  $\kappa$  tunes the flat band energy and the relative position of the two bands, which can overlap for  $|\kappa| \leq 2$ , or can be gapped otherwise. The compact localized states (13.10) are given by

$$\psi_{n,n_0} = A \begin{pmatrix} 1 \\ -1 \end{pmatrix} \delta_{n,n_0} e^{-iE_{FB}t}. \quad (13.13)$$

The detangling procedure is a unitary transformation which is applied to the vector space of each unit cell:

$$\begin{pmatrix} p_n \\ f_n \end{pmatrix} = D\psi_n, \quad D = \frac{1}{\sqrt{2}} \begin{pmatrix} 1 & 1 \\ 1 & -1 \end{pmatrix}, \quad \epsilon_n^\pm = (\epsilon_n^a \pm \epsilon_n^b)/2. \quad (13.14)$$

This yields

$$\begin{aligned} (E + \kappa) p_n &= \epsilon_n^+ p_n + \epsilon_n^- f_n - 2(p_{n-1} + p_{n+1}), \\ (E - \kappa) f_n &= \epsilon_n^+ f_n + \epsilon_n^- p_n. \end{aligned} \quad (13.15)$$

In the ordered case  $\epsilon_n^i = 0$  the flat band states  $f_n$  are decoupled from the dispersive ones  $p_n$ . Onsite perturbations introduce non-zero couplings  $\epsilon_n^\pm \neq 0$  in (13.15) which hybridize the two families of states.

### 13.2 Single Local Defects

In the presence of a flat band, an impurity locally hybridizes one or few renormalized CLS of the flat band with the dispersive bands, turning them into a Fano state which can lead to a Fano resonance.

Consider an onsite energy variation at unit cell  $n_0$  which can be expressed as  $\epsilon_n^{a,b} = \epsilon_n^{a,b} \delta_{n,n_0}$ . It follows

$$E p_n = \epsilon_n^+ \delta_{n,n_0} p_n + \epsilon_n^- \delta_{n,n_0} f_n - 2(p_{n-1} + p_{n+1}), \quad (13.16)$$

$$E f_n = \epsilon_n^+ \delta_{n,n_0} f_n + \epsilon_n^- \delta_{n,n_0} p_n. \quad (13.17)$$

The resulting generalized Fano-Anderson model is shown in Fig. 13.3. Precisely one of the CLS is renormalized, and coupled to the dispersive chain which in addition is perturbed by a simple defect at the site which is coupled to the CLS.

Excluding  $f_{n_0}$  the dispersive wave equation is reduced to

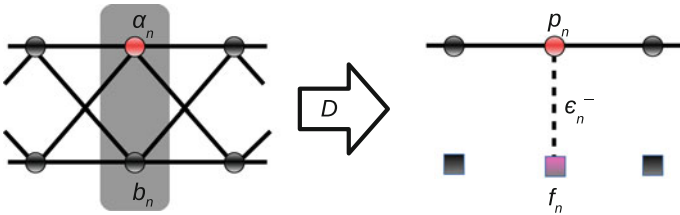
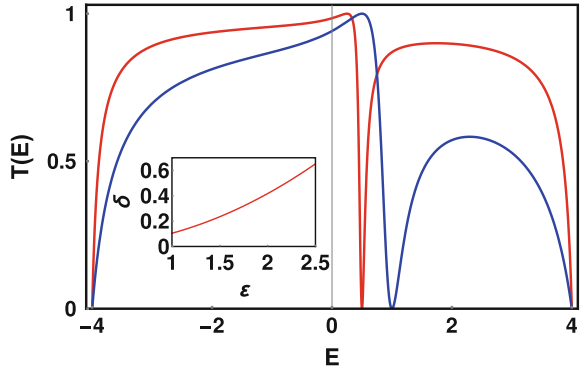


**Fig. 13.3** The cross-stitch lattice (left) and the detangled form (right). Here, the red dot on the cross-stitch lattice represents a local on-site defect. In the detangled chain, a localized state  $f_n$  is coupled to the linear chain due to the presence of defect

**Fig. 13.4** Transmission coefficient for different on-site defect potentials [ $\epsilon_n^a = 1$  (red), 2 (blue)] for the cross-stitch lattice in the presence of a local on-site defect. The inset shows the variation of the width  $\delta$  of the resonance versus the defect potential  $\epsilon = \epsilon_{n_0}^a$



$$E p_n = \left[ \epsilon_n^+ + \frac{(\epsilon_n^-)^2}{E - \epsilon_n^+} \right] \delta_{n,n_0} p_n - 2(p_{n-1} + p_{n+1}) . \quad (13.18)$$

We then obtain the transmission coefficient as

$$T(E) = \frac{16 - E^2}{16 - E^2 + \frac{[2\epsilon_n^+(E - \epsilon_n^+) + (\epsilon_n^-)^2]^2}{(E - \epsilon_n^+)^2}} . \quad (13.19)$$

A Fano resonance appears at  $E = \epsilon_n^+$ . Some scattering outcomes are plotted in Fig. 13.4. A weak local defect of strength  $\epsilon$  will thus lead to a Fano resonance in the dispersive channel. The resonance location is detuned from the original flat band energy by  $\epsilon$ . The width of the resonance is quadratic in  $\epsilon$ . Therefore, the detuning of the resonance off the original flat band energy is well resolved for weak defect strength, and can be used as a detection tool of weak imperfections in a flat band lattice. Our results will hold for any flat band lattice which hosts CLS. The very fact of the existence of a CLS, together with the short rangeness of the tight binding network, ensures that any local defect will renormalize a CLS, and back-couple it locally into one or several dispersive channels, in the manner of a Fano resonance, see e.g. [40].

### 13.3 Disorder

Wave propagation in non-periodic media was studied in the seminal work by Anderson in 1958, where absence of diffusion due to uncorrelated disorder has been predicted e.g. in a one-dimensional tight-binding chain [41]. Experimentally, Anderson localization has been observed e.g. with light waves [42], and Bose-Einstein condensates [43, 44]. Localized states are characterized by an energy-dependent localization length  $\xi$  which controls the asymptotic exponential decay of a wavefunction.

Disorder can be interpreted as a finite density of defects inserted into a system. Each individual defect will act as a Fano resonance in the case of a flat band network. A finite density of such defects then implies a macroscopic set of Fano resonances—all with slightly detuned (due to disorder) resonance energies. The disorder strength controls both the hybridization of Fano defects with the dispersive lattice, and the relative detuning of the Fano resonances. The most interesting limit is then the case of weak disorder, where the individual resonance width becomes narrow, while the different resonances get less detuned and act as a giant macroscopic resonance.

Let us consider a one-dimensional flat band network (13.7) in the presence of a disorder potential in the onsite energy matrix  $\epsilon_n$  where for each leg of the network  $i = 1, \dots, \nu$  the onsite energies are uncorrelated random numbers equidistributed over an interval  $\epsilon_n^i \in [-W/2, W/2]$ . The effect of weak uncorrelated disorder potential has been studied in several examples of class  $U = 1$  and  $U = 2$  flat band networks [13, 17, 18]. In these examples, the scaling law  $\xi(W) \sim W^{-\gamma}$  of the localization length  $\xi$  as function of the disorder strength as  $W \mapsto 0$  shown surprising exponents  $\gamma$  in correspondence of the flat band energy  $E_{FB}$ , in contrast to the exponent  $\gamma = 2$  typical of a dispersive band. In the case of the cross-stitch lattice (13.12), the exponent  $\gamma$  of the scaling law of the localization length  $\xi \sim W^{-\gamma}$  has been estimated for different values of flat band energy  $E_{FB}$ , reporting  $\gamma = 1$  in case of band crossing,  $\gamma = 1/2$  for the flat band located at the edge of the dispersive band, and a saturation to constant value  $\xi \sim c$  for the flat band gapped away from the dispersive one [13]. Similar exponents have been observed for the diamond chain [17] and pyrochlore [18], as well as class  $U = 2$  models such as Stub and one-dimensional Lieb lattice [18]. In higher dimensional lattices, the Fano resonance picture still persists. The computational characterization of eigenstates is performed using the participation number  $P$  (which counts the number of sites strongly excited in an eigen mode).

In the case of the cross-stitch chain with weak disorder we arrive at a whole array of slightly detuned Fano resonances:

$$(E + \kappa) p_n = \left[ \epsilon_n^+ + \frac{(\epsilon_n^-)^2}{(E - t) - \epsilon_n^+} \right] p_n - 2(p_{n-1} + p_{n+1}). \quad (13.20)$$

The probability distribution function of  $z = 1/\epsilon_n^+$  is given by

$$\mathcal{W} = \frac{2}{z^2} \int \mathcal{P}(y) \mathcal{P}\left(\frac{2}{z} - y\right) dy$$

where  $\mathcal{P}(x)$  is the distribution function of  $\epsilon_n^+$ . The heavy tails  $\mathcal{W}(z) \sim 1/z^2$  result in an effective disorder potential for the dispersive modes which has diverging variance. This is due to the the slightly detuned CLS Fano resonances acting as a giant strong scattering potential. This type of disorder potential has been considered in, for example, the exactly solvable Lloyd model [45], where Thouless [46] and Ishii [47] showed that  $\gamma = 1$  within the bulk of the dispersive band and  $\gamma = 1/2$  at the edge, in contrast with the typical  $\gamma = 1$  and  $\gamma = 2/3$  of the Anderson model.

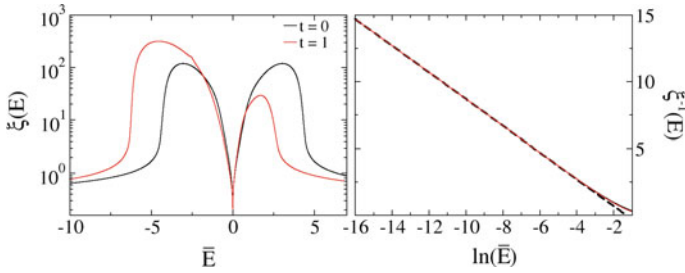


**Fig. 13.5** Left plot: Localization length  $\xi$  versus  $\bar{E} = E - E_{FB}$ . Right plot:  $\xi^{-1}$  versus  $\ln \bar{E}$  for  $\bar{E} > 0$ , same color coding as in left plot. The dashed line corresponds to (13.22). Here,  $W = 4$  and  $t = 0$  (black solid) and  $\kappa = 1$  (red solid). Figure taken from [19]

Any general disorder potential can be represented as a sum of a symmetric and antisymmetric parts:

$$\begin{aligned}
 \text{Symmetric: } \epsilon_n^- = 0 &\Leftrightarrow \epsilon_n^a = \epsilon_n^b, \\
 \text{Antisymmetric: } \epsilon_n^+ = 0 &\Leftrightarrow \epsilon_n^a = -\epsilon_n^b.
 \end{aligned}
 \tag{13.21}$$

The symmetric case  $\epsilon_n^- = 0$  renormalizes the energy of the flat band states, but does not hybridize the CLS with the dispersive states. The antisymmetric case  $\epsilon_n^+ = 0$  instead does not renormalize the CLS energy, but does hybridize them with the dispersive states. This latter case is of interest, since it turns the whole set of CLS into one perfect Fano resonance. For small  $\bar{E} = E - E_{FB}$ , the localization length can be obtained as (see [19])

$$\xi^{-1} = -2 + \ln \frac{W^2}{8|\bar{E}|}, \quad \bar{E} = \pm \frac{\epsilon_0^- \epsilon_1^-}{2} \ll \frac{W^2}{4}. \tag{13.22}$$

Irrespective of the strength of the correlated disorder, the localization length vanishes due to resonant scattering as the energy tends towards flat band energy. The numerically calculated localization length in Fig. 13.5 shows excellent agreement between the numerical data and (13.22). Note that at  $E = \kappa$ , the equations allow only for a trivial solution  $p_n = f_n = 0$ . All the compact states are hybridized and shifted their energies away, but a significant fraction stays close to flat band energy resulting in divergence of density of states at the flat band energy (not shown here—see [19]).

Going from local correlations to global correlations, we can consider the impact of quasiperiodic potentials realized with onsite energies. In particular for the Aubry-André perturbation

$$\epsilon_n^i = \lambda \cos [2\pi (\alpha n + \theta_i)], \quad i = 1, \dots, \nu. \tag{13.23}$$



Each leg is characterized by the potential strength  $\lambda$ , and each sequence is offset by all others by the phase shift parameters  $\theta_i$ . The quasiperiodicity is introduced by the incommensurate parameter in the argument of the *cosine* functions, which without loss of generality can be set equal  $\alpha \in \mathbb{R} \setminus \mathbb{Q}$  in all legs. The set of CLS will then generate a chain of correlated Fano resonances.

Let us consider the cross-stitch network (13.12) defined with the Aubry-André potential (13.23). Without loss of generality, we set the phase shift of the *a*-leg to zero  $\theta_a = 0$ . We will focus on the onsite energy correlations (13.21), which can be achieved by fine tuning of the phase shift  $\theta_b$  on the leg *b*. The most interesting antisymmetric case  $\epsilon_n^+ = 0$  is obtained for  $\theta_b = 1/2$ , which reduces (13.20) to the following eigenvalue problem

$$(E + \kappa) p_n = \frac{(\epsilon_n^-)^2}{E - \kappa} p_n - 2(p_{n-1} + p_{n+1}) . \tag{13.24}$$

where

$$(\epsilon_n^-)^2 = \lambda^2 \cos^2(2\pi\alpha n) = \frac{\lambda^2}{2} [1 + \cos(4\pi\alpha n)] . \tag{13.25}$$

(13.24) then reads as a one-dimensional Aubry-André chain with energy-dependent coefficients

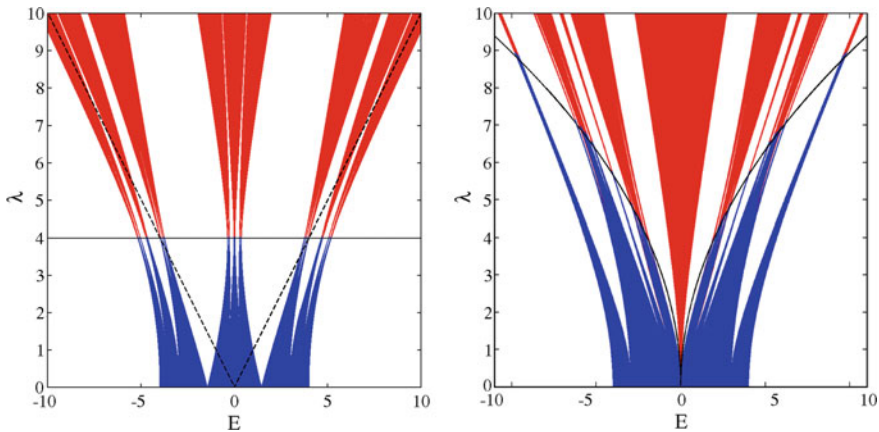


**Fig. 13.6** Spectrum of the cross-stitch lattice. Left plot: symmetric case. The dispersive spectrum shows metal-insulator transition at  $\lambda_c = 4$  (black line). The Fano state spectrum  $\sigma_f$  is omitted (boundaries indicated by black dashed lines). Right plot: antisymmetric case. The mobility edge curve corresponds to (13.27). Here: blue = extended states; red: localized states;  $\kappa = 0$ . Left figure taken from [19]. Right figure taken from [20]

$$\begin{aligned} \tilde{E} p_n &= \tilde{\lambda} \cos(4\pi\alpha n) - (p_{n-1} + p_{n+1}), \\ \text{where } \tilde{E} &:= \frac{E + \kappa}{2} - \frac{\lambda^2}{4(E - \kappa)}, \quad \tilde{\lambda} = \frac{\lambda^2}{4(E - \kappa)} \end{aligned} \quad (13.26)$$

According to [48] the transition between the metallic and insulating regimes occurs when  $\tilde{\lambda} = 2$ , which results in an analytic expression for the mobility edge,  $\lambda_c(E_c)$  :

$$\left| \frac{\lambda_c^2}{4(E_c - \kappa)} \right| = 2 \quad \Rightarrow \quad \lambda_c(E_c) = 2\sqrt{2|E_c - \kappa|}. \quad (13.27)$$

At the flat band energy  $E_{FB} = \kappa$ , the mobility edge shows a square root singularity. The coupling of the dispersive states to the giant Fano resonance, generated by the set of CLS with quasiperiodic modulation of its hybridization strength, carves a tongue of localized states into the metallic regime of the dispersive states, see Fig. 13.6.

In [20], mobility edge transitions between insulating and metallic phase have been obtained for a number of other flat band settings as well.

### 13.4 Nonlinearities

It has been rigorously proved that nonlinear lattice wave equations allow for the existence of coherent time-periodic solutions localized in real space called *discrete breathers*. Due to their time periodicity, discrete breathers act as time-periodic scattering potentials for propagating small amplitude waves. The confined time periodicity of the scattering potential leads to the existence of several scattering channels, opening the door for destructive interference and Fano resonances [49–52].

It turns out, that a subclass of flat band lattices with additional nonlinearities admit *compact discrete breathers*, namely solutions of the nonlinear network equations which are periodic in time and compact in space. These compact breathers are obtained e.g. as the continuation of linear compact localized states. The continuation is accompanied by a renormalization of the CLS frequency, preserving its compactness.

Consider a one-dimensional flat band network in the presence of Kerr nonlinearity. The model equations read

$$\begin{aligned} i\dot{\psi}_n &= H_0\psi_n + H_1\psi_{n+1} + H_1^\dagger\psi_{n-1} + \gamma\mathcal{F}(\psi_n), \\ \mathcal{F}(\psi_n) &= (|\psi_n^1|^2\psi_n^1, \dots, |\psi_n^\nu|^2\psi_n^\nu)^T = \left[ \sum_{i=1}^\nu |\psi_n^i|^2 \mathbf{e}_i \otimes \mathbf{e}_i \right] \psi_n. \end{aligned} \quad (13.28)$$

Let us consider the compact localized states (13.10) of the linear regime  $\gamma = 0$ . Can this solution persist for nonzero  $\gamma \neq 0$  ? Since the nonlinearity acts locally, zero amplitude sites outside the CLS are not affected. For the nonzero amplitude sites of

the CLS (i.e. for  $i = 1, \dots, U$  and  $j = 1, \dots, \nu$ ) we obtain

$$\Omega A_{i,j} = E_{FB} A_{i,j} + \gamma A_{i,j}^3. \quad (13.29)$$

The nonlinear term yields a shift in the frequency  $\Omega = E_{FB} + \gamma A_{i,j}^2$ . This expression is equivalent to

$$\forall a_{i,j} \neq 0 \Rightarrow A_{i,j}^2 = \frac{\Omega - E_{FB}}{\gamma}. \quad (13.30)$$

The linear CLS can be continued as a periodic solution of the nonlinear regime with frequency  $\Omega = E_{FB} + \gamma A^2$  and compact support if and only if for all the non-zero sites  $a_{i,j} \neq 0$  of the linear CLS  $|A_{i,j}|^2 \equiv A^2$ , where  $A$  is some nonzero real number. Linear CLS that satisfy this condition on their amplitude  $A_{i,j}^2 \equiv A^2$  are coined *homogeneous CLS*. *Compact discrete breathers*  $\mathcal{C}_{n_0}$  are continued homogeneous CLS of the linear regime with frequency  $\Omega = E_{FB} + \gamma A^2$  and  $a_{l,j} \in \{0, \pm 1\}$ :

$$\mathcal{C}_{n_0}(t) = A \left\{ \sum_{l=0}^{U-1} v_l \delta_{n,n_0+l} \right\} e^{-i\Omega t}, \quad v_l = \sum_{j=1}^{\nu} a_{l,j} \mathbf{e}_j. \quad (13.31)$$

The above results are independent of the number of bands  $\nu$  as well as the class  $U$  of the linear CLS. In the case of the cross-stitch lattice (13.12), the families of compact discrete breathers are given by

$$\mathcal{C}_{n_0}(t) = A \begin{pmatrix} 1 \\ -1 \end{pmatrix} \delta_{n,n_0} e^{-i\Omega t}. \quad (13.32)$$

The quantity that parametrizes the families of breathers can be either the renormalized frequency  $\Omega$  of the breather amplitude  $A$ .

In order to study the scattering of the propagation of an extended wave, we consider a small perturbation  $\chi_n(t)$  of a compact discrete breather  $\mathcal{C}_{n_0}$ :

$$\psi_n(t) = \mathcal{C}_{n_0}(t) + \chi_n(t). \quad (13.33)$$

We linearize (13.28) with respect to  $\chi_n$  and use  $g \equiv \gamma A^2$ :

$$i\dot{\chi}_n = H_0 \chi_n + H_1 \chi_{n+1} + H_1^\dagger \chi_{n-1} + g \sum_{l=0}^{U-1} \Gamma_l (2\chi_n + \chi_n^* e^{-i2\Omega t}) \delta_{n,n_0+l}, \quad (13.34)$$

where the operators

$$\Gamma_l = \sum_{j=1}^{\nu} a_{l,j}^2 \mathbf{e}_j \otimes \mathbf{e}_j \quad (13.35)$$

are the projector operators of a vector on the space of a compact localized state located between the  $n_0$ -th and the  $(n_0 + U - 1)$ -th unit cells. The time-dependent linearized equations (13.34) can be mapped to a time-independent eigenvalue problem

$$\chi_n = \mathbf{x}_n e^{-iEt} + \mathbf{y}_n^* e^{-i(2\Omega - E)t} \quad (13.36)$$

where  $\mathbf{x}_n, \mathbf{y}_n$  are complex vectors of the two scattering channels,  $\Omega = E_{FB} + g$  is the frequency of the compact discrete breather, and  $E$  is the frequency of the propagating wave in the open channel:

$$\begin{aligned} E\mathbf{x}_n &= H_0\mathbf{x}_n + H_1\mathbf{x}_{n+1} + H_1^\dagger\mathbf{x}_{n-1} + g \sum_{l=0}^{U-1} \Gamma_l (2\mathbf{x}_n + \mathbf{y}_n) \delta_{n,n_0+l}, \\ (2\Omega - E)\mathbf{y}_n &= H_0\mathbf{y}_n + H_1\mathbf{y}_{n+1} + H_1^\dagger\mathbf{y}_{n-1} + g \sum_{l=0}^{U-1} \Gamma_l (2\mathbf{y}_n + \mathbf{x}_n) \delta_{n,n_0+l}. \end{aligned} \quad (13.37)$$

The resulting equations describe two independent scattering channels with energy detuning  $2\Omega$ , and interacting through the non-zero amplitude sites of the compact discrete breather  $\mathcal{C}_{n_0}$ . Here,  $\mathbf{x}_n$  corresponds to the *open* channel, while  $\mathbf{y}_n$  to the *closed* channel. The open channel, away from the alterations induced by the compact breathers located between the  $n_0$ -th and the  $n_0 + (U - 1)$ -th unit cells, support the spectrum of the linear flat band network. Note that the spectra of each of the two channels are composed of several bands (flat and dispersive).

The linearized system (13.34) in the case of the cross-stitch lattice reads

$$\begin{aligned} i\dot{\zeta}_n &= -\zeta_{n-1} - \zeta_{n+1} - \eta_{n-1} - \eta_{n+1} - \kappa\eta_n + g(2\zeta_{n_0} + e^{-i2\Omega t} \eta_{n_0}^*) \delta_{n,n_0}, \\ i\dot{\eta}_n &= -\eta_{n-1} - \eta_{n+1} - \zeta_{n-1} - \zeta_{n+1} - \kappa\zeta_n + g(2\eta_{n_0} + e^{-i2\Omega t} \zeta_{n_0}^*) \delta_{n,n_0}. \end{aligned} \quad (13.38)$$

Here  $\chi_n = (\zeta_n, \eta_n)$ . The expansion (13.36) turns

$$\begin{aligned} \zeta_n &= u_n e^{-iEt} + v_n^* e^{-i(2\Omega - E)t}, \\ \eta_n &= w_n e^{-iEt} + z_n^* e^{-i(2\Omega - E)t}, \end{aligned} \quad (13.39)$$

and it maps (13.38) into a time-independent problem

$$\begin{aligned} Eu_n &= -[u_{n-1} + u_{n+1} + w_{n-1} + w_{n+1} + hu_n] + g(2u_{n_0} + v_{n_0}) \delta_{n,n_0}, \\ Ew_n &= -[w_{n-1} + w_{n+1} + u_{n-1} + u_{n+1} + hu_n] + g(2w_{n_0} + z_{n_0}) \delta_{n,n_0}, \\ (2\Omega - E)v_n &= -[v_{n-1} + v_{n+1} + z_{n-1} + z_{n+1} + hv_n] + g(2v_{n_0} + u_{n_0}) \delta_{n,n_0}, \\ (2\Omega - E)z_n &= -[z_{n-1} + z_{n+1} + v_{n-1} + v_{n+1} + hv_n] + g(2z_{n_0} + w_{n_0}) \delta_{n,n_0}. \end{aligned} \quad (13.40)$$

Both the open (first two equations) and the closed (second two equations) of the problem can be further rotated using the coordinate transformation (13.14), detan-

gling the flat band states  $f_n^1$  and  $f_n^2$  from the dispersive ones  $p_n$  and  $q_n$  respectively. In particular, also the compact localized states  $f_{n_0}^1$  and  $f_{n_0}^2$  located in the  $n_0$ -th unit cell (where the transversal hopping terms are found) are decoupled from the correspondent dispersive states  $p_{n_0}$  and  $q_{n_0}$ , since the alterations and the hopping terms have all the same strength  $g \neq 0$ . A combination of the transformation (13.36) and the detangling procedure (13.14) reduces (13.38) to the following one-dimensional equations of the open and the closed channels:

$$\begin{aligned} E p_n &= -2(p_{n-1} + p_{n+1}) - \kappa p_n + g[2p_{n_0} + q_{n_0}] \delta_{n,n_0}, \\ (2\Omega - E) q_n &= -2(q_{n-1} + q_{n+1}) - \kappa q_n + g[2q_{n_0} + p_{n_0}] \delta_{n,n_0}. \end{aligned} \quad (13.41)$$

Let us at first consider the case  $g = 0$ . Indeed, the dispersive bands  $E_1^O$  and  $E_1^C$  of the open and the closed channel respectively are

$$\begin{aligned} E_1^O &= -\kappa + [-4, 4], \\ E_1^C &= 3\kappa + [-4, 4] \end{aligned} \quad (13.42)$$

It follows that for  $\kappa \leq 2$  (crossing of the flat band  $E_{FB}$  and the dispersive band  $E_1$  of the linear cross-stitch lattice), the dispersive bands overlap  $E_1^O \cap E_1^C \neq \emptyset$ . For  $\kappa > 2$  instead (gapped flat band  $E_{FB}$  and dispersive band  $E_1$  of the linear cross-stitch lattice), the dispersive bands of the open and closed channels are disjoint  $E_1^O \cap E_1^C = \emptyset$ .

Next, let us consider (13.41) when both channels are decoupled. The closed channel admits a localized solution

$$\begin{aligned} q_n &= \mathcal{P} x^{|n-n_0|}, \quad |x| < 1, \quad \mathcal{P} \neq 0, \\ E_L &= 3\kappa + 2g - 2\sqrt{4 + g^2}. \end{aligned} \quad (13.43)$$

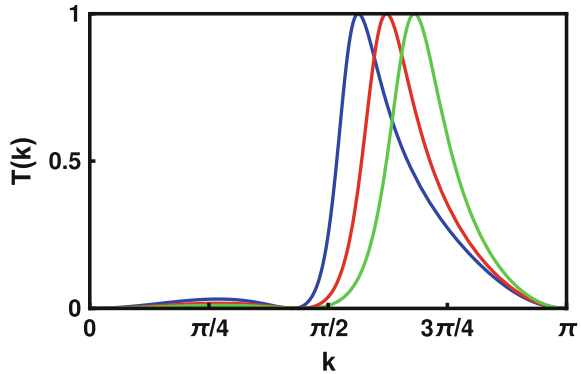
The energy  $E_L$  of this local mode belongs the interval  $\mathcal{E} \equiv [3\kappa - 4, 3\kappa]$ , where  $E_L \rightarrow 3\kappa - 4$  for  $g \rightarrow 0$  and  $E_L \rightarrow 3\kappa$  for  $g \rightarrow \infty$ . Therefore, the bound states (13.43) resonate with the dispersive band  $E_1^O = [-\kappa + 4, -\kappa + 4]$  of the open channel (i) for any  $g > 0$  if  $|\kappa| < 1$ ; (ii) only for  $g \leq \kappa(2 - \kappa)/(\kappa - 1)$  if  $1 < \kappa < 2$ ; the (iii) never if  $\kappa > 2$ .

To compute the transmission coefficient  $T$  we use the transfer matrix approach discussed and used in [12, 51, 52]. Let us define a propagating wave along the  $p_n$  chain

$$p_n = \begin{cases} \tau e^{i\mathbf{k}(n-n_0)} + \sigma e^{-i\mathbf{k}(n-n_0)}, & n < n_0 \\ \rho e^{i\mathbf{k}(n-n_0)}, & n \geq n_0 \end{cases}, \quad (13.44)$$

around the impurity located in the site  $n_0$  (we recall  $\tau + \sigma = \rho$ ). The transmission coefficient  $T(\mathbf{k}) = |\rho/\tau|^2$  follows as

**Fig. 13.7** Transmission coefficient  $T$  as a function of the momentum  $\mathbf{k}$ . Blue  $g = 4$ , Orange  $g = 5$ , Green  $g = 6$



$$T(\mathbf{k}) = \frac{16 \sin^2 \mathbf{k}}{16 \sin^2 \mathbf{k} + \left[ 2g + \frac{g^2}{\sqrt{(2\Omega - E_{\mathbf{k}} + \kappa)^2 - 16 - 2g}} \right]^2}. \tag{13.45}$$

An additional condition required for the transmission coefficient  $T$  is that the argument of the square root of the denominator has to be larger than zero for any wave vector  $\mathbf{k}$ . This requirement translates to the inequality  $g \geq 4 - \kappa$ . Then, a Fano resonance occurs when the denominator diverges, or equivalently when  $\sqrt{(2\Omega - E_{\mathbf{k}} + \kappa)^2 - 16 - 2g} = 0$ . This condition reads as

$$T(\mathbf{k}) = 0 \iff E_{\mathbf{k}} = E_L \iff \mathbf{k} = \arccos \left[ \frac{\kappa + E_L}{4} \right]. \tag{13.46}$$

To summarize, in the nonlinear cross-stitch lattice, a Fano resonance occurs if and only if  $\kappa < 2$ , since otherwise the bound state of the closed channel (13.43) is out of resonance with the dispersive band of the open channel. Furthermore, the condition (13.46) is subject to the requirement  $g \geq 4 - \kappa$ , which translates to  $4 - \kappa \leq g \leq \kappa(2 - \kappa)/(\kappa - 1)$ , if  $1 < \kappa < 2$ . In Fig. 13.7 we show the transmission coefficient  $T$  as function of the wave vector  $\mathbf{k}$  in the case of  $\kappa = 0$  for different values of  $g \geq 4$ . Indeed, zeros of the curves appear, indicating absence of transmission of a propagating wave.

### 13.5 Conclusions

In this chapter, we have discussed phenomena of total reflection of propagating waves in flat band networks, due to impurities, disorder and quasiperiodic potentials, and to compact discrete breathers induced by the presence of nonlinearities. These phenomena have been outlined generally for classes of flat band lattices, and they have been analyzed in detail in the case of the cross-stitch lattice. The flat band lattices

are interesting candidates to visualize Fano resonances because of the presence of compact localized states which serve as Fano states in the presence of proper perturbations. The defect-induced Fano resonance has been shown to result in complete suppression of the propagation. Many defects in lattice can result in distinctive transmission profile characteristics and a macroscopic number of defects takes the role of a disorder which, either correlated or uncorrelated, has a profound effect on the localization of dispersive states with anomalous scaling properties. Experimentally, flat band network Fano resonances can be studied in photonic crystals, optical lattices or even electronic circuits. Further, flat band networks and their Fano resonances can be used to engineer different types of spectral singularities or mobility edges in lattice systems and to control wave transport. In the presence of nonlinearities, novel compact discrete breather solutions turn into tunable Fano resonance scatterers.

**Acknowledgements** This work was supported by the Institute for Basic Science, Project Code (IBS-R024-D1).

## References

1. U. Fano, Sullo spettro di assorbimento dei gas nobili presso il limite dello spettro d'arco. *Il Nuovo Cimento* **12**, 154 (1935)
2. U. Fano, Effects of configuration interaction on intensities and phase shifts. *Phys. Rev.* **124**, 1866 (1961)
3. A.E. Miroshnichenko, S. Flach, Y.S. Kivshar, Fano resonances in nanoscale structures. *Rev. Mod. Phys.* **82**, 2257 (2010)
4. A. Johnson, C. Marcus, M. Hanson, A. Gossard, Charge sensing of excited states in an isolated double quantum dot. *Phys. Rev. B* **71**, 115333 (2005)
5. J. Göres, D. Goldhaber-Gordon, S. Heemeyer, M. Kastner, H. Shtrikman, D. Mahalu, U. Meirav, Fano resonances in electronic transport through a single-electron transistor. *Phys. Rev. B* **62**, 2188 (2000)
6. B.R. Buřka, P. Stefański, Fano and Kondo resonance in electronic current through nanodevices. *Phys. Rev. Lett.* **86**, 5128 (2001)
7. M. Torio, K. Hallberg, S. Flach, A. Miroshnichenko, M. Titov, Spin filters with Fano dots. *Eur. Phys. J. B* **37**, 399 (2004)
8. R. Franco, M. Figueira, E. Anda, Fano resonance in electronic transport through a quantum wire with a side-coupled quantum dot: X-boson treatment. *Phys. Rev. B* **67**, 155301 (2003)
9. M. Rybin, A. Khanikaev, M. Inoue, A. Samusev, M. Steel, G. Yushin, M. Limonov, Bragg scattering induces Fano resonance in photonic crystals. *Photonics Nanostruct.* **8**, 86 (2010)
10. M. Rybin, A. Khanikaev, M. Inoue, K. Samusev, M. Steel, G. Yushin, M. Limonov, Fano resonance between Mie and Bragg scattering in photonic crystals. *Phys. Rev. Lett.* **103**, 023901 (2009)
11. S. Mukhopadhyay, R. Biswas, C. Sinha, Signature of quantum interference and the Fano resonances in the transmission spectrum of bilayer graphene nanostructure. *J. Appl. Phys.* **110**, 014306 (2011)
12. P. Tong, B. Li, B. Hu, Wave transmission, phonon localization, and heat conduction of a one-dimensional Frenkel-Kontorova chain. *Phys. Rev. B* **59**, 8639 (1999)
13. S. Flach, D. Leykam, J.D. Bodyfelt, P. Matthies, A.S. Desyatnikov, Detangling flat bands into Fano lattices. *EPL (Europhys. Lett.)* **105**, 30001 (2014)
14. N. Perchikov, O.V. Gendelman, Flat bands and compactons in mechanical lattices. *Phys. Rev. E* **96**, 052208 (2017)

15. S.D. Huber, E. Altman, Bose condensation in flat bands. *Phys. Rev. B* **82**, 184502 (2010)
16. H. Aoki, M. Ando, H. Matsumura, Hofstadter butterflies for flat bands. *Phys. Rev. B* **54**, R17296 (1996)
17. D. Leykam, S. Flach, O. Bahat-Treidel, A.S. Desyatnikov, Flat band states: disorder and non-linearity. *Phys. Rev. B* **88**, 224203 (2013)
18. D. Leykam, J.D. Bodyfelt, A.S. Desyatnikov, S. Flach, Localization of weakly disordered flat band states. *Eur. Phys. J. B* **90**, 1 (2017)
19. J.D. Bodyfelt, D. Leykam, C. Danieli, X. Yu, S. Flach, Flatbands under correlated perturbations. *Phys. Rev. Lett.* **113**, 236403 (2014)
20. C. Danieli, J.D. Bodyfelt, S. Flach, Flat-band engineering of mobility edges. *Phys. Rev. B* **91**, 235134 (2015)
21. R.A. Vicencio, C. Cantillano, L. Morales-Inostroza, B. Real, C. Mejía-Cortés, S. Weimann, A. Szameit, M.I. Molina, Observation of localized states in Lieb photonic lattices. *Phys. Rev. Lett.* **114**, 245503 (2015)
22. S. Weimann, L. Morales-Inostroza, B. Real, C. Cantillano, A. Szameit, R.A. Vicencio, Transport in sawtooth photonic lattices. *Optics Lett.* **41**, 2414 (2016)
23. T. Brandes, Coherent and collective quantum optical effects in mesoscopic systems. *Phys. Rep.* **408**, 315 (2005)
24. S. Taie, H. Ozawa, T. Ichinose, T. Nishio, S. Nakajima, Y. Takahashi, Coherent driving and freezing of bosonic matter wave in an optical Lieb lattice, *Sci. Adv.* **1** (2015)
25. M. Bellec, U. Kuhl, G. Montambaux, F. Mortessagne, Tight-binding couplings in microwave artificial graphene. *Phys. Rev. B* **88**, 115437 (2013)
26. W. Casteels, R. Rota, F. Storme, C. Ciuti, Probing photon correlations in the dark sites of geometrically frustrated cavity lattices. *Phys. Rev. A* **93**, 043833 (2016)
27. N. Masumoto, N.Y. Kim, T. Byrnes, K. Kusudo, A. Löffler, S. Höfling, A. Forchel, Y. Yamamoto, Exciton-polariton condensates with flat bands in a two-dimensional kagome lattice. *New J. Phys.* **14**, 065002 (2012)
28. W.X. Qiu, S. Li, J.H. Gao, Y. Zhou, F.C. Zhang, Designing an artificial Lieb lattice on a metal surface. *Phys. Rev. B* **94**, 241409 (2016)
29. A. Mielke, Ferromagnetism in the Hubbard model on line graphs and further considerations. *J. Phys. A Math. Gen.* **24**, 3311 (1991)
30. H. Tasaki, Ferromagnetism in the Hubbard models with degenerate single-electron ground states. *Phys. Rev. Lett.* **69**, 1608 (1992)
31. R.G. Dias, G.J.D., Origami rules for the construction of localized eigenstates of the Hubbard model in decorated lattices. *Sci. Rep.* **5**, 16852 (2015)
32. L. Morales-Inostroza, R.A. Vicencio, Simple method to construct flat-band lattices. *Phys. Rev. A* **94**, 043831 (2016)
33. W. Maimaiti, A. Andreanov, H.C. Park, O. Gendelman, S. Flach, Compact localized states and flat-band generators in one dimension. *Phys. Rev. B* **95**, 115135 (2017)
34. A. Ramachandran, A. Andreanov, S. Flach, Chiral flat bands: existence, engineering, and stability. *Phys. Rev. B* **96**, 161104 (2017)
35. J. Vidal, B. Douçot, R. Mosseri, P. Butaud, Interaction induced delocalization for two particles in a periodic potential. *Phys. Rev. Lett.* **85**, 3906 (2000)
36. D. Leykam, S. Flach, Y.D. Chong, Flat bands in lattices with non-Hermitian coupling. *Phys. Rev. B* **96**, 064305 (2017)
37. R. Khomeriki, S. Flach, Landau-Zener Bloch oscillations with perturbed flat bands. *Phys. Rev. Lett.* **116**, 245301 (2016)
38. A.R. Kolovsky, A. Ramachandran, S. Flach, Topological Flat Wannier-Stark bands, *Phys. Rev. B* **97**, 045120 (2018)
39. S. Peotta, P. Törmä, Superfluidity in topologically nontrivial flat bands. *Nat. Commun.* **6**, 8944 (2015)
40. R. Zhu, C. Cai, Fano resonance via quasibound states in time-dependent three-band pseudospin-1 Dirac-Weyl systems. *J. Appl. Phys.* **122**, 124302 (2017)
41. P.W. Anderson, Absence of diffusion in certain random lattices. *Phys. Rev.* **109**, 1492 (1958)



42. Y. Lahini, A. Avidan, F. Pozzi, M. Sorel, R. Morandotti, D.N. Christodoulides, Y. Silberberg, Anderson localization and nonlinearity in one-dimensional disordered photonic lattices. *Phys. Rev. Lett.* **100**, 013906 (2008)
43. J. Billy, V. Josse, Z. Zuo, A. Bernard, B. Hambrecht, P. Lugan, D. Clément, L. Sanchez-Palencia, P. Bouyer, A. Aspect, Direct observation of Anderson localization of matter waves in a controlled disorder. *Nature* **453**, 891 (2008)
44. G. Roati, C. D'errico, L. Fallani, M. Fattori, C. Fort, M. Zaccanti, G. Modugno, M. Modugno, M. Inguscio, in *Pushing The Frontiers of Atomic Physics* (World Scientific, 2009), pp. 190–200
45. P. Lloyd, Exactly solvable model of electronic states in a three-dimensional disordered Hamiltonian: non-existence of localized states. *J. Phys. C* **2**, 1717 (1969)
46. D. Thouless, A relation between the density of states and range of localization for one dimensional random systems. *J. Phys. C* **5**, 77 (1972)
47. K. Ishii, Localization of eigenstates and transport phenomena in the one-dimensional disordered system. *Progress Theor. Phys. Suppl.* **53**, 77 (1973)
48. S. Aubry, G. André, Analyticity breaking and Anderson localization in incommensurate lattices. *Ann. Israel Phys. Soc* **3**, 18 (1980)
49. A. Miroshnichenko, S. Flach, B. Malomed, Resonant scattering of solitons. *Chaos* **13**, 874 (2003)
50. S.W. Kim, S. Kim, The structure of eigenmodes and phonon scattering by discrete breathers in the discrete nonlinear Schrödinger chain. *Physica D* **141**, 91 (2000)
51. S. Flach, A. Miroshnichenko, V. Fleurov, M. Fistul, Fano resonances with discrete breathers. *Phys. Rev. Lett.* **90**, 084101 (2003)
52. R.A. Vicencio, J. Brand, S. Flach, Fano blockade by a Bose-Einstein condensate in an optical lattice. *Phys. Rev. Lett.* **98**, 184102 (2007)

# Chapter 14

## Multiple-Resonance Interference in Metallic Nanohole Arrays



Munehiro Nishida and Yutaka Kadoya

**Abstract** In metallic nanohole arrays, the surface plasmon polaritons on the metal surfaces and the waveguide modes in the nanoholes are combined to form multipole surface plasmons. If these surface bound modes appear in a narrow frequency range, interference between multiple resonances and yields various resonant peak-dip structures in transmission, reflection and absorption spectra. In this chapter, we discuss the theoretical details of the mechanism of the multiple-resonance interference in metallic nanohole array systems using spatial and temporal coupled mode methods.

### 14.1 Introduction

At the interface between a metal and a dielectric, a kind of surface electromagnetic (EM) mode, called surface plasmon polariton (SPP), is created by the coupling between the plasma oscillation in the metal and the EM wave in the dielectric. The SPP excitation confines EM fields near the interface, and causes strong enhancement, which depends strongly on the environment near the metallic surface. Utilizing this peculiarity of SPP, many researches have been conducted aiming to realize highly sensitive biosensors and nanoscale optical devices, controlling the SPP characteristics by metallic nanostructures [1].

A metallic nanohole array is one of the simplest nanostructures; a metallic film perforated by a periodic array of sub-wavelength holes. As was found by Ebbesen et al. [2], the light transmission through this system can be resonantly enhanced by orders of magnitude larger than the expectation of standard aperture theory [3, 4]. Until now, it is revealed that this extraordinary optical transmission (EOT) phenomenon is basically a result of resonances with surface EM modes localized around the metal film [5]. Such surface EM modes also yield anomalous structure in the spectrum of one-dimensional gratings, which is called Wood's anomaly [6–8]. Thus, surface EM modes composed of SPPs play major role in the optical response of the metallic

---

M. Nishida (✉) · Y. Kadoya  
Graduate School of Advanced Science of Matter, Hiroshima University,  
Higashi-Hiroshima 739-8530, Japan  
e-mail: mnishida@hiroshima-u.ac.jp

© Springer Nature Switzerland AG 2018

E. Kamenetskii et al. (eds.), *Fano Resonances in Optics and Microwaves*, Springer  
Series in Optical Sciences 219, [https://doi.org/10.1007/978-3-319-99731-5\\_14](https://doi.org/10.1007/978-3-319-99731-5_14)

331

nanostructures. However, it is important to recognize that the surface EM modes in these systems are not pure SPPs at the flat metal-dielectric interface (SPF) but hybrid modes composed of various elements as shown in this chapter. Much confusion about the origin of EOT was caused by the lack of this recognition.

One of the most important ingredients of this system is the existence of slowly decaying evanescent waveguide modes in a nanohole. Using these modes, the EM field can penetrate rather deeply into the metal region and produce a kind of surface EM mode that has similar property with SPP. This mode appears even when the metal behaves as a perfect electric conductor (PEC) where SPF does not exist [9], and is now commonly called spoof surface plasmon. Moreover, the (spoof) surface plasmons at both sides of the film are coupled through the evanescent fields in the nanoholes, and form two separate “plasmon molecule” levels [10]. In a symmetric environment of equal dielectric constants in the regions of incidence and transmission, there are two types of surface bound modes with symmetric and anti-symmetric charge distributions [11, 12]. The symmetric mode is considered to be a kind of bonding (B) mode similar to the short-range SPP in a thin metallic film. On the other hand, the anti-symmetric mode is an anti-bonding (AB) mode similar to the long-range SPP [13, 14]. In recent paper [12], we have also shown that when the size of the nanohole occupies a large portion of the unit cell, the SPPs at both sides of the film are combined by the higher order waveguide modes of the holes to produce multipole surface plasmons: coupled surface plasmon modes with multipole texture on the electric field distributions.

Another important ingredient is the coupling with the external radiation modes. The SPF is a true surface bound modes whose dispersion is located outside the light cone. However, since the metallic nanohole array is a kind of diffraction grating, SPPs are diffracted and form Bloch-wave modes inside the light cone. Therefore, the surface EM modes in this system are basically considered as leaky surface bound modes (LSBMs) which have the coupling with external radiation fields. The asymmetric line shape observed in the transmission spectra is attributed to the Fano resonance produced by the interference between a directly transmitted wave and a resonantly transmitted wave with the excitation of a leaky bound mode [15–17]. It should be noted that the coupling between the LSBM and the external radiation mode can be changed drastically at the Rayleigh wavelength where the onset of a diffraction order occurs. This may cause abrupt change in the spectrum and yield so-called Rayleigh anomaly in one-dimensional gratings [7, 18].

In this way, there appear various LSBMs with different symmetry that should become degenerate or overlapping. In other words, multiple resonances with different darkness according to their multipole natures coexist within a narrow range of frequencies. In this case, it is expected that the interference between the radiations from multiple resonances yields sharp peak-dip structure in the optical spectra [19–21]. The electromagnetically induced transparency (EIT) found in atomic physics [22] is such a phenomena, in which destructive quantum interference between different excitation pathways to the excited state result in a narrow transparent window within a broader absorption band. Extreme dispersion created within the transparency window leads to the dramatic reduction of the group velocity of the light [23], and

enables to store a light pulse [24, 25]. It has been shown that EIT-like phenomena can be realized in coupled optical resonator systems due to classical destructive interference. This phenomena is called coupled-resonator induced transparency (CRIT) [26, 27].

Since the essential nature of EIT-like phenomena is the interference due to the coupling between the two oscillators (two LSBMs), simple classical oscillator model can explain the qualitative behavior [28]. However, in order to understand the actual optical response caused by these coupled oscillators, it is necessary to take into account that this system is an open wave system connected to the external radiation fields. Especially, there are two types of coupling between the surface modes, namely, the direct internal coupling through near field and the external coupling via the interference of far field and their magnitude relationship affects the formation of resonance states. In addition, the LSBMs have two types of loss, namely, internal material loss and external radiative loss. There is the case when the EIT-like phenomenon leads to the enhancement of absorption instead of reducing it, due to the effect of internal loss [29]. Therefore, we must use theoretical treatment which can deal with the coupling with external radiative field in order to describe the multiple resonance interference in the metallic nanohole array systems.

In this chapter, we try to give the thorough explanation of the essential mechanism of resonant optical response of the metallic nanohole array systems, based on the two types of coupled-mode methods; the spatial coupled-mode (SCM) method based on a modal expansion of the fields in different spatial regions [12, 30, 31], and the temporal coupled mode (TCM) method based on the time-dependent formalism for optical resonators connected to the external radiation via a few ports [27, 32, 33].

## 14.2 Surface Plasmon Polariton in a Metallic Nanohole Array

The system we are concerned in this chapter is square lattice of nanoholes perforated in a thin gold film with the thickness of  $h$  on a substrate whose refractive index (RI) is  $n_2$ , shown in Fig. 14.1a. The film is soaked in a medium whose RI is  $n_1$ . The radius of the hole is denoted by  $r$ , and the period of the array is  $L = 0.5 \mu\text{m}$ . The incident light is assumed to be p-wave, and the projection of the wave vector onto  $xy$  plane,  $\vec{k}$ , is directed along the  $x$ -axis, i.e.  $\vec{k} = (k_x, 0)$ .

Basically, the LSBMs in this system are composed of SPP at the gold-dielectric interfaces. Therefore, the dispersion relations of LSBMs should lie near those of SPPs. The dispersion relation of SPF is expressed as [1]

$$|\vec{k}| = \frac{\omega}{c} \sqrt{\frac{\epsilon_i \epsilon_m}{\epsilon_i + \epsilon_m}}, \quad (14.1)$$

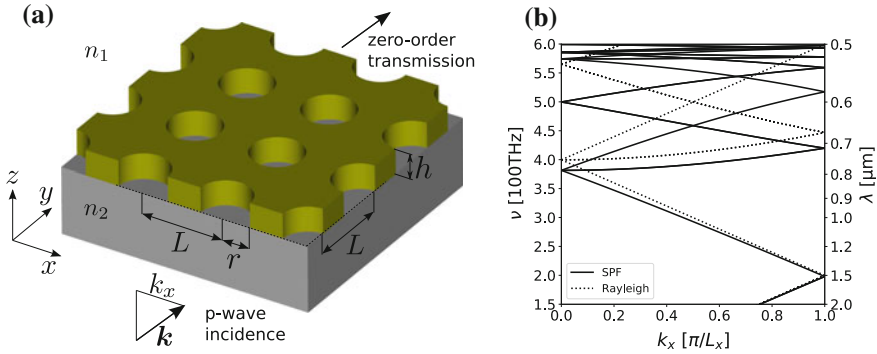


**Fig. 14.1** **a** Schematic diagram of a square lattice of nanoholes perforated in a thin gold film. **b** Empty-lattice band of SPP (solid lines). Dotted lines indicate the Rayleigh frequency at the metal-substrate interface

where  $\omega$  is the angular frequency,  $c$  is the speed of light in a vacuum. The permittivities of the  $i$ th dielectric and the metal are indicated by  $\varepsilon_i = n_i^2$  and  $\varepsilon_m$ , respectively. In the small radius limit of the nanohole, only the diffraction effect remains and so-called empty-lattice band is formed as shown in Fig. 14.1b. This empty-lattice band gives the reference for the band structure of the LSBMs, but the actual shape is deformed considerably near the cutoff frequency of the fundamental waveguide mode of the nanohole, as shown in the following sections.

### 14.3 Method

We use two types of coupled-mode method to calculate the spectra of this system. One is based on a modal expansion of the fields in different spatial regions [12, 30, 31]. Here, we call it spatial coupled-mode (SCM) method. The other is based on the time-dependent formalism for optical resonators connected to the external radiation via a few ports [32]. Here, we call it temporal coupled-mode (TCM) method.

#### 14.3.1 Spatial Coupled-Mode (SCM) Method

The SCM method derives a set of coupled equations for waveguide modes [12, 30, 31]. The EM fields in the free space surrounding the metal film are expressed by a linear combination of plane-wave modes specified by the parallel wave vector  $\vec{k} = \vec{k}_0 + \vec{K}$  and the polarization  $\sigma = p$  or  $s$  with  $\vec{k}_0$  and  $\vec{K}$  being the incident parallel wave vector and the reciprocal lattice vector of the nanohole array, respectively. The EM fields in the nanohole array region are expanded by waveguide modes.

We use Dirac's notation to describe the electric field components parallel to the  $xy$ -plane for the mode  $\alpha$ , such that

$$\vec{E}_\alpha(\vec{r}) = (E_{\alpha x}, E_{\alpha y}) = \langle \vec{r} | \alpha \rangle, \quad (14.2)$$

Here, the mode index  $\alpha$  represents the full information of the modes of a nanohole, such as the "HE<sub>11</sub> horizontal mode" [4]. It may also represent the parallel wave vector  $\vec{k}$  and the polarization  $\sigma$  (= p or s) for plane-wave modes. Since the magnetic field components parallel to the  $xy$ -plane are determined by the position-dependent admittance [12], we use the admittance operator  $\hat{Y}$  to express them, such that

$$\vec{H}_\alpha(\vec{r}) \equiv -\mathbf{e}_z \times \mathbf{H}_\alpha(\vec{r}) = (H_{\alpha y}, -H_{\alpha x}) = \langle \vec{r} | \hat{Y} | \alpha \rangle. \quad (14.3)$$

For the plane-wave mode in the  $i$ th media, this relation is reduced to

$$\langle \mathbf{r} | \hat{Y} | \vec{k} \sigma \rangle = Y_{\vec{k} \sigma} \langle \vec{r} | \vec{k} \sigma \rangle, \quad (14.4)$$

$$Y_{\vec{k} p} = \frac{1}{Z_0} \frac{k_z}{k_\omega}, \quad Y_{\vec{k} s} = \frac{\varepsilon_i}{Z_0} \frac{k_\omega}{k_z}, \quad (14.5)$$

where  $Z_0$  and  $k_\omega$  are the impedance and the wavenumber in the vacuum,  $\varepsilon_i = n_i^2$  is the relative permittivity in the  $i$ th homogeneous medium, and  $k_z$  is the  $z$ -component of the wave vector.

We define the internal product of the two fields as

$$\langle \alpha | \beta \rangle \equiv \iint dx dy \vec{E}_\alpha^* \cdot \vec{E}_\beta, \quad (14.6)$$

$$\langle \alpha | \hat{Y} | \beta \rangle \equiv \iint dx dy \vec{E}_\alpha^* \cdot \vec{H}_\beta = \iint dx dy [\mathbf{E}_\alpha^* \times \mathbf{H}_\beta]_z, \quad (14.7)$$

where  $*$  denotes the complex conjugate. Here, the mode fields are normalized by  $\langle \alpha | \alpha \rangle = 1$ . Then, the orthogonality condition for the plane-wave modes is expressed as,

$$\langle \vec{k} \sigma | \hat{Y} | \vec{k}' \sigma' \rangle = Y_{\vec{k} \sigma} \delta_{\vec{k} \vec{k}'} \delta_{\sigma \sigma'}. \quad (14.8)$$

However, due to the metal loss, the orthogonality condition for the waveguide modes should be modified as

$$\langle \alpha^* | \hat{Y} | \beta \rangle \equiv \int \vec{E}_\alpha^* \cdot \vec{H}_\beta dx dy = Y_\alpha \delta_{\alpha \beta}, \quad Y_\alpha \equiv \langle \alpha^* | \hat{Y} | \alpha \rangle, \quad (14.9)$$

based on the Lorentz reciprocity theorem [34–36].

Using these definitions, the coupled-mode equations can be derived in a similar manner as the original derivation [31]. Imposing the continuity condition of EM

fields at the openings of the holes and the surface impedance boundary conditions (SIBCs) [37] at the surfaces of the metal film, we can derive a coupled system of equations for the coefficients of waveguide modes as follows:

$$\begin{cases} \sum_{\beta} \left( G_{\alpha\beta}^- A_{\beta} + G_{\alpha\beta}^+ e^{ik_{\beta z}h} B_{\beta} \right) = I_{\alpha}, \\ \sum_{\beta} \left( G_{\alpha\beta}'^+ e^{ik_{\beta z}h} A_{\beta} + G_{\alpha\beta}'^- B_{\beta} \right) = 0, \end{cases} \tag{14.10}$$

where  $A_{\alpha}$  ( $B_{\alpha}$ ) is the coefficient for the mode  $\alpha$  propagating in the  $+z$  ( $-z$ ) direction at the bottom (top) interface. Here, the matrix elements  $G_{\alpha\beta}^{\pm}$  ( $G_{\alpha\beta}'^{\pm}$ ) controls the EM coupling between waveguide modes at the bottom (top) interface,  $I_{\alpha}$  takes into account the direct initial illumination over the waveguide mode  $\alpha$ . They are expressed as

$$G_{\alpha\beta}^{\pm} = Y_{\alpha\beta} \mp Y_{\alpha} \delta_{\alpha\beta}, \tag{14.11}$$

$$Y_{\alpha\beta} = \sum_{\vec{k}\sigma} \frac{Y_{\vec{k}\sigma}}{f_{\vec{k}\sigma}^{\pm}} \langle \alpha^* | \vec{k}\sigma \rangle \langle \vec{k}\sigma | \beta \pm \rangle, \tag{14.12}$$

$$I_{\alpha} = 2 \frac{Y_{\vec{k}_0\sigma_0}}{f_{\vec{k}_0\sigma_0}^+} \langle \alpha^* | \vec{k}_0\sigma_0 \rangle, \tag{14.13}$$

where

$$\langle \vec{k}\sigma | \alpha \pm \rangle = \langle \vec{k}\sigma | \alpha \rangle \pm Z_s \langle \vec{k}\sigma | \hat{Y} | \alpha \rangle, \tag{14.14}$$

$$f_{\vec{k}\sigma}^{\pm} = 1 \pm Z_s Y_{\vec{k}\sigma}, \tag{14.15}$$

and  $Z_s$  is the surface impedance given by  $Z_s = \frac{Z_0}{\sqrt{\epsilon_m}}$  with  $\epsilon_m$  being the relative permittivity of the metal. The definition of  $G_{\alpha\beta}'^{\pm}$  is the same as that of  $G_{\alpha\beta}^{\pm}$  except that it is calculated using  $n_1$  instead of  $n_2$ . Additionally, the transmission and reflection coefficients are expressed as

$$t_{\vec{k}\sigma} = \frac{1}{f_{\vec{k}\sigma}^+} \sum_{\alpha} \left\{ \langle \vec{k}\sigma | \alpha + \rangle A_{\alpha} e^{ik_{\alpha z}h} + \langle \vec{k}\sigma | \alpha - \rangle B_{\alpha} \right\}, \tag{14.16}$$

$$\begin{aligned} r_{\vec{k}\sigma} &= -\frac{f_{\vec{k}\sigma}^-}{f_{\vec{k}\sigma}^+} \delta_{\vec{k}\vec{k}_0} \delta_{\sigma\sigma_0} \\ &+ \frac{1}{f_{\vec{k}\sigma}^+} \sum_{\alpha} \left\{ \langle \vec{k}\sigma | \alpha - \rangle A_{\alpha} + \langle \vec{k}\sigma | \alpha + \rangle e^{ik_{\alpha z}h} B_{\alpha} \right\}. \end{aligned} \tag{14.17}$$

In the estimation of  $\langle \vec{k}\sigma | \hat{Y} | \alpha \rangle$ , we use the following approximation,

$$\left\langle \vec{k} \sigma \left| \hat{Y} \right| \alpha \right\rangle \simeq Y_{\vec{k}_0 \sigma, \alpha} \left\langle \vec{k} \sigma \left| \alpha \right\rangle, \quad Y_{\vec{k}_0 \sigma, \alpha} \equiv \frac{\left\langle \vec{k}_0 \sigma \left| \hat{Y} \right| \alpha \right\rangle}{\left\langle \vec{k}_0 \sigma \left| \alpha \right\rangle}, \quad (14.18)$$

in order to keep the reciprocity between the cases of incidence from above and incidence from below.

If we consider  $Y_\alpha$  as the characteristic admittance of a transmission line  $\alpha$ , and the electric field,  $\vec{E}_\alpha(\mathbf{r}) = (A_\alpha e^{ik_\alpha z} + B_\alpha e^{-ik_\alpha z}) \langle \vec{r} | \alpha \rangle$ , and magnetic field,  $\vec{H}_\alpha(\mathbf{r}) = (A_\alpha e^{ik_\alpha z} - B_\alpha e^{-ik_\alpha z}) \langle \vec{r} | \hat{Y} | \alpha \rangle$ , as the voltage and current waves traveling in that line, we can describe the elements in the CM equation (14.10) by the language of the circuit theory [38]. In this point of view,  $I_\alpha$  denotes the input current to the transmission line  $\alpha$ , and  $Y_{\alpha\beta}$  denotes the admittance of the connection circuit connecting the transmission lines  $\alpha$  and  $\beta$ . This connection circuit is composed of the dielectric region and the interface with the metal region.

### 14.3.1.1 Leaky Surface Bound Mode (LSBM)

LSBMs are solutions of Maxwell's equation that can oscillate in time and hold EM energy within the object for a considerable period of time in the absence of incident light. Formally, we would have to derive a non-vanishing output for zero input. In the CM method, the quasi-bound modes correspond to the non-trivial solutions of (14.10). In searching for the LSBMs, we must adopt out-going-wave boundary condition, where one of the branches of the multi-valued function  $k_z$  must be chosen obeying the condition that  $\text{Re}k_z > 0$  for  $|\text{Re}k_z| > |\text{Im}k_z|$  or  $\text{Im}k_z > 0$  for  $|\text{Re}k_z| < |\text{Im}k_z|$  [39].

### 14.3.2 Temporal Coupled-Mode (TCM) Method

We can consider the nanohole array as an optical resonator, and the diffracted waves in the free space as channels connected to the resonator. The temporal coupled mode method has been developed to deal with such a problem [32]. This method is based on the time-dependent formalism for optical resonators connected to the external radiation via a few ports. This method has been applied to the problem of optical transmission through a photonic crystal to explain the asymmetric Fano line shape in the spectra [33]. This theory has been extended to the multiple ports and lossless multimode cavity systems [27]. In this section, we will show the version of two-channel system, which can be applied to our system when only the zero-order diffraction is radiative. In this case, the two channels correspond to  $\left| \vec{k}_0 \text{p} \right\rangle$  for upper and lower dielectric regions. We assume that the system is reciprocal and has inversion symme-



try in  $xy$ -plane. In this case, the reduced scattering matrix for zero-order diffracted waves can be expressed as a symmetric matrix [40].

### 14.3.2.1 Scattering Matrix for a Two-Channel System

If the internal and radiative losses are small enough, the dynamic equations for the amplitudes of the  $n$  modes of an optical resonator can be written in the following form [27, 32, 33]:

$$\frac{d\mathbf{a}}{dt} = -i(\Omega - i\Gamma_i - i\Gamma_e)\mathbf{a} + C^\dagger |s_+\rangle, \quad (14.19)$$

$$|s_-\rangle = S_0 |s_+\rangle + C\mathbf{a}, \quad (14.20)$$

where  $\mathbf{a} = (a_1, a_2, \dots, a_n)$  is the vector which represents the amplitudes of the resonant modes and  $\Omega = \text{diag}(\omega_1, \omega_2, \dots, \omega_n)$  and  $\Gamma_i = \text{diag}(\gamma_{i1}, \gamma_{i2}, \dots, \gamma_{in})$  are  $n \times n$  diagonal matrices which represent resonance frequencies and decay rates due to the internal loss, respectively. The  $n \times n$  matrix,

$$\Gamma_e = \begin{pmatrix} \gamma_1 & \gamma_{12} & \cdots & \gamma_{1n} \\ \gamma_{12}^* & \gamma_2 & \cdots & \gamma_{2n} \\ \vdots & \vdots & \ddots & \vdots \\ \gamma_{1n}^* & \gamma_{2n}^* & \cdots & \gamma_n \end{pmatrix}, \quad (14.21)$$

represents the decay rates due to the radiative loss (diagonal elements) and the external coupling between the resonant modes induced by the radiation in the channels (off-diagonal elements). The amplitude of EM fields in the input and output channels are given by  $|s_{\pm}\rangle = \begin{pmatrix} s_{1\pm} \\ s_{2\pm} \end{pmatrix}$ . The  $2 \times n$  matrix  $C = \begin{pmatrix} c_{11} & c_{12} & \cdots & c_{1n} \\ c_{21} & c_{22} & \cdots & c_{2n} \end{pmatrix}$ , represents the couplings between the resonant modes and the channels. The  $2 \times 2$  matrix

$$S_0 = e^{i\phi} \begin{pmatrix} r_d e^{i\phi_r} & it_d \\ it_d & r_d e^{-i\phi_r} \end{pmatrix}, \quad (14.22)$$

represents the scattering matrix that describes the non-resonant direct scattering processes, which are assumed to obey energy conservation and reciprocity, i.e.  $S_0$  is unitary and symmetric [32, 33]. Here,  $\phi$ ,  $\phi_r$ ,  $r_d$  and  $t_d$  are real numbers and fulfill  $r_d^2 + t_d^2 = 1$ .

Here, we assume that the internal loss is small enough that  $\Gamma_e$  and  $C$  do not depend on it. Then, following the discussion in the lossless case [27] and relying upon only energy conservation and time-reversal symmetry, we can derive

$$C^\dagger C = 2\Gamma_e, \quad S_0 C^* = -C. \quad (14.23)$$

Then, the total scattering matrix  $S$  that obeys  $|s_- \rangle \equiv S |s_+ \rangle$  is given by

$$S = [I + iC [H - \omega I]^{-1} C^\dagger] S_0 = S_0 - iC [H - \omega I]^{-1} C^\dagger, \quad (14.24)$$

$$H \equiv \Omega - i\Gamma_i - i\Gamma_e, \quad (14.25)$$

where  $I$  denotes the  $n \times n$  unit matrix.

### 14.3.2.2 Fano Resonance in a Single Mode System

If there is only one resonant mode, the transmittance becomes,

$$T = t_d^2 \frac{(\delta + \text{Re}[\alpha])^2 + (1 + \text{Im}[\alpha])^2}{\delta^2 + 1}, \quad (14.26)$$

$$\delta = (\omega - \omega_1) / (\gamma_1 + \gamma_{i1}), \quad (14.27)$$

$$\alpha = c_{11}c_{21}e^{-i\phi} / \{t_d(\gamma_1 + \gamma_{i1})\}, \quad (14.28)$$

and gives asymmetric transmission spectrum.

Especially, when the system has mirror symmetry in  $z$ -direction, (14.23) leads [27]

$$c_{11}c_{21} = \gamma_1 e^{i\phi} (r_d + ip_1 t_d), \quad (14.29)$$

where  $p_1 = 1$  for symmetric resonant mode and  $p_1 = -1$  for anti-symmetric resonant mode. In this case, The reflection coefficient  $r$  and transmission coefficient  $t$  are expressed as

$$r = r_d + \frac{i\gamma_1 (r_d + ip_1 t_d)}{\tilde{\omega}_1 - \omega - i\gamma_1}, \quad t = it_d + p_1 \frac{i\gamma_1 (r_d + ip_1 t_d)}{\tilde{\omega}_1 - \omega - i\gamma_1}. \quad (14.30)$$

Then, the transmittance can be expressed as

$$T = t_d^2 \frac{(\delta + p_1 \eta q)^2 + \eta^2}{\delta^2 + 1}, \quad (14.31)$$

$$q = \frac{r_d}{t_d}, \quad \eta = \frac{\gamma_1}{\gamma_{i1} + \gamma_1}, \quad (14.32)$$

which reduces to the Fano formula in the system without internal loss ( $\eta = 1$ ).

### 14.3.2.3 Two Mode System

Let's consider two resonant mode case. Here, we assume mirror symmetry in  $z$ -direction. Using (14.23), we can show that [27, 41, 42]

$$\Gamma_e = \begin{pmatrix} \gamma_1 & \sqrt{\gamma_1 \gamma_2} \delta_{p_1, p_2} \\ \sqrt{\gamma_1 \gamma_2} \delta_{p_1, p_2} & \gamma_2 \end{pmatrix}, \quad C = \begin{pmatrix} \sqrt{\gamma_1} & \sqrt{\gamma_2} \\ p_1 \sqrt{\gamma_1} & p_2 \sqrt{\gamma_2} \end{pmatrix}, \quad (14.33)$$

where  $p_m$  represents the mirror symmetry in  $z$ -direction for the mode  $m (= 1, 2)$ , and we take  $p_m = 1$  for symmetric mode, and  $p_m = -1$  for anti-symmetric mode. The resonant behavior is quite different between the two cases: two resonant modes have opposite symmetry ( $p_1 \neq p_2$ ) or same symmetry ( $p_1 = p_2$ ) [27]. In the following, we use the notation  $\tilde{\omega}_m = \omega_m - i\gamma_m$ .

**Case (I)**  $p_1 = -p_2 = 1$ :

In this case, there is no external coupling between the two resonant modes. The reflection coefficient  $r$  and transmission coefficient  $t$  are expressed as

$$r = r_d + \frac{i\gamma_1 (r_d + it_d)}{\tilde{\omega}_1 - \omega - i\gamma_1} + \frac{i\gamma_2 (r_d - it_d)}{\tilde{\omega}_2 - \omega - i\gamma_2}, \quad (14.34)$$

$$t = it_d + \frac{i\gamma_1 (r_d + it_d)}{\tilde{\omega}_1 - \omega - i\gamma_1} - \frac{i\gamma_2 (r_d - it_d)}{\tilde{\omega}_2 - \omega - i\gamma_2}. \quad (14.35)$$

These equations can be simplified by using the coefficients for a single mode (14.30) as

$$r = r_1 + \frac{i\gamma_2 (r_1 - t_1)}{\tilde{\omega}_2 - \omega - i\gamma_2}, \quad t = t_1 - \frac{i\gamma_2 (r_1 - t_1)}{\tilde{\omega}_2 - \omega - i\gamma_2}. \quad (14.36)$$

From these expressions, we can deduce that if the radiative damping of bonding mode is large, the transmission process via the bonding mode can play a role of non-resonant direct process, and produce Fano resonance. Indeed, when  $\gamma_{i1} \simeq \gamma_{i2} \simeq 0$ ,  $t_d \simeq 0$ , and  $\omega \simeq \omega_2$ , the reflectance and transmittance can be expressed in a form of Fano formula:

$$R \simeq |r_1|^2 \frac{\left(\delta - \frac{1}{q}\right)^2}{\delta^2 + 1}, \quad T \simeq |t_1|^2 \frac{(\delta + q)^2}{\delta^2 + 1}, \quad (14.37)$$

$$q = i \frac{r_1}{t_1} \simeq \frac{\omega_1 - \omega_2}{\gamma_1}, \quad \delta = (\omega - \omega_2) / \gamma_2. \quad (14.38)$$

In this case, the asymmetry parameter  $q$  is determined by the difference between the resonance frequencies. If  $\omega_1 < \omega_2$ ,  $q$  is negative and the frequency of peak is lower than  $\omega_2$  and that of dip is higher than  $\omega_2$ . At the frequency between  $\omega_1$  and  $\omega_2$ , both of the transmission phases acquired during the two resonant processes are considered to be about  $\pi$ , because  $\pi$  phase jump should occur around the resonance frequency  $\omega_1$  for the symmetric mode and the transmission phase of anti-symmetric mode should have  $\pi$  from the start due to the sign change along  $z$  direction. Therefore, it is natural that constructive interference occurs between  $\omega_1$  and  $\omega_2$ .

**Case (2)**  $p_1 = p_2 = p$ :

In this case, the external coupling shifts the poles of  $S$ , namely, the resonant frequencies from the original values  $\tilde{\omega}_m$  to the values which obey

$$\Delta_{12}(\omega) \equiv \det[H - \omega I] = (\tilde{\omega}_1 - \omega - i\gamma_1)(\tilde{\omega}_2 - \omega - i\gamma_2) + \gamma_1\gamma_2 = 0. \quad (14.39)$$

The reflection and transmission coefficients are expressed as

$$r = r_d + \frac{r_d + i p t_d}{\Delta_{12}(\omega)} \{i\gamma_1(\tilde{\omega}_2 - \omega) + i\gamma_2(\tilde{\omega}_1 - \omega)\}, \quad (14.40)$$

$$t = i t_d + p \frac{r_d + i p t_d}{\Delta_{12}(\omega)} \{i\gamma_1(\tilde{\omega}_2 - \omega) + i\gamma_2(\tilde{\omega}_1 - \omega)\}. \quad (14.41)$$

If the external coupling  $\gamma_1\gamma_2$  is neglected in  $\Delta_{12}$ , these equations reduce to those in the case (1) except the sign of the asymmetry parameter.

## 14.4 Waveguide Modes in a Metallic Nanohole

As we show in the following sections, the propagation constant  $k_z$  of the fundamental waveguide mode of the nanohole,  $\text{HE}_{11}$  mode, is the key parameter to determine the resonance of this system. Especially, at the cutoff frequency,  $k_z$  becomes nearly zero and the zero-order Fabry-Perot resonance occurs [30, 43].

Figure 14.2a shows the frequency dependence of the attenuation constants,  $\text{Im}(k_z)$ , for the two TE-like modes, i.e. fundamental  $\text{HE}_{11}$  mode and the second order  $\text{HE}_{21}$  mode. You can see the dipolar and quadrupolar natures of these modes from the electric field distribution shown in 14.2b.

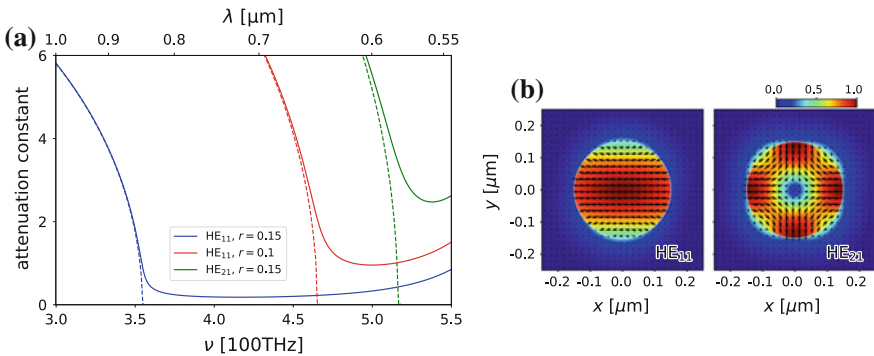


**Fig. 14.2** **a** Attenuation constants of nanohole waveguide modes. Solid (dotted) lines indicate the values calculated using real (lossless) gold permittivity. **b** Electric field distribution of the waveguide modes

## 14.5 Fano Resonance and Short-Circuit Effect

Figure 14.3a shows the zero-order transmission spectra together with the band structure of surface bound modes (solid lines) calculated using SCM method. You can see that band structure of surface bound modes is created near the empty-lattice band of SPP and the resonance peaks follow them.

The blue solid line in Fig. 14.3b represents the profile of transmission spectrum at  $\Gamma$  point. The light-blue dotted line is obtained by the fitting using (14.26) where the resonance frequency  $\omega_1$  and the decay rate  $\gamma_1 + \gamma_{1l}$  are determined by the SCM calculation. The obtained formula for this spectrum is  $T = (0.095)^2 \frac{(\delta-5)^2}{\delta^2+1}$ . Thus, the original Fano formula gives the good fit.

Another striking feature in these transmission spectra is that the transmission is basically quite low on the empty-lattice bands of SPP (dashed lines). This can be clearly explained using SCM theory [5]. From (14.12), you can see that the effective admittance of “connection circuit”  $Y_{\alpha\beta}$  diverges when  $f_{\vec{k}p}^+ = 1 + Z_S Y_{\vec{k}p} \simeq 0$ . This condition is fulfilled if  $k_x \simeq \sqrt{\epsilon_d} k_\omega \sqrt{1 - \epsilon_d/\epsilon_m} \simeq k_\omega \sqrt{\frac{\epsilon_d \epsilon_m}{\epsilon_d + \epsilon_m}}$ , namely, on the dispersion of SPF. Therefore, waveguide mode channels are short-circuited and decoupled from the incident channel on the empty-lattice bands of SPP.

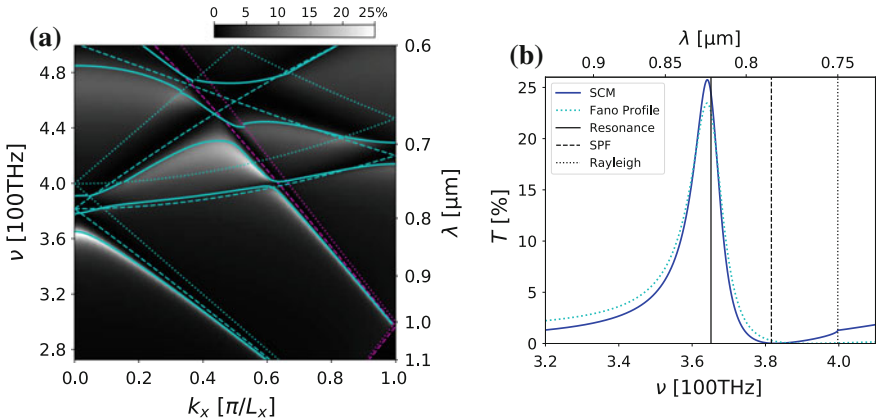


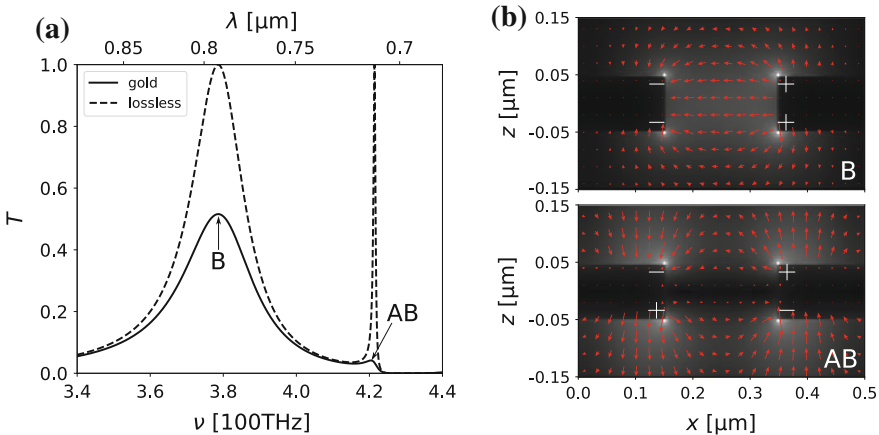
**Fig. 14.3** **a** Zero-order transmission spectra for a square lattice of nanohole with  $r = 0.1 \mu\text{m}$  in air ( $n_1 = 1$ ) on glass substrate ( $n_2 = 1.5$ ). Light-blue solid lines indicate the dispersion of resonant modes, and light-blue dashed (dotted) lines indicate the empty-lattice bands of SPP (Rayleigh frequency) at the metal-substrate interface. Pink dashed and dotted lines indicate those at metal-air interface. **b** Transmission spectra for normal incidence. Blue solid line indicates the transmission spectrum calculated using SCM method. Light blue dotted line represents the fitting using the Fano formula. Black vertical lines indicate the resonance frequency, the frequency of SPF, and the Rayleigh frequency

### 14.6 SPP Molecule and Spoof Surface Plasmon

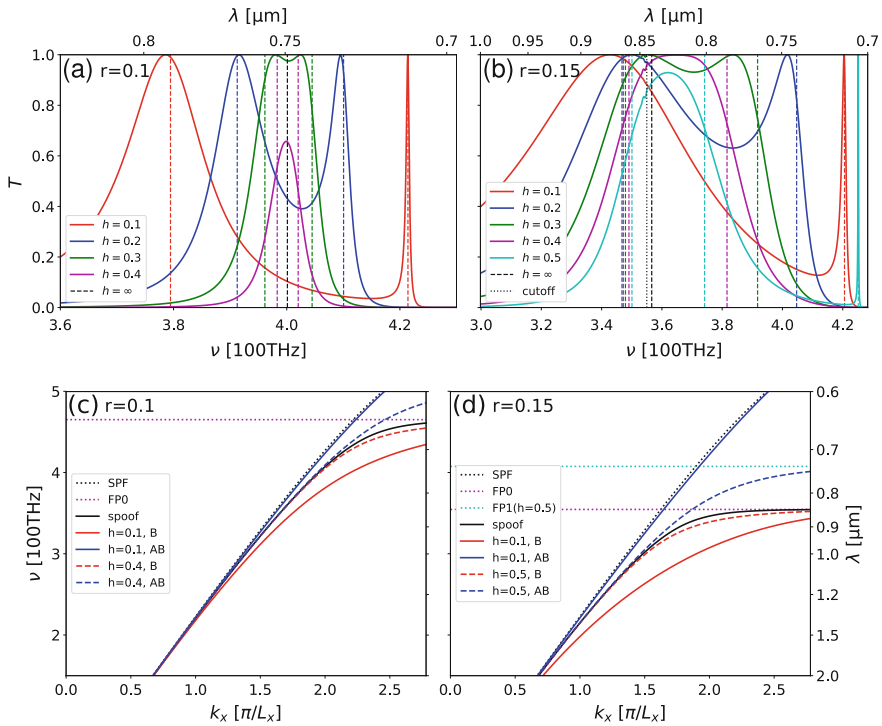
In addition to the diffraction of SPP, there is another effect induced by the nanohole array. EM field can penetrate into the metal region using evanescent or propagating waveguide modes of nanoholes. The SPPs at top and bottom surfaces are considered to be coupled by the waveguide modes and produce “SPP molecule” [10]. Especially, in a system with mirror symmetry in  $z$ -direction, namely,  $n_1 = n_2$  case, there should appear two types of surface bound modes with symmetric and anti-symmetric charge distributions [11, 12]. The symmetric mode is considered to be a kind of bonding (B) mode similar to the short-range SPP in a thin metallic film; on the other hand the anti-symmetric mode is an anti-bonding (AB) mode similar to the long-range SPP [14].

Figure 14.4a shows the zero-order transmission spectra for normal incidence to a lattice of nanohole with the radius of  $r = 0.1 \mu\text{m}$  in water. Eliminating the imaginary part of dielectric constant of gold, there appear two peaks as in the dashed line. The broad resonance at lower frequency is a B mode, which has symmetric charge distribution and the sharp resonance at higher frequency is an AB mode, which has anti-symmetric charge distribution as shown in Fig. 14.4b. The peak height is highly reduced when the real-gold permittivity is used as in the solid line of Fig. 14.4a. These results indicate that the radiative loss of AB mode is so small that the energy is kept around the metal region for a long period of time during which most of the energy is dissipated by the internal loss of gold.

Figure 14.5a shows the metal thickness ( $h$ ) dependence of the transmission spectra for  $r = 0.1 \mu\text{m}$  case. In this case, since the cutoff frequency of the fundamental mode is higher than the resonance frequencies, the coupling between the SPPs at top



**Fig. 14.4** **a** Zero-order transmission spectra for a square lattice of nanohole with the radius  $r = 0.1 \mu\text{m}$  and the film with thickness  $h = 0.1 \mu\text{m}$  in water ( $n_1 = n_2 = 1.333$ ). **b** Electric field distributions in the  $xz$  plane for a bonding (B) mode and an anti-bonding (AB) mode



**Fig. 14.5** **a** Metal thickness dependence of the zero-order transmission spectra for a square lattice of nanohole with the radius  $r = 0.1 \mu\text{m}$  and **b**  $r = 0.15 \mu\text{m}$  in water ( $n_1 = n_2 = 1.333$ ). **c** Dispersion relation of surface bound modes obtained by metamaterial treatment for  $r = 0.1 \mu\text{m}$  and **d**  $r = 0.15 \mu\text{m}$

and bottom interfaces is induced by the decaying mode. Therefore, the strength of coupling is reduced as  $h$  becomes large, and above  $0.4 \mu\text{m}$  the two peaks merges into a single peak whose position coincide with the frequency of the surface bound mode at a single interface on a semi-infinite metal ( $h = \infty$ ) shown by the black dashed vertical line. Other dashed vertical lines represent the frequency of LSBMs found by SCM calculation. You can see that the transmission peaks deviate from the actual resonance frequencies. This is due to the interference between the two resonances as shown in the following sections.

Figure 14.5b also shows the  $h$ -dependence of the transmission spectra for larger hole case with  $r = 0.15 \mu\text{m}$ . In this case, the cutoff frequency of the fundamental mode is in the frequency range where resonances appear, and it seems to change the resonance behavior considerably. The broader resonances of B modes are almost stuck near the cutoff frequency, which is very close to the frequency of the surface bound mode at a single interface ( $h = \infty$ ). You can see that another resonance appears around 420 THz in the thicker film above  $0.5 \mu\text{m}$ . This resonance is induced by the first-order Fabry-Perot resonance in the nanohole as shown below.

In order to reveal the role played by the waveguide mode, we approximately analyze the dispersion relation of the SPP molecule produced by the fundamental waveguide mode using metamaterial treatment as in [5], where only p-polarized waves and the zero-order diffraction mode are considered in (14.10). In a system with mirror symmetry in z-direction, the coefficients for the waveguide mode should obey  $B_\alpha = +A_\alpha$  (symmetric) or  $B_\alpha = -A_\alpha$  (anti-symmetric). Neglecting the imaginary part of the permittivity of gold  $\varepsilon_m$ , the condition for the existence of surface bound mode becomes

$$G_{\alpha\alpha}^+ e^{ik_{\alpha z}h/2} \pm G_{\alpha\alpha}^- e^{-ik_{\alpha z}h/2} = 0, \quad (14.42)$$

$$G_{\alpha\alpha}^\pm = Y_{k_x p} \left( \frac{1 - Z_s Y_{k_x p, \alpha}}{1 + Z_s Y_{k_x p}} \right) |S|^2 \mp Y_\alpha, \quad (14.43)$$

$$|S|^2 \equiv \langle \alpha^* | k_x p \rangle \langle k_x p | \alpha \rangle = |\langle k_x p | \alpha \rangle|^2. \quad (14.44)$$

Solving these equations, the dispersion relations of the SPP molecules for symmetric B mode (+) and anti-symmetric AB mode (−) are given by

$$k_x^\pm = \sqrt{\varepsilon} k_\omega \sqrt{1 + \frac{\varepsilon}{|\varepsilon_m|} \left\{ 1 + \frac{|S|^2 (\gamma_\pm \sqrt{\varepsilon_m} - Z_0 Y_{k_x p, \alpha})}{Z_0 Y_\alpha} \right\}^2}, \quad (14.45)$$

$$\gamma_\pm \equiv \frac{e^{-ik_{\alpha z}h/2} \pm e^{ik_{\alpha z}h/2}}{e^{-ik_{\alpha z}h/2} \mp e^{ik_{\alpha z}h/2}}. \quad (14.46)$$

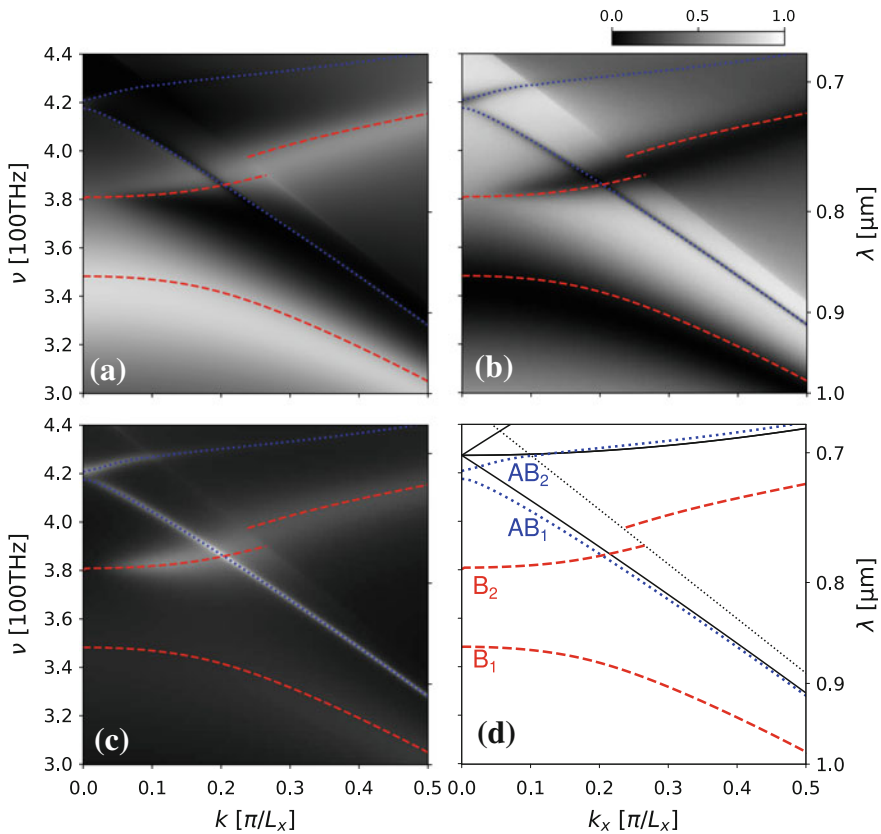
From (14.45), we can see that the dispersion relation is reduced to that of SPF within the SIBC approach, if the coupling between the waveguide mode and the diffraction mode is negligibly small ( $|S|^2 \simeq 0$ ). However, when  $\gamma_\pm$  diverges, the wavenumber also diverges. Although the loss of gold prevents from diverging, this divergence property remains and the dispersion relation flattens when the denominator of  $\gamma_\pm$  approaches zero, which is nothing but the condition for the Fabry-Perot resonance. In other words, the even- (odd-) order Fabry-Perot resonances strongly pull the dispersion of B (AB) mode away from the SPF dispersion into the Fabry-Perot resonance frequency. This situation also applies in the zero-order Fabry-Perot condition, which occurs at the cutoff frequency of the waveguide mode. In the zero-order Fabry-Perot condition, the wave number diverges even in the semi-infinite ( $h \rightarrow \infty$ ) limit where  $\gamma_\pm \rightarrow 1$ , since  $Y_\alpha$  also goes to 0 at cutoff frequency. This is just the spoof surface plasmon.

Figure 14.5c, d show the dispersion relation of (14.45) together with the SPF dispersion (black dotted line) and the Fabry-Perot resonance frequencies (pink dotted line for zero-order and light-blue dotted line for first-order). In the case of  $r = 0.15 \mu\text{m}$ , the dispersion of B mode has the property of spoof surface plasmon and largely deviates from the dispersion of SPP. On the other hand, we can think that the AB mode is SPP-like.



### 14.7 Multipole Surface Plasmon Polariton

Figure 14.6 shows the spectra of (a) zero-order transmission, (b) zero-order reflection and (c) total absorption. The panel (d) shows the dispersion relation of the four LSBMs (two bonding modes,  $B_1$  and  $B_2$ , shown by red dashed lines, and two anti-bonding modes,  $AB_1$  and  $AB_2$ , shown by blue dotted lines) together with the Rayleigh frequencies (black dotted lines) and the empty-lattice band of SPP (black solid lines). The dispersion relations of the surface bound modes are also shown in the panels (a)–(c). We can clearly see that the resonant peaks or dips in the spectrum follow the dispersion relations of LSBMs. Although there is abrupt change of the spectra on the line of the Rayleigh frequency, the profile of change is quite different from the resonant behavior. We conclude that the resonant structure of spectra is produced



**Fig. 14.6** Zero-order **a** transmission, **b** reflection, and **c** total absorption spectra for a square lattice of nanohole with the radius of  $0.15 \mu\text{m}$  in water. The bonding (anti-bonding) modes are shown by the pink dashed (light blue dotted) lines. Black solid (dotted) lines in **d** indicate the empty-lattice bands of SPP (Rayleigh frequency) at the metal-water interface

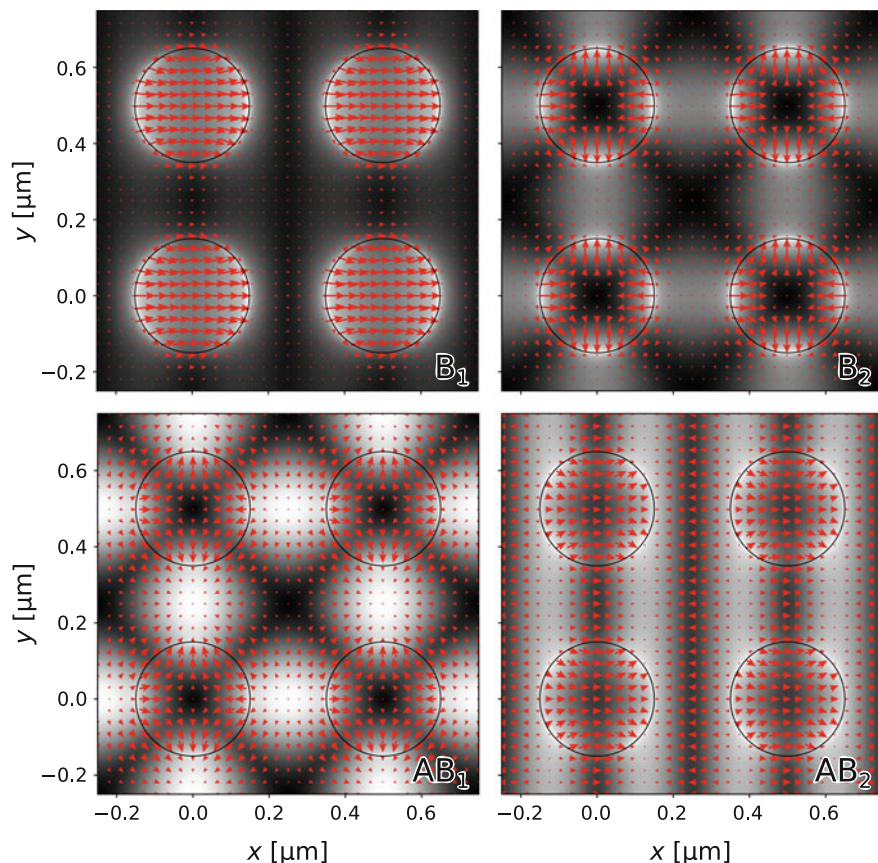


**Fig. 14.7** Electric field distributions of resonance modes at 2 nm above the surface of the golden film for  $k_x = 0$

by LSBMs. However, it is worth noting that the dispersion lines of LSBMs become discontinuous or even vanish on the Rayleigh frequency lines. In the case of one-dimensional gratings on a substrate, there is a situation that a sharp peak appears just on the Rayleigh line due to this effect [44].

Figure 14.7 shows the electric field distributions at 2 nm above the surface of the gold film for the surface bound modes for  $k_x = 0$ . We can see dipole ( $B_1$ ,  $AB_2$ ) and quadrupole ( $B_2$ ,  $AB_1$ ) texture for each branch of the surface bound modes.

In order to see the role played by the waveguide modes to create these multipole textures, we have analyzed the contribution of waveguide modes for each branch. Figure 14.8 shows the rate of contribution of the dipolar  $HE_{11}$  mode (a, c) and the quadrupolar  $HE_{21}$  mode (b, d). The bright color means that the rate of contribution of the mode is high. It is clearly seen that each branch of the B modes is mainly created by a single waveguide mode. This means that spoof-plasmon-like B modes

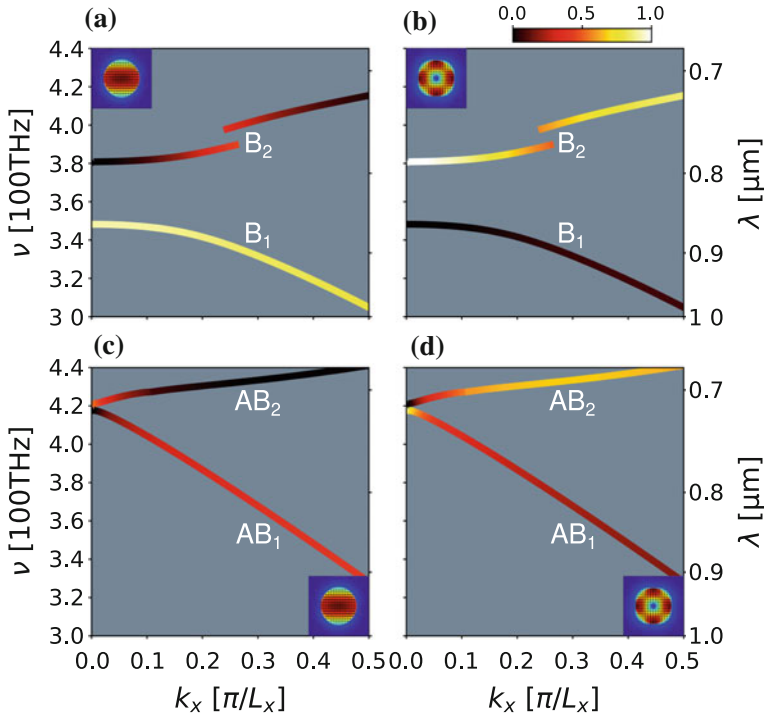


**Fig. 14.8** Rate of contribution of each waveguide mode to create bonding bound modes calculated using the coupled-mode method. Insets show the electric field distributions of waveguide modes

yields higher energy branches with multipole textures according to the higher order waveguide modes. The contribution of the waveguide modes to the AB modes is more complicated. The contribution rates of HE<sub>11</sub> and HE<sub>21</sub> modes are reversed around the  $\Gamma$  point.

### 14.8 Multiple Fano Resonance Interference

These four bound modes produce asymmetric Fano line shape in the transmission spectra. Figure 14.9 shows the transmission (a, c) and reflection (b, d) spectra for normal incidence to a lattice of nanohole with the radius of 0.15  $\mu\text{m}$  in water. In this case, B<sub>2</sub> and AB<sub>1</sub> modes are pure quadrupolar modes, and cannot be excited by the incident light. You can see clear Fano line shape in the green dashed lines (lossless cases) around the resonance concerning AB<sub>2</sub> mode.

Figure 14.10 shows the transmission (a, c) and reflection (b, d) spectra for the oblique incidence with  $k_x = 0.086\pi/L$ , where other conditions are the same as in

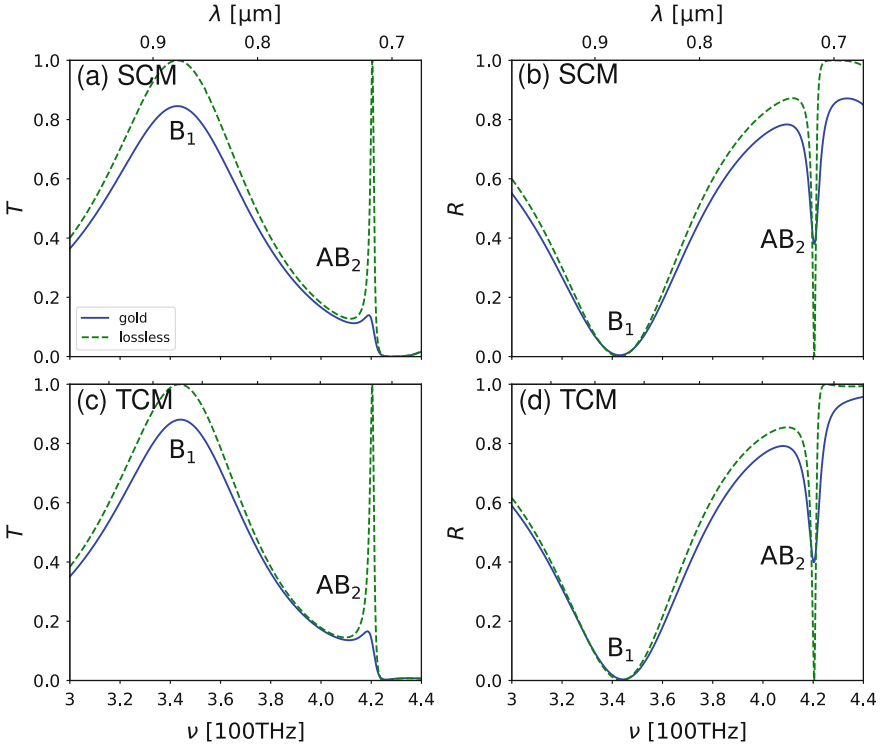


**Fig. 14.9** Transmission (a, c) and reflection (b, d) spectra for normal incidence to a lattice of nanohole with the radius of  $0.15 \mu\text{m}$  in water. The blue solid and green dashed lines are for the real gold and lossless gold systems, respectively. **a** and **b** are obtained by SCM method and **c** and **d** are obtained by TCM method based on two-mode model

Fig. 14.9. This figure also shows the occurrence of Fano-resonance-like phenomena concerning  $B_2$ ,  $AB_1$  and  $AB_2$  modes.

From now on, we will focus our attention to the region under the Rayleigh-frequency line in Fig. 14.6. In this lower left region, only the zero-order diffraction is radiative. Therefore, we can treat this system as a 4-mode or 2-mode cavity system connected to the radiative field by 2 sets of input and output channels. The essential parameters of cavity modes can be extracted from the results of SCM method. The radiative damping rate  $\gamma$  can be estimated from the damping rate for the lossless metal system. By subtracting this rate from the total damping rate, we get the internal damping rate  $\gamma_i$ . In the following, we commonly take the transmission and reflection coefficients as  $t_d = -i [0.22i \tanh \{2(\nu - 346[\text{THz}])\}] + 0.11$ ,  $r_d = -\sqrt{1 - |t_d|^2}$ , part of which may compensate the deficiency of the approximation in the TCM method to express the broad peak of  $B_1$  mode.

Figures 14.9c, d and 14.10 c, d show the results obtained by TCM method using the above procedure, the TCM theory can reproduce qualitative feature of the trans-

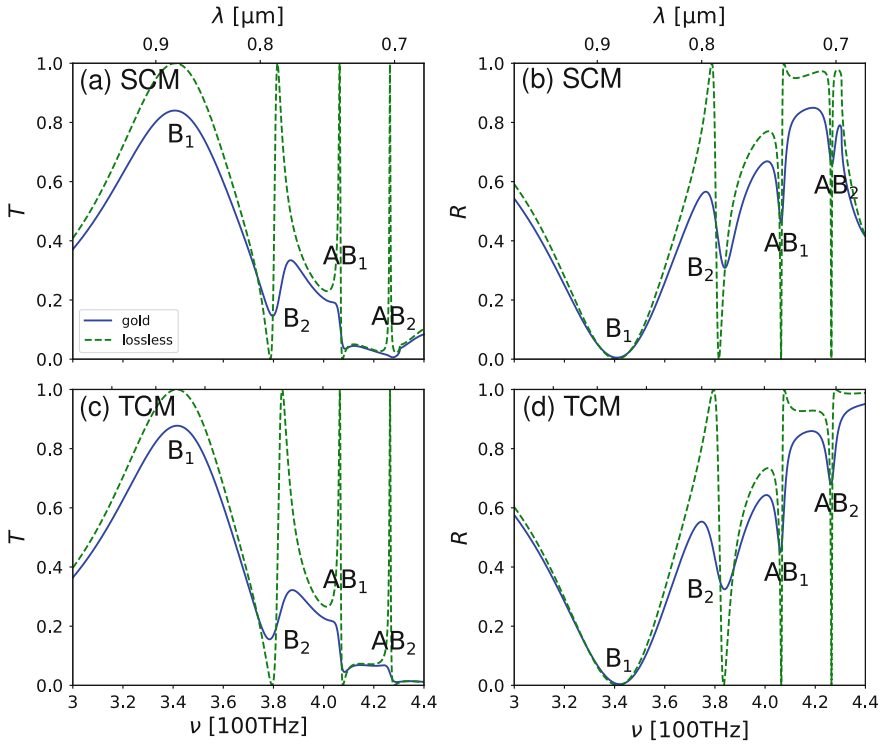


**Fig. 14.10** Transmission (a, c) and reflection (b, d) spectra for the incidence with  $k_x = 0.086\pi/L$  to a lattice of nanohole with the radius of  $0.15 \mu\text{m}$  in water. The blue solid and green dashed lines are for the real gold and lossless gold systems, respectively. **a** and **b** are obtained by SCM method and **c** and **d** are obtained by TCM method based on four-mode model

mission spectra. As we mentioned above, the AB modes and the higher energy B modes have multipole natures, and can be considered as dark modes. The peak and dip structures in the spectra would be attributed to the Fano resonances between the brighter modes and the darker modes [45].

The 4-mode phenomena can be understood by the combination of 2-mode effects. Figure 14.11 shows the results of 2-mode model of TCM method,  $B_1 + B_2$ ,  $B_1 + AB_1$  and  $B_1 + AB_2$ . We can see clear Fano line shapes as expected. The three resonance peaks at higher frequency in Fig. 14.10 are basically understood by the combination of these three Fano resonances, although the detailed line shape is determined by the interference between them. Thus, rather complicated and rich structure in the transmission and reflection spectra of this system can be attributed to the interference between multiple Fano resonances concerning various orders of multipole surface plasmons.

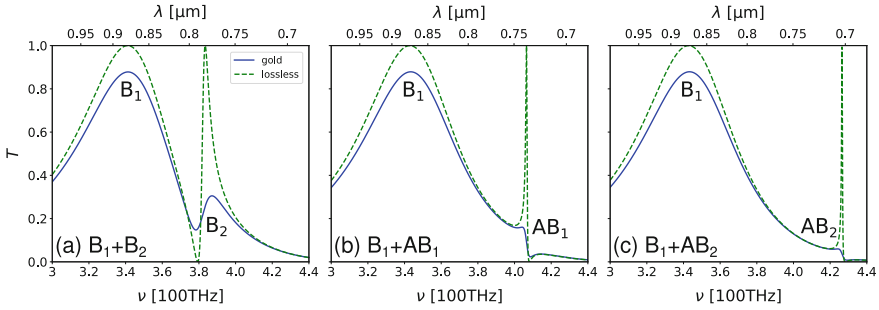


**Fig. 14.11** Transmission spectra obtained by two-mode model of TCM method with **a**  $B_1$  and  $B_2$  modes, **b**  $B_1$  and  $AB_1$  modes, **c**  $B_1$  and  $AB_2$  modes

### 14.9 EIT-like Phenomena

Due to the orthogonality between the B and AB modes, there remain some crossing points in the dispersion curves. Figure 14.12a shows the transmission, reflection, and absorption spectra at the wavenumber  $k_x = 0.2\pi/L$ , which contains the crossing point between  $B_2$  branch and  $AB_1$  branch. Figure 14.12b shows the transmission and reflection spectra calculated by omitting the imaginary part of the dielectric function of gold. Figure 14.12c, d are the results calculated based on the 3-mode model of TCM theory with the parameters extracted from the SCM results in (a) and (b). You can see that the absorption is enhanced strongly around the crossing point. In the results of lossless gold system, (b) and (d), you can see EIT-like line shape with a narrow window within a broader band. These properties are seen more clearly in Fig. 14.12e, f, which are calculated by the 2-mode model of TCM theory using only  $B_2$  and  $AB_1$  modes. The sharpness of the resonance “window” means that the energy remains in the localized modes in a long period of time. If the metal loss is included, almost all the incident energy is consumed around the metal region before it is radiated back. Thus, actual behavior results in a dip both in the transmission and reflection as in Fig. 14.12a, c [29].

This EIT-like phenomenon causes quite high electric-field enhancement. Figure 14.13a and the green dashed line in (b) show the spectra of the averaged field enhancement,  $|\mathbf{E}_{av}|^2/|\mathbf{E}_0|^2$ , where  $|\mathbf{E}_{av}|^2$  denotes the strength of the electric field averaged within a unit cell at 2 nm from the metal surface, and  $|\mathbf{E}_0|^2$  denotes that of incident light. We can see that the field enhancement is increased strongly by the occurrence of degenerate Fano resonance. The blue solid line in (b) represents the maximum values of field enhancement. 14.13c shows the electric field distribution at 2 nm from the metal surface, where quadrupole texture and the hot spots at the hole edges are clearly seen. Thus, the high degrees of freedom of multipole surface plasmons in metallic nanohole arrays will open the possibility to improve the functionality of plasmonic sensors and devices via degenerate Fano resonances.

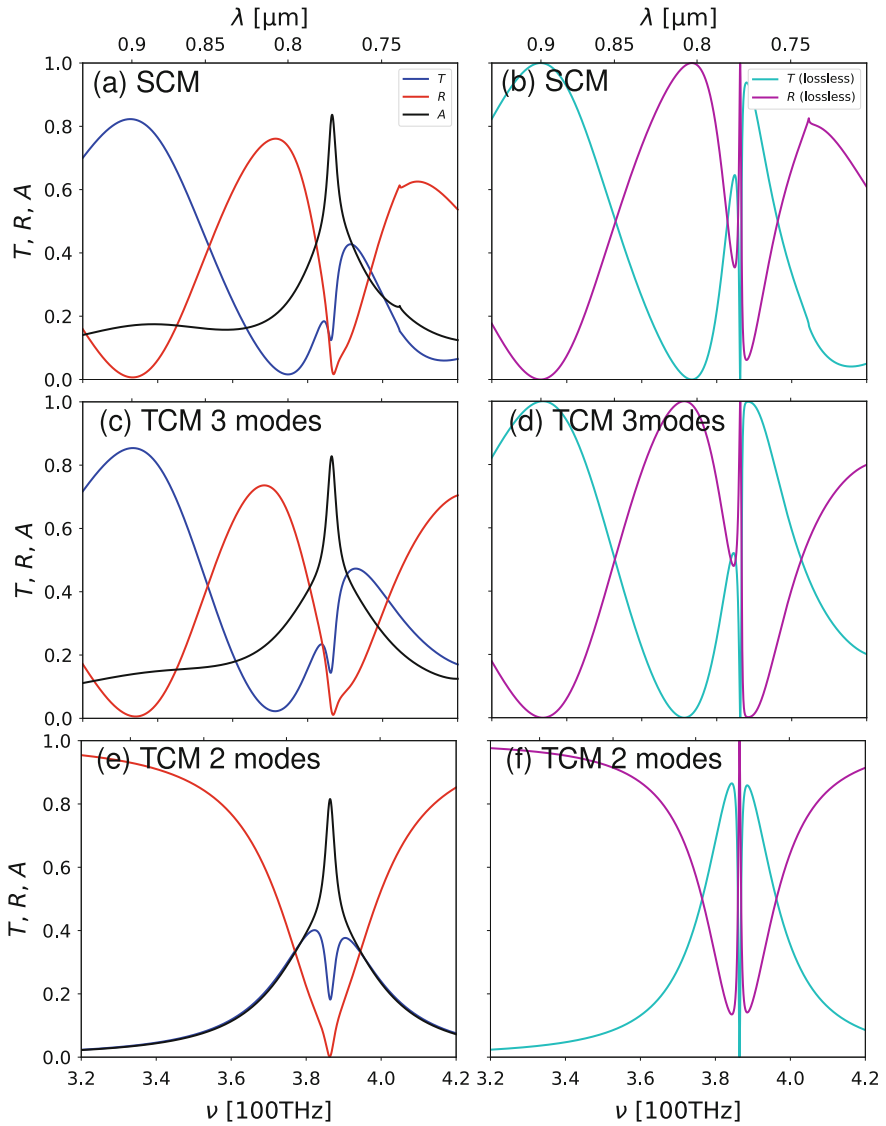


**Fig. 14.12** **a** Reflection (red line), transmission (blue line), and absorption (black line) spectra around the crossing point between  $B_2$  and  $AB_1$  modes. **b** Reflection (pink line) and transmission (light-blue line) spectra for lossless gold system. **c, d** The results of three-mode model of TCM method. **e, f** The results of two-mode model of TCM method

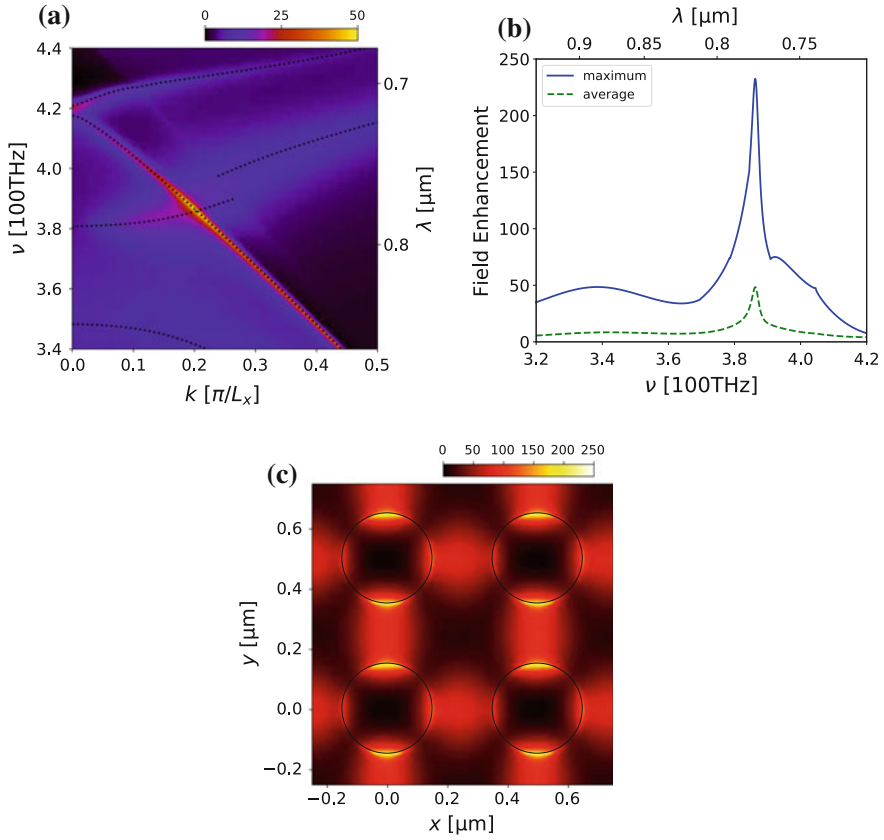


**Fig. 14.13** **a** Spectra of electric field enhancement averaged in the unit cell. **b** Maximum (blue solid line) and averaged (green dashed line) electric field enhancement around the crossing point between  $B_2$  and  $AB_1$  modes. **c** Electric field distribution at the crossing point

## 14.10 Summary

In this chapter, we have shown the essential properties in metallic nanohole array systems, such as spoof surface plasmon and surface plasmon molecule induced by the Fabry-Perot resonance in nanohole waveguides, the Fano resonance due to the interference between resonant and non-resonant transmission processes, short-circuit effect on the dispersion relation of SPF, and multipole surface plasmons produced by the multipolar waveguide modes, based on a set of theoretical formalism; spatial coupled-mode (SCM) method and temporal coupled-mode (TCM) method.

As a result of these properties, various leaky surface bound modes with different darkness according to their multipole natures coexist within a narrow range of frequencies. We have shown that the interference between the radiations from these multiple resonances yields sharp peak-dip structure in the transmission and reflection



spectra. Especially, we have shown that the degeneracy of the surface bound modes induces EIT-like phenomena and yields remarkable features, i.e. high enhancement of absorption and electric-field.

Further study of this system with powerful theoretical tools like SCM and TCM methods will give deeper understandings of not only the Fano resonance but also other important concepts in the open wave system, such as exceptional point [46, 47] or bound state in the continuum [48].

## References

1. S.A. Maier, *Plasmonics: Fundamentals and Applications* (Springer, 2007)
2. T.W. Ebbesen, H.J. Lezec, H.F. Ghaemi, T. Thio, P.A. Wolff, *Nature* **391**(6668), 667 (1998)
3. H.A. Bethe, *Phys. Rev.* **66**(7, 8), 163 (1944)
4. A. Roberts, *J. Opt. Soc. Am. A* **4**(10), 1970 (1987)
5. F.J. García-Vidal, L. Martín-Moreno, T.W. Ebbesen, L. Kuipers, *Rev. Mod. Phys.* **82**, 729 (2010)
6. R. Wood, *Phil. Mag.* **4**(21), 396 (1902)
7. A. Hessel, A.A. Oliner, *Appl. Opt.* **4**(10), 1275 (1965)
8. D. Maystre, in *Plasmonics*, ed. by S. Enoch, N. Bonod (Springer, 1992), pp. 39–83
9. J.B. Pendry, L. Martín-Moreno, F.J. Garcia-Vidal, *Science* **305**, 847 (2004)
10. L. Martín-Moreno, F.J. Garcia-Vidal, H.J. Lezec, K.M. Pellerin, T. Thio, J.B. Pendry, T.W. Ebbesen, *Phys. Rev. Lett.* **86**(6), 1114 (2001)
11. T. Park, N. Mirin, J.B. Lassiter, C.L. Nehl, N.J. Halas, P. Nordlander, *ACS Nano* **2**(1), 25 (2008)
12. M. Nishida, N. Hatakenaka, Y. Kadoya, *Phys. Rev. B* **91**, 235406 (2015)
13. M. Fukui, V.C.Y. So, R. Normandin, *physica status solidi (b)* **91**(1), K61 (1979)
14. D. Sarid, *Phys. Rev. Lett.* **47**, 1927 (1981)
15. U. Fano, *Phys. Rev.* **124**, 1866 (1961)
16. M. Sarrazin, J.P. Vigneron, J.M. Vigoureux, *Phys. Rev. B* **67**, 085415 (2003)
17. C. Genet, M. van Exter, J. Woerdman, *Opt. Commun.* **225**(46), 331 (2003)
18. O.M.L. Rayleigh, *Proc. R. Soc. Lond. A.* **79**(532), 399 (1907)
19. A.E. Miroshnichenko, S. Flach, Y.S. Kivshar, *Rev. Mod. Phys.* **82**, 2257 (2010)
20. H. Feshbach, *Ann. Phys.* **19**(2), 287 (1962)
21. F.H. Mies, *Phys. Rev.* **175**, 164 (1968)
22. M. Fleischhauer, A. Imamoglu, J.P. Marangos, *Rev. Mod. Phys.* **77**, 633 (2005)
23. L.V. Hau, S.E. Harris, Z. Dutton, C.H. Behroozi, *Nature* **397**(6720), 594 (1999)
24. D.F. Phillips, A. Fleischhauer, A. Mair, R.L. Walsworth, M.D. Lukin, *Phys. Rev. Lett.* **86**, 783 (2001)
25. C. Liu, Z. Dutton, C.H. Behroozi, L.V. Hau, *Nature* **409**(6819), 490 (2001)
26. D.D. Smith, H. Chang, K.A. Fuller, A.T. Rosenberger, R.W. Boyd, *Phys. Rev. A* **69**, 063804 (2004)
27. W. Suh, Z. Wang, S. Fan, *IEEE J. Quantum Electron.* **40**(10), 1511 (2004)
28. C.L.G. Alzar, M.A.G. Martinez, P. Nussenzveig, *Am. J. Phys.* **70**(1), 37 (2002)
29. P. Tassin, L. Zhang, R. Zhao, A. Jain, T. Koschny, C.M. Soukoulis, *Phys. Rev. Lett.* **109**, 187401 (2012)
30. F.J. García-Vidal, E. Moreno, J.A. Porto, L. Martín-Moreno, *Phys. Rev. Lett.* **95**, 103901 (2005)
31. F. de León-Pérez, G. Brucoli, F.J. García-Vidal, L. Martín-Moreno, *New J. Phys.* **10**(10), 105017 (2008)
32. H.A. Haus, *Waves and Fields in Optoelectronics* (Prentice Hall, Englewood Cliffs, NJ, 1983)
33. S. Fan, W. Suh, J.D. Joannopoulos, *J. Opt. Soc. Am. A* **20**(3), 569 (2003)
34. H.A. Lorentz, *Versl. Kon. Akad. Wetensch. Amsterdam* **4**, 176 (1895)

35. A.T. de Hoop, *Appl. Sci. Res. Section B* **8**(1), 135 (1960)
36. P. Lalanne, J.P. Hugonin, J.C. Rodier, *Phys. Rev. Lett.* **95**, 263902 (2005)
37. J.D. Jackson, *Classical Electrodynamics*, 3rd edn. (Wiley, New York, 1999)
38. R.E. Collin, *Foundations for Microwave Engineering* (2nd edn.) (McGrawHill, 1992)
39. J.R. Taylor, *Scattering Theory* (Wiley, New York, 1972)
40. N.A. Gippius, S.G. Tikhodeev, T. Ishihara, *Phys. Rev. B* **72**, 045138 (2005)
41. T. Lepetit, B. Kanté, *Phys. Rev. B* **90**, 241103 (2014)
42. A. Kodigala, T. Lepetit, B. Kanté, *J. Appl. Phys.* **117**(2), 023110 (2015)
43. Z. Ruan, M. Qiu, *Phys. Rev. Lett.* **96**, 233901 (2006)
44. R. Kikkawa, M. Nishida, Y. Kadoya, *J. Opt. Soc. Am. B* **34**(12), 2578 (2017)
45. B. Luk'yanchuk, N.I. Zheludev, S.A. Maier, N.J. Halas, P. Nordlander, H. Giessen, C.T. Chong, *Nat. Mater.* **9**(9), 707 (2010)
46. N. Moiseyev, *Non-Hermitian Quantum Mechanics* (Cambridge University Press, Cambridge, UK, 2011)
47. W.D. Heiss, *J. Phys. A Math. Theor.* **45**(44), 444016 (2012)
48. C.W. Hsu, B. Zhen, A.D. Stone, J.D. Joannopoulos, M. Soljačić, *Nat. Rev. Mater.* **1**, 16048 (2016)

# Chapter 15

## Resonant-State Expansion of the Fano Peak in Open Quantum Systems



Naomichi Hatano and Gonzalo Ordóñez

**Abstract** We describe the Fano asymmetry by expanding the transmission amplitude with respect to states with point spectra (discrete eigenstates), including not only bound states but also resonant states with complex eigenvalues. We first introduce a novel complete set that spans the Hilbert space of the central part of an open quantum-dot system. This complete set contains all states of point spectra, but does not contain any states of continuous spectra. We thereby analytically expand the conductance of the dot in terms of all discrete states without any background integrals. This expansion implies that the resonant states produce the main contributions to the electron transmission. We then explain the Fano peak as an interference effect involving resonant states. We find that there are three types of Fano asymmetry according to their origins: the interference between a resonant state and an anti-resonant state, that between a resonant state and a bound state, and that between two resonant states. We derive microscopic expressions of the Fano parameters that describe the three types of Fano asymmetry. We show that the last two types display the asymmetric energy dependence given by Fano, but the first one shows a slightly different form.

### 15.1 Introduction: Resonant States

#### 15.1.1 Landauer Formula and the Transmission Probability

The Landauer formula [1, 2] tells us that the electronic conductance  $\mathcal{G}$  in the situation of Fig. 15.1a (where we ignore the electron-electron interaction) is given by the transmission probability  $T$  of the scattering problem in the infinite space as in Fig. 15.1b:

---

N. Hatano (✉)

Institute of Industrial Science, The University of Tokyo, 5-1-5 Kashiwanoha,  
Kashiwa, Chiba 277-8574, Japan  
e-mail: hatano@iis.u-tokyo.ac.jp

G. Ordóñez

Department of Physics and Astronomy, Butler University, 4600 Sunset Avenue,  
Indianapolis, IN 46208, USA  
e-mail: gordonez@butler.edu

© Springer Nature Switzerland AG 2018

E. Kamenetskii et al. (eds.), *Fano Resonances in Optics and Microwaves*, Springer  
Series in Optical Sciences 219, [https://doi.org/10.1007/978-3-319-99731-5\\_15](https://doi.org/10.1007/978-3-319-99731-5_15)

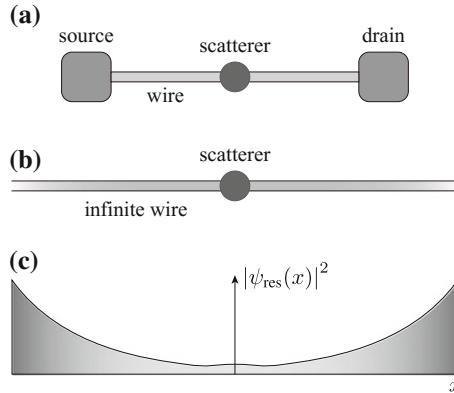


**Fig. 15.1** **a** The situation of electronic conduction in mesoscopic systems. A quantum wire with a quantum scatterer connects a source and a drain. The Landauer formula claims that the electronic conductance of the setup **(a)** is proportional to the transmission probability of the setup **(b)**. The spatial divergence **(c)** of the resonant state of the scattering problem in the setup **(b)** indicates that there are macroscopic numbers of electrons in the source and the drain in the setup **(a)**

$$G = \frac{2e^2}{h} T, \quad (15.1)$$

where  $e$  is the elementary charge of an electron and  $h$  is the Planck constant. The two setups have the following common feature: once an electron goes out of the central quantum scatterer, it never comes back to the scattering area, at least not coherently [3]. This is why the quantum scattering problem in the setup **(b)** can describe the electronic conduction in the setup **(a)**.

The Fano asymmetry of the conductance is therefore equivalent to the Fano asymmetry of the transmission probability. In the present chapter, we introduce the expansion of the transmission probability in terms of all eigenstates of the Hamiltonian with point spectra, including the bound, anti-bound, resonant, and anti-resonant states, but not including the scattering states with a continuous spectrum, thereby excluding the background integral [3–10]. Among the eigenstates with point spectra, the states other than the bound states, namely the resonant and anti-resonant states, mostly contribute to the electronic conduction; this is the point that we emphasize in the present chapter. We describe the Fano asymmetry of the transmission probability in terms of interference between two point-spectral eigenvalues [4].

We will try to make the chapter as self-contained as possible. For the purpose, we will review in the present section the classification of the point-spectral eigenvalues in scattering theory in one dimension with a tutorial example. In the next Sect. 15.2, we will show the resonant-state expansion of the transmission probability with another tutorial example of the tight-binding model. In Sect. 15.3, we finally show our numerical analysis of the Fano asymmetry in the tight-binding model. We find three types of the Fano asymmetry, depending on what pair of point-spectral states interferes with each other.

### 15.1.2 Siegert Boundary Condition: A Tutorial Example

We hereafter refer to the eigenstates with point spectra as the *discrete* eigenstates. The discrete eigenvalues are often defined as poles of the S-matrix, or the transmission amplitude in one dimension. The transmission amplitude is given by the amplitude of the transmitted wave divided by that of the incident wave. Therefore, the poles of the transmission amplitude correspond to the zeros of the amplitude of the incident wave [3, 11, 12]. This means that the wave function of the discrete eigenvalues lacks the incident wave, retaining only the reflected and transmitted waves, in other words, only out-going waves; see Fig. 15.2. This is why the poles of the transmission amplitude are identified with the eigenstates of the time-independent Schrödinger equation under the boundary conditions of out-going waves only, which was first set by Siegert [13].

Let us demonstrate how to solve the time-independent Schrödinger equation under the Siegert boundary condition. We consider the standard equation

$$\left(-\frac{\hbar^2}{2m} \frac{d^2}{dx^2} + V(x)\right) \psi(x) = E\psi(x) \tag{15.2}$$

with the square-well potential

$$V(x) := \begin{cases} -V_0 & \text{for } |x| < a, \\ 0 & \text{for } |x| > a, \end{cases} \tag{15.3}$$

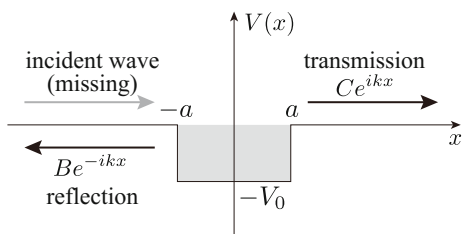
where  $V_0 > 0$ ; see Fig. 15.2. We solve this under the Siegert boundary conditions

$$\psi(x) \sim e^{ik|x|}. \tag{15.4}$$

More precisely, we assume the form

$$\psi(x) = \begin{cases} Be^{-ikx} & \text{for } x < -a, \\ Fe^{ik'x} + Ge^{-ik'x} & \text{for } |x| < a, \\ Ce^{ikx} & \text{for } x > a, \end{cases} \tag{15.5}$$

**Fig. 15.2** The potential function given in (15.3). The discrete eigenstates are given by setting the incident wave to zero, which is the Siegert boundary condition (15.4)



where

$$E = \frac{\hbar^2 k^2}{2m} = \frac{\hbar^2 k'^2}{2m} - V_0. \quad (15.6)$$

We then set the connection conditions at  $x = \pm a$ , which produce four equations. On the other hand, there are four unknown variables, namely the wave number  $k$  (or equivalently the eigenenergy  $E$ ) and the three ratios among the amplitudes  $B$ ,  $C$ ,  $F$  and  $G$ . We therefore obtain discrete solutions, namely point spectra. Note that in finding the standard scattering states, we have another unknown variable, namely the amplitude of the incident wave  $A$ , in which case we obtain solutions for arbitrary  $k$ , namely continuous spectra. This is the basic difference between the present discrete solutions and the continuum scattering solution.

At this point, it is convenient to take advantage of the parity of the potential, finding even and odd solutions separately. Even solutions should satisfy the equations  $B = C$  and  $F = G$ , which yield

$$\psi(x) = \begin{cases} 2F \cos(k'x) & \text{for } 0 < x < a, \\ Ce^{ikx} & \text{for } x > a. \end{cases} \quad (15.7)$$

The connection conditions give

$$2F \cos(k'a) = Ce^{ika}, \quad (15.8)$$

$$-2k'F \sin(k'a) = ikCe^{ika}. \quad (15.9)$$

Dividing the second equation by the first one, we have

$$-k' \tan(k'a) = ik. \quad (15.10)$$

We obtain the even eigensolutions by solving (15.6) and (15.10) simultaneously. Similarly, odd solutions are given by solving (15.6) together with

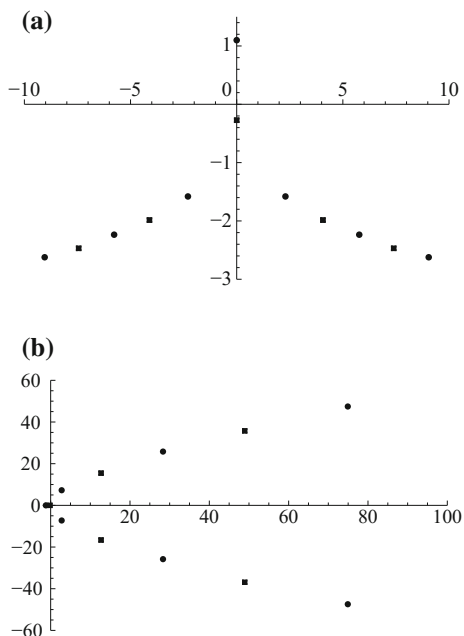
$$k' \cot(k'a) = ik. \quad (15.11)$$

Numerically computing the solutions by the Newton-Raphson method, we obtain the solutions plotted in Fig. 15.3.

### 15.1.3 Resonant and Anti-resonant States

The state on the positive part of the imaginary axis of the complex wave-number plane is a bound state. We can see this by inserting  $k = i\kappa$  with  $\kappa > 0$  into the boundary

**Fig. 15.3** The locations of the discrete eigenstates **a** in the complex-wave-number plane and **b** in the complex energy plane. In both panels, the circles indicate the even solutions of (15.10) and the squares the odd solutions of (15.11)



condition (15.4). It is located on the negative part of the real axis of the complex energy plane.

The states on the fourth quadrant of the complex wave-number plane are historically called resonant states, while those on the third quadrant are called anti-resonant states. These states are located, respectively, on the lower and upper halves of (the second Riemann sheet of) the complex energy plane. We can prove that the time-reversal symmetry of the original problem (15.2) dictates that each resonant state must have its complex conjugate partner of anti-resonant state; although each of resonant and anti-resonant states breaks the time-reversal symmetry, the whole set of the solutions still observes the time-reversal symmetry. The state on the negative part of the imaginary axis in the complex wave-number plane, and correspondingly on the negative part of the real axis in the second Riemann sheet of the complex energy plane, is called an anti-bound state, but we do not pay much attention to it throughout this chapter.

Since all the resonant and anti-resonant states are located on the lower half of the complex wave-number plane, their wave functions diverge spatially away from the scattering potential, being unnormalizable. This is presumably the reason why they are often called unphysical. Let us try in two ways to convince the readers that they are actually physical entities.

We first clarify a physical view of the spatial divergence [3, 12] by multiplying the wave function (15.4) by the temporal part as in

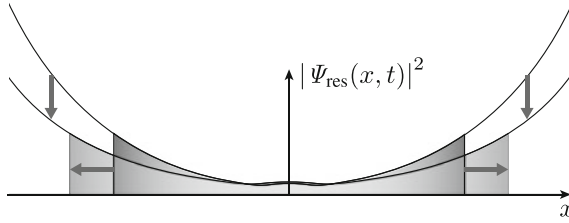


**Fig. 15.4** The proof of the probability conservation. As the time goes by, the wave function decays exponentially. Accordingly, we expand the integration region to follow the exponential spatial divergence

$$\Psi_n(x, t) \sim e^{ik_n|x| - iE_n t}. \quad (15.12)$$

For the resonant states in the fourth quadrant, the real part of the eigen-wave-number  $k_n$  is positive, while the imaginary part of the eigenenergy  $E_n$  is negative. Therefore, the wave amplitude decays exponentially in time and the corresponding amount of the amplitude leaks towards positive and negative infinities. For the anti-resonant states in the third quadrant, the real part of the eigen-wave-number is negative and the imaginary part of the eigenenergy is positive. Therefore, the wave amplitude comes into the central scattering area and the amplitude there grows exponentially in time. The anti-resonant states are time-reversal of the resonant states.

Based on this view, we can prove that the probability is conserved [3, 12, 14] under the following two conditions (Fig. 15.4): first, we calculate the probability in a finite segment  $[-L, L]$  containing the support  $[-a, a]$  of the scattering potential; second, we let the integration area expand as in  $[-L(t), L(t)]$  in order to chase the leaking amplitude for a resonant state. (We shrink the area for an anti-resonant state.) The spatial divergence is exactly cancelled by the temporal decay. This indicates that the spatial divergence is actually essential for the probability conservation.

Let us present another view of the spatial divergence. In what we will show in Sect. 15.2, we reveal that the transmission probability mostly comes from the resonant and anti-resonant states, in other words, the spatially divergent states. This is indeed consistent with the original situation that was considered in the Landauer formula. The Landauer formula assumes free electrons, neglecting electron-electron interactions, and hence we can regard the probability of the present one-electron problem as a quantity proportional to the number of electrons in a many-electron problem. Therefore, the spatial divergence of the resonant and anti-resonant wave functions of the one-electron problem implies that there are macroscopic number of electrons far away from the scattering center. As we see in Fig. 15.1a, the system indeed has two baths (source and drain) away from the scattering potential, both of which have a macroscopic number of electrons under equilibrium. These baths are the cause of the Joule heat generated by the resistance that the Landauer formula gives as the inverse conductance; a microscopic number of electrons out of the source keeps the Fermi distribution of the source during the energy-conserving quantum scattering all the way up until it meets a different Fermi distribution of the drain



and is equilibrated to it. That is when the Joule heat is generated [2]. In this view, it is essential for the Landauer formula to hold that the baths have a macroscopic number of electrons so that their Fermi distributions may never be disturbed by the microscopic number of electrons that participate in the conduction. This situation is reproduced quantum-mechanically by the spatial divergence of the resonant and anti-resonant wave functions; see Fig. 15.1c.

We thus stress that the spatially divergent resonant and anti-resonant states are not at all unphysical; on the contrary, they are indispensable states for the electronic conduction.

## 15.2 Resonant-State Expansion: Another Tutorial Example

### 15.2.1 Transmission Probability and the Green's Function

So far, we have considered a scattering potential in a continuum space. We here move to a discretized model, namely the tight-binding model. As another tutorial example, let us consider the T-shaped quantum-dot model (Fig. 15.5):

$$H := -t_{\text{hop}} \sum_{x=-\infty}^{\infty} (|x+1\rangle\langle x| + |x\rangle\langle x+1|) + \varepsilon_0|0\rangle\langle 0| + \varepsilon_d|d\rangle\langle d| - g(|0\rangle\langle d| + |d\rangle\langle 0|), \quad (15.13)$$

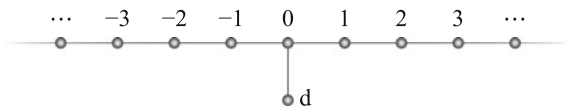
where  $t_{\text{hop}}$  is the hopping amplitude on the quantum wire with  $-\infty < x < \infty$ ,  $\varepsilon_0$  is the potential at the site  $x = 0$ ,  $\varepsilon_d$  is the potential at the quantum-dot site  $d$ , and  $g$  is the hopping amplitude between  $x = 0$  and  $d$ . We hereafter set  $t_{\text{hop}} = 1$  for brevity. The central scattering area consists of the two sites  $|d\rangle$  and  $|0\rangle$ , while the rest is the environment.

As we emphasized in Sect. 15.1.1, the electronic conductance is given by the transmission probability. The energy dependence of the transmission probability of the model above is given by the Green's function in the following form [15]:

$$T(E) = (4 - E^2) \left| \langle 0 | \frac{1}{E - H} | 0 \rangle \right|^2. \quad (15.14)$$

The goal of the present section is to represent the Green's function in terms of all discrete states. In order to do so, we first use the Feshbach formalism [16] to eliminate

**Fig. 15.5** The tutorial model of (15.13)



the infinite number of the environmental degrees of freedom and express the Green's function by means of an effective Hamiltonian as small as a two-by-two matrix. We then expand the Green's function of the effective Hamiltonian with respect to its eigenstates.

### 15.2.2 Feshbach Formalism for the Tight-Binding Model

Let us overview the Feshbach formalism [4, 8, 16] here. Our task is to find the solutions of the eigenvalue problem

$$H|\psi\rangle = E|\psi\rangle. \quad (15.15)$$

It is generally difficult to solve it because  $H$  is an  $\infty$ -by- $\infty$  matrix. The Feshbach formalism gives an effective Hamiltonian for the central scattering area:

$$H_{\text{eff}}(E)(P|\psi\rangle) = E(P|\psi\rangle), \quad (15.16)$$

where

$$P := |d\rangle\langle d| + |0\rangle\langle 0| \quad (15.17)$$

with

$$\begin{aligned} Q &:= I_\infty - P \\ &= \left( \sum_{x=-\infty}^{-1} + \sum_{x=+1}^{+\infty} \right) |x\rangle\langle x|. \end{aligned} \quad (15.18)$$

Here  $I_\infty$  denotes the identity operator in the entire space. The effective Hamiltonian  $H_{\text{eff}}(E)$  in the present tutorial example is a two-by-two matrix.

Let us apply  $P$  and  $Q$  from the left of (15.15) and at the same time insert  $1 = P + Q$  between  $H$  and  $|\psi\rangle$ :

$$PHP(P|\psi\rangle) + PHQ(Q|\psi\rangle) = E(P|\psi\rangle), \quad (15.19)$$

$$QHP(P|\psi\rangle) + QHQ(Q|\psi\rangle) = E(Q|\psi\rangle), \quad (15.20)$$

where we used the facts  $P^2 = P$  and  $Q^2 = Q$ . We now eliminate  $Q|\psi\rangle$  by finding

$$Q|\psi\rangle = \frac{1}{E - QHQ} QHP(P|\psi\rangle) \quad (15.21)$$

from the second equation and inserting it into the first equation, obtaining

$$\left( PHP + PHQ \frac{1}{E - QHQ} QHP \right) (P|\psi\rangle) = E (P|\psi\rangle). \quad (15.22)$$

We thereby realize that the effective Hamiltonian in (15.16) is given by

$$H_{\text{eff}}(E) = PHP + \Sigma(E) \quad (15.23)$$

with the ‘self-energy’

$$\Sigma(E) := PHQ \frac{1}{E - QHQ} QHP. \quad (15.24)$$

### 15.2.3 Green’s Function of the Effective Hamiltonian

In order to calculate (15.14), we need the Green’s function in the  $P$  subspace:

$$PGP = P \frac{1}{E - H} P. \quad (15.25)$$

We will prove here that this Green’s function is equal to the Green’s function of the effective Hamiltonian [8]:

$$P \frac{1}{E - H} P = P \frac{1}{E - H_{\text{eff}}(E)} P. \quad (15.26)$$

The proof is achieved by splitting the total Hamiltonian into the two parts

$$H = (PHP + QHQ) + (PHQ + QHP) \quad (15.27)$$

and carrying out the resolvent expansion:

$$\begin{aligned} P \frac{1}{E - H} P &= P \frac{1}{E - (PHP + QHQ)} P \\ &+ P \frac{1}{E - (PHP + QHQ)} (PHQ + QHP) \frac{1}{E - (PHP + QHQ)} P \\ &+ P \frac{1}{E - (PHP + QHQ)} (PHQ + QHP) \frac{1}{E - (PHP + QHQ)} \\ &\times (PHQ + QHP) \frac{1}{E - (PHP + QHQ)} P + \dots \end{aligned} \quad (15.28)$$

Using the fact  $PQ = QP = 0$ , we find that only the even-order terms survive, obtaining

$$\begin{aligned}
 P \frac{1}{E-H} P &= P \frac{1}{E-PHP} P \\
 &+ P \frac{1}{E-PHP} PHQ \frac{1}{E-QHQ} QHP \frac{1}{E-PHP} P \\
 &+ P \frac{1}{E-PHP} PHQ \frac{1}{E-QHQ} QHP \frac{1}{E-PHP} \\
 &\quad \times PHQ \frac{1}{E-QHQ} QHP \frac{1}{E-PHP} P + \dots \tag{15.29}
 \end{aligned}$$

$$\begin{aligned}
 &= P \frac{1}{E-PHP} P + P \frac{1}{E-PHP} \Sigma \frac{1}{E-PHP} P \\
 &+ P \frac{1}{E-PHP} \Sigma \frac{1}{E-PHP} \Sigma \frac{1}{E-PHP} P + \dots \tag{15.30}
 \end{aligned}$$

Summing up the resolvent expansion with respect to  $\Sigma$ , we end up with [8]

$$P \frac{1}{E-H} P = P \frac{1}{E-(PHP + \Sigma)} P, \tag{15.31}$$

which is equivalent to (15.26). This implies that we can expand the Green's function, and hence the transmission amplitude (15.14), with respect to the eigenstates of the effective Hamiltonian  $H_{\text{eff}}$ . This is what we will do in Sect. 15.2.5.

### 15.2.4 Calculation of the Self-energy

Before finding the eigenstates of the effective Hamiltonian, let us show an easy way [17] to compute the self-energy (15.24). We can find it in a straightforward way [4, 8] but there is a trick to compute it in a much easier way. We first write down the Schrödinger equation (15.15) for  $|x| \geq 1$ :

$$-(\psi_{x+1} + \psi_{x-1}) = E\psi_x, \tag{15.32}$$

where

$$\psi_x := \langle x | \psi \rangle. \tag{15.33}$$

Let us set the Siegert boundary conditions:

$$\psi_x = Ce^{ik|x|} = C \times \begin{cases} e^{-ikx} & \text{for } x \leq -1, \\ e^{ikx} & \text{for } x \geq 1. \end{cases} \quad (15.34)$$

Note that because of the discretized space, the real part of  $k$  is limited to the first Brillouin zone  $-\pi < \text{Re } k < \pi$ . Inserting the wave function (15.34) into (15.32), we have the dispersion relation

$$E = -2 \cos k. \quad (15.35)$$

We also realize in the Schrödinger equation for  $|x| = 1$  that  $\psi_0 = \langle 0|\psi\rangle = C$ .

We next write down the Schrödinger equation for  $x = 0$  and for the dot site  $d$ :

$$-(\psi_1 + \psi_{-1}) - g\psi_d + \varepsilon_0\psi_0 = E\psi_0, \quad (15.36)$$

$$-g\psi_0 + \varepsilon_d\psi_d = E\psi_d. \quad (15.37)$$

Inserting the Siegert boundary condition (15.34) into the first equation, we have

$$-2e^{ik}\psi_0 - g\psi_d + \varepsilon_0\psi_0 = E\psi_0. \quad (15.38)$$

Combining this with the second equation, we can write down the matrix equation

$$\begin{pmatrix} \varepsilon_0 - 2e^{ik} & -g \\ -g & \varepsilon_d \end{pmatrix} \begin{pmatrix} \psi_0 \\ \psi_d \end{pmatrix} = E \begin{pmatrix} \psi_0 \\ \psi_d \end{pmatrix}. \quad (15.39)$$

We identify [17] the two-by-two matrix on the left-hand side as the effective Hamiltonian  $H_{\text{eff}}$  in (15.16). We can indeed confirm [4, 8] (15.23) with

$$PHP = \begin{pmatrix} \varepsilon_0 & -g \\ -g & \varepsilon_d \end{pmatrix}, \quad \Sigma(E) = \begin{pmatrix} -2e^{ik} & 0 \\ 0 & 0 \end{pmatrix}. \quad (15.40)$$

We observe that the self-energy term functions as an effective complex potential at the site  $x = 0$ , which makes the effective Hamiltonian non-Hermitian.

### 15.2.5 Quadratic Eigenvalue Problem

Let us stress here that the eigenvalue problem (15.39) is not a standard one in the sense that the variable  $k$ , which is related to the energy  $E$ , exists on the left-hand side. Therefore, this is a *nonlinear* eigenvalue problem. In fact, we will show that this is formulated as a quadratic eigenvalue problem.

In order to solve the nonlinear eigenvalue problem, we introduce another energy-related variable as follows [5, 8]:

$$\lambda := e^{ik}. \quad (15.41)$$

Because of the dispersion relation (15.35), the energy is given by

$$E = -\left(\lambda + \frac{1}{\lambda}\right). \quad (15.42)$$

We can thereby transform (15.39) into

$$\begin{pmatrix} \varepsilon_0 - 2\lambda & -g \\ -g & \varepsilon_d \end{pmatrix} \begin{pmatrix} \psi_0 \\ \psi_d \end{pmatrix} = -\left(\lambda + \frac{1}{\lambda}\right) \begin{pmatrix} \psi_0 \\ \psi_d \end{pmatrix}, \quad (15.43)$$

which is followed by

$$\left[ \lambda^2 \begin{pmatrix} -1 & 0 \\ 0 & 1 \end{pmatrix} + \lambda \begin{pmatrix} \varepsilon_0 & -g \\ -g & \varepsilon_d \end{pmatrix} + \begin{pmatrix} 1 & 0 \\ 0 & 1 \end{pmatrix} \right] \begin{pmatrix} \psi_0 \\ \psi_d \end{pmatrix} = 0. \quad (15.44)$$

The fact that the left-hand side is a second-order matrix polynomial of  $\lambda$  is the reason why we call it a quadratic eigenvalue problem. More formally, we have the following equation:

$$Z(\lambda) (P|\psi\rangle) = 0, \quad (15.45)$$

where

$$Z(\lambda) := \lambda^2(I_2 - \Theta) + \lambda PHP + I_2 \quad (15.46)$$

with

$$\Theta := PHQHP \quad (15.47)$$

and  $I_2$  is the two-dimensional identity operator. We note

$$E - H_{\text{eff}}(E) = -\frac{Z(\lambda)}{\lambda}. \quad (15.48)$$

There is a standard way of treating the quadratic eigenvalue problem [18]. We double the dimensionality as in [5, 8]

$$\begin{pmatrix} -\lambda I_2 & I_2 \\ I_2 & \lambda(I_2 - \Theta) + PHP \end{pmatrix} \begin{pmatrix} P|\psi\rangle \\ \lambda P|\psi\rangle \end{pmatrix} = 0. \quad (15.49)$$

Note that each matrix element is actually a two-by-two matrix. The first row gives an equation that guarantees the doubled structure of the vector. The second row gives the original quadratic eigenvalue problem (15.45).

We thereby find four solutions of the two-dimensional nonlinear eigenvalue problem (15.39) out of

$$\det \begin{pmatrix} -\lambda I_2 & I_2 \\ I_2 & \lambda(I_2 - \Theta) + PHP \end{pmatrix} = 0, \quad (15.50)$$

which is a fourth-order equation with respect to  $\lambda$ . In order to show the attributes of the solutions, let us solve the equation in the simplest case of  $\varepsilon_0 = \varepsilon_d = 0$ . The equation is then reduced to

$$\lambda^4 + g^2 \lambda^2 - 1 = 0, \quad (15.51)$$

which produces

$$\lambda^2 = \frac{-g^2 \pm \sqrt{g^4 + 4}}{2}. \quad (15.52)$$

The magnitude of the right-hand side is given by

$$0 < \frac{-g^2 + \sqrt{g^4 + 4}}{2} < 1, \quad \frac{-g^2 - \sqrt{g^4 + 4}}{2} < -1. \quad (15.53)$$

Therefore,

$$\lambda_1, \lambda_2 := \pm \sqrt{\frac{-g^2 + \sqrt{g^4 + 4}}{2}} \quad (15.54)$$

are located on the real axis inside the unit circle  $|\lambda| = 1$ , while

$$\lambda_3, \lambda_4 := \pm i \sqrt{\frac{g^2 + \sqrt{g^4 + 4}}{2}} \quad (15.55)$$

are located on the imaginary axis outside the unit circle  $|\lambda| = 1$ ; see Fig. 15.6a. This leads to the following solutions:

$$k_1 := \frac{i}{2} \left[ \ln 2 - \ln \left( -g^2 + \sqrt{g^4 + 4} \right) \right], \quad (15.56)$$

$$k_2 := \frac{i}{2} \left[ \ln 2 - \ln \left( -g^2 + \sqrt{g^4 + 4} \right) \right] + \pi, \quad (15.57)$$

$$k_3 := -\frac{i}{2} \left[ \ln \left( g^2 + \sqrt{g^4 + 4} \right) - \ln 2 \right] + \frac{\pi}{2}, \quad (15.58)$$

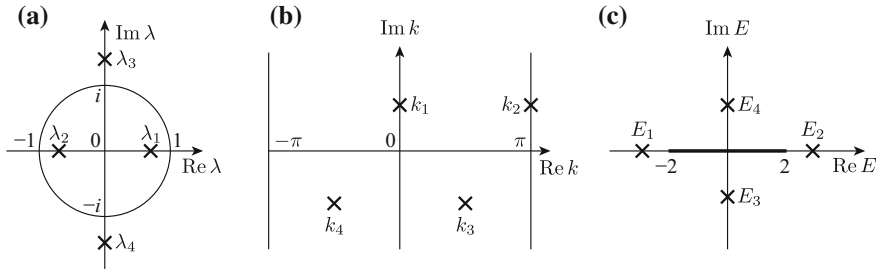


**Fig. 15.6** A schematic view of the locations of the four discrete solutions **a** in the complex  $\lambda$  plane, **b** in the complex-wave-number plane, and **c** in the complex energy plane

$$k_4 := -\frac{i}{2} \left[ \ln \left( g^2 + \sqrt{g^4 + 4} \right) - \ln 2 \right] - \frac{\pi}{2}. \tag{15.59}$$

The former two solutions are located on the upper half of the complex wave-number plane, corresponding to bound states, while the latter two solutions are on the lower half, corresponding to a pair of resonant and anti-resonant states; see Fig. 15.6b. The only difference from the solutions in Fig. 15.3a of the continuous problem in Sect. 15.1 lies in the fact that a bound state  $k = k_2$  exists on the line of  $\text{Re } k = \pi$  in addition to the one  $k = k_1$  on the imaginary axis.

We finally obtain the discrete eigenvalues of the problem (15.15) in the form

$$E_n = -\left( \lambda_n + \frac{1}{\lambda_n} \right). \tag{15.60}$$

For the two bound states, we have

$$E_1, E_2 = \mp \sqrt{2 + \sqrt{g^4 + 4}}, \tag{15.61}$$

which are located below and above the energy band  $E = -2 \cos k$ . For the resonant and anti-resonant states, we have

$$E_3, E_4 = \mp i \sqrt{-2 + \sqrt{g^4 + 4}}, \tag{15.62}$$

which are located on the imaginary axis of the second Riemann sheet of the complex energy plane; see Fig. 15.6c. Again, the only difference from the solutions in Fig. 15.3b is the existence of a bound state  $E = E_2$  above the continuum (the energy band) in addition to the one  $E = E_1$  below it.

In order to find the eigenvectors corresponding to the four eigenvalues, we cast (15.49) into the form of the generalized linear eigenvalue problem:

$$(A - \lambda B) |\Psi\rangle = 0, \tag{15.63}$$



where

$$A := \begin{pmatrix} 0 & I_2 \\ I_2 & PHP \end{pmatrix}, \quad B := \begin{pmatrix} I_2 & 0 \\ 0 & \Theta - I_2 \end{pmatrix}, \quad |\Psi\rangle := \begin{pmatrix} P|\psi\rangle \\ \lambda P|\psi\rangle \end{pmatrix}. \quad (15.64)$$

We can regard the generalized eigenvalue problem as the standard eigenvalue problem of the form  $(B^{-1}A - \lambda)|\Psi\rangle = 0$  as long as  $B$  is invertible. Note that  $B^{-1}A$  is an asymmetric matrix, although  $A$  and  $B$  are symmetric matrices.

We denote the four right- and left-eigenvectors corresponding to the four eigenvalues  $\lambda_n$  in (15.54)–(15.55) by  $|\Psi_n\rangle$  and  $\langle\tilde{\Psi}_n|$  with  $n = 1, 2, 3, 4$ . The left-eigenvector  $\langle\tilde{\Psi}_n|$  is not the Hermitian conjugate of the right-eigenvector  $|\Psi_n\rangle$  because  $B^{-1}A$  is an asymmetric matrix. In order to fix the normalization of the eigenvectors, we take a look at the diagonal matrix element

$$0 = \langle\tilde{\Psi}_n|(A - \lambda_n B)|\Psi_n\rangle = \langle\tilde{\Psi}_n|A|\Psi_n\rangle - \lambda_n \langle\tilde{\Psi}_n|B|\Psi_n\rangle. \quad (15.65)$$

We here normalize the eigenvectors so that  $\langle\tilde{\Psi}_n|B|\Psi_n\rangle = 1$ , which yields the eigenvalue in the form

$$\langle\tilde{\Psi}_n|A|\Psi_n\rangle = \lambda_n. \quad (15.66)$$

We next check the orthogonality of the eigenvectors. For the purpose, we consider the matrix elements

$$\langle\tilde{\Psi}_m|(A - \lambda_n B)|\Psi_n\rangle = 0, \quad (15.67)$$

$$\langle\tilde{\Psi}_m|(A - \lambda_m B)|\Psi_n\rangle = 0 \quad (15.68)$$

for  $m \neq n$ . Subtracting the second equation from the first one, we have

$$(\lambda_m - \lambda_n) \langle\tilde{\Psi}_m|B|\Psi_n\rangle = 0. \quad (15.69)$$

Assuming the lack of degeneracy, we have  $\lambda_m \neq \lambda_n$ , and hence  $\langle\tilde{\Psi}_m|B|\Psi_n\rangle = 0$ , which is followed by  $\langle\tilde{\Psi}_m|A|\Psi_n\rangle = 0$ .

To summarize, we have the diagonalization and the orthonormality

$$\langle\tilde{\Psi}_m|A|\Psi_n\rangle = \delta_{mn}\lambda_n, \quad (15.70)$$

$$\langle\tilde{\Psi}_m|B|\Psi_n\rangle = \delta_{mn} \quad (15.71)$$

for general  $m$  and  $n$ . We can thereby expand the inverse of the four-by-four matrix  $A - \lambda B$  in the form [5, 8]

$$\frac{1}{A - \lambda B} = \sum_{n=1}^4 |\Psi_n\rangle \frac{1}{\lambda_n - \lambda} \langle\tilde{\Psi}_n|. \quad (15.72)$$

### 15.2.6 Resonant-State Expansion of the Green's Function

The next task is to relate the inverse  $(A - \lambda B)^{-1}$  to the Green's function (15.26) so that we may expand the latter in terms of the discrete eigenstates  $\lambda_n$ . We first block-diagonalize the matrix  $A - \lambda B$  by means of the two matrices [5, 8]

$$X(\lambda) := \begin{pmatrix} -\lambda(I_2 - \Theta) - PHP & I_2 \\ I_2 & 0 \end{pmatrix}, \quad Y(\lambda) := \begin{pmatrix} I_2 & 0 \\ \lambda I_2 & I_2 \end{pmatrix} \quad (15.73)$$

as in

$$X(\lambda)(A - \lambda B)Y(\lambda) = \begin{pmatrix} Z(\lambda) & 0 \\ 0 & I_2 \end{pmatrix}, \quad (15.74)$$

where  $Z(\lambda)$  was given in (15.46). We therefore have the relation between the Green's function (15.26) and the inverse  $(A - \lambda B)^{-1}$  in the form [5, 8]

$$\begin{aligned} P \frac{1}{E - H} P &= P \frac{1}{E - H_{\text{eff}}(E)} P \\ &= -\frac{\lambda}{Z(\lambda)} = -\lambda (I_2 \ 0) \frac{1}{Y(\lambda)} \frac{1}{A - \lambda B} \frac{1}{X(\lambda)} \begin{pmatrix} I_2 \\ 0 \end{pmatrix}. \end{aligned} \quad (15.75)$$

Since

$$\frac{1}{X(\lambda)} = \begin{pmatrix} 0 & I_2 \\ I_2 & \lambda(I_2 - \Theta) + PHP \end{pmatrix}, \quad \frac{1}{Y(\lambda)} = \begin{pmatrix} I_2 & 0 \\ -\lambda I_2 & I_2 \end{pmatrix}, \quad (15.76)$$

we arrive at the expansion of the Green's function (15.26) as in [5, 8]

$$\begin{aligned} P \frac{1}{E - H} P &= -\lambda \sum_{n=1}^4 (I_2 \ 0) |\Psi_n\rangle \frac{1}{\lambda_n - \lambda} \langle \tilde{\Psi}_n | \begin{pmatrix} 0 \\ I_2 \end{pmatrix} \\ &= \sum_{n=1}^4 P |\psi_n\rangle \frac{\lambda \lambda_n}{\lambda - \lambda_n} \langle \tilde{\psi}_n | P. \end{aligned} \quad (15.77)$$

Let us finally transform this to a more familiar form by using [8]

$$\begin{aligned} E - E_n &= -\left( \lambda + \frac{1}{\lambda} - \lambda_n - \frac{1}{\lambda_n} \right) = -(\lambda - \lambda_n) \left( 1 - \frac{1}{\lambda \lambda_n} \right) \\ &= \frac{\lambda - \lambda_n}{\lambda \lambda_n} (1 - \lambda \lambda_n), \end{aligned} \quad (15.78)$$

which is followed by [8]

$$P \frac{1}{E - H} P = \sum_{n=1}^4 P |\psi_n\rangle \frac{1 - \lambda \lambda_n}{E - E_n} \langle \tilde{\psi}_n | P. \quad (15.79)$$

We can further show that the sum of the retarded and advanced Green's function

$$G^{R/A} := \frac{1}{E - H \pm i\delta}, \quad (15.80)$$

where  $\delta$  is infinitesimally positive, is given by [4]

$$P \Lambda P = \sum_{n=1}^4 P |\phi_n\rangle \frac{1}{E - E_n} \langle \tilde{\phi}_n | P, \quad (15.81)$$

where

$$\Lambda(E) := P G^R(E) P + P G^A(E) P = 2 \operatorname{Re} (P G^R(E) P) \quad (15.82)$$

for real  $E$ , while the states  $|\phi_n\rangle$  and  $\langle \tilde{\phi} |$  have different normalization from the states  $|\psi_n\rangle$  and  $\langle \tilde{\psi} |$  as in [8]

$$|\phi_n\rangle := \sqrt{1 - \lambda_n^2} |\psi_n\rangle, \quad \langle \tilde{\phi}_n | := \sqrt{1 - \lambda_n^2} \langle \tilde{\psi}_n |. \quad (15.83)$$

In Sect. 15.2.7, we will express the transmission probability, and hence the electronic conductance, by means of  $\Lambda$ . As we emphasized at the end of Sect. 15.1, this expansion reveals that the electronic conduction is dominated by transmission through resonant and anti-resonant states; the bound states in the expansion contribute to the transmission little. Note again that the expansion (15.81) does not contain scattering states.

### 15.2.7 New Formula for the Transmission Probability

We now come back to (15.14) and derive a formula for the transmission probability in terms of the sum (15.82), which enables us to take advantage of the expansion (15.81). We first show that the retarded and advanced Green's functions are given by the Green's function of the effective Hamiltonian  $H_{\text{eff}}(E)$  with  $k$  in the self-energy term in (15.40) set to be positive and negative, respectively.

We proved (15.26) for general complex values of  $E$ . We now set the energy  $E$  to be real for the retarded and advanced Green's functions in (15.80) to be used in the formula for the transmission probability. We therefore consider the Green's function (15.26) of the effective Hamiltonian  $H_{\text{eff}}(E)$  with real  $E$ . Remember that the  $E$  dependence of the effective Hamiltonian comes from the  $k$  dependence of the

self-energy in (15.40). Since the energy  $E$  and the wave number  $k$  are related by the dispersion relation (15.35), two real values of  $k$  give the same real value of  $E$ . The retarded Green's function corresponds to emission from a source at the origin, and hence has only out-going waves, while the advanced Green's function corresponds to absorption into a sink at the origin, and hence has only in-coming waves. We therefore conclude [4, 8] that the retarded Green's function is the Green's function of the effective Hamiltonian with positive  $k$ :

$$PG^R P = P \frac{1}{E - H + i\delta} P = P \frac{1}{E - H_{\text{eff}}(E)} P \Big|_{0 < k < \pi}. \quad (15.84)$$

Conversely, the advanced Green's function is that with negative  $k$ :

$$PG^A P = P \frac{1}{E - H - i\delta} P = P \frac{1}{E - H_{\text{eff}}(E)} P \Big|_{-\pi < k < 0} \quad (15.85)$$

with

$$PG^A(E(k))P = PG^R(E(-k))P, \quad PG^A(E(\lambda))P = PG^R(E(1/\lambda))P. \quad (15.86)$$

These give a formula for the Green's functions [4]:

$$i\Gamma(E) := (PG^R P)^{-1} - (PG^A P)^{-1} \quad (15.87)$$

$$\begin{aligned} &= - [H_{\text{eff}}(E(k)) - H_{\text{eff}}(E(-k))] \Big|_{0 < k < \pi} \\ &= \begin{pmatrix} 2(e^{ik} - e^{-ik}) & 0 \\ 0 & 0 \end{pmatrix} \Big|_{0 < k < \pi} = 4i \sin k \Big|_{0 < k < \pi} |0\rangle \langle 0| \\ &= 2i\gamma |0\rangle \langle 0| \end{aligned} \quad (15.88)$$

for real  $E$ , where

$$\gamma := \sqrt{4 - E^2}. \quad (15.89)$$

More formally, it is written in the form

$$\Gamma = \gamma PHQHP. \quad (15.90)$$

This function in conjunction with the retarded and advanced Green's functions is often used in the Fisher-Lee relation for the transmission probability [15]:

$$T(E) = \text{Tr} (\Gamma G^R \Gamma G^A). \quad (15.91)$$

Since  $\Gamma$  in our simple model has the only finite element for  $|0\rangle\langle 0|$ , the Fisher-Lee relation (15.91) is reduced to [4]

$$T(E) = \gamma^2 \langle 0|G^R|0\rangle \langle 0|G^A|0\rangle = \gamma^2 |\langle 0|G^R|0\rangle|^2, \quad (15.92)$$

which is equivalent to (15.14). We added a factor 1/4 here because the two leads are attached to the same site in our simple model.

We now try to transform (15.92) into an expression in terms of  $\Lambda$  in (15.82). For brevity, we denote  $\langle 0|G^R|0\rangle$ ,  $\langle 0|G^A|0\rangle$  and  $\langle 0|\Lambda|0\rangle$  by  $G_{00}^R$ ,  $G_{00}^A$  and  $\Lambda_{00}$ . We solve

$$\Lambda_{00} = G_{00}^R + G_{00}^A = 2 \operatorname{Re} G_{00}^R, \quad (15.93)$$

which follows from (15.82), together with

$$G_{00}^A - G_{00}^R = 2i\gamma G_{00}^R G_{00}^A, \quad (15.94)$$

which follows from (15.87), or

$$\operatorname{Im} G_{00}^R = -\gamma |G_{00}^R|^2 = -\gamma \left[ (\operatorname{Re} G_{00}^R)^2 + (\operatorname{Im} G_{00}^R)^2 \right]. \quad (15.95)$$

Inserting (15.93) into (15.95), we have

$$\gamma (\operatorname{Im} G_{00}^R)^2 + \operatorname{Im} G_{00}^R + \frac{\gamma}{4} (\Lambda_{00})^2 = 0, \quad (15.96)$$

which produces

$$-\gamma |G_{00}^R|^2 = \operatorname{Im} G_{00}^R = \frac{-1 \pm \sqrt{1 - (\gamma \Lambda_{00})^2}}{2\gamma}. \quad (15.97)$$

The choice of the sign  $\pm$  is given by the sign of

$$\left| \varepsilon_0 + \frac{g^2}{E - \varepsilon_d} \right| - \gamma. \quad (15.98)$$

We finally arrive at [4]

$$T(E) = \frac{1}{2} \left[ 1 \pm \sqrt{1 - (\gamma \Lambda_{00})^2} \right]. \quad (15.99)$$

If the system is more complicated in such a way that two leads are attached to different sites of the central system, the formula becomes more complicated as in [4]

$$T(E) = \left( \frac{1}{4} + \alpha^2 \right) \text{Tr } \Gamma \Lambda \Gamma \Lambda, \quad (15.100)$$

where

$$\alpha^2 = -\frac{1}{4} + \frac{1}{2(S^2 - 4D)} \left( 4 - D \pm \sqrt{(D+4)^2 - 4S^2} \right) \quad (15.101)$$

with

$$S := \text{Tr } \Gamma \Lambda, \quad D := \det \Gamma \Lambda. \quad (15.102)$$

See [4] for the derivation, including the choice of the sign in (15.101).

### 15.3 Fano Asymmetry

Since  $\Lambda$  has the resonant-state expansion of the form (15.81), that is,

$$\Lambda_{00} = \sum_{n=1}^4 \langle 0 | \phi_n \rangle \frac{1}{E - E_n} \langle \tilde{\phi}_n | 0 \rangle, \quad (15.103)$$

we are ready to expand the transmission probability (15.99) with respect to the discrete eigenstates. For later use, let us split  $\Lambda_{00}$  into two parts: namely, the bound-state terms

$$\Lambda^b(E) := \langle 0 | \phi_1 \rangle \frac{1}{E - E_1} \langle \tilde{\phi}_1 | 0 \rangle + \langle 0 | \phi_2 \rangle \frac{1}{E - E_2} \langle \tilde{\phi}_2 | 0 \rangle, \quad (15.104)$$

and the resonant-anti-resonant-state terms

$$\Lambda^{\text{pair}}(E) := \langle 0 | \phi_3 \rangle \frac{1}{E - E_3} \langle \tilde{\phi}_3 | 0 \rangle + \langle 0 | \phi_4 \rangle \frac{1}{E - E_4} \langle \tilde{\phi}_4 | 0 \rangle. \quad (15.105)$$

We again emphasize that the latter produce the dominant contributions.

Because we have the square of  $\Lambda_{00}$  in the formula (15.99), there occur various interference terms. We plot in Fig. 15.7 the following quantities:

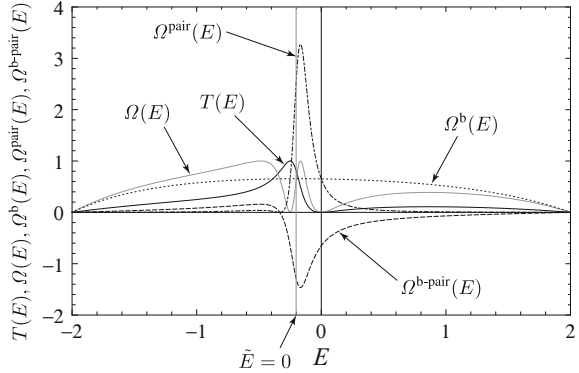
$$\Omega(E) := (\gamma \Lambda_{00})^2 = \gamma^2 (\Lambda^b(E) + \Lambda^{\text{pair}}(E))^2, \quad (15.106)$$

$$\Omega^b(E) := (\gamma \Lambda^b(E))^2, \quad (15.107)$$

$$\Omega^{\text{pair}}(E) := (\gamma \Lambda^{\text{pair}}(E))^2, \quad (15.108)$$

$$\Omega^{\text{b-pair}}(E) := \gamma^2 \Lambda^b(E) \Lambda^{\text{pair}}(E) \quad (15.109)$$

**Fig. 15.7** The transmission probability  $T(E)$  (black solid curve) as well as the quantities  $\Omega(E)$  (gray solid curve),  $\Omega^b(E)$  (dotted curve),  $\Omega^{\text{pair}}(E)$  (chained curve),  $\Omega^{\text{b-pair}}(E)$  (broken curve) for the parameter values  $\varepsilon_0 = 4$ ,  $\varepsilon_d = 0$  and  $g = 1$ . The gray vertical line indicates the real part of the resonant and anti-resonant eigenvalues:  $\text{Re } E_3 = \text{Re } E_4 = 0.200606$



together with the transmission probability  $T(E)$  as given in (15.99). We can first observe that the transmission probability  $T(E)$  (black solid curve) has a Fano asymmetric peak around the real part of the resonant and anti-resonant eigenvalues  $E = \text{Re } E_3 = \text{Re } E_4$  (gray vertical line), which results from the strong asymmetry of the quantity  $\Omega(E)$  (gray solid curve). We next observe that the bound-state contribution  $\Omega^b(E)$  (dotted curve) is a smooth function, whereas the crossing term  $\Omega^{\text{pair}}(E)$  (chained curve) between the resonant and anti-resonant states has a large peak around the energy of the pair and the crossing term  $\Omega^{\text{b-pair}}(E)$  (broken curve) between the bound states and the pair of resonant and anti-resonant states also has a (negatively) large peak around the same point. We can thereby conclude that the quantities  $\Omega^{\text{pair}}(E)$  and  $\Omega^{\text{b-pair}}(E)$  contribute to the asymmetry of  $\Omega(E)$ , and hence to the Fano asymmetry of  $T(E)$ .

Based on this observation, we classify the interference terms into three categories, which thereby result in three types of the Fano asymmetry [4]:

- (i) Interference between a resonant state and the corresponding anti-resonant state;
- (ii) Interference between a bound state and a pair of resonant and anti-resonant states;
- (iii) Interference between two pairs of resonant and anti-resonant states.

In the first case (i), let us assume that for the resonant state  $n = 3$ , the summand in (15.103) takes the form

$$\langle 0 | \phi_3 \rangle \frac{1}{E - E_3} \langle \tilde{\phi}_3 | 0 \rangle = \frac{N e^{i\theta}}{E - E_3}. \tag{15.110}$$

Note that the left-eigenvector  $\langle \tilde{\phi} |$  is generally *not* complex conjugate of the right-eigenvector  $|\phi\rangle$ , and hence the term above is generally complex. Since the anti-resonant contribution  $n = 4$  is its complex conjugate, we have the term in (15.105) in the form

$$A^{\text{pair}}(E) = 2 \frac{N}{|\text{Im } E_3|} \frac{\sin \theta + \tilde{E} \cos \theta}{1 + \tilde{E}^2}, \quad (15.111)$$

where

$$\tilde{E} := \frac{E - \text{Re } E_3}{|\text{Im } E_3|} \quad (15.112)$$

is the normalized energy measure from the separation from  $E = \text{Re } E_3 = \text{Re } E_4$ . The sum of these two terms thereby contribute to the transmission probability  $T(E)$  in the form [4]

$$\Omega^{\text{pair}} \sim \left( \frac{\tilde{E} + q^{\text{pair}}}{1 + \tilde{E}^2} \right)^2, \quad (15.113)$$

where

$$q^{\text{pair}} := \tan \theta. \quad (15.114)$$

The peak of  $\Omega^{\text{pair}}(E)$  around  $\tilde{E} = 0$  observed in Fig. 15.7 underscores the behavior in (15.113).

The parameter (15.114) may be referred to as a Fano parameter, although (15.113) is not the original form derived by Fano [19]:

$$T(E) \sim \frac{(\tilde{E} + q)^2}{1 + \tilde{E}^2}. \quad (15.115)$$

Indeed, many analyses take account only of resonant states, ignoring the corresponding anti-resonant states [19–21]. This may be the reason why the behavior (15.113) has never been pointed out. We will show below for the cases (ii) and (iii) that the Fano asymmetry in these cases take the form of Fano's formula (15.115). The reason why the denominator of (15.115) has a single power of  $1 + \tilde{E}^2$  in contrast to the double power in (15.113) is because the other states that interfere with the resonant state in question do not have singularities at  $E = E_3$  nor at  $E = E_4$ . Conversely, the double power of  $1 + \tilde{E}^2$  in the denominator of (15.113) is due to the fact that both the resonant and anti-resonant states have singularities with the same real part. In other words, the new behavior (15.113) emerges only after we take account of the anti-resonant state in addition to the resonant state [4].

Let us move to the second case (ii). This comes from the crossing term (15.109) in the square of  $\Lambda_{00}$ . We can derive an approximate energy dependence due to this interference by expanding it in terms of  $\tilde{E}$ , which results in the form [4]



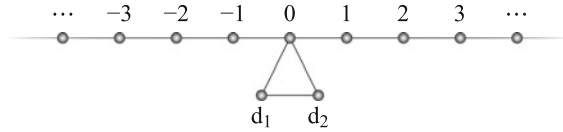


**Fig. 15.8** The model (15.117), which has two pairs of resonant and anti-resonant states in addition to two bound states

$$\Omega^{\text{b-pair}} \sim \frac{(\tilde{E} + q^{\text{b-pair}})^2}{1 + \tilde{E}^2} \tag{15.116}$$

for small  $\tilde{E}$ , where we can define the parameter  $q^{\text{b-pair}}$  microscopically; see [4]. We believe that this corresponds to Fano’s phenomenological analysis [19]. The behavior (15.116) is indeed consistent with Fano’s formula (15.115). The (negative) peak of  $\Omega^{\text{b-pair}}$  around  $\tilde{E} = 0$  observed in Fig. 15.7 confirms (15.116).

In order to discuss the case (iii), we need to move to a more complicated model that has multiple resonant states. The simplest model with two pairs of resonant and anti-resonant states may be the following one [4]:

$$\begin{aligned} H := & -t_{\text{hop}} \sum_{x=-\infty}^{\infty} (|x+1\rangle\langle x| + |x\rangle\langle x+1|) \\ & + \varepsilon_0 |0\rangle\langle 0| + \varepsilon_{d_1} |d_1\rangle\langle d_1| + \varepsilon_{d_2} |d_2\rangle\langle d_2| \\ & - g_{01} (|0\rangle\langle d_1| + |d_1\rangle\langle 0|) - g_{02} (|0\rangle\langle d_2| + |d_2\rangle\langle 0|) - g_{12} (|d_2\rangle\langle d_1| + |d_1\rangle\langle d_2|); \end{aligned} \tag{15.117}$$

see Fig. 15.8. For an appropriate parameter set, it has two pairs of resonant and anti-resonant states in addition to two bound states below and above the energy band. Let us denote the one pair of resonant and anti-resonant states by  $n = 3, 4$  and the other pair by  $n = 5, 6$ . The square of  $\Lambda_{00}$  now has a crossing term between

$$\Lambda_1^{\text{pair}} := \langle 0|\phi_3\rangle \frac{1}{E - E_3} \langle \tilde{\phi}_3|0\rangle + \langle 0|\phi_4\rangle \frac{1}{E - E_4} \langle \tilde{\phi}_4|0\rangle \tag{15.118}$$

and

$$\Lambda_2^{\text{pair}} := \langle 0|\phi_5\rangle \frac{1}{E - E_5} \langle \tilde{\phi}_5|0\rangle + \langle 0|\phi_6\rangle \frac{1}{E - E_6} \langle \tilde{\phi}_6|0\rangle. \tag{15.119}$$

We plot in Fig. 15.9 the following quantities:

$$\Omega(E) := (\gamma \Lambda_{00})^2 = \gamma^2 \left( \Lambda^{\text{b}}(E) + \Lambda_1^{\text{pair}}(E) + \Lambda_2^{\text{pair}}(E) \right)^2, \tag{15.120}$$

$$\Omega_2^{\text{pair}}(E) := \left( \gamma \Lambda_2^{\text{pair}}(E) \right)^2, \tag{15.121}$$

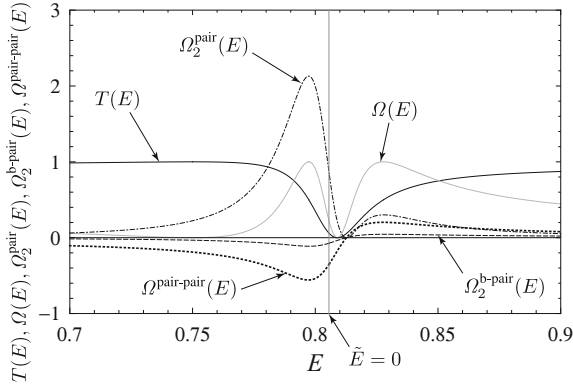


**Fig. 15.9** The transmission probability  $T(E)$  (black solid curve) as well as the quantities  $\Omega(E)$  (gray solid curve),  $\Omega_2^{\text{pair}}(E)$  (chained curve),  $\Omega_2^{\text{b-pair}}(E)$  (broken curve),  $\Omega^{\text{pair-pair}}(E)$  (thick dotted curve) for the parameter values  $\varepsilon_0 = \varepsilon_{d1} = 0, \varepsilon_{d2} = 1/2$  and  $g_{01} = g_{02} = g_{12} = 1/2$ . The gray vertical line indicates the real part of the resonant and anti-resonant eigenvalues:  $\text{Re } E_5 = \text{Re } E_6 = 0.805784$

$$\Omega_2^{\text{b-pair}}(E) := \gamma^2 \Lambda^{\text{b}}(E) \Lambda_2^{\text{pair}}(E) \tag{15.122}$$

$$\Omega^{\text{pair-pair}}(E) := \gamma^2 \Lambda_1^{\text{pair}}(E) \Lambda_2^{\text{pair}}(E) \tag{15.123}$$

together with the transmission probability  $T(E)$  as given in (15.99). The other quantities not shown are smooth in the plotted region. We observe that the interference between the two pairs of resonant and anti-resonant states, quantified by  $\Omega^{\text{pair-pair}}$ , is relatively large in this case.

This interference approximately results in the form [4]

$$\Omega^{\text{pair-pair}} \sim \frac{(\tilde{E} + q^{\text{pair-pair}})^2}{1 + \tilde{E}^2} \tag{15.124}$$

for small  $\tilde{E} := (E - \text{Re } E_5)/|\text{Im } E_5|$ , where we can again define the parameter  $q^{\text{pair-pair}}$  microscopically; see [4]. Each of the two pairs affect the Fano asymmetry of the other pair, although the magnitudes of the Fano parameter can be very different from each other. The interference between two resonant states has been discussed in [20, 21], although we stress again that the corresponding anti-resonant states are mostly ignored.

The values of the Fano parameters around  $E = 0.805784$  are given by

$$q^{\text{pair}} = 0.505055, \tag{15.125}$$

$$q^{\text{b-pair}} = -0.635981, \tag{15.126}$$

$$q^{\text{pair-pair}} = -0.607372 \tag{15.127}$$

for  $\varepsilon_0 = \varepsilon_{d_1} = 0$ ,  $\varepsilon_{d_2} = 1/2$  and  $g_{01} = g_{02} = g_{12} = 1/2$ . The signs of the three parameters indicate the parities of the Fano shapes. The positive value of  $q^{\text{pair}}$  is consistent with the fact that  $\Omega_2^{\text{pair}}(E)$  has a peak on the left and a dip on the right, while the negative values of  $q^{\text{b-pair}}$  and  $q^{\text{pair-pair}}$  agree with the fact that both  $\Omega_2^{\text{b-pair}}(E)$  and  $\Omega^{\text{pair-pair}}(E)$  have a dip on the left and a peak on the right.

## 15.4 Summary

To summarize, we succeeded in expanding the transmission probability, and hence the electronic Landauer conductance, in terms of all discrete states but no continuous states [4, 5, 8]. This expansion makes more transparent to trace the cause of the Fano asymmetry back to the interference between various discrete states. Fano's original argument [19] considered the interference between a bound state and a resonant state, which produced the celebrated formula (15.115). We not only reproduced it but also found a new type of asymmetry with the double power in the denominator, which is caused by interference between a resonant state and its anti-resonant partner [4]; taking account of anti-resonant states made it possible. We also reproduced the asymmetry due to the interference between two resonant-anti-resonant pairs. We found microscopic derivation of the Fano parameters for the three types of the asymmetry [4]. This may let us find experimentally the phase of a resonant state from  $q^{\text{pair}}$  as in (15.114), as well as from  $q^{\text{b-pair}}$  and  $q^{\text{pair-pair}}$ .

We also found in [4] that the Fano parameter of the first type can become complex under an external magnetic field. This is consistent with experiments in [22–24], which indeed observed complex Fano parameters.

## References

1. R. Landauer, IBM J. Res. Dev. **1**, 223 (1957)
2. S. Datta, *Electronic Transport in Mesoscopic Systems* (Cambridge University Press, Cambridge, 1995)
3. N. Hatano, Prog. Theor. Phys. Suppl. **184**, 497 (2010)
4. K. Sasada, N. Hatano, G. Ordóñez, J. Phys. Soc. Jpn. **80**, 104707 (27pp) (2011)
5. S. Klaiman, N. Hatano, J. Chem. Phys. **134**, 154111 (9pp) (2011)
6. N. Hatano, G. Ordóñez, Int. J. Theor. Phys. **50**, 1105 (2011)
7. N. Hatano, Fortschr. Phys. **61**, 238 (2013)
8. N. Hatano, G. Ordóñez, J. Math. Phys. **55**, 122106 (40pp) (2014)
9. G. Ordóñez, N. Hatano, J. Phys. A Math. Theor. **50**, 405304 (34pp) (2017)
10. G. Ordóñez, N. Hatano, Chaos **27**, 104608 (10pp) (2017)
11. L.D. Landau, E.M. Lifshitz, *Quantum Mechanics (Non-relativistic Theory)*, 3rd edn. (Pergamon Press, Oxford, 1977)
12. N. Hatano, K. Sasada, H. Nakamura, T. Petrosky, Prog. Theor. Phys. **119**, 187 (2008)
13. A.J.F. Siegert, Phys. Rev. **56**, 750 (1939)
14. T. Kawamoto, N. Hatano, Phys. Rev. E **84**, 031116 (13pp) (2011)

15. D.S. Fisher, P.A. Lee, *Phys. Rev. B* **23**, 6851 (1981)
16. H. Feshbach, *Ann. Phys. (New York)* **5**, 357 (1958)
17. K. Sasada, N. Hatano, *J. Phys. Soc. Jpn.* **77**, 025003 (2pp) (2008)
18. F. Tisseur, K. Meerberge, *SIAM Rev.* **43**, 235 (2001)
19. U. Fano, *Phys. Rev.* **124**, 1866 (1961)
20. A.F. Sadreev, I. Rotter, *J. Phys. A Math. Gen.* **36**, 11413 (2003)
21. I. Rotter, *J. Phys. A Math. Theor.* **42**, 153001 (51pp) (2009)
22. K. Kobayashi, H. Aikawa, S. Katsumoto, Y. Iye, *Phys. Rev. Lett.* **88**, 256806 (4pp) (2002)
23. K. Kobayashi, H. Aikawa, S. Katsumoto, Y. Iye, *Phys. Rev. B* **68**, 235304 (8pp) (2003)
24. K. Kobayashi, H. Aikawa, A. Sano, S. Katsumoto, Y. Iye, *Phys. Rev. B* **70**, 035319 (6pp) (2004)

# Chapter 16

## Fano Resonances in Slanted Hyperbolic Metamaterial Cavities



F. Vaianella and B. Maes

**Abstract** In this chapter we present the possibility to engineer Fano resonances using multilayered hyperbolic metamaterials, either metal-dielectric or graphene-based multilayers. The proposed cavity designs are composed of multilayers with a central slanted part that allows the excitation of a propagative and an evanescent mode, the interference between these two modes being responsible for highly tunable resonances. The propagating mode can reach an extremely high effective index, making the realization of deeply subwavelength cavities possible, as small as 5 nm for visible light with a metal-dielectric multilayer, and 0.5  $\mu\text{m}$  in the terahertz regime with a graphene-based multilayer. The evanescent mode is rarely analyzed but plays an important role here, as its contribution determines the particular shape of the cavity characteristic. Moreover, these phenomena cannot be described using effective medium theory, and we provide a more rigorous analysis. The reported resonances are very sensitive to any structural changes, but also to small variations of the doping level for the graphene-based multilayers.

### 16.1 Introduction

Enhanced control over all aspects of light is a major research direction over the last decades. In this direction, and thanks to progress in nanofabrication, metamaterials have attracted a large scientific interest with their unusual properties arising from subwavelength features [1–7].

---

This chapter is based in part on material that appeared in [22] which has been revised and updated.

---

F. Vaianella (✉) · B. Maes

Micro- and Nanophotonic Materials Group, Faculty of Science,  
University of Mons, 20, place du Parc, B-7000 Mons, Belgium  
e-mail: fabio.vaianella@umons.ac.be

© Springer Nature Switzerland AG 2018

E. Kamenetskii et al. (eds.), *Fano Resonances in Optics and Microwaves*, Springer Series in Optical Sciences 219, [https://doi.org/10.1007/978-3-319-99731-5\\_16](https://doi.org/10.1007/978-3-319-99731-5_16)

383

Among them, a particular subclass of these materials, the so-called hyperbolic metamaterials (HMMs), presents various interesting properties, such as a very large density of states [8, 9], an extreme refractive index and negative refraction [10, 11]. Typical structures providing these properties are periodic multilayers with subwavelength thicknesses of metal and dielectric [12–16] and arrays of metallic nanorods in a dielectric host [17–19].

Various designs of cavities based on HMMs have been studied, and they present interesting features such as an anomalous scaling law [10], whispering-gallery modes [20], zeroth order Fabry-Perot resonances [21] and Fano resonances [22, 23].

Fano resonances are asymmetrically shaped resonant phenomena that arise from the interference between a slowly varying background and a narrow resonant process [24–26]. Because their features stem from the interplay between two distinct channels, the resonances are very sensitive to any changes, rendering them interesting, among others, for sensing applications [27].

Here we propose very compact, high-quality cavities based on slanted multilayer HMMs, which present Fano resonances. Using rigorous numerical simulations and a thorough modal analysis, we elucidate the mechanism as the simultaneous excitation of a propagating and an evanescent mode. The propagating mode creates Fabry-Perot resonances, whereas the evanescent modes leads to a slowly varying background, so that their interference leads to narrow Fano-type features. This principle cannot be explained using effective medium theory (EMT), and builds on a rarely exploited evanescent mode.

Moreover, because the effective index is very high in the slanted cavity, we can create deep subwavelength cavities of a few nanometers in the visible regime with metal-dielectric structures and a few micrometers in the terahertz regime with graphene-based multilayers. In addition, we show that this mechanism remains valid even in the presence of losses.

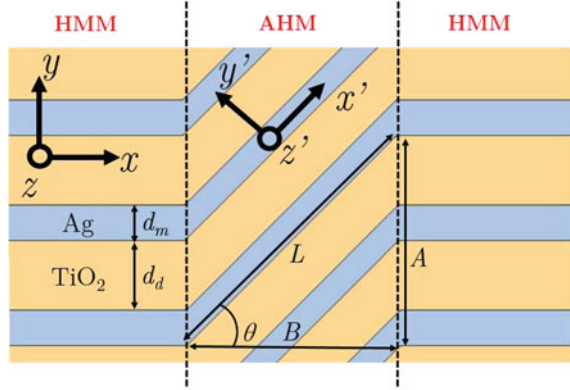
The results of this research for metal-dielectric multilayers have been detailed in [22]. Here we additionally show that the mechanism is more general and also valid for graphene-based multilayers, the latter offering tunability and control on position and sharpness of the Fano resonances through variation of the doping.

In Sect. 16.2 we present the proposed design. Section 16.3 inspects the light behaviour using effective medium theory, leading to an incomplete description. In Sect. 16.4 we calculate the correct characteristics, and explain the observed behaviour for metal-dielectric multilayer, and subsequently for graphene multilayers in Sect. 16.5. Finally, in Sect. 16.6 we discuss the impact of loss in the metal-dielectric multilayer, and Sect. 16.7 concludes.

## 16.2 Design

We study the transmission and reflection of light along the parallel direction (so  $k_{\perp} = k_y = 0$ ) of a HMM with a finite section of tilted layers in the middle (Fig. 16.1). The central tilt section is described by  $A$  (the vertical offset),  $B$  (the horizontal offset) and  $L$  (the parallel length) with  $L = \sqrt{A^2 + B^2} = \frac{A}{\sin \theta}$ , and  $\theta$  is the tilt angle.

**Fig. 16.1** A multilayer HMM with a tilted section in the middle. The fundamental mode is excited from the left. The structure is divided in three parts along the  $x$  direction: Two identical HMMs on the left and right and an asymmetrical HMM (or AHM) in the center



Because we work in the visible and near-infrared region, we use silver (Ag) as metal and  $\text{TiO}_2$  as dielectric, which are well-known to provide good performances at these frequencies [28–30]. We choose  $d_m = 10$  nm for the Ag thickness and  $d_d = 20$  nm for the  $\text{TiO}_2$  thickness. We use a dispersionless index for  $\text{TiO}_2$  with  $n_{\text{TiO}_2} = 2.7$  and a Drude model for Ag:

$$\epsilon_{\text{Ag}} = 1 - \frac{\omega_p^2}{\omega^2 + i\omega\gamma} \quad (16.1)$$

with  $\omega_p = 1.26 \times 10^{16}$  Hz the plasma frequency and  $\gamma$  the collision frequency that we fix equal to zero; we examine the influence of losses in Sect. 16.6.

We work in the regime where only one propagating Bloch mode exists in the HMM, hence the wavelength is larger than 600 nm in our case. We excite the structure from Fig. 16.1 with this propagating mode from the left and look at its reflectance and transmittance for a Bloch momentum  $k_y = 0$ .

In the next section we study this structure using an effective medium theory, which will show its limits to describe such systems.

### 16.3 Effective Medium Theory

For a uniaxial multilayer using effective medium theory, the dispersion relation for TM waves (transverse magnetic, magnetic field along  $z$  direction) is [31, 32]:

$$\frac{k_{\parallel}^2}{\epsilon_{\perp}} + \frac{k_{\perp}^2}{\epsilon_{\parallel}} = k_0^2 \quad (16.2)$$

where  $k_{\parallel}$  ( $k_{\perp}$ ) is the wavevector in the direction parallel (perpendicular) to the layers and  $k_0$  the wavevector in free-space. The permittivity in the parallel and normal

directions depends only on the permittivity of the constitutive materials and their filling fraction:

$$\varepsilon_{\parallel} = f\varepsilon_m + (1 - f)\varepsilon_d, \quad (16.3)$$

$$\varepsilon_{\perp} = \frac{\varepsilon_m \varepsilon_d}{f\varepsilon_d + (1 - f)\varepsilon_m} \quad (16.4)$$

where  $\varepsilon_{\parallel}$  and  $\varepsilon_{\perp}$  are the components of the permittivity in the parallel and perpendicular directions,  $\varepsilon_m$  and  $\varepsilon_d$  are the permittivity of the metal and the dielectric, respectively, and  $f$  is the metal filling fraction.

For the used wavelength regime, these materials turn out to be very particular anisotropic media, namely HMMs, where components of the diagonalized permittivity tensor have opposite sign, and (16.2) is thus the equation of a hyperbola. Consequently, the HMM can support propagating modes with extremely large wavevectors. We note, however, that this equation also has other solutions. There is an evanescent mode (imaginary parallel momentum and real perpendicular momentum), and a mode with real parallel momentum and imaginary perpendicular momentum. These modes are often overlooked, because they are accessible only in certain conditions. We show later on that we fulfill the conditions to excite the evanescent mode, and it will play an important role for the cavity mechanism in the next section.

The geometry explained in the previous section can be divided in three different parts (Fig. 16.1). The left and right parts are ‘standard’ HMMs and are governed by (16.2) with  $\varepsilon_{\perp} = \varepsilon_y$ ,  $\varepsilon_{\parallel} = \varepsilon_x$  and  $k_{\parallel} = k_x$ ,  $k_{\perp} = k_y$ .

The central part however is a hyperbolic medium with the optical axis tilted with respect to the  $x$  direction. In the literature these HMMs with tilted optical axis are sometimes referred to as asymmetric hyperbolic metamaterials (AHMs) [33, 34].

The AHM part of Fig. 16.1 is also governed by (16.2), but with  $\varepsilon_{\perp} = \varepsilon_{y'}$ ,  $\varepsilon_{\parallel} = \varepsilon_{x'}$  and  $k_{\parallel} = k'_{x'}$ ,  $k_{\perp} = k'_{y'}$ . Even if the thicknesses of the Ag and TiO<sub>2</sub> layers in the central part change ( $d'_m = d_m \cos \theta$  and  $d'_d = d_d \cos \theta$ ), we still have the same  $\varepsilon_x = \varepsilon_{x'}$  and  $\varepsilon_y = \varepsilon_{y'}$ , because (16.3) and (16.4) only depend on the filling fraction  $f$ , which remains the same.

Using a coordinate transformation (16.2) in the AHM becomes, in the main coordinates:

$$k_x^{(1,2)} = \frac{k_y \varepsilon_{xy} \pm \sqrt{(\varepsilon_{xy}^2 - \varepsilon_{xx} \varepsilon_{yy})(k_y^2 - k_0^2 \varepsilon_{xx})}}{\varepsilon_{xx}} \quad (16.5)$$

with the the solution  $k_x^{(1)}$  corresponds to the sign “+” in the formula for mode propagating towards smaller  $x$  and  $k_x^{(2)}$  to the sign “-” for waves propagating towards larger  $x$ . Note that in our case of normal incidence,  $k_x^{(1)}$  and  $k_x^{(2)}$  are equal in magnitude.  $\varepsilon_{xx}$ ,  $\varepsilon_{xy}$  and  $\varepsilon_{yy}$  are the permittivity components of the AHM in the main coordinates, which are obtained by applying a rotation matrix to the diagonal permittivity tensor in the tilted coordinates:



$$\bar{\bar{\epsilon}} = \mathcal{R}(\theta) \bar{\bar{\epsilon}}' \mathcal{R}(\theta)^T = \begin{pmatrix} \epsilon_{xx} & \epsilon_{xy} \\ \epsilon_{xy} & \epsilon_{yy} \end{pmatrix} \quad (16.6)$$

with  $\mathcal{R}(\theta)$  the matrix of rotation around the  $z$  axis and  $\bar{\bar{\epsilon}}' = \begin{pmatrix} \epsilon_{x'} & 0 \\ 0 & \epsilon_{y'} \end{pmatrix}$  the permittivity tensor in the tilted coordinates. This leads to

$$\epsilon_{xx} = \epsilon_{x'} \cos^2 \theta + \epsilon_{y'} \sin^2 \theta \quad (16.7)$$

$$\epsilon_{xy} = (\epsilon_{x'} - \epsilon_{y'}) \cos \theta \sin \theta \quad (16.8)$$

$$\epsilon_{yy} = \epsilon_{x'} \sin^2 \theta + \epsilon_{y'} \cos^2 \theta \quad (16.9)$$

For zero momentum in the  $y$  direction (i.e.  $k_y = 0$ ), the momentum in the  $x$  direction is different in the HMMs ( $k_x = \sqrt{\epsilon_y} k_0$ ) and in the AHM ( $k_x = \frac{\sqrt{(\epsilon_{xy}^2 - \epsilon_{xx}\epsilon_{yy}) - k_0^2 \epsilon_{xx}}}{\epsilon_{xx}}$ ), leading to reflection at the interfaces. Thus the introduced design functions as a cavity structure of width  $B$ .

Now that we have defined the effective permittivity components in the HMM and AHM parts, we can easily calculate numerically the scattering characteristics of the structure with the different parts replaced by homogeneous blocks with these effective parameters. The reflectance of light as a function of the tilt angle  $\theta$  and the length  $L$  at a wavelength  $\lambda_0 = 700$  nm is shown in Fig. 16.2.

We observe two distinct behaviours above and below a transition tilt angle of about  $\theta_t \approx 21^\circ$ . This phenomenon can be understood by looking at the isofrequency contours of the HMM and the AHM section, respectively (Fig. 16.3).

Blue curves correspond to the isofrequency contour of propagating modes, thus with real components for the  $x$  and  $y$  momenta (therefore, real part of momenta is

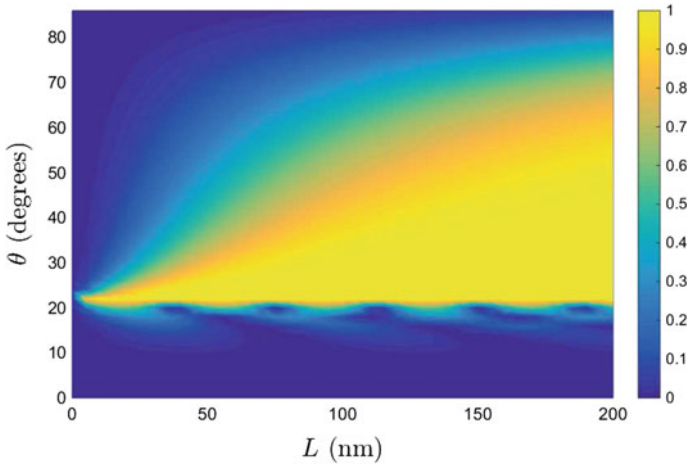


**Fig. 16.2** Reflectance versus tilt length  $L$  and angle  $\theta$  using effective medium theory

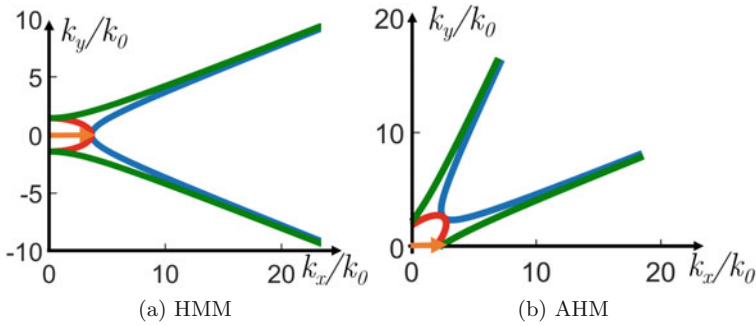


**Fig. 16.3** Isofrequency contours **a** in the HMM, and **b** in the AHM for a tilt angle of  $45^\circ$  with EMT, for  $\lambda_0 = 700$  nm. Blue curve corresponds to propagating waves, green curve corresponds to evanescent waves and red curve corresponds to propagating wave in the  $x$  direction and evanescent in the  $y$  direction. The orange arrow in **(a)** indicates the input wavevector, in **(b)** the dominant (green) mode in the AHM

plotted). Green curves correspond to evanescent modes with imaginary momentum components in both directions (therefore, imaginary part of momenta is plotted). Red curves correspond to modes with real  $x$ -momentum and imaginary  $y$ -momentum (therefore, the real part of the momentum is plotted on the abscissa and the imaginary part is plotted on the ordinate). Note that the isofrequency contours of Fig. 16.3b are just the isofrequency contours of Fig. 16.3a rotated by  $45^\circ$ .

The conservation of the momentum in the transverse direction ( $k_y = 0$ ) imposes in the tilted coordinates ( $x', y'$ ):

$$k_y = k'_x \sin \theta + k'_y \cos \theta = 0 \quad (16.10)$$

so

$$k'_x \sin \theta = -k'_y \cos \theta \quad (16.11)$$

and thus, the mode evanescent in the  $y'$  direction and propagating in the  $x'$  direction (red curves in Fig. 16.3) inside the AHM cannot be excited because (16.11) cannot be fulfilled. The mode evanescent in all directions (green curves in Fig. 16.3) and the propagating one (blue curves in Fig. 16.3) however can be fulfilled (16.11) and can be excited for normal incidence ( $k_y = 0$ ).

The orange arrow in Fig. 16.3a shows the incident momentum inside the HMM. From Fig. 16.3b we see that transverse momentum conservation (the orange arrow in Fig. 16.3b needs to be horizontal) requires that only one mode at a time is excited inside the AHM. The latter mode is either propagating (blue) or evanescent (green), in function of the tilt angle.

The transition angle  $\theta_t$  between the two regimes is determined by the asymptote of the hyperbolic contours (the same asymptote for both blue or green contours), this angle equals

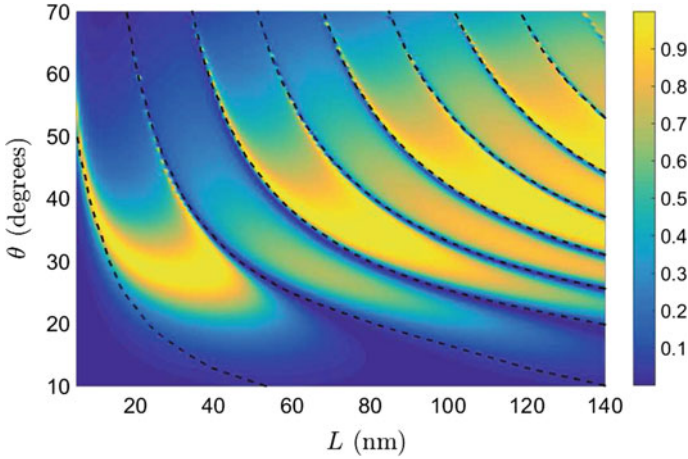


**Fig. 16.4** Exact reflectance in function of  $\theta$  and  $L$ . Black dashed line corresponds to the eight first orders of the Fabry-Perot constructive interferences. The wavelength is 700 nm

$$\theta_t = \text{atan} \left( \sqrt{\frac{\varepsilon_x}{\varepsilon_y}} \right) \approx 21.6^\circ \quad (16.12)$$

at  $\lambda_0 = 700$  nm.

Thus, below  $\theta_t$  only a propagating mode (orange arrow touches blue curve) is excited inside the AHM, so the lobes in the lower part of Fig. 16.2 are Fabry-Perot resonances of the cavity. The fairly weak reflectance of the lobes is typical of Fabry-Perot cavities with low reflection at each interface, which is the case for small tilt angles.

Above  $\theta_t$  only the evanescent mode (orange arrow touches green curve) is excited in the AHM, leading to the absence of Fabry-Perot fringes. Furthermore, the reflectance increases monotonously with  $B (= L \cos \theta)$ , because the mode amplitude decreases exponentially with the length of propagation.

In the next section, we show that this EMT description is actually incomplete, and only provides for qualitative trends compared to the exact simulations.

## 16.4 Rigorous Calculations and Analysis

We employ the commercial finite-element software COMSOL Multiphysics 5.2 to calculate the exact propagation through the structure (Fig. 16.1), with slightly rounded corners to avoid hotspots. The reflectance in function of the tilt angle  $\theta$  and the parallel propagation length  $L$  is shown in Fig. 16.4. The same lobe-like behaviour as with EMT below  $\theta_t$  is present, but the behaviour above  $\theta_t$  is completely different.

In order to understand this difference, we need to take into account the exact dispersion relation obtained by solving Maxwell's equations and applying Bloch's theorem [13, 35]

$$\begin{aligned} \cos(k_y D) = & \frac{(\kappa_d \varepsilon_m + \kappa_m \varepsilon_d)^2}{4\kappa_d \kappa_m \varepsilon_d \varepsilon_m} \cosh(\kappa_d d_d + \kappa_m d_m) \\ & - \frac{(\kappa_d \varepsilon_m - \kappa_m \varepsilon_d)^2}{4\kappa_d \kappa_m \varepsilon_d \varepsilon_m} \cosh(\kappa_d d_d - \kappa_m d_m) \end{aligned} \quad (16.13)$$

with  $D = d_m + d_d$  the period of the multilayer,  $\kappa_{d,m} = \sqrt{k_x^2 - k_0^2 \varepsilon_{d,m}}$  the decay coefficients in the dielectric and metallic layers, respectively. This dispersion relation is also valid in the AHM, by replacing  $(k_x, k_y)$  with  $(k'_x, k'_y)$ ,  $d_{d,m}$  with  $d'_{d,m} = d_{d,m} \cos \theta$  and  $D$  with  $D' = D \cos \theta$ . Combining (16.13) with the transverse momentum conservation condition (16.11) in the AHM, we finally arrive at

$$\begin{aligned} \cos(k'_x D' \tan \theta) = & \frac{(\kappa_d \varepsilon_m + \kappa_m \varepsilon_d)^2}{4\kappa_d \kappa_m \varepsilon_d \varepsilon_m} \cosh(\kappa_d d'_d + \kappa_m d'_m) \\ & - \frac{(\kappa_d \varepsilon_m - \kappa_m \varepsilon_d)^2}{4\kappa_d \kappa_m \varepsilon_d \varepsilon_m} \cosh(\kappa_d d'_d - \kappa_m d'_m) \end{aligned} \quad (16.14)$$

The main conclusion is that two modes satisfy this equation *at the same time* for all tilt angles  $\theta$ : an evanescent one and a propagating one. This result is consistent with the rigorously simulated isofrequency contours (Fig. 16.5), where the blue curve represents the propagating mode and the green curve the evanescent mode.

The orange arrow in Fig. 16.5a shows the incident momentum inside the HMM. In Fig. 16.5b, two horizontal arrows are needed to represent the momentum of the two excited modes inside the AHM. The orange arrow represents the momentum of the propagating mode and the green arrow represents the momentum of the evanescent mode.

The first important difference with the EMT contours of Fig. 16.3 is that the evanescent wave contour (green contours) that was an open curve is now a closed curve for the exact calculations of Fig. 16.5. Secondly, because the structure is periodic, all the information is encoded in the first Brillouin zone, thus the isofrequency contour of the propagating wave (blue curves) is also periodic and is not limited by asymptotes, in contrast with the EMT contours.

For these reasons, inside the AHM, an evanescent and a propagating modes are always excited together. The interferences between these two modes inside the AHM cavity are responsible for the Fano resonances appearing in Fig. 16.4. Indeed, Fano resonances can be described as arising from the interference between a slowly varying background (here: the evanescent wave) and a resonant process (here: the Fabry-Perot oscillations of the propagating mode).

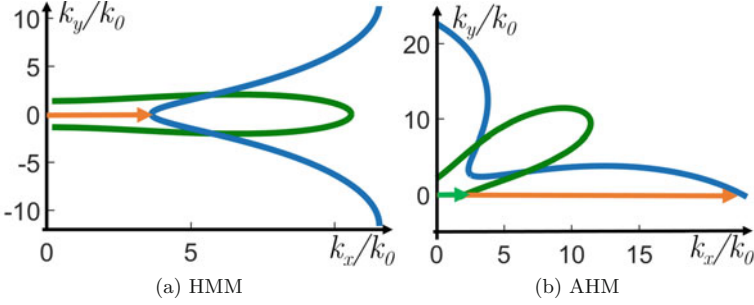
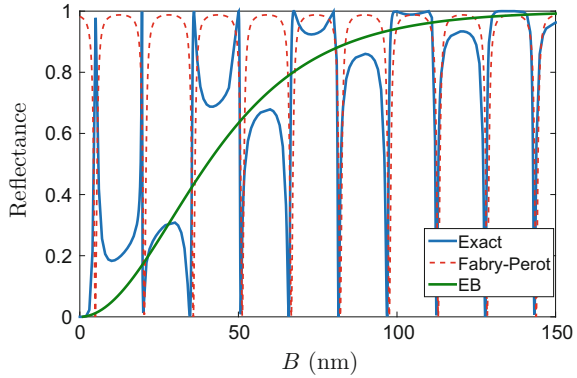


**Fig. 16.5** Exact isofrequency contours **a** in the HMM and **b** in the AHM for a tilt angle of  $45^\circ$  in the first Brillouin zone for  $\lambda_0 = 700$  nm. Blue curves correspond to propagating waves, green curves correspond to evanescent waves. Conservation of the transverse wavevector is illustrated by the orange and green arrows

**Fig. 16.6** Comparison between the exact calculation of the reflectance (blue solid curve) and the slowly varying background of the evanescent mode (green solid curve) and the Fabry-Perot oscillations of the propagating mode (red dashed curve) for  $\theta = 45^\circ$  at  $\lambda_0 = 700$  nm

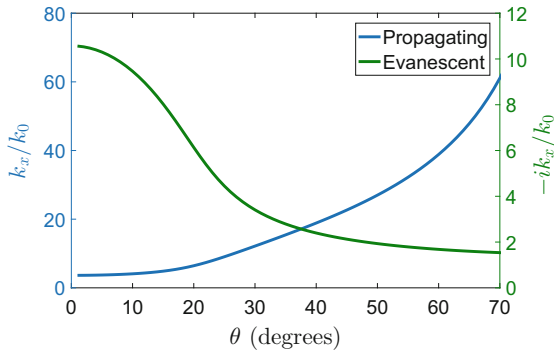


The Fano nature is more visible in Fig. 16.6 (blue curve), which shows the reflectance for an angle  $\theta = 45^\circ$  as a function of the width  $B$  of the cavity. Figure 16.6 further illustrates the cavity principle in detail: the Fabry-Perot oscillations of the propagating mode (red dashed curve) and the slowly increasing evanescent background (green curve) are shown separately. Both reflectance curves are obtained using a transfer matrix method under the hypothesis of an isotropic medium (a good approximation for normal incidence) as:

$$R = |r|^2 = \left| r_{HA} + \frac{t_{HA}t_{AH}r_{AH} \exp(2ik_x B + \varphi)}{1 - r_{AH}^2 \exp(2ik_x B + \varphi)} \right|^2 \quad (16.15)$$

with  $r_{HA}$  and  $r_{AH}$  the Fresnel coefficients of reflection of the propagating (resp. evanescent) mode for the HMM-AHM and AHM-HMM interfaces,  $t_{HA}$  and  $t_{AH}$  the Fresnel coefficient of transmission,  $k_x$  the wavevector in the  $x$  direction of the propagating (resp. evanescent) mode and  $\varphi$  a fitted phase term.

**Fig. 16.7** Momentum in the  $x$  direction  $k_x$  inside the AHM in function of the tilt angle for  $k_y = 0$ . Blue curve and axis represent the propagating mode, green curve and axis represent the evanescent mode



The exact reflectance thus arises from the interference of these two phenomena (leading to the blue curve). When the cavity length  $B$  becomes larger, the effect of the evanescent mode disappears, as its resulting reflectance (green curve) tends to 1, as the mode decays and does not manage to transmit. Then the characteristic only consists of typical Fabry-Perot oscillations from the propagating mode. For smaller lengths we obtain the typical asymmetric double-peak (maximum-minimum or vice-versa) Fano characteristics.

Black dashed lines in Fig. 16.4 show the good correspondance between the Fano resonances and the Fabry-Perot peaks of the propagating mode; the latter are plotted using a typical phase-matching round-trip relation

$$2k_x(\theta)B + 2\varphi(\theta) = 2\pi m \tag{16.16}$$

with  $m$  an integer indicating the order,  $\varphi(\theta)$  the phase change at each interface obtained by fitting, and  $k_x(\theta)$  the wavevector in the  $x$  direction for  $k_y = 0$  obtained from (16.14) (and using  $k_x = k'_x \cos \theta - k'_y \sin \theta$ ). The momentum in the  $x$  direction for the evanescent and propagating modes is shown in Fig. 16.7.

The very high value of the mode index inside the cavity leads to the possibility to create very compact cavities, on the order of 5 nm width for  $\theta = 45^\circ$  (first peak in Fig. 16.6). For the first order ( $m = 1$ ) the reflectance shows a single peak, so no asymmetric double-peak characteristic, which is similar to other contexts, such as a cavity placed on the side of a waveguide [36]. The latter effect is intuitively acceptable as the evanescent mode background (the ‘direct’ channel) has a very large transmission for very thin cavities.

The shapes of the resonances are also present in the spectra of the structure. We show these spectra in two cases for  $\theta = 45^\circ$ , with a reflectance peak for  $A = 5$  nm,  $B = 5$  nm (first order resonance, Fig. 16.8a), and with asymmetric Fano shapes for  $A = 35$  nm,  $B = 35$  nm (third order resonance for  $\lambda_0 = 700$  nm, second order for  $\lambda_0 = 885$  nm, Fig. 16.8b).

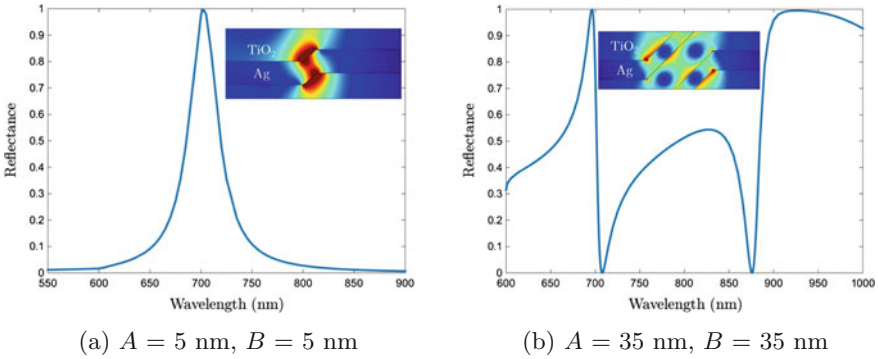


**Fig. 16.8** Reflectance spectra with geometric parameters **a**  $A = 5$  nm,  $B = 5$  nm and **b**  $A = 35$  nm,  $B = 35$  nm. Insets show the magnitude of the electric field at the resonance wavelength  $\lambda_0 = 700$  nm for a single unit cell of the periodic stacks

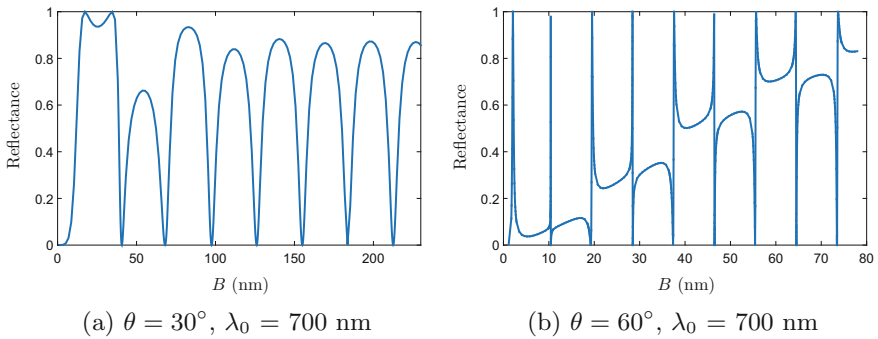


**Fig. 16.9** Reflectance for specific configurations at  $\lambda_0 = 700$  nm: **a**  $\theta = 30^\circ$ . **b**  $\theta = 60^\circ$

The insets of Fig. 16.8 present the magnitude of the electric field at the first order resonance (inset of Fig. 16.8a) and third order resonance (inset of Fig. 16.8b) for the wavelength  $\lambda_0 = 700$  nm. As we can expect, the first order resonance does not present a node in the cavity and the third order profile indicates two nodes. The field inside the cavity for the first order resonance is quite large, so one needs to pay attention to losses, this is discussed in the Sect. 16.5.

The reflectance for two specific tilt angles is presented in Fig. 16.9, showing that cavity engineering is possible in the regime where hyperbolic modes are supported. For an angle  $\theta = 30^\circ$  and  $\lambda_0 = 700$  nm (Fig. 16.9a), the green curve of the isofrequency contour of Fig. 16.5b indicates that the imaginary part of the momentum of the evanescent mode is fairly high, which is true for small  $\theta$  (see also Fig. 16.7). This explains why the asymmetric Fano resonances disappear rapidly, and quickly lead to standard Fabry-Perot features.

For  $\theta = 60^\circ$  and  $\lambda_0 = 700$  nm (Fig. 16.9b) the imaginary part for the evanescent mode is low enough to allow for the existence of Fano resonances over a large range





with

$$\sigma_{\text{intra}} = \frac{2ie^2k_B T}{\hbar^2\pi(\omega + i\tau^{-1})} \ln \left[ 2 \cosh \left( \frac{E_F}{2k_B T} \right) \right] \quad (16.18)$$

$$\begin{aligned} \sigma_{\text{inter}} = & \frac{e^2}{4\hbar} \left[ \frac{1}{2} + \frac{1}{\pi} \arctan \left( \frac{\hbar\omega - 2E_F}{2k_B T} \right) \right] \\ & - \frac{e^2}{4\hbar} \left[ \frac{i}{2\pi} \ln \frac{(\hbar\omega + 2E_F)^2}{(\hbar\omega - 2E_F)^2 + (2k_B T)^2} \right] \end{aligned} \quad (16.19)$$

with  $\sigma_{\text{intra}}$  the conductivity related to the intraband electron-photon scattering processes,  $\sigma_{\text{inter}}$  related to the interband electron transitions,  $E_F$  the doping level,  $\tau$  the electron scattering lifetime,  $T$  the temperature (we use room temperature, 300 K) and  $k_B$  the Boltzmann constant. We neglect spatial dispersion of graphene because the lattice constant is deeply subwavelength in the terahertz regime [51].

For simplicity, we model lossless graphene to compare with the previous section and so we take the imaginary part of the conductivity given by (16.17). We use  $n_1 = 1.5$  for the refractive index of the dielectric (permittivity  $\varepsilon_1 = 2.25$ ) and a period  $P = 1 \mu\text{m}$ . The exact dispersion relation is obtained similarly to equation (16.13) combining the transfer-matrix method (with surface currents) with Bloch's theorem, and one obtains [26, 45, 46]:

$$\cos(k_y P) = \cos(k_{y,1} P) - \frac{i}{2} \sigma Z_0 Z^{(p)} \sin(k_{y,1} P) \quad (16.20)$$

with  $Z_0$  the impedance of free-space,  $k_{y,1} = \sqrt{\varepsilon_1 k_0^2 - k_x^2}$  the wavevector in the dielectric,  $Z^{(p)} = k_{y,1}/(k_0 \varepsilon_1)$  the impedance of the dielectric for TM-polarized waves.

With (16.20) we can calculate the isofrequency contours both in the graphene-based HMM (Fig. 16.11a) and the AHM (with a tilt angle  $\theta = 60^\circ$ , Fig. 16.11b). We can see the magnitude of the wavevectors are much larger than for the metal-dielectric case, reducing drastically the size of the cavity (compared to the wavelength).

In a similar way than in the previous sections, we have highlighted the incident wavevector by the orange arrow in Fig. 16.11a. Note that unlike Fig. 16.5, we have rotated the wavevectors and not the axes here. The effective refractive index at normal incidence is approximatively the refractive index of the dielectric ( $n = 1.5$ ), simplifying drastically the problem of light incoupling that can occur with a metal-dielectric multilayer. Similar to the previous metal-dielectric case, two modes are always excited in the AHM: an evanescent one and a propagating one (green and orange arrows in Fig. 16.11b).

The resonances in this cavity are also Fano resonances, see the blue solid curve in Fig. 16.12, which can again be explained as an interference between the smooth evanescent transmission (solid green curve in Fig. 16.12) and the Fabry-Perot modes of the propagating mode (dashed red curve in Fig. 16.12). Here, because of the large contrast between the refractive index in the HMMs and in the AHM, the peaks are very sharp and the quality factor of the resonances becomes large. Note that Fano

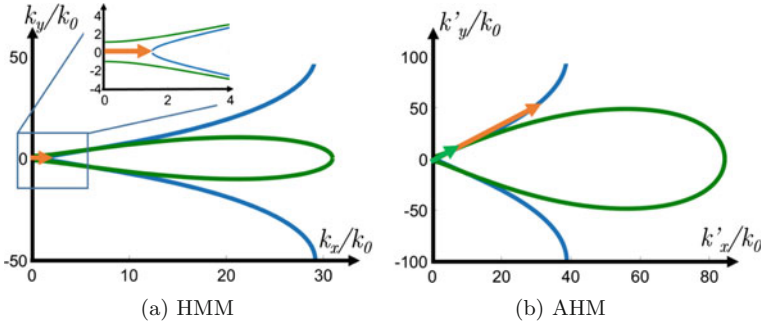


**Fig. 16.11** Exact isofrequency contours **a** in the graphene-based HMM and **b** in the AHM for a tilt angle of  $60^\circ$  in the first Brillouin zone for  $\lambda_0 = 100 \mu\text{m}$  and a doping level  $E_F = 0.1 \text{ eV}$ . Blue curves correspond to propagating waves, green curves correspond to evanescent waves. Conservation of the transverse wavevector is illustrated by the orange and green arrows. The inset in **(a)** shows a zoom on the small momentum part of the isofrequency contours of the HMM

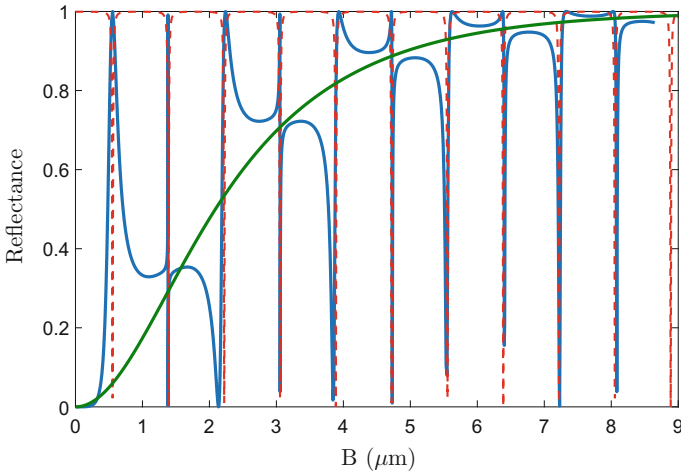


**Fig. 16.12** Comparison between the exact calculation of the reflectance (blue solid curve) and the slowly varying background of the evanescent mode (green solid curve) and the Fabry-Perot oscillations of the propagating mode (red dashed curve) for the graphene-based HMM with a tilt angle  $\theta = 60^\circ$  and  $\lambda_0 = 100 \mu\text{m}$  and a doping level  $E_F = 0.1 \text{ eV}$

resonances for cavities as small as  $0.5 \mu\text{m}$  can be realized, which is drastically smaller than the wavelength in free-space ( $100 \mu\text{m}$ ).

Interestingly, the sharpness of the resonances depends on the particular order. We observe in Fig. 16.12 that odd orders are wider than even orders. By odd order we mean the first, third, fifth ... peaks in Fig. 16.12. This behaviour is caused by an interplay between the evanescent mode and the Fabry-Perot resonances, as confirmed by the fact that for large cavity widths, the evanescent background disappears and the sharpness of the peaks remains constant. The presence of the evanescent mode adds

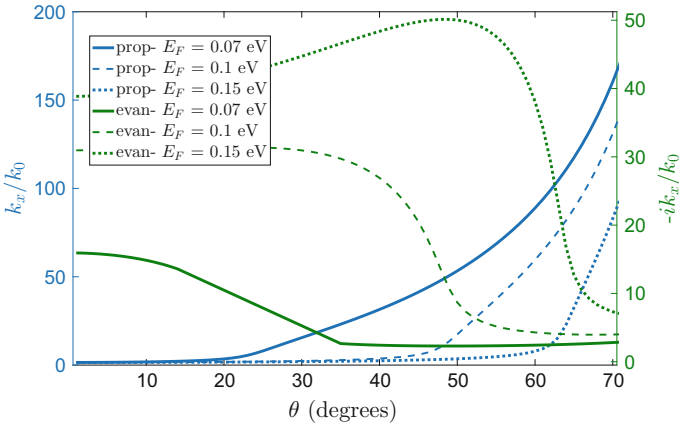


**Fig. 16.13** Momentum in the  $x$  direction  $k_x$  inside the graphene-based AHM in function of the tilt angle for  $k_y = 0$ , and various doping levels  $E_F$ . Blue curves and left axis represent the propagating mode, green curves and right axis represent the evanescent mode

an extra amplitude to the reflection, which interferes with the symmetry of the odd and even Fabry-Perot resonances. This results in a more rapid phase change for the even Fano order and a slower one for the odd ones. This effect is much less visible in the metal-dielectric multilayer case (Fig. 16.6), as the coupling with the two modes is too different there.

By calculating the refractive index inside the cavity, we can also demonstrate that the system is highly tunable. Combining (16.20) with the transverse momentum conservation condition (16.11), we determine the refractive index for the propagating and evanescent mode (Fig. 16.13). Thus, at the angle of Fig. 16.12 ( $\theta = 60^\circ$ ), a small change of the doping level can lead to a drastic change in the wavevector of the propagating and evanescent modes.

For example, a small decrease of the doping level from 0.1 to 0.07 eV changes the refractive index of the propagative mode from about 60 to 100, and of the evanescent mode from about  $4i$  to  $2i$ . This completely modifies the position and sharpness of the Fano resonances, see Fig. 16.14 (blue curve compared to red curve). This tuning is not only geometric, but is also clearly visible in the dispersion spectra. Compare for example the blue curve to the red curve in Fig. 16.15a ( $B = 0.55 \mu\text{m}$ ), and in Fig. 16.15b ( $B = 1.38 \mu\text{m}$ ).

However, an increase of the doping level from 0.1 eV to 0.15 eV strongly reduces the refractive index of the propagative mode, and increases the imaginary part of the wavevector for the evanescent mode. Thus, the Fabry-Perot resonance becomes very broad (as the contrast between the HMM and AHM is low), and the evanescent background disappears for a very small cavity width. For these reasons, the Fano resonances are destroyed when increasing the doping level (Fig. 16.14, yellow curve). The latter is also observed in the reflectance spectra (Fig. 16.15a, b, yellow curve compared to red curve).

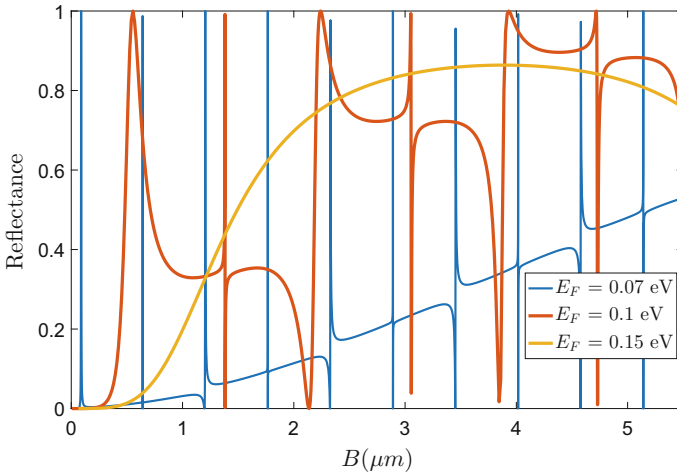


**Fig. 16.14** Reflectance versus the cavity width  $B$  for various doping levels. Blue curve corresponds to  $E_F = 0.07$  eV, red curve to  $E_F = 0.1$  eV, and yellow curve to  $E_F = 0.15$  eV

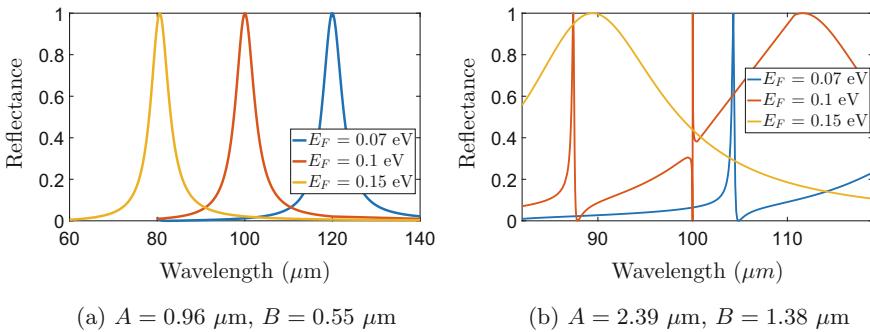


**Fig. 16.15** Reflectance spectra of the graphene-based multilayer for various doping levels: **a**  $A = 0.96$   $\mu\text{m}$ ,  $B = 0.55$   $\mu\text{m}$ , **b**  $A = 2.39$   $\mu\text{m}$ ,  $B = 1.38$   $\mu\text{m}$

### 16.6 Loss Effect

In this section, we return to the metal-dielectric structure, and study the influence of loss on the Fano resonances. Therefore, we use a Drude model with loss for the metal. The collision frequency in (16.1) is now  $\gamma = 0.5 \times 10^{14}$  Hz, which fits well with experimental measurements [10, 52].

Unlike the lossless model, modes with purely real or purely imaginary propagation constant do no longer exist. However, the mainly evanescent and propagating modes still exist (if losses are not too large) and are excited with the provision of momentum conservation (16.11). Furthermore, in order to show the same Fano mechanism as in the previous section, the modal parameters should obey certain conditions. Specifi-

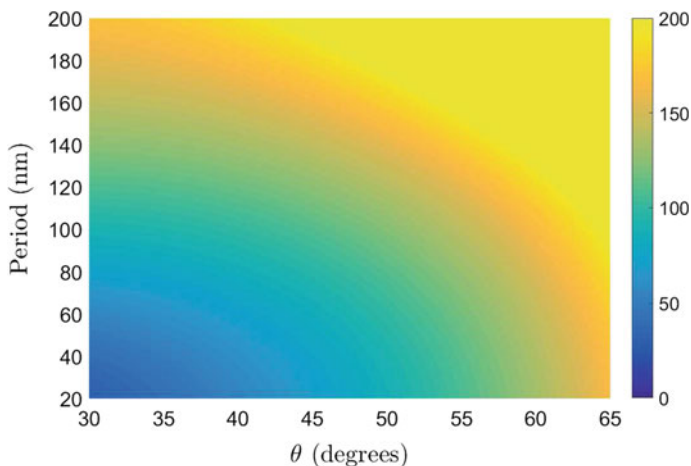


**Fig. 16.16** Ratio between the real and imaginary parts of the refractive index of the propagating mode inside the AHM

cally, the propagating mode should have a large real part and small imaginary part of the modal refractive index in the  $x$  direction, whereas the evanescent mode should have an imaginary part of the mode index in the  $x$  direction in the range between around 1 and 2 (above 2 the Fano resonances disappear quickly, below 1 the slowly varying background is not effective).

We focus on structures with metal filling fraction  $f = \frac{1}{3}$  as in the previous sections. (16.14) is still valid, so we can calculate the refractive index of the modes inside the AHM. Figures 16.16 and 16.17 show the ratio between the real and imaginary parts of

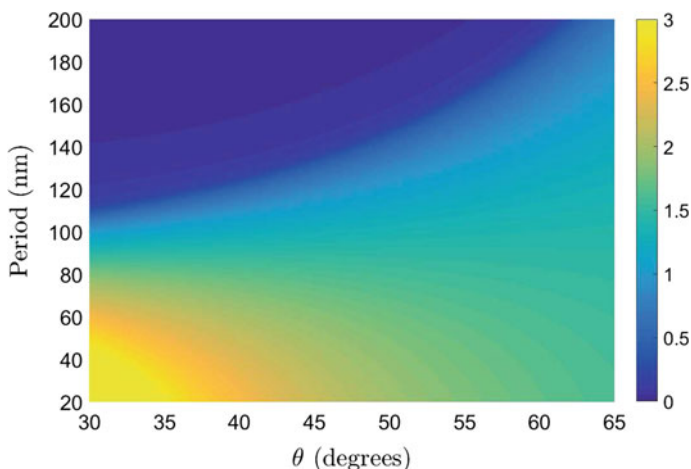


**Fig. 16.17** Imaginary part of the refractive index of the evanescent mode inside the AHM

**Fig. 16.18** Reflectance and transmittance with period 30 nm and tilt angle 65° with losses. Blue curve corresponds to the reflectance, red curve to transmittance

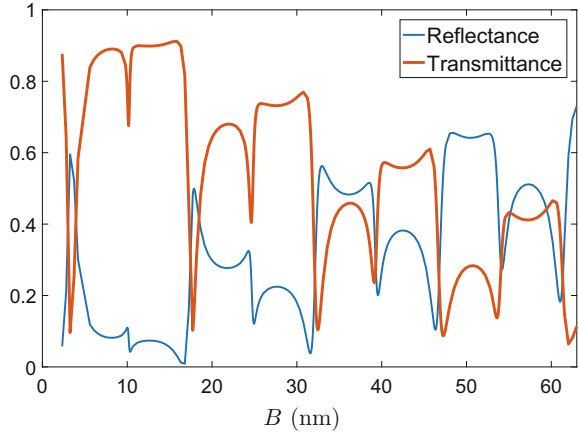
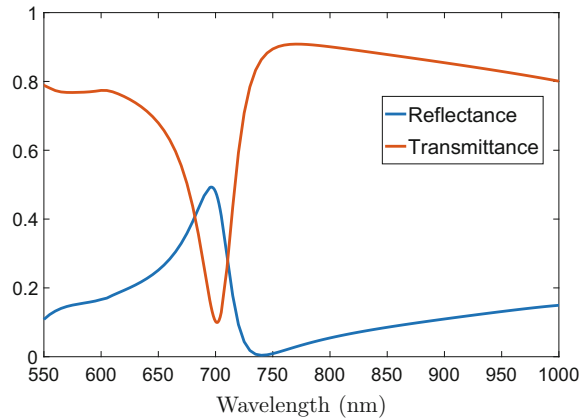


**Fig. 16.19** Reflectance and transmittance spectrum with period 30 nm, tilt angle of 65° and cavity width  $B = 17.7$  nm with losses. Blue curve corresponds to the reflectance, red curve to transmittance



the propagating mode, and the imaginary part of the evanescent mode, respectively. The structure with period of 30 nm and tilt angle of 65° respects the conditions cited above, so we use these parameters for the simulations.

From the field profiles (insets of Fig. 16.8) we can see hotspots created by sharp corners. These hotspots are critical in the presence of loss and can kill the resonance effect, therefore we limit their influence by replacing sharp corners with sections of 10 nm radius circles.

The reflectance and transmittance in function of the cavity width  $B$  is shown in Fig. 16.18. We still observe the Fano resonances and the extreme sensitivity to small changes in the cavity width. The cavity principle thus remains operational, as the spectrum in Fig. 16.19 also illustrates. Note that the decrease in transmittance corresponds to an increase in reflectance, so it is an interference effect, and not only due to metal absorption.

## 16.7 Conclusion

We show in this chapter the possibility to excite Fano resonances in multilayers with a central tilted section that functions as a cavity. Inside this cavity, for normal incidence ( $k_y = 0$ ), a propagating mode and an evanescent mode are always excited, the propagating mode being responsible for Fabry-Perot oscillations, while the evanescent mode ‘direct’ channel leads to a slowly varying background. Furthermore, effective medium theory cannot explain the existence of these resonances, as it only predicts a single mode at a time, either propagating or evanescent.

The relatively large effective index inside the cavity offers the possibility to create very compact extremely subwavelength cavities as small as 5 nm in the visible regime with metal-dielectric multilayers, and 0.5  $\mu\text{m}$  in the terahertz regime with graphene-based multilayers. In addition, the specific characteristics can be tailored, either presenting total transmittance or total reflectance at resonance, or exhibiting an asymmetric spectrum.

For the graphene-based multilayers, the doping level is another parameter to control the position and sharpness of the Fano resonances, with a variation as small as 0.03 eV changing completely the reflectance spectrum. Moreover, compared to the metal-dielectric devices, light incoupling can be easier because the mode index is approximatively equal to the index of the dielectric at normal incidence, avoiding the necessity to rely on incoupling techniques such as gratings or prisms.

Finally, we calculate that for structures with metal losses, these Fano resonances still exist. This bimodal interference mechanism in slanted cavities is therefore quite general and offers new practical possibilities, for instance in the domain of sensing applications.

**Acknowledgements** This work is supported by the Belgian Science Policy Office under the project “Photonics@be” (P7-35) and by the Fonds pour la Formation à la Recherche dans l’Industrie et dans l’Agriculture (FRIA) in Belgium.

## References

1. V. Shalaev, W. Cai, *Optical Metamaterials: Fundamentals and Applications* (Springer, Berlin, 2010)
2. M. Skorobogatiy, *Nanostructured and Subwavelength Waveguides* (John Wiley & Sons, New York, 2012)
3. B. Li, Y. He, S. He, *App. Phys. Exp.* **8**, 082601 (2015)
4. A.V. Kildishev, A. Boltasseva, V.M. Shalaev, *Science* **339**, 1232009 (2013)
5. T. Galfsky, H.N.S. Krishnamoorthy, W. Newman, E.E. Narimanov, Z. Jacob, V.M. Menon, *Optica* **2**, 62 (2015)
6. A.A. Orlov, S.V. Zhukovsky, I.V. Iorsh, P.A. Belov, *Phot. Nano. Fund. Appl.* **12**, 213 (2014)
7. W.D. Newman, C.L. Cortes, Z. Jacob, *J. Opt. Soc. Am. B* **30**, 766 (2013)
8. O.D. Miller, S.G. Johnson, A.W. Rodriguez, *Phys. Rev. Lett.* **112**, 157402 (2014)
9. K.V. Sreekanth, T. Biaglow, G. Strangi, *J. Appl. Phys.* **114**, 134306 (2013)
10. X. Yang, J. Yao, J. Rho, X. Yin, X. Zhang, *Nat. Photonics* **6**, 450 (2012)

11. D. Keene, M. Durach, *Opt. Express* **23**, 18577 (2015)
12. S. Feng, J. Elson, P. Overfelt, *Opt. Express* **13**, 4113 (2005)
13. A.A. Orlov, P.M. Voroshilov, P.A. Belov, Y.S. Kivshar, *Phys. Rev. B* **84**, 045424 (2011)
14. S.V. Zhukovsky, A.A. Orlov, V.E. Babicheva, A.V. Lavrinenko, J.E. Sipe, *Phys. Rev. A* **90**, 013801 (2014)
15. S.V. Zhukovsky, O. Kidwai, J.E. Sipe, *Opt. Express* **21**, 14982 (2013)
16. S.V. Zhukovsky, A. Andryieuski, J.E. Sipe, A.V. Lavrinenko, *Phys. Rev. B* **90**, 155429 (2014)
17. F. Vaianella, B. Maes, *Phys. Rev. B* **93**, 165417 (2016)
18. J. Elser, R. Wangberg, V.A. Podolskiy, E.E. Narimanov, *Appl. Phys. Lett.* **89**, 261102 (2006)
19. N. Vasilantonakis, M.E. Nasir, W. Dickson, G.A. Wurtz, A.V. Zayats, *Laser Photonics Rev.* **9**, 345 (2015)
20. C. Wu, A. Salandrino, X. Ni, X. Zhang, *Phys. Rev. X* **4**, 021015 (2014)
21. Z. Huang, E.E. Narimanov, *Opt. Express* **21**, 15020 (2013)
22. F. Vaianella, B. Maes, *Phys. Rev. B* **94**, 125442 (2016)
23. M. Hasan, I. Iorsh, *Days on Diffraction*, 1 (2015)
24. A.E. Miroschnichenko, S. Flach, Y.S. Kivshar, *Rev. Mod. Phys.* **82**, 2257 (2010)
25. S. Fan, J.D. Joannopoulos, *Phys. Rev. B* **65**, 235112 (2002)
26. I.V. Iorsh, I.V. Shadrivov, P.A. Belov, Y.S. Kivshar, *Phys. Rev. B* **88**, 195422 (2013)
27. B. Luk'yanchuk, N.I. Zheludev, S.A. Maier, N.J. Halas, P. Nordlander, H. Giessen, C.T. Chong, *Nat. Mater.* **9**, 707 (2010)
28. C.L. Cortes, W. Newman, S. Molesky, Z. Jacob, *J. Opt.* **14**, 063001 (2012)
29. B. Dastmalchi, P. Tassin, T. Koschny, C.M. Soukoulis, *Adv. Opt. Mater.* **4**, 177 (2016)
30. P. Tassin, T. Koschny, M. Kafesaki, C.M. Soukoulis, *Nat. Photonics* **6**, 259 (2012)
31. A. Poddubny, I. Iorsh, P. Belov, Y. Kivshar, *Nat. Photonics* **7**, 948 (2013)
32. X. Ni, S. Ishii, M.D. Thoreson, V.M. Shalae, S. Han, S. Lee, A.V. Kildishev, *Opt. Express* **19**, 25242 (2011)
33. I.S. Nefedov, C.A. Valagiannopoulos, S.M. Hashemi, E.I. Nefedov, *Sci. Rep.* **3**, 1 (2013)
34. A.D. Boardman, P. Egan, M. McCall, *EPJ Appl. Metamater.* **2**, 1 (2015)
35. G. Rosenblatt, M. Orenstein, *Opt. Express* **19**, 20372 (2011)
36. B. Maes, P. Bienstman, R. Baets, *J. Opt. Soc. Am. B* **22**, 1778 (2005)
37. X. Li, H. Zhu, K. Wang, A. Cao, J. Wei, C. Li, Y. Jia, Z. Li, X. Li, D. Wu, *Adv. Mater.* **22**, 2743 (2010)
38. Q. Bao, K.P. Loh, *ACS Nano* **6**, 3677 (2012)
39. R. Won, *Nat. Photonics* **4**, 411 (2010)
40. F. Bonaccorso, Z. Sun, T. Hasan, A.C. Ferrari, *Nat. Photonics* **4**, 611 (2010)
41. I.V. Iorsh, I.S. Mukhin, I.V. Shadrivov, P.A. Belov, Y.S. Kivshar, *Phys. Rev. B* **87**, 075416 (2013)
42. A. Andryieuski, A.V. Lavrinenko, *Phys. Rev. B* **86**, 121108(R) (2012)
43. L. Zhang, Z. Zhang, C. Kang, B. Cheng, L. Chen, X. Yang, J. Wang, W. Li, B. Wang, *Opt. Express* **22**, 14022 (2014)
44. K.V. Sreekanth, A. De Luca, G. Strangi, *Appl. Phys. Lett.* **103**, 023107 (2013)
45. I.S. Nefedov, C.A. Valagiannopoulos, L.A. Melnikov, *J. Opt.* **15**, 114003 (2013)
46. M.A.K. Othman, C. Guclu, F. Capolino, *Opt. Express* **21**, 7614 (2013)
47. A.Y. Nikitin, F. Guinea, F. Garcia-Vidal, L. Martin-Moreno, *Phys. Rev. B* **84**, 195446 (2011)
48. L.A. Falkovsky, *J. Phys. Conf. Ser.* **129**, 012004 (2008)
49. L.A. Falkovsky, A.A. Varlamov, *Eur. Phys. J. B* **56**, 281 (2007)
50. C.H. Gan, H.S. Chu, E.P. Li, *Phys. Rev. B* **85**, 125431 (2012)
51. A. Fallahi, J. Perruisseau-Carrier, *Phys. Rev. B* **86**, 195408 (2012)
52. P.B. Johnson, R.W. Christy, *Phys. Rev. B* **6**, 4370 (1972)



# Chapter 17

## Fano Resonance Generation and Applications in 3D Folding Metamaterials



Z. Liu, S. Y. Yang, J. J. Li and C. Z. Gu

**Abstract** The development of nanotechnology has endowed the light-matter interaction with more degrees of freedom, and made the manipulation of optical phenomena more precise and arbitrary. Fano resonance is a type of resonant scattering phenomenon with asymmetric line profile, which was firstly studied in atomic physics and then introduced to photonics and plasmonics. This phenomenon is due to the interference between a discrete bound state and a continuum state, thus a two-body or few-body system is needed to provide different types of states that are necessary in this phenomenon. Artificial metamaterial is a very good candidate to generate Fano resonances because of its designable configuration. In this paper, a new type of structure—3D folding metamaterial—is introduced for Fano resonance generation and application. The structure, fabricated by focused-ion-beam based folding technique, is composed of planar and out-of-plane parts, which are essential for the excitation of the discrete bound states and continuum states. The intensity, frequency and quality factor of the Fano resonances can be modulated by the configuration of the 3D folding structures (shape, size, inclined angle, etc.), thus enlarges its application potential such as index sensing and surface enhanced Raman scattering.

---

Z. Liu · S. Y. Yang · J. J. Li · C. Z. Gu

Beijing National Laboratory for Condensed Matter Physics, Institute of Physics,  
Chinese Academy of Sciences, Beijing 100190, China

S. Y. Yang · J. J. Li · C. Z. Gu

CAS Key Laboratory of Vacuum Physics, School of Physical Sciences, University  
of Chinese Academy of Sciences, Beijing 100190, China

C. Z. Gu (✉)

Collaborative Innovation Center of Quantum Matter, Beijing 100871, China  
e-mail: czgu@iphy.ac.cn

© Springer Nature Switzerland AG 2018

E. Kamenetskii et al. (eds.), *Fano Resonances in Optics and Microwaves*, Springer  
Series in Optical Sciences 219, [https://doi.org/10.1007/978-3-319-99731-5\\_17](https://doi.org/10.1007/978-3-319-99731-5_17)

## 17.1 Fano Resonances Excited in Composite Structures

The Fano resonance got its name from Ugo Fano, who was an “outstanding interpreter of how radiation interacts with atoms and cells” [1]. It was first put forward to explain the sharp asymmetric profile of Rydberg spectral atomic lines based on a superposition principle from quantum mechanics. The ionization of an atom by a high-energy photon can proceed in two distinct ways: (i) through direct excitation of an electron from its bound state into an unbound (continuum) state; (ii) through indirect excitation of two electrons into an intermediate bound state, followed by an Auger-like process of electron ejection. The first process is non-resonant because the electron can be excited as long as the photon energy exceeds the ionization threshold. However, in the second process, it is inherently resonant because the two electrons must be excited into a well-defined auto-ionizing state. Electron-electron interactions are responsible for the excitation and subsequent auto-ionization so the quantum mechanical interference between these two ionization pathways results in highly asymmetric dependence of the ionization cross-section on the photon energy [2, 3].

The asymmetric profile can be described by the formula that put forward by Fano [2, 4] of a scattering cross section:

$$\sigma = \frac{(\varepsilon + q)^2}{\varepsilon^2 + 1} \quad (17.1)$$

where  $q$  is the shape parameter,  $\varepsilon$  is the reduced energy that equals to  $2(E - E_F)/\Gamma$ ,  $E_F$  is the resonant energy and  $\Gamma$  is the width of the autoionized state. The asymmetry parameter  $q$  is a ratio of the transition probabilities to the mixed state and to the continuum. When  $q$  is of the order of unity, both the continuum and discrete transitions are of the same strength, resulting in the asymmetric profile. In the situation  $q = 0$ , it is a unique Fano resonance with symmetrical line shape, which is sometimes called an anti-resonance. In the limit  $|q| \rightarrow \infty$ , the transition to the continuum is very weak, and the line shape is entirely determined by the transition through the discrete state only with the standard Lorentzian profile of a Breit-Wigner resonance [4].

Similar asymmetric profiles can not only be observed in electron-electron interactions but also in other systems such as two weakly coupled harmonic oscillators [4], electron transition in helium [2], or a single quantum dot [5]. In recent years, it has been further extended to photonic crystals, metamaterials (MMs), and other plasmonic systems [6–14]. In analogy with the ionization of atomic system, the metamaterials should also possess two types of resonances, i.e., a discrete bound state (subradiant mode with sharp resonance that weakly coupled to incident light) and a continuum state (superradiant mode with large linewidth that strongly coupled to incident light) [15–17]. For example, for a dolmen structure composed of two horizontal bars and one vertical bar, the coupling between the sharp bonding mode and broad dipole mode results in the asymmetric Fano line shape (Fig. 17.1a) [9]. And when a disk is introduced into the center of the split ring resonators (SRRs), the surface plasmon resonance modes of the SRRs are coupled with the dipole mode of the

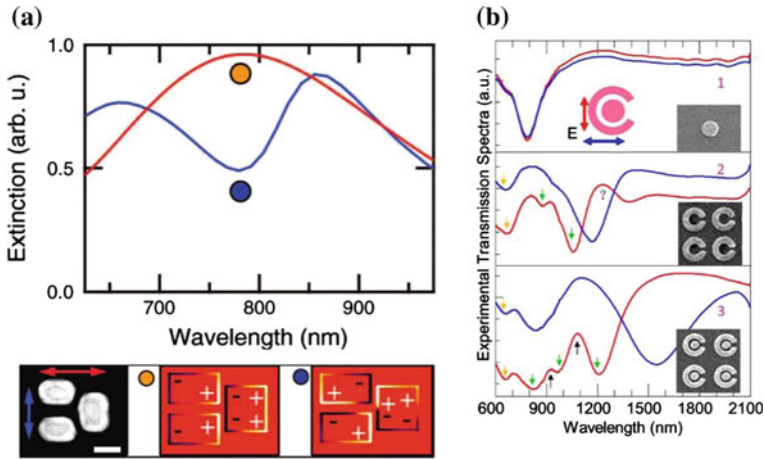


**Fig. 17.1** **a** Fano resonance of an individual dolmen structure (top) and calculated surface charge distributions of the dipolar mode and the Fano extinction dip, respectively (bottom) [9]. **b** Transmission spectra of disk (1), SRR (2), and SRR/D (3) arrays [18]

disk through capacitive interaction, thus an asymmetric line shape appears through the Fano interference (see Fig. 17.1b) [18]. Therefore, in principle, it is promising to construct composite structures composed of different resonant elements to flexibly excite Fano resonances.

## 17.2 Fabrication of 3D Folding Metamaterial

In high frequency region (visible, infrared or terahertz), the feature size of the sub-wavelength metamaterial unit ranges from hundreds of nanometers to tens of microns. Traditional planar techniques such as UV/E-beam lithography, film deposition and plasma etching were applied for the fabrication of high frequency metamaterials, however their configurations were restricted to be two dimensional. 2D metamaterials have intrinsic limitations compared to 3D ones: (i) Negative permeability cannot be achieved by planar SRRs unless oblique incident light radiates on the plane [19]. (ii) The orientations of planar structures are restricted by the substrate so that the density of unit cells and the interaction type with the incident light are limited. (iii) Planar structures usually have smaller scattering cross sections compared to 3D ones thus their resonance intensity are smaller [20, 21]. In order to overcome the above disadvantages, 3D fabrication techniques are necessary to construct 3D metamaterials for diverse Fano resonances.

Up to now, quite a number of 3D fabrication techniques has been developed. These techniques can be classified into two types: one is the combination of the traditional planar techniques, and the other one is brand new techniques beyond the planar ones.

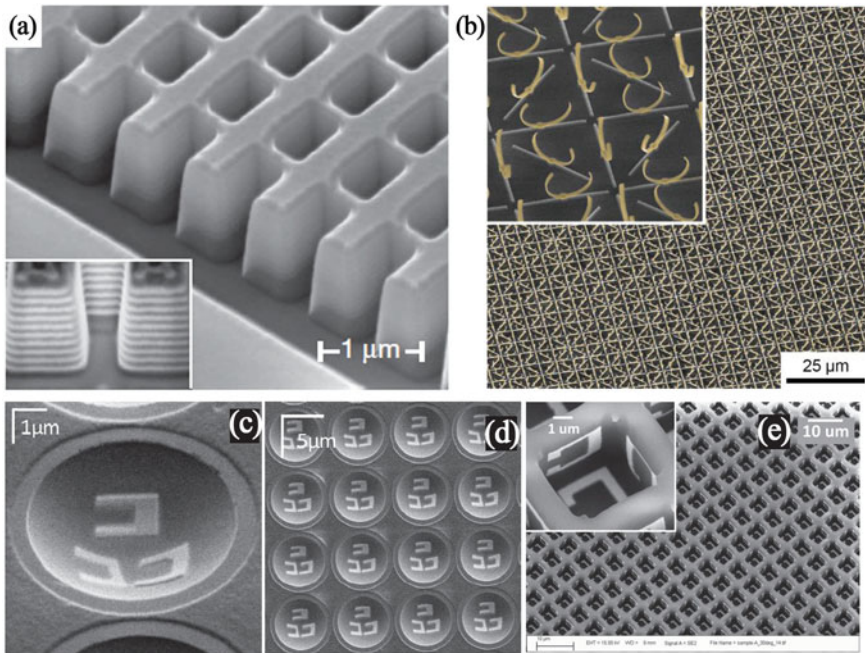


**Fig. 17.2** **a** SEM image of the 21-layer fishnet structure [22]. **b** SEM images of vertical SRRs by stress-driven assembly method [26]. **c–e** SEM images of a composite 3D unit cell with SRRs [31, 32]

### 17.2.1 Combination of Traditional Planar Techniques

In the first type, layer-by-layer stacking is the simplest way that can be thought of. For example, the layer-by-layer fishnet structure composed of Ag and  $\text{MgF}_2$  films have effective negative refractive index over a broad spectral range, where the negative index is provided by the negative permeability from broad metal strips and negative permittivity from narrow metal strips [22], as shown in Fig. 17.2a. In addition, multilayer SRRs [20] with broadband resonance spectra and Yagi-Uda nanoantenna arrays with directional radiations [23] were also studied based on the layer-by-layer stacking method. Besides stacking, rolling up 2D planar unit cells on flexible substrate is also an intuitive way to construct “metamaterial tube” with 3D configuration based on traditional planar techniques [24], but the orientation of these units cells are still severely restricted by the substrate thus they were so called “quasi-3D”.

Stress-driven assembly [25–29] and oblique angle deposition [30–32] are 3D fabrication techniques combining different types of planar processes that the as-fabricated structures are truly 3D. For stress-driven assembly method, the residual stress and strain gradient in single layer [25–27] or bilayer [28, 29] films were used

after the patterns were released from substrate to get vertical structures (Fig. 17.2b), and their radius were determined by material type, film thickness and temperature. For oblique angle deposition, target materials were obliquely deposited onto side walls of grating [30] or containers [31, 32] and the orientation of the 3D units are restricted by the shape and profile of the framework (Fig. 17.2c–e).

### 17.2.2 Brand New Techniques

In the second type, new techniques were developed to replace the existing planar techniques. The most flexible one is direct laser writing (DLW) based on two-photon absorption (TPA) [33]. The probability of the photon absorption is proportional to the square of light intensity thus only in a very small region in the middle of light spot the light intensity is large enough for TPA, therefore the resolution of DLW system is beyond the diffraction limit. A variety of 3D structures were fabricated based on this technique including woodpile photonic crystal [34–36], bi-chiral photonic crystal structure [37] and elasto-mechanical unfeelability cloak [38] (Fig. 17.3a–c). However, there are also disadvantages of DLW: (i) It has very low efficiency due to its dot-by-dot scanning process; (ii) The materials are restricted to the ones that have TPA effect, such as photoresist [39, 40], protein [41], arsenic trisulfide [42], etc. Metal (which is a good candidate for plasmonic metamaterials) is very difficult to be fabricated out of photoresist, but can be indirectly made by electroplating filling in the hole in positive photoresist [21]. Two-photon-induced reduction of metal ions is a solution to directly write metal structures (Fig. 17.3d) [43, 44], but the metal grains are very large that increase the loss of surface plasmon.

Focused ion beam induced folding is also a new technique that beyond the traditional planar technique. In this technique, when focused ion beam irradiates on the bottom of nanowires [45–47] or metal cantilevers [48, 49], the nanowires or metal cantilevers will gradually bend towards the direction of ion beam, and finally be parallel to the ion beam. Therefore, there are two parameters that are most important for the folding process: the ion beam dose (i.e., ion beam scanning times, which is proportional to the bending angle before saturation) and ion beam direction (determines the ultimate bending angle). A schematic of the fabrication strategies for 3D plasmonic structures, e.g. single-folding, double-folding and multi-folding, is illustrated in Fig. 17.4.

First, the metal film is released from the sacrificial layer on substrate and then transferred onto a copper grid by a lift-off process [48]. Self-supported metal film is obtained as shown in Fig. 17.4a. The total size of the pattern area is determined by the size of the hollow grid, which can be chosen flexibly. Then focused-ion-beam is applied onto the film to: (i) cut through the metal film to get in-plane cantilevers with only one edge connected to the rest of the film as shown in Fig. 17.4b–d (red path labeled S1); (ii) scan along specific path to fold the cantilever to a certain inclined angle (blue path). For a typical single-folding process (Fig. 17.4b), line scanning on the base of the cantilevers is processed to fold them to specific angles (labeled S2), the

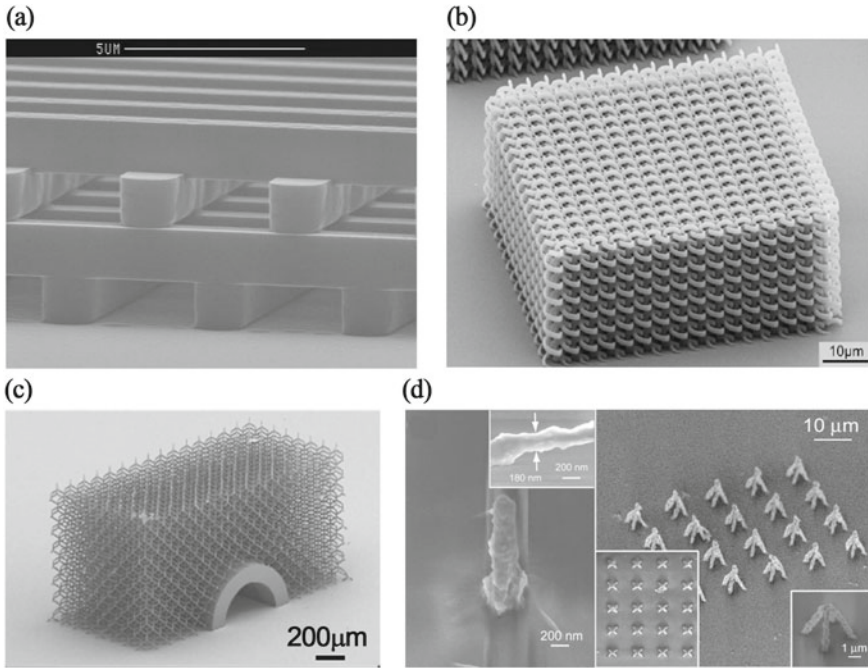


**Fig. 17.3** **a** SEM cross-sectional view of a 3D photonic crystal woodpile structure [36]. **b** SEM images of a Bi-chiral photonic crystal structure [37]. **c** SEM images of elasto-mechanical structures [38]. **d** SEM images of silver pillar and pyramid structures [44]

length-width ratio of which can reach over 10:1. Figure 17.4c illustrates the double-folding process, that smaller cantilevers are firstly cut on a larger cantilever (S1) and line-scanned to be folded up (S2), then followed by an extra line scanning across the base of the large cantilever to make a hierarchy folding configuration (S3). A multi-folding design shown in Fig. 17.4d is carried out by multiple scanning step by step (S2–S5) along one direction of the cantilever. The corresponding scanning electron microscope (SEM) images of structures obtained by the aforementioned three kinds of strategies are displayed in Fig. 17.4e–g, respectively [49]. These images indicate very good degree of control and reproducibility of this in situ ion-beam irradiation-induced folding technique.

An advantage of this 3D nanofabrication approach is that the 3D structures can be prepared with high consistency across a sufficiently large area, e.g., on the order of square millimeters, with a manageable processing time using a step-repeat patterning strategy [48]. In addition, it should be emphasized that not only metal films but also other materials including dielectric, semiconductor and composite multilayer films can be used in this process, which enlarges its application in photonics and plasmonics [50].

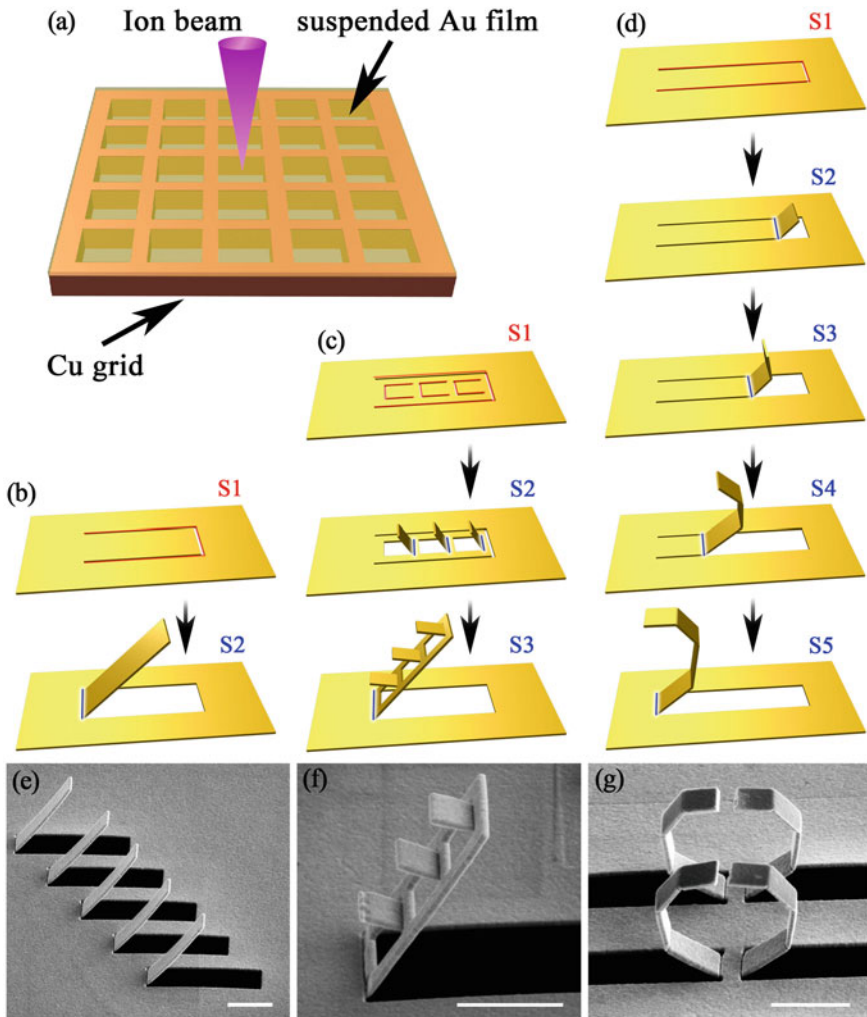


**Fig. 17.4** Fabrication of spatially orientated 3D structures by focused-ion-beam induced folding technique: **a** A suspended gold film on Cu grid. **b–d** Single-folding, double-folding and multi-folding process. **e–g** SEM images of structures achieved with single, double and multi-folding strategy, respectively. The scale bars are 2  $\mu\text{m}$  [49]

### 17.3 Fano Resonances in 3D Folding Metamaterials

An intrinsic property of the 3D folding metamaterial is that, whatever the shape of the folding part is, there is a complementary hole shape on the film. This means that the 3D folding metamaterials are composed of two parts: the out-of-plane part

folded by ion beam, and the planar part containing holes. Therefore, distinct types of resonances can be excited in this composite metamaterial.

### 17.3.1 Unusual Fano Resonance in Composite 3D Structures

In this work, we proposed a MH-VSRR structure that consists of vertical SRRs (VSRRs) standing along an edge of planar metal holes (MHs) to generate Fano resonances, as shown in Fig. 17.5a–c. U-shape SRRs have been widely employed as building blocks for various 2D and 3D MMs [20, 51–56]. Conventionally, the resonances of an SRR can be excited by polarized incident light with the electric field (E-field) parallel to the ‘U’-plane (e.g.,  $k$  parallel to  $z$  direction and E-field parallel to  $x$  direction as shown in Fig. 17.5a), or as to say, the magnetic field (H-field) perpendicular to the ‘U’-plane [53, 57]. Alternatively, when the E-field is perpendicular to the ‘U’-plane in the  $y$  direction, it will induce no electromagnetic resonance for SRR structures, regardless of planar [53, 57], vertical [58, 59] or multi-layered [20, 51] configurations. Here we will show that, the integration of SRRs can significantly change the extraordinary optical transmission (EOT) [60] properties of the original MH arrays. In Fig. 17.5d and f, although the incident light has an  $x$ -polarized E-field component corresponding to the conventional situation, the resonance peaks are rather weak (which will be explained latter) and the red curves (MH-VSRRs) in Fig. 17.5d and f are quite similar to the black curves (EOT property of MHs). When the polarization of the incident light changes to an alternative  $y$  direction, as shown in Fig. 17.5e and h, clear Fano-type asymmetric line shapes (red curves) at both low and high frequencies are observed on the background of broad EOT peak (black curves), with Fano asymmetry factors of  $q = 0.86$  and  $-0.14$  respectively. Here, the ‘broad’ resonance of EOT background can be treated as a continuum state but a discrete bound state seems to be missing, since the VSRRs do not support any resonance under such unconventional excitation scheme [53, 57], making the observed Fano resonances quite unusual.

### 17.3.2 Mechanism of Fano Resonance Excitation

For the EOT mode, it is induced by the surface plasmon polariton that scattered by the metallic hole array on metal/air interface. Only TM mode can exist on the interface, and in the half space on the air side ( $z > 0$ ) the field component can be expressed as:

$$H_y(z) = Ae^{i\beta x}e^{-k_z z} \quad (17.2)$$

$$E_x(z) = iA \frac{1}{\omega \epsilon_0 \epsilon_{\text{air}}} k e^{i\beta x} e^{-k_z z} \quad (17.3)$$



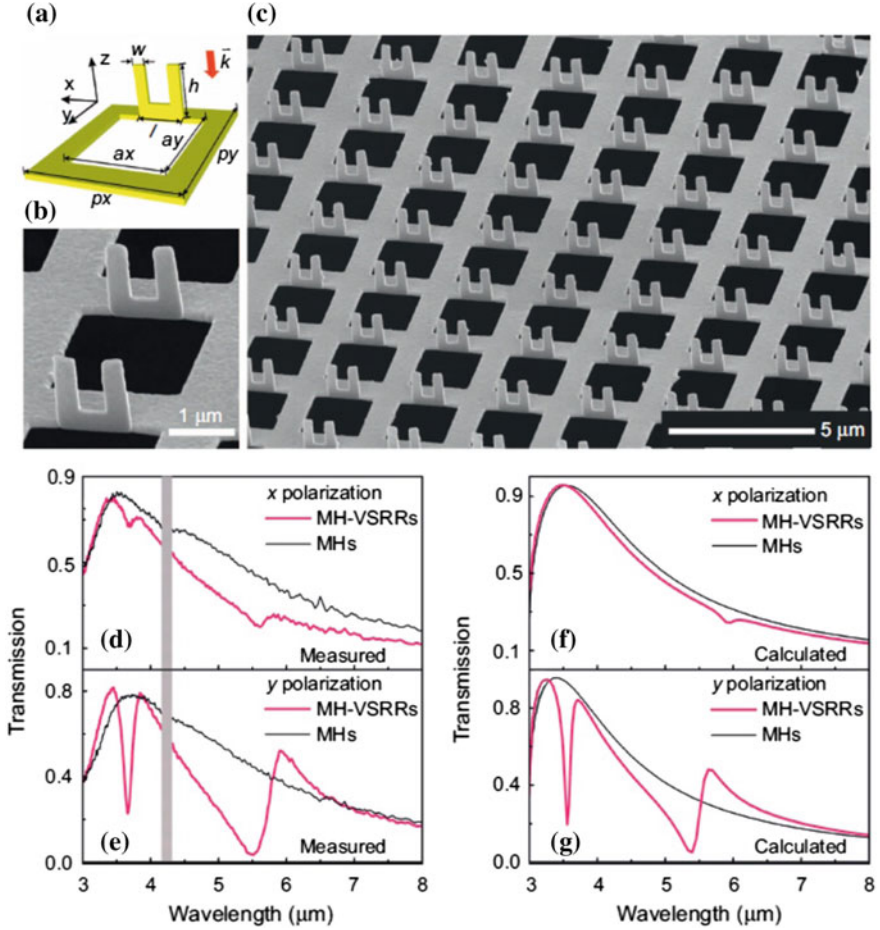


**Fig. 17.5** **a** Schematic of the MH-VSRR structure. **b–c** SEM images of the fabricated MH-VSRRs, with  $h = 1.2 \mu\text{m}$ ,  $l = 1.0 \mu\text{m}$ ,  $w = 340 \text{ nm}$ ,  $a_x = a_y = 2.0 \mu\text{m}$  and  $p_x = p_y = 3.0 \mu\text{m}$ . **d–e** As-measured transmission spectra of the MH-VSRRs shown in **c** under normal incidence with electric field polarized along  $x$ - and  $y$ -direction, respectively. **f–g** Simulated transmission spectra of the MH-VSRRs corresponding to **(d)** and **(e)**, respectively [48]

$$E_z(z) = -A \frac{\beta}{\omega \epsilon_0 \epsilon_{\text{air}}} e^{i\beta x} e^{-k_z z} \quad (17.4)$$

where  $A$  is the field amplitude, and  $\beta = k_0 \sqrt{\epsilon_{\text{air}} \epsilon_{\text{metal}} / (\epsilon_{\text{air}} + \epsilon_{\text{metal}})}$  is the propagation constant of SPP. It is obvious that in the near field region, there are enhanced  $E_z$  component that decays exponentially with distance from the meta/air interface in  $z$  direction. Figure 17.6a shows the electric field distribution (indicated by dark arrows) of a pure metallic hole array without SRRs in the  $yz$  plane in the near field, and the  $E_z$  component is plotted in color. When a vertical SRR is placed within the intensified

$E_z$  field (as the dashed outlines in Fig. 17.6a and green SRR in Fig. 17.6b), the electric resonances of the vertical structure could be naturally and efficiently excited, which could not be directly excited by incident light thus is a “dark mode” [15–17]. Therefore, the Fano resonances are resulted from the coupling between the “bright mode” (SPP scattered by the periodic MH array) and “dark mode” (electric dipole on VSRRs that indirectly excited by evanescent wave of SPP) [61].

The coupling effect can be verified by the simulated surface current distribution at the two resonance dips of both low-order (Fig. 17.6c) and high-order (Fig. 17.6d) modes. As illustrated in Fig. 17.6c, the current distribution at the low-order resonance dip exhibits a 3D configuration, which is a hybridized current flowing between VSRRs and MHs units. This hybridized current is also evident in the experimental and simulated spectra with different arm length  $h$  (Fig. 17.6e and f) that the Fano resonance dips shifted toward longer wavelength as the height of the VSRRs increased. In fact, the resonance wavelength of the low-order mode increases linearly with the ‘empirical length’ ( $EL$ ), which is defined as  $EL = h + (ax - l)/2 + ay/2$  [48]. By contrast, the current distribution at the high-order resonance dip exhibits anti-phase current flow resonances on the arms of VSRRs and edges of MHs, as shown in Fig. 17.6d. This means that the high-order resonance induced by these current flows is a relative local effect and an exotic coupling behavior of the VSRR and MH, which is more dependent on the length of the VSRR arms than on other geometrical parameters.

From Fig. 17.6c, it should be noted that the surface currents concentrate on the outside of the VSRRs, which indicates that if we replace the VSRRs by vertical metal plates, similar responses may be excited. Two samples, 3D metamaterials with vertical SRRs and vertical plates were fabricated as shown in Fig. 17.7a and b, respectively. The measured and simulated spectra are given in Fig. 17.7c and d. As expected, the transmission spectra of both 3D MMs exhibit significant Fano-like resonances for both low-order and high-order modes (labelled #1 and #2), with great distinction compared to the spectrum of the MHs without vertical parts (grey curve in Fig. 17.7c, d). The vertical-part-related Fano resonances indicates that the central part of the vertical SRRs has little effect to the generation of prominent Fano resonances in this evanescent wave excitation scheme (Fig. 17.7e and f). In this way, simple vertical plates can replace complicated VSRRs and two points should be emphasized: Firstly, compared to the 3D MMs with SRRs, the 3D MMs with micro-plates have obvious advantages on fabrication efficiency and yield rate due to their much simpler geometry and mechanical stabilities. Secondly, these observations indicate an underlying physical mechanism responsible for the generation of prominent Fano resonances, which might be universal for the design of other types of 3D MMs with versatile Fano resonances and thus deserves in-depth studies.

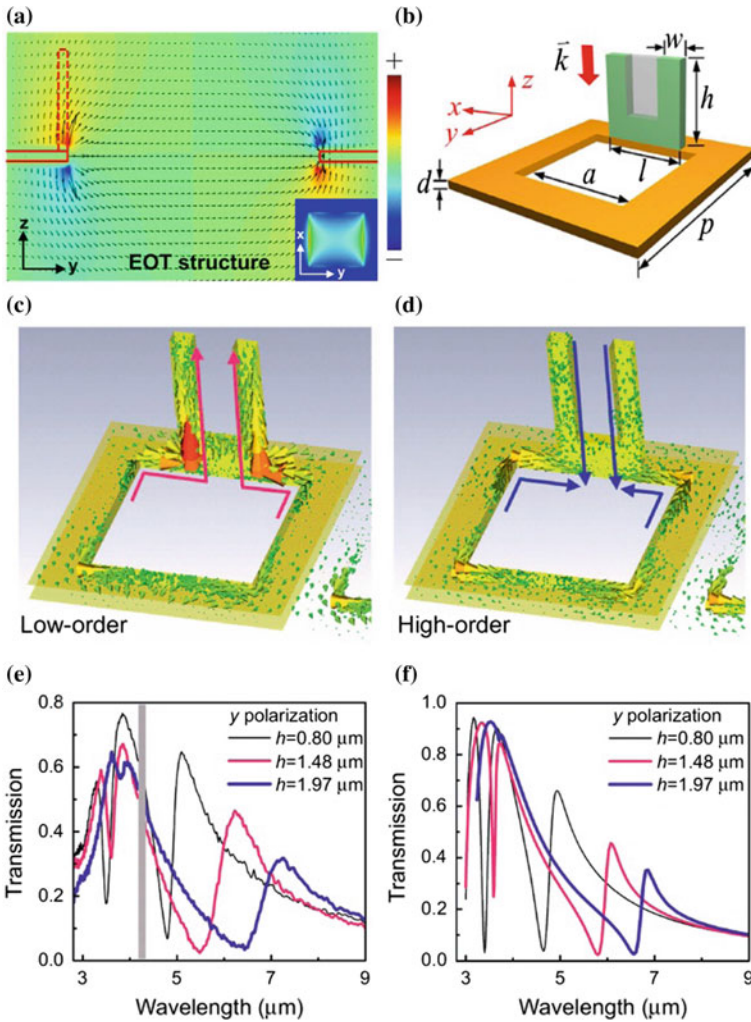


**Fig. 17.6** **a** Simulated E-field distribution (indicated by dark arrows) of a pure metallic hole array without SRRs in the  $yz$  plane.  $E_z$  is plotted in color. **b** Schematic of the unit cell of a 3D MM. **c–d** Simulated current distributions of the sample at the low-order and high-order resonance dips. **e–f** Measured and calculated transmission spectra of the MH-VSRRs under normal incidence with the electric field polarized along the  $y$ -direction [48, 61]

### 17.3.3 Conductive Coupling and Capacitive Coupling

It is now explicit that the Fano resonances of the 3D MM comes from the coupling between the “bright mode” of EOT supported by MH arrays and “dark mode” of electric dipole generated by VSRRs. Generally, the coupling mechanisms of plasmonic

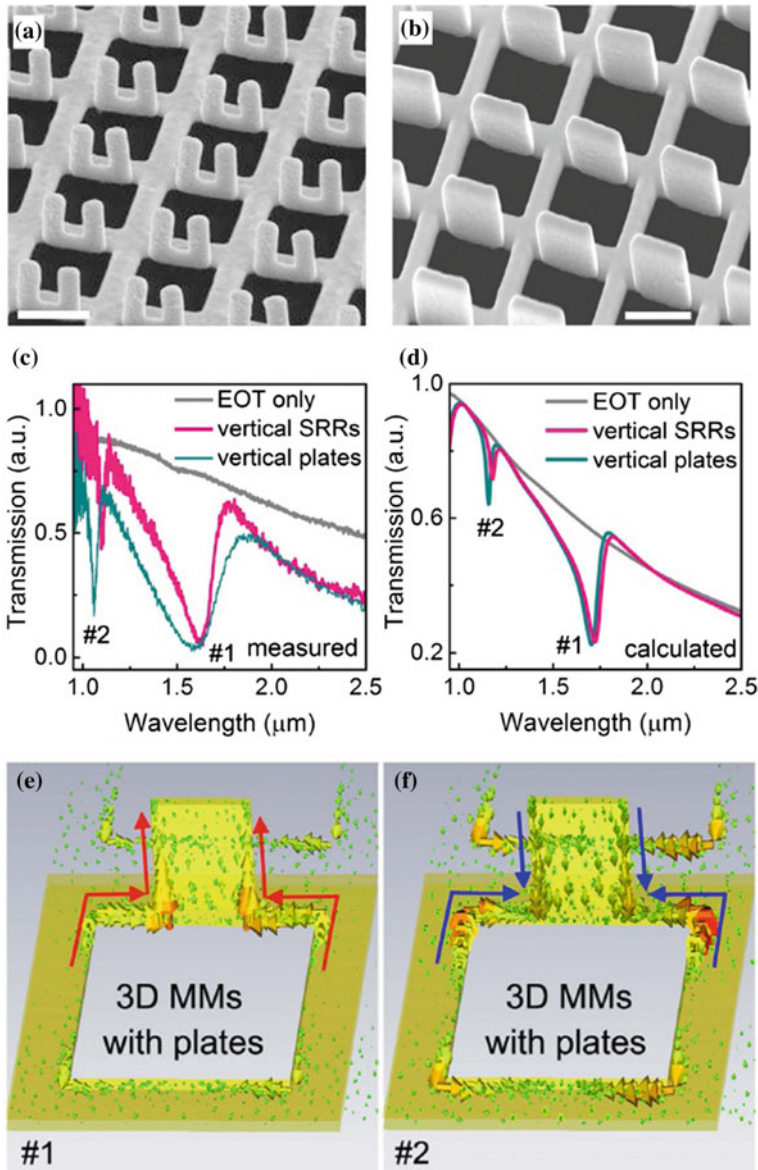


**Fig. 17.7** a–b Side-view SEM images of the fabricated 3D MMs with vertical SRRs and vertical plates, respectively. The scale bars are 500 nm. c–d Measured and calculated transmission spectra of an MHs without any vertical part and two 3D MMs with different vertical structures under y-polarized light excitation. e–f Simulated current distributions of the 3D MMs with vertical plates at two distinct modes #1 and #2 [61]

Fano resonances could be summarized into three types, i.e. capacitive (electric) coupling, inductive (magnetic) coupling and conductive (connective) coupling [62–64]. Among them, the capacitive coupling depends on the charge oscillations on the two sides of the plasmonic gaps [9, 65] and the inductive coupling relies on the current flows in coil-type configurations [18, 64, 66], both of which are well known and have been widely adopted in the generation of plasmonic Fano resonance [4, 7, 67]. In comparison, the conductive coupling has been largely overlooked due to its simple configuration, since the 2D conductive structures look like simple electric connection of individual elements although it has exhibited strong impacts on the modifications of plasmonic properties in systems such as gold nanorod dimers [68, 69], theta-shaped ring-rod nanostructures [63], and THz JSRR structures [62, 70]. In this case, the 2D connected elements were generally treated as single conductive structures and the resulted couplings were traditionally rationalized as the interference between the bright dipole modes and the dark high-order modes [63].

To demonstrate the importance of the 3D conductive coupling mechanism in our MMs, the vertical SRRs are fictitiously lifted from the in-plane MH structure as shown in Fig. 17.8a, which is difficult to be achieved in actual experiment. For  $x$ -polarized excitation, as shown in Fig. 17.8b, the transmission of the 3D MMs with different gap distances shows little spectral shift, and simply represents a linear spectral overlapping between the SRR (green triangles) and MH (black circles) structures, indicating there is almost no couplings between the SRRs and MH structures when the two parts are separated. It should be mentioned that the tiny spectral dip at  $4 \mu\text{m}$  in the case of  $g = 0$  results from the modified magnetic resonance of the SRR when it is connected to the MH structure (identical to the weak resonance peak mentioned in Sect. 3.1).

For comparison, when the incident light is  $y$ -polarized, the coupling scheme is quite different that it gradually transforms from 3D conductive coupling ( $g=0 \text{ nm}$ ) towards capacitive coupling ( $g>0 \text{ nm}$ ). From the normalized transmission spectra of the 3D MM to that of the MH structure shown in Fig. 17.8c, the low-order mode #1 shows significant constructive (enhanced by  $\sim 52\%$  at the peak) and destructive (suppressed by  $\sim 92\%$  at the dip) interference effects when the vertical and planar parts are connected ( $g=0 \text{ nm}$ ). This is quite consistent with the classical understanding that Fano resonance describes both destructive and constructive interferences between a discrete state and a continuum state [4]. When the gap increases, the Fano resonance #1 is found to be highly sensitive on both the resonance wavelength and the amplitude of constructive and destructive interferences. Its peak-to-dip depth drops quickly by 75% when the 3D MM deviates slightly from conductive coupling ( $g=0 \text{ nm}$ ) to capacitive coupling with a gap distance as small as  $\lambda/20$  ( $g=150 \text{ nm}$ ), as shown in Fig. 17.8d, further illustrating the critical role of the 3D conductive coupling. In comparison, both resonance wavelength and amplitude of Fano resonance #2 change slowly with the varied gap distance. This is because for the anti-phase coupling case, the repelling currents in SRR and MH structure are relatively independent thus the existence of gap does not change the type of coupling. Therefore, it is actually capacitive coupling for Fano resonance #2 and the gap size affects its wavelength and amplitude in a much mild way.

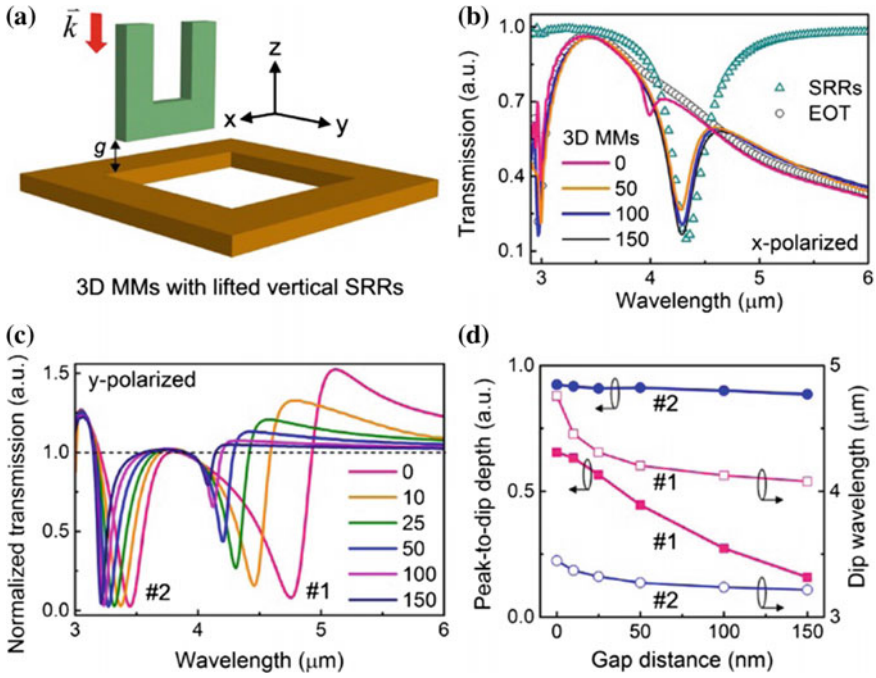


**Fig. 17.8** **a** Schematic of the unit cell of a 3D MM in which the vertical SRR is lifted above the MH structure by a gap distance of  $g$ . **b** Simulated transmission spectra of an MH structure, an SRR array, and 3D MMs with different  $g$  (unit: nm) under  $x$ -polarized excitation. **c** Normalized transmission spectra of the 3D MMs with SRRs to that of MH structure under different gap distances (unit: nm) upon  $y$ -polarized excitation. **d** Absolute peak-to-dip depth and dip wavelength as a function of the gap distance for resonances #1 and #2, respectively [61]

## 17.4 Applications

Fano resonance metamaterials have steep profiles, high quality factors and strong enhancement of electromagnetic field, thereby potentially available for sensing and detecting applications. On one hand, very weak perturbation in the electromagnetic environment of the metamaterial can significantly alter its scattering characteristics, thus the resonance is very sensitive to the refractive index of the environment. On the other hand, the enhanced electromagnetic field could significantly facilitate light-matter interaction, thus helpful in molecule detection by surface enhanced Raman scattering (SERS).

### 17.4.1 Refractive Index Sensing

Refractive index sensing is one of the most common methods to detect material index variation, by which the wavelength shift of resonance peak can be monitored as a function of the index of local dielectric environment. In order to facilitate the study of engineering material in visible and infrared range (e.g., through Abbe number [71]), the 3D MMs were scaled down (a repeating unit of 750 nm on 50-nm-thick Au film as shown in Fig. 17.9a) and still present well-preserved resonance shapes (black curve in Fig. 17.9b) compared with their mid-infrared counterparts [48]. The sensitivity is defined as:

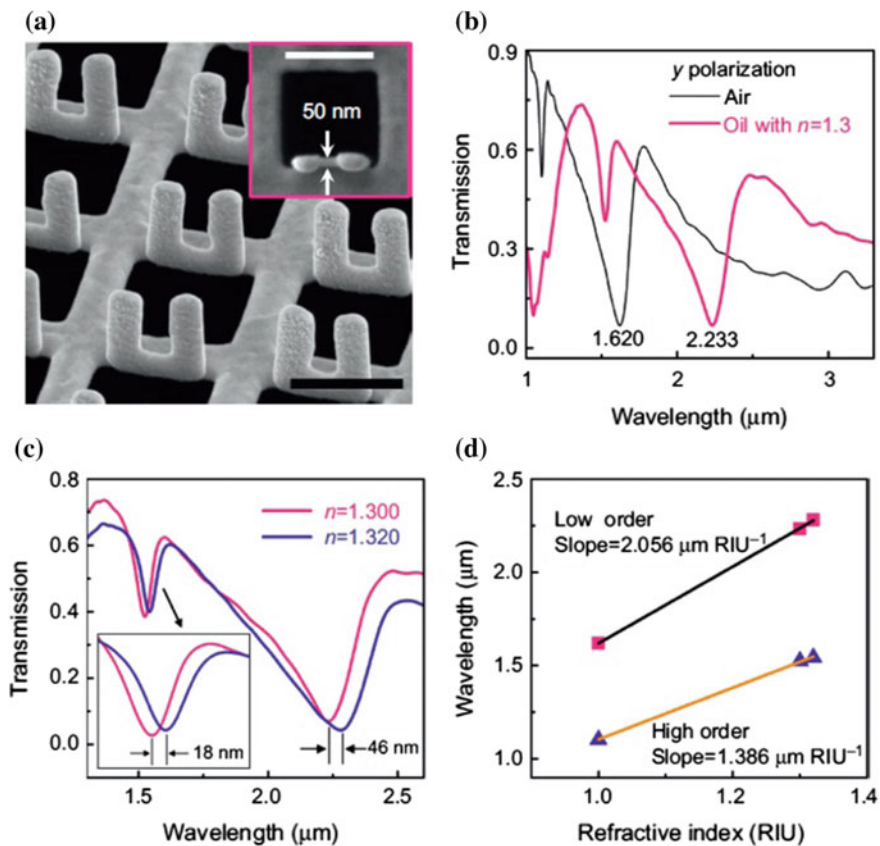


**Fig. 17.9** **a** SEM images of the fabricated nano-structures. **b** Measured transmission spectra of the MH-VSRRs in air and oil with a refractive index of  $1.300 \pm 0.0002$ , respectively. **c** The measured transmission spectra of the MH-VSRRs in oil with refractive indices of 1.300 and 1.320, respectively. **d** The wavelengths of the low-order and high-order Fano resonance dips as a function of the refractive index of the surrounding medium [48]

$$S = \Delta\lambda/\Delta n \quad (17.5)$$

based on the fact that there is a linear relationship between the peak shift  $\Delta\lambda$  and the index variation  $\Delta n$  [72]. The nanoscale 3D MMs were immersed in index matching oil with different refractive indices (Cargille Labs) for transmission measurement. The low-order Fano resonance dip shifts from 1.620  $\mu\text{m}$  in air to 2.233  $\mu\text{m}$  in oil with refractive index of  $1.300 \pm 0.0002$  (shown in Fig. 17.9b), and for oils with very small index differences (1.30 and 1.32) the peak shift can still be recognized demonstrating a large resolution capability (shown in Fig. 17.9c). The relationship between the resonance dip wavelength and refractive index is shown in Fig. 17.9d, and the sensitivity can be calculated according to 17.5, which is the change of the resonance dip wavelength per RIU. The sensitivity was 2040 nm/RIU for the low-order Fano resonance and 1,400 nm/RIU for the high-order mode. In addition, the figure of merit (FOM) values, which equals the refractive index sensitivities divided by the resonance linewidth, are 12.5 and 35 for the low-order and high-order resonance respectively. Both the refractive index sensitivity and FOM values observed in this work appear to be higher than those reported SRR structures in NIR [59, 73].

### 17.4.2 SERS Detection

Figure 17.10a illustrates a scaled-down 3D folding metamaterial containing planar metal holes and vertical metal plates, the designed geometrical parameters of which are  $l = 200$  nm,  $h = 350$  nm,  $a_x = a_y = 360$  nm,  $p_x = p_y = 560$  nm, and  $t = 90$  nm respectively, to match the laser wavelength of 785 nm for SERS detection. Figure 17.10b and c depict the calculated and measured transmission spectrum of the scaled-down 3D metamaterials. The calculated results indicate that the proposed 3D MM exhibit excellent scaling behavior and the high-Q-factor Fano resonance occurs at 785 nm with a Q factor of 76, which matches the frequency of the excitation laser. However, the measured high-Q-factor Fano resonance exhibit a slight red shift to 775 nm with a Q factor of about 24, which is attributed to the larger fabrication tolerance and larger ohmic loss at nanoscale. As a demonstration of the SERS performance of the 3D MM array, we have conducted a comparative experiment using the 3D MM array as SERS substrate for probing 4-mercaptopyridine (4-MP), which has a large scattering cross-section and forms a self-assembled monolayer on metal surfaces similar to alkane thiols and thus has been extensively used in the studies of SERS. The Raman signals were detected separately from an unpatterned area of the gold film as a reference to other three typical areas in the 3D MM arrays (center and edge). The SERS spectra were collected in the Raman shift range of 800–1800  $\text{cm}^{-1}$ . Figure 17.10d shows the measured SERS spectra of the 4-MP molecules on the 3D MM array and the reference gold film, in which a low 4-MP solution concentration of  $1 \times 10^{-6}$  mol/L is directly selected for demonstrating our prior judgment in high-sensitive SERS detection. It can be seen that there are almost no feature peak of the 4-MP molecule on the reference gold film, while three typical areas in 3D



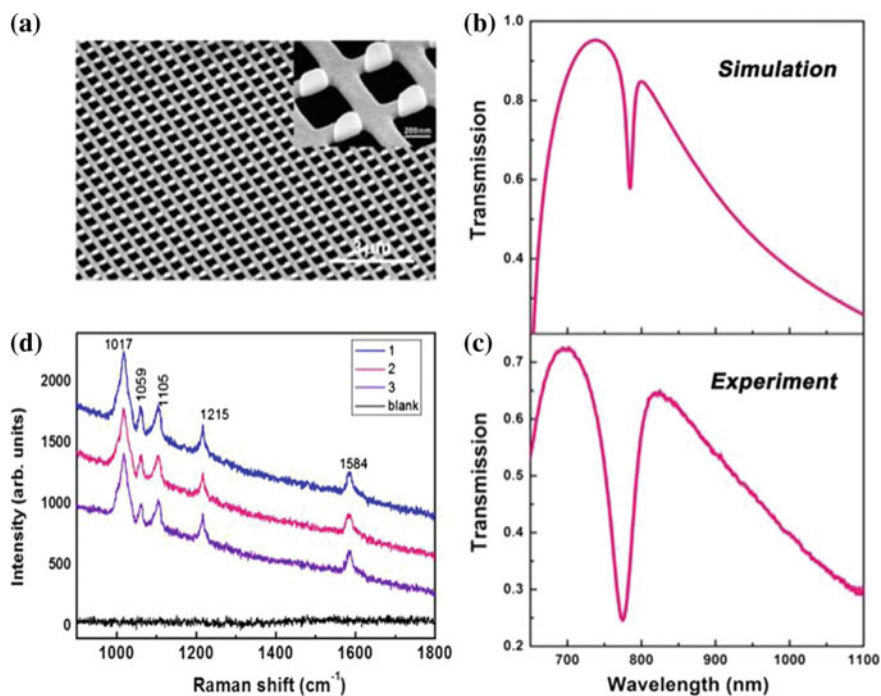


**Fig. 17.10** **a** Oblique view of SEM image of the fabricated scaled-down 3D metamaterials. Inset: zoom in image. **b–c** Calculated and measured optical transmission spectra of the 3D plasmonic metamaterials as a SERS substrate. **d** Experimentally measured Raman spectra of the 4-MP molecules on three typical areas of the 3D metamaterial-based substrate. The laser excitation wavelength is 785 nm

MM arrays all show a strong SERS signal. In addition, the tiny difference in Raman signal intensity of three typical areas in 3D MM arrays maybe originate from the deviation of electric field enhancement in the 3D structure and the error in measurement process, which should be reasonable at such a low concentration. The SERS experiment provides persuasive evidence that the proposed 3D MMs possess significant enhanced SERS performance. The strong spatial electric field enhancement and confinement produced in the 3D MMs by the robust high-Q-factor Fano resonance is responsible for the enhancement of SERS detection. These results strongly substantiate our expectation on utilizing high-Q-factor Fano resonance supported by 3D MMs to boost SERS applications and exhibit promising prospect for light-matter interaction based applications.

## 17.5 Conclusion

The 3D folding metamaterial is a novel type of artificial composite structure composed of planar part and out-of-plane part that support Fano resonances. It has a variety of advantages compared to the existing 3D metamaterials: good controllability on the orientation of the out-of-plane units, nanoscale precision endowed by the focused ion beam spot, and complex configurations based on the multifolding feature. By simply combining MHs and VSRRs together, two Fano resonances were observed due to the coupling between the ‘bright’ mode and ‘dark’ mode excited by the two parts of the 3D units, where the ‘dark’ mode was indirectly excited by the evanescent wave of SPP. The low-order and high-order Fano resonances should be attributed to conductive and capacitive coupling respectively. The Fano resonance on the suspending 3D structures have very large sensitivity (2040 nm/RIU) to distinguish very small differences on refractive index, and can be also used for bio-molecule detection by SERS due to the large electromagnetic field enhancement. It can be expected that by further increasing the complexity of the folding configuration, more resonant modes can be excited to contribute to the research on optical coupling, hybridization and superposition mechanism.

**Acknowledgements** This work is supported by the National Key Research and Development Program of China under (Grant Nos. 2016YFA0200400 and 2016YFA0200800); the National Natural Science Foundation of China (Grants Nos. 91323304, 11504414, 11674387, 11574369, 11574385, 11574368 and 61390503); Strategic Priority Research Program of the Chinese Academy of Sciences (Grant No. XDB07020200).

## References

1. C.W. Clark, Obituary: Ugo Fano (1912–2001). *Nature* **410**, 164–164 (2001)
2. U. Fano, Effects of configuration interaction on intensities and phase shifts. *Phys. Rev.* **124**, 1866–1878 (1961)
3. B. Khanikaev Alexander, C. Wu, G. Shvets, Fano-resonant metamaterials and their applications. *Nanophotonics* **2**, 247–264 (2013)
4. A.E. Miroshnichenko, S. Flach, Y.S. Kivshar, Fano resonances in nanoscale structures. *Rev. Mod. Phys.* **82**, 2257–2298 (2010)
5. M. Kroner et al., The nonlinear Fano effect. *Nature* **451**, 311–314 (2008)
6. B. Luk’yanchuk, N.I. Zheludev, S.A. Maier, N.J. Halas, P. Nordlander, H. Giessen, C.T. Chong, The Fano resonance in plasmonic nanostructures and metamaterials. *Nat. Mater.* **9**, 707–715 (2010)
7. M. Rahmani, B. Luk’yanchuk, M.H. Hong, Fano resonance in novel plasmonic nanostructures. *Laser Photonics Rev.* **7**, 329–349 (2013)
8. V.A. Fedotov, M. Rose, S.L. Prosvirnin, N. Papasimakis, N.I. Zheludev, Sharp trapped-mode resonances in planar metamaterials with a broken structural symmetry. *Phys. Rev. Lett.* **99**, 147401 (2007)
9. N. Verellen, Y. Sonnefraud, H. Sobhani, F. Hao, V.V. Moshchalkov, P. Van Dorpe, P. Nordlander, S.A. Maier, Fano resonances in individual coherent plasmonic nanocavities. *Nano Lett.* **9**, 1663–1667 (2009)

10. R. Singh, I.A.I. Al-Naib, M. Koch, W. Zhang, Sharp Fano resonances in THz metamaterials. *Opt. Express* **19**, 6312–6319 (2011)
11. Y. Francescato, V. Giannini, S.A. Maier, Plasmonic systems unveiled by fano resonances. *ACS Nano* **6**, 1830–1838 (2012)
12. S.H. Mousavi, A.B. Khanikaev, G. Shvets, Optical properties of Fano-resonant metallic meta-surfaces on a substrate. *Phys. Rev. B* **85**, 155429 (2012)
13. C. Wu, A.B. Khanikaev, R. Adato, N. Arju, A.A. Yanik, H. Altug, G. Shvets, Fano-resonant asymmetric metamaterials for ultrasensitive spectroscopy and identification of molecular monolayers. *Nat. Mater.* **11**, 69–75 (2012)
14. R. Singh, I. Al-Naib, C. Wei, C. Rockstuhl, M. Koch, Z. Weili, The Fano resonance in symmetry broken terahertz metamaterials. *IEEE Trans. Terahertz Sci. Technol.* **3**, 820–826 (2013)
15. S. Zhang, D.A. Genov, Y. Wang, M. Liu, X. Zhang, Plasmon-induced transparency in metamaterials. *Phys. Rev. Lett.* **101**, 047401 (2008)
16. S.Y. Yang et al., Multispectral plasmon-induced transparency in hyperfine terahertz metamolecules. *J. Phys. Condens. Matter* **28**, 445002 (2016)
17. S.Y. Yang, C.C. Tang, Z. Liu, B. Wang, C. Wang, J.J. Li, L. Wang, C.Z. Gu, Simultaneous excitation of extremely high-Q-factor trapped and octupolar modes in terahertz metamaterials. *Opt. Express* **25**, 15938–15946 (2017)
18. Q. Zhang, X. Wen, G. Li, Q. Ruan, J. Wang, Q. Xiong, Multiple magnetic mode-based fano resonance in split-ring resonator/disk nanocavities. *ACS Nano* **7**, 11071–11078 (2013)
19. T.J. Yen, W.J. Padilla, N. Fang, D.C. Vier, D.R. Smith, J.B. Pendry, D.N. Basov, X. Zhang, Terahertz magnetic response from artificial materials. *Science* **303**, 1494–1496 (2004)
20. N. Liu, H. Guo, L. Fu, S. Kaiser, H. Schweizer, H. Giessen, Three-dimensional photonic metamaterials at optical frequencies. *Nat. Mater.* **7**, 31–37 (2008)
21. J.K. Gansel, M. Thiel, M.S. Rill, M. Decker, K. Bade, V. Saile, G. von Freymann, S. Linden, M. Wegener, Gold helix photonic metamaterial as broadband circular polarizer. *Science* **325**, 1513–1515 (2009)
22. J. Valentine, S. Zhang, T. Zentgraf, E. Ulin-Avila, D.A. Genov, G. Bartal, X. Zhang, Three-dimensional optical metamaterial with a negative refractive index. *Nature* **455**, 376–380 (2008)
23. D. Dregely, R. Taubert, J. Dorfmüller, R. Vogelgesang, K. Kern, H. Giessen, 3D optical Yagi-Uda nanoantenna array. *Nat. Commun.* **2**, 267 (2011)
24. Z. Chen, R. Mohsen, Y. Gong, C.T. Chong, M. Hong, Realization of variable three-dimensional terahertz metamaterial tubes for passive resonance tunability. *Adv. Mater.* **24**, OP143–OP147 (2012)
25. C.C. Chen et al., Fabrication of three dimensional split ring resonators by stress-driven assembly method. *Opt. Express* **20**, 9415–9420 (2012)
26. C.-C. Chen, A. Ishikawa, Y.-H. Tang, M.-H. Shiao, D.P. Tsai, T. Tanaka, Uniaxial-isotropic metamaterials by three-dimensional split-ring resonators. *Adv. Opt. Mater.* **3**, 44–48 (2015)
27. Z. Tian, L. Zhang, Y. Fang, B. Xu, S. Tang, N. Hu, Z. An, Z. Chen, Y. Mei, Deterministic self-rolling of ultrathin nanocrystalline diamond nanomembranes for 3D tubular/helical architecture. *Adv. Mater.* **29**, 1604572 (2017)
28. W. Huang, S. Koric, X. Yu, K.J. Hsia, X. Li, Precision structural engineering of self-rolled-up 3D nanomembranes guided by transient quasi-static FEM modeling. *Nano Lett.* **14**, 6293–6297 (2014)
29. E. Moiseeva, Y.M. Senousy, S. McNamara, C.K. Harnett, Single-mask microfabrication of three-dimensional objects from strained biphases. *J. Micromech. Microeng.* **17**, N63–N68 (2007)
30. S. Zhang, W.J. Fan, B.K. Minhas, A. Frauenglass, K.J. Malloy, S.R.J. Brueck, Midinfrared resonant magnetic nanostructures exhibiting a negative permeability. *Phys. Rev. Lett.* **94**, 037402 (2005)
31. D.B. Burckel, J.R. Wendt, G.A. Ten Eyck, A.R. Ellis, I. Brener, M.B. Sinclair, Fabrication of 3D metamaterial resonators using self-aligned membrane projection lithography. *Adv. Mater.* **22**, 3171–3175 (2010)

32. D.B. Burckel, J.R. Wendt, G.A. Ten Eyck, J.C. Ginn, A.R. Ellis, I. Brener, M.B. Sinclair, Micrometer-scale cubic unit cell 3D metamaterial layers. *Adv. Mater.* **22**, 5053–5057 (2010)
33. W. Kaiser, C.G.B. Garrett, Two-photon excitation in CaF<sub>2</sub>: Eu<sup>2+</sup>. *Phys. Rev. Lett.* **7**, 229–231 (1961)
34. M. Hermatschweiler, A. Ledermann, G.A. Ozin, M. Wegener, G. von Freymann, Fabrication of silicon inverse woodpile photonic crystals. *Adv. Funct. Mater.* **17**, 2273–2277 (2007)
35. J. Li, B. Jia, G. Zhou, M. Gu, Fabrication of three-dimensional woodpile photonic crystals in a PbSe quantum dot composite material. *Opt. Express* **14**, 10740–10745 (2006)
36. S.Y. Lin et al., A three-dimensional photonic crystal operating at infrared wavelengths. *Nature* **394**, 251–253 (1998)
37. M. Thiel, M.S. Rill, G. von Freymann, M. Wegener, Three-dimensional bi-chiral photonic crystals. *Adv. Mater.* **21**, 4680–4682 (2009)
38. T. Bückmann, M. Thiel, M. Kadic, R. Schittny, M. Wegener, An elasto-mechanical unfeelability cloak made of pentamode metamaterials. *Nat. Commun.* **5**, 4130 (2014)
39. A.S. Quick, A. de los Santos Pereira, M. Bruns, T. Bückmann, C. Rodriguez-Emmenegger, M. Wegener, C. Barner-Kowollik, Rapid thiol-yne-mediated fabrication and dual postfunctionalization of micro-resolved 3D mesostructures. *Adv. Funct. Mater.* **25**, 3735–3744 (2015)
40. A.S. Quick, J. Fischer, B. Richter, T. Pauloechl, V. Trouillet, M. Wegener, C. Barner-Kowollik, Preparation of reactive three-dimensional microstructures via direct laser writing and thiol-ene chemistry. *Macromol. Rapid Commun.* **34**, 335–340 (2013)
41. D. Serien, S. Takeuchi, Chemically responsive protein-photoresist hybrid actuator. in *2015 28th IEEE International Conference on Micro Electro Mechanical Systems (MEMS)* (2015)
42. S.H. Wong, M. Thiel, P. Brodersen, D. Fenske, G.A. Ozin, M. Wegener, G. von Freymann, Highly Selective wet etch for high-resolution three-dimensional nanostructures in arsenic sulfide all-inorganic photoresist. *Chem. Mater.* **19**, 4213–4221 (2007)
43. T. Tanaka, A. Ishikawa, S. Kawata, Two-photon-induced reduction of metal ions for fabricating three-dimensional electrically conductive metallic microstructure. *Appl. Phys. Lett.* **88**, 081107 (2006)
44. Y.-Y. Cao, N. Takeyasu, T. Tanaka, X.-M. Duan, S. Kawata, 3D metallic nanostructure fabrication by surfactant-assisted multiphoton-induced reduction. *Small* **5**, 1144–1148 (2009)
45. A. Cui, W. Li, Q. Luo, Z. Liu, C. Gu, Freestanding nanostructures for three-dimensional superconducting nanodevices. *Appl. Phys. Lett.* **100**, 143106 (2012)
46. A. Cui, W. Li, Q. Luo, Z. Liu, C. Gu, Controllable three dimensional deformation of platinum nanopillars by focused-ion-beam irradiation. *Microelectron. Eng.* **98**, 409–413 (2012)
47. A. Cui, J.C. Fenton, W. Li, T.H. Shen, Z. Liu, Q. Luo, C. Gu, Ion-beam-induced bending of freestanding amorphous nanowires: The importance of the substrate material and charging. *Appl. Phys. Lett.* **102**, 213112 (2013)
48. A. Cui et al., Directly patterned substrate-free plasmonic ‘nanograter’ structures with unusual Fano resonances. *Light Sci. Appl.* **4**, e308 (2015)
49. Z. Liu et al., Spatially oriented plasmonic ‘nanograter’ structures. *Sci. Rep.* **6**, 28764 (2016)
50. Z. Liu, S. Du, A. Cui, Z. Li, Y. Fan, S. Chen, W. Li, J. Li, C. Gu, High-quality-factor mid-infrared toroidal excitation in folded 3D metamaterials. *Adv. Mater.* **29**, 1606298 (2017)
51. N. Liu, H. Liu, S. Zhu, H. Giessen, Stereometamaterials. *Nat. Photon.* **3**, 157–162 (2009)
52. K. Fan, A.C. Strikwerda, H. Tao, X. Zhang, R.D. Averitt, Stand-up magnetic metamaterials at terahertz frequencies. *Opt. Express* **19**, 12619–12627 (2011)
53. N. Katsarakis, T. Koschny, M. Kafesaki, E.N. Economou, C.M. Soukoulis, Electric coupling to the magnetic resonance of split ring resonators. *Appl. Phys. Lett.* **84**, 2943–2945 (2004)
54. X. Xiong, S.-C. Jiang, Y.-H. Hu, R.-W. Peng, M. Wang, Structured metal film as a perfect absorber. *Adv. Mater.* **25**, 3994–4000 (2013)
55. X. Xiong, Z.-H. Xue, C. Meng, S.-C. Jiang, Y.-H. Hu, R.-W. Peng, M. Wang, Polarization-dependent perfect absorbers/reflectors based on a three-dimensional metamaterial. *Phys. Rev. B* **88**, 115105 (2013)
56. A.I. Kuznetsov et al., Split-ball resonator as a three-dimensional analogue of planar split-rings. *Nat. Commun.* **5**, 3104 (2014)

57. E. Tatartschuk, E. Shamonina, L. Solymar, Plasmonic excitations in metallic nanoparticles: resonances, dispersion characteristics and near-field patterns. *Opt. Express* **17**, 8447–8460 (2009)
58. W.T. Chen et al., Optical magnetic response in three-dimensional metamaterial of upright plasmonic meta-molecules. *Opt. Express* **19**, 12837–12842 (2011)
59. P.C. Wu et al., Vertical split-ring resonator based nanoplasmonic sensor. *Appl. Phys. Lett.* **105**, 033105 (2014)
60. T.W. Ebbesen, H.J. Lezec, H.F. Ghaemi, T. Thio, P.A. Wolff, Extraordinary optical transmission through sub-wavelength hole arrays. *Nature* **391**, 667–669 (1998)
61. Z. Liu, Z. Liu, J. Li, W. Li, J. Li, C. Gu, Z.-Y. Li, 3D conductive coupling for efficient generation of prominent Fano resonances in metamaterials. *Sci. Rep.* **6**, 27817 (2016)
62. I. Al-Naib, E. Hebestreit, C. Rockstuhl, F. Lederer, D. Christodoulides, T. Ozaki, R. Morandotti, Conductive coupling of split ring resonators: a path to THz metamaterials with ultrasharp resonances. *Phys. Rev. Lett.* **112**, 183903 (2014)
63. T.G. Habteyes, S. Dhuey, S. Cabrini, P.J. Schuck, S.R. Leone, Theta-shaped plasmonic nanostructures: bringing “Dark” multipole plasmon resonances into action via conductive coupling. *Nano Lett.* **11**, 1819–1825 (2011)
64. S. Panaro, F. De Angelis, A. Toma, Dark and bright mode hybridization: from electric to magnetic Fano resonances. *Opt. Lasers Eng.* **76**, 64–69 (2016)
65. M. Hentschel, M. Saliba, R. Vogelgesang, H. Giessen, A.P. Alivisatos, N. Liu, Transition from isolated to collective modes in plasmonic oligomers. *Nano Lett.* **10**, 2721–2726 (2010)
66. F. Shafiei, F. Monticone, K.Q. Le, X.X. Liu, T. Hartseld, A. Alu, X.Q. Li, A subwavelength plasmonic metamolecule exhibiting magnetic-based optical Fano resonance. *Nat. Nanotechnol.* **8**, 95–99 (2013)
67. B. Luk'yanchuk, N.I. Zheludev, S.A. Maier, N.J. Halas, P. Nordlander, H. Giessen, C.T. Chong, The Fano resonance in plasmonic nanostructures and metamaterials. *Nat. Mater.* **9**, 707–715 (2010)
68. A.M. Funston, C. Novo, T.J. Davis, P. Mulvaney, Plasmon coupling of gold nanorods at short distances and in different geometries. *Nano Lett.* **9**, 1651–1658 (2009)
69. L.S. Slaughter, Y.P. Wu, B.A. Willingham, P. Nordlander, S. Link, Effects of Symmetry breaking and conductive contact on the plasmon coupling in gold nanorod dimers. *ACS Nano* **4**, 4657–4666 (2010)
70. S. Yang, Z. Liu, X. Xia, Y.E. C. Tang, Y. Wang, J. Li, L. Wang, C. Gu, Excitation of ultrasharp trapped-mode resonances in mirror-symmetric metamaterials. *Phys. Rev. B* **93**, 235407 (2016)
71. T. Matsuda, Y. Funae, M. Yoshida, T. Yamamoto, T. Takaya, Optical material of high refractive index resin composed of sulfur-containing aliphatic and alicyclic methacrylates. *J. Appl. Polym. Sci.* **76**, 45–49 (2000)
72. K.A. Willets, R.P. Van Duyne, Localized surface plasmon resonance spectroscopy and sensing. *Annu. Rev. Phys. Chem.* **58**, 267–297 (2007)
73. I.M. Pryce, Y.A. Kelaita, K. Aydin, H.A. Atwater, Compliant metamaterials for resonantly enhanced infrared absorption spectroscopy and refractive index sensing. *ACS Nano* **5**, 8167–8174 (2011)

# Chapter 18

## Fano Resonances in Topological Photonic Systems



Xiang Ni, Maxim A. Gorlach, Daria A. Smirnova, Dmitry Korobkin and Alexander B. Khanikaev

**Abstract** Though Fano resonances were originally discovered in quantum physics, they can emerge in the variety of wave processes including photonic systems. In this chapter, we demonstrate how the concept of Fano resonances can be applied in topological photonics to describe photonic topological states supported by metasurfaces. As we prove, leaky nature of metasurface's modes allows one to probe them from the far field, while the observed Fano-type features in transmittance spectrum can be unequivocally related to the topological properties of photonic bands. This fundamental link between Fano resonances in transmittance and photonic topological states opens an appealing perspective to control scattering of light through the topological characteristics of metasurface.

### 18.1 Introduction

In condensed matter systems, topological phase transitions from trivial phases to the nontrivial ones, characterized by non-vanishing topological indices, give rise to exotic states of matter such as topological insulators, superconductors and superfluids [1–12]. A broad range of phenomena stemming from topological states of quantum matter has recently found a variety of analogues in classical systems, including mechanical, acoustic and photonic designs [13–30]. In the context of photonics, spin-locking and one-way propagation have been shown to drastically alter our view on scattering of electromagnetic waves, and offer unprecedented robustness to defects and disorder. Nevertheless, emulating many of the key manifestations of topological

---

X. Ni · D. A. Smirnova · D. Korobkin · A. B. Khanikaev (✉)  
The City College of the City University of New York, 140th Street  
and Convent Avenue, New York City, NY 10031, USA  
e-mail: khanikaev@ccny.cuny.edu; khanikaev@gmail.com

M. A. Gorlach · D. Korobkin · A. B. Khanikaev  
ITMO University, Saint Petersburg 197101, Russia

physics in condensed matter with photons, such as quantization of the Hall conductance, is not straightforward and often simply impossible, because of the key differences between electrons and photons. In contrast to electrons, photons possess an integer spin, as a consequence they are subject to Bose statistics and they cannot interact with magnetic fields directly. Because of these key differences between electronic and photonic topological phases, topologically protected states of light can only be obtained through judicious design of a photonic system. Conversely, the distinctions of photonic systems make them unique, and may potentially open a whole new realm of research and applications of topology in photonics. One such distinction is related to the fact that photonic modes can leak into free space due to their coupling to the electromagnetic continuum, which may not only alter topological properties, but also make it possible to probe topological photonic phases by spectroscopic means, including Fano resonances. Moreover, topological states of open photonic systems appear to offer a way to control scattering of light via their topological characteristics, which will enable a new class of optical elements whose scattering characteristics are determined via topological effects and thus exhibit considerable robustness.

While Fano resonances were originally discovered in quantum physics [31] to describe asymmetrically shaped photoionization spectral lines of atoms and molecules, due to the fact that wave interference is specific not only to quantum mechanics, a great number of classical systems exhibiting Fano resonance have since been identified. Most recently the concept of Fano resonances was introduced to the field of photonics and metamaterials [32–34]. By analogy with the original atomic system, a photonic structure can possess two scattering pathways via two resonances, which are generally classified as “bright” (i.e., exhibiting strong coupling to incident light and short radiative lifetime) and “dark” (exhibiting weak radiative coupling and long lifetime). Similar to electronic Fano resonances, interference between these scattering pathways may lead to asymmetric scattering characteristics (i.e. transmission and reflection spectra).

The aim of the present chapter is to demonstrate that the concept of Fano resonance can be of significant interest in the context of a new emerging topic of topological photonics, specifically, in the context of open optical systems where the topological modes can be directly probed via far-field measurements.

## **18.2 Theoretical Description of Topological Fano Resonances: Coupled Mode Theory Approach**

To fully consider the topological properties of open topological systems the conventional theory of Fano resonances has to be modified to correctly include pseudo-spin degrees of freedom. In the simplest case this can be achieved by formulating a scattering theory based on coupled mode theory (CMT), where the incident and scattered fields of the continuum couple to the discrete states of a topological system described by its effective Hamiltonian. When only general understanding of

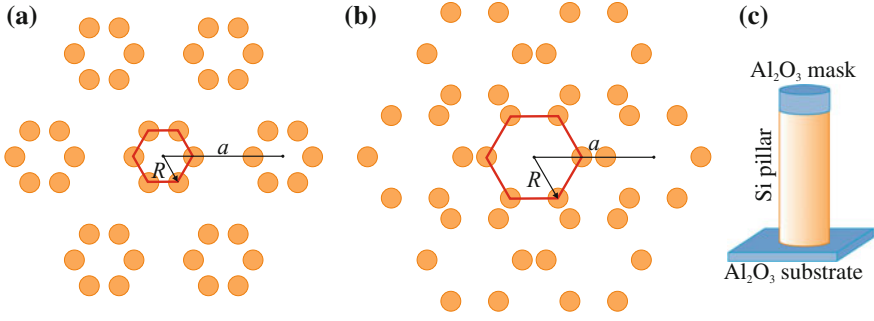


**Fig. 18.1** A schematic view of the topological metasurface under study. **(a, b)** Metasurface with **a** shrunken  $a/R > 3$  and **b** expanded  $a/R < 3$  unit cells. **c** A schematic of a silicon pillar placed on the sapphire substrate

topology is required, such effective Hamiltonians need only to be described near particular point(s) of the Brillouin zone, where band crossings responsible for topological transitions occur. Over the past few years, photonics community developed a powerful toolkit of theoretical and numerical methods for obtaining such Hamiltonians directly from Maxwells equations, e.g by the plane wave expansion method, or rigorous electromagnetic perturbation theory (including electromagnetic analogue of  $\mathbf{k} \cdot \mathbf{p}$ -theory) [24, 35] as detailed below.

As a representative example, we consider a metasurface based on cylindrical Si pillars arranged in hexagon clusters with the edge length  $R$ , placed at the sites of triangular lattice with period  $a$  (Fig. 18.1a, b). The topological properties of its infinite 2D analogue possessing  $C_{6v}$  symmetry have been the subject of several recent studies [36–42]. For  $a/R = 3$ , this system is a conventional honeycomb lattice with the unit cell formed by two cylinders, which exhibits Dirac cones centered at  $K$  and  $K'$  points of the Brillouin zone. However, if the lattice symmetry is reduced by clustering six neighboring pillars so that  $a/R \neq 3$  (distorted lattice), the size of the unit cell increases leading to the reshaping of the first Brillouin zone and as a result the Dirac points appear in the vicinity of the  $\Gamma$  point due to band folding. Additionally, photonic bandgaps open. Previous studies suggested that the shrunken structure with  $a/R > 3$  is topologically trivial, whereas the expanded system with  $a/R < 3$  is topologically nontrivial [36]. To perform spectroscopy measurements of metasurfaces with two topologically distinct geometries, two sets of samples were fabricated (Fig. 18.1a, b) with the same lattice period  $a = 750$  nm, radius of silicon pillars  $r = 75$  nm and height of the pillars  $h = 1.0 \mu\text{m}$  (Fig. 18.1c). The sizes of the clusters  $R$  shown in Fig. 18.1a, b were chosen to be  $a/R = 3.15$  and  $a/R = 2.85$  for shrunken and expanded structures, respectively.

To give an idea how an open topological Fano-resonant system can be described near a Dirac Point, we consider a simple example of the effective Dirac-type Hamiltonian:

$$\hat{H} = \begin{pmatrix} \hat{H}_- & \hat{K} \\ \hat{K}^\dagger & \hat{H}_+ \end{pmatrix}. \quad (18.1)$$



The reasons for choosing such type of effective Hamiltonian are outlined in Sect. 18.4. The  $2 \times 2$  matrices  $\hat{H}_\pm$  and  $\hat{K}$  read

$$\hat{H}_\pm = \begin{pmatrix} \mu(k) & v(\mp k_x - ik_y) \\ v(\mp k_x + ik_y) & -\mu(k) \end{pmatrix}, \quad (18.2)$$

$$\hat{K} = \begin{pmatrix} \alpha(k_x + ik_y)^2 & 0 \\ 0 & -\alpha(k_x - ik_y)^2 \end{pmatrix}, \quad (18.3)$$

where  $+/-$  indicates pseudo-spin up/down state, implying TR-invariant character of the system, the  $2 \times 2$  blocks are written in the basis of dipole ( $p$ ) and quadrupole ( $d$ ) states,  $v$  is the Dirac velocity,  $\mu(k) = \mu + \beta k^2$ ,  $\mu$  and  $\beta$  are the mass term and band parabolicity, respectively. If the terms  $\hat{K}$  and  $\hat{K}^\dagger$  coupling two pseudospins are neglected, the Hamiltonian splits into two decoupled blocks. As such, spin Chern number given by the difference of the Chern numbers for the individual  $2 \times 2$  blocks can be introduced. The result reads:

$$C = \frac{1}{2} [\text{sgn } \mu - \text{sgn } \beta]. \quad (18.4)$$

To describe the evolution of the modes of the open system, we employ the following coupled mode equation [43]:

$$-i\varepsilon |\psi_\pm\rangle = -i\hat{H}_\pm |\psi_\pm\rangle + \varkappa \begin{pmatrix} E_{\text{in}} \\ 0 \end{pmatrix} - \begin{pmatrix} \gamma_0 + \varkappa^2/2 & 0 \\ 0 & \gamma_0 \end{pmatrix} |\psi_\pm\rangle \quad (18.5)$$

Here,  $|\psi_\pm\rangle$  is the ‘‘wavefunction’’ composed of  $p$  (dipole) and  $d$  (quadrupole) modes of the system:  $|\psi_\pm\rangle = (|p_\pm\rangle, |d_\pm\rangle)^T$ .  $\pm$  sign refers to the left- or right-hand circular polarizations of the mode. The first term of (18.5) describes the evolution of the coupled modes in a closed system. The second term is associated with the external driving field. The third term captures the effect of losses that lead to the diminishing of the mode amplitude including both radiative  $\gamma_r = \varkappa^2/2$  and non-radiative  $\gamma_0$  losses, and an explicit expression for  $\hat{H}_\pm$  is given by (18.2).

Once (18.5) is solved with respect to the unknown  $|\psi_\pm\rangle$ , the transmitted wave can be calculated as follows:

$$E_t^{(\pm)} = t_0 E_{\text{in}}^{(\pm)} + c \psi_\pm(p), \quad (18.6)$$

where  $t_0$  is the transmission coefficient of the substrate on which the structure is fabricated and  $\psi_\pm(p)$  is the first (dipole) component of the two-component wave function  $|\psi_\pm\rangle$ . The magnitude of the  $c$  coefficient is determined by the requirement of energy conservation: the change of the mode energy measured by  $\langle \psi_\pm | \psi_\pm \rangle$  should be equal to the intensity of the incoming wave minus the intensity of the transmitted and reflected waves and minus the non-radiative dissipation rate. Since the results turn out to be the same for left- and right circular polarizations, we omit the  $\pm$

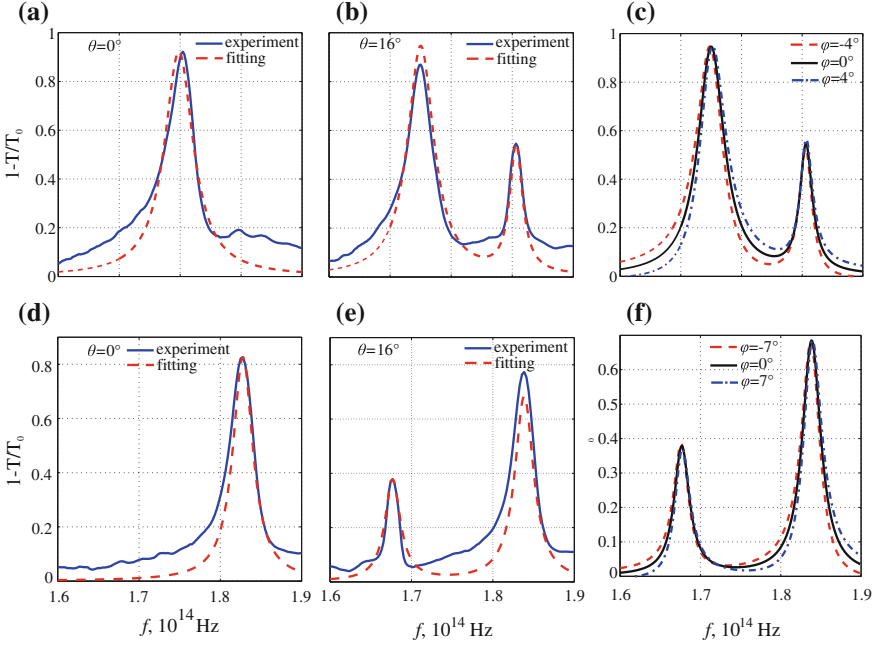


**Fig. 18.2** Fitting of the experimental transmittance spectra  $1 - T/T_0$ , where  $T_0$  is the substrate transmittance, by the analytical model (18.8) for shrunken (top row) and expanded (bottom row) structures with  $a/R = 3.15$  and  $a/R = 2.85$ , respectively. **a, d** Normal incidence. **b, e** Incidence angle  $\theta = 16^\circ$ . **c, f** The influence of the phase shift  $\varphi$  (18.9) on the asymmetry of the transmittance peaks in shrunken and expanded structures, respectively

subscript thus obtaining the result:

$$t = t_0 [1 - \varkappa \psi(p)/E_{\text{in}}] . \quad (18.7)$$

Plugging the solution of (18.5) into the (18.7), we finally derive

$$\tilde{R} \equiv 1 - \frac{|t|^2}{|t_0|^2} = 2\gamma_0 \varkappa^2 \frac{(\varepsilon + \mu(k))^2 + v^2 k^2 + \gamma_0^2}{[\mu^2(k) - \varepsilon^2 + v^2 k^2 + \gamma_0 (\gamma_0 + \varkappa^2/2)]^2 + [2\gamma_0 \varepsilon + \varkappa^2/2 (\mu(k) + \varepsilon)]^2} . \quad (18.8)$$

Equation (18.8) suggests in particular that the peaks in the  $1 - T/T_0$  spectrum are impossible without both radiative and non-radiative losses. Overall, there are six parameters in the effective Hamiltonian:  $\mu$ ,  $\gamma_r = \varkappa^2/2$ ,  $\gamma_0$ ,  $v$  and  $\beta$ . To determine these parameters we used the transmittance spectra measured in the wavelength range from 896 to 2142 nm for the set of the incidence angles from  $0^\circ$  to  $16^\circ$  with the step equal to  $2^\circ$ . Parameters  $\mu$ ,  $\gamma_r$  and  $\gamma_0$  were determined from the spectra

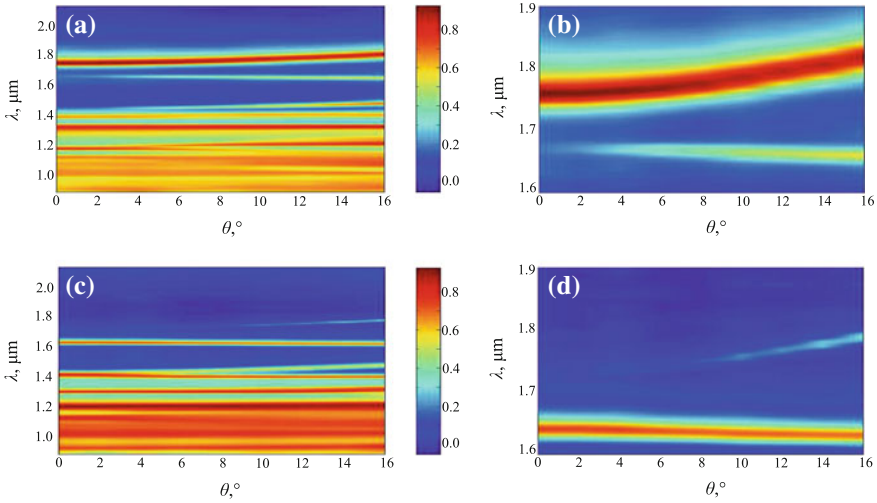


**Fig. 18.3** Measured transmittance spectra for the fabricated dielectric metasurface. Color encodes the magnitude of  $1 - T/T_0$  ( $T$  and  $T_0$  are metasurface and substrate transmittances, respectively) for  $p$ -polarized incident light. **(a, b)** Results for the shrunken structure with  $a/R = 3.15$ : **a** whole studied spectral range; **b** range  $1.6 < \lambda < 1.9 \mu\text{m}$ . **(c, d)** Results for the expanded structure with  $a/R = 2.85$ : **c** whole studied spectral range; **d** range  $1.6 < \lambda < 1.9 \mu\text{m}$

for normal incidence ( $k = 0$ ) since in such scenario these three parameters and the center-of-bandgap frequency  $f_0$  are the only essential parameters determining the transmittance spectrum (see (18.8)). The remaining two parameters,  $v$  and  $\beta$ , were determined from the reflectance spectra for oblique incidence. While analyzing the experimental data on transmittance, we aimed to achieve the best possible fit of the spectral positions, width and height of the characteristic peaks in  $1 - T/T_0$  spectrum (see Fig. 18.2). The results of fitting are presented both for shrunken and expanded structures in Fig. 18.2.

### 18.3 Fitting of Experimental Data with the Analytical Model

The deviations of experimental spectra from the analytical formulas occur due to the structure imperfections (defects, non-cylindrical form of pillars, etc.) as well as due to the approximate nature of the used theoretical model. Specifically, the developed analytical approach does not describe the asymmetry of the transmittance peaks observed in experiment. This asymmetry can be explained by the phase difference between the light reflected from sapphire substrate and from Si pillars which gives rise to Fano-type interference of the two reflected waves. The discussed phase difference can be incorporated into our analytical formula by means of the auxiliary parameter  $\varphi$ :

$$t = t_0 \left[ e^{i\varphi} - \varkappa \psi(p)/E_{\text{in}} \right]. \quad (18.9)$$

While the parameter  $\varphi$  defines the asymmetry of transmittance peaks, its incorporation into the model does not significantly change the numerical results for the remaining parameters. Therefore, in the following we used simplified formulas with smaller number of fitting parameters thus ensuring greater robustness of the developed numerical scheme (18.7)–(18.8).

With the developed technique, we analyzed the experimental data for both shrunken ( $a/R = 3.15$ ) and expanded ( $a/R = 2.85$ ) structures for the range of incidence angles from 0 to 16 degrees (Fig. 18.3). The retrieved values of the effective Hamiltonian parameters are provided in the Table 18.1.

Using (18.4), we calculated spin Chern number for both of the structures confirming the theoretical result that the shrunken structure is topologically trivial, whereas the expanded one is topological. The agreement between the analytical model (18.8) with the fitted parameters (Table 18.1) and the experimental data is further illustrated in Fig. 18.4.

## 18.4 Constructing the Effective Hamiltonian Using the Plane Wave Expansion Method

While discussing the theory of Fano-resonant topological metasurfaces in Sect. 18.2 we assumed a Dirac-type Hamiltonian. Now we support this conclusion by the rigorous derivation based on plane-wave expansion method [24, 35]. To apply this method, we assume that the structure consists of dielectric cylinders with the permittivity that differs only slightly from the permittivity of the background medium. We consider a TM polarization of the wave with the wave vector perpendicular to the axis of cylinder,  $Oz$ . Permittivity of all cylinders along their axes is  $\varepsilon_{zz} \equiv \varepsilon_r$ . The equation for  $E_z$  component of electric field has a form

$$\left[ q^2 \varepsilon(x, y) + \partial_x^2 + \partial_y^2 \right] E_z(x, y) = 0, \quad (18.10)$$

where  $q = \omega/c$ ,  $\varepsilon(x, y) = \varepsilon_r$  inside cylinder and  $\varepsilon(x, y) = 1$  outside of the cylinder. Further we expand the field  $E_z(x, y)$  and the permittivity  $\varepsilon(x, y)$  in Fourier series as follows:

**Table 18.1** Extracted parameters of the effective Hamiltonian for shrunken and expanded metasurfaces

Structure	$\mu$ , THz	$\beta$ , m <sup>2</sup> /s	$v$ , 10 <sup>6</sup> m/s	$\gamma_r$ , THz	$\gamma_0$ , THz	$C$ (Spin Chern number)
Shrunken, $a/R = 3.15$	-5.22	-1.00	4.76	1.83	1.03	0
Expanded, $a/R = 2.85$	5.22	-1.96	7.31	0.437	1.06	1

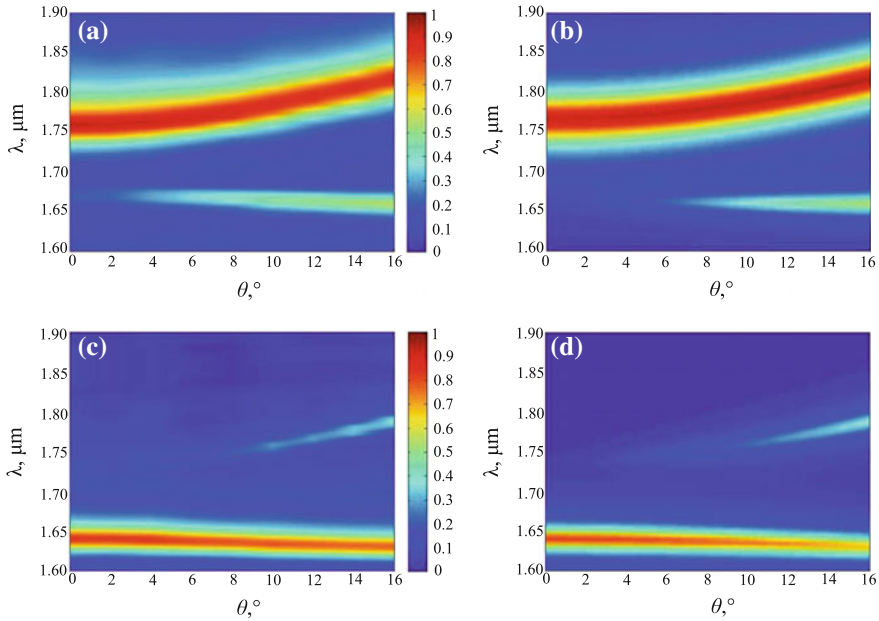


**Fig. 18.4** Comparison of experimental (a, c) versus theoretical (b, d) transmittance spectra. Color encodes the magnitude  $1 - T/T_0$ , where  $T_0$  is the transmittance of the sapphire substrate, whereas  $T$  is the transmittance of the entire structure. Theoretical spectra are computed for the parameter values determined by the experimental data fitting. **a, b** Transmittance spectra for shrunken structure with  $a/R = 3.15$  taken from Table 18.1. **c, d** Transmittance spectra for expanded structure with  $a/R = 2.85$

$$E_z(\mathbf{r}) = \sum_{\mathbf{G}} E_{\mathbf{G}} e^{i(\mathbf{G}+\mathbf{k})\cdot\mathbf{r}}, \quad (18.11)$$

$$\varepsilon(\mathbf{r}) = \sum_{\mathbf{G}} \varepsilon_{\mathbf{G}} e^{i\mathbf{G}\cdot\mathbf{r}}, \quad (18.12)$$

where  $\mathbf{G}$  and  $\mathbf{G}'$  denote reciprocal lattice vectors. Combining (18.11), (18.12) with (18.10), we obtain:

$$q^2 \sum_{\mathbf{G}'} \varepsilon_{\mathbf{G}-\mathbf{G}'} E_{\mathbf{G}'} - [(G_x + k_x)^2 + (G_y + k_y)^2] E_{\mathbf{G}} = 0. \quad (18.13)$$

Now we consider the system of equations in the vicinity of  $\Gamma$  point of the crystal first Brillouin zone (see Fig. 18.5b). We truncate the system leaving only the contributions from  $\Gamma_0$  and six neighboring  $\Gamma$  points denoted by the indices 1–6 in Fig. 18.5b. The length of all reciprocal lattice vectors  $\mathbf{G}_i$  is equal to  $G = 4\pi/(\sqrt{3}a)$ , where  $a = 2R + R'$  is the lattice period,  $R$  is the edge length for a hexagonal cluster, and

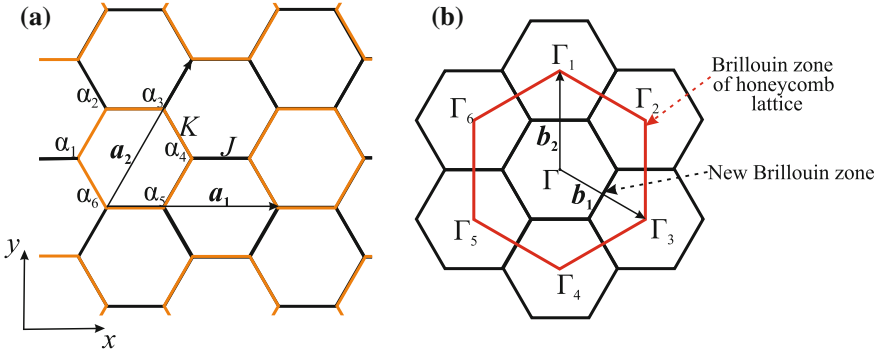


**Fig. 18.5** **a** A schematic representation of triangular lattice formed by hexamer clusters with inter- and intracell tunneling amplitudes equal to  $J$  and  $K$ , respectively.  $\alpha_i, i = 1 \dots 6$  represent Wannier functions. **b** First Brillouin zone of the lattice

$R'$  is the distance between the centers of the nearest rods from the different clusters. The radius of the rod is denoted by  $r$ .

First we calculate the Fourier coefficients  $\varepsilon_{\mathbf{G}-\mathbf{G}'}$  comprising the system (18.13). By definition,

$$\varepsilon_{\mathbf{G}} = \frac{1}{S_0} \int_{S_0} \varepsilon(x, y) e^{-i\mathbf{G}\cdot\mathbf{r}} d^2\mathbf{r}, \quad (18.14)$$

where  $S_0 = a^2 \sqrt{3}/2$  is the area of the structure unit cell. For instance,  $\varepsilon_{\mathbf{G}_0} \equiv \varepsilon_0$  is defined by

$$\varepsilon_0 = 1 + \frac{6\pi(\varepsilon_r - 1)r^2}{S_0}. \quad (18.15)$$

Other coefficients comprising the truncated system (18.13) are as follows:

- $\varepsilon_1 = \varepsilon_{\mathbf{G}_1} = \varepsilon_{\mathbf{G}_2} = \dots = \varepsilon_{\mathbf{G}_6}$ . The expression for  $\varepsilon_1$  reads:

$$\varepsilon_1 = -\frac{4\pi^2 r^2 (\varepsilon_r - 1)}{\sqrt{3} S_0} \frac{2 J_1(Gr)}{Gr} \frac{R - R'}{a} \approx -\frac{4\pi^2 r^2 (\varepsilon_r - 1)}{\sqrt{3} S_0} \frac{R - R'}{a} \equiv -u, \quad (18.16)$$

where  $J_1$  is the Bessel function of the first kind and an assumption  $Gr \ll 1$  is used. If  $\varepsilon_r$  is real, the quantity  $\varepsilon_1$  is also purely real.

- $\varepsilon_3 = \varepsilon_{\mathbf{G}_3-\mathbf{G}_6} = \varepsilon_{\mathbf{G}_2-\mathbf{G}_5} = \varepsilon_{\mathbf{G}_1-\mathbf{G}_4}$ . Under the assumption  $Gr \ll 1$   $\varepsilon_3$  is given by the formula

$$\varepsilon_3 = 2u. \quad (18.17)$$

where  $u$  is defined from (18.16). Quite importantly, the coefficient  $u$  vanishes in the case of a simple honeycomb lattice thus being analogous to the parameter  $J - K$  in tight binding model.

- $\varepsilon_2 = \varepsilon_{G_3-G_1} = \varepsilon_{G_5-G_3} = \varepsilon_{G_1-G_5} = \varepsilon_{G_4-G_2} = \varepsilon_{G_6-G_4} = \varepsilon_{G_2-G_6}$ . This coefficient is also purely real:

$$\varepsilon_2 = -\frac{3\pi r^2 (\varepsilon_r - 1)}{S_0} \frac{2 J_1(Gr\sqrt{3})}{Gr\sqrt{3}} \approx -\frac{3\pi r^2 (\varepsilon_r - 1)}{S_0}, \tag{18.18}$$

The truncated system of equations (18.13) yields the set of the self-consistent equations with respect to the amplitudes  $E_i \equiv E_{G_i}$ :

$$\begin{aligned} & \left[ \varepsilon_0 - q^{-2} k^2 \right] E_0 + \varepsilon_1 E_1 + \varepsilon_1 E_2 + \varepsilon_1 E_3 + \varepsilon_1 E_4 \\ & \quad + \varepsilon_1 E_5 + \varepsilon_1 E_6 = 0, \end{aligned} \tag{18.19}$$

$$\begin{aligned} \varepsilon_1 E_0 + & \left[ \varepsilon_0 - q^{-2} \left( G^2 + 2Gk_y + k^2 \right) \right] E_1 + \varepsilon_1 E_2 + \varepsilon_2 E_3 + \varepsilon_3 E_4 \\ & \quad + \varepsilon_2 E_5 + \varepsilon_1 E_6 = 0, \end{aligned} \tag{18.20}$$

$$\begin{aligned} \varepsilon_1 E_0 + \varepsilon_1 E_1 + & \left[ \varepsilon_0 - q^{-2} \left( G^2 + G\sqrt{3}k_x + Gk_y + k^2 \right) \right] E_2 + \varepsilon_1 E_3 + \varepsilon_2 E_4 \\ & \quad + \varepsilon_3 E_5 + \varepsilon_2 E_6 = 0, \end{aligned} \tag{18.21}$$

$$\begin{aligned} \varepsilon_1 E_0 + \varepsilon_2 E_1 + \varepsilon_1 E_2 + & \left[ \varepsilon_0 - q^{-2} \left( G^2 + G\sqrt{3}k_x - Gk_y + k^2 \right) \right] E_3 + \varepsilon_1 E_4 \\ & \quad + \varepsilon_2 E_5 + \varepsilon_3 E_6 = 0, \end{aligned} \tag{18.22}$$

$$\begin{aligned} \varepsilon_1 E_0 + \varepsilon_3 E_1 + \varepsilon_2 E_2 + \varepsilon_1 E_3 + & \left[ \varepsilon_0 - q^{-2} \left( G^2 - 2Gk_y + k^2 \right) \right] E_4 \\ & \quad + \varepsilon_1 E_5 + \varepsilon_2 E_6 = 0, \end{aligned} \tag{18.23}$$

$$\begin{aligned} & \varepsilon_1 E_0 + \varepsilon_2 E_1 + \varepsilon_3 E_2 + \varepsilon_2 E_3 + \varepsilon_1 E_4 \\ & + \left[ \varepsilon_0 - q^{-2} \left( G^2 - G\sqrt{3}k_x - Gk_y + k^2 \right) \right] E_5 + \varepsilon_1 E_6 = 0 \end{aligned} \tag{18.24}$$

$$\begin{aligned} & \varepsilon_1 E_0 + \varepsilon_1 E_1 + \varepsilon_2 E_2 + \varepsilon_3 E_3 + \varepsilon_2 E_4 \\ & + \varepsilon_1 E_5 + \left[ \varepsilon_0 - q^{-2} \left( G^2 - G\sqrt{3}k_x + Gk_y + k^2 \right) \right] E_6 = 0, \end{aligned} \tag{18.25}$$

where  $k^2 = k_x^2 + k_y^2$ . The matrix of this system is Hermitian. To simplify the analysis, we perform a unitary transformation of the system matrix as follows:

$$U = \frac{1}{\sqrt{3}} \begin{pmatrix} \sqrt{3} & 0 & 0 & 0 & 0 & 0 & 0 \\ 0 & 0 & 1 & 0 & 1 & 0 & 1 \\ 0 & 1 & 0 & 1 & 0 & 1 & 0 \\ 0 & 0 & 1 & 0 & \eta^2 & 0 & \eta \\ 0 & 0 & 1 & 0 & \eta & 0 & \eta^2 \\ 0 & 1 & 0 & \eta^2 & 0 & \eta & 0 \\ 0 & 1 & 0 & \eta & 0 & \eta^2 & 0 \end{pmatrix}, \tag{18.26}$$

where  $\eta = e^{2\pi i/3}$ . After the transformation (18.26) the matrix of the system consists of  $3 \times 3$  and  $4 \times 4$  blocks, the coupling between these blocks is proportional to  $k$ . However, the blocks are not diagonal even for  $k = 0$ .

As a first step, we diagonalize the matrix of the system for  $k = 0$  and small  $u$  (from now on terms proportional to  $u^2, u^3$ , etc. are neglected). The necessary transformation is given by the matrix  $W = W_1 \oplus W_2$ , where matrix  $W_1$

$$W_1 = \begin{pmatrix} 1 & -\sqrt{3}u/(q^{-2}G^2 - 2\varepsilon_2) & -\sqrt{3}u/(q^{-2}G^2 - 2\varepsilon_2) \\ 0 & -1/\sqrt{2} & 1/\sqrt{2} \\ \sqrt{6}u/(q^{-2}G^2 - 2\varepsilon_2) & 1/\sqrt{2} & 1/\sqrt{2} \end{pmatrix} \quad (18.27)$$

diagonalizes the  $3 \times 3$  block of the Hamiltonian for  $k = 0$  with the precision up to the terms linear in  $u$ , and the matrix  $W_2$

$$W_2 = \frac{1}{\sqrt{2}} \begin{pmatrix} 0 & i & 0 & e^{i\pi/6} \\ e^{5i\pi/6} & 0 & e^{i\pi/6} & 0 \\ e^{5i\pi/6} & 0 & e^{-5i\pi/6} & 0 \\ 0 & -i & 0 & e^{i\pi/6} \end{pmatrix}. \quad (18.28)$$

diagonalizes the  $4 \times 4$  block of the Hamiltonian for  $k = 0$ .

Next we would like to exclude the  $3 \times 3$  block of singlet states. To this end we treat coupling between the two blocks of the matrix using degenerate perturbation theory in the special form [44]. To ease the comparison with Sect. 18.2, we also make a redefinition  $k_x \rightarrow k_y$  and  $k_y \rightarrow k_x$ . As a result, we obtain the following eigenvalue problem:

$$\hat{H}_{\text{eff}} |\psi\rangle = \lambda |\psi\rangle. \quad (18.29)$$

Here, the effective  $4 \times 4$  Hamiltonian is given by the expression

$$\hat{H}_{\text{eff}} = \begin{pmatrix} \mu + \beta k^2 & k_x - ik_y & \alpha (k_x + ik_y)^2 & 0 \\ k_x + ik_y & -\mu - \beta k^2 & 0 & -\alpha (k_x - ik_y)^2 \\ \alpha (k_x - ik_y)^2 & 0 & \mu + \beta k^2 & -k_x - ik_y \\ 0 & -\alpha (k_x + ik_y)^2 & -k_x + ik_y & -\mu - \beta k^2 \end{pmatrix} \quad (18.30)$$

with  $\mu = 3uq^2/G$ ,  $\beta = -Gu/(3\varepsilon_2^2 q^2)$ ,  $\alpha = -G/(3\varepsilon_2 q^2)$ , and  $\lambda = -G + q^2(\varepsilon_0 - \varepsilon_2)/G - k^2/G - Gk^2/(3q^2\varepsilon_2)$ . The components of bispinor  $|\psi\rangle$  comprising (18.29) are defined in terms of the field Fourier components:

$$\psi_1 = \frac{1}{\sqrt{6}} \left[ e^{i\pi/6} E_{\mathbf{G}1} + e^{i\pi/2} E_{\mathbf{G}2} + e^{5i\pi/6} E_{\mathbf{G}3} + e^{-5i\pi/6} E_{\mathbf{G}4} + e^{-i\pi/2} E_{\mathbf{G}5} + e^{-i\pi/6} E_{\mathbf{G}6} \right], \quad (18.31)$$

$$\psi_2 = \frac{1}{\sqrt{6}} \left[ e^{i\pi/6} E_{\mathbf{G}1} + e^{5i\pi/6} E_{\mathbf{G}2} + e^{-i\pi/2} E_{\mathbf{G}3} + e^{i\pi/6} E_{\mathbf{G}4} + e^{5i\pi/6} E_{\mathbf{G}5} + e^{-i\pi/2} E_{\mathbf{G}6} \right], \quad (18.32)$$

$$\psi_3 = \frac{1}{\sqrt{6}} \left[ e^{-5i\pi/6} E_{\mathbf{G}1} + e^{5i\pi/6} E_{\mathbf{G}2} + e^{i\pi/2} E_{\mathbf{G}3} + e^{i\pi/6} E_{\mathbf{G}4} + e^{-i\pi/6} E_{\mathbf{G}5} + e^{-i\pi/2} E_{\mathbf{G}6} \right], \quad (18.33)$$

$$\psi_4 = \frac{1}{\sqrt{6}} \left[ e^{i\pi/6} E_{\mathbf{G}1} + e^{-i\pi/2} E_{\mathbf{G}2} + e^{5i\pi/6} E_{\mathbf{G}3} + e^{i\pi/6} E_{\mathbf{G}4} + e^{-i\pi/2} E_{\mathbf{G}5} + e^{i\pi/6} E_{\mathbf{G}6} \right]. \quad (18.34)$$



Note that the derived form of the effective Hamiltonian (18.30) is consistent with (18.1) used in the analysis of experimental spectra.

## 18.5 Perturbative Electromagnetic Theory of Radiative Losses

To support our phenomenological CMT model and elaborate more on the underlying physics, we additionally apply the method of guided mode expansion (GME) to describe the photonic bands of the non-Hermitian PhC slab. In particular, this treatment allows us to get an approximate analytical expression for the radiative coupling, which was not captured by the plane wave expansion method. After the folding due to the permittivity modulation, the localized guided modes of the unperturbed dielectric waveguide fall above the cladding light line, leading to a radiative decay and complex eigenfrequencies. To tackle this leaky behavior, we utilize the approach recently developed in [45–47].

We write the equation for the magnetic field  $\mathbf{H}$ :

$$\nabla \times \left[ \frac{1}{\varepsilon(\mathbf{r})} \nabla \times \mathbf{H}(\mathbf{r}) \right] = q^2 \mathbf{H}(\mathbf{r}), \quad (18.35)$$

where  $q = \omega/c$ , and focus on the TM-like polarization characterized by the components  $(H_x, H_y, E_z)$ . To develop a perturbation theory, we adopt the expansion in the basis of Bloch waves. The high-order waves and radiative waves are assumed to be excited by the basic waves. As follows from Maxwell's equations, in our geometry coupling of the waves is governed by the two physical mechanisms: (i) in-plane permittivity modulation; (ii) the surface coupling stemming from the permittivity discontinuity at the slab interfaces. The latter effect can be incorporated in equations as boundary conditions using the formalism of Dirac  $\delta$ -functions.

We employ the basis of Bloch waves  $\mathbf{V}$  associated with the reciprocal vectors  $\mathbf{G}_j$ ,  $j = 1 \div 6$ . In this way, at the  $\Gamma$  point, the components  $H_{x,y}$  can be expanded as

$$H_x = \sum_{j=1}^6 \frac{G_{jy}}{G} V_j \Theta_0(z) e^{-i\mathbf{G}_j \cdot \mathbf{r}_\perp} \quad (18.36)$$

$$H_y = \sum_{j=1}^6 -\frac{G_{jx}}{G} V_j \Theta_0(z) e^{-i\mathbf{G}_j \cdot \mathbf{r}_\perp}, \quad (18.37)$$

where  $\mathbf{r}_\perp = (x, y)$ ,  $\Theta_0(z)$  is the unperturbed transverse profile of the mode supported by the effective dielectric waveguide,  $\int \Theta_0^*(z) \Theta_0(z) dz = 1$ . At the  $\Gamma$  point, the basic waves have the same transverse profile  $\Theta_0(z)$  and wavenumber  $\beta_0$ . The dispersion relation for TM guided modes is given in the following implicit form

$$\tan\left(\sqrt{\varepsilon_{\text{avg}}q^2 - \beta^2}h\right) = \frac{2\varepsilon_{\text{avg}}\varepsilon_{\text{cl}}\sqrt{(\varepsilon_{\text{avg}}q^2 - \beta^2)(\varepsilon_{\text{cl}}q^2 - \beta^2)}}{\varepsilon_{\text{cl}}^2(\varepsilon_{\text{avg}}q^2 - \beta^2) - \varepsilon_{\text{avg}}^2(\varepsilon_{\text{cl}}q^2 - \beta^2)}, \quad (18.38)$$

where  $\varepsilon_{\text{avg}}$  is the average dielectric permittivity of the slab, and  $\varepsilon_{\text{cl}}$  are the permittivities of the claddings. We assume the permittivities of the upper and lower cladding equal. Here, for simplicity, we neglect TE-TM coupling and coupling to higher-order modes. Thereby, we disregard the  $H_z$  component (responsible for coupling to TE modes) that means the trivial transversality condition of the form  $G_{jx}H_{jx} + G_{jy}H_{jy} = 0$ . We also expand the inverse permittivity in Fourier series  $1/\varepsilon(\mathbf{r}) = \kappa_0(z) + \sum_{\mathbf{G}_j} \kappa_{\mathbf{G}_j} e^{-i\mathbf{G}_j \cdot \mathbf{r}_\perp}$ .

Using these expansions, equations for the field components can be recast to the eigenvalue problem for the modes amplitudes

$$(q^2 - \beta_0^2)\mathbf{V} = \hat{\mathbf{C}}\mathbf{V} \quad (18.39)$$

where  $\mathbf{V} = [V_1, V_2, V_3, V_4, V_5, V_6]^T$ . The coupling matrix  $\hat{\mathbf{C}}$  consists of two parts

$$\hat{\mathbf{C}} = \hat{\mathbf{C}}_1 + \hat{\mathbf{C}}_{\text{rad}}, \quad (18.40)$$

where  $\hat{\mathbf{C}}_1$  and  $\hat{\mathbf{C}}_{\text{rad}}$  correspond to the direct couplings between basic modes and the coupling with the radiative mode ( $H_{0x}$ ,  $H_{0y}$ ), respectively. The matrix elements depend on the parameters of the structure.

Due to the  $\hat{\mathbf{C}}_{6v}$  symmetry of the PC slab, the matrix  $\mathbf{C}$  exhibits the following form

$$\hat{\mathbf{C}}_1 = \begin{pmatrix} 0 & \kappa_1(G^2 + I/2) & \kappa_2(G^2 - I/2) & \kappa_3(G^2 - I) & \kappa_2(G^2 - I/2) & \kappa_1(G^2 + I/2) \\ \kappa_1(G^2 + I/2) & 0 & \kappa_1(G^2 + I/2) & \kappa_2(G^2 - I/2) & \kappa_3(G^2 - I) & \kappa_2(G^2 - I/2) \\ \kappa_2(G^2 - I/2) & \kappa_1(G^2 + I/2) & 0 & \kappa_1(G^2 + I/2) & \kappa_2(G^2 - I/2) & \kappa_3(G^2 - I) \\ \kappa_3(G^2 - I) & \kappa_2(G^2 - I/2) & \kappa_1(G^2 + I/2) & 0 & \kappa_1(G^2 + I/2) & \kappa_2(G^2 - I/2) \\ \kappa_2(G^2 - I/2) & \kappa_3(G^2 - I) & \kappa_2(G^2 - I/2) & \kappa_1(G^2 + I/2) & 0 & \kappa_1(G^2 + I/2) \\ \kappa_1(G^2 + I/2) & \kappa_2(G^2 - I/2) & \kappa_3(G^2 - I) & \kappa_2(G^2 - I/2) & \kappa_1(G^2 + I/2) & 0 \end{pmatrix},$$

where  $\kappa_{1,2,3} = \kappa_{\mathbf{G}_1, \mathbf{G}_1 - \mathbf{G}_3, \mathbf{G}_1 - \mathbf{G}_4}$ ,

$$I = \int_{PC} \left( -\frac{\partial^2}{\partial z^2} + [\delta(z - h/2) - \delta(z + h/2)] \frac{\partial}{\partial z} \right) \Theta_0(z) \Theta_0^*(z) dz. \quad (18.41)$$

Coupling to free-space modes causes the out-of-plane diffraction losses. The profile of the radiative mode ( $H_{0x}$ ,  $H_{0y}$ ) generated by basic waves can be found using the Green's function method [46, 47]:

$$\begin{aligned} H_{0x} &= \kappa_1 \left( V_1 + \frac{1}{2}V_2 - \frac{1}{2}V_3 - V_4 - \frac{1}{2}V_5 + \frac{1}{2}V_6 \right) \tilde{I}_0, \\ H_{0y} &= \kappa_1 \left( -\frac{\sqrt{3}}{2}V_2 - \frac{\sqrt{3}}{2}V_3 + \frac{\sqrt{3}}{2}V_5 + \frac{\sqrt{3}}{2}V_6 \right) \tilde{I}_0, \end{aligned}$$

where  $\tilde{I}_0$  stands for the integral

$$\tilde{I}_0 = \int_{PC} \left( \frac{\partial^2}{\partial z'^2} - [\delta(z' - h/2) - \delta(z' + h/2)] \frac{\partial}{\partial z'} \right) G_0(z, z') \Theta_0(z') dz',$$

and Green's function is the solution of equation

$$(q^2 + \kappa_0 \partial^2 / \partial z^2 + [(\varepsilon_{cl}^{-1} - \kappa_0) \{\delta(z - h/2) - \delta(z + h/2)\}] \partial / \partial z) G_0(z, z') = -\delta(z, z').$$

The coupling of the guided modes with this radiative mode is then calculated by overlap integrals

$$\hat{C}_{\text{rad}} = I_0 \begin{pmatrix} 1 & 1/2 & -1/2 & -1 & -1/2 & 1/2 \\ 1/2 & 1 & 1/2 & -1/2 & -1 & -1/2 \\ -1/2 & 1/2 & 1 & 1/2 & -1/2 & -1 \\ -1 & -1/2 & 1/2 & 1 & 1/2 & -1/2 \\ -1/2 & -1 & -1/2 & 1/2 & 1 & 1/2 \\ 1/2 & -1/2 & -1 & -1/2 & 1/2 & 1 \end{pmatrix},$$

where

$$I_0 = \kappa_1^2 \iint_{PC} \{ [-\partial^2 / \partial z^2 + [\delta(z - h/2) - \delta(z + h/2)] \partial / \partial z] \cdot G_0(z, z') \\ [(\partial^2 / \partial z'^2 - [\delta(z' - h/2) - \delta(z' + h/2)] \partial / \partial z') \Theta_0(z')] \} \Theta_0^*(z) dz' dz \quad (18.42)$$

is a purely imaginary quantity.

To block-diagonalize  $\hat{C}$ , we next perform the unitary transformation  $\hat{C}_{\text{cp}} = U \hat{C} U^{-1}$  with the matrix

$$U = \frac{1}{\sqrt{6}} \begin{pmatrix} 1 & 1 & 1 & 1 & 1 & 1 \\ 1 & e^{i\pi/3} & e^{2i\pi/3} & -1 & e^{-2i\pi/3} & e^{-i\pi/3} \\ 1 & e^{2i\pi/3} & e^{-2i\pi/3} & 1 & e^{2i\pi/3} & e^{-2i\pi/3} \\ 1 & e^{-i\pi/3} & e^{-2i\pi/3} & -1 & e^{2i\pi/3} & e^{i\pi/3} \\ 1 & e^{-2i\pi/3} & e^{2i\pi/3} & 1 & e^{-2i\pi/3} & e^{2i\pi/3} \\ 1 & -1 & 1 & -1 & 1 & -1 \end{pmatrix}.$$

After excluding the first and the sixth rows describing singlet states, we get the matrix in the subspace of the circular-polarized states.

It can be proved using (18.38) that in the vicinity of the  $\Gamma$  point, the propagation constants of the modes are linearly dependent on small deviations  $(k_x, k_y)$  [47]

$$\beta_j = \beta_0 + \tilde{\beta} \left( \frac{G_{jx}}{G} k_x + \frac{G_{jy}}{G} k_y \right), \quad (18.43)$$

that is the right-hand side of (18.39) is additionally corrected with the diagonal matrix  $\Delta \hat{K}$

$$\Delta \hat{K} = 2\beta_0 \tilde{\beta} \begin{pmatrix} k_y & 0 & 0 & 0 & 0 & 0 \\ 0 & \sqrt{3}k_x/2 + k_y/2 & 0 & 0 & 0 & 0 \\ 0 & 0 & \sqrt{3}k_x/2 - k_y/2 & 0 & 0 & 0 \\ 0 & 0 & 0 & -k_y & 0 & 0 \\ 0 & 0 & 0 & 0 & -\sqrt{3}k_x/2 - k_y/2 & 0 \\ 0 & 0 & 0 & 0 & 0 & \sqrt{3}k_x/2 + k_y/2 \end{pmatrix}.$$

As a result, we finally obtain the right-hand side of the eigenvalue problem (18.39) describing a photonic bandstructure of the PhC slab in the proximity of  $\Gamma$  point as follows

$$\begin{aligned} \hat{C}_{\text{cp}} + \Delta \hat{K}_{\text{cp}} = & \begin{pmatrix} (\kappa_1 - \kappa_2 - \kappa_3)G^2 & -\beta_0 \tilde{\beta}(ik_x - k_y) & 0 & 0 \\ \beta_0 \tilde{\beta}(ik_x + k_y) & (\kappa_3 - \kappa_2 - \kappa_1)G^2 & 0 & 0 \\ 0 & 0 & (\kappa_1 - \kappa_2 - \kappa_3)G^2 & \beta_0 \tilde{\beta}(ik_x + k_y) \\ 0 & 0 & -\beta_0 \tilde{\beta}(ik_x - k_y) & (\kappa_3 - \kappa_2 - \kappa_1)G^2 \end{pmatrix} \\ + I & \begin{pmatrix} \frac{\kappa_1 + \kappa_2}{2} + \kappa_3 & 0 & 0 & 0 \\ 0 & \frac{\kappa_2 - \kappa_1}{2} - \kappa_3 & 0 & 0 \\ 0 & 0 & \frac{\kappa_1 + \kappa_2}{2} + \kappa_3 & 0 \\ 0 & 0 & 0 & \frac{\kappa_2 - \kappa_1}{2} - \kappa_3 \end{pmatrix} + I_0 \begin{pmatrix} 3 & 0 & 0 & 0 \\ 0 & 0 & 0 & 0 \\ 0 & 0 & 3 & 0 \\ 0 & 0 & 0 & 0 \end{pmatrix}, \end{aligned} \quad (18.44)$$

where similarly to Sections I and II we redefine  $k_x \rightarrow k_y, k_y \rightarrow k_x$ . In the absence of dissipation, the first and second matrices in (18.44) compose the Hermitian Hamiltonian which contains the Dirac part and real mass-terms. The imaginary part of  $p$  (dipolar) modes eigenfrequencies is determined by  $I_0$  which is directly related to the magnitude of radiative losses  $\gamma_r$ . Thus, the GME method fully confirms applicability of our phenomenological model.

## 18.6 Numerical Calculation of Transmissivity Using Tight-Binding-Based Coupled Mode Theory

One of the most remarkable manifestations of the topological order is the emergence of topologically protected interface states at the boundary of media with different topological invariants. For that reason, we consider here an array of domain walls between shrunken and expanded domains. To prove the existence of interface states on sample consisting of an array of domain walls formed by repetitive stitching of  $N$  unit cells of shrunken and expanded domains, we use the coupled mode theory

described in Sect. 18.2 which contains Hamiltonian constructed by tight binding (TB) method. Intercell and intracell tunneling amplitudes are denoted as  $J$  and  $K$ . The translation vectors of the lattice are equal to  $\mathbf{a}_1 = a (1, 0)$  and  $\mathbf{a}_2 = a (1/2, \sqrt{3}/2)$ , where  $a$  is the lattice period. Bloch vectors are defined as  $k_p = 2\pi/\lambda \sin(\theta)$ , where  $\lambda$  is the wavelength of the incident wave, and  $\theta$  is the angle between propagation direction and normal to the sample. We assume  $O_{xz}$  to be a propagation plane, and electric field is polarized along  $y$  direction. From the symmetry perspective, plane wave excites directly only dipolar modes, while quadrupolar modes are excited indirectly, through their coupling to dipolar modes, and two types of dipolar modes can be excited near zero incident angle  $\theta \approx 0$ , namely  $|u_1\rangle = (1, 1, 0, -1, -1, 0)^T$  and  $|u_2\rangle = (1, 0, 0, -1, 0, 0)^T$ . We consider specifically the case of former mode here, and the second type can be analyzed with a similar approach. omain walls are aligned along  $x$  direction, thus the equations describing such system are as follows (Fig. 18.6)

$$-i\varepsilon |\psi\rangle = -i\hat{H} |\psi\rangle + \varkappa \hat{S}_1 - \hat{L} |\psi\rangle \tag{18.45}$$

where  $\hat{H}$  is constructed from TBM and it reads as

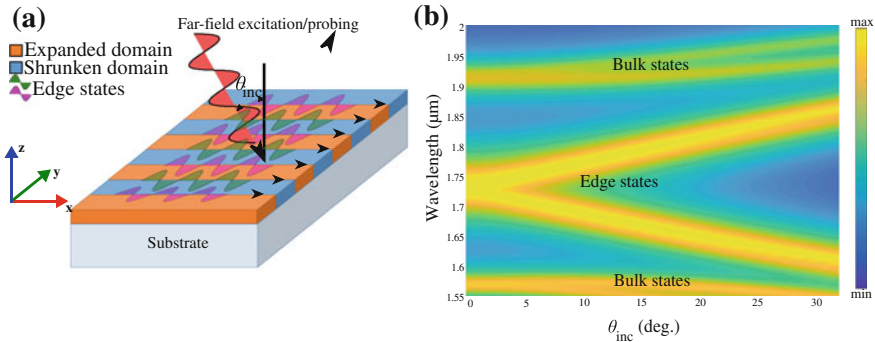


**Fig. 18.6** Far-field spectroscopy of topological edge states **a** Schematic optical setup for far-field mapping of photonic bands corresponding to edge states in a topological meta-grating. **b** The results of TB-CMT calculations of the scattering from topological meta-grating. The number of unit cells for both shrunken lattices and expanded lattices are 6, and other parameters used in TB-CMT model are: on-site energy  $\omega_0 = 173.61$  THz, intra-cell tunneling amplitude  $K = 33.00$  THz, inter-cell tunneling amplitude  $J = 23.00$  THz, radiative loss  $\gamma_r = 0.25$  THz, and non-radiative loss  $\gamma_0 = 0.30$  THz

$$\begin{aligned}\hat{H} = & \text{Diag}(N, N) \otimes \hat{H}_I \oplus \text{Diag}(N, N) \otimes \hat{H}_{II} \\ & + \text{Diag}(2N - 1, 2N) \otimes \hat{H}_m \\ & + \text{Diag}(2N, 2N - 1) \otimes \hat{H}_p\end{aligned}\quad (18.46)$$

with  $\hat{H}_{I/II}$ ,  $\hat{H}_{p/m}$  defined as

$$\hat{H}_I = \begin{pmatrix} 0 & -K & 0 & 0 & 0 & -K \\ -K & 0 & -K & 0 & -J e^{ik(a_2 - a_1)} & 0 \\ 0 & -K & 0 & -K & 0 & -J e^{ik a_2} \\ 0 & 0 & -K & 0 & -K & 0 \\ 0 & -J e^{ik(a_1 - a_2)} & 0 & -K & 0 & -K \\ -K & 0 & -J e^{-ik a_2} & 0 & -K & 0 \end{pmatrix}, \hat{H}_{II} = \hat{H}_I (K \leftrightarrow J), \quad (18.47)$$

$$\hat{H}_m = \begin{pmatrix} 0 & 0 & 0 & 0 & 0 & 0 \\ 0 & 0 & 0 & 0 & 0 & 0 \\ 0 & 0 & 0 & 0 & 0 & 0 \\ -J & 0 & 0 & 0 & 0 & 0 \\ 0 & 0 & 0 & 0 & 0 & 0 \\ 0 & 0 & 0 & 0 & 0 & 0 \end{pmatrix}, \hat{H}_p = \tilde{\hat{H}}_m. \quad (18.48)$$

and  $\hat{S}_1 = E_{\text{in}} |2N\rangle \otimes |u_1\rangle$ , where  $|2N\rangle = (1, 1, \dots, 1)^T$  which has  $2N$  sites.

$$\hat{L} = \text{Diag}(2N, 2N) \otimes \begin{pmatrix} \gamma_0 + \varkappa^2/2 & 0 & 0 & 0 & 0 & 0 \\ 0 & \gamma_0 + \varkappa^2/2 & 0 & 0 & 0 & 0 \\ 0 & 0 & \gamma_0 & 0 & 0 & 0 \\ 0 & 0 & 0 & \gamma_0 + \varkappa^2/2 & 0 & 0 \\ 0 & 0 & 0 & 0 & \gamma_0 + \varkappa^2/2 & 0 \\ 0 & 0 & 0 & 0 & 0 & \gamma_0 \end{pmatrix} \quad (18.49)$$

Periodic boundary conditions are applied at the outer domain walls in the  $y$  direction. In analogy to (18.7), we solve (18.5) and calculate the transmittance.

Compared to the bulk structures without domain wall, the extra periodicity of domain wall along  $y$  direction with lattice constant  $a_y = \sqrt{3}Na_0$  supplies extra diffraction channels for the scattered fields in the wavelength range under study. Due to the continuity of  $E_y$  at boundary  $y = na_y$ , the transmitted field can be written in the following form absorbing the continuity boundary condition [48]

$$E_y^t(\mathbf{r}) = \sum_{m=-\infty}^{\infty} \sum_{n=1}^{\infty} a_{n,m} e^{i(k_x^m x + k_z z)} \sin k_y^n y \quad (18.50)$$

where  $k_x^m = 2\pi/\lambda \sin(\theta) + m2\pi/a$ ,  $k_y^n = n\pi/a_y$ , and

$$k_z = \sqrt{(n_{\text{eff}} 2\pi/\lambda)^2 - k_x^{m2} - k_y^{n2}}, n_{\text{eff}}$$

is the effective index of the substrate. We notice these diffraction modes become leaky if  $k_z$  becomes real, thus both reflectivity and transmissivity drop due to the diffraction losses. To emulate the diffraction losses in tight-binding-based coupled mode approach, we introduce increased losses in all situations when  $k_z$  becomes real. In this way we recover the characteristic Wood's anomaly in the transmittance spectrum.

## 18.7 Conclusion

In conclusion, this chapter demonstrates the link between the well-celebrated concept of Fano resonances and the topological states supported by metasurfaces. Leaky nature of metasurface's modes allows one to probe them from the far field, while the observed Fano-type features in transmittance spectrum can be unequivocally associated with the topological properties of photonic bands.

**Acknowledgements** This work was supported by the Russian Science Foundation (Grant No. 16-19-10538).

## References

1. B.A. Bernevig, T.L. Hughes, S.C. Zhang, *Science* **314**(5806), 1757 (2006). <https://doi.org/10.1126/science.1133734>
2. M.Z. Hasan, C.L. Kane, *Rev. Mod. Phys.* **82**, 3045 (2010). <https://doi.org/10.1103/RevModPhys.82.3045>
3. D. Hsieh, D. Qian, L. Wray, Y. Xia, Y.S. Hor, R.J. Cava, M.Z. Hasan, *Nature* **452**, 970 (2008)
4. C.L. Kane, E.J. Mele, *Phys. Rev. Lett.* **95**, 146802 (2005)
5. C.L. Kane, E.J. Mele, *Phys. Rev. Lett.* **95**, 226801 (2005)
6. X.L. Qi, S.C. Zhang, *Rev. Mod. Phys.* **83**, 1057 (2011)
7. Y. Xia, D. Qian, D. Hsieh, L. Wray, A. Pal, H. Lin, A. Bansil, D. Grauer, Y.S. Hor, R.J. Cava, M.Z. Hasan, *Nat. Phys.* **5**, 398 (2009). <https://doi.org/10.1038/nphys1274>
8. J. Maciejko, T.L. Hughes, S.C. Zhang, *Annu. Rev. Condens. Matter Phys.* **2**, 31 (2011). <https://doi.org/10.1146/annurev-conmatphys-062910-140538>
9. D.N. Sheng, Z.Y. Weng, L. Sheng, F.D.M. Haldane, *Phys. Rev. Lett.* **97**, 036808 (2006)
10. H. Zhang, C.X. Liu, X.L. Qi, X. Dai, Z. Fang, S.C. Zhang, *Nat. Phys.* **5**, 438 (2009)
11. L. Fu, *Phys. Rev. Lett.* **106**, 106802 (2011)
12. P. Dziawa, B.J. Kowalski, K. Dybko, R. Buczko, A. Szczerbakow, M. Szot, E. Lusakowska, T. Balasubramanian, B.M. Wojek, M.H. Berntsen, O. Tjernberg, T. Story, *Nat. Mater.* **11**, 1023 (2012)
13. L. Lu, J.D. Joannopoulos, M. Soljačić, *Nat. Photonics* **8**, 821 (2014). <https://doi.org/10.1038/nphoton.2014.248>
14. F. Haldane, S. Raghu, *Phys. Rev. Lett.* **100**, 013904 (2008)
15. S. Raghu, F.D.M. Haldane, *Phys. Rev. A* **78**, 033834 (2008)
16. Z. Wang, Y. Chong, J. Joannopoulos, M. Soljačić, *Phys. Rev. Lett.* **100**, 013905 (2008)
17. Z. Wang, Y. Chong, J.D. Joannopoulos, M. Soljačić, *Nature* **461**, 772 (2009)
18. Y. Poo, R. Wu, Z. Lin, Y. Yang, C.T. Chan, *Phys. Rev. Lett.* **106**, 093903 (2011)
19. K. Fang, Z. Yu, S. Fan, *Phys. Rev. B* **84**, 075477 (2011)

20. K. Fang, Z. Yu, S. Fan, *Nat. Photonics* **6**, 782 (2012)
21. R.O. Umucalilar, I. Carusotto, *Phys. Rev. A* **84**, 043804 (2011)
22. M. Hafezi, E.A. Demler, M.D. Lukin, J.M. Taylor, *Nat. Phys.* **7**, 907 (2011)
23. M. Hafezi, S. Mittal, J. Fan, A. Migdall, J.M. Taylor, *Nat. Photonics* **7**(12), 1001 (2013). <https://doi.org/10.1038/nphoton.2013.274>
24. A.B. Khanikaev, S.H. Mousavi, W.K. Tse, M. Kargarian, A.H. McDonald, G. Shvets, *Nat. Mater.* **12**, 233 (2013)
25. M.C. Rechtsman, J.M. Zeuner, Y. Plotnik, Y. Lumer, D. Podolsky, F. Dreisow, S. Nolte, M. Segev, A. Szameit, *Nature* **496**, 196 (2013). <https://doi.org/10.1038/nature12066>
26. L. Lu, L. Fu, J.D. Joannopoulos, M. Soljačić, *Nat. Photonics* **7**, 294 (2013)
27. W.J. Chen, S.J. Liang, X.D. Chen, B. Zhu, L. Zhou, J.W. Dong, C.T. Chan, *Nat. Commun.* **5**, 6782 (2014)
28. S.D. Huber, *Nat. Phys.* **12**, 621 (2016)
29. V. Peano, C. Brendel, M. Schmidt, F. Marquardt, *Phys. Rev. X* **5**, 031011 (2015)
30. Z. Yang, F. Gao, X. Shi, X. Lin, Z. Gao, Y. Chong, B. Zhang, *Phys. Rev. Lett.* **114**, 114301 (2015). <https://doi.org/10.1103/PhysRevLett.114.114301>
31. U. Fano, *Phys. Rev.* **124**, 1866 (1961)
32. A.E. Miroshnichenko, S. Flach, Y.S. Kivshar, *Rev. Mod. Phys.* **82**, 2257 (2010)
33. B. Luk'yanchuk, N.I. Zheludev, S.A. Maier, N.J. Halas, P. Nordlander, H. Giessen, C.T. Chong, *Nat. Mater.* **9**, 707 (2010)
34. M.F. Limonov, M.V. Rybin, A.N. Poddubny, Y.S. Kivshar, Fano resonances in photonics, *Nat. Photonics* **11**, 543–554 (2017). <https://www.nature.com/articles/nphoton.2017.142>
35. A. Slobozhanyuk, S.H. Mousavi, X. Ni, D. Smirnova, Y.S. Kivshar, A.B. Khanikaev, *Nat. Photonics* **11**, 130 (2016). <https://doi.org/10.1038/nphoton.2016.253>
36. L.H. Wu, X. Hu, *Phys. Rev. Lett.* **114**, 23901 (2015). <https://doi.org/10.1103/PhysRevLett.114.23901>
37. S. Barik, H. Miyake, W. DeGottardi, E. Waks, M. Hafezi, *New J Phys.* **18**, 113013 (2016). <https://doi.org/10.1088/1367-2630/18/11/113013>
38. J.W. Dong, X.D. Chen, H. Zhu, Y. Wang, X. Zhang, *Nat. Mater.* **16**, 298 (2016). <https://doi.org/10.1038/nmat4807>
39. T. Ma, G. Shvets, *New J. Phys.* **18**, 025012 (2016). <https://doi.org/10.1088/1367-2630/18/2/025012>
40. J. Noh, W.A. Benalcazar, S. Huang, M.J. Collins, K. Chen, T.L. Hughes, M.C. Rechtsman, [arXiv: 1611.02373](https://arxiv.org/abs/1611.02373) [cond-mat.mes-hall] (2016)
41. S. Yves, R. Fleury, T. Berthelot, M. Fink, F. Lemoult, G. Lerosey, *Nat. Commun.* **8**, 16023 (2017). <https://doi.org/10.1038/ncomms16023>
42. Y. Yang, Y.F. Xu, T. Xu, H.X. Wang, J.H. Jiang, X. Hu, Z.H. Hang. [arXiv:1610.07780](https://arxiv.org/abs/1610.07780) (2016)
43. H.A. Haus, *Waves and Fields in Optoelectronics* (Prentice-Hall, Englewood Cliffs, New Jersey, 1984)
44. G.L. Bir, G.E. Pikus, *Symmetry and Strain-Induced Effects in Semiconductors* (Keter Publishing House, Jerusalem, 1974)
45. L.C. Andreani, D. Gerace, *Phys. Rev. B* **73**, 235114 (2006). <https://doi.org/10.1103/PhysRevB.73.235114>
46. Y. Yang, C. Peng, Y. Liang, Z. Li, S. Noda, *Opt. Lett.* **39**(15), 4498 (2014). <https://doi.org/10.1364/OL.39.004498>
47. X. Yin, Y. Liang, L. Ni, Z. Wang, C. Peng, Z. Li, *Phys. Rev. B* **96**, 075111 (2017). <https://doi.org/10.1103/PhysRevB.96.075111>
48. K. Sakoda, *Optical Properties of Photonic Crystals* (Springer, Berlin Heidelberg, 2005)



# Chapter 19

## Fano Resonances in Plasmonic Core-Shell Particles and the Purcell Effect



Tiago José Arruda, Alexandre Souto Martinez, Felipe A. Pinheiro, Romain Bachelard, Sebastian Slama and Philippe Wilhelm Courteille

**Abstract** Despite a long history, light scattering by particles with size comparable with the light wavelength still unveils surprising optical phenomena, and many of them are related to the Fano effect. Originally described in the context of atomic physics, the Fano resonance in light scattering arises from the interference between a narrow subradiant mode and a spectrally broad radiation line. Here, we present an overview of Fano resonances in coated spherical scatterers within the framework of the Lorenz-Mie theory. We briefly introduce the concept of conventional and unconventional Fano resonances in light scattering. These resonances are associated with the interference between electromagnetic modes excited in the particle with

---

T. J. Arruda (✉) · P. W. Courteille  
Instituto de Física de São Carlos (IFSC), Universidade de São Paulo (USP),  
São Paulo, São Carlos 13566-590, Brazil  
e-mail: tiagojarruda@gmail.com

P. W. Courteille  
e-mail: philippe.courteille@ifsc.usp.br

A. S. Martinez  
Faculdade de Filosofia, Ciências e Letras de Ribeirão Preto (FFCLRP),  
Universidade de São Paulo (USP), São Paulo, Ribeirão Preto 14040-901, Brazil  
e-mail: asmartinez@usp.br

F. A. Pinheiro  
Instituto de Física, Universidade Federal do Rio de Janeiro (UFRJ), Rio de Janeiro,  
Rio de Janeiro 21941-972, Brazil  
e-mail: fpinheiro@if.ufrj.br

R. Bachelard  
Departamento de Física, Universidade Federal de São Carlos (UFSCar), São Paulo,  
São Carlos 13565-905, Brazil  
e-mail: bachelard.romain@gmail.com

S. Slama  
Physikalisches Institut, Eberhardt-Karls-Universität Tübingen,  
72076 Tübingen, Germany  
e-mail: sebastian.slama@uni-tuebingen.de

different or the same multipole moment, respectively. In addition, we investigate the modification of the spontaneous-emission rate of an optical emitter at the presence of a plasmonic nanoshell. This modification of decay rate due to electromagnetic environment is referred to as the Purcell effect. We analytically show that the Purcell factor related to a dipole emitter oriented orthogonal or tangential to the spherical surface can exhibit Fano or Lorentzian line shapes in the near field, respectively.

## 19.1 Introduction

The Fano resonance, discovered in the realm of atomic physics by Fano in 1961 [1], is one of the hallmarks of interference in open quantum systems. This interference effect was originally conceived as an interference between a transition to a bound state, coupled weakly to a continuum, and a transition directly to the same continuum [1]. As a signature of quantum interference, the Fano effect has been extensively investigated in electronic transport at the nanoscale, in systems such as quantum dots, quantum wires, and tunnel junctions [2].

Being a wave interference phenomenon, Fano resonances are also present in classical optics and mechanics, where it can be understood as weak coupling between two classical oscillators driven by an external harmonic force [2, 3]. With the advent of metamaterials and plasmonic nanostructures, the Fano effect has recently become an important tool for tailoring and controlling electromagnetic mode interactions at subwavelength scale [4, 5]. In plasmonics, it generally arises from the interference between a localized surface plasmon resonance and a spectrally broad superradiant mode acting as a background radiation [2]. Due to the sharpness of the Fano asymmetric line shape, systems exhibiting the Fano effect are highly sensitive to the local dielectric environment. As a consequence, in plasmonic systems the Fano effect has been explored in the development of optical sensors, nonlinear devices, and low-threshold nanoscopic lasers [5].

Within the Lorenz-Mie scattering theory, the Fano effect results from the interference between electromagnetic modes excited in the scatterer with multipole moments of different orders (e.g., dipole-quadrupole interference) [5] or same orders (e.g., dipole-dipole interference), which is sometimes referred to as unconventional Fano resonance [6–8]. In contrast to the conventional Fano resonance [9], the unconventional Fano effect in light scattering does not depend on the scattering direction, and it can be realized, e.g., with layered [7, 8, 10–12] or high-index [6, 13–15] particles.

Here, we study the influence of an unconventional Fano resonance of a plasmonic nanoshell on a single optical emitter in its vicinity [16]. The presence of a nanostructure is known to enhance the spontaneous-emission rate of optical emitters, which is generally referred to as the Purcell effect [17–21]. Many theoretical and experimental approaches have been developed to maximize [22–24] or minimize [25, 26] the spontaneous-emission rate by changing the electromagnetic environment with engineered nanostructures. In this chapter, we are interested in describing the connection between the Fano resonance usually observed in the Purcell factor [27] and

the unconventional Fano resonance exhibited by plasmonic nanoshells in light scattering [7, 14, 16].

This chapter is organized as follows. We recall the main analytical expressions of the Lorenz-Mie theory for light scattering by coated spherical particles in Sect. 19.2. The concept of conventional and unconventional Fano resonances in plasmonic nanoshells are briefly introduced. In Sect. 19.3, we study the decay rates of single dipole emitters in the vicinity of plasmonic nanoshells. Analytical expressions connecting Fano resonances in light scattering and the Purcell factor of dipole emitters are derived. Finally, in Sect. 19.4, we summarize our main results and contents of this chapter.

## 19.2 Light Scattering by Core-Shell Spheres: Conventional and Unconventional Fano Resonances

Light scattering by small particles is a fundamental topic in classical electrodynamics that has been studied and treated by several researchers, with applications ranging from meteorology and astronomy to biology and medicine [28]. A complete analytic solution for homogeneous dielectric spheres with arbitrary radius was first derived, in an independent way, by Lorenz [29] and Mie [30] more than a century ago. This solution, which is widely known as the Lorenz-Mie theory, is based on the expansion of the electromagnetic fields in terms of spherical wave functions [28]. An interesting generalization of this theory is the case of a spherical scatterer composed of materials with different optical properties, with the core-shell geometry being the simplest one. Historically, the standard Lorenz-Mie theory, which deals with homogeneous spheres, was extended to single-layered spheres by Aden and Kerker [31] in 1951. With the advent of plasmonics and metamaterials, core-shell systems have been extensively applied for experimental and theoretical investigations, such as the plasmonic cloaking technique [32, 33], comb-like scattering response [10], tunable light scattering [34, 35], fluorescence enhancement of optical emitters [16], and Fano resonances [36]. Indeed, the presence of cavities or dielectric materials inside metal-based nanostructures strongly modifies the scattering response due to the so-called plasmon hybridization [37].

In this section, we briefly recall the main analytical expressions used in the Lorenz-Mie theory for single-layered spheres. Our aim is to introduce the concept of the Fano resonance in light scattering by plasmonic nanoshells, which will be further applied to the spontaneous-emission rate of single dipole emitters in Sect. 19.3. With this aim, we present the complete theoretical framework in Sect. 19.2.1. The discussion on plasmonic Fano resonances is treated in Sect. 19.2.2 for a coated nanosphere composed of a silicon (Si) core and a silver (Ag) nanoshell.

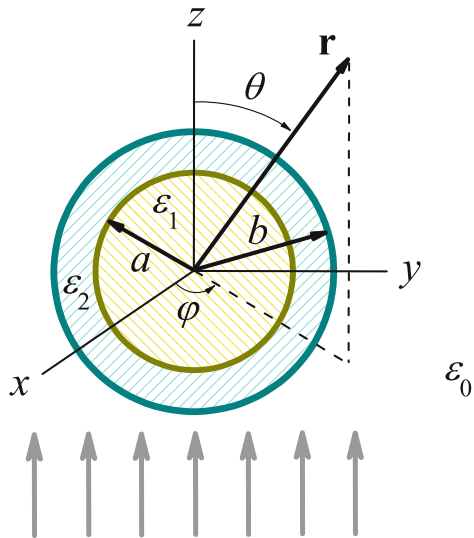
### 19.2.1 The Lorenz-Mie Theory for Single-Layered Spheres

Let us consider a coated sphere interacting with a plane wave  $[\mathbf{E}(\mathbf{r}), \mathbf{H}(\mathbf{r})]e^{-i\omega t}$ , where  $\omega$  is the angular frequency. The coated sphere is composed of a spherical core with radius  $a$  and a single, center-symmetric shell with radius  $b$ , as depicted in Fig. 19.1. The involved media are assumed to be linear, homogeneous and isotropic. In this case, the optical properties of media are described by a scalar electric permittivity  $\epsilon_p$  and a magnetic permeability  $\mu_p$ , with label  $p = 1$  for the core ( $0 \leq r \leq a$ ),  $p = 2$  for the shell ( $a \leq r \leq b$ ) and  $p = 0$  for the surrounding medium ( $r \geq b$ ), which is assumed to be the vacuum. At optical frequencies, naturally occurring media are usually non-magnetic:  $\mu_1 = \mu_2 = \mu_0$ .

The macroscopic Maxwell's equations associated with the system illustrated in Fig. 19.1 provide the vector Helmholtz equation  $(\nabla^2 + k^2)[\mathbf{E}(\mathbf{r}), \mathbf{H}(\mathbf{r})] = (\mathbf{0}, \mathbf{0})$ , where  $k = 2\pi/\lambda$  is the wave number and  $\lambda$  is the wavelength of the light in each medium  $p = \{0, 1, 2\}$ . The interested reader is referred to [28] for a complete and detailed solution of this vector equation. Since the sphere material is non-optically active [38], without loss of generality, we consider the polarization of the incident wave along the  $x$ -direction. In terms of spherical wave functions, the incident and scattered electric fields ( $r \geq b$ ) can be cast as

$$\begin{aligned} \mathbf{E}_{\text{in}}(r, \theta, \varphi) = & -\frac{1}{kr} \sum_{\ell=1}^{\infty} E_{\ell} \left\{ i \cos \varphi \sin \theta j_{\ell}(kr) \ell(\ell + 1) \pi_{\ell}(\cos \theta) \hat{\mathbf{e}}_r \right. \\ & - \cos \varphi \left[ \pi_{\ell}(\cos \theta) \psi_{\ell}(kr) - i \tau_{\ell}(\cos \theta) \psi'_{\ell}(kr) \right] \hat{\mathbf{e}}_{\theta} \\ & \left. - \sin \varphi \left[ i \pi_{\ell}(\cos \theta) \psi'_{\ell}(kr) - \tau_{\ell}(\cos \theta) \psi_{\ell}(kr) \right] \hat{\mathbf{e}}_{\varphi} \right\}, \end{aligned} \quad (19.1)$$

**Fig. 19.1** A non-magnetic core-shell sphere interacting with an electromagnetic plane wave. The inner sphere has radius  $a$  and electric permittivity  $\epsilon_1$ , whereas the outer sphere has radius  $b$  and electric permittivity  $\epsilon_2$ . The surrounding medium is the vacuum  $\epsilon_0$ . An electromagnetic plane wave propagating along the  $z$  axis impinges on the sphere from below



$$\begin{aligned} \mathbf{E}_{\text{sca}}(r, \theta, \varphi) = & \frac{1}{kr} \sum_{\ell=1}^{\infty} E_{\ell} \left\{ \iota \cos \varphi \sin \theta a_{\ell} h_{\ell}^{(1)}(kr) \ell(\ell+1) \pi_{\ell}(\cos \theta) \hat{\mathbf{e}}_r \right. \\ & - \cos \varphi \left[ b_{\ell} \pi_{\ell}(\cos \theta) \xi_{\ell}(kr) - \iota a_{\ell} \tau_{\ell}(\cos \theta) \xi'_{\ell}(kr) \right] \hat{\mathbf{e}}_{\theta} \\ & \left. - \sin \varphi \left[ \iota a_{\ell} \pi_{\ell}(\cos \theta) \xi'_{\ell}(kr) - b_{\ell} \tau_{\ell}(\cos \theta) \xi_{\ell}(kr) \right] \hat{\mathbf{e}}_{\varphi} \right\}, \quad (19.2) \end{aligned}$$

where  $k = \omega \sqrt{\varepsilon_0 \mu_0}$ ,  $E_{\ell} = \iota^{\ell} E_0 (2\ell + 1) / [\ell(\ell + 1)]$ ,  $\pi_{\ell}(\cos \theta) = P_{\ell}^1(\cos \theta) / \sin \theta$ ,  $\tau_{\ell}(\cos \theta) = dP_{\ell}^1(\cos \theta) / d\theta$ , with  $P_{\ell}^1$  being the associated Legendre function of first order. The coefficients  $a_{\ell}$  and  $b_{\ell}$  are the transverse magnetic (TM) and transverse electric (TE) Lorenz-Mie coefficients, respectively, and are determined from boundary conditions. For center-symmetric coated spheres, these coefficients read [28, 39]:

$$a_{\ell} = \frac{\tilde{n}_2 \psi'_{\ell}(kb) - \psi_{\ell}(kb) \mathcal{A}_{\ell}(n_2 kb)}{\tilde{n}_2 \xi'_{\ell}(kb) - \xi_{\ell}(kb) \mathcal{A}_{\ell}(n_2 kb)}, \quad (19.3)$$

$$b_{\ell} = \frac{\psi'_{\ell}(kb) - \tilde{n}_2 \psi_{\ell}(kb) \mathcal{B}_{\ell}(n_2 kb)}{\xi'_{\ell}(kb) - \tilde{n}_2 \xi_{\ell}(kb) \mathcal{B}_{\ell}(n_2 kb)}, \quad (19.4)$$

with the auxiliary functions

$$\mathcal{A}_{\ell}(n_2 kb) = \frac{\psi'_{\ell}(n_2 kb) - A_{\ell} \chi'_{\ell}(n_2 kb)}{\psi_{\ell}(n_2 kb) - A_{\ell} \chi_{\ell}(n_2 kb)}, \quad (19.5)$$

$$\mathcal{B}_{\ell}(n_2 kb) = \frac{\psi'_{\ell}(n_2 kb) - B_{\ell} \chi'_{\ell}(n_2 kb)}{\psi_{\ell}(n_2 kb) - B_{\ell} \chi_{\ell}(n_2 kb)}, \quad (19.6)$$

$$A_{\ell} = \frac{\tilde{n}_2 \psi_{\ell}(n_2 ka) \psi'_{\ell}(n_1 ka) - \tilde{n}_1 \psi'_{\ell}(n_2 ka) \psi_{\ell}(n_1 ka)}{\tilde{n}_2 \chi_{\ell}(n_2 ka) \psi'_{\ell}(n_1 ka) - \tilde{n}_1 \chi'_{\ell}(n_2 ka) \psi_{\ell}(n_1 ka)}, \quad (19.7)$$

$$B_{\ell} = \frac{\tilde{n}_2 \psi'_{\ell}(n_2 ka) \psi_{\ell}(n_1 ka) - \tilde{n}_1 \psi_{\ell}(n_2 ka) \psi'_{\ell}(n_1 ka)}{\tilde{n}_2 \chi'_{\ell}(n_2 ka) \psi_{\ell}(n_1 ka) - \tilde{n}_1 \chi_{\ell}(n_2 ka) \psi'_{\ell}(n_1 ka)}, \quad (19.8)$$

where the functions  $\psi_{\ell}(z) = z j_{\ell}(z)$ ,  $\chi_{\ell}(z) = -z y_{\ell}(z)$  and  $\xi_{\ell}(z) = \psi_{\ell}(z) - \iota \chi_{\ell}(z)$  are the Riccati-Bessel, Riccati-Neumann and Riccati-Hankel functions, respectively, with  $j_{\ell}$  and  $y_{\ell}$  being the spherical Bessel and Neumann functions [28]. The refractive and impedance indices are  $n_p = \sqrt{\varepsilon_p \mu_p / (\varepsilon_0 \mu_0)}$  and  $\tilde{n}_p = \sqrt{\varepsilon_p \mu_0 / (\varepsilon_0 \mu_p)}$ , with  $p = \{1, 2\}$  [39]. For non-magnetic materials ( $\mu_p = \mu_0$ ), one has  $\tilde{n}_p = n_p$  [40]. The solution for a homogeneous sphere of radius  $b$  can be readily obtained by setting  $\varepsilon_1 = \varepsilon_2$  and  $\mu_1 = \mu_2$ , i.e.,  $A_{\ell} = 0 = B_{\ell}$ . It is worth mentioning that these Lorenz-Mie coefficients can be trivially generalized to the case of center-symmetric multi-layered spheres [41].

Analogously, within the core ( $0 \leq r \leq a$ ) and shell ( $a \leq r \leq b$ ) regions, we have the electric fields [39, 42]

$$\begin{aligned} \mathbf{E}_1(r, \theta, \varphi) = & -\frac{1}{n_1kr} \sum_{\ell=1}^{\infty} E_{\ell} \left\{ \iota \cos \varphi \sin \theta d_{\ell} j_{\ell}(n_1kr) \ell(\ell+1) \pi_{\ell}(\cos \theta) \hat{\mathbf{e}}_r \right. \\ & + \cos \varphi [c_{\ell} \pi_{\ell}(\cos \theta) \psi_{\ell}(n_1kr) - \iota d_{\ell} \tau_{\ell}(\cos \theta) \psi'_{\ell}(n_1kr)] \hat{\mathbf{e}}_{\theta} \\ & \left. + \sin \varphi [\iota d_{\ell} \pi_{\ell}(\cos \theta) \psi'_{\ell}(n_1kr) - c_{\ell} \tau_{\ell}(\cos \theta) \psi_{\ell}(n_1kr)] \hat{\mathbf{e}}_{\varphi} \right\}, \quad (19.9) \end{aligned}$$

$$\begin{aligned} \mathbf{E}_2(r, \theta, \varphi) = & -\frac{1}{n_2kr} \sum_{\ell=1}^{\infty} E_{\ell} \left\{ \iota \cos \varphi \sin \theta g_{\ell} j_{\ell}(n_2kr) \ell(\ell+1) \pi_{\ell}(\cos \theta) \hat{\mathbf{e}}_r \right. \\ & + \iota \cos \varphi \sin \theta w_{\ell} y_{\ell}(n_2kr) \ell(\ell+1) \pi_{\ell}(\cos \theta) \hat{\mathbf{e}}_r \\ & + \cos \varphi [f_{\ell} \pi_{\ell}(\cos \theta) \psi_{\ell}(n_2kr) - \iota g_{\ell} \tau_{\ell}(\cos \theta) \psi'_{\ell}(n_2kr)] \hat{\mathbf{e}}_{\theta} \\ & - \cos \varphi [v_{\ell} \pi_{\ell}(\cos \theta) \chi_{\ell}(n_2kr) - \iota w_{\ell} \tau_{\ell}(\cos \theta) \chi'_{\ell}(n_2kr)] \hat{\mathbf{e}}_{\theta} \\ & + \sin \varphi [\iota g_{\ell} \pi_{\ell}(\cos \theta) \psi'_{\ell}(n_2kr) - f_{\ell} \tau_{\ell}(\cos \theta) \psi_{\ell}(n_2kr)] \hat{\mathbf{e}}_{\varphi} \\ & \left. - \sin \varphi [\iota w_{\ell} \pi_{\ell}(\cos \theta) \chi'_{\ell}(n_2kr) - v_{\ell} \tau_{\ell}(\cos \theta) \chi_{\ell}(n_2kr)] \hat{\mathbf{e}}_{\varphi} \right\}, \quad (19.10) \end{aligned}$$

respectively. In terms of the auxiliary functions defined in (19.7) and (19.8), the Lorenz-Mie coefficients  $c_{\ell}$ ,  $d_{\ell}$ ,  $f_{\ell}$ ,  $g_{\ell}$ ,  $v_{\ell}$  and  $w_{\ell}$  read [28, 39]

$$c_{\ell} = \frac{n_1 f_{\ell}}{n_2 \psi_{\ell}(n_1ka)} [\psi_{\ell}(n_2ka) - B_{\ell} \chi_{\ell}(n_2ka)], \quad (19.11)$$

$$d_{\ell} = \frac{n_1 g_{\ell}}{n_2 \psi'_{\ell}(n_1ka)} [\psi'_{\ell}(n_2ka) - A_{\ell} \chi'_{\ell}(n_2ka)], \quad (19.12)$$

$$f_{\ell} = \frac{\iota n_2}{[\psi_{\ell}(n_2kb) - B_{\ell} \chi_{\ell}(n_2kb)] [\xi'_{\ell}(kb) - \tilde{n}_2 \xi_{\ell}(kb) \mathcal{B}_{\ell}(n_2kb)]}, \quad (19.13)$$

$$g_{\ell} = \frac{\iota n_2}{[\psi_{\ell}(n_2kb) - A_{\ell} \chi_{\ell}(n_2kb)] [\tilde{n}_2 \xi'_{\ell}(kb) - \xi_{\ell}(kb) \mathcal{A}_{\ell}(n_2kb)]}, \quad (19.14)$$

$$v_{\ell} = B_{\ell} f_{\ell}, \quad (19.15)$$

$$w_{\ell} = A_{\ell} g_{\ell}. \quad (19.16)$$

Equations (19.1)–(19.16) are the complete Lorenz-Mie solution for center symmetric core-shell spheres [28]. The corresponding magnetic field  $\mathbf{H}(\mathbf{r})$  can be straightforwardly obtained from (19.1), (19.2), (19.9), and (19.10) by Maxwell's curl equations. In the following, we discuss the cross sections and internal field intensities in the context of Fano resonances in plasmonic nanoshells.

## 19.2.2 Fano Resonances in Optical Cross Sections

The cross sections of a spherical particle can be calculated exactly from the net rate of electromagnetic energy crossing an imaginary surface at the far field (for details, see [28]). From the standard Lorenz-Mie theory, by using (19.1) and (19.2), the extinction, scattering and absorption cross sections of a spherical particle irradiated by plane waves are, respectively,

$$\sigma_{\text{ext}} = \frac{2\pi}{k^2} \sum_{\ell=1}^{\infty} (2\ell + 1) \text{Re}(a_{\ell} + b_{\ell}), \quad (19.17)$$

$$\sigma_{\text{sca}} = \frac{2\pi}{k^2} \sum_{\ell=1}^{\infty} (2\ell + 1) (|a_{\ell}|^2 + |b_{\ell}|^2), \quad (19.18)$$

$$\sigma_{\text{abs}} = \sigma_{\text{ext}} - \sigma_{\text{sca}}, \quad (19.19)$$

where  $a_{\ell}$  and  $b_{\ell}$  carry the dependence on the geometrical and optical parameters of the scatterer, and are defined in (19.3) and (19.4) for a single-layered core-shell sphere. Equations (19.17)–(19.19) are calculated from averaging over all possible directions and polarizations. By considering the backward ( $\theta = \pi$ ) and forward ( $\theta = 0$ ) directions, we obtain

$$\sigma_{\text{back}} = \frac{\pi}{k^2} \left| \sum_{\ell=1}^{\infty} (2\ell + 1) (-1)^{\ell} (a_{\ell} - b_{\ell}) \right|^2, \quad (19.20)$$

$$\sigma_{\text{forward}} = \frac{\pi}{k^2} \left| \sum_{\ell=1}^{\infty} (2\ell + 1) (a_{\ell} + b_{\ell}) \right|^2, \quad (19.21)$$

which are the differential backward and forward scattering cross sections, respectively. Usually the optical cross sections are calculated in units of the geometrical cross section  $\sigma_{\text{g}} = \pi b^2$ , where  $b$  is the effective radius of the spherical scatterer.

From (19.17)–(19.21), it is clear that one can achieve interferences between different electric and magnetic scattering amplitudes (namely,  $a_{\ell}$  and  $b_{\ell}$ ) only for directional scattering, e.g.,  $\sigma_{\text{back}}$  and  $\sigma_{\text{forward}}$  [9]. Of particular interest is the case of light scattering by small plasmonic spheres ( $kb \leq 1$ ). In this limiting case, the dipolar Rayleigh scattering ( $\ell = 1$ ) plays the role of a broad spectral resonance, whereas the localized surface plasmon resonance, e.g., quadrupole ( $\ell = 2$ ) or higher order resonance, plays the role of a narrow spectral line interacting with a broad spectral line. As a result, in the vicinity of the narrow plasmon resonance there is a  $\pi$ -phase jump, leading to the coexistence of constructive and destructive interferences with the broad dipole resonance. This interference between the electric scattering amplitudes  $a_1$  and  $a_2$  is described by a characteristic asymmetric line shape, known as the conventional Fano resonance.

### 19.2.2.1 Unconventional Fano Resonances in Plasmonic Nanoshells

Recently, other mechanisms of Fano-like resonances have been described in light scattering by small particles relative to the light wavelength. For instance, Fano resonances were shown to occur beyond the applicability of the Rayleigh approximation in high-index particles, where the interference between electromagnetic modes with the same multipole moment (e.g., dipole-dipole interference) is crucial [6, 13, 15]. These Fano-like resonances also manifest themselves in plasmonic layered particles with moderate permittivities [10], even in the Rayleigh scattering approximation [7].

Since these interferences occur in the total scattering cross section  $\sigma_{\text{sca}}$  and, hence, do not depend on the scattering direction, they were named unconventional Fano resonances [6].

To picture these concepts, let us consider a core-shell nanoparticle consisting of a silicon (Si) core with refractive index  $n_1 = 3.5$  and radius  $a = 60$  nm coated with a dispersive silver (Ag) nanoshell with radius  $b = 90$  nm. The Ag dielectric permittivity is well described by the generalized Drude model [43, 44]

$$\frac{\varepsilon_{\text{Ag}}(\omega)}{\varepsilon_0} = \varepsilon_{\text{int}} - \frac{\omega_{\text{p}}^2}{\omega(\omega + i\gamma)}, \quad (19.22)$$

where  $\varepsilon_{\text{int}} = 3.7$  is a contribution due to interband transitions,  $\omega_{\text{p}} = 9.2$  eV ( $\approx 2\pi \times 2.2 \times 10^{15}$  Hz) is the plasmon frequency associated with conduction electrons, and  $\gamma = 0.02$  eV is the effective dumping rate due to material losses. These Drude parameters for Ag are valid below the frequency of onset for interband transitions:  $\omega/\omega_{\text{p}} < 0.42$  [44]. These are the optical and geometric parameters that we consider for numerical calculations throughout this chapter.

Figure 19.2 shows the plots of the optical cross sections defined in (19.17)–(19.21) as a function of the frequency of the incident electromagnetic wave. For the frequency range  $0.135\omega_{\text{p}} < \omega < 0.225\omega_{\text{p}}$ , the corresponding size parameters of the core-shell sphere are  $0.56 < kb < 0.95$ , so we can restrict our discussion on electric multipole moments up to  $\ell = 2$  (quadrupole). Also, since the involved materials are non-magnetic with moderate permittivities, one has  $b_\ell \approx 0$  for  $kb < 1$ .

In the main plot of Fig. 19.2, one can clearly see that  $\sigma_{\text{sca}}$  presents a Fano line shape, where the dipole-dipole ( $|a_1|^2$ ) resonance occurs at  $\omega \approx 0.170\omega_{\text{p}}$  and the antiresonance (Fano dip) occurs at  $\omega \approx 0.175\omega_{\text{p}}$ . In this same frequency range, the absorption cross section  $\sigma_{\text{abs}}$  exhibits a Lorentzian line shape [45]. In addition, a quadrupole-quadrupole ( $|a_2|^2$ ) resonance also shows up at  $\omega \approx 0.208\omega_{\text{p}}$ , but only contributes to the absorption cross section. However, the overlap of the narrow quadrupole ( $\ell = 2$ ) resonance and the broad dipole resonance ( $\ell = 1$ ) leads to a Fano line shape in the differential scattering cross sections, see the inset of Fig. 19.2.

The unconventional Fano resonance observed in  $\sigma_{\text{sca}}$  and  $\sigma_{\text{ext}}$  can be explained by the interference between out of phase electric fields within the plasmonic nanoshell. Recently, Tribelsky and Miroschnichenko [15] have shown that the Fano line shape associated with high-index spherical particles can be calculated exactly within the Lorenz-Mie theory. Here, we generalize their result to the case of a core-shell sphere. Since we are not interested in magnetic resonances (namely,  $b_\ell$ ) [40, 46], we restrict our discussion on the electric scattering amplitude  $a_\ell$ . Indeed, the magnetic case is completely analogous and the interested reader is referred to [15].

Following [15], we rewrite the electric scattering coefficient  $a_\ell$ :

$$a_\ell = \frac{F_\ell}{F_\ell + iG_\ell} = \frac{\zeta_\ell(\omega) + q_\ell}{\zeta_\ell(\omega) + q_\ell - i[\zeta_\ell(\omega)q_\ell - 1]}, \quad (19.23)$$



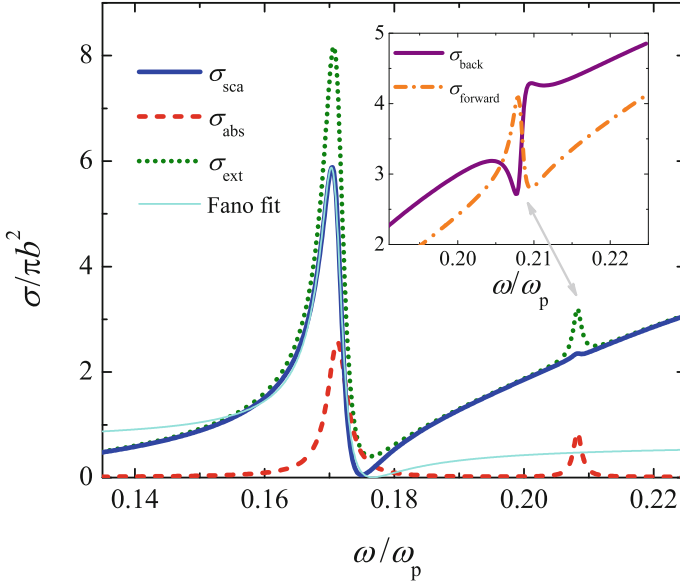


**Fig. 19.2** Optical cross sections in the light scattering by a (Si) core-shell (Ag) nanosphere in free space. The dielectric core has radius  $a = 60$  nm and refractive index  $n_1 = 3.5$ , whereas the plasmonic shell has radius  $b = 90$  nm and electric permittivity  $\varepsilon_2 = \varepsilon_{\text{Ag}}(\omega)$  (19.22). The plot shows the scattering ( $\sigma_{\text{sca}}$ ), absorption ( $\sigma_{\text{abs}}$ ), and extinction ( $\sigma_{\text{ext}}$ ) cross sections (in units of  $\pi b^2$ ) as a function of the frequency  $\omega$  (in units of Ag plasmon frequency  $\omega_p$ ). An unconventional Fano resonance can be observed in  $\sigma_{\text{sca}}$  ( $\omega \approx 0.170\omega_p$ ) associated with the dipole-dipole interference  $a_1 a_1^*$  excited in the shell, where  $a_1$  is the electric Lorenz-Mie coefficient. The inset shows two conventional Fano resonances in the differential backward ( $\sigma_{\text{back}}$ ) and forward ( $\sigma_{\text{forward}}$ ) scattering cross sections at  $\omega \approx 0.208\omega_p$ . These Fano resonances are related to the dipole-quadrupole interference  $a_1 a_2^*$  at the backward and forward directions, respectively

with the new auxiliary functions being

$$F_\ell = n_2 \psi'_\ell(kb) [\psi_\ell(n_2 kb) - A_\ell \chi_\ell(n_2 kb)] - \psi_\ell(kb) [\psi'_\ell(n_2 kb) - A_\ell \chi'_\ell(n_2 kb)], \quad (19.24)$$

$$G_\ell = -n_2 \chi'_\ell(kb) [\psi_\ell(n_2 kb) - A_\ell \chi_\ell(n_2 kb)] + \chi_\ell(kb) [\psi'_\ell(n_2 kb) - A_\ell \chi'_\ell(n_2 kb)], \quad (19.25)$$

where  $\zeta_\ell(\omega) \equiv \zeta'_\ell(\omega) + i\zeta''_\ell(\omega)$  and  $q_\ell$  is the Fano asymmetry parameter. Here,  $\zeta' = \text{Re}(\zeta)$  and  $\zeta'' = \text{Im}(\zeta)$  (not to be confused with derivatives with respect to the argument). Although the demonstration is not trivial [15], one can formally show that

$$\zeta_\ell(\omega) = \frac{F_\ell \psi'_\ell(kb) - G_\ell \chi'_\ell(kb)}{\psi'_\ell(n_2 kb) - A_\ell \chi'_\ell(n_2 kb)}, \quad (19.26)$$

$$q_\ell = \frac{\chi'_\ell(kb)}{\psi'_\ell(kb)}. \quad (19.27)$$

If the sphere is lossless, one has  $\zeta_\ell''(\omega) = 0$  and  $|a_\ell|^2 = (\zeta'_\ell + q_\ell)^2 / [(1 + q_\ell^2)(\zeta_\ell'^2 + 1)]$ , i.e.,  $|a_\ell|^2$  is a normalized Fano lineshape as a function of  $\zeta'_\ell$ . These expressions agree with [15] for  $A_\ell = 0$  (homogeneous sphere).

Considering only the dipole scattering resonance ( $\ell = 1$ ) and defining  $q_{\text{LM}} \equiv q_1$  and  $\zeta(\omega) \equiv \zeta_1(\omega)$ , we finally have

$$\sigma_{\text{sca}} \approx \frac{6\pi}{k^2 (1 + q_{\text{LM}}^2)} \left\{ \frac{\left[ \frac{\zeta'(\omega)}{1 + \zeta''(\omega)} + \frac{q_{\text{LM}}}{1 + \zeta''(\omega)} \right]^2 + \left[ \frac{\zeta''(\omega)}{1 + \zeta''(\omega)} \right]^2}{\left[ \frac{\zeta'(\omega)}{1 + \zeta''(\omega)} \right]^2 + 1} \right\}. \quad (19.28)$$

In the vicinity of a Fano resonance, one can use the approximation  $\zeta'_\ell(\omega)/[1 + \zeta''(\omega)] \approx (\omega - \omega_{\text{res}})/\Omega$ , where  $\Omega$  is associated with the curve linewidth. The function  $\zeta''(\omega)$  has a very complicated analytical expression, and it can be estimated from the dipole resonance [ $\zeta'(\omega_{\text{res}}) = 0$ ]:  $\sigma_{\text{sca}}^{\text{(max)}} = 6\pi(q^2 + \zeta''^2)/[(k^2(1 + q^2)(1 + \zeta''^2)]$ . From Fig. 19.2, one has  $\sigma_{\text{sca}}^{\text{(max)}}(\omega_{\text{res}}) \approx 5.9\pi b^2$  for  $\omega_{\text{res}} \approx 0.170\omega_{\text{p}}$ . Indeed, we have used (19.28) to fit the scattering cross section in Fig. 19.2. For our set of parameters, the effective Fano asymmetry parameter is  $q_{\text{LM}}/(1 + \zeta'') \approx -2.81$ , where  $q_{\text{LM}} \approx -3.84$  and  $\zeta'' \approx 0.368$ .

### 19.2.2.2 Off-Resonance Field Enhancement in Plasmonic Nanoshells

The presence of Fano-like resonances in Lorenz-Mie theory is associated with very interesting optical phenomena, such as the formation of optical vortices and saddle points in the energy flow around particles [9], enhanced light scattering response [34], and off-resonance field enhancement within core-shell scatterers [47, 48]. Indeed, as can be observed in Fig. 19.3, both dipole and quadrupole scattering resonances discussed above are associated with saddle points in the time-averaged energy flow  $\mathbf{S}(\mathbf{r}) = \text{Re}[\mathbf{E}(\mathbf{r}) \times \mathbf{H}^*(\mathbf{r})]/2$  in the vicinity of the Ag nanoshell, where the local electromagnetic field ( $\mathbf{E}$ ,  $\mathbf{H}$ ) is calculated from (19.1) and (19.2).

To show the effect of off-resonance field enhancement, we calculate the corresponding electric field intensity  $\langle |\mathbf{E}|^2 \rangle$  within the coated sphere [7, 42, 49]. Here, the operator  $\langle \dots \rangle = (1/4\pi) \int_{-1}^1 d(\cos \theta) \int_0^{2\pi} d\varphi (\dots)$  is the angle average over  $4\pi$ . Using the exact expression for the electric fields within the core ( $0 \leq r \leq a$ ) and shell ( $a \leq r \leq b$ ), (19.9) and (19.10), we obtain the angle-averaged intensities [7, 42]

$$\frac{\langle |\mathbf{E}_1(\mathbf{r})|^2 \rangle}{|E_0|^2} = \frac{1}{2} \sum_{\ell=1}^{\infty} \left\{ (2\ell + 1) |c_\ell|^2 |j_\ell(n_1 kr)|^2 + |d_\ell|^2 [\ell |j_{\ell+1}(n_1 kr)|^2 + (\ell + 1) |j_{\ell-1}(n_1 kr)|^2] \right\}, \quad (19.29)$$

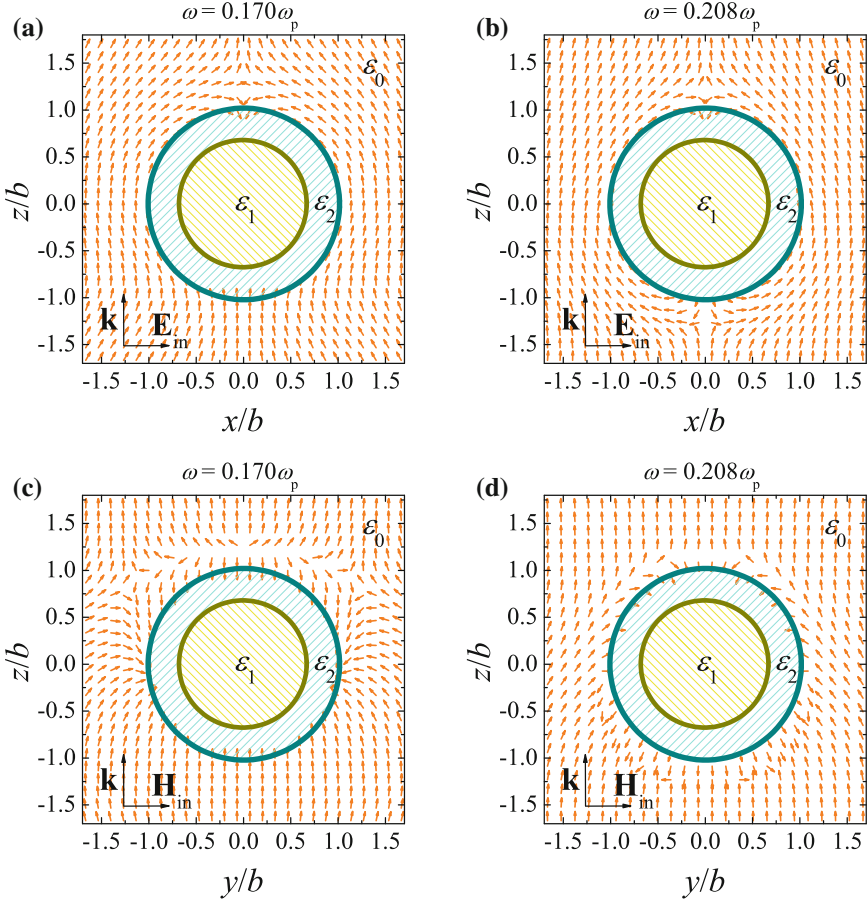


**Fig. 19.3** Time-averaged energy flow (normalized Poynting vector field) in the vicinity of a (Si) core-shell (Ag) nanosphere for dipole ( $\omega \approx 0.170\omega_p$ ) and quadrupole ( $\omega \approx 0.208\omega_p$ ) scattering resonances. The dielectric core has refractive index  $n_1 = 3.5$  and radius  $a = 60$  nm, whereas the Ag nanoshell (19.22) has radius  $b = 90$  nm. The  $xz$  plane shows the presence of a saddle point in the energy flow in the  $z$ -axis around  $z \approx 1.25b$  for dipole resonance **a** and two saddle points for quadrupole resonance **b** around  $z \approx \pm 1.20b$ . The  $yz$  plane shows singular points along the  $y$  direction for dipole **c** and quadrupole **d** resonances

$$\begin{aligned} \frac{\langle |\mathbf{E}_2(\mathbf{r})|^2 \rangle}{|E_0|^2} &= \frac{1}{2} \sum_{n=1}^{\infty} \left\{ (2\ell + 1) [ |f_\ell|^2 |j_\ell(n_2kr)|^2 + |v_\ell|^2 |y_\ell(n_2kr)|^2 ] \right. \\ &\quad + |g_\ell|^2 [ \ell |j_{\ell+1}(n_2kr)|^2 + (\ell + 1) |j_{\ell-1}(n_2kr)|^2 ] \\ &\quad + |w_\ell|^2 [ \ell |y_{\ell+1}(n_2kr)|^2 + (\ell + 1) |y_{\ell-1}(n_2kr)|^2 ] \\ &\quad \left. + 2\text{Re} \left[ (2\ell + 1) f_\ell v_\ell^* j_\ell(n_2kr) y_\ell(n_2^*kr) \right] \right\} \end{aligned}$$

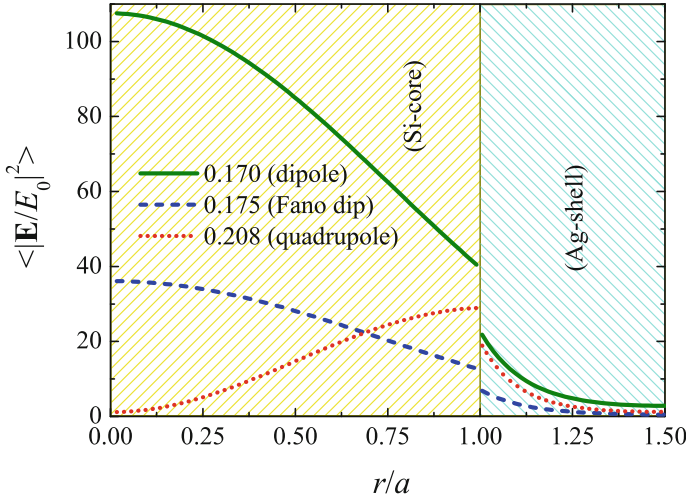


**Fig. 19.4** The angle-averaged electric field intensity inside a (Si) core-shell (Ag) nanosphere in free space, as depicted in Fig. 19.1, as a function of the distance from the center of the scatterer to its surface. The dielectric core has radius  $a = 60$  nm and refractive index  $n_1 = 3.5$ , whereas the plasmonic shell has radius  $b = 90$  nm and electric permittivity  $\varepsilon_2 = \varepsilon_{\text{Ag}}(\omega)$  (19.22). The maximum electric field intensity stored inside the scatterer occurs at the dipole resonance ( $\omega \approx 0.170\omega_p$ ). The intensity at the Fano dip ( $\omega \approx 0.175\omega_p$ ) is comparable to and even greater than the intensity at the quadrupole resonance ( $\omega \approx 0.208\omega_p$ ) inside the core

$$\begin{aligned}
 &+g_\ell w_\ell^* \left[ \ell j_{\ell+1}(n_2 kr) y_{\ell+1}(n_2^* kr) \right. \\
 &\left. + (\ell + 1) j_{\ell-1}(n_2 kr) y_{\ell-1}(n_2^* kr) \right] \Bigg\}, \quad (19.30)
 \end{aligned}$$

where we have used the relations [28]:  $(2\ell + 1) \int_{-1}^1 d(\cos \theta) (\pi_\ell \pi_{\ell'} + \tau_\ell \tau_{\ell'}) = 2\ell^2$   $(\ell + 1)^2 \delta_{\ell\ell'}$ ,  $\int_{-1}^1 d(\cos \theta) (\pi_\ell \tau_{\ell'} + \tau_\ell \pi_{\ell'}) = 0$ , and  $(2\ell + 1) \int_{-1}^1 d(\cos \theta) \pi_\ell \pi_{\ell'} \sin^2 \theta = 2\ell(\ell + 1) \delta_{\ell\ell'}$ , with  $\delta_{\ell\ell'}$  being the Kronecker delta. Note that the electric field intensity  $\langle |\mathbf{E}_2|^2 \rangle$  inside the shell is a quantity sensitive to interference between different electromagnetic modes, i.e.,  $f_\ell v_\ell^*$  and  $g_\ell w_\ell^*$ . This is due to the interference between partial waves generated from Bessel or Neumann functions within the spherical shell. Indeed, one can show that these interferences are related to the unconventional Fano resonance observed in the total scattering cross section [7].

In Fig. 19.4, we show how the electric field intensity  $\langle |\mathbf{E}|^2 \rangle$  depends on the distance from the center of the sphere to its surface  $r = b$ . We study three main frequencies obtained from  $\sigma_{\text{sca}}$  plotted in Fig. 19.2: the dipole resonance ( $\omega \approx 0.170\omega_p$ ), the Fano dip ( $\omega \approx 0.175\omega_p$ ), and the quadrupole resonance ( $\omega \approx 0.208\omega_p$ ). We verify that even at the Fano dip (with  $\sigma_{\text{sca}} \approx 0$ ) it is possible to obtain a large field intensity enhancement inside the (Si) core-shell (Ag) nanosphere. Indeed, the intensity inside the lossless dielectric core ( $r < a$ ) is even greater than the intensity obtained for the

quadrupole resonance, which characterizes an off-resonance field enhancement at the subwavelength scale.

In the following, we use the ideas presented in this section to study how the Fano resonances are connected to the enhancement or suppression of the spontaneous-emission rate of optical emitters near plasmonic nanostructures.

### 19.3 Spontaneous Emission of a Dipole Emitter Near a Plasmonic Nanoshell

Plasmonic surfaces are known to enhance or quench the fluorescence response of quantum emitters due to near- and far-field interactions between emitter and surface [17, 50]. This modification of the spontaneous-emission rate of a quantum emitter due to the electromagnetic environment is generally referred to as the Purcell effect [27]. Historically, this effect was first described by E. M. Purcell in the context of nuclear magnetic resonance [51], and was followed by the reports of K. H. Drexhage on the effects of metallic surfaces on fluorescence decay rate [52] and Chance et al. concerning molecular fluorescence near interfaces [53]. At present, this effect is widely used in several applications involving the enhancement and controlling of light emission and absorption at nanoscale, such as nanoplasmonic devices, nanoscale sensors, and the design of novel optical antennas in surface enhanced spectroscopy and microscopy [27, 50, 54].

This section is devoted to the classical electrodynamics theory that describes the interaction between a single dipole emitter and a coated nanosphere. In quantum electrodynamics, the standard approach to calculate the variation on linewidth and energy level shift of a quantum emitter due to boundary conditions is the first-order perturbation theory [55]. In the weak coupling regime, the excited emitter decays exponentially to its ground state with life time  $\tau = 1/\Gamma$ . A remarkable feature of this approximation is that the decay rate  $\Gamma$  of a quantum emitter in the vicinity of a body, normalized by the spontaneous-emission rate in free space  $\Gamma_0$ , can be calculated in the framework of classical electrodynamics [50, 56–58]. In this case, the excited emitter is modeled as a point dipole source interacting with local electric field at the same position as the quantum emitter, and the Purcell factor  $\Gamma/\Gamma_0$  is derived from the radiated power normalized to free space [18, 59]. This equivalence between classical and quantum calculations in the weak coupling regime occurs due to the fact that both the mode functions of the quantized electromagnetic fields and the classical electric field are derived from the same vector Helmholtz equation [57, 60].

In the following, we present in Sect. 19.3.1 an overview of the fully classical theory used to derive the spontaneous-emission rates of dipole emitters in close proximity of spheres. In Sect. 19.3.2, we calculate the influence of near-field interactions on the radiation efficiency of a dipole emitter near a plasmonic nanoshell. The relation between Fano resonances and the spontaneous-emission rate is discussed in detail in Sect. 19.3.3. It is worth emphasizing that the final expressions for  $\Gamma/\Gamma_0$  derived

in Sect. 19.3.1 agree with the first-order perturbation theory in the weak coupling regime [18, 27].

### 19.3.1 Radiative and Non-radiative Decay Rates of a Dipole Emitter

Let us consider the same geometry investigated in Sect. 19.2: a core-shell sphere of inner radius  $a$  and outer radius  $b$  in free space ( $\epsilon_0, \mu_0$ ). The sphere has optical properties ( $\epsilon_1, \mu_1$ ) for the core ( $r \leq a$ ) and ( $\epsilon_2, \mu_2$ ) for the shell ( $a \leq r \leq b$ ), as depicted in Fig. 19.5. Both core and shell consisting of isotropic and linear materials, and may have absorption and dispersion that satisfies the Kramers-Kronig relations [25, 61]. In addition, we consider a single dipole emitter located at position  $\mathbf{r}'$ , with  $r' = |\mathbf{r}'| > b$ . The dipole emitter is characterized by its electric dipole moment  $\mathbf{d}_0$  and its emission frequency  $\omega$ . The electric field emitted by this electric dipole in the region  $b < r < r'$  can be expanded in terms of vector spherical harmonics [18, 59] and reads

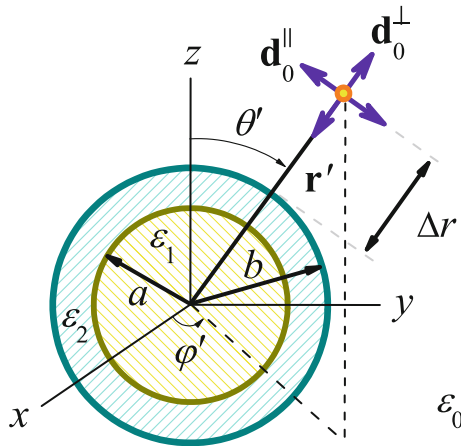


**Fig. 19.5** An optical dipole emitter in the vicinity of a core-shell sphere in free space. The inner sphere has radius  $a$  and electric permittivity  $\epsilon_1$ , whereas the outer sphere has radius  $b$  and electric permittivity  $\epsilon_2$ . The surrounding medium is the vacuum  $\epsilon_0$ . The optical emitter is located at the position  $\mathbf{r}'$ , with  $|\mathbf{r}'| = r' = b + \Delta r$ . There are two basic orientations for the electric dipole moment  $\mathbf{d}_0$  associated with the dipole emitter: it can be orthogonal ( $\mathbf{d}_0^{\perp}$ ) or tangential ( $\mathbf{d}_0^{\parallel}$ ) to the spherical surface. Any arbitrary dipole moment orientation in relation to the sphere can be decomposed in orthogonal and tangential contributions

$$\mathbf{E}_{\text{dip}}^{\mathbf{d}_0}(r, \theta, \varphi) = \sum_{\ell=1}^{\infty} \sum_{m=-\ell}^{\ell} \frac{1}{\ell(\ell+1)} \left\{ \alpha_{\ell m} \frac{1}{k} \nabla \times \left[ j_{\ell}(kr) \hat{\mathbf{L}} Y_{\ell m}(\theta, \varphi) \right] + \beta_{\ell m} j_{\ell}(kr) \hat{\mathbf{L}} Y_{\ell m}(\theta, \varphi) \right\}, \quad (19.31)$$

$$\alpha_{\ell m} = -\iota k^2 \mathbf{d}_0 \cdot \nabla' \times \left[ h_{\ell}^{(1)}(kr') \hat{\mathbf{L}}' Y_{\ell m}^*(\theta', \varphi') \right], \quad (19.32)$$

$$\beta_{\ell m} = -\iota k^3 h_{\ell}^{(1)}(kr') \mathbf{d}_0 \cdot \hat{\mathbf{L}}' Y_{\ell m}^*(\theta', \varphi'), \quad (19.33)$$

where  $k = \omega \sqrt{\varepsilon_0 \mu_0}$ ,  $Y_{\ell m}(\theta, \varphi)$  is the spherical harmonics, and  $\hat{\mathbf{L}} = -\iota \mathbf{r} \times \nabla$  is the angular momentum operator [28]. The derivation of (19.33) can be found in [62]. Here, the superindex  $\mathbf{d}_0$  is just a reminder that the emitted electromagnetic fields depend on the dipole orientation. Also,  $\mathbf{E}_{\text{dip}}^{\mathbf{d}_0}(\mathbf{r})$  for  $r > r'$  can be readily obtained from (19.31)–(19.33) by interchanging  $j_{\ell}$  with  $h_{\ell}^{(1)}$ . Here, the choice of a Hankel function of the first kind  $h_{\ell}^{(1)}$  for outgoing waves is closely related to the assumption of a time harmonic dependence  $e^{-\iota \omega t}$  [28]. From Maxwell's curl equations, this implies a magnetic field  $\mathbf{H}_{\text{dip}}^{\mathbf{d}_0} = -\iota \nabla \times \mathbf{E}_{\text{dip}}^{\mathbf{d}_0} / \omega \mu_0$ .

The electromagnetic wave  $[\mathbf{E}_{\text{dip}}^{\mathbf{d}_0}(\mathbf{r}), \mathbf{H}_{\text{dip}}^{\mathbf{d}_0}(\mathbf{r})]e^{-\iota \omega t}$  impinges on a spherical particle centered at  $r = 0$ , with radius  $b$ , and it is scattered to the far field for  $r > b$ . From the boundary conditions, one can show that the scattered electric field  $\mathbf{E}_{\text{sca}}^{\mathbf{d}_0}(\mathbf{r})$  can be obtained from (19.31) by simply replacing coefficients  $(\alpha_{\ell m}, \beta_{\ell m})$  with  $(a_{\ell m}, b_{\ell m})$  and the function  $j_{\ell}$  with  $h_{\ell}^{(1)}$  [18, 56, 59, 62]. This procedure leads to

$$\mathbf{E}_{\text{sca}}^{\mathbf{d}_0}(r, \theta, \varphi) = \sum_{\ell=1}^{\infty} \sum_{m=-\ell}^{\ell} \frac{1}{\ell(\ell+1)} \left\{ a_{\ell m} \frac{1}{k} \nabla \times \left[ h_{\ell}^{(1)}(kr) \hat{\mathbf{L}} Y_{\ell m}(\theta, \varphi) \right] + b_{\ell m} h_{\ell}^{(1)}(kr) \hat{\mathbf{L}} Y_{\ell m}(\theta, \varphi) \right\}, \quad (19.34)$$

$$a_{\ell m} = -\alpha_{\ell m} a_{\ell}, \quad (19.35)$$

$$b_{\ell m} = -\beta_{\ell m} b_{\ell}, \quad (19.36)$$

where  $\alpha_{\ell m}$  and  $\beta_{\ell m}$  are given by (19.32) and (19.33), respectively. The coefficients  $a_{\ell}$  and  $b_{\ell}$ , which encode the dependence on the sphere parameters, are the usual electric and magnetic Lorenz-Mie coefficients, respectively, given by (19.3) and (19.4).

Using the Green's tensor formalism [18, 56], the solution for the total decay rate associated with an electric dipole moment  $\mathbf{d}_0$  can be expressed as

$$\frac{\Gamma_{\text{total}}^{\mathbf{d}_0}}{\Gamma_0} = 1 + \frac{6\pi \varepsilon_0}{k^3 d_0^2} \text{Im} \left[ \mathbf{d}_0 \cdot \mathbf{E}_{\text{sca}}^{\mathbf{d}_0}(\mathbf{r}') \right], \quad (19.37)$$

where the scattered electric field contains the information of the environment in which the optical emitter is embedded. Equation (19.37) takes into account both radiative and non-radiative contributions, and provides a fully classical computational method

to derive a quantum property of a system [18, 57]. Physically, it is derived from the total power delivered by the optical emitter to the environment [27],  $P_{\text{total}} = -\omega \text{Im}\{\mathbf{d}_0 \cdot [\mathbf{E}_{\text{dip}}^{\mathbf{d}_0}(\mathbf{r}') + \mathbf{E}_{\text{sca}}^{\mathbf{d}_0}(\mathbf{r}')]\}/2$ .

Now, let us now consider two basic orientations for the electric dipole moment in spherical geometry:

$$\mathbf{d}_0^\perp = d_0 \hat{\mathbf{e}}_r, \quad \mathbf{d}_0^\parallel = \frac{d_0}{\sqrt{2}} (\hat{\mathbf{e}}_\theta + \hat{\mathbf{e}}_\varphi), \quad (19.38)$$

where  $\mathbf{d}_0^\parallel$  is chosen for convenience [16]. Without loss of generality, we set the position of the dipole emitter along the positive  $z$ -axis, i.e.,  $r' = z > b$  and  $\theta' = \varphi' = 0$ . As a result, since  $P_\ell^m(\cos \theta') \propto \sin^m \theta'$  as  $\theta' \rightarrow 0$ , only the terms with  $m = 0, \pm 1$  contribute to the sum in (19.31) and (19.34) [56]. Substituting (19.34) into (19.37) for  $\theta' = \varphi' = 0$ , we obtain the total decay rates associated with a dipole moment oriented orthogonal ( $\mathbf{d}_0^\perp$ ) or tangential ( $\mathbf{d}_0^\parallel$ ) to the spherical surface, respectively:

$$\frac{\Gamma_{\text{total}}^\perp(kr')}{\Gamma_0} = 1 - \frac{3}{2} \sum_{\ell=1}^{\infty} \ell(\ell+1)(2\ell+1) \text{Re} \left\{ a_\ell \left[ \frac{h_\ell^{(1)}(kr')}{kr'} \right]^2 \right\}, \quad (19.39)$$

$$\frac{\Gamma_{\text{total}}^\parallel(kr')}{\Gamma_0} = 1 - \frac{3}{4} \sum_{\ell=1}^{\infty} (2\ell+1) \text{Re} \left\{ a_\ell \left[ \frac{\xi'_\ell(kr')}{kr'} \right]^2 + b_\ell h_\ell^{(1)}(kr')^2 \right\}. \quad (19.40)$$

For an electric dipole moment with arbitrary orientation in relation to the spherical surface, one can assume the spatial mean [63]:  $\Gamma_{\text{total}} = (\Gamma_{\text{total}}^\perp + 2\Gamma_{\text{total}}^\parallel)/3$ .

Equations (19.39) and (19.40) contain both radiative and non-radiative contributions to the spontaneous-emission rate [27]. It is convenient to investigate these two contributions separately as they play different roles in near- and far-field interactions [64]. Indeed, for plasmonic spheres, the non-radiative contribution is related to an efficient coupling to surface plasmon modes in the near field. Conversely, the radiative decay rate is associated with the excitation of Mie resonances in the far field.

In classical electrodynamics, the radiative decay rate  $\Gamma_{\text{rad}}^{\mathbf{d}_0}/\Gamma_0$  of a dipole emitter at the position  $\mathbf{r}'$  is calculated via the total radiated power in the presence of the sphere normalized to free space [59]. It can be calculated by integrating the radial component of the Poynting vector at the far field ( $r \rightarrow \infty$ ):  $P_{\text{rad}} = r^2 \int d\Omega \mathbf{S} \cdot \hat{\mathbf{e}}_r \propto r^2 \int_{-1}^1 d(\cos \theta) \int_0^{2\pi} d\varphi |\mathbf{E}_{\text{dip}}^{\mathbf{d}_0}(\mathbf{r}) + \mathbf{E}_{\text{sca}}^{\mathbf{d}_0}(\mathbf{r})|^2$ , where  $\mathbf{E}_{\text{dip}}^{\mathbf{d}_0}(\mathbf{r})$  and  $\mathbf{E}_{\text{sca}}^{\mathbf{d}_0}(\mathbf{r})$  are defined in (19.31) and (19.34), respectively. As a final result, we have

$$\frac{\Gamma_{\text{rad}}^\perp(kr')}{\Gamma_0} = \frac{3}{2} \sum_{\ell=1}^{\infty} \ell(\ell+1)(2\ell+1) \left| \frac{j_\ell(kr') - a_\ell h_\ell^{(1)}(kr')}{kr'} \right|^2, \quad (19.41)$$

$$\begin{aligned} \frac{\Gamma_{\text{rad}}^\parallel(kr')}{\Gamma_0} &= \frac{3}{4} \sum_{\ell=1}^{\infty} (2\ell+1) \left[ \left| \frac{\psi'_\ell(kr') - a_\ell \xi'_\ell(kr')}{kr'} \right|^2 \right. \\ &\quad \left. + \left| j_\ell(kr') - b_\ell h_\ell^{(1)}(kr') \right|^2 \right]. \end{aligned} \quad (19.42)$$



For a detailed calculation of these expressions by using the Poynting vector, the interested reader is referred to [18]. A different approach is discussed by Arruda et al. [16] using the Lorenz-Mie theory, in which the radiative decay rate is calculated straightforwardly from the intensity enhancement factor. Indeed, one can verify that  $\Gamma_{\text{rad}}^{\mathbf{d}_0}(r')/\Gamma_0 = \langle |\mathbf{d}_0 \cdot [\mathbf{E}_{\text{in}}(\mathbf{r}') + \mathbf{E}_{\text{sca}}(\mathbf{r}')]|^2 \rangle / \langle |\mathbf{d}_0 \cdot \mathbf{E}_{\text{in}}(\mathbf{r}')|^2 \rangle$ , where  $\mathbf{E}_{\text{in}}(\mathbf{r})$  and  $\mathbf{E}_{\text{sca}}(\mathbf{r})$  are given by (19.1) and (19.2), respectively, and  $\langle \dots \rangle = (1/4\pi) \int_0^{4\pi} \Omega(\dots)$  is the angle average [16]. Once again, assuming the dipole has no defined orientation in space, one has from (19.41) and (19.42) the spatial mean  $\Gamma_{\text{rad}} = (\Gamma_{\text{rad}}^\perp + 2\Gamma_{\text{rad}}^\parallel)/3$ . In addition, by subtracting (19.41) and (19.42) from (19.39) and (19.40), respectively, we finally obtain the non-radiative decay rates

$$\frac{\Gamma_{\text{nrad}}^\perp(kr')}{\Gamma_0} = \frac{3}{2} \sum_{\ell=1}^{\infty} \ell(\ell+1)(2\ell+1) \left| \frac{h_\ell^{(1)}(kr')}{kr'} \right|^2 \text{Re}(a_\ell - |a_\ell|^2), \quad (19.43)$$

$$\frac{\Gamma_{\text{nrad}}^\parallel(kr')}{\Gamma_0} = \frac{3}{4} \sum_{\ell=1}^{\infty} (2\ell+1) \text{Re} \left\{ \left| \frac{\xi_\ell'(kr')}{kr'} \right|^2 (a_\ell - |a_\ell|^2) + \left| h_\ell^{(1)}(kr') \right|^2 (b_\ell - |b_\ell|^2) \right\}. \quad (19.44)$$

Although we have been discussing the case of an optical emitter with electric dipole radiation in the vicinity of a sphere, analogous expressions can be readily obtained for a magnetic dipole transition by interchanging  $a_\ell$  with  $b_\ell$  [18].

### 19.3.2 Decay Rates and Radiation Efficiency Near a Plasmonic Nanoshell

The theory presented above is general and can be applied to arbitrary non-optically active spheres and single dipole emitters (quantum dots, atoms or molecules) in the weak coupling regime [63–65]. Here, we consider a realistic system for a dipole emitter near a plasmonic core-shell sphere composed of a silicon (Si) core and a silver (Ag) nanoshell. We are interested in a configuration where the presence of a dielectric core strongly modifies the scattering response of a plasmonic nanoshell [14, 35, 66], ultimately leading to unconventional Fano resonances [16, 36]. The optical and geometric parameters are the same of Sect. 19.2: a dielectric (Si) core of refractive index  $n_1 = 3.5$  and radius  $a = 60$  nm coated with a plasmonic (Ag) nanoshell of radius  $b = 90$  nm.

Figure 19.6 shows the Purcell factor  $\Gamma/\Gamma_0$  related to a single dipole emitter near a plasmonic shell as a function of the distance  $\Delta r$  for two basic dipole moment orientations: orthogonal (Fig. 19.6a) or parallel (Fig. 19.6b) to the spherical surface. Based on the scattering cross section  $\sigma_{\text{sca}}$  plotted in Fig. 19.2, we investigate three main frequencies for light emission: dipole scattering resonance ( $\omega \approx 0.170\omega_p$ ),

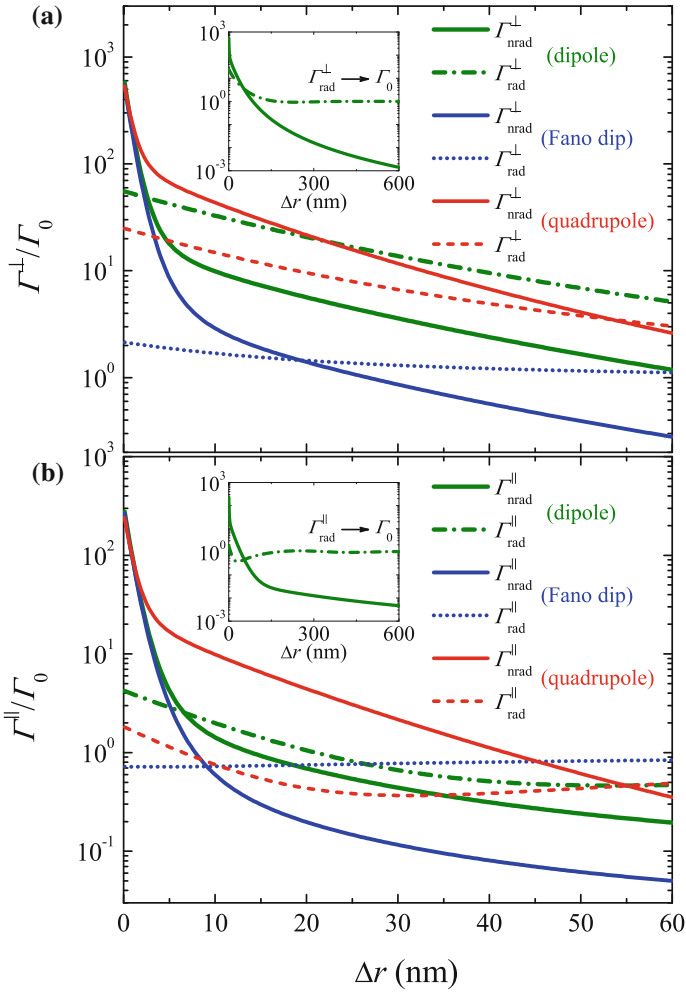


**Fig. 19.6** Spontaneous decay rates  $\Gamma$  of an optical dipole emitter near a (Si) core-shell (Ag) nanosphere in free space as a function of the distance  $\Delta r$  between emitter and sphere. The dielectric core has radius  $a = 60$  nm and refractive index  $n_1 = 3.5$ , and the Ag shell has radius  $b = 90$  nm and electric permittivity  $\varepsilon_2 = \varepsilon_{\text{Ag}}(\omega)$  (19.22). The decay rates are normalized by the corresponding decay rate  $\Gamma_0$  in vacuum. We consider three main frequencies obtained from Fig. 19.2: dipole scattering resonance ( $\omega \approx 0.170\omega_p$ ), Fano dip ( $\omega \approx 0.175\omega_p$ ), and quadrupole resonance ( $\omega \approx 0.208\omega_p$ ). The plots show radiative ( $\Gamma_{\text{rad}}$ ) and non-radiative ( $\Gamma_{\text{nrad}}$ ) decay rates associated with a point dipole oriented orthogonal **a** or parallel **b** to the spherical surface as a function of  $\Delta r$ . The non-radiative decay rates dominate for  $\Delta r \approx 0$  ( $\Gamma_{\text{rad}} \ll \Gamma_{\text{nrad}}$ ). The inset shows that  $\Gamma_{\text{rad}} \rightarrow \Gamma_0$  and  $\Gamma_{\text{nrad}} \rightarrow 0$  for  $\Delta r \gg b$  (far field). At the Fano dip,  $\Gamma_{\text{rad}} \approx \Gamma_0$  irrespective of  $\Delta r$  and dipole orientation

Fano dip ( $\omega \approx 0.175\omega_p$ ), and quadrupole scattering resonance ( $\omega \approx 0.208\omega_p$ ), where  $\omega_p$  is the Ag plasmon frequency.

As can be observed, in the vicinity of the plasmonic nanoshell ( $\Delta r \rightarrow 0$ ), non-radiative channels always dominate over far-field radiative processes, leading to  $\Gamma_{\text{rad}}^{\perp(\ell)} \ll \Gamma_{\text{nrad}}^{\perp(\ell)}$ . In the present system, this effect is mainly associated with ohmic losses on the plasmonic surface. However, as the distance  $\Delta r$  between emitter and nanoshell increases, the non-radiative decay rate decreases faster than the radiative one. At the far field ( $\Delta r \gg b$ ), this results in  $\Gamma_{\text{rad}}^{\perp(\ell)} \rightarrow \Gamma_0$  and  $\Gamma_{\text{nrad}}^{\perp(\ell)} \rightarrow 0$ .

There are some interesting features in Fig. 19.6 that can be explained by light scattering theory. For instance, the non-radiative decay rate  $\Gamma_{\text{nrad}}^{\perp(\ell)}$  associated with the quadrupole scattering resonance ( $|a_2|^2$ ) is greater than that one related to the dipole scattering resonance ( $|a_1|^2$ ). This is an expected result, since the electric quadrupole scattering channel ( $\ell = 2$ ) is mainly associated with absorption, see Fig. 19.2. In addition, note that the light emission at the Fano dip frequency leads to  $\Gamma_{\text{rad}}^{\perp(\ell)} \approx \Gamma_0$  irrespective of the distance  $\Delta r$  between emitter and sphere. Indeed, for a non-dissipative nanoshell, the net spontaneous-emission rate can be identically reduced to its vacuum value depending on the geometrical parameters of the plasmonic coating [25]. This effect is explained by the plasmonic cloaking of the dielectric sphere [32], since  $\sigma_{\text{sca}} \approx 0$  at the Fano dip ( $\omega \approx 0.175\omega_p$ ). However, observe that the plasmonic cloaking is effective only from a certain finite distance  $\Delta r$  of the nanoshell due to unavoidable non-radiative contributions of higher order dark modes ( $\ell > 1$ ) at the near field.

To clarify the role of radiative and non-radiative contributions on the spontaneous-emission rate of an optical emitter, it is convenient to define the radiation efficiency of the light emission. The radiation efficiency  $Q$  of an emitter with negligible internal losses is defined as [27]

$$Q_{\mathbf{d}_0}(kr') = \frac{\Gamma_{\text{rad}}^{\mathbf{d}_0}(kr')}{\Gamma_{\text{rad}}^{\mathbf{d}_0}(kr') + \Gamma_{\text{nrad}}^{\mathbf{d}_0}(kr')}, \quad (19.45)$$

where the corresponding radiative and non-radiative decay rates are calculated in Sect. 19.3.1. Using (19.45), we plot in Fig. 19.7 the competition between far-field radiation and ohmic losses on the surface of the plasmonic nanoshell as a function of  $\Delta r$ . As expected, the radiation efficiency  $Q$  for both dipole moment orientations vanishes at the plasmonic surface ( $\Delta r \approx 0$ ). In particular, note that  $Q_{\perp} > Q_{\parallel}$  in general, which means a more efficient coupling between the electric dipole moment  $\mathbf{d}_0$  oriented orthogonal to the spherical surface than the parallel orientation. Among the chosen light emission frequencies, the lowest values of efficiency at the near field is obtained for the quadrupole scattering resonance frequency  $\omega \approx 0.208\omega_p$ .

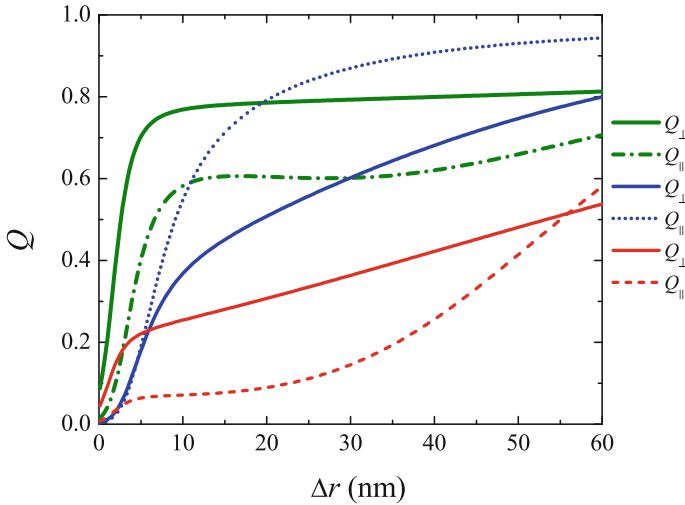


**Fig. 19.7** Radiation efficiency  $Q = \Gamma_{\text{rad}}/\Gamma_{\text{total}}$  associated with a dipole emitter in the vicinity of a plasmonic nanoshell in free space. The system is composed of a (Si) core-shell (Ag) nanosphere with inner radius  $a = 60$  nm and outer radius  $b = 90$  nm. The plots are calculated for an electric dipole moment  $\mathbf{d}_0$  oriented orthogonal ( $Q_{\perp}$ ) or tangential ( $Q_{\parallel}$ ) to the nanoshell as a function of distance  $\Delta r$  for three frequencies obtained from Fig. 19.2: dipole scattering resonance ( $\omega \approx 0.170\omega_p$ , solid and dash-dotted green lines), Fano dip ( $\omega \approx 0.175\omega_p$ , solid and dotted blue lines), and quadrupole resonance ( $\omega \approx 0.208\omega_p$ , solid and dashed red lines). For  $\Delta r \approx 0$  or  $\Delta r \gg b$ , one has  $Q_{\perp(\parallel)} \rightarrow 0$  or  $Q_{\perp(\parallel)} \rightarrow 1$ , respectively

### 19.3.3 The Purcell Effect and Fano Resonances in Plasmonic Nanoshells

The influence of Fano resonances on the Purcell factor is revealed when one considers  $\Gamma/\Gamma_0$  as a function of the light emission frequency  $\omega$  [27]. Recently, it has been analytically demonstrated that the fluorescence enhancement of dipole emitter near a plasmonic nanoshell as a function of the excitation frequency also exhibits an asymmetric Fano line shape [16]. Here, we use the same arguments applied in [16] to describe the Fano effect on the Purcell factor of a dipole emitter in close proximity of plasmonic nanoshells. We focus only on the radiative contribution since we are interested in the dipole mode ( $\ell = 1$ ) excited in the sphere, which is related to the unconventional Fano resonance. For the non-radiative contribution  $\Gamma_{\text{nrad}}^{\perp(\parallel)}$ , the quadrupole mode ( $\ell = 2$ ) excited in the particle dominates the spectrum with a Lorentzian line shape, whereas higher order dark modes ( $\ell > 2$ ) contribute to  $\Gamma_{\text{nrad}}^{\perp(\parallel)}$  in the near field, leading to a broad spectral line ( $Q \rightarrow 0$ , see Fig. 19.7). This influence of higher dark modes is the main reason why the dipole approximation fails to describe near-field interactions between an optical emitter and a plasmonic nanosphere [54]. Conversely, since  $\Gamma_{\text{rad}}^{\perp(\parallel)}$  is related to the far-field radiation, we can restrict our discussion to  $\ell = 1$  for  $kb < 1$  and  $k\Delta r < 1$  in the vicinity of the dipole

scattering resonance ( $|a_1|^2$ ). All the numerical calculations, however, are performed with the exact expressions derived in Sect. 19.3.1.

In Fig. 19.8, we plot  $\Gamma_{\text{rad}}^\perp$  and  $\Gamma_{\text{rad}}^\parallel$  as a function of the light emission frequency  $\omega$ , and for several distances  $\Delta r$  between emitter and plasmonic surface. By comparing Fig. 19.8a and b, we see clearly that  $\Gamma_{\text{rad}}^\perp$  is one order of magnitude greater than  $\Gamma_{\text{rad}}^\parallel$ , confirming that the coupling between emitter and plasmonic nanoshell is stronger for the orthogonal orientation of the dipole moment. More importantly, on one hand, the plots of  $\Gamma_{\text{rad}}^\perp$  exhibit Fano resonances for both dipole ( $\omega \approx 0.170\omega_p$ ) and quadrupole ( $\omega \approx 0.208\omega_p$ ) modes irrespective of  $\Delta r$ . On the other hand, the plots of  $\Gamma_{\text{rad}}^\parallel$  exhibit symmetric Lorentzian profiles for  $\Delta r \ll b$  and, as  $\Delta r$  increases, it develops to a Fano line shape.

As discussed by Arruda et al. [16], the Lorentzian line shape observed in  $\Gamma_{\text{rad}}^\parallel(\omega)$  in the near field, that changes into a Fano line shape in the far field, is a consequence of the core-shell geometry. Physically, the electric dipole moment  $\mathbf{d}_0^\parallel$  associated with the optical emitter induces an oppositely directed dipole moment on the plasmonic nanoshell surface, with almost the same amplitude [58]. This interaction cancels out the broad dipole mode excited in the plasmonic sphere, but does not cancel out the narrow dipole mode ( $\ell = 1$ ) at the plasmonic inner shell surface. According to Refs. [15, 16], we can rewrite the electric Lorenz-Mie coefficient  $a_\ell$ , (19.3), as

$$a_\ell = a_\ell^{\text{PEC}} - \frac{[\psi'_\ell(n_2 kb)g_\ell - \chi'_\ell(n_2 kb)w_\ell]}{n_2 \xi'_\ell(kb)}, \quad (19.46)$$

where  $g_\ell$  and  $w_\ell$  are the Lorenz-Mie coefficients of electromagnetic fields within the plasmonic shell, (19.14) and (19.16), respectively.

The first term in (19.46) is the coefficient of a perfectly electric conducting (PEC) sphere ( $n_2 \rightarrow \infty$ ):  $a_\ell \rightarrow a_\ell^{\text{PEC}} \equiv \psi'_\ell(kb)/\xi'_\ell(kb)$  [28]. Here, this coefficient is related to the broad electric dipole mode ( $\ell = 1$ ), while the second term accounts for the narrow electric dipole mode related to the plasmonic inner shell surface. By inspection of (19.41) and (19.42), it is easily confirmed that the term  $a_1^{\text{PEC}}$  in (19.46) is canceled out for  $r' = b$  and  $\ell = 1$  only in  $\Gamma_{\text{rad}}^\parallel$ , leading to a Lorentzian line shape response as a function of frequency. As the distance between the dipole and the nanoshell becomes greater, the influence of the broad dipole mode in the Purcell factor increases, leading to a Fano resonance.

In Fig. 19.9, we compare  $\Gamma_{\text{rad}}^\perp$  and  $\Gamma_{\text{rad}}^\parallel$  for  $\Delta r = 40$  nm. Both profiles present Fano line shapes, with Fano asymmetry parameters  $q_P^\perp$  and  $q_P^\parallel$  with opposite sign. These Fano parameters are related to the unconventional Fano resonance in the scattering cross section  $\sigma_{\text{sca}}$ , where  $q_{\text{LM}} = \chi'_1(kb)/\psi'_1(kb)$  for  $\ell = 1$ . In particular, observe in Fig. 19.9 that the fitted Fano curves are better for low frequencies (large wavelengths). Assuming the dipole approximation, i.e.,  $kr \ll 1$  and  $kb \ll 1$ , we obtain

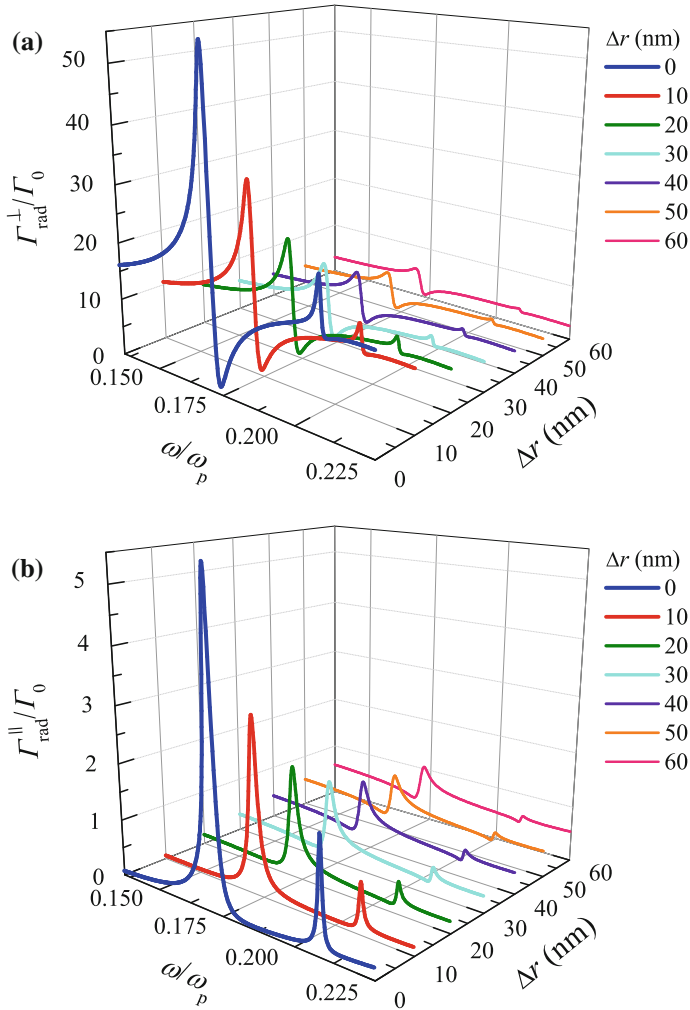


**Fig. 19.8** Radiative decay rates  $\Gamma_{\text{rad}}$  of a dipole emitter near a (Si) core-shell (Ag) nanoparticle as a function of the light emission frequency  $\omega$ . We consider several distances  $\Delta r$  between emitter and coated sphere, which has inner radius  $a = 60$  nm and outer radius  $b = 90$  nm. **a** The plot shows the radiative decay rate  $\Gamma_{\text{rad}}^{\perp}$  of a dipole emitter with orthogonal orientation in relation to the spherical shell. For  $\omega \approx 0.170\omega_p$  (dipole scattering resonance) and  $\omega \approx 0.208\omega_p$  (quadrupole scattering resonance), one has asymmetric Fano line shapes irrespective of the distance  $\Delta r$ . **b** The plot shows  $\Gamma_{\text{rad}}^{\parallel}$  of a dipole emitter with tangential orientation in relation to the spherical surface. For  $\Delta r \approx 0$ , one has symmetric Lorentzian line shapes. From  $\Delta r > 10$  nm, these Lorentzian line shapes change to Fano line shapes

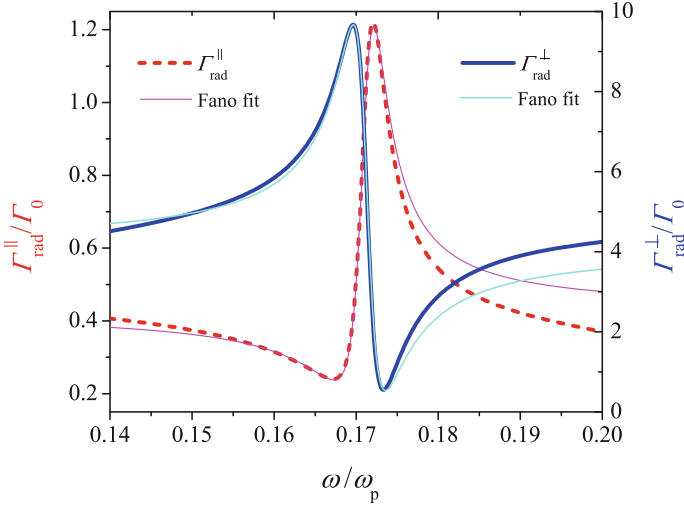


**Fig. 19.9** Radiative decay rates related to an optical emitter located at  $\Delta r = 40$  nm from a (Si) core-shell (Ag) nanoparticle with inner radius  $a = 60$  nm and outer radius  $b = 90$  nm. Both orthogonal ( $\Gamma_{\text{rad}}^{\perp}$ ) and parallel ( $\Gamma_{\text{rad}}^{\parallel}$ ) orientations of the electric dipole moment  $\mathbf{d}_0$  in relation to the spherical surface present a Fano resonance around  $\omega \approx 0.170\omega_p$ , where  $\omega_p$  is the Ag plasmon frequency. The corresponding Fano asymmetry parameters of the Purcell factors are  $q_P^{\perp} \approx -1.2$  and  $q_P^{\parallel} \approx 2.0$

$$\frac{\Gamma_{\text{rad}}^{\perp(\parallel)}(\omega)}{\Gamma_0} \approx F_1^{\perp(\parallel)} \left\{ \frac{\left[ \frac{\zeta'(\omega)}{\zeta''(\omega) + 1} + q_P^{\perp(\parallel)} \right]^2 + \left[ \frac{\zeta''(\omega)}{\zeta''(\omega) + 1} \right]^2}{\left[ \frac{\zeta'(\omega)}{\zeta''(\omega) + 1} \right]^2 + 1} \right\}, \quad (19.47)$$

where the prefactors for the two electric dipole orientations are

$$F_1^{\perp} = \frac{9 [j_1(kr')q_{\text{LM}} + y_1(kr')]^2}{(kr')^2(1 + q_{\text{LM}}^2)}, \quad (19.48)$$

$$F_1^{\parallel} = \frac{9 [\psi_1'(kr')q_{\text{LM}} - \chi_1'(kr')]^2}{4(kr')^2(1 + q_{\text{LM}}^2)}, \quad (19.49)$$

the corresponding Fano asymmetry parameters are

$$q_P^{\perp} = \frac{1}{1 + \zeta''(\omega)} \left[ \frac{y_1(kr')q_{\text{LM}} - j_1(kr')}{j_1(kr')q_{\text{LM}} + y_1(kr')} \right], \quad (19.50)$$

$$q_P^{\parallel} = -\frac{1}{1 + \zeta''(\omega)} \left[ \frac{\chi_1'(kr')q_{\text{LM}} + \psi_1'(kr')}{\psi_1'(kr')q_{\text{LM}} - \chi_1'(kr')} \right], \quad (19.51)$$

where  $\zeta(\omega)$  is defined in (19.26) and  $r' = b + \Delta r$ .

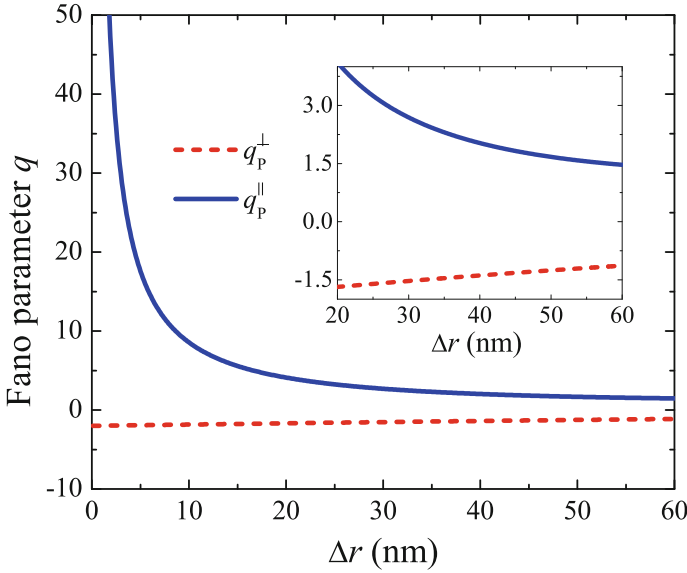


**Fig. 19.10** Fano asymmetry parameters associated with the Purcell factor of an optical emitter in the vicinity of a (Si) core-shell (Ag) nanoparticle with light emission frequency  $\omega = 0.170\omega_p$  (dipole scattering resonance). The coated sphere has inner radius  $a = 60$  nm and outer radius  $b = 90$  nm. The Fano parameters  $q_P^\perp$  and  $q_P^\parallel$  are calculated from (19.50) and (19.51) as a function of the distance  $\Delta r$  between emitter and spherical surface. For the electric dipole moment  $\mathbf{d}_0$  oriented tangential to the spherical surface, we have  $q_P^\parallel \rightarrow \infty$  as  $\Delta r \rightarrow 0$ . The inset shows that  $q_P^\parallel$  is finite for  $\Delta r > 20$  nm and has opposite sign in relation to  $q_P^\perp$ . These curves can be used to fit the plots in Fig. 19.8

From (19.47)–(19.51), it becomes clear that only  $|q_P^\parallel| \rightarrow \infty$  when  $r' \rightarrow b$ , which leads to a Lorentzian line shape in the near field for  $\Gamma_{\text{rad}}^\parallel$ . This fact is shown explicitly in Fig. 19.10, where we plot the corresponding Fano parameters that fit the plots in Fig. 19.8 by using (19.50) and (19.51). In particular, it is worth mentioning that (19.50) and (19.51) can be easily generalized to an arbitrary  $\ell$ , since they are not approximate expressions.

## 19.4 Conclusion

Based on the complete Lorenz-Mie theory, we have investigated the role of Fano resonances in plasmonic core-shell spheres and their influence on the spontaneous-emission rate of optical emitters in close proximity of a nanoshell. We have briefly discussed the appearance of conventional and unconventional Fano resonances in the light scattering by single-layered spheres. Both resonances arise from the interference between electromagnetic modes excited in the particle and can be associated with



the off-resonance field enhancement and saddle points in the energy flow around the particle. For an optical emitter with dipole moment oriented tangentially to a plasmonic nanoshell, we have obtained a symmetric Lorentzian line shape response in the near field that changes into a Fano resonance in the far field, with Fano asymmetry parameter of opposite sign compared to the dipole moment oriented normally to the spherical surface. This effect has been explained by the different role played by the induced electric dipole moment in the plasmonic nanoshell for both dipole moment orientations. More importantly, we have unveiled the relation between Fano resonances in light scattering and the Purcell effect. These analytical results shed light on a fundamental problem of Fano-like resonances in nanoplasmonics, and they may have interesting applications for enhancing and controlling the light emission and absorption of optical dipole emitters near metal-based nanostructures.

**Acknowledgements** The authors thank John Weiner for the fruitful collaboration, discussions and suggestions to improve this study. T.J.A., R.B., and Ph.W.C. acknowledge São Paulo Research Foundation (FAPESP) (Grant Nos. 2015/21194-3, 2014/01491-0, and 2013/04162-5, respectively) for financial support. A.S.M. holds grants from Conselho Nacional de Desenvolvimento Científico e Tecnológico (CNPq) (Grant No. 307948/2014-5). F.A.P. acknowledges The Royal Society-Newton Advanced Fellowship (Grant No. NA150208), Coordenação de Aperfeiçoamento de Pessoal de Nível Superior (CAPES) (Grant No. BEX 1497/14-6), Fundação Carlos Chagas Filho de Amparo à Pesquisa do Estado do Rio de Janeiro (FAPERJ) (Grant No. APQ1-210.611/2016), and CNPq (Grant No. 303286/2013-0) for financial support. S.S. is supported by the Fulbright-Cottrell Award.

## References

1. U. Fano, Effects of configuration interaction on intensities and phase shifts. *Phys. Rev.* **124**, 1866–1878 (1961)
2. A.E. Miroshnichenko, S. Flach, Y.S. Kivshar, Fano resonances in nanoscale structures. *Rev. Mod. Phys.* **82**, 2257–2298 (2010)
3. C.L. Garrido Alzar, M.A.G., Martinez, P. Nussenzveig, Classical analog of electromagnetically induced transparency. *Am. J. Phys.* **70**, 37–41 (2002)
4. C. Stehle, C. Zimmermann, S. Slama, Cooperative coupling of ultracold atoms and surface plasmons. *Nat. Phys.* **10**, 937–942 (2014)
5. B. Luk'yanchuk, N.I. Zheludev, S.A. Maier, N.J. Halas, P. Nordlander, H. Giessen, C.T. Chong, The Fano resonance in plasmonic nanostructures and metamaterials. *Nat. Mater.* **9**, 707–715 (2010)
6. M.I. Tribelsky, A.E. Miroshnichenko, Y.S. Kivshar, Unconventional Fano resonances in light scattering by small particles. *Europhys. Lett.* **97**, 44005 (2012)
7. T.J. Arruda, A.S. Martinez, F.A. Pinheiro, Unconventional Fano effect and off-resonance field enhancement in plasmonic coated spheres. *Phys. Rev. A* **87**, 043841 (2013)
8. H.L. Chen, L. Gao, Tunability of the unconventional Fano resonances in coated nanowires with radial anisotropy. *Opt. Express* **21**, 23619–23630 (2013)
9. B.S. Luk'yanchuk, A.E. Miroshnichenko, Y.S. Kivshar, Fano resonances and topological optics: an interplay of far- and near-field interference phenomena. *J. Opt.* **15**, 073001 (2013)
10. F. Monticone, C. Argyropoulos, A. Alù, Multilayered plasmonic covers for comblike scattering response and optical tagging. *Phys. Rev. Lett.* **110**, 113901 (2013)
11. J. Zhang, A. Zayats, Multiple Fano resonances in single-layer nonconcentric core-shell nanostructures. *Opt. Express* **21**, 8426–8436 (2013)

12. J. Sancho-Parramon, D. Jelovina, Boosting Fano resonances in single layered concentric core-shell particles. *Nanoscale* **6**, 13555–13564 (2014)
13. M.V. Rybin, K.B. Samusev, I.S. Sinev, G. Semouchkin, E. Semouchkina, Y.S. Kivshar, M.F. Limonov, Mie scattering as a cascade of Fano resonances. *Opt. Express* **21**, 30107–30113 (2013)
14. T.J. Arruda, A.S. Martinez, F.A. Pinheiro, Tunable multiple Fano resonances in magnetic single-layered core-shell particles. *Phys. Rev. A* **92**, 023835 (2015)
15. M.I. Tribelsky, A.E. Miroshnichenko, Giant in-particle field concentration and Fano resonances at light scattering by high-refractive-index particles. *Phys. Rev. A* **93**, 053837 (2016)
16. T.J. Arruda, R. Bachelard, J. Weiner, S. Slama, PhW Courteille, Fano resonances and fluorescence enhancement of a dipole emitter near a plasmonic nanoshell. *Phys. Rev. A* **96**, 043869 (2017)
17. M. Kerker, D.-S. Wang, H. Chew, Surface enhanced Raman scattering (SERS) by molecules adsorbed at spherical particles: errata. *App. Opt.* **19**, 4159–4174 (1980)
18. H. Chew, Transition rates of atoms near spherical surfaces. *J. Chem. Phys.* **87**, 1355–1360 (1987)
19. V.V. Klimov, Spontaneous emission of an excited atom placed near a ‘left-handed’ sphere. *Opt. Comm.* **211**, 183–196 (2002)
20. A. Delga, J. Feist, J. Bravo-Abad, F.J. Garcia-Vidal, Quantum emitters near a metal nanoparticle: strong coupling and quenching. *Phys. Rev. Lett.* **112**, 253601 (2014)
21. V.M. Pastukhov, Y.V. Vladimirova, V.N. Zadkov, Photon-number statistics from resonance fluorescence of a two-level atom near a plasmonic nanoparticle. *Phys. Rev. A* **90**, 063831 (2014)
22. V.V. Datsyuk, Ultimate enhancement of the local density of electromagnetic states outside an absorbing sphere. *Phys. Rev. A* **75**, 043820 (2007)
23. D. Szilard, W.J.M. Kort-Kamp, F.S.S. Rosa, F.A. Pinheiro, C. Farina, Purcell effect at the percolation transition. *Phys. Rev. B* **94**, 134204 (2016)
24. D. Lu, J.J. Kan, E.E. Fullerton, Z. Liu, Enhancing spontaneous emission rates of molecules using nanopatterned multilayer hyperbolic metamaterials. *Nat. Nanotechnol.* **9**, 48–53 (2014)
25. W.J.M. Kort-Kamp, F.S.S. Rosa, F.A. Pinheiro, C. Farina, Spontaneous emission in the presence of a spherical plasmonic metamaterial. *Phys. Rev. A* **87**, 023837 (2013)
26. M. Morshed Behbahani, E. Amooghorban, A. Mahdifar, Spontaneous emission and the operation of invisibility cloaks. *Phys. Rev. A* **94**, 013854 (2016)
27. A.E. Krasnok, A.P. Slobozhanyuk, C.R. Simovski, S.A. Tretyakov, A.N. Poddubny, A.E. Miroshnichenko, Y.S. Kivshar, P.A. Belov, An antenna model for the Purcell effect. *Sci. Rep.* **5**, 12956 (2015)
28. C.F. Bohren, D.R. Huffman, *Absorption and Scattering of Light by Small Particles* (Wiley, New York, 1983)
29. L.V. Lorenz, Lysbevaegelsen i og uden for en af plane Lysbolger belyst Kugle. *K. Dan. Vidensk. Selsk. Skr.* **6**, 1–62 (1890)
30. G. Mie, Beiträge zur Optik trüber Medien speziell kolloidaler Goldlösungen. *Ann. Phys.* **25**, 377–445 (1908)
31. A.L. Aden, M. Kerker, Scattering of electromagnetic waves from two concentric spheres. *J. Appl. Phys.* **22**, 1242–1246 (1951)
32. A. Alù, N. Engheta, Achieving transparency with plasmonic and metamaterial coatings. *Phys. Rev. E* **72**, 016623 (2005)
33. M.V. Rybin, D.S. Filonov, P.A. Belov, Y.S. Kivshar, M.F. Limonov, Switching from visibility to invisibility via Fano resonances: theory and experiment. *Sci. Rep.* **5**, 8774 (2015)
34. W. Liu, A.E. Miroshnichenko, R.F. Oulton, D.N. Neshev, O. Hess, Y.S. Kivshar, Scattering of core-shell nanowires with the interference of electric and magnetic resonances. *Opt. Lett.* **38**, 2621–2624 (2013)
35. T.J. Arruda, A.S. Martinez, F.A. Pinheiro, Electromagnetic energy and negative asymmetry parameters in coated magneto-optical cylinders: applications to tunable light transport in disordered systems. *Phys. Rev. A* **94**, 033825 (2016)

36. S. Mukherjee, H. Sobhani, J.B. Lassiter, R. Bardhan, P. Nordlander, N.J. Halas, Fanoshells: nanoparticles with built-in Fano resonances. *Nano Lett.* **10**, 2694–2701 (2010)
37. E. Prodan, C. Radloff, N.J. Halas, P. Nordlander, A hybridization model for the plasmon response of complex nanostructures. *Science* **302**, 419–422 (2003)
38. T.J. Arruda, F.A. Pinheiro, A.S. Martinez, Electromagnetic energy within single-resonance chiral metamaterial spheres. *J. Opt. Soc. Am. A* **30**, 1205–1212 (2013)
39. T.J. Arruda, F.A. Pinheiro, A.S. Martinez, Electromagnetic energy within coated spheres containing dispersive metamaterials. *J. Opt.* **14**, 065101 (2012)
40. T.J. Arruda, A.S. Martinez, Electromagnetic energy within a magnetic sphere. *J. Opt. Soc. Am. A* **27**, 992–1001 (2010)
41. Z.S. Wu, Y.P. Wang, Electromagnetic scattering for multilayered sphere: recursive algorithms. *Rad. Sci.* **26**, 1393–1401 (1991)
42. T. Kaiser, S. Lange, G. Schweiger, Structural resonances in a coated sphere: investigation of the volume-averaged source function and resonance positions. *Appl. Opt.* **33**, 7789–7797 (1994)
43. P.B. Johnson, R.W. Christy, Optical constants of the noble metals. *Phys. Rev. B* **6**, 4370–4379 (1972)
44. P.R. West, S. Ishii, G.V. Naik, N.K. Emani, V.M. Shalaev, A. Boltasseva, Searching for better plasmonic materials. *Laser Photon. Rev.* **4**, 795–808 (2010)
45. Z. Ruan, S. Fan, Temporal coupled-mode theory for Fano resonance in light scattering by a single obstacle. *J. Phys. Chem. C* **114**, 7324–7329 (2010)
46. T.J. Arruda, A.S. Martinez, Electromagnetic energy within a magnetic infinite cylinder and scattering properties for oblique incidence. *J. Opt. Soc. Am. A* **27**, 1679–1687 (2010)
47. A.E. Miroshnichenko, Off-resonance field enhancement by spherical nanoshells. *Phys. Rev. A* **81**, 053818 (2010)
48. T.J. Arruda, A.S. Martinez, F.A. Pinheiro, Omnidirectional absorption and off-resonance field enhancement in dielectric cylinders coated with graphene layers. *J. Opt. Soc. Am. A* **32**, 943–948 (2015)
49. T.J. Arruda, F.A. Pinheiro, A.S. Martinez, Electromagnetic energy stored in inhomogeneous scattering systems. *J. Opt. Soc. Am. A* **34**, 1934–1939 (2017)
50. R. Carminati, A. Caze, D. Cao, F. Peragut, V. Krachmalnicoff, R. Pierrat, Y. De Wilde, Electromagnetic density of states in complex plasmonic systems. *Surf. Sci. Rep.* **70**, 1–41 (2015)
51. E.M. Purcell, Spontaneous emission probabilities at radio frequencies. *Phys. Rev.* **69**, 681 (1946)
52. K.H. Drexhage, Influence of a dielectric interface on fluorescence decay time. *J. Luminesc.* **1**(2), 693–701 (1970)
53. R.R. Chance, A.H. Miller, A. Prock, R. Silbey, Fluorescence and energy transfer near interfaces: the complete and quantitative description of the  $\text{Eu}^{+3}$ / mirror systems. *J. Chem. Phys.* **63**, 1589–1595 (1975)
54. P. Anger, P. Bharadwaj, L. Novotny, Enhancement and quenching of single-molecule fluorescence. *Phys. Rev. Lett.* **96**, 113002 (2006)
55. J.M. Wylie, J.E. Sipe, Quantum electrodynamics near an interface. *Phys. Rev. A* **30**, 1185–1193 (1984)
56. V. Klimov, M. Ducloy, V.S. Letokhov, Radiative frequency shift and linewidth of an atom dipole in the vicinity of a dielectric microsphere. *J. Mod. Opt.* **43**, 2251–2267 (1996)
57. G. D’Aguanno, N. Mattiucci, M. Centini, M. Scalora, M.J. Bloemer, Electromagnetic density of modes for a finite-size three-dimensional structure. *Phys. Rev. E* **69**, 057601 (2004)
58. Y.V. Vladimirova, V.V. Klimov, V.M. Pastukhov, V.N. Zadkov, Modification of two-level-atom resonance fluorescence near a plasmonic nanostructure. *Phys. Rev. A* **85**, 053408 (2012)
59. R. Ruppin, Decay of an excited molecule near a small metal sphere. *J. Chem. Phys.* **76**, 1681–1684 (1982)
60. P.W. Milonni, *The Quantum Vacuum. An Introduction to Quantum Electrodynamics.* (Academic, San Diego, 1994)
61. H.T. Dung, L. Knoll, D.-G. Welsch, Decay of an excited atom near an absorbing microsphere. *Phys. Rev. A* **64**, 013804 (2001)

62. V. Klimov, M. Ducloy, V.S. Letokhov, Spontaneous emission rate and level shift of an atom inside a dielectric microsphere. *J. Mod. Opt.* **43**, 549–563 (1996)
63. D.V. Guzatov, S.V. Vaschenko, V.V. Stankevich, A.Ya. Lunevich, Y.F. Glukhov, S.V. Gaponenko, Plasmonic enhancement of molecular fluorescence near silver nanoparticles: theory, modeling, and experiment. *J. Phys. Chem. C* **116**, 10723–10733 (2012)
64. G. Colas des Francs, A. Bouhelier, E. Finot, J.C. Weeber, A. Dereux, C. Girard, E. Dujardin, Fluorescence relaxation in the near-field of a mesoscopic metallic particle: distance dependence and role of plasmon modes. *Opt. Express* **16**, 17654–17666 (2008)
65. P. Reineck, D. Gomez, S.H. Ng, M. Karg, T. Bell, P. Mulvaney, U. Bach, Distance and wavelength dependent quenching of molecular fluorescence by Au@SiO core-shell nanoparticles. *ACS Nano* **7**, 6636–6648 (2013)
66. T.J. Arruda, A.S. Martinez, F.A. Pinheiro, Electromagnetic energy within coated cylinders at oblique incidence and applications to graphene coatings. *J. Opt. Soc. Am. A* **31**, 1811–1819 (2014)

# Chapter 20

## Fano Resonances in Light Scattering by Finite Obstacles



Andrey Miroschnichenko

**Abstract** Light scattering by finite obstacles, either a single particle or a number of particles in arbitrary configuration, exhibits various resonant effects. It turns out that almost any resonant response, either in directional or total light scattering, can be efficiently described in terms of Fano resonance. One of the peculiar features of the Fano resonance is complete destructive interference, which can be associated with radiationless excitations, such as nontrivial anapole modes.

### 20.1 Introduction

Fano resonance is a universal phenomenon appearing in many fields of physics where wave interference is permitted. Originally, it was introduced to describe the quantum-mechanical interaction between discrete and continuous states [1]. In atomic physics it was used to describe the interference of discrete transitions degenerate with the autoionization continuum. One of the essential features of the Fano resonance is constructive and destructive interferences taking place in a narrow frequency range resulting in asymmetric lineshape [2]. In nuclear physics, for example, the same phenomenon is known as Breit-Wigner or Feshbach resonances [3]. Moreover, Bhatia and Temkin unified the approaches by Fano and Feshbach and gave a derivation of the Fano lineshape by means of Feshbach's projection-operator formalism [4, 5]. In low dimensional semiconductors the degeneracy of discrete and continuum states usually stems from bound excitons and scattering states and the quantum-mechanical coupling is mediated by the Coulomb interaction, including quantum wells and quantum wires [6], bulk semiconductors and superlattices in a magnetic field [7–9]. Fano resonances have been found also in the transport properties of time-periodic potentials [10].

---

A. Miroschnichenko (✉)  
School of Engineering and Information Technology,  
University of New South Wales, Canberra 2600, Australia  
e-mail: andrey.miroschnichenko@unsw.edu.au

Although, the concept of the Fano resonance is quite simple and intuitive, it remains a challenging task for both theoreticians and experimentalists. Despite the existence of the elegant Fano formulae and possibility to fit of, virtually, arbitrary spectra, the main difficulty is to explicitly identify two interfering states and show their mutual coupling. In this Chapter we will study the appearance and origin of the Fano resonance in light scattering by individual and aggregates of nanoparticles.

Light scattering by a finite obstacle can be unequally described in terms of partial wave scattering coefficients, based on multipolar decomposition [11]. Various multipoles can interfere in a given direction either in phase or out-of-phase producing asymmetric line shape, which can be associated with the Fano profile [12, 13]. Such feature can be employed to design effective optical nanoantennas [14, 15].

Alternatively, due to partial waves orthogonality each scattering coefficient can be analysed independently. It turns out that high index dielectric particles exhibit infinite series of sharp asymmetric Fano resonance in any given partial wave scattering [16–18], including complete suppression of scattering [19]. To explain their origin and identify various contributions to destructive interference we analyze the properties of induced field inside dielectric particle by using Cartesian multipoles. In particular, the first zero of the electric dipole partial wave can be described in terms of excitation of anapole state [20], which is a result of destructive interference electric and toroidal dipole moments in the far-field due to their identical radiation profiles [21–24].

It can also be considered as an example of localized source excitation, which produces no radiation in the far-field. It now suggests that higher-order zeros of any partial wave scattering can be treated as nontrivial radiationless localised sources. To describe them properly in terms of Fano resonances one needs to introduce higher-order toroidal multipoles.

## 20.2 Analysis of the Scattered Field

In light scattering by a finite localised object the outside field can be considered as a superposition of incident excitation and induced scattered field produce by the object,  $\mathbf{E}_{\text{total}} = \mathbf{E}_{\text{inc}} + \mathbf{E}_{\text{sca}}$  (and similar for the magnetic field), due to linearity of the Maxwell's equations in the freespace. The incident excitation  $\mathbf{E}_{\text{inc}}$  can be of different origin, including planewave, dipole source, or various vector beams.

### 20.2.1 Scattering Coefficients

To analyse the properties of the induced scattered field  $\mathbf{E}_{\text{sca}}$ , one can employ the multipole decomposition methods. Taking into account that scattering objects are of the order of the incident wavelength or smaller  $D \leq \lambda$ , it is expected that only lower order multipoles will be dominant, simplifying the analysis. One of the convenient method is based on vector spherical harmonics due to their completeness and

orthogonality properties, meaning that arbitrary field can be uniquely decomposed into a series of partial waves. To do that, one needs to record the scattered field on a virtual sphere enclosing the scattering object and project it onto vector spherical harmonics. For an arbitrary object one can evaluate electric  $a_{l,m}$  and magnetic  $b_{l,m}$  scattering coefficients by using the following expressions [25]

$$\begin{aligned}
 a_{l,m} &= C_l \int_0^{2\pi} \int_0^\pi Y_{l,m}^*(\theta, \phi) \mathbf{r} \cdot \mathbf{E}_{\text{sca}} \sin \theta d\theta d\phi \\
 b_{l,m} &= i\eta C_l \int_0^{2\pi} \int_0^\pi Y_{l,m}^*(\theta, \phi) \mathbf{r} \cdot \mathbf{H}_{\text{sca}} \sin \theta d\theta d\phi \\
 C_l &= \frac{(-i)^{l+1} k}{h_l^{(1)}(kr) E_0 \sqrt{\pi(2l+1)l(l+1)}},
 \end{aligned} \tag{20.1}$$

where  $Y_{l,m}$  are the scalar spherical harmonics of order  $(l, m)$ ,  $h_l^{(1)}(\rho)$  is spherical Hankel function describing an outgoing spherical wave,  $k = 2\pi/\lambda$  is the wavenumber of the incident wave,  $E_0$  is the amplitude of the incident field, and  $\eta$  is freespace impedance. It is worthwhile to mention that exactly the same scattering coefficients can be calculated via volumetric integrals of the induced currents inside the object. Moreover, such a method was implemented in commercial numerical solver COMSOL Multiphysics and is available as an add-on [26].

In the case of planewave scattering by a spherical particle, analytical expressions for the scattering coefficients are known, based on the Mie solution [11]

$$a_l^{\text{Mie}} \equiv a_{l,1} = -a_{l,-1} = \frac{m\psi_l(mx)\psi_l'(x) - \psi_l(x)\psi_l'(mx)}{m\psi_l(mx)\xi_l'(x) - \xi_l(x)\psi_l'(mx)} \tag{20.2}$$

$$b_l^{\text{Mie}} \equiv b_{l,1} = b_{l,-1} = \frac{m\psi_l(x)\psi_l'(mx) - \psi_l(mx)\psi_l'(x)}{m\xi_l(x)\psi_l'(mx) - \psi_l(mx)\xi_l'(x)}, \tag{20.3}$$

where  $x = 2\pi R/\lambda$  is the size parameter of the sphere of radius  $R$ ;  $m = \sqrt{\epsilon}$  is the relative refractive index,  $\psi_l(z)$ ,  $\xi_l(z) = \psi_l(z) - i\chi_l(z)$ ,  $\psi_l(z) = zj_l(z)$  and  $\chi_l(z) = -zy_l(z)$  are the Riccati-Bessel functions;  $j_l(z)$ ,  $y_l(z)$  stand for the spherical Bessel functions;  $' \equiv \partial/\partial z$  designates derivative with respect to the entire argument. All other scattering coefficients with  $|m| > 1$  vanish identically. Despite the fact that the Mie solution was obtained more than 100 years ago, it serves as an indispensable tool in analysing and revealing key properties of light scattering till nowadays, including the Fano resonance response, which will be discussed below.

By knowing the coefficients  $a_{l,m}$  and  $b_{l,m}$  the scattered far-field can be reconstructed as a superposition of partial waves [25]

$$\mathbf{H}_{\text{sca}}^{FF} \rightarrow \frac{e^{ikr-i\omega t}}{kr} \sum_{l,m} i^{l-1} \sqrt{\pi(2l+1)} [a_{l,m} \mathbf{X}_{l,m} + i b_{l,m} \mathbf{n} \times \mathbf{X}_{l,m}] \quad (20.4)$$

$$\mathbf{E}_{\text{sca}}^{FF} \rightarrow \eta \mathbf{H}_{\text{sca}}^{FF} \times \mathbf{n},$$

where  $\mathbf{n} = \mathbf{r}/r$  is a unit vector in the radial direction and

$$\mathbf{X}_{l,m} = -\frac{m}{\sqrt{l(l+1)} \sin \theta} Y_{l,m} \hat{\boldsymbol{\theta}} - \frac{i}{\sqrt{l(l+1)}} \frac{\partial Y_{l,m}}{\partial \theta} \hat{\boldsymbol{\phi}} \quad (20.5)$$

are vector spherical harmonics. The time-averaged power radiated per unit solid angle is

$$\frac{dP}{d\Omega} = \frac{\eta}{2k^2} \left| \sum_{l,m} i^{l-1} \sqrt{\pi(2l+1)} [a_{l,m} \mathbf{X}_{l,m} + i b_{l,m} \mathbf{n} \times \mathbf{X}_{l,m}] \right|^2. \quad (20.6)$$

It is also possible to introduce the scattering cross section, that describes the efficiency with which the particle removes the energy from the incident field into the scattered one, by integrating the radiated power over the full solid angle. Based on orthogonality of vector spherical harmonics, the total scattering cross section becomes

$$C_{\text{sca}} = \frac{\pi}{k^2} \sum_{l,m} (2l+1) [|a_{l,m}|^2 + |b_{l,m}|^2]. \quad (20.7)$$

The energy conservation constrain implies that the scattering coefficients are bounded from above with the absolute maximum value of unity,  $|a_{l,m}|, |b_{l,m}| \leq 1$ .

### 20.2.2 Parity and Mirror Symmetries of the Spherical Harmonics

When the scattering object can generate more than one spherical harmonics, they can interfere in the far-field zone. To get a better insight into this process, it is important to understand some symmetry properties of the spherical harmonics. It is known that both scalar and vector spherical harmonics obey the following relations [27]

$$Y_{l,-m} = (-1)^m Y_{l,m}^*, \quad \mathbf{X}_{l,-m} = (-1)^m \mathbf{X}_{l,m}^* \quad (20.8)$$

which implies that real and imaginary parts of a spherical harmonic either symmetric or anti-symmetric upon reflection in  $x-z$  plane, depending on number  $m$ . If, for example, the object is symmetric with respect to  $x-z$  plane then the scattering coefficients will exhibit the same relation due to (20.1).



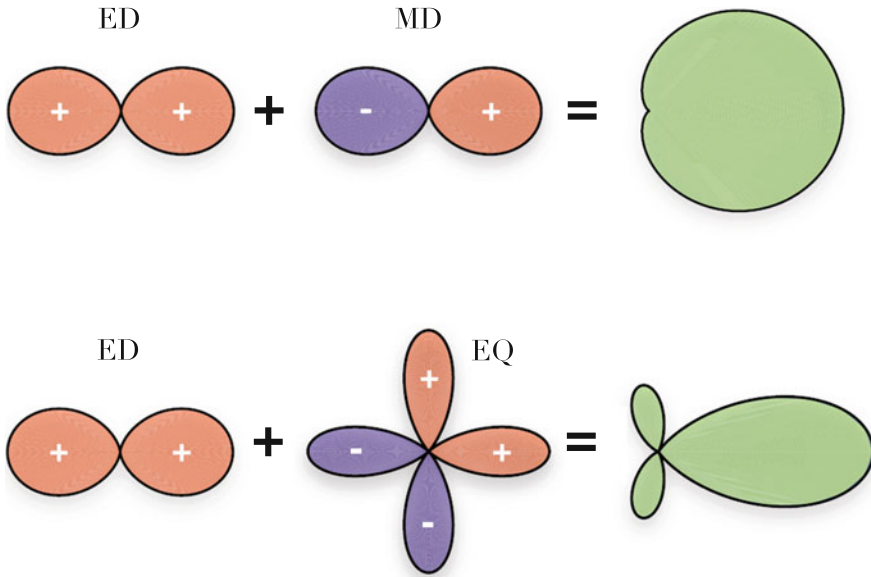


**Fig. 20.1** Schematic illustration of the directional interference of different multipoles with opposite parity (top) electric dipole (ED) with magnetic dipole (MD); and (bottom) electric dipole with electric quadrupole (EQ), showing various scenario when the backward scattering can be completely suppressed

In addition to this, spherical harmonics have definite parity—under spacial inversion ( $\mathbf{r} \rightarrow -\mathbf{r}$  or  $(\theta, \phi) \rightarrow (\pi - \theta, \pi + \phi)$ ) they transform as

$$Y_{l,m}(-\mathbf{r}) = (-1)^l Y_{l,m}(\mathbf{r}), \quad \mathbf{X}_{l,m}(-\mathbf{r}) = (-1)^l \mathbf{X}_{l,m}(\mathbf{r}) \quad (20.9)$$

It allows us to determine the parity of a multipole field. Thus, based on the expressions (20.4), one can see that the parity of fields of an electric multipole of order  $(l, m)$  is  $(-1)^l$ . Specifically, the magnetic field has parity  $(-1)^l$ , while the electric field has parity  $(-1)^{l+1}$ . On contrary, a magnetic multipole of order  $(l, m)$  has the parity  $(-1)^{l+1}$ . In this case, the parity of the magnetic field is changed to  $(-1)^{l+1}$ , while the electric field has the parity  $(-1)^l$ .

It implies, that if there are two electric and magnetic multipoles of the same order  $(l, m)$ , the corresponding electric fields will have different parities  $(-1)^{l+1}$  and  $(-1)^l$ , respectively. Thus, if they interfere constructively in one direction at the same time they interfere destructively in the opposite direction, resulting in unidirectional scattering. The same effect can be achieved by using two electric (or magnetic) multipoles of different orders  $(l, m)$  and  $(l + 1, m)$  (see Fig. 20.1).

### 20.2.3 Forward and Backward Scattering

The scattered power in arbitrary direction is given by (20.6). Among all directions, forward and backward scattering are, usually, of crucial importance in various applications. Assuming that the direction of the incident wave propagation is along  $\hat{\mathbf{z}}$  axis, the forward scattering is characterised by  $\theta = 0$  and  $\phi = 0$ , and backward scattering by  $\theta = \pi$  and  $\phi = 0$ . Using the properties of the scalar spherical harmonics  $Y_{l,m}(0, 0) = \delta_{m,0}\sqrt{\frac{2l+1}{4\pi}}$  and  $Y_{l,m}(\pi, 0) = (-1)^l\sqrt{\frac{2l+1}{4\pi}}\delta_{m,0}$ , and similarly for the derivatives  $\frac{\partial Y_{l,m}}{\partial \theta}(0, 0) = -m\sqrt{\frac{l(l+1)(2l+1)}{16\pi}}\delta_{|m|,1}$  and  $\frac{\partial Y_{l,m}}{\partial \theta}(\pi, 0) = m(-1)^{l+1}\sqrt{\frac{l(l+1)(2l+1)}{16\pi}}\delta_{|m|,1}$  together with the addition theorem the vector spherical harmonics can be simplified to

$$\mathbf{X}_{l,m}(0, 0) = \sqrt{\frac{2l+1}{16\pi}}\delta_{|m|,1}\{\hat{\boldsymbol{\theta}} + im\hat{\boldsymbol{\phi}}\} \quad (20.10)$$

$$\mathbf{n} \times \mathbf{X}_{l,m}(0, 0) = \sqrt{\frac{2l+1}{16\pi}}\delta_{|m|,1}\{-im\hat{\boldsymbol{\theta}} + \hat{\boldsymbol{\phi}}\} \quad (20.11)$$

$$\mathbf{X}_{l,m}(\pi, 0) = \sqrt{\frac{2l+1}{16\pi}}(-1)^{l+1}\delta_{|m|,1}\{\hat{\boldsymbol{\theta}} - im\hat{\boldsymbol{\phi}}\} \quad (20.12)$$

$$\mathbf{n} \times \mathbf{X}_{l,m}(\pi, 0) = \sqrt{\frac{2l+1}{16\pi}}(-1)^{l+1}\delta_{|m|,1}\{im\hat{\boldsymbol{\theta}} + \hat{\boldsymbol{\phi}}\} \quad (20.13)$$

As a result, one can now obtain the the expressions for the scattering in the forward

$$\frac{dP^F}{d\Omega} = \frac{\eta}{32k^2} \left| \sum_{l,|m|=1} i^{l-1}(2l+1)[a_{l,m} + mb_{l,m}]\{\hat{\boldsymbol{\theta}} + im\hat{\boldsymbol{\phi}}\} \right|^2. \quad (20.14)$$

and backward

$$\frac{dP^B}{d\Omega} = \frac{\eta}{32k^2} \left| \sum_{l,|m|=1} i^{l-1}(-1)^{l+1}(2l+1)[a_{l,m} - mb_{l,m}]\{\hat{\boldsymbol{\theta}} - im\hat{\boldsymbol{\phi}}\} \right|^2 \quad (20.15)$$

directions. It is interesting to note, that only modes with  $|m| = 1$  contribute to the forward/backward scattering and lead to interference in these two directions. These expressions can be further simplified in the case of the spherical particle [11]

$$C_{FS} = \frac{\pi}{k^2} \left| \sum_l (2l+1)(a_l^{\text{Mie}} + b_l^{\text{Mie}}) \right|^2 \quad (20.16)$$

$$C_{BS} = \frac{\pi}{k^2} \left| \sum_l (2l+1)(-1)^l (a_l^{\text{Mie}} - b_l^{\text{Mie}}) \right|^2 \quad (20.17)$$

where the variation of the signs clearly demonstrates the role of the parity in opposite directions for electric and magnetic multipoles discussed above (see Sect. 20.2.2).

## 20.3 Light Scattering by a Single Particle

Now we are in the position to analyse various resonant effects of light scattering by an arbitrary object. First, let's consider a subwavelength spherical particle made of a conventional material. It is known that the dominant contribution to the scattering will be an electric dipole one, and the total scattering cross section will exhibit fourth power dependence of frequency, also known as the Rayleigh scattering [11]. This dependence, actually, can be altered if unconventional materials with properly chosen permittivity and permeability are used [28]. This response works quite well below any resonances and the scattering pattern is described by a doughnut-type shape. Being the first non-negligible contribution (under planewave illumination), it is a common understanding that the electric dipole response is always present for an arbitrary scatterer. As we will see later, this is not always the case, and it is possible to suppress it completely. By increasing the particle radius or changing the refractive index various resonant effects can be observed.

### 20.3.1 Directional Fano Resonance

In the case of a plasmonic spherical particle by increasing the radius one can observe a certain hierarchy of resonances, starting from dipole, quadrupole, etc. [29]. At the dipole resonance all other contributions are still negligible, thus, the scattering profile is symmetric in all directions and resembles a doughnut shape profile. The situation changes in the vicinity of the electric quadrupole resonance, where the dipole contribution is important, and leads to a highly asymmetric scattering profile, due to interference of modes of different parities (see Sect. 20.2.2). Taking into account the fact that quadrupole resonances usually have much higher Q-factor we are dealing with a resonant interference phenomenon, which can be associated with the Fano resonance [30, 31]. Indeed, we are having all the essential ingredients here: the quadrupole mode is a resonant state and the dipole mode provides a nonresonant background. By passing through the resonance, the quadrupole mode exhibits  $\pi$ -phase modulation leading to constructive and destructive interference with

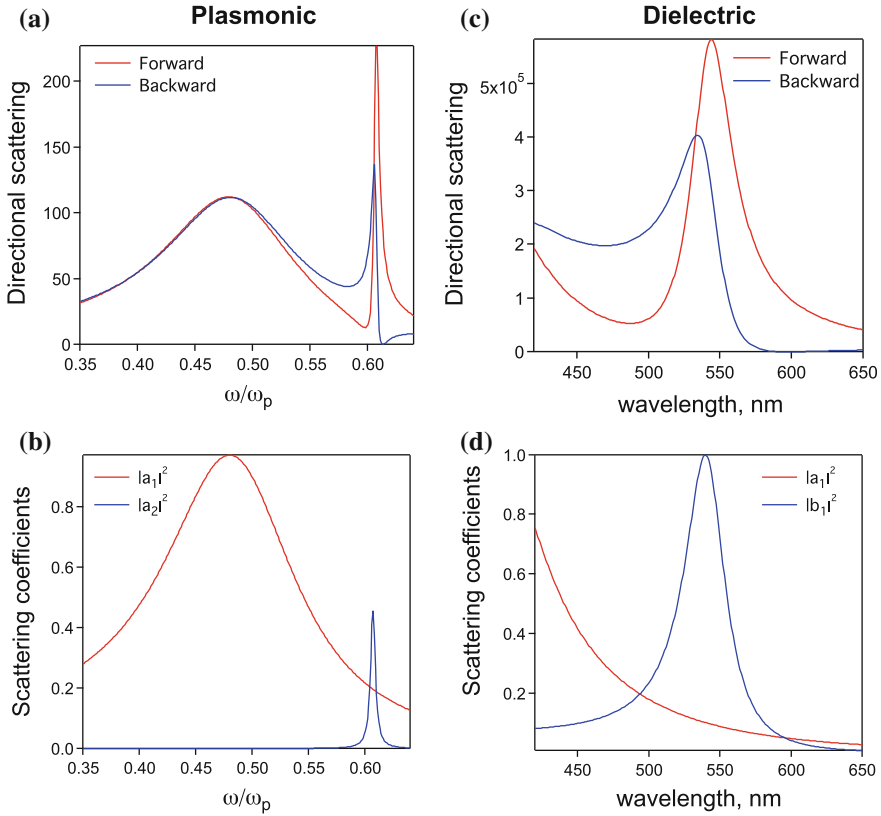


**Fig. 20.2** Directional Fano resonance in the case of plasmonic (a) and dielectric (c) particle. The plasmonic particle is described by the Drude model with  $\gamma = 10^{-3}\omega_p$  and the size parameter is equal to  $x = \omega_p R/c$ . The dielectric particle is described by the refractive index  $n = 4$  and of radius  $R = 65$  nm. The corresponding scattering coefficients leading to the directional Fano resonance are shown in panels (b) and (d), respectively

the dipole mode in certain directions. It can be easily observed, for example, in the forward and backward directions, which both exhibit Fano-type asymmetric profiles (see Fig. 20.2a)

$$C_{FS}^{plas} = \frac{9\pi}{k^2} \left| a_1^{Mie} + \frac{5}{3}a_2^{Mie} \right|^2 \tag{20.18}$$

$$C_{BS}^{plas} = \frac{9\pi}{k^2} \left| a_1^{Mie} - \frac{5}{3}a_2^{Mie} \right|^2 \tag{20.19}$$

The situation changes for high-index dielectric particles. Below any resonances the electric dipole mode is still dominant, but the first resonance will be excited at the magnetic dipole mode. Thus, one might expect the transformation of the scattering

profile, since the parity of the electric and magnetic dipoles is different. Similar expressions for the forward/backward scattering

$$\begin{aligned} C_{FS}^{\text{diel}} &= \frac{9\pi}{k^2} |(a_1^{\text{Mie}} + b_1^{\text{Mie}})|^2 \\ C_{BS}^{\text{diel}} &= \frac{9\pi}{k^2} |(a_1^{\text{Mie}} - b_1^{\text{Mie}})|^2 \end{aligned} \quad (20.20)$$

exhibit asymmetric Fano-type lineshapes in the vicinity of the magnetic dipole resonance (see Fig. 20.2c), where the electric dipole contribution plays the role of non-resonant background. Such variation of the scattering profile was recently observed experimentally for silicon nanoparticles. Importantly, the backward scattering from dielectric particles can completely vanish  $C_{BS}^{\text{diel}} = 0$ , which is known as the first Kerker's condition. It happens when both electric and magnetic scattering are in-phase and of the same strength  $a_1^{\text{Mie}} = b_1^{\text{Mie}}$ . It is analogous to the impedance matching condition and makes high-index dielectric particles the best candidate for optical nanoantennas, where even the simplest spherical particles can exhibit unidirectional scattering. The relative strength of the electric and magnetic dipoles contribution can be effectively controlled in core-shell structures. On contrary, the zero forward scattering can not be achieved, which would imply total zero scattering due to the optical theorem. Nevertheless, it is still possible to minimise it via destructive interference of several modes.

### 20.3.2 Vanishing Partial Wave Scattering and Anapole modes

It turns out, that high-index particles, in addition to magnetic modes, may support other interesting excitations, such as *nonradiating* modes [32]. To understand the possibility and conditions for such excitations, let's revisit the electric dipole response of a spherical particle by using Mie solution. When the particle is small compared to the incident wavelength, the field inside is almost constant and the scattering cross sections follows the Rayleigh dependency (see Fig. 20.3). But, when the particle becomes comparable or larger than the wavelength, one can observe very interesting (although quite strange at first glance) behaviour—vanishing of the electric dipole scattering  $a_1 = 0$  [20]. If in the same time one calculates the internal energy it will be nonzero, meaning, that there is some nontrivial excitation inside the particle. Due to orthogonality of the spherical harmonics and the fact that we are dealing with spherical particle there is no energy leakage to other multipoles, which implies that such an excitation doesn't radiate at all! Thus, we can not, for example, explain vanishing electric dipole scattering as an interference with other multipoles, since it will require scattering cancelation in *all* directions at once. But, the symmetry of various spherical harmonics are all different and such compensation is not possible. Unfortunately, we can not extract any further information on the properties of that excitation based on the Mie theory. We do need to analyse now what is actually

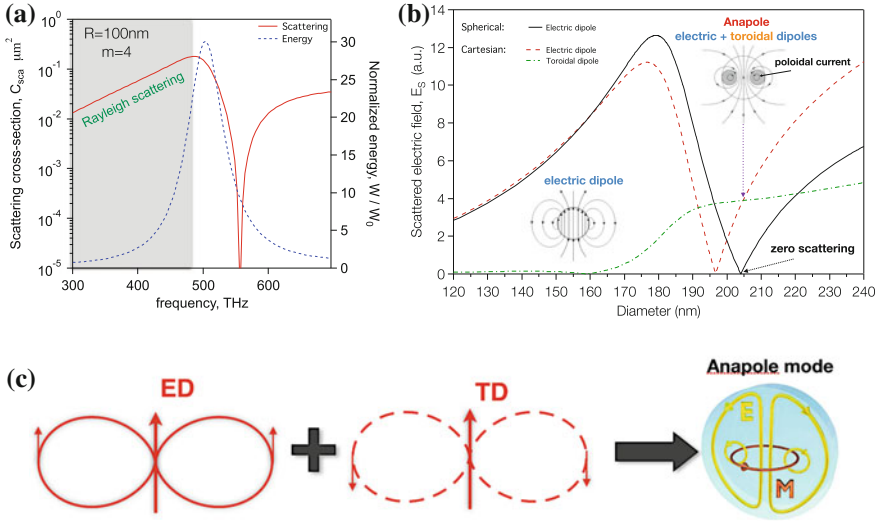


**Fig. 20.3** Example of vanishing of the total electric dipole scattering (a) and nontrivial contributions of Cartesian electric and toroidal dipole contributions (b). Panel (c) schematically illustrates the formation of the anapole state as the destructive field interference of electric and toroidal dipoles in the far-field

excited inside the particle. To do that we can employ alternative description based on Cartesian multipoles. Usually, to describe the electric dipole response one calculates so-called electric dipole moment [27]

$$\mathbf{P} = \frac{i}{\omega} \int \mathbf{J} dV, \tag{20.21}$$

which is, basically, the averaged induced displacement current  $\mathbf{J} = -i\omega\epsilon_0(n^2 - 1)\mathbf{E}_{sph}$  inside the particle. But, it turns out that for high-index particle it produces overestimated scattering cross section

$$C_{sca}^{\mathbf{P}} = \frac{\mu_0\omega^4}{12\pi^2 R^2 c} |\mathbf{P}|^2, \tag{20.22}$$

which is larger than the total one. It implies, that there should be an additional contribution. Recently, there were a lot interest in so-called toroidal dipole moments [33]

$$\mathbf{T} = \frac{1}{10c} \int (\mathbf{r} \cdot \mathbf{J})\mathbf{r} - 2r^2 \mathbf{J} dV, \quad C_{sca}^{\mathbf{T}} = \frac{\mu_0\omega^4 k^2}{12\pi^2 R^2 c} |\mathbf{T}|^2, \tag{20.23}$$

which have the same symmetry of the scattered field as the electric dipole. Thus, their mutual destructive interference in the far-field can lead to complete scattering cancelation and vanishing of the total electric dipole contribution. It now suggests

that the total scattered field should be written as a superposition of two contributions  $\mathbf{E}_{\text{sca}} \approx \mathbf{P} + ik\mathbf{T}$ , and zero scattering  $\mathbf{E}_{\text{sca}} = 0$  occurs when electric and toroidal dipoles scatter light out-of-phase  $\mathbf{P} = -ik\mathbf{T}$ . Indeed, if we calculate both contributions for a single spherical particle, then zero electric dipole scattering will match with the crossing of both contributions (see Fig. 20.3). Such nonradiating configuration is also known as an *anapole*. It has a number of interesting features and can be used to design near-field laser [34], high efficiency harmonic generation [35], or to achieve pure magnetic dipole scattering without admixture of other components under planewave illumination [36] and many other exciting applications [19].

### 20.3.3 Fano Profile of the Scattering Coefficients

By looking more closely at the total electric dipole scattering profile (see Fig. 20.3) one might notice its quite familiar highly asymmetric shape accompanied by a resonant suppression of the scattering, associated with the anapole mode discussed above (see Sect. 20.3.2). Is it a coincidence or there is a deeper reasoning that any scattering coefficient exhibit Fano-type profile? If yes, how can one identify resonant and nonresonant contributions, then? Below, using just a general form for an arbitrary scattering coefficient, we will show that, indeed, it can be described *exactly* in terms of the Fano profile [37]. To start with, due to energy conservation requirement, any scattering coefficient can be written in the following form

$$S = (a_{lm}, b_{lm}) \equiv \frac{F}{F + iG}, \quad (20.24)$$

which implies that  $|S| \leq 1$  for arbitrary values of  $F$  and  $G$ . Then, let us introduce an angle  $\Delta$  according to the expression

$$\tan \Delta \equiv \frac{F}{G}. \quad (20.25)$$

In this case the scattering coefficient  $S$  can be written as

$$S = \frac{\tan \Delta}{\tan \Delta + i} = -ie^{i\Delta} \sin \Delta. \quad (20.26)$$

It turns out, that in this form one can interpret the angle  $\Delta$  and a phase shift, similar to quantum mechanical approach.

The trick now is to decompose this phase shift onto two components, corresponding to two scattering processes. The first one is the scattering by a PEC object of the same geometry, when the field does not penetrate inside and describes the background nonresonant scattering. The second one is the resonant scattering due to excitation of a resonant mode inside the particle. Thus, it permits us to write

$$\Delta \equiv \Delta^{(\text{PEC})} + \Delta^{(\text{res})}, \quad (20.27)$$

and use the simple math to obtain the relation between the total phase shift and each contribution

$$\tan \Delta \equiv \tan(\Delta^{(\text{res})} + \Delta^{(\text{PEC})}) = \frac{\tan \Delta^{(\text{res})} + \tan \Delta^{(\text{PEC})}}{1 - \tan \Delta^{(\text{res})} \tan \Delta^{(\text{PEC})}}. \quad (20.28)$$

If now we introduce the notations

$$\epsilon \equiv -\cot \Delta^{(\text{res})}, \quad q \equiv -\cot \Delta^{(\text{PEC})}, \quad (20.29)$$

the expression for a generic scattering coefficient  $S$  may be rewritten as follows

$$S = \frac{\epsilon + q}{\epsilon + q - i(\epsilon q - 1)}. \quad (20.30)$$

or, alternatively, as

$$|S|^2 = \frac{(\epsilon + q)^2}{(1 + q^2)(1 + \epsilon^2)}. \quad (20.31)$$

which is the conventional Fano profile, normalized to its maximal value [2]. Moreover, one can assign a physical meaning to the introduced notations above (20.29) where  $q$  is the asymmetry parameter and  $\epsilon$  is the normalised resonant energy. What is surprising here is that, in general, the resonant response of an arbitrary scattering coefficient should be described in terms of the Fano resonance, where the background contribution is associated with the scattering induced by a particle shape only (without penetration) and resonant response originates from the excitation of the internal mode of the particle. At the same time, it suggests an alternative description of the scattering cancellation discussed above (see Sect. 20.3.2).

### 20.3.3.1 Case of a Spherical Particle

For a spherical particle one can obtain the expressions for the asymmetry parameter  $q$  and normalised energy  $\epsilon$  in a closed form. Let's take, for example, electric dipole component. It is usually derived from the boundary condition, which can be written in the following form

$$a_1^{\text{Mie}} = a_1^{\text{PEC}} - g_1, \quad a_1^{\text{PEC}} = \frac{\psi_1'(x)}{\xi_1'(x)}, \quad g_1 = a_1^{\text{Mie}} \frac{\psi_1'(mx)}{n\xi_1'(x)} \quad (20.32)$$

where  $g_1$  is the normalized resonant internal electric dipole coefficient [11], and  $a_1^{\text{PEC}}$  is the electric dipole scattering coefficient by a PEC sphere. Then, the background



phase shift  $\Delta^{(\text{PEC})}$  related to the asymmetric parameter  $q$  can be obtained as

$$\tan \Delta^{(\text{PEC})} \equiv \frac{F^{(\text{PEC})}}{G^{(\text{PEC})}} = -\frac{\psi'_1(x)}{\chi'_1(x)} = -\frac{1}{q}, \tag{20.33}$$

After some algebra based on (20.28) it also is possible to obtain the expression for  $\Delta^{(\text{res})}$

$$\tan \Delta^{(\text{res})} = -\frac{\psi'_1(mx)}{F^{(\text{PEC})} F^{(\text{Mie})} + G^{(\text{PEC})} G^{(\text{Mie})}}, \tag{20.34}$$

$$F^{(\text{Mie})} = m\psi'_1(x)\psi_1(mx) - \psi_1(x)\psi'_1(mx), \tag{20.35}$$

$$G^{(\text{Mie})} = -m\chi'_1(x)\psi_1(mx) + \chi_1(x)\psi'_1(mx), \tag{20.36}$$

By exploring the dependency of the electric dipole scattering coefficient  $a_1^{\text{Mie}}$  on the size parameter  $x$ , one can observe that it exhibits an infinite number of resonances, and each of them has an asymmetric profile. The analytically calculated

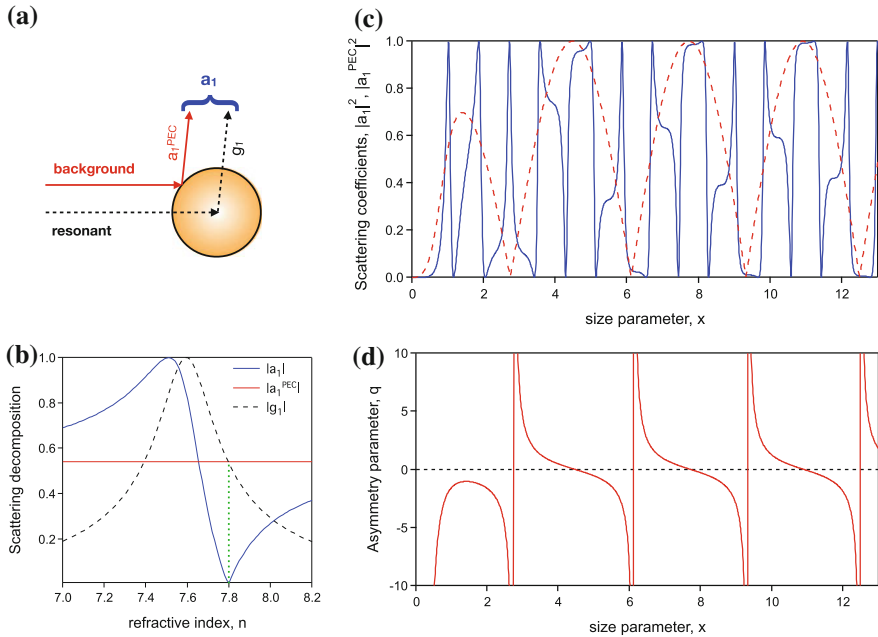


**Fig. 20.4** **a** Illustration of the origin of two scattering contributions resulting in the Fano resonance for any given partial wave. **b** Decomposition of the electric dipole scattering coefficient into background (PEC) and resonant contributions for size parameter  $x = 1$ . **c** Variation of the electric dipole scattering coefficients versus size parameter for a spherical particle with the refractive index  $n = 4$ . **d** Corresponding dependence of the asymmetric Fano parameter  $q$  (20.33)

asymmetry parameter  $q$  describes the Fano lineshape in the vicinity each resonance (see Fig. 20.4).

The presented approach is quite general and can be applied to any scattering coefficient, revealing the origin and importance of the Fano resonance in all scattering processes.

## 20.4 Fano Resonance in *Oligomer* nanostructures

So far we have considered the Fano resonance supported by a single particle. It mostly manifests itself in the asymmetric directional scattering or resonant suppression of a partial wave scattering, associated with nonradiating type sources. But, the observed Q-factor was not so high, which limits the potential applications. Recently, there were a lot of interest in so-called *oligomers* [38–40]—a finite configuration of nanoparticles with rotational symmetry. It turns out that such structures can support high-Q Fano resonances, which might be use for sensing and harmonic generation due to strong near-field enhancement [41–51].

### 20.4.1 *Linear Response*

Initially, the Fano resonance was observed for plasmonic structures [52]. They usually consist of an identical finite number of particles in a ring and an additional particle at the centre of a different size. The origin of the Fano resonance depends on the materials of the particles. In the case of plasmonic nanoparticles it is usually described in terms of near-field hybridisation of so-called super- and sub-radiant modes, which lead to the far-field destructive interference [53–57]. Resonant response of each plasmonic particle is due to electric type localised surface plasmon resonances, which strongly depend on the material of the nanoparticle. The near-field enhancement at the resonance is located in the gap between the particles, which makes them very sensitive to the environment. Thus, the position and spectral lineshape can be strongly affected by the separation of the particles and optical properties of the outside media. It makes them one of the best candidates for the sensing applications with relatively high FOM. In addition to this, in some plasmonic oligomers strong magnetic dipole excitation was observed [58] (Fig. 20.5).

In the case of high-index dielectric materials the origin of the Fano resonance is a bit different. As it was mentioned above, the fundamental resonance of a sub-wavelength dielectric particle is the magnetic dipole, which linearly depends on the nanoparticle dimensions. When the size of the central particle is different to the outer ring particles, their resonances are spectrally shifted. Thus, the Fano resonance emerges as the destructive interference between the resonant response of the central particle, while the particles on the outer ring provide with the nonresonant background scattering [48]. Since the field is mostly localised inside the particles, they

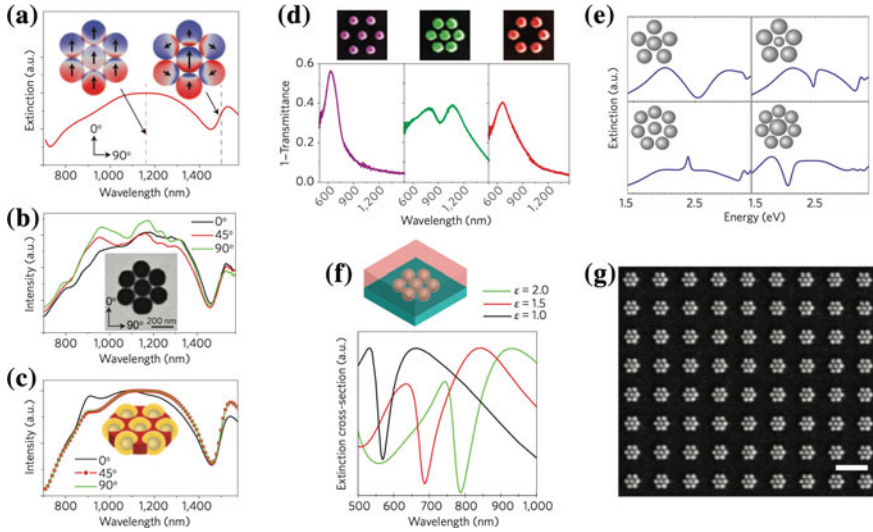


**Fig. 20.5** **a** Calculated dipole amplitudes of the bonding and antibonding collective dipolar plasmon modes in a gold nanoshell heptamer. **b**, **c** Measured (**b**) and calculated (**c**) scattering spectra of a gold nanoshell heptamer. **d** Transmission spectra showing the effects of coupling in lithographically fabricated gold nanodisk heptamers. **e** Extinction spectra showing how the Fano resonance in silver nanosphere hexamers and octumers depend on the size of the central particle. **f** Effect of a surrounding dielectric medium on the extinction spectrum of a silver nanosphere heptamer. **g** Example of a large-scale substrate consisting of lithographically fabricated gold nanodisk heptamers. Scale bar: 1  $\mu\text{m}$ . Reprinted from [13]

are less sensitive to the distance between them, in contrast to the plasmonic counterpart. Nevertheless, it does exhibit strong sensitivity to the refractive index of the environment [43, 44]. Another interesting example is a quadrumer, consisting of four dielectric particles in a square. In such a structure one might observe the interaction between the collective optically induced magnetic response of the quadrumer and the individual magnetic responses of constituent dielectric nanoparticles, leading in a sharp magnetic-magnetic Fano resonance [59] (Fig. 20.6).

It should be mentioned, that the optical response of oligomer type structures can be effectively described by using coupled-dipoles approximation [48, 60]. In the case of plasmonic particles it is usually enough to consider coupled electric dipoles only, while in the case high-index nanoparticles both magnetic and electric dipoles should be taken into account. Moreover, by employing the group theory analysis it can be rigorously proven that oligomers with rotational symmetry should exhibit polarisation independent response under normal incidence [45], which makes them optically isotropic. Interesting enough, all integral characteristics, including extinction, scattering and absorption cross sections do not depend on the incident polarisation, despite the fact that near-field distribution does vary with the polarisation [61]. It was experimentally checked for both plasmonic structures in the visible range [51] and dielectric ones in the MW range [62].

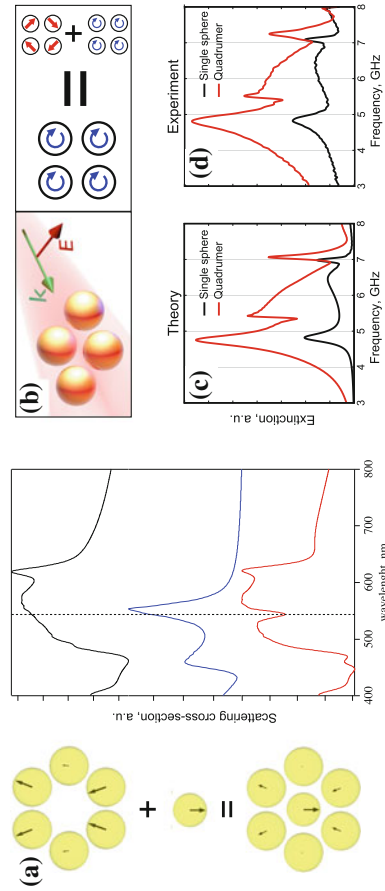


**Fig. 20.6** a Demonstration of the Fano resonance in all-dielectric oligomers made of high-index nanoparticles, which originates from the destructive interference of the resonant response of the central particle and background nonresonant contribution from the outer ring particles [48]. b Magnetic-magnetic Fano resonance in dielectric quadrumers due to resonant interference of collective and individual magnetic dipole excitations [59]

Another related comment, is that the coupled-dipole approximation for many particles can be considered in analogy with the discrete-dipole approximation of a single object. From this perspective, a finite configuration of subwavelength particles can be treated as an “effective” single particle. Then, it allows to interpret the resonant suppression of the total scattering of oligomer-type structures in terms of nonradiating excitations and anapole modes of a single scatterer. The peculiarity of high-index dielectric oligomers is that we are dealing mostly with magnetic dipole response. Thus, it suggests that such structures may support so-called *magnetic anapoles*, which, actually, were recently discussed [24].

### 20.4.2 Chiral Structures and Optical Activity

So far, we have discussed optical response of linearly polarised incident light. It was mentioned that if a structure possesses the rotational symmetry then it should exhibit polarisation independent isotropic response for all cross sections. The situation changes if circular polarised light will be used. It is known, that extinction cross section is a linear response function. Meaning that if we consider two independent excitations of different polarisations, then the response under simultaneous excitation will be a mere superposition of two independent responses. On another hand, the circular polarised light can be considered as a superposition of two orthogonally linearly polarised excitations with a phase shift. Thus, one might expect that extinction cross section should maintain its polarisation independency even for circularly polarised excitation for structures with the rotational symmetry. But, both scattering and absorption cross sections exhibit nonlinear response, which implies that superposition principle is not applicable, in general. As a result, the response for circular polarisation will be different compared to the linear polarisation, or even left and right polarisation. Indeed, it was suggested and recently demonstrated that plasmonic oligomers with rotational but broken mirror symmetries exhibit strong optical dichroism in the vicinity of the Fano resonance [63, 64] (see Fig. 20.7). Despite the fact that the total extinction cross section is the same for both left and right polarisations, both scattering and absorption cross section vary a lot, which can be important in various nonlinear processes [50]. Thus, such planar structure exhibit strong variation in the absorption depending on the incident polarisation, which is related to so-called planar chiral response. It is interesting to note, that if instead of lossy plasmonic structure we would consider lossless dielectric one there will be no optical dichroism, since in this case the absorption cross section will be identically zero and scattering cross section will be equal to extinction, which is polarisation independent. But, the corresponding resonant mode still might be quite different for both excitations, which require further analysis.

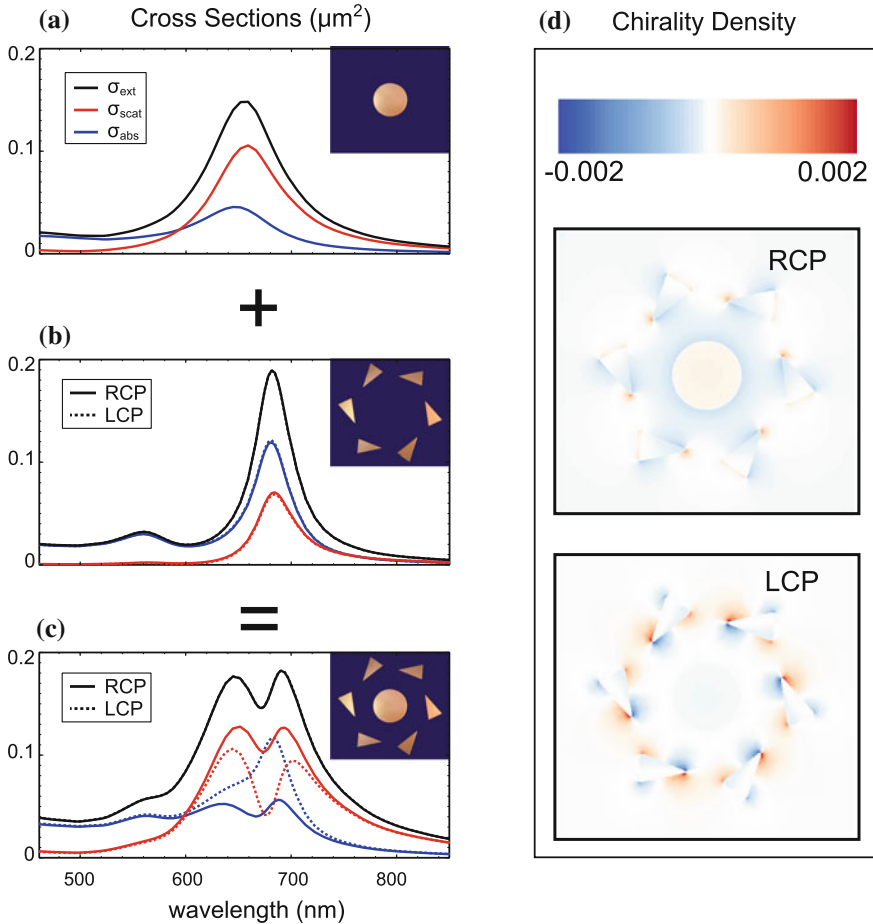


**Fig. 20.7** Simulations demonstrating the role of interference for inducing circular dichroism in the absorption cross section of a planar chiral heptamer. The significant circular dichroism in absorption is observed in the vicinity of the Fano resonance. On the right hand side, the circular dichroism is shown as the magnitude of the near-field chirality density at the Fano resonance [63]

### 20.4.3 Harmonic Generation

Most of high-index materials also possess strong nonlinear response. Thus, at the resonances associated with the strong near-field enhancement inside the particle one might expect various enhance nonlinear effects. Recently, there several demonstrations of second and third harmonic generations in all-dielectric single particles [65], oligomers [66], and metasurfaces [67]. The highest efficiency was observed in the vicinity of magnetic dipole resonances, which exhibit larger mode volume, compared to electric ones. Despite the fact that bulk silicon has an inversion symmetry, finite

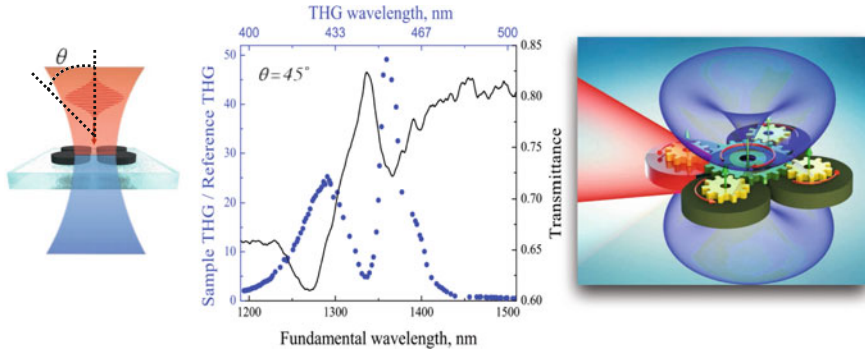


**Fig. 20.8** Third harmonic generation (THG) spectroscopy of dielectric quadrumers showing experimental transmission (black line) and THG (blue dots) spectra under oblique incidence at the angle  $\theta = 45^\circ$  [66]

structures still exhibit relatively strong second harmonic generation, which might be associated not only with surface effects, but also with higher order nonlinear terms due to near-field inhomogeneity. There are also some attempts to identify nonlinear processes due to enhanced magnetic near-field, which might lead to a completely new area of *magnetic nonlinearity* in the visible frequency range.

Another interesting aspect of high-index nanoparticles is that they can support nonradiating anapole states, associated with the Fano resonance (see Sect. 20.3.2). In this case, the scattering at the fundamental frequency can be completely suppressed, resulting in ultra high efficiency of the harmonic generation, which was recently demonstrated [35, 68]. Another typical examples is the magnetic-magnetic Fano resonance in the silicon quadramer, discussed above (see Sect. 20.4.1), where the nontrivial wavelength and angular dependencies of the generated harmonic signal featuring a multifold enhancement of the nonlinear response was observed [66] (Fig. 20.8).

## 20.5 Conclusions

Fano resonance plays a key role in various wave type phenomena, and can be considered as a resonant interference effect. We have demonstrated that it naturally appears in partial wave scattering, which can be used to describe the optical response of an arbitrary finite scattering object or objects. The most generic profile of any scattering coefficient can be described *exactly* in the terms of the Fano formulae (see Sect. 20.3.3), which implies that even isolated partial wave scattering can be decomposed into more than one interfering components. This conclusion is very nontrivial and in some sense even counter-intuitive, taking into account the completeness and orthogonality vector spherical harmonics. We have tried to elucidate this point and

provided at least several alternative descriptions, which allow to shed a light onto this feature and explicitly identified various resonant and nonresonant contributions leading to the Fano type response. In its turn it leads to a number of interesting effects in both linear and nonlinear regimes, including excitation nonradiating anapole modes and high efficiency harmonic generation in the nonlinear materials.

## References

1. U. Fano, Effects of configuration interaction on intensities and phase shifts. *Phys. Rev.* **124**(6), 1866–1878 (1961)
2. A.E. Miroshnichenko, S. Flach, Y.S. Kivshar, Fano resonances in nanoscale structures. *Rev. Modern Phys.* **82**(3), 2257–2298 (2010)
3. G. Breit, E. Wigner, Capture of slow neutrons. *Phys. Rev.* **49**, 519–531 (1936)
4. A.K. Bhatia, A. Temkin, Line-shape parameters for  $^1p$  feshbach resonances in he and  $li^+$ . *Phys. Rev. A* **29**, 1895–1900 (1984)
5. A. Temkin, A.K. Bhatia, *Theory and Calculation of Resonances and Autoionization of Two-electron Atoms and Ions* (Springer, US, Boston, MA, 1985), pp. 1–34
6. W.T. Masselink, P.J. Pearah, J. Klem, C.K. Peng, H. Morkoç, G.D. Sanders, Y.-C. Chang, Absorption coefficients and exciton oscillator strengths in AlGaAs-GaAs superlattices. *Phys. Rev. B* **32**, 8027–8034 (1985)
7. S. Bar-Ad, P. Kner, M.V. Marquezini, S. Mukamel, D.S. Chemla, Quantum confined fano interference. *Phys. Rev. Lett.* **78**, 1363–1366 (1997)
8. V. Bellani, E. PÁrez, S. Zimmermann, L. Viña, R. Hey, K. Ploog, Evolution of fano resonances in two- and three-dimensional semiconductors with a magnetic field. *Solid State Commun.* **97**(6), 459–464 (1996)
9. S. Glutsch, P. Lefebvre, D.S. Chemla, Optical absorption of type-ii superlattices. *Phys. Rev. B* **55**, 15786–15790 (1997)
10. A.A. Clerk, X. Waintal, P.W. Brouwer, Fano resonances as a probe of phase coherence in quantum dots. *Phys. Rev. Lett.* **86**, 4636–4639 (2001)
11. C.F. Bohren, D.R. Huffman, *Absorption and Scattering of Light by Small Particles* (Wiley, 1998)
12. B.S. Luk'yanchuk, A.E. Miroshnichenko, Y.S. Kivshar, Fano resonances and topological optics: an interplay of far- and near-field interference phenomena. *J. Opt.* **15**, 073001 (2013)
13. B. Luk'yanchuk, N.I. Zheludev, S.A. Maier, N.J. Halas, P. Nordlander, H. Giessen, C.T. Chong, The Fano resonance in plasmonic nanostructures and metamaterials. *Nat. Mater.* **9**(9), 707–715 (2010)
14. B. Garcia-Camara, J.F. Algorri, A. Cuadrado, V. Urruchi, J.M. Sanchez-Pena, R. Serna, R. Vergaz, All-optical nanometric switch based on the directional scattering of semiconductor nanoparticles. *J. Phys. Chem. C* **119**(33), 19558–19564 (2015)
15. J. Yan, P. Liu, Z. Lin, H. Wang, H. Chen, C. Wang, G. Yang, Directional Fano resonance in a silicon nano sphere dimer. *ACS Nano* **9**(3), 2968–2980 (2015)
16. M.F. Limonov, M.V. Rybin, A.N. Poddubny, Y.S. Kivshar, Fano resonances in photonics. *Nat. Photonics* **11**(9), 543–554 (2017)
17. M.V. Rybin, D.S. Filonov, P.A. Belov, Y.S. Kivshar, M.F. Limonov, Switching from visibility to invisibility via Fano resonances: theory and experiment. *Sci. Rep.* **5**, 8774 (2015)
18. M.V. Rybin, K.B. Samusev, I.S. Sinev, G. Semouchkin, E. Semouchkina, Y.S. Kivshar, M.F. Limonov, Mie scattering as a cascade of Fano resonances. *Opt. Express* **21**(24), 30107–30113 (2013)
19. B. Luk'yanchuk, R. Paniagua-Dominguez, A.I. Kuznetsov, A.E. Miroshnichenko, Y.S. Kivshar, Suppression of scattering for small dielectric particles: anapole mode and invisibility. *Phil. Trans. R. Soc. Math. Phys. Eng. Sci.* **375**, 2090 (2017)



20. A.E. Miroshnichenko, A.B. Evlyukhin, Y.F. Yu, R.M. Bakker, A. Chipouline, A.I. Kuznetsov, B. Luk'yanchuk, B.N. Chichkov, Y.S. Kivshar, Nonradiating anapole modes in dielectric nanoparticles. *Nat. Commun.* **6**, 8069 (2015)
21. W. Liu, B. Lei, J. Shi, H. Hu, A.E. Miroshnichenko, Elusive pure anapole excitation in homogeneous spherical nanoparticles with radial anisotropy. *J. Nanomater.* **2015**, 672957 (2015)
22. W. Liu, J. Shi, B. Lei, H. Hu, A.E. Miroshnichenko, Efficient excitation and tuning of toroidal dipoles within individual homogeneous nanoparticles. *Opt. Express* **23**(19), 24738–24747 (2015)
23. W. Liu, J. Zhang, B. Lei, H. Hu, A.E. Miroshnichenko, Invisible nanowires with interfering electric and toroidal dipoles. *Opt. Lett.* **40**(10), 2293–2296 (2015)
24. B. Luk'yanchuk, R. Paniagua-Dominguez, A.I. Kuznetsov, A.E. Miroshnichenko, Y.S. Kivshar, Hybrid anapole modes of high-index dielectric nanoparticles. *Phys. Rev. A* **95**, 063820 (2017)
25. P. Grahn, A. Shevchenko, M. Kaivola, Electromagnetic multipole theory for optical nanomaterials. *New J. Phys.* **14**(9), 093033–093112 (2012)
26. <https://www.comsol.com/model/multipole-analysis-of-electromagnetic-scattering-31901>
27. J.D. Jackson, *Classical electrodynamics* (Wiley, 1998)
28. A.E. Miroshnichenko, Non-Rayleigh limit of the Lorenz-Mie solution and suppression of scattering by spheres of negative refractive index. *Phys. Rev. A* **80**, 013808 (2009)
29. M.I. Tribelsky, B.S. Luk'yanchuk, Anomalous light scattering by small particles. *Phys. Rev. Lett.* **97**, 263902 (2006)
30. M.I. Tribelsky, Anomalous light absorption by small particles. *Europhys. Lett. (EPL)* **94**, 14004 (2011)
31. M.I. Tribelsky, S. Flach, A.E. Miroshnichenko, A.V. Gorbach, Y.S. Kivshar, Light scattering by a finite obstacle and Fano resonances. *Phys. Rev. Lett.* **100**, 043903 (2008)
32. G. Gbur, Nonradiating sources and other “invisible” objects. *Prog. Opt.* **45**, 273 (2003)
33. N. Papasimakis, V.A. Fedotov, V. Savinov, T.A. Raybould, N.I. Zheludev, Electromagnetic toroidal excitations in matter and free space. *Nat. Mater.* **15**(3), 263–271 (2016)
34. J.S.T. Gongora, A.E. Miroshnichenko, Y.S. Kivshar, A. Fratallocchi, Anapole nanolasers for mode-locking and ultrafast pulse generation. *Nat. Commun.* **8**, 15535 (2017)
35. T. Shibanuma, G. Grinblat, P. Albella, S.A. Maier, Efficient third harmonic generation from metal-dielectric hybrid nanoantennas. *Nano Lett.* **17**(4), 2647–2651 (2017)
36. T. Feng, Y. Xu, W. Zhang, A.E. Miroshnichenko, Ideal magnetic dipole scattering. *Phys. Rev. Lett.* **118**, 173901 (2017)
37. M.I. Tribelsky, A.E. Miroshnichenko, Giant in-particle field concentration and Fano resonances at light scattering by high-refractive-index particles. *Phys. Rev. A* **93**, 053837 (2016)
38. M. Hentschel, M. Saliba, R. Vogelgesang, H. Giessen, A.P. Alivisatos, N. Liu, Transition from isolated to collective modes in plasmonic oligomers. *Nano Lett.* **10**(7), 2721–2726 (2010)
39. J. Sancho-Parramon, S. Bosch, Dark modes and Fano resonances in plasmonic clusters excited by cylindrical vector beams. *ACS Nano* **6**(9), 8415–8423 (2012)
40. J. Ye, F. Wen, H. Sobhani, J.B. Lassiter, P. Van Dorpe, P. Nordlander, N.J. Halas, Plasmonic nanoclusters: near field properties of the Fano resonance interrogated with SERS. *Nano Lett.* **12**(3), 1660–1667 (2012)
41. D.-J. Cai, Y.-H. Huang, W.-J. Wang, W.-B. Ji, J.-D. Chen, Z.-H. Chen, S.-D. Liu, Fano resonances generated in a single dielectric homogeneous nanoparticle with high structural symmetry. *J. Phys. Chem. C* **119**(8), 4252–4260 (2015)
42. T. Cao, J. Bao, L. Mao, T. Zhang, A. Novitsky, M. Nieto-Vesperinas, C.-W. Qiu, Controlling lateral Fano interference optical force with Au-Ge<sub>2</sub>Sb<sub>2</sub>Te<sub>5</sub> hybrid nanostructure. *ACS Photonics* **3**(10), 1934–1942 (2016)
43. K.E. Chong, B. Hopkins, I. Staude, A.E. Miroshnichenko, J. Dominguez, M. Decker, D.N. Neshev, I. Brener, Y.S. Kivshar, Observation of Fano resonances in all-dielectric nanoparticle oligomers. *Small* **10**(10), 1985–1990 (2014)
44. K.E. Chong, H.W. Orton, I. Staude, M. Decker, A.E. Miroshnichenko, I. Brener, Y.S. Kivshar, D.N. Neshev, Refractive index sensing with Fano resonances in silicon oligomers. *Phil. Trans. R Soc. Math. Phys. Eng. Sci.* **375**(2017), 2090

45. B. Hopkins, D.S. Filonov, S.B. Glybovski, A.E. Miroshnichenko, Hybridization and the origin of Fano resonances in symmetric nanoparticle trimers. *Phys. Rev. B* **92**, 045433 (2015)
46. S. Lepeshov, A. Krasnok, I. Muldhin, D. Zuev, A. Gudovskikh, V. Milichko, P. Belov, A. Miroshnichenko, Fine-tuning of the magnetic Fano resonance in hybrid oligomers via fs-laser-induced reshaping. *ACS Photonics* **4**(3), 536–543 (2017)
47. S.-D. Liu, Y.-B. Yang, Z.-H. Chen, W.-J. Wang, H.-M. Fei, M.-J. Zhang, Y.-C. Wang, Excitation of multiple Fano resonances in plasmonic clusters with D-2h point group symmetry. *J. Phys. Chem. C* **117**(27), 14218–14228 (2013)
48. A.E. Miroshnichenko, Y.S. Kivshar, Fano resonances in all-dielectric oligomers. *Nano Lett.* **12**(12), 6459–6463 (2012)
49. M. Rahmani, B. Luk'yanchuk, M. Hong, Fano resonance in novel plasmonic nanostructures. *Laser Photonics Rev.* **7**(3), 329–349 (2013)
50. M. Rahmani, A.S. Shorokhov, B. Hopkins, A.E. Miroshnichenko, M.R. Shcherbakov, R. Camacho-Morales, A.A. Fedyanin, D.N. Neshev, Y.S. Kivshar, Nonlinear symmetry breaking in symmetric oligomers. *ACS Photonics* **4**(3), 454–461 (2017)
51. M. Rahmani, E. Yoxall, B. Hopkins, Y. Sonnefraud, Y. Kivshar, M. Hong, C. Phillips, S.A. Maier, A.E. Miroshnichenko, Plasmonic nanoclusters with rotational symmetry: polarization-invariant far-field response vs. changing near-field distribution. *ACS Nano* **7**(12), 11138–11146 (2013)
52. N.A. Mirin, K. Bao, P. Nordlander, Fano resonances in plasmonic nanoparticle aggregates. *J. Phys. Chem. A* **113**(16), 4028–4034 (2009)
53. T.J. Davis, D.E. Gomez, K.C. Vernon, Simple model for the hybridization of surface plasmon resonances in metallic nanoparticles. *Nano Lett.* **10**(7), 2618–2625 (2010)
54. F. Hao, P. Nordlander, Y. Sonnefraud, P.V. Dorpe, S.A. Maier, Tunability of subradiant dipolar and Fano-type plasmon resonances in metallic ring/disk cavities: implications for nanoscale optical sensing. *ACS Nano* **3**(3), 643–652 (2009)
55. T. Pakizeh, C. Langhammer, I. Zoric, P. Apell, M. Kall, Intrinsic Fano interference of localized plasmons in Pd nanoparticles. *Nano Lett.* **9**(2), 882–886 (2009)
56. Y. Sonnefraud, N. Verellen, H. Sobhani, G.A.E. Vandenbosch, V.V. Moshchalkov, P. Van Dorpe, P. Nordlander, S.A. Maier, Experimental realization of subradiant, superradiant, and Fano resonances in ring/disk plasmonic nanocavities. *ACS Nano* **4**(3), 1664–1670 (2010)
57. N. Verellen, Y. Sonnefraud, H. Sobhani, F. Hao, V.V. Moshchalkov, P. Van Dorpe, P. Nordlander, S.A. Maier, Fano resonances in individual coherent plasmonic nanocavities. *Nano Lett.* **9**(4), 1663–1667 (2009)
58. F. Shafiei, F. Monticone, K.Q. Le, X.-X. Liu, T. Hartseld, A. Alu, X. Li, A subwavelength plasmonic metamolecule exhibiting magnetic-based optical Fano resonance. *Nat. Nanotechnol.* **8**(2), 95–99 (2013)
59. B. Hopkins, D.S. Filonov, A.E. Miroshnichenko, F. Monticone, A. Alu, Y.S. Kivshar, Interplay of magnetic responses in all-dielectric oligomers to realize magnetic fano resonances. *ACS Photonics* **2**(6), 724–729 (2015)
60. B. Hopkins, A.N. Poddubny, A.E. Miroshnichenko, Y.S. Kivshar, Revisiting the physics of Fano resonances for nanoparticle oligomers. *Phys. Rev. A* **88**, 053819 (2013)
61. B. Hopkins, W. Liu, A.E. Miroshnichenko, Y.S. Kivshar, Optically isotropic responses induced by discrete rotational symmetry of nanoparticle clusters. *Nanoscale* **5**(14), 6395–6403 (2013)
62. D.S. Filonov, A.P. Slobozhanyuk, A.E. Krasnok, P.A. Belov, E.A. Nenasheva, B. Hopkins, A.E. Miroshnichenko, Y.S. Kivshar, Near-field mapping of Fano resonances in all-dielectric oligomers. *Appl. Phys. Lett.* **104**, 021104 (2014)
63. B. Hopkins, A.N. Poddubny, A.E. Miroshnichenko, Y.S. Kivshar, Circular dichroism induced by Fano resonances in planar chiral oligomers. *Laser Photonics Rev.* **10**(1), 137–146 (2016)
64. K.Q. Le, Fano-induced circular dichroism in three-dimensional plasmonic chiral metamolecules. *J. Electron. Mater.* **46**(10), 5577–5581 (2017)
65. M.R. Shcherbakov, D.N. Neshev, B. Hopkins, A.S. Shorokhov, I. Staude, E.V. Melik-Gaykazyan, M. Decker, A.A. Ezhov, A.E. Miroshnichenko, I. Brener, A.A. Fedyanin, Y.S. Kivshar, Enhanced third-harmonic generation in silicon nanoparticles driven by magnetic response. *Nano Lett.* **14**(11), 6488–6492 (2014)

66. A.S. Shorokhov, E.V. Melik-Gaykazyan, D.A. Smirnova, B. Hopkins, K.E. Chong, D.-Y. Choi, M.R. Shcherbakov, A.E. Miroshnichenko, D.N. Neshev, A.A. Fedyanin, Y.S. Kivshar, Multifold enhancement of third-harmonic generation in dielectric nanoparticles driven by magnetic Fano resonances. *Nano Lett.* **16**(8), 4857–4861 (2016)
67. O. Wolf, S. Campione, Y. Yang, I. Brener, Multipolar second harmonic generation in a symmetric nonlinear metamaterial. *Sci. Rep.* **7**, 8101 (2017)
68. G. Grinblat, Y. Li, M.P. Nielsen, R.F. Oulton, S.A. Maier, Enhanced third harmonic generation in single germanium nanodisks excited at the anapole mode, *Nano Lett.* **16**(7), 4635–4640 (2016)

# Chapter 21

## Tuning of Fano Resonance by Waveguide Rotation



### Wave Faucet and Bound States in the Continuum

Almas Sadreev, Artem S. Pilipchuk and Alina A. Pilipchuk

**Abstract** We consider acoustic wave transmission in a non-axisymmetric waveguide composed of a cylindrical resonator of radius  $R$  and length  $L$  and two cylindrical waveguides of radius  $r < R$ . The center lines of the waveguides are shifted relative to the center line of the resonator by a distance  $r_0$  and relative to each other by an azimuthal angle  $\Delta\phi$ . Under variation of  $L$  and fixed  $\Delta\phi$  we find bound states in the continuum (trapped modes) due to full destructive interference of resonant modes leaking into waveguides. Rotation by the angle  $\Delta\phi$  brings complex phases into the coupling strengths of the resonator eigenmodes with propagating modes of the waveguides. As the result interference of neighboring resonances strongly depends on rotation of the waveguide introducing novel way for tuning Fano resonances. In turn rotation of the input waveguide strongly affect the acoustic transmission through the resonator imitating a faucet in wave transmission. Under variation of  $\Delta\phi$  and fixed  $L$  we find symmetry protected trapped modes. For  $\Delta\phi \neq 0$  these trapped modes contribute to the scattering function supporting high vortical acoustic intensity spinning inside the resonator.

## 21.1 Introduction

Bound states in the continuum (BIC) are localized solutions which correspond to discrete eigenvalues coexisting with extended modes of continuous spectrum in resonator-waveguide configurations. The existence of such modes was first reported in [1] at the dawn of quantum mechanics. Since then bound state in the continuum (BIC) has been universally used to designate an BIC in quantum mechanics [2]. In the field of fluid mechanics, Parker [3, 4] is credited to be the first to encounter resonances of pure acoustic nature in air flow over a cascade of flat parallel plates. Nowadays, the BICs are known to exist in various waveguide structures [5–8]. The

---

A. Sadreev (✉) · A. S. Pilipchuk · A. A. Pilipchuk

*Present Address:* Kirensky Institute of Physics, Federal Research Center KSC SB RAS,  
660036 Krasnoyarsk, Russia  
e-mail: almas@tnp.krasn.ru

© Springer Nature Switzerland AG 2018

E. Kamenetskii et al. (eds.), *Fano Resonances in Optics and Microwaves*, Springer  
Series in Optical Sciences 219, [https://doi.org/10.1007/978-3-319-99731-5\\_21](https://doi.org/10.1007/978-3-319-99731-5_21)

497

BICs are of immense interest, especially, in optics thanks to experimental opportunity to confine light in optical microcavities despite that outgoing waves are allowed in the surrounding medium [9–14].

Independently considerable attention has been paid to the BICs in perturbed acoustic waveguides. Many different geometrical configurations with Neumann boundary conditions have been studied. These studies have shown that the existence of trapped modes is very sensitive to choice of geometry. Up to now geometrical configurations were chosen to reduce the effective dimension of the acoustic waveguide. Chronologically, the following specific perturbed acoustic waveguides were considered. In 1951 Ursell [15, 16] considered a sphere placed on the axis of a cylindrical guide and showed that a trapped mode exists for selected radius of the sphere. There is a long history of trapped modes bound below the channel cut-off in two- and three-dimensional nonuniform waveguides due to curvature of the waveguide or a localized bulge [17–20]. However the bound states with isolated discrete eigenvalue embedded in the continuous spectrum above the channel cut-off, BICs, are more unusual. Evans and Porter first provided convincing numerical evidence for BICs of both Neumann and Dirichlet type in the case of a rigid circular cylinder placed on the centre-plane between parallel walls [21]. Linton and McIver [22] proved the existence of an infinite number of trapped modes for the case of cylindrical waveguide containing an axisymmetric obstacle, in particular a thin circular sleeve.

Similarly, the dimension is reduced in acoustical waveguides of rectangular cross-section in  $y_0z$  plane and directed along the  $x$ -axis with obstacle shaped only in the  $x_0y$  plane so that the thickness of the perturbed waveguide along the  $z$ -axis  $d$  is constant. Then the scattering channels are given by the eigenmodes quantized along the  $z$ -axis with corresponding Neumann boundary conditions at the walls positioned at  $z = \pm d/2$ . The utmost case of these structures is a two-dimensional acoustical waveguide formed by two infinite parallel lines at distance  $d$  containing a circle of radius  $R < d$  [23] or multiple circles [24, 25] positioned symmetrically between them. The trapped modes are antisymmetric about the centreline of the guide to determine them as the symmetry protected BICs. More sophisticated BICs of the same symmetry as the symmetry of the continuum were demonstrated recently in [26–30].

A different class is the fully three-dimensional systems. For example, in the case of non-axisymmetric obstacle inside the cylindrical waveguide Hein and Coch [31] numerically computed acoustic resonances and BICs by solving the eigenvalue problem. Here we consider similar non-axisymmetric waveguide but without an obstacle inside as shown in Fig. 21.1. The axisymmetric case shown in Fig. 21.1a preserves the orbital angular momentum  $m$  because of the rotational symmetry around the central axis. That effectively reduces the dimension of the waveguide to two. The BICs with  $m = 0$  were shown to occur under variation of the length of the resonator [28] due to full destructive interference of resonant states [32]. An equivalent explication of the BICs is that under variation of the resonator length the eigenmodes  $\psi_1, \psi_2$  of the same symmetry as the symmetry of propagating modes of the waveguides become degenerate. Then the coupling of the superposed state  $a_1\psi_1 + a_2\psi_2$  with the continuum can be cancelled by a proper choice of the superposition coefficients

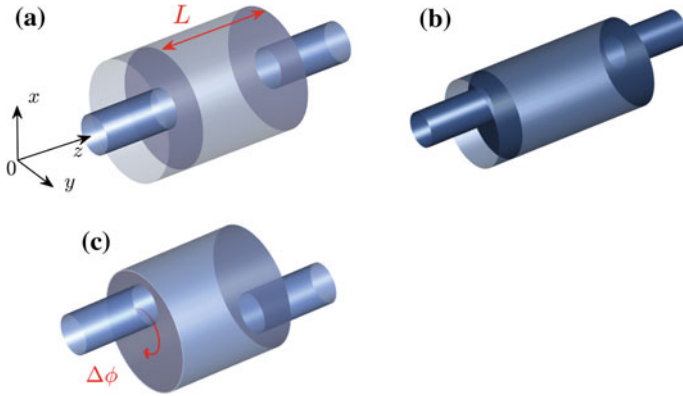


**Fig. 21.1** Cylindrical resonator of radius  $R$  and length  $L$  with two attached cylindrical waveguides of radius  $r < R$ . The whole waveguide system is axisymmetric (a) and non-axisymmetric with aligned waveguides but shifted relative to the center line of resonator by distance  $r_0 = 1.5$  (b) and misaligned relative each other by azimuthal angle  $\Delta\phi$

$a_1$  and  $a_2$  [8]. In the present paper we choose similar strategy for the trapping of acoustic waves by means of the variation of the resonator length by the use of piston-like hollow-stem waveguides tightly fit to the interior boundaries of a cylindric cavity [28]. However this strategy is complemented by rotation of one of the waveguides by the angle  $\Delta\phi$  as shown in Fig. 21.1b. Then one of the waveguides acquires azimuthal difference relative to the other that crucially affects interference of resonances, i.e., Fano resonances and the wave transmission. We show that even tiny rotations result in change of the transmittance from zero to unit qualifying the setup as a wave faucet.





## 21.2 Acoustic Coupled Mode Theory for Open Cylindrical Resonators

Here we apply the method of effective non-Hermitian Hamiltonian [33–36] or equivalently the coupled mode theory, a physically transparent approach to diagnose the BICs. The theory is based on the Feshbach projection technique [33] of the total space, resonator plus waveguides, onto the subspace of the resonator that results in the effective non-Hermitian Hamiltonian. Each subsystem possesses the rotational symmetry and obeys the stationary Helmholtz equation in the cylindrical system of coordinates

$$\left[ \frac{\partial^2}{\partial r^2} + \frac{1}{r} \frac{\partial}{\partial r} - \frac{m^2}{r^2} + \frac{\partial^2}{\partial z^2} + \omega^2 \right] \psi = 0, \tag{21.1}$$

for the velocity potential  $\psi$  where all coordinates are dimensionless through the waveguide width and the frequency  $\omega$  is measured in terms of  $s/d$  where  $s$  is the sound

**Table 21.1** Cut-off frequencies and shapes of propagating modes

Channel	Cut-off frequency	Indices	Mode shape
1	0	$p = 0, q = 1$	
2	1.84118	$p = \pm 1, q = 1$	
3	3.0542	$p = \pm 2, q = 1$	
4	3.831706	$p = 0, q = 2$	

velocity [27]. The propagating modes in the sound hard cylindrical waveguides with Neumann boundary conditions are described by

$$\psi_{pq}(\rho, \alpha, z) = \psi_{pq}(\rho) \frac{1}{\sqrt{2\pi k_{pq}}} \exp(ip\alpha + ik_{pq}z), \tag{21.2}$$

$$\psi_{pq}(\rho) = \begin{cases} \frac{\sqrt{2}}{J_0(\mu_{0q})} J_0(\mu_{0q}\rho), & p = 0, \\ \sqrt{\frac{2}{\mu_{pq}^2 - p^2}} \frac{\mu_{pq}}{J_p(\mu_{pq})} J_p(\mu_{pq}\rho), & p = 1, 2, 3, \dots, \end{cases}$$

where  $\rho, \alpha$  are the polar coordinates in the  $x0y$ -plane,  $\mu_{pq}$  is the  $q$ -th root of equation  $dJ_p(\mu_{pq}\rho)/d\rho|_{\rho=1} = 0$  imposed by the Neumann boundary condition on the walls of sound hard cylindrical waveguide.

$$k_{pq}^2 = \omega^2 - \mu_{pq}^2 \tag{21.3}$$

The propagating bands degenerate with the respect to the sign of OAM are classified by two indices, the OAM index  $p = 0, \pm 1, \pm 2, \dots$  and radial index  $q = 1, 2, 3, \dots$ . Profiles of propagating functions  $\psi_{pq}(\rho) \cos p\alpha$  are depicted in Table 21.1.

The Hilbert space of the closed cylindrical resonator is given by the following eigenmodes

$$\Psi_{mnl}(r, \phi, z) = \psi_{mn}(r) \sqrt{\frac{1}{2\pi}} \exp(im\phi) \psi_l(z), \tag{21.4}$$

where

$$\psi_{mn}(r) = \begin{cases} \frac{\sqrt{2}}{R J_0(\mu_{0n} R)} J_0\left(\frac{\mu_{0n} r}{R}\right), & m = 0 \\ \sqrt{\frac{2}{\mu_{mn}^2 - m^2}} \frac{\mu_{mn}}{R J_m(\mu_{mn} R)} J_m\left(\frac{\mu_{mn} r}{R}\right), & m = 1, 2, 3, \dots, \end{cases} \tag{21.5}$$

$$\psi_l(z) = \sqrt{\frac{2 - \delta_{l,1}}{L}} \cos[\pi(l - 1)z/L],$$

$l = 1, 2, 3, \dots$  and  $z$  is measured in terms of the waveguide radius. The corresponding eigenfrequencies are

$$\omega_{mnl}^2 = \left[ \frac{\mu_{mn}^2}{R^2} + \frac{\pi^2(l-1)^2}{L^2} \right] \quad (21.6)$$

where  $\mu_{mn}$  is the  $n$ -th root of the equation  $\left. \frac{dJ_m(\mu_{mn}r)}{dr} \right|_{r=R} = 0$  which follows from the Neumann BC on the walls of a sound hard cylindrical resonator.

Then the Feshbach projection of the total space of the waveguide shown in Fig. 21.1 onto the subspace of the eigenmodes of the closed cylindrical resonator (21.4) gives us the following effective Hamiltonian [37]

$$\mathbf{H}_{\text{eff}} = \mathbf{H}_B - i \sum_{C=L,R} \sum_{pq} k_{pq} \mathbf{W}_{C,pq} \mathbf{W}_{C,pq}^\dagger, \quad (21.7)$$

where  $\mathbf{W}_{BC}$ ,  $\mathbf{W}_{CB}$  stand for the coupling matrix elements between the eigenmodes (21.4) and the eigenmodes of the scattering channels (21.2) with the frequency  $\omega$ . The full Hamiltonian of an open system is Hermitian only in the total Hilbert space, which is spanned by the bound states and the scattering continuum states. The effective Hamiltonian (21.7) is however non-Hermitian because of the leakage of the eigenmodes (21.4) into the open channels of the waveguides through the holes. That is why the eigenvalues of the non-Hermitian effective Hamiltonian

$$\mathbf{H}_{\text{eff}} \psi_r(r, \phi, z) = z_r \psi_r(r, \phi, z) \quad (21.8)$$

are complex which determine the positions and resonant widths of the resonant states as  $\text{Re}(z_\lambda)$ , and  $-2\text{Im}(z_\lambda)$  correspondingly [34, 35]. The matrix elements of  $\mathbf{W}$  are given by overlapping integrals [37, 38]

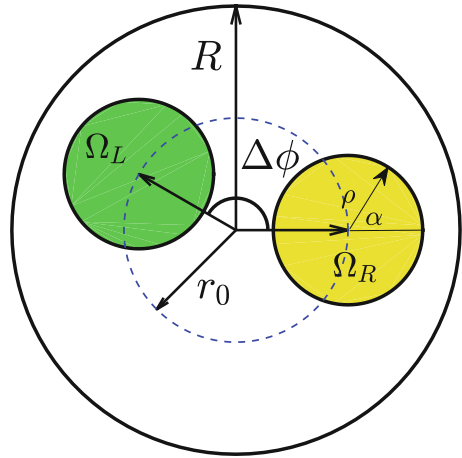
$$\begin{aligned} W_{mnl;pq}^C &= \int_{\Omega_C} \rho d\rho d\alpha \psi_{pq}(\rho, \alpha) \Psi_{mnl}^*(r, \phi, z = z_C) \\ &= \int_0^{2\pi} d\alpha \int_0^1 \rho d\rho \psi_{pq}(\rho, \alpha) \Psi_{mnl}^*(r(\rho, \alpha), \phi(\rho, \alpha), z_C) \\ &= \psi_l(z_C) \int_0^{2\pi} d\alpha \int_0^1 \rho d\rho \psi_{pq}(\rho, \alpha) \psi_{mn}^*(r(\rho, \alpha), \phi(\rho, \alpha)), \end{aligned} \quad (21.9)$$

where  $\Omega_{C=L,R}$  are interfaces positioned at  $z_C = 0, L$  where the waveguides are attached to the resonator as shown in Fig. 21.2. Integration is performed over circular cross section of the attached waveguides as shown in Fig. 21.2. One can link the polar coordinates of the resonator with that of the immovable waveguide

$$r \sin \phi = \rho \sin \alpha, r \cos \phi = r_0 + \rho \cos \alpha$$



**Fig. 21.2** Integration area in the coupling matrix (21.9) shown by filled areas.eps



where  $r_0$  is the distance between the axes of the waveguide and resonator. According to (21.4) we have

$$\psi_l(z = 0) = \sqrt{\frac{2 - \delta_{l,1}}{L}}, \psi_l(z = L) = \psi_l(0)(-1)^{l-1}. \tag{21.10}$$

Although the waveguides are identical they are attached to the resonator at different azimuthal angles as shown in Fig. 21.2 to give rise to an exact relation between the coupling matrix elements

$$W_{mnl;pq}^L = (-1)^{l-1} e^{i(p-m)\Delta\phi} W_{mnl;pq}. \tag{21.11}$$

Here  $W_{mnl;pq} = W_{mnl;pq}^R$  are the coupling matrix elements of the resonator modes specified by integers  $m, n, l$  with  $p, q$  propagating modes of the left waveguide (see Fig. 21.1). Then the matrix of the effective Hamiltonian takes the following form

$$\begin{aligned} \langle mnl | \mathbf{H}_{\text{eff}} | m' n' l' \rangle &= \omega_{mnl}^2 \delta_{mm'} \delta_{nn'} \delta_{ll'} \\ - i \sum_{pq} k_{pq} [1 + (-1)^{l+l'} e^{i(m'-m)\Delta\phi}] &W_{mnl;pq} W_{m' n' l'; pq}^* \end{aligned} \tag{21.12}$$

The transmittance of sound waves in the  $p, q$  propagating channel through the resonator is given by equation [37]

$$T_{pq;pq} = 2ik_{pq} \sum_{mnl} \sum_{m' n' l'} W_{mnl;pq} e^{-im'\Delta\phi} G_{mnl;m' n' l'} W_{m' n' l'; p' q'}^* \tag{21.13}$$

where

$$\mathbf{G} = \frac{1}{\omega^2 - \mathbf{H}_{\text{eff}}}, \tag{21.14}$$

that is propagation of waves through the resonator is described by the Green function which is inverse of the matrix  $\omega^2 - \mathbf{H}_{\text{eff}}$  and coupling matrices of the resonator with the input (left) waveguide and the output (right) waveguide. However the most remarkable feature in (21.13) is complex phases of the coupling matrix elements which contribute into interference of different states  $mnl$ . As we show below that drastically affects Fano resonances.

### 21.3 Trapping in Non Coaxial Waveguide Under Variation of the Resonator Length $L$

In what follows we take both waveguides with unit radius shifted relative to the central axis of the resonator with radius  $R = 3$  by a distance  $r_0 = 1.5$ . We consider transmission in the first channel  $p = 0, q = 1$  in the frequency domain  $0 < \omega < 1.8412$  (see Table 21.1). The transmittance versus the squared frequency and the resonator length  $L$  is shown in Fig. 21.3 for  $\Delta\phi = 0$  and  $\Delta\phi = \pi/4$ . Irrespectively

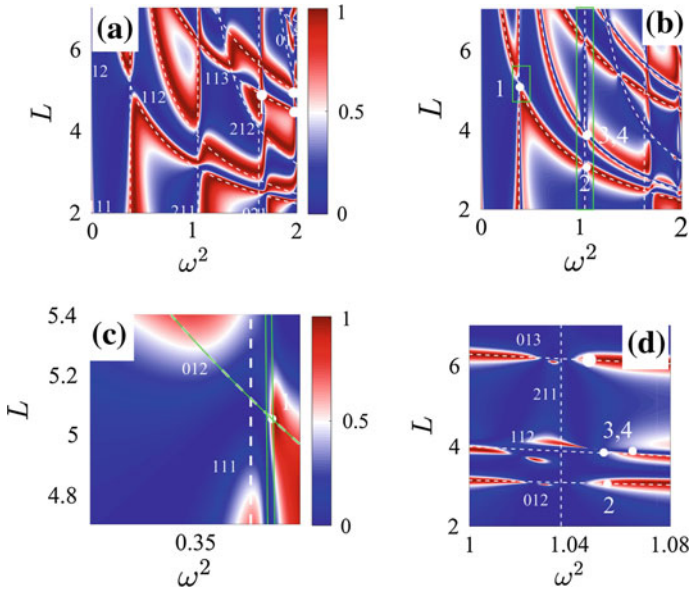
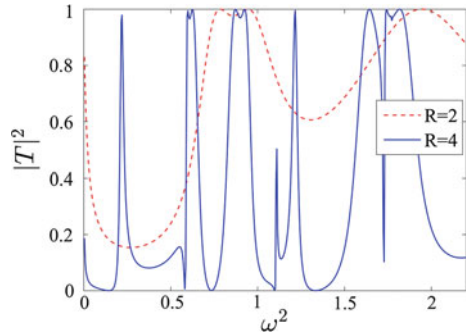


**Fig. 21.3** Transmittance of a cylindrical resonator versus frequency and length of the resonator  $L$  at **a**  $\Delta\phi = 0$  and **b**  $\Delta\phi = \pi/4$ . **c** and **d** zoomed transmittance in the domains isolated by rectangles in **b**. Dash lines show eigenlevels of closed resonator with corresponding indices  $mnl$ . Solid lines show eigenlevels of the resonator shifted by evanescent modes given by the modified Hamiltonian (21.16). The positions of the BICs are shown by closed circles

**Fig. 21.4** The transmittance vs frequency for two values of  $R$  at  $\Delta\phi = 0$  and  $L = 2$



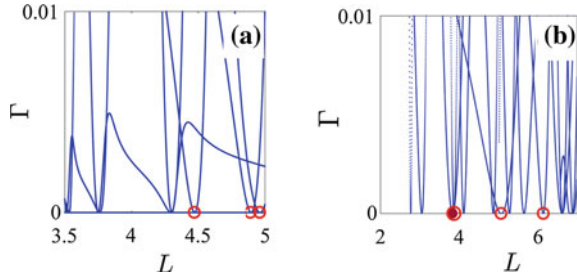
to the choice of the rotation angle the transmittance has resonant behavior which is due to that the resonator is three-dimensional. Indeed, the coupling matrix elements (21.9) can be estimated as  $\frac{1}{RL^{1/2}}$  due to the normalization of the eigenmodes of the resonator (21.5). The resonant widths are proportional to the squared coupling matrix elements, i.e., proportional to  $\frac{1}{R^2L}$ , while the distance between the eigenlevels  $\Delta E$  is proportional to  $R^{-2}$  irrespective to dimension according to (21.6). Hence we obtain an inequality  $R \ll L$  to have the regime of weak coupling [39]. This observation is illustrated in Fig. 21.4. One of the advantages of the effective non-Hermitian Hamiltonian approach is that the BIC can be easily found as the eigenmode of the effective Hamiltonian (see (21.8)) with zero resonant width, i.e., with real eigenvalue  $z_r$  [8, 28]. Each BIC point is searched for by solving the fix point equations [34]

$$\omega_c = \text{Re}(z(\omega_c, L_c, \Delta\phi_c)), \text{Im}(z(\omega_c, L_c, \Delta\phi_c)) = 0.$$

After the fix point equation is solved we can determine the eigenmodes of the effective Hamiltonian with real eigenvalues [8, 28]. As it is seen from (21.13), the above equation corresponds to the case when one of the poles of the S-matrix reaches real axis as was considered by Hein et al. [31]. Then the Green function becomes singular. In order to avoid this singularity in the transmittance the coupling strength becomes zero. Rigorous consideration of these subtle features is given in [8, 40].

The case of waveguides coaxial each other and resonator (Fig. 21.1a) was considered in [28] to show multiple events of BICs due to the mechanism of full destructive interference of leakage modes for crossing of eigenfrequencies for variation of the length  $L$ . Here we consider two distinctive case of non coaxial waveguides: (a) the waveguides are coaxial each other  $\Delta\phi = 0$  but their center lines are shifted relative to the center line of the resonator by a distance  $r_0$  (Fig. 21.1b), and (b) the center lines of the waveguides are shifted relative each other by the azimuthal angle  $\Delta\phi$  (Fig. 21.1c).

**Fig. 21.5** Evolution of resonant widths under variation of the resonator length at  $\Delta\phi = 0$  **a** and  $\Delta\phi = \pi/4$  **b**. Circles mark BICs listed in Tables 21.2 and 21.3



### 21.3.1 $\Delta\phi = 0$

Figure 21.5 shows numerous events of the resonant widths turning to zero with variation of the resonator length  $L$  which evidence BICs. Inside the resonator the BIC trapped mode can be expanded over the eigenmodes of the closed resonator (21.4)

$$\psi_{\text{BIC}}(r, \phi, z) = \sum_{mnl} a_{mnl} \Psi_{mnl}(r, \phi, z). \tag{21.15}$$

The expansion coefficients of the BICs  $a_{mnl}$  are shown in Fig. 21.6 and listed in Table 21.2 where we present only those BICs whose frequencies fit into the frequency window shown in Fig. 21.3a. They are marked by open circles in Fig. 21.5a. One can see that only a few eigenmodes of the resonator participate in the BIC expansion (21.15). The expansion coefficients are real and equal for  $\pm m$ . All BICs listed in Table 21.2 are result of the Friedrich-Wintgen mechanism of destructive interference [8, 32] when the eigenmode  $mln$  with the azimuthal part  $\cos m\phi$  crosses the eigenmode  $m'l'n'$  with the azimuthal part  $\cos m'\phi$ . In Fig. 21.7 we show BICs 1 and 2 listed in Table 21.2 on the surface of the waveguide similar to those shown by Hein et al. [31]. We leave aside here the trivial symmetry protected BICs whose azimuthal dependence is given by  $\sin m\phi$ . One can see that for the waveguides with no phase difference these BICs have zero overlapping with the first channel  $p = 0, q = 1$  shown in Table 21.1.

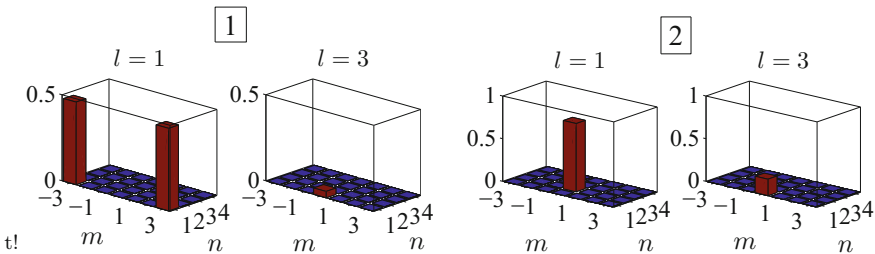


**Fig. 21.6** (Color online) Modal expansion coefficients  $|a_{mnl}|$  of BSCs shown in Fig. 21.6 for the case  $\Delta\phi = 0$

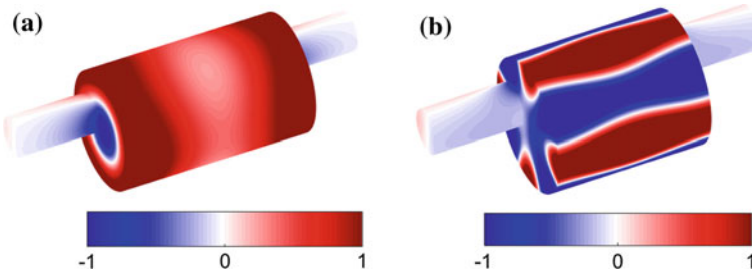


**Fig. 21.7** Patterns of BIC 1 **a** and BIC 2 **b** from Table 21.2 (real parts of modes on the surface of the waveguide) at  $\Delta\phi = 0$

**Table 21.2** BICs at  $\Delta\phi = 0$

BIC	$\omega^2$	$L$	$mn\ell$	$a_{mn\ell}$
1	1.6617	4.8743	021	0.9276
			013	0.3665
2	1.9571	4.9371	$\pm 113$	0.6015
			$\pm 121$	0.5563

### 21.3.2 $\Delta\phi = \pi/4$

Above we considered the BICs for the case when both waveguides were attached to the cylindrical resonator in a non-axisymmetric way for  $\Delta\phi = 0$ . That makes both waveguides identical and summation over  $C = L, R$  in the effective Hamiltonian (21.7) simply gives rise to a factor of 2. Let us now shift the axis of the left waveguide by an azimuthal angle  $\Delta\phi$  compared to the axis of the right waveguide as shown in Fig. 21.1b. To be specific we consider the case  $\Delta\phi = \pi/4$ . Although the continua of the waveguides remain the same the rotation of the left waveguide brings the complex phases in the coupling matrix elements of the resonator eigenmodes with the continua as given by (21.11). That does not affect the transmittance except the points of crossing of the eigenlevels as shown in Fig. 21.3c, d.

As before the BIC points were detected by finding zero resonant width as shown in Fig. 21.5b. However, upon closer inspection in Fig. 21.3c, d we see that these BICs are not exactly in the positions of the degeneracy of the eigenmodes of the closed resonator. The corresponding BICs are listed in Table 21.3 and shown in Fig. 21.8. Here we outline only the most important results. (i) The evanescent modes with imaginary  $k_{pq}$ ,  $p > 0$  contribute into the Hamiltonian of the closed resonator  $\mathbf{H}_R$  to modify it as follows

$$\tilde{\mathbf{H}}_R = \mathbf{H}_R + \sum_{C=L,R} \sum_{p>0,q} k_{pq} \mathbf{W}_{C,pq} \mathbf{W}_{C,pq}^+ \quad (21.16)$$

**Table 21.3** BICs at  $\Delta\phi = \pi/4$ 

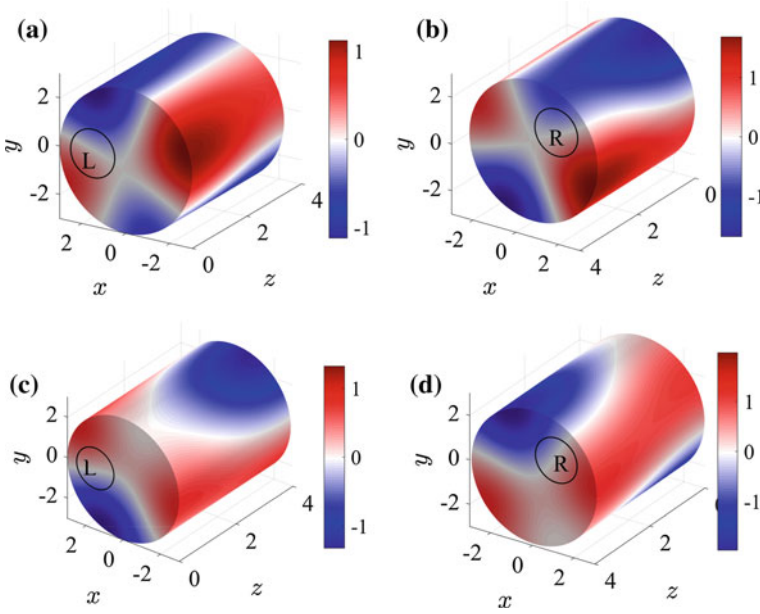
BIC	$\omega^2$	$L$	$mn\ell$	$a_{mn\ell}$	$ a_{mn\ell} $
1	0.385	5.065	012	$-0.113 + 0.272i$	0.294
			111	$-0.478(1-i)$	0.675
			-111	0.675	0.675
2	1.055	3.051	012	$-0.261(1-i)$	0.369
			211	0.656i	0.656
			-211	0.656	0.656
3	1.0535	3.833	211	0.658i	0.658
			-211	0.658	0.658
			112	$-0.237 - 0.098i$	0.256
			-112	$-0.098 - 0.237i$	0.256
4	1.065	3.869	211	-0.505	0.505
			-211	0.505	0.505
			112	$-0.455 - 0.189i$	0.493
			-112	$0.189 + 0.455i$	0.493

As the result the BICs occur in the points of degeneracy of the eigenlevels of this Hamiltonian that explains positions of the BICs shown in Fig. 21.3c. Numerical data of BICs at  $\Delta\phi = \pi/4$  are collected in Table 21.3.

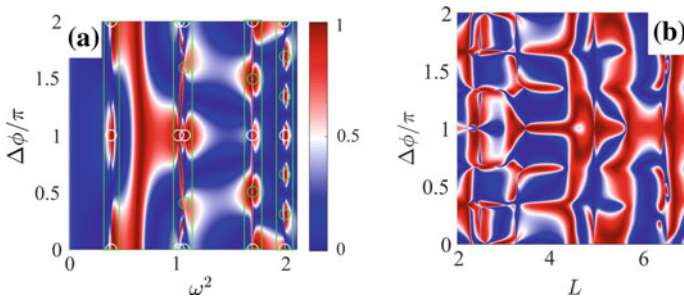
(ii) If the waveguides were coaxial with the resonator the eigenmodes of  $\tilde{\mathbf{H}}_B$  given by the azimuthal parts  $\cos m\phi$  and  $\sin m\phi$  (or equivalently  $e^{im\phi}$  and  $e^{-im\phi}$ ) of the cylindrical resonator would be degenerate. However, as soon as the waveguides are attached non-coaxially this degeneracy with respect to the sign of  $m$  is lifted as shown in Fig. 21.3c by solid lines. That leads to the important consequence that the BICs of the non-coaxial waveguide can not support currents of acoustic intensity [30] in contrast to the case of coaxial waveguides [26]. Figure 21.8 clearly shows that BICs at  $\Delta\phi \neq 0$  are decoupled from the first channel. Assume that the BIC mode is decoupled from the right waveguide owing to degeneracy. In order the BIC mode to be decoupled from the rotated left waveguide the BIC mode has to be twisted to compensate this rotation [30, 41]. Figure 21.8 evidently illustrates the effect of twisting of the BIC by the rotation angle  $\Delta\phi$ .

## 21.4 Wave Faucet

Equation (21.13) shows that the phase factors in the coupling matrix elements due to the rotation of the input waveguide brings an important contribution into interference between resonances. Figure 21.9 vividly illustrates high sensitivity of the transmittance to the rotation angle  $\Delta\phi$ . Figures 21.10 and 21.11 demonstrate that the most strong effect of waveguide rotation occurs at the vicinity of BICs, i.e., in the vicinity of crossing of eigenfrequencies. As seen from Fig. 21.4a the eigenmode 012 crosses the eigenmode  $\pm 111$  around  $L = 5$ . Respectively the

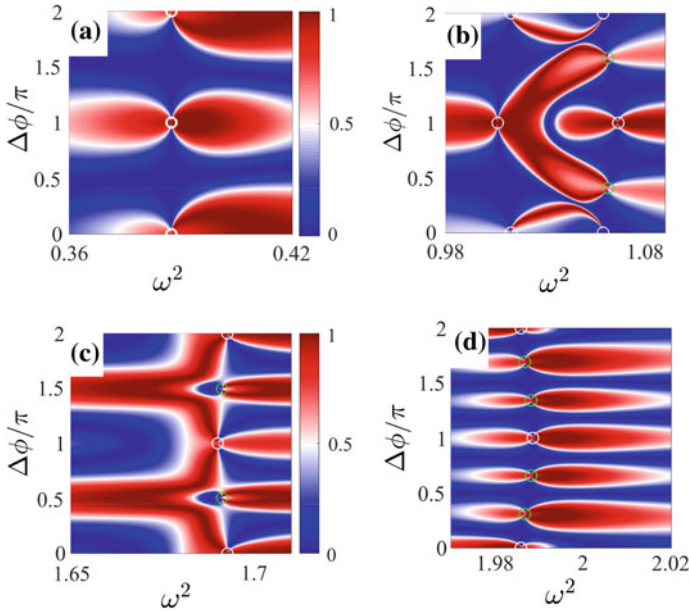


**Fig. 21.8** Patterns of BIC 3 (a, b) and BIC 4 (c, d) shown from the left and right (d) sides of resonator on the surface of the waveguide at  $\Delta\phi = \pi/4$

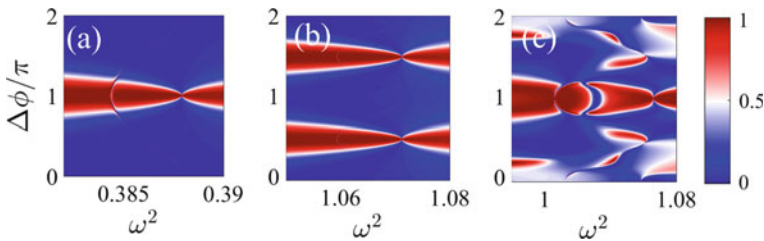


**Fig. 21.9** (Color online) Transmittance of a cylindrical resonator **a** versus frequency and rotation angle  $\Delta\phi$  at  $L = 4$  and **b** versus length and rotation angle at  $\omega^2 = 2$ . The positions of the BICs are shown by open circles

transmittance is basically given by the interference of these resonances. According to (21.11) we have  $W_{012;01}^L = -W_{012;01}^R$ ,  $W_{\pm 111;01}^L = W_{\pm 111;01}^R e^{\mp i\Delta\phi}$ . Therefore for the output waves interfering constructively we have to take  $\Delta\phi = \pm\pi$ , while the full destructive interference takes place at  $\Delta\phi = 0$ . This simple consideration is in excellent agreement with numerics presented in Fig. 21.11a. Along the same line for channels 012 and  $\pm 211$  in the vicinity of  $L = 3$  we have from (21.11)  $W_{012;01}^L = -W_{012;01}^R$ ,  $W_{\pm 211;01}^L = W_{\pm 211;01}^R e^{\mp 2i\Delta\phi}$  to open wave flux through the resonator at  $\Delta\phi = \pi/2, 3\pi/2$  that is illustrated in Fig. 21.11b. At last, in the vicinity



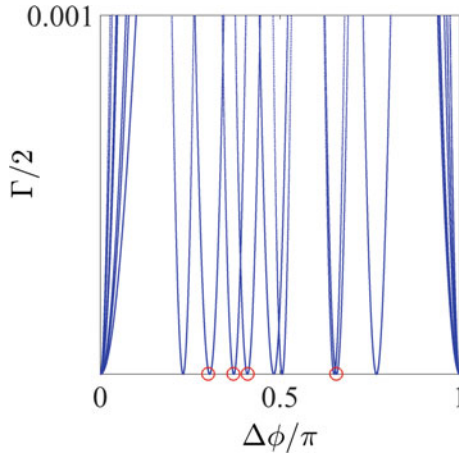
**Fig. 21.10** Transmittance versus frequency and rotation angle  $\Delta\phi$  at  $L = 4$  in frequency domains shown in Fig. 21.9a by rectangles. The positions of the BICs are shown by closed circles. **a** The first frequency domain from 0.36 till 0.42, **b** the second frequency domain from 0.98 till 1.08, **c** the third frequency domain from 1.65 till 1.72, and **(4)** the fourth frequency domain from 1.97 till 2.02



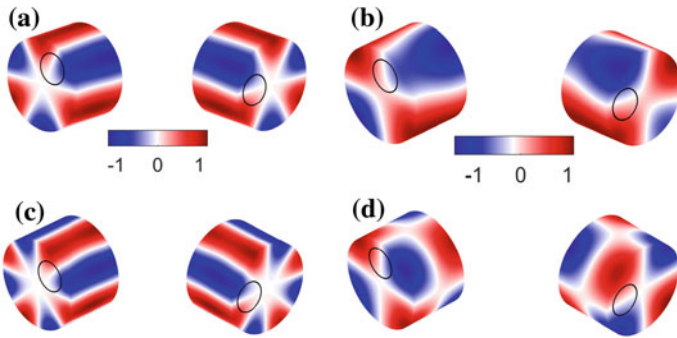
**Fig. 21.11** Transmittance versus the frequency and rotation angle in the vicinity of crossing of the modes **a** 012 and  $\pm 111$  at  $L = 5$ , **b** 012 and  $\pm 211$  at  $L = 3$ , and **c**  $\pm 112$  and  $\pm 211$ ,  $L = 4$

of  $L = 4$  the eigenmodes  $\pm 112$  cross the eigenmodes  $\pm 211$ . Respectively we have  $W_{\pm 211;01}^L = W_{\pm 211;01}^R e^{\mp 2i\Delta\phi}$ ,  $W_{\pm 112;01}^L = -W_{\pm 112;01}^R e^{\mp 2i\Delta\phi}$  to give rise to constructive interference only at  $\Delta\phi = \pi$  that agrees with Fig. 21.11c. Thus, the rotation of the input waveguide strongly tunes Fano resonance [41]. In particular there can be a collapse of Fano resonance when the transmission zero approaches to the transmission maximum that is a signature of wave trapping [6]. These events are shown by open circles in Figs. 21.10 and 21.11 and confirmed by the behavior of the resonant widths vs the rotation angle as shown in Fig. 21.12. Among them we select four BICs shown in Fig. 21.13.





**Fig. 21.12** Evolution of resonant widths under waveguide rotation at  $L = 4$

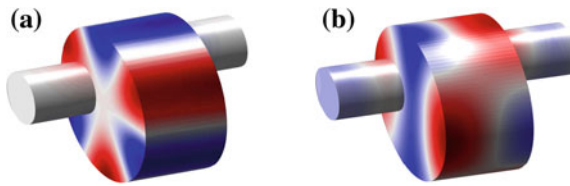


**Fig. 21.13** Patterns of BICs marked by open circles in Fig. 21.12 and listed in Table 21.4 on the surface of the resonator at  $L = 4$ . **a** BIC 1, **b** BIC 3, **c** BIC 2, and **d** BIC 4. Open circles show where the left and right waveguides are attached to the resonator

For  $\Delta\phi \neq 0$  BICs can only be symmetry protected except the cases of a degeneracy of the resonator eigenmodes shown in Fig. 21.3. Indeed, let us consider the first BIC from Table 21.4 whose azimuthal dependence is given by  $\cos[3(\phi - \Delta\phi/2)]$ . In order to decouple this BIC from the right waveguide at  $\Delta\phi = 0$  the nodal line of the BIC mode has to be positioned at  $\phi = 0$  that gives us the equation  $\frac{3}{2}\Delta\phi = \frac{\pi}{2}$ , i.e.,  $\Delta\phi = \frac{\pi}{3}$ . Therefore the BIC mode is  $\cos[3(\phi - \pi/6)]$  which equals zero at  $\phi = 0$ . The left waveguide is rotated by the angle  $\pi/3$  for which the BIC mode is decoupled from the left waveguide too. Numerically according to Table 21.4 we have  $\Delta\phi = 0.308\pi$  which is close to  $\pi/3$ . The small difference is due to the evanescent modes. Similarly for the second BIC we obtain  $\cos[4(\phi - \Delta\phi/2)]$  that gives us  $\Delta\phi = \pi/4$  which is close to numerical result  $\Delta\phi = 0.235\pi$  given in Table 21.4. For the fourth BIC we obtain that  $\Delta\phi = \pi/2$  that well agrees with Table 21.4. The most

**Table 21.4** BICs at  $L = 4$ 

BIC	$\Delta\phi/\pi$	$\omega^2$	$mnl$	$a_{mnl}$
1	0.308	1.9868	311	0.7056
			-311	$0.7056e^{-3i\Delta\phi}$
2	0.2351	3.17304	411	0.705
			-411	$0.705e^{4i\Delta\phi}$
3	0.4171	1.05688	211	0.6898
			-211	$-0.6898e^{-2i\Delta\phi}$
			121	$0.0933 + 0.1215i$
			-121	$a_{121}e^{i\Delta\phi}$
4	0.5055	1.68872	211	0.7043
			-211	$0.7043e^{-2i\Delta\phi}$

**Fig. 21.14** Real parts of scattering function for the parameters close to the BIC point 4 given in Table 21.4. **a**  $\omega = \omega_c$  and **b**  $\omega = \omega_c + 0.01$ 

interesting is the third BIC which is superposed of two modes  $\cos[2(\phi - \Delta\phi/2)]$  and  $\cos[(\phi + \Delta\phi/2)]$ . As the result the BIC mode is twisted as shown in Fig. 21.13.

Although all of the BICs can not support the flows of acoustic intensity, the scattering wave function calculated through the equation [36, 37]

$$\begin{aligned} \psi(r', \phi', z) &= \frac{1}{\sqrt{4\pi k_{01}}} [e^{ik_{01}z} \phi_{10} + \sum_{pq} S_{01L;pqL} e^{-ik_{pq}z} \phi_{pq}(r', \phi')], \quad z < 0, \\ \psi_{mnl}(r, \phi, z) &= -i \sum_{m'n'l'} G_{mnl;m'n'l'} \sqrt{\frac{k_p}{\pi}} W_{m'n'l';01}^L, \quad 0 < z < L, \quad (21.17) \\ \psi_R(r', \phi', z) &= \frac{1}{\sqrt{4\pi k_{01}}} \sum_{pq} S_{01L;pqR} e^{ik_{pq}z} \phi_{pq}(r', \phi')z > L. \end{aligned}$$

is a complex superposition of the BIC and a particular solution of the scattering problem [8]. An example of the scattering function in the vicinity of the BIC 4 from Table 21.4 is shown in Fig. 21.14. One can see that a small deviation from the BIC frequency results in large change of the scattering function. This phenomenon constitutes the important effect of enhancement of the injected wave within the resonator [8, 42, 43].

More interesting is that the scattering function supports vortical acoustic intensity as demonstrated in Fig. 21.15. The mean intensity vector  $\mathbf{j}$  follows minus  $\nabla \arg(\psi)$  according to the equation for the acoustic intensity vector [44–46]

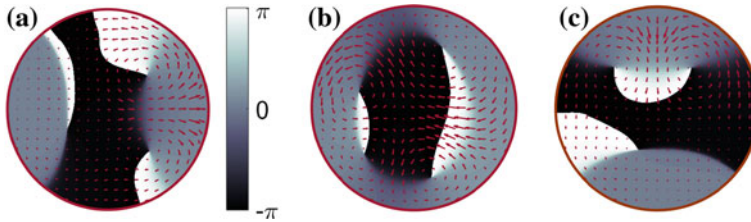


**Fig. 21.15** Current flows at different slices at the vicinity of the BIC 4: **a**  $z = 0$ , **b**  $z = L/2$ , and **c**  $z = L$ . Phase of the scattering function shown in gray

$$\mathbf{j} = -\omega \text{Im}(\psi^* \nabla \psi) = -\omega |\psi|^2 \nabla \arg(\psi), \quad (21.18)$$

where  $\omega$  is the frequency defined below (21.1). The phase of the scattering function  $\arg(\psi)/\pi$  is shown in Fig. 21.15 for selected slices across  $z$ . Figure 21.14 shows the scattering function (21.17) that demonstrates the effect of twisted acoustic pressure field given by real part of  $\psi$ . This figure is complemented with the flows of the acoustic intensity vector (21.18) in Fig. 21.15. Figure 21.15 demonstrates complicated vortical behavior of the flows.

## 21.5 BSCs in Two Continua Different in Phase

Displacement of the waveguide relative to the resonator does not change its continuous spectrum. However the coupling matrix elements of the resonator eigenmodes with the continua are subject to alternation to affect the transmission. In particular under rotation of one of the waveguides the matrix elements acquire phase shift (21.11). Therefore in the framework of the effective non-Hermitian Hamiltonian one can say that two continua become different by phase. First, the problem of the BSC residing in a finite number of continua was considered by Pavlov-Verevkin and coauthors [50]. Rigorous statement about the BSCs was formulated as follows. The interference among  $N$  degenerate states which decay into  $K$  non-interacting continua generally leads to the formation of  $N - K$  BSCs. The equivalent point of view [8, 51] is that the linear superposition of the  $N$  degenerate eigenstates  $\sum_{n=1}^N a_n \psi_n$  can be adjusted to have zero coupling with  $K$  different continua in  $N - K$  ways by variation of the  $N$  superposition coefficients  $a_n$ . Respectively, these coefficients  $a_n$  define an expansion of the BSC over the eigenstates of the closed resonator. The number of continua can grow due to a number of reasons, for example, non-symmetrically attached waveguides, multiple propagation subbands in the waveguides, or two polarizations of the radiation continuum in case of electromagnetic BSCs. Each case puts the problem of constructing BSCs in the case of many continua on the line of art [13, 51].

In the present case of waveguide rotation the number of continua has been doubled for the frequency of sound waves below the second propagation threshold  $\omega < \mu_{11}$  (see Table 21.1). Therefore we could expect BSCs only at the points of threefold degeneracy in compliance with the generic statement [50]. There are indeed numerous points where the eigenlevels  $\omega_{mnl}^2$  double degenerate in  $\pm m$  cross the eigenlevels  $\omega_{0nl}^2$  with BSCs marked by closed circles in Fig. 21.3b, c. However the zoomed picture of transmission in Fig. 21.3d shows that this conclusion is only approximate. Thus, the case needs in special consideration. As shown in Table 21.4 the BSCs are superposed from only a few eigenmodes. Hence we can truncate the effective Hamiltonian to the relevant eigenmodes similar to that in [8, 32].

### 21.5.1 The Mode with $m = 0$ Crosses the Modes with $\pm M$

Let us consider the crossing of the eigenlevel  $\omega_{012}^2 = \pi^2/L^2$  with the degenerate eigenlevel  $\omega_{\pm 111}^2 = \mu_{\pm 11}^2/R^2$  shown in Fig. 21.16 by dash lines. The coupling matrix elements of the eigenmodes with the first propagating channel  $p = 0, q = 1$  (see Table 21.1) of the right waveguide according to (21.2), (21.5) and (21.9) equal

$$W_{mnl;01} = (w_0 \ w_1 \ w_1), \quad w_0 = W_{012;01} = \frac{1}{3}\sqrt{\frac{2}{L}},$$

$$w_1 = W_{\pm 111;01} = 0.269\sqrt{\frac{1}{L}} \quad (21.19)$$

for the given radius of the resonator. We also take into account the coupling with the first evanescent modes  $p = \pm 1, q = 1$  of the waveguide (see Table 21.1)

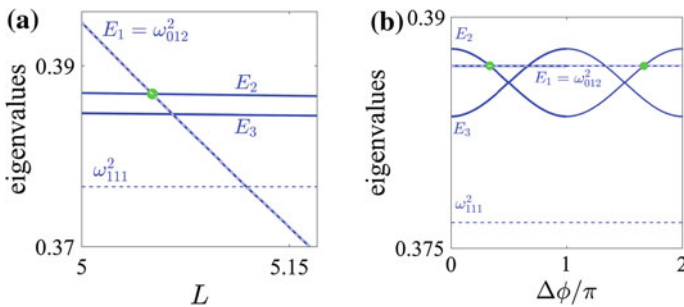


**Fig. 21.16** (Color online). The eigenvalues of the closed resonator (dash lines) and the eigenlevels (21.25) (solid lines) shifted by evanescent modes versus **a** the resonator length at  $\phi = \pi/3$  and **b** rotation angle at  $L = 5.0512$

$$\begin{aligned}
 W_{mnl;11} &= (0 \ v_1 \ v_2), \quad W_{mnl;-11} = (0 \ v_2 \ v_1), \\
 v_1 &= W_{012;11}^L = 0.1141\sqrt{\frac{1}{L}}, \quad v_2 = W_{\pm 111;11} = -0.0141\sqrt{\frac{1}{L}}.
 \end{aligned}
 \tag{21.20}$$

Because of the phase difference between the coupling matrix elements for left and right waveguides we immediately obtain

$$\begin{aligned}
 W_{mnl;01}^R &= (-w_0 \ w_1 e^{i\Delta\phi} \ w_1 e^{-i\Delta\phi}), \\
 W_{mnl;11}^R &= (0 \ v_2 e^{i\Delta\phi} \ v_1 e^{-i\Delta\phi}), \\
 W_{mnl;-11}^R &= (0 \ v_1 e^{i\Delta\phi} \ v_2 e^{-i\Delta\phi}).
 \end{aligned}
 \tag{21.21}$$

The contribution of the higher evanescent modes shown in Table 21.1 is negligible. For open channel  $p = 0, q = 1$  the wave number  $q_{01} = \omega$  while for the next closed channel  $p = \pm 1, q = 1$  the wave number  $k_{11} = iq_{11}, q_{11} = \sqrt{\mu_{11}^2 - \omega^2}$  is imaginary. Then the truncated effective Hamiltonian (21.7) can be rewritten as follows

$$\hat{H}_{eff} = \hat{H}_R + q_{11} \sum_{C=L,R} \sum_{p=\pm 1} \hat{W}_{p=\pm 1,1}^C \{\hat{W}_{p=\pm 1,1}^C\}^\dagger - i\omega \sum_{C=L,R} \hat{W}_{01}^C \{\hat{W}_{01}^C\}^\dagger = \hat{H}_R - i\omega \hat{\Gamma},
 \tag{21.22}$$

where the Hermitian term

$$\hat{H}_R = \begin{pmatrix} \omega_{012}^2 & 0 & 0 \\ 0 & \omega_{111}^2 + 2q_{11}(v_1^2 + v_2^2) & 2q_{11}v_1v_2(1 + e^{-2i\Delta\phi}) \\ 0 & 2q_{11}v_1v_2(1 + e^{2i\Delta\phi}) & \omega_{111}^2 + 2q_{11}(v_1^2 + v_2^2) \end{pmatrix}
 \tag{21.23}$$

is the Hamiltonian of the resonator coupled to the evanescent modes. The anti-Hermitian part takes the following form

$$\hat{\Gamma} = \begin{pmatrix} 2w_0^2 & w_0w_1(1 - e^{i\Delta\phi}) & w_0w_1(1 - e^{-i\Delta\phi}) \\ w_0w_1(1 - e^{-i\Delta\phi}) & 2w_1^2 & w_1^2(1 + e^{-2i\Delta\phi}) \\ w_0w_1(1 - e^{i\Delta\phi}) & w_1^2(1 + e^{2i\Delta\phi}) & 2w_1^2 \end{pmatrix}.
 \tag{21.24}$$

The eigenvalues of the Hamiltonian (21.23) can be easily found as

$$E_1 = \omega_{012}^2, \quad E_{2,3} = \omega_{111}^2 + 2q_{11}[v_1^2 + v_2^2 \pm 2v_1v_2 \cos \Delta\phi].
 \tag{21.25}$$

Thus the evanescent modes of the waveguides non-coaxially attached to the cylindrical resonator lift the degeneracy of eigenmodes  $\pm 111$  as shown in Fig. 21.16 by solid lines. The only case when the degeneracy is restored is the case  $\Delta\phi = \pi/2$ . The corresponding eigenmodes of the Hamiltonian (21.23) are the following

$$\mathbf{X}_1 = \begin{pmatrix} 1 \\ 0 \\ 0 \end{pmatrix}, \quad \mathbf{X}_2 = \frac{1}{\sqrt{2}} \begin{pmatrix} 0 \\ -e^{-i\Delta\phi} \\ 1 \end{pmatrix}, \quad \mathbf{X}_3 = \frac{1}{\sqrt{2}} \begin{pmatrix} 0 \\ e^{-i\Delta\phi} \\ 1 \end{pmatrix}.
 \tag{21.26}$$

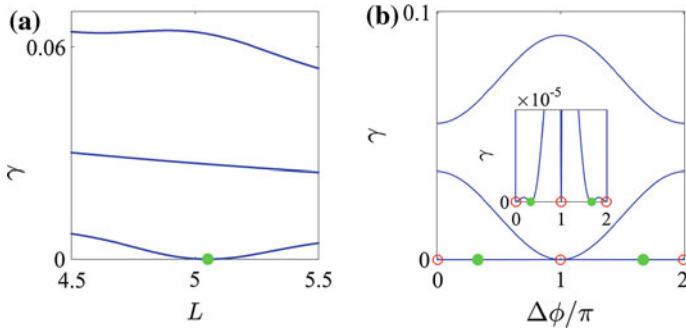


**Fig. 21.17** (Color online). The resonant width versus **a** the resonator length at  $\Delta\phi = \pi/3$  and **b** rotation angle at  $L = 5.0512$ . Circles show the BSC points

Next, let us consider the BSC in the truncated version (21.22). The point of the BSC can be easily diagnosed by zero resonant width as shown in Fig. 21.17. For  $\Delta\phi = \pi/4$  the BSC occurs at  $L = L_c = 5.0512$  marked by closed green circle in Fig. 21.17a. Respectively at  $L = L_c$  the BSC occurs at  $\Delta\phi = \pi/4$  and  $\Delta\phi = 2\pi - \pi/4$ . These points are seen in zoomed insert in Fig. 21.17b.

For  $\Delta\phi = 0$  both continua of left and right waveguides coincide to result in the symmetry protected BSC superposed of degenerate eigenmodes of the closed resonator  $\psi_{111}$  and  $\psi_{-111}$  to be in the following form

$$\psi_{BSC}(r, \phi, z) = A J_1(\mu_{11}r) \sin(\pi z/L) \sin \phi \quad (21.27)$$

which always has zero coupling with the propagation mode  $\psi_{01}(\rho, \alpha, z)$  shown in Table 21.1. As seen from (21.27) this conclusion also holds true for  $\Delta\phi = \pi$ . This BSC is symmetry protected for arbitrary resonator length as shown in Figs. 21.17, 21.9, and 21.10.

As soon as  $\Delta\phi \neq 0$  the continua become different to destroy the symmetry protected BSCs. It could be expected that in the case of two waveguides the point of threefold degeneracy where the  $\omega_{012}$  crosses the double degenerate  $\omega_{111}$  as shown in Fig. 21.16a is a BSC point in accordance with the above consideration. However the BSC point where the resonant width turns to zero (see Fig. 21.17) does not coincide with this point. The computation on the basis of full basis effective Hamiltonian gives the same result. In fact, the evanescent modes split the eigenvalues (21.25). Respectively the point of threefold degeneracy  $\omega_{111}^2 = \omega_{012}^2(L)$  splits into two double degenerate points  $E_1(L) = E_2(L, \Delta\phi)$  and  $E_1(L) = E_3(L, \Delta\phi)$ . As shown in Fig. 21.16a the first case exactly corresponds to the BSC point but not the second.

In the first case we can superpose the eigenmodes (21.26) as  $a\mathbf{X}_1 + b\mathbf{X}_2$  and require zero coupling of this superposed mode with the left waveguide

$$aw_0 + \frac{b}{\sqrt{2}}w_1(1 - e^{-i\Delta\phi}) = 0 \quad (21.28)$$

according to (21.19) and (21.26). It is easy to show that the coupling with the phase shifted continuum of the left waveguide takes the *same* form as (21.28). Thus, the BSC has the following form

$$\psi_{BSC} = w_1(1 - e^{-i\Delta\phi})\psi_{012} + w_0(e^{-i\Delta\phi}\psi_{111} - \psi_{-111}). \tag{21.29}$$

Substituting eigenmodes (21.5) we obtain

$$\psi_{BSC} = 2ie^{-i\Delta\phi/2}[w_1 \sin(\Delta\phi/2)\psi_{01}(r)\psi_2(z) + w_0 \sin(\phi - \Delta\phi/2)\psi_{11}(r)\psi_1(z)]. \tag{21.30}$$

One can see that this BSC does not support spinning currents of acoustic intensity  $\vec{j} = \psi^*\nabla\psi$  in contrast to coaxial waveguides [26]. This is due to evanescent modes of the non-coaxial waveguides which lift the degeneracy of the eigenmodes  $\Psi_{mnl}$  with respect to the sign  $m$ .

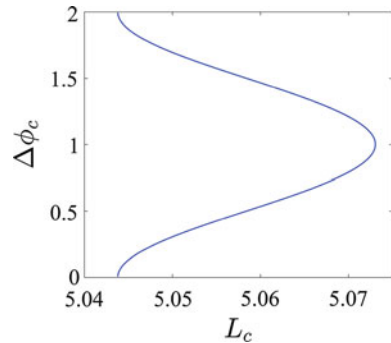
The BSC point is given by the equation  $E_1(L) = E_2(L, \Delta\phi)$  which gives rise to a line of the BSC in the parametric space  $L$  and  $\Delta\phi$  shown in Fig. 21.18. Thus, the only phase difference between the continua allow the BSCs in the point of twofold degeneracy. This is necessary for existence of BSC but not sufficient. Indeed let us consider the another point of degeneracy  $E_1 = E_3$  (see Fig. 21.16a). At this point we adjust the superposition  $a\mathbf{X}_1 + b\mathbf{X}_3$  for cancellation of the coupling with both continua. The analogue of (21.28) takes the following form

$$\pm aw_0 + \frac{b}{\sqrt{2}}w_1(1 + e^{i\Delta\phi})w_1 = 0. \tag{21.31}$$

These equations can not be fulfilled simultaneously to forbid this degeneracy point as the BSC point.

By the use of (21.13) and truncated effective Hamiltonian (21.22) we calculated the transmittance with the results presented in Fig. 21.19. Comparison to Fig. 21.3a, b shows that all features of the transmittance can be well reproduced in the vicinity of the BSCs by the use of truncated basis. One can also see from Fig. 21.19 that the

**Fig. 21.18** (Color online)  
Line of the BSCs in the parametric space of the resonator length and rotation angle  $\Delta\phi$



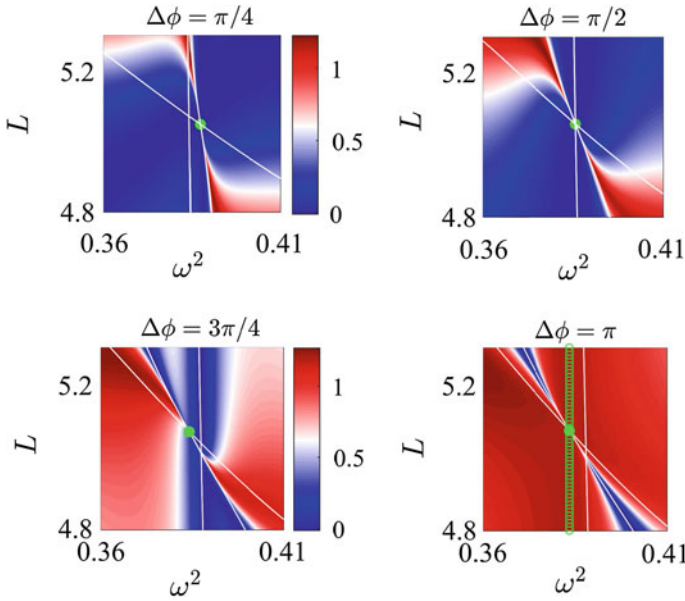


**Fig. 21.19** (Color online) **a** Transmittance versus frequency and resonator length at four fixed rotation angles. Solid green lines show the resonances defined by real part of the complex eigenvalues of the effective Hamiltonian (21.22). Closed circles mark the BSCs which exactly correspond to points of degeneracy of the eigenlevels (21.25)

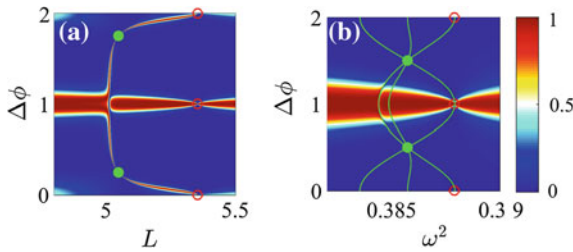


**Fig. 21.20** (Color online) **a** Transmittance vs the resonator length and rotation angle for the frequency tuned onto the frequency of the BSC  $\omega_c^2 = 0.388$ . **b** Transmittance versus the frequency and rotation angle for the length tuned onto the BSC length  $L_c = 5.048$ . Closed circles mark BSC 1 resulted by crossing of eigenlevels (21.25)  $E_1$  and  $E_2$ , open circles mark the symmetry protected BSCs (21.27)

resonant features follow the real parts of the complex eigenvalues of the effective non-Hermitian Hamiltonian (21.22) when  $\Delta\phi \neq 0$ .

Figure 21.20 shows fine features of the transmittance vs two parameters for the third parameter exactly tuned to the BSC. Figure 21.20a demonstrates a Fano resonance collapse in the parametric space of length and rotation angle at the BSC point  $L_c = 5.048$  and  $\Delta\phi_c = \pi/4$  with the frequency exactly tuned to the BSC



**Fig. 21.21** (Color online) Transmittance versus the frequency and rotation angle for the length detuned from the BSC length  $L_c$

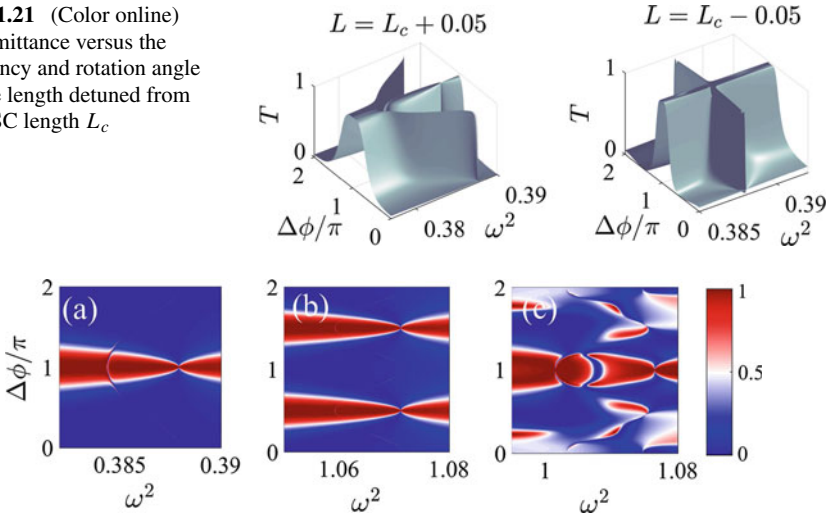


**Fig. 21.22** (Color online) Transmittance versus the frequency and rotation angle in the vicinity of crossing of the modes **a** 012 and 211 at  $L = ?$  and **b** 013 and 211,  $L = 4$

$\omega_c = 0.3873$ . Figure 21.20b shows the transmittance versus the frequency and the rotation angle for the length of the resonator tuned to the BSC length  $L_c = 5.0584$ . Figure 21.20a, b show that the resonator is blocked when  $\Delta\phi = 0$  and open when  $\Delta\phi = \pi$ . Figure 21.21 demonstrates as the transmittance is sensitive to small deviations from the BSC length  $L_c$ .

One can see from (21.19) and (21.21) that at  $\Delta\phi = 0$  the channels 012 and  $\pm 111$  interfere destructively at the right output to block the wave transmission through the resonator. In contrast for  $\Delta\phi = \pi$  the channels interfere constructively at the right output to maximize the transmittance. Along the same line for the channels 012 and  $\pm 211$  the wave faucet will open at  $\Delta\phi = \pi/2, 3\pi/2$  because of the phase factor  $e^{\pm 2i\Delta\phi}$  in the coupling matrix elements (21.21). Respectively, interference of channels of 013 and  $\pm 211$  will realize the wave faucet which opens at  $\Delta\phi = 0, \pi$ . Figure 21.22 completely confirms the above predictions.

### 21.5.2 The Modes $\pm 112$ Cross the Modes $\pm 211$

The coupling matrix elements of the eigenmodes with the first propagating channel  $p = 0, q = 1$  (see Table 21.1) of the right waveguide according to (21.2), (21.5), and (21.9) equal

$$\begin{aligned}
W_{mnl;01}^R &= (w_1 \ w_1 \ w_2 \ w_2), \ w_1 = W_{211;01}^R = 0.1737\sqrt{\frac{1}{L}}, \\
w_2 &= W_{\pm 112;01}^R = 0.2849\sqrt{\frac{2}{L}}.
\end{aligned} \tag{21.32}$$

The coupling matrix elements with the first evanescent modes  $p = 1, n = 1$  of the left waveguide (see Table 21.1) equal

$$\begin{aligned}
W_{mnl;-11}^L &= (v_1 \ v_2 \ v_3 \ v_4), \ W_{mnl;11}^L = (v_2 \ v_1 \ v_4 \ v_3),, \\
v_1 &= W_{-211;11}^L = 0.2197\sqrt{\frac{1}{L}}, \ v_2 = W_{211;11}^L = -0.0187\sqrt{\frac{1}{L}}, \\
v_3 &= W_{-112;11}^L = 0.1709\sqrt{\frac{2}{L}}, \ v_4 = W_{112;11}^R = -0.0157\sqrt{\frac{2}{L}}.
\end{aligned} \tag{21.33}$$

Respectively according to (21.11) we have for the phase shifted coupling matrix elements  $W_{mnl;pq}^R = V_{mnl} W_{mnl;pq}^L$ . The resulting effective non-Hermitian Hamiltonian (21.7)

$$\widehat{H}_{eff} = \widehat{H} - i\omega\widehat{\Gamma}$$

consists of

$$\widehat{H} = q_{11} \begin{pmatrix} \omega_{211}^2/q_{11} + 2v_1^2 & v_1 v_2(1 + e^{4i\Delta\phi}) & v_1 v_3(1 - e^{-i\Delta\phi}) & v_1 v_4(1 - e^{-3i\Delta\phi}) \\ v_1 v_2(1 + e^{-4i\Delta\phi}) & \omega_{211}^2/q_{11} + 2v_2^2 & v_2 v_3(1 - e^{3i\Delta\phi}) & v_1 v_4(1 - e^{i\Delta\phi}) \\ v_1 v_3(1 - e^{i\Delta\phi}) & v_2 v_3(1 - e^{-3i\Delta\phi}) & \omega_{112}^2/q_{11} + 2v_3^2 & v_3 v_4(1 + e^{-2i\Delta\phi}) \\ v_1 v_4(1 - e^{3i\Delta\phi}) & v_2 v_4(1 - e^{-4i\Delta\phi}) & v_3 v_4(1 + e^{2i\Delta\phi}) & \omega_{112}^2/q_{11} + 2v_4^2 \end{pmatrix} \tag{21.34}$$

and

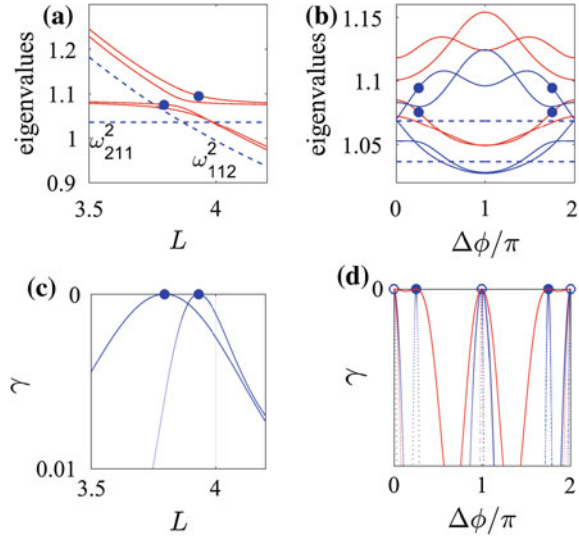
$$\widehat{\Gamma} = \begin{pmatrix} 2|w_1|^2 & w_1^2(1 + e^{4i\Delta\phi}) & w_1 w_2(1 - e^{-i\Delta\phi}) & w_1 w_2(1 - e^{-3i\Delta\phi}) \\ w_1^2(1 + e^{-4i\Delta\phi}) & 2w_1^2 & w_1 w_2(1 - e^{3i\Delta\phi}) & w_1 w_2(1 - e^{i\Delta\phi}) \\ w_1 w_2(1 - e^{i\Delta\phi}) & w_1 w_2(1 - e^{-3i\Delta\phi}) & 2w_2^2 & w_2^2(1 + e^{-2i\Delta\phi}) \\ w_1 w_2(1 - e^{3i\Delta\phi}) & w_1 w_2(1 - e^{-i\Delta\phi}) & w_2^2(1 + e^{2i\Delta\phi}) & 2w_2^2 \end{pmatrix}. \tag{21.35}$$

In contrast to the previous case of crossing of eigenlevels 112 and 012 (the BSC 1), the present case of full matrices impedes analytical consideration of the BSCs. Nevertheless the small size of matrices (21.34) and (21.35) facilitates numerical treatment of the BSCs. Figure 21.23 shows the eigenlevels of the Hamiltonian (21.34)

$$\widehat{H}\mathbf{X}_j = E_j\mathbf{X}_j \tag{21.36}$$

as dependent on the length and rotation angle. One can see that the presence of evanescent modes lifts the degeneracy relative to the sign of  $m$ . Below in Fig. 21.23 we show the resonant widths that demonstrates two BSCs at the points: (1)  $L_c = 3.7947$ ,  $\omega_c^2 =$

**Fig. 21.23** (Color online) The eigenlevels (21.23) (solid lines) as dependent on **a** length of resonator at  $\phi = \pi/41$  and **b** rotation angle at  $L = 3.7947$  (blue) and  $L = 3.9312$  (green) compared to the eigenfrequencies of the closed resonator (dash lines). **c** and **d** Corresponding behavior of the resonant widths defined by imaginary parts of the effective non-Hermitian Hamiltonian (21.34) and (21.35). Closed circles mark the BSCs. Open circles mark the symmetry protected BSCs



1.0756,  $\phi_c = \pi/4$  and (2)  $L_c = 3.9312$ ,  $\omega_c^2 = 1.0946$ ,  $\phi = \pi/4$ . Respectively, in Fig. 21.23b we show the eigenvalues for these BSC lengths.

However in contrast to the former BSCs occurring at the crossing of eigenlevels (21.25) the present BSCs are allocated neither at the crossing of neither the eigenfrequencies  $\omega_{112}$  and  $\omega_{211}$  nor the eigenlevels modified by the evanescent modes as seen from Fig. 21.23. Such phenomenon is generic in open chaotic billiards where the eigenlevels of the closed billiard undergo avoided crossing [52] similar to that shown in Fig. 21.23a. In that case some of the eigenmodes of the Hamiltonian (21.34) can decouple under the evolution of the parameters of the resonator. In the truncated description of the BSCs we obtain the following solutions for the BSCs presented in Table 21.5. Comparison with numerical results in full basis (Table 21.2) shows good agreement with the BSCs (2) and (3). Anyway as seen from Fig. 21.5 the BSCs are expanded over all four eigenmodes  $\pm 211$  and  $\pm 112$  of the closed resonator. Remarkably, in the description of the eigenmodes (21.36)  $\mathbf{X}_j$  we obtain that the numerical amplitudes of the BSC mode  $\psi_{BSC} = \sum_{j=1}^4 b_j \mathbf{X}_j$  are the following

$$\begin{aligned}
 (3) \quad \psi_{BSC} &= \mathbf{X}_2, \quad L_c = 3.7947, \quad \omega_c^2 = 1.0756, \quad \Delta\phi_c = \pi/4, \\
 (4) \quad \psi_{BSC} &= \mathbf{X}_1, \quad L_c = 3.9312, \quad \omega_c^2 = 1.0966, \quad \Delta\phi_c = \pi/4. \quad (21.37)
 \end{aligned}$$

Thus, in this description we have an important result that the BSC is simply one of the eigenmodes of the resonator coupled to the evanescent modes. For this eigenmode to be decoupled from the propagating channel of both waveguides the overlapping integrals

**Table 21.5** BSC solutions 3 and 4 resulted by crossing of modes  $\pm 112$  and  $\pm 211$

BSC number	$\omega^2$	$L$	$\Delta\phi$	$mn\ell$	$a_{mn\ell}$
3	1.0756	3.7947	$\pi/4$	211	0.6715i
				-211	0.6715
				112	-0.2047- 0.0848i
				-112	-0.0848- 0.2047i
4	1.0966	3.9312	$\pi/4$	211	-0.553i
				-211	0.553
				112	-0.407-0.168i
				-112	0.168 + 0.407i

$$W_{j;01}^C = \psi_{01}(z = z_C)\psi_l(z_C) \int_0^{2\pi} d\alpha \int_0^1 \rho d\rho \vec{X}_j(r(\rho, \alpha), \phi(\rho, \alpha)), C = L, R \tag{21.38}$$

have to be zero for selected  $j = 1$  or  $j = 2$ . Figure 21.24 demonstrates that the overlapping integral vanishes at the BSC points. Such BSCs form new class of the

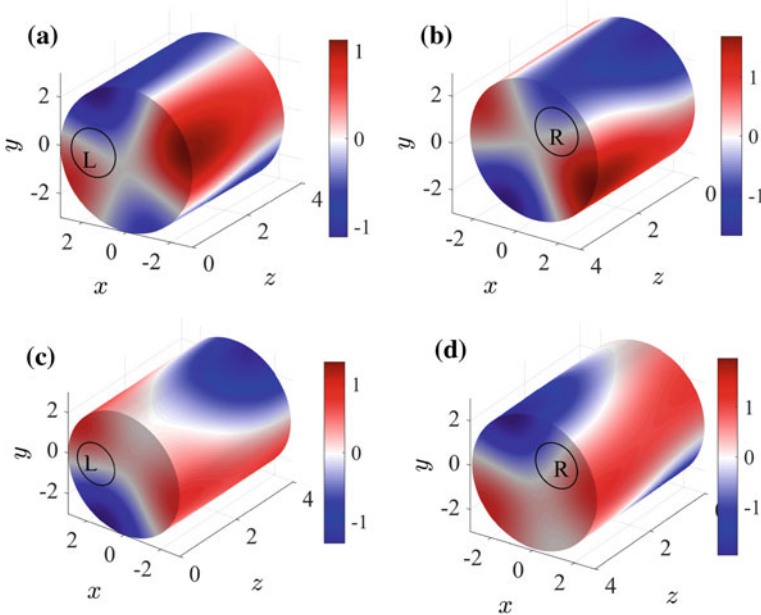
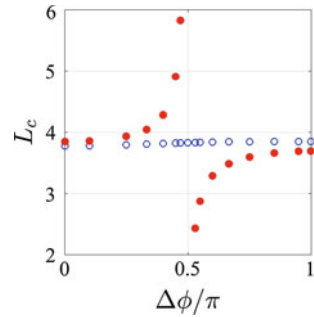


**Fig. 21.24** (Color online) The real parts of the eigenmodes (21.36) of modified Hamiltonian (21.34). **a** and **b**  $X_2$  at the BSC point (3) (21.37) with side of input and output respectively. **c** and **d** the same for the  $X_1$  at the BSC point (4)

**Fig. 21.25** (Color online)  
Lines of the BSCs in the  
parametric space of the  
resonator length and rotation  
angle  $\Delta\phi$



accidental BSCs [13, 52]. Figure 21.24 demonstrates that the BSC modes  $\vec{X}_j$  are twisted to have zero coupling on both interfaces. Again the BSCs occur on lines in the parametric space  $L$  and  $\Delta\phi$  as shown in Fig. 21.25 by open circles. However there is the second line in which the BSC length  $L_c$  diverges when  $\Delta\phi \rightarrow \pi/2$ . Also it is important to note that the BSC modes (21.37) do not support currents of acoustic intensity similar to the BSC 1 and 2.

## 21.6 Conclusions

We considered trapped modes or bound states in the continuum in a non-axisymmetric duct-cavity structure which consists of a cylindrical resonator and two cylindrical waveguides whose axes are shifted relative to the axis of the resonator by a distance  $r_0$ . Moreover the axes of the waveguides can be shifted relative to each other by an azimuthal angle  $\Delta\phi$  as shown in Figs. 21.1b and 21.2. The configuration of attachment does not change the eigenfrequencies of the closed resonator but changes the coupling strengths of the propagating modes of attached waveguides with the resonator. Remarkably, that rotation of, say, the input waveguide provides complex phases in the coupling strength that drastically affect the wave transmission because of interference of resonances giving rise to the effect of wave faucet. The effect can be arranged in a realistic acoustic experiment by the use of piston-like hollow-stem waveguides tightly fit to the interior boundaries of a cylindrical cavity [28].

Assume, that the eigenmodes of the same symmetry undergo degeneracy, say, under variation of the resonator length  $L$  as shown by dash lines in Fig. 21.3. After the waveguides are attached to the resonator these modes become resonances which undergo avoided crossings, i.e., the resonant frequencies are repelled from each other and the degeneracy is lifted. Then in the Friedrich-Wintgen scenario [8, 32] one of resonance can acquire zero resonant width giving rise to the BIC. Although the events of degeneracy are the same in the closed cylindrical resonator, the types of BICs cardinally depend on a way opening the resonator. For  $r_0 = 0$  (the case of axisymmetric waveguide) the OAM  $m$  is an integral of motion to give rise to the BICs

with definite OAM degenerate with respect to the sign of  $m$ . Sound transmission takes place independently in each sector given by the  $m$ , i.e., there is no mode conversion between different the channels with different OAM. That scenario of the BICs and sound transmission in axisymmetric cylindrical waveguide was considered in our first paper [28]. Similar sectorial BICs with preserved OAM were considered in [27, 29, 31].

As soon as  $r_0 \neq 0$  even in the simplest case  $\Delta\phi = 0$  the OAM is not preserved because of the absence of rotational symmetry. In that case we found multiple BICs with nonzero OAM under variation of the resonator length  $L$  which differ from the BICs with zero OAM found in the axisymmetric cylindrical waveguide [28]. Irrespectively to the choice of  $r_0$  the BICs occur at the points of degeneracy of two eigenmodes of the same symmetry of the closed cylindrical resonator. That mechanism of wave localization was first described in [32] and has been experimentally realized in microwave set-ups [47].

For  $\Delta\phi \neq 0$  and fixed arbitrary length of the resonator there are multiple symmetry protected BICs whose azimuthal dependence is given by  $\cos[m(\phi - \Delta\phi/2)]$ . They are degenerate relative to the sign of  $m$  and provide zero overlapping with propagating mode  $p = 0, q = 1$  (see Table 21.1) which is independent of  $\phi$ . Irrespectively of the choice of  $\Delta\phi$  or  $r_0$  the injected wave with zero orbital angular momentum  $m = 0$  transmits and reflects with same OAM when only the first channel is opened for the frequency  $\omega < 1.841$ . However, the case  $\Delta\phi \neq 0$  is of special interest because of twisted flows of the acoustic intensity inside the resonator. In this case the non-axial attachment of the waveguides with the resonator lifts the degeneracy of the resonant modes with respect to the sign of orbital angular momentum. These effects can be controlled by simultaneous variation of the length of the resonator and rotation of one of the waveguides. That results in a high acoustic intensity spinning inside the resonator which can be important for the axial radiation torque [49].

Summing up, the rotation of waveguide relative to the cylindrical resonator results in a complex phase of the coupling strength between the waveguide and resonator. Different setups can be proposed for the coupling strengths to acquire a specific phase difference. However, irrespectively to the choice of the setup the opportunity to vary the phase opens a new instrument to control Fano resonances and the transmittance creating a wave faucet.

**Acknowledgements** This work has been supported by RFBR through Grant 17-02-00440. A. S. acknowledges discussions with E. N. Bulgakov, D. N. Maksimov, H. Schanz, P. Seba, L. Sirko, H.-J. Stöckmann and Shubo Wang.

## References

1. J. von Neumann, E.P. Wigner, Über merkwürdige diskrete eigenwerte (About strange discrete eigenvalue). *Z. Physik* **50**, 291–293 (1929)
2. F. Stillinger, D. Herrick, Bound states in the continuum. *Phys. Rev. A* **11**, 446–454 (1975)

3. R. Parker, Resonance effects in wake shedding from parallel plates: some experimental observations. *J. Sound Vib.* **4**, 62–72 (1966)
4. R. Parker, Resonance effects in wake shedding from parallel plates: calculation of resonant frequencies. *J. Sound Vib.* **5**, 330–343 (1967)
5. J.U. Nöckel, Resonances in quantum-dot transport. *Phys. Rev. B* **46**, 15348–15356 (1992)
6. C.S. Kim, A.M. Satanin, Y.S. Joe, R.M. Cosby, Resonant tunneling in a quantum waveguide: effect of a finite-size attractive impurity. *Phys. Rev. B* **60**, 10962–10970 (1999)
7. O. Olendski, L. Mikhailovska, Bound state evolution in curved waveguides and quantum wires. *Phys. Rev. B* **66**, 035331 (2002)
8. A.F. Sadreev, E.N. Bulgakov, I. Rotter, Bound states in the continuum in open quantum billiards with a variable shape. *Phys. Rev. B* **73**, 235342 (2006)
9. S. Shipman, S. Venakides, Resonant transmission near non robust periodic slab modes. *Phys. Rev. E* **71**, 026611 (2005)
10. D. Marinica, A. Borisov, S. Shabanov, Bound states in the continuum in photonics. *Phys. Rev. Lett.* **100**, 183902 (2008)
11. E. Bulgakov, A. Sadreev, Bound states in the continuum in photonic waveguides inspired by defects. *Phys. Rev. B* **78**, 075105 (2008)
12. Y. Plotnik, O. Peleg, F. Dreisow, M. Heinrich, S. Nolte, A. Szameit, M. Segev, Experimental observation of optical bound states in the continuum. *Phys. Rev. Lett.* **107**, 183901 (2011)
13. C.W. Hsu, B. Zhen, A.D. Stone, J.D. Joannopoulos, M. Soljačić, Bound states in the continuum. *Nat. Rev. Mat.* **1**, 16048–16061 (2016)
14. A. Kodigala, T. Lepetit, Q. Gu, B. Bahari, Y. Fainman, B. Kanté, Lasing action from photonic bound states in continuum. *Nature* **541**, 196–199 (2017)
15. F. Ursell, Trapping modes in the theory of surface waves. *Math. Proc. Camb. Phil. Soc.* **47**, 347–358 (1951)
16. F. Ursell, Trapped modes in a circular cylindrical acoustic waveguide. *Proc. R. Soc. Lond. A* **435**, 575–589 (1991)
17. P. Exner, P. Šeba, P. Štoviček, On existence of a bound state in L-shaped waveguide. *Czech J. Phys. B* **39**, 1181–1191 (1989)
18. J. Goldstone, R.L. Jaffe, Bound states in twisting tubes. *Phys. Rev. B* **45**, 14100–14107 (1992)
19. D. Duclos, P. Exner, Curvature-induced bound states in quantum waveguides in two and three dimensions. *Rev. Math. Phys.* **7**, 73–102 (1995)
20. S.N. Gaultier, N.R.T. Biggs, Acoustic trapped modes in a three-dimensional waveguide of slowly varying cross section. *Proc. R. Soc. A* **469**, 1–17 (2017)
21. D.V. Evans, R. Porter, Trapped modes embedded in the continuous spectrum. *Q. J. Mech. Appl. Math.* **52**, 263–274 (1998)
22. C.M. Linton, P. McIver, Trapped modes in cylindrical waveguides. *J. Mech. Appl. Math.* **51**, 389–412 (1998)
23. M. Callan, C.M. Linton, D.V. Evans, Trapped modes in two-dimensional waveguides. *J. Fluid Mech.* **229**, 51–64 (1991)
24. D.V. Evans, R. Porter, Trapped modes about multiple cylinders in a channel. *J. Fluid Mech.* **339**, 331–356 (1997)
25. T. Utsunomiya, R.E. Taylor, Trapped modes around a row of circular cylinders in a channel. *J. Fluid Mech.* **386**, 259–279 (1999)
26. Y. Duan, M. McIver, Rotational acoustic resonances in cylindrical waveguides. *Wave Motion* **39**, 261–274 (2004)
27. S. Hein, W. Koch, L. Nannen, Trapped modes and Fano resonances in two-dimensional acoustical duct-cavity systems. *J. Fluid Mech.* **692**, 257–287 (2012)
28. A.A. Lyapina, D.N. Maksimov, A.S. Pilipchuk, A.F. Sadreev, Bound states in the continuum in open acoustic resonators. *J. Fluid Mech.* **780**, 370–387 (2015)
29. L. Xiong, W. Bi, Y. Aurégan, Fano resonance scatterings in waveguides with impedance boundary conditions. *J. Acoust. Soc. Am.* **139**, 764–772 (2016)
30. A.A. Lyapina, A.S. Pilipchuk, A.F. Sadreev, Trapped modes in a non-axisymmetric cylindrical waveguide. *J. Sound Vib.* **421**, 48–60 (2018)

31. S. Hein, W. Koch, Acoustic resonances and trapped modes in pipes and tunnels. *J. Fluid Mech.* **605**, 401–428 (2008)
32. H. Friedrich, D. Wintgen, Interfering resonances and bound states in the continuum. *Phys. Rev. A* **32**, 3231–3242 (1985)
33. H. Feshbach, Unified theory of nuclear reactions. *Ann. Phys. (NY)* **19**, 287–313 (1962)
34. J. Okołowicz, M. Płoszajczak, I. Rotter, Dynamics of quantum systems embedded in a continuum. *Phys. Rep.* **374**, 271–383 (2003)
35. F.M. Dittes, The decay of quantum systems with a small number of open channels. *Phys. Rep.* **339**, 215–316 (2000)
36. A.F. Sadreev, I. Rotter, S-matrix theory for transmission through billiards in tight-binding approach. *J. Phys. A Math. Gen.* **36**, 11413–11433 (2003)
37. D.N. Maksimov, A.F. Sadreev, A.A. Lyapina, A.S. Pilipchuk, Coupled mode theory for acoustic resonators. *Wave Motion* **56**, 52–79 (2015)
38. K. Pichugin, H. Schanz, P. Seba, Effective coupling for open billiards. *Phys. Rev. E* **64**, 056227 (2001)
39. V.V. Sokolov, V.G. Zelevinsky, Dynamics and statistics of unstable quantum states. *Nucl. Phys. A* **504**, 562–588 (1989)
40. E.N. Bulgakov, I. Rotter, A.F. Sadreev, Comment on “Bound-state eigenenergy outside and inside the continuum for unstable multilevel systems”. *Phys. Rev. A* **75**, 067401 (2007)
41. A.F. Sadreev, A.S. Pilipchuk, A.A. Lyapina, Tuning of Fano resonances by rotation of continuum: wave faucet. *Euro Phys. Lett.* **117**, 50011 (2017)
42. M. Zhang, X. Zhang, Ultrasensitive optical absorption in graphene based on bound states in the continuum. *Sci. Rep.* **5**(8266), 1–7 (2015)
43. M. Song, Y. Honglin, C. Wang, N. Yao, P. Mingbo, J. Luo, Z. Zhang, X. Luo, Sharp Fano resonance induced by a single layer of nanorods with perturbed periodicity. *Opt. Express* **23**, 2895–2903 (2015)
44. R.V. Waterhouse, D. Feit, Equal-energy streamlines. *J. Acoust. Soc. Am.* **80**, 681–684 (1986)
45. D.M.F. Chapman, Using stream lines to visualized acoustic energy flow across boundaries. *J. Acoust. Soc. Am.* **124**, 48–56 (2008)
46. R.E. Musafir, On non-radiating sources. *J. Sound Vibr.* **332**, 3947–3955 (2013)
47. T. Lepetit, E. Akmansoy, J.-P. Ganne, J.-M. Lourtioz, Resonance continuum coupling in high-permittivity dielectric metamaterials. *Phys. Rev. B* **82**, 195307 (2010)
48. T. Lepetit, B. Kante, Controlling multipolar radiation with symmetries for electromagnetic bound states in the continuum. *Phys. Rev. B* **90**, 241103(R) (2014)
49. L. Zhang, P.L. Marston, Angular momentum flux of nonparaxial acoustic vortex beams and torques on axisymmetric objects. *Phys. Rev. E* **84**, 065601(R) (2011)
50. F. Remacle, M. Munster, V.B. Pavlov-Verevkin, M. Desouter-Lecomte, Trapping in competitive decay of degenerate states. *Phys. Lett. A* **145**, 265–268 (1990)
51. E.N. Bulgakov, A.F. Sadreev, Spin polarized bound states in the continuum in open Aharonov Bohm rings with the Rashba spinorbit interaction. *J. Phys. Condens. Matter* **28**, 265301 (2016)
52. A.S. Pilipchuk, A.F. Sadreev, Accidental bound states in the continuum in an open Sinai billiard. *Phys. Lett. A* **381**, 720–724 (2017)



# Chapter 22

## Interaction of MDM Ferrite Particles with a Microwave-Field Continuum



Eugene Kamenetskii

**Abstract** Magnetic-dipolar modes (MDMs) in a quasi-2D ferrite disk are microwave energy-eigenstate oscillations with topologically distinct structures of rotating fields and unidirectional power-flow circulations. Quantized vortices in MDM oscillations manifest the long-range phase coherence of magnetic dipole-dipole interaction which are described by a complex-valued order parameter field—the magnetostatic-potential (MS-potential) scalar wave function. Because of strong spin–orbit interaction in magnetization dynamics, the MDMs in a quasi-2D ferrite disk are helical resonances. The magnon-photon interaction can be indicated as helical bound states in a microwave continuum. We analyze quasistatic eigenvalue problems for magnon oscillations in subwavelength particles and consider interaction of these particles with a microwave-field continuum.

### 22.1 Introduction

The dual symmetry between electric and magnetic fields underlies the conservation of energy and momentum for electromagnetic fields [1]. It can be connected also with conservation of polarization of the electromagnetic field. In particular, this symmetry underlies the conservation of optical (electromagnetic) helicity [2–4]. It is stated [4] that the dual electromagnetic theory inherently contains straightforward and physically meaningful descriptions of the helicity, spin and orbital characteristics of light.

What kind of the source-free time-varying field structure one can expect to see when an electric or magnetic displacements currents are neglected and so the electromagnetic-field symmetry (dual symmetry) of Maxwell equations is broken? As one of examples of such a symmetry breaking, we can refer to the field structures studied in non-conductive artificial electromagnetic materials that exhibit zero

---

E. Kamenetskii (✉)

Microwave Magnetic Laboratory, Department of Electrical and Computer Engineering, Ben Gurion University of the Negev, Beersheba, Israel  
e-mail: kmntsk@bgu.ac.il

© Springer Nature Switzerland AG 2018

E. Kamenetskii et al. (eds.), *Fano Resonances in Optics and Microwaves*, Springer Series in Optical Sciences 219, [https://doi.org/10.1007/978-3-319-99731-5\\_22](https://doi.org/10.1007/978-3-319-99731-5_22)

527

(or near-zero) permittivity [5, 6]. For these materials, no Maxwell correction (no electric displacement current) exists and the fields are described by three differential equations (instead of the four-Maxwell-equation description of electromagnetic fields). In an assumption that a zero-permittivity medium is magnetically isotropic, one has the static-like fields. Light passing through such a material experiences no phase shift. Evidently, no unified-field retardation effects are observed in structures created by these materials.

For a case of plasmonic (electrostatic) resonances in small metallic samples, one can neglect a magnetic displacement current and consider quasistationary electric fields, which are described by electrostatic-potential functions. In this description, subwavelength sizes of the particles eliminates any effects of the internal electromagnetic retardation processes. Corrections to electrostatic resonance modes due to electromagnetic retardation can be found by using series expansions of the solutions to time harmonic Maxwell equations with respect to the small ratio of the object size to the free-space wavelength. This electromagnetic- retardation process gives coupling between the electric and magnetic fields [7].

Magnetic-dipolar-mode (MDM) oscillations (or magnetostatic-wave oscillations) in small ferrite samples can be considered as an approximation to Maxwell equations when a displacement electric current is negligibly small. The physical justification for such an approximation arises from the fact that in a small (with sizes much less than a free-space electromagnetic wavelength) sample of a magnetic material with strong temporal dispersion (due to the ferromagnetic resonance) one neglects a time variation of electric energy in comparison with a time variation of magnetic energy [8–10]. Subwavelength sizes of such a ferrite particle eliminate any electromagnetic-retardation phenomena and to describe the retardation effects of MDM oscillations one uses the Walker equation for MS-potential scalar wave function  $\psi(\vec{r}, t)$  [11]. The solutions show the existence of non-Maxwellian propagation-wave behaviors for the magnetostatic resonances.

Long-range magnetic-dipolar interactions in confined magnetic structures are not in the scope of classical electromagnetic problems and, at the same time, have properties essentially different from the effects of exchange ferromagnetism. The MDM spectral properties in confined magnetic structures are based on postulates about physical meaning of the magnetostatic (MS) potential function  $\psi(\vec{r}, t)$  as a complex scalar wave function, which presumes long-range phase coherence. MDM oscillations in ferrite spheres excited by external microwave fields were experimentally observed, for the first time, by White and Solt in 1956 [12]. Afterwards, experiments with disk-form ferrite specimens revealed unique spectra of oscillations. While in a case of a ferrite sphere one observed only a few wide absorption peaks of MDM oscillations, for a ferrite disk there was a multiresonance (atomic-like) spectrum with very sharp resonance peaks [13–15]. Analytically, it was shown [16–18] that, contrary to spherical geometry of a ferrite particle analyzed in [11], the Walker equation (together with the homogeneous boundary conditions for function  $\psi$  and its derivatives) for quasi-2D geometry of a ferrite disk gives the Hilbert-space energy-state selection rules for MDM spectra [16–18]. The near fields originated from small ferrite-disk particles with MDM oscillations are the fields with the electric and

magnetic components, but with broken dual (electric–magnetic) symmetry. These fields—called magnetoelectric (ME) fields—have topological properties different from such properties of electromagnetic fields. The ME fields are characterized by power-flow vortices, nonzero helicity, and a torsion degree of freedom [19].

In this chapter we study eigenvalue problems for MDM oscillations in subwavelength ferrite-disk particles, consider the near fields originated from such particles (the ME fields), and analyze interaction of these particles with a microwave-field continuum.

## 22.2 Quasistatic Eigenvalue Problems for Plasmon and Magnon Oscillations in Subwavelength Particles

Magnetic-dipolar resonances in ferrite samples with dimensions much smaller than the wavelength of microwave radiation has its origin in magnetic-potential theory, which describes systems of magnetic dipoles and the magnetostatic potentials produced by these dipoles. To a certain extent, this can be considered as a situation dual to the electrostatic theory describing the localized surface plasmons in nanoparticles with dimensions much smaller than the wavelength of light, which describes systems of electric dipoles and the electrostatic potentials they produce.

Localized surface plasmons excited by light on metal nanoparticle surfaces are observed experimentally by strong scattering at a particular frequency. When the material linear response is described by a bulk dielectric scalar function  $\varepsilon(\omega)$ , the electrostatic resonances can be found as solutions of the equation for an electrostatic potential  $\phi$  [20]:

$$\vec{\nabla} \cdot (\varepsilon(\vec{r}, \omega) \vec{\nabla} \phi) = 0, \quad (22.1)$$

Here an electrostatic potential is found as  $\vec{E} = -\vec{\nabla} \phi$ . For homogeneous negative permittivity particles ( $\varepsilon_p < 0$ ) in a uniform transparent immersion medium ( $\varepsilon_s > 0$ ) and with use of conventional Dirichlet-Neumann boundary conditions for electrostatic-potential function, this equation acquires a form of a linear generalized eigenvalue problem:

$$\vec{\nabla} \cdot (\theta(\vec{r}) \vec{\nabla} \phi) = s \nabla^2 \phi, \quad (22.2)$$

where  $\theta(\vec{r})$  equals 1 inside the particle and zero outside the particle, and  $s = 1/(1 - \varepsilon_p/\varepsilon_s)$ . The eigenmodes (surface plasmons) are orthogonal and are assumed to be normalized as [20, 21]

$$\int \phi_q^*(\vec{r}) \nabla^2 \phi_{q'}(\vec{r}) d^3 r = \delta_{q,q'} \quad (22.3)$$

It was pointed out that for electrostatic resonances in nanoparticles one has a non-Hermitian eigenvalue problem with bi-orthogonal (instead of regular-orthogonal) eigenfunctions [22, 23]. Such an orthonormal set of scalar functions differs from the orthonormal set of scalar functions used in quantum mechanics as derived from the Schrödinger equation. The difference is that the quantum wave equation is Hermitian so that its adjoint is equal to the complex conjugate resulting in complex eigenfunctions that are orthonormal [7].

The spectral solutions for eigenvalue problem for magnetic-dipolar resonances in a small ferrite sample can be obtained based on Walker equation for magnetostatic wave function [11]

$$\vec{\nabla} \cdot (\vec{\mu} \cdot \vec{\nabla} \psi) = 0 \quad (22.4)$$

Here  $\psi$  is a magnetostatic (MS) potential defined as  $\vec{H} = -\vec{\nabla} \psi$ . The equation is obtained based on a constitutive relation for a ferrite,

$$\vec{B} = \vec{\mu}(\omega, \vec{H}_0) \cdot \vec{H}, \quad (22.5)$$

where  $\vec{\mu}(\omega, \vec{H}_0)$  is a tensor of ferrite permeability at the ferromagnetic-resonance frequency range,  $\vec{H}_0$  is a bias magnetic field. Outside the ferrite one has the Laplace equation  $\nabla^2 \psi = 0$ . To obtain the MDM spectral solutions, the boundary conditions for the MS-potential scalar wave function  $\psi(\vec{r}, t)$  and its space derivatives should be imposed.

In the description of quasistatic oscillations in small particles, one uses a classical formalism where the material linear response at frequency  $\omega$  is described by a local bulk dielectric function the permittivity tensor  $\vec{\varepsilon}(\omega)$  or by a local bulk magnetic function the permeability tensor  $\vec{\mu}(\omega)$ . For a case of plasmonic (electrostatic) resonances in small metallic samples, one neglects a magnetic displacement current and has quasistationary electric fields. A dual situation is demonstrated for magnetic-dipolar (magnetostatic) resonances in small ferrite samples, where one neglects an electric displacement current. It is evident that these potentials do not have the same physical meaning as in the problems of “pure” (non-time-varying) electrostatic and magnetostatic fields [1, 10]. Because of the resonant behaviors of small dielectric/metallic or small magnetic objects (confinement phenomena plus temporal-dispersion conditions of tensors  $\vec{\varepsilon}(\omega)$  or  $\vec{\mu}(\omega)$ ), one has scalar wave functions: an electrostatic-potential wave function  $\phi(\vec{r}, t)$  and a magnetostatic-potential wave function,  $\psi(\vec{r}, t)$ , respectively. The main note is that since in the eigenvalue problem, we are on a level of the continuum description of media (based on tensors  $\vec{\varepsilon}(\omega)$  or  $\vec{\mu}(\omega)$ ), the boundary conditions for quasistatic oscillations should be imposed on scalar wave functions  $\phi(\vec{r}, t)$  or  $\psi(\vec{r}, t)$  and their derivatives, but not on the RF functions of polarization (plasmons) or magnetization (magnons). One has to keep in mind that in phenomenological models based on the effective-medium (the

$\tilde{\varepsilon}(\omega)$ - or  $\tilde{\mu}(\omega)$ -continuum) description, no electron-motion equations and boundary conditions corresponding to these equations are used.

Fundamentally, subwavelength sizes should eliminate any effects of the electromagnetic retardation. When one neglects the displacement currents (magnetic or electric) and considers scalar functions  $\phi(\vec{r}, t)$  or  $\psi(\vec{r}, t)$  as the wave functions, one becomes faced with important questions, whether there could be the propagation behaviors inherent for the quasistatic wave processes and, if any, what is the nature of these retardation effects. In a case of electrostatic resonances, the Ampere-Maxwell law gives the presence of a curl magnetic field. With this magnetic field, however, one cannot define the power-flow density of propagating electrostatic-resonance waves. Certainly, from a classical electrodynamics point of view [1], one does not have a physical mechanism describing the effects of transformation of a curl magnetic field to a potential electric field. In like manner, one can see that in a case of magnetostatic resonances, the Faraday law gives the presence of a curl electric field. With this electric field one cannot define the power-flow density of propagating magnetostatic-resonance waves since, from a classical electrodynamics point of view, one does not have a physical mechanism describing the effects of transformation of a curl electric field to a potential magnetic field [1]. So, from Maxwell equations it follows that in a case of electrostatic resonances, characterizing by a scalar wave function  $\phi(\vec{r}, t)$ , the time-varying electric fields cannot be accompanied at all with the RF magnetic fields and, similarly, in a case of magnetostatic resonances, characterizing by scalar wave function  $\psi(\vec{r}, t)$ , the time-varying magnetic fields cannot be accompanied at all with the RF electric field. This fact is perceived, in particular, from the following remarks by McDonald [24, 25].

In frames of the quasiolestatic approximation, we introduce electrostatic-potential function  $\phi(\vec{r}, t)$  excluding completely the magnetic displacement current:  $\frac{\partial \vec{B}}{\partial t} = 0$ . At the same time, from the Maxwell equation (the Ampere-Maxwell law),  $\vec{\nabla} \times \vec{H} = \frac{\partial \vec{D}}{\partial t}$ , we write that  $\vec{\nabla} \times \frac{\partial \vec{H}}{\partial t} = \frac{\partial^2 \vec{D}}{\partial t^2}$ . If a sample does not possess any magnetic anisotropy, we have  $\frac{\partial^2 \vec{D}}{\partial t^2} = 0$ . Similarly, in frames of the quasiolestatic approximation, we introduce magnetostatic-potential function  $\psi(\vec{r}, t)$  excluding completely the electric displacement current:  $\frac{\partial \vec{D}}{\partial t} = 0$ . From Maxwell equation (the Faraday law),  $\vec{\nabla} \times \vec{E} = -\frac{\partial \vec{B}}{\partial t}$ , we obtain that  $\vec{\nabla} \times \frac{\partial \vec{E}}{\partial t} = -\frac{\partial^2 \vec{B}}{\partial t^2}$ . If a sample does not possess any dielectric anisotropy, we have  $\frac{\partial^2 \vec{B}}{\partial t^2} = 0$ . From the above equations on the second derivatives of the fields ( $\frac{\partial^2 \vec{D}}{\partial t^2} = 0$  and  $\frac{\partial^2 \vec{B}}{\partial t^2} = 0$ ), it follows that the electric field in small resonant dielectric/metallic objects as well as the magnetic field in small resonant magnetic objects vary linearly with time. This leads, however, to arbitrary large fields at early and late times, and is excluded on physical grounds. An evident conclusion suggests itself at once: the electric field (for electrostatic resonances) and the magnetic field (for magnetostatic resonances) are constant quantities. Such a conclusion contradicts the fact of temporally dispersive media and thus any resonant conditions. The above analysis definitely means that, from classical electrodynamics, the eigenvalue problem formulated *exceptionally* for

the electrostatic-potential wave function  $\phi(\vec{r}, t)$  do not presume an involvement of alternative magnetic fields in a resonance process and, similarly, the eigenvalue problem formulated *exceptionally* for the magnetostatic-potential function wave  $\psi(\vec{r}, t)$  do not presume an involvement of alternative electric fields in magnetic-dipolar resonances. The curl magnetic field appearing in plasmonic oscillations due to the Ampere-Maxwell law, does not affect the electrostatic result. Similarly, the curl electric field appearing in magnonic oscillations due to the Faraday law does not affect the magnetostatic result.

A role of the magnetic field in plasmonic oscillations in metal nanoparticle becomes appreciable only when in an eigenvalue problem one deviates from the electrostatic approximation to the full-Maxwell-equation description. Corrections to electrostatic resonance modes due to electromagnetic retardation can be found by using series expansions of the solutions to time harmonic Maxwell equations with respect to the small ratio of the object size to the free-space wavelength [7, 26]. It was shown that anomalous light scattering with quite unusual scattering diagrams and enhanced scattering cross sections near plasmon (polariton) resonance frequencies is non-Rayleigh scattering. The observed power-flow patterns cannot be understood within the frame of a dipole approximation and the terms of higher orders with respect to size parameter  $q = 2\pi a/\lambda$  should be taken into account [27–29]. The analogous situation takes place when one considers a role of the electric field in magnetic-dipolar resonances in ferrite samples. In a similar way, corrections to magnetostatic resonance modes due to electromagnetic retardation can be found by using series expansions of the solutions to time harmonic Maxwell equations with respect to the small ratio of the object size to the free-space wavelength [8].

The fact that the retardation effects in the plasmonic or magnonic oscillations appear only when the particle sizes are comparable with the free-space electromagnetic wavelength raises the question on the possibility of existence of non-Maxwellian propagation-wave behaviors for the quasistatic-resonance processes. In electromagnetically subwavelength particles, there can be, for example, space-charge waves in semiconductors [30] and waves of magnetization (spin waves) in ferrites [8]. The latter is the subject of our analysis in the present paper.

Solutions of the spectral problem for magnetostatic-potential wave function give evidence for two distinctive features on MDMs in a ferrite samples. Firstly, there is the existence of non-Maxwellian propagation-wave behaviors for the magnetostatic resonances. Secondly, we show that a case of a quasi-2D ferrite-disk particle, the problem for magnetostatic-potential wave function  $\psi(\vec{r}, t)$  can be considered as Hermitian. In such a ferrite particle, the function  $\psi(\vec{r}, t)$  appears as an orthonormal complex eigenfunction. The adjoint of this function is equal to its complex conjugate quantity. This differs from the resonances in metal nanoparticles where one has a non-Hermitian eigenvalue problem for electrostatic-potential wave function  $\phi(\vec{r}, t)$  [7, 22, 23].

## 22.3 The Spectral Problem for Magnetostatic-Potential Wave Function

### 22.3.1 MDMs in a Ferrite Rod

To show the existence of non-Maxwellian propagation-wave behaviors for the magnetostatic resonances we consider initially propagation of MDMs in a longitudinally-magnetized ferrite rod. MDMs in a ferrite sample are described by two differential equations:  $\vec{H} = -\vec{\nabla}\psi$  and  $\nabla \cdot \vec{B} = 0$ . Taking the constitutive relation for a ferrite,  $\vec{B} = \vec{\mu} \cdot \vec{H}$ , we present the problem in following operator-equation form [16, 17]:

$$\hat{L}V = 0, \quad (22.6)$$

where

$$\hat{L} \equiv \begin{pmatrix} (\vec{\mu})^{-1} \nabla \\ \nabla \cdot 0 \end{pmatrix} \quad (22.7)$$

and

$$V \equiv \begin{pmatrix} \vec{B} \\ \psi \end{pmatrix}. \quad (22.8)$$

The spectral problem for MDMs in a cylindrical ferrite rod is described by a differential-matrix-operator equation [16, 17]

$$\hat{L}_\perp \tilde{V} = i\beta_z \hat{R} \tilde{V}, \quad (22.9)$$

where  $\hat{L}_\perp \equiv \begin{pmatrix} (\vec{\mu})^{-1} \vec{\nabla}_\perp \\ \vec{\nabla}_\perp \cdot 0 \end{pmatrix}$  is the differential-matrix operator,  $\beta_z$  is the MS-wave

propagation constant along the  $z$ -axis,  $\tilde{V} \equiv \begin{pmatrix} \vec{B} \\ \psi \end{pmatrix}$  is the membrane vector function

( $\psi \propto \tilde{\varphi} e^{-i\beta_z z}$ ,  $\vec{B} \propto \vec{\tilde{B}} e^{-i\beta_z z}$ ),  $\hat{R} \equiv \begin{pmatrix} 0 & \vec{e}_z \\ -\vec{e}_z & 0 \end{pmatrix}$ , and  $\vec{e}_z$  is the unit vector along  $z$  axis. Subscript  $\perp$  means differentiation over the in-plane,  $r, \theta$ , coordinates of a waveguide cross section.

Integration by parts on  $S$ —a square of an open MS-wave cylindrical waveguide—of the integral  $\int_S \left[ \hat{L}_\perp \left( \begin{matrix} \widetilde{\vec{B}} \\ \widetilde{\psi} \end{matrix} \right) \right] \left( \begin{matrix} \widetilde{\vec{B}} \\ \widetilde{\psi} \end{matrix} \right)^* dS$  gives the contour integral in a form  $\oint_C (\widetilde{\vec{B}}_r \widetilde{\psi}^* - \widetilde{\vec{B}}_r^* \widetilde{\psi}) dC$ , where  $C$  is a contour surrounding a cylindrical ferrite core and  $\widetilde{\vec{B}}_r$  is a radial component of a membrane function of the magnetic flux density. Operator  $\hat{L}_\perp$  becomes self-adjoint for homogeneous boundary conditions (continuity of  $\widetilde{\varphi}$  and  $\widetilde{B}_r$ ) on contour  $C$ . Based on the homogeneous boundary conditions one obtains the orthogonality relation for MDMs propagating in a ferrite rod:

$$(\beta_m - \beta_n) \int_S (\hat{R} \widetilde{V}_m) (\widetilde{V}_n)^* dS = 0. \quad (22.10)$$

The norm of mode  $n$  is determined as

$$N_n = \int_S (\widetilde{\varphi}_n \widetilde{B}_n^* - \widetilde{\varphi}_n^* \widetilde{B}_n) \cdot \vec{e}_z dS. \quad (22.11)$$

It is easy to show that norm  $N_n$ , being multiplied by a proper dimensional coefficient, corresponds to the power flow of the waveguide mode  $n$  through a waveguide cross section. For monochromatic fields with time variation  $\sim e^{i\omega t}$  we have for the power flow:

$$(p_n)_z = -\frac{i\omega}{4} N_n = \frac{i\omega}{4} \int_S (\widetilde{\varphi}_n^* \widetilde{B}_n - \widetilde{\varphi}_n \widetilde{B}_n^*) \cdot \vec{e}_z dS. \quad (22.12)$$

To show clearly, why this equation characterizes the power flow density, let us consider a general case of propagation of MS waves in a ferrite medium with small losses. The energy balance equation for monochromatic MS waves in such a lossy magnetic media is:

$$-\frac{i\omega}{4} \vec{\nabla} \cdot (\psi \vec{B}^* - \psi^* \vec{B}) = -\frac{i\omega}{4} \left[ \vec{B} \cdot (\vec{\mu}^*(\omega))^{-1} \cdot \vec{B}^* - \vec{B}^* \cdot (\vec{\mu}(\omega))^{-1} \cdot \vec{B} \right]. \quad (22.13)$$

On the right-hand side of this equation, we have the average density of magnetic losses taken with an opposite sign. Thus, the term on the left-hand side is the divergence of the power flow density. Really, in a region of a FMR, the average density of magnetic energy absorption can be expressed as

$$\left\langle \frac{\partial w}{\partial t} \right\rangle_{\text{abs}} = \frac{i\omega}{2} \vec{H}^* \cdot \vec{\mu}^{\text{ah}}(\omega) \cdot \vec{H}, \quad (22.14)$$



where  $\vec{H}$  is an internal radio-frequency magnetic field; superscript ah means “anti-Hermitian”. Since  $\vec{B} \cdot (\vec{\mu}^*(\omega))^{-1} \cdot \vec{B}^* - \vec{B}^* \cdot (\vec{\mu}(\omega))^{-1} \cdot \vec{B} = 2\vec{H}^* \cdot \vec{\mu}^{\text{ah}}(\omega) \cdot \vec{H}$ , the right-hand side of (22.13) describes the density of magnetic losses taken with an opposite sign [8, 31].

For a bias magnetic field directed along  $z$  axis, the permeability tensor has a form:

$$\vec{\mu} = \mu_0 \begin{pmatrix} \mu & i\mu_a & 0 \\ -i\mu_a & \mu & 0 \\ 0 & 0 & 1 \end{pmatrix}, \quad (22.15)$$

where  $\mu$  and  $\mu_a$  are real quantities dependent on both frequency  $\omega$  and a bias magnetic field  $H_0$  [8]. In a general form, we present the solution for the mode  $n$  as

$$\psi_n = C_n \xi_n(z) \tilde{\varphi}_n(r, \theta), \quad (22.16)$$

where  $\xi_n(z)$  is an amplitude factor,  $C_n$  is a dimensional coefficient and  $\tilde{\varphi}_n(r, \theta)$  is a dimensionless membrane function. In a particular case of MS waves propagating in a ferrite waveguide, we have  $\xi_n(z) = e^{-i\beta_n z}$ , where  $\beta_n$  is the propagation constant of mode  $n$ .

For magnetic flux density  $(\vec{B}_n = -\vec{\mu} \cdot \vec{\nabla} \psi_n)$ , we can write

$$\vec{B}_n = \left( \vec{B}_n \right)_z \vec{e}_z + \tilde{B}_n \vec{e}_\perp, \quad (22.17)$$

where

$$\left( \vec{B}_n \right)_z = -C_n \frac{\partial \xi_n(z)}{\partial z} \tilde{\varphi}_n(r, \theta) \quad (22.18)$$

and

$$\tilde{B}_n = -C_n \xi_n(z) \left[ \vec{\mu}_\perp \cdot \vec{\nabla}_\perp \tilde{\varphi}_n(r, \theta) \right] \cdot \vec{e}_\perp. \quad (22.19)$$

Here  $\vec{e}_z$  and  $\vec{e}_\perp$  are unit vectors, directed, respectively, along the rod axis and the cross-section coordinates.

We consider a cylindrical ferrite rod. In this case, the functions  $\tilde{\varphi}_n(r, \theta)$  are the Bessel functions. Let an order of the Bessel function,  $\nu$ , is given and, so, the membrane function  $\tilde{\varphi}_n(r, \theta)$  is determined only by  $r$  variations. For self-adjointness of operator  $\hat{L}_\perp$ , the homogeneous boundary condition should be [16, 17]

$$\mu \left( \frac{\partial \tilde{\varphi}_n}{\partial r} \right)_{r=\mathcal{R}^-} - \left( \frac{\partial \tilde{\varphi}_n}{\partial r} \right)_{r=\mathcal{R}^+} = -\frac{\mu_a}{\mathcal{R}} \nu (\tilde{\varphi}_n)_{r=\mathcal{R}^-}. \quad (22.20)$$

His boundary conditions can be represented as [16, 17]

$$(-\mu)^{\frac{1}{2}} \frac{J'_\nu}{J_\nu} + \frac{K'_\nu}{K_\nu} - \frac{\mu_a \nu}{\beta_n \mathcal{R}} = 0. \tag{22.21}$$

Here  $J_\nu$ ,  $J'_\nu$ ,  $K_\nu$ , and  $K'_\nu$  are the values of the Bessel functions of order  $\nu$  and their derivatives (with respect to the argument) on a lateral cylindrical surface ( $r = \mathcal{R}$ ). From boundary condition (22.20) (or (22.21)) it evidently follows that, for an integer azimuth number  $\nu$  and a given direction of a bias magnetic field (the given sign of parameter  $\mu_a$  [8]), there are different functions,  $\tilde{\varphi}^+$  and  $\tilde{\varphi}^-$ , for positive and negative directions of an angle coordinate when  $0 \leq \theta \leq 2\pi$ .

For MDMs propagating in a waveguide, there is the  $z$  component of the power-flow. On a waveguide cross section, the  $r$  component of the power-flow density is equal to zero. There is, however, a non-zero real azimuth component of the power-flow density:

$$(p_n)_\theta = \frac{i\omega}{4} C_n^2(\xi(z))^2 \left[ -\mu \frac{1}{r} \left( \tilde{\varphi}_n^* \frac{\partial \tilde{\varphi}_n}{\partial \theta} - \tilde{\varphi}_n \frac{\partial \tilde{\varphi}_n^*}{\partial \theta} \right) + i\mu_a \left( \tilde{\varphi}_n^* \frac{\partial \tilde{\varphi}_n}{\partial r} + \tilde{\varphi}_n \frac{\partial \tilde{\varphi}_n^*}{\partial r} \right) \right]. \tag{22.22}$$

With the use of representation  $\tilde{\varphi} = \tilde{\varphi}(r)\tilde{\varphi}(\theta)$ , where  $\tilde{\varphi}(\theta) \propto e^{-i\nu\theta}$ , one has

$$(p_n)_\theta = \frac{\tilde{\varphi}_n(r)}{2} \omega C_n^2(\xi(z))^2 \left[ -\frac{\mu}{r} \tilde{\varphi}_n(r)\nu - \mu_a \frac{\partial \tilde{\varphi}_n(r)}{\partial r} \right]. \tag{22.23}$$

This is a non-zero circulation quantity around a circle  $2\pi r$ . We can see that for a given direction of bias magnetic field there are different power-flow densities  $(p_n(r, z))_\theta$  for different signs of the azimuth number  $\nu$ .

The fact that there are different functions,  $\tilde{\varphi}^+$  and  $\tilde{\varphi}^-$ , for positive and negative directions of an angle coordinate when  $0 \leq \theta \leq 2\pi$  and non-zero circulation of the power-flow density show that operator  $\hat{L}_\perp$  is a self-adjoint, but non-Hermitian operator.

The adjoint of the function  $\tilde{V} = \begin{pmatrix} \tilde{B} \\ \tilde{\varphi} \end{pmatrix}$  is not equal to its complex conjugate quantity. For monochromatic MS waves propagating in an endless ferrite rod, the fact that function  $\tilde{\varphi}_n$  is not a single-valued function (resulting to having the azimuthally rotating-wave solutions), does not bear a real physical meaning. These are not the eigenmodes akin to the well known twisted-wave modes [32, 33] (or, in other words, vortex modes [34]).

### 22.3.2 MDMs in a Ferrite-Disk Particle

In a ferrite disk, considered as a section of a ferrite rod, power flows along the disk axis  $z$  and along the azimuthal coordinate  $\theta$ , becomes coupled. The proper solutions are found based on an analysis of magnetostatic-wave propagation in a helical coordinate system with the pitch defined by a disk thickness [35]. Such an analysis in an endless MS-wave waveguide bears a formal character, but acquires real physical meaning in a case of restricted waveguide sections. We make a supposition that for magnetic-dipolar modes in helical coordinates diagonal and off-diagonal components of the permeability tensor remain the same as in the cylindrical coordinate system. This supposition is clearly acceptable since the long-range magnetic-dipolar field variations have no influence on the character of local spin precession.

The solutions are obtained in Waldron's helical coordinate system  $(r, \phi, \zeta)$  [36]. Following Overfelt's approach [37], the solutions of the Laplace and Walker equations are found as

$$\psi(r, \phi, \zeta) = R(r)P(\phi)Z(\zeta), \quad (2.24)$$

where

$$\begin{aligned} P(\phi) &\sim \exp(\pm iw\phi), \\ Z(\zeta) &\sim \exp(\pm i\beta\zeta). \end{aligned} \quad (2.25)$$

Here the quantities  $w$  and  $\beta$  are assumed to be real and positive. Inside and outside a ferrite rod one has the following four solutions for the MS-potential wave function:

$$\begin{aligned} \psi^{(1)} &\sim e^{-iw\phi} e^{-i\beta\zeta}, \\ \psi^{(2)} &\sim e^{+iw\phi} e^{-i\beta\zeta}, \\ \psi^{(3)} &\sim e^{+iw\phi} e^{+i\beta\zeta}, \\ \psi^{(4)} &\sim e^{-iw\phi} e^{+i\beta\zeta}. \end{aligned} \quad (2.26)$$

We consider the  $\psi^{(1)}$  wave as the forward (propagating in a ferrite rod along  $+z$  axis) right-hand-helix (FR) MS wave. The wave  $\psi^{(2)}$  is the forward left-hand (FL) wave, the wave  $\psi^{(3)}$  is the backward right-hand (BR) wave, and the wave  $\psi^{(4)}$  is the backward left-hand (BL) wave. Functions  $\psi(r)$  are described by the Bessel equations. For a ferrite rod with radius  $\mathfrak{R}$ , we have

$$\frac{\partial^2 \psi(r)}{\partial r^2} + \frac{1}{r} \frac{\partial \psi(r)}{\partial r} - \left[ \frac{\beta^2}{\mu} + \frac{1}{r^2} (w - \bar{p}\beta)^2 \right] \psi(r) = 0 \quad (2.27)$$

inside a ferrite rod ( $r \leq \mathfrak{R}$ ) and

$$\frac{\partial^2 \psi(r)}{\partial r^2} + \frac{1}{r} \frac{\partial \psi(r)}{\partial r} - \left[ \beta^2 + \frac{1}{r^2} (w - \bar{p}\beta)^2 \right] \psi(r) = 0 \quad (2.28)$$

outside a ferrite rod ( $r \geq \Re$ ). Based on the above Bessel equations and boundary conditions one obtains a characteristic equation for helical MS waves. For helical modes  $\psi^{(1)}$  and  $\psi^{(4)}$  there is a characteristic equation in a form:

$$(-\mu)^{1/2} \frac{J'_{(w-\bar{p}\beta)}}{J_{(w-\bar{p}\beta)}} + \frac{K'_{(w-\bar{p}\beta)}}{K_{(w-\bar{p}\beta)}} - \frac{\mu_a(w-\bar{p}\beta)}{\beta\Re} = 0, \tag{22.29}$$

and for helical modes  $\psi^{(2)}$  and  $\psi^{(3)}$  one has:

$$(-\mu)^{1/2} \frac{J'_{(w-\bar{p}\beta)}}{J_{(w-\bar{p}\beta)}} + \frac{K'_{(w-\bar{p}\beta)}}{K_{(w-\bar{p}\beta)}} + \frac{\mu_a(w-\bar{p}\beta)}{\beta\Re} = 0, \tag{22.30}$$

where  $\bar{p} = p/2\pi$ ,  $p$  is the helical pitch. In these equations, the prime denotes differentiation with respect to the argument. There is a mutual transformation of double-helix resonances  $\psi^{(1)} \leftrightarrow \psi^{(4)}$  and  $\psi^{(2)} \leftrightarrow \psi^{(3)}$  for oppositely directed bias magnetic fields. It means that for time reversal one has mutual transformations between the forward right-hand-helix MS wave  $\psi^{(1)}$  and backward right-hand-helix MS wave  $\psi^{(3)}$ , from one side, and between the backward left-hand-helix MS wave  $\psi^{(4)}$  and forward left-hand-helix MS wave  $\psi^{(2)}$ , from the other side. In fact, this is evidence for the  $PT$ -invariance in a lossless ferrite resonator. Because of such  $PT$  invariance, one can obtain an expansion of the fields by the helical MS modes. For helical-mode resonances, one has a non-Hermitian eigenvalue problem. At the same time, there is a  $PT$ -symmetric eigenvalue problem.

When we consider a quasi-2D ferrite disk, we have the possibility to reduce a problem from helical coordinates to a cylindrical coordinate system. With a formal procedure of separation of variables [16], we have MDMs with standing MS waves in the  $z$  direction (the direction of a bias magnetic field) and rotating MS waves in the azimuthal direction. Such a transition, however, has a definite physical meaning: there are two different solutions related to two different directions of bias magnetic field (that is, for a two different signs of the quantity  $\mu_a$ ).

In solving an eigenvalue problem for a quasi-2D ferrite disk in cylindrical coordinate system we use the same non-Hermitian  $\hat{L}_\perp$  and a membrane functions  $\tilde{V} = \begin{pmatrix} \tilde{B} \\ \tilde{\varphi} \end{pmatrix}$ . The solutions for function  $\psi$  are described by (22.16). Inside a ferrite disk,  $\xi(z)$  is expressed by trigonometric functions. The boundary-value-problem solution for (22.9) is written as [18, 19]

$$\psi(r, \theta, z, t) = C_\nu J_\nu \left( \frac{\beta r}{\sqrt{-\mu}} \right) \left( \cos \beta z + \frac{1}{\sqrt{-\mu}} \sin \beta z \right) e^{-i\nu\theta} e^{i\omega t}. \tag{22.31}$$

Here  $\beta$  is a wave number of a MS wave propagating in a ferrite along the  $z$  axis,  $\nu$  is a positive integer azimuth number (related to a bias magnetic field directed along a positive  $z$  axis), and  $J_\nu$  is the Bessel function of order  $\nu$  for a real argument. One-

component eigenmodes propagating in a certain direction of an azimuth coordinate result in appearance on an orbital angular momentum directed along normal bias magnetic field.

## 22.4 Magnetolectric Fields and Helical Bound States in a Microwave-Field Continuum

Analyzing interaction of MDM ferrite particles with a microwave-field continuum, we have to take into consideration unique properties of the near fields. MDMs strongly confine energy in subwavelength scales of microwave radiation. In a vacuum subwavelength region abutting to a MDM ferrite disk, one observes the quantized state of power-flow vortices. Moreover, in such a vacuum subwavelength region, the time-varying electric and magnetic fields can be not mutually perpendicular. Such specific near fields—so-called magnetolectric (ME) fields—give evidence for spontaneous symmetry breakings at the resonance states of MDM oscillations [19, 38].

When, using (22.31), the spectral problem for the MS-potential scalar wave function  $\psi(\vec{r}, t)$  is solved, distribution of magnetization in a ferrite disk is found as  $\vec{m} = -\tilde{\chi} \cdot \vec{\nabla} \psi$ , where  $\tilde{\chi}$  is the susceptibility tensor of a ferrite [8]. The solution for generating scalar wave function  $\psi(\vec{r}, t)$  presumes the presence of orbital angular momenta for the fields. So, magnetization has both the spin and orbital rotation. There is the spin-orbit interaction between these angular momenta. Based on the known magnetization  $\vec{m}$  inside a ferrite, one can find also the electric and magnetic fields distribution at any point outside a ferrite disk. The electric field is defined as [19, 38]

$$\vec{E}(\vec{x}) = -\frac{1}{4\pi} \int_V \frac{\vec{j}^{(m)}(\vec{x}') \times (\vec{x} - \vec{x}')}{|\vec{x} - \vec{x}'|^3} dV', \quad (22.32)$$

For the magnetic field outside a ferrite, we have

$$\vec{H}(\vec{x}) = \frac{1}{4\pi} \left( \int_V \frac{(\vec{\nabla}' \cdot \vec{m}(x'))(\vec{x} - \vec{x}')}{|\vec{x} - \vec{x}'|^3} dV' - \int_S \frac{(\vec{n}' \cdot \vec{m}(x'))(\vec{x} - \vec{x}')}{|\vec{x} - \vec{x}'|^3} dS' \right). \quad (22.33)$$

In these expressions,  $\vec{j}^{(m)} = i\omega\mu_0\vec{m}$  is the density of a magnetic current, frequency  $\omega$  is a discrete quantity of the MDM-resonance frequency;  $V$  and  $S$  are a volume and a surface of a ferrite sample, respectively.

Outside the ferrite disk the electric and magnetic fields defined by (22.32) and (22.33) are potential fields [19, 38]. At the same time, one observes also the curl

component of the electric field. This curl component in a near-field region outside the disk appears due to the time derivative of the local potential magnetic field via the Faraday law. For more clarity, in some places of a further consideration, we will designate potential electric and magnetic fields (expressed by (22.32) and (22.33)), respectively, as  $\vec{E}_p$  and  $\vec{H}_p$ , and a curl component of the electric field (due to the Faraday law in the near-field region) as  $\vec{E}_c$ .

Mutually perpendicular curl electric field and potential magnetic field constitute power-flow density. The near-field regions with mutually parallel potential electric and potential magnetic fields form so-called helicity density. With these two parameters (power-flows density and helicity density), the near fields originated from a MDM ferrite disk—the ME fields—are distinguished with unique topological properties. These twisted evanescent fields are neither virtual nor “real” (free-space propagating) EM photons in vacuum.

For mode  $n$ , the real power flow density is expressed as

$$\vec{p}_n = \text{Re}\left(i\omega\psi_n\vec{B}_n\right) = \text{Re}\left[\left(\vec{E}_c\right) \times \left(\vec{H}_p^*\right)_n\right]. \quad (22.34)$$

In (22.34) we used the identity:

$$\vec{E}_c \times \vec{H}_p^* = i\omega\psi^*\vec{B}. \quad (22.35)$$

This identity can be proven by a simple manipulation with taking into account that  $\vec{\nabla} \cdot \vec{B} = 0$  and  $\vec{H} = -\vec{\nabla}\psi$ :

$$\vec{\nabla} \cdot (\vec{E}_c \times \vec{H}_p^*) = \vec{H}_p^* \cdot \vec{\nabla} \times \vec{E}_c = i\omega\vec{\nabla}\psi^* \cdot \vec{B} = i\omega\vec{\nabla} \cdot (\psi^*\vec{B}). \quad (22.36)$$

Importantly, despite the fact that the expression  $\text{Re}\left(\vec{E} \times \vec{H}^*\right)$  looks like the real and imaginary Poynting vectors, the MS-wave power flow densities cannot be basically related to the EM-wave power flow densities. The Poynting vector is obtained for EM radiation which is described by the *two curl operator* Maxwell equations for the electric and magnetic fields [1]. This is not the case described by (22.34), where, for the MS waves, we have *potential magnetic* and *curl electric* fields.

The ME-field helicity density is expressed as [19, 38, 39]

$$F = \frac{\varepsilon_0}{2}\vec{E} \cdot \nabla \times \vec{E}. \quad (22.37)$$

The product  $\vec{E} \cdot (\vec{\nabla} \times \vec{E})$  is a measure of the screwiness of the electric field. It is equal to the electric field  $\vec{E}$  on the points lying in the screw axis times the vorticity  $\vec{\nabla} \times \vec{E}$ . As the curl of a vector measures its rotation around a point, the product  $\vec{E} \cdot (\vec{\nabla} \times \vec{E})$  gives how much  $\vec{E}$  rotates around itself times its own modulus. This product evaluates to what degree vector  $\vec{E}$  resembles a helix. For time-harmonic

fields ( $\propto e^{i\omega t}$ ), the time-averaged helicity density parameter was calculated in a vacuum near-field region as:

$$F = \frac{\varepsilon_0}{4} \text{Im} \left\{ \vec{E} \cdot \left( \vec{\nabla} \times \vec{E} \right)^* \right\}. \quad (22.38)$$

The ME-field helicity density is nonzero only at the resonance frequencies of MDMs. At the MDM frequency  $\omega = \omega_{\text{MDM}}$ , we have for magnetic induction  $\vec{B} = \frac{i}{\omega_{\text{MDM}}} \left( \vec{\nabla} \times \vec{E} \right)$ . So, (22.38) can be rewritten as

$$F = \frac{\omega_{\text{MDM}} \varepsilon_0}{4} \text{Im} \left\{ i \vec{E} \cdot \vec{B}^* \right\} = \frac{\omega_{\text{MDM}} \varepsilon_0}{4} \text{Re} \left\{ \vec{E} \cdot \vec{B}^* \right\} = \frac{\omega_{\text{MDM}}}{4c^2} \text{Re} \left\{ \vec{E} \cdot \vec{H}^* \right\}, \quad (22.39)$$

where  $c = 1/\sqrt{\varepsilon_0 \mu_0}$ . From this equation, one can see that the helicity density  $F$  transforms as a pseudo-scalar under space reflection  $\mathcal{P}$  and it is odd under time reversal  $\mathcal{T}$ . This is a time-odd, parity-odd pseudoscalar parameter. At the MDM resonances, one observes macroscopically coherent vacuum states near a ferrite disk. These vacuum states of the field experience broken mirror symmetry and also broken time-reversal symmetry. Evidently, for regular electromagnetic fields  $\text{Re} \left\{ \vec{E} \cdot \vec{B}^* \right\} \equiv 0$ ,

We represent now the potential electric field as  $\vec{E}_p = -\vec{\nabla} \vartheta$ , where  $\vartheta$  is an arbitrary electrostatic-potential function. With this representation, we can write:

$$F = \frac{\omega_{\text{MDM}} \varepsilon_0}{4} \text{Re} \left\{ \vec{E} \cdot \vec{B}^* \right\} = -\frac{\omega_{\text{MDM}} \varepsilon_0}{4} \text{Re} \left\{ \vec{\nabla} \vartheta \cdot \vec{B}^* \right\} = -\frac{\omega_{\text{MDM}} \varepsilon_0}{4} \left\{ \vec{\nabla} \cdot \text{Re} \left( \vartheta \vec{B}^* \right) \right\}. \quad (22.40)$$

Here we took into account that  $\nabla \cdot \vec{B} = 0$ . Based on this equation, one can introduce a quantity of the time-averaged ME-energy density:

$$\vec{\nabla} \cdot \text{Re} \left( \vartheta \vec{B}^* \right) \equiv -\tau. \quad (22.41)$$

The quantity  $\vartheta \vec{B}^*$  can be considered as the time-averaged ME-energy flow. For the helicity density we can write:

$$F = \frac{\omega_{\text{MDM}} \varepsilon_0}{4} \tau. \quad (22.42)$$

The regions of the positive and negative helicity density [19, 38, 39] can be described, respectively, as the regions with positive and negative ME-energy density  $\tau$ . Since the helicity factor  $F$  shows what is degree of a twist between the  $\vec{E}$  and  $\vec{H}$  vectors compared to a regular EM-field configuration (with mutually perpendicular  $\vec{E}$  and  $\vec{H}$  vectors), the ME energy can be considered as energy of a torsion degree of freedom. Because of time-reversal symmetry breaking, all the regions with positive helicity become the regions with negative helicity (and vice versa), when one changes a direction of a bias magnetic field:

$$F\vec{H}_{0\uparrow} = -F\vec{H}_{0\downarrow}. \quad (22.43)$$

This equation can be written also as

$$\tau(-\vec{H}_0) = -\tau(\vec{H}_0). \quad (22.44)$$

Let us define the helicity as an integral of the ME-field helicity density over the entire near-field vacuum region of volume  $V'$  (which excludes a region of a ferrite disk):

$$\mathcal{H} = \int_{V'} F dV = \frac{\omega_{\text{MDM}}\varepsilon_0}{4} \int_{V'} \text{Re}\{\vec{E} \cdot \vec{B}^*\} dV = \frac{\omega_{\text{MDM}}\varepsilon_0}{4} \int_{V'} \tau dV. \quad (22.45)$$

The question arises: Whether do we have the ‘‘helicity neutrality’’, i.e.  $\mathcal{H} = \frac{\omega_{\text{MDM}}\varepsilon_0}{4} \int_{V'} \tau dV = 0$ ? To answer this question we can rely on the following simple analysis. With use of the transformation

$$\mathcal{H} = -\frac{\omega_{\text{MDM}}\varepsilon_0}{4} \int_{V'} \text{Re}\{\vec{\nabla} \cdot (\vartheta \vec{B}^*)\} dV = -\frac{\omega_{\text{MDM}}\varepsilon_0}{4} \oint_{S'} \text{Re}\{\vartheta \vec{B}^* \cdot \vec{n}\} dS, \quad (22.46)$$

we can conclude that when the normal component of  $\vec{B}$  vanishes at some boundary inside which the fields  $\vec{B}$  and  $\vec{E}_p$  are confined (i.e. when  $\vec{B} \cdot \vec{n} = 0$  at the boundary), the quantity  $\mathcal{H}$  is equal to zero. The quantity  $\mathcal{H}$  is also equal to zero when the fields are with finite energy and the quantity  $\vartheta \vec{B}^*$  decreases sufficiently fast at infinity.

The problem of electromagnetic-wave scattering by a small ferrite particle with MDM resonances appears as a rather complicated problem. Because of symmetry breakings of the fields, a standard technique of expansion by spherical or cylindrical harmonics is not applicable in such a case. It is evident that for small (quasistatic) MDM ferrite particles one cannot use the classical theory of Rayleigh scattering. While for an incident wave there is no difference between left and right, in the fields scattered by a MDM ferrite particle one should distinguish left from right. To analyze the scattering problem, one should use expansion of the fields by eigenmodes of MS oscillations in a ferrite particle. As we showed above, these oscillations are characterized by the helical-mode resonances.

The ferrite disk is an opened resonator with high-quality MDM oscillations. Sharp MDM resonances can appear as bound states in a microwave-field continuum. Bound states in the continuum (BICs), also known as embedded trapped modes, are localized solutions which correspond to discrete eigenvalues coexisting with extended modes of a continuous spectrum. The BICs are solutions having an infinitely long lifetime. Recent developments show that in a large variety of electromagnetic structures there can be different mechanisms that lead to BICs (see [40] and references therein). One of the main reasons for appearance of the MDM BICs is a symmetry mismatch.



Modes of different symmetry classes (such as reflection or rotation) are completely decoupled. MDM oscillations do not exhibit a rotational symmetry, while a regular waveguide structure is rotationally symmetric. With such a condition, the MDM bound states observed in microwave structures can be classified as the symmetry-protected BICs.

The MDM bound states are embedded in the microwave continuum but not coupled to it. Certainly, if a bound state of one symmetry class is embedded in the continuous spectrum of another symmetry class their coupling is forbidden. Moreover, the ME fields, originated from a MDM ferrite disk, and the EM fields in a microwave structure are described by different types of equations. At any stable state, MDMs cannot radiate EM waves because there is no way to assign a far-field EM-wave polarization that is consistent with vortex ME fields near a MDM ferrite disk. In a short-range interaction, an important aspect concerns the topological nature of the MDM BICs. These topological properties can be understood through eigenpower-flow vortices with corresponding topological charges [19, 38, 39, 41]. Quantized topological charges cannot suddenly disappear. They are protected by special boundary conditions in a quasi-2D ferrite disk. The MDM BICs cannot be removed unless MDM topological charges are cancelled with another structure carrying the opposite topological charges. Such opposite topological charges appear on metal walls of a microwave waveguide [41].

The region where a MDM ferrite disk is localized, is small compared to the characteristic length scale of waveguide modes. The ME near fields originated from a quasi-2D ferrite disk, are characterized by the fields rotating in a plane parallel to the disk plane and decaying along the disk axis. The fields in these contact regions have a torsion structure of rotating power-flow vortices [41–43]. Interaction of MDMs with metal walls of a microwave waveguide results in appearance of topological surface electric currents. The lines of the currents are the right-handed and left-handed flat spirals. Coupling of these spiral surface electric currents with the waveguide fields appears as a non-trivial question. What is a continuum of these waveguide fields? Evidently, there should be a complex-wave microwave continuum with helical-wave topological structure of the fields [41–43]. In a section of a closed lossless hollow waveguide one can observe a continuum of evanescent modes [44]. In addition, in a section of a closed lossless waveguide with anisotropic inclusions, there can be an infinite number of complex conjugate pairs of eigenvalues [45, 46]. Could these complex conjugate pairs of eigenvalues constitute a complex-wave microwave continuum with helical-wave topological structure of the fields? In a view of unique topological properties of ME near fields, we presume existence of such a complex-wave microwave continuum with helical-wave topological structure of the fields. The total system is Hermitian. In our case, it is decomposed into two non-Hermitian sub-systems: (a) *PT*-symmetric bi-orthogonal MDM discrete states and (b) *PT*-symmetric bi-orthogonal complex-wave microwave continuum.

From a number of features attributed to the BICs there is strong resonance field enhancement at discrete resonances. In the case of MDM oscillations in a microwave-field continuum, such a strong field enhancement is shown in numerous numerical studies [19, 42, 47–49]. Another characteristic features inherent in the BICs is a

Fano resonance collapse. For the MDM resonances the effect of Fano resonance collapse was clearly demonstrated in [50]. Thanks to the tenability of the ferrite-disk resonator by an external parameter—the bias magnetic field—the MDM oscillations can become close interacting modes. The structure used in [50] is a microwave cavity with an embedded thin-film ferrite disk. As is shown that as we approach the top of the cavity resonance curve, the minimum of the microwave transmission approaches the maximum of the transmission. At the top of the cavity resonance curve, the levels of the minimum and maximum transmission are in contact. The Fano line shape is completely damped and one observes a single Lorentzian peak. The scattering cross section corresponds to a pure dark mode.

Recently, the MDM BIC phenomena, found further development in a novel technique based on the combination of the microwave perturbation method and the Fano resonance effects observed in microwave structures with embedded small ferrite disks [50, 51]. When the frequency of the MDM resonance is not equal to the cavity resonance frequency, one gets Fano transmission intensity. If the MDM resonance frequency is tuned, by a bias magnetic field, to the cavity resonance frequency, one observes a Lorentzian line shape. The effect of Fano resonance collapse has no relations to the quality factor of a microwave cavity. Use of an extremely narrow Lorentzian peak allows exact probing of the resonant frequency of a cavity loaded by a high lossy material sample. With variation of a bias magnetic field, one can see different frequencies of Lorentzian peaks for different kinds of material samples. This gives a picture of precise spectroscopic characterization of high absorption matter in microwaves, including biological liquids. Importantly, there is no influence of the dissipation effects in the microwave cavity on the quality of the MDM resonances. The poles in the transmission amplitudes are connected with the bound states and their lifetimes.

## 22.5 *G*- and *L*-Magnetic Dipolar Modes

The operator-form (22.6–22.8), gave us possibility to analyze unique topological properties of the fields. We showed that operator  $\hat{L}_\perp$  is a self-adjoint, but non-

Hermitian operator. The adjoint of the function  $\tilde{V} = \begin{pmatrix} \overline{\hat{B}} \\ \hat{\psi} \end{pmatrix}$  is not equal to its

complex conjugate quantity. The MDMs described by operator  $\hat{L}$  are called *L*-modes [17, 18, 35, 49, 52]. The solution of the spectral problem for the *L*-modes are based on two first-order differential equations:  $\vec{\nabla} \cdot \vec{H} = -\vec{\nabla} \cdot \psi$  and  $\nabla \cdot \vec{B} = 0$  with the presentation of MS-potential wave function in a form of (22.16) and with the homogeneous boundary conditions (22.20). It appears, however, that the solutions based on one second-order differential equation (22.4), may lead to physically different results. In this case, the self-adjoint solutions for quasi-2D ferrite-disk particle are obtained with use of another type of membrane functions and with the boundary conditions

different from (22.20). For magnetostatic-potential wave function  $\psi(\vec{r}, t)$ , this gives the possibility to reduce the spectral problem to the Hermitian problem.

For a normally magnetized ferrite disk, the Walker (22.4) is represented as

$$\mu \nabla_{\perp}^2 \psi + \nabla_{\parallel}^2 \psi = 0, \quad (22.47)$$

where  $\mu$  is a diagonal component of the permeability tensor (22.15), subscript  $\perp$  means differentiation over the in-plane,  $r, \theta$ , coordinates and subscript  $\parallel$  means differentiation along the disk axis  $z$ . We present the solution for the mode  $n$  as

$$\psi_n = A_n \xi_n(z) \tilde{\eta}_n(r, \theta), \quad (22.48)$$

where  $A_n$  is a dimensional coefficient and  $\tilde{\eta}_n(r, \theta)$  is a dimensionless membrane function. The amplitude factor  $\xi_n(z)$  is the same as in (22.16).

For the disk geometry, the energy eigenvalue problem is defined by the differential equation [16–19, 52]

$$\hat{G}_{\perp} \tilde{\eta}_n = E_n \tilde{\eta}_n, \quad (22.49)$$

where  $\hat{G}_{\perp}$  is a two-dimensional (with respect to in-plane coordinates of a ferrite disk) differential operator and  $E_n$  is density of accumulated magnetic energy of mode  $n$ . The operator  $\hat{G}_{\perp}$  and energy  $E_n$  are defined as

$$\hat{G}_{\perp} = \frac{g_n}{16\pi} \mu_n \nabla_{\perp}^2, \quad (22.50)$$

$$E_n = \frac{g_n}{16\pi} (\beta_{z_n})^2. \quad (22.51)$$

Here  $g_n$  is a dimensional normalization coefficient for mode  $n$ ,  $\nabla_{\perp}^2$  is the two-dimensional Laplace operator, and  $\beta_{z_n}$  is the propagation constant of mode  $n$  along the disk axis  $z$ . The parameter  $\mu_n$  is to be regarded as an eigenvalue, while the subscript  $n$  labels the available solutions. Outside a ferrite  $\mu_n = 1$ . For self-adjointness of operator  $\hat{G}_{\perp}$ , the homogeneous boundary condition should be [16–19, 52]

$$\mu \left( \frac{\partial \tilde{\eta}_n}{\partial r} \right)_{r=\mathcal{R}^-} - \left( \frac{\partial \tilde{\eta}_n}{\partial r} \right)_{r=\mathcal{R}^+} = 0. \quad (22.52)$$

This boundary conditions is different from (22.20). The MDMs described by operator  $\hat{G}$  are called  $G$ -modes [17, 18, 35, 49, 52].

The normalized scalar-wave membrane function  $\tilde{\eta}$  can be represented as

$$\tilde{\eta} = \sum_n a_n \tilde{\eta}_n. \quad (22.53)$$

The probability to find a system in a certain state  $n$  is defined as

$$|a_n|^2 = \left| \int_{S_c} \tilde{\eta} \tilde{\eta}_n^* dS \right|^2, \tag{22.54}$$

where  $S_c$  is a circular cross section of a ferrite disk. MDM oscillations in a ferrite disk are described by real eigenfunctions:  $(\tilde{\eta}_{-\beta})_n = (\tilde{\eta}_\beta^*)_n$ . The orthogonality conditions are expressed as

$$\int_{S_c} (\tilde{\eta}_\beta)_n (\tilde{\eta}_{-\beta})_{n'} dS = \int_{S_c} \tilde{\eta}_n \tilde{\eta}_{n'}^* dS = \delta_{nn'}. \tag{22.55}$$

The spectral problem gives the energy orthogonality relation for MDMs:

$$(E_n - E_{n'}) \int_{S_c} \tilde{\eta}_n \tilde{\eta}_{n'}^* dS = 0. \tag{22.56}$$

The functions  $\tilde{\eta}_n$  are eigenfunctions of a Hermitian differential operator. Based on (22.50) one can rewrite (22.47) as

$$\widehat{G}_\parallel \psi_n = -E_n \psi_n, \tag{22.57}$$

where

$$\widehat{G}_\parallel = \frac{g_n}{16\pi} \nabla_\parallel^2. \tag{22.58}$$

For a given mode  $n$ , (22.57) looks like the time independent one-dimensional Schrödinger equation for a free particle. For two modes,  $n$  and  $n'$ , one obtains:

$$(E_n - E_{n'}) \psi_n \psi_{n'}^* = \vec{\nabla}_\parallel \cdot (\psi_n \vec{\nabla}_\parallel \psi_{n'}^* - \psi_{n'}^* \vec{\nabla}_\parallel \psi_n). \tag{22.59}$$

The spectral problems for the  $L$  and  $G$  modes are mutually correlated. On a lateral surface of a quasi-2D ferrite disk of radius  $\mathfrak{R}$ , a MS-potential membrane wave function is expressed as:  $(\tilde{\varphi}_\pm)_{r=\mathfrak{R}^-} = \delta_\pm(\tilde{\eta})_{r=\mathfrak{R}^-}$ ,  $\tilde{\eta}$  is a singlevalued membrane function and  $\delta_\pm$  is a double-valued edge wave function on contour  $\mathcal{L} = 2\pi\mathfrak{R}$ . Function  $\delta_\pm$  changes its sign when the regular-coordinate angle  $\theta$  is rotated by  $2\pi$ . As a result, one has the eigenstate spectrum of MDM oscillations with topological phases accumulated by the edge wave function  $\delta$ . On a lateral surface of a quasi-2D ferrite disk, one can distinguish two different functions  $\delta_\pm$ , which are the counterclockwise and clockwise rotating-wave edge functions with respect to a membrane function  $\tilde{\eta}$ . A line integral around a singular contour  $\mathcal{L} : \frac{1}{\mathfrak{R}} \oint_{\mathcal{L}} \left( i \frac{\partial \delta_\pm}{\partial \theta} \right) (\delta_\pm)^* d\mathcal{L} = \int_0^{2\pi} \left[ \left( i \frac{\partial \delta_\pm}{\partial \theta} \right) (\delta_\pm)^* \right]_{r=\mathfrak{R}} d\theta$  is an observable quantity. Because of the existing the geometrical phase factor

on a lateral boundary of a ferrite disk, MDMs are characterized by a pseudo-electric field (the gauge field)  $\vec{\mathcal{E}}$ . The pseudo-electric field  $\vec{\mathcal{E}}$  can be found as  $\vec{\mathcal{E}}_{\pm} = -\vec{\nabla} \times \left( \vec{\Lambda}_{\epsilon}^{(m)} \right)_{\pm}$ . The field  $\vec{\mathcal{E}}$  is the Berry curvature. The corresponding flux of the gauge field  $\vec{\mathcal{E}}$  through a circle of radius  $\mathfrak{R}$  is obtained as:  $K \int_S \left( \vec{\mathcal{E}} \right)_{\pm} \cdot d\vec{S} = K \oint_{\mathcal{L}} \left( \vec{\Lambda}_{\epsilon}^{(m)} \right)_{\pm} \cdot d\vec{\mathcal{L}} = K (\Xi^{(e)})_{\pm} = 2\pi q_{\pm}$ , where  $(\Xi^{(e)})_{\pm}$  are quantized fluxes of pseudo-electric fields,  $K$  is the normalization coefficient. Each MDM is quantized to a quantum of an emergent electric flux. There are the positive and negative eigenfluxes. These different-sign fluxes should be nonequivalent to avoid the cancellation. It is evident that while integration of the Berry curvature over the regular-coordinate angle  $\theta$  is quantized in units of  $2\pi$ , integration over the spin-coordinate angle  $\theta'$  ( $\theta' = \frac{1}{2}\theta$ ) is quantized in units of  $\pi$ . The physical meaning of coefficient  $K$  concerns the property of a flux of a pseudo-electric field. The Berry mechanism provides a microscopic basis for the surface magnetic current at the interface between gyrotropic and nongyrotropic media. Following the spectrum analysis of MDMs in a quasi-2D ferrite disk one obtains pseudo-scalar axion-like fields and edge chiral magnetic currents. Topological properties of ME fields (non-zero helicity factor) arise from the presence of geometric phases on a border circle of a MDM ferrite disk [17–19, 35, 49, 52].

## 22.6 Conclusion

Magnetic-dipolar resonances in ferrite samples with dimensions much smaller than the wavelength of microwave radiation are well described by the magnetostatic-potential wave functions. To a certain extent, this spectral problem is dual to the electrostatic theory describing the localized surface plasmons in nanoparticles with dimensions much smaller than the wavelength of light. For a case of plasmonic (electrostatic) resonances in small metallic samples, one can neglect a magnetic displacement current and consider quasistationary electric fields, which are described by electrostatic-potential functions. In this description, subwavelength sizes of the particles eliminates any effects of the internal electromagnetic retardation processes. Magnetic-dipolar-mode (MDM) oscillations (or magnetostatic-wave oscillations) in small ferrite samples can be considered as an approximation to Maxwell equations when a displacement electric current is negligibly small. The physical justification for such an approximation arises from the fact that in a small (with sizes much less than a free-space electromagnetic wavelength) sample of a magnetic material with strong temporal dispersion (due to the ferromagnetic resonance) one neglects a time variation of electric energy in comparison with a time variation of magnetic energy. Subwavelength sizes of such a ferrite particle eliminate any electromagnetic-retardation phenomena. The main distinguishing feature of the magnetostatic resonances is the existence of non-Maxwellian propagation-wave behaviors.

The near fields originated from small ferrite-disk particles with MDM oscillations are the fields with the electric and magnetic components, but with broken dual (electric–magnetic) symmetry. These fields—called magnetoelectric (ME) fields—have topological properties different from such properties of electromagnetic fields. The ME fields are characterized by power-flow vortices, nonzero helicity, and a torsion degree of freedom.

Interaction of MDMs with metal walls of a microwave waveguide results in appearance of topological surface electric currents. The lines of the currents are the right-handed and left-handed flat spirals. Coupling of these spiral surface electric currents with the waveguide fields appears as a non-trivial question. In a view of unique topological properties of ME near fields, we presume existence of a complex-wave microwave continuum with helical-wave topological structure of the fields. The total microwave system with an embedded ferrite disk resonator is decomposed into two non-Hermitian sub-systems: (a) *PT*-symmetric bi-orthogonal MDM discrete states and (b) *PT*-symmetric bi-orthogonal complex-wave microwave continuum.

In a case of a quasi-2D ferrite-disk particle, the problem for magnetostatic-potential wave function  $\psi(\vec{r}, t)$  can be reduced to the Hermitian problem. In such a ferrite particle, the function  $\psi(\vec{r}, t)$  appears as orthonormal complex eigenfunction. The adjoint of this function is equal to its complex conjugate quantity. This differs from the resonances in metal nanoparticles where one has a non-Hermitian eigenvalue problem for electrostatic-potential wave function.

## References

1. J.D. Jackson, *Classical Electrodynamics*, 2nd edn. (Wiley, New York, 1975)
2. M.M. Coles, D.L. Andrews, Chirality and angular momentum in optical radiation. *Phys. Rev. A* **85**, 063810 (2012)
3. R.P. Cameron, S.M. Barnett, A.M. Yao, Optical helicity, optical spin and related quantities in electromagnetic theory. *New J. Phys.* **14**, 053050 (2012)
4. K.Y. Bliokh, A.Y. Bekshaev, F. Nori, Dual electromagnetism: helicity, spin, momentum and angular momentum. *New J. Phys.* **15**, 033026 (2013)
5. A. Alù, M.G. Silveirinha, A. Salandrino, N. Engheta, Epsilon-near-zero metamaterials and electromagnetic sources: tailoring the radiation phase pattern. *Phys. Rev. B* **75**, 155410 (2007)
6. J. Schilling, Fundamental optical physics: the quest for zero refractive index. *Nat Photonics* **5**, 449 (2011)
7. T.J. Davis, D.E. Gómez, Colloquium: an algebraic model of localized surface plasmons and their interactions. *Rev. Mod. Phys.* **89**, 011003 (2017)
8. A.G. Gurevich, G.A. Melkov, *Magnetization Oscillations and Waves* (CRC Press, 1996)
9. D.D. Stancil, *Theory of Magnetostatic Waves* (Springer-Verlag, New York, 1993)
10. L.D. Landau, E.M. Lifshitz, *Electrodynamics of Continuous Media* (Pergamon Press, Oxford, 1960)
11. L.R. Walker, Magnetostatic modes in ferromagnetic resonance. *Phys. Rev.* **105**, 390 (1957)
12. R.L. White, I.H. Solt Jr., Multiple ferromagnetic resonance in ferrite spheres. *Phys. Rev.* **104**, 56 (1956)
13. J.F. Dillon Jr., Magnetostatic modes in disks and rods. *J. Appl. Phys.* **31**, 1605 (1960)
14. T. Yukawa, K. Abe, FMR spectrum of magnetostatic waves in a normally magnetized YIG disk. *J. Appl. Phys.* **45**, 3146 (1974)

15. E.O. Kamenetskii, A.K. Saha, I. Awai, Interaction of magnetic-dipolar modes with microwave-cavity electromagnetic fields. *Phys. Lett. A* **332**, 303 (2004)
16. E.O. Kamenetskii, Energy eigenstates of magnetostatic waves and oscillations. *Phys. Rev. E* **63**, 066612 (2001)
17. E.O. Kamenetskii, M. Sigalov, R. Shavit, Quantum confinement of magnetic-dipolar oscillations in ferrite discs. *J. Phys. Condens. Matter* **17**, 2211 (2005)
18. E.O. Kamenetskii, Vortices and chirality of magnetostatic modes in quasi-2D ferrite disc particles. *J. Phys. A Math. Theor.* **40**, 6539 (2007)
19. E.O. Kamenetskii, R. Joffe, R. Shavit, Microwave magnetoelectric fields and their role in the matter-field interaction. *Phys. Rev. E* **87**, 023201 (2013)
20. M.I. Stockman, S.V. Faleev, D.J. Bergman, Localization versus delocalization of surface plasmons in nanosystems: can one state have both characteristics? *Phys. Rev. Lett.* **87**, 167401 (2001)
21. K. Li, M.I. Stockman, D.J. Bergman, Self-similar chain of metal nanospheres as an efficient nanolens. *Phys. Rev. Lett.* **91**, 227402 (2003)
22. D.J. Bergman, D. Stroud, Theory of resonances in the electromagnetic scattering by macroscopic bodies. *Phys. Rev. B* **22**, 3527 (1980)
23. I.D. Mayergoyz, D.R. Fredkin, Z. Zhang, Electrostatic (plasmon) resonances in nanoparticles. *Phys. Rev. B* **72**, 155412 (2005)
24. K.T. McDonald, An electrostatic wave (2003). [arXiv:physics/0312025](https://arxiv.org/abs/physics/0312025)
25. K.T. McDonald, Magnetostatic spin waves (2003). [arXiv:physics/0312026](https://arxiv.org/abs/physics/0312026)
26. T.J. Davis, K.C. Vernon, D.E. Gómez, Effect of retardation on localized surface plasmon resonances in a metallic nanorod. *Opt. Express* **17**, 23655 (2009)
27. Z.B. Wang, B.S. Luk'yanchuk, M.H. Hong, Y. Lin, T.C. Chong, Energy flow around a small particle investigated by classical Mie theory. *Phys. Rev. B* **70**, 035418 (2004)
28. M.V. Bashevoy, V.A. Fedotov, N.I. Zheludev, Optical whirlpool on an absorbing metallic nanoparticle. *Opt. Express* **13**, 8372 (2005)
29. M.I. Tribelsky, B.S. Luk'yanchuk, Anomalous light scattering by small particles. *Phys. Rev. Lett.* **97**, 263902 (2006)
30. J. Pozhela, *Plasma and Current Instabilities in Semiconductors: International Series on the Science of the Solid State* (Pergamon, Oxford, New York, 1981)
31. A.I. Akhiezer, V.G. Bar'yakhtar, S.V. Peletminskii, *Spin Waves* (Amsterdam, North-Holland, 1968)
32. J.P. Torres, L. Torner, *Twisted Photons: Applications of Light with Orbital Angular Momentum* (Wiley, 2011)
33. D.L. Andrews, M. Babiker, *The Angular Momentum of Light* (Cambridge University Press, 2012)
34. K.Y. Bliokh, Lorentz-boost eigenmodes. [arXiv:1802.03940](https://arxiv.org/abs/1802.03940)
35. E.O. Kamenetskii, Helical-mode magnetostatic resonances in small ferrite particles and singular metamaterials. *J. Phys. Condens. Matter* **22**, 486005 (2010)
36. R.A. Waldron, A helical coordinate system and its applications in electromagnetic theory. *Q. J. Mech. Appl. Math.* **11**, 438 (1958)
37. P.L. Overfelt, Helical harmonics for static fields. *Phys. Rev. E* **64**, 036603 (2001)
38. R. Joffe, R. Shavit, E.O. Kamenetskii, Microwave magnetoelectric fields: an analytical study of topological characteristics. *J. Magn. Magn. Mater.* **392**, 6 (2015)
39. E.O. Kamenetskii, M. Berezin, R. Shavit, Microwave magnetoelectric fields: helicities and reactive power flows. *Appl. Phys. B* **121**, 31 (2015)
40. C.W. Hsu, B. Zhen, A.D. Stone, J.D. Joannopoulos, M. Soljacic, Bound states in the continuum. *Nat. Rev. Mat.* **1**, 16048 (2016)
41. R. Joffe, E.O. Kamenetskii, R. Shavit, Azimuthally unidirectional transport of energy in magnetoelectric fields: topological Lenz's effect. *J. Mod. Opt.* **64**, 2316 (2017)
42. M. Berezin, E.O. Kamenetskii, R. Shavit, Topological-phase effects and path-dependent interference in microwave structures with magnetic-dipolar-mode ferrite particles. *J. Opt.* **14**, 125602 (2012)

43. M. Berezin, E.O. Kamenetskii, R. Shavit, Topological properties of microwave magnetoelectric fields. *Phys. Rev. E* **89**, 023207 (2014)
44. D.M. Pozar, *Microwave Engineering*, 2nd edn. (Wiley, New York, 1998)
45. G.L. Veselov, S.V. Raevskiy, *The Layered Metallic-Dielectric Waveguides* (in Russian) (Radio i Svyas, Moscow, 1988)
46. A.S. Omar, K.F. Schunemann, Complex and backward-wave modes in inhomogeneously and anisotropically filled waveguides. *Trans. Microw. Theory Tech.* **35**, 268 (1987)
47. E.O. Kamenetskii, G. Vaisman, R. Shavit, Fano resonances in microwave structures with embedded magneto-dipolar quantum dots. *J. Appl. Phys.* **114**, 173902 (2013)
48. E.O. Kamenetskii, R. Joffe, R. Shavit, Coupled states of electromagnetic fields with magnetic-dipolar-mode vortices: magnetic-dipolar-mode vortex polaritons. *Phys. Rev. A* **84**, 023836 (2011)
49. E.O. Kamenetskii, M. Sigalov, R. Shavit, Manipulating microwaves with magnetic-dipolar-mode vortices. *Phys. Rev. A* **81**, 053823 (2010)
50. G. Vaisman, E.O. Kamenetskii, R. Shavit, Magnetic-dipolar-mode Fano resonances for microwave spectroscopy of high absorption matter. *J. Phys. D Appl. Phys.* **48**, 115003 (2015)
51. G. Vaisman, E. Elman, E. Hollander, E.O. Kamenetskii, R. Shavit, Fano resonance microwave spectroscopy of high absorption matter, Patent: US 9651504 B2 (2017)
52. E.O. Kamenetskii, M. Sigalov, R. Shavit, Tellegen particles and magnetoelectric metamaterials. *J. Appl. Phys.* **105**, 013537 (2009)



# Chapter 23

## Weak Coupling, Strong Coupling, Critical Coupling and Fano Resonances: A Unifying Vision



Simone Zanotto

**Abstract** The transversal concepts of weak, strong and critical coupling, and of Fano resonances, are analyzed within a unified framework which relies on a simple classical model of driven-dissipative coupled oscillators. A careful exploration of the system's parameter space has led to the emergence of certain intriguing phenomena, which we named lineshape inheritance, universal absorption lineshape, and strong critical coupling. These concepts may be of relevance when attempting to understand the response of a diversity of systems, especially in the fields of (quantum) light-matter coupling, and of solid-state nanophysics, where the basic scheme of multi-oscillator dissipative resonances is often encountered.

### 23.1 Introduction

The concepts of weak, strong and critical coupling are among the most basic in the physics of resonant systems. They arise from the interplay between the resonator internal losses, the coupling between resonators, and the presence of scattering channels where energy flows into, or from, the system. Weak and strong coupling are concepts also widely explored in the framework of light-matter interaction, in particular with reference to the Purcell effect and to the physics of dressed states, or polaritons [1, 2]. In parallel, the physics of resonances hosts another key concept, that of Fano resonances [3–5]: they emerge from the co-presence of a direct and of an indirect pathway for the scattering process. Otherwise, this can be viewed as the effect of the competition between a resonant and a non-resonant scattering process.

In this chapter we elucidate the connection between the aforementioned concepts, relying on a simple classical model which nonetheless can grasp several key features occurring in complex systems. For instance, it can be applied to a large class of problems in nanoplasmonics, as the underlying quantum nature of the excitations is often washed out by the still large number of electrons involved and/or by the finite temperature at which the experiments are performed and devices are operated.

---

S. Zanotto (✉)

NEST, Istituto Nanoscienze - CNR and Scuola Normale Superiore, 56127 Pisa, Italy  
e-mail: simone.zanotto@nano.cnr.it

© Springer Nature Switzerland AG 2018

E. Kamenetskii et al. (eds.), *Fano Resonances in Optics and Microwaves*, Springer  
Series in Optical Sciences 219, [https://doi.org/10.1007/978-3-319-99731-5\\_23](https://doi.org/10.1007/978-3-319-99731-5_23)

551

Even if smaller objects—such as quantum dots—are considered, i.e. in the so-called *plexcitonic* systems, a semiclassical approximation can still remain a good approach provided that the small object, which is in principle a genuinely quantum two-level system, is excited by a sufficiently small intensity [6–16]. Another frameworks where the present model can be applied is polaritonics, either based on intersubband, on exciton, or on phononic resonances [17–25]. In parallel, it can be applied to purely electromagnetic problems, where the complexity arises from the non-trivial geometry of the resonator, as for instance in coupled photonic cavities [26, 27], in multiplasmon resonators [28] or in disordered systems [29] where it may be computationally prohibitive to numerically model the full devices, making it useful to have at disposal a more comprehensive, high-level model.

However the concepts introduced above are not limited to photonics research, as they only rely on the ideas of oscillation, radiation and dissipation. Hence they can be fruitfully applied to a wealth of physical frameworks, such as acoustics (both macroscopical and microscopical, i.e., nanomechanics) [30], lumped element circuits and networks [31], cavity-controlled chemistry [32], and—most importantly—to all the situations where mixed, hybrid excitations which originate from the interaction of diverse systems occur: nano-opto-mechanical objects [33, 34], hybrid systems [35, 36], etc.

## 23.2 Model System, Parametrization, and Linear Response

The model under consideration is schematized in Fig. 23.1. It is a coupled-mode model, inspired by several works available in the literature [27, 37–42]. A first resonator, here depicted as a two-mirror cavity, is coupled to a second resonant degree of freedom, here represented as a spring-mass resonator. The resonators have (angular) frequencies  $\omega_A$  and  $\omega_B$ , and are coupled through a coupling coefficient  $\Omega$ . The cavity resonator radiates into, and is excited from, two radiative scattering channels through two ports, with couplings  $\kappa_{1,2}$ . In parallel with the resonator A, a non-resonant scattering channel, here depicted by a semi-transparent mirror, is included in the conceptual diagram. It is parametrized by frequency-independent reflection and transmission coefficients  $r$  and  $t$  ( $r^2 + t^2 = 1$  and  $0 \leq r, t \leq 1$ ; see below for the phases). Internal losses of the resonators are represented by the rates  $\gamma_{A,i}$  and  $\gamma_{B,i}$ . In a light-matter coupling framework, where A labels the photonic (or plasmonic) resonator, and B a two-level system (i.e. an atom, a quantum dot, a quantum well, or an assembly of them),  $\gamma_{A,i}$  represents losses such as roughness scattering (i.e., radiative scattering in undesired scattering channels) or dissipation (for instance, in metallic mirrors or plasmonic elements). Instead,  $\gamma_{B,i}$  represents the non-radiative recombination rate of the two-level systems.

Labeling  $a$  and  $b$ , respectively, the amplitudes of the resonators at frequencies  $\omega_A$  and  $\omega_B$ , one gets

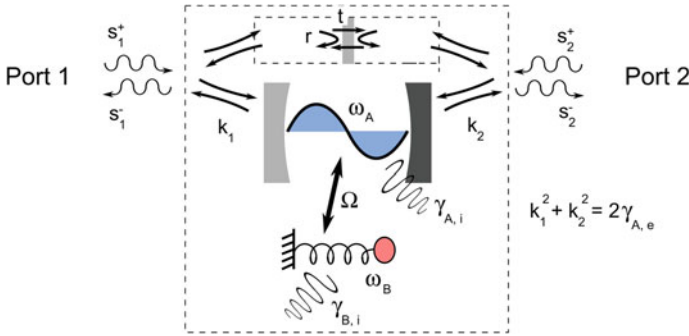


**Fig. 23.1** Schematic representation of the model under analysis. Two resonators (A and B) are coupled each other, and the first (resonator A) is coupled with two scattering channels (ports). The scattering channels are also directly coupled each other through a non-resonant mechanism, represented by a semitransparent mirror, responsible for Fano interference. Resonator A is represented as a two-mirror cavity, and resonator B as a mass-spring system, since one of the possible applications of this model are light-matter coupled systems. The model is classical, but it can be applied also to quantum systems provided that adequate approximations are made (see text for details)

$$\begin{aligned}
 \frac{db}{dt} &= (i\omega_B - \gamma_B)b + i\Omega a \\
 \frac{da}{dt} &= (i\omega_A - \gamma_A)a + i\Omega b + (\langle \kappa |^*) |s^+ \rangle \\
 |s^- \rangle &= C |s^+ \rangle + a | \kappa \rangle
 \end{aligned}
 \tag{23.1}$$

where  $|s^\pm \rangle = (s_1^\pm, s_2^\pm)^T$  are column vectors describing ingoing and outgoing scattering amplitudes. The coupling constants are also arranged in vectors,  $|\kappa \rangle = (\kappa_1, \kappa_2)^T$ . In this notation, the transformation  $|v \rangle \rightarrow \langle v |$  means transposition *and* complex conjugation, while  $|\kappa \rangle \rightarrow |\kappa \rangle^*$  means only complex conjugation.  $C$  is the scattering matrix of the non-resonant process. A constraint stems from the requirement of instantaneous energy conservation of the global process, that is, fulfilment of  $\frac{d}{dt} (|a(t)|^2 + |b(t)|^2) = |s_1^+(t)|^2 + |s_2^+(t)|^2 - |s_1^-(t)|^2 - |s_2^-(t)|^2$ . This is guaranteed by the conditions

$$\begin{aligned}
 \langle \kappa | \kappa \rangle &= 2\gamma_{A,e} \\
 C | \kappa \rangle^* &= -| \kappa \rangle.
 \end{aligned}
 \tag{23.2}$$

The quantity  $\gamma_{A,e}$  is the external damping rate for the cavity, i.e., the radiative damping rate. Combined with the internal damping rate it builds up the total damping rate for resonator A:  $\gamma_A = \gamma_{A,i} + \gamma_{A,e}$ . Since, instead, resonator B has no other loss channels than the internal one,  $\gamma_B = \gamma_{B,i}$ .

By searching for the steady-state solution of (23.1), one gets that the outgoing amplitudes are linearly dependent from the ingoing amplitudes by means of a frequency-dependent scattering matrix:  $|s^- \rangle = S(\omega) |s^+ \rangle$ , where

$$S(\omega) = C - \frac{i(\omega - \omega_B) + \gamma_B}{(\omega - \omega_+)(\omega - \omega_-)} D \quad (23.3)$$

and  $D = |\kappa\rangle (\langle\kappa|^*)$ . The explicit expression of the poles  $\omega_{\pm}$  will be given in the following, while, implementing the constraints introduced above,<sup>1</sup> matrices  $C$  and  $D$  can be written in terms of a minimal set of parameters which evidence the key “ingredients” of the theory:

$$C = e^{i\phi} \begin{pmatrix} r e^{i\psi} & it \\ it & r e^{-i\psi} \end{pmatrix}$$

$$D = -e^{i\phi} \gamma_{A,e} \begin{pmatrix} d_{11} & d_{12} \\ d_{12} & d_{22} \end{pmatrix}$$

where

$$d_{11} = \left( r + \xi \pm it \sqrt{1 - \xi^2} \right) e^{i\psi}$$

$$d_{22} = \left( r - \xi \pm it \sqrt{1 - \xi^2} \right) e^{-i\psi}$$

$$d_{12} = \pm r \sqrt{1 - \xi^2} + it \quad (23.4)$$

The non-resonant process is basically described by the constant reflectance and transmittance  $r$  and  $t$ ;  $\phi$  and  $\psi$  are a global and a relative phase. The resonant process, described by matrix  $D$ , involves an additional parameter  $\xi$ , which quantifies the asymmetry of the decay into the scattering channels. This parameter, constrained in the interval  $[-1, 1]$ , is connected with the coupling coefficients through the relation  $r\xi = (|\kappa_1|^2 - |\kappa_2|^2) / (|\kappa_1|^2 + |\kappa_2|^2)$ . This link between  $\kappa_{1,2}$  and  $r$ , already outlined for single-mode optical resonators [39], is here generalized to the two-oscillator model. If the physical system under analysis possesses a spatial symmetry that exchanges the scattering channels 1 and 2, one must have  $\xi = 0$  and  $\psi = 0$  or  $\pi$ . Furthermore, the arbitrary sign which appears in (23.4) can be chosen at will, and it is connected to the symmetry of the resonant mode. As a limiting case, note that the positions  $r = 1$  and  $\xi = \pm 1$  imply that the two-port system factorizes into two one-port systems, with either port 1 or 2 in interaction with the resonance.

In the scattering matrix (23.3) a resonant denominator with two poles is found. The explicit expression of the poles is

$$\omega_{\pm} = \frac{\omega_A + \omega_B}{2} + i \frac{\gamma_{A,e} + \gamma_{A,i} + \gamma_{B,i}}{2}$$

$$\pm \frac{1}{2} \sqrt{[(\omega_A - \omega_B) - i(-\gamma_{A,e} - \gamma_{A,i} + \gamma_{B,i})]^2 + 4\Omega^2} \quad (23.5)$$

---

<sup>1</sup>The following expressions are the most general ones that fulfill the constraints given in (23.2), and generalize both [27] and [43].

We also write the expression for the zeroes,  $\bar{\omega}_{\pm}$ , which will be useful in the following:

$$\bar{\omega}_{\pm} = \frac{\omega_A + \omega_B}{2} + i \frac{-\gamma_{A,e} + \gamma_{A,i} + \gamma_{B,i}}{2} \pm \frac{1}{2} \sqrt{[(\omega_A - \omega_B) - i(\gamma_{A,e} - \gamma_{A,i} + \gamma_{B,i})]^2 + 4\Omega^2}. \quad (23.6)$$

### 23.3 Lineshape Inheritance to the Strong Coupling Regime

In this section we will discuss what spectral fingerprints should be expected from a two-oscillator system that does not almost present losses other than the radiative ones, but where the coupling between the two oscillator is either vanishing or strong enough to overcome the radiative coupling.

The case of a very weak coupling between the oscillators is essentially that of a single oscillator (oscillator A), radiatively coupled with the scattering channels and embedded in the non-resonant scattering process. This situation describes very well the response of several photonic systems such as dielectric nanoparticles (where the Mie resonances coexist with the background wave transmission) or as dielectric photonic crystal slabs (i.e., guided mode resonators) where the guided mode resonances are embedded in a quasi-flat Fabry-Pérot background. These systems are well known sources of Fano resonances, which, within our formalism, are governed by the parameters  $t$  (or, analogously,  $r$ ),  $\xi$ ,  $\gamma_{A,e}$  and  $\gamma_{A,i}$ .

The upper panels (a–c) in Fig. 23.2 represent this behaviour. The off-resonance transmittance equals  $t^2$ , while on-resonance the lineshape passes from an ordinary to a reversed Lorentzian through the characteristic asymmetric Fano shape. This is true when the system is symmetric ( $\xi = 0$ ); where instead a finite asymmetry is included, it leads to warped lineshapes with smaller contrasts. The contrast is also reduced by the presence of an internal damping  $\gamma_{A,i}$ , while the external damping  $\gamma_{A,e}$  only determines the linewidth. It can be shown that when  $\gamma_{A,i} = 0$  and  $\xi = 0$  the transmittance lineshapes are fully contrasted; given the absence of losses other than the external (radiative) ones, unity contrast is also observed in reflectance. It should be noticed that here we employed the upper sign in (23.4); the other choice would have exchanged  $(\omega - \omega_A) \rightarrow (\omega_A - \omega)$  hence reversing the  $t = 1/\sqrt{2}$  spectrum.

The onset of a large enough coupling  $\Omega$  between the oscillators (Fig. 23.2, panels (d–f)) induces a splitting of the single spectral feature in two separate spectral features, as expected from the physics of strongly coupled oscillators. What is remarkable here is the spectrum resulting when  $t = 1/\sqrt{2}$ : a *double* Fano resonance occurs, whose shape depends *only* on the shape of the original, bare, radiatively coupled resonator, i.e., on the sole value of the parameter  $t$ . This phenomenon, which we name *lineshape inheritance*, is robust and manifests itself also in conjunction with another key phenomenon related to strong coupling: resonance anticrossing. In panel (g) of Fig. 23.2 we report the transmittance lineshapes which occur to the strongly coupled Fano resonators when the frequency of one of them (here, resonator B) is

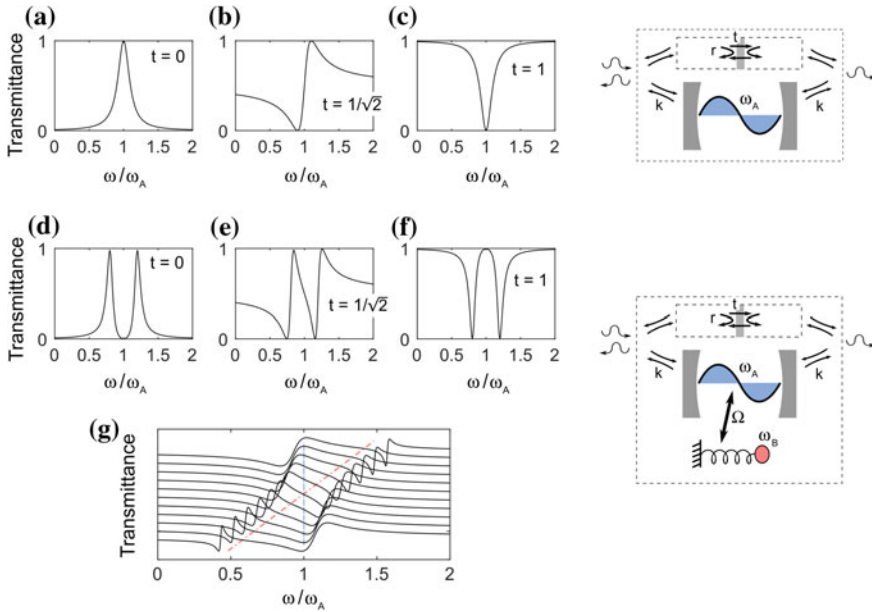


**Fig. 23.2** Lineshape inheritance at the onset of strong coupling. The model system consisting of a resonator coupled with a non-resonant background is responsible for well-known Fano resonances (panels **a–c**). When a second resonator is coupled to the first one, the spectral feature splits in two, as a consequence of the onset of strong coupling between the oscillators (panels **d–f**). Interestingly, the resulting lineshapes inherit from the “parent” system the lineshape, which is only dictated by the value of the off-resonant scattering parameter  $t$ . The lineshape inheritance coexists with the other fingerprint of strong coupling: resonance anticrossing, observed when the frequency of a resonator—here, resonator B—is swept across the frequency of the other (panel **g**). Parameters are:  $\gamma_{A,e} = 0.1 \omega_A$ ,  $\gamma_{A,i} = 0$ ,  $\gamma_{B,i} = 0$ ,  $\Omega = 0$  for panels (a–c) and  $\Omega = 0.2 \omega_A$  for panels (d–g). In panels (d–f) the resonators are matched:  $\omega_A = \omega_B$

swept across the frequency of the other, which is instead kept fixed. It clearly appears that the two splitted resonance maintain their Fano nature, also when they are quite distant on the frequency scale. In this sense, the lineshape inheritance phenomenon is “nonlocal”, as its effects are felt also on spectrally far anomalous features.

To conclude this section we report an experimental observation of the lineshape inheritance phenomenon. This has been observed in a strongly coupled system well known in the community of mid- and far-infrared photonics: intersubband polaritons [22, 44]. They arise when a semiconductor quantum well (or, more usually, a stack of multiple quantum wells) is embedded in a photonic resonator, typically a patch antenna, an LC resonator, or a photonic crystal slab. The device under analysis belongs to the latter category, and its schematic is reported in Fig. 23.3a. A semiconductor waveguide embedding several tens of quantum wells is patterned with an array of metal stripes; the stripe array has a pitch that matches the wavelength of the guided mode, such as to excite the guided mode resonance at a frequency that

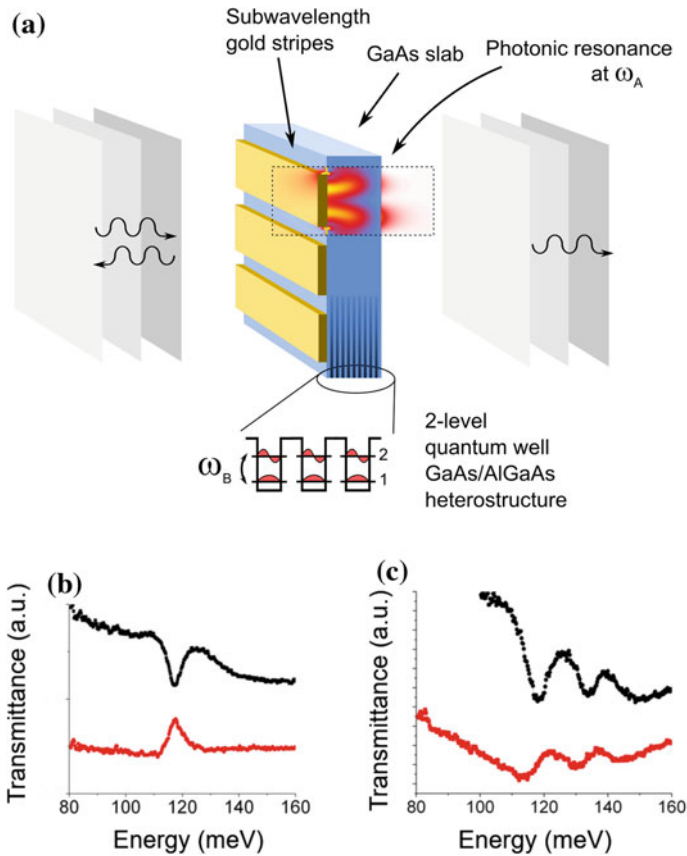


**Fig. 23.3** An experimental situation where lineshape inheritance has been observed. A semiconductor film is patterned with metal stripes, thus implementing a guided mode resonance (also known as leaky mode resonance in photonic crystal slab; the inset shows the internal field at resonance). The photonic resonance is tuned to match the intersubband transition of an ensemble of quantum wells embedded in the membrane itself. When the device is operated below diffraction thresholds, it is a genuine two-port optical system (a). Lineshapes observed when the quantum well transition is switched off (b) and when it is switched on (c). The curves are dips or peaks depending on the geometrical parameters of the metal stripes, and are inherited from the uncoupled to the coupled regime

ultimately matches that of the electron transition between the two confined levels in the quantum well. In such system, the guided mode resonance (i.e., photonic crystal slab resonance) is coupled radiatively with the far-field through plane-wave scattering channels, and meanwhile it is coupled with the electrical dipole transition of the quantum well. As long as the dipole transition can be treated semiclassically as a mechanical oscillator, the model introduced in Sect. 23.2 can be applied. Here, the bare photonic resonance lineshape is dictated by the metallization ratio: at fixed pattern period, narrow stripes are responsible for a dip, while large stripes lead to a peak.

Appropriate tuning of the pattern period allows for tuning the resonance frequency, and eventually to match the quantum well intersubband transition frequency. The transmittance curves recorded from two samples are reported in Fig. 23.3b: here, the quantum wells are inactive and the bare photonic response is observed. When the quantum well transition is instead switched on, the curves of Fig. 23.3c are observed: a strong coupling doublet is observed, preserving the dip or peak character of the uncoupled photonic resonance. This is a clear evidence of the lineshape inheritance phenomenon.

## 23.4 Absorption Properties

### 23.4.1 Universal Absorption Lineshapes

In the previous Section we showed that strong coupling between oscillators, one of which originally behaves as a Fano resonator, induces a splitting of the original spectral feature in two well distinct Fano lines which inherit the shape from the former resonance. However, we based our analysis on transmittance spectra,<sup>2</sup> mostly pushed by the need to compare the model data with experimental results, where transmittance experiments are often the most simple. Nonetheless, transmittance or reflectance experiments alone do not grasp the complete physical picture of a two-port system: rather, absorption spectra provide a complementary picture, more deeply connected with the internal behavior of the system under analysis. Indeed, a resonant, dissipative system absorbs energy mostly when the driving frequency matches its eigenfrequencies. At resonance, the energy is stored within the resonator and dissipated through the internal dissipation mechanisms—for instance, ohmic or dipolar losses in the case of metals or dielectrics, respectively.

In the case of a two-oscillator Fano system under strong coupling, the absorption lineshape *always* present a double-peaked structure, independently from the specific Fano shape observed in transmission or in reflection. This behavior is represented in Fig. 23.4, where a lossy coupled system is analyzed. Here, overall losses are smaller than the coupling constant  $\Omega$ , which guarantees that the overall system is still in the strong coupling regime. On the transmittance traces, these finite losses are responsible for a reduction of the contrast, which is no more of 100% as it was observed in Fig. 23.2d–f. Notice that now the cases of transmittance peaks or of transmittance dips deserve different contrast levels for the transmittance traces: this inequality is balanced for by the reflectance traces (not shown here), which exactly compensate in order to guarantee that the absorption curves are always the same.

We name this behavior *universal lineshape*, since within this model the details of Fano resonances are completely washed out when an appropriate spectroscopic quantity is looked for. More interestingly, the absorption lineshape can be expressed

---

<sup>2</sup>Reflectance behaves similarly.



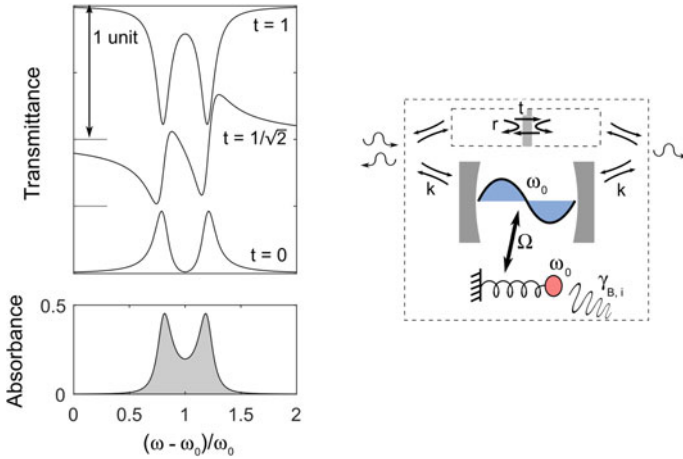


**Fig. 23.4** Universal absorption lineshape occurring for a two-oscillator system displaying Fano doublet in transmittance. The absorption lineshape does not depend on the transmittance lineshape, rather it has always a double-peaked structure. No lineshape inheritance phenomenon takes place here. Parameters are:  $\gamma_{A,e} = 0.1 \omega_A$ ,  $\gamma_{A,i} = 0$ ,  $\gamma_{B,i} = 0.05$ ,  $\Omega = 0.2 \omega_A$

by means of a very simple formula, which stems from appropriate algebraic manipulation of (23.3). Indeed, it can be shown that

$$A(\omega) = \frac{1 - |\det S(\omega)|^2}{2} = \frac{1}{2} \left( 1 - \left| \frac{(\omega - \bar{\omega}_+)(\omega - \bar{\omega}_-)}{(\omega - \omega_+)(\omega - \omega_-)} \right|^2 \right) \tag{23.7}$$

where the explicit expressions of poles and zeros are given in (23.5) and (23.6). Two interesting points are direct consequence of this expression:

- The absorption can never be larger than 1/2. This is because in a lossy system the S-matrix determinant is always restricted to the interval [0, 1].
- The absorption reaches its extremum  $A = 0.5$  if and only if  $\det S = 0$ , i.e., if and only if  $\omega = \bar{\omega}_\pm$ . This point will be elucidated in the following Section, as it is connected with a deep physical insight.

It should be noticed that in the above discussion we assumed the system to be symmetric, i.e., that  $\xi = 0$ . The role of system asymmetry is that of unbalancing the two scattering channels,<sup>3</sup> and to allow for different behaviours for what concerns the amount of energy that can be absorbed in a two-port system; this topic will be clarified in Sect. 23.4.3. However, to get a wider understanding of the absorption phenomena in these systems, which are evidently *two-port systems*, it is useful to introduce another concept, that of coherent absorption, and the closely related one of coherent perfect absorption.

<sup>3</sup>We anticipate that the parameter  $\xi$  does not affect the line shapes.

### 23.4.2 A Detour on Coherent (Perfect) Absorption

When dealing with multi-port systems, speaking of absorption may lead to imprecise pictures, or even be misleading: the amount of energy absorbed in such a system may depend strongly upon the way it is excited. For instance, a two-port optical component may be strongly absorptive when illuminated from one side, and highly reflective (hence not absorptive) when illuminated from the other side [45]. In general, two- and multiport linear optical systems exhibit the phenomenon of *coherent absorption*. Coherent absorption generalizes the concept of ordinary absorption to multiport systems [46, 47]. Here, to appropriately define the absorbance, i.e. “the amount of energy subtracted from the incident field”, it is imperative to define the actual state of the input field. For instance, in a two-port system both ports can be excited by coherent fields; here, an interesting interplay between interference and absorption can be observed. The framework is illustrated in Fig. 23.5a: the most general scattering configuration consists in two input fields  $s_{1,2}^+$  and two output fields  $s_{1,2}^-$ . Applying the  $2 \times 2$  S-matrix formalism it can be shown that the output intensities  $|s_{1,2}^-|^2$  depend sinusoidally on the input beam dephasing. Moreover, also the total output intensity depends sinusoidally on the input dephasing, with minima and maxima that identify the extremal values of energy absorption from a two-port system. This allows to define a *joint absorption*  $A_j$ , i.e., the energy absorbed from the system normalized with respect to the input energy:  $A_j = 1 - (|s_1^-|^2 + |s_2^-|^2) / (|s_1^+|^2 + |s_2^+|^2)$ . This quantity is connected with the S-matrix coefficients through the following formula:

$$A_j = \frac{1+x}{2} A_1 + \frac{1-x}{2} A_2 - \sqrt{1-x^2} A_{\text{mod}} \sin(\Delta\phi + \delta) \quad (23.8)$$

where

$$\begin{aligned} x &= \frac{|s_1^+|^2 - |s_2^+|^2}{|s_1^+|^2 + |s_2^+|^2} \\ \Delta\phi &= \arg(s_1^+ / s_2^+) \\ A_{\text{mod}} &= \sqrt{(1-A_1)(1-A_2) - |\det S|^2} \\ A_1 &= 1 - |s_{11}|^2 - |s_{21}|^2 \\ A_2 &= 1 - |s_{22}|^2 - |s_{12}|^2. \end{aligned} \quad (23.9)$$

The angle  $\delta$  is a quite involved function<sup>4</sup> of the S-matrix amplitudes and phases.

If  $x = \pm 1$ , there is only one input beam active at a time, and the single-beam absorbances  $A_{1,2}$  are recovered. In general, at fixed  $x$ , a sweep of  $\Delta\phi$  allows for  $A_j$  to span an interval, which has extremes

---

<sup>4</sup>Specifically it holds  $\tan \delta = (\rho_2 \sin \psi_2 + \rho_1 \sin \psi_1) / (\rho_2 \cos \psi_2 - \rho_1 \cos \psi_1)$ , where  $\rho_{1,2}$  and  $\psi_{1,2}$  are the amplitudes and phases of the reflection coefficients  $s_{11}$  and  $s_{22}$ , respectively.

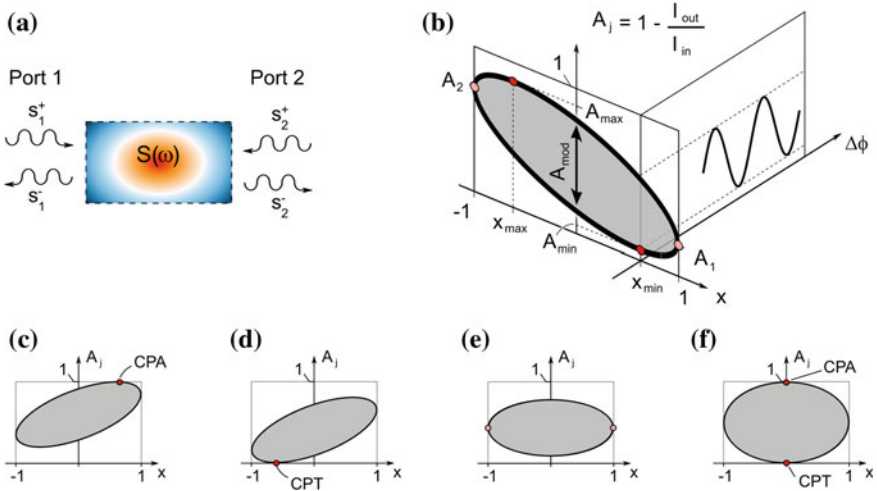


**Fig. 23.5** Coherent absorption in a linear two-port lossy system. **a** Schematic of the system. **b** schematic representing the coherent absorption phenomenon. The energy absorbed when both input are switched on (joint absorption,  $A_j$ ), depends sinusoidally on the input dephasing  $\Delta\phi$ . The set of points accessible by  $A_j$  describes an ellipse when  $x$  is varied ( $x$  measures the imbalance between the input beam intensities, see text). **c–f** Special cases for the coherent absorption ellipse. Coherent perfect absorption (CPA) and coherent perfect transparency (CPT) can be achieved, also simultaneously

$$A_{j,\pm} = \frac{1+x}{2} A_1 + \frac{1-x}{2} A_2 \pm \sqrt{1-x^2} A_{mod}. \quad (23.10)$$

Notably, spanning the beam imbalance  $x$  allows for  $A_{j,\pm}$  to define an ellipse: the *coherent absorption ellipse*, which is depicted in Fig. 23.5b. It has a minimum and a maximum, labeled  $A_{min}$  and  $A_{max}$ , which occur respectively for input beam imbalances  $x_{min}$  and  $x_{max} = -x_{min}$ . These values are strictly connected with the singular value representation of matrix  $S$  [48, 49].

The coherent absorption ellipse has several special cases. One of them occurs when  $A_{max} = 1$ . Upon this condition, perfect absorption is attained; if  $x_{max} \neq \pm 1$  the phenomenon is called *coherent perfect absorption* (CPA, Fig. 23.5c). Indeed, CPA is the result of a precise balance between interference and absorption: the system completely absorbs the incident radiation as the consequence of an appropriate choice of the input fields, which must match the requirements of phase and amplitude dictated by the S-matrix. Not only: in order to have CPA, the S-matrix itself *must* fulfill  $\det S = 0$ . In other words, a system exhibits CPA when one of its eigenvalues is zero, and when the input fields constitute the corresponding eigenvector. Another special case occurs when  $A_{min} = 0$ . Here, *none* of the incident radiation is absorbed, even though the system itself may be absorptive for some other configuration of the input field. This situation is usually referred to as *coherent perfect transparency* (CPT, Fig. 23.5d). The diagrams represented in Fig. 23.5c–d depict the

coherent absorption ellipse for an asymmetric device. If the device is symmetric, i.e., if its S-matrix is invariant for the exchange of the two ports, the ellipse must be symmetric, as depicted in Fig. 23.5e. In the case such a symmetric device exhibits CPA and CPT, both of them occur at  $x = 0$ , i.e., for equal amplitude input beams (Fig. 23.5f); here, the switch between CPA and CPT state can be driven by a sole phase sweep of either one of the two input beams.

It should be noticed that the analysis given so far works *one frequency at a time*: in general, the S-matrix is  $\omega$ -dependent, and the coherent absorption ellipse depends upon the frequency accordingly.

### 23.4.3 Universal Coherent Absorption Lineshapes

Armed with the toolbox of coherent absorption theory, we may now drive towards a complete picture of the absorption phenomenology in the most general Fano-resonant two-port two-oscillator model with asymmetry, as depicted in Fig. 23.1.

All the properties we are looking for stem from the expression of the extremal joint absorbance, (23.10), obtained when employing the S-matrix of (23.3). Quite lengthy calculations result in the expression

$$A_{j,\pm}(\omega, x) = \frac{A_{\text{uni}}(\omega)}{2} \left( 1 + r\xi x \pm \sqrt{(1 - r^2\xi^2)(1 - x^2)} \right) = A_{\text{uni}}(\omega) f_{\pm}(r\xi, x) \quad (23.11)$$

where  $A_{\text{uni}}(\omega) = 1 - |\det S(\omega)|^2$ .

First, it can be noticed that (23.7) is correctly accounted for by (23.11): the single-beam absorptions for the symmetric system described in Sect. 23.4.1 is here retrieved setting  $\xi = 0$  and  $x = \pm 1$ . What is now relevant is that the function  $1 - |\det S(\omega)|^2$  truly plays a role of *universal absorption lineshape*, also when *coherent absorption* is examined. It follows clearly from (23.11) that the coherent absorption ellipse depends upon the frequency only through the factor  $A_{\text{uni}}(\omega)$ , which stretches it without modifying its shape. The ellipse shape is instead described by the function  $f_{\pm}(r\xi, x)$ . In other words, for all the configurations of the input field  $x$  and of the system's lineshape- and asymmetry-governing parameters  $r$  and  $\xi$ , the absorption spectral properties are completely dictated by the sole *resonance* parameters  $\omega_{A,B}$ ,  $\gamma_{A,B}$ , and  $\Omega$ , which enter  $A_{\text{uni}}(\omega)$ .

The form of the function  $f_{\pm}(r\xi, x)$  implies two interesting facts. First, CPT can always be achieved in the present model: indeed, for  $x = -r\xi$  one has  $f_- = 0$ , hence the minimum joint absorption is spectrally flat and equals zero. Second, CPA can be achieved provided that peculiar yet simple conditions are met. One is that  $f_+ = 1$ , i.e.,  $x = r\xi$ , which is a matching condition between the (external) excitation beam imbalance and the (internal) asymmetry properties of the resonator. Another is that  $A_{\text{uni}}(\omega) = 1$ , or alternatively  $|\det S(\omega)|^2 = 0$ , which we already encountered before when analyzing the single-beam absorption of the symmetric system. As anticipated,

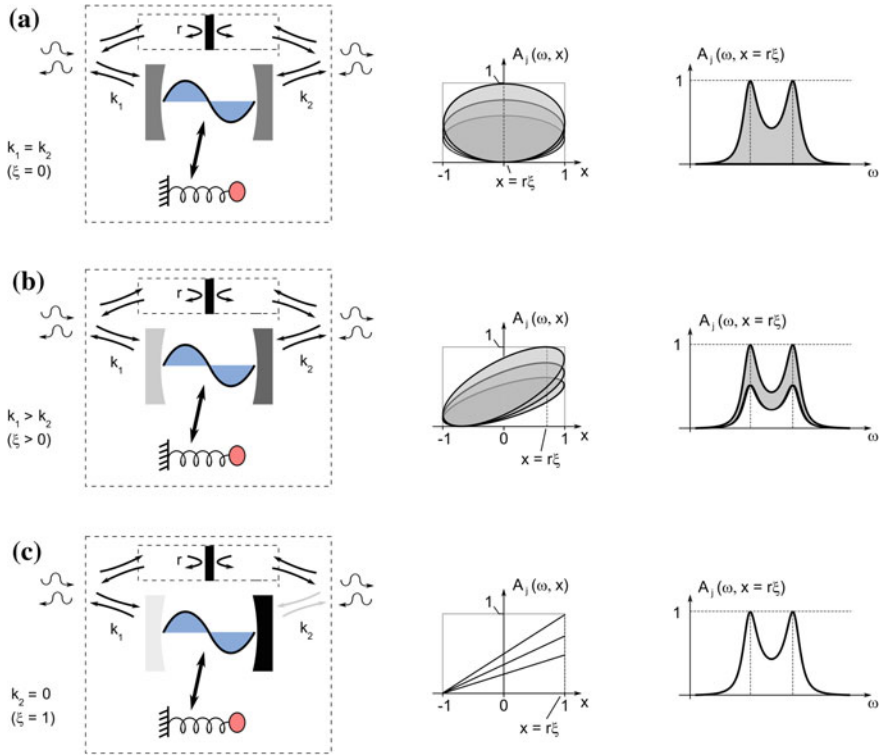


**Fig. 23.6** Universal coherent absorption lineshapes and the role of asymmetry. Rows (a–c) depict three cases with increasing degrees of asymmetry: row (a), symmetric system; row (b), partially asymmetric system, row (c), fully asymmetric system. In case (a) the coherent absorption ellipse is horizontal and the joint absorption spectrum has maximum contrast. For increasing degrees of asymmetry the ellipse becomes more tilted and narrow, and the maximum/minimum joint absorption spectra become closer and closer. Nonetheless, for appropriate choice of the parameters, joint absorption can reach unity at two energy points (strong critical coupling, see Fig. 23.7)

this condition has a profound physical meaning and will be analyzed in depth in the following Section.

To graphically clarify the content of (23.11), let’s focus on a special case that will be further clarified in the following, i.e., the case where  $A_{uni}(\omega)$  has a double-peak structure with the peaks reaching unity. The frequency-dependent coherent absorption ellipses may assume several shapes depending on the parameters  $r$  and  $\xi$ , or, better, on their product<sup>5</sup>  $r\xi$ . To further fix the ideas, suppose that  $r = 1$  (i.e.,  $t = 0$ , with the transmittance lineshapes being peaks, see Fig. 23.2d). Three peculiar cases are reported in Fig. 23.6: in (a) we consider a symmetric system, where the resonator has the same coupling with the two scattering channels. In (b) we consider

<sup>5</sup>This fact is interesting since the product  $r\xi$  is directly connected with the cavity-exterior coupling coefficients  $\kappa$  (see Sect. 23.2).

a system which preferentially decays towards port 1, but which still has some coupling towards port 2. Finally, in (c), the extreme case of a system that only couples with port 1 is represented. Clearly, this system is equivalent to a single-port system, as port 2 only sees a constant and unity reflection dictated by the non-resonant channel. In the middle column of Fig. 23.6 the coherent absorption ellipses are reported: in the symmetric case, the ellipses are clearly symmetrical, always exhibit CPT at  $x = 0$  and show CPA at  $x = 0$ , but only for the frequencies such that  $A_{\text{uni}} = 1$ . In the intermediate case, the ellipse is tilted, always exhibits CPT at  $x = -r\xi$  and has its maximum at  $x = r\xi$ , reaching CPA at the appropriate frequencies. In the extreme case where  $\xi = 1$  the ellipse degenerates in a segment: no more coherent modulation of the absorption is possible. This is a clear consequence of the fact that the system communicates with the exterior with a single port, from which a double-peaked absorption spectrum can however still be observed.

### 23.5 Weak, Strong, and Critical Coupling

The aim of this last Section is to draw a connection between the concepts of weak, strong and critical coupling; to check whether they are compatible or not, and what happens when they indeed coexist. While the transition between weak and strong coupling has been studied since two decades ago [50], the interplay with critical coupling has not been explored until the past few years [51, 52]. We provide here a brief introduction to these concepts.

Weak and strong coupling are concepts mostly employed in the field of quantum light-matter interaction, and refer to the cases where the light-matter coupling can, or cannot, be treated in a perturbative way. In other words, in the weak coupling regime, an ideal two-level system decays radiatively with a rate dictated by the Fermi golden rule. This process is irreversible, as the internal energy of the two-level system is lost towards the radiation bath. On the opposite side stands the strong coupling regime: this occurs under conditions such that the photon emitted by the two-level system could bounce back into the two-level system itself, being reabsorbed, and so on in a loop long enough with respect to the time scales of other competing decay mechanisms. In order to reach the strong coupling regime, the two-level system must be embedded in a resonant cavity such that the characteristic ringing time (i.e., the inverse of the Rabi frequency, eventually dictated by the modal volume of the cavity) is small enough compared to the other decay rates.

Critical coupling—and the related undercoupling and overcoupling concepts—are of key relevance when analyzing driven resonators in general; more closely connected with our aims are the fields of radiofrequency and of photonics, where critical coupling is instrumental to optimize the operation of several resonant-enhanced devices (like filters and detectors). Critical coupling occurs when the external decay rate matches the internal one: in other words, when the time scale needed for a

wavepacket to escape/enter the cavity is equal to the time needed for the wavepacket to be absorbed within the cavity itself. Under this condition, all the energy which is fed into the resonator is absorbed within the resonator itself (and eventually converted into other forms of energy, if required by the application).

In light of these definitions, the two-peak CPA curves presented in Sect. 23.4.1 acquire a clear meaning: *strong and critical coupling can occur simultaneously*. Indeed, CPA is nothing else than critical coupling observed in a two-port system, and the double-peaked spectra are the fingerprint of strong coupling. This observation may be, at a first glance, quite counterintuitive, as it is common knowledge that strong coupling requires low losses to be observed. While this is true in general, a more detailed look at the theory clarifies when and how strong and critical coupling may coexist, and which are the key parameters ruling the phenomenology.

At the basis stands the condition for CPA:  $\det S(\omega) = 0$ . CPA occurs when it exists a real  $\omega$  such that the S-matrix determinant vanishes, i.e., when either one or both zeroes  $\bar{\omega}_{\pm}$  given in (23.6) are purely real. Here we consider the case of tuned oscillators, while the more general case of detuned resonators is described in [53]. Depending on the argument of the square root of (23.6) two situations can be identified:

- Two real zeroes: **strong critical coupling**.

The zeroes occur at

$$\omega_0 \pm \sqrt{\Omega^2 - \gamma_{B,i}^2}$$

when

$$\begin{cases} \gamma_{A,e} = \gamma_{A,i} + \gamma_{B,i} \\ \gamma_{B,i} < \Omega \end{cases} \quad (23.12)$$

- One real zero: **weak critical coupling**.

The zero occurs at

$$\omega_0$$

when

$$\gamma_{B,i}(\gamma_{A,e} - \gamma_{A,i}) = \Omega^2. \quad (23.13)$$

The first case is indeed *strong critical coupling* (SCC) because of the co-presence of spectral feature splitting and (coherent) perfect absorption. In this situation, all the incoming energy is absorbed into the internal dissipation mechanisms of both oscillators A and B. Notice that the SCC occurs on a segment of the parameter space: it is not a single and isolated condition on the parameters, and it can be easily met provided that one is able to tune the damping rate of either resonator A or B, and that the coupling  $\Omega$  is sufficiently large with respect to the accessible values of the damping rates.

In the second case we applied the nomenclature *weak critical coupling* (WCC), which can at a first glance be motivated as being simply the counterpart of strong critical coupling. However, the WCC condition is somewhat subtle and its full com-

prehesion requires further clarification. We will explore these details after analyzing a “phase diagram” which summarizes the phenomenology of SCC and WCC. Figure 23.7 reports such a phase diagram. The solid lines identify the SCC and WCC conditions following from (23.12) and (23.13), on a suitable cartesian plane. We also reported as a dashed line the boundary between the regions where  $|\det S(\omega)|^2$  (or equivalently  $A_{\text{uni}}$ ) is single- or double-peaked, which can be regarded as a definition of weak and strong coupling, respectively.<sup>6</sup> A set of spectra, corresponding to the points reported in the chart on the left, are given in the right panels, which evidence the crossing of strong and weak critical coupling conditions. We remind here that these curves, which do not resemble at all the Fano lineshapes, are indeed observed in systems which do exhibit Fano lineshapes: however, Fano shapes may only be found in transmission and reflection, while (coherent) absorption curves always show the universal curves  $A_{\text{uni}}(\omega) \propto 1 - |\det S(\omega)|^2$  reported in Fig. 23.7.

We now clarify the meaning of *weak critical coupling*. In one sense, WCC can be easily understood by considering the limiting case where resonators A and B are more and more decoupled ( $\Omega \rightarrow 0$ ), but maintain finite damping  $\gamma$ . In this case, the system is essentially a single resonator coupled with the scattering channels, which is the case usually described by radiofrequency and photonics texts about resonator coupling. Equation (23.13) becomes  $\gamma_{A,e} = \gamma_{A,i}$ , which is the usual critical coupling formula. All the energy entering the system through the radiation channels is dissipated within the resonator itself. On the phase diagram, the decoupled system can be thought of as the coupled system where the SCC branch gradually reduces towards a point, and where the WCC hyperbola degenerates to a line (Fig. 23.8a, b). The physics does not depend any more on  $\gamma_{B,i}$ , as resonator B couples less and less to resonator A and eventually not even to the exterior. Thus, the definition of *weak* coupling is justified from the fact that there is no coupling between the resonators.

In another sense, WCC can be viewed as occurring in a system which can show strong coupling (finite  $\Omega$ ), but such that there is almost no internal dissipation of resonator A ( $\gamma_{A,i} \rightarrow 0$ ). The situation is depicted in Fig. 23.8a, c. This single-peaked critical coupling is quite counterintuitive, as it arises from a system where there are still *two* resonators, yet leading to a single-peaked spectrum with perfect absorption. The existence of a single peak is simply that we are considering a region of the phase diagram where the damping—either the *external* damping of resonator A or the *internal* damping of resonator B—are too large compared with the coupling  $\Omega$ . It is interesting to notice that the WCC condition now reads more simply

$$\frac{\Omega^2}{\gamma_{A,e}\gamma_{B,i}} = 1,$$

which is a condition on the *cooperativity*  $C = \Omega^2/2\gamma_{A,e}\gamma_{B,i} = 1/2$ . Meanwhile, it is also significant to observe that in the present case of zero internal losses of resonator A, the boundary between the regions of single- and double-peaked universal lineshape

<sup>6</sup>Notice, however, that the curve which separates the single- from the double-peak region of reflectance and transmittance spectra is different. See also [50] for a discussion on this topic.



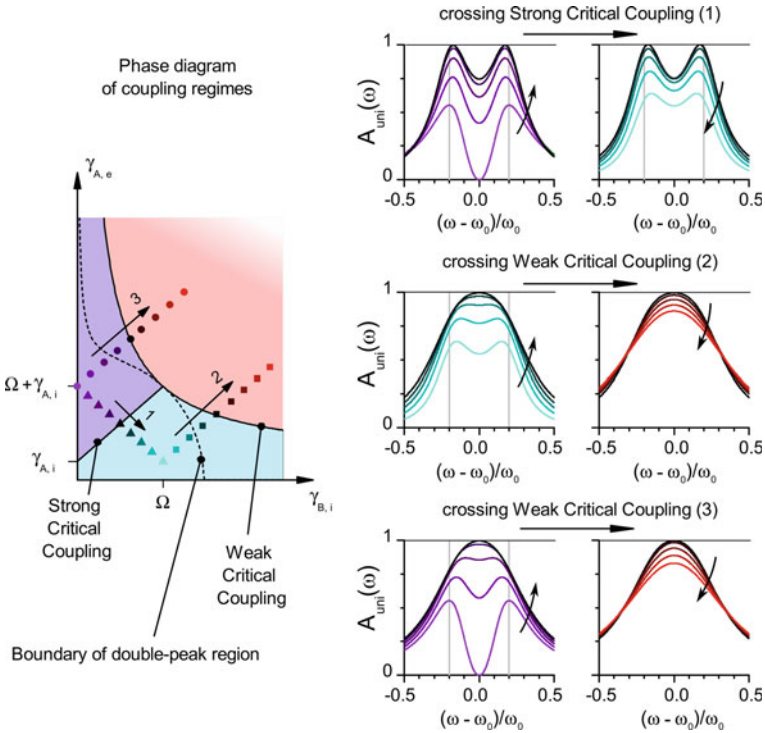


**Fig. 23.7** Phase diagram for the two-oscillator Fano resonant system, following from the analysis of its universal coherent absorption lineshapes. Depending on the relative values of the damping rates  $\gamma$  and of the coupling strength  $\Omega$ , different regimes are observed. Below the dashed line, the absorption lineshape is double-peaked, above it is single-peaked; hence the dashed line can be regarded as the boundary between weak and strong coupling. The solid lines identify the parameter combinations that give rise to (coherent) perfect absorption. Two different regimes can be identified: *strong critical coupling*, where the absorption is double-peaked, and *weak critical coupling*, where the absorption is single-peaked. The panels to the right elucidate the behavior of the lineshapes when exploring different paths in the parameter space

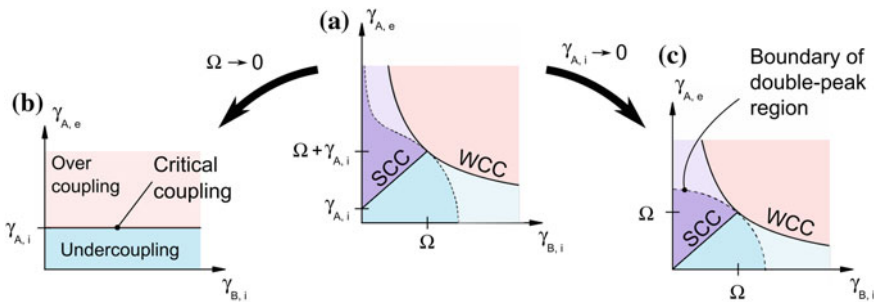


**Fig. 23.8** Limiting cases highlighting the nature of weak critical coupling. The full phase diagram **a** evolves either in those represented in **(b)** or in **(c)**, where, respectively,  $\Omega \rightarrow 0$  or  $\gamma_{A,i} \rightarrow 0$

spectra is described by a simple circumference (see Fig. 23.8a, c), which in formula reads

$$\gamma_{A,e}^2 + \gamma_{B,i}^2 = 2\Omega^2.$$

## 23.6 Conclusions

In conclusion, we have provided a unified vision of strong, weak and critical coupling, based on a simple coupled oscillator model with a nonresonant background usually employed to describe Fano resonances in nanophotonic structures. Exploring the parameter space of the model two significant features emerged: lineshape inheritance, and the universal absorption lineshape. Detailed analysis on the absorption lineshapes—here carried out in the general framework of coherent absorption theory for two-port systems—reveals a further intriguing phenomenon, the strong critical coupling. This regime, where two oscillators are strongly coupled each other and perfectly coupled with the environment, has a novel character and may prove extremely useful to design devices where the quantum physics of strong light-matter coupling is optimally exploited thanks to an effective interface with the exterior. All of this is coupled with the rich and intriguing physics of Fano interference, whose characteristic lineshapes can be harnessed to develop, for instance, advanced filtering functionalities.

**Acknowledgements** The author acknowledges very insightful discussions with Dr. Raffaele Colombelli, Lorenzo Baldacci, and Prof. Alessandro Tredicucci.

## References

1. A. Auffèves, D. Gerace, M. Richard, S. Portolan, M.F. Santos, L.C. Kwek, C.E. Miniatura, *Strong Light-Matter Coupling: From Atoms to Solid-State Systems* (World Scientific, 2013)
2. A.V. Kavokin, J.J. Baumberg, G. Malpuech, F.P. Laussy, *Microcavities* (Oxford University Press, 2007)
3. A.E. Miroschnichenko, S. Flach, Y.S. Kivshar, *Rev. Mod. Phys.* **82**, 2257 (2010). <https://doi.org/10.1103/RevModPhys.82.2257>
4. B. Luk'yanchuk, N.I. Zheludev, S.A. Maier, N.J. Halas, P. Nordlander, H. Giessen, C.T. Chong, *Nat. Mater.* **9**(9), 707 (2010). <http://www.ncbi.nlm.nih.gov/pubmed/20733610>
5. M.F. Limonov, M.V. Rybin, A.N. Poddubny, Y.S. Kivshar, *Nat. Photonics* **11**(9), 543 (2017)
6. R.D. Artuso, G.W. Bryant, *Nano Lett.* **8**(7), 2106 (2008). <https://doi.org/10.1021/nl800921z>. PMID: 18558787
7. A. Manjavacas, F.J.G.d. Abajo, P. Nordlander, *Nano Lett.* **11**(6), 2318 (2011). <https://doi.org/10.1021/nl200579f>. PMID: 21534592
8. A. Ridolfo, O. Di Stefano, N. Fina, R. Saija, S. Savasta, *Phys. Rev. Lett.* **105**, 263601 (2010). <https://doi.org/10.1103/PhysRevLett.105.263601>
9. E. Waks, D. Sridharan, *Phys. Rev. A* **82**, 043845 (2010). <https://doi.org/10.1103/PhysRevA.82.043845>
10. C. Ciuti, I. Carusotto, *Phys. Rev. A* **74**, 033811 (2006). <https://doi.org/10.1103/PhysRevA.74.033811>

11. G.S. Agarwal, Y. Zhu, *Phys. Rev. A* **92**, 023824 (2015). <https://doi.org/10.1103/PhysRevA.92.023824>
12. J. Yang, M. Perrin, P. Lalanne, *Phys. Rev. X* **5**, 021008 (2015). <https://doi.org/10.1103/PhysRevX.5.021008>
13. S. Zhang, D.A. Genov, Y. Wang, M. Liu, X. Zhang, *Phys. Rev. Lett.* **101**, 047401 (2008). <https://doi.org/10.1103/PhysRevLett.101.047401>
14. B. Gallinet, O.J.F. Martin, *Phys. Rev. B* **83**, 235427 (2011). <https://doi.org/10.1103/PhysRevB.83.235427>
15. V. Giannini, Y. Francescato, H. Amrania, C.C. Phillips, S.A. Maier, *Nano Lett.* **11**(7), 2835 (2011). <https://doi.org/10.1021/nl201207n>. PMID: 21635012
16. F. Alpeggiani, S. D'Agostino, L.C. Andreani, *Phys. Rev. B* **86**, 035421 (2012). <https://doi.org/10.1103/PhysRevB.86.035421>
17. D. Dini, R. Köhler, A. Tredicucci, G. Biasiol, L. Sorba, *Phys. Rev. Lett.* **90**, 116401 (2003). <https://doi.org/10.1103/PhysRevLett.90.116401>
18. C. Ciuti, G. Bastard, I. Carusotto, *Phys. Rev. B* **72**, 115303 (2005). <https://doi.org/10.1103/PhysRevB.72.115303>
19. Y. Todorov, A.M. Andrews, R. Colombelli, S. De Liberato, C. Ciuti, P. Klang, G. Strasser, C. Sirtori, *Phys. Rev. Lett.* **105**, 196402 (2010). <https://doi.org/10.1103/PhysRevLett.105.196402>
20. G. Günter, A.A. Anappara, J. Hees, A. Sell, G. Biasiol, L. Sorba, S. De Liberato, C. Ciuti, A. Tredicucci, A. Leitenstorfer, R. Huber, *Nature* **458**(7235), 178 (2009), <http://www.ncbi.nlm.nih.gov/pubmed/19279631>
21. S. Zanotto, G. Biasiol, R. Degl'Innocenti, L. Sorba, A. Tredicucci, *Appl. Phys. Lett.* **97**(23), 231123 (2010), <https://aip.scitation.org/doi/10.1063/1.3524823>
22. S. Zanotto, R. Degl'Innocenti, L. Sorba, A. Tredicucci, G. Biasiol, *Phys. Rev. B* **85**, 035307 (2012). <https://doi.org/10.1103/PhysRevB.85.035307>
23. A. Christ, S.G. Tikhodeev, N.A. Gippius, J. Kuhl, H. Giessen, *Phys. Rev. Lett.* **91**, 183901 (2003). <https://doi.org/10.1103/PhysRevLett.91.183901>
24. C. Weisbuch, M. Nishioka, A. Ishikawa, Y. Arakawa, *Phys. Rev. Lett.* **69**, 3314 (1992). <https://doi.org/10.1103/PhysRevLett.69.3314>
25. C.R. Gubbin, F. Martini, A. Politi, S.A. Maier, S. De Liberato, *Phys. Rev. Lett.* **116**, 246402 (2016). <https://doi.org/10.1103/PhysRevLett.116.246402>
26. S. Fan, P.R. Villeneuve, J.D. Joannopoulos, H.A. Haus, *Phys. Rev. Lett.* **80**, 960 (1998). <https://doi.org/10.1103/PhysRevLett.80.960>
27. S. Fan, W. Suh, J.D. Joannopoulos, *J. Opt. Soc. Am. A* **20**(3), 569 (2003). <http://josaa.osa.org/abstract.cfm?URI=josaa-20-3-569>
28. T.J. Davis, D.E. Gómez, *Rev. Mod. Phys.* **89**, 011003 (2017). <https://doi.org/10.1103/RevModPhys.89.011003>
29. A.N. Poddubny, M.V. Rybin, M.F. Limonov, Y.S. Kivshar, *Nat. Commun.* **3**, 914 (2012)
30. V. Achilleos, G. Theocharis, O. Richoux, V. Pagneux, *Phys. Rev. B* **95**, 144303 (2017). <https://doi.org/10.1103/PhysRevB.95.144303>
31. Y. Sun, W. Tan, H.Q. Li, J. Li, H. Chen, *Phys. Rev. Lett.* **112**, 143903 (2014). <https://doi.org/10.1103/PhysRevLett.112.143903>
32. A. Thomas, J. George, A. Shalabney, M. Dryzhakov, S.J. Varma, J. Moran, T. Chervy, X. Zhong, E. Devaux, C. Genet, J.A. Hutchison, T.W. Ebbesen, *Angew. Chem. Int. Edition* **55**(38), 11462 (2016). <https://doi.org/10.1002/anie.201605504>
33. K.C. Balram, M.I. Davanço, J.D. Song, K. Srinivasan, *Nat. Photonics* **10**(5), 346 (2016)
34. D. Malz, L.D. Tóth, N.R. Bernier, A.K. Feofanov, T.J. Kippenberg, A. Nunnenkamp, *Phys. Rev. Lett.* **120**, 023601 (2018). <https://doi.org/10.1103/PhysRevLett.120.023601>
35. C. Bonizzoni, A. Ghirri, M. Atzori, L. Sorace, R. Sessoli, M. Affronte, *Sci. Rep.* **7**(1), 13096 (2017)
36. Z.L. Xiang, S. Ashhab, J.Q. You, F. Nori, *Rev. Mod. Phys.* **85**, 623 (2013). <https://doi.org/10.1103/RevModPhys.85.623>
37. S. Fan, J.D. Joannopoulos, *Phys. Rev. B* **65**, 235112 (2002). <https://doi.org/10.1103/PhysRevB.65.235112>

38. R.E. Hamam, A. Karalis, J.D. Joannopoulos, M. Soljačić, *Phys. Rev. A* **75**, 053801 (2007). <https://link.aps.org/doi/10.1103/PhysRevA.75.053801>
39. K.X. Wang, Z. Yu, S. Sandhu, S. Fan, *Opt. Lett.* **38**(2), 100 (2013). <http://ol.osa.org/abstract.cfm?URI=ol-38-2-100>
40. K.X. Wang, Z. Yu, S. Sandhu, V. Liu, S. Fan, *Optica* **1**(6), 388 (2014). <http://www.osapublishing.org/optica/abstract.cfm?URI=optica-1-6-388>
41. H. Zhou, B. Zhen, C.W. Hsu, O.D. Miller, S.G. Johnson, J.D. Joannopoulos, M. Soljačić, *Optica* **3**(10), 1079 (2016). <http://www.osapublishing.org/optica/abstract.cfm?URI=optica-3-10-1079>
42. F. Alpeggiani, N. Parappurath, E. Verhagen, L. Kuipers, *Phys. Rev. X* **7**, 021035 (2017). <https://doi.org/10.1103/PhysRevX.7.021035>
43. A. Auffèves-Garnier, C. Simon, J.M. Gérard, J.P. Poizat, *Phys. Rev. A* **75**, 053823 (2007). <https://doi.org/10.1103/PhysRevA.75.053823>
44. S. Zanotto, *Intersubband polaritons in photonic crystal slabs*. Ph.D. thesis, Scuola Normale Superiore, Pisa (2014). <http://metapublishing.org/index.php/MP/catalog/book/45>
45. J.H. Wu, M. Artoni, G.C. La Rocca, *Phys. Rev. Lett.* **113**, 123004 (2014). <https://doi.org/10.1103/PhysRevLett.113.123004>
46. D.G. Baranov, A. Krasnok, T. Shegai, A. Alù, Y. Chong, *Nat. Rev. Mater.* **2**(12), 17064 (2017)
47. J. Yoon, K.H. Seol, S.H. Song, R. Magnusson, *Opt. Express* **18**(25), 25702 (2010). <http://www.opticsexpress.org/abstract.cfm?URI=oe-18-25-25702>
48. L. Ge, L. Feng, *Phys. Rev. A* **95**(1), 013813 (2017). <http://link.aps.org/doi/10.1103/PhysRevA.95.013813>
49. L. Baldacci, S. Zanotto, G. Biasiol, L. Sorba, A. Tredicucci, *Opt. Express* **23**(7), 9202 (2015). <http://www.opticsexpress.org/abstract.cfm?URI=oe-23-7-9202>
50. V. Savona, L. Andreani, P. Schwendimann, A. Quattropani, *Solid State Commun.* **93**(9), 733 (1995). <http://www.sciencedirect.com/science/article/pii/0038109894008655>
51. S. Zanotto, F.P. Mezzapesa, F. Bianco, G. Biasiol, L. Baldacci, M.S. Vitiello, L. Sorba, R. Colombelli, A. Tredicucci, *Nat. Phys.* **10**(11), 830 (2014)
52. J.M. Manceau, S. Zanotto, T. Ongarello, L. Sorba, A. Tredicucci, G. Biasiol, R. Colombelli, *Appl. Phys. Lett.* **105**(8), 081105 (2014)
53. S. Zanotto, A. Tredicucci, *Sci. Rep.* **6**, 24592 (2016)

# Index

## A

- Abraham-Lorentz, 111
- Absorption, 157, 287, 490
- Absorption cross section, 165, 490
- Absorption line bandwidth, 233
- Accidental BSCs, 522
- Acoustic intensity, 516
- Acoustic intensity vector, 511
- Acoustic wave transmission, 497
- Activation, 21
- Adiabatic modes, 132
- Adiabatic population transfer, 91
- Advanced Green's function, 373, 374
- AFM, 23
- Ag nanoshell, 455
- AHB model, 256
- Al layer, 250
- All-dielectric, 490
- Al<sub>2</sub>O<sub>3</sub>, 250
- Ampere-Maxwell law, 531
- Analytical model, 19
- Anapole, 481, 482, 492
- Anapole mode, 474
- Anechoic chamber, 230
- Angle-averaged electric field intensity, 456
- Angle-averaged intensities, 454
- Angle-scan ATR spectroscopy, 244
- Angular Hole Burning (AHB), 256
- Anharmonic, 116
- Anisotropic Fano resonant case, 75
- Anisotropic Fano resonant system, 74
- Anisotropic media, 386
- Anisotropic refractive indices, 256
- Anti-Bonding (AB) mode, 129, 332, 343
- Anti-bound state, 358
- Anticrossing, 133
- Anti-crossing behavior, 71
- Anti-Lorentzian line shape, 164
- Anti-phase coupling, 415
- Anti-phase oscillation, 223
- Anti-resonant state, 358, 361, 370, 373, 377, 378, 380, 381
- Antisymmetric, 320
- Antisymmetric currents, 143
- Antisymmetric dark mode, 226
- Antisymmetric Fano resonance, 45, 46
- Antisymmetric line shapes, 52
- Antisymmetric v-antennas, 226
- apertureless Scanning Near Field Optical Microscopy (aSNOM), 2
- Associated Legendre function, 449
- Asymmetric, 115, 222, 481
- Asymmetric components, 278
- Asymmetric Fano line shape, 464, 466
- Asymmetric Fano profile, 73
- Asymmetric Fano resonance, 81
- Asymmetric Hyperbolic Metamaterials (AHMs), 386
- Asymmetric line shape, 42, 67, 72, 157, 246, 473
- Asymmetric profile, 102, 404, 480
- Asymmetric scattering, 186
- Asymmetric spectral line shape, 58, 404
- Asymmetric transmission, 146, 149
- Asymmetric type design, 232
- Asymmetry, 224, 429, 559
- Asymmetry parameter, 68, 75, 81, 119, 404, 484
- At band topologies, 316
- ATR spectroscopy, 244

- Attenuated Total Reflection (ATR) spectra, 242, 244
- Attenuated transmission band, 234
- Aubry-Andr'e perturbation, 320
- Auger electron, 404
- Autler-Townes Splitting (ATS), 125
- Auto-ionization, 58
- Avoided crossing, 133
- Axion-like fields, 547
- Azobenzene, 252
- B**
- Babinet's principle, 230
- Background integral, 358
- Background scattering, 167, 168
- Backscattering, 211, 299, 478, 481
- Backscattering cancellation, 210
- Backward scattering, 289
- Backward scattering cross sections, 451
- Band folding, 427
- Bessel function, 433, 535
- Bias voltage, 146
- Bi-completeness, 268, 274, 275
- BIC trapped mode, 505
- Bi-orthogonal, 530
- Bi-orthogonality, 194
- Birefringence effect, 40
- Birefringent boundary effect, 41
- Birefringent material, 47
- Birefringent media, 33
- Birefringent mirrors, 41, 50
- Bloch mode, 385
- Bohr's model, 280
- Bloch's theorem, 390, 395
- Bloch wave number, 101
- Bonding (B) mode, 128, 332, 343
- Boundary conditions, 459
- Boundary-value-problem, 538
- Bound state, 358, 370, 373, 377
- Bound state in Continuum (BIC), 86, 275, 497, 522
- Bound states outside the continuum, 92
- Breit-Wigner, 85, 473
- Bright-dark mode interaction, 224
- Bright mode, 242, 412
- Bright or radiative modes, 220
- Bright oscillator, 116, 135
- Brillouin-Wigner-Feshbach projection operator method (BWF method), 262, 265
- Brillouin zone, 390, 391, 396
- Broad, 202, 206, 209
- Broad electric dipole mode, 465
- Broad mode, 205, 213
- Broken centro-symmetry, 23
- Bulk structures, 441
- C**
- Calderón operator, 189
- Capacitive (electric) coupling, 415
- Cartesian multipoles, 482
- Cavity-controlled chemistry, 552
- Center-symmetric multilayered spheres, 449
- Centro-symmetric, 13
- Charge displacement, 112
- Chiral, 33, 489, 490
- Chiral velocity of light, 38
- Chiral material, 49
- Chiral metamaterials, 48
- Chiral resonator, 50, 51
- Chiral resonator boundary, 40
- Chiral structures, 34
- Circular birefringence, 43
- Circular dichroic, 33
- Circular dichroism, 33, 36, 37, 490
- Circular polarisation, 489
- Circular polarizers, 49
- Class, 315
- Classical electrodynamics, 447, 460
- Classical oscillator, 106
- Coated sphere, 448, 468
- Coherence, 527
- Coherent absorption, 560
- Coherent absorption ellipse, 561
- Coherent perfect transparency, 561
- Coincidence probability, 95
- Collapse of Fano resonance, 509
- Collective oscillation of free electrons, 244
- Compact breathers, 324
- Compact discrete breather, 322–324, 326
- Compact Localized States (CLS), 314, 325
- Complementary  $z$  metasurface, 230
- Complete Lorenz-mie solution, 450
- Complex eigenvalue problem, 263, 273, 274
- Complex eigenvalues, 517
- Complex energy plane, 361, 370
- Complex Fano parameters, 381
- Complex phases, 506
- Complex spectral analysis, 280
- Complex spectral representation, 262
- Complex wave-number plane, 361, 370
- Complex-valued oscillator strength, 269, 280
- Comprehensive plasmon polarimetry, 59
- Comprehensive polarimetric platform, 65
- Conductive (connective) coupling, 415
- Constitutive relation, 533
- Constructive, 126

- Constructive/destructive interference, 221
- Continuous spectra, 360
- Continuous Wave (CW), 11
- Continuum state, 404
- Control light, 139
- Cooperativity, 566
- Core-level absorption, 280
- Core-shell sphere, 447, 458
- Coupled antennas, 130
- Coupled-mode method, 334
- Coupled Mode Theory (CMT), 34, 95, 426
- Coupled oscillator model, 106
- Coupled-Resonator Induced Transparency (CRIT), 333
- Coupled resonator model, 141
- Coupled resonators, 137
- Coupled system, 19
- Coupling, 8, 120
- Coupling coefficient, 35, 36, 41
- Coupling matrix elements, 501, 506, 518
- Critical coupling, 123, 551, 564
- Cross section, 21, 450, 453
- Cross-stitch, 316, 321
- Cross-stitch lattice, 312, 317, 321, 323–325
- $C_{6v}$  symmetry, 437
- Currents of acoustic intensity, 507, 522
- Cut wires, 232
- Cylindrical resonator, 499, 507
- Cylindrical scatterer, 162
- Cylindrical waves, 159
- Cytop, 244, 250
  
- D**
- Damping rates, 24
- Damping strength, 221
- Dark field microscope, 65, 78
- Dark mode, 6, 19, 220, 242, 412
- Dark oscillator, 135
- Dark state, 91
- Deceleration of the decay, 90
- Decomposition methods, 77
- Defects, 311
- Degeneracy, 314
- Degenerate Fano resonance, 351
- Degenerate perturbation theory, 435
- Degree of polarization, 60, 62
- Density of states, 9
- Depolarization, 61, 64
- Destructive interference, 126, 209, 313, 486, 505
- Determinant, 98
- 3D folding metamaterial, 403
- Diabatic, 128
- Diattenuating discrete mode, 76
- Diattenuation, 63, 79–81
- Dielectric nanoantenna, 287
- Dielectric nanoparticles, 185
- Dielectric nanostructures, 283, 285
- Dielectric nanowires, 288
- Dielectric oligomers, 288
- Differential decomposition, 67
- Diffraction channels, 441
- Dipolar, 116
- Dipole, 428
- Dipole approximation, 468
- Dipole emitter, 457, 464, 466
- Dipole-dipole interaction, 527
- Dipole-dipole interference, 451
- Dipole-like, 6
- Dipole moment, 226
- Dipole nanoantenna, 225
- Dipole orientation, 462
- Dipole scattering resonance, 454, 462
- Dipole-quadrupole interference, 453
- Dirac cones, 427
- Dirac  $\delta$ -functions
- Dirac-type Hamiltonian, 431
- Directional fano resonances, 186
- Directional scattering, 284, 290, 293, 296, 297
- Direct Laser Writing (DLW), 407
- Dirichlet-Neumann, 529
- Discrete bound state, 404
- Discrete breathers, 322
- Discrete eigenstates, 359, 376
- Discrete state, 113
- Disorder, 311, 318, 326
- Disordered systems, 552
- Disorder potential, 319
- Disperse Red 1 (DR1), 252
- Dispersion equation, 265, 266, 271
- Dispersion relation, 367, 368, 374, 385, 390, 395
- Dissipation, 566
- Dissipative system, 558
- Dolmen metamolecules, 222
- Double-helix resonances, 538
- Double-peaked, 564
- Doubly resonant meta-material, 154
- DR1-doped PMMA, 252
- Dressed bound state, 96
- Dressed mode, 223
- Drude model, 18, 385, 398
- 3D simulations, 19
- Dynamical reciprocity, 106
  
- E**
- Edge chiral magnetic, 547
- Edge wave function, 546

- Effective complex potential, 367
  - Effective hamiltonian, 225, 263, 265, 273, 364–367, 373, 513
  - Effective Medium Theory (EMT), 384, 387, 401
  - Effective non-Hermitian Hamiltonian, 499, 512, 517, 520
  - Effective permittivity, 387
  - Eigenfrequency, 36
  - Eigenfunctions, 193
  - Eigenlevels, 520
  - Eigenmode, 36, 143
  - Eigenvalue, 201
  - Eigen value calibration, 65
  - Eigenvalue problem, 189, 529
  - EIT effect, 137
  - EIT-like metamaterials, 138
  - Electric and magnetic modes, 290
  - Electric Dipole (ED), 202, 208, 474, 477
  - Electric dipole moment, 458
  - Electric dipole oscillation, 142, 145
  - Electric displacement current, 531
  - Electric-field enhancement, 351
  - Electric field intensity, 455
  - Electric Lorenz-Mie coefficient, 465
  - Electric modes, 194, 206
  - Electric multipoles, 479
  - Electric quadruple oscillation, 142
  - Electric Quadrupole (EQ), 202, 477
  - Electric scattering coefficient, 453
  - Electric susceptibility, 139
  - Electromagnetic Induced Transparency (EIT), 5, 42, 102, 106, 125, 137, 157, 164, 174, 180, 249, 332, 351
  - Electromagnetic retardation, 532
  - Electromagnetic scattering, 188
  - Electron Beam Lithography (EBL), 300
  - Electronic conductance, 357, 363
  - Electronic conduction, 373
  - Empirical Length (EL), 412
  - Enantiomeric, 232
  - Energy balance equation, 534
  - Energy conservation, 161
  - Energy eigenvalue problem, 545
  - Energy orthogonality relation, 546
  - Enhanced electric fields, 247
  - Enhanced Yellow Fluorescent (EYFP) molecules, 22
  - Enhancement, 11, 15, 26, 511
  - Enhancement Factor (EF), 17
  - Enhancement of electromagnetic field, 416
  - Entanglement, 4
  - Environmental degrees of freedom, 364
  - Equations of Motion (EOM), 8, 118
  - Evanescent, 72
  - Evanescent coupling, 90
  - Evanescent electromagnetic fields, 246
  - Evanescent mode, 384, 386, 387, 389–393, 396, 397, 399–401, 513, 515, 516, 519, 543
  - Evolution of resonant widths, 505
  - Exact solutions, 24
  - Exceptional point, 103, 267
  - Exceptional point in polarization space, 37
  - Excitation spectrum, 23
  - Expanded structure, 429, 430
  - Extended Coupled Oscillator (ECO), 128, 225
  - Extended Hilbert space, 261, 262, 265, 273, 280
  - External excitation, 197
  - Extinction, 286
  - Extraordinary Optical Transmission (EOT), 331, 410
- F**
- Fabry-Perot cavity, 300
  - Fabry-Perot modes, 395
  - Fabry-Perot resonance, 44, 92, 344, 384, 389, 396
  - Fano absorption profile, 261
  - Fano-Anderson model, 314
  - Fano asymmetric parameter, 163, 167, 453, 467
  - Fano asymmetry, 79, 358, 468, 376–378
  - Fano dip, 6, 456, 462, 463
  - Fano effect, 262, 445
  - Fano enhancement, 19
  - Fano frequency, 68
  - Fano interference, 92, 157, 162, 568
  - Fano interference effect, 180
  - Fano-like interference, 116
  - Fano line shape, 99, 133, 163, 169, 186, 205, 209, 214, 451, 486, 566
  - Fano parameter, 43, 46, 288, 378, 380, 381
  - Fano phase, 75, 77, 78, 80
  - Fano phase shift, 68, 81
  - Fano profile, 483, 292
  - Fano resonance, 19, 42, 85, 137, 142, 149, 172, 186, 221, 283, 284, 287, 289, 339, 383, 390, 393, 395, 397–401, 403, 446, 447, 465, 499, 558, 568
  - Fano resonance collapse, 544
  - Fano-resonant optical spin switching, 47
  - Fano resonant scattering spectra, 78
  - Fano's formula, 379
  - Fano-type absorption profile, 263, 277
  - Fano-type asymmetric spectral profile, 270
  - Fano-type asymmetry, 273



- Fano-type interference, 430
  - Fano-type lineshapes, 481
  - Faraday law, 531
  - Far-field, 12, 298, 426
  - Far-field interactions, 460
  - Far-field radiation, 463
  - Featureless continuum, 90
  - Ferrite disk, 538
  - Ferrite rod, 533
  - Feschbach, 122
  - Feshbach formalism, 363
  - Feshbach projection technique, 499
  - Feshbach resonances, 473
  - Field enhanced spectroscopy, 287, 292
  - Field enhancement, 138, 287
  - Figure of Merit (FOM), 259, 418
  - Filtering, 568
  - First higher mode, 226
  - First Kerker's condition, 289
  - Fisher-Lee relation, 375
  - Flat band lattice, 314, 318
  - Flat band networks, 311, 326
  - Floquet theory, 100
  - Flows of acoustic intensity, 511
  - Fluorescence, 258
  - Fluorescence quenching, 259
  - Fluorescence rate, 9
  - Focused-ion-beam, 403, 407
  - Forward scattering, 211, 289, 293, 294, 299, 478, 481
  - Forward scattering cross sections, 451
  - Fourier series, 431
  - Fourier transform, 21
  - Four-Wave Mixing (FWM), 3, 14, 25
  - Fractional decay, 93
  - Frequency conversion, 4, 137, 149
  - Frequency mixing, 150
  - Fresnel coefficients, 391
  - Friedrich-Wintgen mechanism, 505
  - Fröhlich condition, 202
  - Fundamental dipolar mode, 227
  - Fundamental magnetic dipole, 208
  - Fundamental resonance, 229
  - Fundamental waves, 150
  - FW/BW scattering, 294, 297, 298, 299
  - FW/BW scattering ratio, 299, 301, 302
- G**
- Generalized linear eigenvalue problem, 370
  - Goniometric setup, 230
  - Graphene, 394–398, 401
  - Green dyadic method, 298
  - Green function, 268, 504
  - Green's function, 363, 365, 366, 372, 373, 437
  - Green's tensor formalism, 459
  - Group delay, 144, 146
  - Group velocity, 137
  - Guided Mode Expansion (GME), 436
- H**
- Hamiltonian, 7
  - Harmonic generation, 490, 492
  - Heisenberg equation, 16
  - Helical coordinates, 537
  - Helical-mode resonances, 542
  - Helical MS modes, 538
  - Helical resonances, 527
  - Helicity density, 540
  - Helicity density parameter, 541
  - Helicity neutrality, 542
  - Hermitian, 434
  - Hexamer clusters, 433
  - Higher angular momentum, 179
  - Higher order electric dipole, 202
  - Higher order mode, 237
  - Higher-order multipolar modes, 170
  - High-index, 489
  - High-index dielectric nanostructures, 284, 286
  - High index dielectric particles, 474
  - High index dielectrics, 185
  - High-order mode, 412
  - High-Q-factor, 418
  - High Q Fano resonances, 242
  - High quality factors, 416
  - Homogeneous sphere, 201
  - Honeycomb lattice, 433
  - Horn antennas, 230
  - Hot spot, 6, 25, 27, 389, 400
  - Hybridization, 27, 127, 223, 247, 319
  - Hybridization mechanism, 223
  - Hyperbolic metamaterials, 383, 394
- I**
- Identical resonant elements, 232
  - Impurity, 317, 326
  - Impurity Fano-Anderson model, 263
  - In-coming waves, 374
  - Incommensurate, 321
  - Indefinite material, 45
  - Indefinite mirror, 51
  - Indistinguishable particles, 98
  - Inductive (magnetic) coupling, 415
  - Inherent Q-factor, 42
  - In-phase oscillation, 223
  - Instantaneous charges distribution, 228
  - Instantaneous currents, 233
  - Intensity enhancement factor, 461
  - Interacting modes, 226

- Interaction energy, 35
  - Interaction matrix, 225
  - Interference, 158, 168, 294, 456, 478
  - Interference between resonances, 507
  - Interference of resonances, 499, 522
  - Interference phenomena, 205
  - Interfering modes, 186
  - Intersubband polaritons, 556
  - Inter-tunneling amplitudes, 433
  - Intracell tunneling amplitudes, 433
  - Intrinsic losses, 121
  - Intrinsic Q-factor, 48
  - Ion-beam irradiation-induced folding technique, 408
  - Isofrequency contour, 387, 388, 390, 391, 393, 395, 396
  - Isotropic chiral material, 41
- J**
- Joint absorbance, 560, 562
  - Jones formalism, 60
  - Jones matrix, 61, 63
  - Jones-Mueller formalism, 74
  - Jones vector, 60
  - Joule heat, 362
- K**
- Kerker, 481
  - Kerker's conditions, 210, 289, 291, 295
  - Kerr-type nonlinearity, 105
  - Kretschman, 1
  - Kretschmann configuration, 243, 244
- L**
- Landauer formula, 357, 362
  - LC resonator, 556
  - Leaky Surface Bound Mode (LSBM), 332, 337
  - Left-eigenvector, 377
  - Lifetime, 26, 148
  - Lift-off process, 407
  - Light-based spintronics circuits, 47
  - Light-matter coupling, 564
  - Light-matter interaction, 284
  - Light-tunable Fano resonance, 252
  - Light tuning, 254, 255
  - Light-tuning effect, 255
  - Linear, 26
  - Linearly polarized eigenmodes, 39
  - Linear optical network, 94
  - Linear response, 5
  - Lineshape inheritance, 555
  - Local density of photonic states, 286
  - Localization, 23
  - Localization length, 319, 320
  - Localized solution, 325
  - Localized states, 318
  - Localized Surface Plasmon (LSP), 1, 284, 547
  - Long-range phase, 527
  - Lorentzian line shape, 164, 165, 452, 464, 467
  - Lorentzian profile, 270, 279
  - Lorentzian, 18, 120, 165, 555
  - Lorentz oscillator model, 262
  - Lorenz-Mie coefficients, 449, 450, 465
  - Lorenz-Mie scattering theory, 446
  - Lorenz-Mie theory, 445, 447, 448, 450, 452, 461, 468
  - Loss compensation, 150
  - Low losses, 285
  - Low-order mode, 412
- M**
- Macroscopic degeneracy, 315
  - Magnetic anapoles, 489
  - Magnetic component, 230
  - Magnetic coupling, 150
  - Magnetic current, 539
  - Magnetic-dipolar interactions, 528
  - Magnetic-Dipolar Modes (MDMs), 527
  - Magnetic-dipolar resonances, 547
  - Magnetic Dipole (MD), 277, 477
  - Magnetic dipole oscillation, 145
  - Magnetic displacement current, 531
  - Magnetic eigenmodes, 204
  - Magnetic field enhancement, 296
  - Magnetic LDOS, 286
  - Magnetic modes, 194, 206
  - Magnetic multipoles, 479
  - Magnetic nature, 230
  - Magnetic nonlinearity, 490
  - Magnetic octupole, 208
  - Magnetic quadrupole, 208
  - Magnetic resonances, 285
  - Magnetic-magnetic, 487
  - Magnetolectric (ME) fields, 529, 539
  - Magnetostatic wave function, 530
  - Magnetostatic-wave oscillations, 547
  - Magnonic oscillations, 532
  - Many-body system, 93
  - Markovian approximation, 89
  - Matching condition, 562
  - Material chirality, 48
  - Material independent modes, 187–189
  - Material loss, 48
  - 2×2 matrix method, 243
  - Maxwell's curl equations, 459
  - Maxwell's equations, 390
  - MDM bound states, 543
  - ME-energy flow, 541

- Membrane, 557
- Membrane function, 534, 535, 546
- Memory functions, 89
- Metal-dielectric multilayer, 242
- Metal-enhanced fluorescence, 259
- Metallic nanohole array, 331, 333
- Metal nanoparticles, 1
- Metamaterial, 154, 157, 383, 403
- Metamaterial mirror, 47, 51
- Metasurface, 427, 490
- Microcavity, 99
- Micro/nano resonators, 99
- Microwave, 230
- Microwave-field continuum, 543
- Mie coefficient, 211, 289, 294
- Mie resonance, 292, 460, 555
- Mie scattering coefficients, 292
- Mie solution, 475
- Mie theory, 200, 292, 293, 296, 298, 481
- Mirror symmetry, 71, 476
- Mobility edge, 321
- Mobility edge transitions, 322
- Mode amplitudes, 201
- Modes coupling, 135
- Modulation damping parameter, 122
- Modulation depth, 115
- Morphology-dependent resonances, 190
- Mueller matrix, 63, 64, 66, 78
- $\mu$ -scan ATR spectra, 250
- Multi-level Fano-Anderson model, 88
- Multimode interference, 186
- Multiple conversion paths, 25
- Multiple Fano Resonance Interference, 348
- Multiple resonance interference, 333
- Multipolar Contributions, 296
- Multipole moment, 445
- Multipoles, 212
- Multipole surface plasmon, 332, 346
  
- N**
- Nanoantennas, 285
- Nano-cubes, 290
- Nano-discs/-cylinders, 290
- Nanomechanics, 552
- Nano-optics, 284
- Nanosphere, 290, 453, 456
- Nano-spheroids, 290
- Nanostructures, 157
- Nanowire, 2, 283, 290, 293
- Narrow, 209
- Narrow electric dipole mode, 465
- Narrow modes, 187, 205, 206, 213
- Natural optical rotation, 38, 43, 47
- Near-degeneracy of resonances, 178
- Nearest-neighbor tight-binding approximation, 86
- Near field, 2, 208, 298
- Near-field coupling, 237
- Near-field interactions, 460
- Negative index, 406
- Negative permeability, 406
- Negative permittivity, 406
- Neumann functions, 449
- Non-analytic resonance states, 261, 273, 279, 280
- Non-analytic solution, 271
- Non-analytic states, 278
- Non-axisymmetric duct-cavity structure, 522
- Non-axisymmetric waveguide, 497, 498
- Non-coaxial waveguide, 507, 516
- Non centro-symmetric, 23
- Non-Hermitian, 226, 436
- Non-Hermitian chirality, 36
- Non-Hermitian effective Hamiltonian, 501
- Non-Hermitian materials, 43
- Non-Hermitian operator, 536
- Non-Hermitian photonic structures, 102
- Non-Hermitian resonant system, 37
- Non-Hermitian TCMT equation, 36
- Non-Hermiticity, 125
- Nonlinear, 326
- Nonlinear eigenvalue problem, 367, 369
- Nonlinear optical effects, 106
- Nonlinear response, 7, 10, 20
- Non-linear systems, 116
- Nonlinear terms, 312
- Nonlinearities, 311, 322, 326
- Non-magnetic materials, 449
- Non-orthogonal basis of eigenmodes, 226
- Non-orthogonality of the eigenmodes, 233
- Non-perturbative method, 278
- Nonradiating, 481, 486, 492
- Non-radiative, 428
- Non-radiative decay rates, 458, 461
- Non-radiative losses, 135
- Non-reciprocal transmission, 104
- Nonresonant, 568
- Normalization constant, 268, 269
- Normalized Fano lineshape, 454
- Norm of mode, 534
  
- O**
- Oblique incidence, 228
- Off-resonance field enhancement, 454
- Ohmic loss, 146, 463
- Oligomer, 486, 489, 490

- Oligomers clusters, 224
  - One-dimensional semiconductor superlattice, 264
  - Onsite perturbations, 317
  - Open channels, 501
  - Open photonic systems, 426
  - Optical absorption spectroscopy, 261
  - Optical activity, 489
  - Optical analog of EIT, 174
  - Optical antennas, 285
  - Optical dipole emitter, 458
  - Optical emitters, 446
  - Optical Fano resonances, 288
  - Optical isolator, 105, 106
  - Optical Kerr effect, 48
  - Optical memory, 137
  - Optical nanoantennas, 474
  - Optical non-reciprocity, 105
  - Optical-quantum analogy, 87
  - Optical SAM, 52
  - Optical spintronics, 50
  - Opto-mechanical, 552
  - Orbital angular momenta, 539
  - Orbital rotation, 539
  - Orthogonal, 189
  - Out-going wave, 359, 374
  - Overlap integral, 12, 438
  - Overlapping integrals, 501
  - Overlapping orders, 294
- P**
- Parametric amplification, 150
  - Parametric down-conversion, 96
  - Parametric gain, 152
  - Parametric process, 151
  - Parity, 476
  - Parity-Time (PT) symmetry, 103
  - Partial wave scattering, 491
  - Particle statistics, 93
  - Patch antenna, 556
  - Path interference, 7
  - Pauli exclusion principle, 96
  - PC slab, 437
  - Perfect Electric Conductor (PEC), 483, 484
  - Permanent, 98
  - Permeability tensor, 535
  - Perturbative electromagnetic theory, 436
  - Phase delay, 126
  - Phase diagram, 566
  - Phase difference, 430, 514, 516
  - Phase distribution, 148
  - Phase interference, 44
  - Phase-matched resonance, 37
  - Phase of the background scattering, 163
  - Phase shift, 484
  - PhC slab, 436, 439
  - Phononic, 552
  - Photonic, 34
  - Photonic crystals, 404
  - Photonic crystal slab, 556
  - Photonic crystal waveguides, 92
  - Photonic resonances, 202
  - Photonic simulator, 87
  - Photonic structures, 85
  - Piston-like hollow-stem waveguides, 499, 522
  - Planar Metal Holes (MHs), 410
  - Planar multilayer structures, 242
  - Planar Waveguide (PWG) mode, 242
  - Plane wave, 197, 207
  - Plane wave expansion, 431
  - Plasmonic, 1, 58, 284–286, 288
  - Plasmonic assembly, 225
  - Plasmonic cloaking, 463
  - Plasmonic eigenmodes, 220
  - Plasmonic metasurfaces, 220
  - Plasmonic nanoshell, 445, 454, 457, 464
  - Plasmonic oligomers, 73, 222
  - Plasmonic oscillations, 532
  - Plasmonic sensing, 58
  - Plasmonic systems, 404
  - Plasmon lifetime, 9
  - Plasmon mode, 7
  - Plasmon resonances, 202
  - Plasmon spectrum, 19
  - Plexcitonic, 552
  - PMMA hybridization, 247
  - PMMA waveguide, 246, 248
  - Point spectra, 358, 359
  - Polar decomposition, 67
  - Polaritronics, 552
  - Polarization, 18, 59
  - Polarization algebra, 59, 60
  - Polarization field, 112
  - Polarization mode, 35
  - Polarization sensitive, 255
  - Polarization state, 80, 81
  - Polarization State Analyser (PSA), 66
  - Polarization State Generator (PSG), 66
  - Polarization-angle-dependency, 49
  - Polarization-entangled photons, 94
  - Poles, 554
  - Poly(methyl methacrylate) (PMMA), 250
  - Polynomial, 211
  - Population trapping, 88, 90
  - Positive and negative helicity density, 541
  - Potentials, 326
  - Power-flow vortices, 548
  - Power series, 193

- Poynting vector field, 455  
 Poynting vectors, 540  
 Primitive or diabatic plasmon modes, 223  
 Printed circuit board, 230  
 Probability conservation, 362  
 Probe beam, 253  
 Processing, 34  
 Propagating channel, 502, 520  
 Propagation of waves, 503  
 Pseudo-electric field, 547  
 Pseudoscalar parameter, 541  
 Pseudo-spin, 426  
 $PT$ -invariance, 538  
 $PT$ -symmetric Fano-Anderson model, 104  
 Pump beam, 253  
 Pump laser, 15  
 Pump-probe ATR experiments, 253  
 Pump waves, 153  
 Purcell effect, 8, 446, 457, 464, 469, 551  
 Purcell factor, 461, 465, 468  
 PWG modes, 244, 246–248
- Q**
- Q factor, 251, 479  
 Quadratic eigenvalue problem, 367, 368  
 Quadramer, 487  
 Quadrupolar, 116  
 Quadrupole, 6, 428  
 Quadrupole resonance, 462  
 Quality factor, 141, 231  
 Quantized vortices, 527  
 Quantum Dots (QDs), 8, 90  
 Quantum Emitters (QEs), 3  
 Quantum interference, 96, 262, 280  
 Quantum jump, 280  
 Quantum mechanical decay, 88  
 Quantum wire, 86  
 Quasi-2D ferrite-disk particle, 544  
 Quasi normal modes, 190  
 Quasiperiodic, 326  
 Quasiperiodic potentials, 312  
 Quasistatic-resonance, 532  
 Quenching, 9
- R**
- Rabi frequency, 564  
 Rabi oscillation, 97, 139  
 Rabi splitting, 132  
 Radiation efficiency, 461, 464  
 Radiation loss, 141, 146  
 Radiation pattern, 199, 211  
 Radiation Q-factor, 40  
 Radiative, 428  
 Radiative continuum, 113  
 Radiative damping, 111  
 Radiative decay rate, 458, 460, 466  
 Radiative losses, 189, 231, 439  
 Radiative mode, 141  
 Radiative strengths, 224  
 Radiofrequency, 564  
 Raman scattering, 416  
 Raman signals, 258  
 Rational function, 211  
 Rayleigh anomaly, 70, 72, 332  
 Rayleigh frequency, 342, 346  
 Rayleigh scattering, 451, 479, 542  
 Rectangular Nanowires, 300  
 Reflectance spectra, 430  
 Reflection, 100  
 Reflection and transmission coefficients, 230  
 Reflection matrix, 159, 162  
 Refractive index, 416  
 Refractive index sensitivity, 418  
 Regime of weak coupling, 504  
 Repelling currents, 415  
 Resolvent expansion, 365, 366  
 Resonance, 158, 201, 562  
 Resonance and anti-resonance states, The, 266, 274  
 Resonance formula, 117  
 Resonance frequency shift, 119  
 Resonance quality factor, 236  
 Resonance state, 262  
 Resonant anomaly, 70, 72  
 Resonant frequencies, 206  
 Resonant-modal decay times, 40  
 Resonant mode, 208, 287  
 Resonant state, 358, 361, 370, 373, 377, 378, 380, 381  
 Resonant-state expansion, 358, 372, 376  
 Resonant systems, 551  
 Resonant widths, 501  
 Retardance, 64, 79–81  
 Retardation, 11, 27  
 Retarded Green's function, 373, 374  
 Revival probabilities, 98  
 Riemann sheet, 266, 275  
 Right- and left-eigenvalue problems, 265  
 Right-eigenvector, 377  
 Ring-disk nanocavities, 223  
 Rotating wave approximation, 268  
 Rotational symmetry, 486  
 Rotation angle, 507, 518, 519
- S**
- Scalar spherical harmonics, 475

- Scalar wave function, 528
- Scalar-wave membrane function, 545
- Scattered electric field, 448, 459
- Scattered field, 197
- Scattered power, 186
- Scattering, 157, 286, 289, 313, 323
- Scattering and absorption cross sections, 157, 163
- Scattering cancellation, 484
- Scattering coefficients, 483
- Scattering cross section, 199, 476, 479
- Scattering dip, 209
- Scattering directionality, 292
- Scattering efficiency, 199, 207
- Scattering matrix, 94, 553
- Scattering spectra, 224, 301
- Scattering wave function, 511
- Schrödinger equation, 546
- Screwiness of the electric field, 540
- Second Harmonic Generation (SHG), 3, 12
- Second harmonic waves, 150
- Second Kerker's condition, 289
- Second-quantized scheme, 12
- Second Riemann sheet, 267, 361, 370
- Selection rules, 12
- Self-adjointness of operator, 535, 545
- Self-energy, 274, 365, 366, 374
- Self-oscillation, 35
- Semiconductor, 557
- Semi-infinite one-dimensional semiconductor, 273
- Sensing applications, 220
- SERS detection, 418
- SF11, 244, 250
- Short-circuit effect, 342
- Shrunken structure, 429, 430
- Si pillars, 430
- Siegert boundary condition, 359, 367
- Silent enhancement, 23
- Silicon, 205
- Silicon nanowire, 294, 296, 297
- Silver, 205
- Silver-Müller conditions, 189
- Simulated spectra, 412
- Single-channel limit, 177
- Single impurities, 312
- Single-peaked, 566
- SiO<sub>2</sub>, 250
- Skin depth, 284
- S-matrix, 359, 504
- Sound hard cylindrical waveguide, 500
- Sound transmission, 523
- Spacing, 15
- Spasers, 3
- Spatial Coupled-Mode (SCM) method, 333, 334
- Spatial divergence, 362
- Spatially “rotated” coordinates, 38
- Spectral interference”, 42
- Spectral bands, 315
- Spectral theory, 187, 191
- Spectral width, 18
- Spectrum, 18
- Sphere, 191
- Spherical Bessel, 449
- Spherical wave functions, 448
- Spin Angular Momentum (SAM), 34
- Spin Chern number, 428, 431
- Spin-controlled, 34
- Spin-density Fano parameter, 52
- Spin-dependent Fano resonance, 43, 44, 50, 52
- Spin-dependent Fano-resonant system, 49
- Spin-dependent Fano spectral asymmetry, 42
- Spin-dependent phase information, 44
- Spin eigenmode, 37
- Spinning currents, 516
- Spinor representation, 40
- Spin rotation, 539
- Spin switching, 46, 48
- Split Ring Resonators (SRRs), 6, 143, 222, 404
- Spontaneous decay rates, 462
- Spontaneous emission, 394, 457
- Spontaneous-emission rate, 446, 447, 457
- Spoof surface plasmon, 332, 343, 345
- SPP mode, 244, 246–248
- SPP molecule, 343
- SPR sensors, 259
- Steady-state, 8, 15
- Steep profiles, 416
- Stokes-Mueller formalism, 60, 61
- Stokes vector, 61, 62, 79
- Storage and retrieval of electromagnetic waves, 137, 143, 147
- Storage time, 140, 147
- Stress-driven assembly, 406
- Strong coupling, 235, 551
- Strong critical coupling, 565
- Structured continuum, 90
- Sub-radiant, 69, 131
- Sub-radiant mode, 73, 166, 169, 171, 173, 175
- Subradiant pasmonic mode, 220
- Subwavelength, 479, 486
- Subwavelength dimensions, 284
- Subwavelength scale, 457
- Subwavelength sizes, 528
- Superconductors, 425
- Superfluids, 425
- Super-radiant, 69, 223

- Super-radiant mode, 73, 166, 169, 171, 173, 175
- Superradiant pasmonic mode, 220
- Superscattering, 158, 177–180
- Suppression, 11, 15, 26
- Surface Enhanced Raman Scattering (SERS), 3, 10, 14, 23
- Surface mode, 92
- Surface plasmon molecule, 332
- Surface plasmons, 1, 529
- Surface Plasmon Polariton (SPP), 2, 242, 284, 331, 333
- Surface Plasmon Resonance (SPR), 2
- Susceptibility tensor, 539
- Symmetric, 320
- Symmetric currents, 143
- Symmetric Lorentzian, 271
- Symmetric Lorentzian line shapes, 466
- Symmetry breaking, 223
- Symmetry matching, 237
- Symmetry protected trapped modes, 497
  
- T**
- TB-based CMT, 439
- TE and TM, 297
- TE modes, 193
- TE polarization, 299, 302
- Temporal Coupled Mode (TCM) method, 333, 337
- Temporal Coupled Mode Theory (TCMT), 33, 35, 157, 158, 161, 166, 180, 225
- Temporal decay, 362
- Temporal interpretation of the Fano dynamics, 45
- Temporally dispersive media, 531
- Third Harmonic Generation (THG), 3, 13
- Threefold degeneracy, 515
- Three-level system, 138
- Tight-binding model, 273, 358, 363, 433
- Time evolution, 17
- Time-reversal symmetry, 161, 361
- Time-reversal symmetry breaking, 541
- Time-varying, 154
- TM<sub>0</sub>, 246
- TM<sub>1</sub>, 246
- TM<sub>2</sub>, 246
- TM guided modes, 436
- TM illumination, 298
- TM modes, 193
- TM polarization, 302, 431
- Topological characteristics, 426
- Topological charges, 543
- Topological insulators, 425
- Topological photonic systems, 425
- Topological properties, 544
- Toroidal dipole, 474, 482
- Total decay rate, 459
- Transcis photoisomerization, 252
- Transformation matrix, 40
- Translationally invariant tight binding lattices, 314
- Transmission probability, 357, 363, 373, 374, 376–378, 380, 381
- Transmission spectra, 71
- Transmission, 100, 513
- Transmittance, 499, 509, 516–518
- Transmittance of sound waves, 502
- Transmittance spectra, 429
- Transparency window, 139
- Trapped mode, 141, 498, 522
- Trapping of acoustic waves, 499
- Triangular lattice, 433
- Truncated effective Hamiltonian, 514, 516
- T-shaped quantum-dot model, 363
- Tunable metamaterials, 137, 154
- Tuning of Fano asymmetry, 74
- Twisted acoustic pressure field, 512
- Twisted evanescent fields, 540
- Twisted-wave modes, 536
- Twisting of the BIC, 507
- Two-channel approximation, 102
- Twofold degeneracy, 516
- Two-level Fano-Anderson model, 95
- Two-Photon Absorption (TPA), 23, 407
- Two-port system, 558
- Two-step process, 167
  
- U**
- Ultra-narrow resonance, 102
- Unconventional Fano resonance, 451, 453, 468
- Uncorrelated disorder, 312
- Unidirectional, 481
- Unidirectional scattering, 283
- Unitary transformation, 434, 438
- Universal absorption lineshape, 562
- Universal lineshape, 558
- Unperturbed hermitian hamiltonian, 226
- Unpolarized, 59
- Upper limit for a single channel, 165
- UV/E-beam lithography, 405
- UV plasmonics, 251
  
- V**
- Van Hove singularity, 265
- Varactor diode, 146
- Variable capacitors, 138, 145
- Vector cylindrical harmonics, 293
- Vector Helmholtz equation, 448

Vector spherical harmonics, [475](#), [476](#), [478](#)  
Vector spherical wave functions, [191](#)  
Vertical SRRs (VSRRs), [410](#)  
Virtual bound state, [266](#), [267](#), [275](#)  
Vortex modes, [536](#)

**W**

Waldron's helical coordinate, [537](#)  
Walker equation, [537](#), [545](#)  
Wave faucet, [518](#), [522](#)  
Waveguide, [259](#)  
Waveguide lattice, [86](#)  
Waveguide mode, [341](#)  
Waveguide-plasmon polariton, [69](#)  
Waveguide rotation, [497](#), [507](#), [513](#)  
Waveguiding Plasmonic Crystals (WPC), [69](#)  
Wave number representation, [264](#)

Weak coupling regime, [461](#), [564](#)  
Weak critical coupling, [565](#)  
Weak hybridization, [21](#)  
Whispering gallery modes, [190](#)  
Woods anomaly, [68](#), [70](#), [331](#)

**Y**

Y-polarization, [233](#)

**Z**

Zero-backward scattering, [290](#)  
Zeroes, [555](#)  
Zero net electric dipolar momentum, [237](#)  
Zero scattering, [482](#)  
Z-shaped resonator, [228](#)